Field Testing of Integral Abutments

Sponsored by
the Iowa Highway Research Board
(IHRB Project HR-399)
and
the Iowa Department of Transportation
(CTRE Project 97-03)

Center for Transportation
Research and Education

Department of Civil, Construction and Environmental Engineering

Iowa State University

Final Report • June 2005

Disclaimer Notice

The opinions, findings, and conclusions expressed in this publication are those of the authors and not necessarily those of the Iowa Department of Transportation or the Iowa Highway Research Board. The sponsors assume no liability for the contents or use of the information contained in this document. This report does not constitute a standard, specification, or regulation. The sponsors do not endorse products or manufacturers.

About CTRE/ISU

The mission of the Center for Transportation Research and Education (CTRE) at Iowa State University is to develop and implement innovative methods, materials, and technologies for improving transportation efficiency, safety, and reliability while improving the learning environment of students, faculty, and staff in transportation-related fields.

Technical Report Documentation Page

1. Report No. HR-399	**2. Government Accession No.**	**3. Recipient's Catalog No.**
4. Title and Subtitle Field Testing of Integral Abutments		**5. Report Date** June 2005 **6. Performing Organization Code**
7. Author(s) Robert E. Abendroth and Lowell F. Greimann		**8. Performing Organization Report No.**
9. Performing Organization Name and Address Center for Transportation Research and Education Iowa State University 2901 South Loop Drive, Suite 3100 Ames, IA 50010-8634		**10. Work Unit No. (TRAIS)** **11. Contract or Grant No.**
12. Sponsoring Organization Name and Address Iowa Department of Transportation 800 Lincoln Way Ames, IA 50010		**13. Type of Report and Period Covered** Final Report February 1997 to June 2005 **14. Sponsoring Agency Code**
15. Supplementary Notes		

16. Abstract

Integral-abutment bridges, which do not contain expansion joints, provide a very attractive alternative to the more traditional, stub-abutment bridges that have expansion joints. Jointless bridges have lower construction and maintenance costs than those costs for bridges with expansion joints. The integral connection between the abutment, bridge girders, and piles introduces additional strains and corresponding stresses in the bridge members as a result of thermal expansion and contraction of the bridge superstructure. Experience of bridge engineers from many state departments of transportation who design and construct integral-abutment bridges indicate that these bridges are performing well.

The objectives of this research program were to evaluate the state-of-art for the design of prestressed-concrete (PC), integral-abutment bridges; to validate the assumptions that are incorporated in the current-design procedures for these types of bridges when they are subjected to thermal-loading conditions; and, as appropriate, to revise and improve the current-design procedures for this type of a bridge, as that design relates to the thermally-induced displacements of the abutments and the thermally-induced forces in the abutments and abutment piles.

Two, skewed, PC girder, integral-abutment bridges in the State of Iowa were instrumented over a two-year period to measure structural behavior. Longitudinal and transverse displacements and rotation of the integral abutments, strains in the steel piles and in the PC girders, and temperature distributions were recorded throughout the monitoring period for both bridges. The coefficient of thermal expansion and contraction for the concrete in core specimens that were taken from 20 bridge decks and from several PC girders was experimentally measured at the 100%-dry and 100%-saturated conditions. The longitudinal displacements of the integral abutments correlated well with the recorded change in the bridge temperature. Total, longitudinal, pile strains exceeded the minimum, specified, yield strain of the steel for both bridges. Longitudinal strains in the PC girders were well within acceptable limits. The experimental data were used to calibrate and refine finite-element models of both bridges. Discrepancies were not fully explained for the differences between the predicted and measured, thermal expansion of the bridge and vertical rotations of the integral abutments.

Recommendations for the design of integral-abutment bridges with PC girders and steel piles were advanced, including equations and procedures for the design-temperature range, vertical-temperature gradients in the bridge superstructure, longitudinal displacements of the integral abutments, concrete creep and concrete-shrinkage effects, and coefficients of thermal expansion and contraction for the concrete. Software was presented to estimate the transverse movement of skewed, integral-abutment bridges. Approximate methods were outlined to analyze the abutment pile cap and backwall and to check their designs. Ductility demands placed on the abutment piles during thermal movements were compared to the ductility capacity for the piles when they are subjected to biaxial, cyclic, and reversed loading conditions. Some of the design recommendations were illustrated by examples.

17. Key Words abutments, analysis, bridge, design, ductility, field-tests, finite-element, integral, laboratory-tests, piles, strength, temperature		**18. Distribution Statement** No restrictions.	
19. Security Classification (of this report) Unclassified.	**20. Security Classification (of this page)** Unclassified.	**21. No. of Pages**	**22. Price** NA

FIELD TESTING OF INTEGRAL ABUTMENTS

Iowa DOT Project HR-399

Co-Principal Investigators
Robert E. Abendroth
Associate Professor of Civil Engineering
and
Lowell F. Greimann
Chair and Professor of Civil Engineering
Iowa State University

Research Assistants
Kuok-Hung Lim
Matthew E. Thomas
Brad H. Sayers
Camden L. Kirkpatrick
Wei Chei Ng

Authors
Robert E. Abendroth and Lowell F. Greimann

Preparation of this report was financed in part
through funds provided by the Iowa Department of Transportation
through its research management agreement with the
Center for Transportation Research and Education.

Center for Transportation Research and Education
Iowa State University
ISU Research Park
2901 South Loop Drive, Suite 3100
Ames, IA 50010-8634
Phone: 515-294-8103
Fax: 515-294-0467
www.ctre.iastate.edu

Final Report • June 2005

TABLE OF CONTENTS

LIST OF FIGURES ix

LIST OF TABLES xxiii

ACKNOWLEDGEMENTS xxvii

EXECUTIVE SUMMARY xxix

NOMENCLATURE xxxvii

1. INTRODUCTION 1-1
    1.1. Background 1-1
    1.2. Research scope and objectives 1-3
    1.3. Report organization 1-4

2. LITERATURE REVIEW 2-1
    2.1. Performance of joint-less bridges 2-1
    2.2. Bridge field studies 2-12
    2.3. Pile tests 2-19
        2.3.1. Field tests 2-19
        2.3.2. Laboratory tests 2-20
    2.4. Analytical studies 2-22
        2.4.1. Thermal analyses 2-22
        2.4.2. Integral-bridge analytical studies 2-24
    2.5. Integral-abutment design models 2-31
        2.5.1. Bridge temperature 2-31
        2.5.2. Coefficient of thermal expansion and contraction for concrete 2-33
        2.5.3. Bridge displacement 2-34
        2.5.4. Pile design 2-36
        2.5.5. Abutment backfill 2-41
        2.5.6. Approach slabs 2-42
    2.6. Flange local buckling of I-shaped beams 2-44

3. BRIDGE MONITORING PROGRAM 3-1
    3.1. Overview 3-1
        3.1.1. Bridge selection criterion 3-1
        3.1.2. Bridge descriptions 3-2
        3.1.3. Instrumentation packages 3-4
    3.2. Displacement transducers 3-4
        3.2.1. Guthrie County Bridge 3-5
        3.2.2. Story County Bridge 3-7

3.2.3. Transducers for absolute displacement measurements 3-7
3.2.4. Transducers for relative displacement measurements 3-9
3.3. Strain gages 3-10
3.3.1. Guthrie County Bridge 3-12
3.3.2. Story County Bridge 3-12
3.3.3. Strain gage installation procedure 3-13
3.4. Thermocouples 3-15
3.4.1. Guthrie County Bridge 3-15
3.4.2. Story County Bridge 3-16
3.5. Data-acquisition procedure 3-17
3.5.1. Data-acquisition equipment 3-17
3.5.2. Data-acquisition interval and initial-data reduction 3-18
3.6. Temperature corrections for instrumentation devices 3-20
3.6.1. Corrections for displacement transducers 3-20
3.6.2. Corrections for temperature-compensated, electrical-resistance, strain gages 3-21
3.6.3. Corrections for uncompensated-temperature, electrical-resistance, strain gages 3-23
3.6.4. Corrections for vibrating-wire strain gages 3-25
3.6.5. Corrections for tiltmeters 3-25

4. EXPERIMENTAL RESULTS 4-1
4.1. Experimental data filtering 4-1
4.1.1. Thermocouples 4-1
4.1.2. Displacement transducers 4-2
4.1.3. Pile strain gages 4-4
4.1.4. Girder strain gages 4-9
4.2. Bridge temperatures 4-10
4.2.1. Average, bridge temperatures 4-10
4.2.2. Vertical-temperature gradients 4-12
4.2.3. Transverse-temperature gradients 4-14
4.2.4. Longitudinal-temperature gradients 4-16
4.2.5. Pile temperatures 4-16
4.3. Bridge displacements 4-17
4.3.1. Abutment longitudinal displacements and changes in bridge length 4-17
4.3.2. Abutment rotations in a horizontal plane 4-21
4.3.3. Abutment rotations in a vertical plane 4-22
4.3.4. Abutment transverse displacements 4-25
4.3.5. Relative displacements at the bridge piers 4-26
4.3.6. Relative rotations at the top of an abutment pile 4-27
4.3.7. Relative displacements at the ends of PC girders 4-29
4.4. Bridge member strains 4-29
4.4.1. Pile strains 4-29
4.4.2. Girder strains 4-35

5. FINITE ELEMENT MODELS 5-1
5.1. Structural models 5-1
5.2. Pile-to-soil interaction 5-5
5.3. Abutment backfill models 5-9
5.4. Applied temperature distributions 5-13
5.4.1. Spatial distributions 5-13
5.4.2. Time variations 5-15

6. ANALYTICAL STUDY AND INTERPRETATION OF EXPERIMENTAL RESULTS FOR THE GUTHRIE COUNTY BRIDGE 6-1
6.1. Bridge displacements 6-1
6.1.1. Abutment longitudinal displacements and changes in bridge length 6-3
6.1.2. Abutment transverse displacements 6-6
6.1.3. Abutment rotations in a vertical plane 6-8
6.1.4. Relative displacements at the piers 6-12
6.1.5. Relative rotations at the top of an abutment pile 6-13
6.1.6. Relative displacements and rotations at the ends of the PC girders 6-13
6.2. Pile strains 6-13
6.2.1. Pile flexural-bending strains 6-13
6.2.2. Pile axial strains 6-19
6.3. Girder strains 6-20

7. ANALYTICAL STUDY AND INTERPRETATION OF EXPERIMENTAL RESULTS FOR THE STORY COUNTY BRIDGE 7-1
7.1. Bridge displacements 7-1
7.1.1. Abutment longitudinal displacements and changes in bridge length 7-1
7.1.2. Abutment transverse displacements 7-5
7.1.3. Abutment rotations in a vertical plane 7-6
7.1.4. Relative displacements at the piers 7-7
7.1.5. Relative rotations at the top of an abutment pile 7-8
7.2. Pile strains 7-9
7.2.1. Pile flexural-bending strains 7-9
7.2.2. Pile axial strains 7-14
7.3. Girder strains 7-15

8. INTEGRAL-ABUTMENT DESIGN PROCEDURES 8-1
8.1. AASHTO load cases 8-1
8.2. Bridge temperatures 8-4
8.2.1. Average, bridge temperature 8-4
8.2.2. Vertical-temperature gradient 8-7
8.3. Coefficient of thermal expansion and contraction 8-9
8.4. Creep and shrinkage 8-12
8.4.1. Concrete creep 8-13
8.4.2. Concrete shrinkage 8-15
8.4.3. Soil creep 8-16
8.4.4. Combined effects of concrete creep and shrinkage and soil creep 8-17

8.5. Equivalent cantilever length for piles 8-19
8.6. Bridge superstructure displacements 8-23
8.6.1. Longitudinal displacement of an integral abutment 8-24
8.6.2. Transverse displacement of an integral abutment for a skewed bridge. 8-31
8.6.2.1. Simple model..... 8-33
8.6.2.2. Refined model 8-35
8.6.2.3. Single parameters studies 8-38
8.6.2.3.1. Bridge length and width 8-40
8.6.2.3.2. Abutment height 8-40
8.6.2.3.3. Wingwall-embankment height and wingwall length 8-41
8.6.2.3.4. Number of abutment backwall and wingwall piles 8-41
8.6.2.3.5. Equivalent-cantilever length of a pile 8-41
8.6.2.3.6. Properties of the granular soil behind the abutment 8-42
8.6.2.4. Cross-parameters study 8-42
8.6.2.5. Summary of parameter studies 8-42
8.6.2.6. Upper-bound for transverse displacement 8-44
8.7. Integral-abutment pile displacements 8-47
8.7.1. Longitudinal displacements 8-48
8.7.2. Transverse displacements 8-52
8.8. Abutment design..... 8-52
8.8.1. Loads on an integral abutment..... 8-52
8.8.2. Analytical methods 8-60
8.8.2.1. Pile and girder member-end forces and soil pressures by Analysis Method 1 8-61
8.8.2.2. Pile and girder member-end forces and soil pressures by Analysis Method 2 8-69
8.8.2.3. Internal forces for an abutment..... 8-74
8.8.2.4. Alternate formulation for the internal forces for an abutment..... 8-80
8.8.2.5. Member-load, shear-force, bending moment, and torsional-moment diagrams 8-83
8.8.3. Abutment sidewall and wingwall forces on a backwall 8-83
8.8.4. Design strengths for biaxial bending and biaxial shear plus torsion 8-114
8.8.4.1. Abutment backwall and backwall-pile cap 8-118
8.8.4.2. Abutment wingwall, sidewall, and sidewall-pile cap..... 8-122
8.8.5. Other design strengths 8-125
8.8.5.1. Backwall-to-pile-cap connection 8-126
8.8.5.2. Pile-to-pile-cap connection 8-128
8.8.5.3. Girder-to-backwall connection 8-135
8.9. Pile design 8-145
8.9.1. Strength-limit-state for combined axial compression and bending 8-146
8.9.2. Limit state for pile ductility 8-149
8.9.2.1. Inelastic-rotation capacity for a compact, simply-supported beam 8-149
8.9.2.2. Moment reversal effects on inelastic-rotation capacity..... 8-152
8.9.2.3. Flange local-buckling effects on inelastic-rotation capacity..... 8-154
8.9.2.4. Inelastic-rotation capacity of a fixed-head pile 8-157

8.9.2.5. Inelastic-rotation capacity at different temperature phases 8-159
8.9.2.6. Biaxial-bending effects on inelastic-rotation capacity 8-161
8.9.2.7. Inelastic-rotation demand for a fixed-end beam 8-162
8.9.2.8. Inelastic-rotation demand for uniaxial bending of a fixed-head pile 8-163
8.9.2.9. Inelastic-rotation demand for biaxial bending of a fixed-head pile 8-167
8.9.2.10. Displacement-ductility limit state for uniaxial bending of fixed-head piles 8-168
8.9.2.11. Displacement-ductility limit state for biaxial bending of fixed-head piles 8-170
8.9.3. Capacity to transfer load from a pile to the soil strata..... 8-172
8.10. Maximum bridge length..... 8-173
8.10.1. Non-skewed bridge 8-173
8.10.2. Skewed bridge 8-175
8.11. Pile orientation 8-177

9. DESIGN EXAMPLES..... 9-1
9.1. Average bridge temperature 9-2
9.2. Alpha coefficient for concrete..... 9-2
9.2.1. Bridge deck 9-3
9.2.2. Bridge girders 9-5
9.2.3. Bridge superstructure 9-5
9.3. Equivalent-cantilever length 9-7
9.4. Abutment longitudinal displacements..... 9-11
9.5. Abutment transverse displacements 9-14
9.6. Abutment design 9-15
9.6.1. Backwall-pile-cap design..... 9-15
9.6.2. Composite backwall and backwall-pile-cap design 9-24
9.6.3. Connections 9-36
9.6.3.1. Backwall-to-pile-cap connection..... 9-37
9.6.3.2. Pile-to-pile-cap connection 9-41
9.6.3.3. Girder-to-backwall connection..... 9-47
9.7. Pile design 9-55
9.7.1. Strength limit state..... 9-55
9.7.2. Pile ductility..... 9-58
9.8. Maximum bridge length..... 9-64

10. CLOSING REMARKS 10-1
10.1. Summary..... 10-1
10.2. Conclusions 10-5
10.3. Design recommendations 10-10
10.3.1. Expansion and contraction of a bridge superstructure 10-10
10.3.2. Abutment-pile cap 10-12
10.3.3. Composite backwall and pile cap..... 10-13
10.3.4. Abutment-backwall piles 10-15

10.3.5. Abutment-backwall-to-pile-cap connection 10-17
10.3.6. Pile-to-pile-cap connection 10-18
10.3.7. Girder-to-backwall connection 10-19
10.4. Recommendations for further study 10-20

11. REFERENCES 11-1

APPENDIX A. ALPHA-COEFFICIENT STUDY A-1

APPENDIX B. TRANSMOVE SOFTWARE B-1
B.1. Force equilibrium for an integral abutment B-1
B.2. Displacement and force expressions B-4
B.3. Program installation B-14
B.4. Program interface B-14
B.5. Program algorithm B-15
B.6. Program limitations B-17
B.7. Program execution B-20

LIST OF FIGURES

Figure 1.1. Bridge types 1-6

Figure 1.2. Integral-abutment plan views 1-7

Figure 1.3. Integral-abutment side views 1-8

Figure 3.1. Displacement transducer locations at the Guthrie County Bridge 3-27

Figure 3.2. Displacement transducer locations at the Story County Bridge 3-28

Figure 3.3. Benchmark-post installation 3-29

Figure 3.4. Pier-connection details 3-30

Figure 3.5. Displacement transducer at a pier cap 3-30

Figure 3.6. Displacement transducers at an abutment backwall 3-31

Figure 3.7. Displacement transducers at the bottom of an abutment-pile cap 3-32

Figure 3.8. Strain gages on an HP-shaped pile 3-33

Figure 3.9. Strain-gage locations for the piles at the Guthrie County Bridge 3-34

Figure 3.10. Strain-gage locations for the PC girders and a RC pile cap at the Guthrie County Bridge 3-35

Figure 3.11. Strain-gage locations for the piles at the Story County Bridge 3-36

Figure 3.12. Strain-gage locations for the PC girders and a RC pile cap at the Story County Bridge 3-37

Figure 3.13. Thermocouple locations at the Guthrie County Bridge 3-38

Figure 3.14. Thermocouple locations at the Story County Bridge 3-39

Figure 4.1. Typical thermocouple plots 4-36

Figure 4.2. Typical displacement-transducer plots 4-37

Figure 4.3. Raw strain-gage data for the upper cross section of the pile near the mid-width of the north abutment at the Guthrie County Bridge 4-38

Figure 4.4. Temperature-corrected, pile-strain-gage results for the upper cross section of the pile near the mid-width of the north abutment at the Guthrie County Bridge 4-40

Figure 4.5. Strain gages on an HP10X42, pile cross section 4-42

Figure 4.6. Pile-strain components calculated using all four strain gages at the upper cross section of the pile near the mid-width of the north abutment at the Guthrie County Bridge 4-43

Figure 4.7. Final strain results after completion of the filtering process for the strain gages on the upper cross section of the pile near the mid-width of the north abutment at the Guthrie County Bridge 4-45

Figure 4.8. Final strain components after the completion of filtering process for the upper cross section of the pile near the mid-width of the north abutment at the Guthrie County Bridge 4-47

Figure 4.9. Temperature regions for a partial cross section of a bridge 4-49

Figure 4.10. Average, bridge temperatures for the monitored bridges 4-50

Figure 4.11. Average, bridge temperatures and air temperatures between July 18, 1998 and July 22, 1998 at the Guthrie County Bridge 4-51

Figure 4.12. Vertical-temperature distributions through the depth of the superstructure at the times of minimum and maximum, average, bridge temperatures 4-52

Figure 4.13. Extrapolated temperatures (°F) at the time of maximum and minimum, average, bridge temperatures at the Guthrie County Bridge 4-53

Figure 4.14. Extrapolated temperatures (°F) at the time of maximum and minimum, average, bridge temperatures at the Story County Bridge 4-56

Figure 4.15. Difference between the average temperatures in the bridge deck and in the bottom flanges of the PC girders 4-59

Figure 4.16. Transverse-temperature distribution across the bridge width 4-60

Figure 4.17. Measured, bridge temperatures along the bridge length at the times of the maximum and minimum, average, bridge temperatures 4-61

Figure 4.18. Change in the bridge length 4-62

Figure 4.19. Change in the bridge length versus average, bridge temperature 4-63

Figure 4.20. Change in the longitudinal displacements of north and south abutments versus the average, bridge temperature at the Guthrie County Bridge 4-64

Figure 4.21. Range in the longitudinal displacements at three positions across the width of the abutments 4-65

Figure 4.22. Pile-cap rotations measured with a tiltmeter versus rotations calculated from transducer displacements at the Guthrie County Bridge 4-66

Figure 4.23. Abutment pile-cap rotations 4-67

Figure 4.24. Transverse displacements of the south abutment for the Guthrie County Bridge 4-68

Figure 4.25. Relative displacements at the piers for the Guthrie County Bridge 4-69

Figure 4.26. Relative displacements at the piers for the Story County Bridge 4-70

Figure 4.27. Relative rotation between a pile and a pile cap 4-71

Figure 4.28. Relative displacement between the center PC girder and the south-abutment backwall at the Guthrie County Bridge 4-72

Figure 4.29. Biaxial, flexural-bending strains in the upper, monitored, cross section for the pile near the mid-width of the north abutment for the Guthrie County Bridge 4-73

Figure 4.30. X-axis, flexural-bending strains at two cross sections for the west pile of the north abutment for the Guthrie County Bridge 4-74

Figure 4.31. Biaxial, flexural-bending strains in the upper, monitored, cross section for the center pile of the east abutment for the Story County Bridge 4-75

Figure 4.32. Y-axis, flexural-bending strains at two cross sections for the north pile of the east abutment for the Story County Bridge 4-76

Figure 4.33. Difference between the longitudinal strains in the top and bottom flanges for the east, exterior, PC girder for the Guthrie County Bridge 4-77

Figure 4.34. Difference between the longitudinal strains in the top and bottom flanges for the north, exterior, PC girder for the Story County Bridge 4-78

Figure 5.1. ANSYS finite-element bridge models 5-16

Figure 5.2. Components of the finite-element model for the Guthrie County Bridge 5-17

Figure 5.3. A pile with Winkler-soil models 5-18

Figure 5.4. Typical p-y curve 5-19

Figure 5.5. Non-dimensional, modified, Ramberg-Osgood p-y relationship 5-19

Figure 5.6. Alpha factor for the adhesion of a pile in clay 5-20

Figure 5.7. Soil borings at the Guthrie County Bridge 5-20

Figure 5.8. Soil borings at the Story County Bridge 5-21

Figure 5.9. Horizontal stiffness and vertical stiffness of the soil along the length of the center pile for the south abutment at the Guthrie County Bridge 5-22

Figure 5.10. Horizontal-stiffness design curves for the soil behind a wall 5-23

Figure 5.11. Temperature regions for the bridge decks 5-26

Figure 6.1. Abutment longitudinal displacements predicted by the Guthrie, Series-A Models and experimentally measured at the Guthrie County Bridge 6-23

Figure 6.2. Abutment transverse displacements predicted by the Guthrie, Series-A Models and experimentally measured at the Guthrie County Bridge 6-24

Figure 6.3. Analytically-predicted and experimentally-measured, relative rotations of a pile at the Guthrie County Bridge 6-24

Figure 6.4. X-axis, flexural-bending strains predicted by the Guthrie, Series-A Models and experimentally measured at the Guthrie County Bridge 6-25

Figure 6.5. Y-axis, flexural-bending strains predicted by the Guthrie, Series-A Models and experimentally measured at the Guthrie County Bridge 6-26

Figure 6.6. Orientation of the pile near the mid-width of the south abutment for the Guthrie County Bridge 6-27

Figure 6.7. Y-axis, flexural-bending strains predicted by the Guthrie, Series-B Models and experimentally measured at the Guthrie County Bridge 6-28

Figure 6.8. Strain variation predicted by the Guthrie, Series-A Models along the length of the west pile for the north abutment and experimentally measured at the Guthrie County Bridge 6-29

Figure 6.9. Maximum, predicted, flexural-bending strains in the monitored, abutment piles at the Guthrie County Bridge 6-30

Figure 6.10. Predicted, axial strains in the monitored piles for the north abutment of the Guthrie County Bridge 6-31

Figure 6.11. Strains profiles through the depth of a bridge superstructure 6-32

Figure 6.12. Difference between the longitudinal strains in the top and bottom flanges of the PC girders predicted by the Guthrie, Series-A Models and experimentally measured at the Guthrie County Bridge 6-33

Figure 6.13. Difference between the longitudinal strains in the top and bottom flanges of the PC girders predicted by the Guthrie, Series-B Models and experimentally measured at the Guthrie County Bridge 6-34

Figure 6.14. PC girder strains due to stress predicted by the Guthrie, Series-B, Best-Soil Model for the south span for the Guthrie County Bridge 6-35

Figure 7.1. Abutment longitudinal displacements predicted by the Story, Series-A Models and experimentally measured at the Story County Bridge 7-17

Figure 7.2. Abutment transverse displacements predicted by the Story, Series-A Models and experimentally measured at the Story County Bridge 7-18

Figure 7.3. Analytically-predicted and experimentally-measured, relative rotations of a pile at the Story County Bridge 7-19

Figure 7.4. X-axis, flexural-bending strains predicted by the Story, Series-A Models and experimentally measured at the Story County Bridge 7-20

Figure 7.5. Y-axis, flexural-bending strains predicted by the Story, Series-A Models and experimentally measured at the Story County Bridge 7-21

Figure 7.6. Y-axis, flexural-bending strains predicted by the Story, Series-B Models and experimentally measured at the Story County Bridge 7-22

Figure 7.7. Strain variation predicted by the Story, Series-B Models along the length of the north pile for the east abutment and experimentally measured at the Story County Bridge..... 7-23

Figure 7.8. Maximum, predicted, flexural-bending strains in the monitored, abutment piles at the Story County Bridge 7-24

Figure 7.9. Predicted, axial strains in the monitored piles for the east abutment of the Story County Bridge..... 7-25

Figure 7.10. Difference between the longitudinal strains in the top and bottom flanges of the PC girders predicted by the Story, Series-A Models and experimentally measured at the Story County Bridge 7-26

Figure 7.11. Difference between the longitudinal strains in the top and bottom flanges of the PC girders predicted by the Story, Series-B Models and experimentally measured at the Story County Bridge 7-27

Figure 7.12. PC girder strains due to stress predicted by the Story, Series-B, Best-Soil Model for the east span for the Story County Bridge 7-28

Figure 8.1. Recommended and experimental, temperature ranges..... 8-180

Figure 8.2. Temperature gradient through the depth of a bridge superstructure .. 8-180

Figure 8.3. Alpha coefficients for 100%-dry concrete from selected bridge decks in the State of Iowa 8-181

Figure 8.4. Moisture-correction factor..... 8-181

Figure 8.5. Concrete-age-correction factor..... 8-182

Figure 8.6. Equivalent cantilevers for an abutment pile 8-182

Figure 8.7. Second moment of the distributed, horizontal stiffness of the soil within a soil layer about a reference line A-A..... 8-183

Figure 8.8. Equivalent-cantilever lengths for piles in a uniform soil 8-184

Figure 8.9. Longitudinal displacement and horizontal rotation of a symmetric, single-span, integral-abutment, bridge superstructure..... 8-185

Figure 8.10. Relationship between the horizontal rotation of an integral-abutment bridge and the longitudinal displacement of an integral abutment..... 8-186

Figure 8.11. Simplified model for transverse displacements of an abutment..... 8-187

Figure 8.12. Parameters that affect the transverse displacements of an abutment 8-188

Figure 8.13. Soil-pressure coefficients for the abutment backfill..... 8-189

Figure 8.14. Pile orientations for integral abutments 8-190

Figure 8.15. Influence of the bridge length on the abutment displacement dt 8-191

Figure 8.16. Influence of the bridge width on the abutment displacement dt..... 8-191

Figure 8.17. Influence of the abutment height on the abutment displacement dt ... 8-192

Figure 8.18. Influence of the wingwall-embankment height on the abutment displacement dt ... 8-192

Figure 8.19. Influence of the wingwall length on the abutment displacement dt ... 8-193

Figure 8.20. Influence of the number of backwall piles on the abutment displacement dt ... 8-193

Figure 8.21. Influence of the number of sidewall piles on the abutment displacement dt ... 8-194

Figure 8.22. Influence of the backwall and wsidewall pile, equivalent-cantilever length on the abutment displacement dt ... 8-194

Figure 8.23. Influence of the soil unit-weight on the abutment displacement dt ... 8-195

Figure 8.24. Influence of the soil-internal-friction angle on the abutment displacement dt ... 8-195

Figure 8.25. Influence of the soil-to-abutment, surface-frictional angle on the abutment displacement dt ... 8-196

Figure 8.26. Influence of both bridge length and bridge width on the abutment displacement dt ... 8-196

Figure 8.27. Forces governing the transverse displacement of the bridge during an expansion and a subsequent contraction ... 8-197

Figure 8.28. Relationship between the transverse and longitudinal displacements of an integral abutment ... 8-198

Figure 8.29. Pile moment resistance versus displacement relationship ... 8-199

Figure 8.30. Coordinate axes for an integral-abutment bridge, integral abutment, and abutment-backwall piles ... 8-201

Figure 8.31. Gravity loads on a backwall-pile cap ... 8-202

Figure 8.32. Gravity and thermally-induced loads on an integral abutment without common sidewalls and wingwalls ... 8-203

Figure 8.33. Abutment force geometry for bridge superstructure expansion ... 8-204

Figure 8.34. Displaced shapes for the central portion of an abutment..... 8-205

Figure 8.35. Simplified-frame model in the ℓh-plane for an integral-abutment bridge with gravity loads before the abutments become composite members 8-207

Figure 8.36. Simplified-frame model in the ℓh-plane for an integral-abutment bridge with gravity loads after the abutments become composite members 8-207

Figure 8.37. Simplified-frame model in the ℓh-plane for an integral-abutment bridge with a thermally induced expansion and without a vertical-temperature gradient 8-208

Figure 8.38. Components of the member-end forces for a PC girder that act on an abutment for Analysis Method 1 8-209

Figure 8.39. Components of the member-end forces for an HP-shaped pile that act on an abutment for Analysis Method 1 8-210

Figure 8.40. Components of the member-end forces for an HP-shaped pile that act on an abutment for Analysis Method 2 8-211

Figure 8.41. Gravity loads on the central portion of an abutment-pile cap..... 8-212

Figure 8.42. Gravity and thermally-induced loads on the central portion of an integral abutment..... 8-213

Figure 8.43. Free-body diagram in the vertical XY-plane for the central portion of an integral abutment..... 8-214

Figure 8.44. Free-body diagram in the vertical YZ-plane for the central portion of an abutment-pile cap 8-215

Figure 8.45. Free-body diagram for the central portion of an integral abutment..... 8-216

Figure 8.46. Force coefficients for $W_{soil\text{-}X}$ 8-219

Figure 8.47. Force coefficients for $W_{soil\text{-}friction\text{-}Z}$ 8-219

Figure 8.48. Force coefficients for $W_{abut\text{-}Y}$ 8-220

Figure 8.49. Force coefficients for $P_{pile\text{-}y}$ 8-220

Figure 8.50. Force coefficients for $V_{pile\text{-}X}$ 8-221

Figure 8.51. Force coefficients for $M_{pile\text{-}Z}$ 8-221

Figure 8.52. Force coefficients for $V_{pile\text{-}Z}$ 8-222

Figure 8.53. Force coefficients for $M_{pile\text{-}X}$ 8-222

Figure 8.54. Force coefficients for $M_{pile\text{-}Y}$ 8-223

Figure 8.55. Plan view of an integral abutment..... 8-224

Figure 8.56. Side-elevation view of an integral abutment 8-225

Figure 8.57. Forces induced by thermal expansion of an integral-abutment bridge 8-226

Figure 8.58. Abutment and superstructure forces that are induced by a thermal expansion of an integral-abutment bridge 8-227

Figure 8.59. Free-body diagrams for the corners of an integral abutment..... 8-228

Figure 8.60. Wingwall and sidewall at Corner 1 of an integral abutment..... 8-230

Figure 8.61. Wingwall and sidewall at Corner 2 of an integral abutment..... 8-231

Figure 8.62. Loads on deep-flexural members 8-232

Figure 8.63. Reinforcement for a backwall-pile cap..... 8-232

Figure 8.64. Partial XZ-plane cross section of a backwall-pile cap..... 8-233

Figure 8.65. Reinforcement for an abutment backwall 8-234

Figure 8.66. Reinforcement for a wingwall, sidewall, and sidewall-pile cap..... 8-235

Figure 8.67. Reinforcement for a sidewall and a sidewall-pile cap 8-236

Figure 8.68. Abutment reinforcement in an XY-plane above the pile cap near Corner 2 8-237

Figure 8.69. Abutment reinforcement in an XY-plane within the pile cap near Corner 2 8-238

Figure 8.70. Free-body diagram of an abutment-pile cap with thermally-induced forces..... 8-239

Figure 8.71. Pile-to-pile-cap connection 8-240

Figure 8.72. Concrete punching-shear failure at an abutment pile 8-241

Figure 8.73. Concrete bearing stresses at the end of a PC girder 8-242

Figure 8.74. PC girder member-end forces that act on an integral abutment 8-243

Figure 8.75. Geometric conditions for a simply-supported beam with a concentrated load at the midspan 8-244

Figure 8.76. Displacements for a simply-supported beam loaded at the mid-span 8-245

Figure 8.77. Moment-rotation relationship 8-246

Figure 8.78. Alternating plasticity 8-247

Figure 8.79. Strain distributions that correspond to the M-Φ points shown in Fig. 8.78 8-248

Figure 8.80. Stress distributions that correspond to the M-Φ points shown in Fig. 8.78 8-249

Figure 8.81. Fixed-end beam with sidesway 8-250

Figure 8.82. Moment-rotation relationship for an abutment pile associated with temperature changes for a bridge superstructure 8-251

Figure 8.83. Inelastic-hinge rotation due to live load 8-252

Figure 8.84. Uniaxial-displacement, ductility-limit state for a pile 8-254

Figure 8.85. Soil-pile system for determining the skin-frictional resistance of a pile 8-255

Figure 8.86. Horizontal displacement effects of a pile on the pile length for vertical, skin-frictional resistance 8-256

Figure 9.1. Plan view of the Guthrie County Bridge 9-77

Figure 9.2. Plan view of the south abutment for the Guthrie County Bridge 9-78

Figure 9.3. Vertical cross section of the south abutment for the Guthrie County Bridge 9-79

Figure 9.4. Elevation of the south abutment for the Guthrie County Bridge 9-80

Figure 9.5. Soil profile and horizontal stiffness at the south abutment of the Guthrie County Bridge 9-81

Figure 9.6. Horizontal stiffness of the upper 20 ft of soil at the south abutment of the Guthrie County Bridge 9-82

Figure 9.7. Transmove software parameters for the Guthrie County Bridge 9-83

Figure 9.8. Backwall-pile-cap reinforcement for the Guthrie County Bridge 9-84

Figure 9.9. Composite backwall and backwall-pile-cap reinforcement for the Guthrie County Bridge 9-85

Figure 9.10. Free-body diagram of a backwall-pile cap with factored-level, thermally-induced forces for the Guthrie County Bridge 9-86

Figure 9.11. Partial XZ-plane cross section of a backwall-pile cap for the Guthrie County Bridge 9-87

Figure 9.12. Pile-to-pile-cap connection in the XY-plane for the Guthrie County Bridge 9-88

Figure 9.13. Concrete punching-shear failure at an abutment pile 9-89

Figure 9.14. Concrete bearing stresses at the end of a PC girder for the Guthrie County Bridge 9-90

Figure 9.15. Maximum bridge length for skewed, integral-abutment bridges 9-91

Figure A.1. Geographical locations in the State of Iowa for concrete-core specimens A-4

Figure A.2. Ranges for the α-coefficients for bridge decks in the State of Iowa..... A-5

Figure A.3. Alpha-coefficient ratio for concrete with limestone coarse aggregate..... A-6

Figure A.4. Alpha-coefficient ratio for concrete with gravel coarse aggregate A-6

Figure B.1. Forces on an integral abutment for a skewed bridge due to thermal elongation and rigid-body rotation of the bridge superstructure..... B-21

Figure B.2. Positive displacements for an abutment in the program Transmove B-22

Figure B.3. Displacements at the abutment corners B-23

Figure B.4. User-interface for the Transmove software B-24

Figure B.5. Flowchart for the algorithm of the program Transmove B-25

Figure B.6. Displacement paths in the horizontal plane B-26

LIST OF TABLES

Table 3.1. Characteristics of the instrumented bridges 3-40

Table 3.2. Experimental measurements at the monitored bridges 3-40

Table 3.3. Number of instrumentation devices installed for field monitoring..... 3-41

Table 3.4. Transducers at the Guthrie County Bridge 3-41

Table 3.5. Transducers at the Story County Bridge..... 3-42

Table 3.6. Strain gages for the abutment piles at the Guthrie County Bridge..... 3-43

Table 3.7. Strain gages for the PC girders and a RC pile cap at the Guthrie County Bridge 3-44

Table 3.8. Strain gages for the abutment piles at the Story County Bridge 3-45

Table 3.9. Strain gages for the PC girders and a RC pile cap at the Story County Bridge 3-46

Table 3.10. Thermocouples at the Guthrie County Bridge 3-47

Table 3.11. Thermocouples at the Story County Bridge..... 3-48

Table 4.1. Reliable thermocouple data for the Guthrie County Bridge 4-79

Table 4.2. Reliable thermocouple data for the Story County Bridge..... 4-80

Table 4.3. Reliable displacement-transducer data for the Guthrie County Bridge..... 4-81

Table 4.4. Reliable displacement-transducer data for the Story County Bridge..... 4-81

Table 4.5. Reliable pile-strain-gage data for the Guthrie County Bridge 4-82

Table 4.6. Reliable pile-strain-gage data for the Story County Bridge..... 4-83

Table 4.7. Reliable pile-strain-component data for the Guthrie County Bridge..... 4-84

Table 4.8. Reliable pile-strain-component data for the Story County Bridge 4-85

Table 4.9. Reliable concrete-strain-gage data for the Guthrie County Bridge 4-86

Table 4.10. Reliable concrete-strain-gage data for the Story County Bridge..... 4-87

Table 4.11. Temperatures at the time of the maximum, average, bridge temperature (July 20, 1998, 8:00 p.m.) at the Guthrie County Bridge..... 4-87

Table 4.12. Temperatures at the time of the minimum, average, bridge temperature (January 5, 1999, 4:00 a.m.) at the Guthrie County Bridge..... 4-88

Table 4.13. Temperatures at the time of the maximum, average, bridge temperature (June 20, 1998, 6:00 p.m.) at the Story County Bridge..... 4-88

Table 4.14. Temperatures at the time of the minimum, average, bridge temperature (January 5, 1999, 2:00 a.m.) at the Story County Bridge..... 4-89

Table 4.15. Difference between the longitudinal strains in the top and bottom flanges of the PC girders 4-89

Table 5.1. Properties of the modeled bridges..... 5-27

Table 5.2. Parameters for p-y curves 5-28

Table 5.3. Parameters for f-z curves 5-29

Table 5.4. Parameters for q-z curves 5-29

Table 5.5. Soil properties and displacement parameters for an HP10X42 pile in clay..... 5-30

Table 5.6. Soil properties and displacement parameters for an HP10X42 pile in sand 5-31

Table 5.7. Properties for cohesionless sands..... 5-32

Table 5.8. Approximate, horizontal displacement of a wall to activate passive-soil pressure and active-soil pressure 5-32

Table 6.1. Approximate, initial, non-dimensional slopes for the horizontal stiffness of the abutment backfill based on the Husain and Bagnaroil (1996) design curves in Fig. 5.10b 6-36

Table 6.2. Change in the bridge length predicted by the Guthrie, Series-A Models 6-36

Table 6.3. Change in the bridge length predicted by the Guthrie, Series-B Models 6-37

Table 6.4. Maximum, average, bridge-temperature ranges for reliable, experimental, pile strains at the Guthrie County Bridge 6-38

Table 7.1. Change in the bridge length predicted by the Story, Series-A Models 7-29

Table 7.2. Change in the bridge length predicted by the Story, Series-B Models 7-29

Table 7.3. Maximum, average, bridge-temperature ranges for reliable, experimental, pile strains at the Story County Bridge 7-30

Table 8.1. Load combinations (AASHTO Specifications 1996) 8-257

Table 8.2. Average bridge temperature based on air temperatures 8-257

Table 8.3. Experimentally-measured and recommended, average, bridge temperatures 8-258

Table 8.4. Average design temperatures for concrete-girder bridges in Iowa (Roeder, 2003) 8-258

Table 8.5. Volume proportion for typical concrete mixes (Ng, 1999) 8-259

Table 8.6. Specified alpha coefficients for various types of aggregates 8-259

Table 8.7. Experimental and predicted alpha coefficients for concrete-core specimens at 100%-dry condition (Ng, 1999) 8-260

Table 8.8. Predicted alpha coefficients 8-260

Table 8.9. Experimental and theoretical, longitudinal displacements 8-261

Table 8.10. Parameters for transverse displacements 8-261

Table 8.11. Summary of parameter studies 8-262

Table 8.12. Relative geometric conditions at three cross sections for an abutment 8-263

Table 8.13. Zero-magnitude internal forces for XY-planes of symmetry and asymmetry 8-264

Table 8.14. Internal-force coefficients at three cross sections for an abutment..... 8-265

Table 8.15. Effective girder-reaction coefficients at the center of gravity of an abutment..... 8-266

Table 9.1. Equivalent-cantilever lengths for the abutment piles at Guthrie County Bridge 9-92

Table 9.2. Factored-level internal forces using AASHTO Load Group IV with a D-Load Factor of 1.3 for a pile cap of an abutment backwall at the Guthrie County Bridge..... 9-93

Table 9.3. Design strengths for a pile cap of an abutment backwall at the Guthrie County Bridge 9-94

Table 9.4. Factored-level internal forces using AASHTO Load Group IV with a D, L and I, E, and T-Load Factors of 1.3, 1.3, 1.69, and 1.3, respectively, for a composite backwall and backwall-pile cap at the Guthrie County Bridge..... 9-95

Table 9.5. Design strengths for a composite backwall and backwall-pile cap at the Guthrie County Bridge 9-96

Table 9.6. Effective girder reactions at the center of gravity of a composite backwall and backwall-pile cap at the Guthrie County Bridge..... 9-97

Table 9.7. Geometric and material parameters for the maximum bridge length (based on many of the parameters of the Guthrie County Bridge 9-98

Table A.1. Concrete-core specimens from bridge decks A-7

Table A.2. Concrete-core specimens from PC girders..... A-8

Table A.3. Alpha coefficients for concrete-core specimens taken from bridge decks A-9

Table A.4. Alpha coefficients for concrete-core specimens taken from PC girders A-10

Table A.5. Maximum, alpha-coefficient ratio A-10

Table B.1. Soil and pile forces on an integral abutment..... B-27

ACKNOWLEDGEMENTS

This research project (Project No. HR-399) was sponsored by the Iowa Highway Research Board of the Iowa Department of Transportation (Iowa DOT). The members of the research advisory board were Norm McDonald, Bridge Engineer with the Iowa DOT; Ahmad Abu-Hawash, Chief Structural Engineer with the Iowa DOT; Mark Nahra, Delaware County Engineer; Fouad Daoud, WHKS & Company; and Mike Klapp, Engineering Department – City of Des Moines, Iowa. The authors wish to acknowledge their helpful input and guidance, particularly at the beginning of the project. The authors acknowledge the very cooperative support from Steve Akes, Guthrie County Engineer; Dean Wedemeyer, Assistant Guthrie County Engineer; Harold Jensen, Story County Engineer; Greg Parker, Assistant Story County Engineer; and other staff members for both the Guthrie and Story County Engineering Offices. These representatives from both county engineering offices were very accommodating in making the arrangements to provide traffic control for the installation of the instrumentation devices on the bridges and to provide soil to refill the trenches that were dug in the abutment berms and around abutment piles for the monitored bridges. The authors want to acknowledge the assistance provided by Tom Neumann, Department of Water with the City of Ames, for providing electrical power at the Story County Bridge that was required to operate the data-acquisition system and by William Stabler, Iowa DOT, for use of the maintenance vehicle that provided a platform to help with the installation of the instrumentation devices beneath both of the monitored bridges. Thanks and appreciation are extended to many graduate and undergraduate students from Iowa State University for their help with the excavation of the abutment berms, installation of the instrumentation devices,

and the erection of the security system at both of the monitored bridges. The authors wish to extend special acknowledgement to Douglas L. Wood, Structures Laboratory Manager, for his efforts and assistance with the data-acquisition system and Denise K. Wood, Structures Secretary, for her typing of the final report.

EXECUTIVE SUMMARY

Traditional bridge structures use expansion-joint systems to accommodate the change in the bridge length that is induced by changes in the temperature of the bridge superstructure. The use of bridge-expansion joints incurs initial-construction costs and maintenance costs over the life of the bridge. Integral-abutment bridges do not have expansion joints. The connections between the superstructure and abutments for this type of a bridge are rigid joints. As a result of the restrained displacements of the bridge superstructure that are caused by the integral construction, thermal expansion and contraction and concrete creep and shrinkage of the bridge superstructure induces strains and corresponding stresses in the bridge members.

Many state-bridge engineers design integral-abutment bridges. Most of these designers indicate that these structures are performing well. Transportation agencies typically impose limits, which are usually based on the agency's previous experience, on the total length and skew angle for integral-abutment bridges. Primary concerns of designers and researchers relate to the forces and displacements that are induced in the abutments and abutment piles during the expansion and contraction of the bridge superstructure. Previous monitoring programs for integral-abutment bridges involved measurements of bridge temperatures, longitudinal displacements, soil pressures behind the abutments, strains in the bridge girders, vertical rotations of the abutments, and vertical-temperature gradients through the depth of the bridge girders. Prior research compared bridge responses that were predicted by mathematical models with those responses that were measured during field studies. Numerous analytical models for previous research were developed to study the interaction between an abutment and

the soil backfill, axial forces and bending moments in the superstructure, interaction between the pile and soil, and pile strains that are caused by thermally-induced displacements of the abutments. The literature contains integral-abutment-design recommendations for design-temperature ranges; vertical-temperature gradients through the depth of a bridge superstructure; coefficient of thermal expansion and contraction of concrete; maximum, bridge length; maximum, skew angles; bridge longitudinal and transverse displacements; and pile ductility.

The objectives for the research program that is discussed in this report were to evaluate the state-of-art for the design of prestressed-concrete (PC), integral-abutment bridges; to validate the assumptions that are incorporated in the current-design procedures for these types of bridges when they are subjected to thermal-loading conditions; and, as appropriate, to revise and improve the current-design procedures for this type of a bridge, as that design relates to the thermally-induced displacements of the abutments and the thermally-induced forces in the abutments and abutment piles. The research program involved an experimental-monitoring program, finite-element analyses, and the development of design procedures and recommendations.

Two, PC girder, integral-abutment bridges were monitored over a two-year period for structural behavior. For this study, the bridges were named the Guthrie County Bridge and the Story County Bridge to identify the counties in the State of Iowa where the bridges are located. Instrumentation devices measured the longitudinal and transverse displacements and vertical rotations of the integral abutments; strains in the flanges of several, steel, HP-shaped piles at two cross sections near the tops of the piles; strains in the flanges of several, I-shaped, PC girders near the abutment and pier

for one of the end spans for the bridges; temperatures of the concrete in the flanges and webs of selected PC girders and at the mid-thickness of the reinforced concrete (RC) bridge decks at many locations; and the relative fixity of the selected piles and girders into an abutment for each bridge. Experimental data were recorded to establish the relationships between the daily and seasonal-temperature variations and the measured deformations for the bridges.

Concrete cores were obtained from twenty, RC bridge decks at various locations in the State of Iowa and from PC girders at the production facilities for two, PC producers in the State of Iowa. The coefficient of thermal expansion and contraction (α-coefficient) for the concrete in each of the cores was measured in the laboratory for the 100%-dry and 100%-saturated conditions. The experimentally-measured α-coefficients were compared to the analytically-predicted α-coefficients for several concrete-mix designs to determine the applicability of using the published, empirical, α-coefficient equations for the evaluation of the longitudinal expansion and contraction of bridge superstructures.

The maximum, average, bridge temperature occurred during an early summer evening; and, the minimum, average, bridge temperature occurred in the winter just before sunrise. The maximum, average, bridge temperature lagged behind and exceeded the measured, air temperatures. The longitudinal displacements for the abutments correlated well with the recorded change in average, bridge temperatures. The experimentally-based, maximum, combined-bending strains in the monitored, HP-shaped, abutment piles at the Guthrie County Bridge exceeded the minimum, specified, yield strain of steel. For the Story County Bridge, these pile strains were somewhat less

than the steel-yield strain. However, when these longitudinal strains are added to the sum of the axial, compressive strains induced by the self-weight of the abutments; the dead, live, and impact loads on the bridge superstructure; and the residual, compressive strains in the HP-shaped cross section of the piles, the resulting total longitudinal, compressive strains along a portion of one flange will exceed the steel-yield strain. The experimentally-measured, longitudinal strains at the strain-gage locations in the selected PC girders were well within acceptable limits. The integral connections between the PC girders and the abutment backwall, and between the abutment piles and the abutment-pile cap essentially behaved as rigid joints.

The experimental data were used to calibrate and refine the finite-element models of the Guthrie County Bridge and Story County Bridge. These models included the RC deck; PC girders; piers; abutment piles; intermediate diaphragms; and integral abutments. Values of the α-coefficients of the concrete were based on the results from the laboratory tests that were conducted on the concrete-core samples. Some discrepancies occurred between the longitudinal displacements and vertical rotations of the integral abutments that were analytically predicted by the finite-element models and experimentally measured during the bridge monitoring. The cause was not completely determined for these discrepancies.

Recommendations are presented for the design of an integral-abutment pile cap; a composite, abutment backwall and pile cap; and HP-shaped, backwall piles for an integral-abutment bridge with PC girders. The design recommendations that are based on the results from previous work by the authors of this report, by other researchers, and from the findings for this research include empirical equations and procedures for

establishing the design-temperature range; vertical-temperature gradients for the bridge superstructure, longitudinal and transverse displacements for the integral abutments, concrete-creep and concrete-shrinkage effects; and an effective, coefficient of thermal expansion and contraction for the bridge.

A software program was developed to calculate the transverse displacements of an abutment for a skewed, integral-abutment bridge. The computer program, which is based on an analytical model that was presented by others, includes enhancements that improve the accuracy of the predictions for the transverse displacements of an integral abutment. This program was used in a sensitivity analysis to evaluate the effect that many of the design parameters for an integral-abutment bridge have on the transverse displacements of integral abutments.

Two analysis methods are presented to predict the member-end forces for the piles and girders and the soil pressures and soil-frictional forces that act on an integral abutment, when an integral-abutment bridge is subjected to gravity and thermal loadings. The first analysis method involves the use of two-dimensional, frame models of an integral-abutment bridge. The second analysis method does not require the use of a structural model for the entire bridge. This analysis method considers that the member-end forces for the abutment piles are based on the maximum resistance for each pile, and that the maximum, soil pressures and the corresponding, soil-frictional forces are based on full-passive-soil resistance. Both analysis methods include the effect of soil settlement from the bottom of the abutment-pile cap and the application of equivalent-cantilever lengths for the abutment piles. Either analysis method can be applied along with the boundary conditions that are associated with the planes of

symmetry and asymmetry for particular, abutment loads and specific, abutment cross sections to evaluate the internal forces in an abutment-pile cap or in a composite, abutment backwall and pile cap. Free-body diagrams for the central portion of an abutment-pile cap and a composite, abutment backwall and pile cap are presented to assist in the evaluation of the internal forces for an abutment.

As documented in the field studies and elsewhere, the abutment piles for integral-abutment bridges experience strains beyond the steel-yield strain for annual-temperature changes in the bridge deck. To accommodate these large pile strains, pile-ductility demands are quantified by equations. The ductility capacity of an HP-shaped, abutment pile that is subjected to biaxial, cyclic, and load reversals, which involve alternating plasticity of the pile, is described and represented by an equation.

Bridge length may be limited by the pile-ductility limit state. To maximize the ductility capacity for an abutment pile, the upper portion of the pile length should be in a pre-bored hole that is filled with a material, which has a very low stiffness (such as a bentonite slurry), and the y-axis (weak axis) for the pile should be oriented perpendicular to the longitudinal axis of the bridge. Procedures that are based on pile ductility are presented to approximate the maximum length for a non-skewed and a skewed, integral-abutment bridge with PC girders. Since numerous parameters that are associated with a particular PC-girder, integral-abutment bridge affect the maximum length for that bridge, specific length limitations are not provided for the maximum length verses the bridge-skew angle. However, longer, integral-abutment bridges can be constructed than those that are currently being constructed using the present, Iowa DOT, length limits. Annotated examples that incorporate the design recommendations

are presented for the Guthrie County Bridge. For the Guthrie County Bridge, the designs for the abutment-pile cap; composite, abutment backwall and pile cap; and backwall piles and the connections between the pile cap and the backwall, between the backwall piles and a pile cap, and between an interior PC girder and an abutment backwall were checked using the design recommendations and current-design equations.

Further experimental studies would contribute to a better understanding of integral-abutment bridges that have one or more of the following attributes: steel girders, longer lengths, curved horizontal alignments, and PC abutment piles. Additional verification for the simplified model that was used to predict the transverse displacements of an integral abutment could be accomplished with more field studies. A better understanding of the behavior of the soil behind an integral abutment could be obtained with additional, bridge-monitoring programs. With better soil-pressure representations, analytical models for integral-abutment bridges would more accurately predict the behavior for these types of bridges.

NOMENCLATURE

A_1	=	bearing area;
A_2	=	effective area of the concrete support that is geometrically similar to and has the same centroid as the area A_1;
A_3	=	bearing area for the bearing stress q_{3Y};
A_c	=	area of concrete along the vertical and horizontal edges of the shearing surfaces for a concrete-punching-shear failure at the end of a PC girder;
A_{cp}	=	area that is enclosed by the perimeter of the concrete cross section
A_d	=	total, cross-sectional area for the bridge deck;
$A_{element}$	=	surface area of the finite-element;
A_g	=	total, cross-sectional area for all of the PC girders across the bridge width;
A_j	=	area of a particular region of the total cross section for the bridge superstructure;
A_{vf}	=	area of the shear-friction reinforcement;
B	=	buoyancy force;
	=	width for a portion of an abutment-pile cap and an integral abutment that occurs between two, vertical, cross sections through the abutment;
B_M	=	ratio of the moments $\Sigma M_{pile\text{-}\ell}$ to $\Sigma M_{pile\text{-}t}$;
B_{abut}	=	abutment thickness;
B_{pile}	=	pile width;
B_{sw}	=	width of the sidewall;
B_{swcap}	=	width of the sidewall-pile cap;
B_{wwe}	=	width of the wingwall at the end of the wingwall;

C	=	minimum width of the concrete confinement along the perimeter of the bearing area;
C_i	=	compression-flange, local-buckling factor;
CF	=	centrifugal force that is induced by the live load;
D	=	dead load;
D_i	=	temperature-phase factor that is applied to the inelastic-rotation capacity;
E	=	earth pressure;
	=	modulus of elasticity of the material;
	=	modulus of elasticity for the HP-shaped, steel, abutment piles;
$E_{c,eff}$	=	effective, modulus of elasticity for the initial slope of the stress-strain curve for concrete;
E_{ci}	=	initial, modulus of elasticity for the concrete at an age of t_i-days After concrete casting;
E_d	=	modulus of elasticity of the concrete in the bridge deck;
E_{eff}	=	effective, modulus of elasticity for the bridge superstructure;
E_g	=	modulus of elasticity of the concrete in the PC girders;
EQ	=	earthquake load;
F_X	=	girder-reaction force that acts in the X-axis direction of the abutment backwall;
F_X-forces	=	forces that are directed parallel to the X-axis for an abutment;
F_Y	=	girder-reaction force that acts in the Y-axis direction of the abutment backwall;
F_Y-forces	=	forces that are directed parallel to the Y-axis for an abutment;
F_Z	=	girder-reaction force that acts in the Z-axis direction of the abutment backwall;
F_Z-forces	=	forces that are directed parallel to the Z-axis for an abutment;

F_{af} = tangential force for the soil that acts against the back face of an integral abutment in the simplified model for the transverse displacement of an abutment;
= horizontal force that acts along the length of an abutment and is induced by the coefficient of friction of the soil against the abutment backwall and the forces F_{po} and $F_{pp\text{-}po}$;

F_{ap} = normal force for the soil pressure that acts on the backface of an integral abutment in the simplified model for the transverse displacements of an abutment;

$F_{bpile\text{-}X}$ = force resultant for the backwall pile forces that act along the X-axis of the abutment;

$F_{bpile\text{-}Z}$ = force resultant for the backwall pile forces that act along the Z-axis of the abutment;

F_n = sum of the components of the horizontal forces that are induced by the displacement at the top of each of the abutment-backwall piles (N_{pa} piles) and that acts normal to the abutment length;

F_{ni} = horizontal force at the top of the ith pile in an abutment backwall that Is normal to the abutment face;

F_p = sum of the components of the horizontal forces that are induced by The displacement at the top of each of the abutment-backwall piles (N_{pa} piles) and that acts parallel to the abutment length;

F_{pi} = horizontal force at the top of the ith pile in an abutment backwall that is parallel to the abutment face;

$F_{piernorm}$ = component of the force that is induced by the displacement at the top of the pier and that acts on the bridge superstructure in the direction that is normal to the length of the pier;

$F_{pierparal}$ = component of the force that is induced by the displacement at the top of the pier and that acts on the bridge superstructure in the direction that is parallel to the length of the pier;

F_{pn1} = sum of the components of the horizontal forces that are induced by the displacement at the top of each of the Sidewall 1 piles (N_{p1} piles) and that acts normal to the length, ℓ_{w1}, of the common sidewall and wingwall;

F_{pn2} = sum of the components of the horizontal forces that are induced by The displacement at the top of each of the Sidewall 2 piles (N_{p2} piles) and that acts normal to the length, ℓ_{w2}, of the common sidewall and wingwall;

F_{po} = horizontal force that is induced by the at-rest-soil-pressure p_o and that acts normal to the backwall of the abutment and over the height, h_{abut}, and length, ℓ_{abut}, of the abutment;

F_{pp1} = sum of the components of the horizontal forces that are induced by the displacement at the top of each of the Sidewall 1 piles (N_{p1} piles) and that acts parallel to the length, ℓ_{w1}, of the common sidewall and wingwall;

F_{pp2} = sum of the components of the horizontal forces that are induced by the displacement at the top of each of the Sidewall 2 piles (N_{p2} piles) and that acts parallel to the length, ℓ_{w2}, of the common sidewall and wingwall;

$F_{pp\text{-}po}$ = horizontal force that is induced by the difference between the passive-soil pressures p_{p2} and p_{p3} and the at-rest-soil pressure p_o and that acts normal to the back of the abutment and over the height, h_{abut}, and length, $\ell_{pp\text{-}po}$, of the abutment that is subjected to the passive-soil pressure;

F_{s1} = horizontal force that is induced by the passive-soil pressure p_{pw1} and that acts normal to Sidewall and Wingwall 1 and over the height, h_1, and length, ℓ_{w1}, of the abutment;

F_{s2} = horizontal force that is induced by the passive-soil pressure p_{pw2} and that acts normal to Sidewall and Wingwall 2 and over the height, h_2, and length, ℓ_{w2}, of the abutment;

$F_{s\&w1soil\text{-}t}$ = resultant force for the passive-soil pressures that act on Sidewall 1 and Wingwall 1 and along the t-axis direction of the bridge superstructure;

$F_{s\&w2soil\text{-}Z}$ = resultant force for the passive-soil pressures that act on Sidewall 2 and Wingwall 2 and along the length of the abutment backwall;

$F_{soil\text{-}X}$ = resultant force for the passive-soil pressure that acts on the backwall and along the X-axis direction of the abutment;

$F_{soil\text{-}Z}$ = resultant force for the soil-frictional forces that acts on the backwall and along the Z-axis direction of the abutment;

$F_{supstr\text{-}X}$ = internal, resultant force between the superstructure and an abutment that acts in a direction that is parallel to the X-axis of an abutment;

$F_{supstr\text{-}Z}$ = internal, resultant force between the superstructure and an abutment that acts in a direction that is parallel to the Z-axis of an abutment;

F_{xi} = horizontal force at the top of the ith backwall pile and in the x-axis directions of the pile cross section;

F_y = steel-yield stress for the HP-shaped, steel, abutment piles;

F_{yi} = horizontal force at the top of the ith backwall pile and in the y-axis directions of the pile cross section;

F_{ys} = yield strength of the shear reinforcement;

G = shear modulus of elasticity;

H = abutment-backwall height;
= wall height;
= horizontal load at the top of a pile;
= relative humidity percent;

H_{east} = height of the east abutment for the Story County Bridge;

H_{north} = height of the north abutment for the Guthrie County Bridge;

H_{south} = height of the south abutment for the Guthrie County Bridge;

H_{west} = height of the west abutment for the Story County Bridge;

I = impact load;
= moment of inertia of the pile cross section with respect to the axis of bending;
= moment of inertia of the beam cross section with respect to the axis of bending;

I_k = second moment of the $k_h(z)$ curve about the reference line A-A at a depth of ℓ_o;

I_{ki} = I_{k1} for the first soil layer;
= I_{k2} for the second soil layer;
= I_{k3} for the third soil layer;

I_x	=	moment of inertia with respect to the x-axis of a pile cross section;
I_y	=	moment of inertia with respect to the y-axis of a pile cross section;
ICE	=	ice pressure;
J	=	soil parameter;
J_c	=	property of the concrete area A_c that is similar to the polar moment of inertia;
K_{spring}	=	total, horizontal stiffness for the soil that is attributed to each wall, finite element;
L	=	original gage length when the strain-gage reading was initialized;
	=	live load;
	=	bridge length;
	=	beam span length;
L_e	=	equivalent-cantilever length for a pile;
L_{eb}	=	equivalent-cantilever length of the pile that is based on the elastic-buckling load of the pile;
L_{eh}	=	equivalent-cantilever length of the pile that is based on the horizontal stiffness of the pile in the soil;
L_{ehx}	=	equivalent-cantilever length of a pile that is based on the horizontal stiffness of the pile in the soil for x-axis (strong-axis) bending of the pile;
L_{ehy}	=	equivalent-cantilever length of a pile that is based on the horizontal stiffness of the pile in the soil for y-axis (weak-axis) bending of the pile;
L_{em}	=	equivalent-cantilever length of the pile that is based on the maximum moment in the pile;
$L_{em\ell}$	=	length L_{em} in the ℓh-plane for ℓ-axis bending of the pile;
L_{emt}	=	length L_{em} in the ℓh-plane for t-axis bending of the pile;
L_{emx}	=	length L_{em} in the ℓh-plane for x-axis bending of the pile;
L_{emy}	=	length L_{em} in the ℓh-plane for y-axis bending of the pile;

L_{ex}	=	length L_e related to x-axis buckling, bending, or horizontal stiffness;
L_{ext1}	=	length of the first exterior span for the bridge;
L_{ext2}	=	length of the second exterior span for the bridge;
L_{ey}	=	length L_e related to y-axis buckling, bending, or horizontal stiffness;
L_{int}	=	length of the interior span for the bridge;
L_{max}	=	maximum bridge length;
L_{pile}	=	pile length;
L_{wire}	=	length of the extension wire for a displacement transducer;
LF	=	longitudinal force that is induced by the live load;
M	=	bending moment at the joint between the abutment pile cap and the backwall;
	=	mid-span moment;
	=	moment resistance;
M_X	=	internal bending moment about the X-axis of an abutment cross section;
	=	girder-reaction moment that acts in the X-axis direction of the abutment backwall;
	=	internal bending moment about the X-axis of an abutment at the joint between an abutment backwall and the abutment-pile cap;
M_{X1}	=	X-axis-bending moment in the abutment at Cross Section 1;
$M_{X1'}$	=	X-axis bending moment in the abutment at Cross Section 1';
$M_{X1.5}$	=	X-axis bending moment in the abutment at Cross Section 1.5;
M_{X2}	=	X-axis bending moment in the abutment at Cross Section 2;
M_{Xi}	=	X-axis-bending moment in the abutment at the ith cross section;
M_X-moments	=	moments whose vectors are directed parallel to the X-axis for an abutment;

M_Y	=	internal bending moment about the Y-axis of an abutment cross section;
	=	girder-reaction moment that acts in the Y-axis direction of the abutment backwall;
M_{Y1}	=	Y-axis-bending moment in the abutment at Cross Section 1;
$M_{Y1'}$	=	Y-axis-bending moment in the abutment at Cross Section 1';
$M_{Y1.5}$	=	Y-axis-bending moment in the abutment at Cross Section 1.5;
M_{Y2}	=	Y-axis-bending moment in the abutment at Cross Section 2;
M_{YC1}	=	resultant, internal, support-bending-moment reaction for the horizontally-cantilevered sidewall and wingwall near Corner 1 of the abutment;
M_{YC2}	=	resultant, internal, support-bending-moment reaction for the horizontally-cantilevered sidewall and wingwall near Corner 2 of the abutment;
M_{Yi}	=	Y-axis-bending moment in the abutment at the ith cross section;
M_Y-moments	=	moments whose vectors are directed parallel to the Y-axis for an abutment;
M_Z	=	internal torsional moment about the Z-axis of an abutment cross section;
	=	girder-reaction moment that acts in the Z-axis direction of the abutment backwall;
	=	internal bending moment about the Z-axis of an abutment at the joint between an abutment backwall and the abutment-pile cap;
M_{Z1}	=	torsional moment in the abutment at Cross Section 1;
$M_{Z1'}$	=	torsional moment in the abutment at Cross Section 1';
$M_{Z1.5}$	=	torsional moment in the abutment at Cross Section 1.5;
M_{Z2}	=	torsional moment in the abutment at Cross Section 2;
M_{Zi}	=	torsional moment in the abutment at the ith cross section;
M_Z-moments	=	moments whose vectors are directed parallel to the Z-axis for an abutment;

M_{af} = moment induced by the soil-frictional force, F_{af} about the "point-of-fixity" for the bridge superstructure;

M_{ap} = moment induced by the soil force F_{ap} about the "point-of-fixity" for the bridge superstructure;

$M_{bpile\text{-}Y}$ = moment resultant for the backwall pile moments that act about the Y-azis of the abutment;

$M_{girder\text{-}X}$ = total of the moment components at the abutment-end of a PC girder that act along the X-axis for an abutment;

$M_{girder\text{-}Y}$ = total of the moment components at the abutment-end of a PC girder that act along the Y-axis for an abutment;

$M_{girder\text{-}Z}$ = total of the moment components at the abutment-end of a PC girder that act along the Z-axis for an abutment;

$M_{girder\text{-}h}$ = weak-axis (h-axis) bending moment at the abutment-end for a PC girder;

$M_{girder\text{-}\ell}$ = torsional moment (ℓ-axis moment) for a PC girder;

$M_{girder\text{-}\ell X}$ = X-axis is component for the moment $M_{girder\text{-}\ell}$;

$M_{girder\text{-}\ell Z}$ = Z-axis component for the moment $M_{girder\text{-}\ell}$;

$M_{girder\text{-}t}$ = strong-axis (t-axis) bending moment at the abutment-end for a PC girder;

$M_{girder\text{-}tX}$ = X-axis component for the moment $M_{girder\text{-}t}$;

$M_{girder\text{-}tZ}$ = Z-axis component for the moment $M_{girder\text{-}t}$;

$M_{h'}$ = girder-bending moment that acts about an axis that is parallel to the h-axis of the bridge superstructure and was resolved at a point on the front face of the abutment backwall and at an elevation that matches the center of gravity y_{ncg};

$M_{\ell'}$ = girder-torsional moment that acts about an axis that is parallel to the ℓ-axis of the bridge superstructure and was resolved at a point on the front face of the abutment backwall and at an elevation that matches the center of gravity y_{ncg};

$M_{\ell C1}$ = resultant, internal, support-torsional-moment reaction at an assumed fixed support that is located at the center of bearing for the exterior girder for a horizontally-cantilevered sidewall and wingwall near Corner 1 of the abutment;

$M_{\ell C2}$ = resultant, internal, support-torsional-moment reaction at an assumed fixed support that is located at the center of bearing for the exterior girder for a horizontally-cantilevered sidewall and wingwall near Corner 2 of the abutment;

M_{nX} = nominal-moment strength for uniaxial bending about the X-axis for an abutment cross section;

M_{nX}^{+} = positive, X-axis, nominal-bending moment for an abutment cross section;

M_{nX}^{-} = negative, X-axis, nominal-bending moment for an abutment cross section;

M_{nY} = nominal-moment strength for uniaxial bending about the Y-axis for an abutment cross section;

M_{nx} = nominal, x-axis-bending resistance of an abutment pile when only x-axis bending is present;

M_{ny} = nominal, y-axis-bending resistance of an abutment pile when only y-axis bending is present;

M_p = theoretical-plastic, moment strength;

$M_{pile\text{-}X}$ = total of the moment components at the top of a pile that act along the X-axis for an abutment;

$M_{pile\text{-}Y}$ = total of the moment components at the top of a pile that act along the Y-axis for an abutment;

$M_{pile\text{-}Z}$ = total of the moment components at the top of a pile that act along the Z-axis for an abutment;

$M_{pile\text{-}h}$ = torsional moment in a pile at the top of the pile;

$M_{pile\text{-}\ell}$ = bending moment at the top of an abutment pile that acts about the ℓ-axis for the bridge;

$M_{pile\text{-}\ell X}$ = X-axis component for the moment $M_{pile\text{-}\ell}$;

$M_{pile\text{-}\ell Z}$ = Z-axis component for the moment $M_{pile\text{-}\ell}$;

$M_{pile\text{-}t}$ = bending moment at the top of an abutment pile that acts about the t-axis for the bridge;

$M_{pile\text{-}tX}$ = X-axis component of the moment $M_{pile\text{-}t}$;

$M_{pile\text{-}tZ}$ = Z-axis component of the moment $M_{pile\text{-}t}$;

$M_{pile\text{-}x}$ = strong-axis (x-axis) bending moment in a pile at the top of the pile;

$M_{pile\text{-}xX}$ = X-axis component of the moment $M_{pile\text{-}x}$;

$M_{pile\text{-}xZ}$ = Z-axis component of the moment $M_{pile\text{-}x}$;

$M_{pile\text{-}y}$ = weak-axis (y-axis) bending moment in a pile at the top of the pile;

$M_{pile\text{-}yX}$ = X-axis component of the moment $M_{pile\text{-}y}$;

$M_{pile\text{-}yZ}$ = Z-axis component of the moment $M_{pile\text{-}y}$;

$M_{pile\text{-}z}$ = torsional moment (z-axis moment) in a pile at the top of the pile;

$M_{pp\text{-}po}$ = moment about the point-of-fixity of the bridge superstructure due to the force $F_{pp\text{-}po}$;

M_{px} = x-axis, plastic-moment strength for a pile;

M_{py} = y-axis, plastic-moment strength for a pile;

M_r = factored-level, flexural-bending resistance;

M_{rx} = factored-level, flexural resistance for bending about the x-axis of an abutment pile when only x-axis bending is present ($M_{rx} = \phi_f M_{nx}$);

M_{ry} = factored-level, flexural resistance for bending about the y-axis of an abutment pile when only y-axis bending is present ($M_{ry} = \phi_f M_{ny}$);

$M_{soil\text{-}Y}$ = resultant moment for the passive-soil pressures and soil-frictional forces that act on the backwall and about the Y-axis of the abutment;

$M_{supstr\text{-}Y}$ = internal, resultant moment between the bridge superstructure and an abutment that acts about the Y-axis of the abutment;

$M_{swC1\text{-}Y}$ = Sidewall 1 bending moment at the effective, critical-moment, cross section and that acts along the Y-axis direction for the backwall;

$M_{swC1\text{-}\ell}$ = Sidewall 1 bending moment at the effective, critical-moment, cross section and that acts along the ℓ-axis direction for the bridge superstructure;

$M_{swC1\text{-}t}$ = Sidewall 1 bending moment at the effective, critical-moment, cross section and that acts along the t-axis direction for the bridge superstructure;

$M_{swC2\text{-}Y}$ = Sidewall 2 bending moment at the effective, critical-moment, cross section and that acts along the Y-axis direction for the backwall;

$M_{swC2\text{-}\ell}$ = Sidewall 2 bending moment at the effective, critical-moment, cross section and that acts along the ℓ-axis direction for the bridge superstructure;

$M_{swC2\text{-}t}$ = Sidewall 2 bending moment at the effective, critical-moment, cross section and that acts along the t-axis direction for the bridge superstructure;

$M_{t'}$ = girder-bending moment that acts about an axis that is parallel to the t-axis of the bridge superstructure and was resolved at a point on the front face of the abutment backwall and at an elevation that matches the center of gravity y_{ncg};

M_{tC1} = resultant, internal, support-bending-moment reaction at an assumed fixed support that is located at the center of bearing for the exterior girder for a horizontally-cantilevered sidewall and wingwall near Corner 1 of the abutment;

M_{tC2} = resultant, internal, support-bending-moment reaction at an assumed fixed support that is located at the center of bearing for the exterior girder for a horizontally-cantilevered sidewall and wingwall near Corner 2 of the abutment;

M_{uX} = factored-level, bending moment about the X-axis of an abutment cross section;

M_{uXmax} = maximum of the factored-level, X-axis-bending moments in an abutment at Cross Sections 1, 1.5, and 2;

M_{uX1} = factored-level for the moment M_{X1};

$M_{uX1.5}$ = factored-level for the moment $M_{X1.5}$;

M_{uX2} = factored-level for the moment M_{X2};

M_{uY} = factored-level, bending moment about the Y-axis of an abutment cross section;

M_{nY}^{+} = positive, Y-axis, nominal-bending moment of an abutment cross section;

M_{ny}^{-} = negative Y-axis, nominal-bending moment of an abutment cross section;

M_{uY1} = factored-level for the moment M_{Y1};

$M_{uY1.5}$ = factored-level for the moment $M_{Y1.5}$;

M_{uY2} = factored-level for the moment M_{Y2};

M_{uZ} = factored-level for the moment M_{Z};

M_{uZ1} = factored-level for the moment M_{Z1};

$M_{uZ1.5}$ = factored-level for the moment $M_{Z1.5}$;

M_{uZ2} = factored-level for the moment M_{Z2};

$M_{uh'}$ = factored-level for the moment $M_{h'}$;

$M_{u\ell\text{-gravity}}$ = first-order, factored-level, gravity-load, bending moment at the top a fixed-head, abutment pile and about the ℓ-axis for the bridge;

$M_{u\ell'}$ = factored-level for the moment $M_{\ell'}$;

$M_{upile\text{-}X}$ = factored-level for pile moment $M_{pile\text{-}X}$;

$M_{upile\text{-}Y}$ = factored-level for pile moment $M_{pile\text{-}Y}$;

$M_{upile\text{-}Z}$ = factored-level for pile moment $M_{pile\text{-}Z}$;

$M_{u\ell}$ = total, factored-level, bending moment that acts about an axis that is parallel to the ℓ-axis for the bridge superstructure;

M_{ut} = total, factored-level, bending moment that acts about an axis that is parallel to the t-axis for the bridge superstructure;

$M_{ut\text{-}gravity}$ = first-order, factored-level, gravity-load, bending moment at the top a fixed-head, abutment pile and about the t-axis for the bridge;

$M_{ut'}$ = factored-level for the moment $M_{t'}$;

$M_{u\ell 2nd}$ = factored-level, second-order, bending moments that act about an axis that is parallel to the ℓ-axis of the bridge superstructure ($M_{u\ell 2nd} = P_{upile\text{-}Y}\Delta_t$);

M_{ut2nd} = factored-level, second-order, bending moments that act about an axis that is parallel to the t-axis of the bridge superstructure ($M_{ut2nd} = P_{upile\text{-}Y}\Delta_\ell$);

M_{ux} = factored-level, bending moment, including second-order bending effects with respect to bending about the x-axis of an abutment pile;

M_{uy} = factored-level, bending moment, including second-order bending effects, with respect to bending about the y-axis of an abutment pile;

M_w = elastic-bending moment at the top of an abutment pile due to the abutment rotation θ_w about the t-axis for the bridge;

M_{wx} = x-axis component of the moment M_w for an abutment pile,

M_{wy} = y-axis component of the moment M_w for an abutment pile,

M_y = theoretical, yield-moment strength;

N = load-group number;
= average, standard-penetration blow count;

N_{corr} = corrected, standard-penetration-test blow count at the pile tip;

N_p = number of piles for the abutment along the band-width B;

N_{p1} = number of piles for the abutment sidewall near Corner 1;

N_{p2} = number of piles for the abutment sidewall near Corner 2;

N_{pa} = number of piles for the abutment backwall;

P = vertical load at the top of a pile;
= vertical load that is applied along the side face of a deep beam;

P_Y = internal, vertical force along the Y-axis of an abutment at the joint between an abutment backwall and the abutment-pile cap;

P_{Z1} = axial force in the abutment at Cross Section 1;

$P_{Z1'}$ = axial force in the abutment at Cross Section 1';

$P_{Z1.5}$ = axial force in the abutment at Cross Section 1.5;

P_{Z2} = axial force in the abutment at Cross Section 2;

P_{Zi} = axial force in the abutment at the ith cross section;

P_{abut} = axial force in an integral abutment;
= axial force in an integral-abutment pile cap;

P_{down} = downward, concentrated load at the mid-span of a beam;

P_{ebH} = horizontal-bearing force along the bottom half of the pile-embedment depth into the bottom of the abutment pile cap for an abutment pile;

P_{ebV} = vertical-bearing force at the top of an abutment pile ($P_{ebV} = P_{pile\text{-}Y}$);

$P_{egC1\text{-}\ell}$ = axial force in the exterior girder near Corner 1 of the abutment that is induced by the passive-soil pressure forces, which act on Sidewall 1 and Wingwall 1, and by the Sidewall 1 pile forces;

$P_{egC2\text{-}\ell}$ = axial force in the exterior girder near Corner 2 of the abutment that is induced by the passive-soil pressure forces, which act on Sidewall 2 and Wingwall 2, and by the Sidewall 2 pile forces;

$P_{girder\text{-}X}$ = total of the force components at the abutment-end of a PC girder that act along the x-axis for an abutment;

$P_{girder\text{-}\ell}$ = axial force in a PC girder;

$P_{girder\text{-}\ell X}$ = X-axis component for the force $P_{girder\text{-}\ell}$;

$P_{girder\text{-}\ell Z}$ = Z-axis component for the force $P_{girder\text{-}\ell}$;

$P_{igC1\text{-}\ell}$ = axial force in the first interior girder near Corner 1 of the abutment that is induced by the passive-soil pressure forces, which act on Sidewall 1 and Wingwall 1, and by the Sidewall 1 pile forces;

$P_{igC2\text{-}\ell}$ = axial force in the first interior girder near Corner 2 of the abutment that is induced by the passive-soil pressure forces, which act on Sidewall 2 and Wingwall 2, and by the Sidewall 2 pile forces;

$P_{\ell'}$ = girder axial force that was resolved at a point on the front face of the abutment backwall and at an elevation that matches the center of gravity y_{ncg};

P_{max} = maximum, concentrated load at the mid-span of a beam;

P_n = nominal-bearing strength of the concrete;
= nominal, compressive resistance for an abutment pile;

$P_{piernorm}$ = pier force that acts normal to longitudinal axis of a pier;

$P_{pierparal}$ = pier force that acts parallel to longitudinal axis of a pier;

$P_{pile\text{-}Y}$ = total of the force components at the abutment-end of a pile that act along the Y-axis for an abutment;

$P_{pile\text{-}h}$ = axial force at the top of an abutment pile;
= first-order, factored-level, axial force at the top of an abutment pile;

$P_{pile\text{-}z}$ = axial force in pile at the top of the pile;

P_r = factored-level, axial-compressive resistance when only axial load is present for an abutment pile ($P_r = \phi_c P_n$);

$P_{swC1\text{-}\ell}$ = Sidewall 1 axial force at the effective, critical-moment, cross section and that acts along the ℓ-axis direction of the bridge superstructure;

$P_{swC2\text{-}\ell}$ = Sidewall 2 axial force at the effective, critical-moment, cross section and that acts along the ℓ-axis direction of the bridge superstructure;

P_u = factored-level, axial-compressive load for an abutment pile;

P_{uY} = factored-level for the internal force P_Y;

P_{uZ1} = factored-level for the force P_{Z1};

$P_{uZ1.5}$ = factored-level for the force $P_{Z1.5}$;

P_{uZ2} = factored-level for the force P_{Z2};

$P_{u\ell'}$ = factored-level for the force $P_{\ell'}$;

P_{up} = upward, concentrated load at the mid-span of a beam;

$P_{upile\text{-}Y}$ = factored-level for pile force $P_{pile\text{-}Y}$;

P_Z = axial force in the integral abutment that is caused by the soil and pile forces that act on the sidewall, sidewall-pile cap, and wingwall near Corner 1;

R = original gage resistance for a strain gage;
= rib shortening effect;
= relative-stiffness factor for a pile in soil;
= inelastic-curvature, capacity factor;

R_{XC1} = total, X-axis component for the forces $R_{\ell C1}$ and R_{tC1};

R_{XC2} = total, X-axis component for the forces $R_{\ell C2}$ and R_{tC2};

R_{YC1} = resultant, internal, vertical-support reaction for the horizontally-cantilevered sidewall and wingwall near Corner 1 of the abutment;

R_{YC2} = resultant, internal, vertical-support reaction for the horizontally-cantilevered sidewall and wingwall near Corner 2 of the abutment;

R_{ZC1} = total, Z-axis component for the forces $R_{\ell C1}$ and R_{tC1};

R_{ZC2} = total, Z-axis component for the forces $R_{\ell C2}$ and R_{tC2};

R_n = nominal resistance;

$R_{\ell C1}$ = resultant, internal, longitudinal-support reaction, which acts parallel to the ℓ-axis of the bridge superstructure, for the horizontally-cantilevered sidewall and wingwall near Corner 1 of the abutment;

$R_{\ell C2}$ = resultant, internal, longitudinal-support reaction, which acts parallel to the ℓ-axis of the bridge superstructure, for the horizontally-cantilevered sidewall and wingwall near Corner 2 of the abutment;

R_{tC1} = resultant, internal, transverse-support reaction, which acts parallel to the t-axis of the bridge superstructure, for the horizontally-cantilevered sidewall and wingwall near Corner 1 of the abutment;

R_{tC2} = resultant, internal, transverse-support reaction, which acts parallel to the t-axis of the bridge superstructure, for the horizontally-cantilevered sidewall and wingwall near Corner 2 of the abutment;

R_u	=	factored-level-load effect;
	=	relative-initial, stiffness factor;
S	=	Initial, non-dimensionalized slope of a design curve for the lateral stiffness of a backfill soil;
	=	shrinkage;
S_{east}	=	initial, non-dimensionalized slope S of a design curve for the lateral stiffness of the soil behind the east abutment at the Story County Bridge;
S_{gage}	=	strain-gage factor;
S_{ni}	=	lateral stiffness of the ith pile in the direction that is normal to the length of the abutment;
S_{norm}	=	horizontal stiffness of a pier in the direction that is normal to the length of the pier;
$S_{norm\ j}$	=	horizontal stiffness of the jth "fixed" pier in the direction that is normal to the vertical plane (elevation view) of the pier;
S_{north}	=	initial, non-dimensionalized slope S of a design curve for the lateral stiffness of the soil behind the north abutment at the Guthrie County Bridge;
S_{paral}	=	horizontal stiffness of a pier in the direction that is parallel to the length of the pier;
$S_{paral\ j}$	=	horizontal stiffness of the jth "fixed" pier in the direction that is parallel to the vertical plane (elevation view) of the pier;
S_{pi}	=	lateral stiffness of the ith pile in the direction that is parallel to the length of the abutment;
S_s	=	lateral stiffness of the wingwall pile in the direction that is normal to the length of the wingwall;
S_{south}	=	initial, non-dimensionalized slope S of a design curve for the lateral stiffness of the soil behind the south abutment at the Guthrie County Bridge;
S_w	=	lateral stiffness of the wingwall pile in the direction that is parallel to the length of the wingwall;

S_{west}	=	initial, non-dimensionalized slope S of a design curve for the lateral stiffness of the soil behind the west abutment at the Story County Bridge;
S_x	=	elastic-section modulus with respect to the x-axis of a pile cross section;
S_y	=	elastic-section modulus with respect to the y-axis of a pile cross section;
SF	=	streams-flow pressure;
T	=	temperature effect;
T_{ave}	=	average, bridge temperature;
$T_{construction}$	=	mean, construction temperature for the bridge;
T_{cr}	=	concrete-cracking, torsional-moment strength;
T_j	=	temperature measured by a thermocouple in a particular region in the total cross section for the bridge superstructure;
$T_{max\ air}$	=	experimentally-measured, maximum, air temperature for the hottest day;
$T_{max\ ave}$	=	maximum, average, bridge temperature for the concrete superstructure;
$T_{max\ shade}$	=	maximum, air temperature that is measured in the shade;
$T_{min\ air}$	=	experimentally-measured, minimum, air temperature for the coldest day;
$T_{min\ ave}$	=	minimum, average, bridge temperature for the concrete superstructure;
$T_{min\ shade}$	=	minimum, air temperature that is measured in the shade;
T_{nZ}	=	nominal, torsional strength about the Z-axis for an abutment cross section;
T_u	=	factored-lever torsional moment;
T_{uZ}	=	factored-level, torsional moment about the Z-axis for an abutment cross section;

V	=	horizontal force at the joint between the pile cap and the backwall;
	=	vertical force at the top of a pile;
V_A	=	shear stress at Point A in the abutment backwall behind a PC girder;
V_C	=	shear stress at Point C in the abutment backwall behind a PC girder;
V_X	=	internal-shear force in the X-axis direction for an abutment;
	=	internal, horizontal-shear force along the X-axis of an abutment at the joint between an abutment backwall and the abutment-pile cap;
V_{X1}	=	transverse-shear force in the abutment at Cross Section 1;
$V_{X1'}$	=	transverse-shear force in the abutment at Cross Section 1';
$V_{X1.5}$	=	transverse-shear force in the abutment at Cross Section 1.5;
V_{X2}	=	transverse-shear force in the abutment at Cross Section 2;
V_{Xi}	=	transverse-shear force in the abutment at the ith cross section;
V_Y	=	internal-shear force in the Y-axis direction for an abutment;
V_{Y1}	=	vertical-shear force in the abutment at Cross Section 1;
$V_{Y1'}$	=	vertical-shear force in the abutment at Cross Section 1';
$V_{Y1.5}$	=	vertical-shear force in the abutment at Cross Section 1.5;
V_{Y2}	=	vertical-shear force in the abutment at Cross Section 2;
V_{Yi}	=	vertical-shear force in the abutment at the ith cross section;
V_Z	=	internal, horizontal-shear force along the Z-axis of an abutment at the joint between an abutment backwall and the abutment-pile cap;
V_c	=	nominal shear strength of the concrete;
V_{eXC1}	=	internal, member-end shear force in the abutment for the first horizontal span of the backwall and backwall-pile cap between the exterior and the first interior girder near Corner 1 of the abutment;

V_{eXC2} = internal, member-end shear force in the abutment for the first horizontal span of the backwall and backwall-pile cap between the exterior and the first interior girder near Corner 2 of the abutment;

V_{eYC1} = internal, member-end shear force for the first, horizontal span of the composite, backwall and backwall-pile cap between the exterior girder and first-interior girder near Corner 1 of the abutment;

V_{eYC2} = internal, member-end shear force for the first, horizontal span of the composite, backwall and backwall-pile cap between the exterior girder and first-interior girder near Corner 2 of the abutment;

$V_{egC1\text{-}Y}$ = shear force in the exterior girder that is induced by the force couple that consists of the vertical reactions for the exterior and the first interior girder that is assumed to resist the torque $M_{\ell 12}$;

$V_{egC2\text{-}Y}$ = shear force in the exterior girder that is induced by the force couple that consists of the vertical reactions for the exterior and the first interior girder that is assumed to resist the torque $M_{\ell C2}$;

$V_{girder\text{-}Y}$ = total of the force components at the abutment-end of a PC girder that act along the Y-axis for an abutment;

$V_{girder\text{-}Z}$ = total of the force components at the abutment-end of a PC girder that act along the Z-axis for an abutment;

$V_{girder\text{-}h}$ = vertical-shear force at the abutment-end for a PC girder;

$V_{girder\text{-}t}$ = transverse-shear force at the abutment-end of a PC girder;

$V_{girder\text{-}tX}$ = X-axis component for the force $V_{girder\text{-}t}$;

$V_{girder\text{-}tZ}$ = Z-axis component for the force $V_{girder\text{-}t}$;

V_{iXC1} = internal, member-end shear force in the abutment for the second horizontal span of the backwall and backwall-pile cap between the first and the second interior girder near Corner 1 of the abutment;

V_{iXC2} = internal, member-end shear force in the abutment for the second horizontal span of the backwall and backwall-pile cap between the first and the second interior girder near Corner 2 of the abutment;

V_{iYC1} = internal, member-end shear force for the second, horizontal span of the composite, backwall and backwall-pile cap between the first-interior girder and second-interior girder near Corner 1 of the abutment;

V_{iYC2} = internal, member-end shear force for the second, horizontal span of the composite, backwall and backwall-pile cap between the first-interior girder and second-interior girder near Corner 2 of the abutment;

$V_{igC1\text{-}Y}$ = shear force in the first-interior girder that is induced by the force couple that consists of the vertical reactions for the exterior and the first interior girder that is assumed to resist the torque $M_{\ell 12}$;

$V_{igC2\text{-}Y}$ = shear force in the first-interior girder that is induced by the force couple that consists of the vertical reactions for the exterior and the first interior girder that is assumed to resist the torque $M_{\ell C2}$;

$V_{h'}$ = girder-shear force that acts parallel to the h-axis of the bridge superstructure and was resolved at a point on the front face of the abutment backwall and at an elevation that matches the center of gravity y_{ncg};

$V_{t'}$ = girder-shear force that acts parallel to the t-axis of the bridge superstructure and was resolved at a point on the front face of the abutment backwall and at an elevation that matches the center of gravity y_{ncg};

V_{nX} = nominal, shear strength in the X-axis direction for an abutment;

V_{nY} = nominal, shear strength in the Y-axis direction for an abutment;

$V_{pile\text{-}X}$ = total of the force components at the abutment-end of a pile that act along the X-axis for an abutment;

$V_{pile\text{-}Z}$ = total of the force components at the abutment-end of a pile that act along the Z-axis for an abutment;

$V_{pile\text{-}\ell}$ = ℓ-axis, shear force at the top of an abutment pile;

$V_{pile\text{-}\ell X}$ = X-axis component of the shear force $V_{pile\text{-}\ell}$;

$V_{pile\text{-}\ell Z}$ = Z-axis component of the force $V_{pile\text{-}\ell}$;

$V_{pile\text{-}t}$ = t-axis, shear force at the top of an abutment pile;

$V_{pile\text{-}tX}$ = X-axis component of the shear force $V_{pile\text{-}t}$;

$V_{pile\text{-}tZ}$ = Z-axis component of the shear force $V_{pile\text{-}t}$;

$V_{pile\text{-}x}$ = x-axis, shear force in a pile at the top of a pile;

$V_{pile\text{-}xX}$ = X-axis component of the force $V_{pile\text{-}x}$;

$V_{pile\text{-}xZ}$ = Z-axis component of the force $V_{pile\text{-}x}$;

$V_{pile\text{-}y}$ = y-axis, shear force in a pile at the top of a pile;

$V_{pile\text{-}yX}$ = X-axis component of the force $V_{pile\text{-}y}$;

$V_{pile\text{-}yZ}$ = Z-axis component of the force $V_{pile\text{-}y}$;

V_{px} = lateral loads (x-axis-shear force in the pile that correspond to the plastic-moment resistances of the pile for y-axis bending at the top of a pile;

V_{py} = lateral loads (y-axis-shear force in the pile that correspond to the plastic-moment resistances of the pile for x-axis bending at the top of a pile;

$V_{sw1p\text{-}\ell}$ = Sidewall 1, pile-shear force that acts in a direction that is parallel to the ℓ-axis for the bridge superstructure;

$V_{sw1p\text{-}t}$ = Sidewall 1, pile-shear force that acts in a direction that is parallel to the t-axis for the bridge superstructure;

$V_{sw2p\text{-}\ell}$ = Sidewall 2, pile-shear force that acts in a direction that is parallel to the ℓ-axis for the bridge superstructure;

$V_{sw2p\text{-}t}$ = Sidewall 2, pile-shear force that acts in a direction that is parallel to the t-axis for the bridge superstructure;

$V_{swC1\text{-}t}$ = Sidewall 1 shear force at the effective, critical-moment, cross section and that acts along the t-axis direction for the bridge superstructure;

$V_{swC1\text{-}Y}$ = Sidewall 1 shear force at the effective, critical-moment, cross section and that acts along the Y-axis direction for the backwall;

$V_{swC2\text{-}t}$ = Sidewall 2 shear force at the effective, critical-moment, cross section and that acts along the t-axis direction for the bridge superstructure;

$V_{swC2\text{-}Y}$	=	Sidewall 2 shear force at the effective, critical-moment, cross section and that acts along the Y-axis direction for the backwall;
V_u	=	factored-level shear force that acts on the concrete-punching-shear failure surface;
V_{uX}	=	factored-level, shear force in the X-axis direction for an abutment;
V_{uXmax}	=	maximum of the factored-level, shear forces that act along the X-axis of an abutment at Cross Sections 1, 1.5, and 2;
V_{uX1}	=	factored-level for the shear force V_{X1};
$V_{uX1.5}$	=	factored-level for the shear force $V_{X1.5}$;
V_{uX2}	=	factored-level for the shear force V_{X2};
V_{uY}	=	factored-level, shear force in the Y-axis direction for an abutment;
V_{uY1}	=	factored-level for the shear force V_{Y1};
$V_{uY1.5}$	=	factored-level for the shear force $V_{Y1.5}$;
V_{uY2}	=	factored-level for the shear force V_{uY2};
V_{uZ}	=	factored-level, shear force in the Z-axis direction for an abutment;
$V_{uh'}$	=	factored-level for the force $V_{h'}$;
$V_{ugirder\text{-}Y}$	=	factored-level for the shear force $V_{girder\text{-}Y}$;
$V_{upile\text{-}X}$	=	factored-level for the pile force $V_{pile\text{-}X}$;
$V_{upile\text{-}Z}$	=	factored-level for the pile moment $V_{pile\text{-}Z}$;
$V_{ut'}$	=	factored-level for the force $V_{t'}$;
V/S	=	volume-to-surface-area ratio for the member;
W	=	wind load on the structure;
	=	bridge width;
	=	uniform load that acts on a deep beam;

W_{DL1} = uniform, dead load on the bridge superstructure that is present before the abutment pile cap and backwall form a composite member;

W_{DL2} = uniform, dead load on the bridge superstructure that is present after the abutment pile cap and backwall form a composite member;

W_{I} = uniform, impact load on the bridge superstructure;

W_{LL} = uniform, live load on the bridge superstructure;

W_{abut} = uniform, self-weight of an abutment pile cap and backwall;

$W_{soil\text{-}X}$ = passive-soil-pressure force per unit length of the backwall;

$W_{sw1s\text{-}t}$ = passive-soil-pressure force per unit length of Sidewall 1;

$W_{sw1w\text{-}Y}$ = self-weight per unit length of Sidewall 1;

$W_{sw1wcap\text{-}Y}$ = self-weight per unit length of the pile cap for Sidewall 1;

$W_{sw2s\text{-}Z}$ = passive-soil-pressure force per unit length of the trapped that is adjacent to Sidewall 2;

$W_{sw2w\text{-}Y}$ = self-weight per unit length of Sidewall 2;

$W_{sw2wcap\text{-}Y}$ = self-weight per unit length of the pile cap for Sidewall 2;

$W_{soil\text{-}friction\text{-}Z}$ = soil-frictional force per unit length of the abutment;

W_{uabut} = factored-level for the abutment weight W_{abut};

$W_{usoil\text{-}X}$ = factored-level for the soil force $W_{soil\text{-}X}$;

$W_{usoil\text{-}friction\text{-}Z}$ = factored-level for the soil force $W_{soil\text{-}friction\text{-}Z}$;

$W_{ww1sa\text{-}t}$ = passive-soil-pressure force per unit length of Wingwall 1 at the construction joint with Sidewall 1;

$W_{ww1sb\text{-}t}$ = passive-soil-pressure force per unit length of Wingwall 1 at the free end of the wingwall;

$W_{ww1wa\text{-}Y}$ = self-weight per unit length of Wingwall 1 at the connection to the sidewall;

$W_{ww1wb\text{-}Y}$ = self-weight per unit length of Wingwall 1 at the free end of the wingwall;

$W_{ww2sa\text{-}Z}$ = passive-soil-pressure force per unit length of the trapped soil that is adjacent to Wingwall 2 at the construction joint with Sidewall 2;

$W_{ww2wa\text{-}Y}$ = self-weight per unit length of Wingwall 2 at the connection to the sidewall;

$W_{ww2wb\text{-}Y}$ = self-weight per unit length of Wingwall 2 at the free end of the wingwall;

$W_{ww2sb\text{-}Z}$ = passive-soil-pressure force per unit length of the trapped soil that is adjacent to Wingwall 2 at the free end of the wingwall;

WL = wind load on the live load (100 pounds per linear foot);

X = abutment-coordinate axis that is normal to the abutment face;

Y = abutment-coordinate axis that is parallel to the abutment height;
= horizontal displacement at the top of a wall;

Z = abutment coordinate axis that is along the abutment width;

Z_x = x-axis, plastic-section modulus for a pile;

Z_y = y-axis, plastic-section modulus for a pile;

a = one half of the difference between the dimensions B and c;

a_1 = difference between the length ℓ_o and the depth d_1;

a_2 = difference between the length ℓ_o and the sum of the depths d_1 and d_2;

a_p = effective height of concrete-bearing region, which is the height of the “Whitney-Stress-Block” that is associated with the concrete, flexural-compressive strength;

a_{p1} = a_p for concrete-bearing stresses q_{1t1} and q_{2t1};

a_{p2} = a_p for concrete-bearing stresses q_{1t2};

a_{p3} = a_p for concrete-bearing stresses q_{2t2};

b = concrete-bearing width;

b_o	=	perimeter of the failure surface for a concrete-punching-shear failure;
b_1	=	effective-bearing width for the concrete-bearing stresses q_{1h};
b_2	=	effective-bearing width for the concrete-bearing stresses q_{2h};
b_{bf}	=	width of the bottom flange for a PC girder;
b_f	=	flange width for an I-shaped beam;
	=	flange width for an HP-shaped pile;
b_{tf}	=	width of the top flange for a PC girder;
b_o	=	perimeter of the concrete-failure surface
c	=	center-to-center spacing of the backwall piles;
	=	depth or width of a beam cross section;
c_3	=	one-half of the dimension a_2;
c_{AB}	=	distance from the centroidal axis for the three-sided, shearing planes to Points A and B;
c_{CD}	=	distance from the centroidal axis for the three-sided, shearing planes to Points C and D;
c_a	=	adhesion between a pile and a clay soil;
$c_{bwp\text{-}t}$	=	distance from the outside face of the sidewall-pile cap to the center of the end backwall pile that is measured along the transverse direction of the bridge superstructure;
c_c	=	concrete clear cover;
$c_{girderC1\text{-}\ell}$	=	distance from the front edge of the sidewall to the center of bearing for an exterior girder that is measured along the ℓ-axis direction for the bridge superstructure at Corner 1 of an abutment;
$c_{girderC1\text{-}t}$	=	distance from the outside face of an abutment sidewall to the center of bearing for an exterior girder that is measured along the t-axis direction for the bridge superstructure at Corner 1 of an abutment;

$c_{girderC2\text{-}\ell}$ = distance from the front edge of the sidewall to the center of bearing for an exterior girder that is measured along the ℓ-axis direction for the bridge superstructure at Corner 2 of an abutment;

$c_{girderC2\text{-}t}$ = distance from the outside face of an abutment sidewall to the center of bearing for an exterior girder that is measured along the t-axis direction for the bridge superstructure at Corner 2 of an abutment;

$c_{pile\text{-}t}$ = distance from the outside face of a sidewall to the center of an end, backwall pile that is measured along the t-axis for the bridge;

$c_{swp\text{-}\ell}$ = distance from the end of a sidewall-pile cap to the center of gravity for a sidewall pile that is measured along the ℓ-axis direction for a bridge superstructure;

$c_{swp\text{-}t}$ = distance from the end of a sidewall-pile cap to the center of gravity for a sidewall pile that is measured along the t-axis direction for a bridge superstructure;

c_u = cohesion from an unconsolidated, undrained test;

d = depth of an I-shaped beam;
= depth of an HP-shaped pile;
= effective depth of an abutment backwall for through-thickness bending of the backwall;

d_1 = depth for the first soil layer within the length ℓ_o;

d_2 = depth for the second soil layer within the length ℓ_o;

d_3 = depth for the third soil layer within the length ℓ_o;

d_{c2i} = distance from the ith backwall pile to Corner 2;

d_{eff} = effective depth to the centroid of the tension reinforcement;
= average of the effective depths d_{eff1} and d_{eff2};

d_{eff1} = maximum effective depth at the end of a PC girder to the centroid of the tension reinforcement in the abutment backwall;

d_{eff2} = minimum effective depth at the end of a PC girder to the centroid of the tension reinforcement in the abutment backwall;

d_{emb} = pile-embedment depth into the bottom of a pile cap;

dR_1	=	relative displacement at Corner 1 of an abutment when a horizontal rotation, β, of the bridge superstructure occurs about the "point-of fixity" for the bridge;
$dR_{1\ell}$	=	displacement component, which is directed along the longitudinal direction of the bridge, for the relative displacement dR_1;
dR_{1n}	=	displacement component that is directed normal to the abutment length of the relative displacement dR_1;
dR_{1p}	=	displacement component that is directed parallel to the abutment length of the relative displacement dR_1;
dR_{1t}	=	displacement component, which is directed along the transverse directions of the bridge, for the relative displacement dR_1;
dR_2	=	relative displacement at Corner 2 of an abutment when a horizontal rotation, β, of the bridge superstructure occurs about the "point-of fixity" for the bridge;
$dR_{\ell 2}$	=	displacement component that is directed along the longitudinal direction of the bridge for the relative displacement dR_2;
dR_{n2}	=	displacement component that is directed to the abutment length of the relative displacement dR_2;
dR_{p2}	=	displacement component that is directed parallel to the abutment length of the relative displacement dR_2;
dR_{t2}	=	displacement component that is directed along the transverse direction of the bridge for the relative displacement dR_2;
$d\ell$	=	abutment displacement in the longitudinal direction of a bridge;
$d\ell_1$	=	longitudinal displacements at Corner 1 of an integral abutment;
$d\ell_2$	=	longitudinal displacements at Corner 2 of an integral abutment;
$d\ell_{contract}$	=	maximum displacement of the abutment along the longitudinal direction of the bridge during initial contraction of the bridge;
	=	maximum displacement of the abutment along the longitudinal direction of the bridge for bridge contraction from the point of maximum-initial expansion;
	=	absolute, horizontal displacement along the longitudinal direction for a bridge of a pile head from its original non-displaced position for a contraction of a bridge superstructure;

$d\ell_{expand}$	=	maximum displacement of the abutment along the longitudinal direction of the bridge during the initial expansion of the bridge;
	=	maximum displacement of the abutment along the longitudinal direction of the bridge for bridge expansion from the point of maximum, initial contraction;
	=	absolute, horizontal displacement along the longitudinal direction for a bridge of a pile head from its original nondisplaced position for a expansion of a bridge superstructure;
$d\ell_i$	=	displacement of the ith backwall pile in the longitudinal direction of the bridge;
$d\ell_n$	=	displacement component that is directed normal to the abutment length of the length $d\ell$;
$d\ell_p$	=	displacement components that is directed parallel to the abutment length of the length $d\ell$;
$d\ell_{re\text{-}contract}$	=	maximum displacement of the abutment along the longitudinal direction of the bridge during the re-contraction of the bridge from the point of maximum expansion;
$d\ell_{re\text{-}expand}$	=	maximum displacement of the abutment along the longitudinal direction of the bridge during the re-expansion of the bridge from the point of maximum contraction;
	=	absolute, horizontal displacement along the longitudinal direction for a bridge for a pile head from its original un-displaced position for a re-expansion of a bridge superstructure;
dP_{s1}	=	horizontal displacements of the abutment in the longitudinal direction of the bridge at the mid-length of Sidewall and Wingwall 1;
dP_{s2}	=	horizontal displacements of the abutment in the longitudinal direction of the bridge at the mid-length of Sidewall and Wingwall 2;
dn_1	=	normal displacement at Corner 1 of an integral abutment;
dn_2	=	normal displacement at Corner 2 of an integral abutment;
dn_3	=	normal displacement at the mid-length of an abutment;
dp_1	=	parallel displacement at Corner 1 of an integral abutment;
dp_2	=	parallel displacement at Corner 2 of an integral abutment;

dt	=	abutment displacement in the transverse direction of a bridge;
dt_1	=	transverse displacement at Corner 1 of an integral abutment;
dt_2	=	transverse displacement at Corner 2 of an integral abutment;
dt_3	=	transverse displacement at the mid-length of an abutment;
dt_i	=	displacement of the ith backwall pile in the transverse direction of the bridge;
dt_{max}	=	maximum displacement for the displacement dt;
dt_o	=	transverse displacement of an abutment that is induced by the at-rest-soil pressure behind the abutments;
dt_{s1}	=	horizontal displacements of the abutment in the transverse direction of the bridge at the mid-length of Sidewall and Wingwall 1;
dt_{s2}	=	horizontal displacements of the abutment in the transverse direction of the bridge at the mid-length of Sidewall and Wingwall 2;
dx_i	=	horizontal displacement pile at the top of the ith backwall pile along the x-axis for the cross section;
dy_i	=	horizontal displacement pile at the top of the ith backwall pile along the y-axis for the cross section;
e	=	shear-span length for a deep beam;
e_{gY}	=	vertical eccentricity of the girder-end forces with respect to the centroid of an abutment cross section;
e_h	=	vertical eccentricity of the girder-end forces from the assumed axes of zero-strain bending for the concrete-bearing stresses q_{1t2} and q_{2t2};
e_ℓ	=	horizontal eccentricity of the girder-end forces from the assumed axes of zero-strain bending for the concrete-bearing stresses q_{1t1} and q_{2t1};
e_{pY}	=	vertical eccentricity of the pile-end forces with respect to the centroid of an abutment cross section;
e_{sX}	=	horizontal eccentricity of the soil-frictional force with respect to the centroid of an abutment cross section;

e_{sY} = vertical eccentricity of the soil pressure with respect to the centroid of an abutment cross section;

$e_{sw1p\text{-}\ell}$ = horizontal eccentricity of the pile force $V_{sw1p\text{-}t}$, with respect to the center of bearing for the exterior girder near Corner 1 of the abutment;

$e_{sw1p\text{-}t}$ = horizontal eccentricity of the pile force $V_{sw1p\text{-}\ell}$, with respect to the center of bearing for the exterior girder near Corner 1 of the abutment;

$e_{sw2p\text{-}\ell}$ = horizontal eccentricity of the pile force $V_{sw2p\text{-}t}$, with respect to the center of bearing for the exterior girder near Corner 2 of the abutment;

$e_{sw2p\text{-}t}$ = horizontal eccentricity of the pile force $V_{sw2p\text{-}\ell}$, with respect to the center of bearing for the exterior girder near Corner 2 of the abutment;

$e_{sw1s\text{-}\ell}$ = horizontal eccentricity of the soil force $W_{sw1s\text{-}t}$, with respect to the center of bearing for the exterior girder near Corner 1 of the abutment;

$e_{sw2s\text{-}X}$ = horizontal eccentricity of the soil force $W_{sw2s\text{-}Z}$, with respect to the center of bearing for the exterior girder near Corner 2 of the abutment;

$e_{ww1sa\text{-}\ell}$ = horizontal eccentricity of the soil force $W_{ww1sa\text{-}t}$, with respect to the center of bearing for the exterior girder near Corner 1 of the abutment;

$e_{ww1sb\text{-}\ell}$ = horizontal eccentricity of the soil force $W_{ww1sb\text{-}t}$, with respect to the center of bearing for the exterior girder near Corner 1 of the abutment;

$e_{ww2sa\text{-}X}$ = horizontal eccentricity of the soil force $W_{ww2sa\text{-}Z}$, with respect to the center of bearing for the exterior girder near Corner 2 of the abutment;

$e_{ww2sb\text{-}X}$ = horizontal eccentricity of the soil force $W_{ww2sb\text{-}Z}$, with respect to the center of bearing for the exterior girder near Corner 2 of the abutment;

e_X = distance between the ℓth-coordinate axes and the ℓ’t’h’-coordinate axes that is measured along the X-axis of the abutment;

e_Z = distance between the ℓth-coordinate axes and the ℓ't'h'-coordinate axes that is measured along the Z-axis of the abutment;

$e1_{sw1p\text{-}Y}$ = Yℓ-plane and Yt-plane, vertical eccentricity for Sidewall 1, pile forces $V_{sw1p\text{-}\ell}$ and $V_{sw1p\text{-}t}$, respectively, with respect to the effective, critical-moment cross section;

$e1_{sw1p\text{-}\ell}$ = XZ-plane, horizontal eccentricity for Sidewall 1, pile force $V_{sw1p\text{-}t}$ with respect to the effective, critical-moment cross section;

$e1_{sw1p\text{-}t}$ = XZ-plane, horizontal eccentricity for Sidewall 1, pile force $V_{sw1p\text{-}\ell}$ with respect to the effective, critical-moment cross section;

$e1_{sw1s\text{-}Y}$ = Yt-plane, vertical eccentricity for Sidewall 1, soil force $W_{sw1s\text{-}t}$ with respect to the effective, critical-moment cross section;

$e1_{sw1s\text{-}\ell}$ = XZ-plane, horizontal eccentricity for Sidewall 1, soil force $W_{sw1s\text{-}t}$ with respect to the effective, critical-moment cross section;

$e1_{sw1w\text{-}\ell}$ = Yℓ-plane, horizontal eccentricity for Sidewall 1, self-weight force $W_{sw1w\text{-}Y}$ with respect to the effective, critical-moment cross section;

$e1_{sw1w\text{-}t}$ = Yt-plane, horizontal eccentricity for Sidewall 1, self-weight force $W_{sw1w\text{-}Y}$ with respect to the effective, critical-moment cross section;

$e1_{sw1wcap\text{-}\ell}$ = Yℓ-plane, horizontal eccentricity for Sidewall 1 pile cap, self-weight force $W_{sw1wcap\text{-}Y}$ with respect to the effective, critical-moment cross section;

$e1_{sw1wcap\text{-}t}$ = Yt-plane, horizontal eccentricity for Sidewall 1 pile cap, self-weight force $W_{sw1wcap\text{-}Y}$ with respect to the effective, critical-moment cross section;

$e1_{sw2p\text{-}Y}$ = Yℓ-plane and Yt-plane, vertical eccentricity for Sidewall 2, pile forces $V_{sw2p\text{-}\ell}$ and $V_{sw2p\text{-}t}$, respectively, with respect to the effective, critical-moment cross section;

$e1_{sw2p\text{-}\ell}$ = XZ-plane, horizontal eccentricity for Sidewall 2, pile force $V_{sw2p\text{-}t}$ with respect to the effective, critical-moment cross section;

$e1_{sw2p\text{-}t}$ = XZ-plane, horizontal eccentricity for Sidewall 2, pile force $V_{sw2p\text{-}\ell}$ with respect to the effective, critical-moment cross section;

$e1_{sw2s\text{-}Y}$ = Yt-plane, vertical eccentricity for Sidewall 2, trapped-soil force $W_{sw2s\text{-}Z}$ with respect to the effective, critical-moment cross section;

$e1_{sw2s\text{-}X}$ = XZ-plane, horizontal eccentricity for Sidewall 2, trapped-soil force $W_{sw2s\text{-}Z}$ with respect to the effective, critical-moment cross section;

$e1_{sw2w\text{-}\ell}$ = Yℓ-plane, horizontal eccentricity for Sidewall 2, self-weight force $W_{sw2w\text{-}Y}$ with respect to the effective, critical-moment cross section;

$e1_{sw2w\text{-}t}$ = Yt-plane, horizontal eccentricity for Sidewall 2, self-weight force $W_{sw2w\text{-}Y}$ with respect to the effective, critical-moment cross section;

$e1_{sw2wcap\text{-}\ell}$ = Yℓ-plane, horizontal eccentricity for Sidewall 2 pile cap, self-weight force $W_{sw2wcap\text{-}Y}$ with respect to the effective, critical-moment cross section;

$e1_{sw2wcap\text{-}t}$ = Yt-plane, horizontal eccentricity for Sidewall 2 pile cap, self-weight force $W_{sw2wcap\text{-}Y}$ with respect to the effective, critical-moment cross section;

$e1_{ww1sa\text{-}Y}$ = Yt-plane, vertical eccentricity for Wingwall 1, soil force $W_{ww1sa\text{-}t}$ with respect to the effective, critical-moment cross section;

$e1_{ww1sb\text{-}Y}$ = Yt-plane, vertical eccentricity for Wingwall 1, soil force $W_{ww1sb\text{-}t}$ with respect to the effective, critical-moment cross section;

$e1_{ww1sa\text{-}\ell}$ = XZ-plane, horizontal eccentricity for Wingwall 1, soil force $W_{ww1sa\text{-}t}$ with respect to the effective, critical-moment cross section;

$e1_{ww1sb\text{-}\ell}$ = XZ-plane, horizontal eccentricity for Wingwall 1, soil force $W_{ww1sb\text{-}t}$ with respect to the effective, critical-moment cross section;

$e1_{ww1wa\text{-}\ell}$ = Yℓ-plane, horizontal eccentricity for Wingwall 1, self-weight force $W_{ww1wa\text{-}Y}$ with respect to the effective, critical-moment cross section;

$e1_{ww1wa\text{-}t}$ = Yt-plane, horizontal eccentricity for Wingwall 1, self-weight force $W_{ww1wa\text{-}Y}$ with respect to the effective, critical-moment cross section;

$e1_{ww1wb\text{-}\ell}$ = Yℓ-plane, horizontal eccentricity for Wingwall 1, self-weight force $W_{ww1wb\text{-}Y}$ with respect to the effective, critical-moment cross section;

$e1_{ww1wb\text{-}t}$ = Yt-plane, horizontal eccentricity for Wingwall 1, self-weight force $W_{ww1wb\text{-}Y}$ with respect to the effective, critical-moment cross section;

$e1_{ww2sa\text{-}Y}$ = Yt-plane, vertical eccentricity for Wingwall 2, trapped-soil force $W_{ww2sa\text{-}Z}$ with respect to the effective, critical-moment cross section;

$e1_{ww2sb\text{-}Y}$ = Yt-plane, vertical eccentricity for Wingwall 2, trapped-soil force $W_{ww2sb\text{-}Z}$ with respect to the effective, critical-moment cross section;

$e1_{ww2sa\text{-}X}$ = XZ-plane, horizontal eccentricity for Wingwall 2, trapped-soil force $W_{ww2sa\text{-}Z}$ with respect to the effective, critical-moment cross section;

$e1_{ww2sb\text{-}X}$ = XZ-plane, horizontal eccentricity for Wingwall 2, trapped-soil force $W_{ww2sb\text{-}Z}$ with respect to the effective, critical-moment cross section;

$e1_{ww2wa\text{-}\ell}$ = Yℓ-plane, horizontal eccentricity for Wingwall 2, self-weight force $W_{ww2wa\text{-}Y}$ with respect to the effective, critical-moment cross section;

$e1_{ww2wa\text{-}t}$ = Yt-plane, horizontal eccentricity for Wingwall 2, self-weight force $W_{ww2wa\text{-}Y}$ with respect to the effective, critical-moment cross section;

$e1_{ww2wb\text{-}\ell}$ = Yℓ-plane, horizontal eccentricity for Wingwall 2, self-weight force $W_{ww2wb\text{-}Y}$ with respect to the effective, critical-moment cross section;

$e1_{ww2wb\text{-}t}$ = Yt-plane, horizontal eccentricity for Wingwall 2, self-weight force $W_{ww2wb\text{-}Y}$ with respect to the effective, critical-moment cross section;

f = vertical-skin-frictional resistance of the soil at a depth z along the pile length;

f_A = correction factor for the age of the concrete;

f_M = correction factor for the moisture content in the concrete;

f_T = correction factor for temperature conditions (1.0 for a controlled environment and 0.86 for an outside exposure);

f_c' = 28-day, concrete-compressive strength;

f_{ci} = compressive stress applied to the concrete;

f_s = calculated, service-level, tension stress in the reinforcement;

f_u = ultimate, vertical, skin-frictional resistance of the soil at the depth z along the pile length;

f_y = minimum-specified, yield strength for the reinforcement;

h = bridge-coordinate axis that is in the vertical direction;
= overall depth of a PC girder;
= wall height;
= overall depth of a deep beam;

h_1	=	soil-embankment height at Corner 1;
	=	soil-backfill height;
h_2	=	sidewall height at Corner 2;
h_{abut}	=	abutment height;
h_{cap}	=	abutment pile-cap height;
h_{girder}	=	PC-girder depth;
h_{wa}	=	wingwall height at the construction joint between the wingwall and the sidewall;
h_{wb}	=	wingwall height at the free end of the wingwall;
k	=	earth-pressure coefficient;
k_1	=	soil-pressure coefficients at Corner 1 of the abutment;
k_2	=	soil-pressure coefficients at Corner 2 of the abutment;
k_3	=	soil-pressure coefficient at the mid-width of an abutment;
k_a	=	Rankine's active-soil-pressure coefficient;
k_c	=	factor that accounts for the influence of the volume-to-surface-area ratio for the member;
k_e	=	equivalent, uniform, horizontal stiffness of the layered soil;
k_f	=	factor that accounts for the concrete strength;
k_h	=	initial, horizontal stiffness of the soil at the depth z along the pile length;
	=	humidity factor;
$k_h(z)$	=	variation of the stiffness k_h with soil depth;
k_o	=	Rankine's at-rest-soil-pressure coefficient;
k_p	=	Rankine's passive-soil-pressure coefficient;
k_{pmax}	=	maximum, passive-soil-pressure coefficient;

k_{pw1} = passive-soil pressure coefficients for the soil that acts against Sidewall 1 and Wingwall 1;

k_{pw2} = passive-soil pressure coefficients for the soil that acts against Sidewall 2 and Wingwall 2;

k_q = initial-vertical stiffness of the strata at the pile tip;

k_s = size factor;

k_x = flexural stiffness of an HP-shaped pile with respect to bending about the strong-axis (x-axis) of the pile cross section;

k_v = initial, vertical stiffness of the soil at the depth z along the pile length;
= flexural stiffness of an HP-shaped pile with respect to bending about the weak-axis (y-axis) of the pile cross section;

kn_1 = passive-soil-pressure coefficients for the soil pressures that act normal to the abutment backwall at Corner 1 of an abutment;

kn_2 = passive-soil-pressure coefficients for the soil pressures that act normal to the abutment backwall at Corner 2 of an abutment;

kn_3 = passive-soil-pressure coefficients for the soil pressures that act normal to the abutment backwall at the mid-point of the length $l_{pp\text{-}po}$ of an abutment;

ℓ = distance from the "point-of-fixity" for the bridge to an abutment (for a symmetric bridge, $\ell = L/2$);
= bridge-coordinate axis that is parallel to the bridge length;
= total pile length;
= span length for a deep beam;

ℓ' = length of a pile that is available to resist the vertical load by skin friction;

ℓ_{abut} = abutment length ($\ell_{abut} = W/\cos\theta$);

ℓ_c = depth of soil below which the horizontal displacement at the pile head has negligible effects on the transverse displacement of the pile and on the shear force and bending moment in the pile at that depth;

ℓ_e	=	equivalent-embedded length for the pile, which is the depth from the soil surface below the bottom of any pre-bored hole to the fixed base of the equivalent cantilever;
	=	end distance, which is measured along the ℓ-axis direction for the bridge superstructure, from the center of the abutment backwall to the end of a PC girder;
ℓ_{emb1}	=	smallest girder-embedment length into a skewed abutment backwall;
ℓ_{emb2}	=	largest girder-embedment length into a skewed abutment backwall;
ℓ_n	=	length of pile that is ineffective for skin-frictional resistance;
ℓ_o	=	active length for a pile in bending;
$\ell_{pp\text{-}po}$	=	length of the abutment that is subjected to passive-soil pressure;
ℓ_{sw1}	=	length of Sidewall 1;
ℓ_{sw1c}	=	horizontal-cantilever length of Sidewall 1;
ℓ_{sw2}	=	length of Sidewall 2;
ℓ_{sw2c}	=	horizontal-cantilever length of Sidewall 2;
ℓ_{w1}	=	length of the exterior face of the abutment that is parallel to the longitudinal direction of the bridge near Corner 1 of the abutment;
ℓ_{w2}	=	length of the exterior face of the abutment that is parallel to the longitudinal direction of the bridge near Corner 2 of the abutment;
ℓ_{ww1}	=	length of Wingwall 1;
ℓ_{ww2}	=	length of Wingwall 2;
ℓ_u	=	pile length above the undisturbed-soil strata, which includes the depth of a properly-filled, pre-bored hole;
n	=	number of regions in the total cross section for the bridge superstructure;
	=	shape parameter for the modified Ramberg-Osgood curve;
p	=	horizontal resistance of the soil at a depth z along the pile length;
	=	horizontal pressure of the soil at a depth h;

p_{cp} = perimeter of the concrete cross section;

p_o = at-rest-soil pressure that acts normal to the backwall of the abutment;

p_{p1} = the passive-soil pressure that acts normal to the backwall of the abutment at Corner 1;

p_{p2} = passive-soil pressure that acts normal to the backwall of the abutment at Corner 2;

p_{p3} = passive-soil pressure that acts normal to the backwall of the abutment at the mid-point of the length $P_{pp\text{-}po}$;

p_{pw1} = passive-soil pressure that acts normal to Sidewall and Wingwall 1 of the abutment;

p_{pw2} = passive-soil pressure that acts normal to Sidewall and Wingwall 2 of the abutment;

p_u = ultimate, horizontal resistance of the soil at the depth z along the pile length;

q = bearing resistance at the pile tip;

q_1 = concrete-bearing stress that acts normal to the sloped surface of the top flange for a PC girder;

q_2 = concrete-bearing stress that acts normal to the sloped surface of the bottom flange for a PC girder;

q_{1X} = concrete-bearing stress along the bottom half of the pile-embedment depth into the bottom of the abutment pile cap;

q_{1h} = concrete-bearing stresses, which correspond to the girder-shear force $V_{h'}$ and a bending moment $M_{t'}$, and that act near the front face of the abutment backwall;

q_{1t1} = concrete-bearing stresses that act on the sides of the embedded portion of a PC girder near the end of the girder and in a direction that is parallel to the t-axis of the bridge superstructure;

q_{1t2} = concrete-bearing stresses that act on the sides and near the top of the embedded portion of a PC girder and in a direction that is parallel to the t-axis of the bridge superstructure;

q_{2X} = concrete-bearing stress along the top half of the pile-embedment depth into the bottom of the abutment pile cap;

q_{2h} = concrete-bearing stresses, which correspond to the girder-shear force $V_{h'}$ and a bending moment $M_{t'}$, and that act near the end of the girder;

q_{2t1} = concrete-bearing stresses that act on the sides of the embedded portion of a PC girder near the front face of an abutment backwall and in a direction that is parallel to the t-axis of the bridge superstructure;

q_{2t2} = concrete-bearing stresses that act on the sides and near the bottom of the embedded portion of a PC girder and in a direction that is parallel to the t-axis of the bridge superstructure;

q_{3Y} = concrete-bearing stress that is induced by the pile axial load;

$q_{3\ell}$ = concrete-bearing stress which corresponds to the girder-axial force $P_{\ell'}$;

q_n = nominal concrete-bearing stress;

q_{n1} = non-confined, nominal, concrete-bearing-design stress;

q_{n2} = confined, nominal, concrete-bearing stress;

q_u = ultimate, bearing stress at the pile tip;

q_{u1} = concrete-bearing stresses and that act normal to the sloped inside face of the top flange;

q_{u1X} = factored-level for the concrete-bearing stress q_{1X};

q_{u1Z} = factored-level for the concrete-bearing stress q_{1Z};

q_{u1h} = factored-level for the concrete-bearing stress q_{1h};

q_{u1t} = total, factored-level, concrete-bearing stresses and that acts on the side of a girder and near the front face of an abutment backwall;

q_{u1t1} = factored-level for the concrete-bearing stress q_{1t1};

q_{u1t2} = factored-level for the concrete-bearing stress q_{1t2};

q_{u2} = concrete-bearing stresses and that act normal to the sloped inside face of the bottom flange;

q_{u2X} = factored-level for the concrete-bearing stress q_{2X};

q_{u2Z} = factored-level for the concrete-bearing stress q_{2Z};

q_{u2h} = factored-level for the concrete-bearing stress q_{2h};

q_{u2t} = total, factored-level, concrete-bearing stresses and that acts on the side of a girder and near the embedded end of a PC girder;

q_{u2t1} = factored-level for the concrete-bearing stress q_{2t1};

q_{u2t2} = factored-level for the concrete-bearing stress q_{2t2};

$q_{u3\ell}$ = factored-level for the concrete-bearing stress $q_{3\ell}$;

r_d = reinforcement-distribution factor;

s = spacing for the vertical reinforcement;

s_{girder} = center-to-center spacing for the PC girders;

t = bridge-coordinate axis that is parallel to the bridge width;
= number of days that the concrete was exposed to drying;

t_f = flange thickness for a I-shaped beam;
= flange thickness for an HP-shaped pile;

t_h = height of the concrete haunch between the underside of the slab and the top of the bridge girder;

t_s = thickness of the bridge deck;

t_w = web thickness for a I-shaped beam;
= web thickness for an HP-shaped pile;
= web thickness for a PC girder;

$w_{soil\ active}$ = active-soil pressure that acts at the bottom of the back face of the abutment pile cap;

$w_{soil\ passive}$ = passive-soil pressure that acts at the bottom of the back face of the abutment pile cap;

$w_{soil\text{-}X}$ = active or passive-soil pressure at the bottom of the back face of the abutment;

$w_{soil\text{-}X\ell L}$ = ℓ-axis component of the soil pressure $w_{soil\text{-}X}$ at left abutment;

$w_{soil\text{-}X\ell R}$ = ℓ-axis component of the soil pressure $w_{soil\text{-}X}$ at right abutment;

$w_{soil\text{-}Z}$ = passive-soil pressure that acts at the bottom of Sidewall 2;

$w_{soil\text{-}t}$ = passive-soil pressure that acts at the bottom of Sidewall 1;

$w_{usoil\text{-}X}$ = factored-level for the soil pressure $w_{soil\text{-}X}$;

x = pile-coordinate axis that is parallel to the pile flanges;
= transverse distance between Corner 2 and the location along the length of the abutment where the soil pressure is equal to the at-rest-soil pressure;

x_{sw1cg} = horizontal distance from the outside face of Sidewall 1 to the center of gravity for a Yt-plane cross section of the composite sidewall and sidewall-pile cap near Corner 1 of the abutment;

x_{sw2cg} = horizontal distance from the outside face of Sidewall 2 to the center of gravity for a Yt-plane cross section of the composite sidewall and sidewall-pile cap near Corner 2 of the abutment;

y = pile-coordinate axis that is within the plane of the pile web;
= horizontal displacement of the pile at a depth z along the pile length;

y_{50} = displacement at one-half of the ultimate-soil reaction;

y_{cg} = vertical distance from the top of the bridge deck to the center of gravity for the composite bridge girder;

y_{max} = maximum, lateral displacement below which the skin friction of the pile remains effective;

y_{ncg} = vertical distance from the top of the bridge deck to the center of gravity for the non-composite bridge girder;

y_{sw1cg} = vertical distance from the top face of Sidewall 1 to the center of gravity for a Yt-plane cross section of the composite sidewall and sidewall-pile cap near Corner 1 of the abutment;

y_{sw2cg} = vertical distance from the top face of Sidewall 2 to the center of gravity for a Yt-plane cross section of the composite sidewall and sidewall-pile cap near Corner 2 of the abutment;

y_u	=	horizontal displacement y for the pile that is associated with an elastic-plastic, soil material when the resistance p equals the resistance p_u;
z	=	depth of soil to a particular point along the pile length;
	=	depth of soil to a particular point along the abutment height;
	=	relative, vertical displacement between the pile and the soil at the depth z along the pile length;
	=	vertical settlement of the pile tip;
	=	pile-coordinate axis that is parallel to the pile length;
z_c	=	vertical displacement at maximum force;
β	=	load factor that is dependent on the load type;
	=	soil parameter;
	=	rotation of the bridge superstructure about the “point-of-fixity” for the bridge (counter-clockwise rotations are positive rotations);
β_1	=	“Whitney-Stress-Block” factor that is a function of the concrete-compression strength;
β_{CA}	=	concrete-mix proportion by volume for the course aggregate;
β_{FA}	=	concrete-mix proportion by volume for the fine aggregate;
β_c	=	ratio of the longer-to-shorter dimension of the loaded-concrete area;
β_P	=	concrete-mix proportion by volume for the cement paste;
β_{max}	=	maximum rotation of the bridge superstructure about the “point-of-fixity” for the bridge (counter-clockwise rotations are positive rotations);
Γ	=	displacement-magnification factor that is based on a 98% statistical-confidence level to account for uncertainties in the expansion and contraction of a PC-girder bridge;
Δ	=	horizontal displacement at the top of the pile;
	=	horizontal displacement at the top of a wall;
	=	sidesway for a fixed-end beam;
	=	displacement demand;
Δ_{R1}	=	displacement parameter at Corner 1 of the abutment;

Δ_{R2}	=	displacement parameter at Corner 2 of an abutment;
Δ_{X1}	=	X-axis displacement for the elastic curve of the abutment at Cross Section 1;
$\Delta_{X1'}$	=	X-axis displacement for the elastic curve of the abutment at Cross Section 1';
$\Delta_{X1.5}$	=	X-axis displacement for the elastic curve of the abutment at Cross Section 1.5;
Δ_{X2}	=	X-axis displacement for the elastic curve of the abutment at Cross Section 2;
Δ_{Xi}	=	X-axis displacement for the elastic curve of the abutment at the ith cross section;
Δ_{Y1}	=	Y-axis displacement for the elastic curve of the abutment at Cross Section 1;
$\Delta_{Y1'}$	=	Y-axis displacement for the elastic curve of the abutment at Cross Section 1';
$\Delta_{Y1.5}$	=	Y-axis displacement for the elastic curve of the abutment at Cross Section 1.5;
Δ_{Y2}	=	Y-axis displacement for the elastic curve of the abutment at Cross Section 2;
Δ_{Yi}	=	Y-axis displacement for the elastic curve of the abutment at the ith cross section;
Δ_{Z1}	=	Z-axis displacement for the elastic curve of the abutment at Cross Section 1;
$\Delta_{Z1'}$	=	Z-axis displacement for the elastic curve of the abutment at Cross Section 1';
$\Delta_{Z1.5}$	=	Z-axis displacement for the elastic curve of the abutment at Cross Section 1.5;
Δ_{Z2}	=	Z-axis displacement for the elastic curve of the abutment at Cross Section 2;

Δ_{Zi} = Z-axis displacement for the elastic curve of the abutment at the ith cross section;

Δ_{active} = horizontal displacement of a wall for full-active-soil pressure;

Δ_c = displacement capacity;

Δ_{cx} = lateral-displacement capacity in the x-axis direction at the top of abutment pile for y-axis bending of the pile;

Δ_{cy} = lateral-displacement capacity in the y-axis direction at the top of abutment pile for x-axis bending of the pile;

$\Delta_{e\text{-}fixed}$ = sidesway for the fixed-end beam during elastic behavior;

$\Delta_{e\text{-}simple}$ = deflection at the mid-span of the simply-supported beam during elastic behavior;

Δ_h = horizontal displacement at the top of a pile;

$\Delta_{i\text{-}fixed}$ = sidesway for the fixed-end beam after the moment at the mid-span of the beam equals the theoretical-plastic moment, M_p;

$\Delta_{i\text{-}simple}$ = deflection at the mid-span of the simply-supported beam after the moment at the mid-span of the beam equals the theoretical-plastic moment, M_p;

$\Delta_{\ell 1}$ = horizontal displacement of the abutment in the longitudinal direction of the bridge at Corner 1;

$\Delta_{\ell 2}$ = horizontal displacement of the abutment in the longitudinal direction of the bridge at Corner 2;

Δ_{n1} = horizontal displacement of the abutment that is normal to the abutment face at Corner 1;

Δ_{n2} = horizontal displacement of the abutment that is normal to the abutment face at Corner 2;

Δ_{ni} = horizontal displacement of the ith pile in the direction that is normal to the length of the abutment;

Δ_p = horizontal displacement at the top of a pile that is associated with the theoretical, initial M_p behavior;

Δ_{p1}	=	horizontal displacement of the abutment that is parallel to the abutment face at Corner 1;
Δ_{p2}	=	horizontal displacement of the abutment that is parallel to the abutment face at Corner 2;
$\Delta_{p\text{-}fixed}$	=	sidesway for the fixed-end beam when the moment at the mid-span of the beam first equals the theoretical-plastic moment, M_p;
$\Delta_{p\text{-}simple}$	=	deflection at the mid-span of the simply-supported beam when the moment at the mid-span of the beam first equals the theoretical-plastic moment, M_p;
$\Delta_{passive}$	=	horizontal displacement of a wall to reach the full-passive-soil pressure;
Δ_{pi}	=	horizontal displacement of the ith pile in the direction that is parallel to the length of the abutment;
Δ_{pr}	=	plastic-dispalcement ratio (Δ_{px}/Δ_{py});
Δ_{px}	=	horizontal displacement of the pile head along the x-axis direction for the pile that is associated with the plastic-moment strength M_{py};
Δ_{py}	=	horizontal displacement of the pile head along the y-axis direction for the pile that is associated with the plastic-moment strength M_{px};
Δ_v	=	vertical displacement at the top of a pile;
Δ_x	=	x-axis component of the displacement Δ;
	=	horizontal displacement of the pile head along the x-axis for the pile;
Δ_y	=	y-axis component of the displacement Δ;
	=	horizontal displacement of the pile head along the y-axis for the pile;
ΔL	=	change in a measured length;
ΔL_{wire}	=	change in the length of the extension wire of a displacement transducer;
ΔR	=	change in the resistance for a strain gage;

ΔT = change in temperature;
= change in the average temperature of the bridge superstructure;

ΔT_1 = minimum, absolute value of $T_{max\ ave}$ - $T_{construction}$ and $T_{min\ ave}$ – $T_{construction}$;
= change in the temperature of the concrete at the top surface of the bridge slab;

ΔT_2 = maximum, absolute value of $T_{max\ ave}$ – $T_{construction}$ and $T_{min\ ave}$ – $T_{construction}$;
= change in the temperature of the concrete at 4-in. below the top surface of the bridge slab;

ΔT_3 = change in the temperature of the concrete at the bottom surface of the bridge girders;

$\Delta T_{average}$ = average, bridge-temperature range;

$\Delta T_{contract}$ = change in the temperature of the bridge, which is equal to the difference between the temperatures $T_{min\ ave}$ and $T_{construction}$, for the initial contraction of the bridge superstructure;
= change in the temperature of the bridge, which is equal to the difference between the temperatures $T_{min\ ave}$ and $T_{max\ ave}$, for the contraction of the bridge superstructure from the point of maximum-initial expansion;

ΔT_{expand} = change in the temperature of the bridge superstructure, which is equal to the difference between the temperatures $T_{max\ ave}$ and $T_{construction}$, for the initial expansion of the bridge superstructure;
= change in the temperature of the bridge superstructure, which is equal to the difference between the temperatures $T_{max\ ave}$ and $T_{min\ ave}$, for the expansion of the bridge superstructure from the point of maximum-initial contraction;

$\Delta T_{re\text{-}contract}$ = change in the temperature of the bridge superstructure, which equals the difference in the temperatures $T_{min\ ave}$ and $T_{max\ ave}$ that starts at the point of maximum expansion;

$\Delta T_{re\text{-}expand}$ = change in the temperature of the bridge superstructure, which is equal to the difference between the temperatures $T_{max\ ave}$ and $T_{min\ ave}$, that starts at the point of maximum contraction;

ΔT_{solar} = change in the temperature of the bridge superstructure due to solar radiation;

$\Delta T_{specimen}$ = change in the temperature of the specimen;

ΔT_{vibr}	=	change in the temperature of the vibrating wire in the strain gage;
ΔT_{wire}	=	change in the temperature of the extension wire for a displacement transducer;
$\Delta \ell_L$	=	horizontal displacement of the left abutment in the longitudinal direction of the bridge;
$\Delta \ell_R$	=	horizontal displacement of the right abutment in the longitudinal direction of the bridge;
$\Delta \ell_{re\text{-}expand}$	=	relative, horizontal displacement along the longitudinal direction for a bridge of the top of a pile from its maximum, displaced position that is associated with the maximum contraction of a bridge superstructure;
$\Delta \varepsilon$	=	change in strain;
$\Delta \varepsilon_1$	=	change in the temperature-corrected, total, strain-gage reading measured by Strain gage 1;
$\Delta \varepsilon_2$	=	change in the temperature-corrected, total, strain-gage reading measured by Strain gage 2;
$\Delta \varepsilon_3$	=	change in the temperature-corrected, total, strain-gage reading measured by Strain gage 3;
$\Delta \varepsilon_4$	=	change in the temperature-corrected, total, strain-gage reading measured by Strain gage 4;
$\Delta \varepsilon_a$	=	change in the pile longitudinal strain induced by the axial force in the pile;
	=	change in strain due to different α-coefficients for the strain gage and the specimen;
$\Delta \varepsilon_{app}$	=	change in the apparent strain;
$\Delta \varepsilon_{app\text{-}dummy}$	=	change in the apparent strain for the “dummy-strain” gage;
$\Delta \varepsilon_{bottom}$	=	change in the strain in the bottom flange of a PC girder;
$\Delta \varepsilon_{dummy}$	=	change in the strain that was measured by the “dummy-strain” gage;

$\Delta\varepsilon'_{dummy}$	=	adjusted change in the “dummy-gage” strain for the first temperature correction;
$\Delta\varepsilon_m$	=	change in the measured strain;
$\Delta\varepsilon_{stress}$	=	change in the strain due to the induced change in stress;
$\Delta\varepsilon_t$	=	change in the pile longitudinal strain induced by the normal-warpage, torsional moment in the pile;
$\Delta\varepsilon_{temp}$	=	change in the strain due to the change in temperature;
$\Delta\varepsilon_{top}$	=	change in the strain in the top flange of a PC girder;
$\Delta\varepsilon_{total}$	=	change in the total strain;
$\Delta\varepsilon_x$	=	difference between the change in the longitudinal strains in the top and bottom flanges of a PC girder;
	=	change in the pile longitudinal strain induced by the x-axis, bending moment in the pile;
$\Delta\varepsilon_y$	=	change in the pile longitudinal strain induced by the y-axis, bending moment in the pile;
$\Delta\varepsilon_\alpha$	=	strain-temperature correction for the change in strain;
$\Delta\sigma$	=	change in the stress;
θ	=	skew angle for a bridge (angle between the t-axis for the bridge and the Z-axis for an abutment);
	=	relative, mid-span rotation due to bending of a cross section for a beam;
θ_{X1}	=	X-axis rotation for the elastic curve of the abutment at Cross Section 1;
$\theta_{X1'}$	=	X-axis rotation for the elastic curve of the abutment at Cross Section 1’;
$\theta_{X1.5}$	=	X-axis rotation for the elastic curve of the abutment at Cross Section 1.5;
θ_{X2}	=	X-axis rotation for the elastic curve of the abutment at Cross Section 2;

θ_{Xi} = X-axis rotation for the elastic curve of the abutment at the ith cross section;

θ_{Y1} = Y-axis rotation for the elastic curve of the abutment at Cross Section 1;

$\theta_{Y1'}$ = Y-axis rotation for the elastic curve pf the abutment at Cross Section 1';

$\theta_{Y1.5}$ = Y-axis rotation for the elastic curve of the abutment at Cross Section 1.5;

θ_{Y2} = Y-axis rotation for the elastic curve of the abutment at Cross Section 2;

θ_{Yi} = Y-axis rotation for the elastic curve of the abutment at the ith cross section;

θ_{Z1} = Z-axis rotation for the elastic curve of the abutment at Cross Section 1;

$\theta_{Z1'}$ = Z-axis rotation for the elastic curve of the abutment at Cross Section 1';

$\theta_{Z1.5}$ = Z-axis rotation for the elastic curve of the abutment at Cross Section 1.5;

θ_{Z2} = Z-axis rotation for the elastic curve of the abutment at Cross Section 2;

θ_{Zi} = Z-axis rotation for the elastic curve of the abutment at the ith cross section;

θ_{abut} = rotation of an integral abutment in the vertical plane due to the differential displacement between the top and bottom of the abutment;

θ_{c} = critical-skew angle beyond which transverse displacements will occur for an integral abutment;

$\theta_{e\text{-}fixed}$ = two times the angle between the tangent line that is drawn at the mid-span of the fixed-end beam to the elastic curve of the displaced shape for elastic behavior and a line that is parallel to the undisplaced shape for the beam;

$\theta_{e\text{-}simple}$ = relative, mid-span angle between the tangent lines to the elastic curve for the displaced shape of the simply-supported beam that are drawn through the supports when elastic behavior occurs for the beam;

θ_i = inelastic rotation for a beam;

$\theta_{i\text{-}fixed}$ = two times the angle between the tangent line that is drawn at the mid-span of the fixed-end beam to the elastic curve of the displaced shape for inelastic behavior and a line that is parallel to the un-displaced shape for the beam;

$\theta_{i\text{-}simple}$ = relative, mid-span angle between the tangent lines to the elastic curve for the displaced shape of the simply-supported beam that are drawn through the supports when inelastic behavior occurs for the beam;

θ_{ic} = inelastic-rotation capacity for an abutment pile;

θ_{icx} = inelastic-rotation capacity for x-axis bending of an abutment pile;

θ_{icy} = inelastic-rotation capacity for y-axis bending for an abutment pile;

θ_{id} = total, inelastic-rotation demand at the top of the pile;

$\theta_{id\text{-}partrev}$ = inelastic-rotation demand for partial reversal of the horizontal displacement at the top of an abutment pile;

θ_{idx} = total, inelastic-rotation demand at the top of the pile for x-axis bending;

θ_{idy} = total, inelastic-rotation demand at the top of the pile for y-axis bending;

$\theta_{imax\text{-}simple}$ = maximum, inelastic rotation $\theta_{i\text{-}simple}$ that occurs when the moment resistance is reduced to the M_p-strength due to buckling;

$\theta_{ip\text{-}fixed}$ = inelastic rotation of the plastic hinge at the supports for the fixed-end beam with sidesway;

$\theta_{ip\text{-}simple}$ = inelastic-rotation between the tangent lines that are drawn to the elastic curve of the displaced shape of the beam on each side of the mid-span, plastic-hinge location;

θ_{ipc} = inelastic-rotation capacity that is associated with the angle $\theta_{imax\text{-}simple}$ at the plastic-hinge location;

$\theta_{ipc\text{-}simple}$ = inelastic-rotation capacity of the idealized, simple-beam, plastic hinge;

θ_p = relative, mid-span angle at first yielding of the extreme fibers in the cross section;

$\theta_{p\text{-}fixed}$ = two times the angle between the tangent line that is drawn at the mid-span of the fixed-end beam to the elastic curve of the displaced shape when the mid-span moment first equals the theoretical-plastic moment, M_p, and a line that is parallel to the un-displaced shape for the beam;

$\theta_{p\text{-}simple}$ = relative, mid-span angle between the tangent lines to the elastic curve for the displaced shape of the simply-supported beam that are drawn through the supports when theoretical and initial M_p behavior occurs for the beam;

$\theta_{px\text{-}simple}$ = x-axis component of $\theta_{p\text{-}simple}$;

$\theta_{py\text{-}simple}$ = y-axis component of $\theta_{p\text{-}simple}$;

θ_r = skew angle for a pile, which is the angle between a line that is parallel to the t-axis (transverse-axis) for a bridge and the y-axis (weak-axis) for anHP-shaped, abutment pile;

θ_{tg} = abutment rotation, which is in a vertical plane that is parallel to the longitudinal direction of the bridge, due to the vertical-temperature gradient;

θ_u = relative, mid-span angle when the strain-hardening, moment strength decreases to the M_p-strength due to buckling;

θ_w = abutment rotation, which is in a vertical plane that is parallel to the longitudinal direction of the bridge, due to the factored-level, live and impact loads;

θ_y = relative, mid-span angle at the initial development of the M_p-strength for the idealized behavior;

ΣH_{fp} = horizontal reaction at the fixed pier for the single-equivalent girder;

$\Sigma M_{pile\text{-}t}$ = bending moment in the single-equivalent pile about the t-axis at each abutment;

$\Sigma P_{pile\text{-}h}$ = axial force in the single-equivalent pile at each abutment;

ΣR_{ep} = vertical reaction at the expansion pier for the single-equivalent girder;

ΣR_{fp} = vertical reaction at the fixed pier for the single-equivalent girder;

$\Sigma V_{pile\text{-}\ell}$ = ℓ-axis shear force in the single-equivalent pile at each abutment;

$\psi(t,t_i)$ = concrete-creep coefficient, which is the ratio of the concrete-creep strain ε_{cr} to the concrete strain ε_{cf};

α = coefficient of thermal expansion and contraction (α-coefficient);
= soil parameter;
= reduction factor for piles in clay;

α_1 = rotation angle between a line that is drawn parallel to the transverse axis (t-axis) for the bridge and a line drawn along the displacement dR_1 at Corner 1 of an abutment;

α_2 = rotation angle between a line that is drawn parallel to the transverse axis (t-axis) for the bridge and a line drawn along the displacement dR_2 at Corner 2 of an abutment;

α_{CA} = α-coefficient for the coarse aggregate;

α_{FA} = α-coefficient for the fine aggregate;

α_S = α-coefficient for a saturated and hardened, neat-cement paste;
= α-coefficients for the specimen;

α_c = α-coefficient for the concrete;

α_d = α-coefficient for the concrete in the bridge deck;

α_{dry} = α-coefficient for the concrete at the 100%-dry condition;

α_e = effective, α-coefficient for a concrete-bridge superstructure;

α_g = α-coefficients for the concrete in the PC girders;

α_{gage} = α-coefficient for the strain gage;

α_s	=	bearing-condition-edge factor for a concrete-punching-shear failure;
$\alpha_{specimen}$	=	α-coefficient for the specimen;
α_{vibr}	=	α-coefficient for the vibrating wire in the strain gage;
α_{wire}	=	α-coefficient of the extension wire of a displacement transducer;
γ	=	unit-weight of the soil;
	=	overall-load factor;
γ_v	=	proportion of the moment that is transferred in the connection by shear stress;
γ'	=	effective, unit-weight of the soil;
γ'_{sat}	=	effective, saturated, unit-weight of the soil;
γ_{dry}	=	dry, unit-weight of the soil;
γ_{gage}	=	temperature, coefficient-of-resistivity of the strain-gage material;
δ	=	soil-to-abutment, surface-friction angle;
ε_1	=	strain measured by Strain gage 1;
ε_2	=	strain measured by Strain gage 2;
ε_3	=	strain measured by Strain gage 3;
ε_4	=	strain measured by Strain gage 4;
ε_{50}	=	axial strain at one-half of the peak-stress difference from a triaxial test;
ε_a	=	axial strain in the pile;
ε_c	=	maximum compressive strain at the extreme-compression fiber of the cross section (ε_c = 0.003 in./in.);
ε_{cf}	=	initial, elastic, concrete strain when the concrete is loaded at an age of t_i-days after concrete casting;

$\varepsilon_{cf}(t,t_i)$	=	effective strain for the concrete at an age of t-days after casting when a compressive stress f_{ci} is applied to the concrete and remains constant from an age of t_i-days to t-days after concrete casting;
ε_{cr}	=	concrete-creep strain;
	=	concrete-creep strain at an age of t-days after concrete casting;
ε_i	=	longitudinal strain in the pile;
ε_ℓ	=	average, longitudinal strain in the bridge superstructure;
ε_{sh}	=	concrete-shrinkage strain;
ε_t	=	normal-warpage, torsional strain in the pile;
$(\varepsilon_{th})_{contract}$	=	thermal strain for the maximum contraction of the bridge superstructure from the point of the maximum-initial expansion;
	=	thermal strain for initial contraction of the bridge superstructure;
$(\varepsilon_{th})_{expand}$	=	thermal strain for the maximum, initial expansion of the bridge superstructure;
	=	thermal strain for the maximum expansion of the bridge superstructure from the point of maximum, initial contraction;
$(\varepsilon_{th})_{re\text{-}contract}$	=	thermal strain for maximum re-contraction of the bridge superstructure from the point of maximum expansion;
$(\varepsilon_{th})_{re\text{-}expand}$	=	thermal strain for maximum re-expansion of the bridge superstructure from the point of the maximum contraction;
$(\varepsilon_{total})_{contract}$	=	total, longitudinal strain in the bridge superstructure for the maximum contraction of the bridge superstructure from the point of maximum-initial expansion;
	=	total, longitudinal strain in the bridge superstructure for the maximum, initial contraction of the bridge superstructure;
$(\varepsilon_{total})_{expand}$	=	total, longitudinal strain in the bridge superstructure for the maximum, initial expansion;
	=	total, longitudinal strain in the bridge superstructure for the maximum, expansion of the bridge superstructure from the point of maximum-initial contraction;
ε_x	=	x-axis, bending strain in the pile;
ε_y	=	y-axis, bending strain in the pile;

$(\varepsilon_{cr}+\varepsilon_{sh})_{1\text{-year}}$	=	combined, concrete creep and shrinkage strain in the bridge superstructure over the 1-year period after the completion of bridge construction;
$(\varepsilon_{cr}+\varepsilon_{sh})_{28\text{-day}}$	=	concrete creep and shrinkage strains in the bridge superstructure over the 28-day period after the completion of bridge construction;
ζ_{bf}	=	angle between the sloped face of the bottom flange of a PC girder and a horizontal line;
ζ_{tf}	=	angle between the sloped face of the top flange of a PC girder and a horizontal line;
λ	=	ACI Code specified concrete-weight factor friction for the shear-friction, design strength (λ = 1.0 for normal-weight concrete);
μ	=	Poisson's ratio;
	=	ACI Code specified coefficient of friction for the shear-friction, design strength ($\mu = 0.6\lambda$, where the factor λ is set equal to 1.0 for normal-weight concrete);
μ_s	=	soil-to-abutment, surface-friction constant ($\mu_s = \tan \delta$);
ξ	=	shape factor for a beam cross section;
η	=	transitional, bridge-skew angle, θ, for generalized behavior regarding parameter studies;
$\sigma'_{horizontal}$	=	effective, horizontal stress in the soil at a depth z;
$\sigma'_{vertical}$	=	effective, vertical stress in the soil at a depth z;
σ_c	=	effective longitudinal stress at the center of gravity of the bridge superstructure;
ϕ	=	angle of internal friction for the soil;
	=	resistance factor;
ϕ_b	=	resistance factor for bending;
ϕ_c	=	resistance factor for concrete bearing;
	=	resistance factor for axial compression;

ϕ_f	=	resistance factor for flexure;
$\phi_{ic\text{-}rev\text{-}simple}$	=	inelastic-curvature capacity for a full-reversal of loads on a simply-supported beam;
$\phi_{ic\text{-}simple}$	=	inelastic-curvature capacity for uni-directional loads on a simply-supported beam;
ϕ_p	=	beam curvature that is associated with the theoretical, plastic-moment strength, M_p;
ϕ_{rc}	=	resistance factor for compression that is applied to the inelastic-rotation capacity for the pile (ϕ_{rc} = 0.85);
ϕ_v	=	resistance factor for shear;
	=	resistance factor for torsion; and
ϕ_y	=	beam curvature that is associated with the theoretical, yield moment strength, M_y.

1. INTRODUCTION

1.1. Background

Integral-abutment bridges have their abutments constructed integrally with the bridge girders and deck for the end spans, while non-integral-abutment bridges have an expansion joint between the abutment and bridge superstructure. Figure 1.1 shows elevations of a single-span, integral-abutment bridge and non-integral abutment bridge. The non-integral-abutment bridge (Fig. 1.1a) has stub abutments that are supported by vertical and battered piles, while an integral-abutment bridge (Fig. 1.1b) has abutments that are supported by only vertical piles. The lateral flexibility of the vertical piles in an integral-abutment bridge permits longitudinal, bridge movements that are induced by temperature changes of the bridge. To reduce the lateral resistance to horizontal displacements near the top of the piles, a pre-drilled hole that is filled with a low stiffness material, such as a bentonite slurry, surrounds each pile.

Common terminology for the different parts of an integral abutment is not used by all bridge engineers. The integral-abutment terminology that is presented in this report may not necessarily be the same as that is used by some bridge engineers. Schematic drawings that illustrate the geometrical conditions of an integral abutment are shown in Figs. 1.2 and 1.3. When an integral-abutment bridge has Iowa DOT Type-A or Type-B and sometimes Type-C, prestressed concrete (PC) girders, the abutment wingwalls are cantilevered from the back of the abutment (Figs. 1.2a and 1.3a). For this abutment configuration, the abutment piles are placed only in a single row to support the straight-wall abutment. When an integral-abutment bridge has Iowa DOT, Type-D and

sometimes Type-C, PC girders, abutment sidewalls are constructed integrally with the abutment and an additional abutment pile is, or additional piles are, placed directly under the end of each sidewall to help support the resulting U-shaped abutment (Figs. 1.2b and 1.3b). With this abutment configuration, the wingwalls are cantilevered from the ends of the sidewalls.

For an integral-abutment bridge, a monolithic joint at each abutment is formed by casting the concrete for an abutment pile cap around the upper portion of the abutment piles, by casting the concrete for the abutment backwall around the ends of the bridge girders at the same time that the end portion of the bridge deck is cast, and by developing force and moment resistance at the construction joint between the pile cap and backwall for the abutment. For the orientation for the HP-shaped piles shown in Fig. 1.2, expansion and contraction of the bridge superstructure will induce displacements of the abutment that will primarily cause bending about the y-axis (weak-axis) of the pile cross section. Even for this pile orientation, bending of the abutment piles about the x-axis (strong-axis) for the pile cross section can occur when the bridge-skew angle is larger than a specific amount, which is based on soil properties for the abutment backfill. Other plan-view orientations for an HP-shaped pile have been used by bridge engineers for integral-abutment bridges.

The designers of integral-abutment bridges need to evaluate the forces that are induced in the abutment and abutment piles and establish the ductility requirements for the abutment piles due to the longitudinal and transverse displacements of an integral abutment. Integral construction creates additional strains and stresses in the bridge elements that are caused by the thermal expansion and contraction of the bridge and by

the creep and shrinkage of the concrete. The displacement of the abutments into and away from the soil backfill behind an abutment creates pressures on the backwall and induces forces in the supporting piles. The passive-soil pressures from the backfill and the horizontal reactions from the piles induce axial forces, shear forces, and bending moments in the bridge superstructure.

1.2. Research scope and objectives

The integral-abutment research presented in this report addresses bridges that have a reinforced concrete (RC) deck; I-shaped, PC girders; and HP-shaped, steel, abutment piles. The geometric parameters that were considered included either straight or skewed-bridge alignments; straight-line or U-shaped abutments; multiple-span girders; fixed and expansion piers; a single row of piles for each abutment backwall; and several, plan-view orientations for the abutment piles. Different types of backfill were also considered for the soil behind the abutments. The research concentrated on the design of the integral abutments and their pile foundations for load combinations that involve temperature effects, which caused expansion and contraction of the bridge superstructure.

To provide direction for the research, the following four objectives were formulated by the Iowa State University (ISU) researchers: (1) Evaluate the state-of-the-art for the behavior and design of integral-abutment bridges; (2) present additional information on the behavior of integral-abutment bridges; (3) validate the assumptions that are incorporated in the current, pile-design procedures for integral-abutment bridges; (4) develop recommendations for a rational design of integral abutments and

the abutment piles for thermally-induced forces and displacements. To accomplish these objectives, the research efforts were categorized by the ISU research team into the following seven tasks: (1) Conduct a literature review of integral-abutment-bridge analysis and design; (2) develop a bridge-monitoring program to obtain long-term air and concrete temperatures; pile and girder strains; longitudinal and transverse displacements for the abutments; relative, longitudinal displacements between the bridge girders and the pier caps; pile-head rotations relative to the abutment pile cap; and abutment rotations in a vertical plane that is parallel to the length of a bridge; (3) monitor two, integral-abutment bridges that have different, plan-view, geometric shapes for the abutments (straight-line abutments and a U-shape abutments) to establish their response to thermal loading; (4) develop finite-element bridge models that were calibrated and refined using the experimental results for the monitored, integral-abutment bridges; (5) compare analytically-predicted and experimentally-measured, abutment displacements and member strains to verify the accuracy of the finite-element, bridge models; (6) establish procedures and recommendations for the design of integral-abutment backwalls, pile caps, abutment piles, and connection details that are required to resist thermally-induced forces and displacements; and (7) present design examples for the members and some of their connections in an integral abutment.

1.3. Report organization

This chapter presented a general discussion on integral-abutment bridges and non-integral-abutment bridges and described the objectives, tasks, and scope of the

research on integral-abutment bridges. Chapter 2 presents the findings of a review of the published literature that addressed many directly and indirectly related aspects of integral-abutment bridge design. The field-monitoring program for two integral-abutment bridges is described in Chapter 3, and the experimental results for these bridges are presented in Chapter 4. In Chapter 5, finite-element models are described for the two bridges that were monitored during the research. These models included soil interaction with the abutment piles and backwall. Chapters 6 and 7 present comparisons between the analytically-predicted and experimentally-measured bridge displacements, pile strains, and girder strains for the two bridges. Integral-abutment, design procedures are discussed in Chapter 8. To illustrate many of the concepts that were presented in Chapter 8, annotated design examples for one of the monitored bridges are given in Chapter 9. A brief summary of the research program, conclusion developed by the ISU researchers, and suggestions for future research involving integral-abutment bridges is presented in Chapter 10. Chapter 11 contains the references for the research. Appendix A gives supplemental information on the coefficient of thermal expansion and contraction of concrete-core samples that were taken from bridge decks and PC girder webs. Appendix B presents user information for the computer program Transmove, that calculates the transverse displacements of integral abutments.

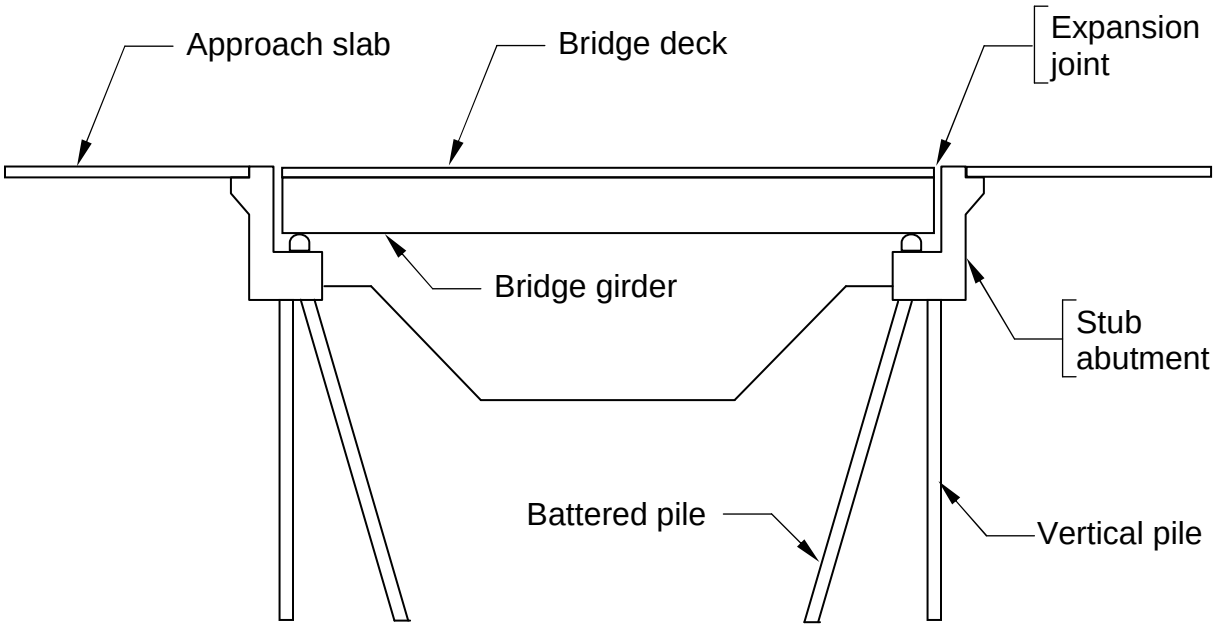

(a) Single-span bridge with expansion joints

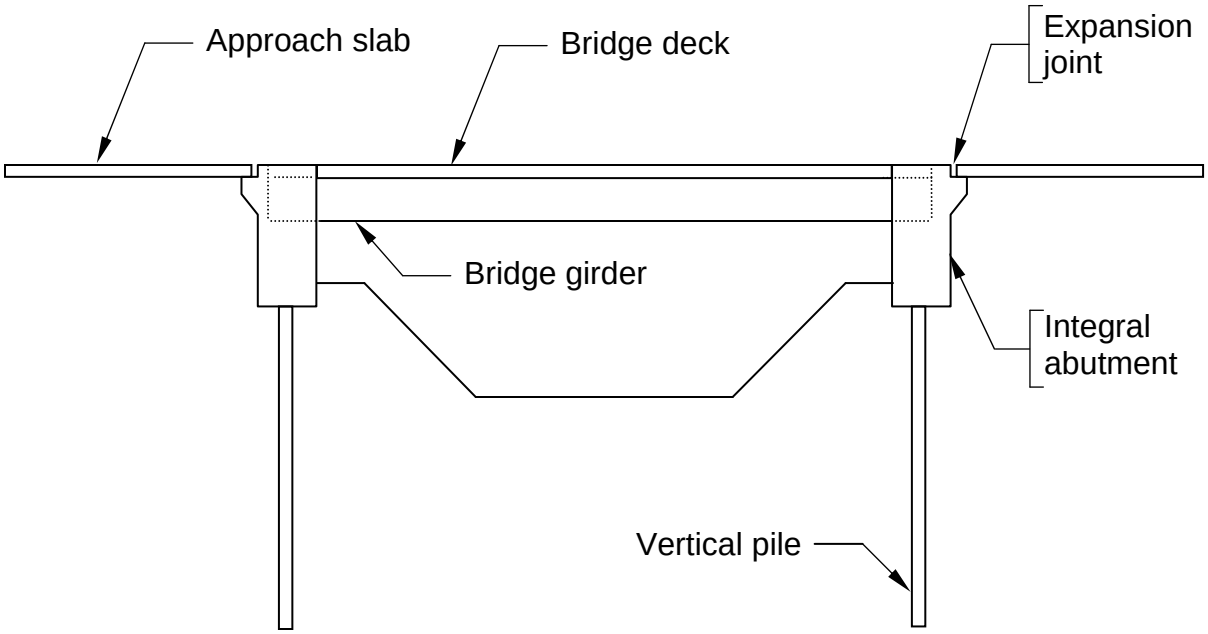

(b) Single-span, integral-abutment bridge

Figure 1.1. Bridge types

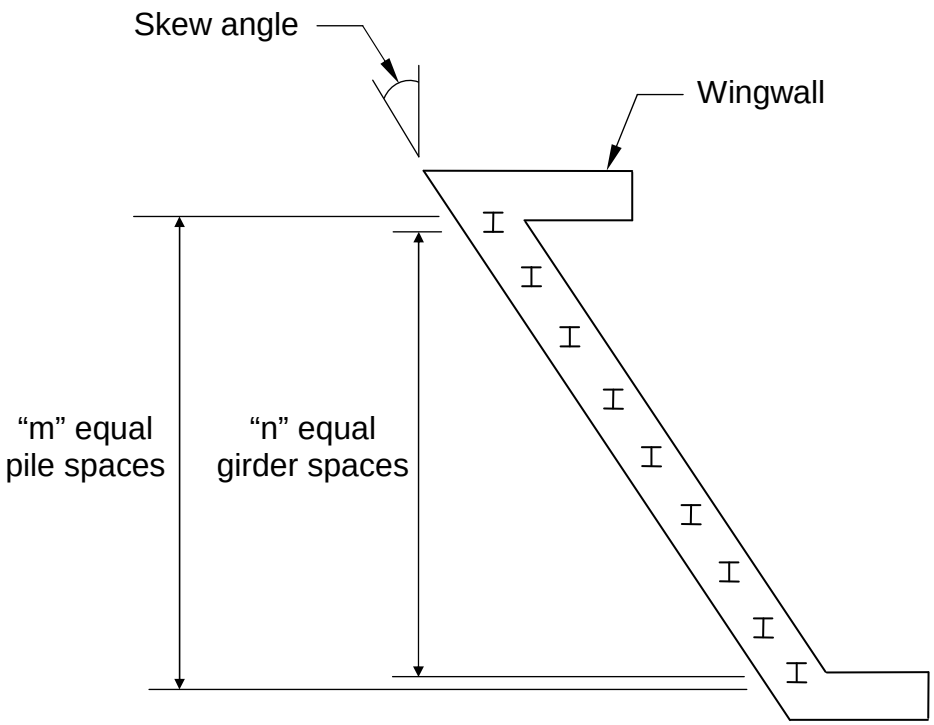

(a) Iowa Type-A, B, or C PC girders

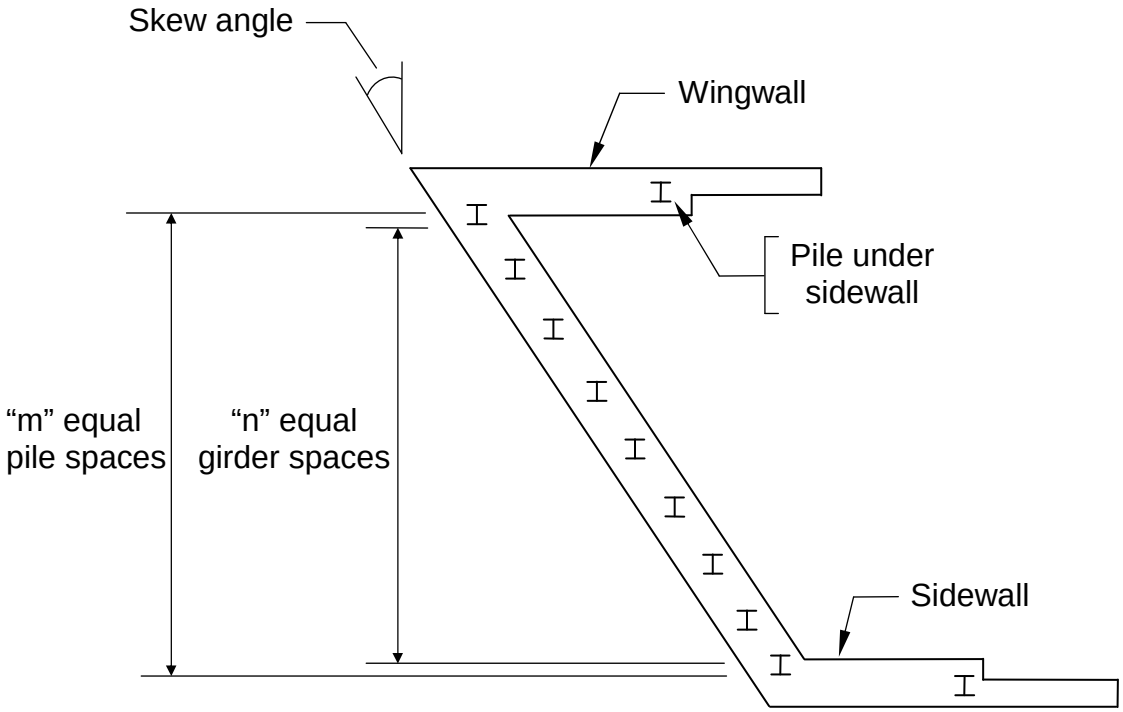

(b) Iowa Type-D PC girders

Figure 1.2. Integral-abutment plan views

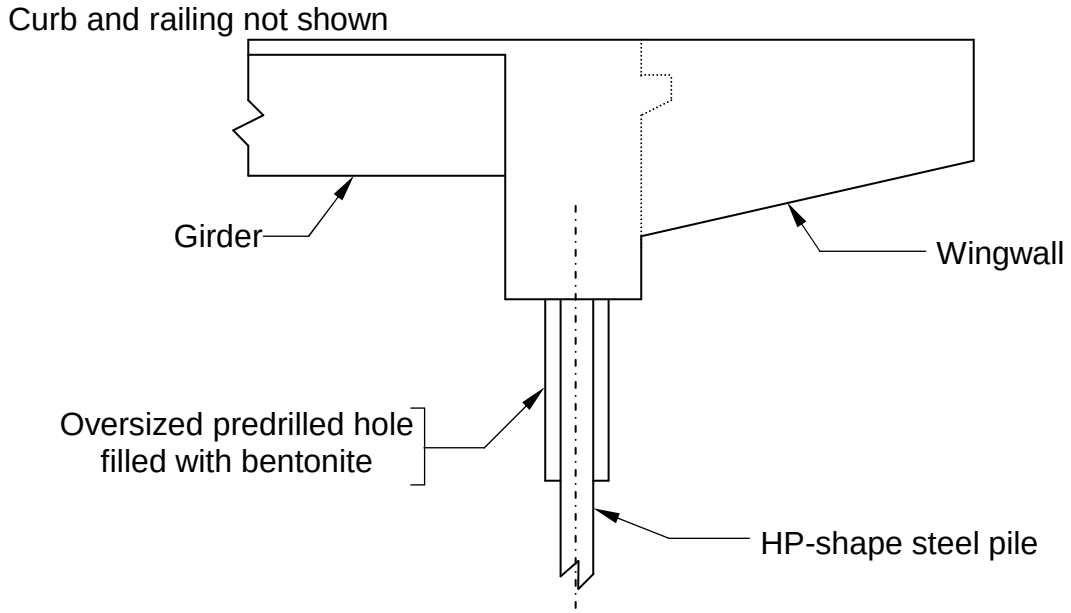

(a) Iowa Type-A, B, or C PC girder

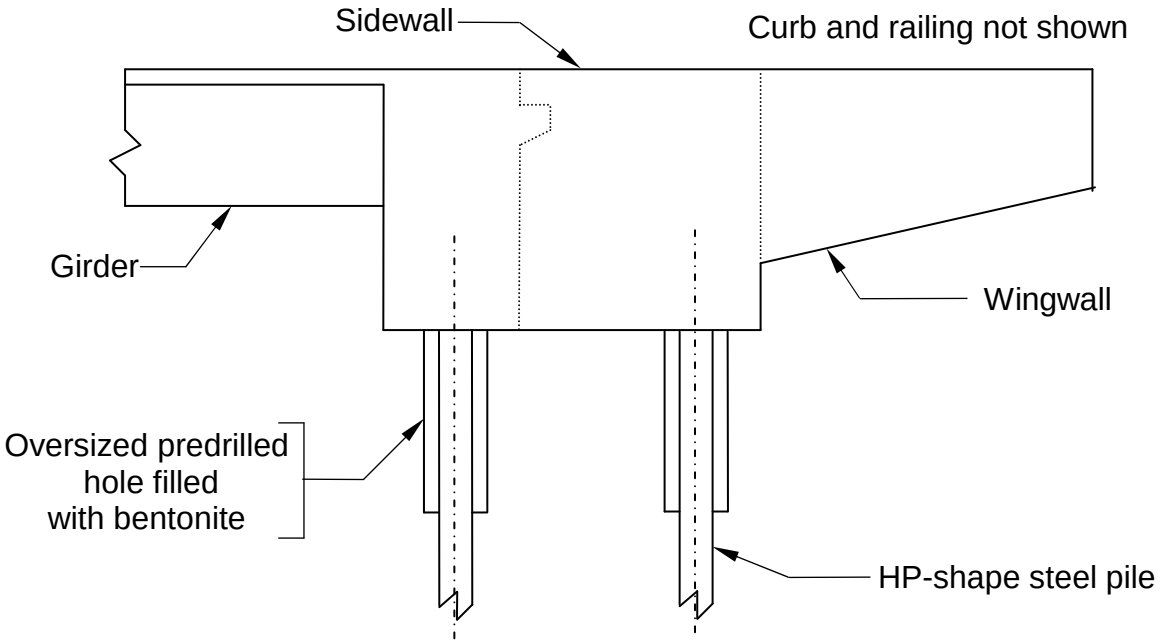

(b) Iowa-D PC girder

Figure 1.3. Integral-abutment side views

2. LITERATURE REVIEW

2.1. Performance of joint-less bridges

Twenty-nine of the fifty-two design agencies that responded to a survey, which was conducted by Greimann, et al. (1984), indicated that their design agency permit the construction of integral-abutment bridges. In the early 1980's, more than half of the design agencies oriented the integral-abutment piles for strong-axis bending when a bridge experiences longitudinal expansion and contraction that is induced by temperature changes in the bridge superstructure, and only four of twenty-nine design agencies that used integral-abutment bridges required pre-bored holes for the abutment piles. The results of the 1983 survey by Greimann, et al. revealed that only the states of Iowa and South Dakota and the District Construction Office of the Federal Highway Administration (FHWA), Region 15 indicated that piling stresses due to horizontal movement are calculated for integral-abutment bridges. Although the States of Alaska and Idaho indicated that such calculations are warranted only for integral-abutment bridges that involve some unique feature. At the date of this survey, most of the remaining states essentially neglected the stresses that are induced in the abutment piles by the horizontal displacement of the pile heads. However, some states required some type of an abutment detail, such as driving the piles into a pre-bored hole, to reduce pile stresses.

This survey revealed that the construction details for an integral bridge vary widely from state to state. Pile-head details reflected either hinge, fixed, or partially restrained conditions at the tops of an abutment pile, and pile caps may or may not be used. In some states, the approach slabs are tied to the abutment backwalls with

dowels, while in other states, an expansion joint is provided between an approach slab and the bridge slab. Even though a granular backfill material was most widely used behind the abutments, some states do not specify a specific type of a backfill. The abutment wingwalls may be in-line or flared. However, some states did not allow the use of U-shaped, abutment walls because of design uncertainty, backfill compaction difficulty, and the additional design details that are required for the joint between the wingwalls and an approach slab. The State of New York recommended avoiding wingwall lengths in excess of 10 ft, while the State of Tennessee required designers to use a comprehensive analysis, if wingwall lengths were greater than 12-ft long.

According to Greimann, et al. (1984), bridge-length limitations for integral-abutment bridges were for, the most part, established on the basis of experience and engineering judgment. Many state departments of transportation have progressively increased their bridge-length limitations, primarily as a result of observed satisfactory bridge performance. As of 1983, the bridge-length limitations for non-skewed, integral-abutment bridges were 150 ft to 400 ft for steel-girder bridges, 150 ft to 800 ft for concrete-girder bridges, and 200 ft to 800 ft for prestressed-concrete (PC) girder bridges. Most states use the same length limitations for skewed, integral-abutment bridges. Most state highway departments have their own empirically-based limitations and criteria that are applied for the design of integral abutments.

A literature review was conducted by Wolde-Tinsae and Klinger (1987) to determine the extent of joint-less-bridge or minimal-jointed-bridge design and construction by highway agencies in the United States of America, Canada, Australia, and New Zealand. At the ends of a bridge either integral or semi-integral abutments

have been used by the bridge design agencies to eliminate an expansion joint at this location. An integral abutment forms a rigid joint between a bridge superstructure and substructure; while, semi-integral abutments restrain translation, but not rotation between these bridge components. Abutment details that were used by several bridge engineers are included in the report by those authors.

The design and construction of integral bridges in the State of Tennessee was discussed by Loveall (1985) and Wasserman (1987). As of 1987, the maximum, total length of joint-less, steel-girder bridges and PC-girder bridges in that state was set at about 400 ft and 800 ft, respectively. However, these authors commented that their longest joint-less bridge is a 927-ft long, concrete bridge. Loveall and Wasserman noted that bridge engineers in Tennessee use a temperature range of 0 °F to 120 °F for steel-girder superstructures and a temperature range of 20 °F to 90 °F for concrete-girder superstructures. With these temperature ranges and these maximum bridge lengths, the longitudinal movement at each end of a bridge is about 2 in. To establish these long bridge lengths, Wasserman (1987) stated that the bridge designers consider pile translation and rotation capacities, modify foundation conditions when feasible, use a reduced modulus of elasticity for long-term loads on concrete substructures, allow plastic hinges to form in the steel piles or to construct internal hinges in parts of the structure, and use expansion bearings where necessary. Wasserman (1987) also noted that the State of Tennessee is also eliminating expansion joints during rehabilitation of some of their existing bridges. He discussed and showed some details for some of their retro-fit procedures to eliminate a bridge-expansion joint.

Wolde-Tinsae, et al. (1988) assessed the performance of joint-less bridges in the States of California, New York, and Tennessee, discussed some of the problems that were encountered by these states for these types of bridges, and described some corrective measures that were used by these states to improve the performance of integral bridges. These authors reported that the bridges, which they evaluated in these three states, are performing as intended and, in most cases, have not experienced major, structural problems nor long-term, serviceability problems. For joint-less bridges that are about 450 ft or more in length, some of the problems that were encountered included the settlement of the approach slabs and the development of compression-induced bumps in the roadway at the ends of the bridges. Other problems that were discussed by Wolde-Tinsae were minor pattern and transverse cracks in the bridge decks, concrete shrinkage cracks in the deck along the negative moment regions above the piers, and cracking of the concrete approach slabs.

A brief historical perspective on integral bridges that started with references to arches in nature and Roman times and ended with the present was provided by Burke (1993). He discussed attributes and limitations of integral bridges. The attributes included simple design, joint-less construction, rapid construction, earthquake resistance, facilitates future bridge widening, and improved distribution of live loads. The limitations included the development of high stresses in the abutment piles, limited range of application, special construction procedures, special approach slab details, additional research regarding soil pressures and concrete creep and shrinkage effects on bridge behavior, and minimal guidance by design specifications. Burke concluded that the positive aspects outweigh the negative aspects of integral bridges.

Russell and Gerken (1994) provided an overview of design considerations that need to be addressed for integral-abutment bridges. They noted that these type of bridges must accommodate the movements that are caused by changes in the bridge temperature and concrete creep and shrinkage and the forces that are induced by the restraints to those moments, which are associated with integral-abutment bridges. Regarding temperature effects on bridge movements, these authors commented that seasonal-temperature changes primarily affect the total change in the bridge length, while daily-temperature changes primarily affect thermal gradients through the depth of the bridge superstructure. Russell and Gerken noted that both temperature and humidity affect short-term creep and shrinkage of the concrete; therefore, an increase in temperature and a simultaneous decrease in the relative humidity may not cause a change in the bridge length that is based only on the change in the temperature. These authors discussed the resistance to bridge movements that are provided by the abutment stiffness, soil pressures behind the abutments, and pier stiffness. Russell and Gerken remarked that topics, which require further investigations for integral-abutment bridges, include abutment-pile capacity and stability, skewed and curved bridges, and continuity details in multiple-span bridges.

The design and performance of integral-abutment and semi-integral-abutment bridges in Ontario, Canada was reported by Husain and Bagnariol (1998). These authors reported that the first integral-abutment bridges were constructed in this Canadian Province in the early 1960's, and that during the 1990's the Ministry of Transportation of Ontario (MTO) has become more active regarding the design and construction of these types of bridges. Husain and Bagnariol that the MTO, bridge-

monitoring program has shown that both the integral-abutment and semi-integral-abutment bridges exhibit good performance and that only minimal signs of distress were observed by the bridge inspectors.

Alampalli and Yannotti (1998) discussed the performance of integral bridges and joint-less-bridge decks that were constructed in the State of New York. Only the reported findings of these authors for integral bridges with PC girders are discussed here. A condition-rating system was used by the State of New York, bridge inspectors to describe the results of their visual inspections of various bridge components. Alampalli and Yannotti applied statistical methods to evaluate the performance of integral, PC-girder bridges. Some of their conclusions for these types of bridges were that the condition of the bridge deck and abutments directly correlated with the span length for the bridge. Lower deck and abutment ratings occurred for bridges with long-span lengths. The skew angle for a bridge significantly affected the performance of the deck slabs and the approach slabs. Bridges with large-skew angles produced lower condition ratings for both the bridge deck and the approach slabs. These authors noted that abutments that had straight wingwalls performed better than abutments that had flared wingwalls. Also, the condition ratings for the bridge components were not significantly influenced by the type of an abutment pile. Alampalli and Yannotti remarked that the integral bridges in New York have performed very well and that many of their constriction details are quite satisfactory, while some other details need to be improved.

Problems that have occurred with integral-abutment and semi-integral-abutment bridges in the State of Ohio were described by Burke (1999). The author discussed

concrete-deck cracks that formed at the acute corners of new, integral-type bridges and at the end diaphragms of a bridge that was converted from a formally end-jointed, continuous, steel-girder bridge to an integral bridge. This author commented on some of the approaches that bridge engineers with the Ohio Department of Transportation (Ohio DOT) tried to prevent concrete cracks in early-age, deck slabs. Burke noted that the use of high-performance concrete, which is less permeable than normal concrete, can produce more transverse, concrete cracking of bridge decks. To help prevent deck cracking, special-concrete-construction policies were instituted by the Ohio DOT. These construction procedures include casting the concrete sections of a bridge deck that provide continuity for the bridge (continuity connections) at sunrise, casting deck slabs and these continuity connections at night, casting these continuity connections along after the deck-slab sections were cast, and using crack sealers on the fresh concrete of bridge decks.

Also, Burke (1999) discussed displacements that were observed for the vertical joint between the superstructure of a two-span, continuous-deck-type bridge and the lateral wingwalls for the bridge abutments. The joint fillers for these vertical joints, which were at the acute corners of the bridge deck, were compressed to about one-half of their original thickness; while these joint fillers, which were at the obtuse corners of the bridge deck, were loose within these joints. This bridge had a substantial skew angle and semi-integral abutments. Burke commented that skewed, semi-integral-abutment bridges have a tendency to incrementally, progressively, and horizontally rotate towards the acute corners for the bridge deck. Also, for these bridge types, Burke noted that adequately designed, guide bearings for the bridge superstructure are

needed at the abutments to resist horizontal rotation of these bridges and to provide long-term stability for the semi-integral abutments.

A recent survey of current practices for the design of integral-abutment bridges was performed by Kunin and Alampalli (1999, 2000) for the New York State Department of Transportation. The questionnaire covered various aspects of the design and performance of integral-abutment bridges that included bridge lengths, skew-angle limits, design assumptions, design procedures, and analysis procedures. A total of 39 state and provincial transportation agencies in the United States and Canada responded to the survey. Thirty-one of the agencies indicated they had experience with integral-abutment bridges. For the most part, only minor problems occurred with this type of a bridge. The reported problems included minor cracking in the deck near the piers, concrete cracking and spalling in bearing areas, drainage problems for the abutment backfill, and settlement of the bridge-approach slabs. Only the State of Arizona, based on their experience with expensive repairs of the approach slabs, did not recommend the use of integral-abutment bridges.

Kunin and Alampalli (1999, 2000) noted that the majority of the bridge-design agencies use the AASHTO Specifications for calculating concrete-shrinkage strains and selecting the coefficient of thermal expansion and contraction of steel and concrete elements. Different integral-abutment, bridge-design assumptions and limitations are applied by the design agencies. The maximum, permissible length for integral-abutment bridges varied greatly amongst the agencies. Bridge engineers for the State of Tennessee permit the construction of the longest, PC-girder, integral-abutment bridges. The maximum length for this type of a bridge in Tennessee is 800 ft. Most

design agencies limit the bridge-skew angle to 30 deg. The length limit for PC-girder, integral-abutment bridges has not significantly changed during the years that elapsed between the surveys that were conducted by Greimann, et al. (1984) and Kunin and Alampalli (1999, 2000).

According to Kunin and Alampalli (1999, 2000), passive-soil pressure is usually applied in the design of integral-abutment bridges. However, a few agencies neglect the effect of earth pressure on the abutments during longitudinal expansion of the bridge. The States of Alaska and North Dakota assume a specific, soil pressure regardless of the actual design conditions. One-third of the responding design agencies apply special construction details to reduce backfill pressures on the abutment walls. These details included using a granular embankment with an underdrain, attaching a foam backing on the abutment wall, and providing a gap between the abutment wall and a geotextile-reinforced backfill. Most of the agencies neglect the effects of the bridge skew on soil pressure. About two-thirds of the responses use U-shaped abutments. Normally, the wingwalls are rigidly attached to the abutment backwall, by either being poured monolithically with or rigidly tied with reinforcement to the backwall. Wingwalls are generally designed using active-soil and passive-soil pressures.

Kunin and Alampallis' survey (1999, 2000) revealed that most design agencies use steel, HP-shaped piles to support integral-abutment bridges. However, some agencies use PC pipe and concrete-filled, steel-shell piles. When HP-shaped piles are used, the design agencies frequently orientate the abutment piles for y-axis (weak-axis) bending when changes in the bridge length occur due to changes in the temperature. More than half of the design agencies consider combined axial-load and bending

moment for the design of the abutment piles. Depending on the pile-to-abutment connection detail, fixed, pinned, or free pile-head conditions are used in the bridge analysis. According to these researchers, twelve of the thirty agencies that design integral bridges require the use of pre-bored holes for the abutment piles. The number of design agencies that require pre-bored holes has increased significantly from that reported by Greimann, et al. (1984). These prebored holes are filled with bentonite slurry or sand, or these holes are left unfilled.

The approach slabs for integral-abutment bridges have the largest number of incidences of poor performance, according to Kunin and Alampalli (1999, 2000). These authors noted that approach-slab problems included settlement, transverse or longitudinal cracking, and cracking of asphalt overlays at the ends of the approach slabs. Generally, approach slabs bear on a ledge or corbel extending from the back of an abutment, and an approach slab may or may not be connected to the abutment. The respondents to their survey indicated that these details for an approach slab were used with approximately the same frequency. An expansion joint for an integral-abutment bridge may be placed at the joint between the abutment and the approach slab or at the joint between the approach slab and the pavement slab. Kunin and Alampalli noted that regardless of the location of the expansion, similar performances were observed for the approach slab.

Also, Kunin and Alampalli (1999, 2000) noted that seventeen, bridge-design agencies used both PC girders and steel girders for integral-abutment bridges. Thirteen of these agencies stated that differences were not observed in the performance of their bridges with either type of bridge girder. However, the remaining four of these

seventeen agencies reported that bridge performance differences were observed between their PC-girder and steel-girder bridges. The differences included concrete-creep or concrete-shrinkage problems for their PC-girder bridges and greater girder rotations at their bearings for steel-girder bridges than that for their PC-girder bridges. The design agency for the State of New York noticed less concrete cracking in the bearing areas at an abutment for their steel-girder bridges than that for their PC-girder bridges.

The Precast/Prestressed Concrete Institute (PCI), through the work of its Subcommittee on Integral Bridges, published a report (PCI, 2001) on the state-of-the-art of integral-bridge design. This report discusses the basic concepts for integral bridges and includes chapters that address general-design concepts for bridge superstructures, abutments, and piers; a chapter that highlights analysis models for integral bridges; and an appendix that presents five, case studies of in-service bridges. Details are presented for continuity of the superstructure at the piers that can be used for only slab continuity and for both slab and PC-girder continuity. The report discusses and illustrates several types of abutment details and presents suggestions for treating each end of an approach slab. Regarding structural analyses of joint-less bridges, the PCI report states that a two-dimensional, bridge model is usually sufficient for analyzing typical, integral bridges. For more complex bridges, such as those with large skew angles or horizontal curves, a three-dimensional, finite-element model that includes site-specific conditions should be applied to more accurately predict bridge behavior. An example is included in the report to illustrate calculations of pile forces, passive-soil forces, and pier forces.

2.2. Bridge field studies

Jorgenson (1983) conducted an experimental monitoring program of a 450-ft long, six-span, integral-abutment bridge that has five, PC, box girders. The bridge has a pressure-relief system that was installed directly behind the abutments and an expansion joint in the approach slabs, which was located at a distance of 20 ft from each abutment. The instrumentation devices included thermocouples to measure air and concrete-deck temperatures and slope indicators to measure the change in the slope along the length of selected abutment piles. Bridge-length measurements were made using a steel tape, and elevations were established using surveying techniques. Even though the bridge appeared to be geometrically symmetric, the displacements at each abutment were not equal to each other. The maximum movement at south and north abutments was 1.96 in. and 0.74 in., respectively. Based on the results of the field measurements and an analytical model of the bridge, Jorgenson concluded that the abutment piles experienced yielding when the south abutment was fully displaced.

An Iowa State University research project (Girton, et al. 1989 and 1991), which was sponsored by the Iowa Department of Transportation, involved the monitoring of temperatures, displacements, and strains in two, skewed, integral-abutment bridges. A steel-girder bridge and a PC-girder bridge were monitored over a two-year-time period for changes in bridge length, strains in one abutment pile, and deck and girder temperatures. Bridge-length changes and pile-bending strains showed daily and seasonal variations that were associated with thermal effects. For each bridge, a bi-

linear, temperature distribution was established through the depth of the composite-deck-and-girder superstructure.

Sandford and Elgaaly (1994) measured soil pressures behind the abutments of a steel, rigid-frame bridge. They used sixteen, soil-pressure transducers and determined that the soil pressure behind the abutment varied with soil depth. For an expansion condition of the bridge, the soil pressure did not always increase with soil depth. The maximum, soil pressure was estimated to have occurred at about one-third of the depth of the abutment backwall. Also, the researchers examined the effect of the bridge-skew angle on the soil pressure. The soil pressures acting the backside of the abutment were higher at the obtuse-angle corner of the bridge deck than at the acute-angle corner of the bridge deck. These researchers noted that soil pressures did not increase with successive seasons, and that the differences in the horizontal, soil pressures across the width of the abutment diminished over time.

Thermally-induced, superstructure displacements in a jointed bridge were measured by Pentas, et al. (1994a, 1994b). In their study, a multi-span bridge with both steel and PC girders was instrumented with thermocouples and linear-variable, displacement transducers (LVDTs). The LVDTs were used to measure relative, longitudinal movements between the adjoining girders sections at several expansion-joint locations. The relative-displacement measurements were made near the top and bottom of the bridge girders. These transducer measurements were used to calculate relative rotations between the girder ends. Unsymmetrical movements were recorded for the expansion joint along the width of the bridge. These measurements were not believed to be caused by transverse, temperature gradients in the bridge deck, but

rather due to the variability in the longitudinal stiffness of the neoprene supports for the bridge girders. These researchers concluded that a total-station, surveying instrument did not produce measured displacements that were very useful.

Several field investigations of thermally-induced bridge movements were completed in England. Darley and Alderman (1995) measured the thermally-induced cyclic movements of two, portal-frame bridges that contain massive concrete abutments. They determined that most of the bridge expansion was accommodated by movements of the abutments rather than by induced, vertical curvature of the bridge deck. Displacement measurements were made using high-precision, electronic, surveying equipment. This study did not continuously monitor, bridge displacements. Deck temperatures were measured with thermocouples that were installed throughout the depth of the concrete deck.

Darley, et al. (1996) instrumented a bridge with thermocouples, earth-pressure cells, and an inclinometer tube during its construction. The inclinometer tube was installed in one abutment to measure displacements and rotations of that abutment. The vibrating-wire, pressure cells were placed flush with the face of the abutment backwall to measure the soil pressures, which acted on that wall of the abutment. The measured soil pressures increased with the depth of the soil. Bridge temperatures were measured at six locations throughout the depth of the deck near one of the abutments and at the mid-span for one of the bridge spans.

For a two-span, composite, steel-girder bridge with integral backwalls, Hoppe and Gomez (1996) monitored strains, temperatures, and soil pressures during and for two-and-a-half years after the completion of the bridge construction. Soil pressures

were monitored near the base of the backwalls behind both abutments and directly below the strain gage that was installed on the backwall for one of the abutments. The soil pressures within the backfill soil were found to be nearly constant and close to the predicted, at-rest-soil pressure. When bridge expansion occurred, the measured, soil pressures indicated the development of passive-soil pressure at each end of the bridge. Hoppe and Gomez noted problems with the approach slabs for this bridge. In the first two years after the construction of the bridge, repeated resurfacing of the approach slabs was necessary due to excessive settlement of the approach slabs. The rate of settlement for the approach slabs decreased in the second year after the construction of the bridge.

MacGregor, et al. (1997) instrumented the Confederation Bridge in Canada to monitor strains, temperatures, and deflections in order to experimentally confirm some assumptions that were made during the design of this bridge. The Confederation Bridge is a multi-span, concrete, box-girder bridge. At the expansion joints, cable-tension, displacement transducers were installed. High-precision, surveying techniques were used to measure vertical and horizontal displacements of the bridge superstructure. Thermocouples recorded temperatures throughout the depth of the concrete-box girders. Vibrating-wire, strain gages were embedded in the box girders to determine the longitudinal strain distribution throughout the depth of the girders. Pyranometers were also installed to measure the intensity of solar radiation. A total of about 750, instrumentation devices were installed on the bridge.

Field tests of a steel-girder, integral-abutment bridge were performed by Oesterle, et al. (1999) from Construction Technologies Laboratories (CTL) to determine

the temperature gradients in a bridge superstructure. These researchers determined that the positive-temperature gradient recommended by the AASHTO LRFD Specifications (1998) was conservative, but the temperature gradient followed the general shape of the experimentally-measured, temperature gradients within the cross-section for the bridge. The maximum, experimentally-measured temperatures were approximately 60 percent of the recommended, maximum, AASHTO temperature.

Long-term monitoring of a non-skewed, PC-girder, integral-abutment bridge in Minnesota was performed by Lawver, et al. (2000). The abutment piles were oriented for weak-axis bending when the bridge superstructure was subjected to temperature changes. Longitudinal abutment movement was primarily a translational movement that induced double-curvature bending of the abutment piles. Tensile strains, which were recorded in a reinforcing bar in the approach slab near the connection of the slab to the deck of the bridge, were measured in the winter, as the superstructure pulled the abutment away from the backfill.

Since Lawver, et al. (2000) applied strain gages to the abutment piles during the construction of the bridge, measurements were made of the induced, axial strains in specific piles that were caused by the weight of the bridge superstructure. For the combined, dead load and thermal movements of the bridge, the maximum, axial, compressive strain in an abutment pile was 392 micro-strains. As the temperature of the bridge deck increased, the axial strains increased in an interior pile and decreased in an exterior pile for the abutment. The maximum, compressive strains in an abutment pile that were induced by combined, axial forces and bending moments were larger than the yield strain of the steel for the pile. This maximum strain was measured in the

flange tips of the pile near the pile cap and on the approach-slab side of the monitored, exterior pile.

Also, Lawver, et al. (2000) conducted static, live-load tests on this bridge. These researchers directed highway-maintenance personnel from the State of Minnesota to drive dump trucks loaded with sand to various locations on the bridge. The results from these live-load tests indicated that the three spans of the bridge essentially acted independent from each other. The connection details for the bridge girders at the bridge piers prevent continuity of the PC girders over the piers. Therefore, when live loads were applied to the bridge deck, the structure did not behave as a completely-continuous, multi-span structure. The experimentally-based, mid-span moments for the exterior spans were approximately 30 percent smaller than the analytically-predicted, mid-span moments for a pinned-end-span model and about 20 percent greater than those moments that were predicted for a span model which was pinned at one end and fixed at the other end. The center span essentially behaved as a simple span for the applied live loads.

Investigators at the University of Minnesota (Huang, 2004) studied the behavior of a prestressed concrete integral-abutment bridge in Rochester, Minnesota. This publication is the final report for the work that was initially reported by Lawyer (2000). These researchers monitored abutment horizontal movements, abutment rotations, abutment pile strains, earth pressure, pier pile strains, prestressed girder strains, concrete deck strains, thermal gradients and weather from 1996 to 2004. Two live load tests were also conducted. A three-dimensional, finite-element model of the bridge including soil-structure interaction was calibrated to the live load tests and the seasonal

data. The finite-element model was used to investigate the effect of pile configurations, soil conditions, bridge length and skew, and wingwalls configurations, on bridge performance. Significant findings of this work included:

- The abutment substructure provided small rotation restraint to the end-span girders.
- Environmental loading effects were as large as or larger than the live load effects.
- The 131 ^{o}F, measured temperature range was larger than the 80 ^{o}F, temperature range given in the AASHTO, Load and Resistance Factor Design Specifications (2002).
- The measured thermal gradients were 9 ^{o}F to 10 ^{o}F smaller than that specified in the AASHTO, Load and Resistance Factor Design Specifications (2002).
- Bridge shortening steadily increased, presumably because the concrete creep and shrinkage period may have been extended for this particular bridge at a relatively, high-humidity site. Average pile curvatures steadily increased.
- Inconsistent abutment movement data were observed between horizontal extensometers, crack meters, and surveys and results "should be viewed with caution."
- Nearly two percent of the flange cross section had longitudinal strains that exceeded the steel yield strains.
- The measured, coefficient of thermal expansion and contraction, which was between 6.1 and 6.4 microstrains per ^{o}F, was greater than the AASHTO recommended value of 6.0 microstrains per ^{o}F.
- Earth pressure readings were reliable in the narrow temperature range of 50 ^{o}F to 77 ^{o}F.

These researchers recommended a simplified, pile-design approach, and they investigated and eliminated low-cycle fatigue as a design consideration. Some of their other recommendations included:

- A 130 ^{o}F temperature range should be used for PC girder bridges.
- Four to six-foot depth, predrilled holes should be used for the abutment piles.

- A pile analysis method that addressed:
    - A strength analysis that was similar to Greimann, et al. (1987a) with slight modifications for the effective-pile length.
    - Concrete creep and shrinkage effects should be included in the design of the bridge, but a method is not clearly identified.
    - The abutment piles should be oriented to bend about the weak axis during thermal expansion and contraction of the bridge superstructure.
    - Pile can be designed for only vertical loads with an allowable stress of 9 ksi, as verified using axial force and bending moment interaction curves. Presumably, this approach would satisfy pile-ductility limitations. With this approach, bridge length limits would be conservative relative to other investigators.
- To reduce concrete stress and improve pile behavior, a hinged connection should be used between the abutment-pile cap and abutment diaphragm.
- The configuration for an abutment wingwall has little effect on the behavior of the abutment piles.

2.3. Pile tests

2.3.1. Field tests

To experimentally verify the strength of an isolated pile, Greimann, et al. (1987a) conducted field tests of a pile-and-girder system that was subjected to three, load cases: (1) vertical load only, (2) horizontal displacement of pile head only, and (3) combined horizontal displacement of pile head with subsequent vertical load. Both tests (1) and (3) reached the same ultimate vertical load, that is, the horizontal displacement had no effect on the vertical-load capacity. Also, these researchers conducted one-tenth-scale, pile-model tests in sand. The experimental results from both the field and model tests were used to develop the vertical and horizontal, load-displacement properties of the soil. These properties were input into the finite-element, computer

program “Integral Abutment Bridge Two-Dimensional”. The experimental and analytical results compared well for the test cases.

2.3.2. Laboratory tests

The use of PC piles in integral-abutment bridges was investigated by Kamel, et al. (1996). These researchers studied the lateral-load versus lateral-displacement relationship for both PC piles and steel, HP-shaped piles. The steel piles experienced greater lateral displacements than that for the PC piles before the allowable-moment strength was developed for a cross section of the pile. Laboratory tests of piles in loose sand, which is sometimes placed in pre-bored holes for integral-abutment piles, revealed that the density of the sand had a significant effect on the lateral displacements of both types of piles. The lateral displacements of a pile head were dependent on the lateral stiffness of the soil against the upper 10 ft of the pile length. The lateral stiffness of the soil below this depth had a negligible effect on the lateral displacement at the pile head. This behavior was observed for both the PC piles and the steel, HP-shaped piles.

Small-scale-model tests on steel, H-shaped piles, which were subjected to lateral and vertical loads, were performed by Amde, et al. (1997). Experimentally-measured, lateral displacements of the pile, computed bending moments in the pile due to lateral displacements of the pile head, and vertical-load capacities for the pile were compared with those results that were predicted by a nonlinear, finite-element program, which was developed by Wolde-Tinsae, et al. (1982) for the soil-to-pile interaction. Soil force versus displacement relationships were approximated using the Ramberg-Osgood Model (Desai and Wu 1976), which is described in Chapter 5 of this report. The finite-

element predictions for the lateral displacements at the pile head were greater than the experimentally-measured displacements at the pile head for the same lateral load. The finite-element model underestimated the vertical-load capacity of a friction pile. For a combined axial and lateral load on the piles, the vertical resistance of the soil was exceeded before a plastic hinge developed in the steel piles. This behavior was observed in the experimental tests and for the analytical analyses.

Laboratory tests of an HP10 x 42, a 14-in.-dia. pipe, and a 12-in-sq. PC pile were performed by Arsoy, et al. (2002) to simulate 75 years of service life for a pile in an integral-abutment bridge. The pile-embedment details into a reinforced concrete (RC) block were modeled after the construction details for this type of a bridge that are used by the Virginia Department of Transportation (Virginia DOT). For the HP-shaped pile and the pipe pile, the steel grade was A572 Gr. 50 and A252 Gr. 3, respectively. The PC pile was the standard, Virginia DOT pile that had five, ½-in. diameter, 270-ksi, low-relaxation-steel strands. The amount of prestress in the pile was equivalent to an axial compressive stress of 920 psi. Small and large amplitude-displacement cycles were applied to the test pile to represent daily and seasonal, respectively, temperature changes of a bridge superstructure. A total of about 27,000, horizontal-displacement-control cycles were applied to one end of a test pile. The HP-shaped pile was oriented for weak-axis bending and was stressed up to 50 percent of the nominal, yield stress for the pile. Axial loads were simultaneously applied with the horizontal displacements for only the HP-shaped pile. Testing limitations prevented simultaneously applying an axial load to the laterally-displaced pipe and PC piles. Based on the test results, Arsoy, et al. concluded that the HP-shaped pile was the best choice of the three types of piles for an

integral abutment. Since the steel-pipe pile was substantially stiffer than the HP-shaped pile, an abutment would be subjected to larger stresses that could damage an abutment, if a pipe pile was used rather than an HP-shaped pile. Since the tested PC pile developed tension cracks that were spaced along the length of the pile, these authors did not recommend using PC piles for integral-abutment bridges. Arsoy noted that this type of a pile may experience progressive, concrete cracking and damage, when cyclic-horizontal displacements occur at the pile head.

2.4. Analytical studies

2.4.1. Thermal analyses

Many analytical and experimental studies have been conducted to investigate bridge temperatures. The analytical studies usually make use of a heat-flow model that can incorporate air temperature, solar radiation, wind effects, and bridge material properties in the analysis. Field studies are often conducted to confirm analytical results. The simplest method of measuring bridge-member temperatures involves using thermocouples that are embedded in the bridge superstructure.

Two-dimensional, temperature distributions were computed by Elbadry and Ghali (1983) for varying climatic input and bridge, cross-sectional properties. For a bridge with a constant cross section along its length, temperature variations along the bridge length were determined to be negligible. Finite-element-modeling techniques were applied to calculate longitudinal stresses in concrete bridges due to non-uniform temperature distributions in a cross section for a bridge. Maximum, longitudinal stresses were predicted to occur when there was a large range in the daily, ambient temperature; when solar radiation was a maximum; and when the wind speed was low.

Elbadry and Ghali determined that an asphalt topping on a concrete, bridge deck increased the temperature-induced stresses in a cross section for a concrete bridge.

Potgieter and Gamble (1989) used a one-dimensional model to predict temperature gradients through the depth of bridge superstructures. Using national-weather data as input for their model, these researchers estimated the maximum, vertical, temperature gradients for bridges that are located in different regions throughout the continental United States. Their study revealed that solar radiation had the greatest effect on this temperature gradient. Negative, temperature gradients, which occur when the top of a bridge deck is cooler than the bottom flange of the bridge girders, were revealed by these researchers to occur at night. Potgieter and Gamble predicted that for bridges, which are located in the mid-west region of the United States, about a 45 °F difference occurs between the maximum, bridge-deck temperature and the minimum temperature throughout the depth of a bridge superstructure. An asphalt overlay on a concrete, bridge deck was determined not to cause an increase in the temperature gradient in the concrete superstructure from that for a bridge with a concrete-deck surface. These researchers stated that an asphalt re-surface acts as an insulation layer and reduces the maximum temperature in the concrete deck. Positive-temperature gradients, which occur when the top of a bridge deck is hotter than the bottom flange of the bridge girders, were predicted by Potgieter and Gamble (1989). Their temperature gradients are similar to those recommended by the AASHTO LRFD Specifications (1998). Temperature differences of less than 4 °F were observed in the bottom 6 in. of a bridge superstructure.

Thermal analyses of bridges involving various parameters were conducted by Moorty and Roeder (1992). Their results suggest that in some climatic regions of the United States, the recommended, design-temperature range in the AASHTO Standard Specifications (1996) is too low for concrete bridges and is too high for steel bridges. Also, these researchers examined temperature-dependent displacements of skewed and curved bridges with different joint configurations. Moorty and Roeder suggested that integral abutments in skewed bridges might increase the abutment movements in the transverse direction of a bridge compared to those displacements for the same bridge without integral abutments.

Time-dependent, weather models for estimating ambient-air temperature and solar radiation were developed by Hulsey and Powell (1993). These predicted, thermal parameters were compared with historical weather data for locations in Columbia, Missouri and Fairbanks, Alaska. The temperature models can be incorporated into finite-element or finite-difference programs to calculate temperatures within bridge structures.

2.4.2. Integral-bridge analytical studies

Previous analytical studies investigated many aspects of integral bridges. Research has included soil pressures behind a translating abutment, pile-to-soil interaction, bridge displacements, stresses in bridge members, and concrete creep and shrinkage effects.

A two-dimensional, frame model was developed by Girton, et al. (1989) to predict the longitudinal displacements of an abutment in an integral-abutment bridge. A frame model was developed to predict the longitudinal displacement of the bridge. This

analytical model incorporated the flexural stiffness of the piles and axial and flexural stiffness of the bridge superstructure. These researchers neglected the displacement restraint of the soil backfill. A bi-linear, temperature distribution through the depth of the superstructure was applied to the model. Also, Girton, et al. developed a two-dimensional, frame model to predict pile strains that are induced by longitudinal, thermal movements of an abutment.

A lateral-frame model was developed by Girton, et al. (1989) to predict pile strains that are induced by the lateral movement of a skewed abutment. Equivalent cantilevers were used to model the piles, with an axial spring at the bottom of the equivalent-cantilever length. This spring represented the axial shortening and vertical slippage of the pile. Transverse, abutment movements were calculated for an applied, lateral force that corresponded with the transverse component of a normal, passive-soil and soil-frictional forces that acted on the abutment.

A comprehensive, analytical study of five, in-service, integral-abutment bridges was undertaken by Thippeswamy and GangaRao (1995). Due to page limitation for the journal article, the bridge that was reported in the paper was the Lone Tree Road Bridge in Black Hawk County, Iowa. Their analyses were performed using two-dimensional, frame models with different rotational-restraint conditions for the supports. Also, the orientation of the abutment piles in these analytical models was set to produce either weak-axis or strong-axis bending of the piles, when the modeled bridge experienced a change in temperature. The loading conditions that were considered by these authors involved gravity, soil pressure, concrete creep and shrinkage, differential support settlement, and temperature. Some of the conclusions that Thippeswamy and

GangaRao reached were that temperature loading produced significant stresses in the bridge, concrete creep reduced the induced bending stresses, concrete shrinkage relieved some of the effect of concrete creep, soil pressures induced negligible stresses in the bridge, and support settlements induced significant stresses in multiple-span integral bridges.

An analytical investigation to determine the effects of thermal loading and soil-to-structure interaction on the performance of steel-girder, integral-abutment bridges was conducted by Siros (1995). When a uniform temperature change was applied along the length of the bridge superstructure, and a temperature gradient was applied across the depth of the concrete deck, stresses in the concrete deck and steel girders were calculated for various boundary conditions for the abutments. For these analyses, the bottom surface of the abutments were considered to be either fixed; pinned; or horizontally restrained by springs with an equivalent, horizontal stiffness that was based on either an upper-bound or a lower-bound, soil stiffness. When the lateral stiffness of the abutment backfill was set equal to an upper-bound limit for the soil stiffness, the predicted stresses that were induced in the bridge deck and girders were about 9 and 28 percent of the allowable stresses for the concrete and steel, respectively. When the lateral stiffness of the abutment backfill was set equal to a lower-bound limit for the soil stiffness, those stresses became 8 and 22 percent of the allowable stress for the concrete deck and steel girders, respectively.

Also, Siros (1995) developed a non-linear, three-dimensional model of a composite, steel girder, integral-abutment bridge to predict the stresses in the concrete deck and steel girders that are induced by concrete creep. He compared these

stresses with those same stresses that were predicted by his linear, two-dimensional, analytical model for the same bridge. Since small differences occurred between the stresses that were predicted by the two, analytical models. Siros justified the use of a two-dimensional, analytical model of a bridge to predict the effect of concrete creep on bridge behavior. The stresses in the concrete deck that were induced by concrete creep ranged between 26 and 49 percent of the induced, dead-load stresses, and the corresponding stresses in the steel girders ranged between 2 and 21 percent of the induced, dead-load stresses. Concrete creep increased the positive and negative, longitudinal stresses in the steel girders and reduced the longitudinal stresses in the concrete deck.

A three-dimensional, finite-element analysis of a three-span, non-skewed, steel-girder, integral-abutment bridge was performed by Ting and Faraji (1998). These researchers used the Georgia Institute of Technology's, GT-STRUDL program (1991). The bridge deck and abutments were modeled using bending and stretching-plate elements, and the girders, piles, piers, and pier caps are modeled as beam elements. Two, geometric conditions were considered by Ting and Faraji for the horizontal alignment between the girders and the deck. One model neglected and another model considered the vertical eccentricity between the center of gravity of the girders and the mid-thickness of the bridge deck. The soil backfill behind the abutments and the soil along the length of the piles were modeled as uncoupled, non-linear springs that were located at the finite-element nodes for the abutment wall and piles. The non-linear properties for the soil were based on the soil-stiffness, design curves by Clough and Duncan (1991) and by O'Neal and Murchison (1983). Ting and Faraji conducted a soil-

parameter study that involved four sets of soil compactions. For the soil against the abutments and the soil along the piles, the soil densities were loose and loose, loose and dense, dense and dense, and dense and loose, respectively.

Ting and Faraji (1998) determined that the vertical eccentricity between the center of gravity of the girders and the mid-thickness of the bridge deck must be considered to properly predict bridge behavior. Neglecting this vertical eccentricity for an analytical model of a bridge, greatly decreases the flexural rigidity of the bridge superstructure. For the finite-element models that included this vertical eccentricity, the horizontal stiffness of the soil behind the abutments significantly affected the displacements of the abutments. Longitudinal displacements at the base of an abutment ranged between 0.36 and 0.38 in. for a loose-soil backfill and between 0.26 and 0.28 in. for a dense-soil backfill. The abutment rotation in a vertical plane was approximately 0.060 deg. for a loose-soil backfill and about 0.100 deg. for a dense-soil backfill. The maximum, bending moments in the abutment piles, which occurred at the abutment-to-pile connection, ranged between 55 and 80 k-ft for a loose-soil backfill and between 20 and 35 k-ft for a dense-soil backfill. The abutment backfill nearly reached a full-passive-soil-pressure condition. The distribution of the soil pressures over the depth of an abutment was slightly nonlinear. The lowest, soil pressures occurred near the bottom of an abutment.

As part of this same research, Ting and Faraji (1998) developed two-dimensional, finite-element models for the same bridge that they analyzed using three-dimensional, finite-element models. One-seventh of the bridge cross section was modeled, since the bridge contained seven piles per abutment and seven girders. The

support conditions for the girders at the bridge piers were considered to be either pins, rollers, or a pier model that included nonlinear-soil springs. For non-skew bridges, the horizontal displacements for the abutments and piles, the bending moments in the abutment piles, and the bending moments in the girders that were predicted by two-dimensional analytical models that had the bridge piers modeled as roller supports correlated well with those analytical responses that were predicted by their three-dimensional, finite-element models for the bridges.

A nonlinear, finite-element analysis that involved the interaction between an abutment and the soil backfill was conducted by Oesterle, et al. (1999). These researchers determined that the Rankine, passive-soil-pressure model provided an adequate estimation of the soil pressures against the back of a bridge abutment when large abutment movements were caused by expansion of the bridge superstructure. Also, these researchers noted that the Clough and Duncan (1991), soil-stiffness, design curve for soil pressure, which was based on wall movement, provided a reasonable, upper-bound value for the soil pressure against an abutment that experiences large displacements. A high, soil pressure occurs near the base of an abutment, and this base pressure decreases with an increase in the abutment rotation. Oesterle, et al. determined that a decrease in the compaction of the soil backfill from 90 to 80 percent will decrease the resultant, passive-soil-pressure force by a factor of about two and a half. Also, these researchers determined that a decrease in the slope of the in-situ, soil backfill from 45 to 30 deg. will decrease the resultant, passive-soil-pressure force by a factor of about two.

Lehane, et al. (1999) developed a simplified, elastic model to predict the axial forces and bending moments that are induced in the superstructure of a frame-type, integral bridge, when thermal expansion occurs for the bridge superstructure. An expression for an equivalent, linear-stiffness modulus for a cohesionless-soil backfill was developed for a range of in-situ, dry-soil densities; for the effective stress of the soil; and for average, shear-strain levels. A simplified, plane-frame model that incorporated an equivalent abutment height and a translational, linear spring at the deck level was developed to represent the abutment-and-soil-backfill system. The results from the simplified, analytical model correlated well with the results predicted by a more detailed, finite-element model.

Interactions between abutment piles and foundation soils, between approach fills and foundation soils, between abutments and approach fills, and between abutments and their piles were analytically investigated by Arsoy, et al. (2002). These researchers used finite-element models for isolated piles and for integral-type bridges. These analytical models included finite elements for approach fills and foundation soils. Their proto-type bridge had three, 100-ft-long spans; W44 x 285, steel girders; a 10-in.-thick, RC deck; 10-ft high by 3-ft wide abutments; and HP10 x 42 steel piles. Both integral abutments and semi-integral abutments and three, soil conditions (dense, medium dense, and loose sand) were incorporated in their study. Based on the parametric analyses that were conducted, Arsoy, et al. concluded that the presence of approach fills significantly reduces the forces in the abutment piles from that which would occur without an approach fill because the approach fill drags the foundation soil in the same direction as the movement of the pile head. These researchers concluded that semi-

integral abutments induce significantly smaller, pile stresses than those induced by integral abutments, when both types of abutments had the same amount of horizontal displacement at the top of the abutment piles.

2.5. Integral-abutment design models

2.5.1. Bridge temperature

Bridges need to be designed to accommodate the displacements that are induced by variations in the temperature of the structure. The AASHTO Standard Specification (1996) requires that consideration shall be given to the locality in which the structure will be built and to the lag between the air temperature and the bridge temperature. The two, specified, design-temperature ranges for steel structures are from 0 °F to 120 °F for bridges located in moderate climates and from -30 °F to 120 °F for bridges located in cold climates. Concrete structures shall be designed for changes in temperatures of +30 °F and -40 °F for moderate climates and +35 °F and -45 °F for cold climates. The design temperature range is much smaller for concrete structures than that for steel structures.

MacGregor, et al. (1997) established bridge-design temperatures for the Confederation Bridge. For this bridge, the maximum, average, bridge temperature was 9 °F above the 2½ %, dry-bulb temperature in July and the minimum, average, bridge temperature was 5 °F above the 2½ %, dry-bulb temperature in January. Also, vertical gradients for the temperature through the depth of the superstructure were specified for this bridge. By assuming a bridge temperature when the bridge became a continuous structure, changes in bridge temperature were calculated and used for the thermal loads on the bridge. Statistical methods were applied to predict a 100-year,

temperature drop that was based on the daily, average temperature for 46 years. Since the bridge has a large thermal mass, the temperature of the superstructure was related to the 3-day, average, minimum temperature.

A method for determining the average, bridge-temperature range and for establishing the vertical distribution of temperature in bridge superstructure that can be applied for the design of an integral-abutment and joint-less bridges was developed by Oesterle, et al. (1999). The design temperatures are based on the 24-hour, mean, shade- temperature data given in the American Society of Heating, Refrigeration, and Air-conditioning Engineers (ASHRAE) Handbook (1993). The effect of solar radiation can be incorporated in the temperature evaluation. Oesterle, et al. recommended using the vertical distribution for the temperatures through the depth of a bridge superstructure that is provided in Art. 3.12.3 of the AASHTO LRFD Specifications (1994) for the design of continuous-girder structures.

To provide bridge engineers with bridge-temperature data, Roeder (2003) presented design maps of the contiguous 48 states of the United States of America that show temperature contour lines for extreme, average minimum and average maximum, bridge temperatures. Different bridge-temperature maps are provided for steel bridges with concrete decks and for concrete bridges. To develop these temperature maps, Roeder considered the relationship between bridge temperature and climatic conditions that occurred over more than 60 continuous years. This researcher used these temperature maps as a part of his proposed, design recommendations for bridge movements. Roeder verified his design recommendations in a comparative study of predicted and measured, bridge temperatures and displacements. The author's paper

discusses installation temperatures and bridge movements for mechanical and elastomeric bearings and for expansion joints. Roeder stated that his proposed design recommendations, which are currently under review for adoption into the AASHTO Specifications, will produce some significant changes in the predicted thermal movements of some bridges. This researcher concluded that concrete bridges will experience smaller movements than that for steel-girder bridges with concrete decks, but the difference in the movements is not as large as that suggested in the AASHTO Specifications (1998); and that the proposed thermal movements for steel-girder bridges and concrete-girder bridges are comparable or smaller than those movements, which are presently required movement in most regions of the United States of America, and larger than those movements, which are presently required in the north central part of the country.

2.5.2. Coefficient of thermal expansion and contraction for concrete

The American Concrete Institute (ACI) publication ACI 209R (1998) provides a lower-bound and an upper-bound value for the coefficient of thermal expansion and contraction (α-coefficient) for concrete of 4.7×10^{-6} in./in./°F and 6.5×10^{-6} in./in./°F, respectively. These α-coefficients can be used to estimate a range of thermal movement for highways and bridges. Also, ACI 209R provides an empirical equation to determine an α-coefficient that is based on environmental conditions for exposed concrete and for the characteristics of the aggregates.

In the absence of more precise information regarding the α-coefficient for concrete, Oesterle, et al. (1999) recommended the use of an α-coefficient of concrete equal to 6.0×10^{-6} in./in./°F. This magnitude for the α-coefficient is conservative. These

researchers experimentally determined an average, α-coefficient of concrete that was equal to 4.9×10^{-6} in./in./°F.

When a specific, concrete-mix design is available, Emanual and Hulsey (1997) developed a method that can be applied to determine an accurate value for the α-coefficient of concrete. Their approach incorporated the characteristics of the aggregates, the concrete-mix proportions, moisture content, temperature, and age of the cured concrete.

2.5.3. Bridge displacement

Modification factors (Γ-factors) that are applied to the calculated, longitudinal displacements for an integral abutment to account for the variability of several, design parameters were developed by Oesterle, et al. (1999). These parameters included the α-coefficient of the concrete, concrete creep and shrinkage strains, bridge temperature when the bridge becomes an integral structure, modulus of elasticity of the concrete, and lateral stiffness of the soil behind the abutment. These researcher's design recommendations for determining the change in the length of a bridge include an initial expansion phase, an initial contraction phase, and a re-expansion phase. According to these researchers, any initial, longitudinal expansion of a bridge superstructure, which occurs immediately after the completion of the bridge construction, consists of thermal expansion of the bridge superstructure and a reduction in that expansion due to concrete creep and shrinkage. To determine the magnitude of concrete creep and shrinkage contraction, the duration of the initial expansion is assumed by Oesterle, et al. to be equal to one-quarter of the construction season and the girders are assumed to be 90-days old when the bridge deck is cast. According to these researchers, any initial,

longitudinal contraction of a bridge superstructure, which occurs immediately after the completion of the bridge construction, includes thermal contraction of the bridge superstructure and an increase in that contraction due to concrete creep and shrinkage. To evaluate the magnitude of this initial contraction, the predicted, maximum, concrete creep and shrinkage strains are used and the girders are assumed to be 10-days old when the bridge deck is cast. Re-expansion of a bridge superstructure involves an increase in the average, bridge temperature that is equal to the entire design-temperature range. For this bridge re-expansion, the concrete creep and shrinkage are not included, since they are assumed to have already occurred prior to the bridge re-expansion.

Oesterle, et al. (1999) experimentally investigated concrete creep and shrinkage by subjecting 6-in. dia. by 12-in. long, concrete cylinders to several environmental and stress conditions. For their test specimens, these researchers determined that concrete creep and shrinkage strains decreased the temperature-induced elongation strains by approximately 12 and 3 percent for non-freezing and freezing conditions, respectively. Oesterle, et al. recommended the use of the concrete creep and shrinkage strains that are provided by ACI Committee 209 (1998). Articles 5.4.2.3.2 and 5.4.2.3.3 of the AASHTO LRFD Specifications (1998) on concrete creep and concrete shrinkage, respectively, are based on the recommendations from ACI Committee 209.

Oesterle, et al. (1999) determined that a free expansion of a bridge superstructure provided a reasonable estimate for bridge re-expansion. The passive-soil pressure for the soil behind the abutments and the flexural stiffness for the bridge piers provide negligible restraint regarding longitudinal displacements of a bridge

superstructure. Confirmation of this expansion behavior was observed for the PC-girder, integral-abutment bridge that was monitored by Lawver, et al. (2000). This bridge experienced a thermal expansion equal to about 96 percent of the total theoretical elongation, when the bridge was treated as an unrestrained structure for longitudinal expansion.

Abutment movements that are transverse to the length of a bridge need to be investigated for the design of skewed, integral-abutment bridges. Based on typical, soil-friction angles for a granular backfill, Oesterle, et al. (1999) recommended that transverse displacements for an integral abutment need to be calculate when the skew angle for a bridge is greater than 20 deg. These researchers presented a design chart for determining the magnitude of the transverse displacement of an abutment that included the thermal expansion of the abutment and was based on the skew angle for a bridge, the length of the bridge, and the bridge-length-to-width ratio.

2.5.4. Pile design

Greimann, et al. (1987a, 1987b) and Abendroth and Greimann (1989a, 1989b) presented procedures for designing the abutment piles in an integral-abutment bridge for thermally-induced, lateral translation and applied vertical loads. To model an abutment pile as an isolated, structural member with idealized, end-restraint, boundary conditions, Greimann et al. (1989a) and Abendroth and Greimann (1989a, 1989b) developed three equivalent-cantilever lengths. These equivalent lengths, which were based on the flexural buckling; maximum, bending moment; and horizontal stiffness of a pile in soil, were used by these researchers in two alternative, design methods. Alternative One is quite conservative and does not permit plastic redistribution of

internal forces. Alternative Two is also conservative, but for this design method, plastic redistribution is permitted to occur in an abutment pile. To use Alternative Two, the pile cross section must have sufficient, inelastic-rotation capacity before local buckling occurs in an element of the cross section. To illustrate the application of both design alternatives, Greimann, et al. (1987a) presented a design example for a friction pile and another design example for an end-bearing pile. A continuation of the integral-abutment research at Iowa State University was performed by Girton, et al. (1989 and 1991). This research provided additional confirmation of the design procedures for the piles in an integral abutment.

Methods for determining the effective lengths of laterally loaded piles that are used in the equivalent-cantilever method for modeling the pile-and-soil system were investigated by Chen (1997a, 1997b, 1997e). This researcher made comparisons between the effective lengths that were obtained by approximate methods used in design and more precise, analytical methods. Chen's work revealed that none of the approximate methods for the pile-and-soil system consistently provided conservative results for the effective lengths of laterally-loaded piles. Chen proposed a numerical procedure to predict the effective length of laterally-loaded, steel, HP-shaped piles. Design tables were provided for establishing the effective-pile length for the bending moment, horizontal stiffness, and buckling of piles supported in various soil conditions. The author recommended that the design of laterally-loaded piles should be based on the more conservative of either the author's proposed method or the approach presented in the AASHTO LRFD Specifications (1994). Chen recommended using a 10 to 20-ft depth for a pre-bored hole that is backfilled with loose sand for each abutment

pile; using stub-type abutments with a single row of piles oriented for weak-axis bending that would be induced by movements of the abutments in the longitudinal direction of the bridge; setting a 600-ft long, maximum length for an integral-abutment bridge; setting a 20-deg., maximum, bridge-skew angle for PC-girder, integral bridges; and attaching the approach slabs to the abutments.

When the calculated horizontal displacements at the tops of the abutment piles exceeds the displacement limits for a specific, pile size and orientation, Oesterle, et al. (1999) presented several, pile-design options to improve the ductility for a pile. Their first option was to increase the size of the pile cross section. Their second option was to re-orientate the pile for strong-axis bending (the pile web is parallel to the bridge length) when the bridge superstructure experiences a thermally-induced, longitudinal movement. For either of these options, Oesterle, at al. stated that the pile-displacement limit will increase for a pile. However, these researchers noted that the increased flexural stiffness of the pile will cause a larger moment to be induced at the top of the pile when the bridge superstructure is subjected to temperature changes. Based on the recommendations by Yang, et al. (1985), Oesterle, et al. suggested a third option that involved the use of a pre-bored hole for each abutment pile. Prior to casting the abutment-pile cap, these holes should be filled with loose sand. These researchers stated that loose sand along the upper portion of a pile increases the flexibility of the pile for lateral displacements of the pile head. A fourth option, which was proposed by Oesterle, et al. to increase the lateral-displacement capacity of the abutment piles, was to use semi-integral abutments rather than integral abutments. Two types of semi-integral abutments were suggested by these researchers. The first type of an abutment

has a pinned-pile-head condition. The second type of an abutment permits horizontal translation between the abutment and the pile cap, which eliminates lateral displacement at the top of an abutment pile. These researchers noted that both types of semi-integral abutments will increase the cost of the bridge construction compared to other types of abutments. Also, Oesterle, et al. commented that these types of semi-integral abutments and may require future costs to maintain the abutment.

A design example for HP10 x 42 piles in a 426-ft long, three-span, integral-abutment bridge with steel girders was presented by Wasserman (2001). The pile behavior was modeled using a computer program that accounts for the elastic-plastic, soil-and-structure interaction to establish the point of inflection in a pile. Wasserman used the computer program "COM624P"-Laterally Loaded Pile Analysis Program for the Micro-computer, Version 2.0, which was presented in a Federal Highway Administration (FHWA) final report (Report No. FHWA-5A-91-048). The author notes that more refined programs such as "L Pile" and "Florida Pier" are available on the Florida DOT web site www.dot.state.fl.us/structures/. Wasserman's example also includes an evaluation of the strength of the pile-to-pile cap connection. Regarding the pile orientation, Wasserman stated that y-axis (weak-axis) bending, which is induced by pile-head displacement, provides the least resistance to lateral displacement. However, Wasserman stated that due to flange-local buckling, this pile orientation will be more limiting regarding the displacement at the top of the pile than that associated with x-axis (strong-axis) bending.

For the design of steel, HP-shaped, abutment piles for an integral bridge, engineers apply interaction relationships that involve axial compression and bending

moment(s). These strength-behavioral models for combined loading were established for typical beam-column members in structural frames, which have specific effective lengths for flexural buckling and unbraced lengths for lateral-torsional buckling. Ingram, et al. (2003) disputed the applicability of the AASHTO Standard Specification (1996) and the AISC LRFD Specification (1998), beam-column-interaction equations for integral-abutment piles that are surrounded by soil. These researchers performed field tests on two, HP10 x 42 piles that were driven about 38 ft into soil. A pre-bored hole was not used for either pile. The first pile was driven into a compacted fill, and the second pile was driven into virgin clay. Each pile had a RC abutment that was cast around the top of the pile. The pile tests were monitored using strain gages along the length of the piles, load cells, and displacement transducers. Vertical and horizontal loads were applied to the test piles. From these field tests, axial load and bending moment resistances were experimentally established for the test piles.

To analytically predict and axial load versus bending moment, interaction relationships for the test piles, Ingram, et al. (2003) applied the AASHTO Standard Specification (1996); AISC LRFD Specification (1998); and a plastic-limit-strength criteria, which neglected any member length effects on axial load and bending moment resistances. These researchers graphically illustrated the three interaction relationships for the test piles and showed experimental data points on these same graphs. The experimentally determined pile resistances were more closely predicted by the plastic-limit-strength criteria than by the AASHTO or AISC member-resistance models. Ingram, et al. concluded that the AASHTO and AISC interaction-design equations, which consider member length effects, do not accurately model the behavior of a pile in soil.

2.5.5. Abutment backfill

Koch and Schaefer (1992) determined that the development of voids in the soil beneath the approach slabs for integral-abutment bridges was primarily due to the thermally-induced movements of the abutments. Their study of 79, integral-abutment bridges in South Dakota revealed that soil voids beneath approach slabs occurred for 78 of these bridges. These researchers determined that this type of soil void will occur even when a 97%-relative compaction is used for the approach-slab fill. Koch and Schaefer noted that uplift of approach slabs was encountered when high-compaction levels were used for the abutment backfill.

Experimentally-measured, lateral-soil pressures for skewed, integral-abutment bridges were used by Sanford, et al. (1994) to develop soil-pressure envelopes in the vertical and horizontal directions. The authors recommended vertical and horizontal, soil pressures for a steel, rigid-frame, integral-abutment bridge. The maximum, lateral-soil pressure was assumed to occur at one-third of the abutment depth from the surface of the roadway. This depth was approximately at the bottom of the bridge girders. The experimentally-measured, soil pressures acting on the abutments were larger on the obtuse-angle side of the bridge deck for a skewed, integral abutment bridge.

Springman, et al. (1996) provided several comments regarding the soil backfill for integral abutments. These researchers recommended that a medium-dense to dense, granular backfill should be used behind integral abutments. A soil backfill with a lower stiffness was not recommended, since cyclical, horizontal displacements of an abutment over time will compact the backfill material. Also, if a loose backfill is used, settlement will occur for the approach slabs. These researchers noted that the length of the soil-

settlement region behind an abutment is equal to about 60 percent of the height of the abutment. Springman, et al. stated that the grain size for a granular backfill should be in the sand-to-gravel-size range, and that the backfill should not contain silt because silt will allow capillary action to occur for water in the backfill. The presence of silt in a backfill will increase the effective stresses in the soil and increase the maximum, passive-soil pressure on the abutment.

In an attempt to minimize the development of voids in the soil beneath approach slabs for integral-abutment bridges, Reid, et al. (1998) studied the effect of placing a vertical layer of rubber-tire chips between the backfill soil and the back of an abutment. The rubber-tire chips reduced the soil pressures in the backfill for their bridge models; but, a soil void still developed similar to that observed in a bridge model without rubber-tire chips. These researchers concluded that the lack of compaction of the rubber-tire chips might have caused the development of the voids in the soil.

Oesterle, et al. (1999) stated that high compaction of the backfill soil behind an abutment is not advantageous, since voids will still occur in the soil, and the passive-soil pressure is lower for a loose backfill compared to that for a dense backfill. These researchers recommended the use of a well-graded, granular soil with approximately 90%-relative compaction. This level of soil compaction approximately represents the medium-dense, soil condition that was defined by Clough and Duncan (1991).

2.5.6. Approach slabs

The potential of damaging an approach slab due to temperature-induced movements of an integral-abutment bridge was discussed by Burke (1987). As the superstructure for this type of a bridge contracts during the winter, the joint between the

bridge deck and an approach slab will open, if the approach slab is not tied to the abutment, or the joint between an approach slab and an adjacent pavement slab will open, if the approach slab is tied to the abutment. An open roadway joint can become filled with debris. Then, when the bridge superstructure expands in the summer, the debris-filled joint will close, which will cause the approach slab to be compressed between the abutment and the pavement slab. Compression of an approach slab may fracture a rigid pavement or deteriorate a flexible pavement. In his 1987 paper, Burke discussed various approach-slab designs that have been used to minimize problems with these slabs.

The Ohio DOT has experienced problems with approach slabs for integral bridges. As a follow-up on his 1987 paper, Burke (1999) noted that distress in these slabs was caused by repeated, seasonal-temperature cycles and the accumulation of debris in the joint between the back of an abutment and an approach slab. The approach slabs were pushed away from the ends of a bridge. As traffic crosses these joints, the approach-slab seats on the abutments and the ends of the approach slabs at these joints were fractured, which caused settlement of the approach slabs. To prevent this type of a failure, the Ohio DOT ties their approach slabs to the bridge abutments using dowel bars that are diagonally oriented through the seats for the approach slabs. Burke noted that if straight-bar extensions of the longitudinal reinforcement in a bridge deck are used to tie the approach slabs to the bridge, settlement of an approach slab will cause concrete cracks to develop in the top surface of these slab and yielding of this tie reinforcement.

In this same paper, Burke (1999) stated that approach slabs should be the same width as the bridge deck and have curbs that are in alignment with the curbs for the bridge deck to prevent soil erosion of the roadway shoulders, embankment surfaces, and abutment foundation soil due to water run-off from a bridge. Also, the joint between the approach slabs and the highway pavement needs to be properly designed to accommodate the cyclic movements of the bridge and approach slab. Burke discussed details that the Ohio DOT has used at these joints for different lengths of integral bridges.

In a paper on integral-abutment design, Wasserman (2002) discussed the design of approach slabs. He recommended that reinforced-concrete slabs (approach pavements) should be used to provide a transition between a highway and a bridge to prevent the development of a bump, if the embankment settles. He stated that approach pavements provide better horizontal distribution of vertical loads that are applied close to the ends of a bridge. Wasserman noted that approach pavements should be anchored into the backwall for an abutment. In this same paper, Wasserman provided recommendations on the soil backfill that should be used behind the abutments and on methods that should be incorporated in the bridge construction to provide for proper drainage behind the abutments.

2.6. Flange local buckling of I-shaped beams

Many experimental tests of simply-supported, steel beams that involved mid-span, concentrated loads were preformed by Lukey and Adams (1969), Adams et al. (1965), Kuhlmann (1989), and Kemp (1985). These tests were conducted to determine the influence of inelastic flange-local buckling, web-local buckling, and lateral-torsional

buckling on the flexural ductility of the beams. The results for the tests on beams that were classified as a compact section indicated that the inelastic-rotation capacity is governed by the slenderness ratio for lateral-torsional buckling. Also, the test results revealed that when a greater portion of the web element for a cross section is in compression due to combined, axial compression and bending, the member may experience a considerable loss of flexural ductility compared to that same cross section without an axial compression force.

Factors affecting the rotation capacity of plastically-designed members were investigated by Kemp (1986). By using theoretical-slenderness ratios of plate elements which take into account of the present of a simultaneous, axial-compression force, Kemp (1985) established interaction criterion for web-local buckling and flange-local buckling with lateral-torsional buckling by recognizing the relationship between mode of failures and the plastic length of plate elements. Kemp's investigations indicated that the loss of flexural ductility is particularly severe when constraints to flange-local buckling are released by web-local buckling prior to lateral-torsional buckling or where resistance to lateral-torsional buckling is reduced by the onset of flange-local buckling.

Takanashi, et al. (1989) investigated the elastic-plastic behavior of steel and composite beams that were subjected to various, displacement rates. Dynamic and quasi-static tests were performed on the steel beams and composite beams that had different element, width-to-thickness ratios. The beams were tested using either monotonic or cyclic-reverse loading. The dynamic tests were conducted at displacement rates of 0.06 in./sec., 6 in./sec., and 12 in./sec. The test results for both the monotonic and the cyclic-reverse loadings indicated that the maximum, moment

capacities for the steel beams and composite beams increased as the displacement rate increased. Also, these tests revealed that the deformation capacities of the steel beams slightly increased as the displacement rate increased, and that the elastic stiffness and the unloading stiffness in the plastic range were not influenced by the displacement rate.

A theoretical relationship between the inelastic-rotation capacity of a cross section for a beam and the web and flange, width-to-thickness ratios was established by Kato (1989). This researcher combined a simplified, moment-versus-rotation relationship with a statistical, critical stress for stub-columns. Kato compared his theoretical relationship to the results for experimental tests that were performed by other researchers, including Lukey and Adam (1967), on steel beams. Kato's prediction for the inelastic-rotation capacity for a cross section of an I-shaped beam agreed fairly well with the experimentally-based, rotation capacities.

Interaction effects between local buckling of an element for a cross section of a steel beam and lateral-torsional buckling of the beam was studied by Daali and Korol (1994). These researchers utilized the relationship between rotation capacity and an effective, slenderness ratio, which was developed by Kemp (1991), to estimate the moment-rotation capacity of several, steel beams. Daali and Korol modified Kemp's interaction relationship to produce a better prediction for Kemp's experimental observations. The modified, buckling-interaction relationship agreed well with the experimental results for beams that were tested by Lukey and Adam (1969) and Kuhlmann (1989). Daali and Korol showed that members with slenderness values, which are close to the limits given by design specifications, may not be able to

redistribute moments adequately under seismic loading. These researchers proposed a critical lateral, slenderness ratio that is associated with the potential ductility for a member.

Toshikiro (1997) studied the elastic-plastic behavior of cantilever columns that had a variable cross-section and were subjected to horizontal, cyclic load. His numerical study was based on a plastic-zone theory. Toshikiro's investigation revealed that columns will collapse due to instability of the column under cyclic loading, which cannot be predicted by general buckling and bending strengths of columns.

An evaluation of the contemporary, international, design specifications for the plastic-design, flexural requirements of I-shaped, steel beams was performed by Kemp (1996). He noted that current-design specifications over-emphasize local buckling of the cross-sectional elements as the primary, strain-weakening effect, while they underestimate the simultaneous interaction of an axial-compressive force and inelastic bending. Kemp proposed to resolve the anomalies between the in-practice, design specifications and the test results. Kemp investigated 44 tests of I-shaped, steel beams that were subjected to only flexural bending and 14 tests on similar beams that were subjected to combined bending and axial force. He compared the buckling strengths from those tests to the predicted, buckling strengths for a theoretical model. Kemp did not identify any significant relationship between rotation capacity and the element, width-to-thickness ratio for web-local buckling and flange-local buckling. Despite the considerable amount of scatter in the experimental-data points, Kemp detected a vague relationship between the rotational capacity and the slenderness ratio for lateral-torsional buckling. Kemp developed an effective, slenderness ratio for lateral-torsional

buckling that accounts for the interaction between web-local buckling, flange-local buckling, and lateral buckling. Kemp was able to establish a well-defined relationship between rotation capacity and an effective, slenderness ratio for lateral-torsional buckling. Also, test results showed that the presence of axial compression on the specimens caused a reduction in the available, rotation capacity for the member. In many of the tests, the rotation capacities were less than one-half of the rotation capacities that corresponded to a test specimen without an axial-compression force.

3. BRIDGE MONITORING PROGRAM

3.1. Overview

One of the objectives of the research was to monitor two, integral-abutment bridges for temperature-induced, displacements and strains. The instrumentation installed at each bridge site consisted of displacement transducers and a tiltmeter to measure bridge movements, strain gages to measure longitudinal strains in members, and thermocouples to measure air and concrete temperatures. Additional discussions of the bridge monitoring program are presented in the M.S. creative-component report for Kirkpatrick (1998) and in the M.S. theses for Thomas (1999) and Sayers (2000).

3.1.1. Bridge selection criterion

The bridge-selection process involved an evaluation of integral-abutment bridges that have Iowa Type-B, Type-C, or Type-D, prestressed concrete (PC) girders; a skewed alignment; and a relatively long, total length. A list of 91 bridges that have those geometric conditions and are located on the state-highway-road and county-road systems in the State of Iowa was complied for further consideration. Since abutment geometry is influenced by the PC girder size, one bridge was to have U-shaped abutments and Iowa Type-D, PC girders, and the other bridge was to have straight-wall abutments and Iowa Type-C, PC-girders. Each bridge that was considered had advantages and disadvantages with respect to field monitoring. The advantages were a long length that would induce significant thermal movements along the length of the bridge, a large skew angle that would induce possible thermal movements in the

transverse direction to the bridge length, symmetric geometry that would produce symmetric responds to temperature changes, significant clearance above a river that would minimize the potential for flooding of the instrumentation devices, minimal amounts of highway traffic that would minimize the effect of bridge vibrations on the instrumentation readings, rip-rap or earth berms that would simplify the installation of benchmark posts for monitoring bridge displacements, and steel-intermediate diaphragms that would allow for the passage of the instrumentation wiring along the bridge length. From the generated list of potential bridges, two integral-abutment bridges were selected for long-term, field monitoring of displacements, longitudinal member strains, and internal concrete temperatures at specific locations. Each bridge has three spans, a skewed alignment, and cross a river.

Both of the selected bridges are county-road bridges on the secondary-road system. The first bridge, which is in Guthrie County, is located just south of the Town of Panora, Iowa on Route P28, where the highway crosses the Middle Raccoon River. This bridge will be referred to as the Guthrie County Bridge. The second bridge, which is in Story County, is located just northwest of the City of Ames, Iowa on Route E26, where the highway crosses Squaw Creek. This bridge will be referred to as the Story County Bridge.

3.1.2. Bridge descriptions

The Guthrie County Bridge is a three-span-continuous, 318-ft long, PC girder bridge with a right-side-ahead, 30-deg., skew angle. This bridge has a U-shaped abutment with a single row of ten, HP 10 x 42, steel piles under the reinforced-concrete (RC) backwall, and an HP10x42 pile under each wingwall. The piles under the RC

backwall are oriented with their webs parallel to the abutment face. The wingwall piles are oriented with the webs perpendicular to the longitudinal axis of the bridge. The piles were driven to a depth of at least 45 ft into shale bedrock at the south abutment and to a depth of at least 40 ft into shale bedrock at the north abutment. Pre-bored holes that were filled with bentonite slurry were specified for the piles at this bridge. A spread footing that is keyed into the shale bedrock supports the each Tee-shaped pier. At the south pier, which is an expansion pier, the bridge girders bear on 3.75-in. thick, steel-reinforced, neoprene pads. The RC diaphragm at this pier does not extend down to the top of the pier cap. At the north pier, which is a fixed pier, the RC, pier diaphragm is cast into keyways in the top of the pier cap. The keyways are lined along their sides and bottom with an expansion-joint filler. Between the keyways, the pier diaphragm is cast against a continuous neoprene pad. The bridge girders bear on 1-in. thick, neoprene pads at this pier. A summary of the geometric characteristics of the Guthrie County Bridge is given in Table 3.1.

The Story County Bridge is a three-span-continuous, 201 ft - 4 in. long, PC girder bridge with a right-side-ahead, 15-deg. skew angle. Each RC abutment is supported on a single row of seven, HP10 x 42, steel piles that are oriented with their webs parallel to the abutment face. The wingwalls are cantilevered from the abutment backwall. The abutment piles are driven to bedrock or to a minimum bearing strength of 34 tons. The specified length of the abutment piles was 40 ft. An 8-ft deep, pre-bored hole that was filled with sand was provided for each abutment pile. The two, pedestal-type piers have a single line of twelve, HP10 x 42, steel piles that are encased by concrete. The bridge superstructure is supported at the piers, which are fixed piers, by 1-in. thick, neoprene

pads. The connection details between the full-depth, pier diaphragms and the pedestal-type piers is the same as the connection detail at the fixed pier for the Guthrie County Bridge. A summary of the geometric characteristics of the Story County Bridge is given in Table 3.1.

3.1.3. Instrumentation packages

To quantify the displacements and member strains that were induced by temperature changes, a system of instrumentation was developed for long-term, field monitoring of each bridge. Table 3.2 lists the behavioral responses that were measured for each bridge. Table 3.3 lists the number of each type of instrumentation device that was installed at each bridge site.

The instrumentation devices are described in Sections 3.2 through 3.4. To individually identify each device that was installed on a bridge, each device was assigned an acronym-based-code name. The first part of the code refers to the instrument type and the remaining letters or numbers indicate the location of the device on the bridge and/or the type of measurement.

3.2. Displacement transducers

At each bridge, longitudinal displacements (translations parallel to the longitudinal axis of the bridge) of one abutment were measured at three locations across the width of the RC pile cap. Also, transverse displacements (translations perpendicular to the longitudinal axis of the bridge) of this abutment were measured at the ends of the RC pile cap. Longitudinal displacements of the other abutment pile cap at each bridge were measured at the mid-width of the bridge. Displacement

transducers were mounted on each bridge to record differential displacements between a pile and the RC pile cap of one abutment and between the center PC girder and the piers. Additional displacement transducers were installed at the Guthrie County Bridge to measure differential displacement between the center PC girder and the RC abutment backwall. Displacement transducers were installed at each bridge to establish the relative displacements between two points at a set gage distance so that relative rotations could be evaluated between structural elements in the bridges. A tiltmeter was mounted at the mid-width of the pile cap of one abutment of each bridge to measure rotations of the pile cap in a vertical plane that was parallel to the longitudinal axis of the bridge.

3.2.1. Guthrie County Bridge

Bridge movements at the Guthrie County Bridge were measured with fourteen, string-potentiometer, displacement transducers and a tiltmeter. Table 3.4 lists the instrumentation code and defines the acronyms for the transducers that were installed on the Guthrie County Bridge. The first group of letters of an instrumentation code represents the type of device (SP = string-type potentiometer and TM = tiltmeter). The second group letters represent the location on the bridge where the device was installed. The third group of letters indicates the type of displacement that was measured by the device. Figure 3.1 shows the location of these transducers on the Guthrie County Bridge. Seven of the transducers (SP-SW-LB, SP-SC-LT, SP-SC-LB, SP-SE-LB, SP-NC-L, SP-SW-T, and SP-SE-T) were used to measure absolute displacements of the abutments. These seven transducers were mounted on benchmark posts that were installed about 10 ft from the bridge abutments. Six

displacement transducers (SP-SC-RGT, SP-SC-RGB, SP-SC-RPB, SP-SC-RPF, SP-SP-RPL, SP-NP-RPL) were mounted on the bridge to record differential displacements between bridge elements. The displacement transducer (SP-NP-RPL) that measured the relative longitudinal displacements between the pier cap and the center PC girder at the north pier was installed in July 1998. The tiltmeter (TM-SC-LR) was mounted at the center of the south-abutment pile cap to measure rotations of this pile cap in the vertical plane that is parallel to the longitudinal axis of the bridge.

To verify the stability of one of the benchmark posts, a displacement transducer (SP-SC-LV) was installed to measure any differential longitudinal movement between two adjacent posts. These two posts were installed approximately 4-ft apart and were located below the center PC girder near the south abutment at the Guthrie County Bridge, as shown in Fig. 3.1. A transducer was bolted to the post that was farther from abutment and the transducer string was attached to the post that was closest to the abutment. Any differential displacements between these two posts that was recorded by the transducer after adjusting for the temperature-induced, change in the wire length would indicate some instability in one or both of the benchmark posts and the transducer attachment assemblies.

Abutment rotations in the vertical plane that is parallel with the bridge length were calculated using the measured displacements from a pair of post-mounted displacement transducers (SP-SC-LT and SP-SC-LB) at the mid-width of the south abutment. These transducers measured absolute longitudinal displacements at two points that were at a set distance apart and in vertical alignment on the pile cap. This abutment rotation was also measured by a tiltmeter.

3.2.2. Story County Bridge

Eleven, string-potentiometer, displacement transducers and a tiltmeter were installed at the Story County Bridge to measure bridge displacements. Table 3.5 lists the transducers and Fig. 3.2 shows the location of the transducers for the Story County Bridge. Six of these displacement transducers (SP-EN-L, SP-EC-L, SP- ES-L, SP-WC-L, SP-EN-T, and SP-ES-T) were used to measure displacements of the abutments. These transducers were mounted on benchmark posts that were installed near the bridge abutments. To verify the stability of one of the benchmark posts, a displacement transducer (SP-EC-LV) was installed to measure any differential movement between two adjacent posts. The remaining four displacement transducers (SP-EC-RPB, SP-EC-RPF, SP-EP-RPL, SP-WP-RPL) were mounted on the bridge to record differential displacements between bridge elements. The tiltmeter (TM-EC-LR) was mounted at the center of the east-abutment pile cap to measure rotations in the vertical plane parallel to the longitudinal axis of the bridge.

3.2.3. Transducers for absolute displacement measurements

For each bridge site, benchmark posts, which consisted of a steel pipe that was supported by a concrete foundation, were used to provide a fixed reference point for the displacement transducers. Figure 3.3 shows a typical longitudinal cross section near an abutment. The top of the concrete foundation for most of the benchmark posts was located about 3 to 4 ft below grade. The steel posts for the transducers that measured the transverse movements of the south abutment of the Guthrie County Bridge were installed by first drilling a 16-in. diameter hole to a depth of about 10 ft. A truck-mounted auger was used to drill these holes. Then, concrete for these post foundations was cast

into the hole to a depth of about 5 ft below grade and the steel post was placed in the fresh concrete. Each steel post was surrounded by a 12-in. diameter, corrugated-plastic pipe that was filled with batt insulation to prevent the soil backfill from contacting the steel posts and to insulate the concrete foundation for the posts.

Each post-mounted transducer was firmly bolted to a benchmark post and its sensor cable was linked to a RC abutment with a steel wire that had a known coefficient of thermal expansion and contraction. As a bridge abutment moved relative to a benchmark post, the displacement was measured by the transducer when the sensor wire moving into and out of the transducer. For the longitudinal displacement measurements at the south abutment of the Guthrie County Bridge, the transducer wires for SP-SW-LT, SP-SC- LT, and SP-SE-LT were attached to the RC abutment at a point that was approximately 3 in. below the top of the pile cap. The wires for SP-SW-LB, SP-SC-LB, and SP-SE-LB were attached at a point that was approximately 3 in. above the bottom of the pile cap. The vertical distance between the transducer wires was the gage distance used for calculating the pile-cap rotations in a plane parallel to the longitudinal axis of the bridge. The wires for the displacement transducers measuring transverse displacements of the south abutment and longitudinal displacements of the north abutment at the Guthrie County Bridge were attached at the mid-height of the pile cap. At the Story County Bridge, all of the abutment displacement measurements were made at the mid-height of the pile cap. To protect the transducers and extension wires from vandalism and extreme weather conditions, the post-mounted, transducer- measurement systems were enclosed by wood housings.

3.2.4. Transducers for relative displacement measurements

The design drawings for the Guthrie County Bridge showed that the north pier is a fixed pier, and the south pier is an expansion pier. At the north pier, a full-depth, pier diaphragm was keyed into the pier cap. For the Story County Bridge, the design drawings show that the east and west piers are fixed piers. The pier details are shown in Fig. 3.4. Since differential, longitudinal displacements of a bridge superstructure over a fixed pier were expected to be negligible, a transducer to measure relative, displacements was not initially installed at the north pier of the Guthrie County Bridge. A transducer to measure relative displacements at the south pier was installed at the same time that the other instrumentation was placed on this bridge. Figure 3.4a shows that expansion joint filler was used in the keyways and between the diaphragm and the pier cap. Therefore, relative displacements between a bridge superstructure and the pier cap for a fixed pier will occur when the joint material deforms during the expansion and contraction of the bridge. On July 17, 1998, a displacement transducer (SP-NP-RPL) was installed to measure relative, superstructure movement over the north pier of the Guthrie County Bridge. Since the Story County Bridge was the second bridge to be monitored, transducers were installed at both fixed piers when the other instrumentation devices were placed on this bridge.

The transducers, which were used to measure relative displacements at the piers, were mounted to the undersides of the center PC girder, as shown in Fig. 3.5. When possible, a transducer wire was directly attached to the concrete pier cap. However, at the south pier of the Guthrie County Bridge, the 3.75-in. thick, neoprene bearing pad below each PC girder at this pier created a large space between the bottom

of a girder and the top of the pier cap. A steel plate was used to extend the plane for the vertical face of the pier cap. The displacement transducer wire was attached to this steel plate.

At the Guthrie County Bridge, displacement transducers were installed on one side of the top and bottom flanges of the center, PC girder near the south abutment, as shown in Fig. 3.6. These transducers were used to measure relative movements of this girder with respect to the RC abutment backwall. Each transducer was attached to the inside of a steel box, and each box was attached to wood 2 x 6's that were glued and screwed to the vertical face of a PC girder flange. Relative displacements between a PC girder and a RC abutment backwall were not measured at the Story County Bridge.

At each bridge, two displacement transducers that were clamped to a steel pile were used to measure vertical, relative displacements between the underside of a RC, abutment pile cap and a pile, as shown in Fig. 3.7. At the Guthrie County Bridge, the transducers were mounted to a pile near the mid-width of the south abutment. At the Story County Bridge, these transducers were mounted to the center pile under the east abutment. The horizontal separation between the two transducers allowed for the determination of the relative rotation between the pile cross section, where the transducers were attached at 18 in. below the bottom of the pile cap, and the bottom of the pile cap. This relative rotation was in the vertical plane parallel to the longitudinal axis of the bridge.

3.3. Strain gages

Several types of strain gages were used to monitor strains in selected members of each bridge. At the Guthrie County Bridge and Story County Bridge, weldable,

electrical-resistance, strain gages were applied to several steel, HP-shaped, abutment piles. Also, at the Guthrie County Bridge, bondable, electrical-resistance, strain gages were applied to the flanges of selected PC girders and to the exposed face of a RC, abutment pile cap. While at the Story County Bridge, vibrating-wire, strain gages were used to measure strains in selected PC girders and at a particular location in an abutment pile cap. A vibrating-wire, strain gage consists of a taut wire stretched between two anchor blocks. Changes in strain in the specimen are indicated by the change of natural frequency of this taut wire.

In most instances, each abutment pile that was instrumented had a total of eight, electrical-resistance, strain gages that were applied to the outside faces of the flanges near the flange tips, as shown in Fig. 3.8. An arrangement of four strain gages was used at two cross sections that were located at 9 in. and 33 in. below the bottom of the pile cap. If four, longitudinal strains are known at a monitored, pile cross section, the x-axis and y-axis bending, axial, and torsional-warpage strains can be computed from the measured strains. Strain gages were used at two pile cross sections to possibly permit the determination of the moment gradient along the pile length.

Strain gages were attached to the vertical face of the top and bottom flanges of selected PC girders at a cross section that was located at 5 ft from the face of support at each end of a girder. These gages were positioned at the mid-thickness of each flanges and on one side of a girder. These gages were used to establish the total, longitudinal strains in the selected PC girder at this location. The strain gages that were attached to the abutment pile caps were placed in a single, horizontal line at the mid-height of the pile cap and at a spacing that was equal to one-half of the pile spacing.

These gages were used to determine whether significant horizontal bending occurred in the pile cap due to the expansion of the bridge superstructure.

3.3.1. Guthrie County Bridge

At the Guthrie County Bridge, five abutment piles were instrumented with strain gages, as shown in Fig. 3.9. At the south abutment of this bridge, the two exterior piles and a pile near the mid-width of the abutment were monitored. At the north abutment, a pile near the mid-width of the abutment and the west exterior pile was instrumented. Table 3.6 lists the instrumentation code and the description of the acronyms for the strain gages that were installed on the abutment piles at the Guthrie County Bridge.

Twenty-one, bondable, electrical-resistance, strain gages were applied to measure strain in concrete elements of the Guthrie County Bridge. The location for these gages is shown in Fig. 3.10. Table 3.7 lists the gage locations. Sixteen gages were bonded to four PC girders, and the remaining five gages were bonded to the north face of the pile cap for the south abutment. A “dummy” strain gage was used to correct the measured strains in the other strain gages for temperature changes.

3.3.2. Story County Bridge

Four abutment piles at the Story County Bridge were instrumented with strain gages. The locations for these gages are shown in Fig. 3.11, and the descriptions of the acronym for these gages are listed in Table 3.8. At the east abutment, gages were used to monitor the two exterior piles and the center pile. At the west abutment, only the center pile was instrumented with strain gages. Three of the four monitored piles had had eight strain gages whose locations are shown in Fig. 3.8. Due to the lack of

channels in the multiplexer, one of the four strain gage was omitted at the bottom cross section of the south pile of the east abutment to permit the use of a “dummy” strain gage to correct the measured strains for changes in the temperature. This pile was instrumented with seven strain gages. At the Story County Bridge, twelve, vibrating-wire strain gages were attached to four, PC girders and four, vibrating-wire strain gages were mounted to the west face of the pile cap for the east abutment. These 16 gages are listed in Table 3.9, and the location of each of the gages is shown in Fig. 3.12.

3.3.3. Strain gage installation procedure

To provide access for installing the strain gages on the steel piles, the soil was removed around the upper portions of the selected piles. The excavation procedure consisted of removing the stone rubble from the berm in front of a pile and removing the soil around the pile to a depth of about 42 in. to expose the pile flanges. At a gage location the flange was scraped to remove any soil and an electric grinder was used to expose clean, bare steel. This surface was sanded to produce a flat and smooth surface for installation of the gage.

Each weldable, electrical-resistance gage (Hitec model HBW-35-125-6-3VH-SS) consisted of a strain gage that had been bonded to a thin, metal tab by the manufacturer. This metal tab for each gage was attached to the steel pile with a series of closely spaced, small, tack welds. To strengthen the connection between a metal tab and a pile surface, Superglue was applied around the edges of the tab. At the Guthrie County Bridge, these gages were protected from moisture penetration by applying a silicone caulk over the gages. At the Story County Bridge, asphalt cement was used to protect the pile gages.

The bondable, electrical-resistance, strain gages that were applied to the PC girders and the RC pile cap at the Guthrie County Bridge were attached to the concrete surfaces with epoxy adhesives that are produced by Measurements Group, Inc. Several of the gages were installed at temperatures too cold to use the AE-10 epoxy. These gages were bonded to the concrete with a faster setting epoxy Mbond-300. The Mbond-300 adhesive has low-peel strength compared to that for the AE-10 adhesive.

The concrete surface at each strain gage location was cleaned and prepared in accordance with the gage-application instructions. The epoxy was mixed and spread onto the concrete surface. The gages were positioned on the epoxy bed and held in place with a bracket designed to apply pressure to the gage while the epoxy set. After the epoxy had set, the gage was covered with a strip of butyl rubber to keep moisture away from the gage and epoxy. Several gages had to be re-bonded to the concrete after they became loose during the application of the weatherproofing protection. The strain gages were re-bonded to the concrete with the AE-10 epoxy and heat was applied to properly cure the epoxy. The strain gage at the 1SCB location on the Guthrie County Bridge was accidentally peeled-off when removing a clamping bracket in July of 1998. This gage was not re-bonded to the concrete.

Each vibrating-wire, strain gage that was installed at the Story County Bridge was attached to the PC girders or the RC abutment pile cap by firmly clamping the gage anchor blocks into the two mounting blocks that had been bonded to the concrete surfaces using a high-modulus, epoxy cement. To protect the gage installation, a one-half-cylindrical section of a 4-in. diameter, PVC pipe was placed over the gage. The pipe covering was glued to the concrete surface.

After the strain gages were installed on a bridge, the electrically-shielded extension wires that connected each gage to the data-acquisition system were soldered to the wire leads on the gage. These connections were protected against moisture infiltration by using a shrink tube around each of the three conductor wires. This group of wires was enclosed in another shrink tube that was filled with a waterproof material.

3.4. Thermocouples

To measure the temperature of the concrete and to establish temperature gradients at selected locations in each of the instrumented bridges, thermocouples were installed along the length, across the width, and through the depth of the bridge superstructures. Thermocouples were embedded in the RC deck and PC girders at several locations by drilling a hole in the concrete member, placing a thermocouple into the hole, and filling the hole with a cement grout. Deck temperatures were measured at 4 in. from the bottom of the slab and girder temperatures were measured at a depth of about ¾ in. into the member.

Also, thermocouples were used to measure the air temperature near the displacement transducer wires so that temperature corrections could be made to the raw-displacement data. These thermocouples were suspended in the air near the mid-length of the transducer wires. The thermocouples that were used to measure bridge temperatures are described in Sections 3.4.1 and 3.4.2.

3.4.1. Guthrie County Bridge

Forty-one thermocouples, which are listed in Table 3.10, were installed at the locations shown in Fig. 3.13 for the Guthrie County Bridge. The “E” in the instrument

code indicates that the thermocouple was embedded into the concrete members. Most of the thermocouples were installed in the south span (Span 1) of this bridge. In this span, concrete temperatures were measured near the south abutment, at the mid-span, and near the south pier in both of the exterior, PC girders and in the center, PC girder. The remaining thermocouples in the bridge superstructure were embedded in the slab and in the center, PC girder at the midspan of the center span (Span 2) and at both ends of the west span (Span 3). At each of the instrumented, PC-girder cross sections, thermocouples were embedded into the top and bottom flanges of the girders. At several of these locations, temperatures were measured in the slab and in the PC-girder web. An additional thermocouple was installed in the north face and near the mid-width of the pile cap for the south abutment.

3.4.2. Story County Bridge

Table 3.11 lists the 46 thermocouples that were installed in the superstructure of the Story County Bridge. The thermocouple locations, which are shown in Fig. 3.14, were similar to those that were selected for the Guthrie County Bridge. Most of the thermocouples were placed in the east span. There were some changes made for the locations of the thermocouple compare to those used for the Guthrie County Bridge. To obtain a more complete transverse temperature distribution, more thermocouples were embedded in the slab at the midspan of the east span at the Story County Bridge than were used in the south span at the Guthrie County Bridge. These additional thermocouples were placed in the slab near the PC girders and midway between the girders.

3.5. Data-acquisition procedure

Data acquisition was accomplished using data-loggers and peripherals that were manufactured by Campbell Scientific, Inc. A CR10X data-logger provided the excitation voltage for most of the instrumentation devices and recorded voltage output from most of the instrumentation devices at each bridge. The data were initially stored in the memory of the CR10X data-logger until the data was downloaded to a laptop computer. A modern (Model COM 200) was used to communicate with the data-logger at the Guthrie County Bridge from an office in the Town Engineering Building on the campus of Iowa State University. Data collected at the Story County Bridge were downloaded to a laptop computer by directly connecting the computer to the CR10X data-logger at the bridge side. Multiplexers (Model AM416) were used to increase the number of instrumentation devices that could be interface with each CR10X data-logger.

3.5.1. Data-acquisition equipment

At the Guthrie County Bridge, the data-logger and six multiplexers were bolted into two electrical boxes. These boxes were attached to the bottom surface of the bridge deck at a location that was about 20 ft from the south abutment and near the center PC-bridge girder. Another multiplexer was located at the north end of the bridge. This multiplexer was bolted into another electrical box that was attached to the south face of the north abutment. A data-logger and seven multiplexers were used at the Story County Bridge. These units were bolted into two electrical boxes that were attached to the west face of the east abutment backwall between two of the PC-bridge girders.

Additional Campbell Scientific, data-acquisition equipment that was used at the bridge sites included two units that recorded strain in the electrical-resistance and vibrating-wire strain gages. At the Guthrie County Bridge and Story County Bridge, a Terminal Input Module, TIM (Model 4FWB350) was used to measure strain changes in the electrical-resistance, strain gages installed on the bridges. All of the electrical-resistance, strain gages at each bridge were multiplexed through one TIM unit. A Vibrating-Wire Sensor Interface (Model AVW1) was used to provide excitation and measure strain changes in the vibrating-wire, strain gages installed at the Story County Bridge.

3.5.2. Data-acquisition interval and initial-data reduction

Since daily-temperature variations occur quickly compared to the seasonal-temperature variations, temperature measurements were frequently recorded to establish the variations in the daily temperatures. For the Guthrie County Bridge, all instrumentation readings were recorded at 20-minute intervals between December 17, 1997 and May 15, 1998. After May 15, 1998, the data collection frequency was changed to every 30 minutes to reduce the volume of data that needed to be stored and analyzed, yet maintain sufficient sensitivity to record changes in the bridge response due to daily-temperature variations. At the Story County Bridge, the instrumentation measurements were recorded at 30-minute intervals for the entire monitoring period from July 18, 1998 to May 15, 2000. Even with a 30-minute, data-collection interval over the direction of the monitoring periods at each bridge site, the volume of data was too large to efficiently analyze and plot. To facilitate the analysis and graphical presentation of the measured data and still maintain accuracy for the daily-temperature

variations, the volume of data was reduced by deleting three of every four filtered-data points. Therefore, the reported data represents measurements at two-hour-long, time intervals.

Each time data were collected, the data-logger recorded each instrumentation measurement six times. Rather than computing a simple average of the six recorded data values for each instrumentation device, an algorithm was developed and applied to discard any questionable data that was recorded if highway traffic was on the bridge. The algorithm used two criteria for determining an allowable range of data values. For the first criterion, an outlier data was defined as a data that was more than one-standard deviation away from the mean value of the six, measured values. For a normal distribution of data, this criterion would imply that 32 percent of the six, measured values should be discarded. The second criterion was based on the median of the six, measured values. If the standard deviation for a set of six, data values was small and if the first criterion would eliminate good data, the implied data outlier was not eliminated, unless the magnitude of the suspected data was more than a fixed amount away from the median value. The limits of acceptable deviations from the median value were different for each instrument type: 0.0015 in. for the displacement transducers, 7.5 micro-strains for the strain gages, 0.36 °F for the thermocouples. These deviation values were based on the expected repeatability of the instrumentation measurements. After the filtering algorithm had discarded the questionable data, a mean value of the remaining data values from the original data set for each instrumentation device was calculated and used as the representative instrumentation reading for that particular time.

3.6. Temperature corrections for instrumentation devices

Since the instrumentation devices were subjected to the same temperatures as the bridges, temperature corrections were made for some of the train and displacement data. The strain measurements made with the electrical-resistance strain gages were more sensitive to temperature-induced errors than the measurements that were made by the other instrumentation devices.

Thermocouples were installed near some of the instrumentation devices to measure the temperature of the surrounding air or material containing the instrumentation device. The temperatures of the displacement transducer extension wires were measured with thermocouples placed near the mid-length of these wires in each of the wooden-box enclosures. The temperature of the vibrating-wire, strain gages was measured with a thermistor that was built into each strain gage. The temperatures of the electrical-resistance, strain gages that were applied to the steel piles were measured with thermocouples that were mounted with an adhesive to a pile surface near those strain gages. The temperatures of the electrical-resistance, strain gages that were bonded to PC girders were measured by a thermocouple that was embedded in the girder near the location of the strain gage.

3.6.1. Corrections for displacement transducers

Laboratory tests (Kirkpatrick, 1997) of a displacement transducer showed that these devices were insensitive to temperature changes. However, the steel extension wire that linked the displacement transducer wire to the bridge experienced a change in its length, L_{wire}, when the temperature changed. The change in length, ΔL_{wire}, of an extension wire due to a change in the temperature, ΔT_{wire}, of the wire is given by:

$$\Delta L_{wire} = \alpha_{wire} \Delta T_{wire} L_{wire} \tag{3.1}$$

where, α_{wire} is the coefficient of thermal expansion and contraction of the wire (α_{wire} = 6.33 X 10^{-6} in./in./°F, as specified by the manufacturer). The change in the wire length was added to the displacement transducer measurement to obtain the correct displacement magnitude.

3.6.2. Corrections for temperature-compensated, electrical-resistance, strain gages

Since the strain gages were attached to the elements of a bridge that were not at a state-of-zero strain and zero stress and since the gages were initialized to read zero strain, each strain gage will measure a change in strain rather than an absolute strain. Therefore, the change in strain, $\Delta\varepsilon$, is defined as the change in a measured length, ΔL, divided by the original-gage length, L, when a strain-gage reading was initialized. The change in total strain, $\Delta\varepsilon_{total}$, is expressed as:

$$\varepsilon_{total} = \varepsilon_{stress} + \varepsilon_{temp} \tag{3.2}$$

where, $\Delta\varepsilon_{stress}$ is the change in the strain due to the change in stress, $\Delta\sigma$, and $\Delta\varepsilon_{temp}$ is the change in the strain due to the change in temperature, ΔT. Rewriting Eq. 3.2,

$$\varepsilon_{total} = \frac{\sigma}{E} + \alpha \quad T \tag{3.3}$$

where, α is the coefficient of thermal expansion and contraction (α-coefficient) and E is the modulus of elasticity of the material for the particular bridge element.

An experimental strain was determined by measuring the change in resistance of a strain gage. For an electrical-resistance, strain gage, two temperature related corrections are required to obtain the change in strain due to stress, $\Delta\varepsilon_{stress}$.

The first temperature correction was necessary because a change in temperature affects the length of the wire grid for a strain gage and the resistance of the gage material (Dally and Riley, 1991). The ratio of the temperature-induced change in the resistance, ΔR, to the original resistance, R, for a strain gage is given by

$$\left(\frac{R}{R}\right)_T = (\alpha_{specimen} - \alpha_{gage})\, S_{gage}\, \Delta T + \gamma_{gage} \Delta T \qquad (3.4)$$

Where, $\alpha_{specimen}$ and α_{gage} are the α-coefficients for the specimen and gage, respectively; S_{gage} is the strain-gage factor; and γ_{gage} is the temperature, coefficient-of-resistance of the strain-gage material.

Temperature-compensated, electrical-resistance, strain gages were used for measuring strain due to stress on the steel piles. Temperature-compensated gages were selected to minimize the change in the temperature-induced resistance for the gage. However, over a wide-temperature range, the gage readings still needed to be corrected for temperature changes because of the nonlinearity of the resistance coefficient and the α-coefficients (Dally and Riley, 1991). An apparent strain (Measurements Group, Inc., 1983) is a temperature-induced strain that is not caused by stress in the specimen. The apparent strain, $\Delta\Sigma_{app}$, that was induced by the change in the gage-material properties over a wide range in temperature was expressed by a fourth-order, polynomial function that was provided by the strain-gage manufacturer.

The second temperature correction was necessary because each electrical-resistance, strain gage was one of the resistors in a Wheatstone, quarter-bridge circuit. The electrical resistance of the Wheatstone-bridge circuit that consisted of the entire data acquisition system was affected by changes in temperature. To correct this

temperature induced error, a “dummy”, electrical-resistance, strain gage was attached to an unrestrained steel bar that was placed into the same electrical box that contained the data-logger. The adjusted change in the “dummy-gage” strain, $\Delta\varepsilon'_{dummy}$, for the first temperature correction is given by

$$\Delta\varepsilon'_{dummy} = \Delta\varepsilon_{dummy} - \Delta\varepsilon_{app\text{-}dummy} \tag{3.5}$$

where, $\Delta\varepsilon_{dummy}$ is the change in the strain that was measured by the “dummy-strain” gage and $\Delta\varepsilon_{app\text{-}dummy}$ is the change in the apparent strain for the “dummy-strain” gage. The strain in the unrestrained steel bar should be equal to zero, since the bar was free of stress. If $\Delta\varepsilon'_{dummy}$ was not equal to zero, this corrected change in the “dummy-gage” strain represents the strain error for the Wheatstone-bridge circuit. Both temperature corrections were applied to the change in the strain that was measured by the temperature-compensated, electrical-resistance strain gages to obtain the strain due to stress, $\Delta\varepsilon_{stress}$, at each gage location, which is given by

$$\Delta\varepsilon_{stress} = \Delta\varepsilon_{m} - \Delta\varepsilon_{app} - \Delta\varepsilon_{dummy} + \Delta\varepsilon_{app\text{-}dummy} \tag{3.6}$$

where, $\Delta\varepsilon_{m}$ is the change in the measured strain.

3.6.3. Corrections for the uncompensated-temperature, electrical-resistance, strain gages

Temperature-compensated, electrical-resistance gages were not used for PC girder at the Guthrie County Bridge. The strain gages that were mounted on the PC girders for this bridge could be referred to as temperature-uncompensated, strain gages. These strain gages had an effective α-coefficient equal to that of mild steel (6.5 x 10^{-6} in./in./°F). An additional temperature correction was needed for this type of a

strain gage to account for the difference in the α-coefficient for the gage and that for the PC girder.

To illustrate this temperature correction for these gages, a simple example is presented for an unrestrained-bar specimen. For a small increase in the temperature of the bar the total strain in the bar equals $\alpha_{specimen}$ ($\Delta T_{specimen}$), where, $\alpha_{specimen}$ is the α-coefficient for the specimen and $\Delta T_{specimen}$ is the change in the temperature of the specimen. The strain due to stress, $\Delta\varepsilon_{stress}$, is equal to zero for an unrestrained bar. However, because of the difference in α-coefficient for the gage and that for the specimen, the strain gage will have a non-zero, strain reading. The strain-temperature correction for the change in the strain, $\Delta\varepsilon_{\alpha}$, that is due to the different α-coefficients for the strain gage and the specimen is given by

$$\Delta\varepsilon_{\alpha} = (\Delta T_{specimen})\ (\alpha_{gage} - \alpha_{specimen}) \tag{3.7}$$

For temperature-compensated gages, α_{gage} equals $\alpha_{specimen}$ and $\Delta\varepsilon_{\alpha}$ is equal to zero. Three temperature corrections must be applied to the strains that are measured by the temperature-uncompensated, electrical-resistance, strain gages. These temperature corrections are for the apparent strain, $\Delta\varepsilon_{app}$, in the primary strain gage, the Wheatstone bridge circuit error, $\Delta\varepsilon'_{dummy}$, that were established by the “dummy” strain gage, and the gage α-coefficient, $\Delta\varepsilon_{\alpha}$. All three temperature corrections were applied to the change in the strain that was measured by this type of a strain gage to obtain the strain due to stress, $\Delta\varepsilon_{stress}$, at each gage location, which is expressed as

$$\Delta\varepsilon_{stress} = \Delta\varepsilon_{m} - \Delta_{app} - \Delta\varepsilon_{dummy} + \Delta\varepsilon_{app\text{-}dummy} - \Delta\varepsilon_{\alpha} \tag{3.8}$$

The strains in the PC girders that were predicted by the finite-element models of the Guthrie County Bridge and the Story County Bridge, which are presented in Chapters 6 and 7, respectively, are the strains due to stress.

3.6.4. Corrections for the vibrating-wire strain gages

If a vibrating-wire gage is subject to temperature changes, the wire length and, hence, the natural frequency of vibration for the wire will change without, necessarily, a directly associated expansion or contraction between the gage mounting blocks. The temperature correction for the vibrating-wire, strain gages was similar to that for temperature-uncompensated, electrical-resistance, strain gages, except that the first temperature correction for the apparent strain, $\Delta\varepsilon_{app}$, is not used. The strain-temperature correction for the change in strain, $\Delta\varepsilon_{\alpha}$, that is due to different α-coefficients is given by

$$\Delta\varepsilon_{\alpha} = \alpha_{vibr} (\Delta T_{vibr}) \tag{3.9}$$

The strain due to stress, $\Delta\varepsilon_{stress}$, at the location of a vibrating-wire, strain gage is expressed as

$$\Delta\varepsilon_{stress} = \Delta\varepsilon_{m} - \Delta\varepsilon_{dummy} + \Delta\varepsilon_{app\text{-}dummy} - \Delta\varepsilon_{\alpha} \tag{3.10}$$

3.6.5. Corrections for tiltmeters

Temperature variations can affect the output of an electrolytic tiltmeter by affecting the zero value and the scale factor for the tiltmeter. The scale factor correlates measured voltage to an angular-rotation magnitude. To some degree, the tiltmeters were temperature-compensated by their internal circuitry. However, increased accuracy was obtained by using the results from temperature tests that were conducted by the

manufacturer, Applied Geomechanics, Inc. Two temperature coefficients were provided by the manufacturer for each tiltmeter and the temperature corrections were made in accordance with instructions that were provided by the tiltmeter supplier (Roctest, 1997).

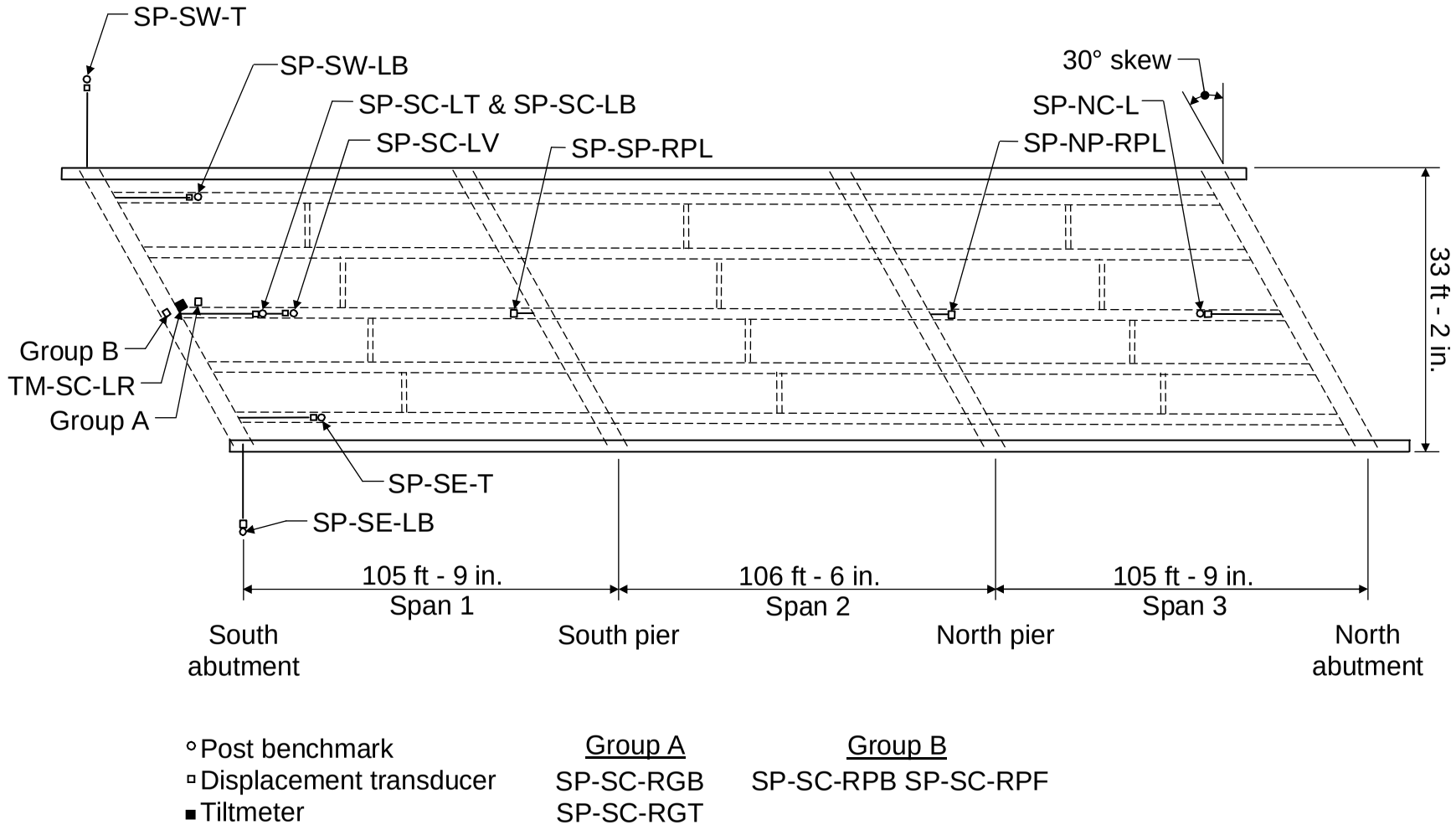

Figure 3.1. Displacement transducer locations at the Guthrie County Bridge (not to scale)

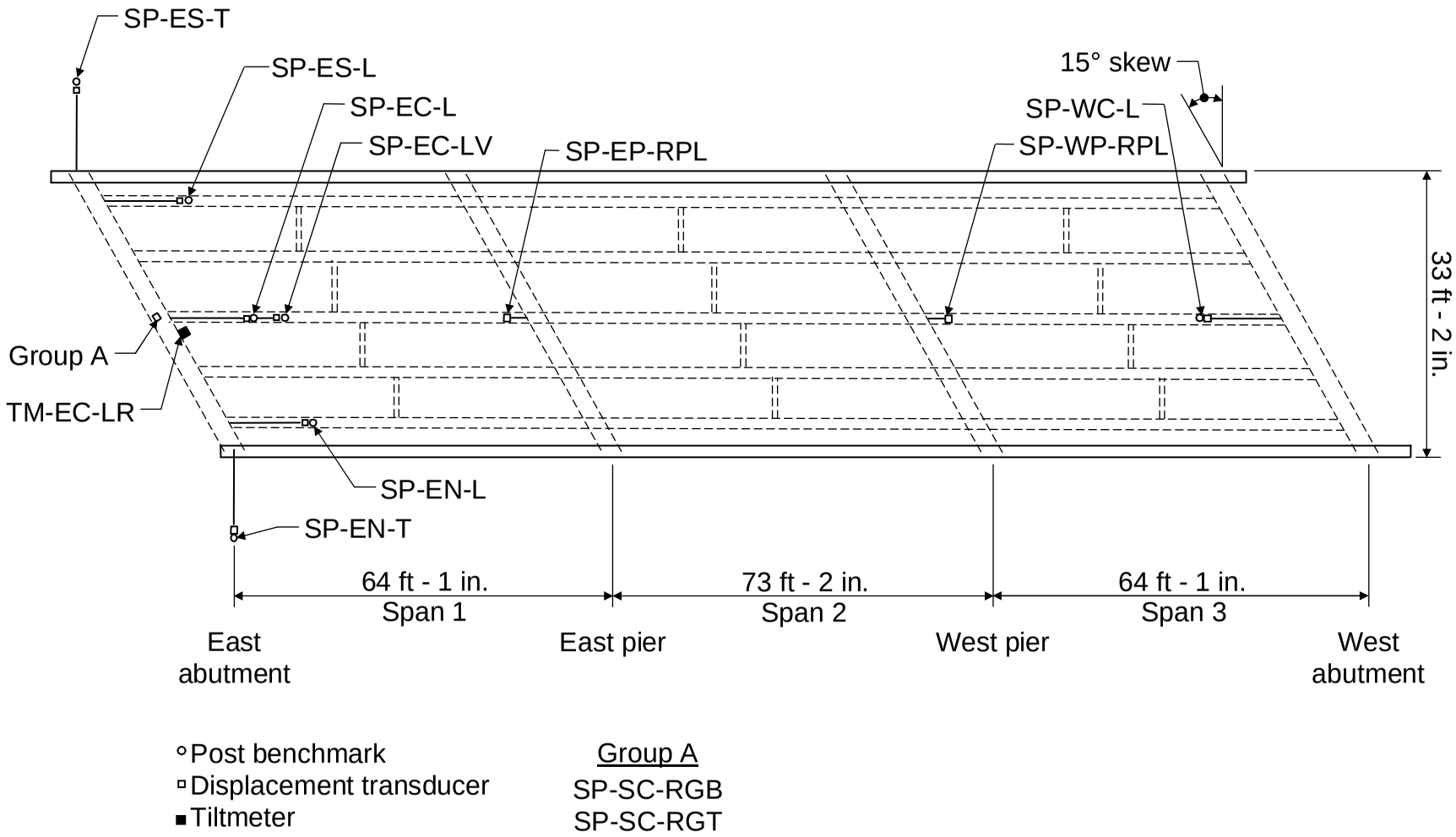

Figure 3.2. Displacement transducer locations at the Story County Bridge (not to scale)

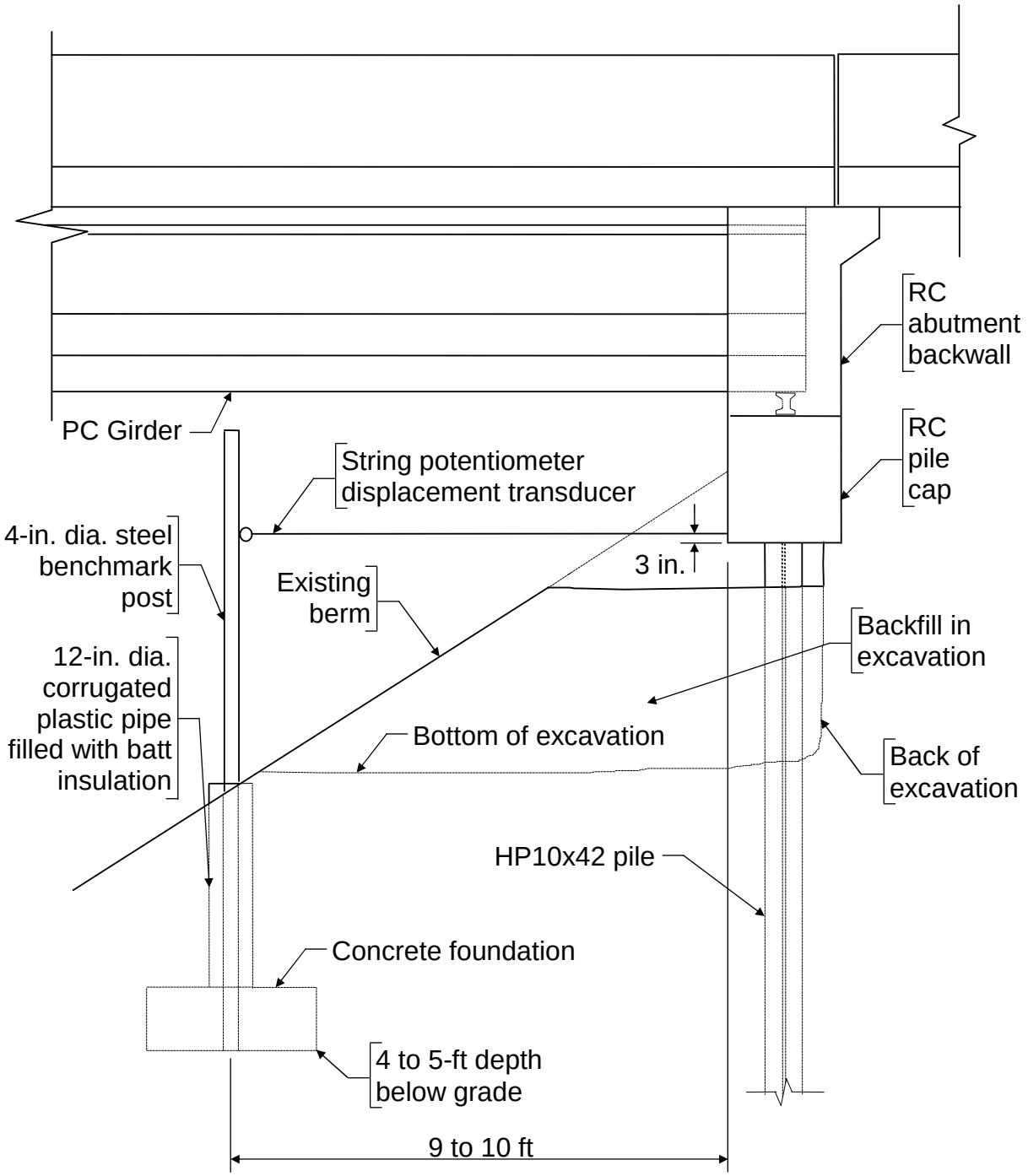

Figure 3.3. Benchmark-post installation (not to scale)

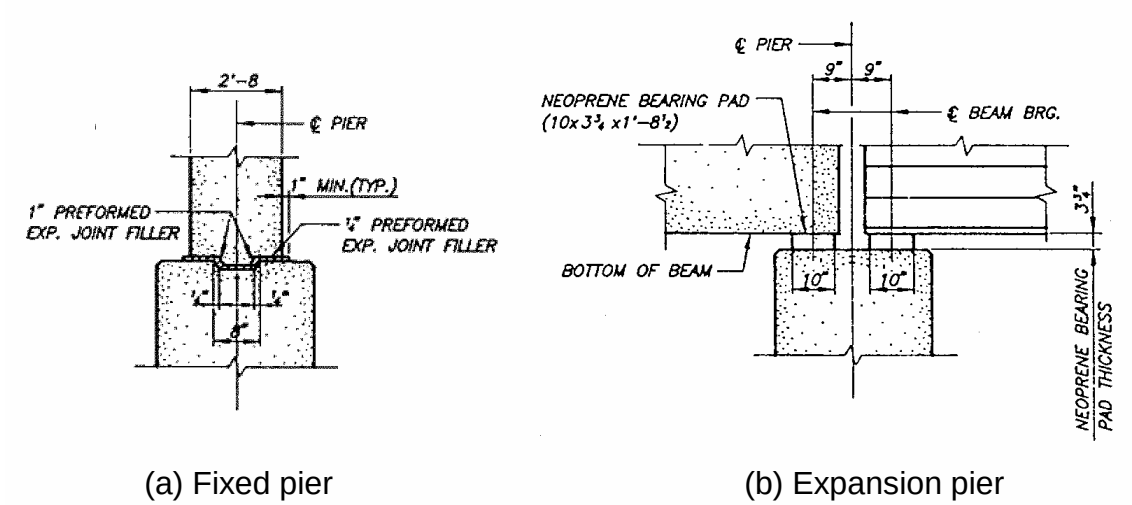

(a) Fixed pier (b) Expansion pier

Figure 3.4. Pier-connection details (Iowa DOT, 1984)

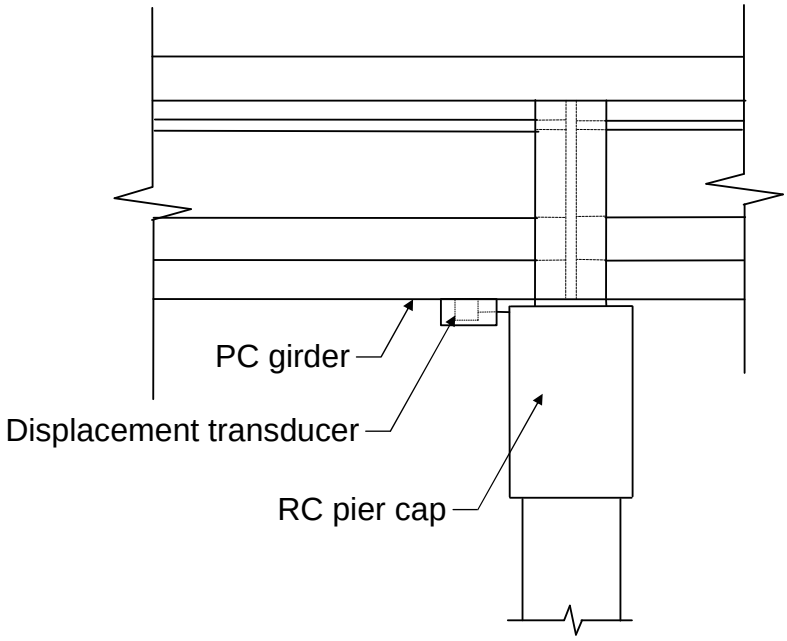

Figure 3.5. Displacement transducer at a pier cap

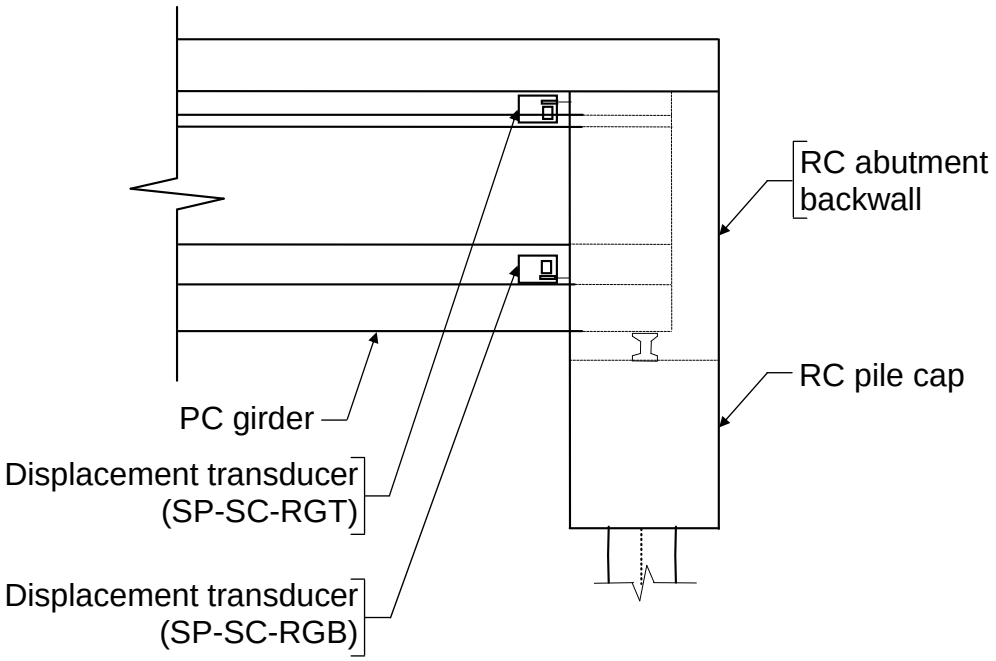

Figure 3.6. Displacement transducers at an abutment backwall

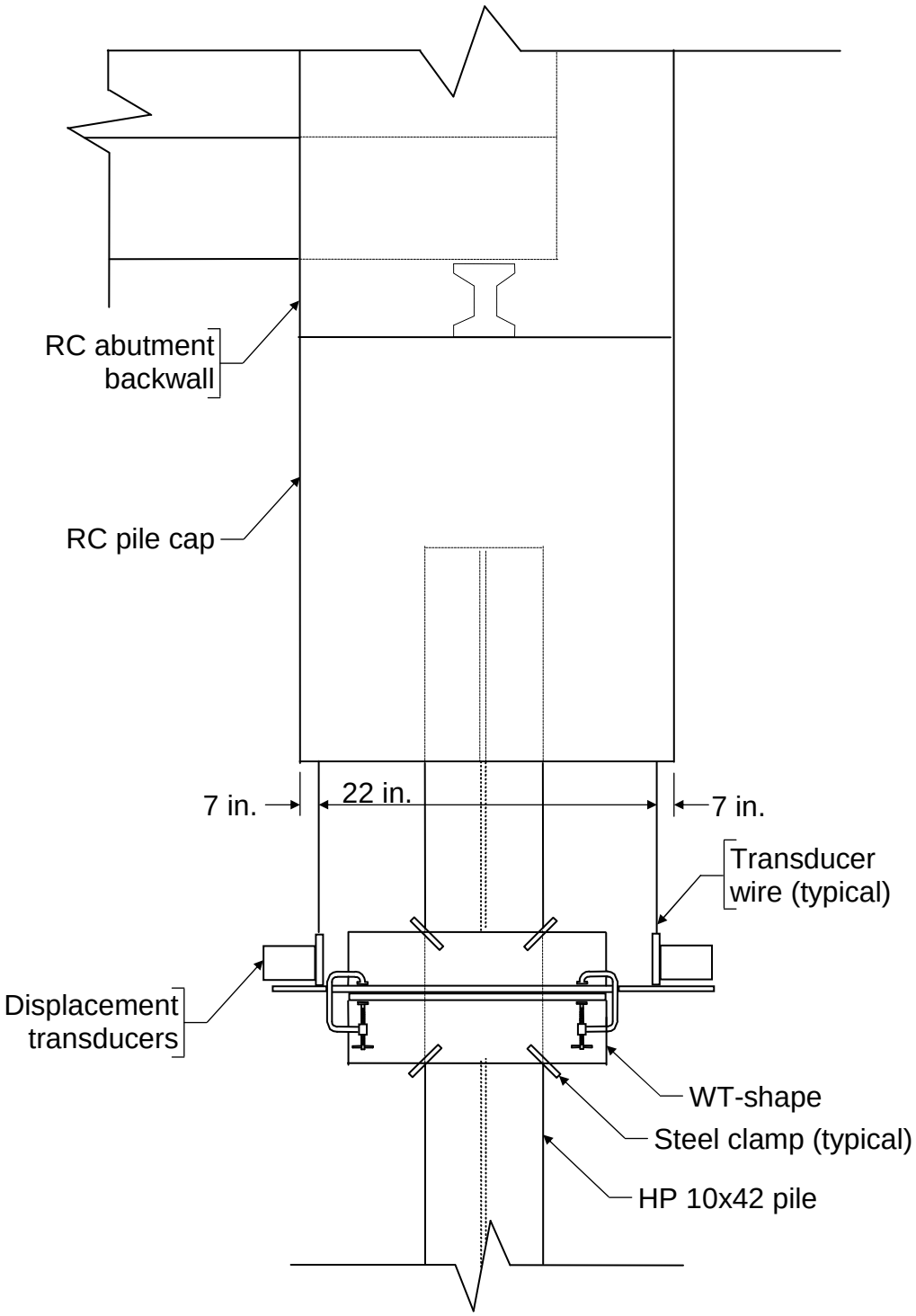

Figure 3.7. Displacement transducers at the bottom of an abutment-pile cap

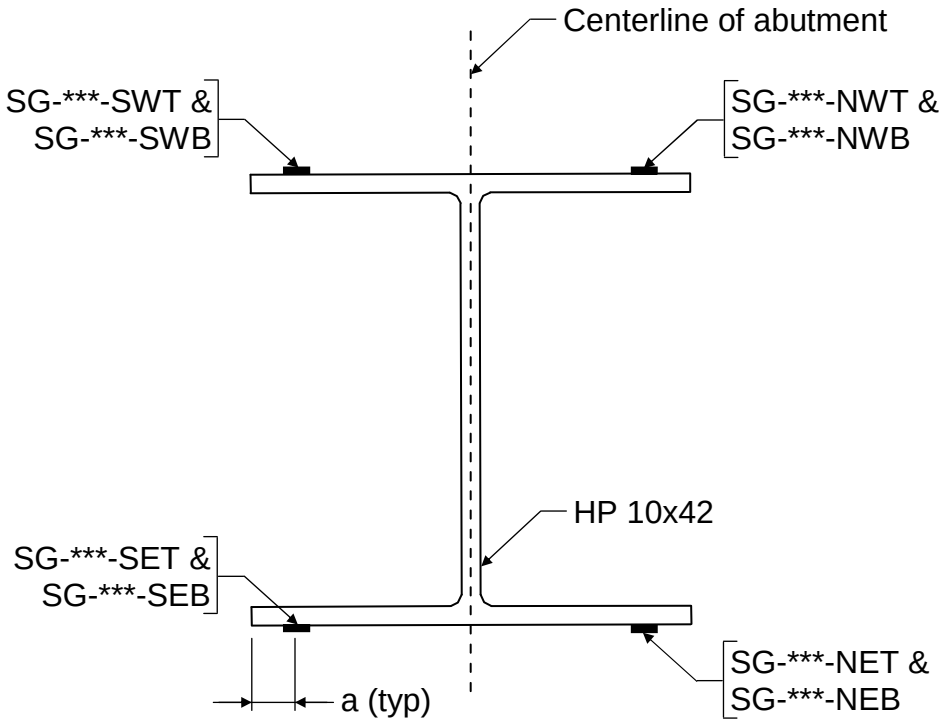

a = 1 in. for the monitored piles at both bridges, except a = 1/2 in. at the NW pile for the Guthrie County Bridge

Figure 3.8. Strain gages on an HP-shaped pile

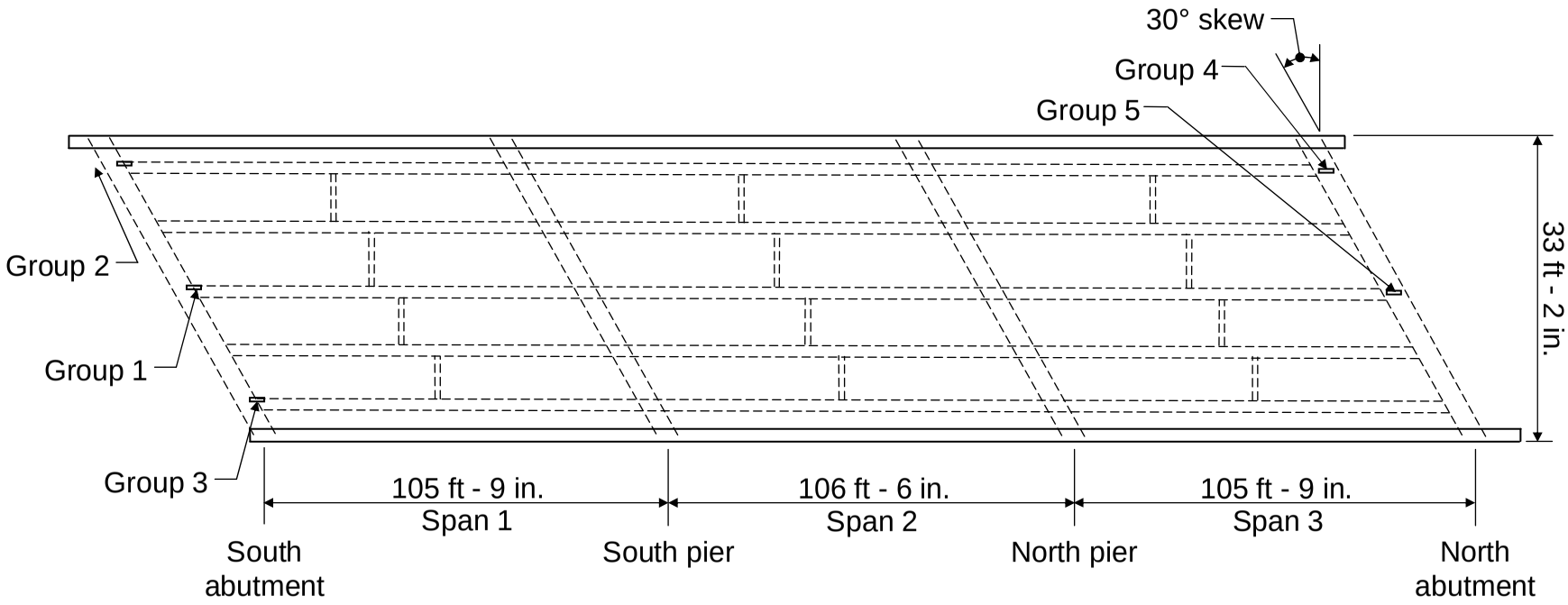

Group 1	Group 2	Group 3	Group 4	Group 5
SG-SCP-SWT	SG-SWP-SWT	SG-SEP-SWT	SG-NWP-SWT	SG-NCP-SWT
SG-SCP-NWT	SG-SWP-NWT	SG-SEP-NWT	SG-NWP-NWT	SG-NCP-NWT
SG-SCP-SET	SG-SWP-SET	SG-SEP-SET	SG-NWP-SET	SG-NCP-SET
SG-SCP-NET	SG-SWP-NET	SG-SEP-NET	SG-NWP-NET	SG-NCP-NET
SG-SCP-SWB	SG-SWP-SWB	SG-SEP-SWB	SG-NWP-SWB	SG-NCP-SWB
SG-SCP-NWB	SG-SWP-NWB	SG-SEP-NWB	SG-NWP-NWB	SG-NCP-NWB
SG-SCP-SEB	SG-SWP-SEB	SG-SEP-SEB	SG-NWP-SEB	SG-NCP-SEB
SG-SCP-NEB	SG-SWP-NEB	SG-SEP-NEB	SG-NWP-NEB	SG-NCP-NEB

Figure 3.9. Strain-gage locations for the piles at the Guthrie County Bridge (not to scale)

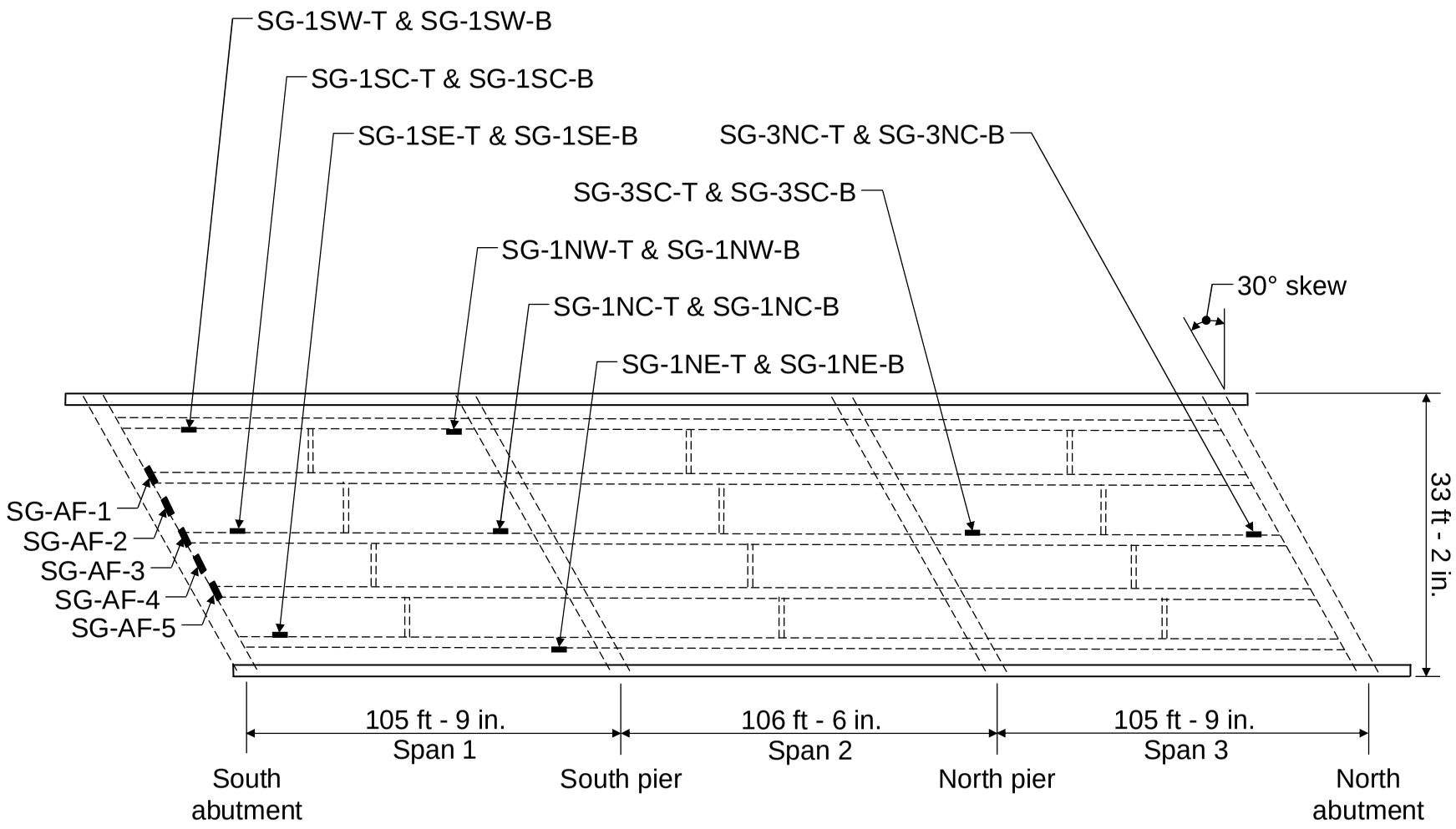

Figure 3.10. Strain-gage locations for the PC girders and a RC pile cap at the Guthrie County Bridge (not to scale)

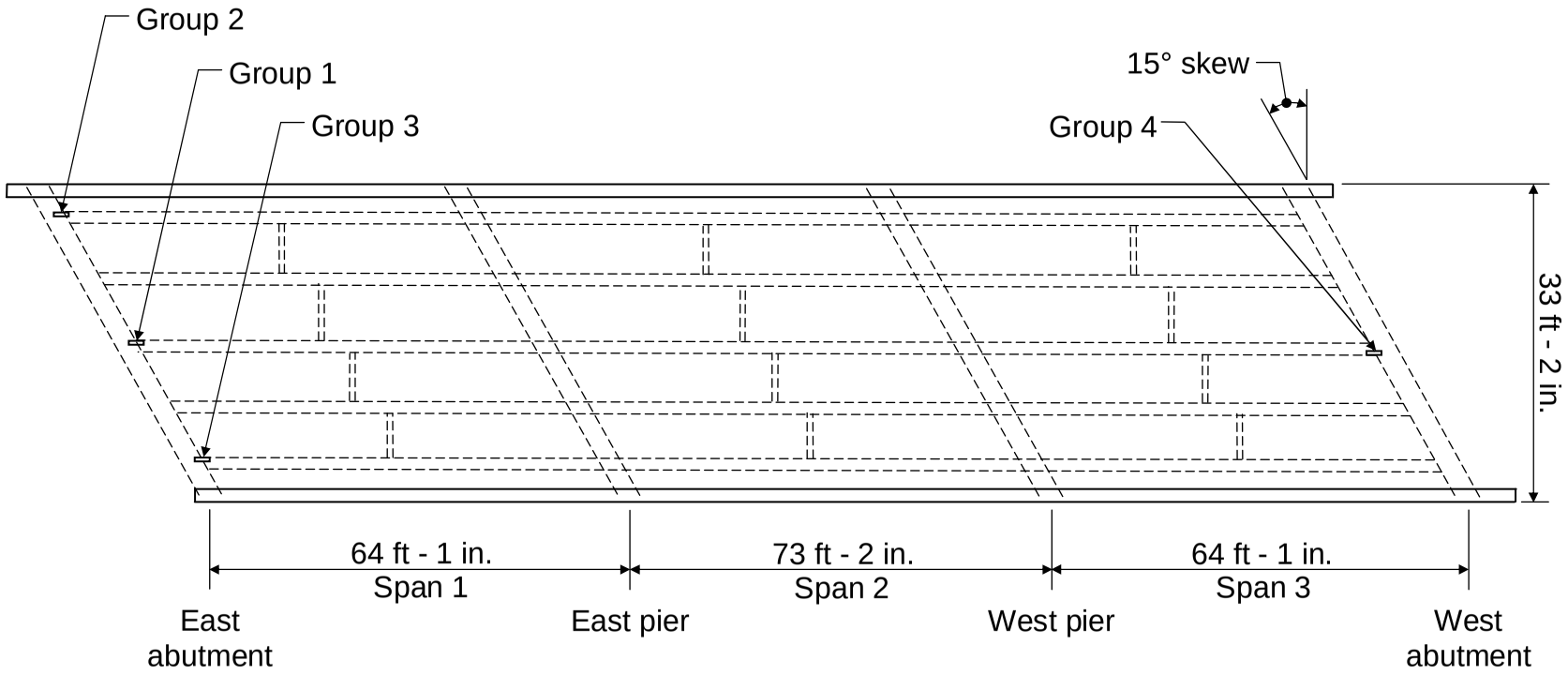

Group 1	Group 2	Group 3	Group 4
SG-ECP-SWT	SG-ESP-SWT	SG-ENP-SWT	SG-WCP-SWT
SG-ECP-NWT	SG-ESP-NWT	SG-ENP-NWT	SG-WCP-NWT
SG-ECP-SET	SG-ESP-SET	SG-ENP-SET	SG-WCP-SET
SG-ECP-NET	SG-ESP-NET	SG-ENP-NET	SG-WCP-NET
SG-ECP-SWB	SG-ESP-SWB	SG-ENP-SWB	SG-WCP-SWB
SG-ECP-NWB	SG-ESP-NWB	SG-ENP-NWB	SG-WCP-NWB
SG-ECP-SEB	SG-ESP-NEB	SG-ENP-SEB	SG-WCP-SEB
SG-ECP-NEB		SG-ENP-NEB	SG-WCP-NEB

Figure 3.11. Strain-gage locations for the piles at the Story County Bridge (not to scale)

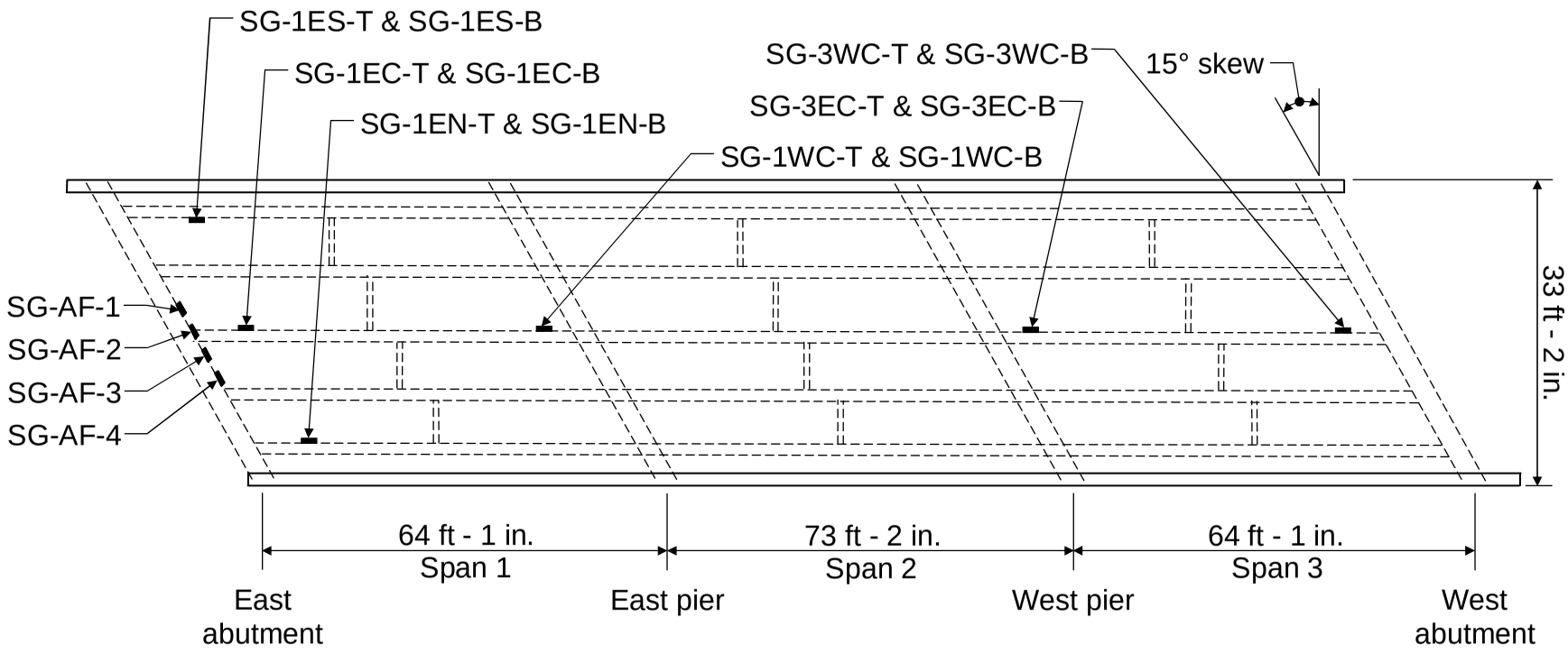

Figure 3.12. Strain-gage locations for the PC girders and a RC pile cap at the Story County Bridge (not to scale)

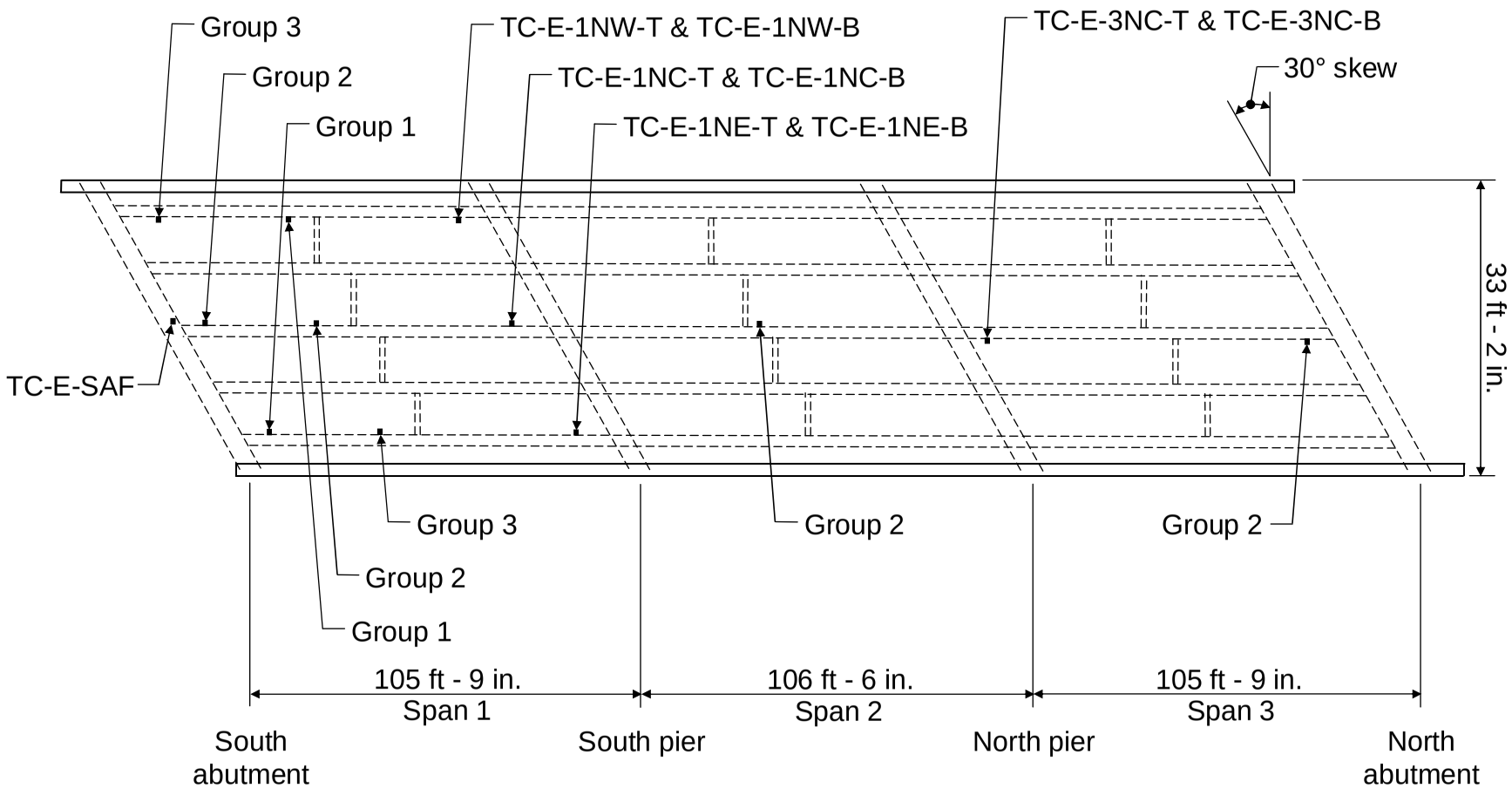

Group 1	Group 2	Group 3	Group 4	Group 5	Group 6	Group 7	Group 8
TC-E-1SE-S	TC-E-1SC-S	TC-E-1SW-S	TC-E-1MSE-S	TC-E-1MSC-S	TC-E-1MSW-S	TC-E-2MSC-S	TC-E-3NC-S
TC-E-1SE-T	TC-E-1SC-T	TC-E-1SW-T	TC-E-1MSE-T	TC-E-1MSC-T	TC-E-1MSW-T	TC-E-2MSC-T	TC-E-3NC-T
TC-E-1SE-W	TC-E-1SC-W	TC-E-1SW-W	TC-E-1MSE-W	TC-E-1MSC-W	TC-E-1MSW-W	TC-E-2MSC-W	TC-E-3NC-W
TC-E-1SE-B	TC-E-1SC-B	TC-E-1SW-B	TC-E-1MSE-B	TC-E-1MSC-B	TC-E-1MSW-B	TC-E-2MSC-B	TC-E-3NC-B

Figure 3.13. Thermocouple locations at the Guthrie County Bridge (not to scale)

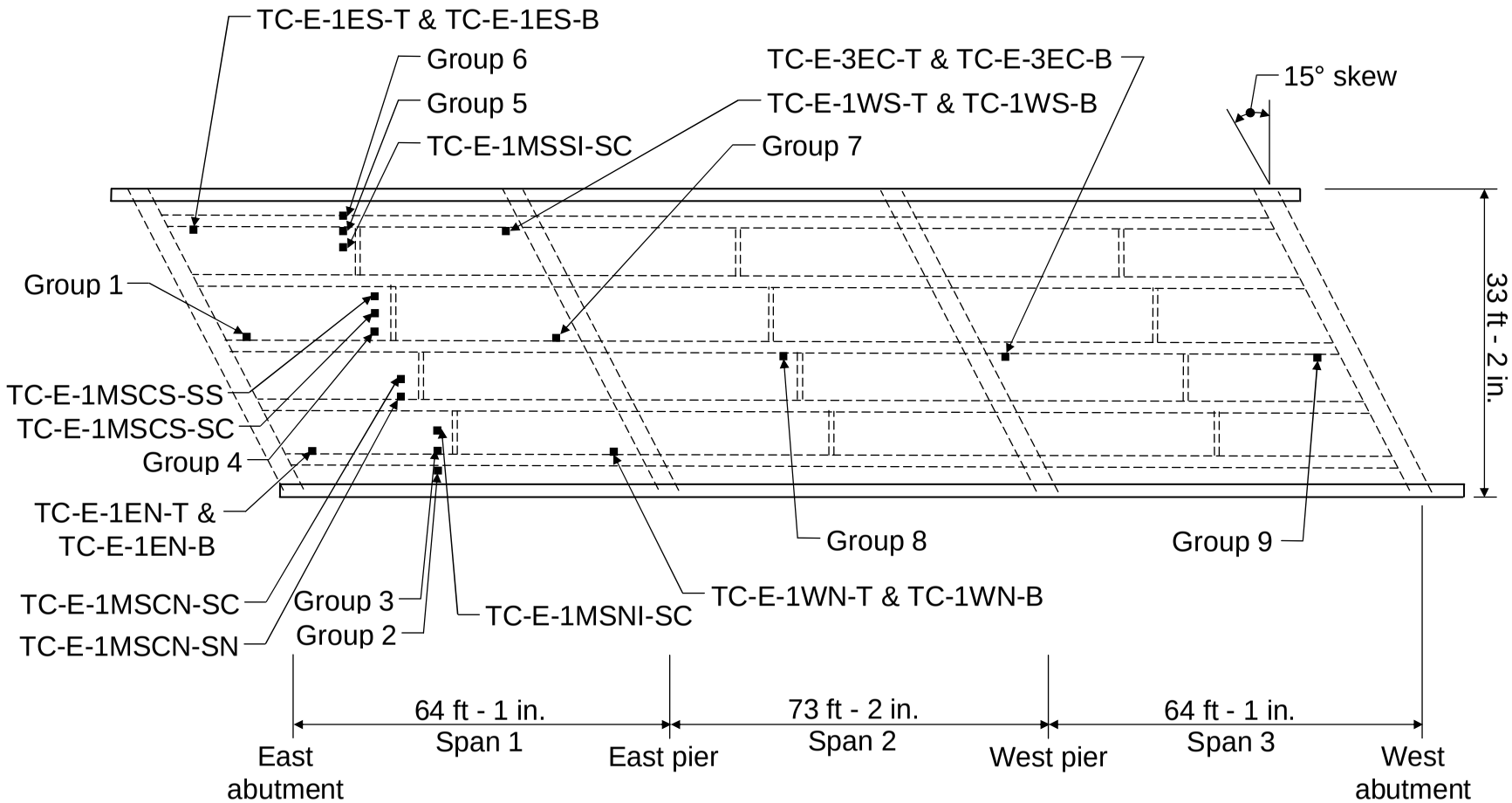

Group 1	Group 2	Group 3	Group 4	Group 5	Group 6	Group 7	Group 8	Group 9
TC-E-1EC-S	TC-E-1MSNX-S	TC-E-1MSNI-S	TC-E-1MSCS-SN	TC-E-1MSSI-SS	TC-E-1MSSX-S	TC-E-1WC-S	TC-E-2MSC-S	TC-E-3WC-S
TC-E-1EC-T	TC-E-1MSNX-W	TC-E-1MSNI-T	TC-E-1MSCS-T	TC-E-1MSSI-T	TC-E-1MSSX-W	TC-E-1WC-T	TC-E-2MSC-T	TC-E-3WC-T
TC-E-1EC-W	TC-E-1MSNX-B	TC-E-1MSNI-W	TC-E-1MSCS-W	TC-E-1MSSI-W	TC-E-1MSSX-B	TC-E-1WC-W	TC-E-2MSC-W	TC-E-3WC-W
TC-E-1EC-B		TC-E-1MSNI-B	TC-E-1MSCS-B	TC-E-1MSSI-B		TC-E-1WC-B	TC-E-2MSC-B	TC-E-3WC-B

Figure 3.14. Thermocouple locations at the Story County Bridge (not to scale)

Table 3.1. Characteristics of the instrumented bridges

Parameter	Guthrie County Bridge	Story County Bridge
Total bridge length	318 ft - 0 in.	201 ft - 4 in.
Spans	105.75, 106.5, 105.75 ft	64.08, 73.17, 64.08 ft
Skew	30°	15°
Abutment pile arrangement	U-shaped	Single row
Number of piles per abutment	12	7
Bridge orientation	North-south	East-west
PC girders (number/type)	5, Iowa Type-D	5, Iowa Type-C
Pier type	Tee pier	Pedestal pier
Bridge width	30 ft	30 ft

Table 3.2. Experimental measurements at the monitored bridges

Measurement	Guthrie County Bridge	Story County Bridge
Longitudinal abutment displacements	Each abutment	Each abutment
Transverse abutment displacements	One abutment	One abutment
Strains in steel piles	Five piles	Four piles
Strains in PC girders	Eight locations	Six locations
Displacements of a pile relative to RC pile cap	One pile location	One pile location
Vertical temperature gradient through superstructure	12 locations	14 locations
Relative displacements of bridge superstructure over piers	Each pier	Each pier
Strains in RC pile cap	One abutment	One abutment

Table 3.3. Number of instrumentation devices installed for field monitoring

Instrumentation	Guthrie County Bridge	Story County Bridge
Displacement transducers	16	11
Tiltmeters	1	1
Strain gages on piles	40	31
Strain gages on girders	16	12
Strain gages on pile cap	5	4
Thermocouples	43	46
Total	121	105

Table 3.4. Transducers at the Guthrie County Bridge

Instrument Code	Location	Measurement
SP-SW-LB	South abutment at West end	Longitudinal movement at Bottom of pile cap
SP-SC-LT	South abutment at Center of width	Longitudinal movement at Top of pile cap
SP-SC-LB	South abutment at Center of width	Longitudinal movement at Bottom of pile cap
SP-SE-LB	South abutment at East end	Longitudinal movement at Bottom of pile cap
SP-NC-L	North abutment at Center of width	Longitudinal movement of pile cap
SP-SW-T	South abutment at West edge	Transverse movement of pile cap
SP-SE-T	South abutment at East edge	Transverse movement of pile cap
SP-SC-LV	South abutment near Center of width	Relative Longitudinal displacement between benchmark posts for Verification
SP-SC-RGT	South abutment at Center girder	Relative displacement between abutment backwall and Girder Top flange
SP-SC-RGB	South abutment at Center girder	Relative displacement between abutment backwall and Girder Bottom flange
SP-SC-RPB	South abutment at Center of width	Relative displacement between bottom of Pile cap near Back face and pile
SP-SC-RPF	South abutment at Center of width	Relative displacement between bottom of Pile cap near Front face and pile
SP-SP-RPL	South Pier	Relative movement of superstructure over south Pier along Longitudinal axis
SP-NP-RPL	North Pier	Relative movement of superstructure over north Pier along Longitudinal axis
TM-SC-LR	South abutment at Center of width	Longitudinal Rotation of the south abutment pile cap

Table 3.5. Transducers at the Story County Bridge

Instrument Code	Location	Measurement
SP-EN-L	East abutment, North end	Longitudinal movement of pile cap
SP-EC-L	East abutment, Center	Longitudinal movement of pile cap
SP-ES-L	East abutment, East end	Longitudinal movement of pile cap
SP-WC-L	West abutment, Center	Longitudinal movement of pile cap
SP-EN-T	East abutment, North edge	Transverse movement of pile cap
SP-ES-T	East abutment, South edge	Transverse movement of pile cap
SP-EC-LV	East abutment, Center	Relative Longitudinal displacement between benchmark posts for Verification
SP-EC-RPB	East abutment, Center	Relative displacement between bottom of Pile cap near Back face and pile
SP-EC-RPF	East abutment, Center	Relative displacement between bottom of Pile cap near Front face and pile
SP-EP-RPL	East Pier	Relative movement of superstructure over east Pier along Longitudinal axis
SP-WP-RPL	West Pier	Relative movement of superstructure over west Pier along Longitudinal axis
TM-EC-LR	East abutment, Center	Longitudinal Rotation of the pile cap

Table 3.6. Strain gages for the abutment piles at the Guthrie County Bridge

Instrument Code	Member	Gage Location
SG-SWP-SWT	South abutment, West Pile	South West flange corner, Top cross section
SG-SWP-NWT	South abutment, West Pile	North West flange corner, Top cross section
SG-SWP-SET	South abutment, West Pile	South East flange corner, Top cross section
SG-SWP-NET	South abutment, West Pile	North East flange corner, Top cross section
SG-SWP-SWB	South abutment, West Pile	South West flange corner, Bottom cross section
SG-SWP-NWB	South abutment, West Pile	North West flange corner, Bottom cross section
SG-SWP-SEB	South abutment, West Pile	South East flange corner, Bottom cross section
SG-SWP-NEB	South abutment, West Pile	North East flange corner, Bottom cross section
SG-SCP-SWT	South abutment, Center Pile	South West flange corner, Top cross section
SG-SCP-NWT	South abutment, Center Pile	North West flange corner, Top cross section
SG-SCP-SET	South abutment, Center Pile	South East flange corner, Top cross section
SG-SCP-NET	South abutment, Center Pile	North East flange corner, Top cross section
SG-SCP-SWB	South abutment, Center Pile	South West flange corner, Bottom cross section
SG-SCP-NWB	South abutment, Center Pile	North West flange corner, Bottom cross section
SG-SCP-SEB	South abutment, Center Pile	South East flange corner, Bottom cross section
SG-SCP-NEB	South abutment, Center Pile	North East flange corner, Bottom cross section
SG-SEP-SWT	South abutment, East Pile	South West flange corner, Top cross section
SG-SEP-NWT	South abutment, East Pile	North West flange corner, Top cross section
SG-SEP-SET	South abutment, East Pile	South East flange corner, Top cross section
SG-SEP-NET	South abutment, East Pile	North East flange corner, Top cross section
SG-SEP-SWB	South abutment, East Pile	South West flange corner, Bottom cross section
SG-SEP-NWB	South abutment, East Pile	North West flange corner, Bottom cross section
SG-SEP-SEB	South abutment, East Pile	South East flange corner, Bottom cross section
SG-SEP-NEB	South abutment, East Pile	North East flange corner, Bottom cross section
SG-NCP-SWT	North abutment, Center Pile	South West flange corner, Top cross section
SG-NCP-NWT	North abutment, Center Pile	North West flange corner, Top cross section
SG-NCP-SET	North abutment, Center Pile	South East flange corner, Top cross section
SG-NCP-NET	North abutment, Center Pile	North East flange corner, Top cross section
SG-NCP-SWB	North abutment, Center Pile	South West flange corner, Bottom cross section
SG-NCP-NWB	North abutment, Center Pile	North West flange corner, Bottom cross section
SG-NCP-SEB	North abutment, Center Pile	South East flange corner, Bottom cross section
SG-NCP-NEB	North abutment, Center Pile	North East flange corner, Bottom cross section
SG-NWP-SWT	North abutment, West Pile	South West flange corner, Top cross section
SG-NWP-NWT	North abutment, West Pile	North West flange corner, Top cross section
SG-NWP-SET	North abutment, West Pile	South East flange corner, Top cross section
SG-NWP-NET	North abutment, West Pile	North East flange corner, Top cross section
SG-NWP-SWB	North abutment, West Pile	South West flange corner, Bottom cross section
SG-NWP-NWB	North abutment, West Pile	North West flange corner, Bottom cross section
SG-NWP-SEB	North abutment, West Pile	South East flange corner, Bottom cross section
SG-NWP-NEB	North abutment, West Pile	North East flange corner, Bottom cross section

Table 3.7. Strain gages for the PC girders and a RC pile cap at the Guthrie County Bridge

Instrument Code	Member	Gage Location
SG-1SW-T	1st span, South end of the West girder	Top flange
SG-1SW-B	1st span, South end of the West girder	Bottom flange
SG-1SC-T	1st span, South end of the Center girder	Top flange
SG-1SC-B	1st span, South end of the Center girder	Bottom flange
SG-1SE-T	1st span, South end of the East girder	Top flange
SG-1SE-B	1st span, South end of the East girder	Bottom Flange
SG-1NW-T	1st span, North end of the West girder	Top flange
SG-1NW-B	1st span, North end of the West girder	Bottom flange
SG-1NC-T	1st span, North end of the Center girder	Top flange
SG-1NC-B	1st span, North end of the Center girder	Bottom flange
SG-1NE-T	1st span, North end of the East girder	Top flange
SG-1NE-B	1st span, North end of the East girder	Bottom flange
SG-3NC-T	3rd span, North end of the Center girder	Top flange
SG-3NC-B	3rd span, North end of the Center girder	Bottom flange
SG-3SC-T	3rd span, South end of the Center girder	Top flange
SG-3SC-B	3rd span, South end of the Center girder	Bottom flange
SG-AF-1	south Abutment pile cap Face	Position no. 1
SG-AF-2	south Abutment pile cap Face	Position no. 2
SG-AF-3	south Abutment pile cap Face	Position no. 3
SG-AF-4	south Abutment pile cap Face	Position no. 4
SG-AF-5	south Abutment pile cap Face	Position no. 5

Table 3.8. Strain gages for the abutment piles at the Story County Bridge

Instrument Code	Member	Gage Location
SG-ENP-SWT	East abutment, North Pile	South West flange corner, Top cross section
SG-ENP-NWT	East abutment, North Pile	North West flange corner, Top cross section
SG-ENP-SET	East abutment, North Pile	South East flange corner, Top cross section
SG-ENP-NET	East abutment, North Pile	North East flange corner, Top cross section
SG-ENP-SWB	East abutment, North Pile	South West flange corner, Bottom cross section
SG-ENP-NWB	East abutment, North Pile	North West flange corner, Bottom cross section
SG-ENP-SEB	East abutment, North Pile	South East flange corner, Bottom cross section
SG-ENP-NEB	East abutment, North Pile	North East flange corner, Bottom cross section
SG-ECP-SWT	East abutment, Center Pile	South West flange corner, Top cross section
SG-ECP-NWT	East abutment, Center Pile	North West flange corner, Top cross section
SG-ECP-SET	East abutment, Center Pile	South East flange corner, Top cross section
SG-ECP-NET	East abutment, Center Pile	North East flange corner, Top cross section
SG-ECP-SWB	East abutment, Center Pile	South West flange corner, Bottom cross section
SG-ECP-NWB	East abutment, Center Pile	North West flange corner, Bottom cross section
SG-ECP-SEB	East abutment, Center Pile	South East flange corner, Bottom cross section
SG-ECP-NEB	East abutment, Center Pile	North East flange corner, Bottom cross section
SG-ESP-SWT	East abutment, South Pile	South West flange corner, Top cross section
SG-ESP-NWT	East abutment, South Pile	North West flange corner, Top cross section
SG-ESP-SET	East abutment, South Pile	South East flange corner, Top cross section
SG-ESP-NET	East abutment, South Pile	North East flange corner, Top cross section
SG-ESP-SWB	East abutment, South Pile	South West flange corner, Bottom cross section
SG-ESP-NWB	East abutment, South Pile	North West flange corner, Bottom cross section
SG-ESP-NEB	East abutment, South Pile	North East flange corner, Bottom cross section
SG-WCP-SWT	West abutment, Center Pile	South West flange corner, Top cross section
SG-WCP-NWT	West abutment, Center Pile	North West flange corner, Top cross section
SG-WCP-SET	West abutment, Center Pile	South East flange corner, Top cross section
SG-WCP-NET	West abutment, Center Pile	North East flange corner, Top cross section
SG-WCP-SWB	West abutment, Center Pile	South West flange corner, Bottom cross section
SG-WCP-NWB	West abutment, Center Pile	North West flange corner, Bottom cross section
SG-WCP-SEB	West abutment, Center Pile	South East flange corner, Bottom cross section
SG-WCP-NEB	West abutment, Center Pile	North East flange corner, Bottom cross section

Table 3.9. Strain gages for the PC girders and a RC pile cap at the Story County Bridge

Instrument Code	Member	Gage Location
SG-1EN-T	1st span, East side, North girder	Top flange
SG-1EN-B	1st span, East side, North girder	Bottom flange
SG-1EC-T	1st span, East side, Center girder	Top flange
SG-1EC-B	1st span, East side, Center girder	Bottom flange
SG-1ES-T	1st span, East side, South girder	Top flange
SG-1ES-B	1st span, East side, South girder	Bottom flange
SG-1WC-T	1st span, West side, Center girder	Top flange
SG-1WC-B	1st span, West side, Center girder	Bottom flange
SG-3WC-T	3rd span, West side, Center girder	Top flange
SG-3WC-B	3rd span, West side, Center girder	Bottom flange
SG-3EC-T	3rd span, East side, Center girder	Top flange
SG-3EC-B	3rd span, East side, Center girder	Bottom flange
SG-AF-1	east Abutment Face	Position no. 1
SG-AF-2	east Abutment Face	Position no. 2
SG-AF-3	east Abutment Face	Position no. 3
SG-AF-4	east Abutment Face	Position no. 4

Table 3.10. Thermocouples at the Guthrie County Bridge

Instrument Code	Member	Gage Location
TC-E-SAF	South Abutment pile cap Face	Mid-height
TC-E-1SE-S	1st span, South end of the East girder	Slab
TC-E-1SE-T	1st span, South end of the East girder	Top flange
TC-E-1SE-W	1st span, South end of the East girder	Web
TC-E-1SE-B	1st span, South end of the East girder	Bottom flange
TC-E-1SC-S	1st span, South end of the Center girder	Slab
TC-E-1SC-T	1st span, South end of the Center girder	Top flange
TC-E-1SC-W	1st span, South end of the Center girder	Web
TC-E-1SC-B	1st span, South end of the Center girder	Bottom flange
TC-E-1SW-S	1st span, South end of the West girder	Slab
TC-E-1SW-T	1st span, South end of the West girder	Top flange
TC-E-1SW-W	1st span, South end of the West girder	Web
TC-E-1SW-B	1st span, South end of the West girder	Bottom flange
TC-E-1MSE-S	1st span, Mid-Span, East girder	Slab
TC-E-1MSE-T	1st span, Mid-Span, East girder	Top flange
TC-E-1MSE-W	1st span, Mid-Span, East girder	Web
TC-E-1MSE-B	1st span, Mid-Span, East girder	Bottom flange
TC-E-1MSC-S	1st span, Mid-Span, Center girder	Slab
TC-E-1MSC-T	1st span, Mid-Span, Center girder	Top flange
TC-E-1MSC-W	1st span, Mid-Span, Center girder	Web
TC-E-1MSC-B	1st span, Mid-Span, Center girder	Bottom flange
TC-E-1MSW-S	1st span, Mid-Span, West girder	Slab
TC-E-1MSW-T	1st span, Mid-Span, West girder	Top flange
TC-E-1MSW-W	1st span, Mid-Span, West girder	Web
TC-E-1MSW-B	1st span, Mid-Span, West girder	Bottom flange
TC-E-1NE-T	1st span, North end of the East girder	Top flange
TC-E-1NE-B	1st span, North end of the East girder	Bottom flange
TC-E-1NC-T	1st span, North end of the Center girder	Top flange
TC-E-1NC-B	1st span, North end of the Center girder	Bottom flange
TC-E-1NW-T	1st span, North end of the West girder	Top flange
TC-E-1NW-B	1st span, North end of the West girder	Bottom flange
TC-E-2MSC-S	2nd span, Mid-Span, Center girder	Slab
TC-E-2MSC-T	2nd span, Mid-Span, Center girder	Top flange
TC-E-2MSC-W	2nd span, Mid-Span, Center girder	Web
TC-E-2MSC-B	2nd span, Mid-Span, Center girder	Bottom flange
TC-E-3SC-T	3rd span, South end of the Center girder	Top flange
TC-E-3SC-B	3rd span, South end of the Center girder	Bottom flange
TC-E-3NC-S	3rd span, North end of the Center girder	Slab
TC-E-3NC-T	3rd span, North end of the Center girder	Top flange
TC-E-3NC-W	3rd span, North end of the Center girder	Web
TC-E-3NC-B	3rd span, North end of the Center girder	Bottom flange

Table 3.11. Thermocouples at the Story County Bridge

Instrument Code	Member	Gage Location
TC-E-1EN-T	1st span, East end of North girder	Top flange
TC-E-1EN-B	1st span, East end of North girder	Bottom flange
TC-E-1EC-S	1st span, East end of Center girder	Slab
TC-E-1EC-T	1st span, East end of Center girder	Top flange
TC-E-1EC-W	1st span, East end of Center girder	Web
TC-E-1EC-B	1st span, East end of Center girder	Bottom flange
TC-E-1ES-T	1st span, East end of South girder	Top flange
TC-E-1ES-B	1st span, East end of South girder	Bottom flange
TC-E-1MSNX-S	1st span, Mid-Span, North girder, Exterior side	Slab
TC-E-1MSNX-W	1st span, Mid-Span, North girder, Exterior side	Web
TC-E-1MSNX-B	1st span, Mid-Span, North girder, Exterior side	Bottom flange
TC-E-1MSNI-SN	1st span, Mid-Span, North girder, Interior side	in Slab span, North side
TC-E-1MSNI-SC	1st span, Mid-Span, North girder, Interior side	in Slab span, Center
TC-E-1MSNI-T	1st span, Mid-Span, North girder, Interior side	Top flange
TC-E-1MSNI-W	1st span, Mid-Span, North girder, Interior side	Web
TC-E-1MSNI-B	1st span, Mid-Span, North girder, Interior side	Bottom flange
TC-E-1MSCN-SN	1st span, Mid-Span, Center girder, North side	in Slab span, North side
TC-E-1MSCN-SC	1st span, Mid-Span, Center girder, North side	in Slab span, Center
TC-E-1MSCS-SN	1st span, Mid-Span, Center girder, South side	in Slab span, North side
TC-E-1MSCS-SC	1st span, Mid-Span, Center girder, South side	in Slab span, Center
TC-E-1MSCS-SS	1st span, Mid-Span, Center girder, South side	in Slab span, South side
TC-E-1MSCS-T	1st span, Mid-Span, Center girder, South side	Top flange
TC-E-1MSCS-W	1st span, Mid-Span, Center girder, South side	Web
TC-E-1MSCS-B	1st span, Mid-Span, Center girder, South side	Bottom flange
TC-E-1MSSI-SC	1st span, Mid-Span, South girder, Interior side	in Slab span, Center
TC-E-1MSSI-SS	1st span, Mid-Span, South girder, Interior side	in Slab span, South
TC-E-1MSSI-T	1st span, Mid-Span, South girder, Interior side	Top flange
TC-E-1MSSI-W	1st span, Mid-Span, South girder, Interior side	Web
TC-E-1MSSI-B	1st span, Mid-Span, South girder, Interior side	Bottom flange
TC-E-1MSSX-S	1st span, Mid-Span, South girder, Exterior side	Slab
TC-E-1MSSX-W	1st span, Mid-Span, South girder, Exterior side	Web
TC-E-1MSSX-B	1st span, Mid-Span, South girder, Exterior side	Bottom flange
TC-E-1WC-S	1st span, West end of Center girder	Slab
TC-E-1WC-T	1st span, West end of Center girder	Top flange
TC-E-1WC-W	1st span, West end of Center girder	Web
TC-E-1WC-B	1st span, West end of Center girder	Bottom flange
TC-E-2MSC-S	2nd span, Mid-Span, Center girder	Slab
TC-E-2MSC-T	2nd span, Mid-Span, Center girder	Slab
TC-E-2MSC-W	2nd span, Mid-Span, Center girder	Web
TC-E-2MSC-B	2nd span, Mid-Span, Center girder	Bottom flange
TC-E-3WC-S	3rd span, West end of Center girder	Slab
TC-E-3WC-T	3rd span, West end of Center girder	Top flange
TC-E-3WC-W	3rd span, West end of Center girder	Web
TC-E-3WC-B	3rd span, West end of Center girder	Bottom flange
TC-E-3EC-T	3rd span, East end of Center girder	Top flange
TC-E-3EC-B	3rd span, East end of Center girder	Bottom flange

4. EXPERIMENTAL RESULTS

This chapter presents the results of the experimental monitoring program that was conducted for the two, in-service, integral-abutment bridges. The Guthrie County Bridge was monitored from December 17, 1997 until April 1, 2000, and the Story County Bridge was monitored from July 12, 1998 to April 1, 2000. Additional discussions of the experimental results are presented in the MS theses for Thomas (1999) and Sayers (2000).

4.1. Experimental data filtering

With the massive amount of accumulated data, gages were expected to occasionally produce outlying-data points. The initial, data-reduction process that was discussed in Section 3.5.2 eliminated many of the questionable data. Also, some of the gages were expected to produce unreliable data or completely fail during the monitoring period due to a variety of reasons. Problems that were encountered with some of the instrumentation devices include water infiltration, which damaged the connections for gages to bridge elements; moisture that accumulated at wire splices; and gage malfunctions. Erroneous data was identified and, if possible, corrected or eliminated before the experimental results were presented in this report.

4.1.1. Thermocouples

Since thermocouples measure absolute temperatures, the raw data was presented without modifications in most instances. Each thermocouple reading was plotted versus time to determine if the thermocouple was properly functioning. Discrete jumps and drifting were not encountered with the temperature data. Either the

thermocouples worked and produced reliable temperatures, which followed an expected pattern of temperature over time, or they did not work and produced temperature readings outside of the expected range. Temperature data were discarded if they were obviously incorrect. Figures 4.1a and 4.1b show graphs of temperature versus time that were measured by a thermocouple (TC-E-1SC-S for the Guthrie County Bridge) with reliable data over the entire monitoring period and a thermocouple (TC-E-1SW-S for the Guthrie County Bridge) with some time periods of unreliable temperature data that is indicated by the large spikes in the temperatures, respectively. For Fig. 4.1a, the maximum, temperature range is shown to the right of the plot. When a thermocouple was considered to produce reliable data over the entire monitoring-time period, the experimental, temperature range is the difference between the maximum and minimum, measured temperatures. When a thermocouple failed during the monitoring-time period, the experimental, temperature range is the difference between the overall maximum and minimum of the reliable temperature readings. Tables 4.1 and 4.2 indicate the months during which each thermocouple was properly functioning for the Guthrie County Bridge and Story County Bridge, respectively.

4.1.2. Displacement transducers

Data from each of the displacement transducers were plotted versus time to determine if these gages were properly functioning. The displacement plots were compared with the plots of the average, bridge temperature to verify that the recorded displacements correlated with temperature changes. Faulty displacement measurements included sudden jumps in a displacement or the drifting of a displacement over time. Displacement data were considered reliable after a

displacement jump if the displacements that were measured after the discontinuity correlated with temperature. However, a new temperature cycle was started for that displacement, since the absolute displacement was not continuous across a displacement jump. Displacements that continuously increased or decreased with time and did not correlate with changes in temperature indicated a drift in the measured displacement. A displacement drift would occur if a transducer malfunctioned or if a benchmark post which supported that transducer moved. Measurements were considered unreliable if they contained a displacement drift.

Figure 4.2a shows a plot of displacement versus temperature from a displacement transducer (SP-SC-LB for the Guthrie County Bridge) with reliable data over the entire monitoring-time period. Figure 4.2b shows a plot of a displacement transducer (SP-SE-LB for the Guthrie County Bridge) with an apparent jump in the displacement that occurred on July 5, 1999. The experimental, displacement range was determined for a time period over which the gage was continuously producing reliable data. In the case of a distinct jump in a displacement, the experimental, displacement range can be determined from the maximum and minimum displacement in the time period before the jump and after the jump, as shown by the bars in Fig. 4.2b. This figure also shows that the displacements indicate a possible displacement drift, since the displacements during the 1999-yearly cycle did not return to the displacement amounts for the previous 1998-yearly cycle. The displacement data was inconclusive as to whether a displacement drift occurred or if the side of the abutment at the obtuse angle of the bridge deck displaced over time towards the river. Tables 4.3 and 4.4

indicate the months during which reliable data was obtained from each displacement transducer for the Guthrie County Bridge and Story County Bridge, respectively.

4.1.3. Pile strain gages

The strain gages on the abutment piles required a more in-depth filtering process to determine their reliability than that for the other instrumentation devices because the weldable-strain gages had a higher rate of failure than that for the other instrumentation devices. The strain measurements for each of the monitored piles were plotted versus time and compared for similar patterns to graphs of the longitudinal displacements versus time for the abutment that was supported by the pile. Problems that were encountered with the strain gages for the piles included jumps in the strain values, drifting of strain values over time, and failure of the gages. Strain-gage data was individually checked for each gage and was also checked by computing the axial; bending; and torsional, normal-warpage strains for each of the monitored pile cross sections.

A significant amount of pile-strain data was discarded due to drifting of the strain-gage readings over time, which was most likely caused by moisture infiltration into the splice between a strain-gage, lead wire and the gage-extension wire. These splices were covered with shrink-wrap tubing. Several of the lead-wire splices for the pile, strain gages at the Guthrie County Bridge were examined on February 28, 1999. Several wire splices were disconnected to reveal that moisture had infiltrated into the wire splices. The inside surface of the outer layer of the shrink-wrap tubing was wet. Also, the shrink-wrap tubing that was originally placed around each of the three-wire, strain-gage conductors was no longer tightly closed around the conductor insulation.

Several splices were rehabilitated by applying heat to dry the splice and by coating the splice with a waterproof caulk to prevent any future moisture infiltration.

The measured strains from the gages SG-NCP-SWT, SG-NCP-NWT, SG-NCP-SET, and SG-NCP-NET at the top cross section of the pile near the mid-width of the north abutment at the Guthrie County Bridge are shown in Fig. 4.3. Initial, data reduction was completed to eliminate strain values that were outside of the limits that were specified in Section 3.5.2. Figure 4.4 shows temperature-corrected pile strains for the same strain gages whose raw-strain data was shown in Fig. 4.3. The temperature corrections included the non-linear gage and the Wheatstone-Bridge corrections that were described in Section 3.6.2. The “dummy” gage that used to correct the Wheatstone-Bridge resistor was installed in March 1998. Therefore, individual, strain-gage results could not be obtained before this date. The Wheatstone-Bridge completion error was most noticeable for gages with small strain ranges, such as that shown in Fig. 4.4b for gage SG-NCP-NWT for the Guthrie County Bridge. The measured strains were checked for jumps and drifts in the same manner as that used for checking the acceptability of the measured displacements. Smaller, individual, strain errors were difficult to isolate when they were plotted over long-term periods. Investigating each gage over daily or weekly-time periods was impractical when large amounts of data existed, so another method was investigated to assess the reliability of the strain-gage readings. The method used that detected less visible errors in individual, strain-gage readings involved plotting the average axial; bending; and torsional, normal-warpage-strain components over time. These strain components should correlate with the abutment displacement over seasonal cycles. At each pile cross section that was

monitored with four, strain gages, as shown in Fig. 4.5, the longitudinal strain, ε_i, in the pile is a superposition of the axial strain, ε_a; x-axis, bending strain, ε_x; y-axis, bending strain, ε_y; and torsional, normal-warpage strains, ε_t. The strain relationships are given by Eq. 4.1 through 4.4. The subscripts 1, 2, 3, and 4 correspond to the Strain gages 1, 2, 3, and 4, respectively, shown in Fig. 4.5.

$$\varepsilon_1 = \varepsilon_a + \varepsilon_x - \varepsilon_y + \varepsilon_t \tag{4.1}$$

$$\varepsilon_2 = \varepsilon_a + \varepsilon_x + \varepsilon_y - \varepsilon_t \tag{4.2}$$

$$\varepsilon_3 = \varepsilon_a - \varepsilon_x + \varepsilon_y + \varepsilon_t \tag{4.3}$$

$$\varepsilon_4 = \varepsilon_a - \varepsilon_x - \varepsilon_y - \varepsilon_t \tag{4.4}$$

Since the strain gages measure the change in strain from their initialized values and when a properly functioning strain gage is located near each flange tip on an HP-shaped, pile cross section, the change in the pile longitudinal strains induced by the axial force, torsional moment, x-axis-bending moment, and y-axis-bending moment in the pile, can be determined from Eqs. 4.5, 4.6, 4.7, and 4.8, respectively, as discussed by Girton, et al., (1991).

$$\varepsilon_a = (\varepsilon_1 + \varepsilon_2 + \varepsilon_3 + \varepsilon_4)/4 \tag{4.5}$$

$$\varepsilon_t = (\varepsilon_1 - \varepsilon_2 + \varepsilon_3 - \varepsilon_4)/4 \tag{4.6}$$

$$\varepsilon_x = (\varepsilon_1 + \varepsilon_2 - \varepsilon_3 - \varepsilon_4)/4 \tag{4.7}$$

$$\varepsilon_y = (-\varepsilon_1 + \varepsilon_2 + \varepsilon_3 - \varepsilon_4)/4 \tag{4.8}$$

where, $\Delta\varepsilon_1$, $\Delta\varepsilon_2$, $\Delta\varepsilon_3$, and $\Delta\varepsilon_4$ are the changes in the temperature-corrected, total, strain-gage readings, which are evaluated from Eq. 3.8, for the four gages on a cross section of a pile.

As described in Section 3.6.2, the “dummy-gage” correction was required for the calculation of axial strains, since any Wheatstone-Bridge completion error is additive. Hence, axial strain could not be computed for the Guthrie County Bridge piles before the “dummy” gage was installed in March of 1998 and after the “dummy-gage” readings became unreliable in July of 1999. For the other three, strain components, the Wheatstone-Bridge completion strain error is eliminated when taking the difference in the strain-gage readings. These strain components were computed when reliable, individual, strain-gage data were available.

Torsional, normal-warpage strains can be assumed to be near zero, as shown in Figure 4.6a, for a pile cross section with four, reliable, strain gages. The ANSYS, finite-element models also verified that these torsional strains were negligible. With nearly zero daily and seasonal variations in the torsional, normal-warpage strains, any strain jumps were easily identified for individual gages. Also, axial strains, which had low-daily and low-seasonal variations, were used as a second check for the reliability of the gages in a pile cross section. An examination of Fig. 4.6b shows that a strain jump occurred in July of 1998 for axial strain in the upper, cross section for the pile near the mid-width of the north abutment for the Guthrie County Bridge. A similar jump in axial strain occurred for every instrumented-pile cross section at the Guthrie County Bridge. The individual, strain-gage readings and the axial-strain components were considered to be unreliable for only the time period that had the jump in the strain. The strain-jump

error was eliminated when the bending strains shown in Figs. 4.6c and 4.6d for x-axis and y-axis bending, respectively, and torsional, normal-warpage strains shown in Fig. 4.6a were computed from Eqs. 4.5 through 4.8, since this error equally affected each gage.

When other strain jumps or drifts were noticed in the strain-component plots, individual, strain gages were more thoroughly investigated. Using the assumption that the torsional, normal-warpage strains were negligible, a specific combination of two strain gages in a pile cross section could be used to determine axial, x-axis-bending, or y-axis-bending strains in the pile at that cross section. When only two or three gages were properly functioning, pile-strain components were calculated from Eqs. 4.9, 4.10, and 4.11.

$$\Delta\varepsilon_a = (\Delta\varepsilon_1 + \Delta\varepsilon_3)/2 \text{ or } (\Delta\varepsilon_2 + \Delta\varepsilon_4)/2 \tag{4.9}$$

$$\Delta\varepsilon_x = (\Delta\varepsilon_1 - \Delta\varepsilon_4)/2 \text{ or } (\Delta\varepsilon_2 - \Delta\varepsilon_3)/2 \tag{4.10}$$

$$\Delta\varepsilon_y = (\Delta\varepsilon_2 - \Delta\varepsilon_1)/2 \text{ or } (\Delta\varepsilon_3 - \Delta\varepsilon_4)/2 \tag{4.11}$$

The plots of the strain components evaluated by Eq. 4.9 through 4.11 were compared with the plots of longitudinal abutment displacement versus time for the abutment that was supported by these monitored piles. If the strain components correlated well with the abutment displacements, the gage readings were considered to be reliable. If the strain components did not correlate well with the abutment displacements, at least one of the two gage readings was in error. The two-gage combinations were used to determine which gage or gages were causing errors in the strain-component calculations at the particular, pile cross section.

After applying this filtering process for the upper cross section for the pile near the mid-width of the north abutment for the Guthrie County Bridge, the individual, strain-gage plots and strain-component plots are shown in Fig. 4.7 and 4.8, respectively. The reported, strain range for each of the strain components was determined from the time period with the largest, strain range in an uninterrupted data set. The reported ranges for the strain components are shown as a bar on the right-hand side of the plot in Fig. 4.8. The maximum range of the torsional, normal-warpage strain was considered negligible and was not shown in Fig. 4.8a.

Tables 4.5 and 4.6 indicate the reliability of the strain gages on the monitored piles for the Guthrie County Bridge and Story County Bridge, respectively. The "dummy" gage at the Guthrie County Bridge failed in June of 1999, making the individual, strain-gage readings incorrect after the failure. As discussed before, the bending and warpage-normal, torsion strains can still be evaluated after the failure of the "dummy" gage, since the Wheatstone-Bridge completion error is eliminated using Eqs. 4.5 through 4.8. The months for which reliable, strain components were calculated at the monitored, pile cross sections for the Guthrie County Bridge and Story County Bridge are listed in Tables 4.7 and 4.8, respectively.

4.1.4. Girder strain gages

The same process that used to filter the pile-strain data was applied to the experimentally-measured, girder strains. A strain gage was attached to one side of each flange of selected PC girders. The gage was oriented along the longitudinal direction of the girder at each of the monitored cross sections. Assuming that the axial; y-axis bending; and torsional, normal-warpage strains were negligible, the measured,

longitudinal strains in the girder flanges were essentially x-axis-bending strains, $\Delta\varepsilon_x$, that were induced by the stress and temperature. The difference between the change in the top-flange strain, $\Delta\varepsilon_{top}$, and bottom-flange strains, $\Delta\varepsilon_{bottom}$, in a PC girder is given by

$$\Delta\varepsilon_x = \Delta\varepsilon_{top} - \Delta\varepsilon_{bottom} \tag{4.12}$$

The months for which girder, strain-gage data and x-axis, bending-strain differences were reliable are shown in Table 4.9 and 4.10 for the Guthrie County Bridge and Story County Bridge, respectively. The strain jump that was detected in July of 1998 for the pile-strain gages at the Guthrie County Bridge was also noticed for the girder strains. The strain jump equally affected all of the strain gages on the girders; therefore, that strain error was eliminated when Eq. 4.12 was applied to calculate the differences in the longitudinal strains in the girder flanges.

4.2. Bridge temperatures

The temperatures that were measured with the thermocouples, which were embedded in the concrete superstructure for each bridge, were analyzed to establish an average, bridge temperature and the thermal gradients in each bridge. This section describes the experimental, temperature results that were obtained for each bridge.

4.2.1. Average, bridge temperatures

Average, bridge temperatures of a bridge superstructure were computed for each time interval during the monitoring period. The average, bridge temperature is the weighted average of the temperatures that were measured by all of the thermocouples, which were embedded in a bridge superstructure. A uniform temperature was assumed to exist for each region and for each portion of the total cross section of the

superstructure, as shown by the shaded areas in Fig. 4.9. This partial cross section, which represents one bridge girder and its tributary slab width, was divided into four regions: bride deck, girder top flange, girder web, and girder bottom flange. The average, bridge temperature, T_{ave}, was calculated as

$$T_{ave} = \frac{\sum_{j=1}^{n} T_j A_j}{\sum_{j=1}^{n} A_j} \tag{4.13}$$

where, T_j is the temperature measured by a thermocouple in a particular region of the total cross section for the bridge superstructure, A_j is the area of that particular region, and n is the number of regions in the total cross section for the bridge superstructure. Graphs of the average, bridge temperatures versus time for the Guthrie County Bridge and the Story County Bridge are shown in Fig. 4.10.

At the Guthrie County Bridge, the maximum, average, bridge temperature of 101 °F occurred in the early evening hours of July 20, 1998 and July 22, 1999. At the Story County Bridge, a maximum, average, bridge temperature of 104 °F occurred in the early evening hours of July 20, 1998 and July 20, 1999. The highest, slab temperatures were also recorded at these times.

The minimum, average, bridge temperature measured at the Guthrie County Bridge was -12 °F, which occurred before the sunrise on January 5, 1999. At the Story County Bridge, the minimum, average, bridge temperature of -10° F was measured before sunrise on January 5, 1999. The maximum ranges in average, bridge temperatures for each monitored bridge are shown in Fig. 4.10. The range in the average, bridge temperatures was 113 °F and 115 °F for the Guthrie County Bridge and Story County Bridge, respectively.

The maximum, average, bridge temperatures were warmer than the air temperatures measured by a thermocouple placed under each bridge. Figure 4.11 shows that for the Guthrie County Bridge, the average, bridge temperature lagged behind and exceeded the measured, air temperature. A 98 °F, maximum, air temperature was recorded on July 20, 1998 by the National Weather Service (NWS) for Des Moines, Iowa, which is within 30 miles of this bridge.

4.2.2. Vertical-temperature gradients

Temperature distributions through the depth of the superstructure for each bridge were established from the experimentally-measured, concrete temperatures. These temperatures were measured by the thermocouples that were installed in the bridge deck and in selected, PC girders for each bridge. Vertical-thermal gradients induce bending moments, which cause longitudinal stresses to develop in the superstructure, of continuous bridges. A positive, vertical-thermal gradient occurs when the temperature at the top of a bridge deck is greater than the temperature at the bottom of the PC girders. The largest, positive-thermal gradients occurred at the times of the maximum, average, bridge temperatures.

Bi-linear, temperature distributions through the depth of a PC-girder, bridge superstructure were evaluated by Girton, et al. (1989). For their monitored, PC-girder bridge, these researchers showed that there was a moderate, thermal gradient through the depth of the girders and a steep, thermal gradient through the depth of the slab. Since the temperatures of the deck for the Guthrie County Bridge and Story County Bridge were only measured at the mid-thickness of the slab, precise temperature distributions were not established for the slab.

Using the temperature measurements recorded in the top flange, web, and bottom flange of the PC girders, a best-fit, linear, thermal gradient for the girders was established for each instrumented cross section. The temperature at the top and bottom of the PC girders was calculated using a linear extrapolation of the temperature gradient in the girder. The thermal gradient in the slab was determined by assuming that a bi-linear, temperature distribution existed through the superstructure depth, as shown by Girton, et al. (1989). The temperature at the bottom of the slab, which was assumed to be the same as the extrapolated temperature at the top of the PC girder, and the measured temperature at the mid-thickness of the deck slab established the linear, thermal gradient through the depth of the bridge deck. The temperature at the top of the deck slab was determined by a linear extrapolation of the thermal gradient for the slab. Tables 4.11 and 4.12 list the experimentally-measured and analytically-extrapolated, bridge temperatures at the time of the maximum and minimum, average, bridge temperatures, respectively, at the Guthrie County Bridge. Tables 4.13 and 4.14 list the same temperature information for the Story County Bridge. Figure 4.12 shows the measured temperatures at all of the thermocouple locations in the superstructure of the Guthrie County Bridge and Story County Bridge, at the time of the maximum and minimum, average, bridge temperatures. This figure also shows the bi-linear, thermal-gradient lines that were used to estimate the temperatures at the top of the RC bridge deck and at the top and bottom of the PC girders. Figure 4.13 and 4.14 show the extrapolated, top-of-slab, top-of-girder, and bottom-of-girder temperatures for the Guthrie County Bridge and Story County Bridge, respectively, at the time of the maximum and minimum, average, bridge temperatures.

Very steep, thermal gradients occurred through the depth of a bridge slab at the time of the maximum temperature. Based on a linear extrapolation of the average, thermocouple-temperature values, the average, extrapolated temperature at the top of the RC slab was 126 °F for the Guthrie County Bridge, and 132 °F for the Story County Bridge. At the times of the minimum, average, bridge temperature, there were slightly positive-thermal gradients in the girder and negative-thermal gradients in the slab. A negative-thermal gradient in the slab was found to develop during the night by Pentas, et al. (1994) and Potgieter and Gamble (1989).

Figure 4.15 shows the difference between the average temperature in the RC bridge deck and the average temperature in the bottom flange of the PC girders at the Guthrie County Bridge and Story County Bridge. The magnitude of the slope at the thermal gradient varies seasonally, as well as daily, as indicated by Fig. 4.15. The magnitude of the maximum, vertical-temperature gradient is much larger during the summer, due to the increased exposure of the bridge to solar radiation, than that during the winter. Negative-temperature gradients through the depth of the superstructure occur more frequently in the winter months.

4.2.3. Transverse-temperature gradients

The Story County Bridge had a large number of thermocouples in the slab to measure temperature variations across the width of the bridge. Thermocouples were not installed in the concrete barriers for either bridge. Figure 4.16a shows the temperatures across the width of the Story County Bridge for two hot days and two cold days, at the time of the maximum and minimum, average, bridge temperatures. For the abscissa scale in the graph, positive distances are measured from the bride centerline

towards the north and negative distances are measured from the bridge centerline towards the south. Temperature measurements that were recorded in the slab between the continuous, Jersey-type, concrete barriers and in the center portion of the east span did not indicate a horizontal-temperature gradient. The temperatures that were measured in the slab near the edges of the bridge that were beneath these concrete barriers were significantly cooler than the rest of the slab at the time of the maximum, average, bridge temperature. The concrete barriers shade the edge of the slab and provide additional thermal mass at that location. At the time of the minimum, average, bridge temperature on January 5, 1999, the slab temperatures were warmer at the edges of the bridge than between the concrete barriers.

Small variations in the slab temperature across the bridge width were measured away from the bridge edges. However, these variations may have been due to differences in the vertical positions of the thermocouples in the slab. If the slab thermocouples were not all installed at the same depth, the steep, vertical-temperature gradient in the slab, when the maximum temperatures occur, can create an apparent transverse-temperature variation.

A limited number of thermocouples were installed across the width of the Guthrie County Bridge. Figure 4.16b shows the temperature distribution across the width of this bridge. Temperatures near the centerline of the bridge were slightly higher than those measured near the exterior girders, but the difference was not significant. Since an open-type, RC guardrail was used at the Guthrie County Bridge, less thermal mass exists at the edges of this bridge than that for the Story County Bridge. Since thermocouples were not placed in the slab directly beneath the open guardrail and since

the thermocouples were at about a 15-ft transverse spacing, the ISU researchers could not determine whether a transverse-temperature gradient existed across the width of the Guthrie County Bridge.

4.2.4. Longitudinal-temperature gradients

Temperatures were measured at six locations along the longitudinal axis of the Guthrie County Bridge and Story County Bridge. Figure 4.17 shows the temperatures measured through the depth of the superstructure at the selected cross sections along the length of the monitored bridges at the time of the maximum and minimum, average, bridge temperatures. For a particular depth in the bridge superstructure, the differences in the measured temperatures along the bridge length were not significant. Previous analytical work by MacGregor, et al. (1997) and Potgieter and Gamble (1989) has shown that longitudinal temperature variations along the length of a bridge are not significant.

4.2.5. Pile temperatures

The temperatures of several abutment piles were measured near the bottom of the pile cap at each bridge. Even though about 20 in. of the length for the instrumented piles were left exposed to the air, the changes in the pile temperature were not as extreme as the changes in the superstructure temperatures. At the time of the maximum, average, bridge temperature of 101 °F for the Guthrie County Bridge, the average, pile temperature was approximately 80 °F. At the time of the minimum, average, bridge temperature of -12 °F, the piles at this bridge had a temperature of

approximately 10 °F. Therefore, range in the pile temperature range was 70 °F at the Guthrie County Bridge.

At the Story County Bridge, the pile temperatures were approximately 75° F and 15 °F at the time of the maximum and minimum, average, bridge temperatures of 104 °F and –10 °F, respectively. For the Story County Bridge, the range in the pile temperatures was 60 °F. The temperature range of the piles will decrease along the length of the pile, since the piles are embedded in soil.

4.3. Bridge displacements

This section describes the abutment longitudinal and transverse displacements, abutment rotations in a vertical plane that is parallel to the longitudinal axis of the bridge, rotations in a horizontal plane and differential displacements between several bridge elements.

4.3.1. Abutment longitudinal displacements and changes in bridge length

Longitudinal displacements that were parallel to the longitudinal axis of the bridge were measured for each abutment of the Guthrie County Bridge and Story County Bridge with displacement transducers that were mounted on benchmark posts. The measured, abutment displacements were used to calculate the change in length of a bridge and the rigid-body motion of an abutment in a horizontal plane.

The change in the bridge length was determined by summing the experimentally-measured, longitudinal displacements of the abutments at the mid-width of the abutment pile cap at each end of the bridge. Figure 4.18 shows the change in bridge length of the Guthrie County Bridge and the Story County Bridge between December

17, 1997 and April 1, 2000 and between October 17, 1998 and April 1, 2000, respectively. Since the monitored displacements and rotations were relative deformations, reference times and dates were established for each bridge. For the Guthrie County Bridge, the reference time and date was at 11:20 p.m. on March 9, 1998. This time and date coincided with the first, “dummy”, strain-gage reading. For the Story County Bridge, the reference time and date was at 1:30 a.m. on October 1, 1998. Positive and negative displacements indicate expansion and contraction, respectively, of the bridge superstructures with respect to these reference times and dates.

The experimentally-based range in the length of the Guthrie County Bridge was 1.77 in. The maximum change in average, bridge temperature, and thus the maximum change in the bridge length, occurred during the time period between July 20, 1998 and January 5, 1999. The displacement transducer SP-NC-LB produced unreliable data from August of 1999 through October of 1999, but resumed producing reliable data after November of 1999.

At the Story County Bridge, the maximum change in bridge length was 0.96 in. over the time period between January 5, 1999 and July 5, 1999. For this bridge, the maximum expansion did not occur on the day (July 20, 1999) of the maximum, average, bridge temperature. The range of the average, bridge temperature between January 5, 1999 and July 5, 1999 was 110 °F, which is less than the maximum, 115 °F-range for the average, bridge temperature. The same maximum, average, bridge temperature was recorded on July 20, 1998, but the installation was not complete for the displacement transducers whose measurements were used to calculate the change in

the bridge length. The change in bridge length had exceeded the magnitude measured on July 20, 1999 for only a few other times for which the average, bridge temperature was about 5 °F less than that measured on July 20, 1999. The ISU researchers believe that the experimentally-based change in the bridge length was incorrect on July 20, 1999. Each of the displacement transducers that were used to determine the change in the length of the Story County Bridge produced unreliable data in October of 1998.

Figure 4.19 shows the change in the bridge length versus the average, bridge temperature for the monitored bridges. The longitudinal displacement data correlated well with the recorded change in the average, bridge temperature. Since the average, bridge temperature is an indicator of the influence of temperature on the longitudinal expansion and contraction of the bridge superstructure, this analysis was made to show a general trend in the bridge displacement results.

Equal abutment displacements in the longitudinal direction of the bridge did not occur at the ends of the Guthrie County Bridge. The longitudinal displacements measured at the north abutment were approximately twice as large as those measured at the south abutment. Except for the pier details, the bridge geometry is symmetric. The pier details were discussed in Section 3.2.4 and the relative movements of the bridge superstructure over the piers are discussed in Section 4.3.5. Since, the south pier is an expansion pier, the ISU researchers predicted that the longitudinal displacement at the south abutment would exceed those of the north abutment. However, the experimentally-measured, abutment displacements revealed that the longitudinal displacements at the north abutment were greater than those at the south abutment. The horizontal stiffness of the abutment backfill may have caused this

unexpected result for the abutment displacements. Factors that affect the stiffness of the backfill include the soil type, compaction, and moisture content of the backfill material.

The relationship between the displacements in the longitudinal direction of the bridge for each abutment and the average, bridge temperature at the Guthrie County Bridge is shown in Fig. 4.20. Non-linear displacements at each abutment were observed at this bridge. The south abutment experienced a decrease and the north abutment experienced an increase in the rate of displacement for an average, bridge temperature greater than about 60 °F. The net effect of these abutment displacements produced a change in the bridge length that was approximately linear with respect to changes in the average, bridge temperature. The ISU researchers believe that these non-linear, abutment-displacement responses were caused by changes in the horizontal stiffness of the soil behind each abutment. As the south abutment was pushed against the soil, the backfill stiffness increased, since the soil had not reached its maximum, passive resistance. As the north abutment was pushed against its backfill, the stiffness of the backfill reached its maximum, passive resistance. After the maximum, passive-soil pressure is reached, soil pressures do not increase with additional displacement.

At the Story County Bridge, the abutment displacements along the longitudinal direction of the bridge were more symmetric than those for the Guthrie County Bridge. Both piers for the Story County Bridge are fixed piers as shown in Fig. 3.6. For this bridge, the west abutment displacements accounted for approximately 55 percent of the change in the bridge length. The longitudinal displacements at each abutment of the Story County Bridge remained linear over the entire range of bridge temperatures.

4.3.2. Abutment rotations in a horizontal plane

Displacements in the longitudinal direction of each bridge were measured at three positions across the width of one of the abutments to determine whether that abutment moved as a rigid body. Any difference in these longitudinal displacements would be due to a rigid-body rotation of the abutment about a vertical axis and/or to horizontal curvature of the abutment.

The change in longitudinal positions of three points that were located along the width of the south-abutment pile cap for the Guthrie County Bridge is shown in Fig. 4.21a. Positive distances for the abscissa scale in the graph are measured normal to the longitudinal axis of the bridge and towards the acute-angle corner of the bridge deck. The displacements shown for July 20, 1998, which was the day that had the maximum, abutment displacement at the mid-width of the pile cap, were calculated relative to the displacements that were measured on January 5, 1999, which was the day that had the minimum, abutment displacement at the mid-width of the pile cap. Over this time period, the south abutment rotated in a counterclockwise direction in a horizontal plane. The longitudinal displacement of this abutment near the acute-angle corner of the bridge deck was greater than that for the obtuse-angle corner of the bridge deck.

The longitudinal displacements of three points across the width of the east abutment of the Story County Bridge are shown in Fig. 4.21b. A jump in the displacement reading at the south corner of the east abutment occurred on June 2, 1999; therefore, the three, longitudinal, abutment displacements could not be compared for the largest range in the average, bridge temperature. The displacements shown for

May 29, 1999 were calculated relative to the displacements that were measured on January 5, 1999, which was the day that had minimum, abutment displacement at the mid-width of the pile cap. Over this time period, which had a 95 °F change in the average, bridge temperature, the east abutment at the Story County Bridge did not rotate in a horizontal plane. The magnitude of the longitudinal displacement at the mid-width of the abutment was slightly larger than the longitudinal displacement at the ends of the abutment. The differences in these displacements indicate that the abutment was subject to flexural bending in a horizontal plane.

4.3.3. Abutment rotations in a vertical plane

At one abutment for each of the monitored bridges, the rotations of the abutment pile cap were measured in a vertical plane that was parallel to the longitudinal axis of the bridge. For the Guthrie County Bridge, two displacement transducers and a tiltmeter were used to measure the rotation of the south-abutment pile cap. For the Story County Bridge, a tiltmeter was used to measure rotation of the east-abutment pile cap.

The abutment rotations at the Guthrie County Bridge were initially calculated by dividing the difference between the experimentally-measured, longitudinal displacements at the top and bottom of the pile cap by the vertical distance between the two transducers that were used to measure the displacements. The accuracy of this method was questioned by the ISU researchers, when apparent, relative movements were detected between the benchmark post that supported the two displacement transducers and an adjacent benchmark post. If the post that supported the transducers was moving, the accuracy of the small difference in longitudinal

displacements was uncertain. To reliably measure the abutment rotations, a temperature-compensated tiltmeter was mounted to the face of the pile cap at the mid-width of the south abutment for the Guthrie County Bridge. The tiltmeter was at the same location and in vertical alignment with the two displacement transducers that were positioned to measure the longitudinal displacements of the abutment. Since all of the input ports for the data-acquisition system were used, two transducers that measured the abutment displacements at the top of the pile cap at the east and west ends of the south abutment were removed to permit the connection of the tiltmeter to the data-acquisition system. The pair of displacement transducers at the mid-width of the south-abutment, pile cap was kept in place to determine the validity of the previous, rotation measurements at that location.

Figure 4.22 shows a graph of the south-abutment, pile-cap rotations that were calculated from the longitudinal displacements, which were measured by the two, displacement transducers versus those same rotations that were measured by the tiltmeter at the Guthrie County Bridge. Even though the experimentally-based, computed rotations were less than the directly-measured rotations; the figure shows that good correlation occurred between the two methods of establishing the rotations. The ISU researchers concluded that both methods of obtaining the rotations for the pile cap were reliable.

Figure 4.23 shows the rotations of the pile caps at the mid-width of the south abutment for the Guthrie County Bridge and at the mid-width of the east abutment for the Story County Bridge. A positive rotation for an abutment, pile cap occurs when the displacement at the top of the pile cap relative to the displacement at the bottom of the

pile cap is towards the span of the bridge. The magnitudes for the ranges in the measured rotations of the abutment, pile caps were similar at both bridges. The pile cap at the Guthrie County Bridge and Story County Bridge rotated through a range of about 0.087 deg. and 0.075 deg., respectively. In one day, the measured, pile-cap rotation for each bridge varied by as much as 0.040 deg. These rotations were greater during the summer than during the winter. During the summer, the average, bridge temperature and the daily range in the vertical-thermal gradients that were induced by solar radiation were larger than those which occurred during the winter, as shown in Figs. 4.10 and 4.15, respectively.

A positive, vertical-temperature gradient will cause the concrete superstructure for a bridge to arch upwards. Unless the abutment was rigidly held, a rotation of the abutment would occur about a horizontal axis. Abutment rotations are also caused by the restraining, horizontal forces that are applied to an abutment by the piles and the soil backfill. As an abutment displaces along the longitudinal direction of the bridge due to thermal expansion, forces are induced in the soil backfill and in the steel piles. The induced, shear forces, at the tops of the abutment piles are located below the center of gravity of the cross section of the bridge superstructure. The eccentricity for these shear forces and the induced, bending moment at the top of a fixed-head pile produce a negative, bending moment at the end of the bridge. Also, since the resultant for the passive-soil pressure will probably be located below the center of gravity of the superstructure, an additional, negative, bending moment is induced at the end of the bridge. These end forces on the bridge superstructure will cause a rotation of the

abutment, pile cap that is in the same direction as the rotation induced by a positive, vertical-temperature gradient.

4.3.4. Abutment transverse displacements

At each bridge, post-mounted transducers measured the transverse displacement of an abutment at each end of the pile cap. Displacement measurements at each end of an abutment were necessary because the change in position of the ends of an abutment is a combination of two effects: (1) temperature-dependant volumetric expansion or contraction of the concrete in the pile cap, and (2) rigid-body translation of the abutment due to the longitudinal expansion or contraction of a skewed bridge. Based on the magnitude of the skew angle, skewed bridges may experience a rotation in a horizontal plane. Expansion of an integral-abutment bridge activates soil pressures behind the abutments. For a skew, integral-abutment bridge, a component of this passive-soil force is perpendicular to the longitudinal axis of the bridge and directed towards the acute-angle corner of the bridge deck.

To determine the magnitudes for the expansion or contraction and translation of an abutment, the ISU researchers assumed that a uniform, thermal expansion or contraction of a pile cap occurred along the width of an abutment. The change in the length of a pile cap was equal to the algebraic sum of the horizontal displacements that were measured at each end of the pile cap. The translation of the center of gravity of a pile cap was calculated as one-half of the algebraic difference in these measured, horizontal displacements.

Figure 4.24 shows the measured, transverse displacements of the center of gravity of the south-abutment, pile cap for the Guthrie County Bridge. Positive

displacements indicate that the abutment translated towards the acute-angle corner of the bridge deck. The south abutment in the Guthrie County Bridge did not return to the same lateral position after each yearly cycle of temperature changes. Over the monitored-time period shown in the figure, the south abutment of this bridge experienced a residual displacement towards the acute-corner of the bridge deck.

The transverse displacements that were measured at the northeast corner of the east abutment for the Story County Bridge did not appear to be realistic, since these displacements did not correlate well with the average, bridge temperatures. These displacements were much higher than the comparable displacements that were measured at the Guthrie County Bridge, whose skew angle is larger than that for the Story County Bridge. Therefore, the thermal expansion of this abutment pile cap and the transverse displacement of the center of gravity of this pile cap could not be computed using the measured, transverse displacements.

4.3.5. Relative displacements at the bridge piers

For both bridges, relative, longitudinal movements of the bridge superstructure over the pier caps were measured between the bottom of the center PC girder and top of the RC pier cap. The pier details (Fig. 3.6) for the Guthrie County Bridge show that the south pier is an expansion pier and the north pier is a fixed pier. Therefore, less longitudinal restraint for relative displacement exists between the superstructure and the south pier than that between the superstructure and the north pier. These relative displacements at the Guthrie County Bridge are shown in Fig. 4.25. The range in the relative displacements of the superstructure over the south and north piers of the Guthrie County Bridge were approximately 0.165 in. and 0.069 in., respectively. The

relative magnitudes of these measured displacements are in agreement with the types of pier that were used at these locations. The daily ranges for the relative displacements of the superstructure over the fixed pier were smaller during the winter than those ranges during the summer. The smaller, relative displacements during the winter were related to the magnitude of the daily changes in the bridge temperature. These temperature changes were smaller during the winter than those during the summer. At the Guthrie County Bridge, the daily variations in the relative displacements of the bridge superstructure over the expansion pier were nearly constant over the entire monitoring period.

The construction details between the bridge superstructure and both of the pier diaphragms at the Story County Bridge are similar to the pier details for the fixed pier at the Guthrie County Bridge. The relative displacements between the superstructure and the piers at the Story County Bridge are shown in Fig. 4.26. The ranges for the relative displacements at the east and west piers were 0.039 in. and 0.028 in. These displacements were smaller than those measured over the fixed pier at the Guthrie County Bridge. The range of motion of the superstructure over the piers at the Story County Bridge was smaller during the winter than those during the summer.

4.3.6. Relative rotations at the top of an abutment pile

Relative, vertical displacements between the abutment pile near the mid-width of an abutment and its RC pile cap were measured at each bridge. Using these displacements, rotations were calculated by dividing the difference between the measured, relative, vertical displacements at the front and at the back of the pile cap by the horizontal distance between these displacement transducers. This relative rotation

was the rotation between the bottom of the pile cap and a point that was 18 in. below the pile cap, where the transducers were attached to the pile. Figure 4.27 shows these experimentally-based, relative rotations for the pile near the mid-width of the south and east abutments for the Guthrie County Bridge and Story County Bridge, respectively. A positive, relative rotation for the top of an abutment pile is associated with a pile curvature that has its center of curvature on the side of the pile that is facing the span of the bridge. During the Summer of 1999, the experimentally-based, relative rotations of the monitored pile at the Story County Bridge were significantly smaller than those recorded during the Summer of 1998. However, the range for these relative rotations from July to December of 1998 was nearly the same as that from July to December of 1999. This rotation response indicates that a directional shift in this relative rotation was occurring over time. For the time period of reliable measurements for both displacement transducers that were used to compute the relative, pile rotation at the Guthrie County Bridge, a directional shift was not observed for that relative rotation.

The range for the relative, pile rotation at these piles was 0.128 deg. and 0.234 deg. at the Guthrie County Bridge and the Story County Bridge, respectively. Even though the Story County Bridge is about two-thirds of the length of the Guthrie County Bridge, the relative rotation was larger at the Story County Bridge than that of the Guthrie County Bridge. The ISU researchers attributed this rotation abnormality to the difference in the horizontal stiffness of the material that surrounds the upper portion of the abutment piles at these bridges. The 8-ft deep, pre-bored holes for the abutment piles were filled with loose sand and bentonite slurry at the Story County Bridge and Guthrie County Bridge, respectively. Approximately a 36 to 48-in. depth of these

materials were excavated for the installation of the instrumentation devices. The material in the pre-bored holes was not disturbed below this depth.

4.3.7. Relative displacements at the ends of PC girders

Relative displacements that were measured between the top and bottom flanges of the center, PC girder and the south-abutment backwall at the Guthrie County Bridge are shown in Fig. 4.28. The displacements measured at the top flange location changed significantly in the Spring of 1998 compared to the measurements over the remainder of the monitoring period. The initial measurements by the upper, displacement transducer were not considered to be reliable. After May of 1998, the relative displacements that were measured by both transducers are small and similar in magnitude. No evidence of concrete cracking was observed in the RC abutment backwall or in the PC girder near the abutments for either bridge.

4.4. Bridge member strains

Strain gages were used to measure strain in the abutment, HP-shaped, steel piles, PC girders, and a RC pile cap at each bridge. The strain gages provided an indication of the magnitudes of the stresses and deformations that were induced in these bridge elements.

4.4.1. Pile strains

As integral-abutment bridges expand and contract, the top of the abutment piles move with the abutment. For fixed-head, abutment piles, the abutment and the bridge superstructure restrained the rotation of the tops of the piles for bending about the

principal axes of the piles. The longitudinal strains induced in the steel piles were measured by electrical-resistance, strain gages that were welded to the pile flanges. The measured, pile strains indicated that biaxial bending of the piles occurred and that a moment gradient developed along the upper portion of a pile.

The abutment piles for the Guthrie County Bridge are oriented with their webs parallel to the abutment face. Since the bridge has a 30-deg., skew angle, the pile-head displacement in a horizontal plane will induce both x-axis and y-axis, flexural-bending strains in the piles. Figure 4.29 shows the x-axis and y-axis, flexural-bending strains at the monitored, upper, cross section of the pile near the mid-width of the north abutment for the Guthrie County Bridge. The upper, cross section was located at 9 in. below the bottom of the pile cap. The range in the x-axis and y-axis, flexural-bending strains were approximately 510 and 620 micro-strains, respectively. For structural steel with a yield stress of 36 ksi, the yield strain is equal to 1240 micro-strains. If the y-axis, flexural-bending strains, which were measured at one inch from the flange tips, are linearly extrapolated to the extreme fibers of the cross section, the calculated, maximum, y-axis, flexural-bending strain was 770 micro-strains. At the extreme-fiber location in the monitored, upper, cross section of the pile, the ratio of the maximum x-axis to y-axis, flexural-bending strains was equal to 0.66.

At two, diagonally opposite, flange tips of an HP-shaped, steel pile, the x-axis and y-axis bending strains are additive. For the pile near the mid-width of the north abutment of the Guthrie County Bridge, the total range in the flexural-bending strains at these diagonally opposite, flange tips for the cross section that is located at 9 in. below the pile cap was 1300 micro-strains. Since the x-axis and y-axis, bending moments will

be the largest at the pile head, the combined, flexural-bending strain in the steel pile at a cross section that is located at the bottom of the pile cap would be higher than 1300 micro-strains. This range in strain is approximately equal to the yield strain for A36 steel. When the combined-bending, compressive strain is added to the sum of the axial, compressive strains in the steel piles due to the dead load of the bridge and the residual, compressive strains at the flange tips of an HP-shaped pile, a portion of one flange of the pile yielded in compression.

Larger bending strains were measured in the abutment piles at 9 in. below the pile cap than at 33 in. below the pile cap. Unfortunately, many of the strain gages that were attached to the lower, cross section of the piles at the Guthrie County Bridge failed early in the monitoring period. Vertical extrapolation of the y-axis flexural-bending strains to the cross section of a pile at the bottom of the pile cap was not possible for any of the monitored piles at the Guthrie County Bridge.

Figure 4.30 shows the x-axis, flexural-bending strains measured at the two, instrumented, cross sections along the length of the west pile for the north abutment of the Guthrie County Bridge. The x-axis, flexural-bending, strain measurements in the lower, cross section were reliable until October of 1998. During times when the strain gages at both pile cross sections provided reliable data, the patterns for the x-axis, flexural-bending strains that were measured at the two, cross sections were similar. The range in the x-axis, flexural-bending strains measured at the upper and lower, cross sections between December 17, 1997 and October 1, 1998 was approximately 350 and 260 micro-strains, respectively. The difference in the measured, x-axis, flexural-bending strains between these two, cross sections indicates that a moment gradient

occurred along the length of the pile. If the soil pressure against the pile between the instrumented, cross sections was negligible, a linear-moment gradient would exist along this length of the pile. The upper, 8-ft length of a pile at the Guthrie County Bridge was in a pre-bored hole that was filled with bentonite slurry. This highly-plastic material has a low stiffness; therefore, a negligible amount of horizontal pressure would be exerted against the pile between the instrumented, cross sections when the pile displaces due to temperature changes of the bridge superstructure. The x-axis, flexural-bending strain at the bottom of the pile cap was calculated by applying a linear extrapolation to the measured, x-axis, flexural bending strains at the two, monitored, cross sections for the pile. For the west pile of the north abutment of the Guthrie County Bridge, the extrapolated, x-axis, flexural-bending strain in the steel pile at the bottom of the pile cap was approximately 380 micro-strains.

Figure 4.31 shows the x-axis and y-axis, flexural-bending strains in the pile cross section that was located at 9 in. below the bottom of the pile cap for the pile near the mid-width of the east abutment for the Story County Bridge. Between the middle of August of 1998 and early July of 1999, the range in measured x-axis and y-axis, flexural-bending strains at this pile cross section was approximately 190 and 610 micro-strains, respectively. The linearly extrapolated, y-axis, flexural-bending strain at the pile flanges tips for this cross section was about 760 micro-strains. For this pile cross section, the ratio of the x-axis to the y-axis, flexural-bending strains was about 0.25. This bending-strain ratio for the abutment piles of the Story County Bridge was lower than that for the abutment piles of the Guthrie County Bridge. The abutment piles at the Story County Bridge were also oriented with their webs parallel to the abutment face.

Since the 15-deg., skew angle for the Story County Bridge was smaller than the 30-deg., skew angle for the Guthrie County Bridge, the components of abutment displacements that induced x-axis, bending moments in the abutment piles for the Story County Bridge was smaller than those displacement components that induced x-axis, bending moments in the abutment piles for the Guthrie County Bridge. The superposition of the flexural-bending strains measured at the monitored, upper, cross section of the center pile of the east abutment at the Story County Bridge resulted in a combined, flexural-bending, strain range of approximately 950 micro-strains. The combined, flexural-bending strain in the steel pile at a cross section that is located at the bottom of the pile cap would be even higher than 950 micro-strains. When the combined-bending, compressive strain is added to the sum of the axial, compressive strains in the steel piles due to the dead load of the bridge and with the residual, compressive strains at the flange tips of an HP-shaped pile, a portion of one flange of the HP-shaped pile has probably yielded in compression.

At the Story County Bridge, the magnitude of the flexural-bending strains at the monitored, lower, cross sections for the piles were also less than the flexural-bending strains at the monitored, upper, cross sections for the piles. Figure 4.32 shows the y-axis, flexural-bending strains at the two, instrumented, cross sections in the north pile of the east abutment for the Story County Bridge. The range in y-axis, flexural-bending strain in the upper and lower, monitored, cross sections in this pile was approximately 730 and 230 micro-strains, respectively. The difference between the y-axis, flexural-bending strains at the two, cross sections in the pile at the Story County Bridge was

greater than that for the Guthrie County Bridge because the skew angle for the Story County Bridge was smaller than that for the Guthrie County Bridge.

The pre-bored holes for the abutment piles of the Story County Bridge were filled with sand. When the monitored, abutment piles were exposed by excavating soil in the abutment berm to install the instrumentation devices, the sand was removed from around the top of these piles. Therefore, no lateral restraint was present between the monitored, cross sections when these piles were laterally displaced by the expansion and contraction of the bridge superstructure. A linear extrapolation of the y-axis, flexural-bending strains at the two, cross sections for the north pile of the east abutment was used to calculate the y-axis, flexural-bending strain in the pile cross section at the bottom of the pile cap. At the flange tips of this pile cross section, the range for the y-axis, flexural-bending strains was approximately 1140 micro-strains, which approached the theoretical, yield strain of 1240 micro-strains for the steel pile. When the x-axis and y-axis, flexural-bending, compressive strains; axial, compressive strains due to the dead load of the bridge; and the residual, compressive strains at the flange tips are superimposed, a portion of one flange of the pile cross section yielded in compression.

For the Guthrie County Bridge and Story County Bridge, a significant number of strain gages malfunctioned due to moisture infiltration into the wire splices, as discussed in Section 4.1.3. Therefore, the ISU researchers were not able to make additional comparisons of the strains induced in the monitored piles. An extrapolation of the pile strains from the instrumented, pile cross sections up to the pile cross section at the bottom of the pile cap was not possible if the strain readings were not available or were unreliable at either the upper or lower, cross sections for a monitored pile.

4.4.2. Girder strains

Longitudinal-strain profiles through depth of selected PC bridge girders were established from the strains that were measured by the strain gages that were attached to the top and bottom flanges of the girders. Figure 4.33 shows the difference between the measured, total, longitudinal strain in the top and bottom flanges of an exterior, PC girder near an abutment and near a pier for an exterior span of the Guthrie County Bridge. Figure 4.34 shows similar strain differences for the north, exterior, PC girder in the east-end span of the Story County Bridge. The daily variation for the differences in the total, longitudinal strain near an abutment was larger than those near a pier. This strain difference indicates that less curvature of the PC girders occurred near the piers than that near the abutments. Table 4.15 lists the ranges for the differences in the total, longitudinal strain between the top and bottom flanges for the PC girders across the width of the Guthrie County Bridge and Story County Bridge.

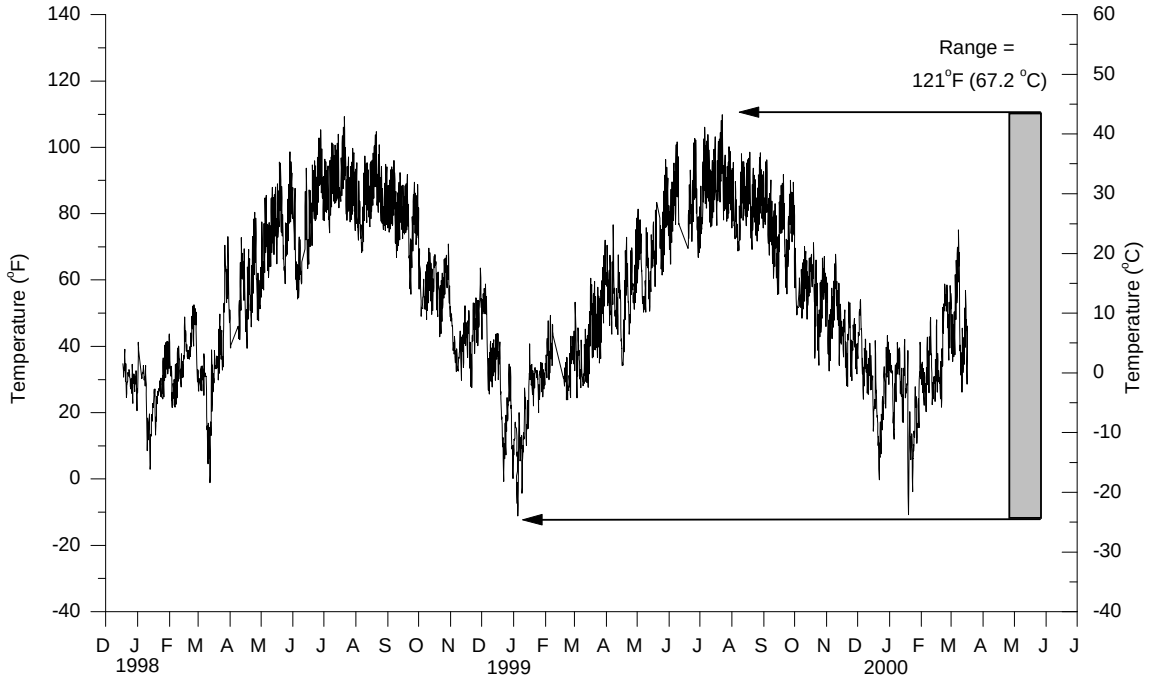

(a) Reliable thermocouple (Guthrie TC-E-1SC-S)

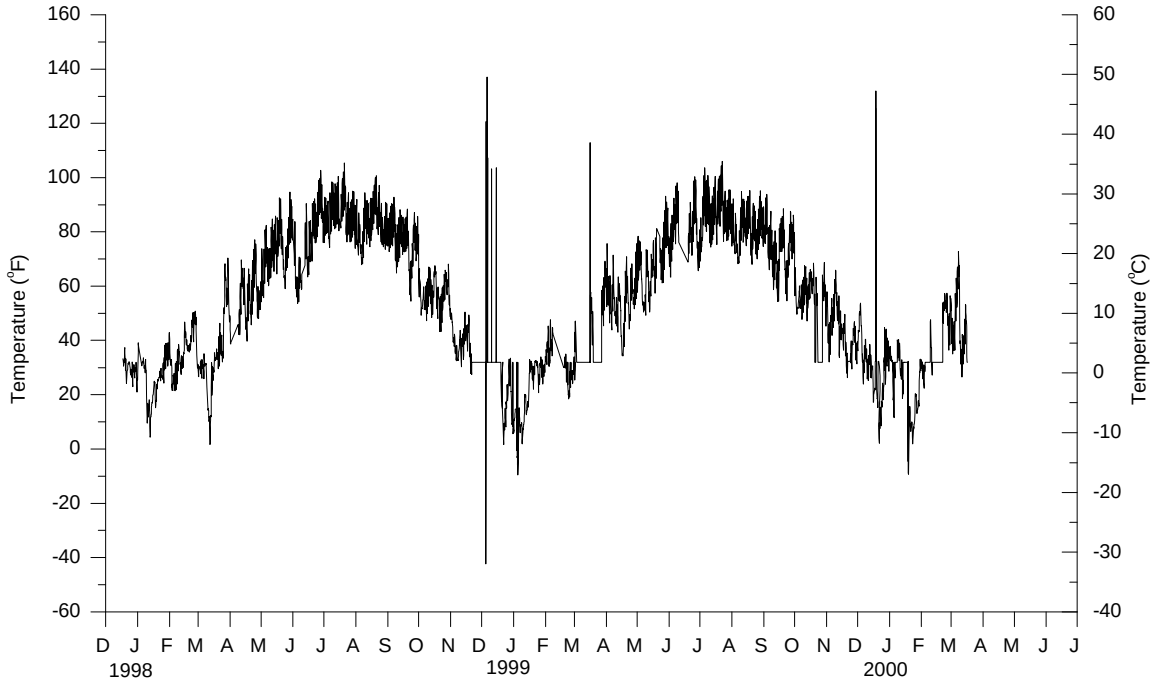

(b) Thermocouple with errors (Guthrie TC-E-1SW-S)

Figure 4.1. Typical thermocouple plots

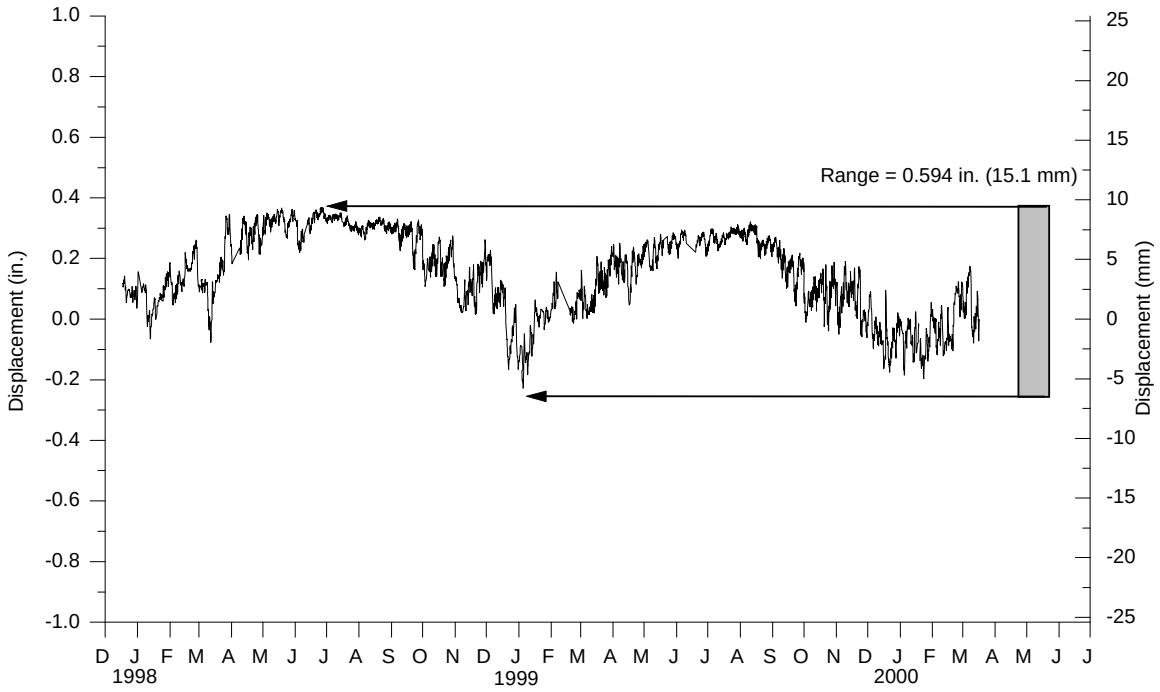

(a) Reliable displacement transducer (Guthrie SP-SC-LB)

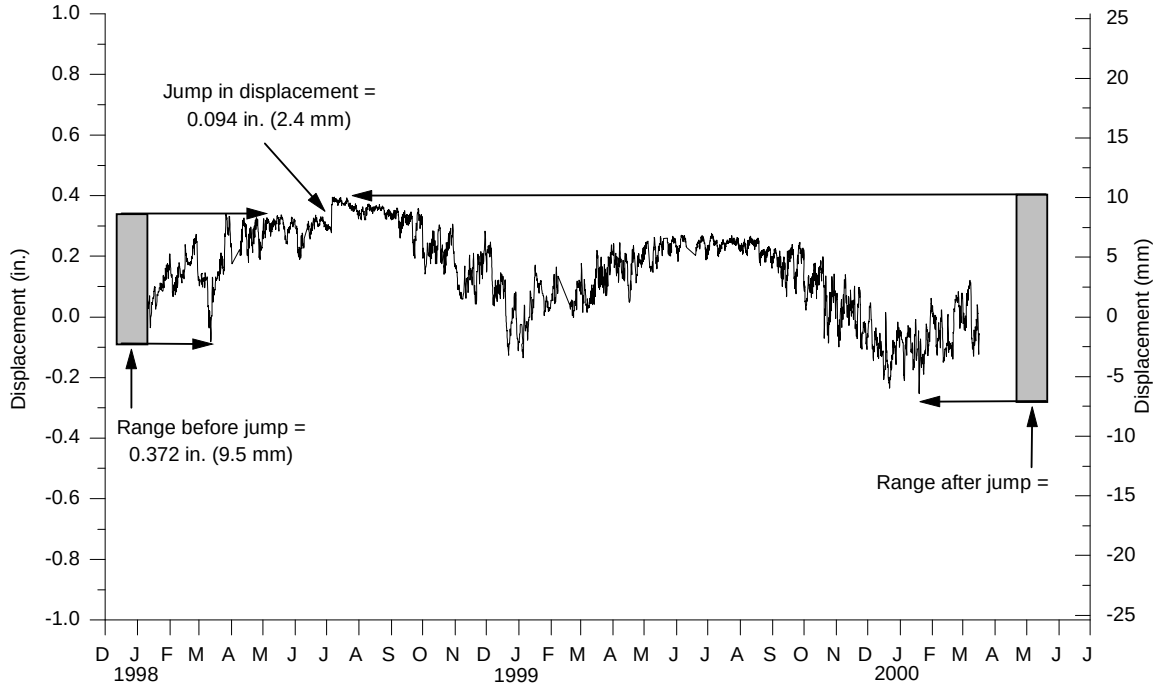

(b) Displacement transducer with error (Guthrie SP-SE-LB)

Figure 4.2. Typical displacement-transducer plots

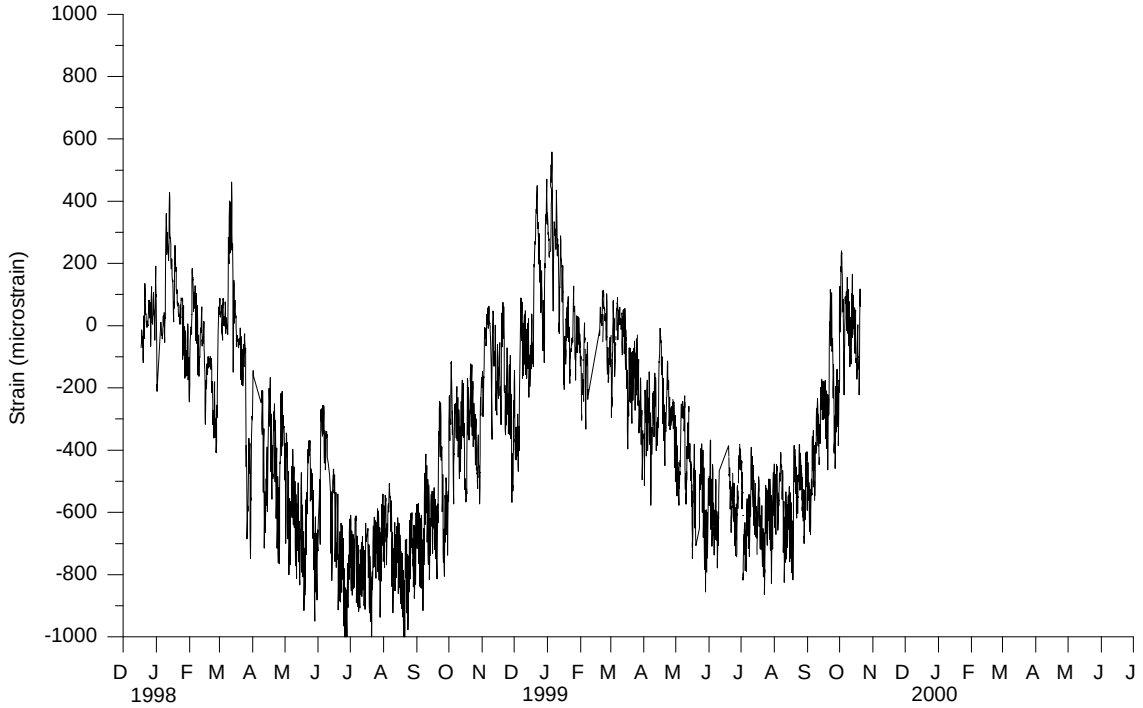

(a) Strain gage (SG-NCP-SWT) near the southwest flange tip

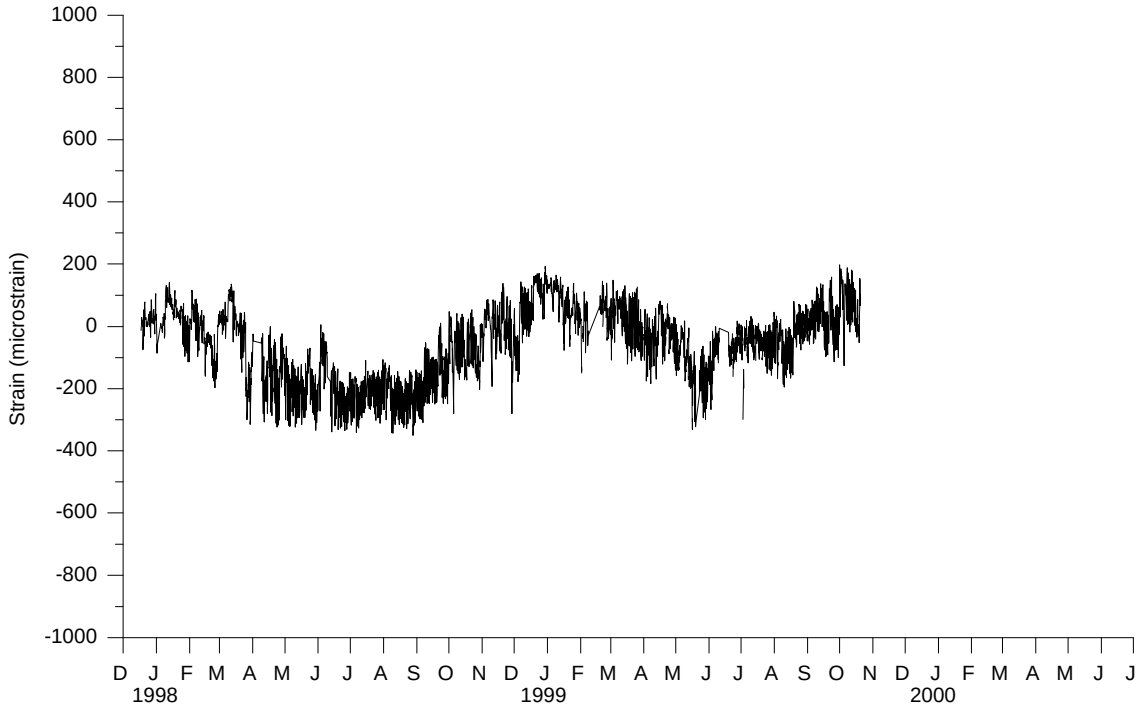

(b) Strain gage (SG-NCP-NWT) near the northwest flange tip

Figure 4.3. Raw strain-gage data for the upper cross-section of the pile near the mid-width of the north abutment at the Guthrie County Bridge

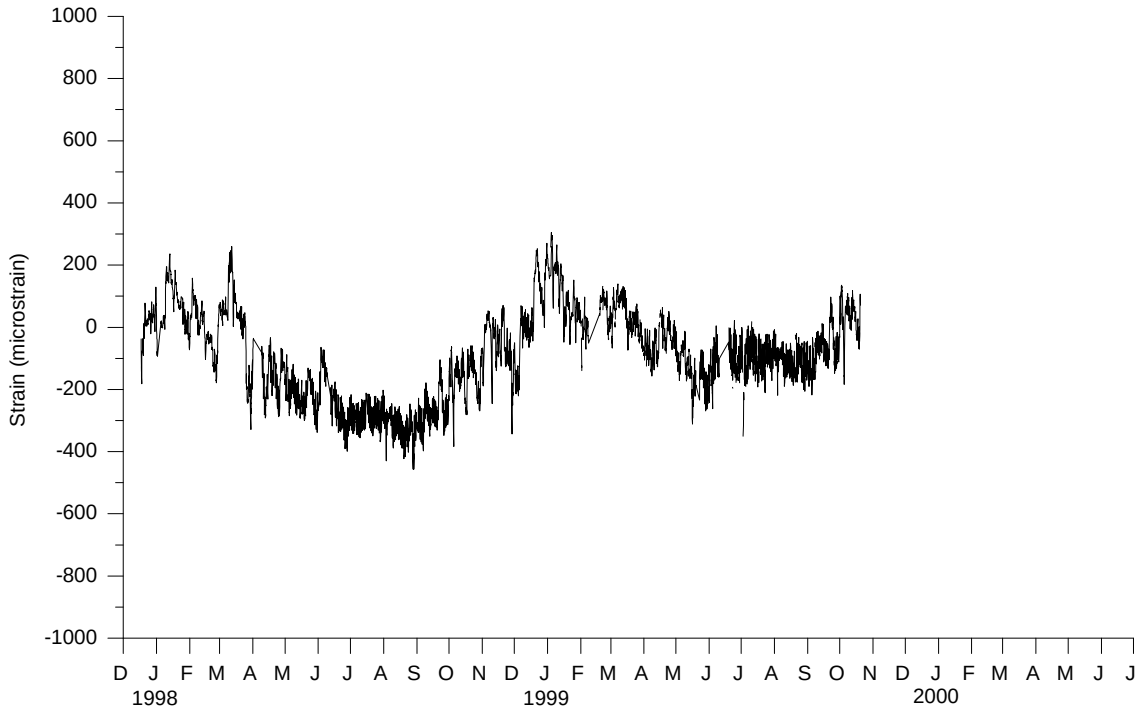

(c) Strain gage (SG-NCP-SET) near the southeast flange tip

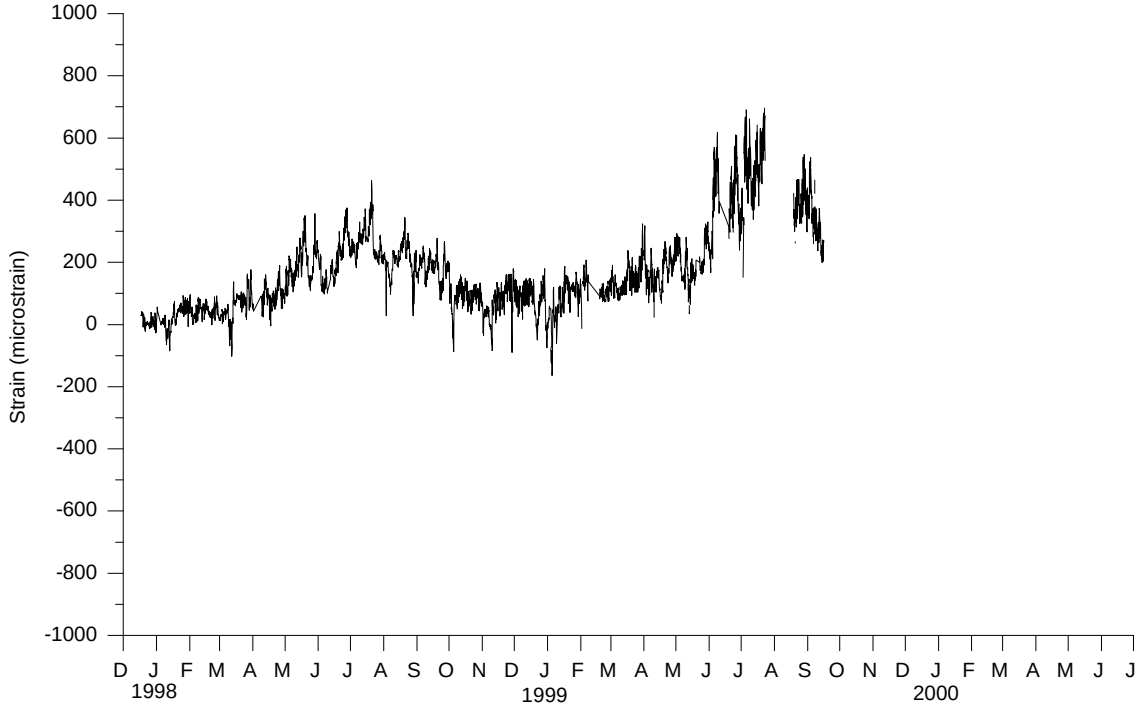

(d) Strain gage (SG-NCP-NET) near the northeast flange tip

Figure 4.3. (continued)

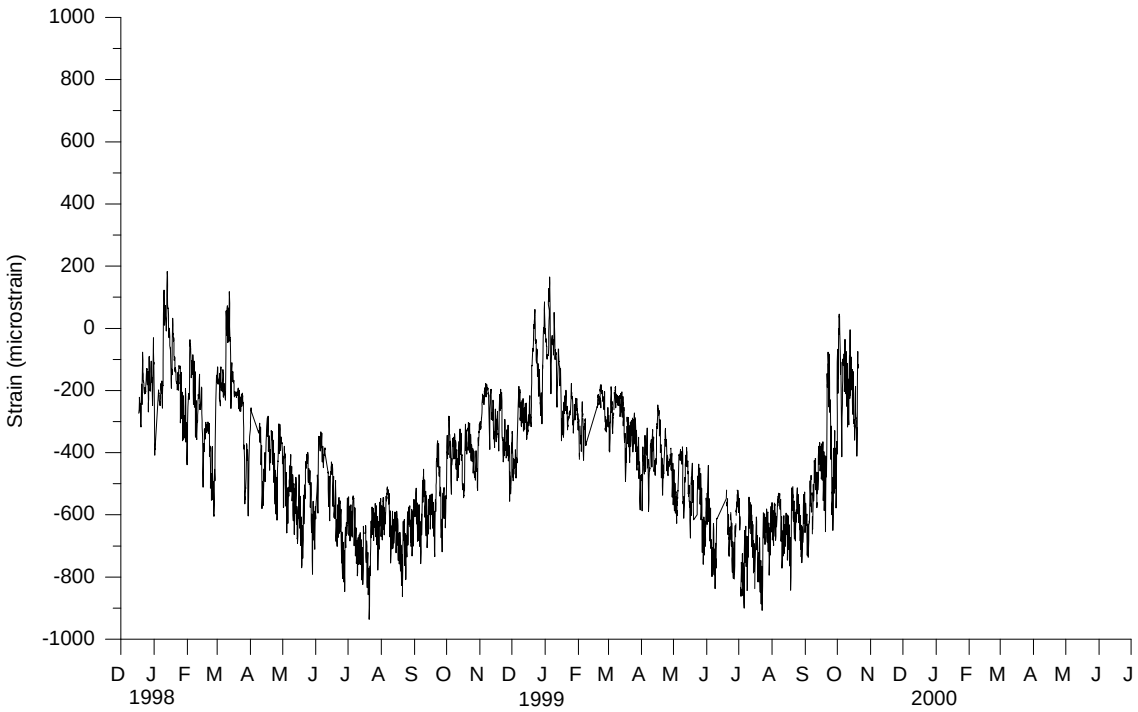

(a) Strain gage (SG-NCP-SWT) near the southwest flange tip

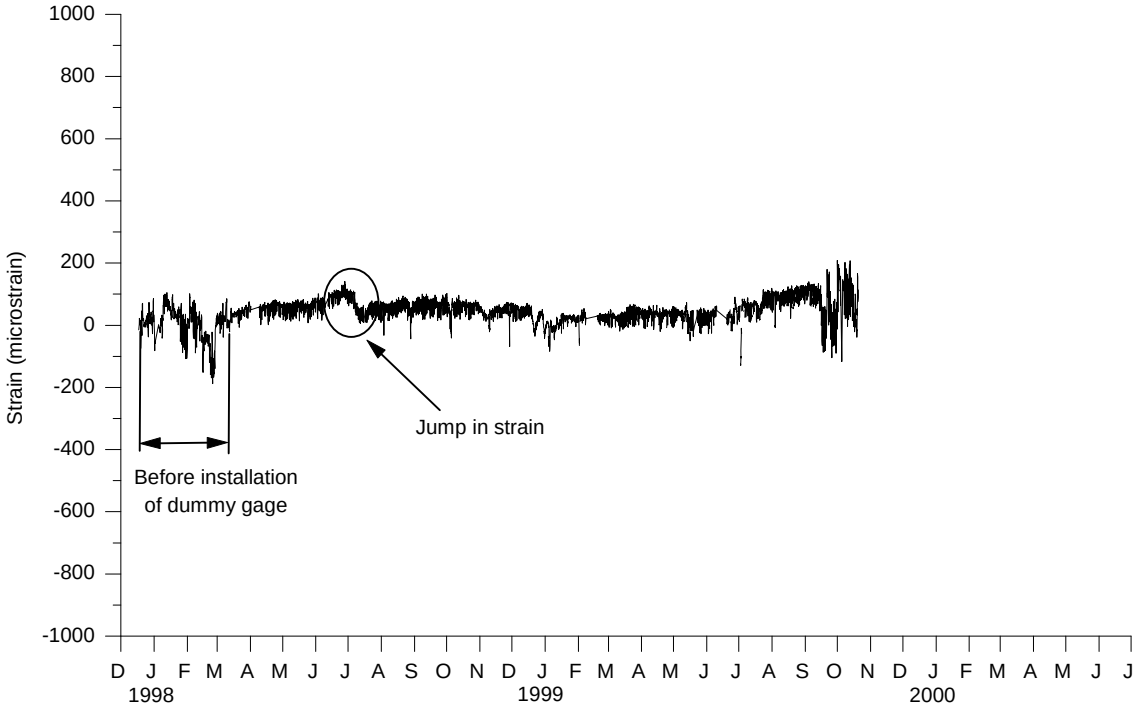

(b) Strain gage (SG-NCP-NWT) near the northwest flange tip

Figure 4.4. Temperature-corrected, pile-strain-gage results for the upper cross section of the pile near the mid-width of the north abutment at the Guthrie County Bridge

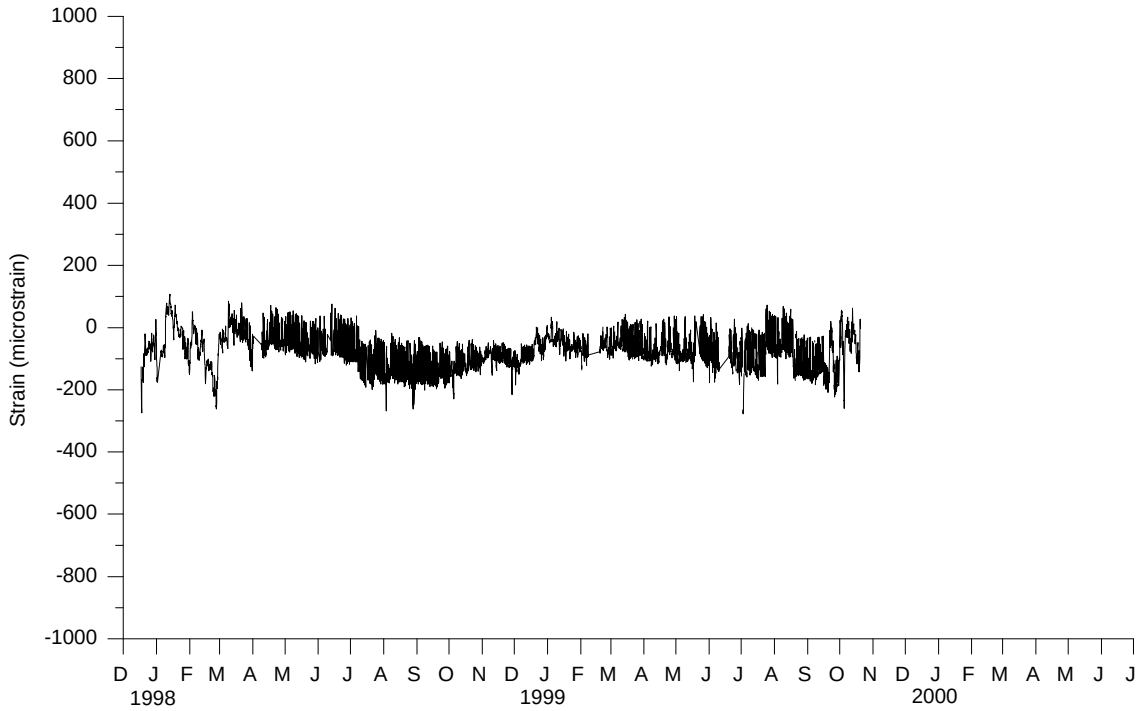

(c) Strain gage (SG-NCP-SWT) near the southeast flange tip

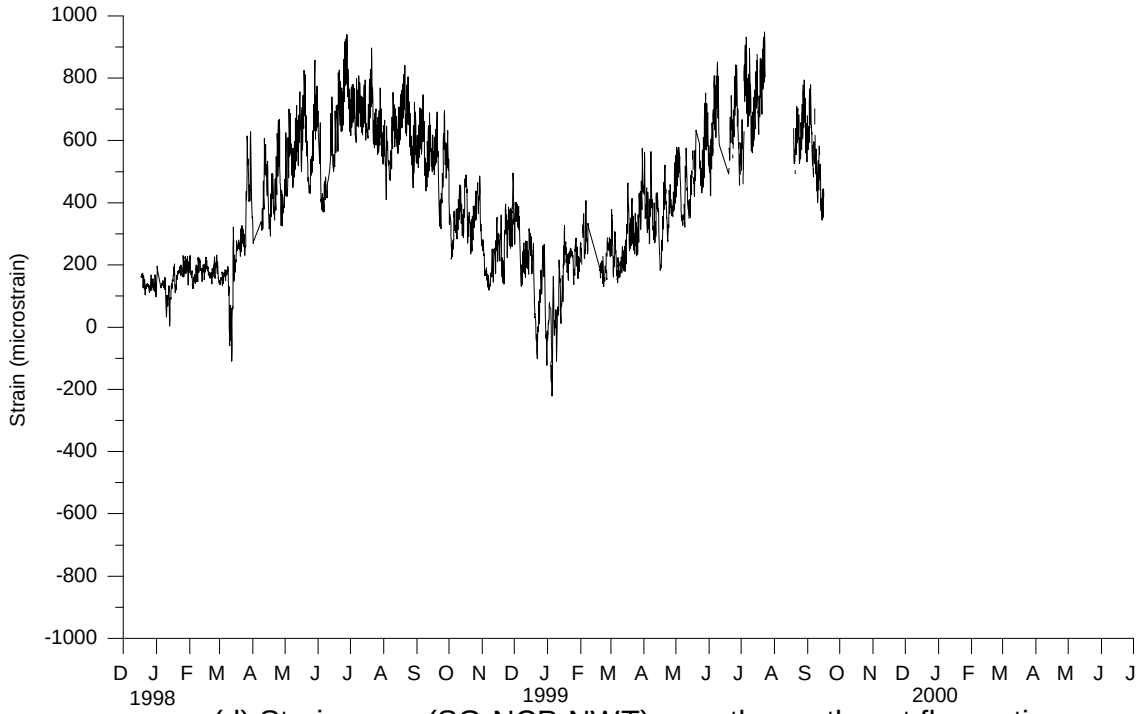

(d) Strain gage (SG-NCP-NWT) near the northeast flange tip

Figure 4.4. (continued)

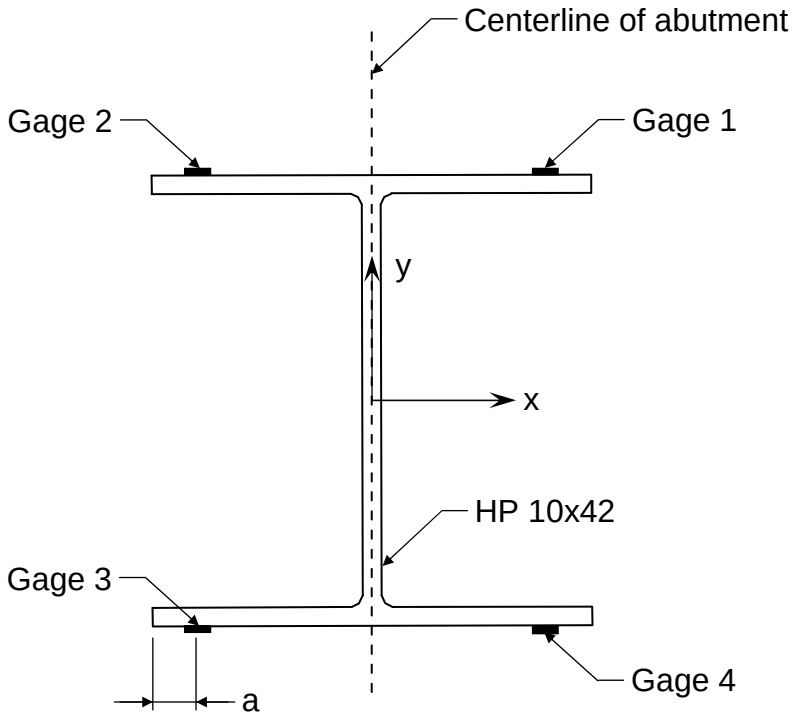

a = 1 in. typical for the monitored piles at both bridges, except
a = 1/2 in. at the NW pile for the Guthrie County Bridge

Figure 4.5. Strain gages on an HP10X42, pile cross section

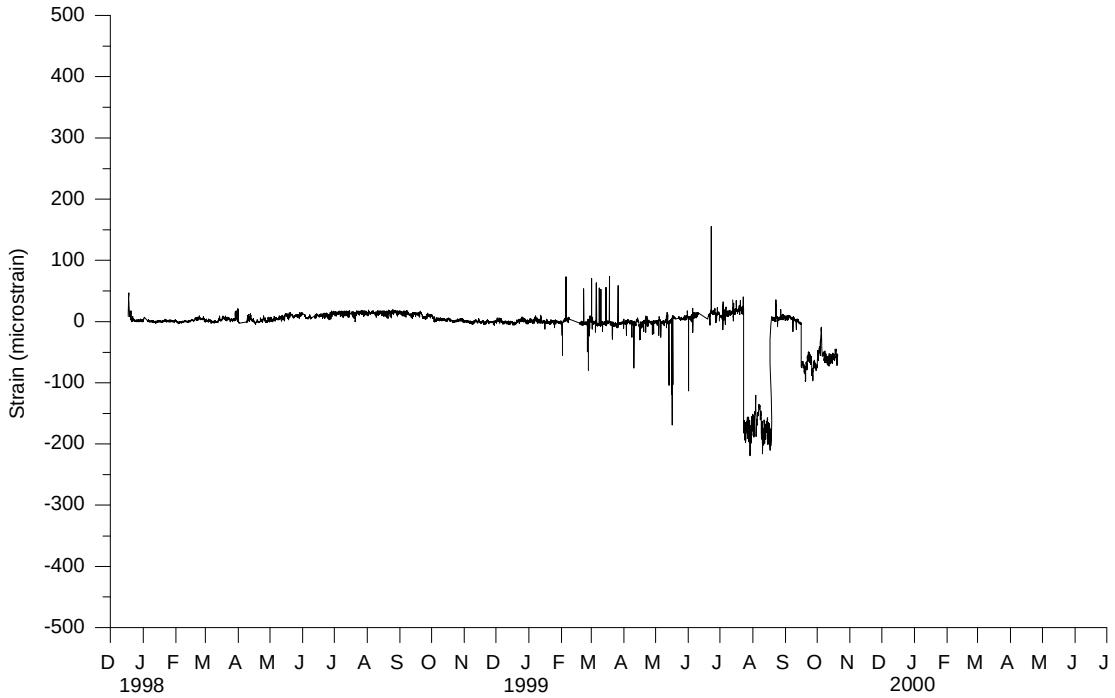

(a) Normal warpage torsional strain

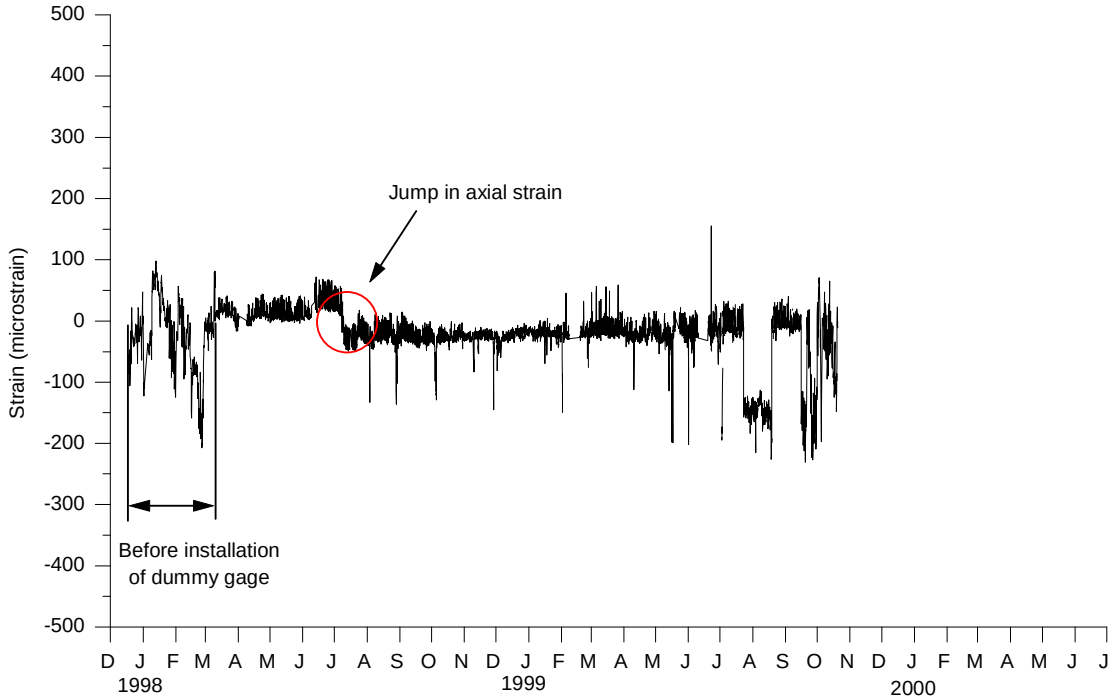

(b) Axial strain

Figure 4.6. Pile-strain components calculated using all four strain gages at the upper cross section of the pile near the mid-width of the north abutment at the Guthrie County Bridge

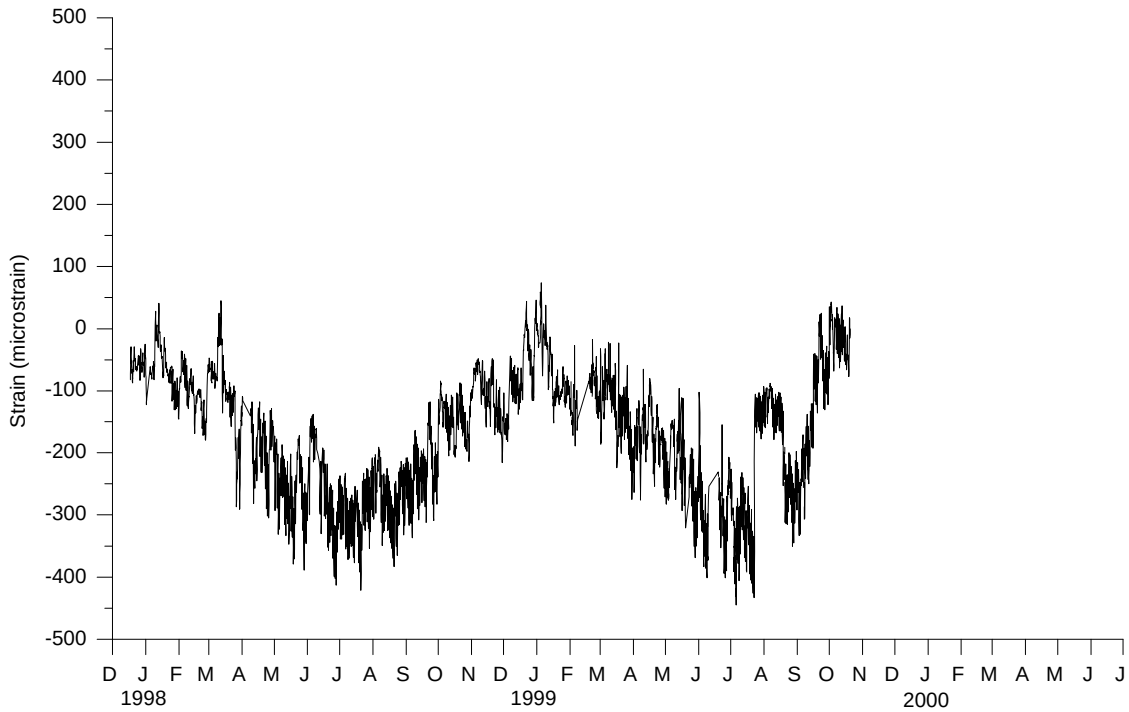

(c) X-axis bending strain

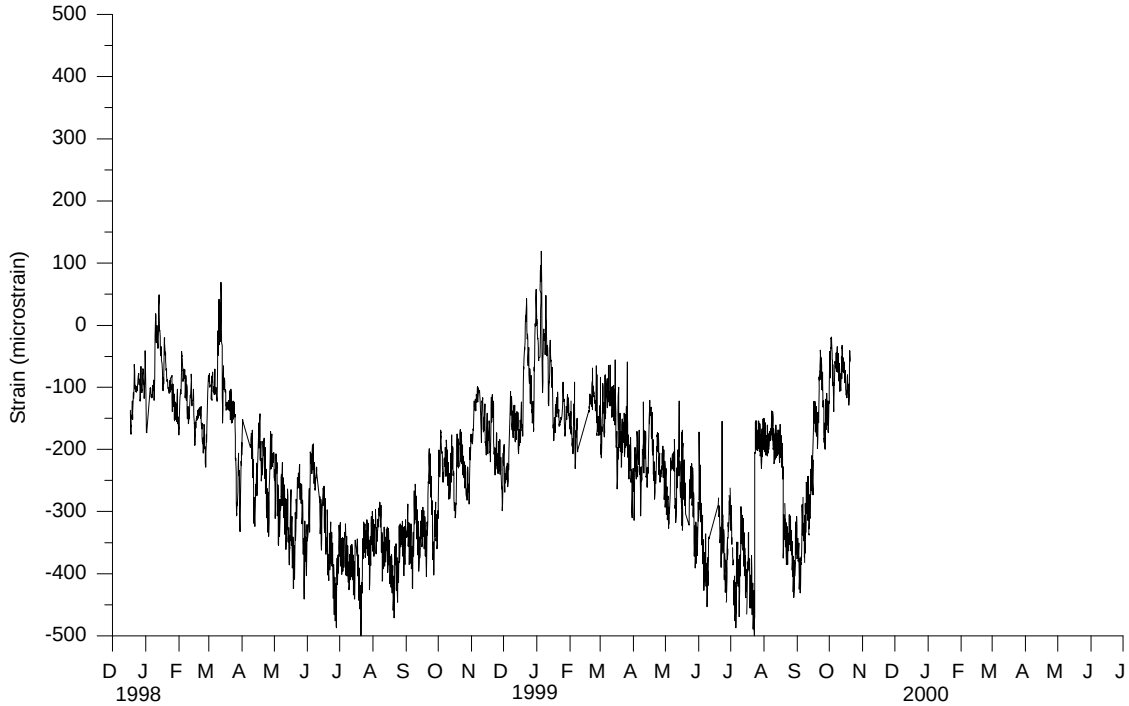

(d) Y-axis bending strain

Figure 4.6. (continued)

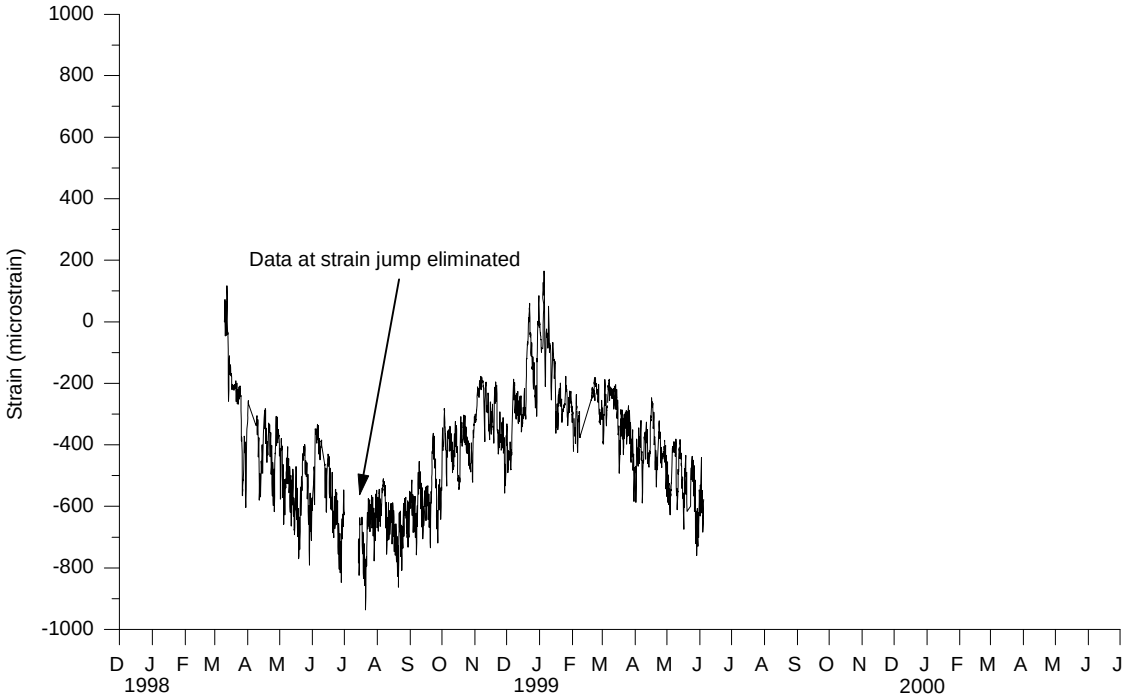

(a) Strain gage (SG-NCP-SWT) near the southwest flange tip

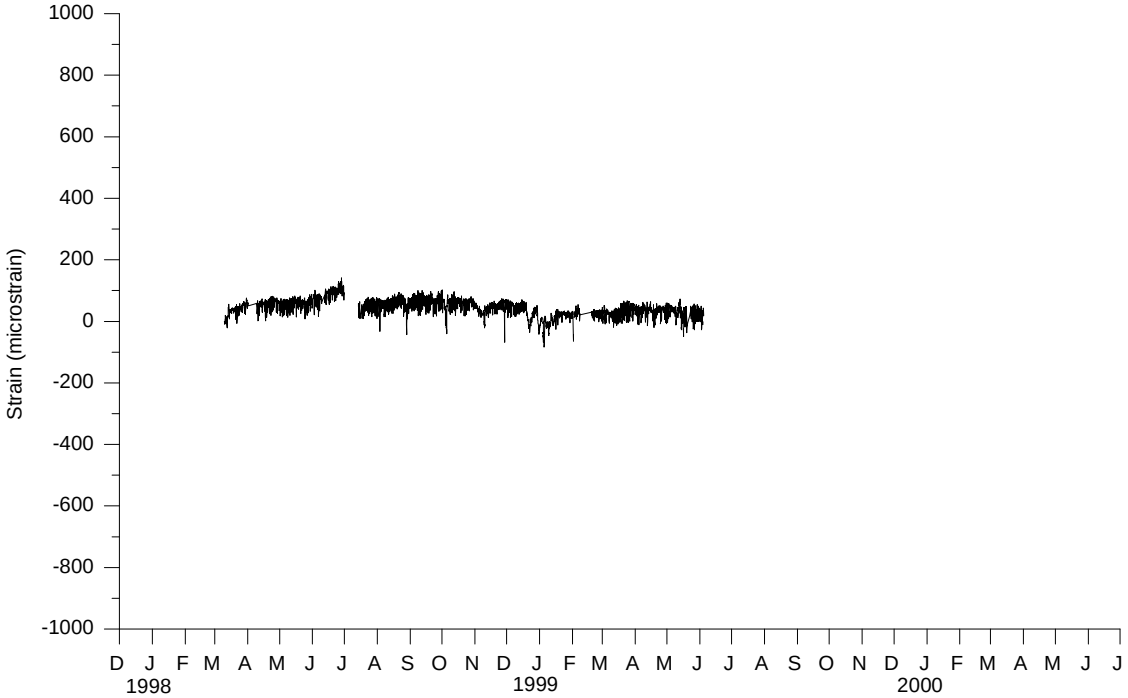

(b) Strain gage (SG-NCP-NWT) near the northwest flange tip

Figure 4.7. Final strain results after completion of the filtering process for the strain gages on the upper cross section of the pile near the mid-width of the north abutment at the Guthrie County Bridge

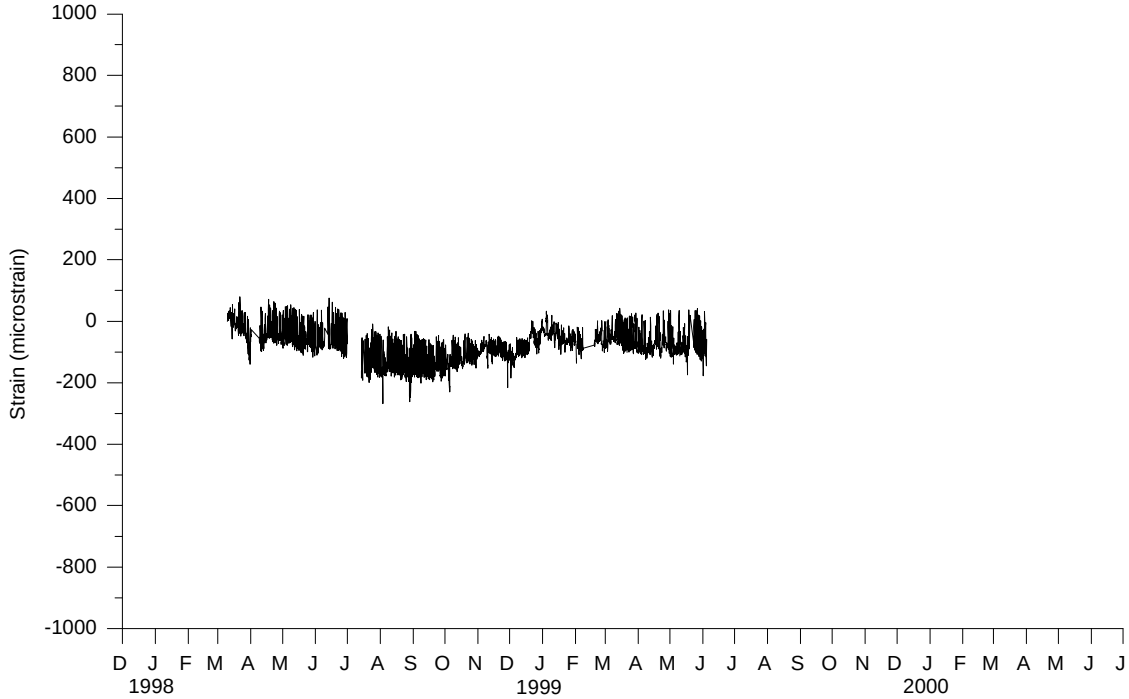

(c) Strain gage (SG-NCP-SET) near the southeast flange tip

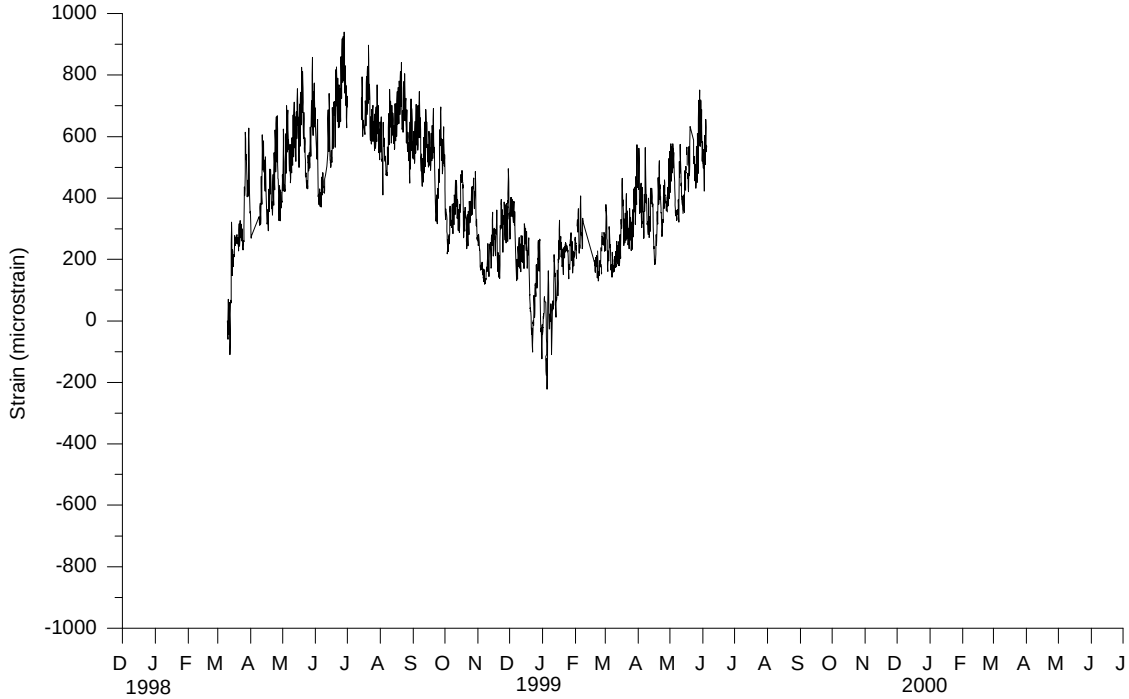

(d) Strain gage (SG-NCP-NET) near the northeast flange tip

Figure 4.7. (continued)

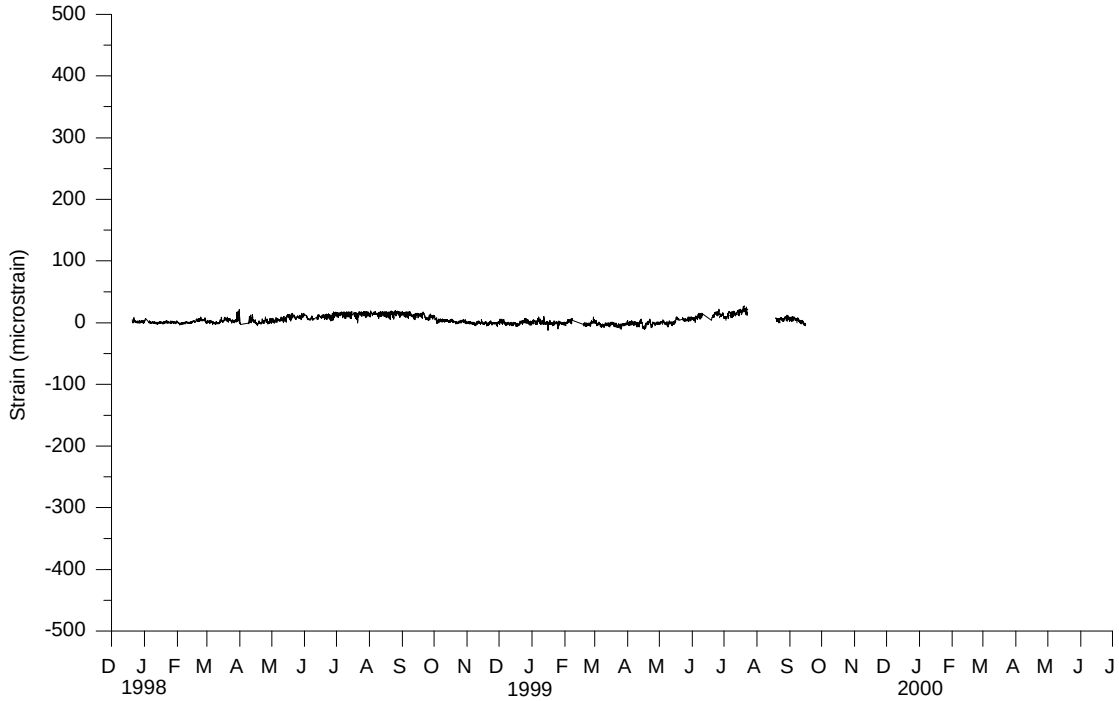

(a) Normal warpage torsional strain

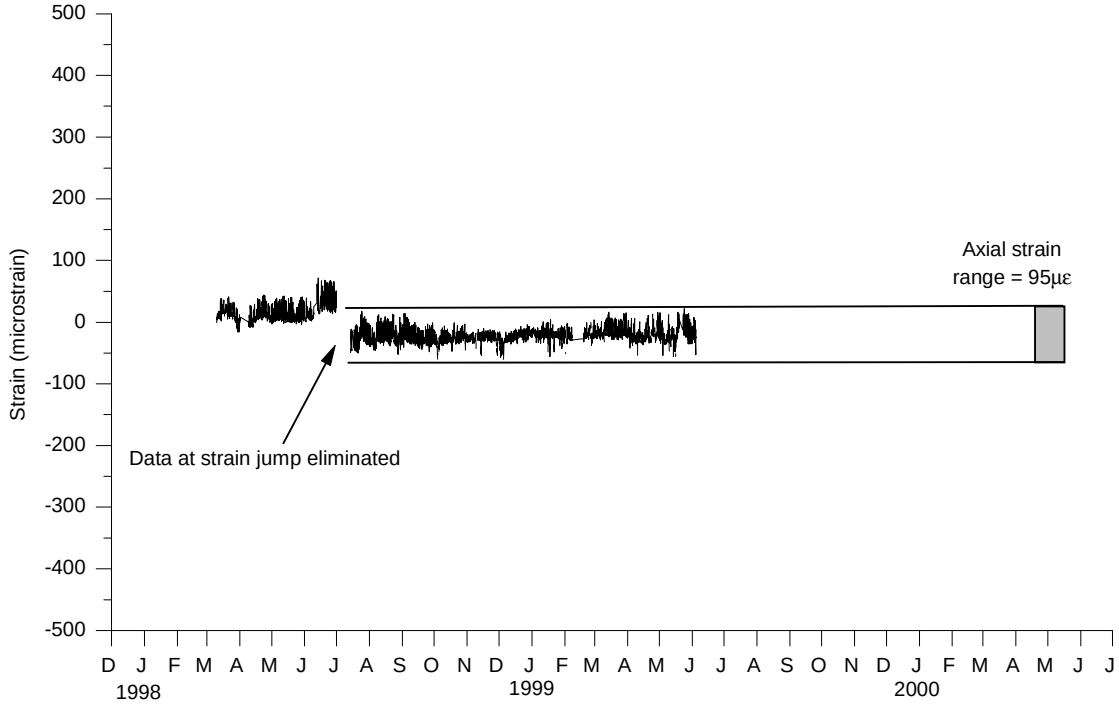

(b) Axial strain

Figure 4.8. Final strain components after the filtering process for the upper cross section of the pile near the mid-width of the north abutment at the Guthrie County Bridge

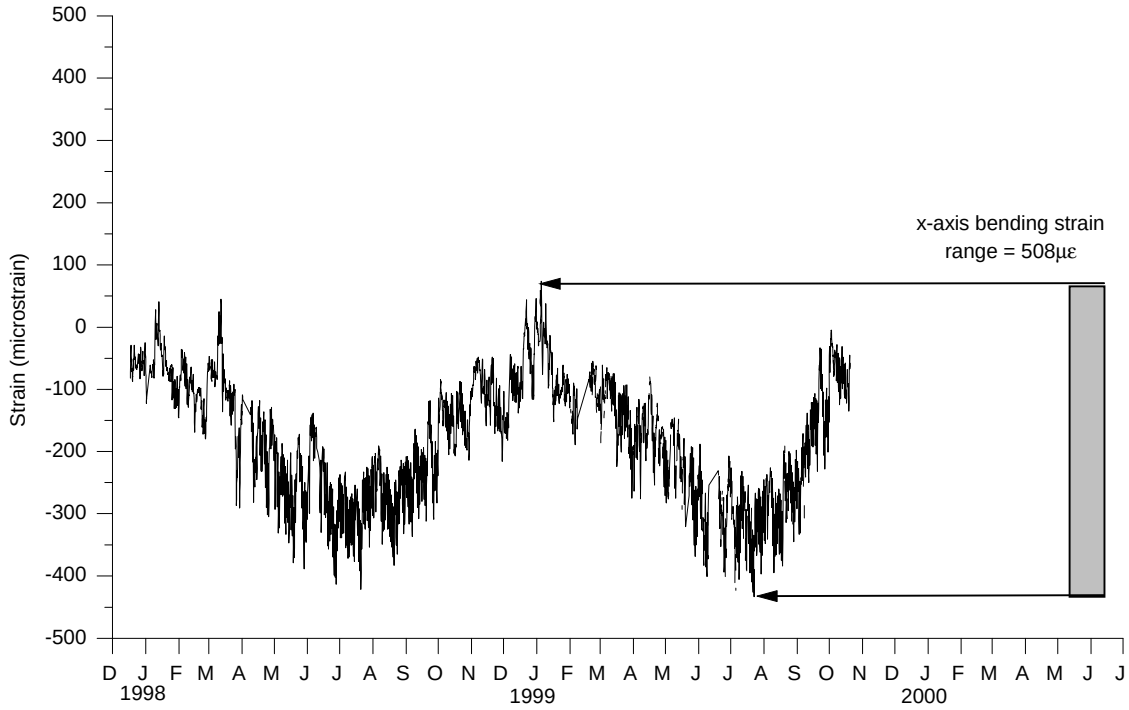

(c) X-axis bending strain

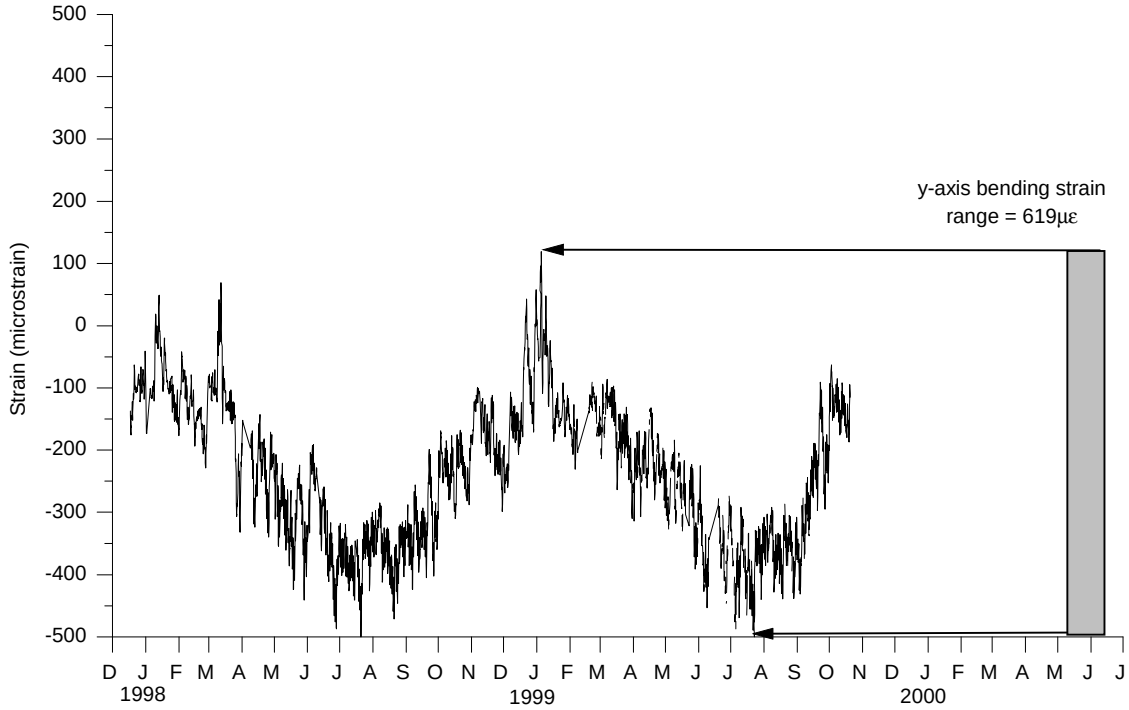

(d) Y-axis bending strain

Figure 4.8. (continued)

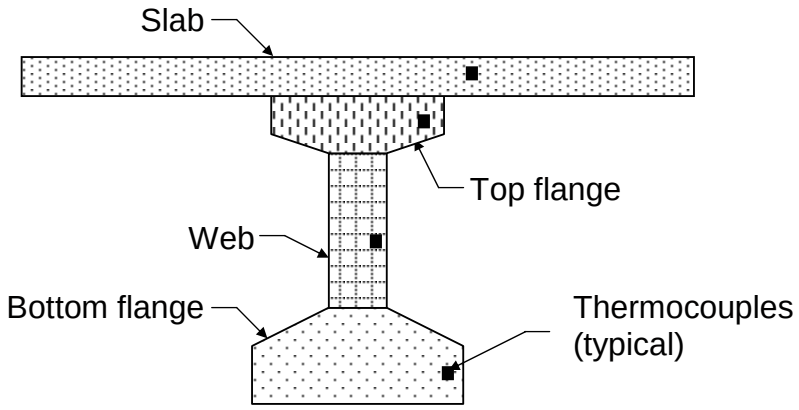

Figure 4.9. Temperature regions for a partial cross section of a bridge (not to scale)

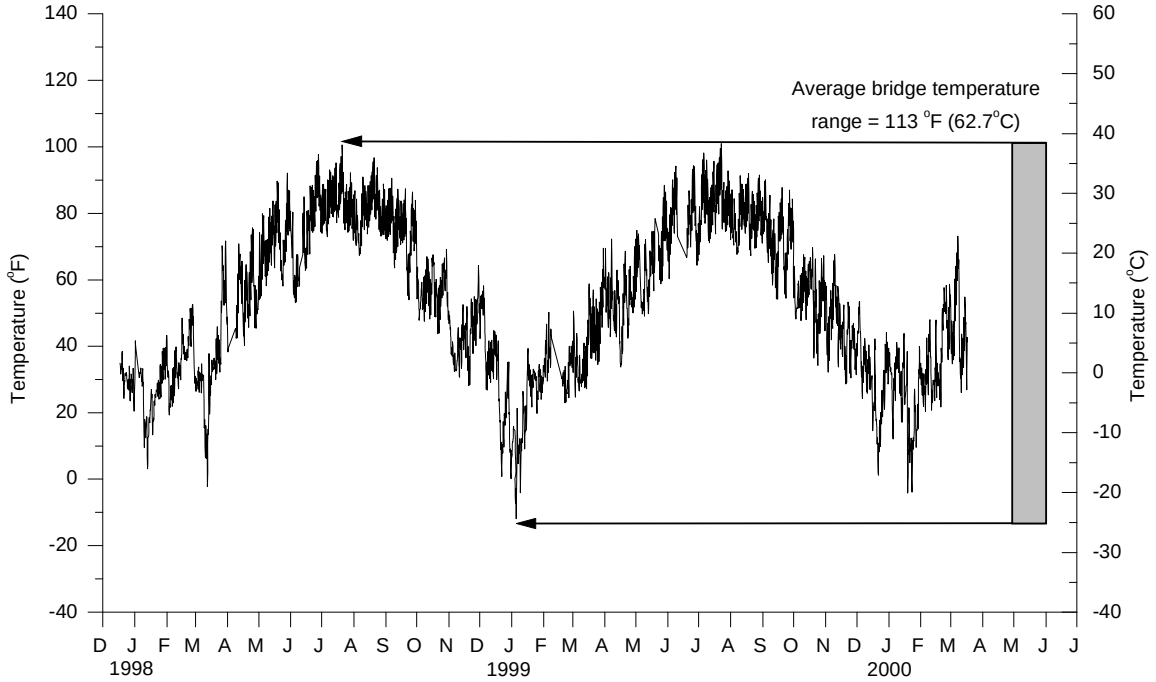

(a) Guthrie County Bridge

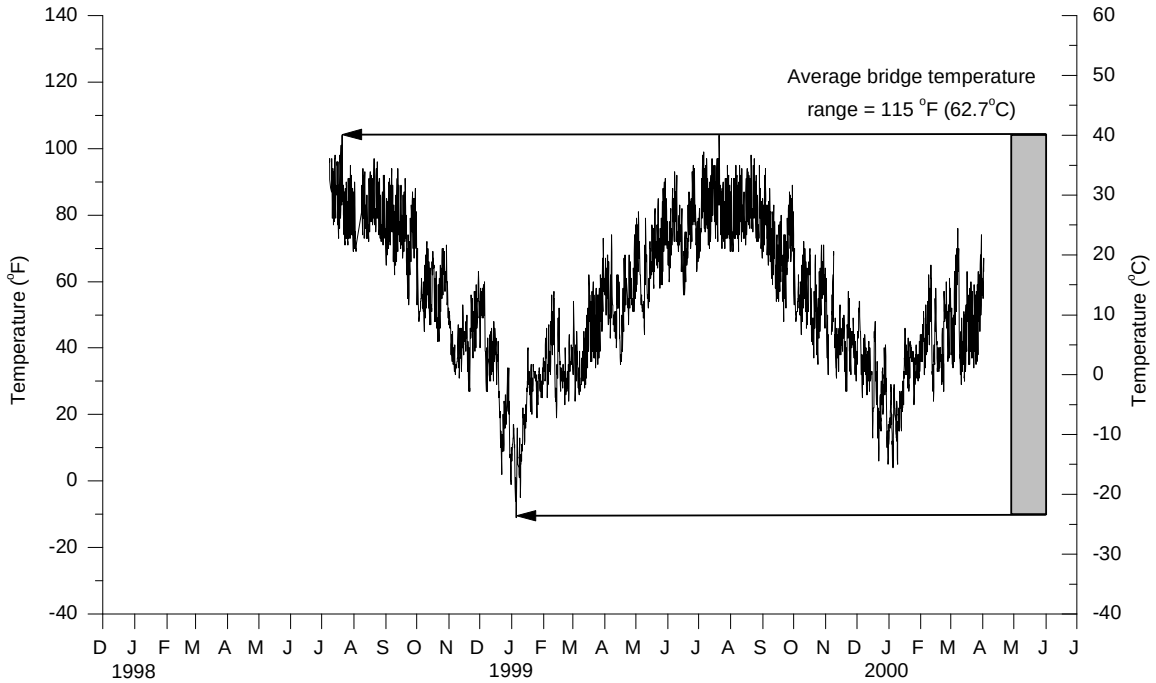

(b) Story County Bridge

Figure 4.10. Average, bridge temperatures for the monitored bridges

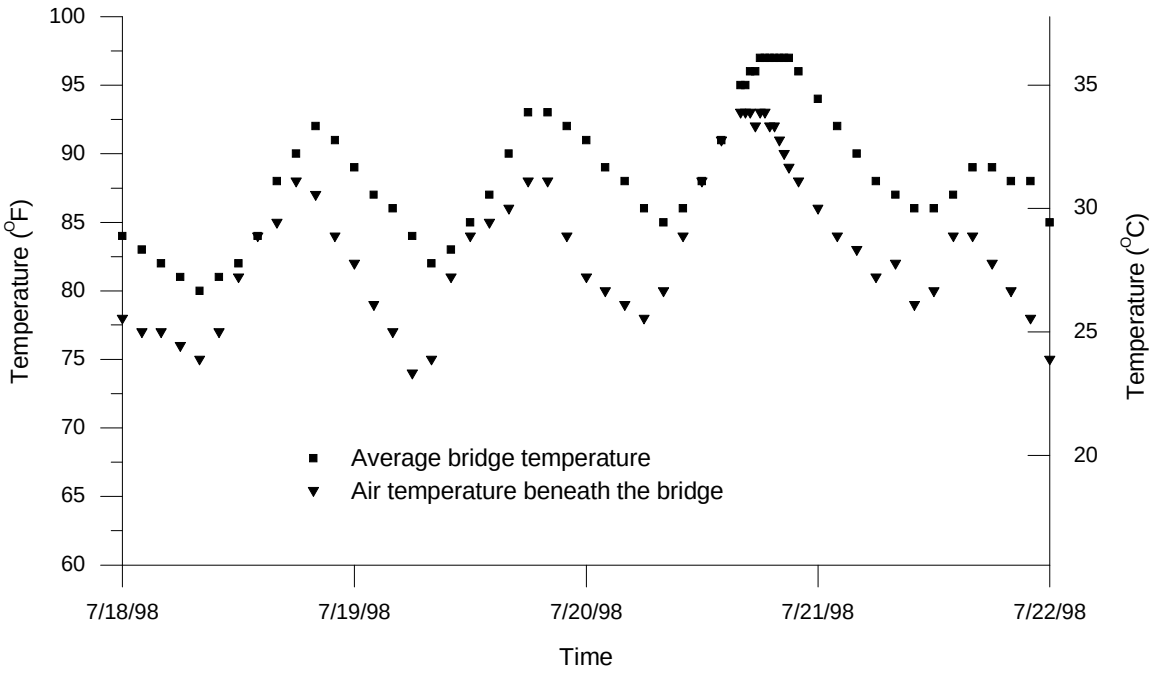

Figure 4.11. Average, bridge temperatures and air temperatures between July 18, 1998 and July 22, 1998 at the Guthrie County Bridge

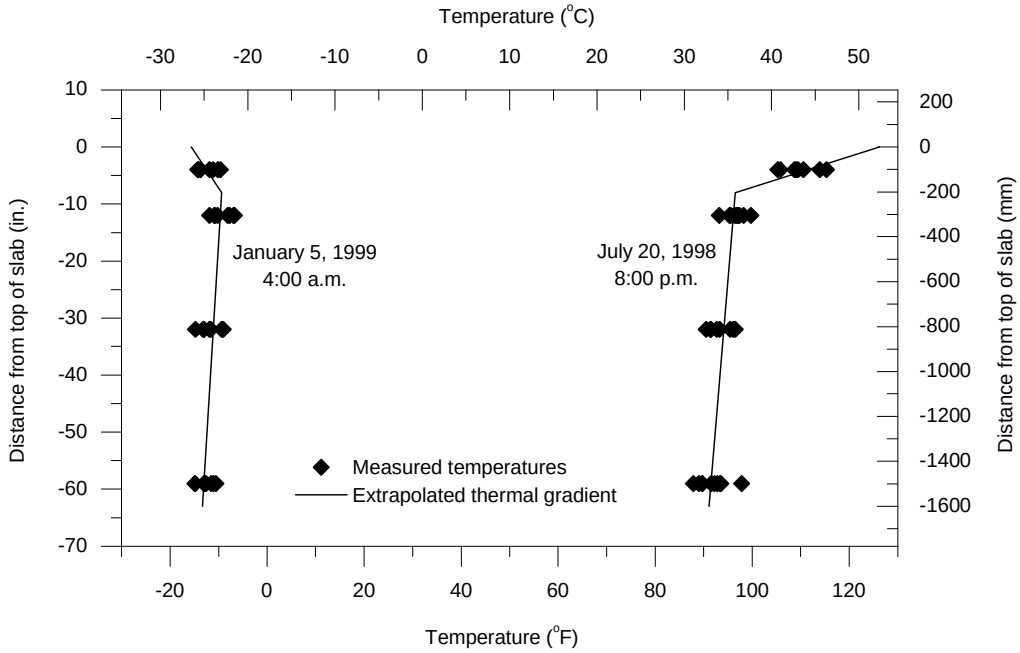

(a) Guthrie County Bridge

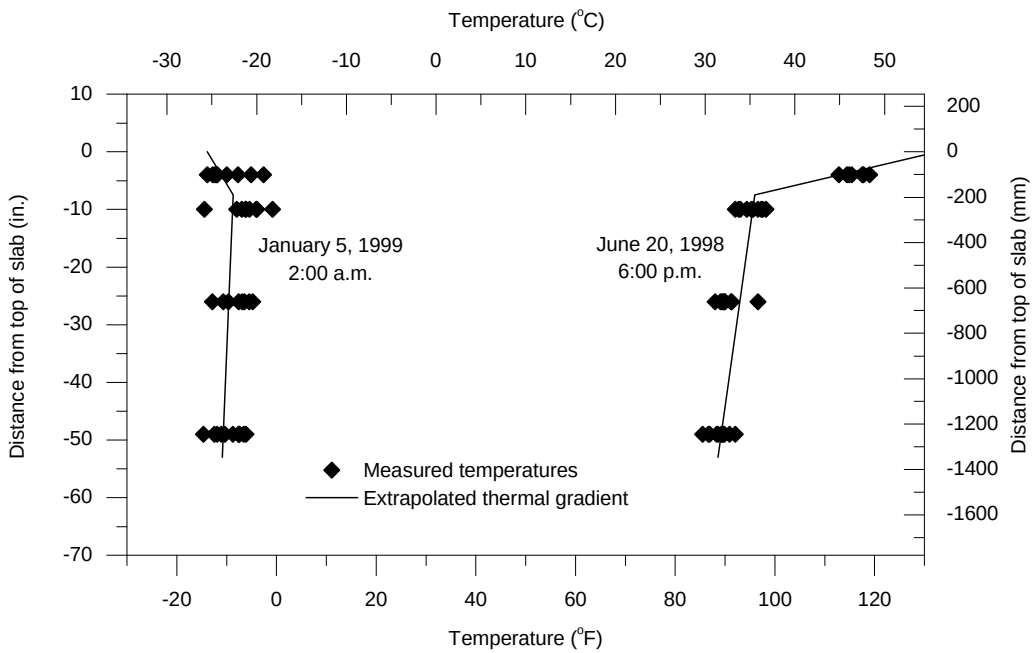

(b) Story County Bridge

Figure 4.12. Vertical-temperature distributions through the depth of the superstructure at the times of minimum and maximum, average, bridge temperatures

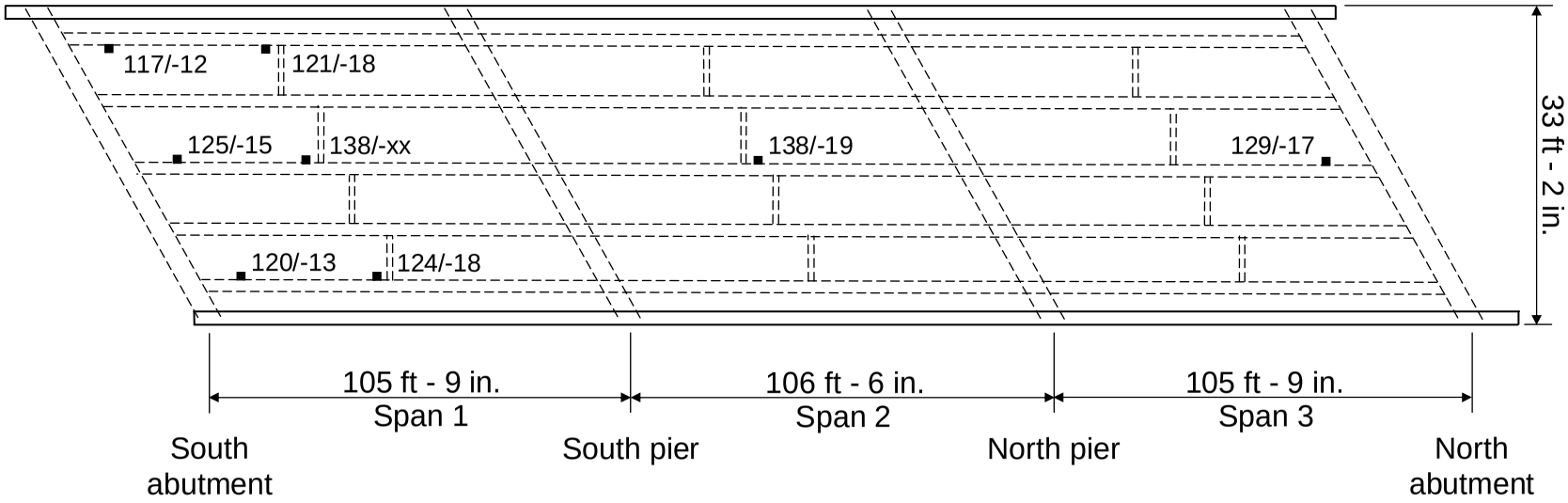

(a) At the top of the bridge deck

Figure 4.13. Extrapolated temperatures (°F) at the time of the maximum and minimum, average, bridge temperatures at the Guthrie County Bridge

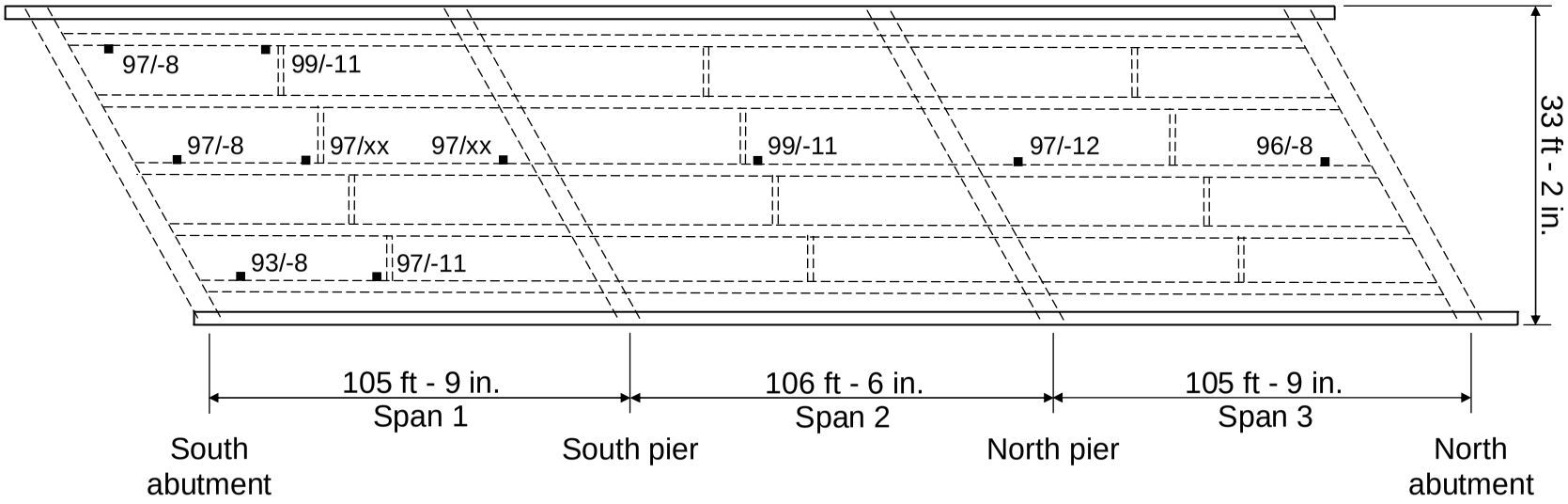

(b) At the top of the PC girders

Figure 4.13. (continued)

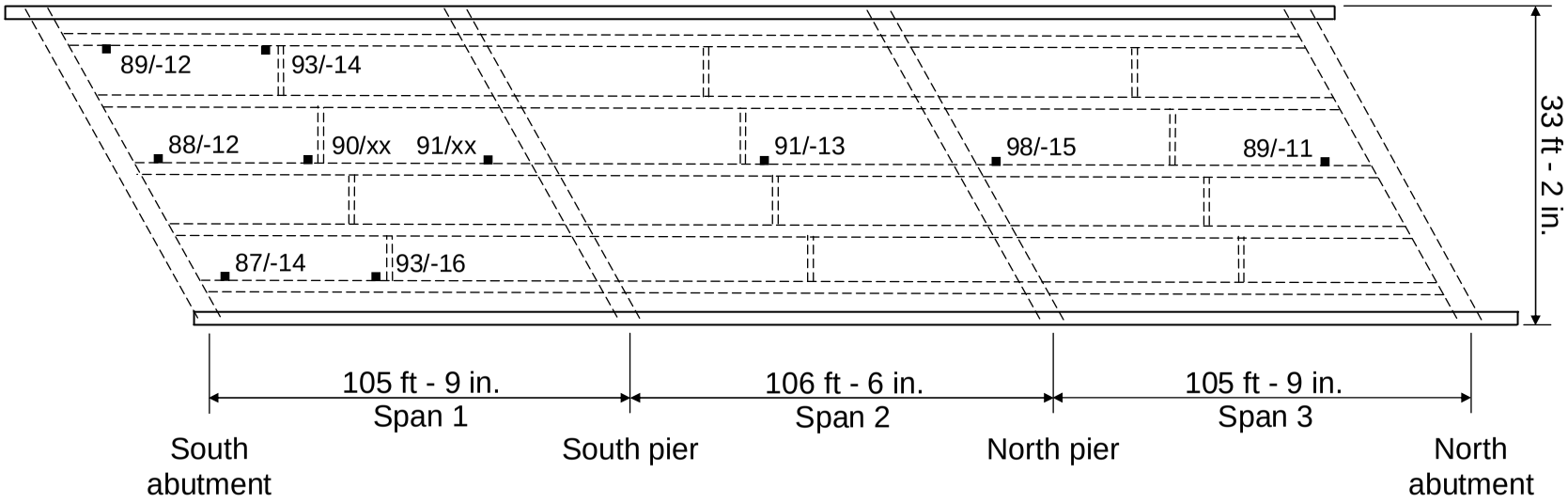

(c) At the bottom of the PC girders

Figure 4.13. (continued)

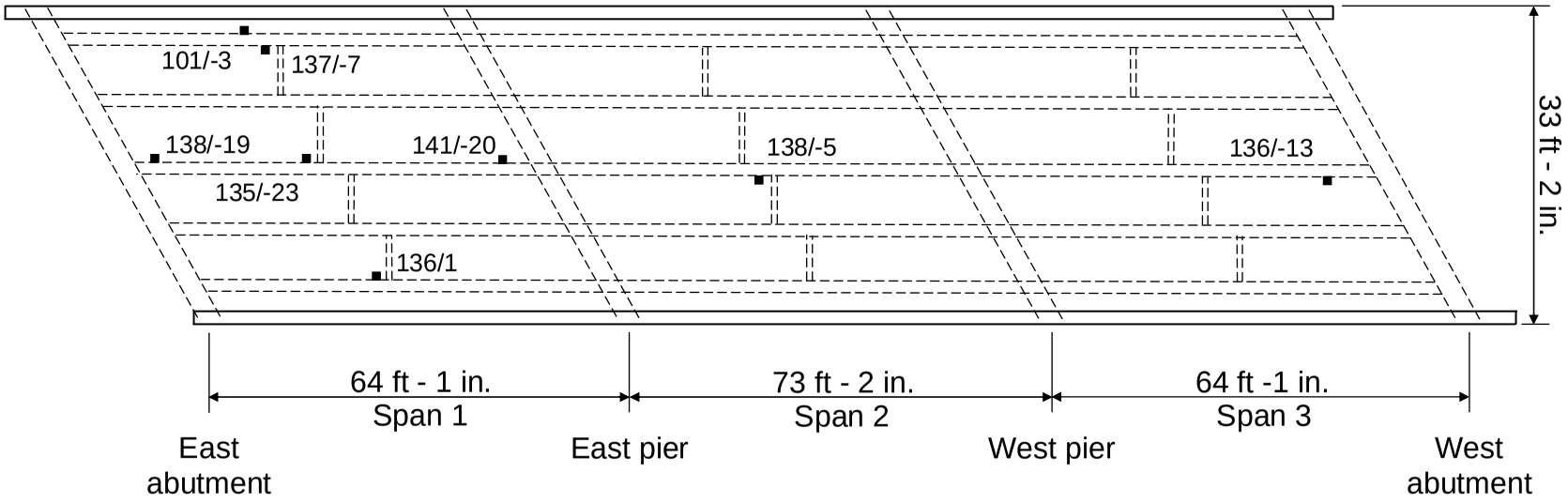

(a) At the top of the bridge deck

Figure 4.14. Extrapolated temperatures (°F) at the time of the maximum and minimum, average, bridge temperatures at the Story County Bridge

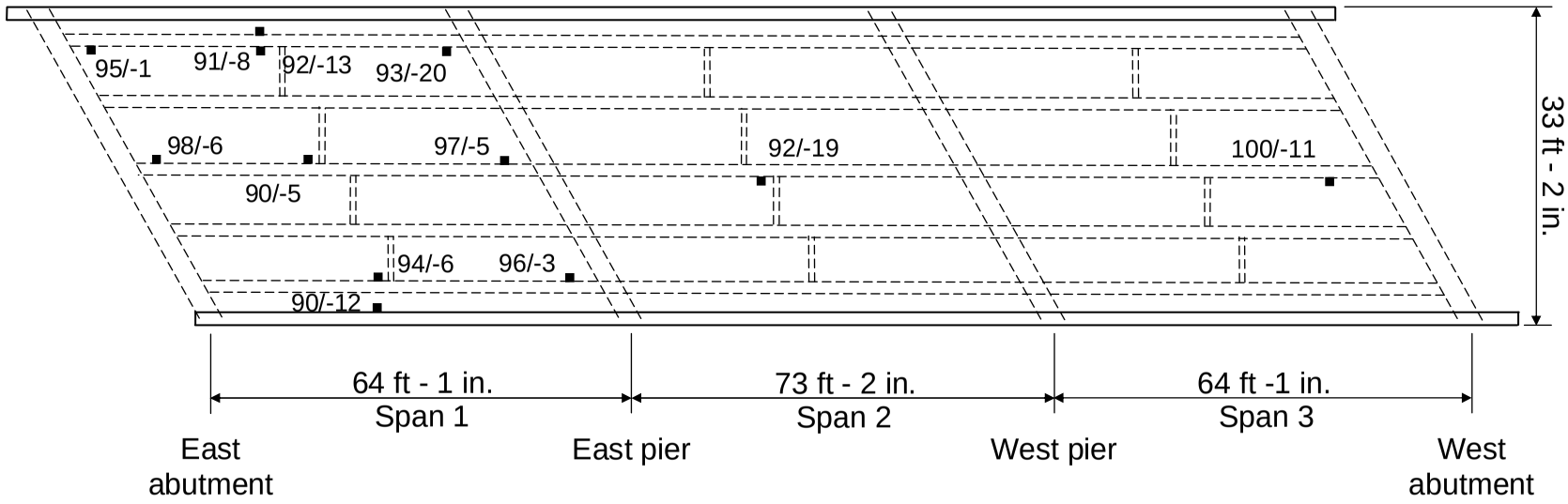

(b) At the top of the PC girders

Figure 4.14. (continued)

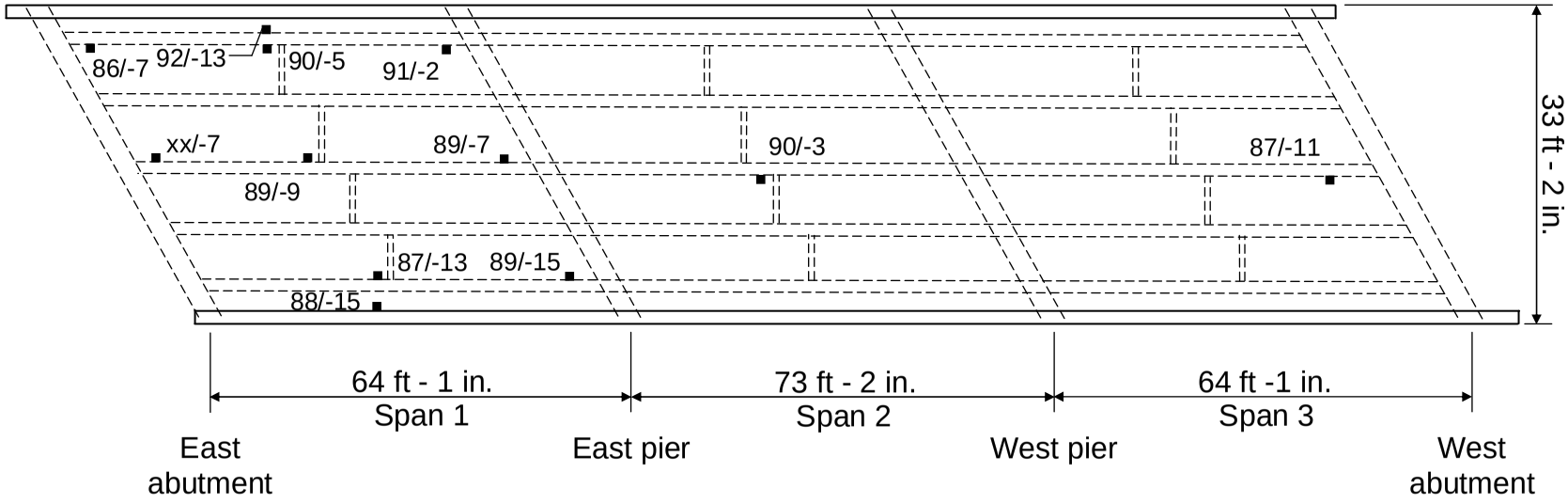

(c) At the bottom of the PC girders

Figure 4.14. (continued)

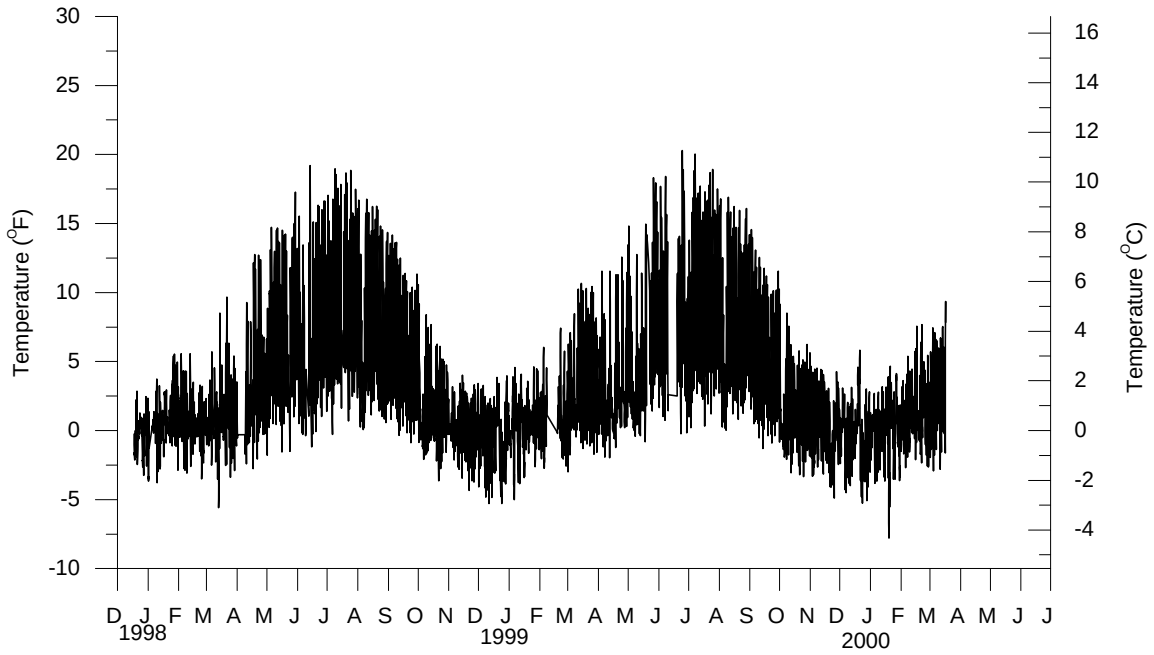

(a) Guthrie County Bridge

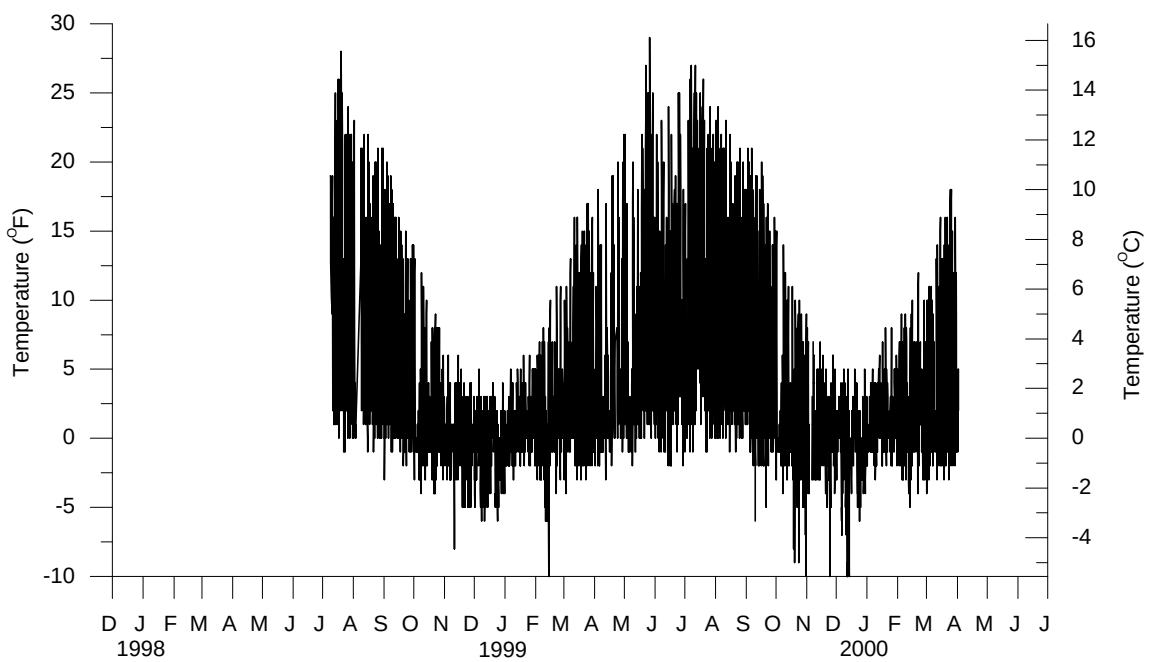

(b) Story County Bridge

Figure 4.15. Difference between the average temperatures in the bridge deck and in the bottom flanges of the PC girders

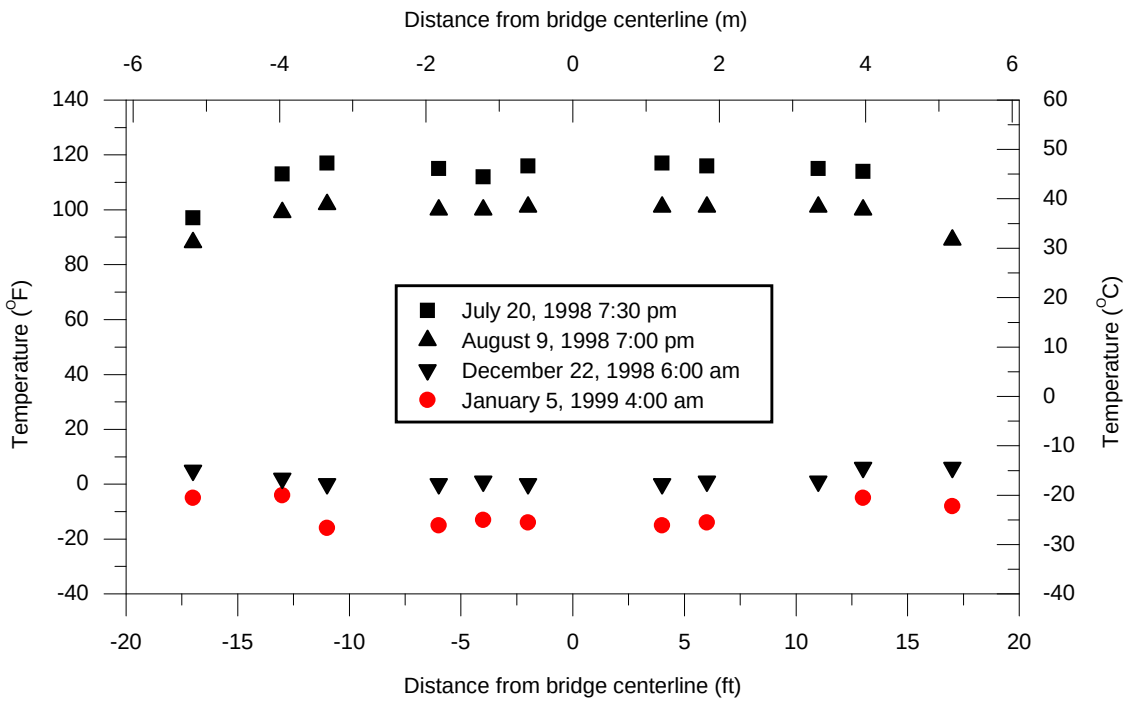

(a) Story County Bridge

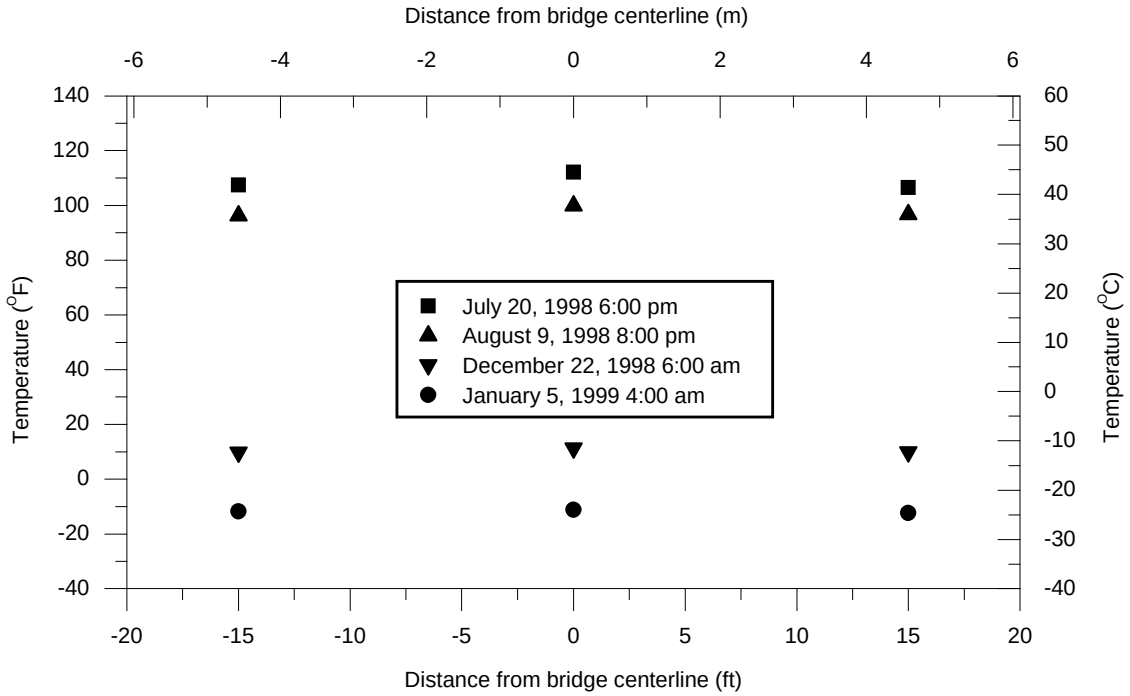

(b) Guthrie County Bridge

Figure 4.16. Transverse-temperature distribution across the bridge width

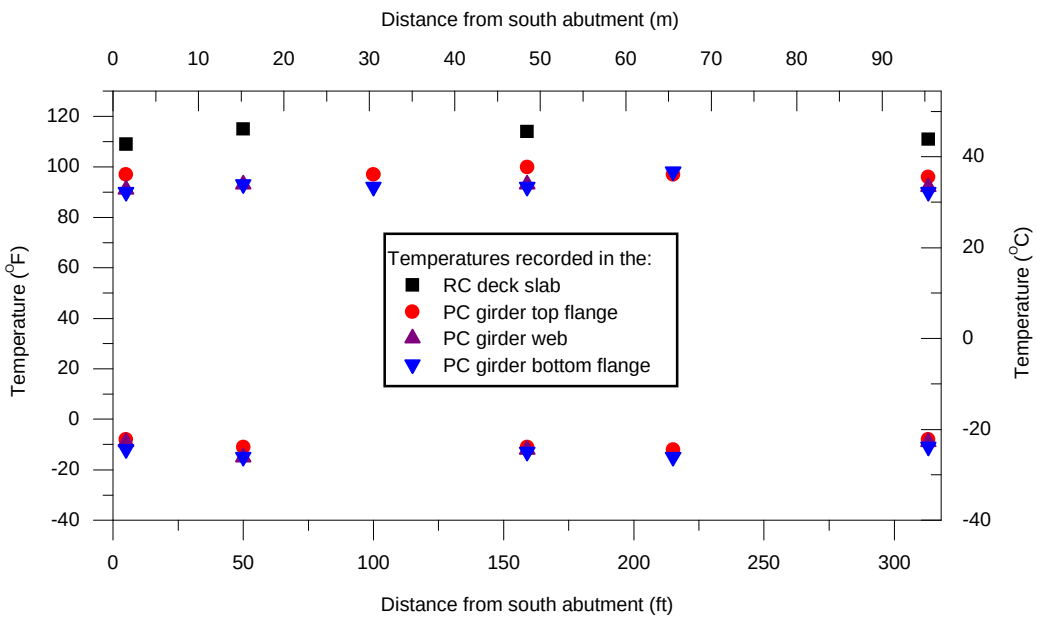

(a) Guthrie County Bridge (July 20, 1998 and January 5, 1999)

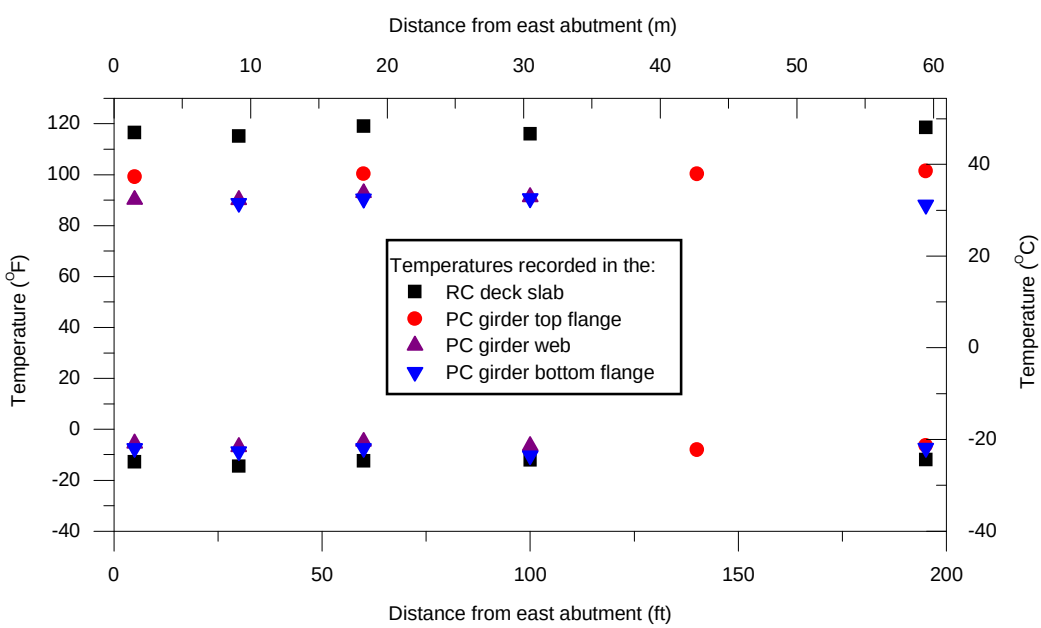

(b) Story County Bridge (July 20, 1998 and January 5, 1999)

Figure 4.17. Measured, bridge temperatures along the bridge length at the times of the maximum and minimum, average, bridge temperatures

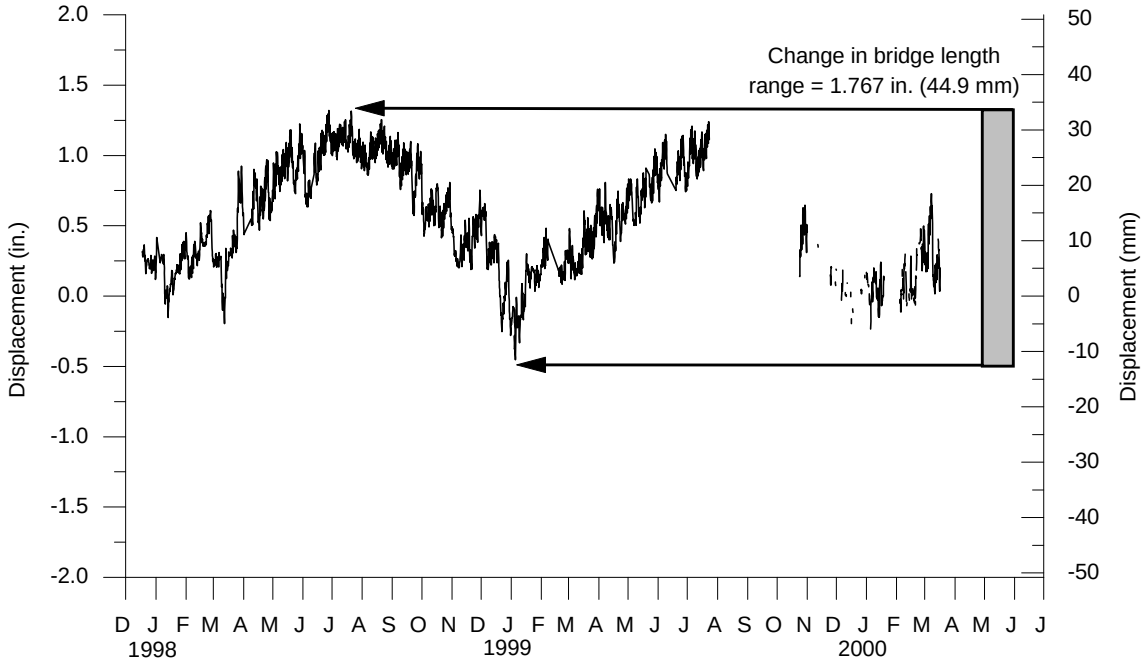

(a) Guthrie County Bridge

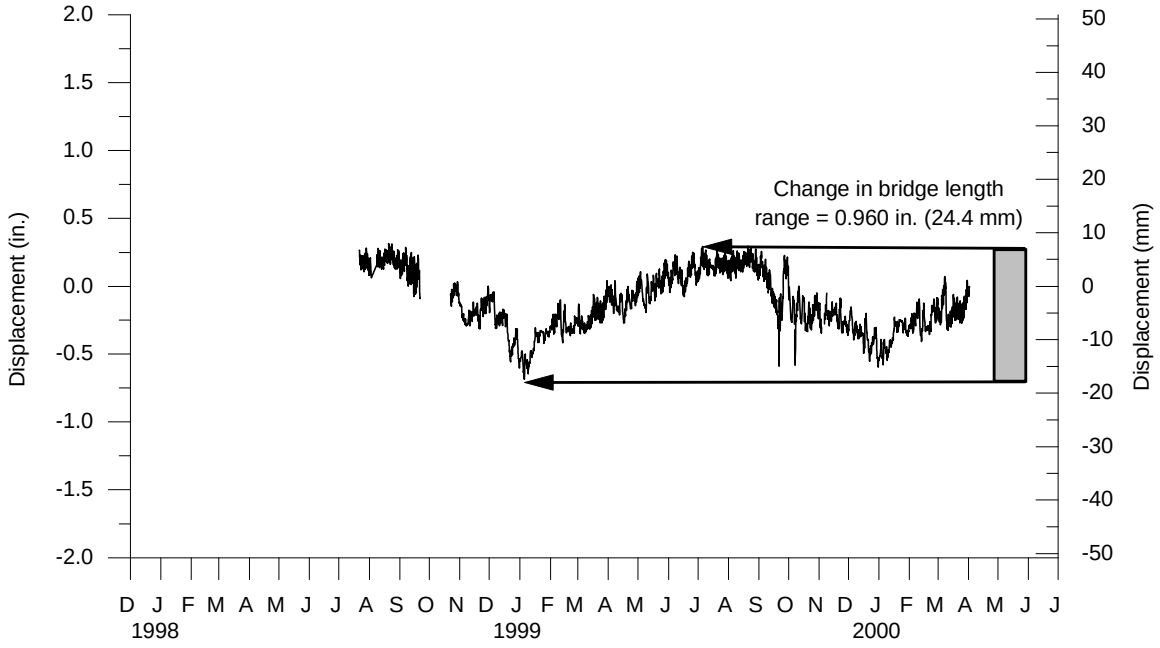

(b) Story County Bridge

Figure 4.18. Change in the bridge length

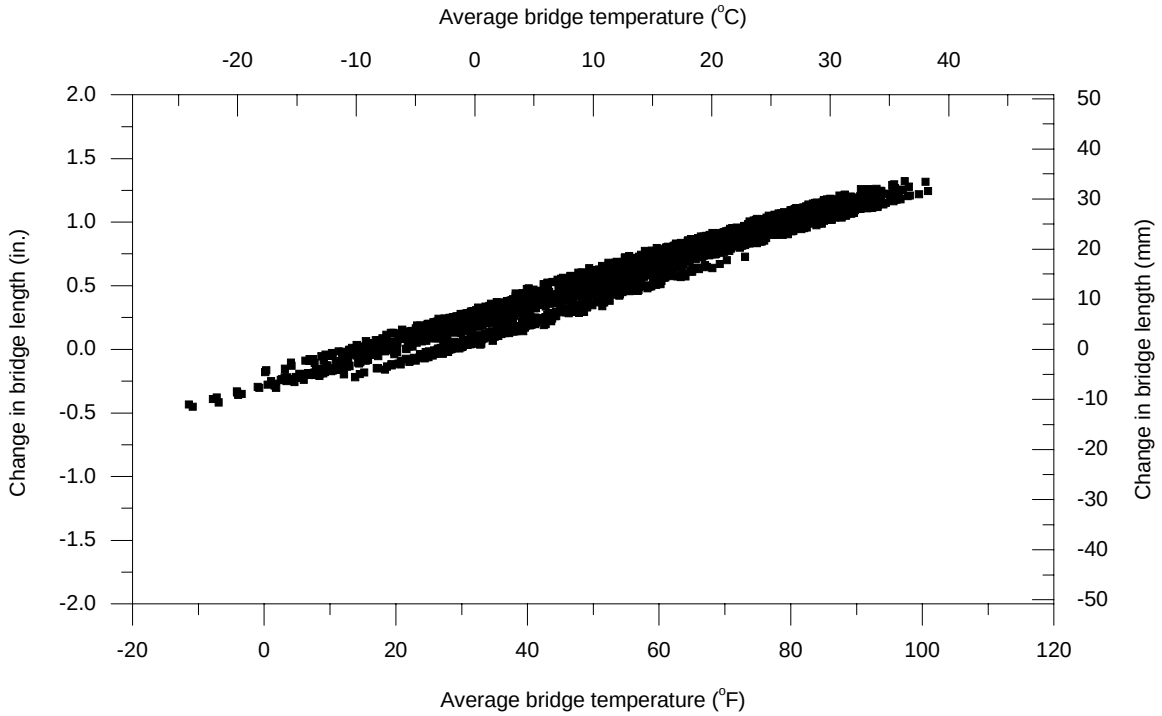

(a) Guthrie County Bridge

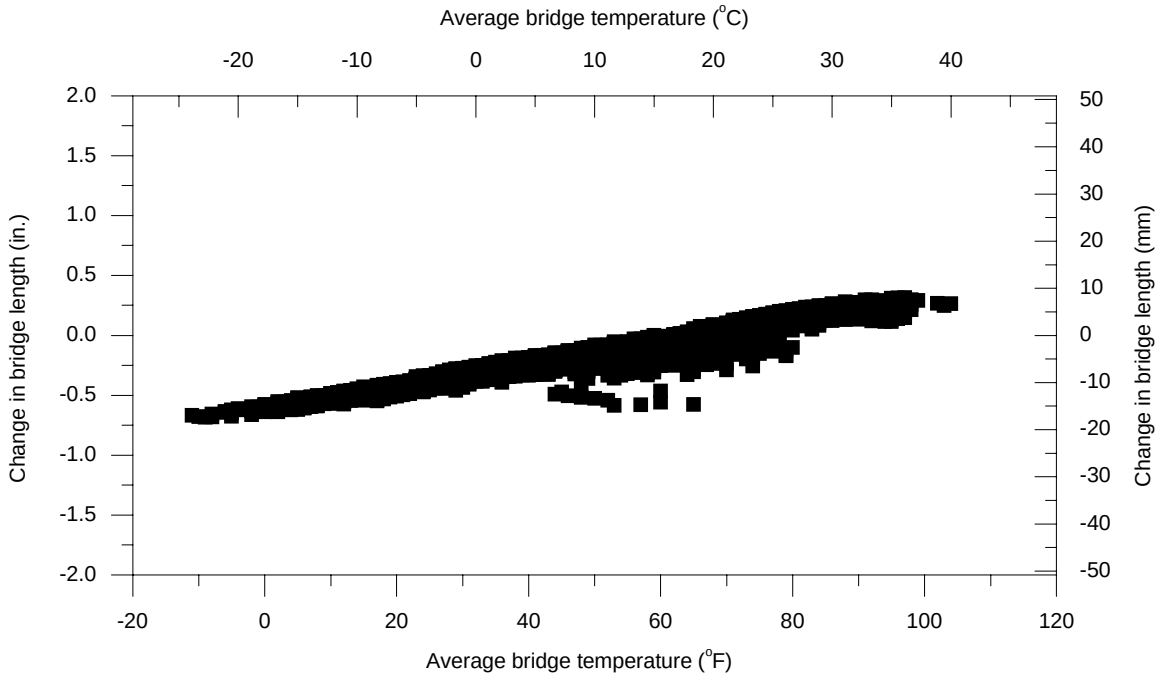

(b) Story County Bridge

Figure 4.19. Change in the bridge length versus average, bridge temperature

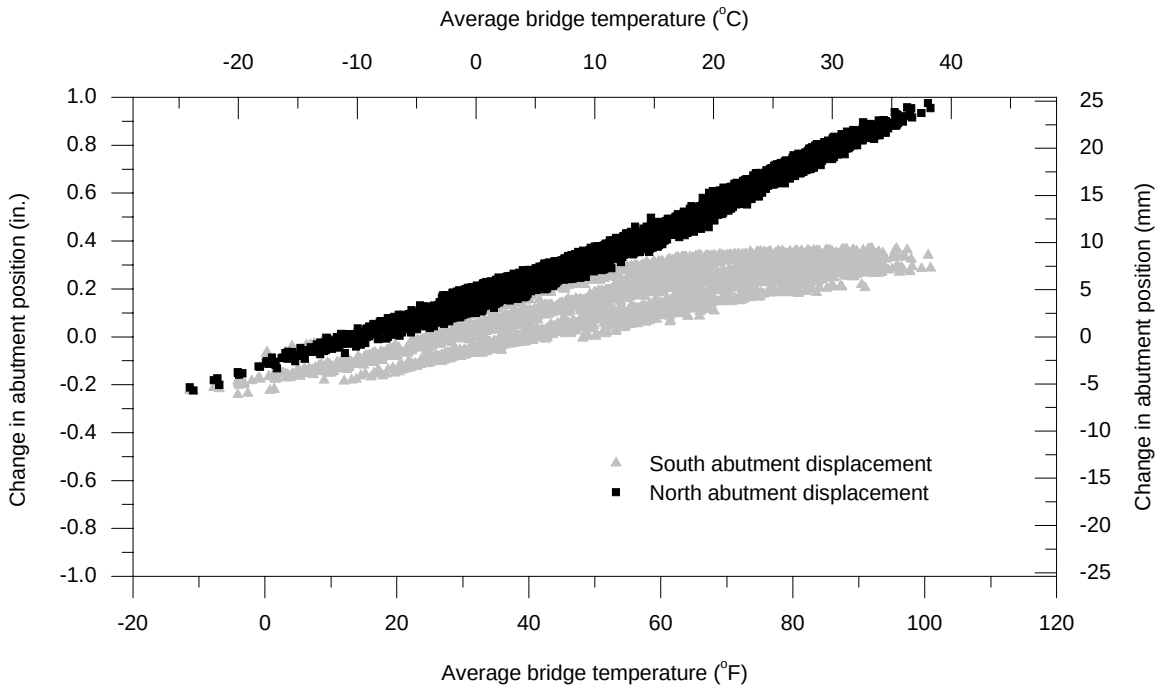

Figure 4.20. Change in the longitudinal displacements of the north and south abutments versus the average, bridge temperature at the Guthrie County Bridge

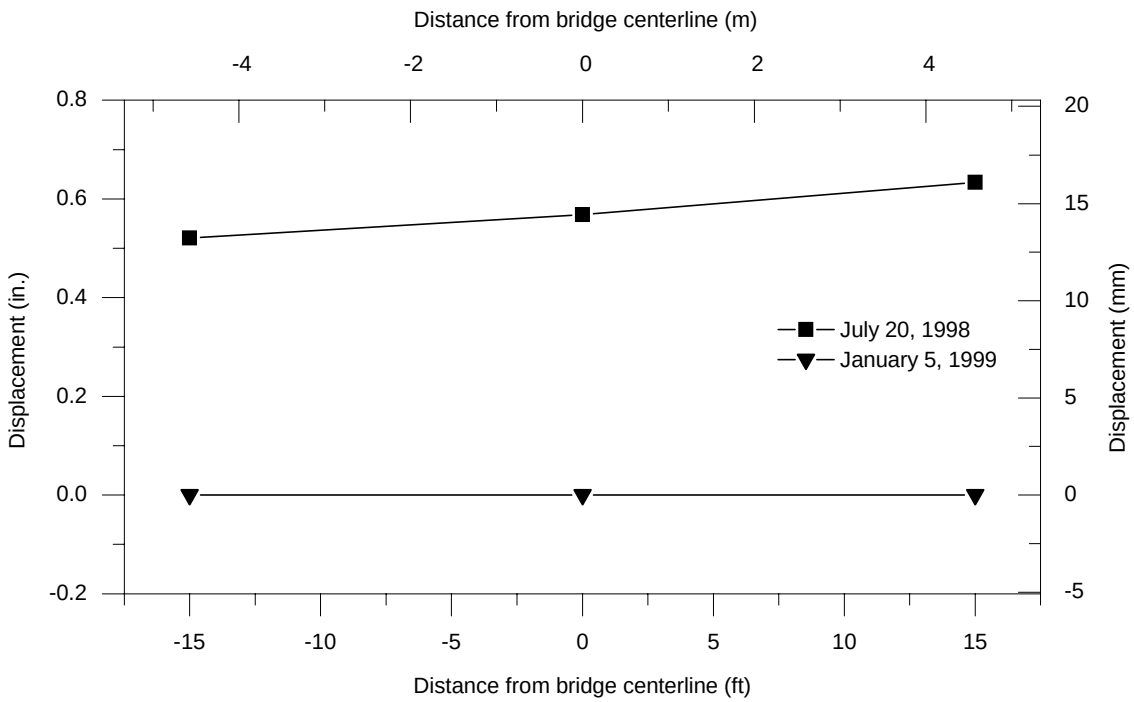

(a) South abutment at the Guthrie County Bridge

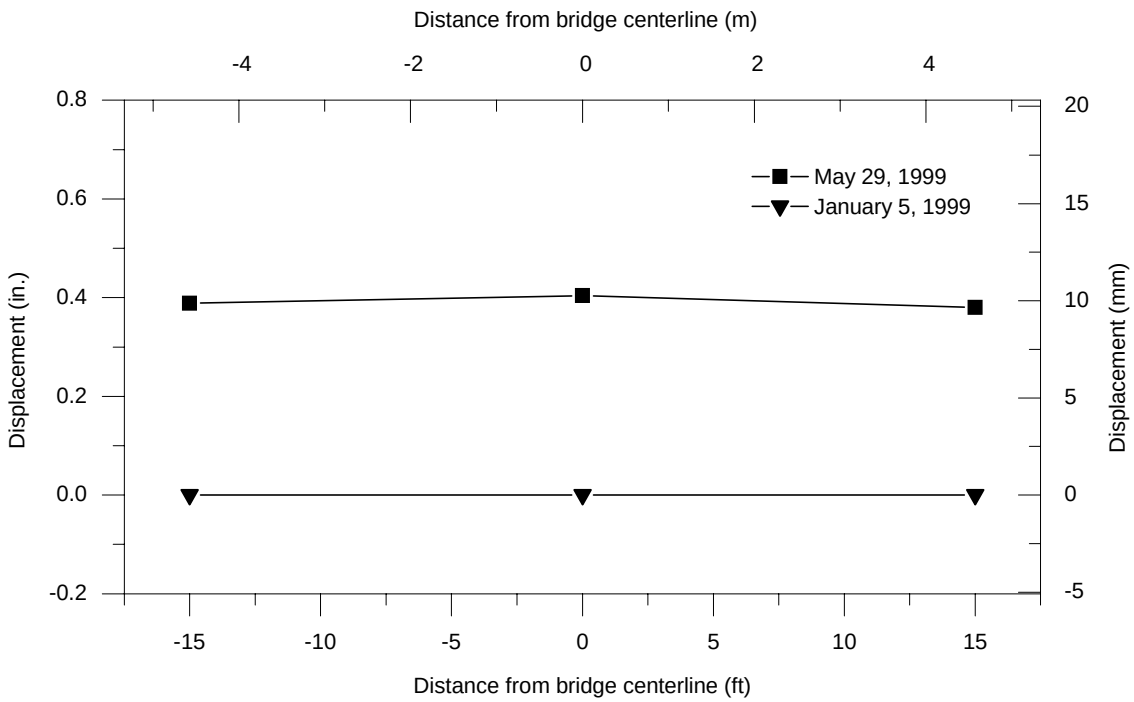

(b) East abutment at the Story County Bridge

Figure 4.21. Range in the longitudinal displacements at three positions across the width of the abutments

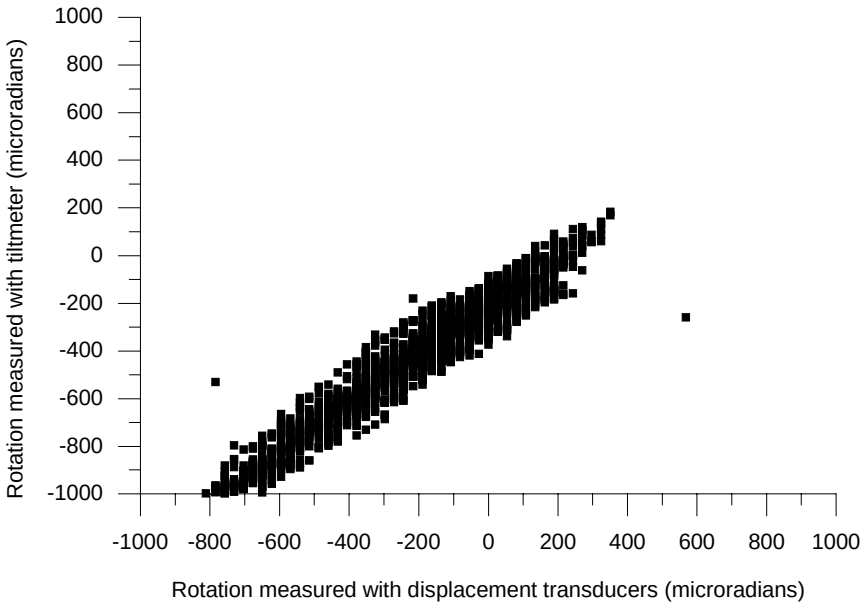

Figure 4.22. Pile-cap rotations measured with a tiltmeter versus rotations calculated from transducer displacements at the Guthrie County Bridge

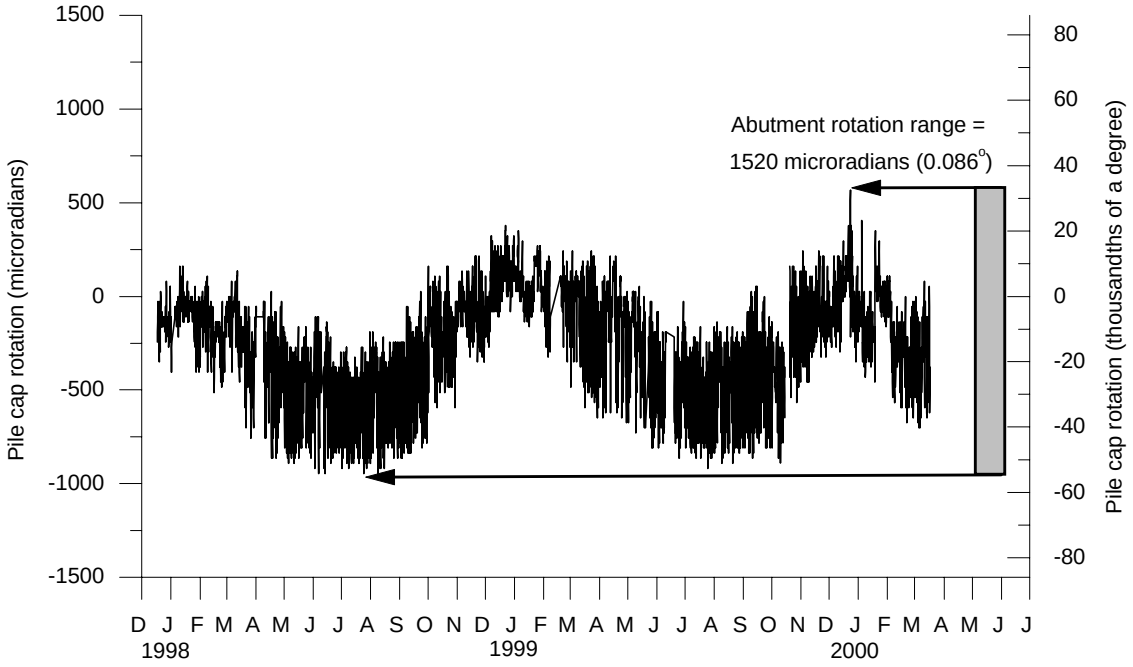

(a) South abutment at the Guthrie County Bridge

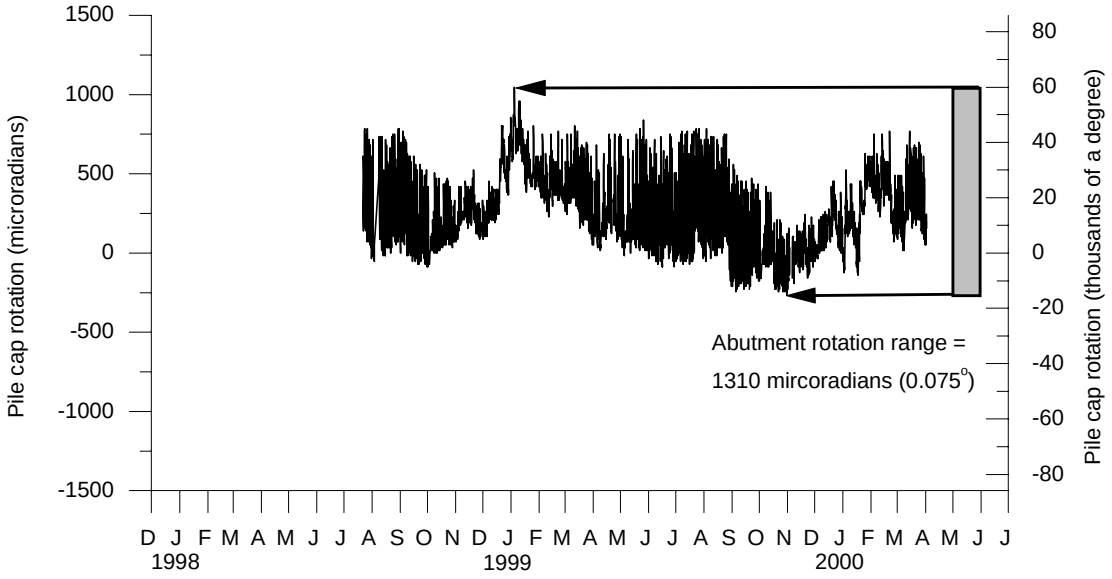

(a) South abutment at the Guthrie County Bridge

Figure 4.23. Abutment pile-cap rotations

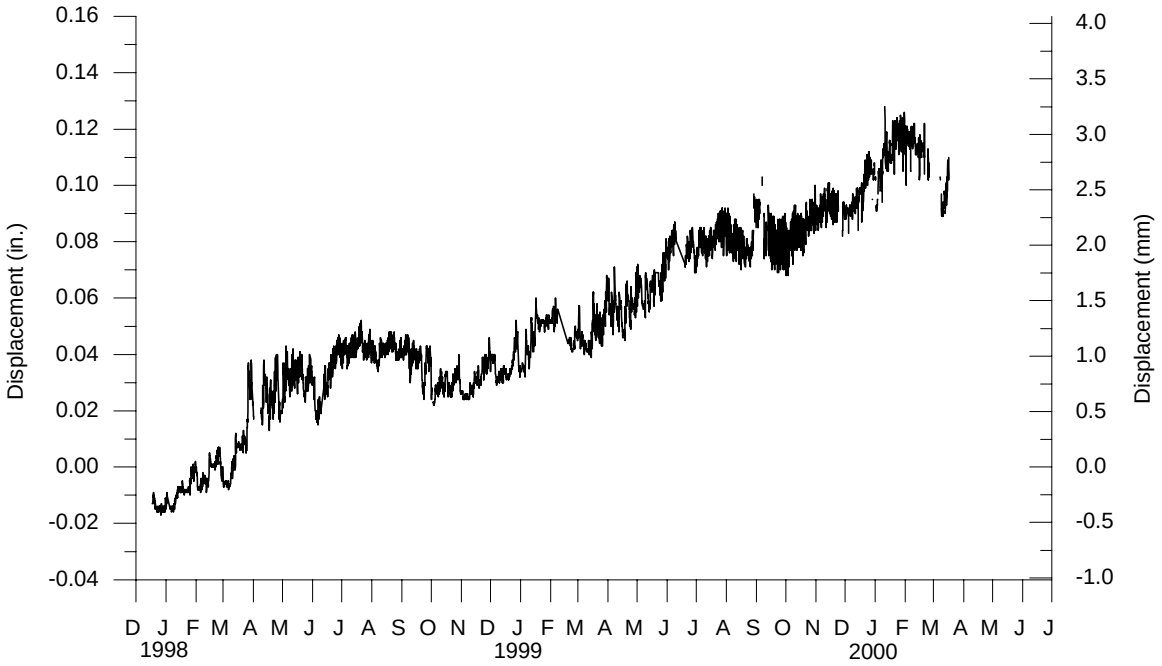

Figure 4.24. Transverse displacements of the south abutment for the Guthrie County Bridge

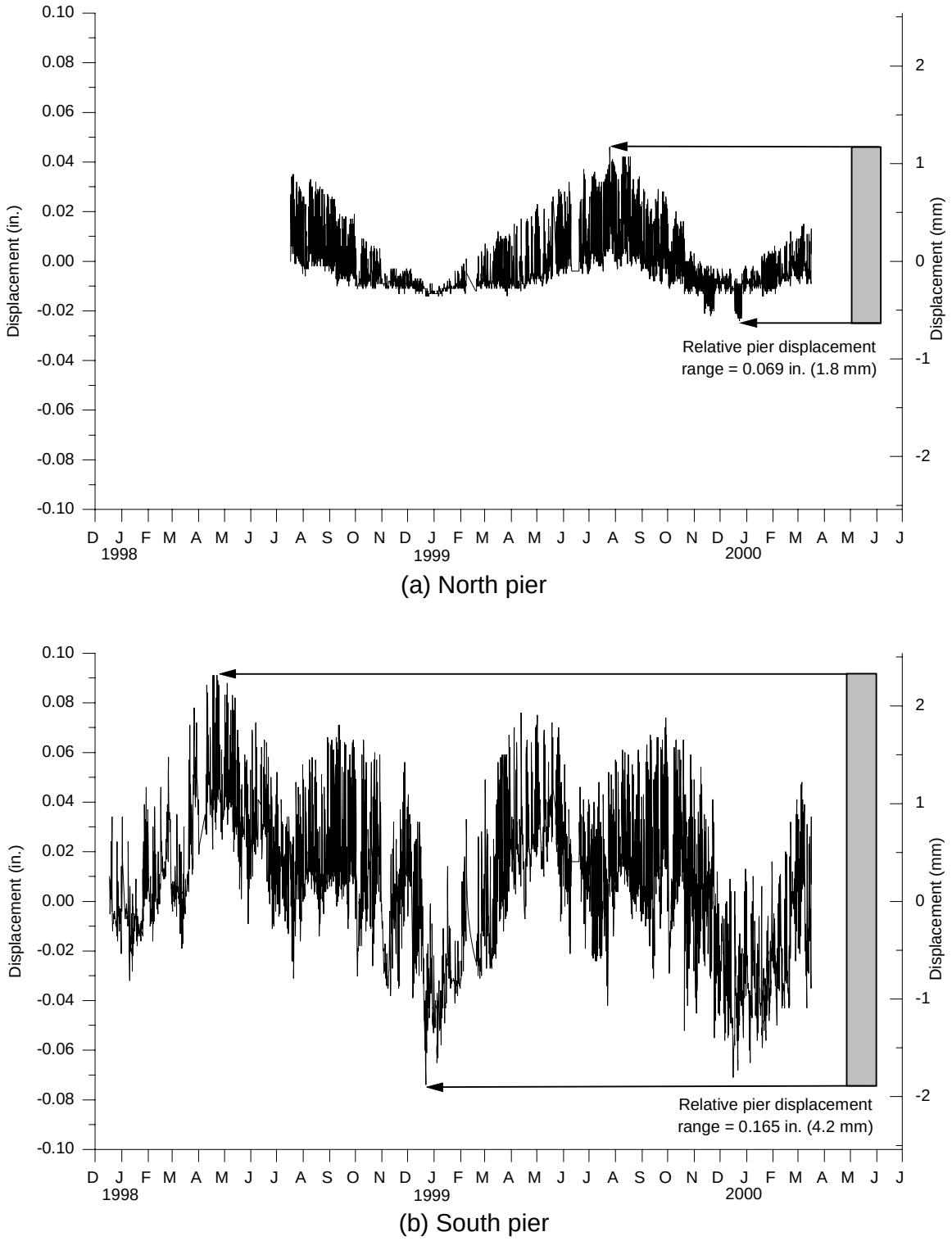

Figure 4.25. Relative displacements at piers for the Guthrie County Bridge

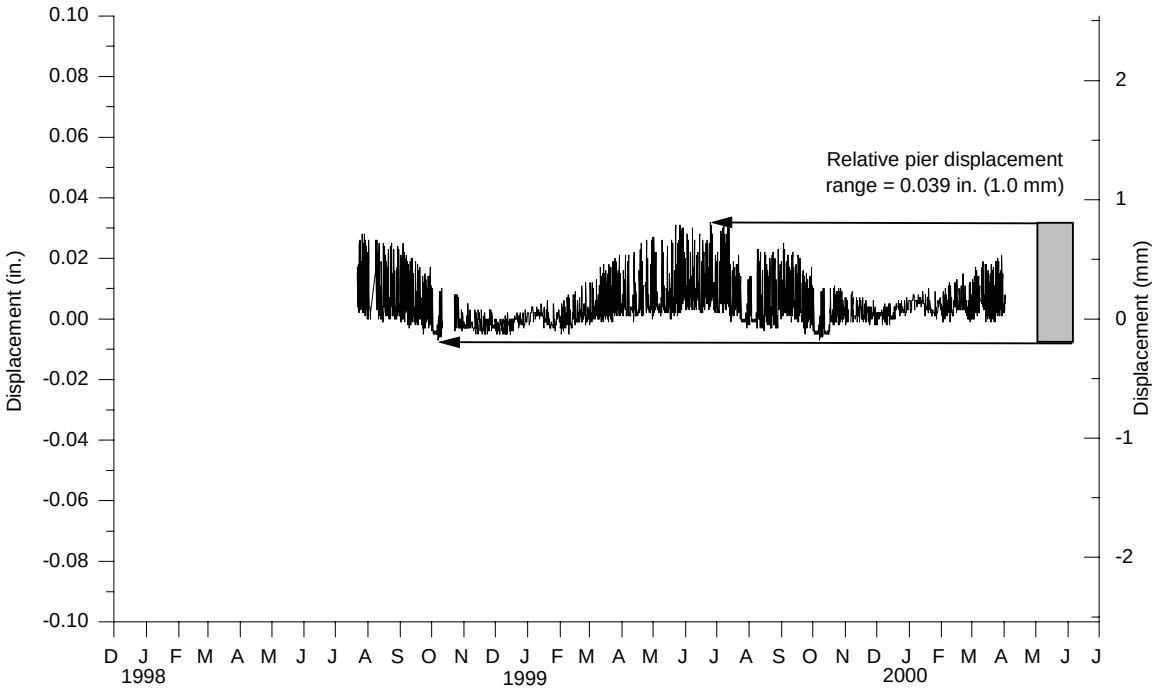

(a) West pier

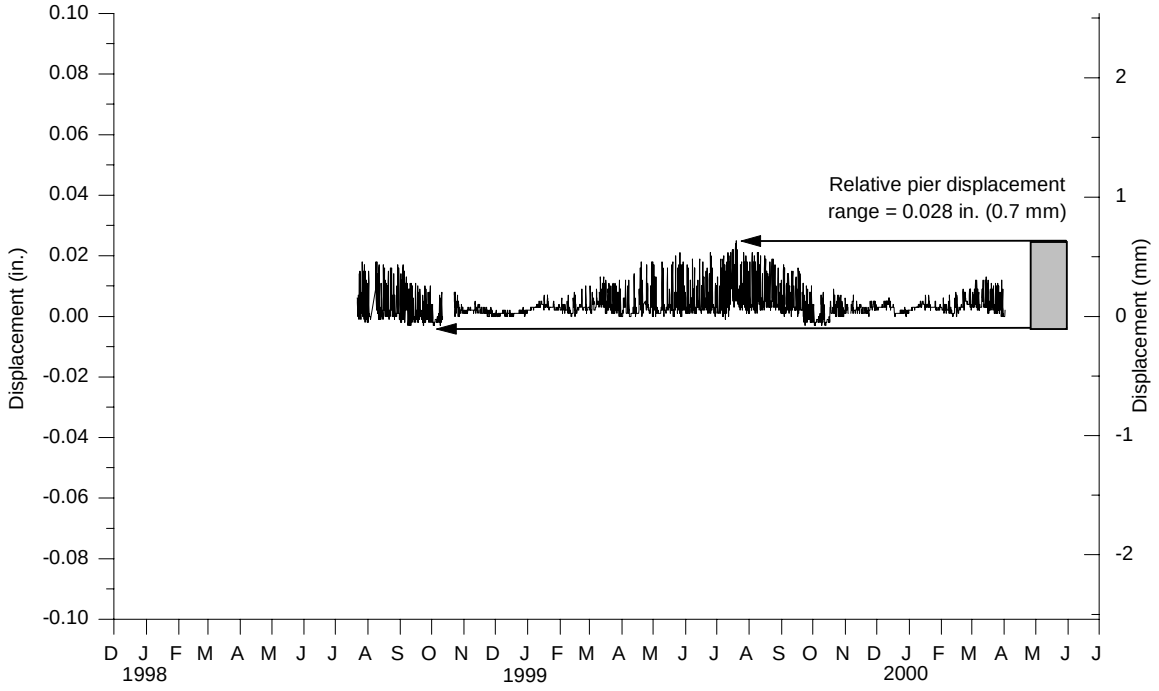

(b) East pier

Figure 4.26. Relative displacements at the piers for the Story County Bridge

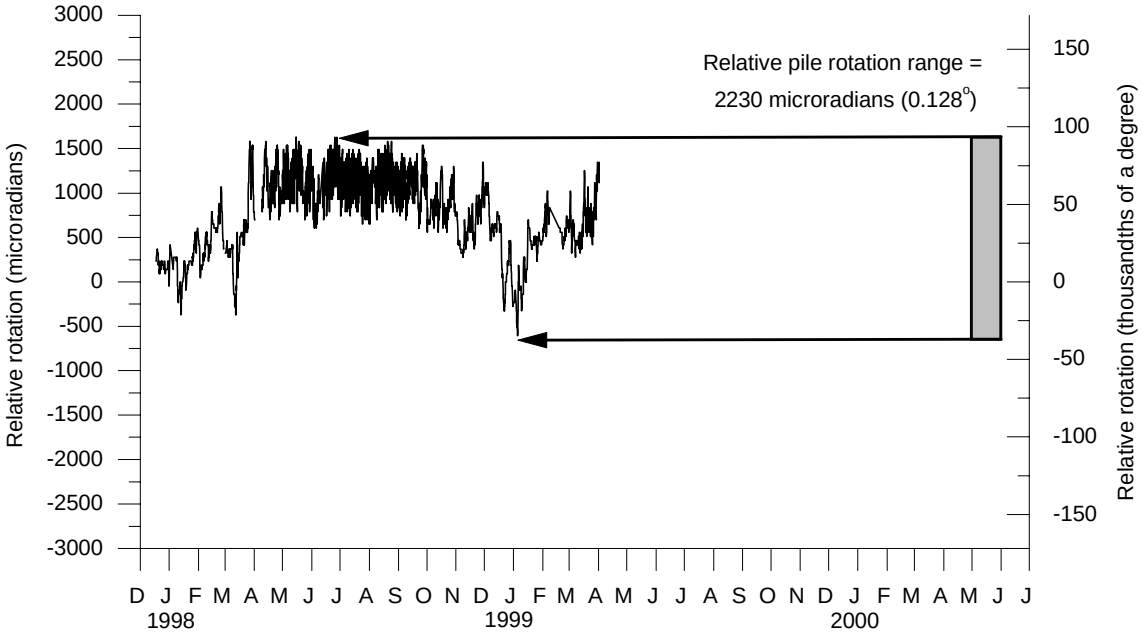

(a) Guthrie County Bridge

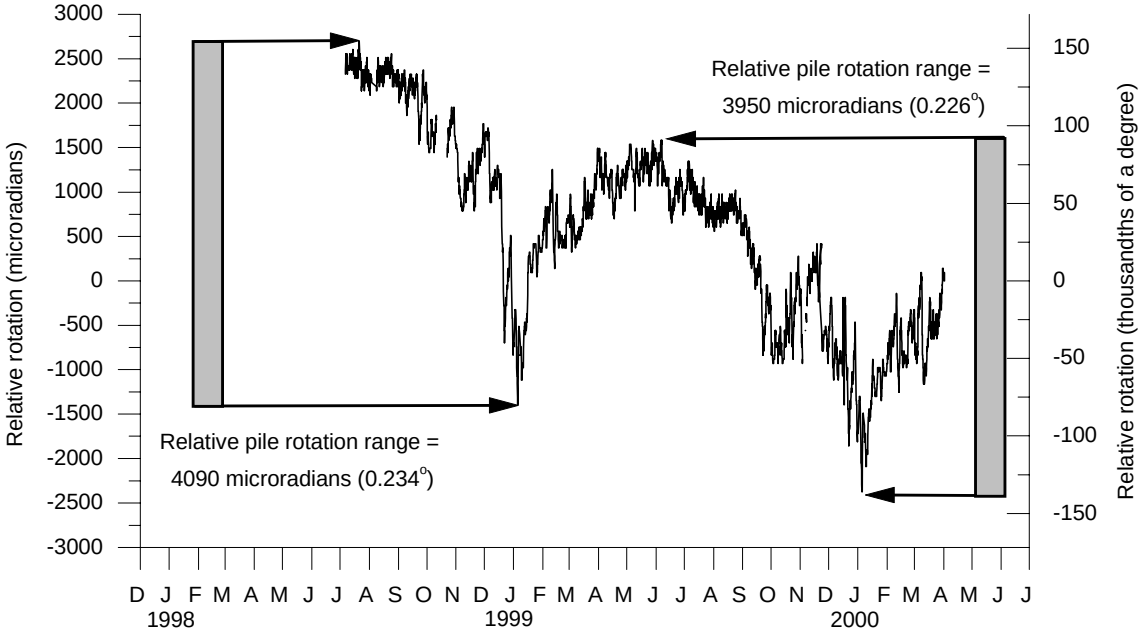

(a) Guthrie County Bridge

Figure 4.27. Relative rotation between a pile and a pile cap

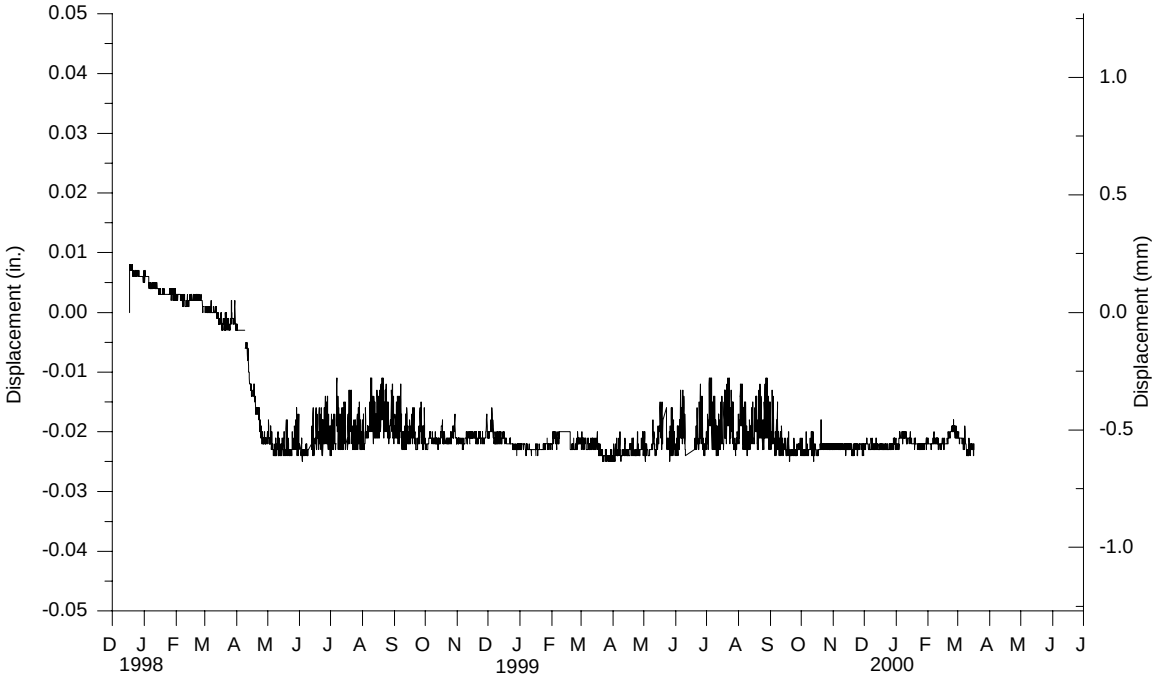

(a) Displacement at the top flange

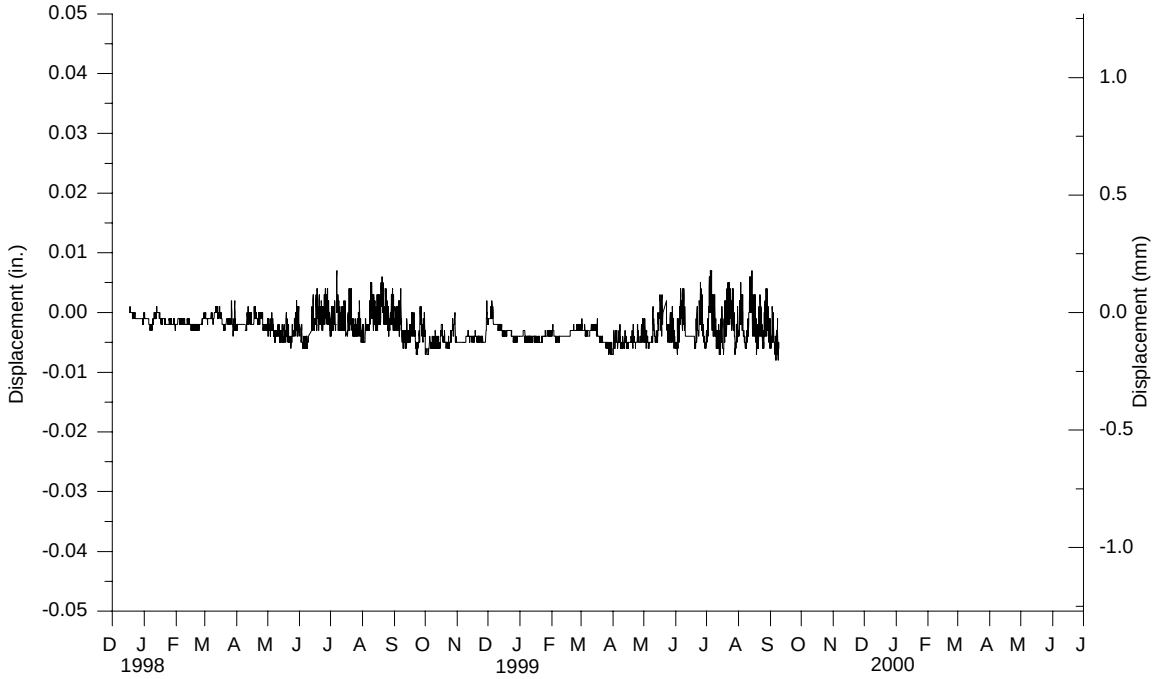

(b) Displacement at the bottom flange

Figure 4.28. Relative displacement between the center PC girder and the south-abutment backwall at the Guthrie County Bridge

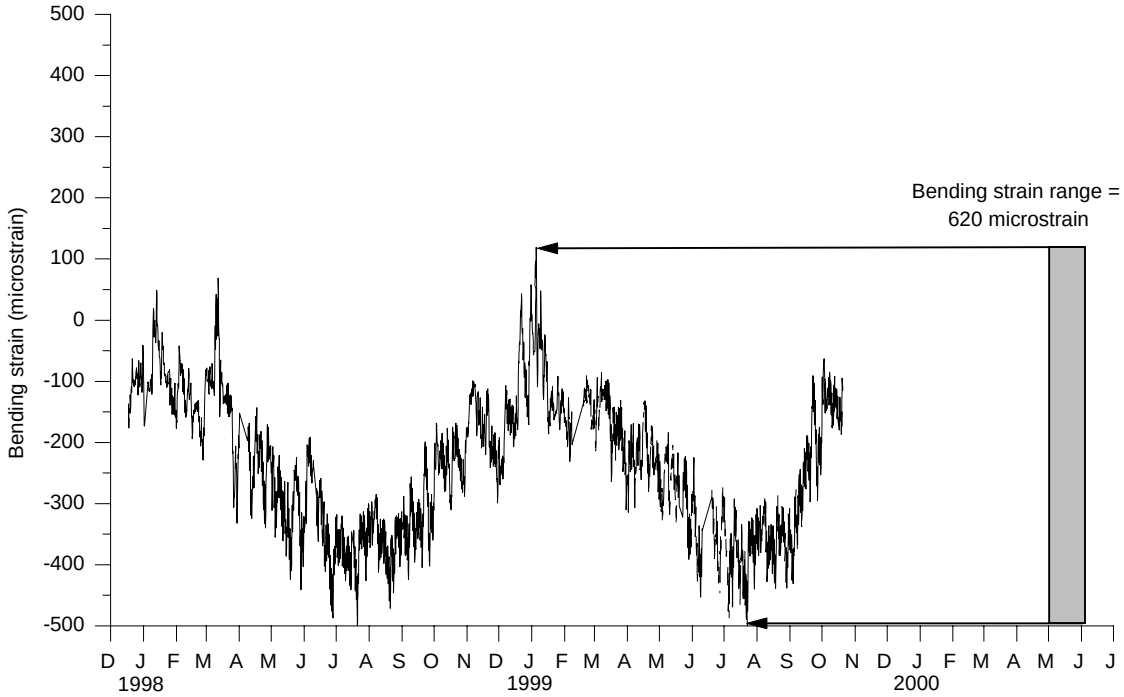

(a) Y-axis bending strain

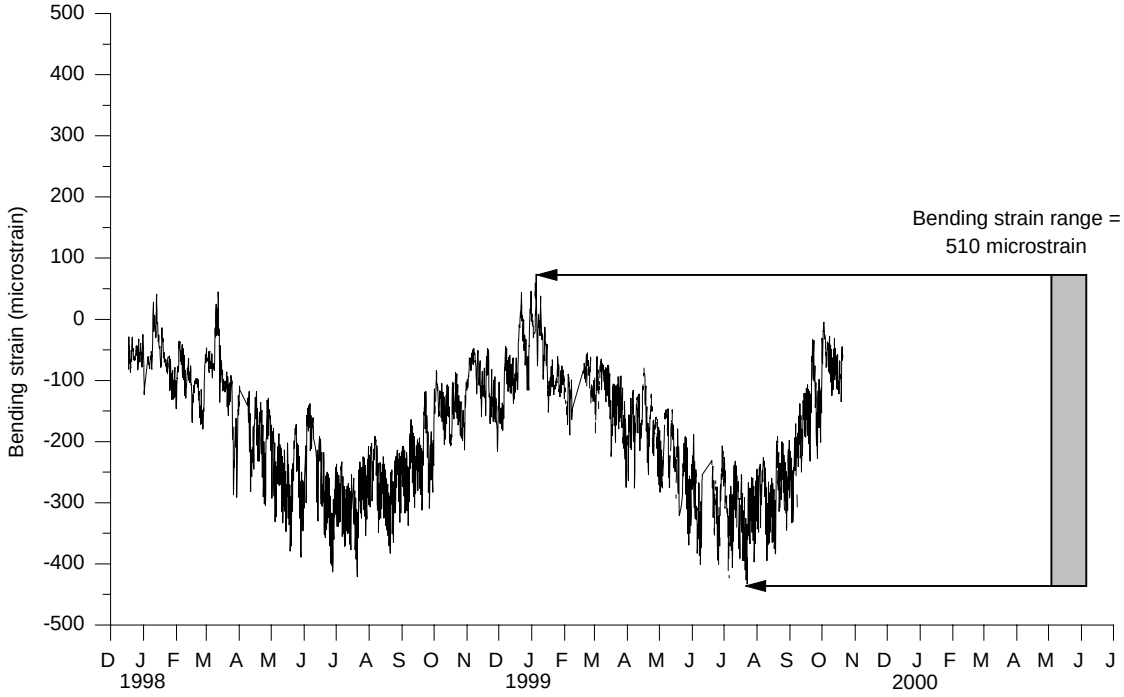

(b) X-axis bending strain

Figure 4.29. Biaxial, flexural-bending strains in the upper, monitored, cross section for the pile near the mid-width of the north abutment for Guthrie County Bridge

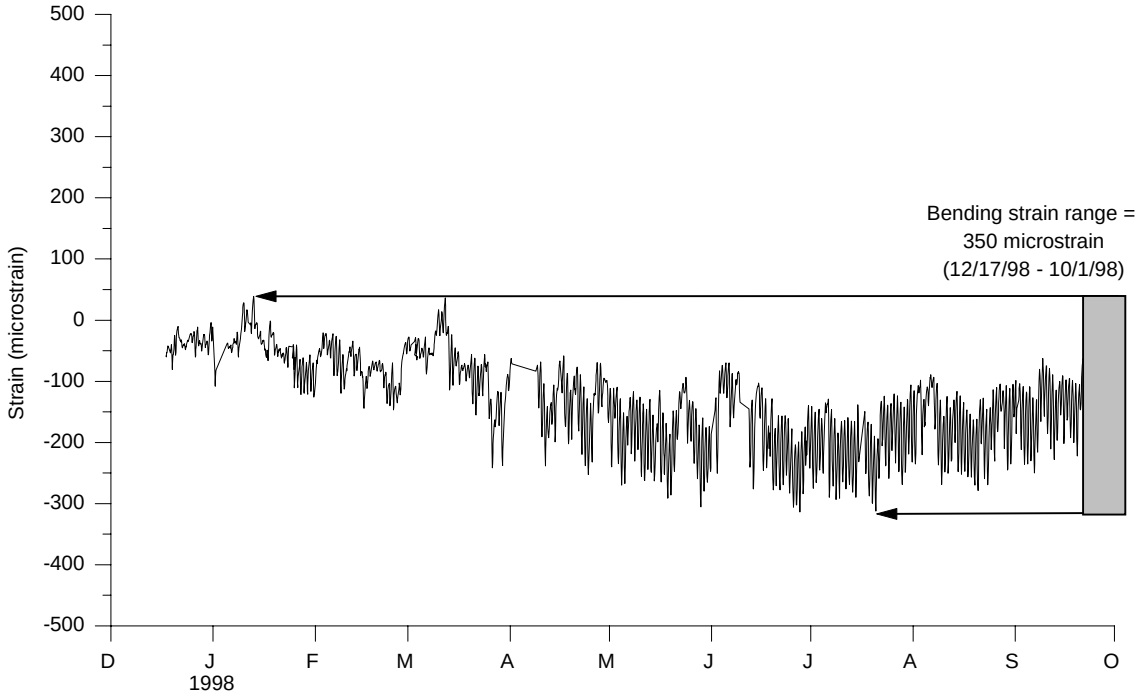

(a) Bending strain at 9 in. below the bottom of the pile cap

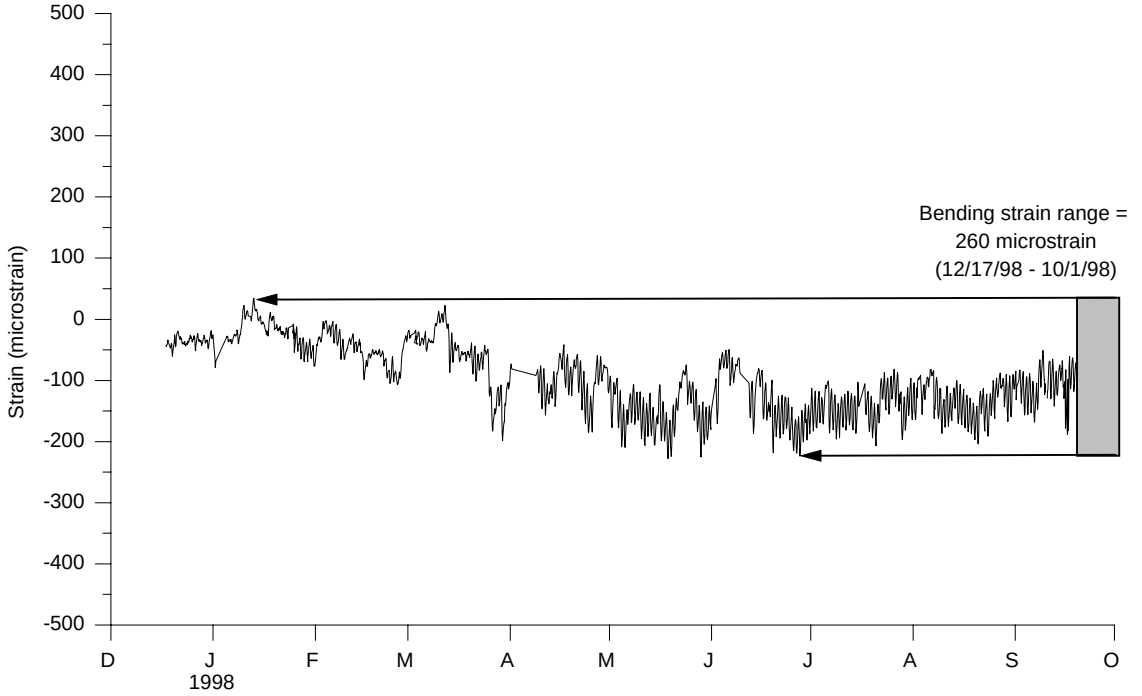

(b) Bending strain at 33 in. below the bottom of the pile cap

Figure 4.30. X-axis, flexural-bending strains at two cross sections for the west pile of the north abutment for the Guthrie County Bridge

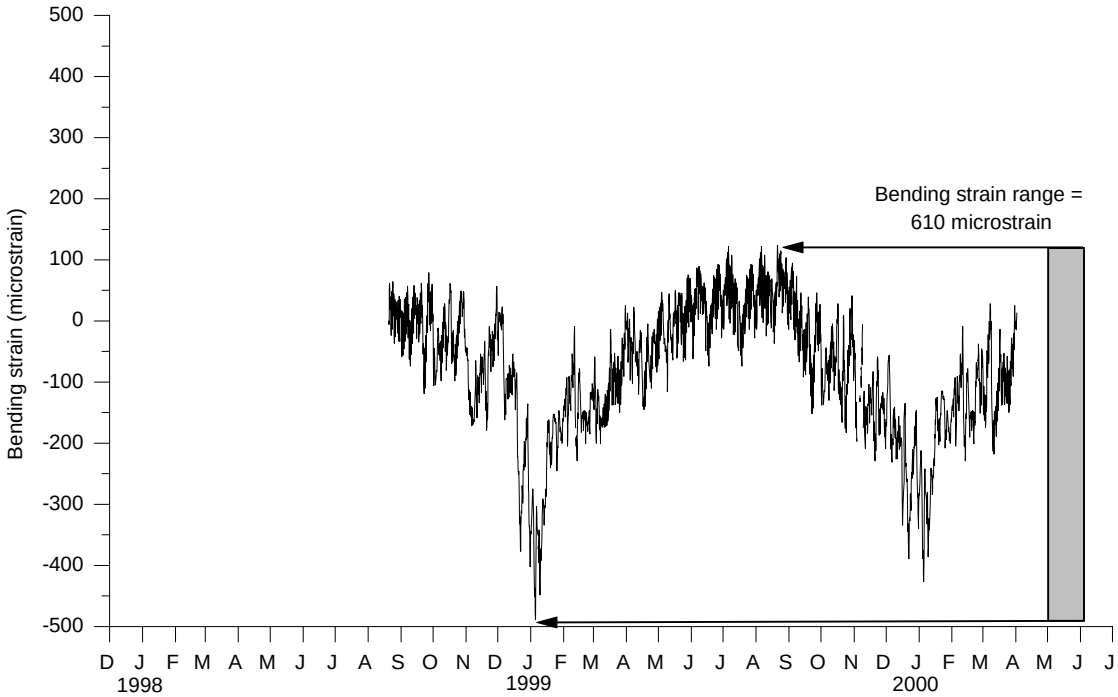

(a) Y-axis bending strain

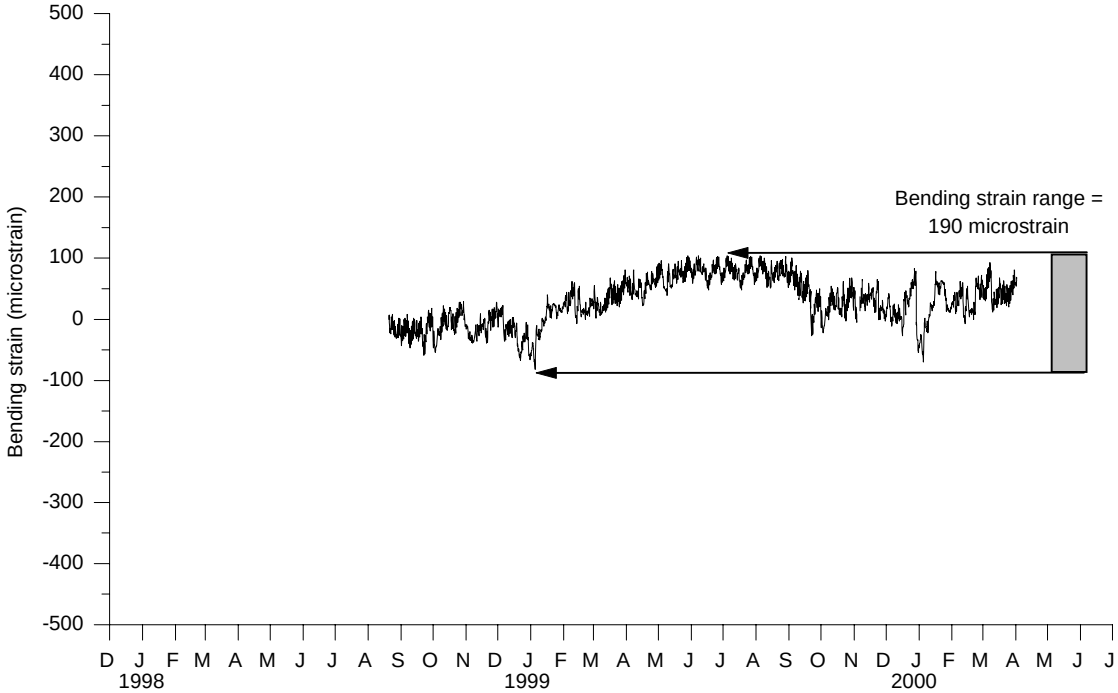

(b) X-axis bending strain

Figure 4.31. Biaxial, flexural-bending strains in the upper, monitored, cross section for the center pile of the east abutment for the Story County Bridge

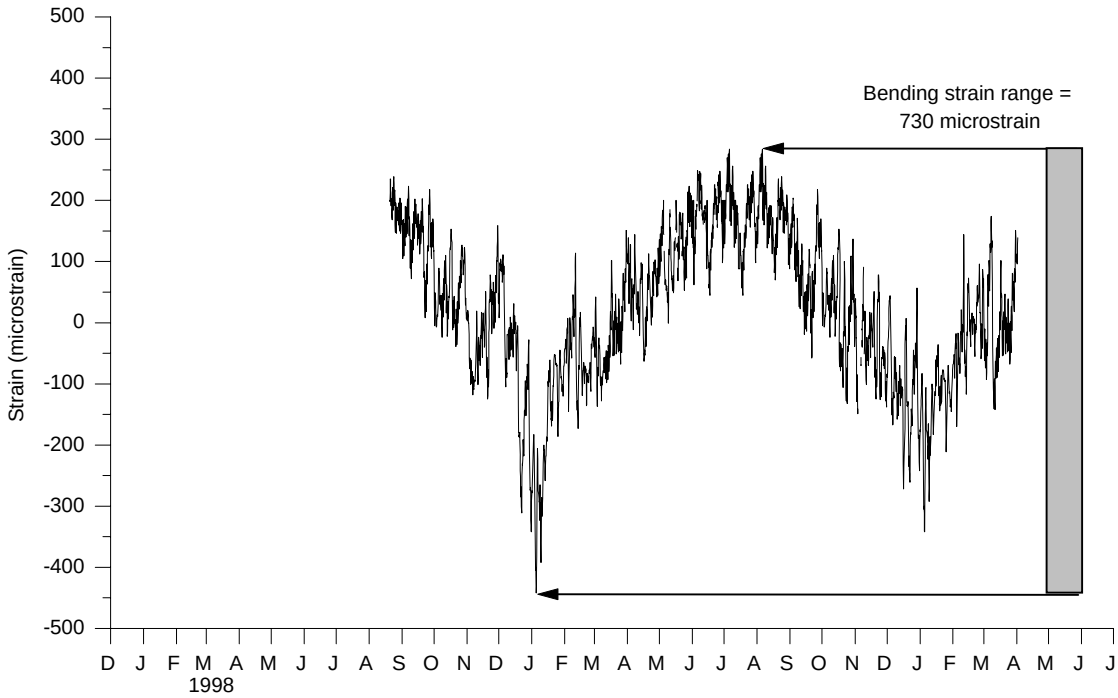

(a) Bending strain at 9 in. below the bottom of the pile cap

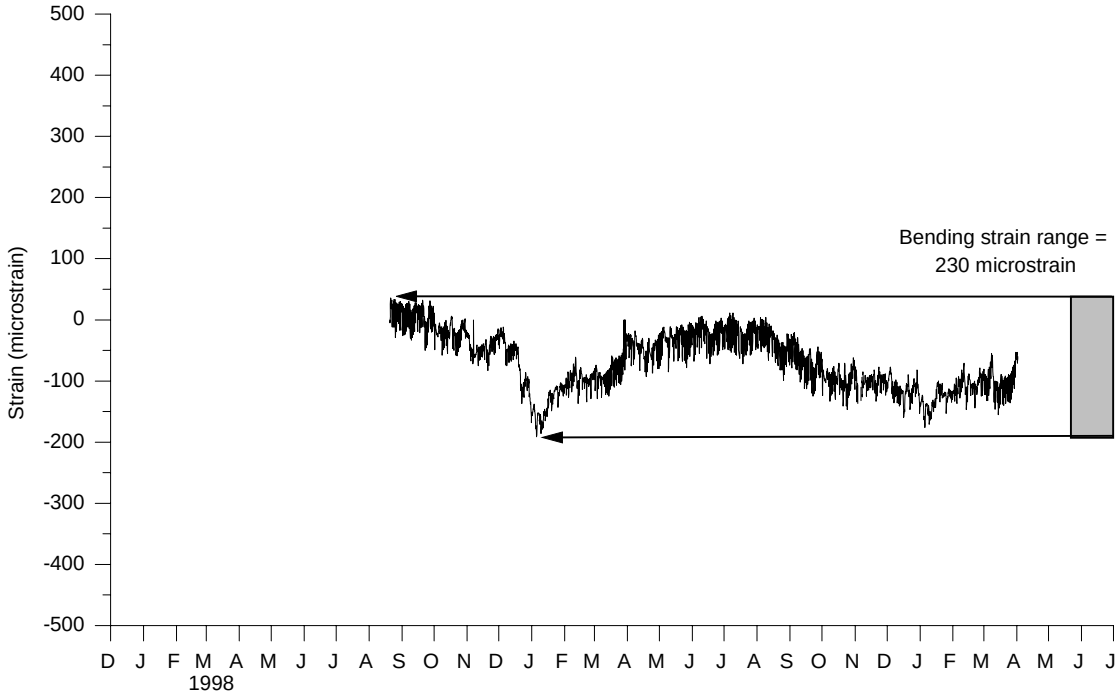

(b) Bending strain at 33 in. below the bottom of the pile cap

Figure 4.32. Y-axis, flexural-bending strains at two cross-sections for the north pile of the east abutment for the Story County Bridge

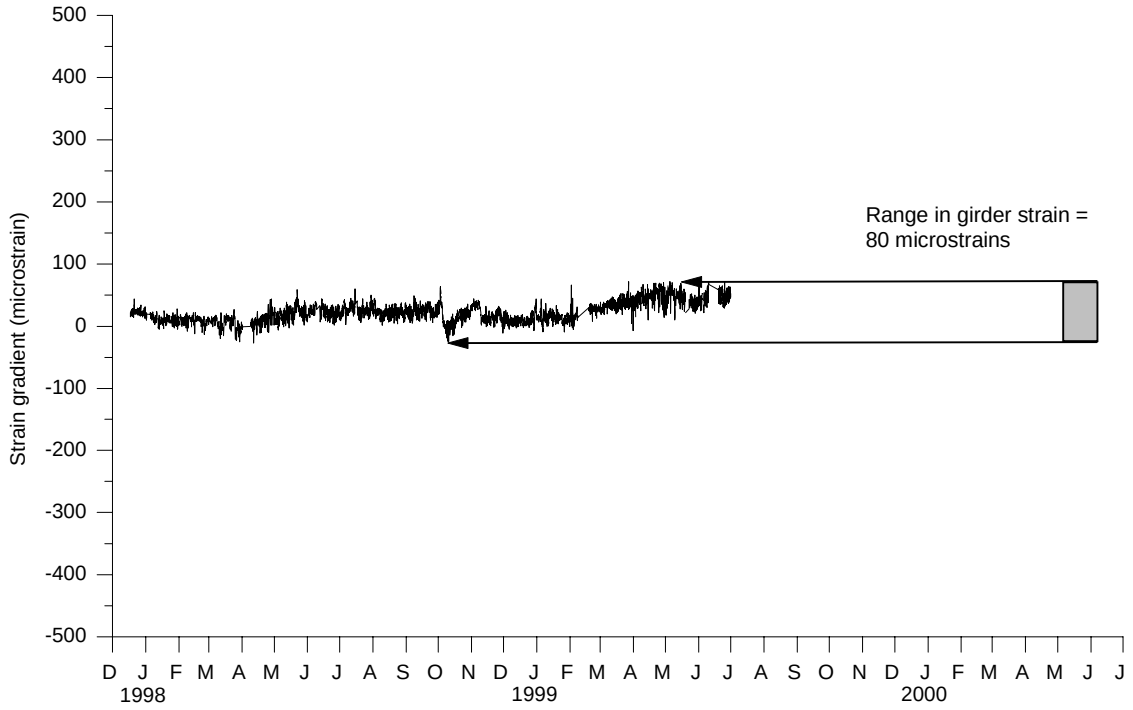

(a) Near the south pier

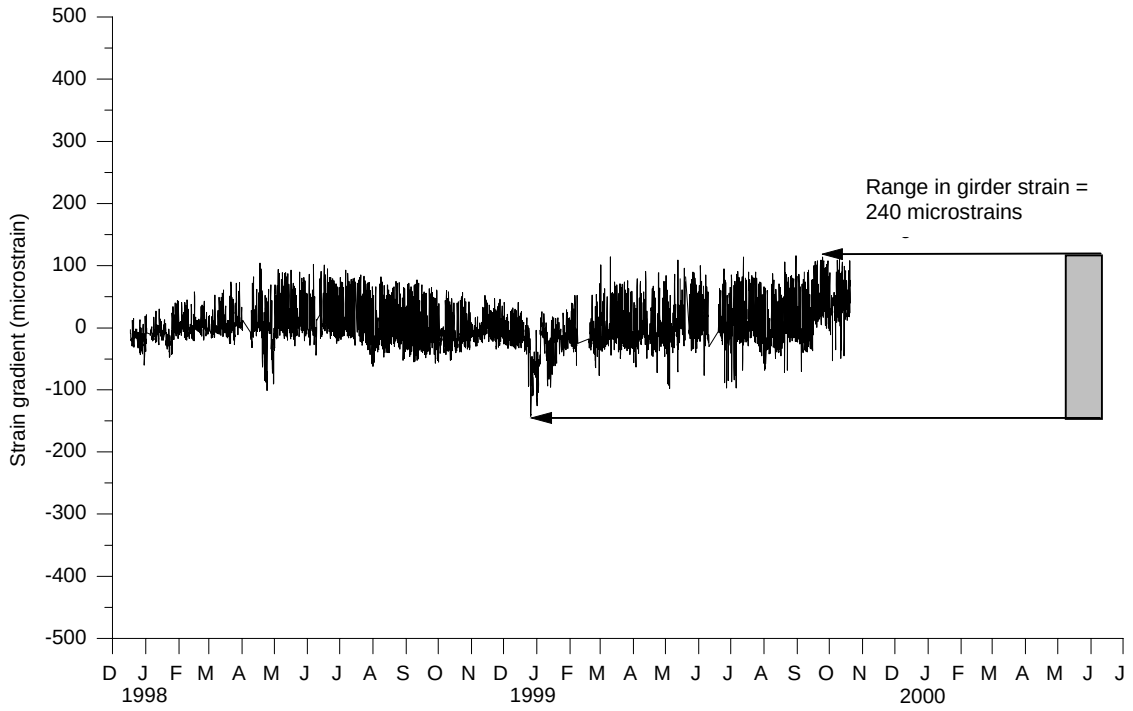

(b) Near the south abutment

Figure 4.33. Difference between the longitudinal strains in the top and bottom flanges for the east, exterior, PC girder for the Guthrie County Bridge

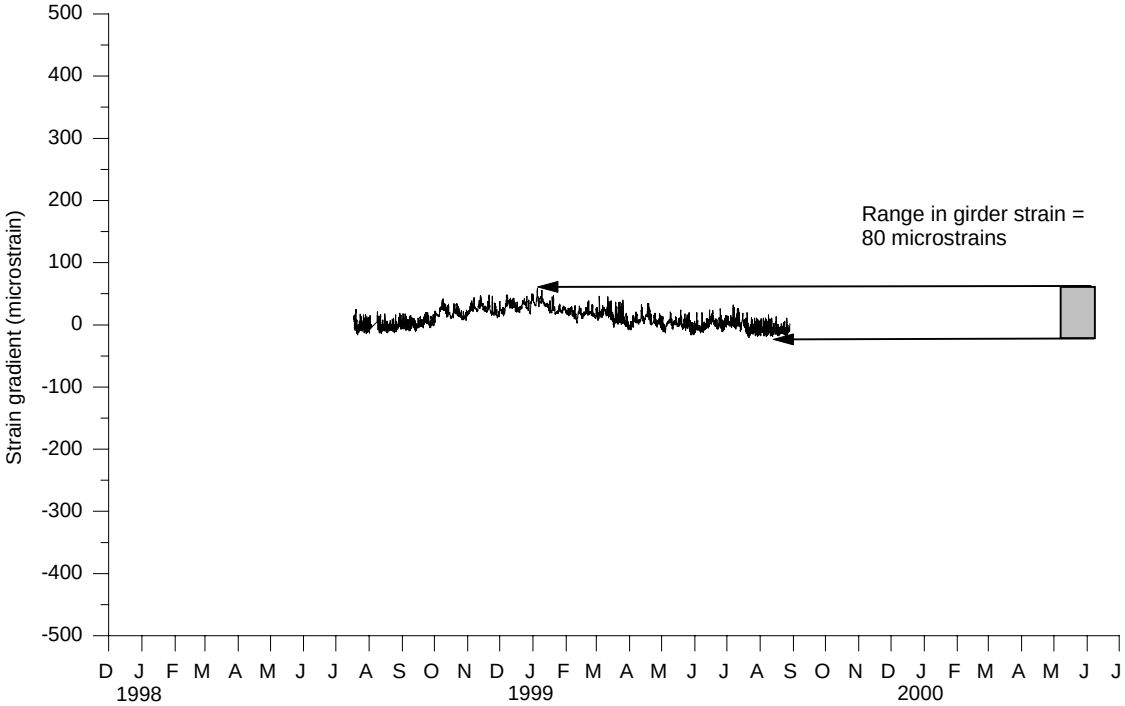

(a) Near the east pier

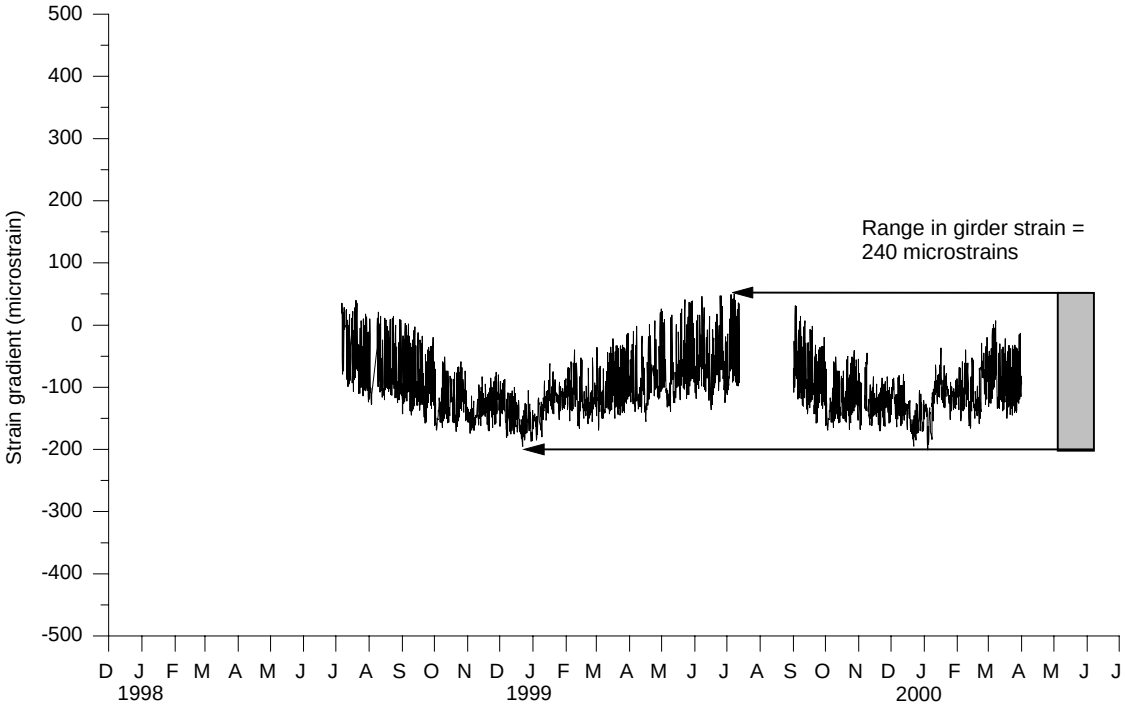

(b) Near the east abutment

Figure 4.34. Difference between the longitudinal strains in the top and bottom flanges for the north, exterior, PC girder for the Story County Bridge

Table 4.1. Reliable thermocouple data for the Guthrie County Bridge

Location	Instrument Code	1998												1999												2000		
		J	F	M	A	M	J	J	A	S	O	N	D	J	F	M	A	M	J	J	A	S	O	N	D	J	F	M
Group 1	TC-E-1SE-S	■	■	■	■	■	■	■	■	■	■	■	■	■	■	■	■	■	■	■	■	■	■	■	■	■	■	■
	TC-E-1SE-T	■	■	■	■	■	■	■	■	■	■	■	■	■	■	■	■	■	■	■	■	■	■	■	■	■	■	■
	TC-E-1SE-W	■	■	■	■	■	■	■	■	■	■	■	■	■	■	■	■	■	■	■	■	■	■	■	■	■	■	■
	TC-E-1SE-B	■	■	■	■	■	■	■	■	■	■	■	■	■	■	■	■	■	■	■	■	■	■	■	■	■	■	■
Group 2	TC-E-1SC-S	■	■	■	■	■	■	■	■	■	■	■	■	■	■	■	■	■	■	■	■	■	■	■	■	■	■	■
	TC-E-1SC-T	■	■	■	■	■	■	■	■	■	■	■	■	■	■	■	■	■	■	■	■	■	■	■	■	■	■	■
	TC-E-1SC-W							■	■	■	■	■	■	■	■													
	TC-E-1SC-B	■	■	■	■	■	■	■	■	■	■	■	■	■	■	■	■	■	■	■	■	■	■	■	■	■	■	■
Group 3	TC-E-1SW-S	■	■	■	■	■	■	■	■	■	■			■	■	■	■	■	■	■	■	■	■	■	■	■	■	■
	TC-E-1SW-T	■	■	■	■	■	■	■	■	■	■	■	■	■	■	■	■	■	■	■	■	■	■	■	■	■	■	■
	TC-E-1SW-W	■	■	■	■	■	■	■	■	■	■	■	■	■	■	■	■	■	■	■	■	■	■	■	■	■	■	■
	TC-E-1SW-B	■	■	■	■	■	■	■	■	■	■	■	■	■	■	■	■	■	■	■	■	■	■	■	■	■	■	■
Group 4	TC-E-1MSE-S	■	■	■	■	■	■	■	■	■	■	■	■	■	■	■	■	■	■	■	■	■	■	■	■	■	■	■
	TC-E-1MSE-T	■	■	■	■	■	■	■	■	■	■	■	■	■	■	■	■	■	■	■	■	■	■	■	■	■	■	■
	TC-E-1MSE-W	■	■	■	■	■	■	■	■	■	■	■	■	■	■	■	■	■	■	■	■	■	■	■	■	■	■	■
	TC-E-1MSE-B	■	■	■	■	■	■	■	■	■	■	■	■	■	■	■	■	■	■	■	■	■	■	■	■	■	■	■
Group 5	TC-E-1MSC-S	■	■	■	■	■	■	■	■	■	■	■	■	■			■	■	■	■	■	■	■	■	■	■	■	■
	TC-E-1MSC-T																											
	TC-E-1MSC-W	■	■	■	■	■	■	■	■	■	■	■	■	■			■	■	■	■	■	■	■	■	■	■	■	■
	TC-E-1MSC-B	■	■	■	■	■	■	■	■	■	■	■	■	■			■	■	■	■	■	■	■	■	■	■	■	■
Group 6	TC-E-1MSW-S	■	■	■	■	■	■	■	■	■	■	■	■	■	■	■	■	■	■	■	■	■	■	■	■	■	■	■
	TC-E-1MSW-T	■	■	■	■	■	■	■	■	■	■	■	■	■	■	■	■	■	■	■	■	■	■	■	■	■	■	■
	TC-E-1MSW-W	■	■	■	■	■	■	■	■	■	■	■	■	■	■	■	■	■	■	■	■	■	■	■	■	■	■	■
	TC-E-1MSW-B	■	■	■	■	■	■	■	■	■	■	■	■	■	■	■	■	■	■	■	■	■	■	■	■	■	■	■
Group 7	TC-E-2MSC-S		■	■	■	■	■	■	■	■	■	■	■	■	■	■	■	■	■	■	■	■	■	■	■	■	■	■
	TC-E-2MSC-T		■	■	■	■	■	■	■	■	■	■	■	■	■	■	■	■	■	■	■	■	■	■	■	■	■	■
	TC-E-1MSC-W		■	■	■	■	■	■	■	■	■	■	■	■	■	■	■	■	■	■	■	■	■	■	■	■	■	■
	TC-E-2MSC-B		■	■	■	■	■	■	■	■	■	■	■	■	■	■	■	■	■	■	■	■	■	■	■	■	■	■
Group 8	TC-E-3NC-S	■	■	■	■	■	■	■	■	■	■	■	■	■	■	■	■	■	■	■	■	■	■	■	■	■	■	■
	TC-E-3NC-T	■	■	■	■	■	■	■	■	■	■	■	■	■	■	■	■	■	■	■	■	■	■	■	■	■	■	■
	TC-E-3NC-W	■	■	■	■	■	■	■	■	■	■	■	■	■	■	■	■	■	■	■	■	■	■	■	■	■	■	■
	TC-E-3NC-B	■	■	■	■	■	■	■	■	■	■	■	■	■	■	■	■	■	■	■	■	■	■	■	■	■	■	■
Near DCDTs	TC-A-SEIT	■	■	■	■	■	■	■	■	■	■	■	■	■	■	■	■	■	■	■	■	■	■	■	■	■	■	■
	TC-A-SCIT	■	■	■	■	■	■	■	■	■	■	■	■	■	■	■	■	■	■	■	■	■	■	■	■	■	■	■
	TC-A-SWIT		■	■	■	■	■																					
	TC-A-SWXT	■	■	■	■	■	■	■	■	■	■	■	■	■	■	■	■	■	■	■	■	■	■	■	■	■	■	■
	TX-A-NCIT	■	■	■	■	■	■	■	■	■	■	■	■	■	■	■	■	■	■	■	■	■	■	■	■	■	■	■
Various girder locations	TC-E-1NE-T																											
	TC-E-1NE-B	■	■	■	■	■	■	■	■	■	■	■	■	■			■	■	■	■	■	■	■	■	■	■	■	■
	TC-E-1NC-T	■	■	■	■	■	■	■	■	■	■	■	■	■			■	■	■	■	■	■	■	■	■	■	■	■
	TC-E-1NC-B	■	■	■	■	■	■	■	■	■	■	■	■	■			■	■	■	■	■	■	■	■	■	■	■	■
	TC-E-1NW-T	■	■	■	■	■	■	■	■	■	■	■	■	■			■	■	■	■	■	■	■	■	■	■	■	■
	TC-E-1NW-B																											
	TC-E-3SC-T	■	■	■	■	■	■	■	■	■	■	■	■	■	■	■	■	■	■	■	■	■	■	■	■	■	■	■
	TC-E-3SC-B				■	■	■	■	■	■	■	■	■	■	■	■	■	■	■	■	■	■	■	■	■	■	■	■
Piles	TC-S-SWP	■	■	■	■	■	■	■	■	■	■	■	■	■	■	■	■	■	■	■	■	■	■	■	■	■	■	■
	TC-S-SCP	■	■	■	■	■	■	■	■	■	■	■	■	■	■	■	■	■	■	■	■	■	■	■	■	■	■	■
	TC-S-SEP	■	■	■	■	■	■	■	■	■	■	■	■	■	■	■	■	■	■	■	■	■	■	■	■	■	■	■
	TC-S-NCP	■	■	■	■	■	■	■	■	■	■	■	■	■	■	■			■	■	■							
	TC-S-NWP	■	■	■	■	■	■	■	■		■	■	■	■	■	■	■	■	■	■	■	■	■	■	■	■	■	■
Abutment	TC-E-SAF	■	■	■	■	■	■	■	■	■	■	■	■	■	■	■	■	■	■	■	■	■	■	■	■	■	■	■
Air temp.	TCAIRTEMP								■	■	■	■	■	■	■	■	■	■	■	■	■	■	■	■	■	■	■	■
Data-logger	mp6tempC	■	■	■	■	■	■	■	■	■	■	■	■	■	■	■	■	■	■	■	■	■	■	■	■	■	■	■

Legend		
	■	Thermocouple data were reliable for the month
		Thermocouple data were unreliable for the month

Table 4.2. Reliable thermocouple data for the Story County Bridge

Location	Instrument Code	1998												1999												2000		
		J	F	M	A	M	J	J	A	S	O	N	D	J	F	M	A	M	J	J	A	S	O	N	D	J	F	M
Group 1	TC-E-1EC-S																											
	TC-E-1EC-T																											
	TC-E-1EC-W																											
	TC-E-1EC-B																											
Group 2	TC-E-1MSNX-S																											
	TC-E-1MSNX-W																											
	TC-E-1MSNX-B																											
Group 3	TC-E-1MSNI-SN																											
	TC-E-1MSNI-T																											
	TC-E-1MSNI-W																											
	TC-E-1MSNI-B																											
Group 4	TC-E-1MSCS-SN																											
	TC-E-1MSCS-T																											
	TC-E-1MSCS-W																											
	TC-E-1MSCS-B																											
Group 5	TC-E-1MSSI-SS																											
	TC-E-1MSSI-T																											
	TC-E-1MSSI-W																											
	TC-E-1MSSI-B																											
Group 6	TC-E-1MSSX-S																											
	TC-E-1MSSX-W																											
	TC-E-1MSSX-B																											
Group 7	TC-E-1WC-S																											
	TC-E-1WC-T																											
	TC-E-1WC-W																											
	TC-E-1WC-B																											
Group 8	TC-E-2MSC-S																											
	TC-E-2MSC-T																											
	TC-E-2MSC-W																											
	TC-E-2MSC-B																											
Group 9	TC-E-3WC-S																											
	TC-E-3WC-T																											
	TC-E-3WC-W																											
	TC-E-3WC-B																											
Various Locations	TC-E-1MSCN-SC																											
	TC-E-1MSCN-SN																											
	TC-E-1-EN-T																											
	TC-E-1-EN-B																											
	TC-E-1MSCS-SS																											
	TC-E-1MSCS-SC																											
	TC-E-1ES-T																											
	TC-E-1ES-B																											
	TC-E-1MSNI-SC																											
	TC-E-1MSSI-SC																											
	TC-E-1WN-T																											
	TC-E-1WN-B																											
	TC-E-1WS-T																											
	TC-E-1WS-B																											
	TC-E-3EC-T																											
	TC-E-3EC-B																											
	TC-AIRTEMP																											

Legend		
		Thermocouple data were reliable for the month
		Thermocouple data were unreliable for the month

Table 4.3. Reliable displacement-transducer data for the Guthrie County Bridge

Displacement	Instrument Code	1998												1999												2000		
		J	F	M	A	M	J	J	A	S	O	N	D	J	F	M	A	M	J	J	A	S	O	N	D	J	F	M
Longitudinal abutment displacement	SP-SE-LB	■	■	■	■	■	■	■	■	■	■	■	■	■	■	■	■	■	■	■	■	■	■	■	■	■	■	■
	SP-SC-LT	■	■	■	■	■	■	■	■	■	■	■	■	■	■	■	■	■	■	■	■	■	■	■	■	■	■	■
	SP-SC-LB	■	■	■	■	■	■	■	■	■	■	■	■	■	■	■	■	■	■	■	■	■	■	■	■	■	■	■
	SP-SW-LB	■	■	■	■	■	■	■	■	■	■	■	■	■	■	■	■											
	SP-NC-LB	■	■	■	■	■	■	■	■	■	■	■	■	■	■	■	■	■	■	■				■	■	■	■	■
Transverse abutment	SP-SE-T	■	■	■	■	■	■	■	■	■	■	■	■	■	■	■	■	■	■	■	■	■	■	■	■	■	■	■
	SP-SW-T	■	■	■	■	■	■	■	■	■	■	■	■	■	■	■	■	■	■	■								
Relative girder	SP-SC-RGB	■	■	■	■	■	■	■	■	■	■	■	■	■	■	■	■	■	■	■	■	■						
	SP-SC-RGT					■	■	■	■	■	■	■	■	■	■	■	■	■	■	■	■	■	■	■	■	■	■	■
Relative pile	SP-SC-RPB	■	■	■	■	■	■	■	■	■	■	■	■	■	■	■												
	SP-SC-RPF	■	■	■	■	■	■	■	■	■	■	■	■	■	■	■	■	■	■	■	■	■	■	■	■	■	■	■
Relative pier	SP-SP-RPL	■	■	■	■	■	■	■	■	■	■	■	■	■	■	■	■	■	■	■	■	■	■	■	■	■	■	■
	SP-NP-RPL								■	■	■	■	■	■	■	■	■	■	■	■	■	■	■	■	■	■	■	■
Abut. rotation	TM-SC-LR								■	■	■	■	■	■	■	■	■	■	■	■	■	■	■	■	■	■	■	■

Legend		
	■	Displacement transducer data were reliable for the month
		Displacement transducer data were unreliable for the month

Table 4.4. Reliable displacement-transducer data for the Story County Bridge

Displacement	Instrument Code	1998												1999												2000		
		J	F	M	A	M	J	J	A	S	O	N	D	J	F	M	A	M	J	J	A	S	O	N	D	J	F	M
Longitudinal abutment	SP-EN-L								■	■		■	■	■	■	■	■	■	■	■	■	■	■	■	■	■	■	■
	SP-EC-L								■	■		■	■	■	■	■	■	■	■	■	■	■	■	■	■	■	■	■
	SP-ES-L								■	■		■	■	■	■	■	■	■			■	■	■	■	■	■	■	■
	SP-WC-L								■	■		■	■	■	■	■	■	■	■	■	■			■	■	■	■	■
Transverse abutment	SP-ES-T								■	■		■	■	■	■	■	■	■	■	■	■	■	■	■	■	■	■	■
	SP-EN-T																											
Relative pile	SP-EC-RPB								■	■		■	■	■	■	■	■	■	■	■	■	■	■	■	■	■	■	■
	SP-EC-RPF								■	■		■	■	■	■	■	■	■	■	■	■	■	■	■	■	■	■	■
Relative pier	SP-EP-L								■	■		■	■	■	■	■	■	■	■	■	■	■	■	■	■	■	■	■
	SP-WP-L								■	■		■	■	■	■	■	■	■	■	■	■	■	■	■	■	■	■	■
Abut. rotation	TM-SC-LR								■	■	■	■	■	■	■	■	■	■	■	■	■	■	■	■	■	■	■	■

Legend		
	■	Displacement transducer data were reliable for the month
		Displacement transducer data were unreliable for the month

Table 4.5. Reliable pile-strain-gage data for the Guthrie County Bridge

Pile	Instrument Code	1998												1999												2000		
		J	F	M	A	M	J	J	A	S	O	N	D	J	F	M	A	M	J	J	A	S	O	N	D	J	F	M
South abutment: West Pile	SG-SWP-SWT																											
	SG-SWP-SET																											
	SG-SWP-NWT																											
	SG-SWP-NET																											
	SG-SWP-SWB																											
	SG-SWP-SEB																											
	SG-SWP-NWB																											
	SG-SWP-NEB																											
South abutment: Center Pile	SG-SCP-SWT																											
	SG-SCP-SET																											
	SG-SCP-NWT																											
	SG-SCP-NET																											
	SG-SCP-SWB																											
	SG-SCP-SEB																											
	SG-SCP-NWB																											
	SG-SCP-NEB																											
South abutment: East Pile	SG-SEP-SWT																											
	SG-SEP-SET																											
	SG-SEP-NWT																											
	SG-SEP-NET																											
	SG-SEP-SWB																											
	SG-SEP-SEB																											
	SG-SEP-NWB																											
	SG-SEP-NEB																											
North abutment: West Pile	SG-NWP-SWT																											
	SG-NWP-SET																											
	SG-NWP-NWT																											
	SG-NWP-NET																											
	SG-NWP-SWB																											
	SG-NWP-SEB																											
	SG-NWP-NWB																											
	SG-NWP-NEB																											
North abutment: Center Pile	SG-NCP-SWT																											
	SG-NCP-SET																											
	SG-NCP-NWT																											
	SG-NCP-NET																											
	SG-NCP-SWB																											
	SG-NCP-SEB																											
	SG-NCP-NWB																											
	SG-NCP-NEB																											

Legend	
	Pile strain gage data were reliable for the month
	Pile strain gage data were unreliable for the month
	Dummy gage data were reliable from April of 1998 through May of 1999

Table 4.6. Reliable pile-strain-gage data for the Story County Bridge

Pile	Instrument Code	1998												1999												2000		
		J	F	M	A	M	J	J	A	S	O	N	D	J	F	M	A	M	J	J	A	S	O	N	D	J	F	M
East abutment: North Pile	ENPSET								■	■	■	■	■	■	■	■	■	■	■	■	■	■		■	■	■	■	■
	ENPSWT								■	■		■	■	■	■	■	■	■	■	■	■	■	■	■	■	■	■	■
	ENPNET								■	■	■	■	■	■	■	■	■	■	■	■	■	■	■	■	■	■	■	■
	ENPNWT								■	■	■	■	■	■	■	■	■	■	■	■	■	■	■	■	■	■	■	■
	ENPSEB								■	■	■	■	■	■	■	■	■	■	■	■	■	■	■	■	■	■	■	■
	ENPSWB								■	■	■	■	■	■	■	■					■	■	■	■	■	■	■	■
	ENPNEB								■	■	■	■	■	■	■	■	■	■	■	■	■	■	■	■	■	■	■	■
	ENPNWB								■	■	■	■	■	■														
East abutment: Center Pile	ECPSET								■	■	■	■	■	■	■	■	■	■	■	■	■	■	■	■	■	■	■	■
	ECPSWT								■	■	■	■	■	■	■	■	■	■	■	■	■	■	■	■	■	■	■	■
	ECPNET												■	■	■	■	■	■	■	■	■	■	■	■	■	■	■	■
	ECPNWT								■	■	■	■	■	■	■	■	■	■	■	■	■	■	■	■	■	■	■	■
	ECPSEB																											
	ECPSWB																											
	ECPNEB								■	■	■	■	■	■	■	■	■	■	■	■	■	■	■	■	■	■	■	■
	ECPNWB																											
East abutment: South Pile	ESPSET								■	■	■	■	■	■	■	■	■	■	■	■	■	■	■	■	■	■	■	■
	ESPSWT								■	■	■	■	■	■														
	ESPNET								■	■	■	■	■	■	■	■	■	■	■	■	■	■	■	■	■	■	■	■
	ESPNWT											■	■	■	■	■	■	■	■	■	■	■	■	■	■	■	■	■
	ESPSEB																											
	ESPSWB								■	■	■	■	■	■	■	■												
	ESPNEB																											
	ESPNWB								■	■	■	■	■	■	■	■	■	■	■	■		■	■	■	■	■	■	■
West abutment: Center Pile	WCPSET											■	■	■	■	■	■	■	■	■	■							
	WCPSWT																											
	WCPNET								■	■	■	■	■	■	■	■	■	■	■									
	WCPNWT								■	■	■	■	■	■	■	■	■	■	■	■	■	■						
	WCPSEB								■	■	■	■	■	■	■	■	■	■	■	■	■	■	■	■	■	■	■	■
	WCPSWB								■	■	■	■	■	■	■	■	■											
	WCPNEB								■	■	■	■	■	■	■	■	■	■										
	WCPNWB								■	■	■	■	■	■	■	■	■	■	■	■	■	■	■	■	■	■	■	■

Legend		
	■	Pile strain gage data were reliable for the month
		Pile strain gage data were unreliable for the month

Table 4.7. Reliable pile-strain-component data for the Guthrie County Bridge

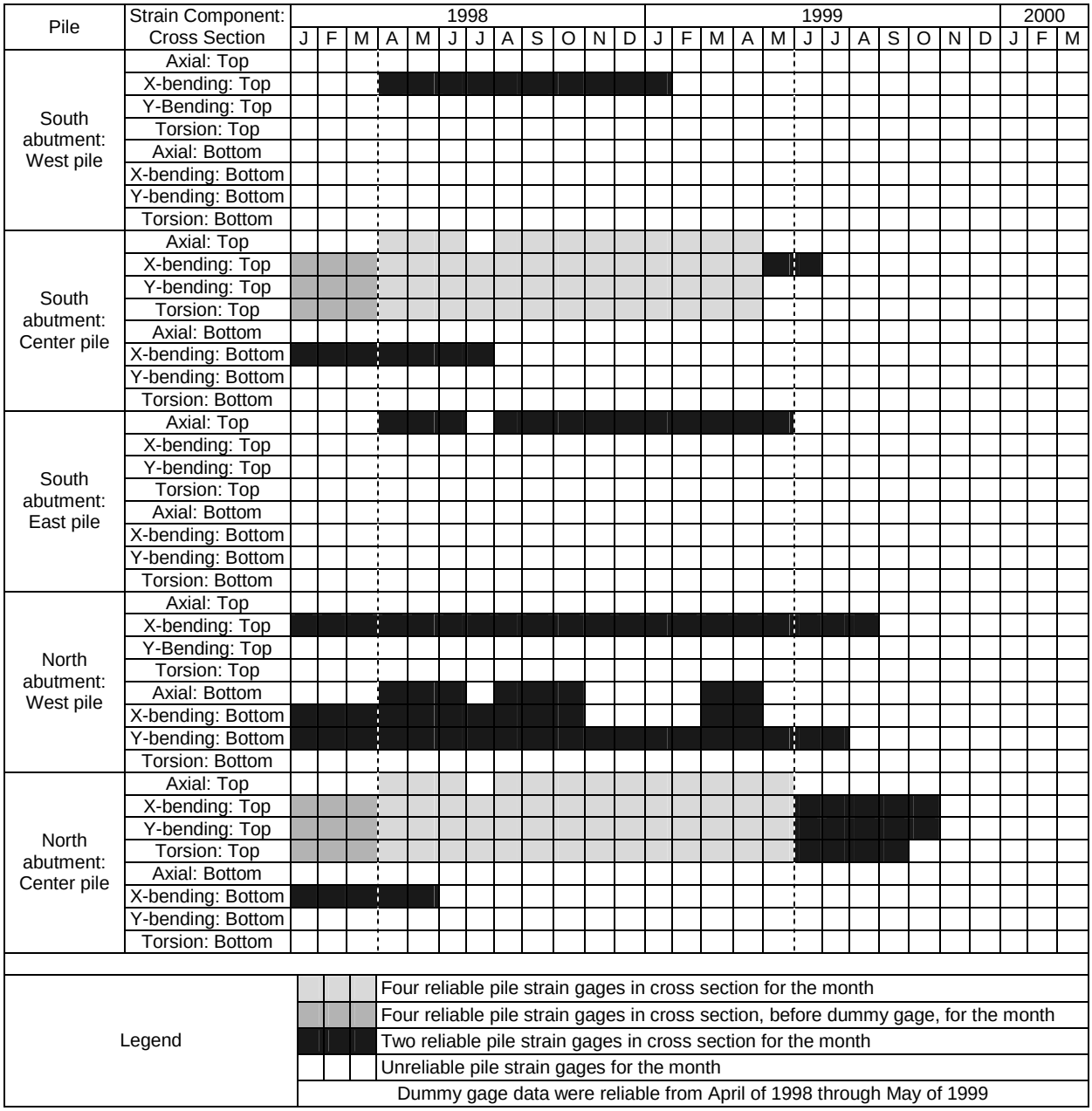

Table 4.8. Reliable pile-strain-component data for the Story County Bridge

Pile	Strain Component: Cross Section	1998												1999												2000		
		J	F	M	A	M	J	J	A	S	O	N	D	J	F	M	A	M	J	J	A	S	O	N	D	J	F	M
East abutment: North pile	Axial: Top																											
	X-bending: Top																											
	Y-bending: Top																											
	Torsion: Top																											
	Axial: Bottom																											
	X-bending: Bottom																											
	Y-bending: Bottom																											
	Torsion: Bottom																											
East abutment: Center pile	Axial: Top																											
	X-bending: Top																											
	Y-bending: Top																											
	Torsion: Top																											
	Axial: Bottom																											
	X-bending: Bottom																											
	Y-bending: Bottom																											
	Torsion: Bottom																											
East abutment: South pile	Axial: Top																											
	X-bending: Top																											
	Y-bending: Top																											
	Torsion: Top																											
	Axial: Bottom																											
	X-bending: Bottom																											
	Y-bending: Bottom																											
	Torsion: Bottom																											
West abutment: Center pile	Axial: Top																											
	X-bending: Top																											
	Y-bending: Top																											
	Torsion: Top																											
	Axial: Bottom																											
	X-bending: Bottom																											
	Y-bending: Bottom																											
	Torsion: Bottom																											

Legend	
	Four reliable pile strain gages in the cross-section for the month
	Two reliable pile strain gages in the cross-section for the month
	Unreliable pile strain gages for the month

Table 4.9. Reliable concrete-strain-gage data for the Guthrie County Bridge

Girder	Instrument Code	1998												1999												2000		
		J	F	M	A	M	J	J	A	S	O	N	D	J	F	M	A	M	J	J	A	S	O	N	D	J	F	M
Individual girder strain gages																												
East	SG-1SE-T																											
	SG-1SE-B																											
	SG-1NE-T																											
	SG-1NE-B																											
Center	SG-1SC-T																											
	SG-1SC-B																											
	SG-1NC-T																											
	SG-1NC-B																											
	SG-3NC-T																											
	SG-3NC-B																											
	SG-3SC-T																											
	SG-3SC-B																											
West	SG-1SW-T																											
	SG-1SW-B																											
	SG-1NW-T																											
	SG-1NW-B																											
Girder	Support Location	1998												1999												2000		
		J	F	M	A	M	J	J	A	S	O	N	D	J	F	M	A	M	J	J	A	S	O	N	D	J	F	M
Differences between longitudinal strains in flanges																												
East	South abutment																											
	South pier																											
Center	South abutment																											
	South pier																											
	North pier																											
	North abutment																											
West	South abutment																											
	South pier																											

Legend		
		Girder strain gage data were reliable for the month
		Girder strain gage data were unreliable for the month

Table 4.10. Reliable concrete-strain-gage data for the Story County Bridge

Girder	Instrument Code	1998												1999												2000		
		J	F	M	A	M	J	J	A	S	O	N	D	J	F	M	A	M	J	J	A	S	O	N	D	J	F	M
Individual girder strain gages																												
North	1EN-T																											
	1EN-B																											
Center	1EC-T																											
	1EC-B																											
	1WC-T																											
	1WC-B																											
	3EC-T																											
	3EC-B																											
	3WC-T																											
	3WC-B																											
South	1ES-T																											
	1ES-B																											
Girder	Support Location	1998												1999												2000		
		J	F	M	A	M	J	J	A	S	O	N	D	J	F	M	A	M	J	J	A	S	O	N	D	J	F	M
Differences between longitudinal strains in flanges																												
North	East abutment																											
Center	East abutment																											
	East pier																											
	West pier																											
	West abutment																											
South	East abutment																											

Legend		
		Girder strain gage data were reliable for the month
		Girder strain gage data were unreliable for the month

Table 4.11. Temperatures at the time of the maximum, average, bridge temperature (July 20, 1998, 8:00 p.m.) at the Guthrie County Bridge

Gage	Measured Temperatures (°F)				Extrapolated Bi-linear Temperatures (°F)		
	Slab	Top Flange	Web	Bottom Flange	Top of Slab	Top of Girder	Bot. of Girder
1MSE	109.1	97.0	96.1	93.6	123.7	97.4	93.4
1MSW	108.7	98.2	96.5	93.3	121.2	98.7	93.0
1SC	109.4	97.1	91.4	89.7	125.4	96.6	88.4
1SE	105.3	93.3	90.5	87.9	120.2	93.4	87.3
1SW	105.8	95.6	95.5	89.0	116.7	97.1	89.2
3NC	110.6	96.4	91.5	89.6	128.8	96.1	88.5
2MSC	113.9	99.7	92.7	92.2	132.9	98.7	90.5
1MSC	115.3	n.a.	93.3	92.8	138.4	96.8	90.2
3SC	n.a.	97.3	n.a.	97.8	n.a.	97.3	97.9
1NW	n.a.	95.3	n.a.	n.a.	n.a.	n.a.	n.a.
1NC	n.a.	96.7	n.a.	91.6	n.a.	97.0	91.2
1NE	n.a.	n.a.	n.a.	92.6	n.a.	n.a.	n.a.
Average	109.8	96.7	93.4	91.8	126.3	96.5	91.1

Table 4.12. Temperatures at the time of the minimum, average, bridge temperature (January 5, 1999, 4:00 a.m.) at the Guthrie County Bridge

Gage	Measured Temperatures (°F)				Extrapolated Bi-linear Temperatures (°F)		
	Slab	Top Flange	Web	Bottom Flange	Top of Slab	Top of Girder	Bot. of Girder
1MSE	-14.3	-10.8	-14.8	-14.9	-18.0	-11.4	-15.8
1MSW	-13.7	-10.2	-13.2	-13.0	-17.5	-10.7	-13.8
1SC	-11.2	-8.1	n.a.	-11.6	-15.3	-7.9	-11.8
1SE	-10.2	-7.0	-13.0	-13.0	-13.0	-7.9	-14.4
1SW	-9.6	-6.8	-11.8	-11.1	-11.9	-7.8	-12.3
3NC	-11.8	-7.7	-9.1	-10.6	-17.1	-7.6	-10.9
2MSC	-14.2	-10.9	-11.6	-12.6	-18.5	-10.8	-12.7
1MSC	n.a.	n.a.	n.a.	n.a.	n.a.	n.a.	n.a.
3SC	n.a.	-11.8	n.a.	-14.8	n.a.	-11.7	-15.1
1NW	n.a.	n.a.	n.a.	n.a.	n.a.	n.a.	n.a.
1NC	n.a.	n.a.	n.a.	n.a.	n.a.	n.a.	n.a.
1NE	n.a.	n.a.	n.a.	n.a.	n.a.	n.a.	n.a.
Average	-12.2	-9.2	-11.8	-12.7	-15.6	-9.4	-13.3

Table 4.13. Temperatures at the time of the maximum, average, bridge temperature (June 20, 1998, 6:00 p.m.) at the Story County Bridge

Gage	Measured Temperatures (°F)				Extrapolated Bi-linear Temperatures (°F)		
	Slab	Top Flange	Web	Bottom Flange	Top of Slab	Top of Girder	Bot. of Girder
1EN	n.a.	n.a.	n.a.	n.a.	n.a.	n.a.	n.a.
1EC	117.5	96.6	89.4	n.a.	137.5	97.5	n.a.
1ES	n.a.	94.3	n.a.	85.5	n.a.	94.7	85.5
1MSNX	n.a.	n.a.	89.1	88.3	n.a.	89.7	88.3
1MSNI	115.4	95.3	88.0	86.6	136.5	94.3	86.6
1MSC	112.8	n.a.	89.6	88.6	135.2	90.4	88.6
1MSSI	114.5	92.7	89.8	89.8	136.8	92.2	89.8
1MSSX	95.7	n.a.	91.2	92.0	100.8	90.6	92.0
1WS	n.a.	93.1	n.a.	90.9	n.a.	93.2	90.9
1WC	119.0	97.6	91.3	89.4	141.1	96.9	89.4
1WN	n.a.	95.6	n.a.	89.3	n.a.	95.9	89.3
2MSC	114.9	92.0	90.0	89.5	138.0	91.7	89.5
3WC	117.8	98.2	96.6	86.9	135.6	100.0	86.9
3EC	n.a.	97.2	n.a.	n.a.	n.a.	n.a.	n.a.
Average	114.1	97.0	91.6	90.4	132.9	95.9	88.6

Table 4.14. Temperatures at the time of the minimum, average, bridge temperature (January 5, 1999, 2:00 a.m.) at the Story County Bridge

Gage	Measured Temperatures (°F)				Extrapolated Bi-linear Temperatures (°F)		
	Slab	Top Flange	Web	Bottom Flange	Top of Slab	Top of Girder	Bot. of Girder
1EN	n.a.	-4.1	n.a.	n.a.	n.a.	n.a.	n.a.
1EC	-12.8	-7.0	-5.5	-7.6	-19.3	-6.3	-7.2
1ES	n.a.	-0.8	n.a.	-6.1	n.a.	-0.6	-6.8
1MSNX	-7.8	n.a.	-12.9	-14.7	n.a.	-11.5	-15.1
1MSNI	-2.6	-5.4	-10.7	-11.1	1.0	-6.3	-12.6
1MSC	-13.9	n.a.	-6.9	-8.8	-22.5	-5.4	-9.2
1MSSI	-10.0	-14.5	-7.6	-8.0	-6.8	-13.2	-4.7
1MSSX	-5.1	n.a.	-9.7	-12.5	-2.6	-7.5	-13.1
1WS	n.a.	n.a.	n.a.	-6.6	n.a.	-19.5	-2.2
1WC	-12.4	-6.1	-4.8	-7.6	-19.6	-5.3	-7.3
1WN	n.a.	-3.9	n.a.	-11.9	n.a.	-3.4	-14.8
2MSC	-12.0	n.a.	-6.5	-10.4	-4.5	-19.4	-3.1
3WC	-11.9	-6.3	n.a.	-7.4	-17.6	-6.2	-7.8
3EC	n.a.	-8.0	n.a.	n.a.	n.a.	n.a.	n.a.
Average	-11.3	-8.9	-9.4	-10.7	-13.9	-8.7	-10.9

Table 4.15. Difference between the longitudinal strains in the top and bottom flanges of the PC girders

Bridge	Girder	Strain difference (micro-strains)	
		Abutment	Pier
Guthrie County Bridge	West girder	170	n.a.
	Center girder	200	70[a]
	East girder	240	80
Story County Bridge	South girder	180	n.a.
	Center girder	230[b]	80
	North girder	160	n.a.

[a]Average of the strain difference near the north and south piers.
[b]Average of the strain difference near the east and west abutments.

5. FINITE ELEMENT MODELS

This chapter discusses the finite-element models that were developed for the Guthrie County Bridge and the Story County Bridge using the ANSYS computer-software program (Swanson Analysis System, Inc., 1992). Additional discussion of the finite-element models for both of these in-service, integral-abutment bridges is presented in the MS thesis for Sayers (2000).

5.1. Structural models

The Guthrie County Bridge, finite-element model contained 12,244 nodes and 7,762 elements. The Story County Bridge model contained 11,920 nodes and 6,630 elements. The finite-element models used shell, beam, spring, truss, and general-matrix elements. The finite-element models for the Guthrie County Bridge and Story County Bridge are shown in Fig. 5.1. Portions of the finite-element model for the Guthrie County Bridge are shown in Fig. 5.2.

Shell elements (ANSYS SHELL93 elements) were used to model the reinforced concrete (RC) deck, abutments, and piers. Both quadrilateral-shell elements with four, corner nodes and four, mid-side nodes and triangular-shell elements with three, corner nodes and three, mid-side nodes were used for the analytical models for the bridges. Each node had three, translational degrees-of-freedom and three, rotational degrees-of-freedom. The thickness of each shell element matched the thickness of the particular bridge member in the structure. The aspect ratios of the shell elements were generally less than 2 to 1. This ratio was less than the 5 to 1 maximum, aspect ratio specified by the AASHTO LRFD Specifications (1998). The prestressed concrete (PC) bridge

girders; steel, HP-shaped piles; and the Guthrie County Bridge guardrail were modeled using three-dimensional, beam elements (ANSYS BEAM44 elements). Two nodes defined a beam element with a third node used to orient the cross-sectional axes. The two, end nodes for this element were located at the center of gravity of the beam member. Geometric-beam properties including the area, depth, and moments of inertia were assigned to these elements.

Full-composite action was modeled between the slab and girders. Constraint equations (ANSYS CERIG commands) were used to create rigid links that connected the vertically-aligned nodes of the finite elements for the slab and girders. These constraint equations coupled the translational and rotational, degrees-of-freedom between the element nodes for the slab and girders.

A truss element (ANSYS LINK8 element) was used to model each steel intermediate diaphragm between the PC girders in the Guthrie County Bridge. A truss element is a uniaxial, tension-compression element with three, translational, degrees-of-freedom at both of its nodes. The connection between an intermediate diaphragm and the web of a PC girder was modeled as a pinned connection. Shell elements were used to model the RC intermediate diaphragms in the Story County Bridge.

Full-moment continuity was modeled between the steel piles and the RC abutments. The abutment piles are embedded about 36 in. into the bottom of the pile caps at both bridges. As shown in Fig. 5.2a, the nodes for the beam elements that modeled the piles share the corner nodes of the shell elements for the pile cap at the location of the embedded pile. This modeling detail created a rigid connection between

these members. The piles that support the piers of the Story County Bridge are embedded within the entire height of the piers.

The north pier at the Guthrie County Bridge is a fixed pier. As was shown in Fig. 3.4a, a fixed pier has the RC pier diaphragm cast against and into keyways in the RC pier cap. A compressible, expansion-joint material exists between pier cap and diaphragm and along the sides and bottom of the keyways. The connection between the RC diaphragm and pier cap is not completely fixed, since small, relative movements along the longitudinal direction of the bridge can occur between the bridge superstructure and a fixed pier when shear deformations occur within the expansion-joint material on the horizontal surfaces of the pier cap and by compressive deformations the expansion-joint material on the sides of the keyways. A general-matrix element (ANSYS MATRIX27 element) was developed using structural-analysis, matrix methods (Weaver and Gere, 1990) to model the connection of the concrete diaphragm and the pier cap. The general-stiffness element incorporates the translational stiffness and rotational stiffness of the connection and allows for small, relative movements.

The south pier of the Guthrie County Bridge is an expansion pier. For an expansion pier, an air space exists between the bottom of the RC pier diaphragm and the top of the RC pier cap. At this type of a pier, the PC bridge girders bear on 3.75-in. thick, neoprene pads, as shown in Fig. 3.4b. The low-shear modulus (G = 0.10 ksi) of the thick, neoprene pad provides minimal resistance to the translation of the superstructure over the piers. Linear-spring elements (ANSYS COMBIN14 elements) were used to model the vertical, compressive stiffness and the shear stiffness of the

bearing pads that support the girders at the piers. Material properties for the neoprene pads were obtained from Lee (1994).

The details for the connection between the bridge superstructure and both piers at the Story County Bridge are similar to those details for the fixed pier at the Guthrie County Bridge. Because the relative movements measured at the fixed pier on the Guthrie County Bridge were very small, the relative movements were neglected between the bridge superstructure and the piers for the Story County Bridge. Therefore, common nodes for the elements were used at the bearing points between the bridge superstructure and the pier caps for this bridge.

The pier footings for the Guthrie County Bridge were cast against shale bed rock. The bearing stiffness and the sliding-frictional stiffness for the shale were assumed to be equal to 100 ton/ft^3 and the 50 ton/ft^3, respectively, as recommended by Barkan (1992).

The bridge elements and the material properties for the Guthrie County Bridge and Story County Bridge are listed in Table 5.1. The material properties are the 28-day, concrete-compressive strength, f'_c; modulus of elasticity, E; shear modulus, G; Poisson's ratio, μ; and coefficients of thermal expansion and contraction, α. These material properties were established from the information that is shown on the design drawings for each bridge. Values of the coefficient of thermal expansion and contraction, α-coefficient, were based on the laboratory tests that were conducted by Ng (1999).

5.2 Pile-to-soil interaction

Figure 5.3 shows a pile has a vertical load, P, and a horizontal load, H, that are applied at the top of the pile. These loads induce a vertical displacement, Δ_v, and a horizontal displacement, Δ_h, at the top of the pile. The soil that surrounds the pile is represented by vertical and lateral springs along the length of the pile and an end-bearing, point spring. Winkle-soil models (Fleming, et al., 1985 and Poulos and Davis, 1980) were used to model the force versus displacement relationships between the soil and a pile. These models neglect any interaction between the soil springs as a pile is displaced. Linear-spring elements (ANSYS COMBIN14 elements) were used to model the soil stiffness in the finite-element models.

Soil characteristics of each of the three types of springs can be described by soil-resistance versus displacement curves. The first characteristic is represented by a p-y curve, which describes the relationship between the horizontal resistance (horizontal force per unit length of pile) of the soil at a depth z along the pile length and the corresponding horizontal displacement of the pile at that depth. The second characteristic is represented by an f-z curve, which describes the relationship between the vertical-skin-frictional resistance (vertical force per unit length of pile) of the soil at a depth z along the pile length and the relative, vertical displacement between the pile and the soil at that depth. The third characteristic is represented by a q-z curve, which describes the relationship between the bearing resistance (vertical force on the effective, pile-tip area) at the pile tip and the vertical settlement of the pile tip. All three types of curves assume non-linear, soil behavior.

Non-linear, pile-to-soil interaction models were presented by a number of researchers (Duncan and Chang, 1970; Finn, et al., 1977; Martin, 1975; Streeter et al., 1974; Pyke, 1979 and Mattock and Reese, 1960). The modified, Ramberg-Osgood model (Desai and Wu, 1976) was used to approximate the p-y, f-z, and q-z soil-resistance and displacement curves for the modeling of the non-linear pile-to-soil interaction. The p-y relationship is given by

$$p = \frac{k_h y}{\left[1 + \left|\frac{y}{y_u}\right|^n\right]^{\frac{1}{n}}} \tag{5.1}$$

with,

$$y_u = \frac{p_u}{k_h} \tag{5.2}$$

where, k_h is the initial, horizontal stiffness for the soil; p is the horizontal resistance for the soil; p_u is the ultimate, horizontal resistance for the soil at the depth z along the pile length; n is the shape parameter for the modified, Ramberg-Osbood curve; y is the horizontal displacement of the pile; and y_u is the horizontal displacement y for the pile that is associated with an elastic-plastic, soil material when the resistance p equals the resistance p_u, as shown in Fig. 5.5. Figure 5.6 shows the effect of the shape parameter, n, on the soil-resistance and displacement behavior. Equations that are similar to Eqs. 5.1 and 5.2 were used for the Ramberg-Osbood f-z curve (with f_u, the ultimate, vertical, skin-frictional resistance developed between the pile and soil at the depth z along the pile length, and k_v, the initial, vertical stiffness of the soil at the depth z along the pile length) and the Ramberg-Osgood q-z curve (with q_u, the ultimate, bearing stress at the pile tip, and k_q, the initial, vertical stiffness of the soil strata at the pile top). The soil

parameters for the Ramberg-Osgood curves were empirically determined from basic soil properties as presented in Greimann, et al. (1984, 1987a), which are repeated here in Tables 5.2, 5.3, and 5.4 (Poulus and Davis, 1980; Davisson, 1970; Ha and O'Neill, 1981; US Steel Corp. 1965; and Wolde-Tinsae et al., 1982). As noted in Table 5.3, the adhesion, c_a, between a pile and a clay soil is a function of the cohesion, c_u, from an unconsolidated, undrained test, and a reduction factor, α, that is established from Fig. 5.6. The Ramberg-Osgood parameters for an HP10 x 42, steel pile that is driven in clay and sand are listed in Tables 5.5 and 5.6, respectively.

For practical purposes, the stiffness, k_h is often assumed to be constant or to vary linearly with depth. The uncertainty associated with estimating the soil behavior from standard, soil tests is usually consistent with the errors caused by selecting a simple function for the soil-modulus versus depth relationship (Matlock and Reese, 1960). For the parameters presented in Tables 5.2 through 5.6, the sub-grade-reaction modules for clay soils are assumed to be constant within a soil layer and to vary linearly with depth for granular soils.

The finite-element models for the Guthrie County Bridge and Story County Bridge incorporated linear, Winkler-pile-soil models that were based on the initial stiffness of the soil. Spring elements that represented the horizontal stiffness of the soil normal to flange and normal to web, the vertical skin-friction stiffness, and the end-bearing stiffness were applied at the corresponding element nodes for a pile.

Soil parameters were based on the soil-boring data that is shown in Fig. 5.7 for the abutment locations of the Guthrie County Bridge, and as shown in Fig. 5.8 for piles at the abutment and piers of the Story County Bridge. These soil-boring logs were

obtained from the design drawings for the bridges. Soil stiffness was calculated using the expressions and values presented in Tables 5.2 through 5.4. The soil-boring data was used to establish the soil type (clay or sand) for each soil layer. The standard-penetration, blow count, N, was used to determine the approximate, soil parameters from Tables 5.5 or 5.6. Effective, soil-unit weights were estimated by considering the moisture conditions at the bridge sites. At the Guthrie County Bridge, saturated-soil conditions were encountered at the north abutment, and dry-soil conditions were encountered at the south abutment. At the Story County Bridge, the soil in the berm adjacent to the abutments was dry when it was excavated for installing strain gages on the selected piles. Over the monitoring period, the soil near the north pile of the east abutment became saturated. Soil near the other monitored piles remained dry or because slightly damp. Soil for finite-element model of the Story County Bridge was assumed to be dry at all locations. Figure 5.9 shows the distribution for the horizontal stiffness and vertical stiffness for the soil along and at the node points for a pile in the south abutment at the Guthrie County Bridge.

For the Guthrie County Bridge, the piles were driven through an 8-ft deep, 16-in. diameter, pre-bored hole. During the bridge construction, bentonite slurry was used to fill the pre-bored holes. Bentonite slurry is a soft mixture that has water as the majority of its composition (Filz, et al., 1997). During the excavation of the piles for installing the strain gages on the selected piles for this bridge, the ISU researchers noted that the bentonite had a consistency of a pliable, clay-type soil. The stiffness of the bentonite slurry was considered minimal; therefore, the horizontal stiffness and vertical stiffness of this material were neglected for the finite-element model of the Guthrie County Bridge.

The abutment piles at the Story County Bridge were driven in similar pre-bored holes. After the piles were driven, loose sand was placed in the pre-bored holes. For the finite-element model of the Story County Bridge, loose-sand properties were used for the portion of the pile lengths in the pre-bored holes.

5.3. Abutment backfill models

Linear-spring elements (ANSYS COMBIN14 elements) were used to model the soil backfill behind the abutments. At each discrete point where the interface conditions between the bridge structure and soil were modeled, one spring was oriented normal to the bridge member and two springs were oriented orthogonal to each other and parallel to the surface of the bridge member. The tangential springs represented the frictional forces induced by the soil on the abutment surface.

Other researchers have presented design curves to determine the magnitude of the lateral pressure for the soil behind rigid, retaining walls that is induced by wall movement towards the backfill (passive movement) and away from the backfill (active movement) (Clough and Duncan, 1991; Barker, et al., 1991; Canadian Geotechnical Society, 1992; Husian and Bagnaroil, 1996; and Dept. of the Navy, 1971). Effective-soil pressures induced by wall movements can be expressed in terms of an earth-pressure coefficient, k, given by

$$k = \frac{\sigma'_{horizontal}}{\sigma'_{vertical}} \tag{5.3}$$

where, $\sigma'_{horizontal}$ is the effective, horizontal stress in the soil at a depth z; $\sigma'_{vertical}$ is the effective, vertical stress in the soil, which is equal to $\gamma' z$, at a depth z; γ' is the effective,

unit-weight of the soil; and z is the depth of soil to a particular point along the backwall height.

The Rankine theory (Clayton, et al., 1993) was applied to determine earth-pressure coefficients. For a wall at rest, Rankine's coefficient of at-rest-soil pressure, k_o, is given by

$$k_o = 1 - \sin\phi \tag{5.4}$$

where, ϕ is the angle of internal friction for the soil. For a rigid wall that is pushed into a soil mass, Rankine's passive-soil-pressure coefficient, k_p, is evaluated as

$$k_p = \tan^2 (45° + \phi/2) \tag{5.5}$$

As a wall is moved away from the soil, Rankine's active-soil-pressure coefficient, k_a, is expressed as

$$k_a = \tan^2 (45° - \phi/2) \tag{5.6}$$

Design curves for a wall subjected to soil pressure that were presented by the Canadian Foundation Engineering Manual (Canadian Geotechnical Society, 1992), Husain and Bagnaroil (1996), and Clough and Duncan (1991) are shown in Fig. 5.10. The design curve for the Canadian Foundation Engineering Manual (Fig. 5.10a), shows the wall height and horizontal displacement at the top of the wall as the dimensions H and Y, respectively. While for the design curve presented by Hussian and Bagnaroil (Fig. 5.10b) and by Cough and Duncan (Fig. 5.10c), these variables are represented by the dimensions h and Δ and by the dimensions H and Δ, respectively. The Canadian Foundation Engineering Manual contains design curves similar to those proposed in NAVFAC DM-7 (Dept. of the Navy, 1971) that include wall-friction effects. The National Cooperative Highway Research Program (NCHRP) (Barket, et al., 1991) adopted

design curves for cohesionless soil that were based on the work of Clough and Duncan's recommendations.

Ting and Faraji (1998) compared soil pressures that were predicted by applying numerous design curves with soil pressures established by experimental studies. They concluded that the NCHRP design curve underestimates the ultimate, passive-soil pressure and overestimates the initial, lateral stiffness for dense and medium-dense sand. These researchers determined that the Canadian Foundation Engineering Manual (CFEM) design curve closely matched the experimental data for dense and medium sands. Ting and Faraji noted that both the NCHRP and CFEM design curves provide an accurate representation of the experimental data for a loose backfill.

Ting and Faraji stated that if the rotation of a wall about its base causes the top of the wall to displace further into the soil than that for a pure translational movement, higher soil pressure will be induced in the top portion of the wall with slightly lower pressures at the bottom of the wall than the soil pressures that are induced by the pure translational movement. Ting and Faraji stated that a triangular, soil-pressure distribution along the height of a wall will adequately represent the soil pressure against the wall with this type of a displacement.

For the finite-element models, linear springs were used to approximate the force versus displacement relationship of the granular backfill behind the abutments. The horizontal stiffness for each of the Winkler-soil springs was based on passive-soil stiffness to represent the effect of the abutment being pushed into the backfill during the bridge expansion. The initial slope for the passive-soil, force versus displacement curves presented in Fig. 5.10 were used to represent the horizontal stiffness of the soil

backfill behind the abutments in the finite-element models. The maximum, passive-soil force, $F_{passive,}$ at a given depth z on a finite element for an abutment is given by

$$F_{passive} = (k_{passive} - k_o)\ \sigma'_{vertical}\ A_{element} \tag{5.7}$$

where, $A_{element}$ is the surface area of the finite element and $\sigma'_{vertical}$ is the effective, vertical stress that was calculated for the depth of the element centroid below the top surface of the abutment backfill. The total, horizontal stiffness, K_{spring}, for the soil that is attributed to each wall, finite element is expressed by

$$K_{spring} = F_{passive}/\Delta_{passive} \tag{5.8}$$

where, $\Delta_{passive}$ is the horizontal displacement of a wall for full-passive-soil pressure. For each finite element in the abutment, nodal-spring stiffness was computed by evenly distributing the magnitude of K_{spring} to each of the corner nodes for the abutment wall element.

The backfill soil behind the abutments of the Guthrie County Bridge and Story County Bridge is a compacted, granular soil. To establish soil properties for a compacted, granular backfill, the soil properties for a loose, medium, and dense-sand backfill, which were recommended by Winklehorn and Fang (1975) and are listed in Table 5.7, were used as a guide. For these general classifications for sand, Clough and Duncan (1991) presented approximate values for the ratio of the horizontal displacements Δ_{active} and $\Delta_{passive}$ for the full-active-soil pressure and full-passive-soil-pressure conditions, respectively, to the height, H, of a wall. These non-dimensionalized, displacement parameters are listed in Table 5.8. The frictional stiffness of the abutment backfill was initially assumed to be equal to one-half of the normal stiffness, as recommended by Barkan (1962). The frictional stiffness was

adjusted if this initial stiffness value did not produce adequate predictions for the transverse displacements for the abutments. Both bridge finite-element models were calibrated by adjusting the backfill stiffness until abutment displacements that were predicted by the finite-element model were close to the experimentally-measured displacements, as discussed in Chapters 6 and 7.

5.4. Applied temperature distributions

5.4.1. Spatial distributions

The experimental, temperature data were used to estimate longitudinal, transverse, and vertical-temperature distributions that were applied to the finite-element models for a given point in time. Analysis of the experimental, temperature data for the Guthrie County Bridge and Story County Bridge was described in Section 4.2. The length for each span of the Guthrie County Bridge was divided into fifteen temperature regions, as shown in Fig. 5.11a. The temperature regions were selected based on the location of the thermocouples in the most intensely instrumented span (the south span) for this bridge. The width of the bridge was divided into five temperature regions. Each of these regions was attributed to a PC bridge girder. Since thermocouples were not installed in the second and fourth PC girders, the temperature distributions for these girders were computed as the average of the temperature distributions for the adjacent girders. The few thermocouples in the middle and north spans of the Guthrie County Bridge recorded temperatures that were similar to the recorded temperatures at similar locations in the south span. Therefore, the temperature distribution for the middle and north spans was assumed to be the same as that of the south span of this bridge. The

temperatures that were recorded by the thermocouples that were located close to the abutments were also used for the locations that are close to the piers.

For a given point in time, vertical-temperature gradients through the slab thickness and girder depth were established in each of the fifteen temperature regions for each span of the finite-element model for the Guthrie County Bridge. For regions that did not have thermocouples in vertical alignment, interpolated vertical-temperature gradients were established from the available, experimental, temperature measurements. For each span, bi-linear, vertical-temperature distributions, which were defined by the temperatures at the top of slab, bottom of slab/top of girder, and bottom of girder at points along the length and width of the slab, were applied as a loading condition to the finite-element model of the Guthrie County Bridge.

For the finite-element model of the Story County Bridge, a simpler temperature distribution in the superstructure was used as a loading condition. As discussed in Section 4.2.4, temperature variations along the length of the bridge were not significant. Except for under the solid guardrail, as shown in Fig. 4.16, the temperatures were relatively constant over the width of the bridge. Figure 5.11b shows the three temperature regions that were used in each span of the Story County Bridge. Two, vertical-temperature gradients through the depth of this superstructure were applied as a loading condition for each span of this finite-element model.

For the finite-element models of the Guthrie County Bridge and Story County Bridge, temperature changes for the substructures were selected by the ISU researchers. A thermocouple, which was embedded in the exposed face and near the mid-width of an abutment, measured the concrete temperatures at this location. Since

the back face of the abutment was in contact with soil, the concrete temperature on this face at depths that are a few feet below the roadway were assumed not to change with changes in air temperatures. Temperatures for the portion of the piles that were left exposed in the excavations were based on thermocouples readings at these locations. Pier temperatures were estimated from the average, concrete temperature of the bridge.

5.4.2. Time variations

The range in the experimentally-measured, bridge-member temperatures, between the times of the coldest and hottest average, bridge temperature for the Guthrie County Bridge and Story County Bridge, was applied as a loading condition to the respective, finite-element, bridge models. Bridge member strains that were induced by the thermal loading were predicted by the finite-element models. The calculated member strains at the locations of the strain gages that were applied to the bridges were of particular interest.

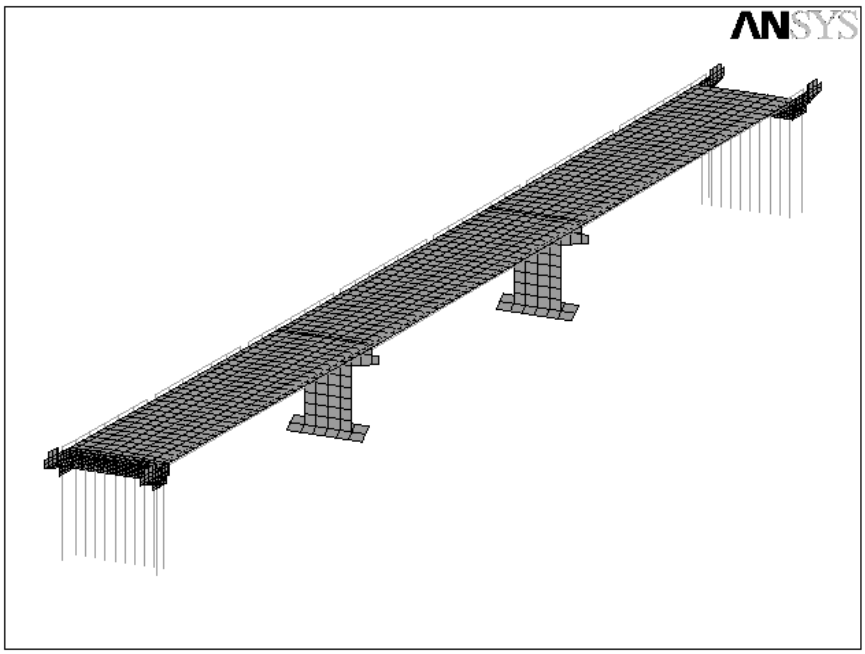

(a) Guthrie County Bridge

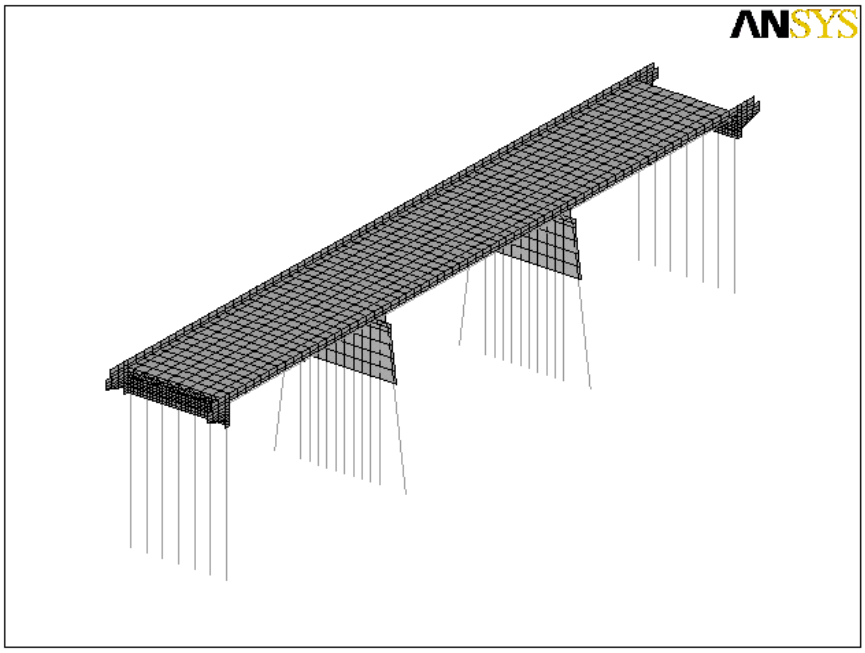

(b) Story County Bridge

Figure 5.1. ANSYS finite-element bridge models

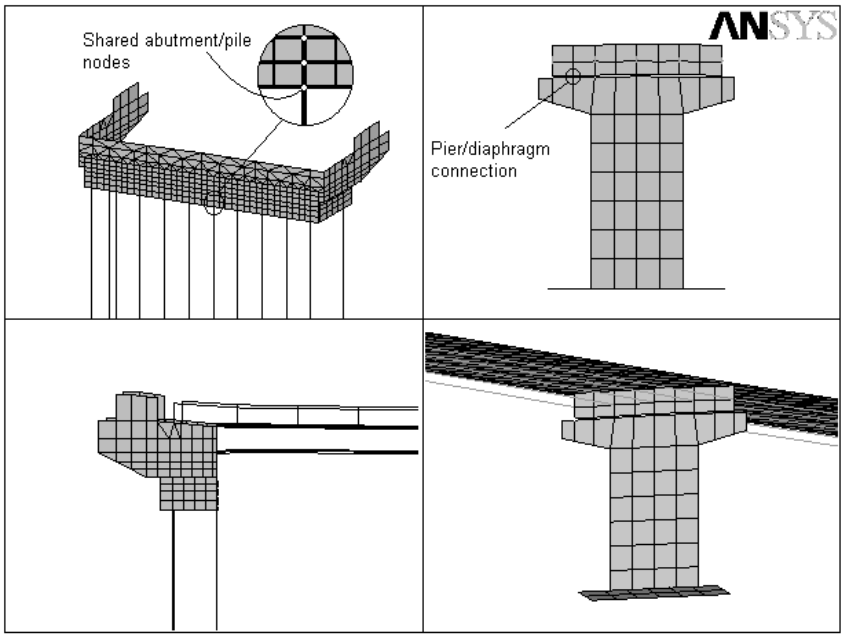

(a) Abutment and pier

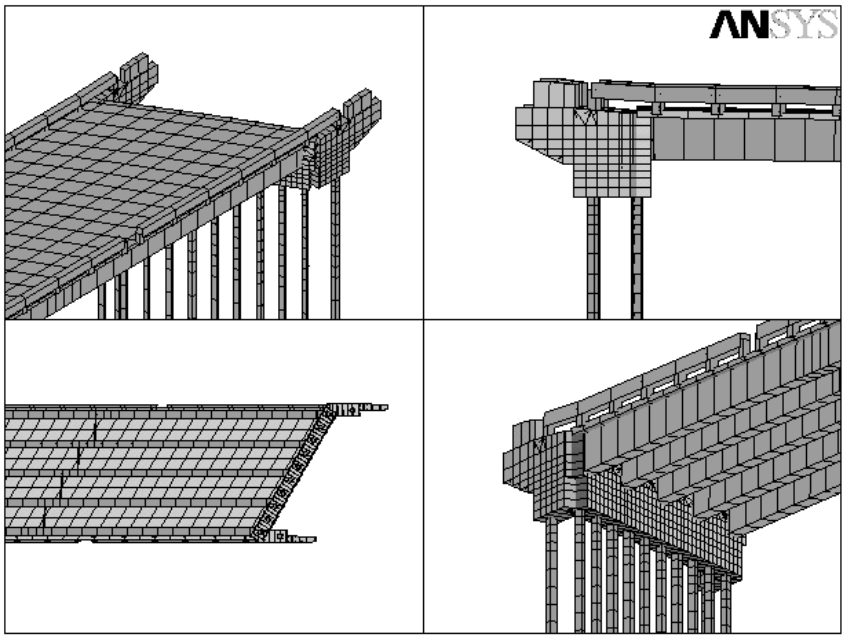

(b) Bridge deck, girders, and abutment

Figure 5.2. Components of finite-element model for the Guthrie County Bridge

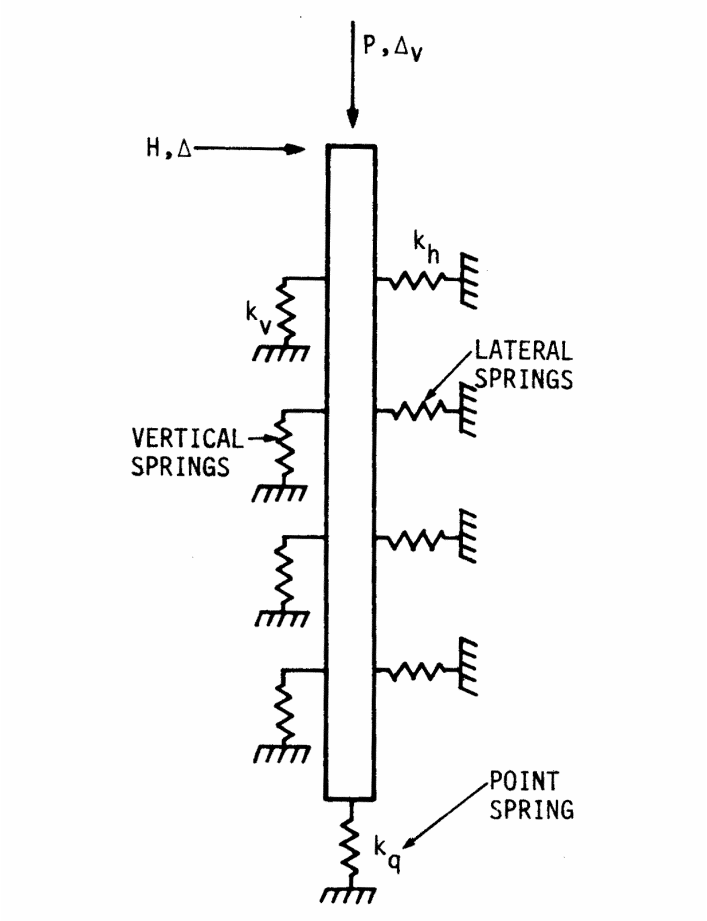

Figure 5.3. A pile with Winkler-soil models

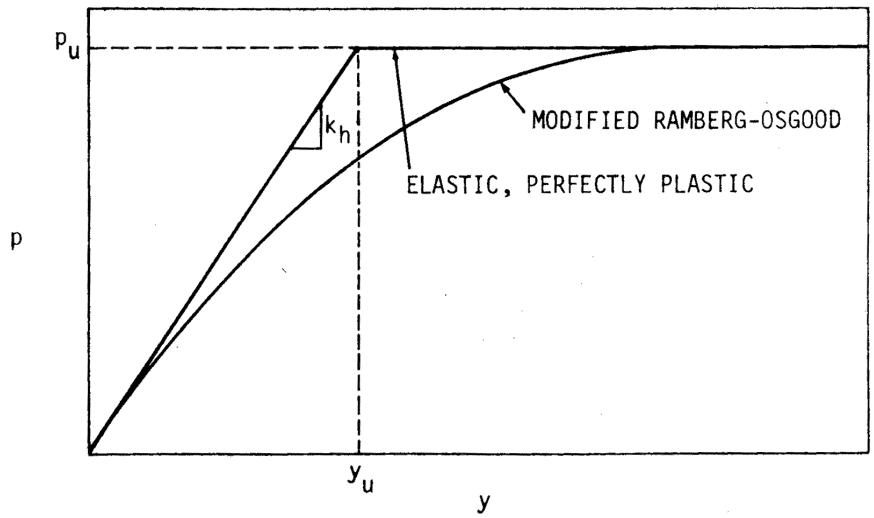

Figure 5.4. Typical p-y curve (Greimann, et al., 1987)

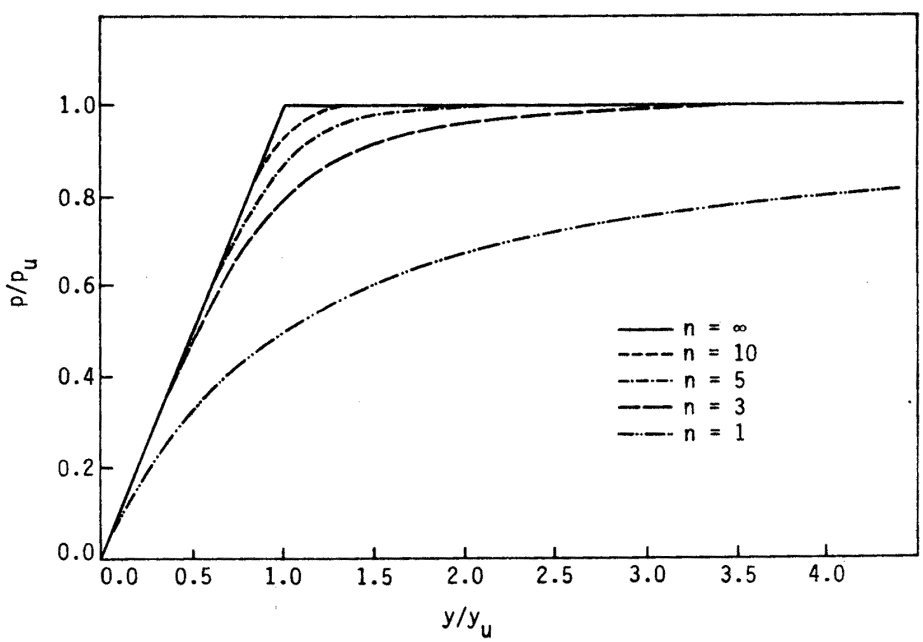

Figure 5.5. Non-dimensional, modified, Ramberg-Osgood p-y relationship (Greimann, et al., 1987)

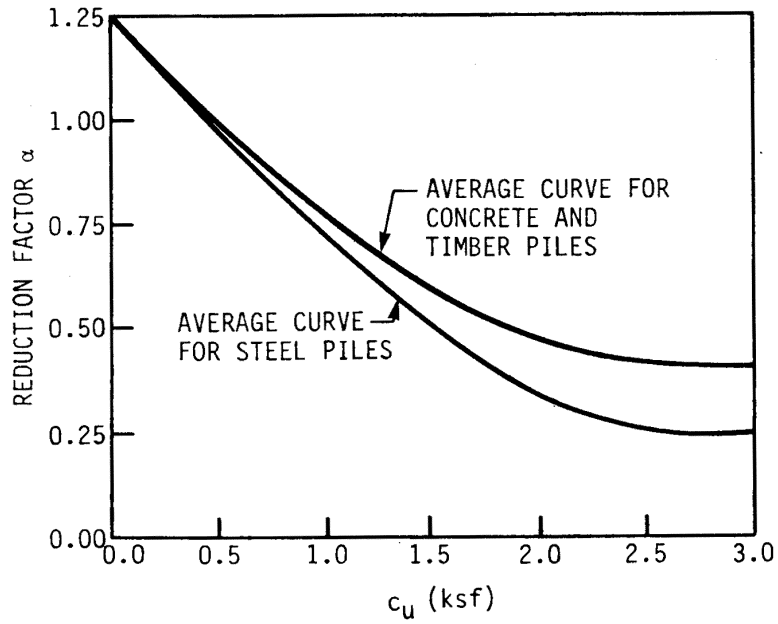

Figure 5.6. Alpha factor for the adhesion of a pile in clay (Greimann, et al., 1984)

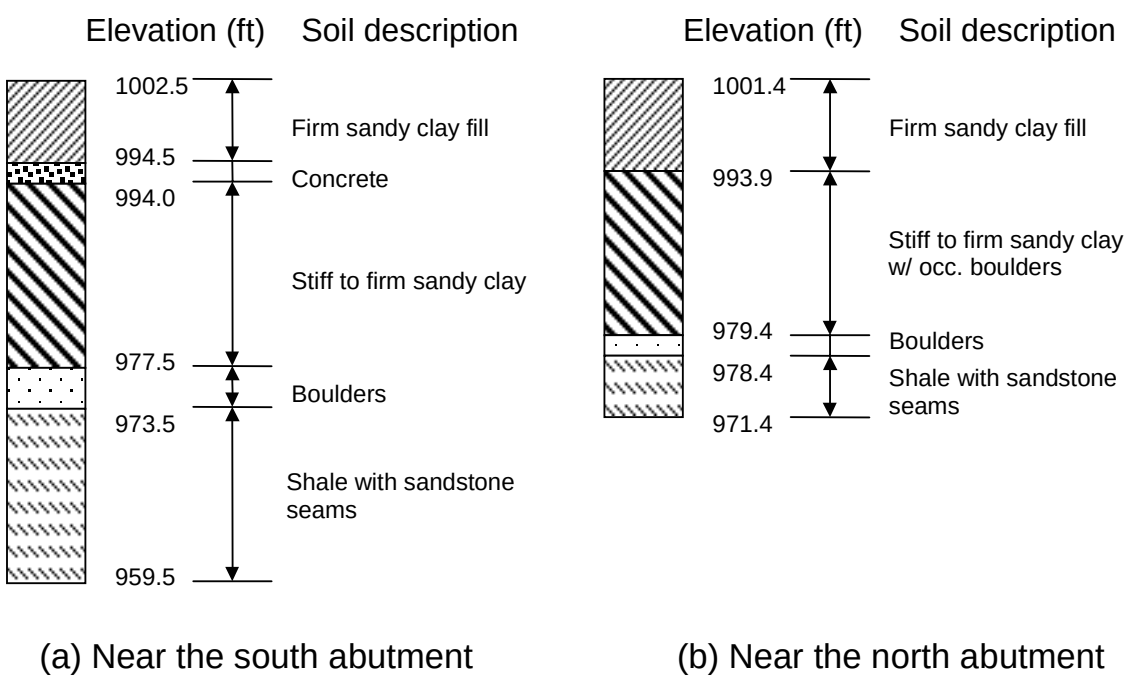

(a) Near the south abutment (b) Near the north abutment

Figure 5.7. Soil borings at the Guthrie County Bridge (not to scale) (adapted from the Iowa DOT bridge drawings)

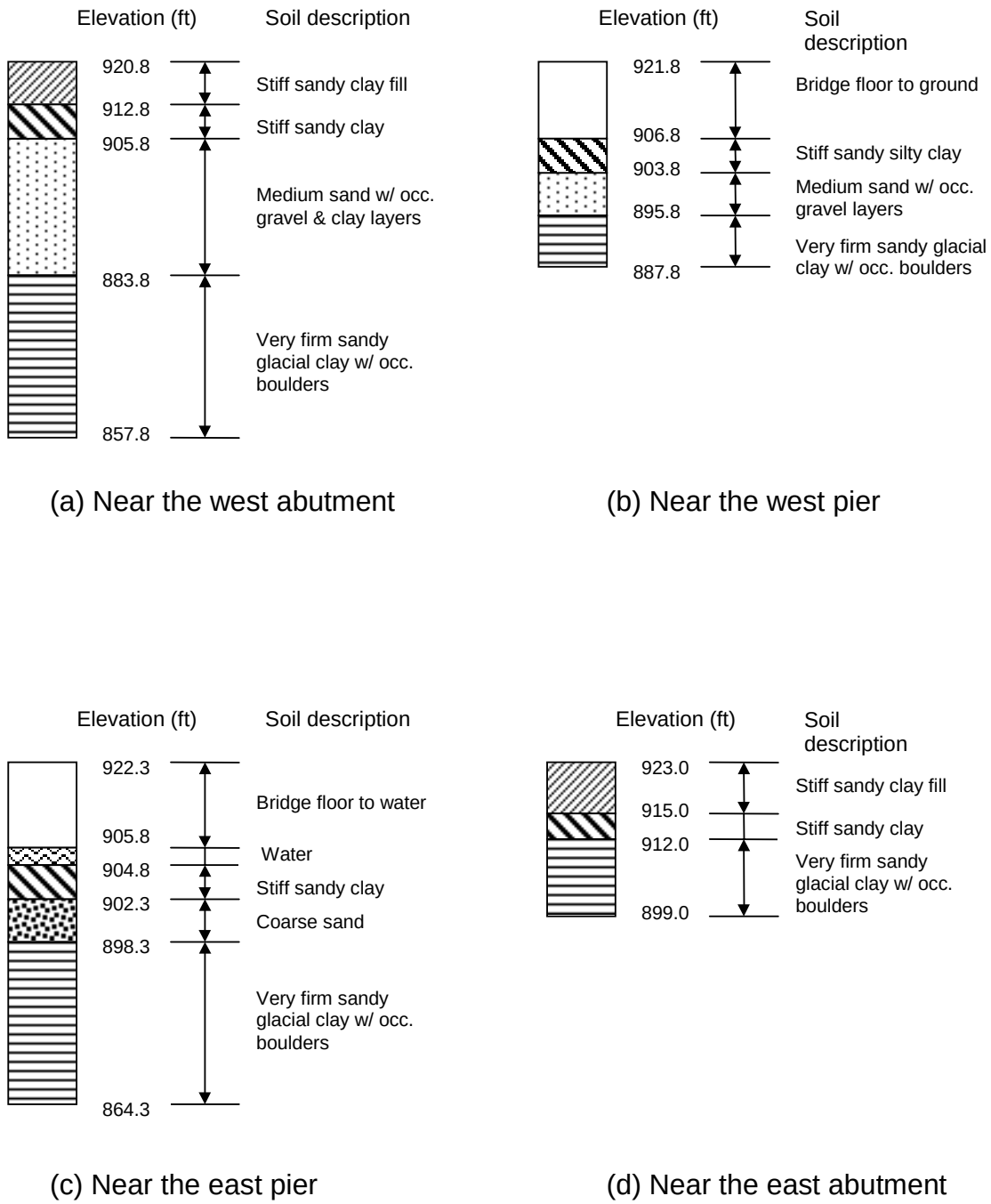

Figure 5.8. Soil borings at the Story County Bridge (not to scale) (adapted from the Iowa DOT bridge drawings)

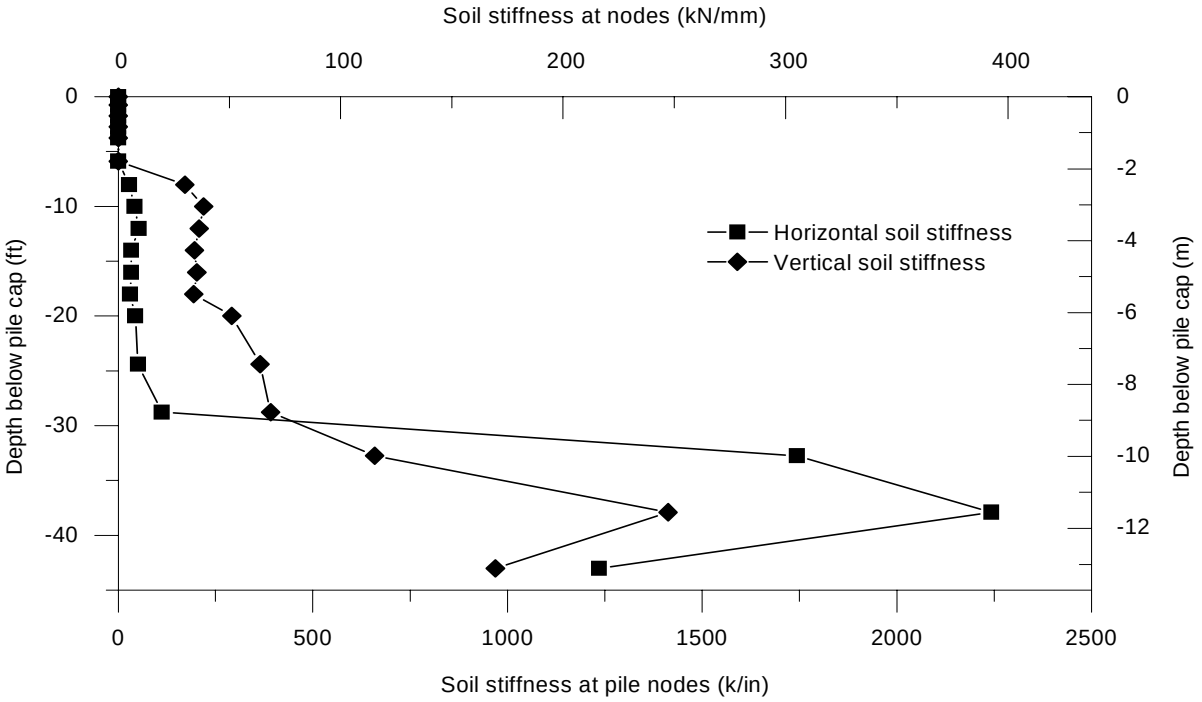

Figure 5.9. Horizontal stiffness and vertical stiffness of the soil along the length of the center pile for the south abutment at the Guthrie County Bridge

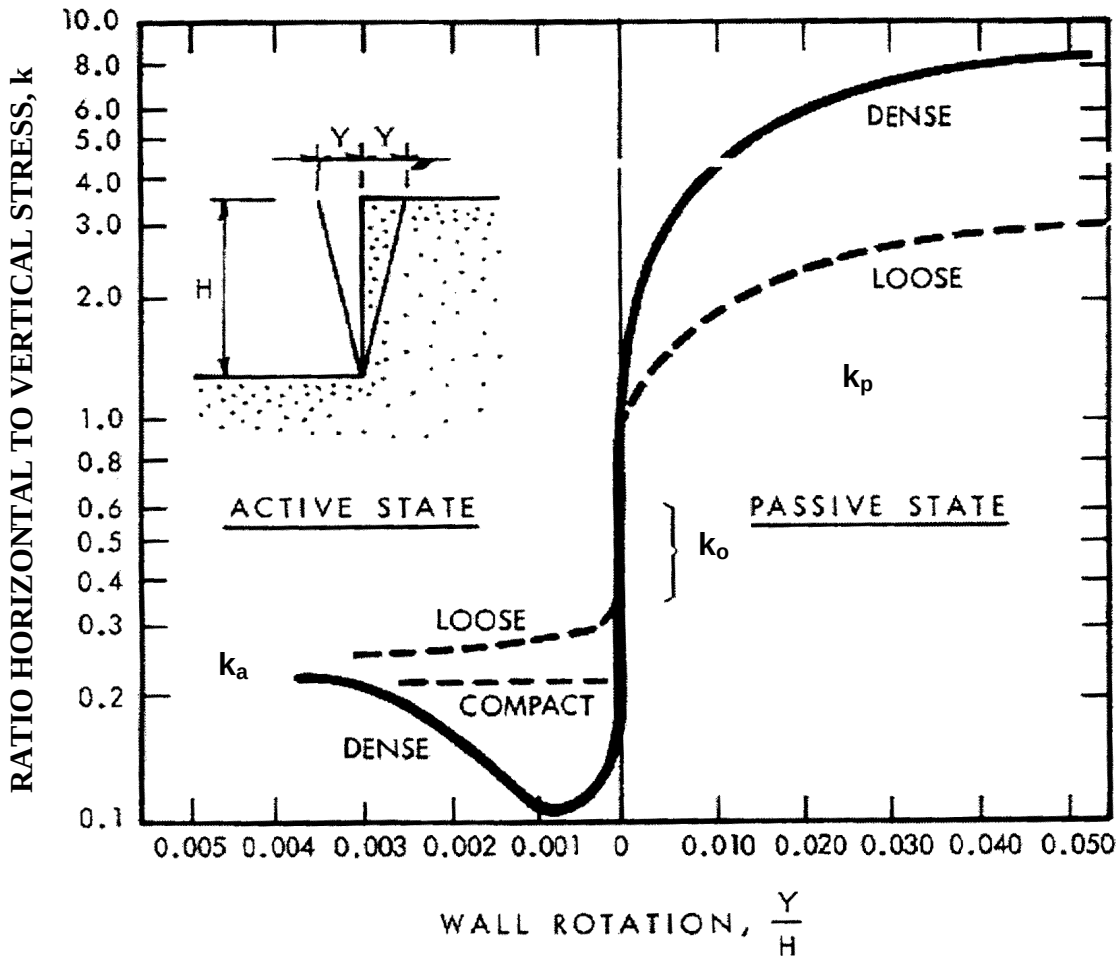

a) Canadian Foundation Engineering Manual (1992)

Figure 5.10. Horizontal-stiffness design curves for the soil behind a wall

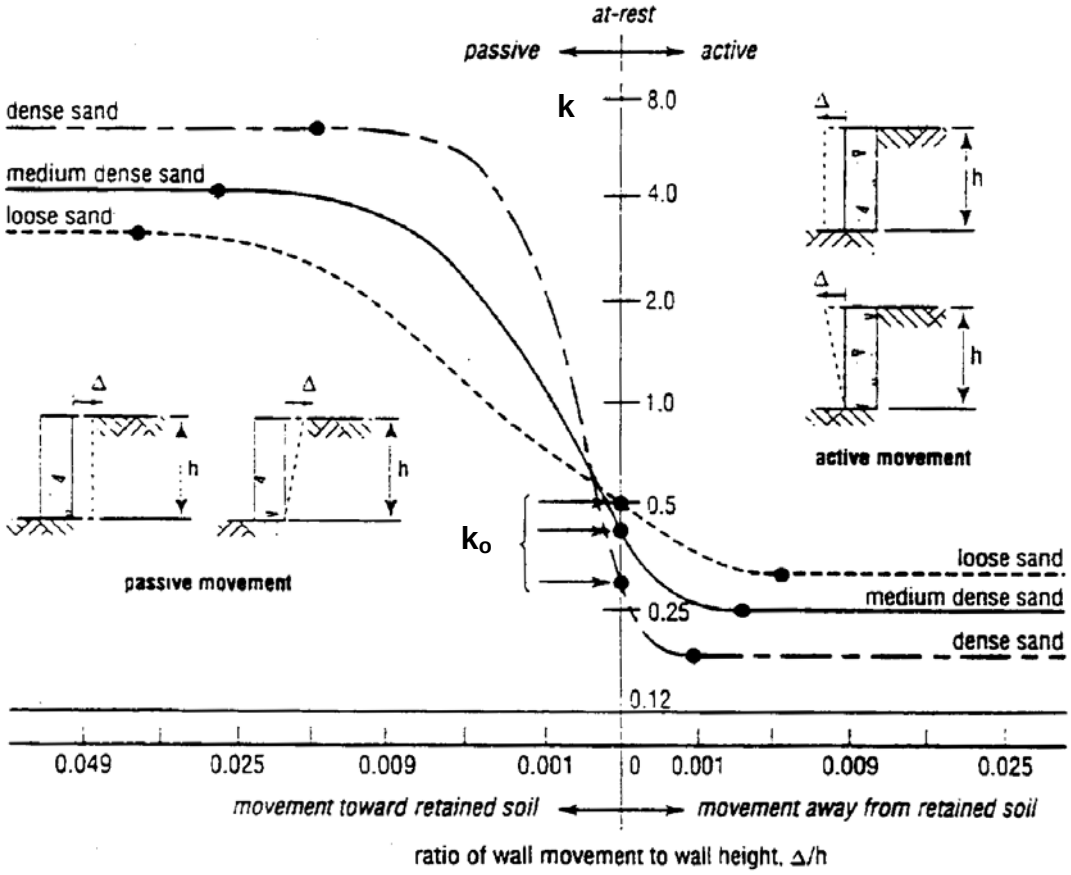

(b) Husain and Bagnaroil (1996)

Figure 5.10. (continued)

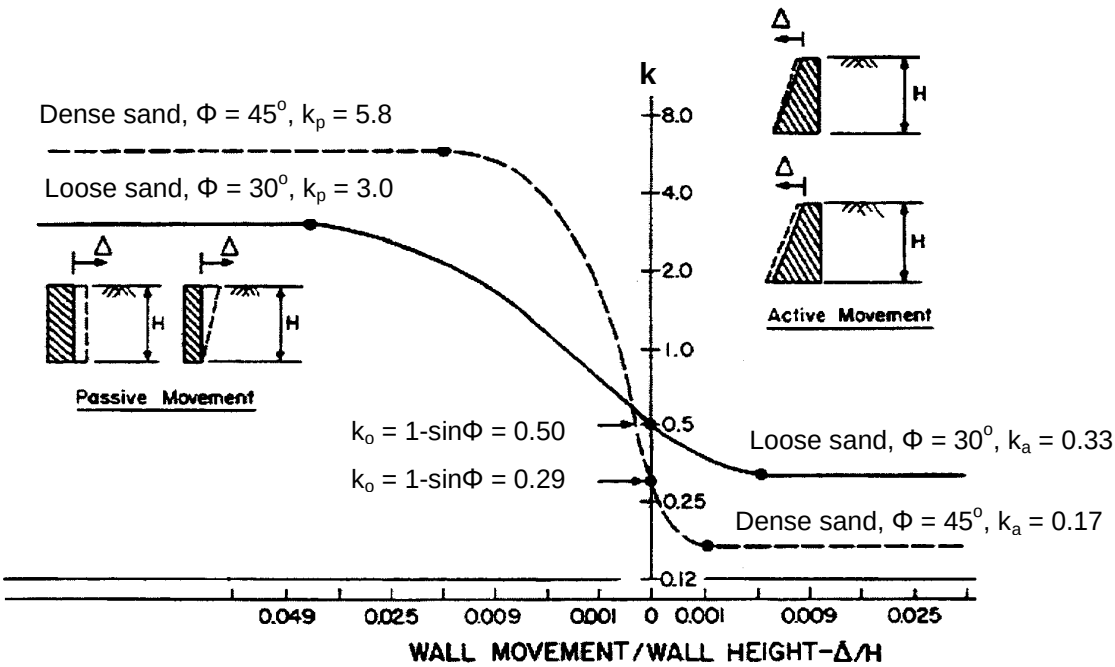

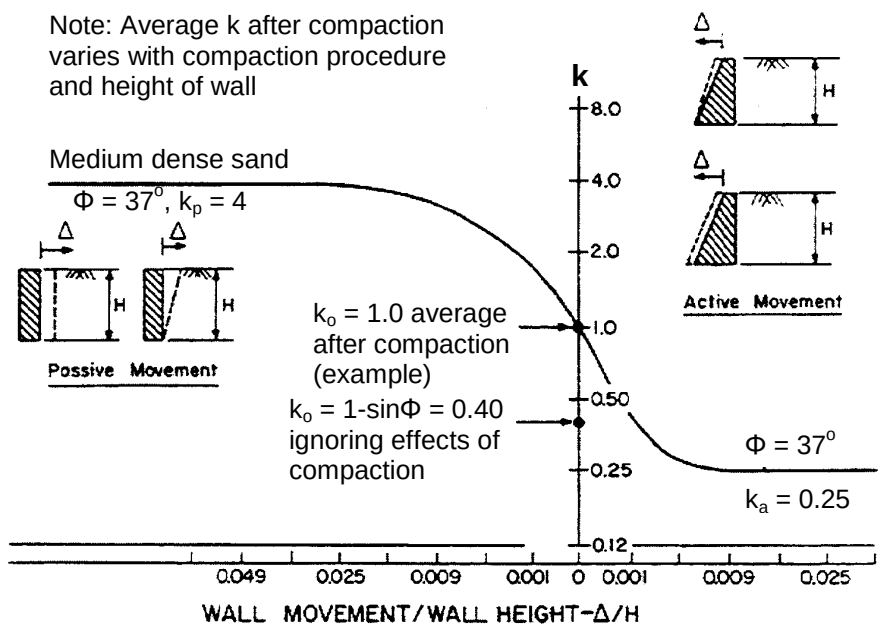

(c) Clough and Duncan (1991)

Figure 5.10. (continued)

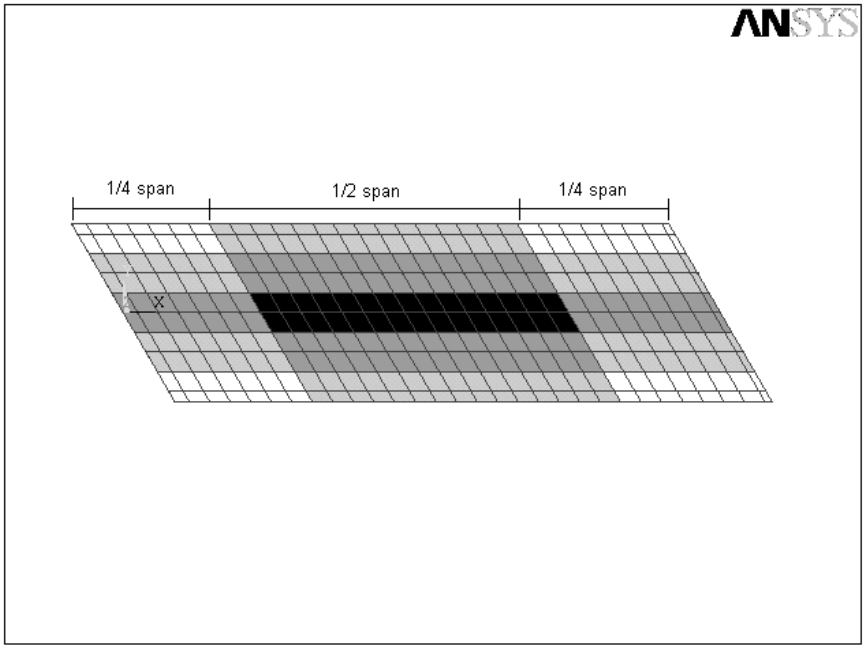

(a) Guthrie County Bridge

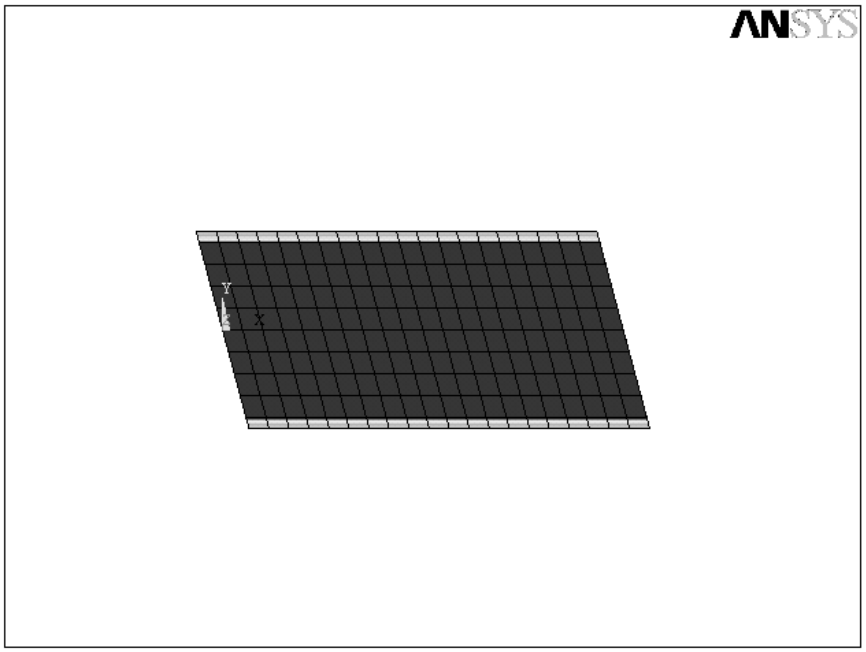

(b) Story County Bridge

Figure 5.11. Temperature regions for the bridge decks

Table 5.1. Properties of the modeled bridges

Material and Property		Guthrie County Bridge	Story County Bridge
Cast-in-place concrete	Compressive strength, f'_c (ksi)	3.5	3.5
	Modulus of elasticity, E (ksi)	3400	3400
	Shear modulus, G (ksi)	1420	1420
	Poisson's ratio, μ	0.20	0.20
	Dry coefficient of thermal expansion and contraction, α-coefficient (in./in./°F)	5.8×10^{-6}	4.8×10^{-6}
	Maximum coefficient of thermal expansion and contraction, α-coefficient (in./in./°F)	6.4×10^{-6}	5.3×10^{-6}
Prestressed concrete	Compressive strength, f'_c (ksi)	6.0	5.0
	Modulus of elasticity, E (ksi)	4400	4000
	Shear modulus, G (ksi)	1710	1680
	Poisson's ratio, μ	0.20	0.20
	Dry coefficient of thermal expansion and contraction, α-coefficient (in./in./°F)	4.3×10^{-6}	4.3×10^{-6}
	Maximum coefficient of thermal expansion and contraction, α-coefficient (in./in./°F)	4.7×10^{-6}	4.7×10^{-6}
Steel	Coefficients of thermal expansion and contraction α-coefficient (in./in./°F)	6.5×10^{-6}	6.5×10^{-6}

Table 5.2. Parameters for p-y curves

Soil Type	n	p_u (use smallest value)	k_h
Soft clay and stiff clay	1.0	$p_u = 9c_uB_{pile}$ $p_u = \left[3 + \frac{\gamma'}{c_u}z + \frac{0.5}{B_{pile}}z\right]c_uB_{pile}$	$\frac{p_u}{y_{50}}$
Very stiff clay	2.0	$p_u = 9c_uB_{pile}$ $p_u = \left[3 + \frac{\gamma'}{c_u}z + \frac{2.0}{B_{pile}}z\right]c_uB_{pile}$	$\frac{p_u}{2y_{50}}$
Sand	3.0	$p_u = \gamma' z[B_{pile}(k_p - k_a) + zk_p\tan\alpha\tan\beta$ $+ zk_o\tan\beta(\tan\phi - \tan\alpha)]$ $p_u = \gamma' zk_p^3 + 2k_p^2k_o\tan\phi - k_aB_{pile}$	$\frac{J\gamma' k}{1.35}$

where,
c_u = cohesion from an unconsolidated, undrained test;
B_{pile} = pile width;
γ' = effective, unit-weight of the soil;
z = depth from soil surface;
k_p = Rankine's passive-earth-pressure coefficient, which equals $\tan^2(45° + \phi/2)$;
k_a = Rankine's active-earth-pressure coefficient, which equals $\tan^2(45° - \phi/2)$;
k_o = Rankine's at-rest-earth-pressure coefficient, which equals $(1 - \sin\phi)$;
α = soil parameter ($\phi/2$ for dense or medium sand and $\phi/3$ for loose sand);
β = soil parameter $(45° + \phi/2)$;
ϕ = angle of internal friction for the soil;
J = soil parameter (200 for loose sand, 600 for medium sand, and 1500 for dense sand);
y_{50} = displacement at one-half of the ultimate-soil reaction: ($2.5B_{pile}\,\varepsilon_{50}$ for soft and stiff clay and $2.0B_{pile}\,\varepsilon_{50}$ for very stiff clay); and
ε_{50} = axial strain at one-half of the peak-stress difference from a tri-axial test; or use 0.02 for soft clay, 0.01 for stiff clay, or 0.005 for very stiff clay.

Table 5.3. Parameters for f-z curves

Soil Type	n	f_u		k_v
		H piles	Others	
Clay	1.0	The least of: $2(d+b_f)c_u$ $2(d+2b_f)c_a$ $2(dc_u + b_fc_a)$	The lesser of c_u or c_a times pile perimeter	$\frac{10f_u}{z_c}$
Sand	2.0	$0.02N[2(d+2b_f)]$	0.04 N times pile perimeter	$\frac{10f_u}{z_c}$

where,
b_f = flange width for an HP-shape;
d = depth for an HP-shape;
c_u = cohesion from an unconsolidated, undrained test, which is approximately equal to 97N + 114 (psf);
c_a = adhesion between soil and pile, αc_u (see Fig. 5.6 for α);
N = average, standard-penetration blow count; and
z_c = vertical displacement at maximum force (0.4 in. for sand and 0.25 in. for clay).

Table 5.4. Parameters for q-z curves

Soil Type	n	q_u	k_q
Clay	1.0	$9c_u$	$\frac{10q_u}{z_c}$
Sand	1.0	$8N_{corr}$	$\frac{10q_u}{z_c}$

where,
N_{corr} = corrected, standard-penetration-test blow count at the pile tip; equal to N, if $N \leq 15$, or equal to $15 + 0.5(N-15)$, if $N > 15$.

Table 5.5. Soil properties and displacement parameters for an HP10X42 pile in clay

Properties and Parameters		Soft Clay	Stiff Clay	Very Stiff Clay
Soil Properties	Blow Count, N	3	15	40
	Effective, saturated unit weight, γ'_{sat} (pcf)	50	60	65
	Dry unit weight, γ'_{dry} (pcf)	90-110	115-135	120-140
	Undrained cohesion, c_u (psf)	400	1,600	5,000
p-y Parameters	n	1.0	1.0	1.0
	Saturated conditions p_u (klf) (use smaller value)	3.0 or 1.0 + 0.24z	12 or 3.9 + 0.85z	37 or 12.5 + 10.1z
	Saturated conditions k_h (ksf) (use smaller value)	72 or 24 + 5.8z	580 or 190 + 41z	2,200 or 750 + 610z
f-z Parameters	n	1.0	1.0	1.0
	Saturated conditions f_u (klf) (use smaller value)	1.3	3.6	6.2
	Saturated conditions k_v (ksf)	620	1,700	2,960
q-z Parameters	n	1.0	1.0	1.0
	Saturated conditions q_u (ksf)	3.6	14	45
	Saturated conditions k_q (kcf)	1,700	6,700	21,000

Table 5.6. Soil properties and displacement parameters for an HP10X42 pile in sand

Properties and Parameters		Loose Sand	Medium Sand	Dense Sand
Soil Properties	Blow Count, N	5	15	30
	Effective, saturated unit weight, γ'_{sat} (pcf)	55	60	65
	Dry unit weight, γ_{dry} (pcf)	90-125	110-130	110-140
	Angle of friction, ϕ (deg.)	30	35	40
p-y Parameters	n	3.0	3.0	3.0
	Saturated conditions p_u (klf)	$0.070z^2 + 0.12z$ for $z \leq 20$ ft 1.5z for z > 20 ft	$0.15z^2 + 0.17z$ for $z \leq 18$ ft 2.9z for z > 18 ft	$0.26z^2 + 0.24z$ for $z \leq 22$ ft 5.9z for z > 22 ft
	Saturated conditions k_h (ksf)	8.0z	27z	72z
f-z Parameters	n	1.0	1.0	1.0
	Saturated conditions f_u (klf)	0.5	1.5	3.0
	Saturated conditions k_v (ksf)	150	450	900
q-z Parameters	n	1.0	1.0	1.0
	Saturated conditions q_u (ksf)	40	120	180
	Saturated conditions k_q (kcf)	12,000	36,000	55,000

Table 5.7. Properties for cohesionless sands

Type of Backfill	Angle of Internal Friction, ϕ (deg).	Typical Dry Unit Weight, γ_{dry} (lb/ft^3)	Typical Effectove Saturated Unit Weight, γ_{sat} (lb/ft^3)
Loose sand	30	90-125	55-65
Medium sand	35	110-130	60-70
Dense sand	40	110-140	65-80

Table 5.8. Approximate, horizontal displacement of a wall to activate passive-soil pressure and active-soil pressure

Type of Backfill	Displacement Required to Reach Active Soil-Pressure, Δ_{active}/H	Displacement Required to Reach Passive Soil-Pressure, $\Delta_{passive}/H$
Loose sand	0.004	0.04
Medium-dense sand	0.002	0.02
Dense sand	0.001	0.01

6. ANALYTICAL STUDY AND INTERPRETATION OF EXPERIMENTAL RESULTS FOR THE GUTHRIE COUNTY BRIDGE

This chapter presents the longitudinal, translational, and rotational displacements for the integral abutments; relative displacements at the piers; relative rotations at the top of an abutment pile; relative displacements and rotations at the ends of the PC girders; axial and flexural-bending strains in particular abutment piles; and longitudinal girder strains in selected PC girders that were predicted by the finite-element models for the Guthrie County Bridge. Comparisons are presented and discussed between those analytically-predicted and experimentally-measured, bridge responses that were induced by changes in the bridge temperature. Additional discussions of the analytical and experimental results for this in-service, integral-abutment bridge are presented in the MS thesis for Sayers (2000).

6.1. Bridge displacements

Changes in the bridge length that were induced by temperature changes were investigated using finite-element models for the Guthrie County Bridge. The change in the bridge length is a function of the bridge temperature, coefficients of thermal expansion and contraction, α-coefficients, of the bridge members, and forces restraining bridge movements that are provided by the piers, soil behind the abutments, and abutment piles. Magnitudes for the α-coefficients and other material properties for the Guthrie County Bridge are presented in Table 5.1. The applied temperature distribution on the bridge structure is discussed in Section 5.4. The temperature ranges applied to the analytical models were for a temperature rise from the coldest day to the hottest day.

The horizontal stiffness of the backfill behind the abutments is the major factor in restraining the displacements of the abutments in the longitudinal direction of a bridge. The horizontal stiffness of the soil adjacent to the piles affects the flexural-bending forces induced in the pile, but has a negligible effect on the abutment displacements (Winklehorn and Fang, 1975). The abutment-backfill material was specified in the design drawings to be a compacted, granular backfill. The insitu properties of the backfill were not known.

To model the horizontal stiffness of the abutment backfill, the initial slope of the Husain and Bagnaroil (1996) design curves (Fig. 5.10b), was used for the linear stiffness of the soil springs in the finite-element models. The analytical models for the Guthrie County Bridge did not account for the nonlinear characteristics of the backfill. The non-dimensional, initial slope, S, of the design curves for the horizontal stiffness of the backfill is approximated by

$$S = \frac{(k_p - k_o)}{/H} \tag{6.1}$$

where, Rankine's, passive-soil-pressure coefficient, k_p, and the at-rest-soil-pressure coefficient, k_o, and the corresponding ratio of wall horizontal displacement to wall height, Δ/H, were chosen along the initial slope of the design curve for the backfill stiffness. A summary of the approximate, initial, non-dimensionalized slopes for the horizontal stiffness for the three classifications of granular backfill is provided in Table 6.1.

The calibration of the finite-element models for the Guthrie County Bridge involved abutment displacements during the time period with the largest range in the average, bridge-temperature. The temperature range corresponded to the temperature change from the coldest, average, bridge temperature on January 5, 1999 at 4:00 a.m.

to the hottest, average, bridge temperature on July 20, 1998 at 8:00 p.m. The maximum, experimental range in the average, bridge-temperature was 113 °F.

6.1.1. Abutment longitudinal displacements and changes in bridge length

For the finite-element models, the horizontal stiffness for the abutment backfill was adjusted until the analytically-predicted abutment displacements, which were in the longitudinal direction of the bridge and at the mid-width of the north and south abutments, and the analytically-predicted displacements in the transverse direction of the bridge at the ends of the south abutment were within an acceptable degree of accuracy of these experimentally-measured displacements. As discussed in Chapter 4, there was a significant difference in the experimentally-measured, longitudinal displacements at the north and south abutments for the Guthrie County Bridge. The longitudinal displacement of the north abutment was approximately twice that of the south abutment. Therefore, the horizontal stiffness of the backfill behind the south abutment must be greater than that behind the north abutment. Since a significant amount of water was observed in the soil at the north abutment and no water was detected in the soil at the south abutment, a saturated and a dry, abutment backfill was assumed to exist behind the north abutment and south abutment, respectively.

If the 100%-dry condition for the α-coefficients of the concrete is selected to evaluate the effect of temperature on bridge length, the change in the length of the bridge will be underestimated. In reality, the α-coefficients for the concrete members are somewhere between that for the 100%-dry and 100%-saturated conditions. For the finite-element models for the Guthrie County Bridge, the maximum values for the α-

coefficients of the concrete were used to predict the temperature induced displacements for the abutments.

The calibrated, finite-element models of the Guthrie County Bridge are labeled as the Guthrie, Series-A Models. The analytical model, whose predicted, abutment displacements closely matched the corresponding, experimentally-measured displacements, was named the Guthrie, Series-A, Best-Soil Model. For this model, the initial, non-dimensionalized slope for the horizontal force versus displacement relationship (horizontal-stiffness parameter) of the south abutment backfill, S_{south}, was set equal to 520, which is slightly greater than that for a dry, granular, medium-dense soil as defined by the Husain and Bagnaroil (1996) design curves (Fig. 5.10b). The initial, horizontal-stiffness parameter of the backfill behind the north abutment, S_{north}, was set equal to 380 for a saturated, granular soil. This stiffness is approximately equal to that for a medium-dense soil.

The analytically-predicted, abutment displacements were compared with the experimentally-measured, abutment displacements to determine if the soil was adequately represented in the calibrated, finite-element model. The Guthrie, Series-A, Best-Soil Model had displacement errors of less than 2 percent for the longitudinal displacements at the mid-width of the north and south abutments. The analytically-predicted, transverse displacements at the east and west corners of the south abutment were within 10 percent of the experimentally-measured displacements at those locations.

To study the sensitivity of the abutment displacements to the horizontal stiffness of the soil, Guthrie, Series-A Models were analyzed with an upper-bound and a lower-

bound, soil stiffness for the soil that was adjacent to the piles at both abutments and behind the south abutment. The horizontal stiffness of the soil behind the north abutment was adjusted so that the ratio of the experimentally-measured, longitudinal displacement at the north abutment to that at the south abutment essentially matched that same ratio for the experimentally-measured, abutment displacements.

For the Guthrie County Bridge, the four, finite-element models with bounds placed on the horizontal stiffness of the soil were (1) lower-bound backfill and lower-bound soil around piles, (2) upper-bound backfill and upper-bound soil around piles, (3) upper-bound backfill and lower-bound soil around piles, and (4) lower-bound backfill and upper-bound soil around piles. The lower-bound, soil stiffness was approximately midway between the stiffness of a loose-soil and a medium-dense soil. The upper-bound, soil stiffness was approximately one-quarter of the way from the stiffness of a medium-dense soil to the stiffness of a dense soil. A summary of the horizontal stiffness of the soil and the corresponding change in bridge length for the Guthrie, Series-A Models is listed in Table 6.2. This table also lists the measured change in the length of the Guthrie County Bridge.

For the Guthrie County Bridge, the ratio of the experimentally-measured, horizontal displacement of the south abutment to its height, Δ/H_{south}, was equal to 0.005. A ratio of this magnitude corresponds with the linear portion of the wall-stiffness, design curve for a medium-dense soil that is shown in Fig. 5.10b. Therefore, the approximation of a linear, horizontal stiffness appears to be valid for the soil behind the south abutment. However, the experimental displacement results, which were shown in Fig. 4.20, clearly indicate that this soil stiffness was nonlinear. The ratio of the experimentally-measured,

horizontal displacement of the north abutment to its height, Δ/H_{north}, was equal to 0.011. A ratio of this magnitude implies that the horizontal stiffness for the backfill behind this abutment was slightly beyond the linear range for medium-dense sand. The ISU researchers considered that a linear approximation for the horizontal stiffness of the soil behind both abutments was adequate for this analysis.

The analytically-predicted displacements in the longitudinal direction of the bridge at the ends and at the mid-width of the south and north abutment at the Guthrie County Bridge are shown in Fig. 6.1. These displacements were experimentally measured at mid-width and ends of the south abutment and at the mid-width of the north abutment. These abutment displacements were larger at the acute-angle corner of the bridge deck than those at the obtuse-angle corner of the bridge deck. The largest and smallest abutment displacements that were predicted by the four, finite-element models are labeled the maximum and minimum, respectively, data points in Fig. 6.1. To indicate an approximate elastic curve along the width of an abutment, the analytically-predicted, displacement-data points were connected by straight lines. The maximum displacements occurred for the least-stiff-soil conditions (lower-bound backfill and lower-bound soil around pile). Conversely, the minimum abutment displacements occurred for the stiffest-soil conditions (upper-bound backfill and upper-bound soil around piles). The finite-element model with the best-soil conditions predicted abutment displacements that closely matched the experimentally-measured displacements.

6.1.2. Abutment transverse displacements

Abutment displacements in the transverse direction of a skewed bridge can occur since the passive-soil pressure acts normal to the abutment backwall. A component of

this force acts perpendicular to the longitudinal axis of the bridge. If the skew angle is large enough, this soil-force component pushes the abutment in the transverse direction of the bridge and towards the acute-angle corner of the bridge deck. Thermal expansion of an abutment induces abutment displacements that are additive with the transverse displacement of the abutment at the acute-angle corner of the bridge deck that are induced by the passive-soil pressure behind the abutment.

For the finite-element models of the Guthrie County Bridge, the stiffness of the tangential soil-springs on the back face of an abutment was set equal to a percentage of the normal-spring stiffness for the backfill. Initially, the stiffness of the tangential springs was assumed to equal one-half of that for the normal springs, as recommended by Barkan (1992). For this magnitude of tangential-spring stiffness, the analytically-predicted, transverse displacements of the south abutment were too large. When the tangential-spring stiffness were set equal to the normal-spring stiffness for the Guthrie, Series-A, Best-Soil Model, the analytically-measured, transverse, abutment displacements essentially matched the experimentally-measured, transverse, abutment displacements. Figure 6.2 shows the analytically-predicted and experimentally-measured ranges for the displacements at the corners of the south abutment for the Guthrie County Bridge. Positive displacements shown in Fig. 6.2 are towards the acute-angle of the bridge deck. These displacement ranges were in the transverse direction of the bridge, and they are based on temperatures between the coldest day on January 5, 1999 and hottest day on July 20, 1998. Transverse displacements were not experimentally measured at the north abutment of this bridge.

6.1.3. Abutment rotations in a vertical plane

Abutment rotation in a vertical plane that is parallel to the longitudinal axis of the bridge is caused by the moment produced by the resultant horizontal force, which equals the sum of the force due to the passive-soil pressure behind the abutment and the pile forces that restrain bridge expansion, that acts below the center of gravity of the superstructure; the temperature gradient existing through the depth of the superstructure; and the difference between the α-coefficients for the concrete in the deck and girders. The experimental rotation for the south abutment of the Guthrie County Bridge was extremely small. The range for the rotation of this abutment was approximately 0.080 deg.

The Guthrie, Series-A, Best-Soil Model overestimated the field-measured rotation of the south abutment by nearly a factor of two. The ISU researchers tried to correct the predicted abutment rotations by (1) applying a horizontal restraining force at the deck level to represent the force that is induced when the bridge pushes against an approach slab, (2) reducing the temperature gradient through the depth of the superstructure, (3) reducing the difference in the α-coefficient for the concrete in the deck and girders, and (4) using different profiles for the passive-soil pressure behind the abutments.

The ISU researchers observed that the width of the expansion joint between the approach slab and the bridge deck narrowed as the Guthrie County Bridge expanded due to an increase in the average, bridge temperature. Therefore, the approach slab slide on the corbel that supported the approach slab at the end of the bridge. The finite-element model for the bridge was reanalyzed with a restraining force that was applied at the top of the abutment to represent the friction force between the approach slab and

the corbel. The application of this frictional force had a negligible effect on the predicted, abutment rotation.

When the finite-element model of the Guthrie County Bridge was reanalyzed with a reduction in the vertical-temperature gradient and a reduction in the difference in the α-coefficient for the concrete in the girders and deck, only a slight reduction occurred in predicted, abutment rotation. The analytical prediction for the abutment rotation still overestimated the experimental measurement. Even if the passive-soil pressure distribution behind the abutment was modeled with the maximum pressure at the ground level and zero pressure at the bottom of the abutment pile cap, the analytically-predicted, abutment rotation was still larger than the measured rotation. The cause was not determined for the discrepancy between the predicted and measured, abutment rotations.

The predicted, flexural-bending strains for the abutment piles were affected by the overestimation of the abutment rotation. For the pile orientation used in the Guthrie County Bridge, the abutment rotation affects both x-axis and y-axis, flexural-bending strains. The x-axis, flexural-bending strains were not investigated with these finite-element models, since these strains were only slightly affected by the abutment rotation. When a pile head translates in the longitudinal direction of the bridge due to an increase in the average, bridge temperature; abutment rotation caused by the passive-soil pressure; a positive vertical-temperature gradient through the depth of the superstructure; and the induced forces at the top of the pile, the rotational restraint is reduced at the top of the pile. A reduction in the rotational restraint at a pile head will cause a reduction in the flexural-bending strains for the pile. The y-axis, flexural-

bending strains in the abutment piles that were predicted by the Guthrie, Series-A, Best-Soil Model were less than the experimentally-measured, flexural-bending strains.

To analytically model the Guthrie County Bridge more closely, another set of finite-element models was developed with the rotation of the south abutment set equal the experimentally-measured rotation. Since experimentally-measured rotations were not available for the north abutment, the finite-element models did not have constraints set on the rotation of this abutment. These finite-element models were named the Guthrie, Series-B Models. Except for the rotational constraints that were applied to the south abutment, the displacement-calibration method that was used for the Guthrie, Series-A Models was applied to the Guthrie Series-B Models. These rotation constraints were imposed to each of the nodes for the pile cap and backwall for the south abutment. Rotation constraints were not imposed to the nodes in the wingwalls for this abutment. Since the maximum α-coefficient for the concrete in the bridge superstructure caused the analytical models to overestimate the abutment displacements, the 100%-dry α-coefficient was used for the slab and girders in the Guthrie, Series-B Models. The calibrated backfill stiffness was adjusted until the analytically-predicted, longitudinal and transverse displacements for the south abutment were approximately equal to the experimentally-measured, abutment displacements. The calibrated, backfill stiffness for the Guthrie, Series-B Models was not as stiff as that for the Guthrie, Series-A Models. The calibrated, horizontal-stiffness parameter of the south abutment backfill, S_{south}, for the Guthrie, Series-B, Best-Soil Model was 440, which is approximately equal to the initial, non-dimensionalized, slope for the horizontal force versus displacement relationship of a dry, granular, medium-dense soil.

The Guthrie, Series-B Models were used to investigate the upper-bound and lower-bound, soil-stiffness models. The four, previously described, soil-stiffness-bound models (lower-bound backfill and lower-bound soil around piles, upper-bound backfill and upper-bound soil around piles, upper-bound backfill and lower-bound soil around piles, and lower-bound backfill and upper-bound soil around piles) were used to determine the minimum and maximum limits for the y-axis, flexural-bending strains in the south abutment piles. Since the rotation of the abutment had only a small effect on the x-axis, flexural-bending strains, these strains were not investigated with these finite-element models. The non-dimensionalized, horizontal-stiffness parameters for the abutment backfill and changes in the bridge length for the Guthrie, Series-B Models, and the experimentally-measured change in the bridge length are listed in Table 6.3. The calibrated, horizontal stiffness for the soil behind the south abutment in the Guthrie, Series-B Models was about 84 percent of that stiffness in the Guthrie, Series-A Models. Except for the lower-bound backfill and upper-bound soil around pile model, the soil stiffness behind the north abutment of the Guthrie, Series-B models was about 75 percent of that stiffness for the Guthrie, Series-A Models. The Guthrie, Series-B Models predicted different displacements at the ends of the abutments. The horizontal displacement of the abutment in the longitudinal direction of the bridge at the acute-angle corner of the bridge deck was greater than that displacement at the obtuse-angle corner of the bridge deck. This displacement relationship was confirmed by the experimental measurements at the Guthrie County Bridge.

6.1.4. Relative displacements at the piers

Relative displacements between the pier cap and the center PC girder were measured in the longitudinal direction of the bridge at both piers of the Guthrie County Bridge. The range in the relative displacements at the south pier, which is an expansion pier, was larger than that at the north pier, which is a fixed pier. Between June 20, 1998 and January 5, 1999, the experimental range for the relative displacements at the south pier was 0.040 in. The Guthrie, Series-A, Best-Soil Model predicted a 0.023-in., relative displacement at this pier. The finite-element models with the upper-bound and lower-bound, soil stiffness predicted a relative displacement at the south pier of 0.033 in. and 0.011 in., respectively. All of the finite-element models for the Guthrie County Bridge underestimate the experimentally-measured, relative displacement at the south pier.

The fixed-pier detail for the north pier at the Guthrie County Bridge was not completed fixed regarding relative displacements between the pier diaphragm and the pier cap, since the pier diaphragm bears on a continuous neoprene pad that rests on the top of the pier cap and the keyways between the pier diaphragm and the pier cap is lined with a compressible, expansion-joint filler. Between June 20, 1998 and January 5, 1999, the experimentally-measured range for the relative displacement at the north pier was 0.027 in. The analytical prediction for this displacement was 0.014 in. Even though the analytical models underestimated the relative movement between the PC girders and the north pier cap, the ISU researchers considered the difference between the analytical and experimental displacements to be too small to affect the longitudinal displacements of the abutments.

6.1.5. Relative rotations at the top of an abutment pile

At the Guthrie County Bridge, the relative rotation was measured between the bottom of the pile cap for the south abutment and a point that was 18 in. below the pile cap on the pile near the mid-width of the abutment. The experimental range for this relative rotation was approximately 0.100 deg. As shown in Fig. 6.3, the Guthrie, Series-A Models underestimated the range in this rotation, and the Guthrie, Series-B Models provided better predictions for the range in this relative rotation. When the vertical rotation at the south abutment was set equal to the experimentally-measured rotation for the Guthrie, Series-B Models, good correlation occurred between the analytical and experimental, relative rotation at the top of this instrumented pile.

6.1.6. Relative displacements and rotations at the ends of the PC girders

Relative displacements in the longitudinal direction of the bridge between the top and bottom flange of the center PC girder and the face of the south-abutment backwall were measured at the Guthrie County Bridge. These experimentally-measured displacements were extremely small compared to other displacement measurements. The analytical predictions for the relative rotation between the PC girder at the location of the transducers and the abutment backwall were less than 0.0006 deg.

6.2. Pile strains

6.2.1. Pile flexural-bending strains

The finite-element models for the Guthrie County Bridge predicted that the abutment pile near the acute-angle corner of the bridge deck had the largest horizontal displacement along the longitudinal direction of the bridge and the greatest y-axis,

flexural-bending strains compared to those displacements and strains for the other piles in the same abutment. The greatest, x-axis, flexural-bending strains were predicted to occur in the piles near the ends of the abutments, since at these locations, the transverse abutment displacements were the largest.

Analytically-predicted and experimentally-measured, pile strains were compared to determine the accuracy of the finite-element models for predicting bridge responses to temperature changes. The comparisons of the pile bending strains were made using different temperature ranges over which the strain gages provided continuous and reliable measurements. The largest temperature range occurred between the maximum and minimum, average, bridge temperatures on July 20, 1998 and January 5, 1999, respectively. A couple of piles had strain data that was reliable over at least a 100 °F-temperature range for the average, bridge temperature. The experimentally-measured, pile strains were minimally affected by small changes in the average, bridge temperature. This observation was especially true at the south abutment where the abutment was nearly stationary for average, bridge temperatures above 60 °F. Table 6.4 lists the abutment; pile location; depth of the pile cross section below the bottom of the pile cap; dates for the coldest and hottest temperatures for the temperature range; and the average, bridge-temperature ranges for which continuous and reliable, experimentally-measured, x-axis and y-axis, pile, bending-strain data was available.

The x-axis and y-axis, flexural-bending-strain ranges from the Guthrie, Series-A models are shown in Figs. 6.4 and 6.5. In these figures, the first letter in the pile notation that is shown along the abscissa scale for the graph refers to the abutment (S for south, N for north). The second letter in the pile notation refers to the pile location in

the abutment (W for west, C for near the mid-width, and E for east). The maximum, flexural-bending strains occurred when the displacement of the pile head was large and when the soil adjacent to the pile had the largest horizontal stiffness, which corresponded to the finite-element model with the lower-bound backfill and upper-bound soil around piles. The minimum, flexural-bending strains occurred when the pile-head displacement is small and the soil adjacent to the pile had the least horizontal stiffness, which corresponded to the finite-element model with the upper-bound backfill and lower-bound soil around piles.

The bridge design drawings show that the webs of the abutment piles are oriented parallel to the face of the abutment. However, the pile near mid-width of the south abutment of the Guthrie County Bridge evidently twisted when it was driven. This pile is rotated approximately 25 deg. in the clockwise direction from the intended orientation, as shown in Fig. 6.6. This twisted-pile orientation essentially induces only y-axis, flexural-bending strains when this abutment displaces in the longitudinal direction of the bridge. The majority of the x-axis, flexural-bending strains in this pile are induced by the abutment displacements along the transverse direction of the bridge.

Since the vertical rotation of the south abutment was overestimated by the Guthrie, Series-A Models, these finite-element models underestimated the y-axis, flexural-bending strains in the SC pile at the top cross section, as shown in Fig. 6.5. The vertical rotation of the abutment causes some rotational release of a fixed, pile-head condition. Flexural-bending strains in a pile are reduced when a pile head is allowed to rotate. The predicted, y-axis, flexural-bending strains at the other pile cross

sections could not be compared to experimentally-measured strains, since reliable, strain data were not available at those pile cross sections.

For the Guthrie, Series-A, Best-Soil Model, the y-axis, flexural-bending strains in the NC pile at the top cross section and the NW pile at the bottom cross section had a good correlation with the experimental measurements, as shown in Fig. 6.5. This strain correlation may indicate that the predicted, north-abutment rotations did not exceed the experimentally-measured rotations. However, this hypothesis cannot be confirmed, since vertical rotations were not measured at this abutment. As shown in Fig. 6.4, the x-axis, flexural-bending strains that were predicted by the Guthrie, Series-A Models for the SW, SC, NW, and NC piles at the top cross section and for the SC and NW piles at the bottom cross section correlated well with the experimentally-measured, x-axis, flexural-bending strains.

The overestimation of the vertical rotation of the south abutment that was predicted by the Guthrie, Series-A Models was corrected by setting the abutment rotation equal to the measured rotation in the Guthrie, Series-B Models. For these latter finite-element models, the predicted ranges for the y-axis, flexural-bending strains in the south abutment piles are shown in Fig. 6.7. Since the Guthrie, Series-B Models were analyzed to determine the effect of incorporating the measured rotation at the south abutment on the predicted strains in the south-abutment piles, the ranges for the induced strains in the piles for the north abutment were not presented in the figure. Experimentally-measured, y-axis, flexural-bending strains, which were reliable for the temperature ranges that are listed in Table 6.4, were only available at the top cross section of the pile near the mid-width of the south abutment. At this cross section for

the SC pile, good correlation occurred between the analytically-predicted and experimentally-measured, bending strains. A comparison of the analytical results shown in Figs. 6.5 and 6.7 indicates the effect of the abutment rotation on the y-axis, flexural-bending strains at the two cross sections of the monitored piles in the south abutment. As expected, the largest difference in the magnitude of these predicted, pile strains occurred with the Guthrie, Series-B Models for a particular horizontal stiffness of the backfill soil. The overestimated, abutment rotation caused a discrepancy in the range of the predicted, y-axis, flexural-bending strain of between 100 and 200 micro-strains.

The maximum, x-axis and y-axis, flexural-bending strains along the length of the west pile in the north abutment of the Guthrie County Bridge that were predicted by the Guthrie, Series-A Models are shown in Fig. 6.8. These pile strains are the maximum strains that occurred at the flange tips for the two cross sections. Data points for the maximum, experimentally-measured, x-axis, flexural-bending strains that were mathematically extrapolated to the flange tips at 9 in. and 33 in. below the pile cap are included in Fig. 6.9a. These measured strains correspond to those strains that are shown in Fig. 4.30. The measured, x-axis, flexural-bending strain for the lower, monitored, cross section of this pile was only available for an average, bridge-temperature range of 103 °F. Figure 6.9b also shows the maximum, experimentally-measured, y-axis, flexural-bending strain that was mathematically extrapolated to the flange tips for the pile cross section at 33 in. below the pile cap.

For the analytical models, the maximum, flexural-bending strains in the pile occurred at the bottom of the abutment pile cap, and an inflection point was located

approximately 5 ft below the bottom of the pile cap. The maximum, flexural-bending strains below the inflection point in the pile were approximately 60% of those strains at the bottom of the pile cap. Figure 6.8 shows that the predicted, x-axis and y-axis, flexural-bending strains were negligible in the lower portion of the pile length.

The maximum, predicted, x-axis and y-axis, flexural-bending strains at the flange tips for the piles at the east-end, near the mid-width, and west-end of each abutment and the pile in the south-west wingwall at the acute-angle corner of the bridge deck are shown in Fig. 6.9. The finite-element models with the best estimate of the soil properties were used to predict the flexural-bending strains in the pile cross section at the bottom of the pile cap. The Guthrie, Series-A, Best-Soil Model was used to predict the x-axis and y-axis, flexural-bending strains in the north-abutment piles and to predict the x-axis, flexural-bending strains in the south-abutment piles. The Guthrie, Series-B, Best-Soil Model was used to predict the y-axis, flexural-bending strains in the south-abutment piles.

Abutment displacements in the longitudinal direction of the bridge were the greatest at the acute-angle corners of the bridge deck. Hence, the largest flexural-bending strains were in the abutment piles that were near these locations. The Guthrie, Series-A, Best-Soil Model, predicted an 1800-micro-strain, maximum, combined x-axis and y-axis, flexural-bending strain for the east pile of the north abutment (NE pile) in the pile cross section that is located at the bottom of the pile cap. This predicted strain exceeded the 1240-micro-strain, yield strain for A36 steel. For the west pile of the south abutment (SW pile), this finite-element model predicted a maximum, combined, flexural-bending strain of about 930 micro-strains in a similar pile cross section. If the SW pile

had a rotationally, fixed-head condition, the predicted, maximum, combined, flexural-bending strain was approximately 1130 micro-strains. The predicted, maximum, combined, flexural-bending strain for the northeast wingwall pile in the pile cross section that is located at the bottom of the pile cap was about 1300 micro-strains. The majority of this strain was due to y-axis, flexural-bending of that pile.

6.2.2. Pile axial strains

Changes in the axial strains in the abutment piles were a daily phenomenon. As previously shown in Fig. 4.8b, these strains did not have a seasonal correlation with the average, bridge temperature or abutment displacement. Figure 6.10 shows the range in the predicted, axial strains in four piles for the north abutment of the Guthrie County Bridge. This figure also shows the experimental range of the axial strains in the pile near the mid-width of the north abutment (NC pile) that was computed using Eq. 4.5. The maximum, experimental, axial-tension-strain range was about 95 micro-strains for this pile. The axial strain predicted by the Guthrie, Series-A, Best-Soil Model for the NC pile was a tension strain of approximately 110 micro-strains. The experimental, axial strains in the other pile cross sections in the Guthrie County Bridge were inconclusive and were not included in the comparison study of the predicted and measured, axial strains.

Axial forces in the piles for the wingwalls and backwall resist the vertical rotation of an integral abutment. The magnitude of the predicted, axial strains in the north-east-wingwall pile was approximately five times larger than those strains in the piles for the north abutment. The predicted range in the axial strain for the north-east-wingwall pile

is shown in Fig. 6.10. Compressive, axial strains were induced in the wingwall piles when the bridge expanded due to an increase in the average, bridge temperature.

6.3. Girder strains

A thermal expansion of a bridge superstructure will cause the passive-soil pressures of the abutment backfill and end forces in the abutment piles to induce moments at the ends of the bridge. If the bridge is assumed to be a continuous structure with three equal spans, the moment in the bridge superstructure at the interior supports (piers) will be 20 percent of the applied moment at the end supports (abutments). Strain gages were used to measure the strain in the top and bottom flanges of selected PC girders, as described in Section 4.4.2. The differences between the strains in the top and bottom flanges of the girders near the abutment were noticeably larger than those strain differences near the piers, as shown in Fig. 4.33.

The theoretical-strain profiles through the depth of a bridge superstructure are shown in Fig. 6.11. The temperature profile and the corresponding, unrestrained, change in strains, $\Delta\varepsilon_{temp}$, due to the changes in temperature have a nonlinear distribution, as shown in Figs. 6.11b and 6.11c, respectively. The vertical profile for the bridge temperatures was assumed to be bilinear, as discussed in Chapter 4. Also, recall that the α-coefficient of the concrete in the bridge deck was greater than that for the PC girders at the Guthrie County Bridge. A profile through the depth of a bridge superstructure for the change in the total strain, $\Delta\varepsilon_{total}$, that is shown in Fig. 6.11d was assumed to be linear according to the simple-bending theory that plane sections remain plane before and after bending. The shaded areas in Fig. 6.11e represent the change in strains due to the induced change in stress, $\Delta\varepsilon_{stress}$, which are determined by

$$\varepsilon_{stress} = \varepsilon_{total} - \varepsilon_{temp} \tag{6.2}$$

Typically, compressive, longitudinal strains are expected in the RC deck and tensile, longitudinal strains are expected in the PC girders due to the different α-coefficients for the concrete in the deck and girders and positive, vertical-temperature gradient through the depth of the superstructure. An unrestrained deck would expand further than an unrestrained girder due to the larger temperature increase and larger α-coefficient for the slab than those for the girders of the Guthrie County Bridge. For strain compatibility at the joint between the bridge deck and the girders, axial and bending strains are induced in the superstructure members as the deck is compressed and the girders are stretched to develop the final-strain profile shown in Fig. 6.11e. The ranges for the difference between longitudinal strains in the top and bottom flanges of selected PC girders that were predicted by the Guthrie, Series-A Models are shown in Fig. 6.12. For some of the girders, the experimentally-based strain differences are also shown in the figure. The strain ranges shown are based on absolute values of the total strains in the PC girder, cross sections that were located near the abutments and the piers. At the PC girder cross sections that were located near the abutments, the ranges for the strain differences that were predicted by the Guthrie, Series-A Models were larger than the corresponding, experimentally-based, strain differences. Overestimation of the abutment rotations that was described in Section 6.1.3 may account for the overestimation of the PC girder strains. Figure 6.13 presents girder-strain information, which is similar to that shown in Fig. 6.12. For Fig. 6.13, the Guthrie, Series-B Models were used to predict the ranges for the differences in the PC girder strains. The Guthrie, Series-B Models provided a better correlation between the predicted and the

experimental strains than that provided by the Guthrie, Series-A Models. Since the vertical rotations at the north abutment were not experimentally measured, the Guthrie, Series-B Models, which set the vertical rotation at the south abutment equal to the experimentally-measured rotation at the south abutment, could not adequately predict the girder strains near the north abutment.

The Guthrie, Series-B, Best-Soil Model was used to predict the force-induced, longitudinal strains in the PC girder cross sections near each end of the south span for the Guthrie County Bridge. These predicted strains, which are shown in Fig. 6.14, were due to stresses in the girders. The flexural-bending strains at the extreme top fibers of the PC girders and axial strains in the PC girders are shown in Figs. 6.14a and 6.14b, respectively. The bending strains were induced by moments about the horizontal axis (x-axis) for the composite- girder cross section. A maximum, combined axial and flexural-bending strain of approximately 170 micro-strains in tension was predicted in the top flange of the east PC girder for the cross section that was located near the south abutment. Using Hooke's Law and a modulus of elasticity for the concrete in the PC girder from Table 5.1, the equivalent stress for this strain is about 750 psi. The restraint to vertical rotation of an abutment that is provided by the in-plane flexural stiffness of the abutment wingwalls and the axial stiffness of the wingwall pile and the backwall piles near a wingwall caused the bending strains to be higher in the exterior, PC girders than those strains that were induced in the interior, PC girders.

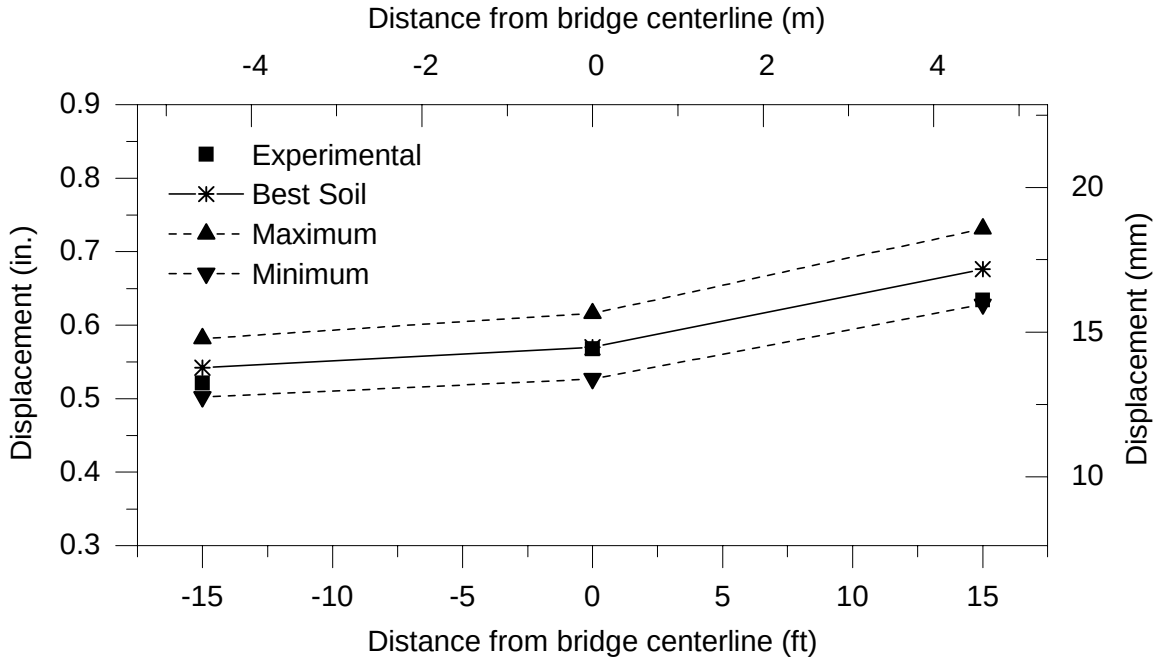

(a) South abutment

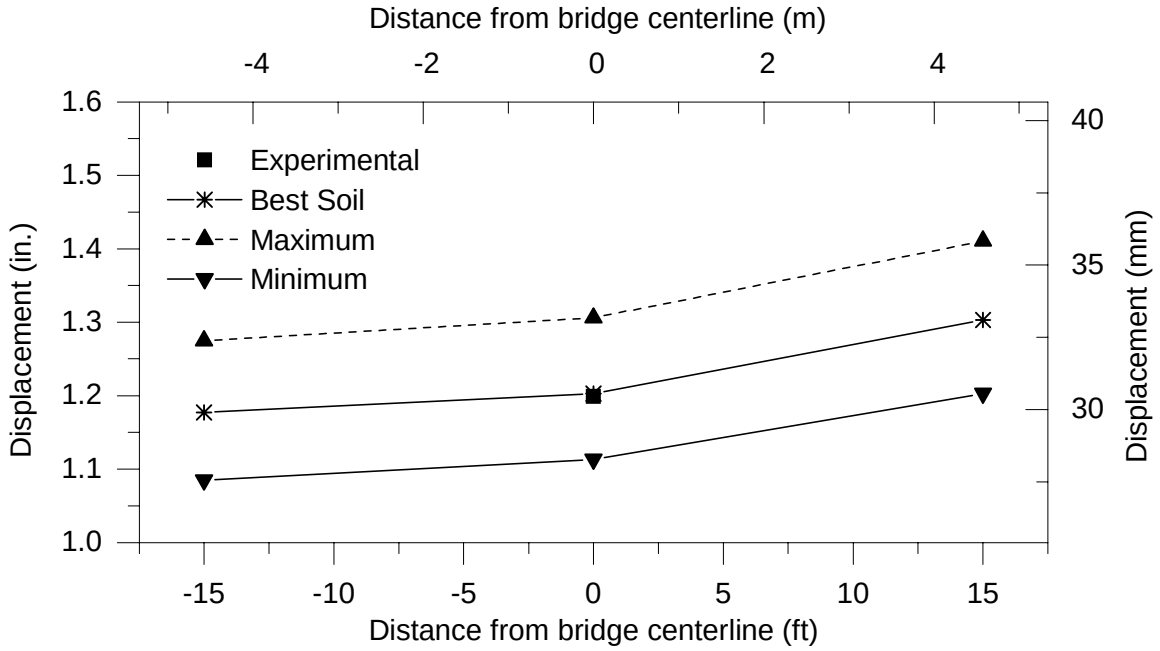

(b) North abutment

Figure 6.1. Abutment longitudinal displacements predicted by the Guthrie, Series-A Models and experimentally measured at the Guthrie County Bridge

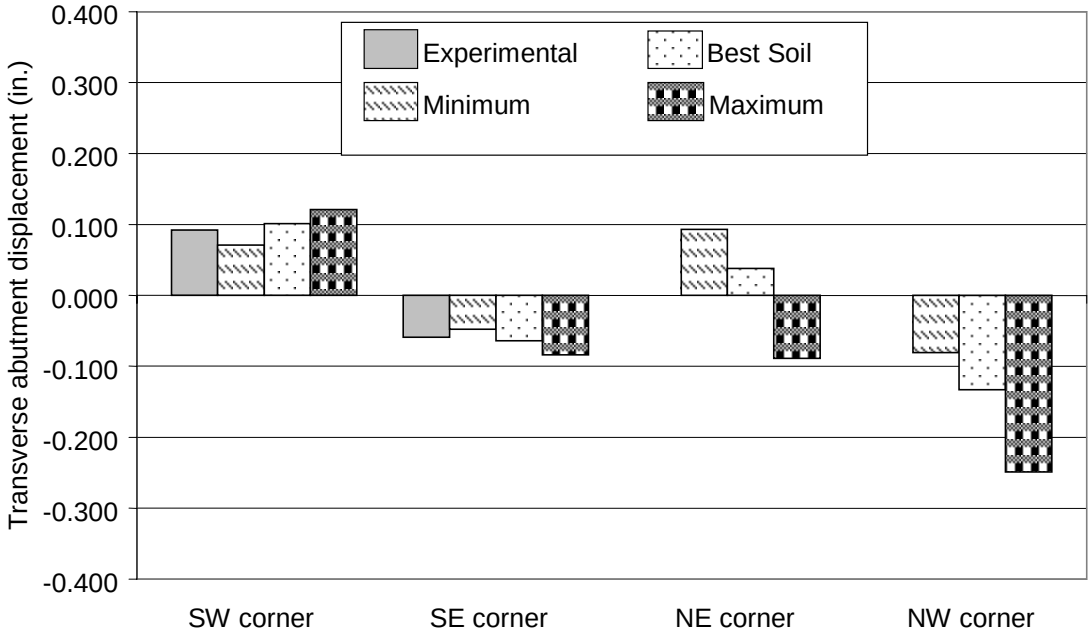

Figure 6.2. Abutment transverse displacements predicted by the Guthrie, Series-A Models and experimentally measured at the Guthrie County Bridge

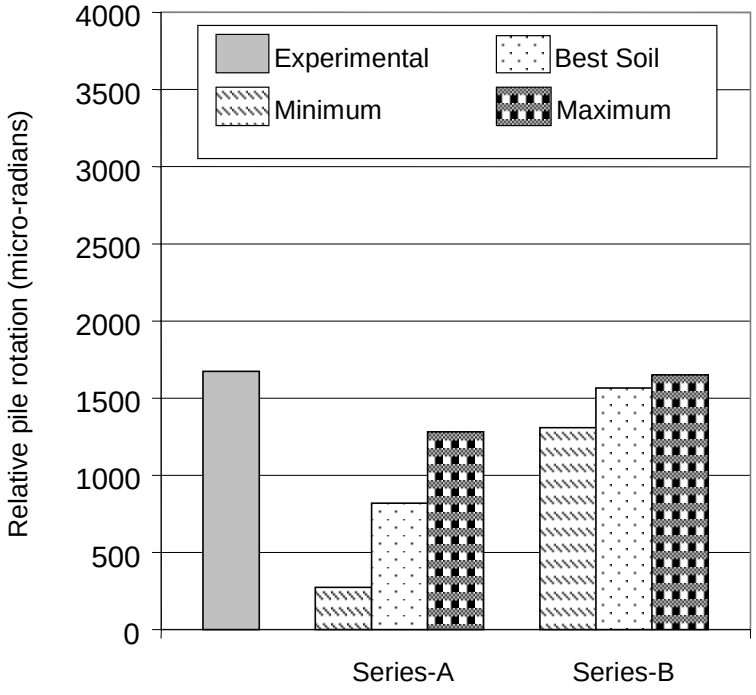

Figure 6.3. Analytically-predicted and experimentally-measured, relative, rotations of a pile at the Guthrie County Bridge

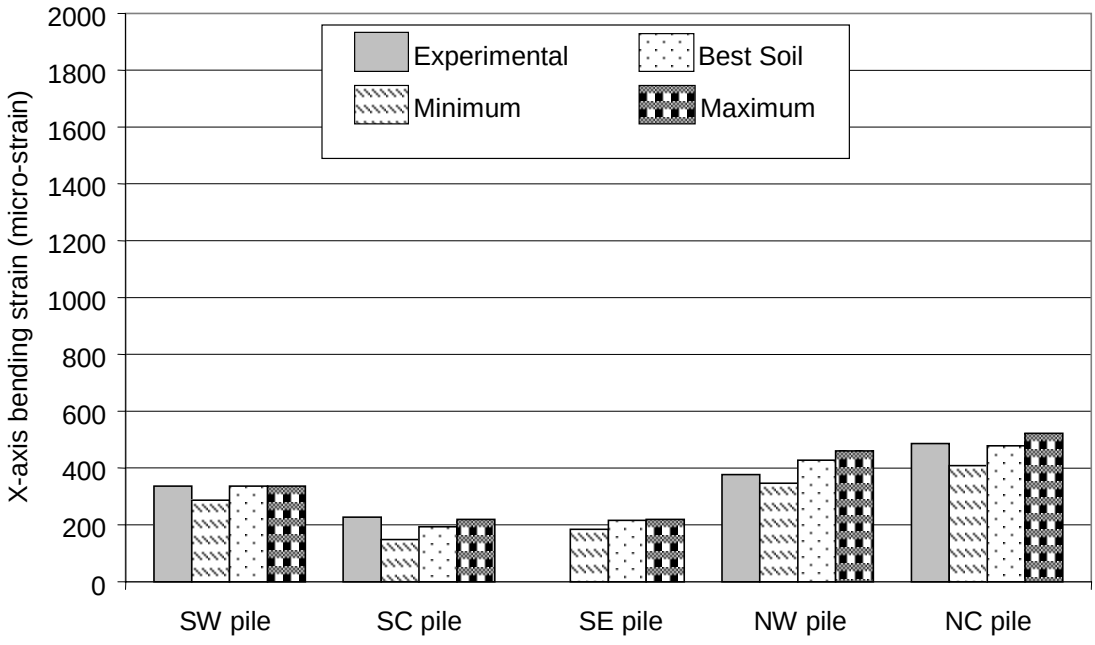

(a) Upper cross section at 9 in. below the pile cap

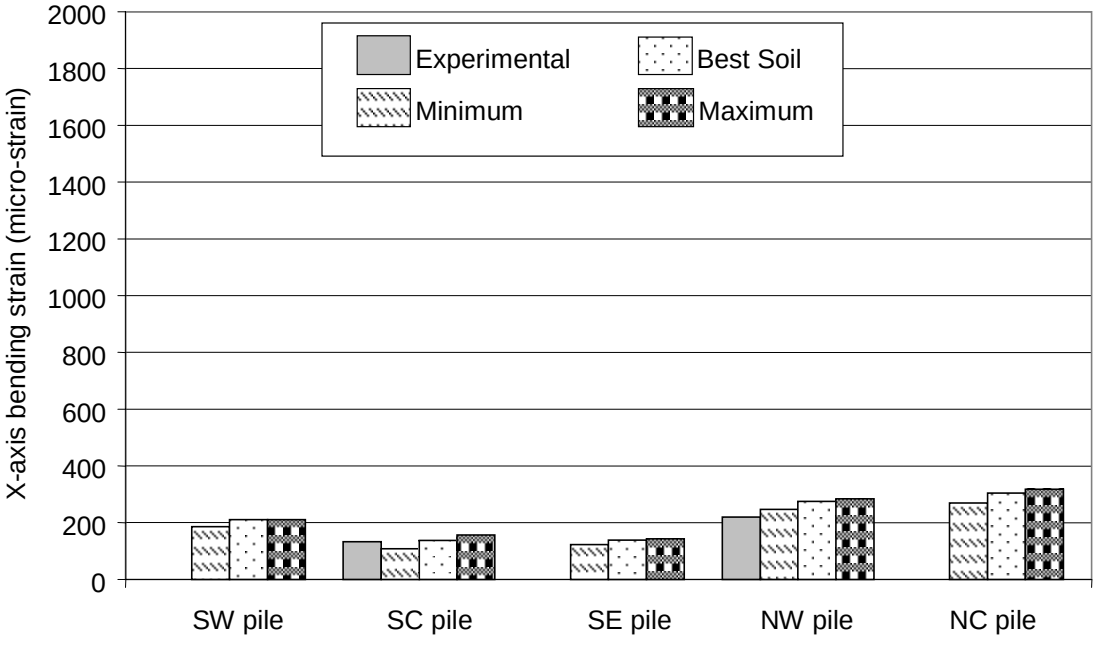

(b) Lower cross section at 33 in. below the pile cap

Figure 6.4. X-axis, flexural-bending strains predicted by the Guthrie, Series-A Models and experimentally measured at the Guthrie County Bridge

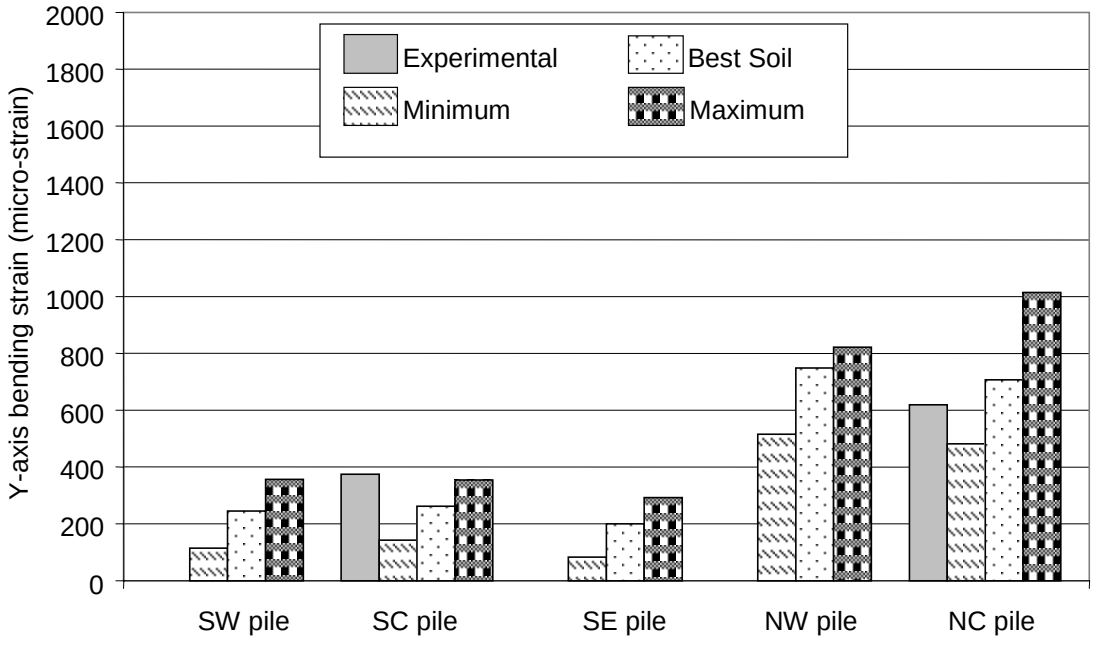

(a) Upper cross section at 9 in. below the pile cap

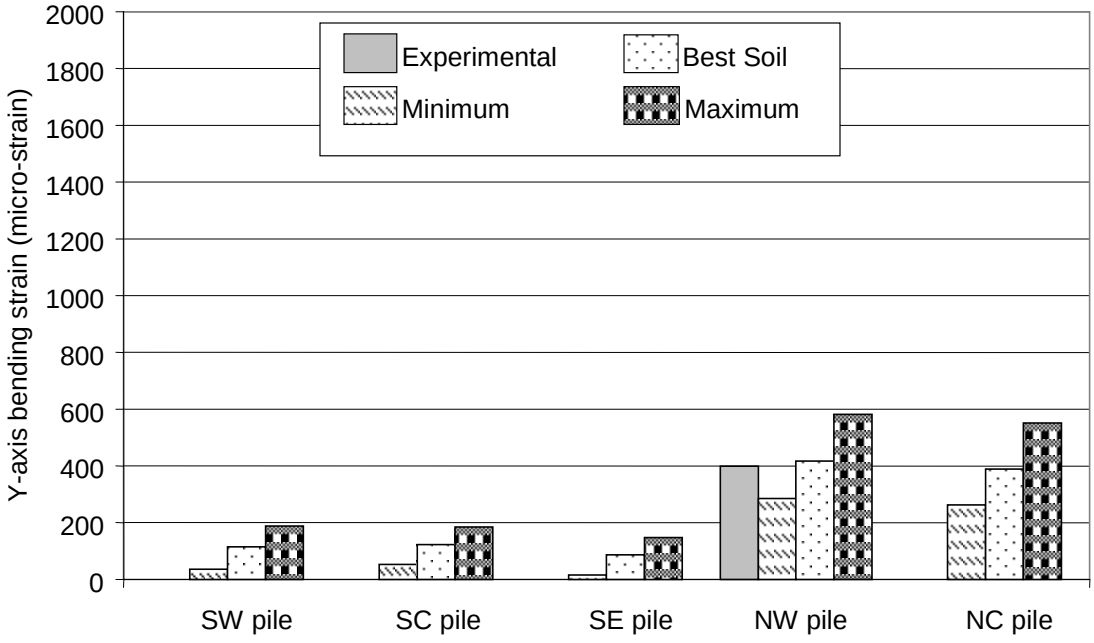

(b) Lower cross section at 33 in. below the pile cap

Figure 6.5. Y-axis, flexural-bending strains predicted by the Guthrie, Series-A Models and experimentally measured at the Guthrie County Bridge

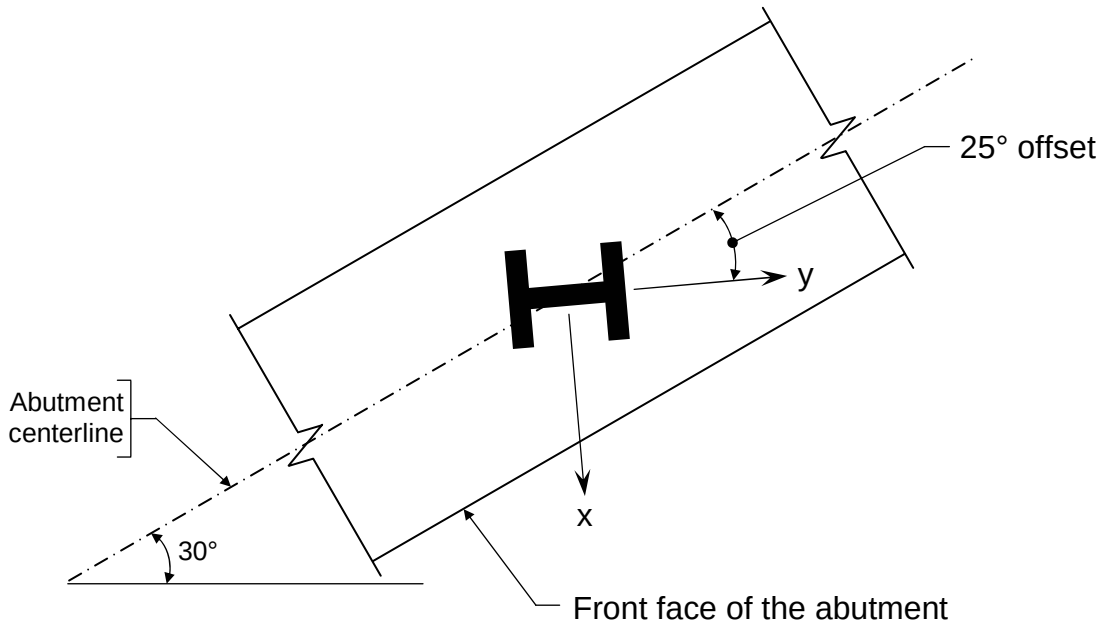

Figure 6.6. Orientation of the pile near the mid-width of the south abutment for the Guthrie County Bridge

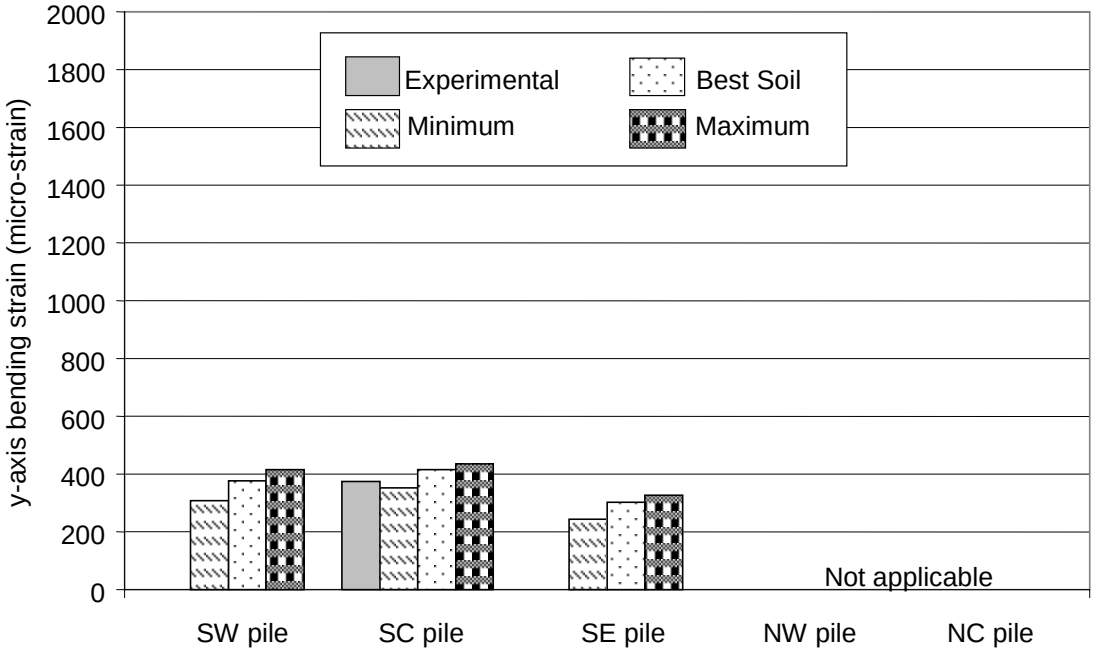

(a) Upper cross section at 9 in. below the pile cap

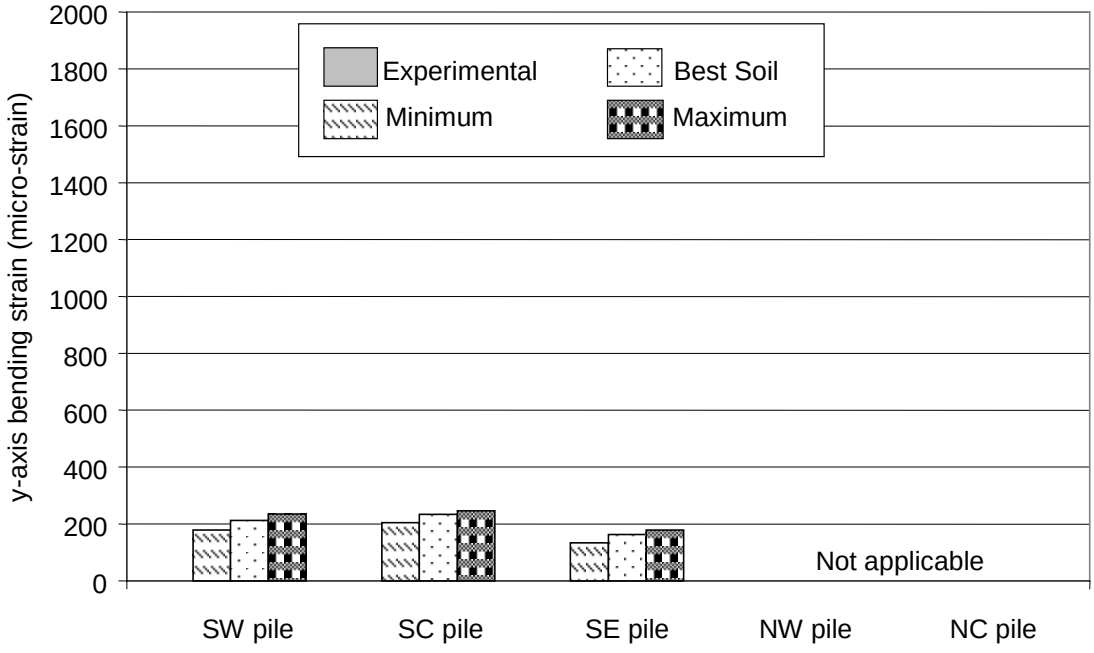

(b) Lower cross section at 33 in. below the pile cap

Figure 6.7. Y-axis, flexural-bending strains predicted by the Guthrie, Series-B Models and experimentally measured at the Guthrie County Bridge

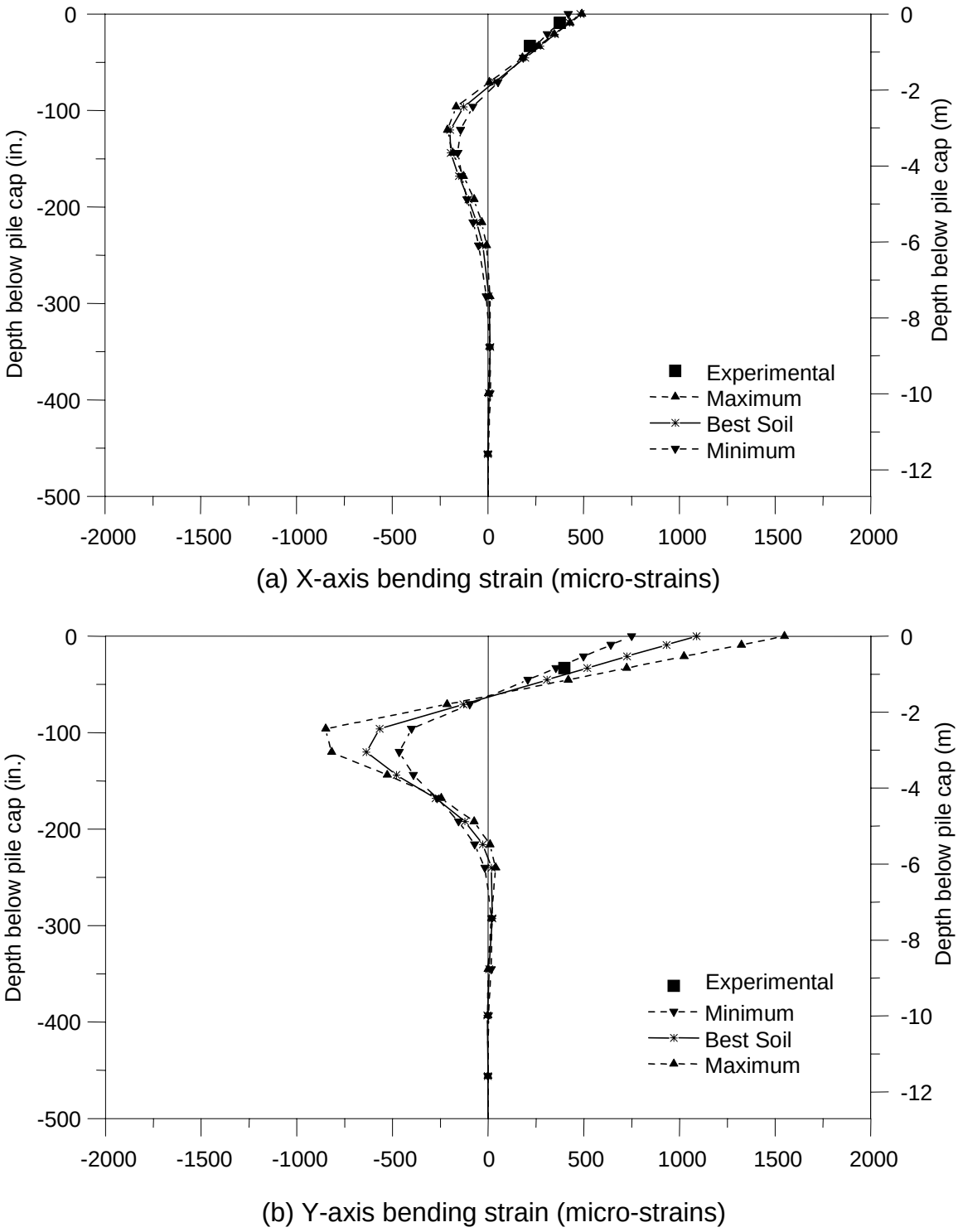

Figure 6.8. Strain variation predicted by the Guthrie, Series-A Models along the length of the west pile for the north abutment and experimentally measured at the Guthrie County Bridge

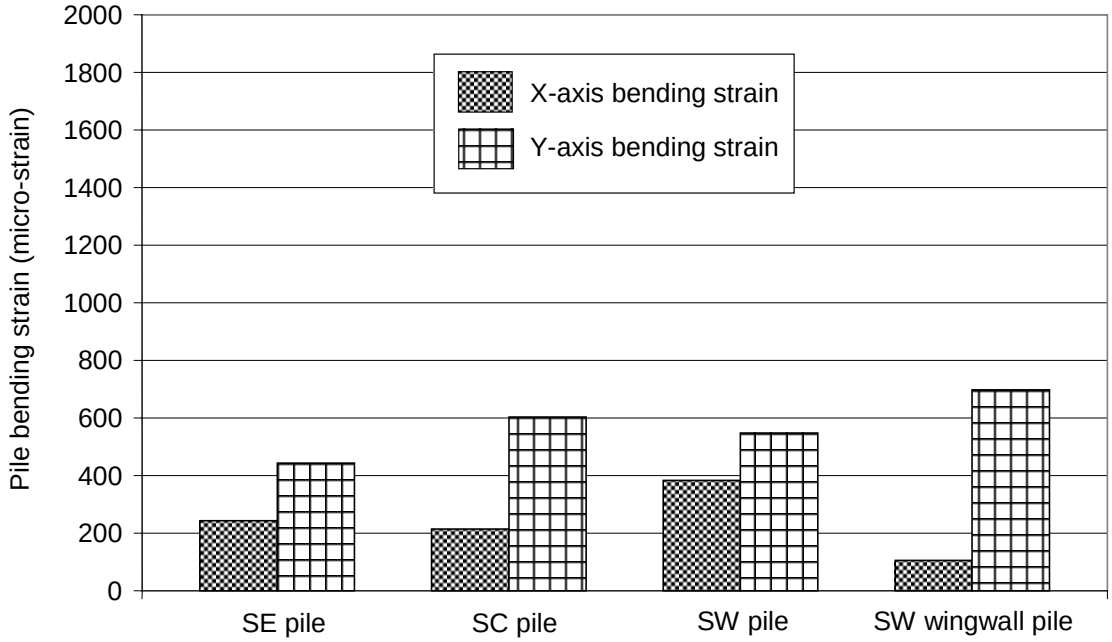

(a) South abutment

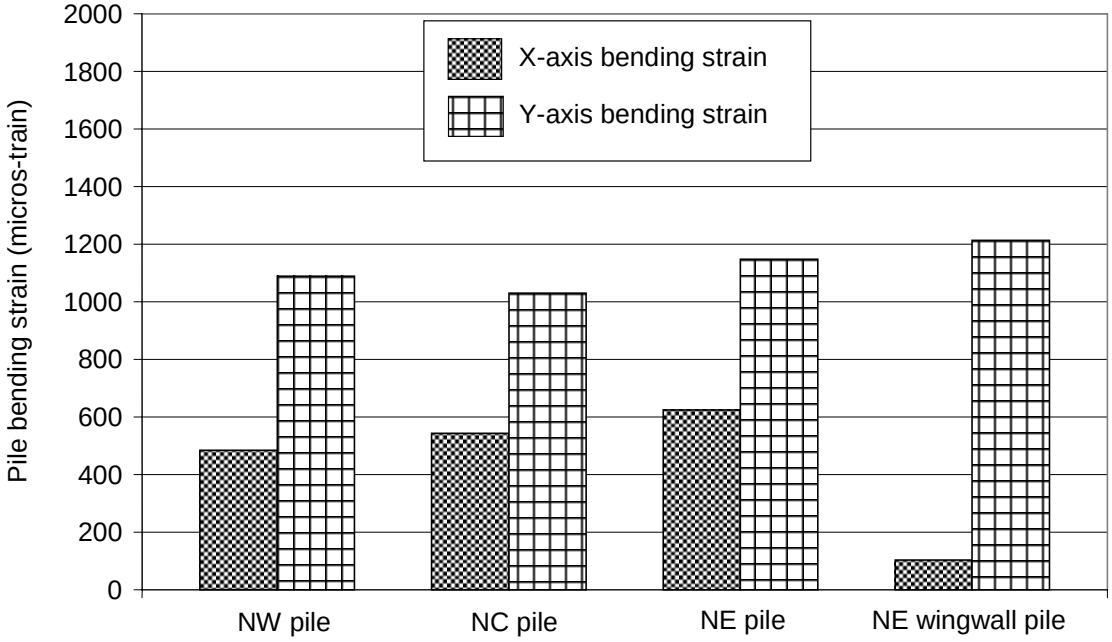

(b) North abutment

Figure 6.9. Maximum, predicted, flexural-bending strains in the monitored, abutment piles at the Guthrie County Bridge

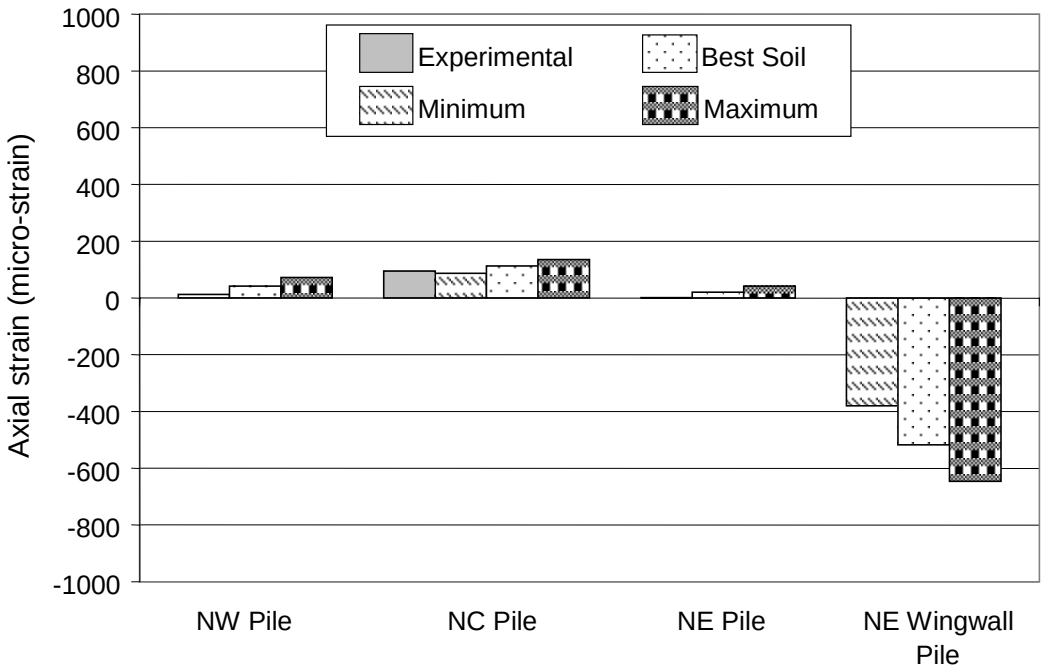

Figure 6.10. Predicted, axial strains in the monitored piles for the north abutment of the Guthrie County Bridge

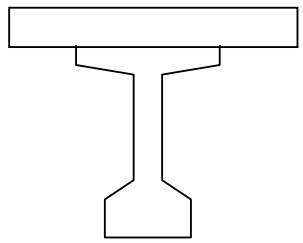

(a) Partial cross section of a bridge superstructure

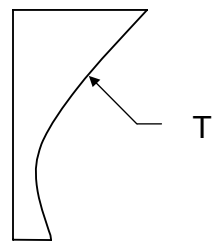

(b) Typical temperature profile

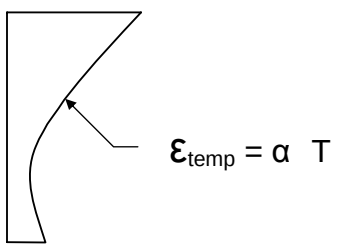

(c) Typical unrestrained strain profile due to temperature

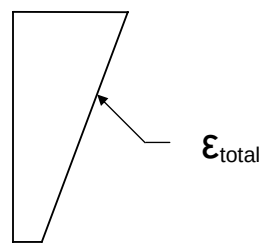

(d) Total-strain profile

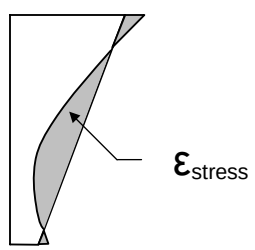

(e) Final strain profile showing the strain due to stress

Figure 6.11. Strains profiles through the depth of a bridge superstructure (adapted from Oesterle, et al., 1999)

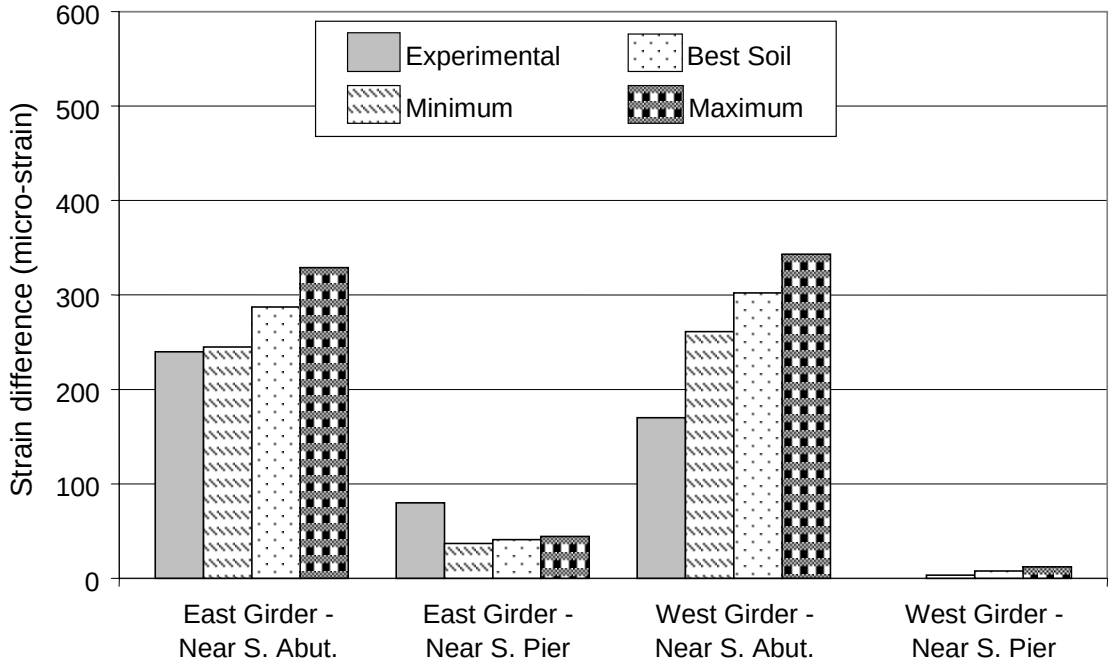

(a) East and west girder

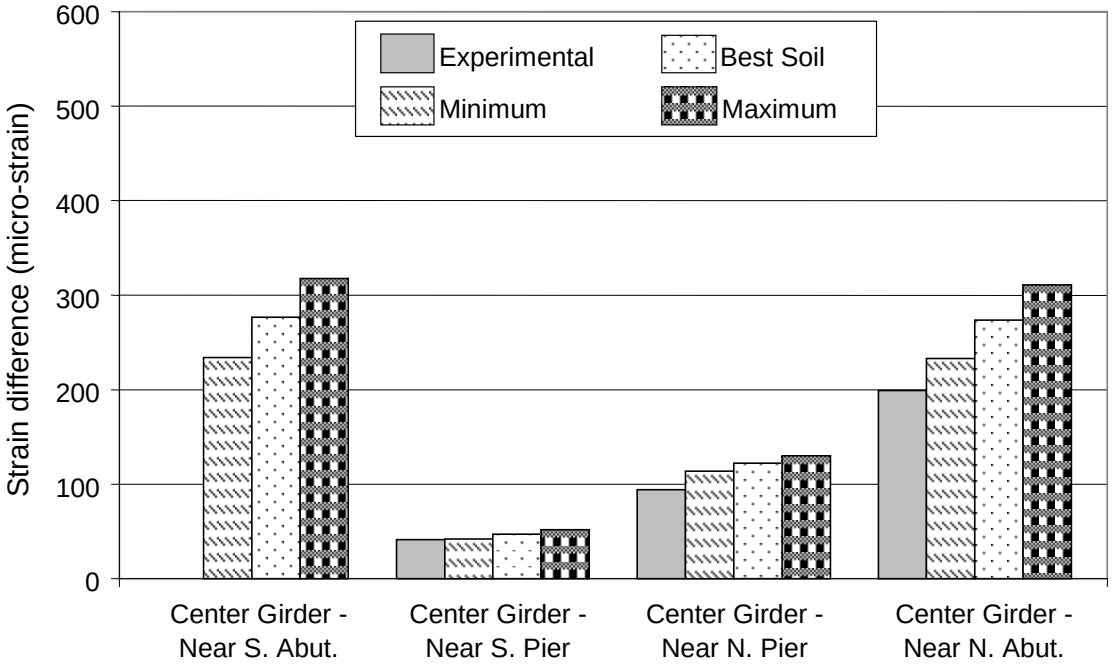

(b) Center girder

Figure 6.12. Difference between the longitudinal strains in the top and bottom flanges of the PC girders predicted by the Guthrie, Series-A Models and experimentally measured at the Guthrie County Bridge

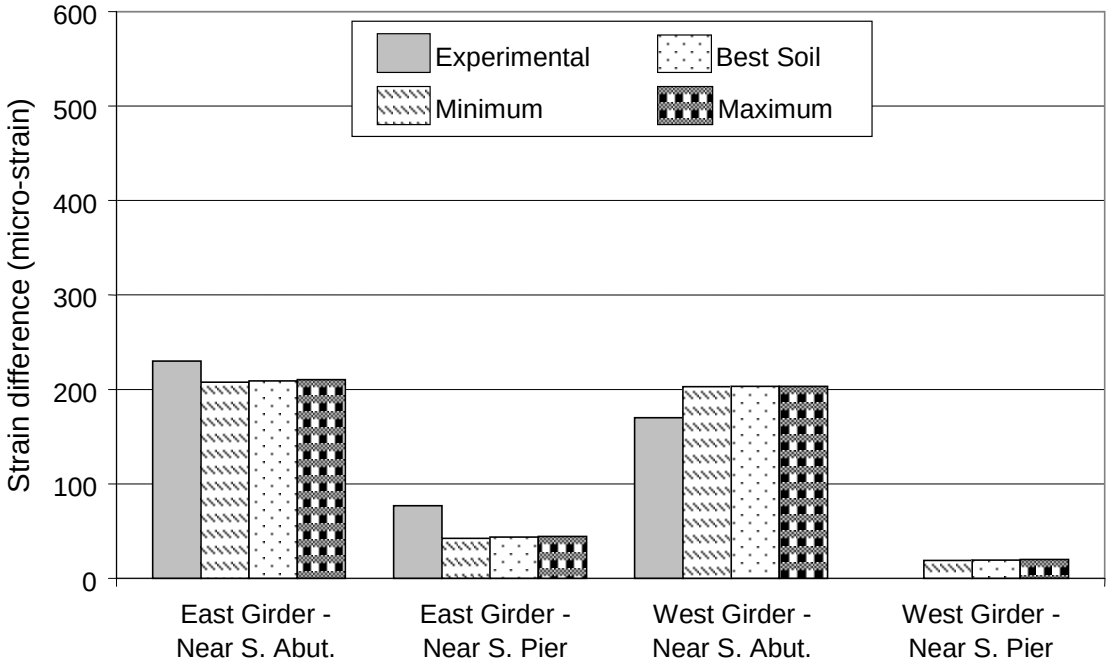

(a) East and west girder

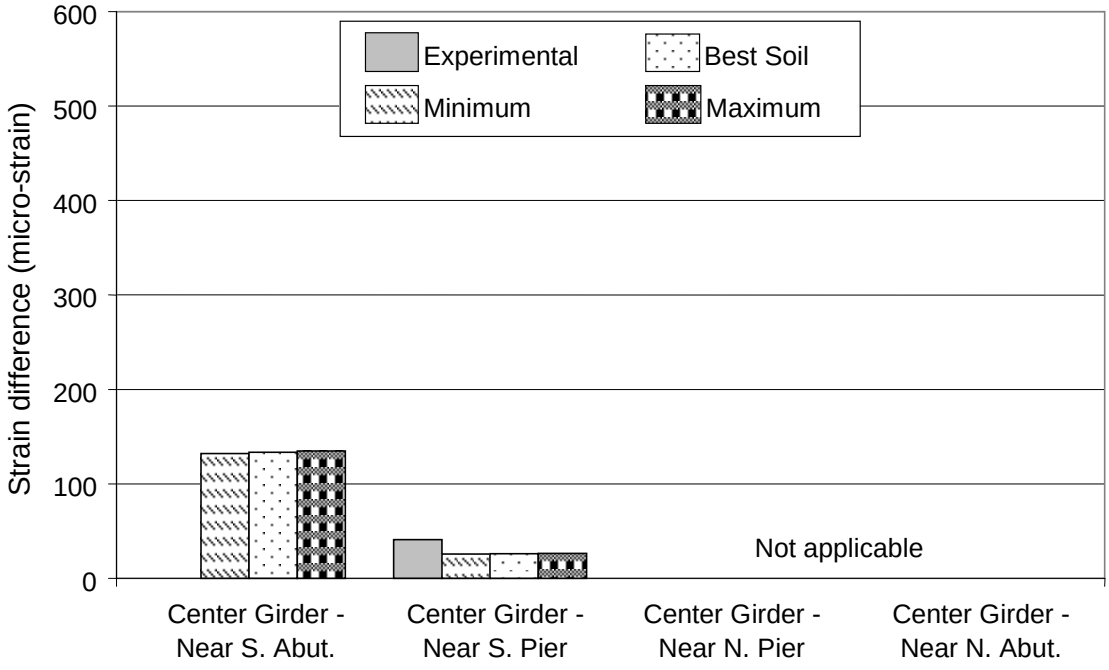

(b) Center girder

Figure 6.13. Difference between the longitudinal strains in the top and bottom flanges of the PC girders predicted by the Guthrie, Series-B Models and the experimentally measured at the Guthrie County Bridge

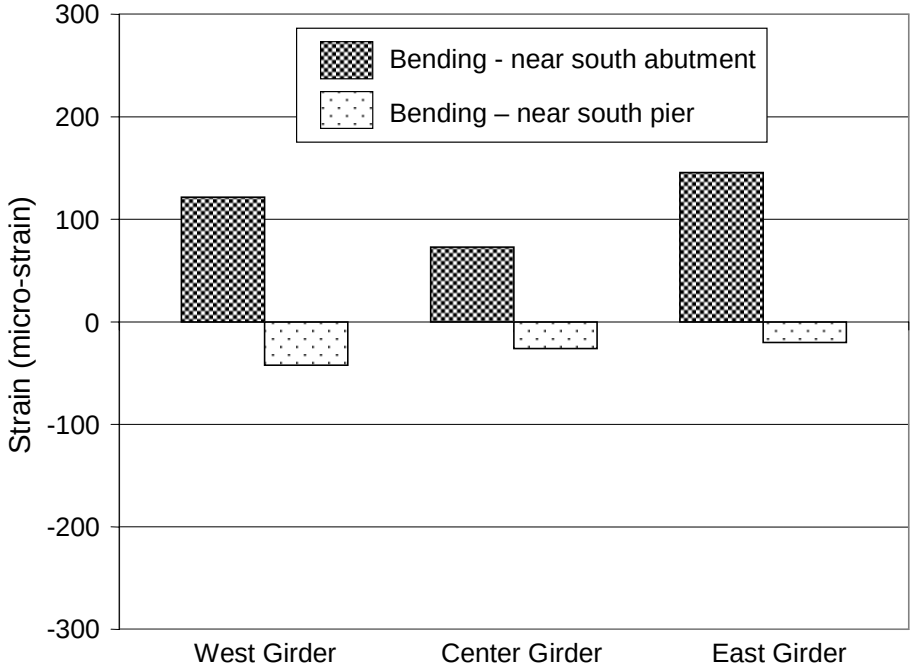

(a) X-axis bending strains

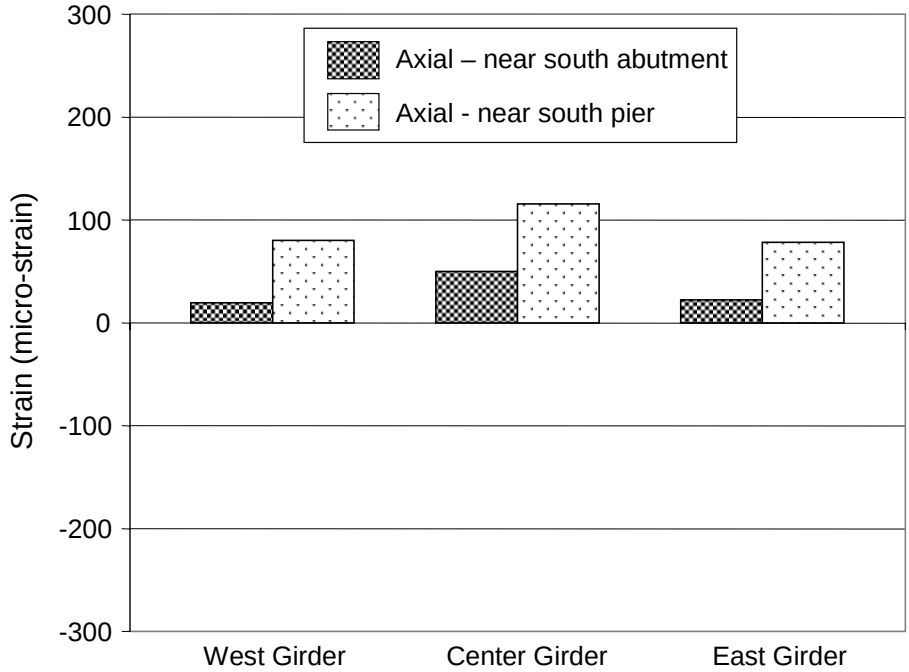

(b) Axial strains

Figure 6.14. PC girder strains due to stress predicted by the Guthrie, Series-B, Best-Soil Model for the south span for the Guthrie County Bridge

Table 6.1. Approximate, initial, non-dimensional slopes for the horizontal stiffness of the abutment backfill based on the Husain and Bagnaroil (1996) design curves in Fig. 5.10b

Type of Backfill	Initial Non-Dimensionalized Slope, S
Loose sand	130
Medium-dense sand	400
Dense sand	2000

Table 6.2. Change in bridge length predicted by the Guthrie, Series-A Models

Evaluation Method		S_{south}	S_{north}	Change in Bridge Length (in.)	Change from Best-Soil Model (%)
Guthrie- Series-A Models	Best-Soil	520	380	1.772	----
	Lower-bound backfill and lower-bound soil around piles	261	154	1.918	+8.2
	Upper-bound backfill and upper-bound soil around piles	783	607	1.647	-7.1
	Upper-bound backfill and lower-bound soil around piles	783	637	1.642	-7.3
	Lower-bound backfill and upper-bound soil around piles	261	134	1.911	+7.8
Experimental		----	----	1.767	-0.3

Table 6.3. Change in the bridge length predicted by the Guthrie, Series-B Models

Evaluation Method		S_{south}	S_{north}	Change in Bridge Length (in.)	Change from Best-Soil Model (%)
Guthrie- Series-B Models	Best-Soil	435	284	1.772	----
	Lower-bound backfill and lower-bound soil around piles	218	114	1.918	+8.2
	Upper-bound backfill and upper-bound soil around piles	653	454	1.647	-7.1
	Upper-bound backfill and lower-bound soil around piles	653	480	1.642	-7.3
	Lower-bound backfill and upper-bound soil around piles	218	85	1.911	+7.8
Experimental		----	----	1.767	-0.3

Table 6.4. Maximum, average, bridge-temperature ranges for reliable, experimental, pile strains at the Guthrie County Bridge

Abutment	Pile	Depth Below Pile Cap (in.)	Coldest Average Bridge Temp. Date	Hottest Average Bridge Temp. Date	Average Bridge Temp. Range (°F)
Pile x-axis Flexural-Bending					
South	West	9	1/5/99	7/20/98	113
South	West	33	n.a.	n.a.	n.a.
South	Center	9	1/5/99	7/20/98	113
South	Center	33	3/12/98	6/27/98	100
South	East	9	n.a.	n.a.	n.a.
South	East	33	n.a.	n.a.	n.a.
North	West	9	1/5/99	7/20/98	113
North	West	33	3/12/98	7/20/98	103
North	Center	9	1/5/99	7/20/98	113
North	Center	33	n.a.	n.a.	n.a.
Pile y-axis Flexural-Bending					
South	West	9	n.a.	n.a.	n.a.
South	West	33	n.a.	n.a.	n.a.
South	Center	9	1/5/99	7/20/98	113
South	Center	33	n.a.	n.a.	n.a.
South	East	9	n.a.	n.a.	n.a.
South	East	33	n.a.	n.a.	n.a.
North	West	9	n.a.	n.a.	n.a.
North	West	33	1/5/99	7/20/98	113
North	Center	9	1/5/99	7/20/98	113
North	Center	33	n.a.	n.a.	n.a.

7. ANALYTICAL STUDY AND INTERPRETATION OF EXPERIMENTAL RESULTS FOR THE STORY COUNTY BRIDGE

This chapter presents the longitudinal, translational, and rotational displacements for the integral abutments; relative displacements at the piers; relative rotations at the top of an abutment pile; axial and flexural-bending strains in particular abutment piles; and longitudinal girder strains in selected PC girders that were predicted by the finite-element models for the Story County Bridge. Comparisons are presented and discussed between those analytically-predicted and experimentally-measured, bridge responses that were induced by changes in the bridge temperature. Additional discussions of the analytical and experimental results for this in-service, integral-abutment bridge are presented in the MS thesis for Sayers (2000).

7.1. Bridge displacements

The analysis techniques and the comparative studies for the analytically-predicted and experimentally-measured, displacements and strains were the same as those that were applied in the investigation of the Guthrie County Bridge. The α-coefficients of the concrete members and other material properties for the Story County Bridge are listed in Table 5.1. The temperature distribution for the bridge structure was discussed in Section 5.4. The temperature ranges that were used for the analytical models involved a temperature rise from the coldest day to the hottest day.

7.1.1 Abutment longitudinal displacements and changes in bridge length

The experimentally-measured, east-abutment and west-abutment displacements in the longitudinal direction of the Story County Bridge were more equal to each other

than those displacements for the north and south abutments for the Guthrie County Bridge. The longitudinal displacements at the west abutment for the Story County Bridge were approximately 25 percent greater than those displacements at the east abutment for this bridge. When the soil was excavated to install the strain gages on the selected abutment piles, less water was encountered in the soil under the abutments for the Story County Bridge than under the abutments for the Guthrie County Bridge. The backfill was assumed to be dry behind both abutments for finite-element models of the Story County Bridge.

Following an analysis approach that was similar to that used for the Guthrie County Bridge, two series of finite-element models were developed to analyze the Story County Bridge. For the Story, Series-A Models, the maximum, α-coefficient was selected for the concrete in the RC slab, piers, and abutments and PC girders, since the use of the 100%-dry α-coefficient for the concrete in those members caused an underestimation for the actual change in bridge length of the Story County Bridge. For the Story, Series-B Models, which had the vertical rotation of the east abutment set equal to the experimentally-measured rotation at this abutment, the 100%-dry α-coefficient was used for the concrete members. The horizontal stiffnesses for the soil behind the abutments in the finite-element models of the Story County Bridge were adjusted until the analytically-predicted abutment displacements were approximately equal to the experimentally-measured displacements. The experimental data that was used for the calibration of the finite-element models was for the time period from January 5, 1999 at 2:00 a.m. to July 5, 1999 at 4:00 p.m. that produced the maximum, reliable, change in the bridge length. The maximum, average, bridge temperature

actually occurred on July 20, 1999, but the measurement of the bridge length was considered unreliable on this date (see Section 4.3.1).

For the Story, Series-A, Best-Soil Model, the initial, non-dimensionalized slope, S_{east}, for the horizontal stiffness versus displacement relationship of the backfill behind the east abutment was set equal to 344. This magnitude for the horizontal-stiffness parameter is slightly less than that for a dry, granular, medium-dense soil, as defined by the Husain and Bagnaroil (1996) design curves (Fig. 5.10b). The horizontal-stiffness parameter, S_{west}, for the backfill behind the west abutment was set equal to 261. This magnitude for the horizontal-stiffness parameter is about halfway between that of a loose and medium-dense, dry, granular soil.

The limits on the acceptable errors in the predicted displacements of the abutments for the finite-element models of the Story County Bridge were the same as those for the analytical models of the Guthrie County Bridge. For the Story, Series-A, Best-Soil Model, the error in the predicted, longitudinal displacements at the mid-width of the east and west abutments was less than 2 percent of the experimentally-measured displacements. The predicted, transverse displacement at the south corner of the east abutment, was within 10 percent of the experimentally-measured displacement at that location.

As discussed in Section 6.1.1, upper-bound and lower-bound, soil-stiffness models were developed with a fixed change in the horizontal stiffness of the abutment backfill and the soil surrounding the piles. A listing of the soil stiffness and the corresponding change in the bridge length that was predicted by the Story, Series-A

Models is given in Table 7.1. The table also lists the experimentally-measured change in the length of the Story County Bridge.

The finite-element models were analyzed to predict abutment displacements at the ends and at the mid-width of each abutment. Longitudinal displacements of the abutments were experimentally measured at the ends and at the mid-width of the east abutment and at the mid-width of the west abutment. Figure 7.1 shows the analytically-predicted and experimentally-measured, longitudinal displacements at these locations. The analytical models predicted that the abutments displaced further longitudinally at the acute-angle corner than at the obtuse-angle corner of the bridge deck. Experimental measurements at the south corner of the east abutment were not reliable over the maximum range of the average, bridge temperatures and are not included in Fig. 7.1. The largest, abutment displacements for the four, soil-stiffness-bound models are referred to as the maximum in Fig. 7.1. The maximum displacement occurred with the least- stiff-soil condition, which corresponded to the finite-element model with the lower-bound backfill and lower-bound soil around piles. Conversely, the minimum displacement shown in this figure occurred with the stiffest-soil condition, which corresponded to the finite-element model with the upper-bound backfill and upper-bound soil around piles.

For the Story County Bridge, the ratio of the experimentally-measured, horizontal displacement of the east abutment to its height, Δ/H_{east}, was equal to 0.004. The ratio of the experimentally-measured, horizontal displacement of the west abutment to its height Δ/H_{west}, was equal to 0.005. Ratios of these magnitudes correspond with the linear portion of the wall-stiffness, design curve for a medium-dense soil shown in Fig. 5.10b.

The experimentally-measured, longitudinal displacements for the abutments were significantly less than those displacements that were required to induce the full-passive, soil-pressure condition. Therefore, the approximation of a linear, horizontal stiffness behind both abutments was a valid assumption. For the remainder of the chapter, the comparisons between the analytically-predicted and experimentally-measured deformations and strains are based on the maximum, average, temperature range of 115 °F that occurred between January 5, 1999 at 2:00 a.m. and July 20, 1999 at 5:30 p.m.

7.1.2. Abutment transverse displacements

For the Story County Bridge, experimentally-measured, transverse displacements at the east abutment were reliable only at the acute-angle corner of the bridge deck. This transverse displacement was used to calibrate the finite-element models. When Barkan's (1992) recommendation, which states that the transverse stiffness for the backfill behind the abutments should be set equal to one-half of the normal stiffness for the backfill, was applied in the finite-element models of the Story County Bridge, the predicted transverse displacements of the abutments were too large. Barkan's recommendation for the transverse stiffness of abutment backfill was also shown to be too low by the finite-element-models predictions for the abutment displacements of the Guthrie County Bridge. For the Story, Series-A, Best-Soil Model to correctly predict the transverse displacement of the east abutment, the ratio of the tangential-spring stiffness to normal-spring stiffness was set equal to 0.85.

The ranges for the analytically-predicted, transverse displacements at the corners of the abutments for the Story County Bridge are shown in Fig. 7.2. Positive

displacements shown in this figure are towards the acute-angle corner of the bridge deck. Figure 7.2 also shows the experimentally-measured range of the transverse displacements at the south corner of the east abutment. Experimentally-measured, transverse displacements were not reliable at the north corner of the east abutment and were not monitored and both corners of the west abutment for the Story County Bridge.

7.1.3. Abutment rotations in a vertical plane

The Story, Series-A, Best-Soil Model overestimated by a factor of two the east abutment rotations in a vertical plane that is parallel to the longitudinal axis of the bridge. This amount of overestimation in the abutment rotation was also encountered with the Guthrie, Series-A Models. Again, the cause was not determined for the discrepancy between the predicted and measured abutment rotation. To more accurately model the Story County Bridge, the Story, Series-B Models were developed with rotational constraints that were applied to the element nodes for the east abutment. These rotational constraints set the analytical rotation of the east abutment equal to the experimentally-measured rotations at this abutment. The range in the experimentally-measured rotations for the east abutment of the Story County Bridge was approximately equal to 0.075 deg. Since the west abutment rotations were not experimentally monitored, the Story, Series-B Models did not have predetermined, rotational restraints applied to the nodes at this abutment.

The Story, Series-B, Best-Soil model was calibrated by adjusting the horizontal stiffness of the soil so that the displacements predicted by this analytical model essentially matched those displacements that were predicted by the Story, Series-A, Best-Soil Model for the maximum range in average, bridge temperatures. The

computed, horizontal stiffness of the backfill behind the abutments of the Story, Series-B Models was less than that for the Story, Series-A Models. The non-dimensionalized, horizontal-stiffness parameter for the east-abutment backfill, S_{east}, of the Story, Series-B, Best-Soil Model was equal to 289, which is less than the initial, non-dimensionalized slope to Husain and Bagnaroil (1996) design curve (Fig. 5.10b) for a dry, granular, medium-dense soil.

The four, soil-stiffness-bound models (lower-bound backfill and lower-bound soil around piles, upper-bound backfill and upper-bound soil around piles, upper-bound backfill and lower-bound soil around piles, and lower-bound backfill and upper-bound soil around piles that were previously described in Section 6.1.1) were used to determine the minimum and maximum limits for the y-axis, flexural-bending strains in the piles for the east abutment. The x-axis, flexural-bending strains were not investigated with these models, since these strains were only slightly affected by the abutment rotation. The non-dimensionalized, horizontal-stiffness parameters for the abutment backfill and changes in the length for the Story, Series-B Models and the experimentally-measured changes in the bridge length are listed in Table 7.2.

7.1.4. Relative displacements at the piers

Fixed pier details, shown in Fig. 5.3a, were specified for both piers at the Story County Bridge. As discussed in Section 5.1, the finite elements for the pier diaphragm and the pier-cap shared nodes at the interface between these members. Therefore, relative translation between the bridge superstructure and the pier caps was neglected in the finite-element models for the Story County Bridge. The maximum, experimental

measurements for the relative displacements at both piers for this bridge were less than 0.040 in., as shown in Fig. 4.25.

7.1.5. Relative rotations at the top of an abutment pile

At the Story County Bridge, the relative rotation was measured between the bottom surface for the pile cap of the east abutment and a cross section for the pile that is near the mid-width of this abutment. The referenced pile cross section was located at 18 in. below the bottom of the pile cap. Referring back to Fig. 4.27, an experimentally-measured range for this relative rotation, which is not labeled in the figure, was approximately 0.168 deg. This relative rotation occurred between the coldest temperature on January 5, 1999 and the hottest temperature on July 20, 1999. As discussed in Section 4.3.6, the experimentally-measured, relative rotations of the pile were questionable, since a shift in the relative rotation appears to have occurred between the two ranges for this rotation that are shown in Fig. 4.27. As shown in Fig. 7.3, the Story, Series-A Models underestimated the experimentally-measured, relative rotation at the top of the pile near the mid-width of the east abutment. The relative rotation for this pile that was predicted by the Story, Series-B Models was larger than the relative rotation that was predicted by the Story, Series-A Models. However, the experimentally-measured, relative rotation was still greater than the predicted rotation at the top of this pile.

The Story County Bridge had larger, analytically-predicted and experimentally-measured, relative rotations at the top of the pile near the mid-width of the east abutment than those corresponding relative rotations at the top of the pile near the mid-width of the south abutment for the Guthrie County Bridge. A greater horizontal

stiffness for the material along the upper portion of the abutment piles at the Story County Bridge, than that for the abutment piles at the Guthrie County Bridge, may have caused these differences in the relative rotation at the top of the piles for the two bridges. As previously discussed, the pre-bored holes, through which the piles were driven, were filled with sand and bentonite slurry at the Story County Bridge and Guthrie County Bridge, respectively.

7.2. Pile strains

7.2.1. Pile flexural-bending strains

As described in Section 6.2, the analytically-predicted, pile strains were compared with the corresponding, experimentally-measured, pile strains when reliable data was available over the time period for the maximum range in the average, bridge temperatures. The strain gages on the abutment piles for the Story County Bridge properly functioned over a longer period of time than that for the strain gages on the abutment piles for the Guthrie County Bridge. Table 7.3 shows the maximum ranges in the average, bridge temperature over which reliable, pile bending-strain data was obtained at the Story County Bridge.

The ranges for the x-axis and y-axis, flexural-bending strains in the abutment piles that were predicted by the Story, Series-A Models and the reliable, experimentally-measured strains are shown in Figs. 7.4 and 7.5. For these figures, the first letter in the pile notation along the abscissa scale for the graphs refers to the particular abutment (E for the east abutment and W for the west abutment) that is supported by the pile. The second letter in the pile notation refers to the pile location (N for the north end, C for the mid-width, and S for the south end) in the abutment. As discussed in Section 6.2.1, the

finite-element models that incorporated the lower-bound, horizontal stiffness for the abutment backfill and the upper-bound, horizontal stiffness for the soil surrounding the piles predicted the maximum, flexural-bending strains. Conversely, the analytical models that had the upper-bound, horizontal stiffness for the abutment backfill and the lower-bound, horizontal stiffness for the soil around the piles predicted the minimum, flexural-bending strains.

For both the Story County Bridge and Guthrie County Bridge, the webs of the abutment piles are oriented parallel to the abutment face. The Story County Bridge has a 15-deg., skew angle, which is smaller than the 30-deg., skew angle at the Guthrie County Bridge. If the pile orientation with respect to the abutment face does not change with a decrease in the skew angle for an integral-abutment bridge, the ratio of y-axis to x-axis bending strains in the abutment piles will increase. Therefore, this bending-strain ratio was larger for the abutment piles in the Story County Bridge than that ratio for the abutment piles in the Guthrie County Bridge.

Figure 7.4 shows that the magnitudes for the x-axis, flexural-bending strains that were predicted by the Story, Series-A Models were reasonably close to the corresponding, experimentally-measured strains in the upper cross section for the center and south piles (EC and ES piles, respectively) for the east abutment. The predicted, x-axis, flexural-bending strains in both cross sections for the north pile (EN pile) in the east abutment and in the lower cross section for the center pile (WC pile) for the west abutment underestimated the experimentally-measured strains in these pile cross sections.

As shown in Fig. 7.5, the Story, Series-A Models underestimated the experimentally-measured y-axis, flexural-bending strains in the monitored piles of the east abutment. As discussed in Section 6.2, if the abutment rotations in a vertical plane that is parallel to the longitudinal axis of the bridge are overestimated, and if the pile web is parallel to the face of the abutment, the analytical model will underestimate the y-axis, flexural-bending strains in the abutment piles. For bridges with small skew angles and this pile orientation, the rotations of the abutment in a vertical plane that is parallel to the longitudinal direction of the bridge had a negligible effect on the x-axis, flexural-bending strains in the abutment piles. This rotation for the east abutment was overestimated by the Story, Series-A Models, as discussed in Section 7.1.3.

Figure 7.5 shows that the y-axis, flexural-bending strains in the upper cross section of the center pile (WC pile) in the west abutment that were predicted by the Story, Series-A Models were in reasonable agreement with the experimentally-measured strains at this location. This result may indicate that the west-abutment rotation, which was predicted by the Story, Series-A Models, may have been close to the actual rotation of this abutment. This hypothesis could not be confirmed since the abutment rotations were not measured at the west abutment of the Story County Bridge.

The Story, Series-B Models were developed with the vertical rotation of the east abutment set equal to the experimentally-measured rotation of this abutment. These finite-element models were analyzed to predict the y-axis, flexural-bending strains in the upper and lower cross sections of the three experimentally-monitored piles for the east abutment of the Story County Bridge. Figure 7.6 shows these predicted strains and the experimental strains in four of the six pile cross sections. The y-axis, flexural-bending

strains for the two cross sections of the WC pile in the west abutment are not shown in Fig. 7.6 because the vertical rotations were not experimentally measured for that abutment. Without a measured rotation, the west-abutment rotation in the Story, Series-B Models could not be set equal to any predetermined value. Figure 7.6 shows that the Story, Series-B Models provided a better prediction of the experimentally-measured, pile strains than the corresponding strains that were predicted by the Story, Series-A Models.

The variation in the predicted, x-axis and y-axis, flexural-bending strains along the length of the north pile in the east abutment are shown in Fig. 7.7. These strains, which were predicted by the Story Series-B Models, are at the flange tips for this pile. The graphs for the minimum, maximum, and best-soil, flexural-bending strains that are shown in the figure correspond to the finite-element models that predicted a horizontal displacement at the mid-width of the east abutment that represented a minimum, maximum, and best-fit to the experimentally-measured displacement at that location. In Fig. 7.7b, the experimentally-measured, y-axis, flexural-bending strains were mathematically extrapolated to the flange tips of the north pile. For both x-axis and y-axis bending of the pile, the maximum, flexural-bending strains occurred at the pile cross section that was located directly below the pile cap, and an inflection point in this pile was located approximately 5 ft below the pile cap. As seen in the figure, the bending strains were smaller for x-axis bending than for y-axis bending of the pile, and these strains were negligible for bending about both axes for this pile in the lower portion of the pile length.

The maximum, predicted, x-axis and y-axis, flexural-bending strains that occurred at the flange tips for the three, experimentally-monitored piles along the width of each abutment at the Story County Bridge are shown in Fig. 7.8. The Story, Series-A, Best-Soil Model was used to predict the x-axis, flexural-bending strains in all six piles and to predict the y-axis, flexural-bending strains for the three piles in the east abutment. The Story, Series-B, Best-Soil Model was used to predict the y-axis, flexural-bending strains for the three piles in the south abutment.

Since the difference in the longitudinal displacements for the east and west abutments of the Story County Bridge was small, a small difference occurred in the flexural-bending strains in the piles for the east and west abutments, as shown in Fig. 7.8. The maximum, predicted, combined, flexural-bending strain in the south pile of the east abutment for the Story County Bridge was approximately 1100 micro-strains. If this pile had the same horizontal translation at the pile head but had zero vertical rotation of the abutment (the “perfectly”, fixed-head, rotation condition), the maximum, predicted, combined, flexural-bending strain was approximately 1400 micro-strains. The predicted 1100 micro-strains for the combined-bending strain is slightly less than the 1240-micro-strain, yield strain for A36 steel. The maximum, predicted, combined, flexural-bending strain in the north pile of the east abutment for this bridge was about 1180 micro-strains, which is slightly less than the yield strain for A36 steel. When residual strains and the strains that are induced by the dead and live loads for the bridge are added to these combined-bending strains, yielding occurred over some portions of the HP-shaped, cross sections for the piles in each abutment for the Story County Bridge.

7.2.2. Pile axial strains

For the Story County Bridge, the abutment piles were located only under the abutment backwall. Since piles were not placed under the abutment wingwalls, the wingwalls were cantilevered from the abutment backwall for this bridge. Temperature induced axial strains that were predicted by the Story, Series-B Models for three piles in the east abutment are shown in Fig. 7.9. Compressive, axial strains were predicted for the exterior piles, and tensile, axial strains were predicted for the interior piles in this abutment. The maximum, predicted, axial-compressive strain occurred in the exterior pile (ES pile) for the east abutment near the acute-angle corner of the bridge deck. These pile, axial-strain result are contrary to the findings of Lawver, et al. (2000) who conducted their own monitoring program of an integral-abutment bridge. These researchers noted that the axial strains decreased in the exterior piles and increased in an interior pile for their monitored abutment.

Since the axial strains in the abutment piles that were computed from the experimentally-measured, longitudinal strain in the abutment piles of the Story County Bridge were questionable, these strains were not compared with the analytical results that are shown in Fig. 7.9. After the first week in December of 1998, the dummy-strain gage that was installed at the Story County Bridge did not measure strains that correlated well with changes in temperature. Therefore, the strain measurements by the “dummy” gage were considered to be unreliable after that week. Before and during this week, the ranges in the experimentally-based, axial strain in the monitored piles were usually less than 100 micro-strains and, the experimentally-based, daily variations for the axial strains in these piles were approximately 50 micro-strains.

7.3. Girder strains

The analytically-predicted and experimentally-measured ranges for the difference in the total, longitudinal strains in the top and bottom flanges of the exterior and center, PC girders near the ends of the east span of the Story County Bridge are shown in Figs. 7.10 and 7.11 for the Story, Series-A Models and Story, Series-B Models, respectively. Figure 7.10 also shows the difference in these strains near the ends of the center, PC girder that is in the west span of this bridge. The differences in the longitudinal strains in the flanges of the PC girders in the west span for the bridge were not presented in Fig. 7.11, since the Story, Series-B Models were developed only for a set vertical rotation of the east abutment. As was the case with the Guthrie, Series-A Models, the Story, Series-A Models overestimated the range for the difference in the experimentally-measured, girder-flange strains. These strain differences are affected by the rotation of the abutment in a vertical plane that is parallel to the longitudinal axis of the bridge. Larger abutment rotations produce larger bending strains in the PC girders. As shown in Fig. 7.11, the differences in the flange strains that were predicted by the Story, Series-B Models for the PC girders in the east span of the bridge were in closer agreement with the experimentally-based, strain differences than those strain differences shown in Fig. 7.10 that were predicted Story, Series-A Models. Therefore, the Series-B, finite-element models more correctly modeled the bridge than the Series-A, finite-element models regarding the longitudinal strains that were induced in the girders in the span that was adjacent to the abutment with the set vertical rotation.

Strains due to stress in the exterior and center, PC girders for cross sections near the ends of the east span of the Story County Bridge were predicted by the Story,

Series-B, Best-Soil Models. The predicted, girder strains due to stress are shown in Fig. 7.12. The x-axis, flexural-bending strains, which are shown in Fig. 7.12a, are at the uppermost fibers in the top flange of the girders. The predicted, axial strain in the girders that are shown in Fig. 7.12b counteracted the flexural-bending strain in the extreme fibers of the top flange of the girders. The maximum, predicted, combined strain due to stress, in the top flange of a PC girder was a tensile strain of approximately 125 micro-strains. If Hooke's Law and a modulus of elasticity for concrete that is listed in Table 5.1 is applied, the corresponding, tensile stress is about 500 psi. The axial strain was additive with the flexural-bending strain in the extreme fiber of the bottom flange of the girders. The maximum, predicted, combined strain due to stress in the bottom flange of a PC girder was a compressive strain of approximately 180 micro-strain. Again, if a linear stress versus strain relationship is applied and the modulus of elasticity for the concrete from Table 5.1 is used, the corresponding, compressive stress is about 720 psi.

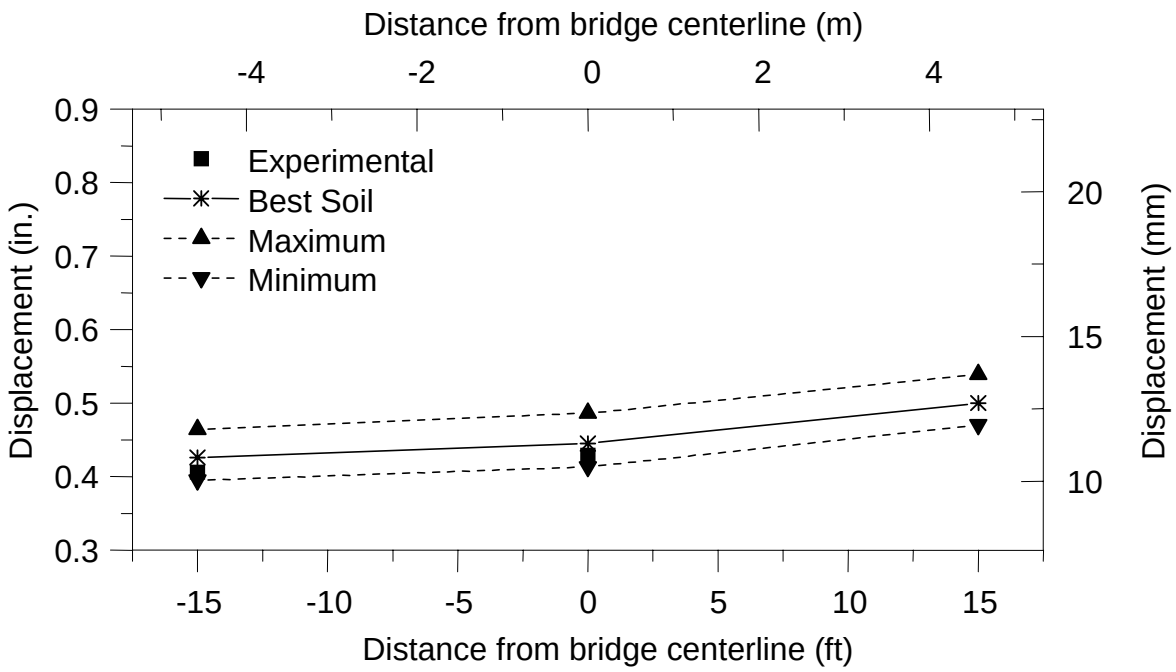

(a) East abutment

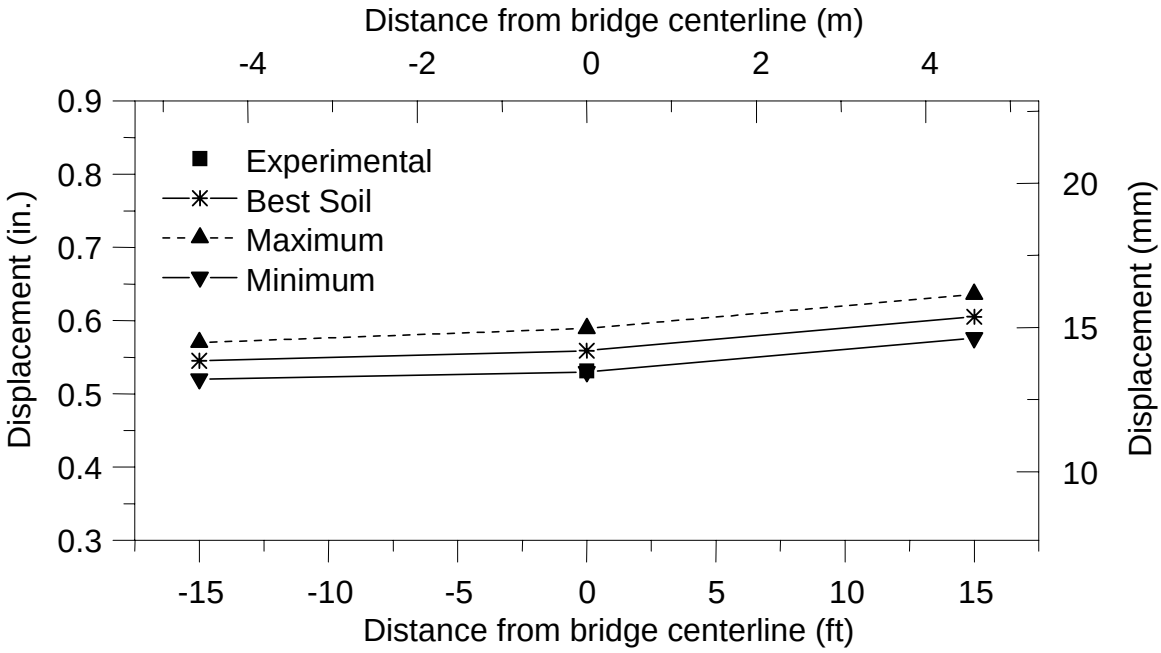

(b) West abutment

Figure 7.1. Abutment longitudinal displacements predicted by the Story, Series-A Models and the experimentally measured at the Story County Bridge

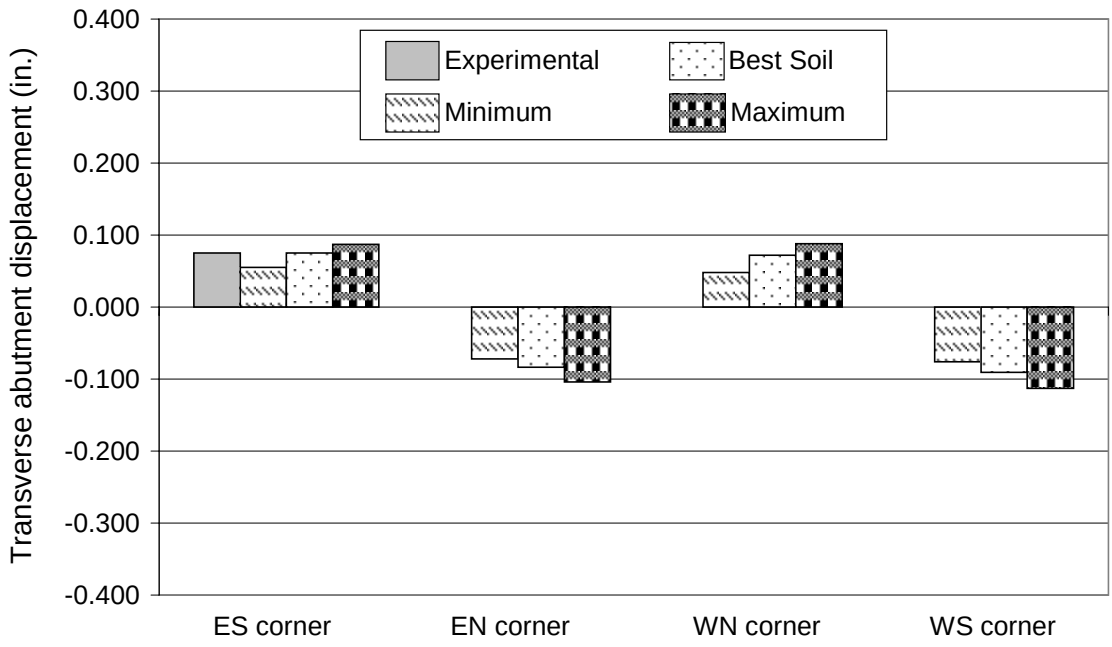

Figure 7.2. Abutment transverse displacements predicted by the Story, Series-A Models and experimentally measured at the Story County Bridge

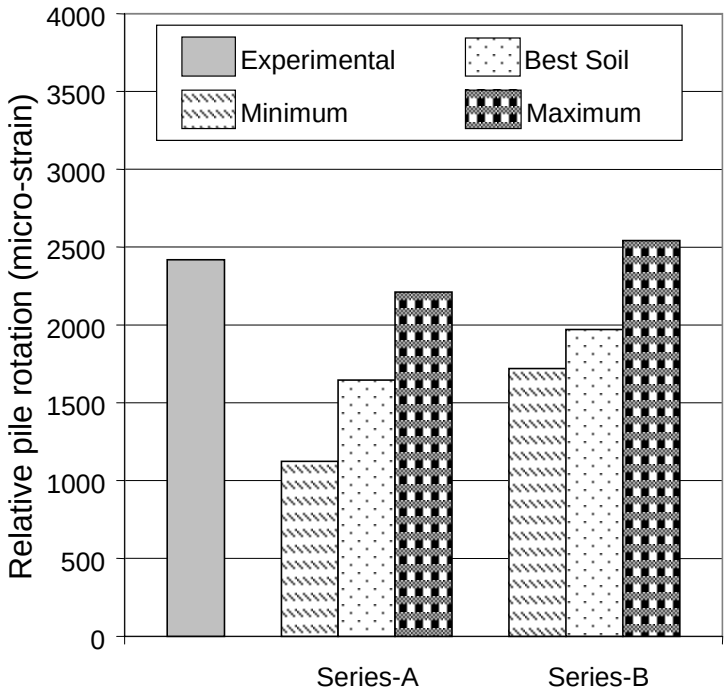

Figure 7.3. Analytically-predicted and experimentally-measured, relative rotations of a pile at the Story County Bridge

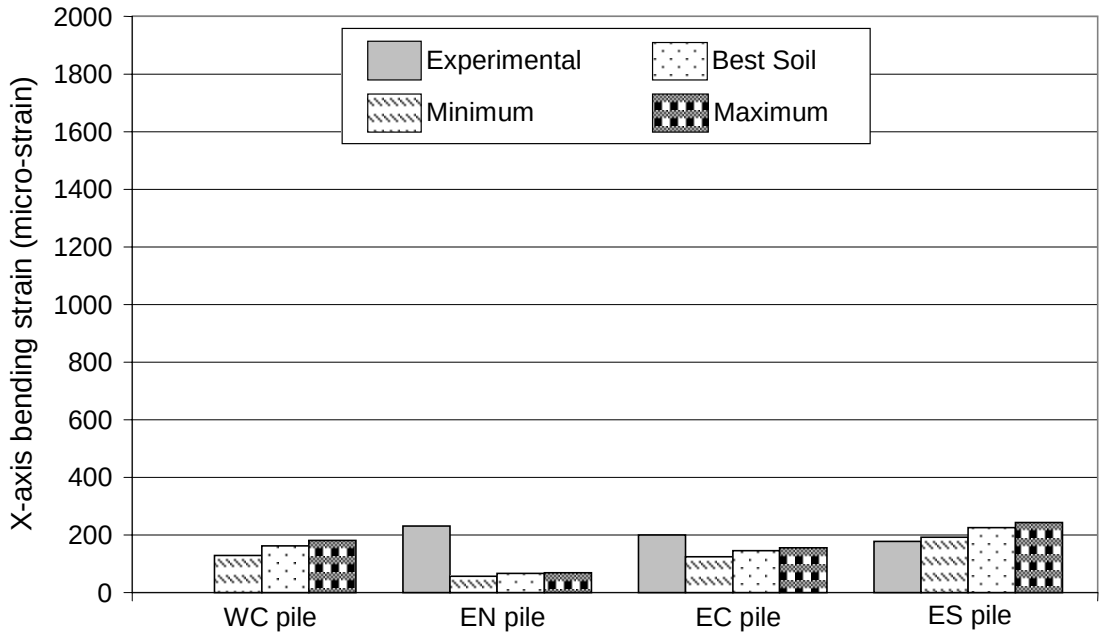

(a) Upper cross section at 9 in. below the pile cap

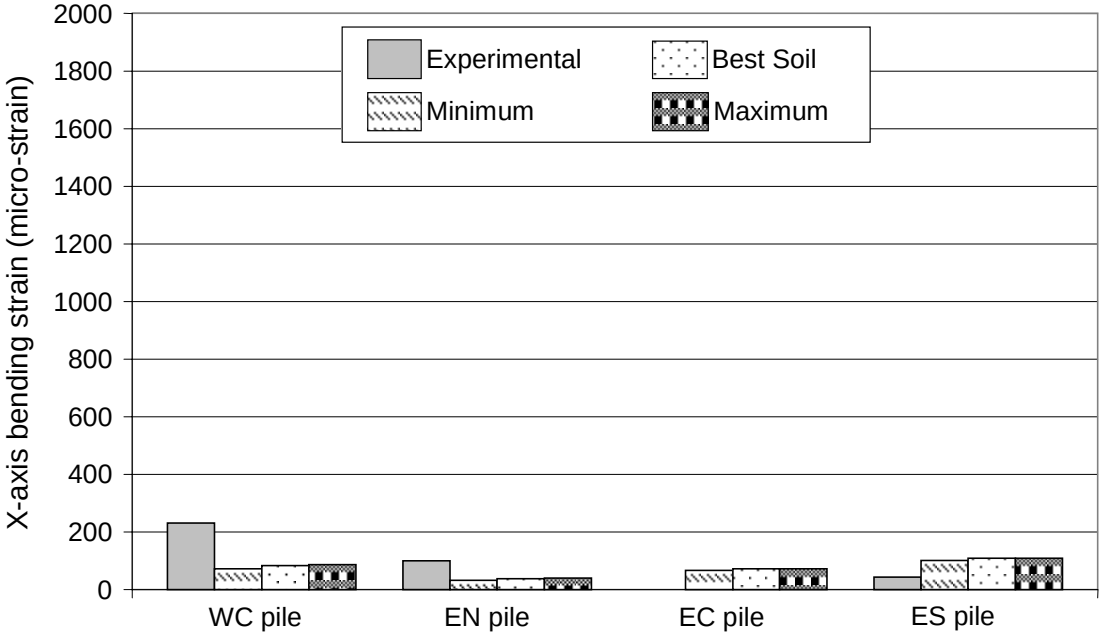

(b) Lower cross section at 33 in. below the pile cap

Figure 7.4. X-axis, flexural-bending strains predicted by the Story, Series-A Models and experimentally measured at the Story County Bridge

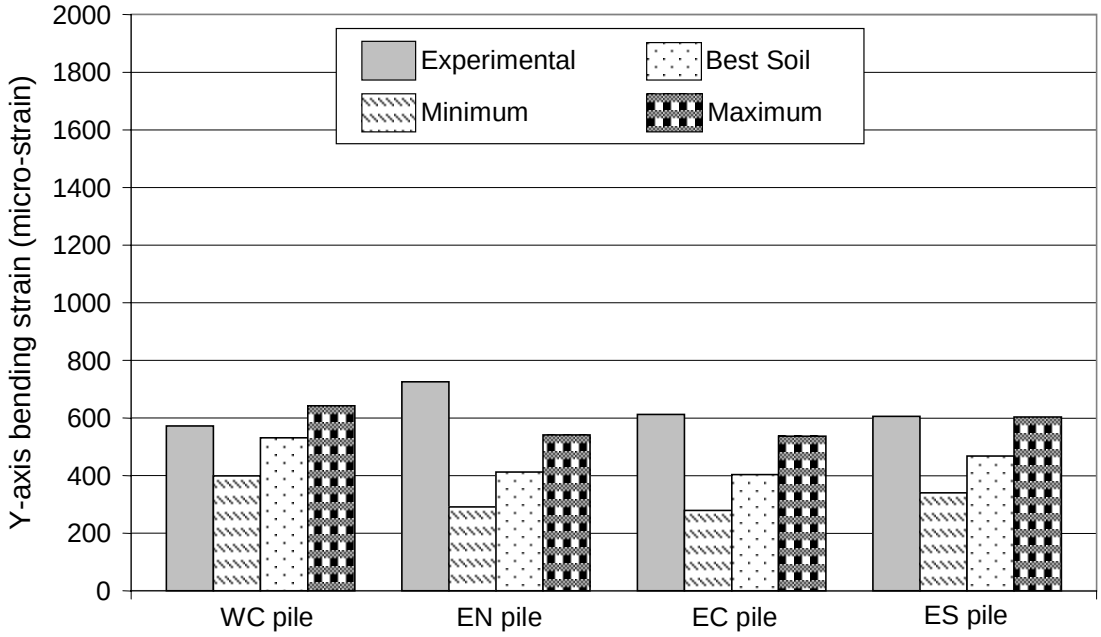

(a) Upper cross section at 9 in. below the pile cap

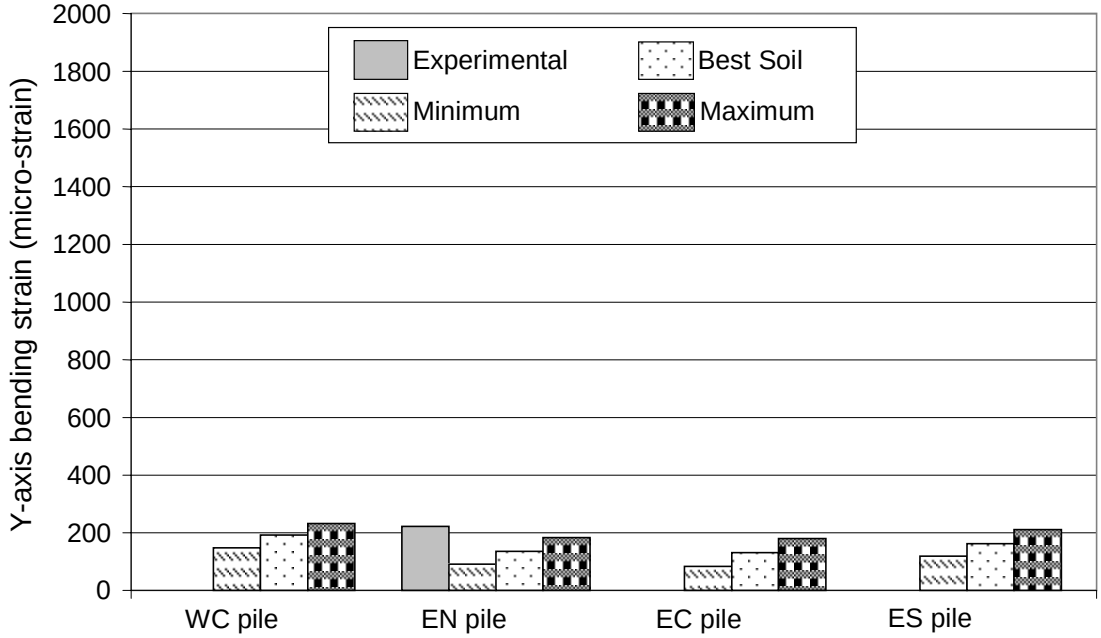

(b) Lower cross section at 33 in. below the pile cap

Figure 7.5. Y-axis, flexural-bending strains predicted by the Story, Series-A Models and experimentally measured at the Story County Bridge

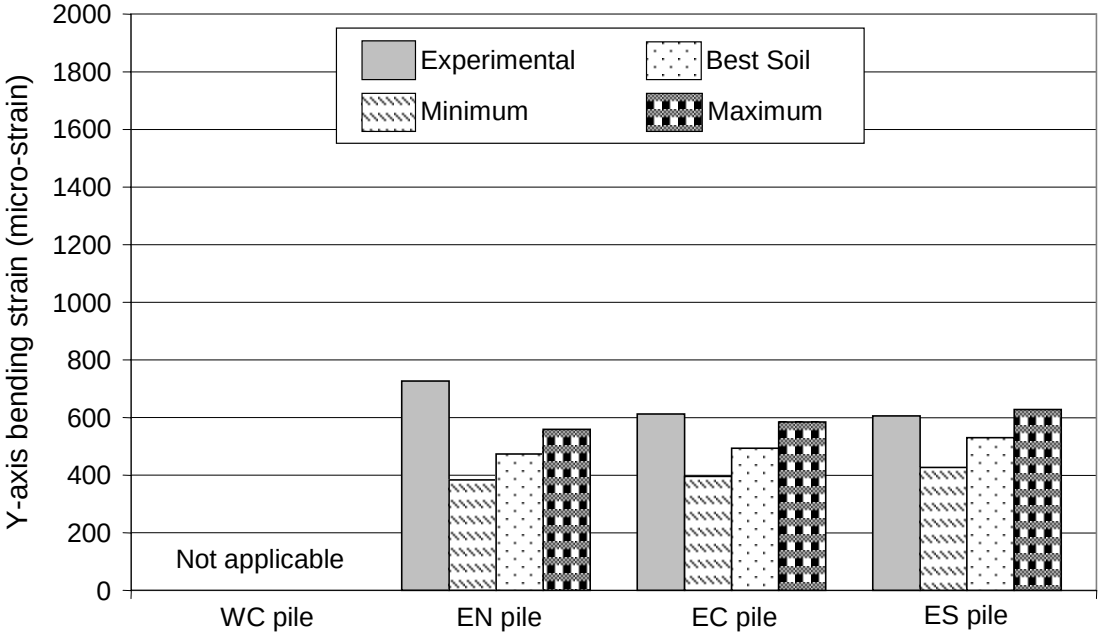

(a) Upper cross section at 9 in. below the pile cap

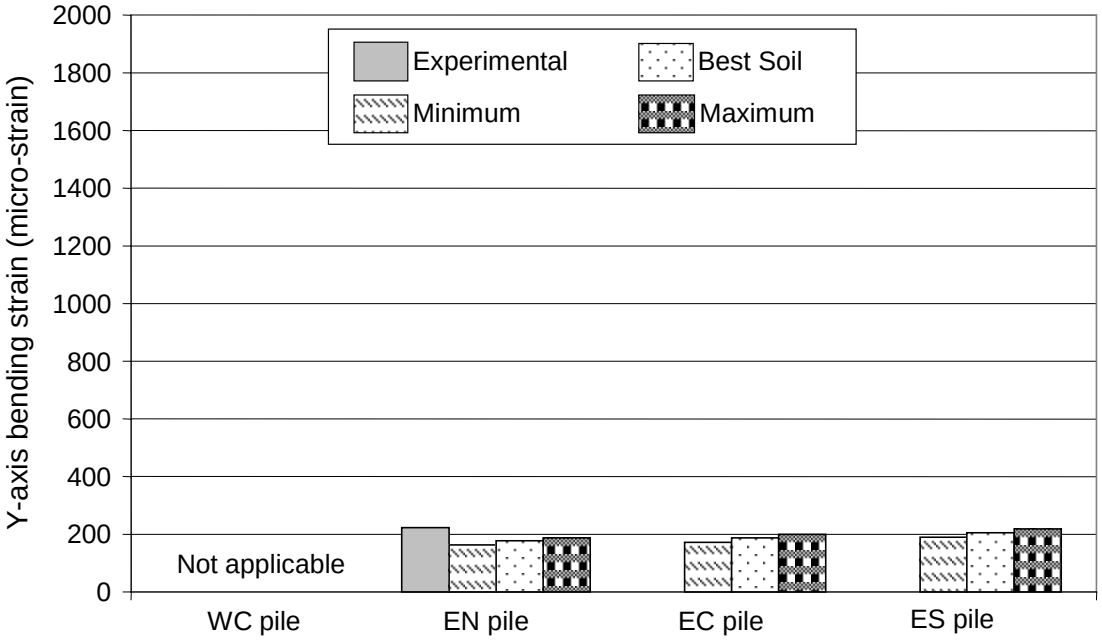

(b) Lower cross section at 33 in. below the pile cap

Figure 7.6. Y-axis, flexural-bending strains predicted by the Story, Series-B Models and experimentally measured at the Story County Bridge

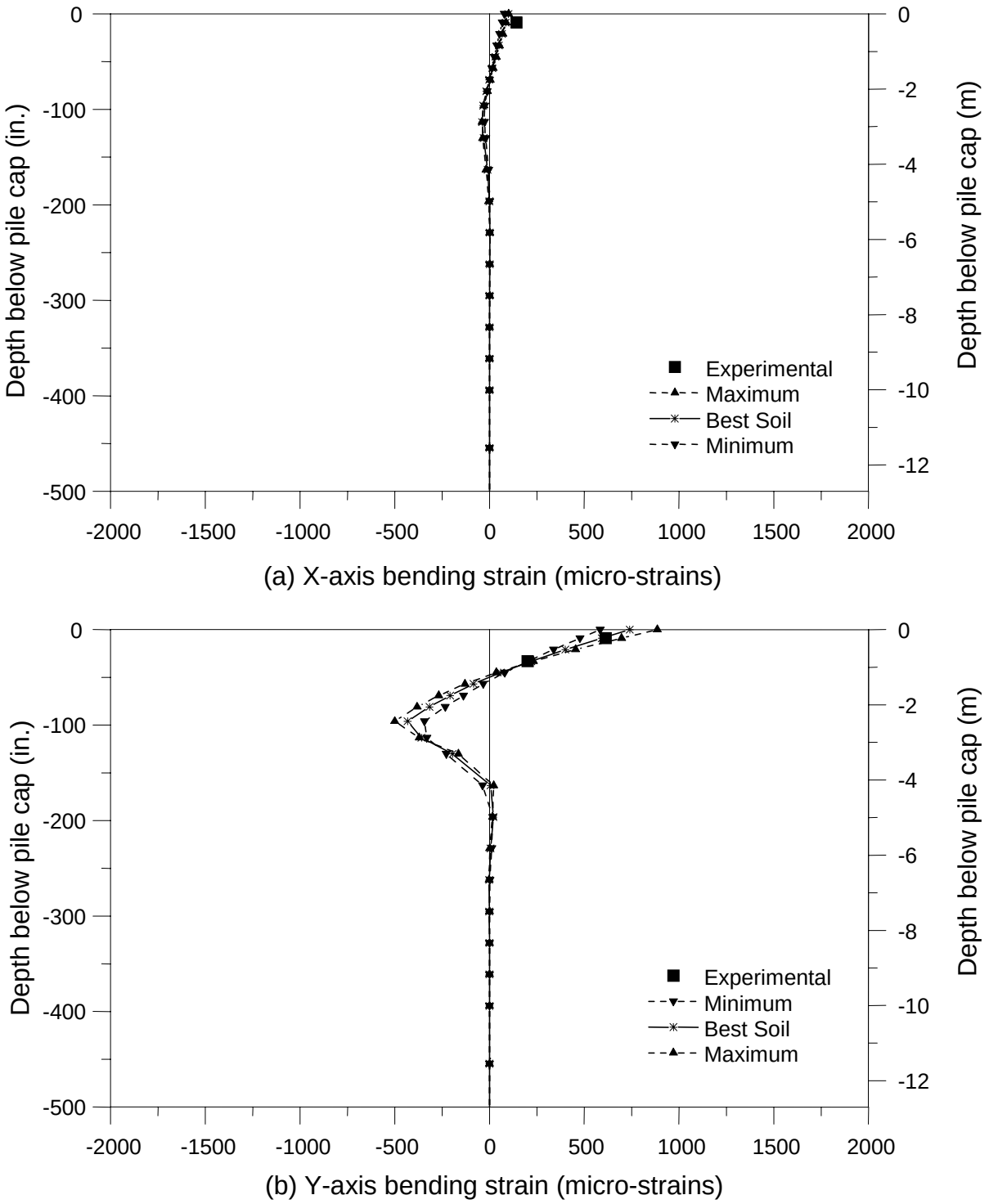

Figure 7.7. Strain variation predicted by the Story, Series-B Models along the length of the north pile for the east abutment and experimentally measured at the Story County Bridge

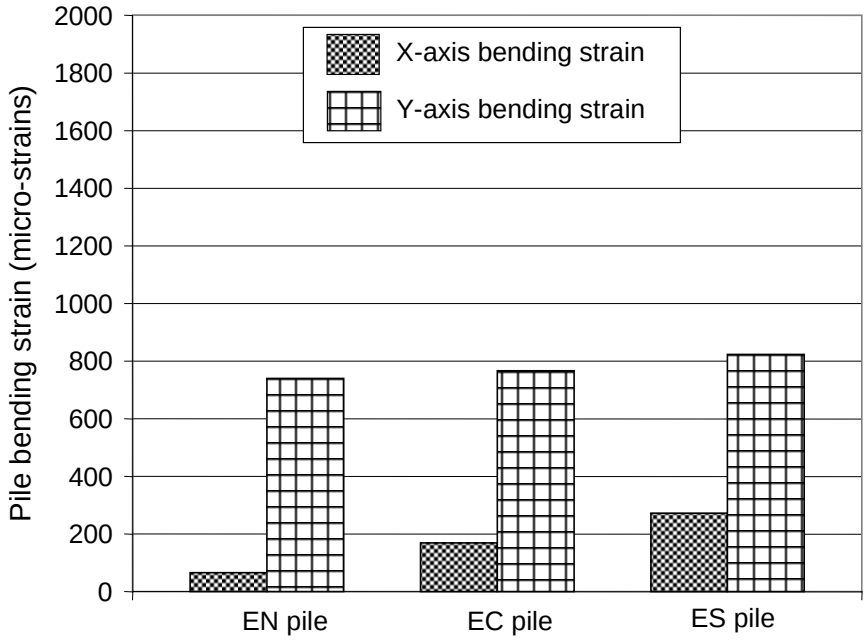

(a) East abutment

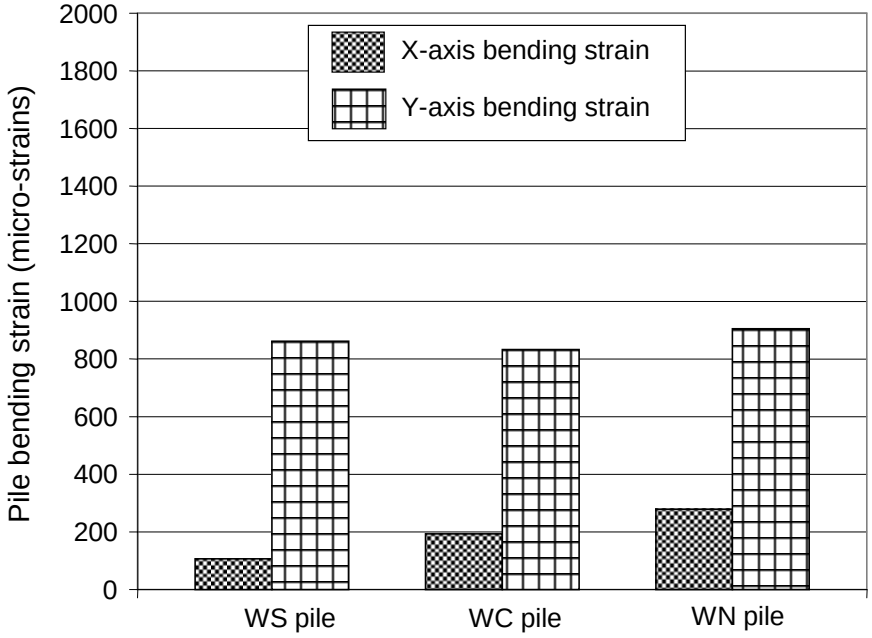

(b) West abutment

Figure 7.8. Maximum, predicted, flexural-bending strains in the monitored abutment piles at the Story County Bridge

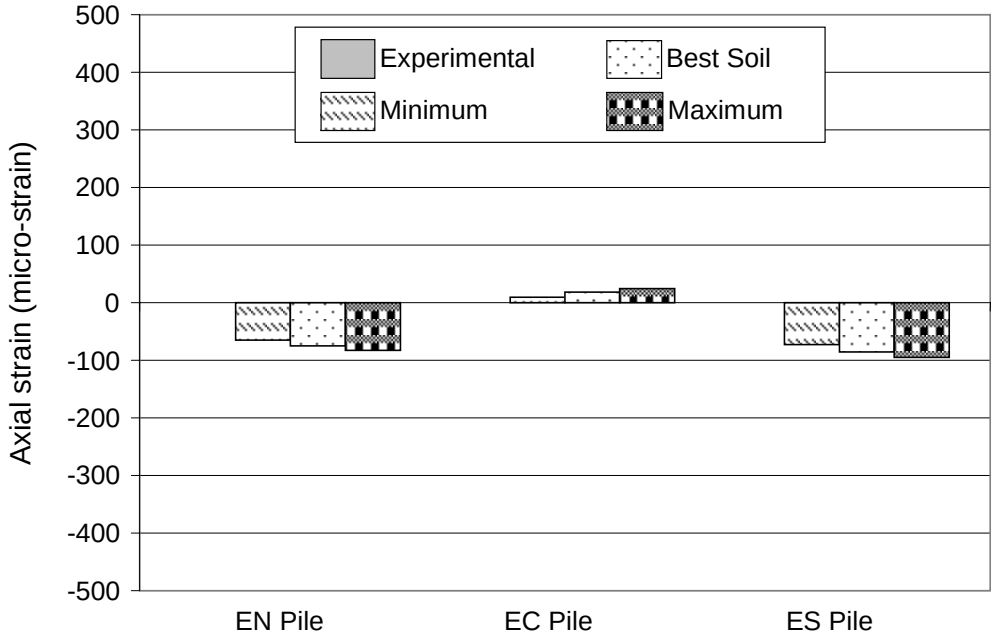

Figure 7.9. Predicted, axial strains in the monitored piles for the east abutment of the Story County Bridge

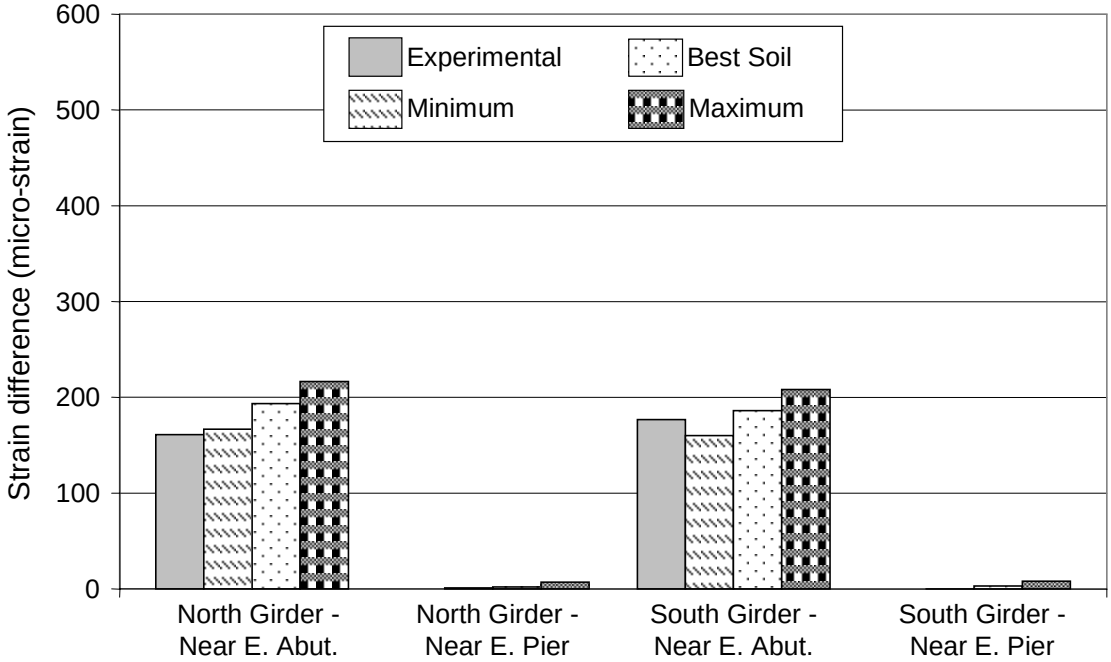

(a) North and South girder

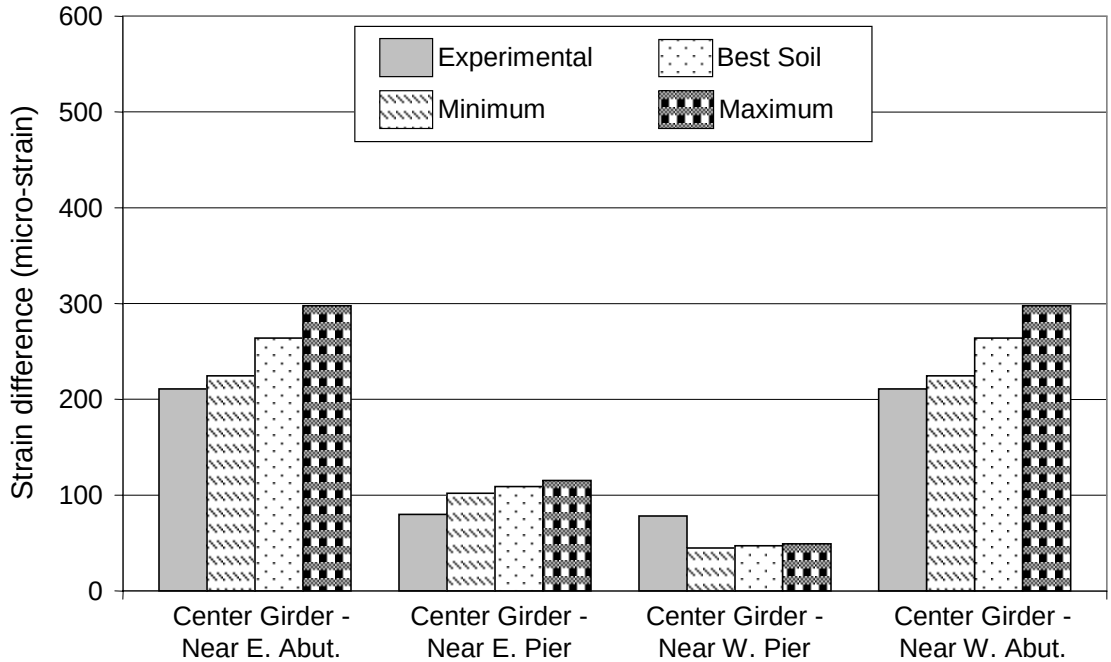

(b) Center girder

Figure 7.10. Difference between the longitudinal strains in the top and bottom flanges of the PC girders predicted by the Story, Series-A Models and experimentally measured at the Story County Bridge

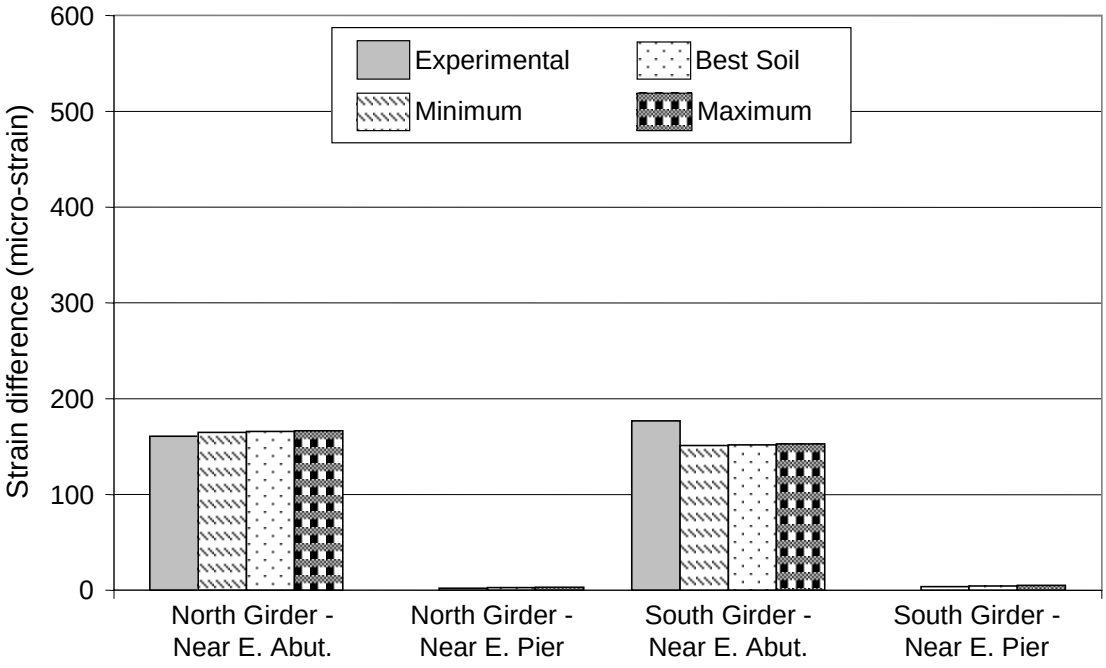

(a) North and South girder

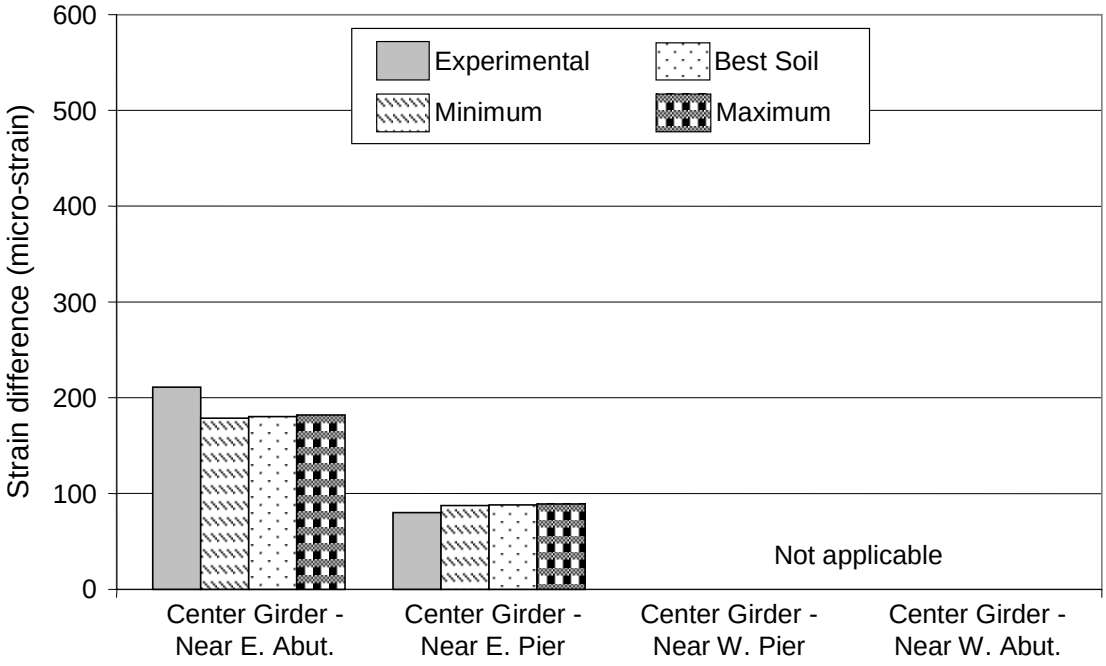

(b) Center girder

Figure 7.11. Difference between the longitudinal strains in the top and bottom flanges of the PC girders predicted by the Story, Series-B Models and experimentally measured at the Story County Bridge

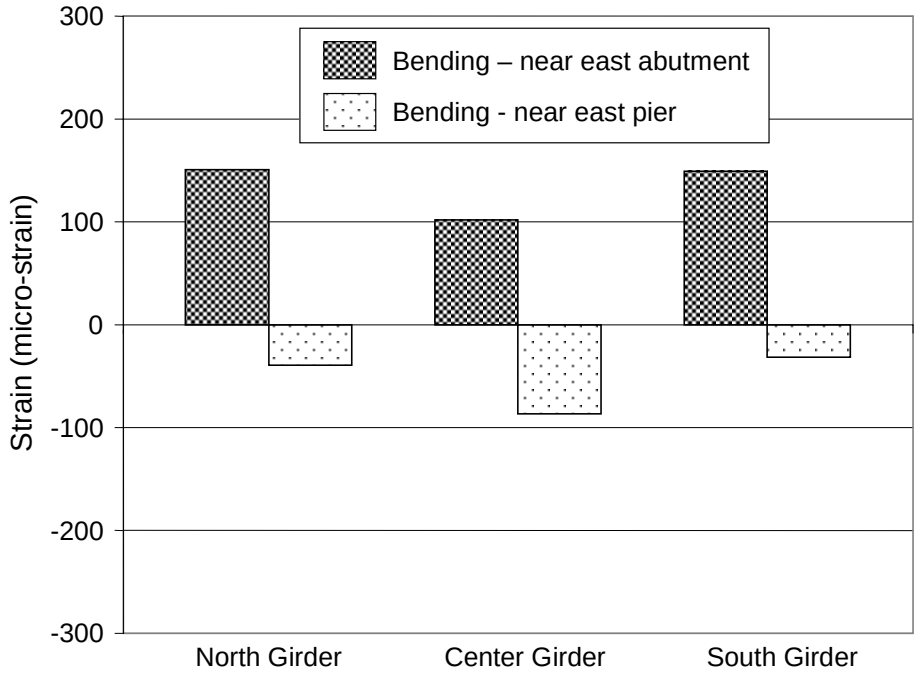

(a) X-axis bending strains

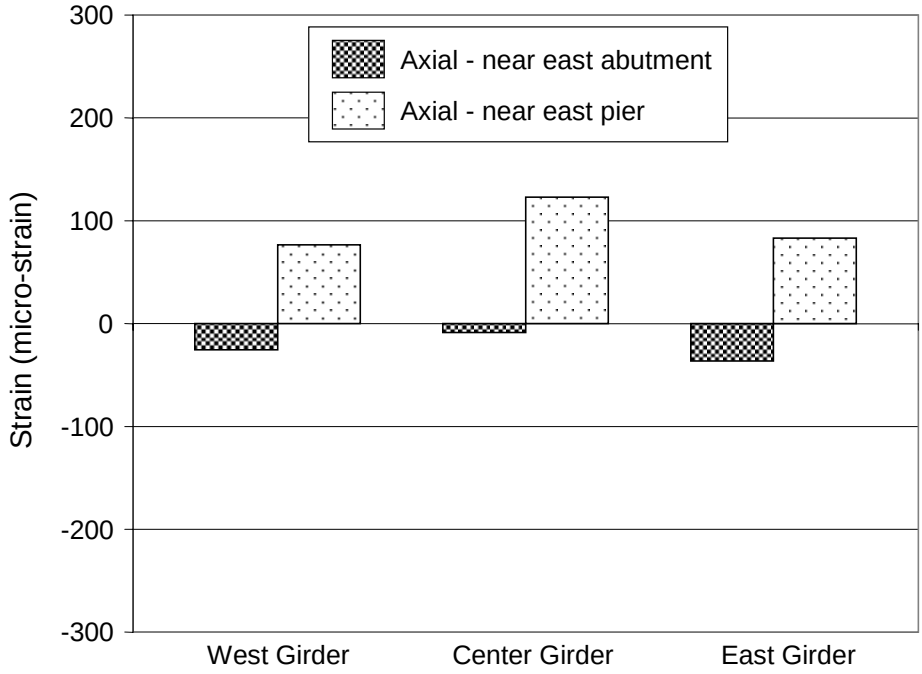

(b) Axial strains

Figure 7.12. PC girder strains due to stress predicted by the Story, Series-B, Best-Soil Model for the east span for the Story County Bridge

Table 7.1. Change in the bridge length predicted by the Story, Series-A Models

Evaluation Method		S_{east}	S_{west}	Change in Bridge Length (in.)	Change from Best-Soil Model (%)
Story, Series-A Models	Best-Soil	344	261	0.964	----
	Lower-bound backfill and lower-bound soil around piles	172	131	1.039	+7.8
	Upper-bound backfill and upper-bound soil around piles	515	392	0.901	-6.5
	Upper-bound backfill and lower-bound soil around piles	515	392	0.919	-4.7
	Lower-bound backfill and upper-bound soil around piles	172	131	1.015	+5.3
Experimental		----	----	0.960	-0.4

Table 7.2. Change in the bridge length predicted by the Story, Series-B Models

Evaluation Method		S_{east}	S_{west}	Change in Bridge Length (in.)	Change from Best-Soil Model (%)
Story, Series-B Models	Best-Soil	289	218	0.967	----
	Lower-bound backfill and lower-bound soil around piles	144	109	0.985	+1.9
	Upper-bound backfill and upper-bound soil around piles	435	326	0.949	-1.9
	Upper-bound backfill and lower-bound soil around piles	435	326	0.954	-1.3
	Lower-bound backfill and upper-bound soil around piles	144	109	0.981	+1.4
Experimental		----	----	0.960	-0.7

Table 7.3. Maximum, average, bridge-temperature ranges for reliable, experimental, pile strains at the Story County Bridge

Abutment	Pile	Depth Below Pile Cap (in.)	Coldest Average Bridge Temp. Date	Hottest Average Bridge Temp. Date	Average Bridge Temp. Range (°F)
Pile x-axis Flexural-Bending					
West	Center	9	n.a.	n.a.	n.a.
West	Center	33	1/5/99	8/20/99	108
East	North	9	1/5/99	7/20/99	115
East	North	33	1/5/99	7/20/99	115
East	Center	9	1/5/99	7/20/99	115
East	Center	33	n.a.	n.a.	n.a.
East	South	9	1/5/99	7/20/99	115
East	South	33	1/5/99	8/20/99	108
Pile y-axis Flexural-Bending					
West	Center	9	1/5/99	6/25/99	106
West	Center	33	1/5/99	7/20/99	115
East	North	9	1/5/99	7/20/99	115
East	North	33	1/5/99	7/20/99	115
East	Center	9	1/5/99	7/20/99	115
East	Center	33	1/5/99	7/20/99	115
East	South	9	1/5/99	7/20/99	115
East	South	33	n.a.	n.a.	n.a.

8. INTEGRAL-ABUTMENT DESIGN PROCEDURES

The main objective of this research was to develop guidelines for the design of integral-abutment bridges that have PC girders and steel, HP-shaped piles. The results from the field monitoring and finite-element analyses of the Guthrie County Bridge and Story County Bridge were used in conjunction with previously proposed, design models by other researchers, which were described in Chapter 2, and by Iowa State University (ISU) researchers, which are presented in this chapter, to develop the ISU design guidelines. Abutment design examples, which are presented in Chapter 9, illustrate many of the recommended, design procedures for an integral abutment when a bridge is subjected to loading conditions that involve temperature. The Guthrie County Bridge was selected for the design examples.

Several specifications are applied in this chapter to evaluate the required and provided design strength of the selected components and connections for an integral abutment. The American Association of State Highway and Transportation Officials (AASHTO) Standard Specifications for Highway Bridges (1996), AASHTO Load and Resistance Factor Design (LRFD) Bridge Design Specifications (1994, 1998, 2004), American Concrete Institute (ACI) Building Code Requirements for Structural Concrete (1998, 2002), American Institute of Steel Construction (AISC) Allowable Stress Design (1989), and AISC LRFD Specification for Structural Steel Buildings (1994, 1999) are cited this and the following chapters. Since, each of these design specifications may not adequately address all of the required design criteria for integral abutments, several

specifications were applied for this research. Additional discussion as to why a particular design specification was selected is presented in the applicable sections of this chapter.

8.1. AASHTO load cases

A more rational design approach and a more consistent factor of safety are provided by either a load-factor design method or a load-and-resistance-factor design method than that associated with a service-level (allowable stress) design method. Since bridge design engineers with the Office of Bridges and Structures at the Iowa Department of Transportation have used the AASHTO Standard Specifications for Highway Bridges (1996) to a greater extent than the AASHTO LRFD Bridge Design Specifications (1994, 1998, 2004), the ISU researchers selected the load-factor design method in the AASHTO Standard Specifications for Highway Bridges (1996) to determine the load combinations that need to be applied for the design of an integral abutment. Article 3.22 of the AASHTO Standard Specifications lists the load combinations that need to be considered for the load-factor design of a structure. The combination of loads and their load factors, which are given in the AASHTO Eq. (3-10), are expressed here as

$$\text{Group (N)} = \gamma[\beta_D D + \beta_L(L+I) + \beta_c CF + \beta_E E + \beta_B B + \beta_S SF + \beta_W W + \beta_{WL} WL + \beta_L LF + \beta_R(R+S+T) + \beta_{EQ} EQ + \beta_{ICE} ICE] \quad (8.1)$$

where, N is the load-group number, γ is an overall-load factor β is a load factor that is dependent on the load type, D is the dead load, L is the live load, I is the impact load, E is the earth pressure, B is the buoyancy force, W is the wind load on the structure, WL is

the wind load on the live load (100 pounds per linear foot), LF is the longitudinal force that is induced by the live load, CF is the centrifugal force that is induced by the live load, R is the rib shortening effect, S is the shrinkage, T is the temperature effect, EQ is the earthquake load, SF is the stream-flow pressure, and ICE is the ice pressure. A complete list of all the load combinations and load factors γ and β for load-factor design is provided in Table 8.1. For this table, the load factors β_D and β_E were set equal to 1 and 1.3, respectively. Group X loads are for culvert design. For the design of an integral abutment, the loads that need to be considered are dead, live, earth pressure, and temperature loads. Therefore, the critical-load combinations for load-factor design of an integral abutment are given by:

$$\text{Group I} = 1.3[D + 1.67(L+I) + 1.3E] \tag{8.2}$$

$$\text{Group IA} = 1.3[D + 2.2(L+I)] \tag{8.3}$$

$$\text{Group IV} = 1.3[D + (L+I) + 1.3E + T] \tag{8.4}$$

When only gravity loads are applied to the bridge, the Group IA loading combination is used by the Iowa Department of Transportation for live loadings that are less than the AASHTO, H20-load case. For live loads that are equal to or greater than AASHTO, HS20-load case, the Group I loading combination will govern the gravity-load condition. For a thermal-load condition, the Group IV loading combination should be used. The material presented in this chapter will focus on the forces and displacements that are induced by thermal loading.

8.2. Bridge temperatures

A change in the average, bridge temperature causes a change in the length of a bridge. When the temperature change through the depth of a bridge superstructure is not constant, the bridge will experience a curvature in the vertical plane. The average, bridge temperature and vertical-temperature gradients are discussed in the following sections.

8.2.1. Average bridge temperature

The average, temperature range of the bridge superstructure is a major factor that causes the change in the length of a bridge and induces abutment displacements. This temperature range is a function of the air temperature, solar radiation, wind velocity, and type of bridge structure. Discussion of the experimental, average, bridge temperatures is in Section 4.2.1.

Oesterle, et al. (1999) from Construction Technologies Laboratories (CTL) provided empirical equations for the minimum and maximum, average, bridge temperatures, $T_{min\ ave}$ and $T_{max\ ave}$, respectively, for concrete superstructures. Their equations, which include the air temperature and solar radiation, are given by

$$T_{min\ ave} = 1.00\ T_{min\ shade} + 9\ °F \tag{8.5}$$

$$T_{max\ ave} = 0.97\ T_{max\ shade} - 3\ °F + \Delta T_{solar} \tag{8.6}$$

where, $T_{min\ shade}$ and $T_{max\ shade}$ are the minimum and maximum, respectively, air temperatures that are measured in the shade and ΔT_{solar} is the change in the temperature of the bridge superstructure due to solar-radiation. The shade temperatures

are given by the American Society of Heating, Refrigeration and Air-Conditioning Engineers (ASHRAE, 1993). The ASHRAE shade temperatures are outdoor-air temperatures that are based on a 99%-confidence interval. These maximum and minimum, shade temperatures are expected to be only exceeded for approximately 30 hours per year. Oesterle, et al. experimentally determined that air temperatures measured at 1:00 pm and at the mid-height of the bridge girders correlated well with the computed, average, bridge temperatures.

Experimental data from the Guthrie County Bridge and Story County Bridge verified the CTL procedure for predicting the average, bridge temperatures from measured, air temperatures. If the experimentally-measured, maximum and minimum, air temperatures $T_{max\ air}$ and $T_{min\ air}$, for the hottest day and coldest day, respectively, are used in place of the shade temperatures in Eqs. 8.5 and 8.6 with ΔT_{solar} set equal to 13 °F for concrete-girder bridges in the State of Iowa (Oesterle, et al. 1999), the resulting, average, bridge temperatures are within a few degrees of the experimental-measured, average, bridge temperatures that is computed by Eq. 4.13 at the Guthrie County Bridge and Story County Bridge, as shown in Table 8.2. Therefore, the CTL procedure is acceptable for estimating the average, bridge temperature from the measured, air temperatures.

Ranges for the experimental, average, bridge temperature for the Guthrie County Bridge and Story County Bridge that were monitored in this project and for the PC-girder bridge (Boone County Bridge) that was studied by Girton, et al. (1989, 1991) are listed in Table 8.3. The minimum and maximum, shade temperatures as reported by ASHRAE (1993) for the Des Moines, Iowa area, which should be used in Eqs. 8.5 and 8.6, are –9

°F and 93 °F, respectively. The average, bridge temperatures recommended for design by CTL (Oesterle et al., 1999) and in Article 3.12.2 of the AASHTO LRFD Specifications (1998) are shown in Table 8.3. The recommended, design-temperature ranges for the CTL and AASHTO models underestimate the average, bridge temperatures for the monitored, concrete bridges.

Since the ASHRAE temperature values in the CTL equations are not conservative, the ISU researchers recommend that the minimum and maximum, average, bridge temperatures that are presented as "Procedure B" in Article 3.12.2.1 of the AASHTO LRFD Bridge Design Specifications (AASHTO, 2004) be applied in the design of integral-abutment bridges. This specification provides a more accurate approach to establish bridge temperatures than that presented in previous AASHTO bridge design specifications (AASHTO, 1994, 1996, and 1998). The temperature approach used in this edition of the AASHTO LRFD Bridge Design Specifications is based on the research by Roeder (2003). This specification presents maps of the United States that show temperature isobars of minimum and maximum, bridge temperatures for steel-girder and concrete-girder bridges. The temperatures that are listed in Table 8.4 were established by using a visual interpolation of the temperature map for concrete bridges. From Table 8.4, the minimum and maximum, average, bridge temperatures for the central Iowa region are $T_{min\ ave}$ = - 6 °F and $T_{max\ ave}$ = + 109 °F, respectively, as listed in Table 8.3. The average, bridge-temperature range, $\Delta T_{average}$, is given by

$$\Delta T_{average} = T_{max\ ave} - T_{min\ ave} \tag{8.7}$$

The ISU design-temperature recommendation is more conservative than that based on the AASHTO and CTL design models. The ISU, recommended, design-temperature range, $\Delta T_{average}$, is essentially the same as the experimentally-measured, temperature range at the Story County Bridge and Boone County Bridge and only slightly greater than the temperature range that was measured at the Guthrie County Bridge. Figure 8.1 shows the CTL, AASHTO, and ISU recommended temperature ranges of 100 ^{o}F, 80 ^{o}F, and 118 ^{o}F, respectively, for the average, bridge temperature for bridges the Des Moines, Iowa area and the experimental, average, bridge temperature ranges for the Guthrie County Bridge, Story County Bridge, and Boone County Bridge of 117 ^{o}F, 118 ^{o}F, and 118 ^{o}F, respectively.

8.2.2. Vertical-temperature gradient

A vertical-temperature gradient within an integral-abutment bridge can induce bending stresses in the bridge members and abutment rotations in a vertical plane that is parallel to the length of the bridge. The thermal gradient will be the largest on clear summer days, when the solar radiation is the greatest. Article 3.12.3 in the AASHTO LRFD Specification (1998) recommends the temperature gradient through the depth of a PC-girder, bridge superstructure that is shown in Fig. 8.2. The change in the temperatures, ΔT_1 and ΔT_2, of the concrete at the top and at 4 in. below the top surface of the bridge slab, respectively, that produce a temperature gradient are estimated in Article 3.12.3 of the AASHTO LRFD Specifications (1998) to be 46 °F and 12 °F, respectively, for bridges that are located in the State of Iowa. The change in the temperature, ΔT_3, of the concrete at the bottom surface of the bridge girders shall not

exceed 5 °F; however, the temperature ΔT_3 shall be set equal to zero, when the actual temperature change at this location is not available to the designer. For concrete superstructures that are equal to or deeper than 16 in., the dimension A is set equal to 12 in. For concrete superstructures that are less than 16-in. deep, the dimension A is set equal to 4 in. less than the actual depth of the superstructure.

If low, night-time temperatures occur after high, day-time temperatures, a negative-temperature gradient can occur, since rapid cooling exists for a bridge superstructure. The AASHTO LRFD Specifications (1998), note that the negative-temperature gradient should be established by multiplying the positive-temperature gradient values by -0.30 for plain-concrete decks and by -0.20 for decks with an asphalt overlay. Negative-temperature gradients are only specified for concrete superstructures that are greater than 24-in. deep.

Extrapolated, vertical-temperature gradients (Fig. 4.12) for the hottest day at the Guthrie County Bridge and Story County Bridge were similar to the AASHTO LRFD Specifications (1998), positive-temperature gradient (Fig. 8.2) for concrete bridges. A bilinear, temperature gradient was determined for these bridges. A steeper, temperature gradient occurred in the concrete deck than that established in the PC girders. An increase in the temperature-gradient value at the bottom of the girders was not experimentally determined since a limited number of thermocouples were used along the depth of the girders. Negative-temperature gradients (Fig. 4.12) were observed during the bridge-monitoring period. The ISU researchers recommended the use of the AASHTO LRFD Specifications, positive-temperature and negative-temperature gradients for PC-girder bridges.

8.3. Coefficient of thermal expansion and contraction

Experimental testing was performed at ISU by Ng (1999) to determine typical values for the coefficient of thermal expansion and contraction (α-coefficient) for the concrete that is used for bridge superstructures in the State of Iowa. Concrete-core samples were tested at 100%-dry and 100%-wet (saturated) conditions. A summary of the experimental, α-coefficient study is given in Appendix A. Figure 8.3 shows the ranges in the experimental, α-coefficients for 20 bridge decks in the State of Iowa. Figures A-1 and A-2 in Appendix A show the bridge locations and corresponding 100%-dry concrete, α–coefficient range for those bridges, respectively, on a map for the State of Iowa. The experimental, α-coefficients were usually less than 6.0 x 10^{-6} in./in./°F, which is the α-coefficient that is recommended in Article 5.4.2.2 of the AASHTO LRFD Specifications (1998) when more precise data are not available.

Ng (1999) computed α-coefficients, α_c, for the concrete in the core specimens by applying the Emanuel and Hulsey (1977) empirical equation, which is expressed as

$$\alpha_c = f_T\left(f_M f_A \beta_P \alpha_S + \beta_{FA}\alpha_{FA} + \beta_{CA}\alpha_{CA}\right) \tag{8.8}$$

where, f_T is the correction factor for temperature conditions (1.0 for a controlled environment and 0.86 for an outside exposure); f_M is the correction factor for the moisture content in the concrete, which is shown in Fig. 8.4; f_A is the correction factor for the age of the concrete, which is shown in Fig. 8.5; β_P is the concrete-mix proportion by volume for the cement paste, β_{FA} is the concrete-mix proportion by volume for the fine aggregate, and β_{CA} is the concrete-mix proportion by volume for the coarse aggregate,

which are listed in Table 8.5; α_S is the α-coefficient for a saturated and hardened, neat-cement paste (α_S = 6.0 x 10^{-6} in./in./°F); and α_{FA} is the α-coefficient for the fine aggregate and α_{CA} is the α-coefficient for the coarse aggregate. The α-coefficients that are specified by ACI Committee 209 (1998), by the AASHTO Guide—Thermal Effects in Concrete Bridge Superstructures (1989), and by PCA (1988) for concrete aggregates are listed in Table 8.6. Quartz sand is typically used for the fine aggregate in concrete-mix designs for bridge superstructures in the State of Iowa. For this aggregate, Table 8.6 lists a maximum α-coefficient of 6.6 x 10^{-6} in./in./°F.

The experimental, α-coefficients and the computed, α-coefficients that were determined from Eq. 8.8 with the ACI, AASHTO, and PCA aggregate α-coefficients for the 100%-dry condition (f_M = 1.2 from Fig. 8.4) of the concrete in the bridge decks of the Guthrie County Bridge and Story County Bridge are listed in Table 8.7 (The experimental α-coefficients for the concrete-core samples that were taken from other bridge decks in the State of Iowa are presented in Table A.3 of Appendix A). Ng (1999) evaluated the α-coefficient of the concrete in PC girders that were manufactured by two, precast-concrete producers (Raider Precast Concrete and Iowa Prestressed Concrete) in the State of Iowa. The experimental α-coefficients and the computed α-coefficients from Eq. 8.8 with the ACI, AASHTO, and PCA, aggregate α-coefficients for the 100%-dry condition of the concrete from two girders are also listed in Table 8.7. For these girders, Eq. 8.8 overestimated the α-coefficient for 100%-dry concrete. Differences between the experimental, α-coefficients and the empirical, α-coefficients were less than 15%. If experimental, α-coefficients are not available, the ISU researchers recommend that the

Emanuel and Hulsey's expression (Eq. 8.8) be applied for the determination of the α-coefficient when the concrete-mix design and aggregate types are known.

Ng (1999) multiplied the average, experimental, α-coefficient for the 100%-dry condition in Table 8.7 by the α-coefficient ratio in Eq. A.1, to calculate the α-coefficients that are listed in Table 8.8. These predicted, α-coefficients, which are listed in Table 5.1, were used for the finite-element analyses of the Guthrie County Bridge and Story County Bridge that are presented in Chapters 6 and 7, respectively.

A revised, design equation was derived for predicting an α-coefficient of concrete that includes moisture effects when no experimental results are available. By applying the maximum, combined effect of f_M and f_A, which occurs at the 45%-moisture-saturation condition, Emanuel and Hulsey's equation (Eq. 8.8) (see Appendix A) becomes

$$\alpha_C = 0.86\left(1.58\beta_P\alpha_S + \beta_{FA}\alpha_{FA} + \beta_{CA}\alpha_{CA}\right) \tag{8.9}$$

The predicted α-coefficients using Eq. 8.9 are listed in Table 8.8. Note that the predicted, α-coefficients by Eq. 8.9 for the PC girders in the Guthrie County Bridge and Story County Bridge are much higher than those predicted by Ng (1999).

The α-coefficients are not the same for the different concrete elements in a bridge superstructure. Therefore, an effective α-coefficient, α_e, for a concrete-bridge superstructure is needed to calculate the thermally-induced changes in the length of a bridge (Oesterle, et al. 1999). For a bridge with a RC deck and PC girders, α_e is given by

$$\alpha_e = \frac{\left(\alpha_g E_g A_g\right) + \left(\alpha_d E_d A_d\right)}{\left(E_g A_g + E_d A_d\right)} \tag{8.10}$$

where, α_g is the α-coefficient for the concrete in the PC girders; E_g is the modulus of elasticity of the concrete in the PC girders; A_g is the total, cross-sectional area for all of the PC girders; α_d is the α-coefficient for the concrete in the bridge deck; E_d is the modulus of elasticity of the concrete in the bridge deck; and A_d is the total, cross-sectional area for the bridge deck. The effective, α-coefficients for the Guthrie County Bridge and Story County Bridge are listed in Table 8.8.

8.4. Creep and shrinkage

Concrete creep and shrinkage decreases the initial, thermal expansion and increases the initial, thermal contraction of a bridge superstructure. These volumetric changes for the concrete bridge deck and PC girders affect the horizontal displacements at the top of the abutment piles. As the pile heads displace, passive-soil pressures are induced along the length of the upper portion of the piles and flexural-bending strains are induced in the piles. When soil is subjected to lateral pressures, the soil will creep over time. Soil creep along the length of an abutment pile will reduce the pile curvature and cause a decrease in the flexural-bending strains in the pile. Concrete creep, concrete shrinkage, and soil creep and discussed in the following sections. The ISU researchers selected the AASHTO LRFD Specifications (1998) to address concrete creep and shrinkage strains because this specification provides detailed discussions for these internal member strains.

8.4.1. Concrete creep

Article 5.4.2.3.2 of the AASHTO LRFD Specifications (1998), which is based on the work by Collins and Mitchell (1997) and as recommended by ACI Committee 209 (1998), accounts for concrete creep in prestressed-concrete construction by applying an effective, modulus of elasticity, $E_{c,eff}$, for the initial slope of the stress-strain curve for concrete. The modulus $E_{c,eff}$ is expressed as

$$E_{c,eff} = \frac{E_{ci}}{1+\psi(t,t_i)} \tag{8.11}$$

where, E_{ci} is the initial, modulus of elasticity for the concrete at an age of t_i-days after concrete casting and the parameter $\psi(t,t_i)$ is the ratio of the concrete-creep strain, ε_{cr}, at an age of t-days after concrete casting to the initial, elastic, concrete strain, ε_{cf}, when the concrete is loaded at an age of t_i-days after concrete casting is the concrete-creep coefficient, which is given by

$$\psi(t,t_i) = \frac{\varepsilon_{cr}}{\varepsilon_{cf}} \tag{8.12}$$

with t-days being equal to or greater than t_i-days. An approximation for the concrete-creep coefficient, which is expressed by the AASHTO LRFD Eq. (5.4.2.3.2.1), is rewritten here as

$$\psi(t,t_i) = 3.5k_c k_f \left(1.58 - \frac{H}{120}\right) t_i^{-0.118} \left[\frac{(t-t_i)^{0.6}}{10+(t-t_i)^{0.6}}\right] \tag{8.13}$$

where, H is the relative-humidity percent, k_c is a factor that accounts for the influence of the volume-to-surface-area ratio, V/S, for the member, and k_f is a factor that accounts for

the concrete strength. The AASHTO, LRFD Eqs. (C5.4.2.3.2-1) and (5.4.2.3.2-2), for the k_c-factor and the k_f-factor, respectively, are rewritten here as

$$k_c = \left(\frac{45+t}{26e^{0.36(V/S)}+t}\right)\left(\frac{1.80+1.77e^{-0.54(V/S)}}{2.587}\right) \tag{8.14}$$

$$k_f = \frac{1}{0.67+\left(\frac{f_c^{'}}{9000}\right)} \tag{8.15}$$

where, f'_c. is the 28-day, concrete-compressive strength (in psi units). In determining the age of the concrete at the time of initial loading, one day of accelerated curing can be regarded as adding 7 days to the age of concrete. An effective strain for concrete at an age of t-days after casting the concrete when a compressive stress f_{ci} is applied to the concrete and remains constant from an age of t_i-days to t-days after casting the concrete is approximated as

$$\varepsilon_{cf}(t,t_i) = \frac{f_{ci}}{E_{c,eff}} \tag{8.16}$$

From Eq. (8.12), the concrete-creep strain is given by

$$\varepsilon_{cr} = \varepsilon_{cf}(t,t_i) - \varepsilon_{cf} = \psi(t,t_i)\varepsilon_{cf} \tag{8.17}$$

Article C5.4.2.3.2 of the AASHTO LRFD Specification (1998) states that the creep strain of concrete, which is subjected to permanent loads, is about 1.5 to 4.0 times the initial, elastic, compressive strain.

The shortening in the length for a bridge superstructure due to the concrete- creep strains is affected by the magnitude of the prestress force in the PC girders at the time when the RC deck has cured and when the bridge becomes an integral structure. Since the RC deck will restrain concrete-creep for the PC girders, an effective longitudinal stress, σ_c, at the center of gravity of the bridge superstructure would need to be established to determine the change in the length of a bridge. The magnitude of the stress σ_c is a function of the dead loads of the bridge deck and parapets; prestress force in the PC bridge girders; and resultant, horizontal, soil-pressure forces that act behind the abutment backwalls. Applying the relationship between stress and strain for elastic behavior, Eq. 8.17 can be rewritten as

$$\varepsilon_{cr} = \psi(t, t_i)\frac{\sigma_c}{E_{eff}} \tag{8.18}$$

where, E_{eff} is the effective, modulus of elasticity for the bridge superstructure. Since the concrete-creep strains are proportional to the magnitude of the compressive stress in the bridge superstructure, the ISU researchers believe that the full-passive-soil pressure for the abutment backfill should be used to induce the largest, concrete-creep strains in a bridge superstructure.

8.4.2. Concrete shrinkage

Article 5.4.2.3.3 of the AASHTO LRFD Specifications (1998) states that for moist-cured concrete without shrinkage-prone aggregates, the concrete-shrinkage strains can be calculated as

$$\varepsilon_{sh} = -k_s k_h \left(\frac{t}{35+t} \right) (0.51 x 10^{-3}) \tag{8.19}$$

where, t is the number of days that the concrete was exposed to drying, k_s is a size factor, and k_h is a humidity factor. The k_s-factor, which is expressed by the AASHTO LRFD Eq. (C5.4.2.3.3-1), is rewritten here as

$$k_s \left(\frac{45+t}{26e^{0.36(V/S)}+t} \right) \left(\frac{1064-94(V/S)}{923} \right) \tag{8.20}$$

The k_h-factor can be approximated by Eq. 8.21 when H < 80% and by Eq. 8.22 when H $\geq$ 80%.

$$k_h = \frac{140-H}{70} \tag{8.21}$$

$$k_h = \frac{3(100-H)}{70} \tag{8.22}$$

Article 5.4.2.3.1 of the AASHTO LRFD Specification (1998) permits the use of an approximation for the concrete-shrinkage strains. At 28 days and after one year has elapsed since the concrete was cast, the concrete-shrinkage strains can be approximated as 200 micro-strains and 500 micro-strains, respectively. Also, the AASHTO LRFD Specifications permits the use of the ACI Committee 209 recommendations (1998) to determine concrete-creep and concrete-shrinkage strains.

8.4.3. Soil creep

The creep rate of soil is affected by the type and amount of clay in the soil. Mitchell (1993) noted that time-dependent deformations in a soil are caused by primary

consolidation of the soil as water escapes from the pore spaces in the soil and by secondary compression of the soil, which is volumetric creep. Soil creep is affected by the viscous resistance of the soil structure. Also, Mitchell stated that the plasticity index for a soil accounts for the type and amount of clay. For a consolidation pressure of 4200 psf on a test-soil specimen with 10%, 20%, 30%, and 40% clay sizes finer than 80 μ in., Mitchell showed in Fig. 10.22 of his text that the average, steady-state, creep rate was about 3, 6, 9, and 13 in./in./min., respectively, corresponding to plasticity indexes of about 10, 40, 70, 80%, respectively. Creep of the soil along the upper portion of the length for an integral-abutment pile reduces the flexural-bending strains in the pile that are induced by the horizontal displacements at the pile head.

8.4.4. Combined effects of concrete creep and shrinkage and soil creep

A high level of uncertainty exists in the prediction of the amount and relative rate of concrete creep, concrete shrinkage, and soil creep that occurs for an integral-abutment bridge. Over time, concrete creep and shrinkage will shorten the length of a bridge. When the average temperature for a bridge superstructure is equal to the construction temperature at the time the bridge became an integral structure, concrete creep and shrinkage of the bridge superstructure will shift the tops of the abutment piles from their as-built, un-flexed position towards the center of the bridge. The flexing of the piles against the non-granular soil along the pile length will induce plastic deformation and time-dependent creep of the soil. Over time, the lateral-soil pressures on the abutment piles will decrease from an intensity that is as high as the full-passive-soil-pressure condition to a stress condition between the active-soil-pressure and the at-rest-soil-pressure condition.

Since soil creep occurs over a shorter period of time than concrete creep and shrinkage, the ISU researchers believe that the decrease in the flexural-bending strains in the abutment piles that is caused by the creep of soil effectively negates the increase in these pile strains due to concrete creep and shrinkage of the bridge superstructure.

Most of the concrete-volumetric changes that are caused by concrete shrinkage happen over a relatively short period of time (about one year after concrete casting) when compared to the anticipated life of a bridge. During the time period when significant amounts of concrete creep and shrinkage occur, soil consolidation and soil creep will take place along the length of the upper portion of an abutment pile that is located below the pre-bored hole. This soil response will reduce the flexural-bending strains and the ductility demand for the abutment piles from that which are induced by just the thermal contraction and concrete creep and shrinkage of the bridge superstructure.

The ISU researchers believe that the probability is essentially negligible for the maximum live and impact loads to be acting on a bridge when the coldest, average, bridge temperature occurs during the first year after the bridge becomes an integral structure. Live and impact loads affect the ductility demand for an abutment pile, as discussed in Section 8.10.2.8. If this highly unlikely combination of events would occur, the ISU researchers would consider such an event to be a one-time, overload condition that would not be detrimental to the abutment piles. Beyond the first year after the completion of the construction for an integral-abutment bridge, concrete creep and shrinkage will have little, if any, effect on the performance of the piles in an integral abutment.

For investigating the ductility of integral-abutment piles, the ISU researchers believe that neglecting the longitudinal displacements of an integral abutment that are caused by concrete creep and shrinkage of the bridge superstructure might be only slightly non-conservative. Any attempt to accurately quantify the pile-head displacements due to concrete creep, concrete shrinkage, and soil creep and consolidation would not be successful. Therefore, the ISU researchers recommend that concrete creep and shrinkage can be neglected for either the thermal expansion or contraction of a bridge superstructure when evaluating the effect of pile-head displacements on pile performance (see Section 8.9). Concrete creep and shrinkage do affect the movement of a bridge superstructure. Therefore, these material deformations must be included when calculating displacements of a bridge superstructure (see Section 8.6).

8.5. Equivalent cantilever length for piles

Piles are designed to resist the vertical loads in integral-abutment bridges. As a result of thermal expansion and contraction of the bridge superstructure, the tops of the abutment piles are subjected to horizontal displacements. These piles can be analyzed as beams supported continuously by the surrounding soil, as discussed in Chapter 5. However, because the lateral deformations of an integral-abutment pile will be generally confined to the upper portion of a pile, the pile can be idealized as an equivalent-cantilever member, as shown in Fig. 8.6 (Greimann, et al. 1987a). When a pre-bored hole is used, it should be filled with a material that has very-low stiffness, such as that for bentonite slurry. The bottom of the equivalent cantilever is fixed and the rotational-

restraint conditions at the top of the equivalent cantilever can be either pinned or fixed, which is based on the connection detail at the pile head.

The equivalent-cantilever length, L_e, for a pile is a function of both the pile properties and the soil profiles at the location of the pile. The equivalent-cantilever length is given by

$$L_e = \ell_e + \ell_u \tag{8.23}$$

where, ℓ_e is the equivalent, embedded length for the pile, which is the depth from the soil surface below the bottom of any pre-bored hole to the fixed base of the equivalent cantilever; and ℓ_u is the pile length above the undisturbed-soil strata, which includes the depth of a properly-filled, pre-bored hole.

For a pile embedded in soil, there is a length, ℓ_c, along the pile for which the horizontal displacement at the pile head has minimal effects on the horizontal displacement of the pile and on the shear forces and bending moments in the pile at the soil depth that corresponds with the lower end of the length ℓ_c. Beyond the length ℓ_c, horizontal displacements and bending moments are a small percentage (about 4%) of those at the pile head. If a pile is longer than the length ℓ_c, the pile will essentially behave as an infinitely-long pile. For a single layer of soil that has a constant horizontal stiffness throughout the depth of the soil, the length ℓ_c is given by

$$\ell_c = 4R \tag{8.24}$$

where, the relative-stiffness factor, R, for a pile in soil is expressed as

$$R = \sqrt[4]{\frac{EI}{k_h}} \tag{8.25}$$

where, I is the moment of inertia of the pile cross section with respect to the axis of bending ($I = I_x$ for x-axis bending and $I = I_y$ for y-axis bending) and k_h is the horizontal stiffness of the soil. If the soil profile is layered or does not have a constant horizontal stiffness along the depth of the soil, the horizontal stiffness k_h is replaced with an equivalent, horizontal stiffness, k_e. An iterative procedure for evaluating the horizontal stiffness k_e, which was presented by Greimann, et al. (1987a) is represented here as

Step 1: Assume an initial value for the equivalent-horizontal stiffness k_e of the layered soil.

Step 2: Evaluate the active length, ℓ_o, of the pile in bending, which is assumed to be equal to one-quarter of the deflected-wave shape for the pile or about one-half of the length ℓ_c, by applying the expression

$$\ell_o = 2\sqrt[4]{\frac{EI}{k_e}} \tag{8.26}$$

Step 3: Calculate the second moment, I_k, of the $k_h(z)$ curve about the reference line A-A, shown in Fig. 8.7, at a depth of ℓ_o, by the expression

$$I_k = \int_o^{\ell_o} k_h(z)(\ell_o - z)^2 dz, \tag{8.27}$$

where, $k_h(z)$ represents the variation of the stiffness k_h with soil depth.

Step 4: Evaluate a new estimate for the equivalent, horizontal stiffness, k_e, of the soil by applying the expression

$$k_e = \frac{3I_k}{\ell_o^{\,3}} \tag{8.28}$$

Step 5: Return to Step 2 and repeat Steps 2, 3, and 4 until convergence is obtained for the stiffness k_e.

After the length ℓ_c is established, Fig. 8.8 is used with the ratio $\frac{\ell_u}{\ell_c}$ to establish the ratio $\frac{\ell_e}{\ell_c}$ for a particular pile behavior that is associated with the equivalent cantilever.

Equivalent cantilevers can be used to calculate the displacement, force and moment at the top of a pile. There are three types of equivalencies that are used for the integral-abutment system: (1) the horizontal stiffness of the equivalent cantilever is equal to the horizontal stiffness of a pile that is in soil, (2) the maximum moment in the equivalent cantilever is equal to the maximum moment in a pile that is in soil, and (3) the elastic-buckling load of a equivalent cantilever is equal to elastic-buckling load of a pile that is in soil. The equations for determining the three, equivalent-cantilever lengths are plotted in Fig. 8.8 in a non-dimensional format for fixed-head and pinned-head piles embedded in a uniform soil.

For computing the displacements at the pile head and the maximum bending moments in the pile due to thermal movements, the equivalency that is based on the horizontal stiffness of the pile in the soil medium is used to determine the equivalent-cantilever length, L_{eh}, for the pile. For computing the forces and moments in the pile due to gravity load, the equivalency that is based on the maximum moment in the pile is used

to establish the equivalent-cantilever length, L_{em}. The elastic-buckling-load equivalency is used when computing the axial-compressive strength of the pile as a structural member. For this case, the equivalent-cantilever length is the elastic-buckling, equivalent-cantilever length, L_{eb}.

8.6. Bridge superstructure displacements

Figure 8.9 shows the plan views for the non-displaced and displaced positions for the bridge deck of a single-span, geometrically-symmetric, skewed, integral-abutment bridge. The bridge has identical soil conditions at each abutment, and it is subjected to thermal expansion. Point A and Point A' correspond to generic, non-displaced and displaced points, respectively, on the bridge deck at the mid-thickness of one of the integral abutments. The magnitude of the displacement of Point A to Point A' along the longitudinal and transverse directions for the bridge is measured by the distances $d\ell$ and dt, respectively. These displacements, which occur in a horizontal plane, are induced by the thermal expansion or contraction, concrete creep and shrinkage, and rotation of the bridge deck in the horizontal plane. The rotation of the bridge deck, which is measured by the angle β, is caused by the passive-soil pressures that act on the backwalls of the skewed abutments. When the bridge experiences a thermal expansion, the rotation occurs in a counter-clockwise direction for the geometry shown in the figure, and occurs about the "point-of-fixity" for the bridge. The "point-of-fixity" is a point on the bridge deck where the translational displacements are assumed to be equal to zero. Corners 1 and Corners 2 of the bridge deck are defined as the acute-angle corners and obtuse-angle corners, respectively, for the slab.

Thermal expansion and contraction of an abutment that occurs along its length is limited by the presence of the soil mass behind the abutment. The temperature range for the soil in the abutment backfill is significantly smaller than the range in the air temperature. The soil in contact with an abutment will significantly reduce the temperature range for an abutment compared to that for the portion of the concrete superstructure that is not adjacent to the abutment backfill. For the bridge-deck model shown in Fig. 8.9, the ISU researchers assumed that the abutment length was not affected by the change in the temperature of the bridge deck. Therefore, transverse expansion or contraction of the bridge deck was neglected for calculating the displacements $d\ell$ and dt of an integral abutment.

8.6.1. Longitudinal displacement of an integral abutment

A generalized relationship between the rotation angle β and the longitudinal displacement $d\ell$ at the mid-length of an abutment for an integral-abutment bridge is shown in Fig. 8.10. After the end portion of the bridge deck and abutment backwall are cast and the concrete has cured to form an integral-bridge structure, the soil behind the abutment is placed and compacted. For this stage of bridge construction, the soil forces that act on the bridge are caused by the soil pressures from the backfill soil. The longitudinal expansion and contraction of an integral-abutment bridge that occurs at the mid-width of the bridge can be assumed to be approximately equal to the free expansion and contraction of an unrestrained structure, since the soil pressures behind the abutments and the horizontal restraint provided by the abutment piles and pier structures have an insignificant effect on the average, longitudinal strain in the bridge superstructure. Oesterle, et al. (1999) recommended using the total concrete-creep and

concrete-shrinkage strains that are given by AASHTO LRFD Specifications (1998), rather than applying the more exact procedures of ACI Committee 209 (1998) to account for these strains.

The CTL method (Oesterle, et al. 1999) that is described in this section can be used to determine the displacements $d\ell_{expand}$, $d\ell_{contract}$, and $\Delta\ell_{re\text{-}expand}$ of an integral abutment for initial expansion, initial contraction, and re-expansion, respectively, for a bridge superstructure. Displacement-magnification factors, Γ, that are based on a 98%, statistical-confidence level were developed by the CTL researchers to account for uncertainties in the expansion and contraction of a PC-girder bridge.

The procedure for determining the displacements for a point that is located at the mid-width of a bridge, at the mid-thickness of an integral abutment, and at the center-of-gravity of the bridge superstructure involves the following steps:

Step 1: Determine the mean, construction temperature, $T_{construction}$, for the bridge. A typical, mean, construction temperature for bridges that are constructed in the State of Iowa is approximately 60 °F.

Step 2: Determine the minimum and maximum, average, bridge temperatures, $T_{min\ ave}$ and $T_{max\ ave}$, respectively, as described in Section 8.2.1.

Step 3: Determine the location for the “point-of-fixity” for a bridge. Researchers at CTL recommend using a procedure given by Zederbaum (1969) for determining the “point-of-fixity” for jointless bridges with semi-integral piers. The location of the “point-of-fixity” is influenced by the flexural stiffness of the piers, passive-soil restraint at the abutments, and the flexural stiffness of the abutment piles, with respect to the longitudinal direction of the bridge. For a geometrically symmetric

bridge, the "point-of-fixity" is located at the mid-length and mid-width of the bridge. For this symmetric case, the distance, ℓ, from the "point-of-fixity" to the an abutment is given by

$$\ell = \frac{L}{2} \tag{8.29}$$

where, L is the bridge length.

Step 4: Determine the maximum expansion of the bridge shortly after construction. The change in the temperature of the bridge, which is equal to the difference between the maximum, average, bridge temperature and the mean, construction temperature, is evaluated as

$$\Delta T_{expand} = T_{max\ ave} - T_{construction} \tag{8.30}$$

The corresponding thermal strain for the maximum, initial expansion of the bridge superstructure is expressed by

$$(\varepsilon_{th})_{expand} = \alpha_e (\Delta T_{expand}) \tag{8.31}$$

where, α_e is the effective, coefficient of thermal expansion and contraction that is evaluated using either experimental α-coefficients or the Emanuel and Hulsey's (1977) expression. As discussed in Sections 8.4.1 and 8.4.4, the initial, concrete-creep strain, ε_{cr}, and concrete-shrinkage strain, ε_{sh}, can not be accurately predicted due to the uncertainties associated with the elapse time between the casting of the concrete for both the PC bridge girders and the bridge deck and when the maximum expansion occurs for the bridge. Since

these strains reduce the maximum expansion of the bridge, concrete creep and shrinkage should be conservatively neglected for the evaluation of the expansion of the bridge superstructure. For the expansion of a bridge, the maximum displacement of an abutment along the longitudinal direction of the bridge that is measured from the original, non-displaced position, which was shown in Fig. 8.9, is given by

$$d\ell_{\text{expand}} = \Gamma(\varepsilon_{\text{th}})_{\text{expand}}\,\ell \tag{8.32}$$

A Γ-displacement factor of 1.60 or 2.05 was recommended by Oesterle, et al. (1999) to account for uncertainties in the maximum expansion of a PC girder bridge when experimental α-coefficients, or Emanuel and Hulsey's (1977) expression, respectively, is used in the evaluation of the coefficient α_e.

Step 5: Determine the maximum, long-term contraction of the bridge superstructure. The change in the temperature of the bridge, which equals the difference between the minimum, average, bridge temperature and the mean, construction temperature, is evaluated as

$$\Delta T_{\text{contract}} = T_{\text{min ave}} - T_{\text{construction}} \tag{8.33}$$

The corresponding thermal strain for the maximum contraction of the bridge superstructure is given by

$$(\varepsilon_{\text{th}})_{\text{contract}} = \alpha_e(\Delta T_{\text{contract}}) \tag{8.34}$$

Concrete creep and shrinkage will increase the magnitude of the contraction of the bridge superstructure so that the total, longitudinal strain in the bridge superstructure for the maximum contraction of the bridge superstructure is given by

$$\left(\varepsilon_{\text{total}}\right)_{\text{contract}} = \left(\varepsilon_{\text{th}}\right)_{\text{contract}} + \varepsilon_{\text{cr}} + \varepsilon_{\text{sh}} \tag{8.35}$$

The concrete-creep strains, ε_{cr}, and concrete-shrinkage strains, ε_{sh}, are evaluated as discussed in Sections 8.4.1 and 8.4.2, respectively. If for some reasons, the concrete strains ε_{cr} and ε_{sh} can not be evaluated by accurate methods, the ISU researchers recommend that a strain of 500 micro-strains be used to approximate the total of these concrete-material strains. For the bridge contraction, the maximum displacement of an abutment along the longitudinal direction of the bridge from the original non-displaced position, which was shown in Fig. 8.9, is evaluated as

$$\mathrm{d}\ell_{\text{contract}} = \Gamma\left(\varepsilon_{\text{total}}\right)_{\text{contract}} \ell \tag{8.36}$$

A Γ-displacement factor of 1.35 or 1.45 was recommended by Oesterle, et al. (1999) to account for uncertainties in the maximum, thermal contraction of a PC girder bridge, when experimental α-coefficients or Emanuel and Husley's (1977) expression, respectively, is used in the evaluation of the coefficient α_e. There may be occasions for which both the concrete-creep and concrete-shrinkage strains may be neglected if a significantly long period of time has elapsed

between the casting of the concrete for the majority of the bridge and the portion of the bridge deck that is adjacent to and integral with an abutment.

Step 6: Determine the maximum re-expansion of the bridge starting at the point of maximum contraction. The change in temperature of the bridge superstructure, which equals the difference between the maximum and minimum, average, bridge temperatures is given by

$$\Delta T_{\text{re-expand}} = T_{\text{max ave}} - T_{\text{min ave}} \tag{8.37}$$

The corresponding thermal strain for the maximum re-expansion of the bridge superstructure is expressed as

$$(\varepsilon_{\text{th}})_{\text{re-expand}} = \alpha_e (\Delta T_{\text{re-expand}}) \tag{8.38}$$

Concrete creep and shrinkage are neglected for the bridge re-expansion, since these strains are assumed to have already taken place by this time. For the re-expansion phase, the movement for an abutment from its maximum-contracted location is due to the thermal strain of the bridge re-expansion. This abutment displacement, which occurs at the mid-width of the abutment and is measured along the longitudinal direction of the bridge, is evaluated as

$$\Delta \ell_{\text{re-expand}} = \Gamma (\varepsilon_{\text{th}})_{\text{re-expand}} \ell \tag{8.39}$$

A Γ-displacement factor of 1.20 was recommended by Oesterle, et al. (1999) to account for uncertainties in the thermal re-expansion of a PC girder bridge,

when either experimental α-coefficients or Emanuel and Husley's (1977) expression is used in the evaluation of the coefficient α_e.

With repetitions of seasonal-temperature changes, a cyclic, abutment displacement versus temperature relationship will occur that involves successive re-expansion and re-contraction phases. If the stress versus strain relationships for the materials in the bridge members remains elastic, if the force versus deformation behavior relationships for the soil behind the abutments and around the abutment piles remained linear, and if geometrical linearity exists throughout the structure, the hysteresis loops for abutment displacements versus temperature would overlap. The re-expansion and re-contraction phases would not change over time. However, since the temperature-induced, abutment-displacement response is actually non-linear, these hysteresis loops will not overlap each other. The ISU researchers believe that the Γ-factors, which were established by the CTL researchers and are applied in Eqs. 8.32, 8.36, and 8.39, account for the non-linearity of the abutment-displacement responses.

Experimentally-measured, longitudinal displacements of the abutments for Guthrie County Bridge and Story County Bridge and the theoretical, re-expansion displacements for those abutments that were evaluated using Eq. 8.39, without applying the Γ-displacement factor are listed Table 8.9. The change in the bridge length that is shown in this table was calculated as the sum of the abutment displacements. Two, theoretical displacements were calculated for re-expansion of a bridge. The first set of predicted displacements was based on the experimentally-measured, temperature ranges from Table 8.3 and the experimental α-coefficients (Ng's 1999 predictions) from Table 8.8.

These theoretical displacements are conservative because Ng's (1999) α-coefficients in Table 8.8 were obtained by applying the maximum, α-coefficient ratio to the experimental values (see Appendix A). The second set of displacement predictions were based on the ISU, recommended-design values for the average, bridge temperature from Table 8.3 and the α-coefficient for the concrete that is listed in the column labeled Eq. 8.9 in Table 8.8. The second set of abutment-displacement magnitudes are conservative because the recommended, design-temperature range is larger than the experimentally-measured range and the α-coefficient predicted by Eq. 8.9 is conservative compared to that predicted by Eq. 8.8. Regardless of the pier types (a fixed pier or an expansion pier), the predicted displacements of the integral abutments along the longitudinal direction of the bridge are assumed to be equal to one-half of the total change in the length of the bridge. Other factors that cause the predicted displacements for the abutments of the Guthrie County Bridge and Story County Bridge to be conservative, include neglecting the restraining effect of the abutment backfill and the flexural stiffness of the abutment piles and pier structures on the longitudinal movement of the bridge. Also, the α-coefficient for the concrete in the PC girders was calculated using the concrete-mix proportion of sample girders at Raider Precast Concrete because the concrete-mix proportion of the in-place, PC girders was not known.

8.6.2. Transverse displacement of an integral abutment for a skewed bridge

The skew angle; wingwalls for straight-line abutments (see Fig. 1.2a) or common sidewalls and wingwalls for U-shaped abutments (see Fig. 1.2b); width of the bridge; abutment backfill; and temperature affect the magnitude of the transverse movement of

an abutment in a skewed, integral-abutment bridge. If the bridge-skew angle is less than the frictional angle for the soil against the concrete of the abutment backwall, the bridge will initially rotate in a counterclockwise direction for the geometric conditions that are shown in Fig. 8.9 after the placement of the soil behind the abutment and before any thermal expansion or contraction and concrete creep and shrinkage of the bridge superstructure occurs. This initial, angular rotation, which occurs in a horizontal plane and is shown in Fig. 8.10, is the rotation angle β_o that is caused by the at-rest-soil pressure behind the abutments. A maximum, rotation angle, β_{max}, will occur for longitudinal expansion of a bridge superstructure, when the soil backfill is at its full-passive-soil-pressure state. Any additional bridge expansion beyond this soil-pressure condition will not induce any additional soil pressure behind the abutment; therefore, further bridge rotation will not occur in the horizontal plane.

Oesterle, et al. (1999) reported that abutment displacements in a direction that is transverse to the bridge length should be considered when the skew angle, θ, of a bridge exceeds 20 deg. This conclusion was based on an assumed, surface-friction angle of 22 deg. to 26 deg. for the soil against the abutments. When the soil-friction angle exceeds the bridge-skew angle, transverse displacements can occur for an integral abutment. Oesterle, et al. non-dimensionalized the transverse displacements for an integral abutment by dividing the transverse displacement, dt, by the longitudinal displacement, $d\ell$, for the abutment. These displacements are in the transverse and longitudinal directions, respectively, of the bridge. The displacement $d\ell$ that corresponds to the displacements $d\ell_{expand}$, $d\ell_{contract}$, and $\Delta\ell_{re\text{-}expand}$ is computed using the procedures presented in Section 8.6.1.

8.6.2.1. Simple model

A simplified, bridge model that neglects the presence of the abutment piles and wingwalls can be used to explain the CTL theory that was presented by Oesterle, et al. (1999) for transverse displacements of integral abutments, which occur during the initial expansion of a bridge. Only the soil forces behind the abutment backwalls are applied to the model. For the skewed, symmetric, bridge model shown in Fig. 8.11, identical soil properties are assumed to exist behind each abutment. The "point-of-fixity" (Point C in the figure) is located at the center of the plan-view area of the bridge deck. A more complex model for transverse movements of integral abutments is presented in Section 8.6.2.2. When the temperature of a bridge superstructure is increased, the bridge will expand and the abutments will displace into the soil behind the abutments. As shown in Fig. 8.11, the soil will exert a normal force, F_{ap}, on the back of each abutment to restrain the bridge elongation. These forces will induce a counter-clockwise moment, M_{ap}, about Point C. This moment is expressed as

$$M_{ap} = 2(F_{ap})(\ell)(\sin \theta) \tag{8.40}$$

where, the angle θ is the bridge-skew angle and the length ℓ is equal to one-half of the bridge length, L. The moment M_{ap} is resisted by the moment M_{af} that is produced by the soil-frictional force, F_{af}, that acts along the back of each abutment. The soil-frictional force is expressed as

$$F_{af} = \mu_s F_{ap} \tag{8.41}$$

where, μ_s is the soil-to-abutment, surface-friction constant (μ_s = tan δ, with δ being the soil-to-abutment, surface-friction angle); and F_{ap} is a maximum when the full-passive-soil pressure is developed in the soil behind the abutment during the expansion of the bridge. The moment M_{af} is given by

$$M_{af} = 2(F_{af})(\ell)(\cos\theta) \tag{8.42}$$

For the plan view of the skewed bridge shown in Fig. 8.11, the sum of these moments about the "point-of-fixity" (Point C) of the bridge gives

$$\Sigma M_c = (F_{ap})(\ell)(\sin\theta) - (F_{af})(\ell)(\cos\theta) \tag{8.43}$$

The bridge will rotate only when the moment M_{ap} that is induced by the passive-soil pressure F_{ap} is larger than the moment M_{af} that is provided by the soil-frictional force F_{af}. A critical-skew angle, θ_c, occurs when these moments are equal to each other. By setting Eq. 8.43 equal to zero, letting $\theta = \theta_c$, knowing that μ_s = tan δ, and applying Eq. 8.41, the relationship between the angle θ_c and the angle δ is expressed as

$$\tan\theta_c = \tan\delta \tag{8.44}$$

A skewed, integral-abutment bridge will rotate only when the skew angle, θ, exceeds the angle θ_c or, equivalently, the angle δ. The NCHRP Report No.343, Manual for the Design of Bridge Foundations (Barker, et al., 1991), lists a range for the friction angle, δ, of 22 to 26 deg. for clean gravel, gravel-sand mixtures, and well-graded rock fill with spalls against formed concrete. Using this range for the angle θ_c, a bridge designer

might imply that transverse displacements of an integral abutment do not need to be considered when the skew angle for an integral-abutment bridge is equal to or less than 20 deg. However, when the abutment-pile forces, soil forces on the wingwalls or on the common sidewall and wingwalls, and pier forces are included in the moment equilibrium condition, a bridge may rotate even if the skew angle for the bridge is smaller than the angle θ_c that is evaluated by the simplified model for a bridge. In other words, a bridge with a 20-deg. skew angle might rotate even when the soil-friction angle is equal to 22 deg. For the simplified, bridge model, forces are not applied to rotate the bridge back towards its initial position when the bridge superstructure contracts. Thus, the bridge will remain in the rotated position during contraction of the bridge superstructure.

8.6.2.2. Refined model

The CTL research by Oesterle, et al. (1999) involved many parameters including the abutment height, h_{abut}; soil-backfill height, h_1; angle of internal-friction for the soil, ϕ; unit-weight of the soil, γ; soil-to-abutment, surface-friction angle, δ; equivalent-cantilever length, L_e, for the piles; bridge width, W; bridge length, L; and orientation of piles. Some of these parameters are shown in Fig. 8.12. Except for the forces that bridge piers exert on a bridge superstructure, Fig. B.1 in Appendix B shows the forces that are involved in the transverse displacement of an integral abutment. The nomenclature for these forces and parameters are defined in that appendix.

Two modifications were made by the ISU researchers to the approach that Oesterle, et al. (1999) used for establishing the transverse displacements of an integral abutment. These changes involved the distribution of the soil pressure against the

backwall of an abutment and the approach used to compute the maximum, transverse displacement of the abutment. When passive-soil pressures exist along a portion of the entire length, ℓ_{abut}, of an abutment, the CTL approach assumes that a linear, soil-pressure distribution occurs along the length $\ell_{pp\text{-}po}$ of the abutment that is subjected of passive-soil pressure. As shown in Fig. 8.13, the minimum and maximum, soil pressures for this soil-pressure distribution occur at Corner 1 and Corner 2, respectively, of an abutment. The passive-soil pressures at the abutment corners, which are functions of the soil-pressure coefficients k_1 and k_2, are determined from Fig. 5.10 after the displacements are known at Corner 1 and Corner 2, respectively. A linear distribution for the soil-pressures across the length $\ell_{pp\text{-}po}$ of the abutment will underestimate the magnitude of soil-pressure distribution when a region of the soil has reached its maximum, passive-soil-pressure magnitude. As shown in Fig. 8.13, a better approximation for the passive-soil pressure distribution along the length $\ell_{pp\text{-}po}$ can be achieved by introducing an additional, soil-pressure coefficient k_3 at the mid-length of the distance $\ell_{pp\text{-}po}$. The coefficient k_3 can be established using the same approach as that used to evaluate the soil-pressure coefficients k_1 and k_2. The displacement at the mid-length of an abutment can be assumed to be equal to the average of the displacements at the abutment corners.

The second modification to the CTL theory involved a change in the fundamental approach that is used to establish the transverse displacement of an integral abutment. With the CTL analysis, a bridge is assumed to elongate due to the maximum, temperature change and then rotate in a horizontal plane until moment equilibrium is satisfied about the “point-of-fixity” for the bridge. This displacement approach does not

satisfy the actual, load-displacement path for a bridge. Bridge displacements in a horizontal plane involve simultaneous elongation and rotation of the bridge superstructure. An iterative-displacement procedure was used by the ISU researchers to establish the abutment displacements. For each successive, 1° F increase in the average, bridge temperature, the bridge elongates and then rotates in a horizontal plane until moment equilibrium is satisfied about the "point-of-fixity" for the bridge. This step-wise, displacement algorithm is applied until the maximum, transverse displacement, dt_{max}, is obtained for the abutment.

The CTL bridge model (Oesterle, et al. 1999) for transverse displacement of an integral abutment does not include the forces that are induced on a bridge superstructure by the translational resistance that is associated with the flexural stiffness of the bridge piers. These forces for a particular pier are functions of the degree-of-fixity for the pier foundation, flexural and shear rigidity of the pier structure, and the type of connection between the pier cap and the bridge superstructure. As evidenced during the experimental monitoring of both the Guthrie County Bridge and the Story County Bridge, relative displacements were measured between the pier cap and a bridge girder for both a "fixed" pier and an "expansion" pier. These relative displacements were caused by deformations in the bearing pads for the PC girders at the "fixed and expansion piers" and in the neoprene liners within the concrete keyways at the "expansion" piers. Because of the uncertainties associated with predicting the deformations at the connections between the pier caps and the bridge superstructure, the ISU researchers did not include the effects of the pier structures in resisting transverse and longitudinal displacements of the integral abutments.

A computer program that includes these modifications to the CTL, transverse-displacement theory was developed by the ISU researchers to study abutment displacements. The procedure for using the software entitled “Transmove” is described in Appendix B. This program was used to predict the transverse displacements of the integral abutments for the Guthrie County Bridge, Story County Bridge, and for the parameter studies that are presented in the following sections of this report.

8.6.2.3. Single parameter studies

In addition to the effective, coefficient of thermal expansion and contraction, α_e, for a bridge superstructure that is computed by Eq. 8.10; the magnitude of the abutment displacement, $d\ell$, in the longitudinal direction of a bridge that is discussed in Section 8.6.1; and the skew angle, θ, for a bridge, the other parameters that affect the transverse displacement of an integral abutment can be divided into three categories. These categories are bridge geometry, pile properties, and soil properties. These parameters are listed in Table 8.10 along with their values that were used for the parameter studies. The bridge-geometric parameters are the bridge width, W; bridge length, L; abutment height, h_{abut}; soil-embankment height at Corner 1, h_1; wingwall height at Corner 2, h_2; length of the abutment wingwall or common wall for the abutment sidewall and wingwall near Corner 1, ℓ_{w1}; and length of the abutment wingwall or common wall for the abutment sidewall and wingwall near Corner 2, ℓ_{w2} (see Fig. 8.12). The pile-property parameters are the number of piles for the abutment backwall, N_{pa}; number of piles for the abutment sidewall near Corners 1 and 2, N_{p1} and N_{p2}, respectively; equivalent-cantilever length, L_e, for the abutment piles; and pile orientation. As shown in Fig. 8.14,

the four orientations for an HP-shape pile in an integral abutment are: Type-A that has the y-axis of the pile parallel to the bridge skew, Type-B that has the y-axis of the pile perpendicular to the bridge skew, Type-C that has the y-axis of the pile parallel to transverse axis (t-axis) of the bridge, and Type-D that has the y-axis of the pile perpendicular to the t-axis of the bridge. For Type-A, Type-B, and Type-D pile orientations, Fig. 8.14 shows the skew angle, θ_r, for a pile between the t-axis and the y-axis. For Type-C pile orientation, the angle θ_r equals 0 deg. The soil-property parameters are the unit-weight of the soil, γ; angle of internal friction for the soil, ϕ; and the soil-to-abutment, surface-friction angle, δ.

The program "Transmove" was used to establish the effect of each parameter on the magnitude of transverse displacements, dt, for an integral abutment for bridge expansion. For the parameter studies, the parameters that have identical values were combined into a single parameter. These parameters are h_2 and h_{abut}, ℓ_{w1} and ℓ_{w2}, and N_{p1} and N_{p2}. The parameter $d\ell$, which is the displacement of an abutment along the longitudinal direction of a bridge, is a linear function of L, ΔT, and α_e; therefore, the product $(\alpha_e)(\Delta T)(L)$, which is the total expansion for a bridge, was considered as a single parameter. Also, the soil stiffness at both abutments was assumed to be the same, and the thermal expansion was ignored for an abutment backwall and pile cap.

For the parameter studies, base, lower-bound, and upper-bound values were selected for the bridge-geometric, pile-property, and soil-property parameters. The base value for a parameter was chosen as an intermediate value between a lower-bound value and an upper-bound value for that parameter. An initial analysis was performed to predict the displacement dt that was associated with the base value for each parameter

for a particular bridge-skew angle, θ. In subsequence analysis, the magnitude of a single parameter was replaced with a value ranging between the lower-bound and upper-bound values. For example, when the effect of the bridge length was studied, the base-length value of 300 ft was replaced with lengths of 100 ft, 200 ft, 400 ft, or 500 ft, while the other parameters were set equal to their base values. The results for the parameter studies are presented in a graphical format.

8.6.2.3.1. Bridge length and width

Figures 8.15 and 8.16 show that a change in the bridge length and bridge width, respectively, affects the transverse displacements of an integral abutment when the bridge-skew angle, θ, exceeds about 23 deg. For angles θ larger than about 27 deg., an increase in the bridge length, L, or bridge width, W, causes a significant increase in the displacement dt.

8.6.2.3.2. Abutment height

For bridge-skew angles, θ, larger than about 23 deg., the height of an integral abutment, h_{abut} (equal to h_2), affects the displacement dt, as shown in Fig. 8.17. These graphs indicate that for angles θ between about 23 and 40 deg., an increase in the height h_{abut} causes an increase in the displacement dt. For angles θ greater than about 40 deg., the three graphs for the height h_{abut} equal to 8 ft, 10 ft, and 12 ft almost overlap one another; therefore, the displacement dt essentially is not affected by a change in the height of the abutment.

8.6.2.3.3. Wingwall-embankment height and wingwall length

A change in the wingwall-embankment height, h_1, and wingwall or common sidewall and wingwall length ℓ_{w1}, which equals ℓ_{w2}, affects the magnitude of the displacement dt for bridge-skew angles, θ, greater than about 23 deg., as shown in Figs. 8.18 and 8.19, respectively. For angles θ between about 23 and 37 deg., an increase in the height h_1 essentially has no significant effect on the displacement dt, as shown in Fig. 8.18. However, for angles θ greater than about 37 deg., an increase in the height h_1 causes a slight decrease in the displacement dt. For angles θ greater than about 23 deg., an increase in wingwall or common sidewall and wingwall length causes a significant decrease in the displacement dt, as shown in Fig. 8.19.

8.6.2.3.4. Number of abutment backwall and sidewall piles

Figures 8.20 and 8.21 show that for bridge-skew angles, θ, greater than about 23 deg., the number of abutment backwall piles, N_{pa}, and sidewall piles, N_{p1}, which equals N_{p2}, respectively, for an integral abutment essentially have no significant effect on the displacement dt. The three curves for N_{pa} equal to 8 ft, 10 ft, and 12 ft shown in Fig. 8.20 and for the three curves for N_{p1} and N_{p2} equal to 0, 1, and 2 shown in Fig. 8.21 essentially overlap one another.

8.6.2.3.5. Equivalent-cantilever length of a pile

As shown in Fig. 8.22, a simultaneous increase in the equivalent-cantilever length, L_e, of both the abutment backwall and sidewall piles causes a decrease in displacement dt for bridge-skew angles, θ, between about 23 and 50 deg. For angles θ greater than about 50 deg., the length L_e essentially has no influence on the displacement dt.

8.6.2.3.6. Properties of the granular soil behind the abutment

Figures 8.23, 8.24, and 8.25 show that an increase in the soil unit-weight, γ, and soil internal-frictional angle, ϕ, have less of an influence on the displacement dt than that for an increase in the soil-to-abutment, surface-frictional angle, δ. For bridge-skew angles, θ, between about 23 and 37 deg., an increase in the unit weight γ or the friction angle ϕ essentially has no effect on the displacement dt. However, for angles θ greater than about 37 deg., an increase in the unit weight γ causes a slight increase in the displacement dt, while an increase in the friction angle ϕ causes a slight decrease in the displacement dt. For angles θ greater than about 23 deg., an increase in the friction angle δ causes a decrease in the displacement dt; however, the influence of the friction angle δ on the displacement dt reduces as the angle θ increases.

8.6.2.4. Cross-parameter study

Figure 8.26 shows the influence of simultaneous changes in bridge length, L, and bridge width, W, on the displacement dt. A change in bridge length will have a larger influence on the displacement dt than that for a change in bridge width. Other cross-parameters studies were performed, but the results are not presented in this report. The ISU researchers did not observe any design-related benefits in the presentation of the results from those additional cross-parameter studies.

8.6.2.5. Summary of parameter studies

The parameter studies were conducted to examine the effect of different parameters on the transverse displacement of an integral abutment during initial

expansion of a bridge superstructure. The parameter studies that were presented in Section 8.6.2.3 and a cross-parameter study that was presented in Section 8.6.2.4 revealed that the amount of transverse displacement of an integral abutment for a skewed bridge is a function of many parameters. The relationship with and influence on the transverse displacement, dt, of an integral abutment for each of the examined parameters are listed in Table 8.11. The relationship between a parameter and the displacement dt is either “positive”, “negative” or “insignificant”. A “positive” relationship means that an increase in the magnitude of the parameter caused an increase in the displacement dt; while, a “negative” relationship means that an increase in the magnitude of the parameter caused a decrease in the displacement dt. An “insignificant” relationship means that a distinct correlation was not established between an increase in the magnitude of the parameter and either an increase or decrease in the displacement dt. The influence of a particular parameter on the displacement dt is qualitatively labeled as “significant”, “moderate”, “minor”, and “negligible”. These qualitative descriptions were established after comparing the influence of each parameter on the displacement dt. A parameter with a “negligible” influence does not mean that the parameter has no effect on the displacement dt, but implies that the influence of that parameter on the displacement dt is negligible compared to the influence that the other parameters have on the displacement dt. One can conclude from Table 8.11 that the most effective way to minimize the magnitude of the transverse displacement of an integral abutment that is induced by an increase in the temperature of a bridge superstructure for a bridge with a skew angle greater than about 23 deg. is by adjusting the parameters that have a “significant” or “moderate” influence on the displacement dt, rather than by adjusting the

parameters with a “minor” or “negligible” influence on the displacement dt. For most integral-abutment bridges, the transverse displacement of an abutment during contraction of the bridge superstructure is small.

8.6.2.6. Upper-bound for transverse displacement

The ISU researchers used the Transmove program (see Appendix B) to study the transverse displacement behavior of integral-abutments bridges by subjecting a wide variety of integral-abutment, bridge models to numerous cycles of sequential expansion and contraction of the bridge superstructure for different temperature ranges. To evaluate the magnitude of the transverse displacement for the loading, unloading, and reloading of the backfill soil, the soil-behavioral characteristics that are shown in Fig. 5.10b were applied. Even though the assumed lateral stiffness of the soil is not exactly correct for cyclic-load response for the soil, the ISU researchers believe that the predicted, transverse displacements for the abutment are acceptable for design purposes.

During the expansion or contraction of a symmetric, integral-abutment bridge, the forces shown in Fig. 8.27a or Fig. 8.27b, respectively, act on the abutments and bridge superstructure. The forces shown at the ends of the bridge are the resultant forces for the soil pressures, soil friction, and pile-head forces that act on the abutments. The forces $F_{piernorm}$ and $F_{pierparal}$, which are shown at a bridge pier, are the resultant forces for the restraint provided by the pier structure in the directions that are normal and parallel, respectively, to the pier. As noted in Section 8.7.2, since the translational restraint of the bridge superstructure that is provided by bridge piers was neglected, the forces $F_{piernorm}$ and $F_{pierparal}$ were assumed to be equal to zero for the evaluation of the transverse

displacement of an integral abutment. Complete descriptions for the forces that act on an integral abutment are given in Appendix B. If the bridge-skew angle shown in Fig. 8.27 is large enough, the bridge rotates in the counter-clockwise direction (as shown in Fig. 8.9) during an expansion phase and rotates in the clockwise direction during a contraction phase. This plan-view, bridge rotation causes transverse displacements of the abutments. Generic displacement relationships between the longitudinal displacement, $d\ell$, and the transverse displacement, dt, for an integral abutment are shown in Fig. 8.28. Before any temperature change occurs to induce a thermal expansion or contraction of a bridge superstructure, a transverse displacement of an abutment might occur after the abutment was backfilled during the bridge construction. The transverse displacement dt_o shown in Fig. 8.28 is induced by the at-rest-soil pressure behind the abutments.

If the first, temperature-induced movement of the bridge superstructure is an initial expansion, the relationship between the displacements $d\ell$ and dt is given by the curved line between the point corresponding to the displacement dt_o and Point A shown in Fig. 8.28a. Point A corresponds with the maximum, average, bridge temperature. For the subsequent contraction phase, the temperature of the bridge superstructure decreases, which causes the bridge to contract and rotate back towards its original non-displaced position. However, the clockwise rotation of the bridge is resisted by forces that are shown in Fig. 8.27b. These forces are the passive-soil forces, F_{s1}' and F_{s2}'; that act on Wingwall 1 and Wingwall 2, respectively, (see Fig. 8.12) for the abutments and the frictional force, F_{af}, between the soil and the backwalls for the abutments. The bridge will not completely rotate back to its original, non-displaced position. The abutment

displacements that occur during this contraction phase of bridge movement are represented by the curved-line AB shown in Fig. 8.28a. Re-expansion of the bridge superstructure from the maximum, contracted position that is represented by Point B in Fig. 8.28a induces additional transverse displacements of an abutment. Repeated cycles of expansion and contraction cause the abutment displacement dt to increase at a decreasing rate. This displacement response is illustrated in Fig. 8.28a by the shift from the curved line AB to the curved line CD. The displacement dt converges to the maximum displacement dt_{max}. Further temperature cycles will not produce any additional transverse displacement for an abutment.

If the first, temperature-induced movement of the bridge superstructure is an initial contraction, the soil pressure behind the backwall decreases from the at-rest- soil pressure to the active-soil pressure. This reduction in soil pressure creates a tendency for the bridge to rotate clockwise from the displaced position that corresponds with the rotation angle β_o shown in Fig. 8.10 back towards its original non-displaced position. This clockwise rotation is essentially prevented by the forces that restrained the clockwise rotation of the bridge during the contraction phase that followed the initial expansion for the bridge. Therefore, minimal rotation of the bridge occurs during the initial-contraction phase.

As illustrated in Fig. 8.28b and as described above and in Section 8.6.2.1, minimal transverse movement of an integral abutment occurs during the bridge-contraction phases. After several temperature cycles occur, a maximum amount of plan-view rotation of a bridge superstructure occurs and the transverse displacement of an integral abutment will remain constant despite any further increments in bridge expansion. This

upper limit for the transverse displacement of an integral abutment is denoted as the displacement dt_{max}. The magnitude for the displacement dt_{max} is independent of the temperature versus abutment-displacement response history and is only dependent on the bridge and soil system. The soil properties for the abutment backfill and the geometric properties of the bridge superstructure and substructure will affect the magnitude of the displacement dt_{max}. Figure 8.28 shows that, regardless of whether initial expansion or initial contraction of a bridge superstructure occurs first, the upper limit for the displacement dt_{max} is the same for both cases. This displacement behavior for an integral abutment was confirmed by using the Transmove program to predict abutment displacements for several temperature histories for the superstructure of an integral-abutment bridge. Since the upper-bound value for the displacement dt_{max} is usually small, the displacement dt_{max} can be used in the design for the abutment and abutment piles. The displacement dt_{max} is evaluated by using the Transmove program.

8.7. Integral-abutment pile displacements

The displacements at the top of an integral-abutment pile are the same as those displacements for the abutment that occur at the same location, since the pile is cast integrally into the abutment-pile cap. When the flexural stiffness of the superstructure for an integral-abutment bridge is significantly larger than that for all of the piles of an integral abutment, the tops of the abutment piles can be assumed to be fixed against rotation in a vertical plane that is parallel to the longitudinal direction of the bridge. Also, in a vertical plane that is normal to the longitudinal direction of the bridge, the rotation of an abutment-pile head, which is cast into the bottom of an abutment, can be assumed to

be equal to zero, since the flexural stiffness of the integral abutment is significantly larger than the flexural stiffness of a single pile. Therefore, only the longitudinal and transverse displacements need to be considered at the tops of the abutment piles.

The concept of a fixed-pile head for rotations in the vertical plane that is parallel to the longitudinal direction of the bridge superstructure was confirmed during the experimental portion of this research. The range in the measured, abutment-pile-cap rotations at the south abutment of the Guthrie County Bridge and the east abutment of the Story County Bridge were 1520 micro-radians (0.086 deg.) and 1310 micro-radians (0.075 deg.), respectively, as shown in Figs. 4.23a and 4.23b, respectively. The range in the relative, measured rotation between a monitored, abutment pile and the pile cap at the south abutment of the Guthrie County Bridge and that at the east abutment of the Story County Bridge were 2230 micro-radians (0.128 deg.) and 4090 micro-radians (0.234 deg.), as shown in Figs. 4.27a and 4.27b, respectively.

8.7.1. Longitudinal displacements

Figure 8.29a shows a graph of the moment resistance, M_n, for an abutment pile versus the horizontal displacement, $d\ell$, that occurs along the longitudinal direction of the bridge and at the top of a fixed-head pile during cycles of bridge expansion and contraction, when initial expansion of the bridge superstructure occurs after the bridge becomes an integral structure. The effects of soil creep on the moment resistance versus displacement relationship are not illustrated in this figure. As discussed in Section 8.4.4, soil consolidation and creep would cause the moment that is induced in the pile to decrease with time. A more precise graph of moment resistance versus

horizontal displacement would depend on the rate of temperature change and the rate of soil creep.

If initial contraction of the bridge superstructure occurs after the bridge becomes an integral structure, Fig. 8.29b shows the pile, moment resistance versus displacement behavior, which is similar to that shown in Fig. 8.29a. Without considering the effects of soil creep, consecutive cycles of moment versus longitudinal displacement gradually shift to the left over time because concrete-creep and concrete-shrinkage strains shorten the bridge length. The displacements $d\ell_{expand}$, $d\ell_{contract}$, and $d\ell_{re\text{-}expand}$ are the absolute, horizontal displacements along the longitudinal direction for a bridge of a pile head from its original, non-displaced position for an expansion, contraction, and re-expansion, respectively, of a bridge superstructure. For a re-expansion of a bridge superstructure, the displacement $\Delta\ell_{re\text{-}expand}$ represents a relative, horizontal displacement along the longitudinal direction for a bridge of the top of a pile from its maximum, displaced position, that is associated with the maximum contraction of the bridge superstructure.

The maximum, absolute, horizontal displacements of the top of an integral-abutment pile that is associated with bridge expansion and contraction will be represented by Point A (Fig. 8.29a) or Point A' (Fig. 8.29b) and by Point C (Fig. 8.29a) or Point C' (Fig. 8.29b), respectively. The pile displacement that corresponds with Point A (Fig. 8.29a) will be larger than that associated with Point A' (Fig. 8.29b) because the concrete-creep and concrete-shrinkage strains will be larger for Point A' than those for Point A. More time will elapse before the pile head experiences the maximum expansion condition for a bridge when initial contraction occurs first compared to that when initial expansion occurs first. The pile-head displacement that is associated with Points C (Fig.

8.29a) and C' (Fig. 8.29b), will be essentially identical because both of these points are associated with the passage of a long period of time since the bridge became an integral structure. Therefore, the bridge superstructure has already experienced the maximum amount of shortening due to concrete creep and shrinkage. Figures 8.29a and 8.29b illustrate critical, longitudinal displacements $d\ell_{expand}$, $d\ell_{contract}$, and $\Delta\ell_{re\text{-}expand}$ at the top of an integral-abutment pile, which correspond to Displacement Cases 1, 2, and 3, respectively. These abutment displacements were also considered by researchers at CTL (Oesterle, et al., 1999).

Based on the discussion in Section 8.4.4 and in the previous paragraphs, soil creep will permit a relaxation of the flexural-bending strains in the abutment piles during concrete creep and shrinkage of a bridge superstructure. Therefore, the effects of concrete creep and shrinkage can be neglected for the evaluation of the pile-ductility demand. The displacements, $d\ell_{expand}$ and $d\ell_{contract}$ (Displacement Cases 1 and 2, respectively) that are used for the pile-ductility demand should be calculated using the equations in Section 8.6.1, but without the concrete-creep and concrete-shrinkage strains. The relative displacement $\Delta\ell_{re\text{-}expand}$ (Displacement Case 3), which corresponds with a temperature range from the coldest day that corresponds with Point C or C', to the hottest day that corresponds with Point D or D' in Figs. 8.29a or 8.29b, respectively, should be used to check pile-ductility demand that involves full reversal of longitudinal displacements at the pile head. However, the ISU researchers believe that using the actual temperature range that is defined by Eq. 8.37 would be result in a very conservative design regarding pile ductility. The effect of long-term, soil consolidation and soil creep will produce a steady-state condition for the flexural-bending strains in the

abutment piles that is somewhere near the mid-point between Points C and D in Fig. 8.29a and between Points C' and D' in Fig 8.29b. This soil behavior effectively shifts the origin of the graph shown in each of these figures towards the left for the subsequent, re-expansion and re-contraction cycles of the bridge superstructure. The steady-state location of the origin for the graph of bending-moment resistance versus horizontal displacement of the abutment piles represents the existence of no flexural-bending strains in the abutment piles. To account for the effects of soil consolidation and soil creep on only the required ductility for the abutment piles that is associated with the Displacement Case 3, the ISU researchers recommend using a temperature range that is equal to one-half of the actual temperature range that is defined by Eq. 8.37. For the ductility demand of the abutment piles that involves Displacement Case 3, the concrete-creep and concrete-shrinkage strains for the bridge superstructure can be neglected, just as they were for Displacement Cases 1 and 2. However, the actual temperature range, which is defined by Eq. 8.37 for Displacement Case 3, should also be used to determine the maximum, passive-soil pressure that acts on the abutment for the abutment design.

The offsetting effects of concrete creep and shrinkage and soil consolidation and creep were not considered by Huang, et al. (2004). Those authors state that concrete creep and shrinkage needs to be included in the design of the abutment piles for an integral-abutment bridge. The ISU researchers believe that since the rates of soil consolidation and soil creep are faster than the rates of concrete creep and concrete shrinkage, concrete creep and shrinkage can be neglected for the ductility demand of the abutment piles.

8.7.2. Transverse displacements

The transverse displacement at the top of an abutment pile can be assumed to be the same as that displacement for the integral abutment. An upper-bound magnitude for this displacement is the displacement dt_{max}, as discussed in Section 8.6.2.6.

8.8. Abutment design

The design of an integral abutment for thermally-induced movements involves the determination of the loads on the abutment, calculation of the internal forces on the elements of the abutment, and the evaluation of the design strengths for the abutment. These topics are discussed in the following sections.

8.8.1. Loads on an integral abutment

During the lifetime of a bridge, an abutment is subjected to service-level loads. These loads are dead load, D; live load, L; temperature load, T; and earth-pressure load, E. The load combinations in the AASHTO Standard Specifications (1996) that are applicable for the design of an integral abutment are listed in Section 8.1, namely, Load Group I, Group IA, and Group IV. Consistent with the scope of this research project, only the load combination that involves thermal loads will be considered for the design of an integral abutment. The AASHTO Standard Specifications, Load Group IV is re-written as

$$\text{Group IV: } 1.3[D+(L+I)+1.3E+T] \qquad [8.4]$$

In all load cases, the live load needs to be placed to produce the most critical loading on the abutment. Examples of the gravity and thermal load computations for the Guthrie County Bridge are presented in Chapter 9. The methodology presented in this chapter

can also be applied to design an abutment-pile cap and composite, abutment backwall and pile cap for the other load combinations that are listed in the AASHTO Standard Specifications.

The design of an abutment-pile cap and backwall is affected by the bearing resistance of the soil beneath the pile cap and the sequence of construction for the abutment. After the abutment piles are driven and cut-off to the proper elevation and after the pre-bored holes through which the piles were driven are filled with an appropriate material, the abutment-pile cap is formed and the concrete is cast on compacted soil. The weight of the wet concrete for the pile cap is initially supported by the soil beneath the pile cap. After the concrete in the pile cap has cured to sufficient strength, the girders are erected and braced with intermediate diaphragms. The abutment ends of the girders are supported by a short length of an S3x7.5 steel section that is positioned on the top surface and at the mid-width of the pile caps. If the soil beneath the abutment-pile cap settles immediately after the concrete has cured for the pile cap, all of the gravity loads are transferred from the soil to the abutment piles. The pile cap needs to be designed to resist its own self-weight; the self-weight of the abutment backwall; and the dead-load, girder reactions that include the self-weight of the girders and those portions of the slab that were cast.

The casting of the abutment backwall and wingwalls (or common sidewall and wingwalls) completes the abutment construction for straight-line abutments (see Fig. 1.2a) or U-shaped abutments (see Fig. 1.2b). After the concrete in the abutment backwall has cured, the backwall and pile cap form a composite member. If the soil beneath the abutment-pile cap had not previously settled, but settles after the abutment

becomes a composite member, the entire abutment needs to be designed to resist the self-weight of the pile cap and backwall, all superstructure dead loads, lane and truck live loads with impact effects, and thermally-induced loads.

A change in the air temperature at a bridge site will cause a change in the average temperature for the bridge superstructure. An increase in the average, bridge temperature induces a thermal expansion of the bridge superstructure and causes the integral abutments to be pushed back into the soil behind the abutments. The horizontal displacement of an abutment along the longitudinal direction of the bridge induces passive-soil pressures, which act normal to the back face of the abutment, pile- shear forces, and pile-bending moments. If the integral-abutment bridge has a skewed alignment, soil-frictional forces are induced along the back face of the abutments. If the bridge-skew angle is large enough, the thermal expansion of the bridge superstructure causes a rotation of the bridge about the “point-of-fixity” for the bridge. This plan-view, bridge rotation induces soil pressures along the abutment wingwall or common, sidewalls and wingwalls.

Another loading condition for an integral-abutment bridge involves temperature changes that produce vertical-temperature gradients through the depth of a bridge superstructure. A positive-temperature gradient induces a positive, vertical curvature for the bridge superstructure. Therefore, within the central portion of a bridge span for a continuous structure, the deformed shape of this portion of the elastic curve has a concave-downward shape. A negative-temperature gradient induces negative, vertical curvature and a concave-upwards shape for the elastic curve of the deformed shape for the central portion of a span for a continuous-bridge superstructure.

Coordinate axes for an abutment, the bridge superstructure, and an abutment pile need to be established to orientate the directions of the loads that are applied to an abutment and to correlate the directions for the induced internal forces between the bridge girders, abutment piles, abutment-pile cap, and the integral abutment. Figure 8.30 shows three, rectangular-coordinate systems that were used to define the orientation of the bridge members. The XYZ, ℓht, and xyz-coordinate-axis systems are for an abutment-pile cap or for an integral abutment, for the bridge superstructure, and for the abutment piles, respectively. The X-axis, Y-axis, and Z-axis are the axes that are normal to the abutment face, parallel to the abutment height, and along the abutment length, respectively. The ℓ-axis, h-axis, and t-axis are the axes that are parallel to the bridge length, in the vertical direction and, parallel to the bridge width, respectively. Each pile has its own local, rectangular, xyz-coordinate-axis system. The x-axis, y-axis, and z-axis for an HP-shaped pile are parallel to the width of the pile flanges, within the plane of the pile web, and along the pile length, respectively. The bridge-skew angle, θ, is measured in the horizontal plane between the t-axis for the bridge superstructure and the Z-axis for an abutment. The orientation for an abutment pile is defined by the pile-skew angle, θ_r, which is measured in the horizontal plane between a reference line that is parallel to the t-axis for the bridge superstructure and the y-axis for the pile.

Figure 8.30 shows the abutment piles to be symmetrically located about the mid-length of the abutment and that a pile does not exist along the ℓ-axis of the bridge superstructure. The center-to-center spacing for the piles; the width for a portion of an abutment-pile cap and an integral abutment that occurs between two, vertical, cross sections through the abutment; and the abutment thickness are given by the dimensions

c, B, and B_{abut}, respectively. If a pile exists at the mid-length of an abutment, the central portion of the abutment would be offset by one-half of the pile spacing c; however, the origin at the XYZ and ℓth-coordinate-axis systems would still remain at the center of the length and width for the abutment.

Figure 8.31 shows the loads that act on an abutment-pile cap before the abutment becomes integral with the bridge superstructure for a bridge that has five, PC girders and ten, abutment piles that are located under each abutment backwall. The pile cap for the abutment sidewalls are not shown for clarity of the figure. The forces that act on the pile cap are oriented with respect to the XYZ-coordinate-axis system for the pile cap. Each bridge girder induces a downward, dead-load, vertical reaction, $V_{girder\text{-}Y}$, on the top of the pile cap. The weight of the hardened concrete in the pile cap plus the weight of the uncured concrete in the abutment backwall is represented by the load $W_{abut\text{-}Y}$. Each abutment pile induces an upward vertical force, $P_{pile\text{-}Y}$, on the bottom of the pile cap.

A composite, abutment backwall and pile cap for an integral-abutment bridge that has five, PC girders and ten piles for each abutment backwall is shown in Fig. 8.32. The abutment sidewalls and wingwalls are not shown for clarity of the figure. The member-end forces that act on an integral abutment and the soil pressure and soil frictional force that act on the back face of the abutment are oriented with respect to the X-Y-Z coordinate-axis system for an abutment. The total of the X, Y, and Z-axis components for the PC-girder end-forces, which are in the ℓth-coordinate-axis system for a girder, are the forces $P_{girder\text{-}X}$, $V_{girder\text{-}Y}$, and $V_{girder\text{-}Z}$, respectively. The total of the X, Y, and Z-axis components for the PC-girder end-moments, which are in the ℓth-coordinate-axis system for a girder, are the moments $M_{girder\text{-}X}$, $M_{girder\text{-}Y}$, and $M_{girder\text{-}Z}$, respectively. The total of the

X, Y, and Z-axis components for the end-forces for an abutment pile, which are in the xyz-coordinate-axis system for a pile, are the forces $P_{pile\text{-}Y}$, $V_{pile\text{-}X}$, and $V_{pile\text{-}Z}$, respectively. The total of the X, Y, and Z-axis components for the end-moments for an abutment pile, which are in the xyz-coordinate-axis system for a pile, are the moments $M_{pile\text{-}X}$, $M_{pile\text{-}Y}$, and $M_{pile\text{-}Z}$, respectively. The directions for the member-end forces that are shown in Fig. 8.32 correspond to a longitudinal expansion and a clockwise rotation of a bridge superstructure with respect to the "point-of-fixity" for a bridge with a counter-clockwise, skew angle, θ. If a longitudinal contraction and a counter-clockwise rotation for a bridge superstructure occur with this skew-angle direction, then, except for the axial load in the piles, the direction for the member-end forces would be reversed from that shown in Fig. 8.32. If the bridge-skew angle, θ, is less than the critical-skew angle, θ_c, for the bridge, plan-view rotations of the bridge superstructure and displacements of the integral abutments in the transverse direction for the bridge will not occur with thermal expansion of the bridge superstructure. Depending on the direction of the displacements for an abutment along the bridge length, either, active-soil or passive-soil pressures occur on an abutment. The soil pressure, $w_{soil\text{-}X}$, which is shown in Fig. 8.32 at the bottom of the abutment-pile cap, acts normal to the back face of an abutment. The soil-frictional force, $W_{soil\text{-}friction\text{-}Z}$, which is shown behind the abutment in Fig. 8.32, acts along the back face of the abutment and at two-thirds of the abutment height, h_{abut}, and in a direction that restrains the plan-view rotation of the bridge superstructure. This frictional force has units of force per unit length. For clarity of Fig. 8.32, the girder and pile forces are shown at locations that are slightly removed from their actual points of application. The girder forces act at the center-line of an abutment-pile cap, and are assumed to act at the

intersection point for the longitudinal axis of a composite, PC girder and a vertical line at the mid-thickness of an integral abutment. The pile forces are assumed to act at the mid-depth of the pile embedment into the bottom of the abutment-pile cap. Abutment cross sections are indicated by the dotted lines that are shown in Figs. 8.30, 8.31, and 8.32.

Free-body diagrams for a portion of an integral abutment and for an abutment pile are shown in Fig. 8.33. A XZ-plane cross section, a YZ-plane elevation, and a XY-plane cross section for a portion of an integral abutment are shown in Figs. 8.33a, 8.33b, and 8.33d, respectively. A YZ-plane elevation and a XY-plane elevation for an abutment pile are shown in Figs. 8.33c and 8.33e, respectively. These diagrams illustrate the orientation in the various planes for each of the free-body diagrams for the forces from a PC girder, abutment pile, and the soil that act on an abutment when the bridge superstructure experiences a thermal expansion. The thermal expansion of the bridge causes the abutment to displace along the longitudinal axis (ℓ-axis) and possible along the transverse axis (t-axis) of the bridge superstructure. The head of an abutment pile may experience horizontal displacements with respect to the principal axes of the pile that will induce biaxial bending of the pile. The YZ-plane and XY-plane elevation views for an abutment pile show the member-end forces at the top and bottom of an effective-cantilever length, ℓ_{ehX} and ℓ_{ehZ}, respectively, for the pile that are calculated as

$$\ell_{ehX} = \frac{M_{pile-X}}{V_{pile-Z}} \tag{8.45}$$

$$\ell_{ehZ} = \frac{M_{pile-Z}}{V_{pile-X}} \tag{8.46}$$

where, $V_{pile\text{-}X}$ and V_{pileZ} are the total of the X and Z-axis components of the pile-shear forces $V_{pile\text{-}x}$ and $V_{pile\text{-}y}$, which are calculated by Eqs. 8.59 and 8.60 in Section 8.8.2.2.

The locations of the PC girders with respect to the locations of the piles along the length of an abutment are a function of the bridge-skew angle and the spacing of the PC girders and piles. For a generalized analysis that would cause the most critical loading on an abutment, the ISU researchers only considered an abutment geometry that had the PC girders located at alternate mid-spans between the abutment piles, as shown in Figs. 8.31 and 8.32. This geometrical arrangement for the girders simplified the structural analyses of an abutment for the soil, pile, and girder forces that act on the abutment. These abutment loads have force and moment components that are directed along one or more of the X, Y, and Z-axes for an abutment. Multiple-force components occur when the line-of-action for an abutment load is eccentric to the center-of-gravity for a cross section in the XY plane for an abutment.

When the PC girders are located at alternate mid-spans for an abutment that is supported by piles, the abutment loads will induce either a symmetric or an asymmetric shape for the elastic curve of the displaced abutment. Figure 8.34 shows displaced shapes for the central portion of an abutment length. These elastic curves were drawn with respect to zero displacement and zero rotation at the location of a PC girder. Cross Sections 1 and 1', 1.5 and 1.5', and 2 occur at the ends, quarter-points, and mid-length, respectively, of the central portion of the abutment. With the pile spacing equal to one-half of the length B, these abutment cross sections are also located at the mid-point between two interior girders, at abutment piles, and at an interior girder, respectively. Figure 8.34a, 8.34b, and 8.34c and Figures 8.34d, 8.34e, and 8.34f show the relative

displaced shapes for an abutment that are induced by F_X, F_Y, and F_Z-forces and M_X, M_Y, and M_Z-moments, respectively. Inflection points (I.P.) are indicated by the solid circles shown on the elastic curves, and zero and non-zero displacements and rotations are specified at Cross Sections 1, 2, and 1' in these figures.

Table 8.12 lists the geometric-boundary conditions for abutment displacements Δ_{Xi}, Δ_{Yi}, and Δ_{Zi} and rotations θ_{Xi}, θ_{Yi}, and θ_{Zi} in the X, Y, and Z-axis directions of an abutment at the ith cross section, when i = 1, 1.5, and 2, that are induced by the load and moment components, which are associated with the abutment loads, when the abutment is considered to be fixed at the location of the bridge girders. The column labeled "geometry" in the table lists whether the displaced shape of the elastic curve for the abutment is assumed to be symmetric or asymmetric. For symmetric behavior, planes of symmetry exist at Cross Sections 1, 2, and 1' as shown in Figs. 8.34a, 8.34b, and 8.34f. For asymmetric behavior, planes of asymmetry exist at these same cross sections for the abutment, as shown in Figs. 8.34c to 8.34e.

8.8.2. Analytical methods

Two analysis methods can be used to establish the girder and pile, member-end forces and soil forces that act on an abutment-pile cap and an integral abutment. The first method (Analysis Method 1) requires structural analyses of the bridge. The complexity of the analytical models for a bridge can vary from a three-dimensional, finite-element model that includes all of the bridge members for the superstructure and substructures, soil interaction with the bridge-substructure members, and material non-linearity to more conventional, two-dimensional, frame models that involve the use of member equivalents for the bridge members and computed soil forces, which act on the

abutments. The second method (Analysis Method 2), which does not require the use of analytical models for the entire bridge, requires the use of specific conditions for planes of symmetry and asymmetry and assumed member-end forces. An abutment can be designed for the axial, shear, and bending-moment strengths for the members that frame to an abutment and for full-passive-soil pressures and corresponding soil-frictional forces that act on the back face of an abutment.

8.8.2.1. Pile and girder member-end forces and soil pressures by Analysis Method 1

A simplified, two-dimensional, frame model for a partially constructed, three-span, integral-abutment bridge is shown in Fig. 8.35. At this stage of the bridge construction, the abutments are not integrally connected to the bridge superstructure. This model, which is in the ℓh-plane, can be used to establish the maximum, dead loads that act on an abutment-pile cap. The exterior-span lengths, L_{ext1} and L_{ext2}, and the interior-span length, L_{int}, are measured between the centerlines of supports for the PC girders. The members for this model, are a single-equivalent girder and a single-equivalent pile with a monolithic, RC, pile cap at each abutment. The geometric properties for these equivalent members are a function of the number of PC girders and abutment piles that are within a band-width B along the length of an abutment and that are associated with displacements and rotations in the ℓh-plane. When specific bridge-deck-section castings are used, the portions of the length of the bridge deck with cured concrete will act compositely with the PC girders. Therefore, if the concrete in the bridge deck over the piers and in the pier diaphragms has cured, the equivalent girder will behave as a continuous-span member, as shown in Fig. 8.35, rather than as a series of simple-span members. If the bridge contractor is permitted to use a concrete retarder, which keeps

the concrete in a plastic state for a longer period of time, and is allowed to cast the entire bridge deck, the pier diaphragms, and the abutment backwalls during a single concrete casting, the equivalent girders should be modeled as a series of single-span members. At this stage of the bridge construction that involves either bridge-deck casting method, the bridge is not an integral structure with the abutments. Therefore, an internal roller can be used to model the boundary conditions that exist at the end of the equivalent girder at each abutment. The equivalent pile at each abutment is a cantilever column. The equivalent-cantilever length, L_{emt}, in the ℓh-plane for the abutment piles is the length that is based on moment equivalence for t-axis-pile bending, as discussed in Section 8.5 for a pinned-head pile. To simplify the analytical model, the geometric and material properties for the bridge piers are not included in this model. The pier structures are represented by the pinned support and roller support for a fixed pier and an expansion pier, respectively. The reactions ΣR_{fp} and ΣR_{ep} are the vertical reactions for the equivalent girder that occur at the fixed pier and expansion pier, respectively. Since no horizontal loads are applied to the bridge members and since an internal roller essentially exists at the abutment ends for the equivalent girder at this stage of the bridge construction, the horizontal reaction ΣH_{fp} at the fixed pier for the single-equivalent girder is equal to zero. The load W_{DL1} represents all of the dead loads for the bridge superstructure that are present before the abutment-pile cap and backwall form a composite member. The load W_{abut} represents the self-weight of abutment-pile cap and backwall. At the end of the equivalent-cantilever length for the piles the reactions, ΣP_{pile-h}, $\Sigma V_{pile-\ell}$, and ΣM_{pile-t} are the axial force, ℓ-axis-shear force, and bending moment in the

single-equivalent pile about the t-axis at each abutment. For this model, the forces $\Sigma V_{pile-\ell}$ and the moments ΣM_{pile-t} are equal to zero.

Figure 8.36 shows a simplified, two-dimensional, frame model in the ℓh-plane that can be used to analyze the same three-span, integral-abutment bridge that was shown in Fig. 8.35 for gravity loading after the abutments are integral with the bridge superstructure. For this bridge model, the single-equivalent girder is a composite beam for the entire length of the bridge and a single-equivalent pile at each abutment has a monolithic, abutment-pile cap and backwall at the top of this member. Again, the geometric properties for these single-equivalent members are a function of the number of PC girders and abutment piles that are within a band-width B along the length of an abutment and that are associated with the displacements and pile rotations in the ℓh-plane. The equivalent-cantilever length, L_{emt}, in the ℓh-plane for the abutment piles is the length that is based on moment equivalence for t-axis-pile bending, as discussed in Section 8.5, for a rotationally-fixed-head pile, since the tops of the abutment piles are monolithically cast into the pile cap. The loads W_{DL2}, W_{LL}, and W_I represent all of the superstructure dead loads, live loads, and impact loads, respectively. The frame reactions ΣP_{pile-h}, $\Sigma V_{pile-\ell}$, ΣM_{pile-t}, ΣR_{ep}, ΣR_{fp}, and ΣH_{fp} are all obtained from the structural analysis of this frame model for the bridge.

Figure 8.37 shows a simple, two-dimensional, frame model in the ℓh-plane that can be used to analyze the same integral-abutment bridge, which was shown in Figs. 8.35 and 8.36, for thermal loading, without a vertical-temperature gradient. The thermal loads involve longitudinal expansion of the bridge superstructure and passive-soil pressures that are induced by the bridge expansion. Since the bridge has one

expansion pier and one fixed pier, the horizontal displacements $\Delta\ell_L$ and $\Delta\ell_R$ at the left and right abutments, respectively, and in the longitudinal direction of the bridge may not be equal to each other. These abutment displacements are calculated from Eq. 8.39. The maximum, soil pressure, $w_{soil\text{-}X}$, which occurs at the bottom of an abutment-pile cap, acts normal to the back face of the abutment. The magnitude for this passive-soil pressure is a function of the abutment displacement, $(\Delta\ell_{re\text{-}expand})(\cos\theta)$, in the direction that is parallel to the X-axis for the abutment. Figure 5.10b can be used to establish the passive-soil-pressure coefficient, k_p, for this displacement. The soil pressure $w_{soil\text{-}X}$ is expressed as

$$w_{soil\text{-}X} = k_p\,\gamma\,h_{abut} \tag{8.47}$$

where, γ is the unit weight of the backfill soil and h_{abut} is the total height of the abutment. An upper-bound value for the soil pressure $w_{soil\text{-}X}$ is the full-passive-soil pressure. The components of the maximum, passive-soil pressures, $w_{soil\text{-}X\ell L}$ and $w_{soil\text{-}X\ell R}$, along the longitudinal direction of the bridge, which are shown in Fig. 8.37 at the left abutment and right abutment, respectively, are calculated by multiplying the soil pressure that is established from Eq. 8.47 by the cosine of the bridge-skew angle, θ.

The geometric properties for the single-equivalent girder and single-equivalent pile at each abutment are the same as those properties that are used for the single-equivalent members for the bridge model that was shown in Fig. 8.36. For this bridge model, the equivalent-cantilever length, $L_{eh\ell}$, in the ℓh-plane for the abutment piles is the length that is based on horizontal-stiffness equivalence for ℓ-axis-pile displacement, as discussed in Section 8.5 for a rotationally-fixed-head pile.

The loading for this bridge model involves the induced displacements $\Delta\ell_L$ and $\Delta\ell_R$ and the triangular, soil-pressure distributions at each abutment. The support reactions $\Sigma P_{pile\text{-}h}$, $\Sigma V_{pile\text{-}\ell}$, $\Sigma M_{pile\text{-}t}$, ΣR_{ep}, ΣR_{fp}, and ΣH_{fp} for the bridge are obtained from a structural analysis of this frame model. The maximum magnitude for the bending moment $\Sigma M_{pile\text{-}t}$ that can be induced in an equivalent-pile member is based on the plastic-moment strength for a pile cross section with respect to the t-axis for the bridge superstructure. For the simple-frame model shown in Fig. 8.37, the effect of the axial load on the plastic-moment strength of the pile is neglected and the plastic-moment strength is assumed to be obtainable, even if the flange for an HP-shaped pile is not classified as a compact flange. A steel cross section that is classified as a non-compact section may still be able to develop its plastic-moment strength; however, the inelastic-rotation capacity of the cross section is limited below that for a compact cross section. When the non-seismic, flange-width-to-thickness ratio limitation is considered in defining a compact section, only six and two of the eleven, HP-shaped, cross sections that are listed in the AISC LRFD Manual of Steel Construction (2001), are compact cross sections for a steel-yield stress equal to 36 ksi and 50 ksi, respectively. Additional discussing regarding the inelastic-rotation capacity of compact and non-compact cross sections is presented in Section 8.9.2.

When the maximum, moment resistance for an abutment pile is assumed to be equal to its plastic-moment strength, an integral abutment will be subjected to the largest forces from the abutment piles. When the pile-skew angle, θ_r, is equal to zero (see Fig. 8.30 and the Type-C, pile orientation shown in Fig. 8.14) and when the bridge-skew angle, θ, is less than the critical-skew angle, θ_c, that induces abutment displacements

along the t-axis for the bridge, the plastic-moment strength for a pile is the y-axis, plastic-moment strength, M_{py}. Then, the single-equivalent member, pile moment, $\Sigma M_{pile\text{-}t}$, must satisfy

$$\Sigma M_{pile\text{-}t} \leq N_p M_{py} \tag{8.48}$$

where, N_p is the number of piles along the band-width B for each abutment. When the angle θ_r is not equal to zero and/or when the angle θ is equal to or greater than the angle θ_c, the abutment piles are subjected to biaxial bending. Applying a conservative, linear, biaxial-bending, interaction relationship that is based on yielding of a pile, the single-equivalent member, pile moment, $\Sigma M_{pile\text{-}t}$, must satisfy

$$\Sigma M_{pile-t} \leq N_p M_{py} \left[\frac{1}{(\cos\theta_r - B_M \sin\theta_r) + \left(\frac{Z_y}{Z_x}\right)(\sin\theta_r + B_M \cos\theta_r)} \right] \tag{8.49}$$

where, Z_x and Z_y are the plastic-section modulus for x-axis bending and y-axis bending, respectively, of the HP-shaped, pile cross section; and, B_M is the ratio of the longitudinal-bending moment, $\Sigma M_{pile\text{-}\ell}$, to the transverse-bending moment, $\Sigma M_{pile\text{-}t}$. If the angle θ_r is equal to zero and if the angle θ is less than the angle θ_c, Eq. 8.48 and Eq. 8.49 are equivalent. The bending-moment, resistance factor, ϕ_b, that is associated with Eqs. 8.48 and 8.49 was set equal to unity to correlate the moment strength with the formation of a plastic hinge in the fixed-head, abutment piles at the bottom of the equivalent-cantilever length, $L_{eh\ell}$, for ℓ-axis bending of an abutment pile and at the top of the pile. For a rotationally-fixed-pile head, the corresponding longitudinal-shear force, $\Sigma V_{pile\text{-}\ell}$, for the single-equivalent-pile member is given by

$$\Sigma V_{pile\text{-}\ell} = \frac{2\Sigma M_{pile\text{-}t}}{L_{eh\ell}} \tag{8.50}$$

As discussed in Section 8.6.2, thermal expansion or contraction of a bridge superstructure can produce abutment displacements along the t-axis for the bridge, when the bridge-skew angle, θ, is larger than a critical-skew angle, θ_c. After many seasonal-temperature cycles, the abutment displacement dt will not exceed the displacement dt_{max}, which is shown in Fig. 8.28 and is evaluated using the computer program "Transmove" (see Appendix B). When the tops of the abutment piles experience the displacement dt_{max}, a transverse-shear force, $\Sigma V_{pile\text{-}t}$, and longitudinal-bending moment, $\Sigma M_{pile\text{-}\ell}$, are induced in the single-equivalent-pile member for the simplified-frame model shown in Fig. 8.36. For fixed-head piles, these member-end forces are expressed by

$$\Sigma V_{pile-t} = N_p \left[\frac{(12EI)(dt_{max})}{L_{eht}^3} \right] \tag{8.51}$$

$$\Sigma M_{pile-\ell} = N_p \left[\frac{(6EI)(dt_{max})}{L_{eh\ell}^2} \right] \tag{8.52}$$

where, I is the moment of inertia for the single-equivalent-pile member with respect to bending about an axis that is parallel to the ℓ-axis of the bridge; and, L_{eht} is the equivalent-cantilever length in the ht-plane for the abutment piles that is based on horizontal-stiffness equivalence for t-axis, pile displacement, as discussed in Section 8.5 for a fixed-head pile.

After a plastic hinge forms in the abutment piles, further expansion of the bridge superstructure that is caused by an increase in the average, bridge temperature will induce inelastic rotation of the plastic hinges and will not increase the bending moments in the abutment piles. The abutment piles must have sufficient, flexural ductility to permit the required inelastic rotation at the plastic-hinge locations. The topic of pile ductility is discussed in Section 8.9.2.

The simple, two-dimensional, frame model, without the gravity loads, shown in Fig. 8.36 can be used to analyze the same three-span, integral-abutment bridge for vertical-temperature gradients. For this analysis, the vertical-temperature distributions through the depth of the bridge superstructure are the loads on the bridge. For this bridge model, the equivalent-cantilever length, L_{emt}, in the ℓh-plane is used for the abutment piles.

Figures 8.38 and 8.39 show the components for the member-end forces for a PC girder and an abutment pile, respectively, that act along the X-axis, Y-axis, and Z-axis for an abutment-pile cap (see Fig. 8.31) and an integral abutment (see Fig. 8.32). The lines-of-action for the girder, member-end forces, $V_{girder\text{-}h}$ and $M_{girder\text{-}h}$, and the abutment pile, axial forces, $P_{pile\text{-}h}$, and $M_{pile\text{-}h}$ are parallel to the Y-axis for the abutment. The components for the member-end forces, which are shown in Figs. 8.38 and 8.39, have subscripts that correlate with the coordinate axes for the bridge superstructure and an abutment. For example, the force-component $P_{girder\text{-}\ell x}$ that is shown in Fig. 8.38a represents the positive, X-axis, force components for the axial load in a girder, which is directed along the longitudinal axis (ℓ-axis) for the bridge superstructure. The other member-end, force components for a girder and an abutment pile were designated in a similar manner.

The relationship between the components of these member-end forces and the coordinate-axis systems for an abutment, an abutment pile, and the bridge superstructure is given by direction cosines that involve the bridge-skew angle, θ. From Figs. 8.38, the total of the components for the member-end forces for a bridge girder along the X, Y, and Z-axes of an abutment are given by

$$\begin{Bmatrix} P_{girder-X} \\ V_{girder-Y} \\ V_{girder-Z} \end{Bmatrix} = \begin{bmatrix} \cos\theta & 0 & \sin\theta \\ 0 & 1 & 0 \\ -\sin\theta & 0 & \cos\theta \end{bmatrix} \begin{Bmatrix} P_{girder-\ell} \\ V_{girder-h} \\ V_{girder-t} \end{Bmatrix} \tag{8.53}$$

$$\begin{Bmatrix} M_{girder-X} \\ M_{girder-Y} \\ M_{girder-Z} \end{Bmatrix} = \begin{bmatrix} \cos\theta & 0 & \sin\theta \\ 0 & 1 & 0 \\ -\sin\theta & 0 & \cos\theta \end{bmatrix} \begin{Bmatrix} M_{girder-\ell} \\ M_{girder-h} \\ M_{girder-t} \end{Bmatrix} \tag{8.54}$$

From Fig. 8.39, the total of the components for the member-end forces for an abutment pile along the X, Y, and Z-axes of an abutment are expressed as

$$\begin{Bmatrix} V_{pile-X} \\ P_{pile-Y} \\ V_{pile-Z} \end{Bmatrix} = \begin{bmatrix} \cos\theta & 0 & \sin\theta \\ 0 & 1 & 0 \\ -\sin\theta & 0 & \cos\theta \end{bmatrix} \begin{Bmatrix} V_{pile-\ell} \\ P_{pile-h} \\ V_{pile-t} \end{Bmatrix} \tag{8.55}$$

$$\begin{Bmatrix} M_{pile-X} \\ M_{pile-Y} \\ M_{pile-Z} \end{Bmatrix} = \begin{bmatrix} \cos\theta & 0 & \sin\theta \\ 0 & 1 & 0 \\ -\sin\theta & 0 & \cos\theta \end{bmatrix} \begin{Bmatrix} M_{pile-\ell} \\ M_{pile-h} \\ M_{pile-t} \end{Bmatrix} \tag{8.56}$$

8.8.2.2. Pile and girder member-end forces and soil pressures by Analysis Method 2

A conservative approach can be used to establish the member-end forces, $V_{girder\text{-}Y}$, shown in Fig. 8.31, for the analysis of an abutment-pile cap. An upper-bound magnitude

for the dead-load, member-end, vertical-shear force, $V_{girder\text{-}Y}$, for a PC-girder, is based on the assumption that an exterior span for a PC girder is simply supported at the abutment-pile cap and at the pier for this span. Since the uniform, dead load $W_{abut\text{-}Y}$ is equal to the weight per unit length for the abutment backwall and pile cap, the axial force in the piles, $P_{pile\text{-}Y}$, is determined from vertical equilibrium of the portion of the abutment-pile cap that occurs between the vertical planes of symmetry and that has a length B, as shown in Fig. 8.31. Planar, free-body diagrams for this central portion of an abutment-pile cap are presented and discussed in Section 8.8.2.3.

Also, a conservative approach can be used to establish the member-end forces $P_{pile\text{-}Y}$, $V_{pile\text{-}X}$, $V_{pile\text{-}Z}$, $M_{pile\text{-}X}$, $M_{pile\text{-}Y}$, and $M_{pile\text{-}Z}$ and the soil pressure $w_{soil\text{-}X}$ and soil-frictional force $W_{soil\text{-}friction\text{-}Z}$ shown in Fig. 8.32. An upper-bound magnitude for the axial force $P_{pile\text{-}Y}$ in an abutment pile is the pile-vertical-load capacity. Realistic, upper-bound magnitudes for the moments $M_{pile\text{-}X}$ and $M_{pile\text{-}Y}$ for an abutment pile were established by first assuming that the ratio of the bending moment in an abutment pile to the plastic-moment strength for each principal axis of the pile is inversely proportional to the predicted horizontal displacement of the pile head along the principal axes of the pile. This proportionality relationship is given by

$$\left(\frac{M_{pile-x}/M_{px}}{M_{pile-y}/M_{py}}\right)=\left(\frac{\Delta_y/\Delta_{py}}{\Delta_x/\Delta_{px}}\right) \tag{8.57}$$

where, the moments $M_{pile\text{-}x}$ and $M_{pile\text{-}y}$ are the pile moments with respect to bending about the x-axis and y-axis, respectively, for a pile and the displacements Δ_x and Δ_y are the horizontal displacements of the pile head along the x-axis and y-axis directions,

respectively, for the pile. The displacements Δ_{px} and Δ_{py} are those displacements that are associated with the development of the plastic-moment strengths M_{py} and M_{px}, respectively, for a pile with elastic-plastic, material properties. A steel-yield, moment-interaction criteria that is expressed by Eq. 8.58 is applied to establish the relationship between the predicted moments and the plastic-moment strengths for each principal axis of the pile.

$$\left(\frac{M_{pile-x}}{M_{px}}\right)+\left(\frac{M_{pile-y}}{M_{py}}\right)=1 \tag{8.58}$$

Equations 8.57 and 8.58 can be used to establish upper-bound magnitudes for the bending moments $M_{pile\text{-}x}$ and $M_{pile\text{-}y}$. These pile-bending moments are expressed as

$$M_{pile-x}=M_{px}\left[\frac{(\Delta_y/\Delta_{py})}{(\Delta_x/\Delta_{px})+(\Delta_y/\Delta_{py})}\right] \tag{8.59}$$

$$M_{pile-y}=M_{py}\left[\frac{(\Delta_x/\Delta_{px})}{(\Delta_x/\Delta_{px})+(\Delta_y/\Delta_{py})}\right] \tag{8.60}$$

For an abutment pile, the principal-axis, member-end-shear forces are associated with the member-end-bending moments. Upper-bound magnitudes for the shear forces $V_{pile\text{-}x}$ and $V_{pile\text{-}y}$ that are along the x-axis and y-axis, respectively, for a fixed-head pile are established from

$$V_{pile-x}=\frac{2M_{pile-y}}{L_{ehy}} \tag{8.61}$$

$$V_{pile\text{-}y}=\frac{2M_{pile-x}}{L_{ehx}} \tag{8.62}$$

where, L_{ehx} and L_{ehy} are the equivalent-cantilever lengths that are based on horizontal-stiffness of the pile in the soil for x-axis (strong-axis) bending and y-axis (weak-axis) bending, respectively, of the pile, as discussed in Section 8.5.

The remaining member-end force for an abutment pile is the torsional moment, $M_{pile\text{-}h}$. This torque is caused by any plan-view rotation of the superstructure for an integral-abutment bridge, which is defined by the angle β that is shown in Fig. 8.9. The integral connection between the abutments and the bridge superstructure produces an abutment rotation and corresponding twisting of the abutment piles through an angular rotation in the XY-plane equal that is equal to the angle β. As discussed in Section 8.6.2, rotation of a bridge superstructure about the "point-of-fixity" will only occur when the bridge-skew angle, θ, is equal to or greater than the critical-skew angle, θ_c. Since the angle β is small, the torsional resistance of an HP-shape is small in comparison to the bending-moment resistances for the piles, the ISU researchers recommend that the torsional-moment strength $M_{pile\text{-}h}$ be set equal to zero for establishing the forces on an integral abutment using Analysis Method 2.

The components for the principal-axis, member-end forces of an abutment pile, which are shown in Fig. 8.40, have subscripts that correlate with the coordinate axes for an abutment pile and an abutment. For example, the force-component $V_{pile\text{-}xX}$, which is shown in Fig. 8.40b, represents the positive, X-axis, force component for the shear force in a pile that is directed along the major-principal axis (x-axis) for the pile. The other member-end, force components for an abutment pile were labeled in a similar manner. The relationship between the components of the pile, member-end forces and the

coordinate-axis systems for a pile and an abutment is given by direction cosines that involve the bridge-skew angle, θ, and the pile-skew angle, θ_r. From Fig. 8.40, the total of the components for the member-end forces for a pile along the X, Y, and Z-axes of an abutment are established from

$$\begin{Bmatrix} V_{pile-X} \\ P_{pile-Y} \\ V_{pile-Z} \end{Bmatrix} = \begin{bmatrix} \cos(\theta-\theta_r) & 0 & \sin(\theta-\theta_r) \\ 0 & -1 & 0 \\ -\sin(\theta-\theta_r) & 0 & \cos(\theta-\theta_r) \end{bmatrix} \begin{Bmatrix} V_{pile-x} \\ P_{pile-z} \\ V_{pile-y} \end{Bmatrix} \tag{8.63}$$

$$\begin{Bmatrix} M_{pile-X} \\ M_{pile-Y} \\ M_{pile-Z} \end{Bmatrix} = \begin{bmatrix} \cos(\theta-\theta_r) & 0 & \sin(\theta-\theta_r) \\ 0 & -1 & 0 \\ -\sin(\theta-\theta_r) & 0 & \cos(\theta-\theta_r) \end{bmatrix} \begin{Bmatrix} M_{pile-x} \\ M_{pile-z} \\ M_{pile-y} \end{Bmatrix} \tag{8.64}$$

An upper-bound magnitude for the soil pressure, w_{soil-X}, which acts normal to the back face of an abutment, is the full-passive-soil pressure. This maximum, passive-soil pressure is evaluated as

$$w_{soil-X} = k_{pmax}\, \gamma\, h_{abut} \tag{8.65}$$

where, k_{pmax} is the maximum, passive-soil-pressure coefficient from Fig. 5.10b. The maximum, soil-frictional force, $W_{soil-friction-Z}$, that corresponds with the passive-soil pressure is given by

$$W_{soil-friction-Z} = (w_{soil-X})\left(\frac{1}{2}\right)(h_{abut})(\mu_s) \tag{8.66}$$

where, h_{abut} is the height of the integral-abutment backwall and μ_s is the soil-to-abutment, surface-friction constant (μ_s = tan δ, with δ being the soil-to-abutment, surface-friction

angle). The other forces that act on the integral abutment shown in Fig. 8.32 are the uniform dead load $W_{abut\text{-}Y}$ for the abutment backwall and pile cap and the unknown member-end forces for the PC girders, which are the axial force, $P_{girder\text{-}X;}$ shear forces, $V_{girder\text{-}Y}$ and $V_{girder\text{-}Z}$; and bending moments, $M_{girder\text{-}X}$, $M_{girder\text{-}Y}$, and $M_{girder\text{-}Z}$. These member-end forces for a PC girder are determined from vertical, horizontal, and rotational equilibrium of the portion of the integral abutment that has a length B, as shown in Fig. 8.32. Free-body diagrams for this central portion of an integral abutment are presented and discussed in Section 8.8.2.3. If the resulting, member-end forces for a PC girder are greater than the associated strengths for the composite PC-girder, either the upper-bound values for the member-end forces for the piles are conservative values or the composite PC-girder is under designed.

8.8.2.3. Internal forces for an abutment

The internal axial force, shear forces, bending moments, and torsional moment at a cross section of an abutment-pile cap or an integral abutment that are induced by gravity and thermal loads can be determined either by applying indeterminate, structural analyses (Internal-Force Procedure 1) of the continuous foundation or by applying determinate, structural analyses (Internal-Force Procedure 2) of a geometrically-simplified portion of the foundation. The foundation loads for the internal-force procedures are the member-end forces for the bridge girders and the abutment piles and the soil pressures and soil-frictional forces on the back of an abutment. These abutment loads can be determined by either applying Analysis Method 1, which was discussed in Section 8.8.2.1, or by applying Analysis Method 2, which was described in Section 8.8.2.2.

For the Internal-Force Procedure 2, the bridge girders are assumed to be located at the mid-point between the abutment piles for alternate spans of the abutment-pile cap and integral abutment. With these girder locations, planes of either symmetry or asymmetry, which were illustrated in Fig. 8.34, exist at the ends of the portions of an abutment that have a length B for each type of load that acts on the foundation. Figure 8.34 shows that the relative displacements and rotations for the elastic curve of an abutment with respect to a PC girder, which are along X, Y, and Z-axes for an abutment and which are induced by the different forces that act on an abutment, are equal to zero at the location of a bridge girder (Cross Section 2). Therefore, the portion of an abutment between a bridge girder and the mid-point between the girders along the length of an abutment can be modeled as a member that is supported by a bridge girder and that has displacement, rotation, and force conditions, which are imposed at the end of the member. The geometric conditions are shown in Fig. 8.34 at Cross Sections 1 and 2.

Isometric views of a free-body diagram for a central portion of an abutment-pile cap and an integral abutment are shown in Figs. 8.41 and 8.42, respectively. The vertical cross sections, which were represented by Cross Sections 1 and 1' in Fig. 8.34, at the ends of these free-body diagrams have three internal forces and three internal moments. At Cross Section 1, the axial force, transverse-shear force, vertical-shear force, X-axis-bending moment, Y-axis-bending moment, and torsional moment are P_{Z1}, V_{X1}, V_{Y1}, M_{X1}, M_{Y1}, and M_{Z1}, respectively. At Cross Section 1', these forces and moments are $P_{Z1'}$, $V_{X1'}$, $V_{Y1'}$, $M_{X1'}$, $M_{Y1'}$, and $M_{Z1'}$, respectively. A total of 16 forces act on

the portion of an abutment-pile cap that is shown in Fig. 8.41, and a total of 33 forces act on the portion of an integral abutment that is shown in Fig. 8.42.

Static equilibrium will permit six unknown forces to be calculated for a three-dimensional free-body. If the member-end forces for the abutment piles, soil pressures, and soil-frictional forces are known and when symmetric and asymmetric conditions are applied to the free-body diagrams shown in Figs. 8.41 and 8.42, the remaining unknown forces can be calculated by independently analyzing the portion of the abutment between Cross Sections 1 and 1' as a member for the abutment loads $W_{soil\text{-}X}$, $W_{soil\text{-}friction\text{-}Z}$, $W_{abut\text{-}Y}$, $P_{pile\text{-}Y}$, $V_{pile\text{-}X}$, $M_{pile\text{-}Z}$, $V_{pile\text{-}Z}$, $M_{pile\text{-}X}$, and $M_{pile\text{-}Y}$. The zero-magnitude force conditions that exist on symmetric and asymmetric Cross Sections 1 and 1' are listed in Table 8.13. The subscript i that is included for some of the internal forces refers to any vertical cross section between the ends of the portion of an abutment shown in Figs. 8.41 and 8.42.

Coefficients for the shear forces, axial forces, bending moments, and torsional moments at Cross Sections 1, 1.5, and 2 are listed in Table 8.14. Cross Section 1.5 occurs at the location of an abutment pile, which is midway between Cross Sections 1 and 2. For some of the force coefficients, two values are listed in the table. The first force coefficient applies to the left side of a force discontinuity, and the second force coefficient applies to the right side of a force discontinuity. Some of the internal-force coefficients involve eccentricities of the applied abutment loads. Figure 8.43 shows a XY-plane, cross-sectional view for the portion of an integral abutment shown in Fig. 8.42. The resultant force for the soil pressure and soil-frictional force occurs at a depth equal to two-thirds of the abutment height, h_{abut}, from the top of the abutment. The member-

end forces for a bridge girder act at Point A shown in the figure. The eccentricities for the soil pressure, soil-frictional force, girder-end forces, and pile-end forces with respect to the centroid of an abutment cross section, which are the distances e_{sY}; e_{sY} and e_{sX}; e_{gY}; and e_{pY}, respectively, are expressed by

$$e_{sY} = \frac{1}{6} h_{abut} \tag{8.67}$$

$$e_{sX} = \frac{1}{2} B_{abut} \tag{8.68}$$

$$e_{gY} = \frac{1}{2} h_{abut} - y_{cg} \tag{8.69}$$

$$e_{pY} = \frac{1}{2} (h_{abut} - d_{emb}) \tag{8.70}$$

where, B_{abut} is the abutment thickness, y_{cg} is the distance from the top of the bridge deck to the center of gravity for the composite bridge girder, and d_{emb} is the embedment depth for an abutment pile into the bottom of the abutment-pile cap. Eccentric loads do not occur on the portion of the abutment-pile cap that was shown in Fig. 8.41, since the resultant for the girder vertical reaction and the self-weight of the abutment-pile cap occur at the mid-width of the abutment.

By using the internal-force coefficients from Table 8.14 and the principle of superposition, the internal forces can be established on a cross section of an abutment. For the design of the portion of an abutment-pile cap that was shown in Fig. 8.41, the only applicable load case is the gravity-load case, which involves the abutment loads $W_{abut\text{-}Y}$, $P_{pile\text{-}Y}$, and $V_{girder\text{-}Y}$. Figure 8.44 shows a XZ-plane, elevation view of this portion of an abutment-pile cap with these loads. For this load case, all of the internal forces on

Cross Sections 1 and 1' are equal to zero, except for the moments M_{x1} and M_{x2}, which are equal in magnitude but act in opposite directions. The moment M_{x1} is evaluated as

$$M_{x1} = \left(\frac{B^2}{24}\right)(W_{abut-Y}) - \left(\frac{B}{16}\right)(P_{pile-Y}) \tag{8.71}$$

After the moment M_{X1} is calculated from Eq. 8.71, the shear-force and bending-moment diagrams that are presented in Section 8.8.2.5 for the abutment loads $W_{abut\text{-}Y}$ and $P_{pile\text{-}Y}$ can be drawn for the central portion of the integral abutment that is shown in Fig. 8.44.

For the design of an integral abutment (composite backwall and pile cap), the ten abutment loads that are listed in Table 8.14 may contribute to the internal forces that act on a cross section of an abutment. Figure 8.45 shows six free-body diagrams for a central portion of the integral abutment, which is shown in Fig. 8.42. Multiple free-body diagrams were provided to give clarity for the abutment loads that are listed in Table 8.14 and for the member-end forces for a PC girder.

The total for the internal forces at Cross Section 1 for the portion of the integral abutment, which is shown in Figs. 8.42 and 8.44 and is subjected to the abutment loads that are listed in Table 8.14, are evaluated using Eqs. 8.72 to 8.77.

$$V_{X1} = +(e_{sX})(W_{soil-friction-Z}) + \left(\frac{9}{4B}\right)(M_{pile-Y}) \tag{8.72}$$

$$V_{Y1} = -(e_{sY})(W_{soil-friction-Z}) + \left(\frac{9e_{sY}}{4B}\right)(V_{pile-Z}) - \left(\frac{9}{4B}\right)(M_{pile-X}) \tag{8.73}$$

$$P_{Z1} = 0 \tag{8.74}$$

$$M_{X1} = -\left(\frac{B^2}{24}\right)(W_{abut-Y}) + \left(\frac{B}{16}\right)(P_{pile-Y}) \tag{8.75}$$

$$M_{Y1} = -\left(\frac{B^2}{24}\right)(W_{soil\text{-}X}) - \left(\frac{B}{16}\right)(V_{pile-X}) \tag{8.76}$$

$$M_{Z1} = 0 \tag{8.77}$$

where, the soil-frictional force, $W_{soil\text{-}friction\text{-}Z}$, per unit length of the abutment and soil-pressure force, $W_{soil\text{-}X}$, per unit length of the abutment are given by

$$W_{soil\text{-}friction\text{-}Z} = (W_{soil\text{-}X})(\mu_s) \tag{8.78}$$

$$W_{soil\text{-}X} = \frac{1}{2}(w_{soil-X})(h_{abut}) \tag{8.79}$$

and, μ_s is the soil-to-abutment, surface-friction constant ($\mu_s = \tan\delta$, with δ being the soil-to-abutment, surface-friction angle); and w_{soil} is the maximum, soil pressure at the bottom of the back face for the abutment (see Fig. 8.42). After the internal forces on Cross Section 1 are computed using Eqs. 8.72 to 8.77, the axial force, shear force, bending moment, and torsional moment diagrams that are presented in Section 8.8.2.5 for the abutment loads $W_{soil\text{-}X}$, $W_{soil\text{-}friction\text{-}Z}$, $W_{abut\text{-}Y}$, $P_{pile\text{-}Y}$, $V_{pile\text{-}X}$, $M_{pile\text{-}Z}$, $V_{pile\text{-}Z}$, $M_{pile\text{-}X}$, and $M_{pile\text{-}Y}$ can be drawn for a central portion of the integral abutment. For skewed, integral-abutment bridges, a soil-frictional force, $W_{soil\text{-}friction\text{-}Z}$, develops along the back face of the abutments when the bridge superstructure experiences a thermal expansion or contraction. As discussed in Section 8.6.2, an integral-abutment bridge will rotate about the "point-of-fixity" and induce transverse displacements, dt, of the abutments when the bridge-skew angle, θ, is close to or exceeds the soil-friction angle, γ.

Figure 8.45e shows the asymmetrical, axial forces that may be applied along the Z-axis for an integral abutment. The geometric-boundary conditions, which are associated with these axial forces; are relative to Cross Section 2, and are shown in Fig. 8.34c are: $\Delta_{Z1} = \Delta_{Z1'} \neq 0$ and $\Delta_{Z2} = 0$. When the soil pressures on the abutment wingwalls that are induced by the rotation of the bridge superstructure about the "point-of-fixity" are neglected, the axial forces P_{Z1} and $P_{Z1'}$ are equal to zero.

The asymmetric torsional moments, which are applied along a central portion of an integral abutment, as shown in Fig. 8.45f, induce the symmetric displacement of the top and bottom forces of an abutment as shown in Fig. 8.34f. The member rotations about the Z-axis of an abutment for the type of load are: $\theta_{Z1} = \theta_{Z1'} \neq 0$ and $\theta_{Z2} = 0$. The internal torsional moments M_{Z1} and $M_{Z1'}$ on Cross Sections 1 and 1', respectively, are equal to zero.

8.8.2.4. Alternate formulation for the internal forces for an abutment

An alternate formulation (Internal-Force Procedure 3) can be used to establish the moment M_{x1} for an abutment-pile cap. Since the vertical faces at each end of the free-body diagram shown in Fig. 8.44 are planes of symmetry, the shear forces, V_{X1}, $V_{x1'}$, V_{Y1}, and $V_{Y1'}$, and the torsional moments, M_{Z1} and $M_{Z1'}$, on these faces (Cross Sections 1 and 1') are all equal to zero. The moments M_{Y1} and $M_{Y1'}$, and axial forces P_{Z1} and $P_{Z1'}$ are equal to zero because no temperature-induced, horizontal forces are applied to the abutment-pile cap at this stage of the bridge construction. The free-body shown in Fig. 8.44 has identical segments adjacent to each end. Therefore, geometric-boundary conditions require that the rotations about the X-axis at each end and at the mid-length

of the elastic curve for this free-body must be equal to zero, as shown in Fig. 8.34b. The deflection in the Y-axis direction of the elastic curve for this free-body at each of these three locations is not equal to zero. The internal moment M_{X1}, which is evaluated by applying the moment-area method for the change in the rotation between the mid-length and end of the free-body and vertical, static equilibrium for the forces on the free-body, is the same as that expressed by Eq. 8.71.

The Internal-Force Procedure 3 can be used to establish the internal forces in an integral abutment (composite backwall and pile cap). Figures 8.45a and 8.45b show the symmetric forces and asymmetric forces, respectively, that induce flexural bending in the YZ-plane for a central portion of an integral abutment. For the symmetrically applied forces, the global, symmetric-boundary conditions are $V_{Y1} = V_{Y1'} = 0$, $M_{X1} = M_{X1'}$, $\theta_{X1} = \theta_{X1'} = 0$, $\theta_{X2} = 0$, $\Delta_{Y1} = \Delta_{Y1'} \neq 0$, and $\Delta_{Y2} \neq 0$. An expression for the bending moment M_{X1} is established by applying the moment-area method for the change in the slope to the elastic curve for the deformed shape of the abutment between Cross Sections 1 and 2. Since the rotations θ_{X1} and θ_{X2} are equal to zero, the change in the slope must also be equal to zero. When the moment-area expression is solved for the bending moment M_{X1}, the resulting equation is Eq. 8.75.

For the asymmetrically applied forces in the YZ-plane that are shown in Fig. 8.45b, the global, asymmetric-boundary conditions are $V_{Y1} = - V_{Y1'}$, $M_{X1} = M_{X1'} = 0$, $\theta_{X1} = \theta_{X1'} = 0$, $\theta_{X2} = 0$, $\Delta_{Y1} = \Delta_{Y1'} = 0$, and $\Delta_{Y2} = 0$. If shear deformations are neglected, the uniformly applied moment $(W_{soil\text{-}friction\text{-}Z})$ (e_{sY}) does not induce any displacement of the elastic curve for the abutment. For this applied moment, the shear force V_{Yi} is constant and equal to the applied moment. For all the applied asymmetric forces that cause

flexural bending in the YZ-plane, an expression for the shear force V_{Y1} is established by applying the moment-area method for the tangential deviation to the elastic curve for the deformed shape of the abutment at Cross Section 1 from a tangent line that represents the slope of the elastic curve at Cross Section 2. Since the displacements Δ_{Y1} and Δ_{Y2} and the rotation θ_{X2} are all equal to zero, the expression for this tangential deviation must also be equal to zero. When the moment-area expression is solved for the shear force V_{Y1}, the resulting equation is Eq. 8.73. When both the symmetric and asymmetric forces for YZ-plane bending are simultaneously applied to the abutment, the shear force V_{Y1} and the bending moment M_{X1} are still expressed by Eqs. 8.73 and 8.75, respectively, due to the force conditions on the planes of symmetry and asymmetry for Cross Sections 1 and 1'.

Figures 8.45c and 8.45d show the symmetric and asymmetric forces, respectively, that induce flexural bending in the XZ-plane for a central portion of an integral abutment. For the symmetrically applied forces, the global, symmetric-boundary conditions are $V_{X1} = -V_{X1'} = 0$, $M_{Y1} = M_{Y1'}$, $\theta_{Y1} = \theta_{Y1'} = 0$, $\theta_{Y2} = 0$, $\Delta_{X1} = \Delta_{X1'} \neq 0$, and $\Delta_{X2} \neq 0$. For the asymmetrically applied forces, the global, asymmetric-boundary conditions are $V_{X1} = V_{X1'}$, $M_{Y1} = M_{Y1'} = 0$, $\theta_{Y1} = \theta_{Y1'} \neq 0$, $\theta_{Y2} = 0$, $\Delta_{X1} = \Delta_{X1'} = 0$, and $\Delta_{X2} = 0$. After analyzing the portion of the abutment between Cross Sections 1 and 2 using the moment-area method for the change in the slope between these two cross sections when the symmetric forces are applied to the abutment and for the tangential deviation of the elastic curve between these two cross sections when the asymmetric forces are applied to the abutment, the shear force V_{X1} and bending moment M_{Y1} are expressed by Eqs. 8.72 and 8.76, respectively.

8.8.2.5. Member-load, shear-force, bending-moment, and torsional-moment diagrams

The member-load, V_X-shear force, V_Y-shear force, P_Z-axial force, M_X-bending moment, M_Y-bending moment, and M_Z-torsional moment diagrams for the portion of an integral abutment with a length B between Cross Sections 1 and 1' are shown in Figs. 8.46, 8.47, 8.48, 8.49, 8.50, 8.51, 8.52, 8.53, and 8.54 for the abutment loads $W_{soil\text{-}X}$, $W_{soil\text{-}friction\text{-}Z}$, $W_{abut\text{-}Y}$, $P_{pile\text{-}Y}$, $V_{pile\text{-}X}$, $M_{pile\text{-}Z}$, $V_{pile\text{-}Z}$, $M_{pile\text{-}X}$, and $M_{pile\text{-}Y}$, respectively. These loads are the abutment loads that were listed in Table 8.14. Recall that the girders are assumed to be located at the center of alternate spans for the abutment, which is vertically supported by the piles, and that Cross Sections 1 and 1', 1.5 and 1.5', and 2 are located at the mid-point between two abutment piles for the portion of the abutment length without a PC girder, at an abutment pile, and at the mid-point between two abutment piles for a portion of the abutment length with a PC girder, respectively. The magnitudes for the loads, forces, and moments are expressed as a coefficient of the particular abutment load. For example, the maximum, negative-bending moment in an integral abutment that is caused by the application of the maximum, passive-soil pressure, which corresponds with the abutment load $W_{soil\text{-}X}$ shown in Fig. 8.46, is equal to $-(B^2/12)(W_{soil\text{-}X})$.

8.8.3. Abutment sidewall and wingwall forces on a backwall

Figure 8.55 shows a plan view of an integral abutment, which has common side and wingwalls, for a skewed, integral-abutment bridge. The skewed-geometry for an abutment produced an acute-angle corner (Corner 1) for the bridge slab and a corresponding, obtuse-angle corner between the abutment backwall and sidewall at one

end of the backwall and an obtuse-angle corner (Corner 2) for the bridge slab and a corresponding acute-angle corner between the abutment backwall and sidewall at the other end of the backwall. For the portion of the abutment near Corner 1, the lengths ℓ_{sw1} and ℓ_{ww1} are the lengths of the sidewall and wingwall, respectively, and the length ℓ_{w1} is the length of the exterior face of the abutment that is parallel to the longitudinal direction of the bridge. For the portion of the abutment near Corner 2, these lengths are ℓ_{sw2}, $\ell_{ww2,}$ and ℓ_{w2}, respectively. Figure 8.55 shows that the lengths ℓ_{sw1} and ℓ_{sw2} are measured from the point where the inside face of the sidewall intersects with the back face of the abutment backwall. The other end of the sidewall is defined by the construction joint between the sidewall and the wingwall. Other dimensions shown in Fig. 8.55 are the dimensions B_{swcap}, B_{sw}, and B_{wwe}; $c_{girderC1\text{-}t}$ and $c_{girderC2\text{-}t}$; $c_{girderC1\text{-}\ell}$ and $c_{girderC2\text{-}\ell}$; $c_{pile\text{-}t}$; $c_{swp\text{-}\ell}$ and $c_{swp\text{-}t}$; and c and s_{girder}, which are the width of the sidewall-pile cap, sidewall, and wingwall at the end of the wingwall, respectively; the distance from the outside face of an abutment sidewall to the center of bearing for an exterior girder that is measured along the t-axis direction for the bridge superstructure at Corner 1 and Corner 2, respectively; the distance from the front edge of the sidewall to the center of bearing for an exterior girder that is measured along the ℓ-axis direction for the bridge superstructure at Corner 1 and Corner 2, respectively; the distance from the outside face of a sidewall to the center of an end, backwall pile that is measured along the t-axis for the bridge; the distance from the end of a sidewall-pile cap to the center of gravity for a sidewall pile that is measured along the ℓ-axis direction and t-axis direction, respectively, for the bridge superstructure; and the center-to-center spacing for the backwall piles and

the PC girders, respectively. The dimensions $c_{girderC1\text{-}\ell}$ and $c_{girderC2\text{-}\ell}$, which are functions of the geometry for the bridge, are expressed, respectively, as

$$c_{girderC1-\ell} = \left(\frac{B_{abut}}{2\cos\theta}\right) - \left(c_{girderC1-t} - B_{sw}\right)\tan\theta \tag{8.80}$$

$$c_{girderC2-\ell} = \left(\frac{B_{abut}}{2\cos\theta}\right) + \left(c_{girderC2-t} - B_{sw}\right)\tan\theta \tag{8.81}$$

A side-elevation view for an integral abutment is shown in Fig. 8.56. The sidewall is supported by its own foundation that consists of a pile cap and one or sometimes two piles. The trapezoidal-shaped wingwall, which cantilevers from the end of the sidewall, is supported by the sidewall for the abutment.

Figure 8.57 shows the directions for the resultants of the thermally-induced forces that act on the various components of a bridge, when a thermal expansion of the bridge superstructure occurs for a skewed bridge that has two piers and a bridge-skew angle, 2, which is large enough to cause a plan-view, clockwise rotation of the bridge and transverse displacements of the abutments. The force and moment resultants, $F_{bpile\text{-}X}$, $F_{bpile\text{-}Z}$, and $M_{bpile\text{-}Y}$, are the backwall-pile forces and moment that act along the X-axis and Z-axis and about the Y-axis, respectively, of the abutment. Sidewall 1, pile-shear forces, $V_{sw1p\text{-}\ell}$ and $V_{sw1p\text{-}t}$ and the Sidewall 2, pile-shear forces $V_{sw2p\text{-}\ell}$ and $V_{sw2p\text{-}t}$ act in a direction that is parallel to the ℓ-axis and t-axis, respectively, for the bridge superstructure. The pier forces, $P_{piernorm}$ and $P_{pierparal}$, act normal and parallel, respectively, to longitudinal axis of the piers. The force and moment resultants $F_{soil\text{-}X}$, $F_{soil\text{-}Z}$, and $M_{soil\text{-}Y}$, which act along the X-axis and Z-axis and about the Y-axis of the

abutment, respectively, are caused by the passive-soil pressure and soil-frictional forces that act on the abutment backwalls. The resultant force, $F_{s\&w1soil\text{-}t}$, for the passive-soil pressure acts normal to Sidewall 1 and Wingwall 1 and along the t-axis direction for the bridge superstructure. At Corner 2 of an abutment, trapped soil exists adjacent to the abutment, which caused the direction for the resultant force, $F_{s\&w2soil\text{-}Z}$, for the passive-soil pressure at this location to be parallel to the length of the abutment backwall.

The magnitude and distribution of the horizontal pressure from the soil on the common sidewall and wingwall is a function of the displacement direction and magnitude; soil properties; geometry of the vertical faces for these walls; and through-thickness, flexural stiffness of the wingwall or common sidewall and wingwall. As shown in Fig. 8.56b, a triangular-pressure distribution should be used for the passive-soil pressure. The passive-soil pressure $w_{soil\text{-}t}$ that acts at the bottom of Sidewall 1 is equal to the passive-soil pressure that is associated with transverse displacement, dt, of the integral abutment. The passive-soil pressure $w_{soil\text{-}Z}$ that acts at the bottom of Sidewall 2 is equal to the passive-soil pressure that is associated with transverse displacement, dt, and longitudinal displacement, $d\ell$, of the integral abutment. The maximum, transverse displacement dt_{max} can be used instead of the displacement dt. The displacement dt_{max} and the corresponding, passive-soil pressures, k_{pw1} and k_{pw2}, for the soil that is against Wingwall 1 and Sidewall 1 and for the trapped soil that is adjacent to Wingwall 2 and Sidewall 2, respectively, is computed by the software program “Transmove” (see Appendix B). Since the displacement dt_{max} is substantially smaller than the abutment displacement, $d\ell$, along the longitudinal direction of the bridge, the soil pressure $w_{soil\text{-}t}$ normally will be smaller than the full-passive-soil pressure. However, the soil pressure

$w_{soil\text{-}Z}$ probably will be equal to the full-passive-soil pressure because the trapped soil near Corner 2 of the abutment causes the soil to displace in a direction that is parallel to the length of the abutment backwall. If the program Transmove is not used to establish the passive-soil pressures on an abutment sidewall and wingwall, Fig. 5.10b in Chapter 5 can be used to predict the passive-soil pressure after the abutment displacement dℓ is calculated as a free expansion of the bridge superstructure and the abutment displacement dt is estimated by some other analysis technique.

The passive-soil pressure that acts at the bottom of Wingwall 1 and Wingwall 2 are less than the passive-soil pressures $w_{soil\text{-}t}$ and $w_{soil\text{-}Z}$, respectively, that act at the bottom of Sidewall 1 and Sidewall 2, respectively, because the heights, h_{wa} and h_{wb}, for a trapezoidal-shaped wingwall at the construction joint between a wingwall and a sidewall and at the free end of a wingwall, respectively, are less than the height of a sidewall, as shown in Fig. 8.56a. The sidewall height is equal to the height, h_{abut}, of the composite, backwall and backwall-pile cap. The passive-soil pressures that act at the bottom of the two ends of Wingwall 1 and Wingwall 2 are established by multiplying the passive-soil pressures $w_{soil\text{-}t}$ and $w_{soil\text{-}Z}$, respectively, by the ratio of the wingwall height at those locations to the height of the corresponding sidewall. When a passive-soil pressure is assumed to occur on one side of a wall, soil pressure is assumed not to act on the other side of that same wall because a gap may develop along the other side of a wall.

Figure 8.58 shows XZ-plane, free-body diagrams for the abutments and the two end spans for a bridge superstructure. The external, resultant forces that are shown on the free-body diagrams for Abutment 1 and Abutment 2 (Figs. 8.58a and 8.58d, respectively) and for the free-body diagrams for End Slab 1 and End Slab 2 (Figs. 8.58b

and 8.58c, respectively) are the same forces that were shown in Fig. 8.57. The internal, resultant forces, $F_{supstr\text{-}X}$, $F_{supstr\text{-}Z}$, and $M_{supstr\text{-}Y}$, represent the internal forces that occur between the bridge superstructure and an abutment. These forces and moment, which act in the directions that are parallel to the X-axis and Z-axis and about the Y-axis of an abutment, respectively, are associated with the internal stresses in the PC-bridge girders and the RC slab. A bridge superstructure must be in static equilibrium. For a symmetrical bridge that has two piers, the internal, resultant forces that act at the ends of the bridge superstructure and the external, pier forces are equal in magnitude and act in opposite directions on each side of the "fixed point" (center of the XZ-plane rotation) for the bridge.

Figures 8.59a and 8.59b show an enlarged, XZ-plane, plan views of a portion of an integral abutment near Corner 1 and Corner 2, respectively, for a skewed, integral-abutment bridge. Also shown in these figures are the passive-soil-pressure forces, backwall-pile forces, sidewall-pile forces, and PC-girder forces and moments, which act in a horizontal plane on these portions of an abutment, when the bridge superstructure experiences a longitudinal expansion and a clockwise rotation. The passive-soil-pressure force that acts along a unit length of Sidewall 1 is the force $W_{sw1s\text{-}t}$, and the passive-soil-pressure forces that act on a unit length of Wingwall 1 at the connection with Sidewall 1 and at the free end of the wingwall are the soil forces $W_{ww1sa\text{-}t}$ and $W_{ww1sb\text{-}t}$, respectively. For Sidewall 2 and Wingwall 2, these passive-soil-pressure forces, which act on a unit length of the trapped soil that is adjacent to the sidewall and wingwall, are the forces $W_{sw2s\text{-}Z}$, $W_{ww2sa\text{-}Z}$, and $W_{ww2sb\text{-}Z}$, respectively.

Each sidewall with its pile cap and wingwall combination behaves as a horizontal cantilever that is supported by the composite, abutment backwall and backwall-pile cap. If a Yt-plane, fixed support for these horizontally-cantilevered walls at Corner 1 of the abutment is assumed to be located at the bearing point for the exterior, PC-bridge girder on the backwall-pile cap, which is shown in Fig. 8.59a, six, resultant, internal, support reactions can be evaluated at this vertical cross section. Positive force vectors and moment vectors for these reactions are directed along the positive t-axis, ℓ-axis, and Y-axis directions. The resultant, transverse-support reaction, R_{tC1}, which acts in a direction that is parallel to the positive t-axis of the bridge superstructure and which is shown as the solid-line force in the insert for Fig. 8.59a, is given by

$$R_{tC1} = W_{sw1s-t}\left(\ell_{sw1} + \frac{B_{abut}}{\cos\theta}\right) + \frac{1}{2}\left(W_{ww1sa\text{-}t} + W_{ww1sb\text{-}t}\right)\ell_{ww1} + V_{sw1p\text{-}t} \tag{8.82}$$

For this same Yt-plane, fixed support, the resultant, internal, longitudinal-support reaction, $R_{\ell C1}$, which acts in a direction that is parallel to the positive ℓ-axis of the bridge superstructure, is expressed as

$$R_{\ell C1} = -V_{sw1p-\ell} \tag{8.83}$$

These reactions can be resolved into component forces, which act in a direction that is parallel to the positive X-axis and positive Z-axis for the composite, backwall and backwall-pile cap. The resultant, internal, forces R_{XC1} and R_{ZC1} at Corner 1 of the abutment are given, respectively, by

$$R_{XC1} = R_{tC1}\sin\theta + R_{\ell C1}\cos\theta \tag{8.84}$$

$$R_{ZC1} = R_{tC1}\cos\theta - R_{\ell C1}\sin\theta \tag{8.85}$$

An axial force, P_Z, in the integral abutment that is caused by the soil and pile forces that act on the sidewall, sidewall-pile cap, and wingwall near Corner 1 is not constant along the length of the abutment because the resultant, internal force R_{ZC1} and a corresponding resultant, internal force R_{ZC2}, which is associated with Corner 2 of the abutment, are dissipated into the bridge superstructure along the length of the abutment backwall. Most of these internal forces will be transferred into the bridge superstructure over a relatively short distance from the corners of the abutment.

The resultant, internal, vertical-support reaction, R_{YC1}, which acts in a direction that is parallel to the positive Y-axis of an abutment backwall, is evaluated by

$$R_{YC1} = \left(W_{sw1w\text{-}Y} + W_{sw1wcap\text{-}Y}\right)\ell_{sw1c} + \left(\frac{W_{ww1wa\text{-}Y} + W_{ww1wb\text{-}Y}}{2}\right)\ell_{ww1} - P_{sw1p\text{-}Y} \tag{8.86}$$

where, as shown in Figs. 8.60b and 8.60c, $W_{sw1w\text{-}Y}$, $W_{sw1wcap\text{-}Y}$, $W_{ww1wa\text{-}Y}$, and $W_{ww1wb\text{-}Y}$ are the self-weights of Sidewall 1, the pile cap for that sidewall, Wingwall 1 at the connection to the sidewall, and Wingwall 1 at the free end of the wingwall, respectively, and the length ℓ_{sw1C} is the horizontal-cantilever length for Sidewall 1. This length, which is established by Eq. 8.87, is the distance between the end of the sidewall, which is adjacent to the wingwall, and a critical vertical cross section that is located at a point mid-way between the vertical-intersection lines that are formed at the intersection of the inside face of the sidewall-pile cap and the inside face of the corresponding sidewall and the back face of the abutment backwall.

$$\ell_{sw1c} = \ell_{sw1} + \frac{1}{2}\left(B_{swcap} - B_{sw}\right)\tan\theta \tag{8.87}$$

For the horizontally-cantilevered sidewall and wingwall at Corner 1 of the abutment, the resultant, internal, support-bending-moment reaction, M_{YC1}, which is shown as the solid-line moment in the insert for Fig. 8.59a and whose moment vector acts in a direction that is parallel to the positive Y-axis of the abutment backwall, is expressed as

$$M_{YC1} = -W_{sw1s-t}\left(\ell_{sw1} + \frac{B_{abut}}{\cos\theta}\right)e_{sw1s-\ell} - \left[\left(\frac{W_{ww1sa-t}}{2}\right)\ell_{ww1}\,e_{ww1sa-\ell}\right]$$

$$-\left[\left(\frac{W_{ww1sb-t}}{2}\right)\ell_{ww1}\,e_{ww1sb-\ell}\right] - \left(V_{sw1p-t}e_{sw1p-\ell}\right) + \left(V_{sw1p-\ell}e_{sw1p-t}\right) \tag{8.88}$$

The horizontal eccentricities $e_{sw1s-\ell}$, $e_{ww1sa-\ell}$, and $e_{ww1sb-\ell}$ for the soil forces that act on the sidewall and its pile cap and on the wingwall, respectively, and the horizontal eccentricities $e_{sw1p-\ell}$ and e_{sw1p-t} for the pile forces with respect to the center of bearing for the exterior girder near Corner 1 of the abutment are functions of the bridge geometry. These force eccentricities are given, respectively, by

$$e_{sw1s-\ell} = \left(\frac{\ell_{sw1}}{2}\right) - \left(c_{girderC1-t} - B_{sw}\right)\tan\theta \tag{8.89}$$

$$e_{ww1sa-\ell} = \left(\frac{\ell_{ww1}}{3}\right) + \ell_{sw1} + \left(c_{girderC1-t} - B_{sw}\right)\tan\theta \tag{8.90}$$

$$e_{ww1sb-\ell} = \left(\frac{2\ell_{ww1}}{3}\right) + \ell_{sw1} + \left(c_{girderC1-t} - B_{sw}\right)\tan\theta \tag{8.91}$$

$$e_{sw1p-\ell} = \ell_{sw1} + \left(\frac{B_{abut}}{2\cos\theta}\right) + \left(c_{girderC1-t} - B_{sw}\right)\tan\theta - c_{swp-\ell} \tag{8.92}$$

$$e_{sw1p-t} = c_{girderC1-t} - \left(\frac{B_{swcap}}{2}\right) \tag{8.93}$$

The moment M_{YC1} is resisted by the bridge superstructure within a relatively short distance from Corner 1 of the abutment. An approximate model can be used to provide a mechanism to transfer the moment M_{YC1} into the bridge superstructure. The ISU researchers assumed that a force couple that involves an axial force in the exterior girder and the first interior girder for the bridge superstructure resists the moment M_{YC1}. For this model, the composite backwall and backwall-pile cap is subjected to Y-axis bending and corresponding X-axis, member-end, shear forces. For the first, horizontal span of the backwall and backwall-pile cap between the exterior girder and first-interior girder near Corner 1 of the abutment, the internal, member-end shear forces, V_{eXC1}, in the abutment are given by

$$V_{eXC1} = \left[\frac{\left(M_{YC1} + \frac{M_{YC1}}{2}\right)}{\left(\frac{s_{girder}}{\cos\theta}\right)}\right] \tag{8.94}$$

For the second, horizontal span of the composite, backwall and backwall-pile cap between the first-interior girder and second-interior girder, the induced, internal, member-end shear forces, V_{iXC1}, are expressed by

$$V_{iXC1} = \left[\frac{\left(\frac{M_{YC1}}{2} + \frac{M_{YC1}}{4} \right)}{\left(\frac{s_{girder}}{\cos\theta} \right)} \right] \tag{8.95}$$

In Eqs. 8.94 and 8.95, the moment terms $M_{YC1}/2$ and $M_{YC1}/4$ are the "carry-over moments" for the continuous, composite, backwall and backwall-pile cap that is horizontally supported by the bridge girders. These shear forces are in addition to the shear forces that are induced in this member by the soil forces and pile forces and moments for the abutment backwall and its pile cap. For Corner 1 of the abutment, the corresponding axial forces, $P_{egC1\text{-}\ell}$ and $P_{igC1\text{-}\ell}$ in the exterior girder and the first-interior girder, respectively, are expressed as

$$P_{egC1-\ell} = \left[\frac{\left(\frac{3M_{YC1}}{2} \right)}{s_{girder}} \right] + R_{\ell C1} \tag{8.96}$$

$$P_{igC1-\ell} = \left[\frac{\left(\frac{9M_{YC1}}{4} \right)}{s_{girder}} \right] \tag{8.97}$$

These axial forces are in addition to the axial forces that are induced by the passive-soil pressure and pile shear forces and bending moments on the composite, backwall and backwall-pile cap. The girder forces $P_{egC1\text{-}\ell}$ and $P_{igC1\text{-}\ell}$ are a tension force in the exterior girder and a compression force in the first-interior girder, respectively.

Since vertical eccentricities occur between the lines-of-action for the sidewall-pile shear forces, $V_{sw1p\text{-}\ell}$ and $V_{sw1p\text{-}t}$; for the passive-soil-pressure force, $W_{sw1s\text{-}t}$, that acts on

the composite sidewall and sidewall-pile cap; and for the passive-soil-pressure forces, $W_{ww1sa\text{-}t}$ and $W_{ww1sb\text{-}t}$, that act on the wingwall and the center of gravity for the composite backwall and backwall-pile cap, a resultant, internal, support-bending-moment reaction, M_{tC1}, and a resultant, internal, support-torsional-moment reaction, $M_{\ell C1}$, develops at the assumed, Yt-plane, fixed support at the bearing point for the exterior, PC girder. The bending-moment reaction M_{tC1} and torsional-moment reaction $M_{\ell C1}$, whose moment vectors act in directions that are parallel to the positive t-axis and positive ℓ-axis directions, respectively, are given by

$$M_{tC1} = -\left(P_{sw1p\text{-}Y} e_{sw1p\text{-}\ell}\right) + \left[V_{sw1p\text{-}\ell}\left(\frac{h_{abut}}{2} - \frac{d_{emb}}{2}\right)\right] + M_{sw1p\text{-}t} - \left(W_{sw1w\text{-}Y} + W_{sw1wcap\text{-}Y}\right)\ell_{sw1c} e_{sw1s\text{-}\ell}$$

$$- \left(W_{ww1wa\text{-}Y} e_{ww1sa\text{-}\ell} + W_{ww1wb\text{-}Y} e_{ww1sb\text{-}\ell}\right)\frac{\ell_{ww1}}{2} \tag{8.98}$$

$$M_{\ell C1} = -\left(P_{sw1p\text{-}Y} e_{sw1p\text{-}t}\right) + \left[V_{sw1p\text{-}t}\left(\frac{h_{abut}}{2} - \frac{d_{emb}}{2}\right)\right] + M_{sw1p\text{-}\ell} + \left[W_{sw1s\text{-}t}\left(\ell_{sw1} + \frac{B_{abut}}{\cos\theta}\right)\left(\frac{h_{abut}}{6}\right)\right]$$

$$- \left[W_{ww1sa\text{-}t}\left(\frac{h_{abut}}{2} - \frac{2h_{wa}}{3}\right) + W_{ww1sb\text{-}t}\left(\frac{h_{abut}}{2} - \frac{2h_{wb}}{3}\right)\right]\frac{\ell_{ww1}}{2}$$

$$+ \left[W_{sw1w\text{-}Y}\left(c_{girderC1\text{-}t} - \frac{B_{sw}}{2}\right) + W_{sw1wcap\text{-}Y}\left(c_{girderC1\text{-}t} - \frac{B_{swcap}}{2}\right)\right]\ell_{sw1c}$$

$$+ \left[W_{ww1wa\text{-}Y}\left(c_{girderC1\text{-}t} - \frac{B_{sw}}{2}\right) + W_{ww1wb\text{-}Y}\left(c_{girderC1\text{-}t} - \frac{B_{wwe}}{2}\right)\right]\frac{\ell_{ww1}}{2} \tag{8.99}$$

The moment M_{tC1} can be assumed to be dissipated into the bridge superstructure through strong-axis bending of the exterior, PC-bridge girder. An analytical model, which is similar to the one that was used to describe how the moment M_{YC1} is resisted by the bridge superstructure, can also be used to provide a mechanism for distributing the torque $M_{\ell C1}$ into the bridge superstructure. A force couple that consists of the vertical reactions for the exterior and the first interior girder can resist the torque $M_{\ell C1}$. A positive torque is resisted by a downward reaction at the exterior girder and an upward reaction at the first interior girder. For Corner 1 of the abutment the corresponding shear forces $V_{egC1\text{-}Y}$ and $V_{igC1\text{-}Y}$ in the exterior and first interior girder, respectively, given by

$$V_{egC1-Y} = \left[\frac{\left(\frac{3M_{\ell C1}}{2} \right)}{s_{girder}} \right] + R_{YC1} \tag{8.100}$$

$$V_{igC1-Y} = \left[\frac{\left(\frac{9M_{\ell C1}}{4} \right)}{s_{girder}} \right] \tag{8.101}$$

For this model, the composite backwall and backwall-pile cap is subjected to X-axis bending and corresponding Y-axis, member-end, shear forces. For the first, vertical span of the backwall and backwall-pile cap between the exterior girder and first-interior girder near Corner 1 of the abutment, the internal, member-end shear forces, V_{eYC1}, in the abutment are given by

$$V_{eYC1} = \left[\frac{\left(M_{\ell C1} + \frac{M_{\ell C1}}{2} \right)}{\left(\frac{s_{girder}}{\cos\theta} \right)} \right] \tag{8.102}$$

For the second, horizontal span of the composite, backwall and backwall-pile cap between the first-interior girder and second-interior girder, the induced, internal, member-end shear forces, V_{iYC1}, are expressed by

$$V_{iYC1} = \left[\frac{\left(\frac{M_{\ell C1}}{2} + \frac{M_{\ell C1}}{4} \right)}{\left(\frac{s_{girder}}{\cos\theta} \right)} \right] \tag{8.103}$$

In Eqs. 8.102 and 8.103, the moment terms $M_{\ell C1}/2$ and $M_{\ell C1}/4$ are the "carry-over moments" for the continuous, composite, backwall and backwall-pile cap that is vertically supported by the bridge girders. These shear forces are in addition to the shear forces that are induced in this member by the soil forces and pile forces and moments for the abutment backwall and its pile cap.

The moment M_{tC1} and torque $M_{\ell C1}$ can be resolved into X-axis and Z-axis components using Eqs. 8.104 and 8.105, respectively.

$$M_{XC1} = +M_{\ell C1}\cos\theta + M_{tC1}\sin\theta \tag{8.104}$$

$$M_{ZC1} = -M_{\ell C1}\sin\theta - M_{tC1}\cos\theta \tag{8.105}$$

Positive moment vectors for the moments M_{XC1} and M_{ZC1} are directed along the positive X-axis and Z-axis directions, respectively.

Again, by assuming a Yt-plane, fixed support condition at the bearing point for the exterior, PC girder for the horizontally-cantilevered, sidewall with its pile cap and wingwall near Corner 2 of the abutment that is shown in Fig. 8.59b, six, resultant, internal, support reactions can be evaluated at this vertical cross section. Positive force vectors and moment vectors for these reactions are directed along the positive t-axis, ℓ-axis, and Y-axis directions. The resultant, internal, support reaction, R_{XC2}, which acts in a direction that is parallel to the positive X-axis of the abutment backwall, is given by

$$R_{XC2} = V_{sw2p-\ell} \cos\theta - V_{sw2p-t} \sin\theta \tag{8.106}$$

The resultant, internal, support reaction, R_{ZC2}, which acts in a direction that is parallel to the positive Z-axis of the abutment backwall, for this sidewall and its pile cap and wingwall is established by

$$R_{ZC2} = -W_{sw2s-Z}\, \ell_{sw2} \cos\theta - \frac{1}{2}\left(W_{ww2sa\text{-}Z} + W_{ww2sb\text{-}z}\right) \ell_{ww2} \cos\theta$$
$$- \left(V_{sw2p-t} \cos\theta\right) - \left(V_{sw2p-\ell} \sin\theta\right) \tag{8.107}$$

The insert for Fig. 8.59b shows the resultant, internal, reactive forces, $R_{\ell C2}$ and R_{tC2} as solid-line forces. These forces act in directions that are parallel to the positive ℓ-axis and positive t-axis, respectively, for the bridge superstructure. The forces $R_{\ell C2}$ and R_{tC2}, which are equal to the total of the ℓ-axis and t-axis components of the forces R_{XC2} and R_{ZC2}, are respectively equal to

$$R_{\ell C2} = R_{XC2} \cos\theta - R_{ZC2} \sin\theta \tag{8.108}$$

$$R_{tC2} = -R_{XC2}\sin\theta + R_{ZC2}\cos\theta \tag{8.109}$$

Applying the simplified model that was used to describe the load-transfer mechanism for the forces at Corner 1 of the abutment, the force $R_{\ell C2}$ induces an axial force in the exterior girder at Corner 2 of the abutment that is in addition to the axial force that is induced in this girder by the soil forces and pile forces and moments for the composite, backwall and backwall-pile cap.

The resultant, internal, vertical-support reaction, R_{YC2}, which acts in a direction that is parallel to the positive Y-axis of an abutment backwall is evaluated by

$$R_{YC2} = \left(W_{sw2w-Y} + W_{sw2wcap-Y}\right)\ell_{sw2c} + \left(W_{ww2wa-Y} + W_{ww2wb-Y}\right)\frac{\ell_{ww2}}{2} - P_{sw2p\text{-}Y} \tag{8.110}$$

where, as shown in Fig. 8.61, $W_{sw2w\text{-}Y}$, $W_{sw2capw\text{-}Y}$, $W_{ww2wa\text{-}Y}$, and $W_{ww2wb\text{-}Y}$ are the self-weights of Sidewall 2, the pile cap for that sidewall, Wingwall 2 at the connection to the sidewall, and Wingwall 2 at the free end of the wingwall, respectively, and the length ℓ_{sw2C} is the horizontal-cantilever length for Sidewall 2. This length, which is expressed by Eq. 8.111), is the distance between the end of the sidewall, which is adjacent to the wingwall, and a critical vertical cross section that is located at a point mid-way between the vertical-intersection lines that are formed at the intersection of the inside face of the sidewall-pile cap and the inside face of the corresponding sidewall and the back face of the abutment backwall.

$$\ell_{sw2c} = \ell_{sw2} - \frac{1}{2}\left(B_{swcap} - B_{sw}\right)\tan\theta \tag{8.111}$$

For the horizontally-cantilevered sidewall and wingwall at Corner 2 of the abutment, the resultant, internal, support-bending-moment reaction, M_{YC2}, which is shown as the solid-lime moment in the insert for Fig. 8.59b and whose moment vector acts in a direction that is parallel to the positive Y-axis of the abutment backwall, is expressed as

$$M_{YC2} = -\left(W_{sw2s-Z}\,\ell_{sw2}\,e_{sw2s-X}\cos\theta\right) - \left[\frac{1}{2}\left(W_{ww2sa-Z}\right)\ell_{ww2}\,e_{ww2sa-X}\cos\theta\right]$$

$$-\left[\frac{1}{2}\left(W_{ww2sb-Z}\right)\ell_{ww2}\,e_{ww2sb-X}\cos\theta\right]$$

$$-\left(V_{sw2p-t}\,e_{sw2p-\ell}\right) - \left(V_{sw2p-\ell}\,e_{sw2p-t}\right) \tag{8.112}$$

The eccentricities e_{sw2s-X}, $e_{ww2sa-X}$, and $e_{ww2sb-X}$ for the soil forces that act on the sidewall and its pile cap and on the wingwall, respectively, and the eccentricities $e_{sw2p-\ell}$, and e_{sw2p-t} for the pile forces with respect to the center of bearing for the exterior girder near Corner 2 of the abutment are functions of the bridge geometry. These force eccentricities are given, respectively, by

$$e_{sw2s-X} = \left(\frac{\ell_{sw2}\cos\theta}{2}\right) + \left(\frac{B_{abut}}{2}\right) \tag{8.113}$$

$$e_{ww2sa-X} = \left[\left(\frac{\ell_{ww2}}{3}\right) + \ell_{sw2}\right]\cos\theta + \left(\frac{B_{abut}}{2}\right) \tag{8.114}$$

$$e_{ww2sb-X} = \left[\left(\frac{2\ell_{ww2}}{3}\right) + \ell_{sw2}\right]\cos\theta + \left(\frac{B_{abut}}{2}\right) \tag{8.115}$$

$$e_{sw2p-\ell} = \ell_{sw2} + \left(\frac{B_{abut}}{2\cos\theta}\right) - \left(c_{girderC2-t} - B_{sw}\right)\tan\theta - c_{swp-\ell} \tag{8.116}$$

$$e_{sw2p-t} = c_{girderC2-t} - \left(\frac{B_{swcap}}{2}\right) \tag{8.117}$$

The moment M_{YC2} is assumed to induce internal, end-member, shear forces, V_{eXC2}, in the composite, backwall and backwall-pile cap for the first-horizontal span between the exterior and first-interior girder near Corner 2 of the abutment. These internal, shear forces are given by

$$V_{eXC2} = \left[\frac{\left(M_{YC2} + \frac{M_{YC2}}{2}\right)}{\left(\frac{s_{girder}}{\cos\theta}\right)}\right] \tag{8.118}$$

For the second-horizontal span of the composite, backwall and backwall-pile cap between the first-interior and second-interior girder, the assumed, induced, internal, end-shear forces, V_{iXC2}, are expressed by

$$V_{iXC2} = \left[\frac{\left(\frac{M_{YC2}}{2} + \frac{M_{YC2}}{4}\right)}{\left(\frac{s_{girder}}{\cos\theta}\right)}\right] \tag{8.119}$$

In Eqs. 8.118 and 8.119, the moment terms $M_{YC2}/2$ and $M_{YC2}/4$ are the "carry-over moments" for the continuous, composite, backwall and backwall-pile cap that is horizontally supported by the bridge girders. These shear forces in the abutment induce the axial forces, $P_{egC2-\ell}$ and $P_{igC2-\ell}$ in the exterior girder and first interior girder,

respectively, that are given by Eqs. 8.120 and 8.121, respectively. These shear forces and axial forces are in addition to the shear forces and axial forces that are induced in these two girders by the soil forces and pile forces and moment for the abutment backwall and its pile cap.

$$P_{egC2-\ell} = \left[\frac{\left(\frac{3M_{YC2}}{2} \right)}{s_{girder}} \right] - R_{\ell C2} \tag{8.120}$$

$$P_{igC2-\ell} = \left[\frac{\left(\frac{9M_{YC2}}{4} \right)}{s_{girder}} \right] \tag{8.121}$$

The girder forces $P_{egC2\text{-}\ell}$ and $P_{igC2\text{-}\ell}$ are a compression force in the exterior girder and a tension force in the first-interior girder, respectively.

Since vertical eccentricities occur between the lines-of-action for the sidewall-pile shear forces, $V_{sw2p\text{-}\ell}$ and $V_{sw2p\text{-}t}$; for the passive-soil-pressure force, $W_{sw2s\text{-}Z}$, that acts against the trapped soil, which is adjacent to the composite, sidewall and sidewall-pile cap; and for the passive-soil-pressure forces, $W_{ww2sa\text{-}Z}$ and $W_{ww2sb\text{-}Z}$, that act against the trapped soil, which is adjacent to the wingwall and the center of gravity for the composite, backwall and backwall-pile cap, a resultant, internal, support-bending-moment reaction, M_{tC2}, and a resultant, internal, support-torsional-moment reaction, $M_{\ell C2}$, develops at the assumed, Yt-plane, fixed support at the bearing point for the exterior, PC girder. The bending-moment reaction M_{tC2} and the torsional-moment

reaction $M_{\ell C1}$, whose moment vectors act in directions that are parallel to the positive t-axis and positive ℓ-axis, respectively, for the bridge superstructure are given by

$$
\begin{aligned}
M_{tC2} = & -\left(P_{sw2p\text{-}Y} e_{sw2p\text{-}\ell}\right) + \left[V_{sw2p\text{-}\ell}\left(\frac{h_{abut}}{2} - \frac{d_{emb}}{2}\right)\right] \\
& + M_{sw2p\text{-}t} + \left[W_{sw2s\text{-}Z}\,\ell_{sw2}\left(\frac{h_{abut}}{6}\right)\cos\theta\sin\theta\right] \\
& - \left[W_{ww2sa\text{-}Z}\left(\frac{h_{abut}}{2} - \frac{2h_{wa}}{3}\right) + W_{ww2sb\text{-}Z}\left(\frac{h_{abut}}{2} - \frac{2h_{wb}}{3}\right)\right]\frac{\ell_{ww2}}{2}\cos\theta\sin\theta \\
& + \left\{W_{sw2w-Y}\left[\frac{e_{sw2s-X}}{\cos\theta} - \left(c_{girderC2-t} - \frac{B_{sw}}{2}\right)\tan\theta\right]\right. \\
& \qquad \left. + W_{sw2wcap-Y}\left[\frac{e_{sw2s-X}}{\cos\theta} - \left(c_{girderC2-t} - \frac{B_{swcap}}{2}\right)\tan\theta\right]\right\}\ell_{sw2c} \\
& + \left\{W_{ww2wa-Y}\left[\frac{e_{ww2sa-X}}{\cos\theta} - \left(c_{girderC2-t} - \frac{B_{sw}}{2}\right)\tan\theta\right]\right. \\
& \qquad \left. + W_{ww2wb-Y}\left[\frac{e_{ww2sb-X}}{\cos\theta} - \left(c_{girderC2-t} - \frac{B_{wwe}}{2}\right)\tan\theta\right]\right\}\frac{\ell_{ww2}}{2}
\end{aligned}
\tag{8.122}
$$

$$
\begin{aligned}
M_{\ell C2} = & +\left(P_{sw2p\text{-}Y} e_{sw2p\text{-}t}\right) + \left[V_{sw2p\text{-}t}\left(\frac{h_{abut}}{2} - \frac{d_{emb}}{2}\right)\right] + M_{sw2p\text{-}\ell} + \left[W_{sw2s\text{-}Z}\,\ell_{sw2}\left(\frac{h_{abut}}{6}\right)\cos^2\theta\right] \\
& - \left[W_{ww2sa\text{-}Z}\left(\frac{h_{abut}}{2} - \frac{2h_{wa}}{3}\right) + W_{ww2sb\text{-}Z}\left(\frac{h_{abut}}{2} - \frac{2h_{wb}}{3}\right)\right]\frac{\ell_{ww2}}{2}\cos^2\theta \\
& + \left[W_{sw2w-Y}\left(c_{girderC2-t} - \frac{B_{sw}}{2}\right) + W_{sw2wcap-Y}\left(c_{girderC2-t} - \frac{B_{swcap}}{2}\right)\right]\ell_{sw2c}
\end{aligned}
$$

$$+\left[W_{ww2wa-Y}\left(c_{girderC2-t}-\frac{B_{sw}}{2}\right)+W_{ww2wb-Y}\left(c_{girderC2-t}-\frac{B_{wwe}}{2}\right)\right]\frac{\ell_{ww2}}{2} \tag{8.123}$$

The moment M_{tC2} can be assumed to be dissipated into the bridge superstructure through strong-axis bending of the exterior, PC-bridge girder. An analytical model, which is similar to the one that was used to describe how the moment M_{YC2} is resisted by the bridge superstructure, can also be used to provide a mechanism for distributing the torque $M_{\ell C2}$ into the bridge superstructure. A force couple that consists of the vertical reactions for the exterior and the first interior girder can resist the torque $M_{\ell C2}$. A positive torque is resisted by an upward reaction at the exterior girder and a downward reaction at the first interior girder. For Corner 2 of the abutment the corresponding shear forces $V_{egC2\text{-}Y}$ and $V_{igC2\text{-}Y}$ in the exterior and first interior girder, respectively, given by

$$V_{egC2-Y}=\left[\frac{\left(\frac{3M_{\ell C2}}{2}\right)}{s_{girder}}\right]-R_{YC2} \tag{8.124}$$

$$V_{igC2-Y}=\left[\frac{\left(\frac{9M_{\ell C2}}{4}\right)}{s_{girder}}\right] \tag{8.125}$$

For this model, the composite backwall and backwall-pile cap is subjected to X-axis bending and corresponding Y-axis, member-end, shear forces. For the first, vertical span of the backwall and backwall-pile cap between the exterior girder and first-interior

girder near Corner 2 of the abutment, the internal, member-end shear forces, V_{eYC2}, in the abutment are given by

$$V_{eYC2} = \left[\frac{\left(M_{\ell C2} + \frac{M_{\ell C2}}{2} \right)}{\left(\frac{s_{girder}}{\cos\theta} \right)} \right] \tag{8.126}$$

For the second, horizontal span of the composite, backwall and backwall-pile cap between the first-interior girder and second-interior girder, the induced, internal, member-end shear forces, V_{iYC2}, are expressed by

$$V_{iYC2} = \left[\frac{\left(\frac{M_{\ell C2}}{2} + \frac{M_{\ell C2}}{4} \right)}{\left(\frac{s_{girder}}{\cos\theta} \right)} \right] \tag{8.127}$$

In Eqs. 8.126 and 8.127, the moment terms $M_{\ell C2}/2$ and $M_{\ell C2}/4$ are the "carry-over moments" for the continuous, composite, backwall and backwall-pile cap that is vertically supported by the bridge girders. These shear forces are in addition to the shear forces that are induced in this member by the soil forces and pile forces and moments for the abutment backwall and its pile cap.

The moment M_{tC1} and torque $M_{\ell C1}$ can be resolved into X-axis and Z-axis components by using Eqs. 8.128 and 8.129, respectively.

$$M_{XC2} = +M_{\ell C2}\cos\theta + M_{tC2}\sin\theta \tag{8.128}$$

$$M_{ZC2} = -M_{\ell C2}\sin\theta - M_{tC2}\cos\theta \tag{8.129}$$

Positive moment vectors for the moments M_{XC2} and M_{ZC2} act along the positive, X-axis and Z-axis directions, respectively.

To establish the internal forces that act at an effective, critical-moment, tY-plane, cross section of a composite, sidewall and sidewall-pile cap, a vertical plane was taken through the sidewall at a point mid-way between the vertical-intersection lines that are formed at the intersection of the inside face of a sidewall-pile cap and the inside face of the corresponding sidewall and the back face of the abutment backwall. The horizontal-cantilever lengths for the abutment sidewalls between these vertical cross sections and the construction joint at the connection to the wingwall are the dimensions ℓ_{sw1C} and ℓ_{sw2C} near Corner 1 and Corner 2, respectively, of the abutment, as shown in Figs. 8.60 and 8.61, respectively. These figures show several free-body diagrams for the portion of an integral abutment between the critical-moment, cross section and the free end of the wingwall. The directions for the soil forces and pile forces and moments that are shown in these figures are based on a thermal expansion and a plan-view, clockwise rotation about the "point-of-fixity" for the bridge superstructure.

Figures 8.60a, 8.60b, and 8.60c show the forces that act in the XZ-plane, Yℓ-plane, and Yt-plane, respectively, at the center of gravity of the Yt-plane, effective, critical-moment, cross section for the composite, sidewall and sidewall-pile cap near Corner 1 of the abutment. These forces and moments are the axial force $P_{swC1\text{-}\ell}$, shear forces $V_{swC1\text{-}t}$ and $V_{swC1\text{-}Y}$, bending moments $M_{swC1\text{-}t}$ and $M_{swC1\text{-}Y}$ and torsional moment $M_{swC1\text{-}\ell}$. Positive force vectors and moment vectors for these internal forces and moments were selected to act in directions that are parallel to the positive t-axis, ℓ-axis,

and Y-axis directions. The center of gravity for the Yt-plane cross section through the sidewall and its pile cap is located at the distances x_{sw1cg} and y_{sw1cg} from the outside face and top face, respectively, of Sidewall 1 near Corner 1 of the abutment. In the XZ-plane (see Fig. 8.60a), the horizontal eccentricities, with respect to the effective, critical-moment section, for the sidewall-pile forces $V_{sw1p\text{-}t}$ and $V_{sw1p\text{-}\ell}$ are the dimensions $e1_{sw1p\text{-}\ell}$ and $e1_{sw1p\text{-}t}$, respectively. The horizontal eccentricities for the soil force $W_{sw1s\text{-}t}$ that acts on the sidewall and the soil forces $W_{ss1sa\text{-}t}$ and $W_{ss1sb\text{-}t}$ that act at the ends of the wingwall are the dimensions $e1_{sw1s\text{-}\ell}$, $e1_{ww1sa\text{-}\ell}$, and $e1_{ww1sb\text{-}\ell}$, respectively. In the Yℓ-plane (see Fig. 8.60b), the self-weight of the sidewall, the sidewall-pile cap, the wingwall at the end of the wingwall that is adjacent to the sidewall, and the wingwall at the free end of the wingwall are the loads $W_{sw1w\text{-}Y}$, $W_{sw1wcap\text{-}Y}$, $W_{ww1wa\text{-}Y}$, and $W_{ww1wb\text{-}Y}$, respectively. The horizontal eccentricities for the self-weight in this plane are the dimensions $e1_{sw1w\text{-}\ell}$, $e1_{sw1w\text{-}\ell}$, $e1_{sw1wa\text{-}\ell}$, and $e1_{sw1wb\text{-}\ell}$, respectively. In the Yt-plane, the eccentricities for the vertical and horizontal forces for the sidewall pile are the dimensions $e1_{sw1p\text{-}t}$ and $e1_{sw1p\text{-}Y}$, respectively. Also for this plane, the vertical eccentricities for the soil forces that act on the sidewall and its pile cap, that act on the wingwall at the connection with the sidewall, and that act on the free end of the wingwall are the dimensions $e1_{sw1s\text{-}Y}$, $e1_{ww1sa\text{-}Y}$, and $e1_{ww1sb\text{-}Y}$, respectively. Also, in the Yt-plane, the horizontal eccentricities for the self-weight of the sidewall-pile cap, sidewall, and wingwall are the dimensions $e1_{sw1wcap\text{-}t}$, $e1_{sw1w\text{-}t}$, and $e1_{ww1wa\&b\text{-}t}$, respectively. All of these eccentricities, which are functions of the bridge geometry at Corner 1 of the abutment, are given by

$$e1_{sw1p-\ell} = \ell_{sw1} + \frac{1}{2}\left(B_{swcap} - B_{sw}\right)\tan\theta - c_{swp\text{-}\ell} \tag{8.130}$$

$$e1_{sw1p-t} = \frac{1}{2}B_{swcap} - x_{sw1cg} \tag{8.131}$$

$$e1_{sw1p-Y} = h_{abut} - \frac{1}{2}d_{emb} - y_{sw1cg} \tag{8.132}$$

$$e1_{sw1s-\ell} = \frac{1}{2}\ell_{sw1} + \frac{1}{2}\left(B_{swcap} - B_{sw}\right)\tan\theta \tag{8.133}$$

$$e1_{sw1s-Y} = \frac{2}{3}h_{abut} - y_{sw1cg} \tag{8.134}$$

$$e1_{ww1sa-\ell} = \frac{1}{3}\ell_{ww1} + \ell_{sw1} + \frac{1}{2}\left(B_{swcap} - B_{sw}\right)\tan\theta \tag{8.135}$$

$$e1_{ww1sa-Y} = \frac{2}{3}h_{wa} - y_{sw1cg} \tag{8.136}$$

$$e1_{ww1sb-\ell} = \frac{2}{3}\ell_{ww1} + \ell_{sw1} + \frac{1}{2}\left(B_{swcap} - B_{sw}\right)\tan\theta \tag{8.137}$$

$$e1_{ww1sb-Y} = \frac{2}{3}h_{wb} - y_{sw1cg} \tag{8.138}$$

$$e1_{sw1wcap-\ell} = e1_{sw1s-\ell} \tag{8.139}$$

$$e1_{sw1wcap-t} = e1_{sw1p-t} \tag{8.140}$$

$$e1_{sw1w-\ell} = e1_{sw1s-\ell} \tag{8.141}$$

$$e1_{sw1w-t} = x_{sw1cg} - \frac{1}{2}B_{sw} \tag{8.142}$$

$$e1_{ww1wa-\ell} = e1_{ww1sa-\ell} \tag{8.143}$$

$$e1_{ww1wa-t} = e1_{sw1w-t} \tag{8.144}$$

$$e1_{ww1wb-\ell} = e1_{ww1sb-\ell} \tag{8.145}$$

$$e1_{ww1wb-t} = x_{sw1cg} - \frac{1}{2}B_{wwe} \tag{8.146}$$

The axial force, shear forces, bending moments, and torsional moments at the effective, critical-moment, Yt-plane, cross section are induced by the passive-soil pressure, pile forces and moments, and self-weight of the sidewall and its pile cap and the wingwall. The soil forces that are shown in Fig. 8.60a correspond with the passive-soil pressures $w_{soil\text{-}t}$ that is shown in Fig. 8.60c. If the axial force in a sidewall pile is assumed to be equal to the pile-driving capacity that is listed in the design drawing for a bridge and the shear forces and bending moments at the head of the sidewall pile are assumed to be equal to those forces and moments that are associated with the plastic, biaxial-bending, moment resistance of the HP-shaped pile, which was discussed in Section 8.8.2.2, the forces and moments can be calculated at the effective, critical-moment, Yt-plane, cross section by applying static equilibrium to the free-body diagrams that are shown in these figures. These forces and moments are evaluated for the critical-moment section near Corner 1 of the abutment using Eqs. 8.147 thru 8.152.

$$P_{swC1\text{-}\ell} = -V_{sw1p\text{-}\ell} \tag{8.147}$$

$$V_{swC1\text{-}t} = V_{sw1p\text{-}t} + W_{sw1s\text{-}t}\ell_{sw1c} + \frac{1}{2}\left(W_{ww1sa\text{-}t} + W_{ww1sb\text{-}t}\right)\ell_{ww1} \tag{8.148}$$

$$V_{swC1\text{-}Y} = -P_{sw1p\text{-}Y} + \left(W_{sw1w\text{-}Y} + W_{sw1wcap\text{-}Y}\right)\ell_{sw1c} + \frac{1}{2}\left(W_{ww1wa\text{-}Y} + W_{ww1wb\text{-}Y}\right)\ell_{ww1} \tag{8.149}$$

$$\begin{aligned} M_{swC1\text{-}Y} = &-\left(V_{sw1p\text{-}t}e1_{sw1p\text{-}\ell}\right) - \left(V_{sw1p\text{-}\ell}e1_{sw1p\text{-}t}\right) - \left(W_{sw1s-t}\ell_{sw1c}e1_{sw1s-\ell}\right) \\ &- \left[\frac{1}{2}\left(W_{ww1sa-t}\right)\ell_{ww1}e1_{ww1sa-\ell}\right] - \left[\frac{1}{2}\left(W_{ww1sb-t}\right)\ell_{ww1}e1_{ww1sb-\ell}\right] \end{aligned} \tag{8.150}$$

$$M_{swC1-t} = -\left(P_{sw1p-Y}e1_{sw1p-\ell}\right) + \left(V_{sw1p-\ell}e1_{sw1p-Y}\right) + M_{sw1p-t}$$

$$+\left(W_{sw1w-Y}\ell_{sw1c}e1_{sw1w-\ell}\right)+\left(W_{sw1wcap-Y}\ell_{sw1c}e1_{sw1wcap-\ell}\right)$$

$$+\left[\frac{1}{2}\left(W_{ww1wa-Y}\right)\ell_{ww1}e1_{ww1wa-\ell}\right]+\left[\frac{1}{2}\left(W_{ww1wb-Y}\right)\ell_{ww1}e1_{ww1wb-\ell}\right] \tag{8.151}$$

$$M_{swC1-\ell}=M_{sw1p-\ell}+\left(P_{sw1p-Y}e1_{sw1p-t}\right)+\left(V_{sw1p-t}e1_{sw1p-Y}\right)$$

$$+\left(W_{sw1s-t}\ell_{sw1c}e1_{sw1s-Y}\right)$$

$$-\left\{\left[\frac{\left(W_{ww1sa}e1_{ww1sa-Y}\right)+\left(W_{ww1sb}e1_{ww1sb-Y}\right)}{2}\right]\ell_{ww1}\right\}$$

$$-\left\{\left[\left(W_{sw1wcap-Y}e1_{sw1wcap-t}\right)-\left(W_{sw1w-Y}e1_{sw1w-t}\right)\right]\ell_{sw1c}\right\}$$

$$+\left\{\left[\left(W_{ww1wa}e1_{ww1wa-t}\right)+\left(W_{ww1wb}e1_{ww1wb-t}\right)\right]\frac{\ell_{ww1}}{2}\right\} \tag{8.152}$$

Near Corner 2 of an integral abutment, Figs. 8.61a, 8.61b, and 8.61c show the axial force $P_{swC2-\ell}$, shear forces V_{swC2-t} and V_{swC2-Y}, bending moments M_{swC2-t} and M_{swC2-Y} and torsional moment $M_{swC2-\ell}$ that act in the XZ-plane, Yℓ-plane, and Yt-plane, respectively, at the center of gravity of the Yt-plane, effective, critical-moment, cross section for the composite, sidewall and sidewall-pile cap. Again, positive force vectors and moment vectors for these internal forces and moments were selected to act in directions that are parallel to the positive t-axis, ℓ-axis, and Y-axis directions. The center of gravity for the Yt-plane cross section through the sidewall and its pile cap is located at the distances x_{sw2cg} and y_{sw2cg} from the outside face and top, respectively, of the sidewall near Corner 2 of the abutment.

In the XZ-plane (see Fig. 8.61a), the horizontal eccentricities, with respect to the effective, critical-moment section, for the sidewall-pile forces $V_{sw2p\text{-}t}$ and $V_{sw2p\text{-}\ell}$ are the dimensions $e1_{sw2p\text{-}\ell}$ and $e1_{sw2p\text{-}t}$, respectively. The horizontal eccentricities for the soil force $W_{sw2s\text{-}Z}$ that acts on trapped soil, which is adjacent to the sidewall and its pile cap, and the soil forces $W_{ss2sa\text{-}Z}$ and $W_{ss2sb\text{-}Z}$ that act on the trapped soil, which is adjacent to the ends of the wingwall are the dimensions $e1_{sw2s\text{-}X}$, $e1_{ww2sa\text{-}X}$, and $e1_{ww2sb\text{-}X}$, respectively. In the Yℓ-plane (see Fig. 8.61b), the self-weight of the sidewall, the sidewall-pile cap, the wingwall at the end of the wingwall that is adjacent to the sidewall, and the wingwall at the free end of the wingwall are the loads $W_{sw2w\text{-}Y}$, $W_{sw2wcap\text{-}Y}$, $W_{ww2wa\text{-}Y}$, and $W_{ww2wb\text{-}Y}$, respectively. The horizontal eccentricities for the self-weight in this plane are the dimensions $e1_{sw2w\text{-}\ell}$, $e1_{sw2wcap\text{-}\ell}$, $e1_{ww2wa\text{-}\ell}$, and $e1_{ww2wb\text{-}\ell}$, respectively. In the Yt-plane, the eccentricities for the vertical and horizontal pile forces are the dimensions $e1_{sw2p\text{-}t}$ and $e1_{sw2p\text{-}Y}$, respectively. Also for this plane, the vertical eccentricities for the soil forces that act on the trapped soil, which is adjacent to the sidewall and its pile cap; that act on the trapped soil, which is adjacent to the wingwall at the connection with the sidewall; and that acts on the trapped soil, which is adjacent to the free end of the wingwall are the dimensions $e1_{sw2s\text{-}Y}$, $e1_{sw2sa\text{-}Y}$, and $e1_{sw2sb\text{-}Y}$, respectively. Also, in the Yt-plane, the horizontal eccentricities for the self-weight of the sidewall-pile cap, sidewall, and wingwall are the dimensions $e1_{sw2wcap\text{-}t}$, $e1_{sw2w\text{-}t}$, and $e1_{ww2wa\&b\text{-}t}$, respectively. All of these eccentricities, which are functions of the bridge geometry at Corner 2 of the abutment, are given by

$$e1_{sw2p-\ell} = \ell_{sw2} - \frac{1}{2}\left(B_{swcap} - B_{sw}\right)\tan\theta - c_{swp\text{-}\ell} \tag{8.153}$$

$$e1_{sw2p-t} = \frac{1}{2}B_{swcap} - x_{sw2cg} \tag{8.154}$$

$$e1_{sw2p-Y} = h_{abut} - \frac{1}{2}d_{emb} - y_{sw2cg} \tag{8.155}$$

$$e1_{sw2s-X} = \left[\frac{1}{2}\ell_{sw2} - \frac{1}{4}\left(B_{swcap} - B_{sw}\right)\tan\theta\right]\cos\theta \tag{8.156}$$

$$e1_{sw2s-Y} = \frac{2}{3}h_{abut} - y_{sw2cg} \tag{8.157}$$

$$e1_{ww2sa-X} = \left[\frac{1}{3}\ell_{ww2} + \ell_{sw2} - \frac{1}{2}\left(B_{swcap} - B_{sw}\right)\tan\theta\right]\cos\theta \tag{8.158}$$

$$e1_{ww2sa-Y} = \frac{2}{3}h_{wa} - y_{sw2cg} \tag{8.159}$$

$$e1_{ww2sb-X} = \left[\frac{2}{3}\ell_{ww2} + \ell_{sw2} - \frac{1}{2}\left(B_{swcap} - B_{sw}\right)\tan\theta\right]\cos\theta \tag{8.160}$$

$$e1_{ww2sb-Y} = \frac{2}{3}h_{wb} - y_{sw2cg} \tag{8.161}$$

$$e1_{sw2wcap-\ell} = \frac{e1_{sw2s-X}}{\cos\theta} \tag{8.162}$$

$$e1_{sw2wcap-t} = e1_{sw2p-t} \tag{8.163}$$

$$e1_{sw2w-\ell} = \frac{e1_{sw2s-X}}{\cos\theta} \tag{8.164}$$

$$e1_{sw2w-t} = x_{sw2cg} - \frac{1}{2}B_{sw} \tag{8.165}$$

$$e1_{ww2wa-\ell} = \frac{e1_{ww2sa-X}}{\cos\theta} \tag{8.166}$$

$$e1_{ww2wa-t} = e1_{sw2w-t} \tag{8.167}$$

$$e1_{ww2wb-\ell} = \frac{e1_{ww2sb-X}}{\cos\theta} \tag{8.168}$$

$$e1_{ww2wb-t} = x_{sw2cg} - \frac{1}{2}B_{wwe} \tag{8.169}$$

The axial force, shear forces, bending moments, and torsional moments at this vertical cross section are induced by the passive-soil pressure, pile forces and moments, and self-weight of the sidewall and its pile cap and the wingwall. The soil forces that are shown in Figs. 8.61a correspond with the passive-soil pressures w_{soil-Z} that is shown in Fig. 8.61c. If the axial force in a sidewall pile is assumed to be equal to the pile-driving capacity that is listed in the design drawing for a bridge and the shear forces and bending moments at the head of the sidewall pile are assumed to be equal to those forces and moments that are associated with the plastic, biaxial-bending, moment resistance of the HP-shaped pile, which was discussed in Section 8.8.2.2, the forces and moments can be calculated at the effective, critical-moment, Yt-plane, cross section that is shown in Fig. 8.61 by applying static equilibrium to the free-body diagrams that are shown in these figures. These forces and moments are evaluated for the critical-moment section near Corner 2 of the abutment using Eqs. 8.170 thru 8.175.

$$P_{swC2-\ell} = -V_{sw2p-\ell} - \left(W_{sw2s-Z}\ell_{sw2c}\cos\theta\sin\theta\right)$$

$$-\left[\left(\frac{W_{ww2sa-Z} + W_{ww2sb-Z}}{2}\right)\ell_{ww2}\cos\theta\sin\theta\right] \tag{8.170}$$

$$V_{swC2-t} = V_{sw2p-t} + \left(W_{sw2s-Z}\ell_{sw2c}\cos^2\theta\right)$$

$$+\left(\frac{W_{ww2sa\text{-}Z}+W_{ww2sb\text{-}Z}}{2}\right)\ell_{ww2}\cos^2\theta \tag{8.171}$$

$$V_{swC2\text{-}Y}=-P_{sw2p\text{-}Y}+\left[\left(W_{sw2w\text{-}Y}+W_{sw2wcap-Y}\right)\ell_{sw2c}\right]$$

$$+\left(\frac{W_{ww2wa\text{-}Y}+W_{ww2wb\text{-}Y}}{2}\right)\ell_{ww2} \tag{8.172}$$

$$M_{swC2\text{-}Y}=-\left(V_{sw2p\text{-}t}e1_{sw2p-\ell}\right)+\left(V_{sw2p\text{-}\ell}e1_{sw2p-t}\right)$$

$$-\left(W_{sw2s\text{-}Z}\ell_{sw2c}e_{sw2s\text{-}X}\cos\theta\right)$$

$$-\left[\left(\frac{W_{ww2sa-Z}}{2}\right)\ell_{ww2}e1_{ww2sa-X}\cos\theta\right]$$

$$-\left[\left(\frac{W_{ww2sb\text{-}Z}}{2}\right)\ell_{ww2}\,e_{ww2sb\text{-}X}\cos\theta\right] \tag{8.173}$$

$$M_{swC2-t}=-\left(P_{sw2p-Y}e1_{sw2p-\ell}\right)+\left(V_{sw2p-\ell}e1_{sw2p-Y}\right)+M_{sw2p-t}$$

$$+\left[\left(W_{sw2s-Z}\ell_{sw2c}e1_{sw2s-Y}\right)\cos\theta\sin\theta\right]$$

$$-\left[\left(W_{ww2sa-Z}e1_{ww2sa-Y}\right)+\left(W_{ww2sb-Z}e1_{ww2sb-Y}\right)\right]\frac{\ell_{ww2}}{2}\cos\theta\sin\theta$$

$$+\left(W_{sw2w-Y}\ell_{sw2c}e1_{sw2w-\ell}\right)+\left(W_{sw2wcap-Y}\ell_{sw2c}e1_{sw2wcap-\ell}\right)$$

$$+\left[\frac{1}{2}\left(W_{ww2wa-Y}\right)\ell_{ww2}e1_{ww2wa-\ell}\right]+\left[\frac{1}{2}\left(W_{ww2wb-Y}\right)\ell_{ww2}e1_{ww2wb-\ell}\right] \tag{8.174}$$

$$M_{swC2\text{-}\ell}=-M_{sw2p-\ell}+\left(P_{sw2p-Y}e1_{sw2p\text{-}t}\right)-\left(V_{sw2p-t}e1_{sw2p-Y}\right)$$

$$-\left(W_{sw2s-Z}\ell_{sw2c}\;e1_{sw2s-Y}\cos^2\theta\right)$$

$$+\left\{\left[\left(W_{ww2sa}e1_{ww2sa-Y}\right)+\left(W_{ww2sb}e1_{ww2sb-Y}\right)\right]\frac{\ell_{ww2}}{2}\cos^2\theta\right\}$$

$$-\left(W_{sw2wcap-Y}e1_{sw2wcap-t}\right)+\left(W_{sw2w-Y}e1_{sw2w-t}\right)$$

$$+\left\{\left[\left(W_{ww2wa}e1_{ww2wa-t}\right)+\left(W_{ww2wb}e1_{ww2wb-t}\right)\right]\frac{\ell_{ww2}}{2}\right\} \tag{8.175}$$

8.8.4. Design strengths for biaxial bending and biaxial shear plus torsion

The selection of an appropriate design specification to be applied for the evaluation of the resistance of reinforced-concrete members was based on applying a single specification for the design of all reinforced-concrete members, on specific limitations that are associated with a particular design specification, and on the familiarity of bridge engineers with a particular design specification. Regarding a specific limitation of a design specification, the service-load method and the load-factor method in the AASHTO Standard Specifications for Highway Bridges (1996) do not address the topic of torsional resistance for concrete members. The AASHTO LRFD Bridge Design Specifications (1998) addresses many of the design criteria that are needed for the design of reinforced-concrete members; however, this specification is not applied at the present time by engineers with the Office of Bridges and Structures at the Iowa Department of Transportation to design members of a bridge substructure. Because of these reasons and to take a slightly more conservative approach for the design of the reinforced-concrete members an integral abutment, the ISU researchers used the load factors from the AASHTO Standard Specification and selected the ACI Building Code (1999, 2002) to evaluate of the design resistances for shear force, bending moment, and torsional

moment. The ACI Code resistance factors were applied to compute these design resistances.

Article 9.1 of the ACI Building Code (1999, 2002) specifies the strength limit-states as

$$\phi R_n \geq R_u \tag{8.176}$$

where, ϕ is a resistance factor, R_n is a nominal resistance, and R_u is a factored-level-load effect. When a member cross section is subjected to combined forces and moments, the interaction of those forces and moments need to be considered in the design of that member. Therefore, the strength-limit state given by Eq. 8.176 needs to be re-written as an interaction expression. A single interaction relationship that involves axial force, biaxial-shear forces, biaxial-bending moments, and torsional moments is not presented in design specifications, textbooks, or published literature on reinforced-concrete design. Conventional design practice suggests the use of two, linear, interaction relationships. When the axial force has an insignificant effect on the design of a concrete cross section, the ISU researchers recommend the application of Eq. 8.177 for biaxial-bending moments and Eq. 8.178 for biaxial-shear forces and torsion, respectively, for a reinforced-concrete member that has an XY-plane cross section and that has a longitudinal axis that is the Z-axis.

$$\frac{M_{uX}}{\phi_b M_{nX}} + \frac{M_{uY}}{\phi_b M_{nY}} \leq 1.0 \tag{8.177}$$

$$\frac{T_{uZ}}{\phi_v T_{nZ}} + \frac{V_{uX}}{\phi_v V_{nX}} + \frac{V_{uY}}{\phi_v V_{nY}} \leq 1.0 \tag{8.178}$$

where, M_{uX} and M_{uY} are the factored-level, bending moments about the X-axis and Y-axis, respectively; M_{nX} and M_{nY} are the nominal, moment strengths for uniaxial bending about the X-axis and Y-axis, respectively; T_{uZ} is the factored-level, torsional moment about the Z-axis; V_{uX} is the factored-level, shear force in the X-axis direction; V_{uY} is the factored-level, shear force in the Y-axis direction; T_{nZ} is the nominal, torsional strength about the Z-axis; V_{nX} is the nominal, shear strength in the X-axis direction; V_{nY} is nominal, shear strength in the Y-axis direction for an abutment cross section; and ϕ_b and ϕ_v are the resistance factors for bending and for shear and torsion, respectively. The ACI Building Code (2002) sets the resistance factors ϕ_b and ϕ_v equal to 0.90 and 0.75, respectively.

When the overall depth of a cross section is relatively large in comparison with the length of a span or with the shear span, flexural-bending strains are no longer linear throughout the depth of that cross section. Therefore, the shear-strength and moment-strength behavior for the member are affected by the non-linear, flexural-strain distribution. Three categories of deep-flexural members, which are shown in Fig. 8.62, have a span, ℓ, to overall depth, h, ratio of about five or less, or have a shear span, e, less than about twice their depth (Nelson and Winter, 1991 and Wang and Salmon, 1998). Article 10.7 of the ACI Building Code (1999) defines a deep-flexural member for a continuous span, as a member with an overall-depth-to-clear-span ratio, h/ℓ, greater than 2/5. The same article in the 2002 edition of the ACI Code (2002) has revised the definition for deep-flexural members, as a member with an h/d-ratio greater than 0.20, or as a member that has a concentrated load within a distance of twice the depth of the

member from a support. A Category-A, deep-flexural member, which is shown in Fig. 8.62a, has loads applied on one horizontal surface and the support reactions are on the opposite horizontal surface for the beam. A Category-B, deep-flexural member, which is shown in Fig. 8.62b, has the applied loads and support reactions on the same horizontal surface of the beam. A Category-C, deep-flexural member, which is shown in Fig. 8.62c, has the loads applied throughout the depth of the member.

Article 10.7 of the ACI Building Code (1999, 2002) applies for flexural and shear design. Nelson and Winter (1991) stated that the bending strength of a deep-flexural member can be predicted with sufficient accuracy using the same methods that are used to predict the bending strength of a beam that is not classified as a deep-flexural member. Also, these authors noted that the shear strength of a deep-flexural member can be as much as two or three times greater than the strength predicted from the ACI Building Code equations for a flexural member that is not classified as a deep-flexural member. Article 11.8 of the ACI Building Code (1999, 2002) states that the special-shear provisions for a deep-flexural member only apply for a Category-A, deep-flexural member. The shear-strength design for Category-B and Category-C, deep-flexural members can be considered to be the same as that for a beam that is not classified as a deep-flexural member. Article 11.8 of the ACI Building Code (1999, 2002) requires a continuous, deep-flexural member to be designed for shear in accordance with the non-deep-flexural member, shear-strength criteria. However, the ACI Building Code, special provisions for flexural members must be followed for that design. The special provisions involve the location of the critical-shear section, nominal-shear strength, shear strength

provided by the shear reinforcement, and minimum areas for the vertical-shear reinforcement and horizontal-shear reinforcement.

8.8.4.1. Abutment backwall and backwall-pile cap

A backwall-pile cap is subjected to vertical, dead-load reactions from the bridge girders, the self-weight of the pile cap and the abutment backwall, and the axial force in the abutment piles, as was shown in Fig. 8.31. Since all of these vertical forces act in the YZ-plane for the pile cap, only X-axis-bending moment and Y-axis-shear forces are induced in an XY-plane cross section of the pile cap. When the backwall-pile cap resists dead loads in the YZ-plane, the pile cap is classified as a Category-A, deep-flexural member.

The composite, backwall and backwall-pile cap for an integral abutment that was shown in Fig. 8.32 is subjected to member-end forces from the composite, bridge girders and piles; passive-soil pressures; and soil-frictional forces that induce an internal axial force, biaxial-shear forces, biaxial-bending moments, and torsional moments in the abutment. The internal-axial force that exists in a composite, backwall and backwall-pile cap is assumed to have a negligible effect on the design of an abutment, since the cross-sectional area of an integral abutment cross is very large. The composite, backwall and backwall-pile cap is classified as Category-C, deep-flexural member for the loads that are applied in YZ-plane, since the gravity load and girder reactions are applied along the depth of the beam. The composite, backwall and backwall-pile cap is classified as a Category-A, deep-flexural member for the loads that are applied parallel to the XZ-plane, since the soil pressure acts on the back face of the abutment and the girder axial loads, which are significantly larger than the pile horizontal reactions, act on the front face of

the abutment. The ACI, special-shear provisions apply in the design of a backwall-pile cap for gravity loads and in the design of an integral abutment for horizontal loads. For the shear design of an integral abutment that is subjected to only vertical loads, the ACI, special-shear provisions do not apply for this part of the design.

The abutment backwalls and backwall-pile caps for the integral-abutment bridges that are constructed in the State of Iowa contain the steel-bar reinforcement that is shown in Figs. 8.63 thru 8.65. Longitudinal #k bars are placed along the vertical and top horizontal faces of the pile cap, pairs of #m bar, closed-looped stirrups that are evenly spaced between the piles, #j bar, spiral reinforcement around each pile, and #o bent bars at the front and back faces of the pile cap at each pile comprise the reinforcement in an backwall-pile cap. An embedment depth, d_{emb}, is specified for the piles that are evenly spaced along the abutment length. Figure 8.64 shows a partial, XZ-plane cross section through a pile cap for an abutment backwall. For the geometrical configuration shown in the figure, a bridge girder is located midway between two piles for alternate spans of the abutment cap. The distance B represents the length of the pile cap that was analyzed in Section 8.8.2.3.

Figure 8.65 shows an XY-plane cross section for a composite, backwall and backwall-pile cap of an integral abutment. The #s bar, longitudinal reinforcement within the backwall represents only a minimal amount of steel. Closed-looped stirrups are not used along the full depth of the cross section for flexural-shear reinforcement or torsional-shear reinforcement. The abutment backwall and its pile cap are tied together with large-diameter, vertical-dowel, #p bars in the front face and back face of the abutment backwall. These bars do not extend to the bottom of the backwall-pile cap and

they are not hooked at their ends. Only the vertical bars in the back face of the abutment backwall are lapped with equal-sized, #q bent bars that extend into the bridge deck.

Since the PC girders are embedded into the abutment backwall (see Fig. 8.65), the typical connection between a PC girder and the abutment would require that the longitudinal, #s bar, reinforcement, which is along the front face to the abutment backwall, to terminate at the sides faces of the bridge girders. With this type of a reinforcement detail, continuity of the longitudinal reinforcement in the abutment does not exist for the negative-bending-moment resistance of the composite, backwall and backwall-pile cap in the XZ-plane of the abutment, when passive-soil pressures occur behind the abutment, and for the torsional-moment resistance of this composite section in the XY-plane of the abutment. Without the continuity of the reinforcing bars, the horizontal-support condition for the abutment at each PC-girder location is a simple support. Then, the portions of the abutment between the PC girders resemble single-span, notched-end beams that are horizontally supported by the PC girders. If the magnitude of the required, XZ-plane, negative-bending moment in an abutment at the location of a PC girder or the magnitude of the required, XY-plane, torsional moment in an abutment requires continuity of the longitudinal steel along the inside face of the abutment backwall for adequate bending-moment resistance or torsional-moment resistance, the ISU researchers recommend the placement of PVC sleeves through the webs of the PC girders to permit sections of #s bars to pass through the girder webs and be lapped with the longitudinal #s bars along this face of the abutment backwall. The horizontal alignment of these PVC sleeves would need to correspond with the skew angle for the bridge.

Article 11.6 of the ACI Code (2002) specifies that when the torsional strength of the concrete in a cross section of an integral abutment is not sufficient to resist the torsional moment (M_Z-moment in an XZ-plane of the abutment), closed-looped stirrups must be provided and that equally-spaced, longitudinal reinforcement shall be placed around the perimeter of the cross section of the abutment. These longitudinal bars are to be located just inside of the closed-looped stirrups. Also, a longitudinal bar is required to be positioned at the corners of the cross section for the member.

For a non-skewed, integral-abutment bridge, the transverse reinforcement in the bridge deck that is located over the abutment can be considered to be effective for the bending-moment-strength and torsional-moment-strength design of the integral abutment. However, for a skewed, integral-abutment bridge, the transverse reinforcement in the bridge deck is oriented at an angle to the longitudinal direction of the abutment. When a skewed alignment for the transverse reinforcement in the bridge deck is used, these bars are terminated at the back face of the abutment. Therefore, this reinforcement can not be used to provide bending-moment strength and torsional-moment strength for the abutment. The ISU researchers recommend that when required for bending-moment strength and torsional-moment strength for an abutment of a skewed, integral-abutment bridge, additional longitudinal reinforcement (along the Z-axis of the abutment) must be used within the width of the abutment and within the thickness of the bridge deck.

As discussed in Section 8.8.3, the connection of an abutment sidewall to the backwall will induce significant Y-axis-bending moments into the portion of the abutment backwall between the exterior girder and the first interior girder. The ISU researchers recommend that the longitudinal reinforcement in the vertical faces of the backwall,

which is required near the connection with the sidewall, be extended to the first interior girder. To accommodate this reinforcement placement, the horizontal reinforcement must pass through the web of the exterior PC girder. Again, PVC sleeves would need to be placed through the webs of the exterior girders prior to casting the concrete for these girders.

8.8.4.2. Abutment wingwall, sidewall, and sidewall-pile cap

A wingwall for an integral abutment cantilevers from the end of an abutment sidewall or, if the abutment does not have a sidewall, from the abutment backwall. The wingwall is classified as a deep-flexural member in the YZ-plane and a non-deep-flexural member in the XZ-plane. The composite, sidewall and sidewall-pile cap is classified as a deep-flexural member in the YZ-plane and XZ-plane. Since the span-to-depth ratios for an abutment wingwall and sidewall are small, special shear provisions and reinforcement size and spacing requirements, such as those in the ACI Code (2002), need to be applied for the design of these walls.

An abutment wingwall is subjected to biaxial-shear forces and biaxial-bending moments. These forces and moments at a vertical cross section of an abutment wingwall are induced by the passive-soil pressures that act on the wingwall and by the self-weight of the wingwall. Each sidewall of an abutment is subjected to an axial force, biaxial-shear forces, biaxial-bending moments, and torsional moments. These forces and moments at a vertical cross section of an abutment sidewall are induced by the passive-soil pressures that act on the sideside and wingwall and by the sidewall pile that is embedded into the bottom of the sidewall-pile cap.

For a composite, sidewall and sidewall-pile cap, the location for the critical-shear section near the connection of this portion of the abutment to the composite, backwall and backwall-pile cap is dependent on the direction of the transverse-shear force that is induced by the passive-soil pressures. The torsional moment that occurs in a composite, sidewall and sidewall-pile cap may require that closed-looped stirrups be used not only within the sidewall-pile cap but also within the sidewall and that additional longitudinal bars be used along the vertical, top, and bottom faces of the sidewall and its pile cap. The general reinforcement requirements in the ACI Code (2002) that apply for flexural shear and torsional shear in the composite, sidewall and sidewall-pile cap are the same as those that were discussed for the composite, backwall and backwall-pile cap in Section 8.8.4.1. An effective, critical-moment section for a composite, sidewall and sidewall-pile cap is essentially located at the back face of the abutment backwall.

Figures 8.66 thru 8.69 show the steel reinforcement in an abutment wingwall, sidewall, and sidewall-pile cap that is used by the Iowa DOT for their integral-abutment bridges. A comparison of Figs. 8.63 and 8.67 reveals that the reinforcement, which is used in the sidewall-pile cap, is similar to that which is used in a backwall-pile cap. However, two differences are noted in the amount of reinforcement for these pile caps. One less #k longitudinal bar is used in the sidewall-pile cap and the pairs of #o bent bars that surround a pile at the bottom of the backwall-pile cap are not present around the sidewall pile. The vertical reinforcement (#p bar) in the abutment backwall (see Fig. 8.65) is significantly larger than the vertical reinforcement (#u bar) in an abutment sidewall (see Figs. 8.66 and 8.67).

As shown in Fig. 8.68, the exterior, PC girder interrupts the continuity of the front-face, horizontal reinforcement for the abutment backwall at the connection to the sidewall. When passive-soil pressure acts on the outside face of the sidewall and wingwall, the acute angle between the sidewall and the backwall at Corner 2 of the abutment will tend to close and cause a vertical concrete crack to develop in the front face of the backwall adjacent to the PC girder. A similar situation exists at the obtuse-angle corner (Corner 1) of the abutment. The ISU researchers recommend that the #h corner bars that are shown in Fig. 8.68 be extended through PVC sleeves that pass through the web of an exterior girder. Then, these corner bars would be lapped with the #s bars in the front face of the abutment backwall and with the #v bars that are in the outside face of the abutment sidewall. At this same joint, when passive-soil pressures act on the inside face of the sidewall and wingwall, the acute-angle corner of the abutment that is shown in Fig. 8.68 will tend to open and induce tension in the #s bars that are in the back face of the abutment backwall. Minimal embedment length is available for a straight-end extension of these #s bars into the abutment sidewall. Again, a similar situation exists at the obtuse-angle corner of the abutment. The ISU researchers recommend that if the thickness, B_{sw}, of the sidewall is not large enough to fully develop the #s bars, a standard ACI hook should be used at this end of the #s bars to provide sufficient anchorage for these bars.

Figure 8.69 shows the relationship between the longitudinal reinforcement in the backwall-pile cap and in a sidewall-pile cap. The HP-shaped pile at the end of the abutment backwall prevents a full extension into the backwall-pile cap of the #w bars that are at the inside face of the sidewall-pile cap. When passive-soil pressures act on the

inside face of this abutment wingwall and sidewall, as shown in Fig. 8.59b, the #w bars in this face of the sidewall-pile cap will be in tension. The #w bars need to have sufficient development length into the backwall-pile cap. These bars may need to be bent at their ends of allow the bars to clear the pile and extend to the front face of the backwall-pile cap.

8.8.5. Other design strengths

During an expansion cycle and a re-expansion cycle for a bridge superstructure, the soil behind an integral abutment and the abutment piles restrain the movement of an abutment. The primary resistance to the movement of an integral abutment along the ℓ-axis for a bridge superstructure during a thermally-induced, contraction cycle is provided by the abutment piles. Since the total resistance to bridge contraction is relatively small compared to the resistance to bridge expansion, the expansion and re-expansion cycles for a bridge superstructure will govern the design of an integral abutment for thermally-induced forces. Figure 8.43 shows an XY-plane, cross-sectional view of a composite backwall and backwall-pile for an integral abutment and the forces that act on the abutment when a thermal expansion occurs for the bridge superstructure. A horizontally-loaded, backwall-pile cap can be analyzed as a cantilever beam that is supported by the bottom of the abutment backwall, as shown in Fig. 8.70. A horizontally-loaded, composite backwall and backwall-pile cap can be analyzed as a continuous, deep flexural member that is horizontally supported by the PC girders, as shown in Fig. 8.32. Design criteria for the abutment backwall-to-pile-cap connection, pile-to-pile-cap connections, girder-to-abutment connections, and sidewall-to-backwall connections are discussed in the Sections 8.8.5.1, 8.8.5.2, 8.8.5.3, and 8.8.5.4, respectively.

8.8.5.1. Backwall-to-pile-cap connection

Figure 8.70 shows a free-body diagram in the XY-plane of backwall-pile cap with the forces and moments that act on the pile cap during longitudinal expansion or re-expansion of a bridge superstructure. This figure corresponds to the lower portion of Fig. 8.43. The total forces for the components of the pile-end forces in a plane that is parallel to the XY-plane of the abutment are the vertical force, $P_{pile\text{-}Y}$, horizontal force, $V_{pile\text{-}X}$, and bending moment, $M_{pile\text{-}Z}$. These forces are effectively applied at the mid-height of the pile-embedment depth, d_{emb}, into the bottom of the pile cap. These pile forces and moments and the soil pressures are resisted by a distributed vertical force, P_Y, horizontal force, V_X, and bending moment, M_Z, that act the mid-thickness of the abutment and along the entire length of the interface between the abutment-pile cap and the abutment backwall.

The vertical reinforcement that the Iowa DOT uses across the construction joint between the backwall-pile cap and the backwall is the #p dowel bars, which were shown in Fig. 8.65. Oesterle, et al. (1999) recommended that 75 percent of the required vertical reinforcement, which crosses this construction joint, should be evenly distributed within a distance that is equal to 25 percent of the center-to-center spacing of the PC girders. The remaining 25 percent of this reinforcement should be evenly distributed along the middle 50 percent of the girder spacing. Along the front face of the abutment at this construction joint, Oesterle, et al. (1999) recommended that at least the minimum amount of flexural reinforcement, which is specified in Article 10.5 of the ACI Building Code (2002), be provided across this joint and along a distance that is equal to 25 percent of the girder spacing on each side of the girders. For the remaining, front-face

regions of the abutment length, these CTL researchers recommended that at least the minimum amount of temperature and shrinkage reinforcement, which is specified for slabs in Article 7.12 of the ACI Building Code, be provided across this joint.

To control the crack width for the concrete at this joint, Oesterle, et al. (1999) recommended that the spacing, s, for this vertical, flexural reinforcement in each face of an abutment should satisfy

$$s \leq \left(\frac{540}{f_s}\right) - 2c_c \tag{8.179}$$

$$s \leq 12\left(\frac{36}{f_s}\right) \tag{8.180}$$

where, c_c is the concrete cover for the reinforcing bars that is measured from the nearest tension surface of the concrete to the closest surface of the flexural-tension reinforcement and f_s is the calculated, service-level, tension stress in the reinforcement that is expressed in ksi units. The stress f_s can be approximated as 60 percent of the minimum-specified-yield strength, f_y, for the reinforcement. These bar spacing limits are the same as those that are specified in Article 10.6.4 of the ACI Building Code (2002). Rather than providing different amounts of vertical reinforcement across this construction joint for the front and back faces of an abutment, the ISU researchers recommend using a uniform distribution of vertical reinforcement in each abutment face. The amount of reinforcement must be at least equal to the maximum amount of reinforcement across this joint that was recommended by Oesterle, et al. (1999). The spacing for this reinforcement must satisfy Eqs. 8.179 and 8.180. Also, the reinforcement across this joint must satisfy the shear-friction requirements, bar-development-length requirements,

and dowel-bar requirements in Articles 11.7, 12.1, and 15.8, respectively, of the ACI Building Code (2002).

The $M_{pile\text{-}Z}$ moment from each abutment pile needs to be effectively resisted near the mid-depth of the pile-embedment length into the bottom of the pile cap. Therefore, the ISU researchers recommend that adequate anchorage below the mid-depth of the pile-embedment length be provided for the #p-dowel-bar, vertical reinforcement shown in Fig. 8.65. Therefore, the #p-dowel bars may need to be extended to the bottom of the pile cap and an ACI 90^0 Standard hook may need to be used at the end of these bars to develop the required tensile strength for this reinforcement. Oesterle, et al. (1999) suggested that a strut-and-tie model can be applied to design for the transfer of the bending moment and shear force between an abutment pile and the pile cap. The AASHTO LRFD Specifications (1994) provides information regarding this method of an analysis.

8.8.5.2. Pile-to-pile-cap connection

The strength of the connection between the pile and the pile cap, shown in Figs. 8.71 and 8.72, must be adequate to prevent three types of failure during the maximum expansion or contraction of a bridge superstructure. These potential failures are a concrete-bearing failure at the top of a pile, when the axial load in the pile is at its maximum value; a concrete-bearing failure along the sides of a pile; and a concrete punching-shear failure along the sides of a pile.

The vertical-bearing force, P_{ebV}, at the top of a pile is expressed as

$$P_{ebV} = q_{3Y}A_3 \tag{8.181}$$

where, q_{3Y} is the concrete-bearing stress, shown in Figs. 8.71a and 8.71c, that is induced by the pile axial load, $P_{pile\text{-}Y}$, and A_3 is the bearing area. The force P_{ebV} will be equal to the force $P_{pile\text{-}Y.}$ The horizontal-bearing force, P_{ebH}, along the bottom half of the pile-embedment depth is given by

$$P_{ebH} = q_{1X} a_p b \tag{8.182}$$

with,

$$q_{1X} = q_{2X} + \frac{V_{pile\text{-}X}}{a_p b} \tag{8.183}$$

$$q_{2X} = \frac{M_{pile\text{-}Z} + \left(\frac{a_p}{2}\right) V_{pile\text{-}X}}{a_p b \left(d_{emb} - a_p\right)} \tag{8.184}$$

$$a_p = \beta_1 \left(\frac{d_{emb}}{2}\right) \tag{8.185}$$

where, a_p, b, and d_{emb} are the effective height of the concrete-bearing regions; concrete-bearing width; and pile-embedment depth, respectively; q_{1X} and q_{2X} are the concrete-bearing stresses along the bottom half and top half, respectively, of the pile-embedment depth into the bottom of the abutment pile cap, that are shown in Figs. 8.71b and 8.71c for a thermal expansion of the bridge superstructure; and β_1 is the "Whitney-Stress-Block" factor that is a function of the concrete-compression strength. The height a_p is the height of the "Whitney-Stress-Block" that is associated with the concrete, flexural-compressive strength.

Oesterle, et al. (1999) stated that Wassermann and Walker (1996) suggested an upper-bound limit of $1.9f_c'$ for the nominal, concrete-bearing stress for a pile that is embedded in concrete. An example problem in Wassermann and Walkers' publication (1986) was presented that evaluated the concrete-bearing stresses for an HP10X42 pile, which was embedded 12 in. into an abutment-pile cap. These authors compared a computed, factored-level, horizontal-bearing stresses for the pile on the surrounding concrete with a nominal, concrete-bearing stress that was equal to $3.78f_c'$. This nominal-bearing stress was based on experimental test results for eight, large inserts that were cast into a concrete slab (Burdette, et al., 1983). The inserts were used to attach machinery to a concrete floor slab at a gas centrifuge enrichment plant in Portsmouth, Ohio. Using a simple, analytical model of each of the inserts, Burdette, et al. calculated a horizontal, concrete-bearing stress for the Whitney-Stress Block near the surface of the slab for the analytical model that corresponded with the applied horizontal force that caused a failure of the particular test specimen. For the eight test specimens, the computed, ultimate, concrete-bearing stresses were equal to $2.78f_c'$, $3.55f_c'$, $3.62f_c'$, $3.65f_c'$, $3.88f_c'$, $4.02f_c'$, $4.31f_c'$, and $4.43f_c'$, and the average, concrete-bearing stress for the eight specimens was equal to $3.78f_c'$. Burdette, et al. noted that they had problems casting the concrete for the test specimens and that the low bearing strength for one of the specimen was not representative of the other specimens because the concrete surrounding this insert had begun to set before proper consolidation of the concrete was obtained and that the surface of the concrete around this insert was pocketed more than that for the other specimens. The ISU researchers believe that Oesterle, et al. (1999)

must have applied a factor of safety to Burdette, et al.'s average, bearing stress to obtain an upper-bound, concrete-bearing stress of $1.9f_c'$.

The end-bearing strength of axially-loaded, HP-shaped piles that were embedded into RC pile caps was investigated by researchers at GAI Consultants, Inc. for the Steel Pile Sub-Committee of the Committee on Construction Codes and Standards of the American Iron and Steel Institute (AISI, 1980). For the pile specimens that were tested, the ultimate, concrete-bearing stress at the end of the piles was calculated to be between about $8f_c'$ and $10f_c'$. The researchers at GAI Consultants concluded that pile-cap plate are not required at the tops of HP-shaped piles for bearing resistance, if the piles are subjected to axial-compressive loads and sufficient pile-embedment length, pile edge distance, and pile spacing is provided, and if adequate reinforcement is used in the RC pile cap.

The nominal, concrete-bearing strength, P_n, that is specified by Article 10.17 at the ACI Building Code (2002) is given by

$$P_n = 0.85f_c' A_1 \sqrt{\frac{A_2}{A_1}} \leq 1.7f_c' A_1 \qquad (8.186)$$

where, f_c' is the 28-day, compressive strength of the concrete; A_1 is the bearing area; A_2 is the effective area of the concrete support, which has an area that is geometrically similar to and has the same centroid as the area A_1. The increase in the nominal bearing strength by the term $\sqrt{\frac{A_2}{A_1}}$ is permitted because of the concrete confinement around the perimeter of the bearing area A_1. For the ACI Code, the upper-bound,

nominal, concrete-bearing stress that is equal to $1.7f_c'$. However, this maximum, bearing stress is for bearing on a concrete surface, and not for bearing on a concrete surface for a large steel insert that is embedded into the concrete. The ACI Code, design, concrete-bearing strength, $P_n\phi_c$, includes a resistance factor, ϕ_c, that is equal to 0.65.

For the connection between an abutment pile and an abutment-pile cap that has spiral reinforcement around the pile, as shown in Fig. 8.72, the ISU researchers believe that the portion of a steel pile that is embedded into the pile cap is representative of a large steel insert in a mass of concrete. Therefore, the ISU researchers recommend using a design, concrete-bearing stress of $2.46f_c'$ (0.65 times $3.78f_c'$) along the sides of the pile-embedment length. For bearing at the top of an embedded, HP-shaped pile, the ISU researchers recommend the use of the same design, concrete-bearing stress, rather than a more liberal design concrete-bearing stress of 5.20fc' (0.65 times $8f_c'$) that is based on AISI (1980). This higher bearing stress could be used at the top of a pile if the abutment piles were subjected only to axial-compressive loads. Since the abutment piles are subjected to axial compression, biaxial-bending moments, and biaxial-shear forces, the design, concrete-bearing stress should probably be somewhere between $2.46f_c'$ and $5.20f_c'$. For most applications, the computed, factored-level, concrete-bearing stress at the top of an abutment pile will be less than the lower-bound, design, concrete-bearing stress. Therefore, a pile-cap plate, which is similar to a base plate for a column, would not be needed across the pile head to reduce the concrete-bearing stresses.

When the factored-level, horizontal, concrete-bearing stress q_{u1X} and q_{u2X} are evaluated using Eqs. 8.183 and 8.184, respectively, the dimension b is normally taken to be equal to the pile dimension that is normal to the direction of these bearing stresses. If

the concrete-bearing stress q_{u1X}, which is the largest of the horizontal-bearing stresses, is too high, the presence of the spiral-bar reinforcement, which is shown in Figs. 8.72a and 8.72b, might be able to be considered to increase the effective, concrete-bearing width, b, to the diameter of the spiral. An increase bearing width would reduce the horizontal bearing stresses. If the bearing stresses are still too high, a longer embedment depth, $d_{emb,}$ must be used to reduce these bearing stresses.

A concrete-punching-shear failure through a vertical face of the pile cap may occur with large, horizontal, concrete-bearing stresses, which are directed normal to the face of the pile cap, as shown in Fig. 8.71b. These bearing stresses are induced by the pile forces $V_{pile\text{-}X}$ and $M_{pile\text{-}Z}$ that are shown in Fig. 8.71c. At the location of the concrete-bearing stress q_{1X}, the perimeter for a concrete-punching-shear failure is smaller than that associated with the concrete-bearing stress q_{2X} because of the free edge at the bottom of the pile cap.

Figure 8.72 shows a plan-view cross section, a vertical cross section, and an elevation of the concrete-bearing area adjacent to an abutment pile at the bottom of the pile cap. A portion of the spiral reinforcement and two legs of a bent tie pass through the sides of the potential concrete-punching-shear failure surfaces. Article 11.12 of the ACI Code (2002) discusses concrete-punching-shear. For the concrete-bearing stress q_{1X}, the loaded-concrete area has the dimensions of the Whitney-Stress Block depth, a_p, by the depth, d, of the HP pile. The nominal, concrete strength is the smallest strength established by Eqs. 8.187 thru 8.189.

$$V_c = \left(2 + \frac{4}{\beta_c}\right)\sqrt{f_c^{'}}\ b_o d_{eff} \tag{8.187}$$

$$V_c = \left(\frac{\alpha_s d_{eff}}{b_o} + 2\right)\sqrt{f_c^{'}}\ b_o d_{eff} \tag{8.188}$$

$$V_c = 4\sqrt{f_c^{'}}\ b_o d_{eff} \tag{8.189}$$

where, β_c is the ratio of the longer-to-shorter dimension of the loaded-concrete area; α_s is a bearing-condition-edge factor, which is equal to 30 for a concrete-punching-shear failure shape that has one edge of that failure surface truncated by a concrete face; b_o is the perimeter of the concrete-failure surface; and d_{eff} is the effective depth to the centroid of the tension reinforcement. The design shear strength, $\Phi_v V_n$, with a resistance factor, Φ_v, that is equal to 0.75, must be not be less than the required, factored-level, shear strength, V_u, to satisfy the punching-shear, limit state.

The required, factored-level, shear strength is the shear force that acts on the failure surface. This force, which is equal to the applied load for bearing of the pile on the concrete at the end of the pile-embedment depth into the bottom of the pile cap, is expressed as

$$V_u = q_{u1X} a_p d \tag{8.190}$$

where, q_{u1X} is the factored-level, horizontal, concrete-bearing stress at the bottom of the pile-embedment depth.

If the concrete-punching-shear design strength adjacent to a pile is not adequate, bent-bar ties, shown in Figs. 8.72a and 8.72b, which are distributed over the bearing

length a_p, can be designed to resist a concrete-punching-shear failure. See Section 8.8.5.1 regarding the development of the #p-bar-dowel, vertical reinforcement, which is shown in Figs. 8.65 and 8.72 to connect the abutment backwall to the backwall-pile cap.

8.8.5.3. Girder-to-backwall connection

An abutment backwall must be designed to resist the concrete-bearing stresses that occur at the embedded end of a PC girder. These bearing stresses are induced by the girder axial force, $P_{girder\text{-}\ell}$, shear forces, $V_{girder\text{-}h}$ and $V_{girder\text{-}t}$, bending moments, $M_{girder\text{-}h}$ and $M_{girder\text{-}t}$, and torsional moment, $M_{girder\text{-}\ell}$. Oesterle, et al. (1999) stated that the connection between a bridge girder and an abutment backwall is similar the connection between a RC column and a RC flat slab in a building. Article 11.12.6 of the ACI Building Code (2002) provides design criteria for evaluating a punching-shear, limit state for a flat slab that is based the axial force and bending moment in the column and on section properties for a shear-failure zone in the slab. However, the connection between a PC girder and an abutment backwall is not identical to the connection between a building column and a flat slab. For an integral-abutment bridge, the end of a bridge girder is embedded into the abutment backwall; and, if the bridge has a skewed alignment, the longitudinal axis of the girder is not perpendicular to the front face of the abutment backwall. Since these geometric conditions are not present in a building-column-to-slab connection, the ISU researchers recommend that the connection between a PC girder and an abutment backwall should be analyzed and designed for the concrete-bearing stresses, which are shown in Fig. 8.73. To establish these bearing stresses, the ISU researchers recommend the application of the same static-equilibrium,

analysis technique that was used in Section 8.8.5.2 to determine the concrete-bearing stresses for an abutment pile that is embedded into a pile cap.

The force $V_{girder\text{-}t}$ and bending moment $M_{girder\text{-}h}$, are assumed to be resisted by the bearing stress q_{1t1} and q_{2t1} that act against the sides of the embedded portion of a PC girder and in a direction that is parallel to the t-axis of the bridge superstructure, as shown in Fig. 8.73b. The torsional moment $M_{girder\text{-}\ell}$ is considered to be resisted by a force couple that is formed by the bearing stresses q_{1t2} and q_{2t2} that also act against the sides of the embedded portion of a PC girder and in a direction that is parallel to the t-axis of the bridge superstructure, as shown in Fig. 8.73c. The force $P_{girder\text{-}\ell}$ is assumed to induce the bearing stress $q_{3\ell}$, which acts on the end of the girder and in a direction that is parallel to the ℓ-axis of the bridge superstructure; and, the force $V_{girder\text{-}h}$ and bending moment $M_{girder\text{-}t}$ are considered to induce the bearing stresses q_{1h} and q_{2h}, which act on the top and bottom flanges of the PC girder and in a direction that is parallel to the h-axis of the bridge superstructure, as shown in Fig. 8.73d.

For a structural analysis of an integral-abutment bridge, the member-end forces for a PC girder are located at the joint that represents the intersection of the member axes for the composite girder and the composite, abutment backwall and pile cap. The member-end forces for a PC girder that act on the backwall of an integral abutment are computed from

$$\begin{Bmatrix} P_{girder-\ell} \\ V_{girder-h} \\ V_{girder-t} \end{Bmatrix} = \begin{bmatrix} \cos\theta & 0 & -\sin\theta \\ 0 & 1 & 0 \\ \sin\theta & 0 & \cos\theta \end{bmatrix} \begin{Bmatrix} F_X \\ F_Y \\ F_Z \end{Bmatrix} \tag{8.191}$$

$$\begin{Bmatrix} M_{girder-\ell} \\ M_{girder-h} \\ M_{girder-t} \end{Bmatrix} = \begin{bmatrix} \cos\theta & 0 & -\sin\theta \\ 0 & 1 & 0 \\ \sin\theta & 0 & \cos\theta \end{bmatrix} \begin{Bmatrix} \left(M_X + F_Z\, e_{gY}\right) \\ M_Y \\ \left(M_Z - F_X\, e_{gY}\right) \end{Bmatrix} \tag{8.192}$$

For an interior girder, the forces F_X, F_Y, and F_Z and the moments M_X, M_Y, and M_Z are listed in Table 8.15 for each type of abutment load. These forces and moments, which are the girder reactions at Cross Section 2 of the integral abutment and which are associated with the Internal-Force Procedure 2, were shown in the free-body diagrams for Figs. 8.46 thru 8.54 for each type of abutment load. Figures 8.74a and 8.74b shows the forces and moments, respectively, that are directed along the X-axis and Z-axis for the integral abutment and the components of those forces along the ℓ-axis and t-axis for the bridge superstructure. The point of application for these forces and moments was at the center-of-gravity of the composite, backwall and backwall-pile cap, which is located at the mid-height and mid-width of the abutment cross section. As shown in Fig. 8.74d, the center-of-gravity for the cross section of a composite, bridge girder at the mid-width of the abutment is directly above the center-of-gravity for the abutment cross section that is at the girder location. Because of the vertical eccentricity, e_{gY}, for a girder, the horizontal forces F_X and F_Z induce a bending moment about a parallel Z-axis and a parallel X-axis, respectively, at the center-of-gravity of the girder cross section at the abutment.

These girder-end forces are eccentric by the distances e_ℓ and e_h to the assumed axes of zero-strain bending for the concrete-bearing stresses that are shown in Figs. 8.73b, 8.73c, and 8.73d. The horizontal eccentricity, e_ℓ, of the girder-end forces is a

function of the girder-embedment length into the abutment backwall. When a bridge has a skewed alignment, as shown in Fig. 8.73a, the girder-embedment lengths ℓ_{emb1} and ℓ_{emb2}, which are shown in Fig. 8.73b, are not the same on each side of the girder. The ISU researchers suggest that the shorter, girder-embedment length should be used to establish the concrete-bearing stresses. For the geometry shown in Fig. 8.73b, this length is the length ℓ_{emb1}. Then, the eccentricity e_ℓ is given by

$$e_\ell = \ell_{emb1} - \ell_e + \frac{b_{bf}}{2}\tan\theta \tag{8.193}$$

where, ℓ_e is the end distance, which is measured along the ℓ-axis direction for the bridge superstructure, from the center of the abutment backwall to the end of the girder. A positive, end distance is measured towards the back face of the abutment.

The ISU researchers suggest that the thickness, t_s, of the bridge deck and the height, t_h, of a concrete haunch between the underside of the slab and the top of the bridge girder be neglected to simplify the calculation of the horizontal and vertical, concrete-bearing stresses. Then, the eccentricity, e_h, which is equal to the vertical distance between the center of gravities for the vertical cross sections of a composite girder and a non-composite girder, is evaluated as

$$e_h = y_{ncg} - y_{cg} \tag{8.194}$$

where, y_{ncg} and y_{cg} are the vertical distances from the top of the bridge deck to the center of gravity for a non-composite girder and composite girder, respectively.

The concrete-bearing stresses are evaluated using static equilibrium of the free-body diagrams of the end portion of a PC girder that are shown in Figs. 8.73b, 8.73c, and 8.73d. For these figures, the girder-end forces were resolved to a point at the front face of the abutment backwall. The girder forces and moments at this location are expressed as

$$\begin{Bmatrix} P_{\ell'} \\ V_{h'} \\ V_{t'} \end{Bmatrix} = \begin{bmatrix} \cos\theta & 0 & -\sin\theta \\ 0 & 1 & 0 \\ \sin\theta & 0 & \cos\theta \end{bmatrix} \begin{Bmatrix} F_X \\ F_Y \\ F_Z \end{Bmatrix} \tag{8.195}$$

$$\begin{Bmatrix} M_{\ell'} \\ M_{h'} \\ M_{t'} \end{Bmatrix} = \begin{bmatrix} \cos\theta & 0 & -\sin\theta \\ 0 & 1 & 0 \\ \sin\theta & 0 & \cos\theta \end{bmatrix} \left\{ \begin{Bmatrix} M_X \\ M_Y \\ M_Z \end{Bmatrix} + \begin{bmatrix} 0 & +e_Z & +e_Y \\ -e_Z & 0 & -e_X \\ -e_Y & +e_X & 0 \end{bmatrix} \begin{Bmatrix} F_X \\ F_Y \\ F_Z \end{Bmatrix} \right\} \tag{8.196}$$

where, the distances e_X and e_Y, which are shown in Fig. 8.74c, are given by

$$e_X = \frac{B_{abut}}{2} \tag{8.197}$$

$$e_Z = \left(\frac{B_{abut}}{2}\right)\tan\theta \tag{8.198}$$

For the free-body diagram shown in Fig. 8.73b, the concrete-bearing stresses q_{1t1} and q_{2t1}, which correspond to a shear-force vector $V_{t'}$ and bending-moment vector $M_{h'}$ that act along the positive directions for the t'-axis and h'-axis, respectively, are evaluated as

$$q_{2t1} = \frac{M_{h'} + \left(\dfrac{a_{p1} + b_{bf}\tan\theta}{2}\right)V_{t'}}{a_{p1}h_{girder}\left(\ell_{emb1} - a_{p1}\right)} \tag{8.199}$$

$$q_{1t1} = q_{1t2} + \left(\frac{V_{t'}}{a_{p1} h_{girder}} \right) \tag{8.200}$$

where, b_{bf} and h_{girder} are the width of the bottom flange and depth, respectively, for the PC girder. The depth of the Whitney-stress block, a_{p1}, is computed as

$$a_{p1} = \beta_1 \left(\frac{\ell_{emb1}}{2} \right) \tag{8.201}$$

For the free-body diagram shown in Fig. 8.73c, the concrete-bearing stresses q_{1t2} and q_{2t2}, which correspond to a torsional-moment vector $M_{\ell'}$ that acts along the positive direction for the ℓ-axis, are given by

$$q_{2t2} = \frac{M_{t'}}{a_{p3} \ell_{emb1} \left(h_{girder} - \frac{a_{p2}}{2} - \frac{a_{p3}}{2} \right)} \tag{8.202}$$

$$q_{1t2} = \left(\frac{a_{p3}}{a_{p2}} \right) q_{2t2} \tag{8.203}$$

The Whitney-stress block depths a_{p2} and a_{p3} are computed as

$$a_{p2} = \beta_1 \left(y_{ncg} - t_s - t_h \right) \tag{8.204}$$

$$a_{p3} = \beta_1 \left(h_{girder} - y_{ncg} + t_s + t_h \right) \tag{8.205}$$

For the free-body diagram shown in Fig. 8.73d, the concrete-bearing stresses q_{1h} and q_{2h}, which correspond to a shear-force vector $V_{h'}$ that acts along the negative

direction for the h'-axis direction and a bending-moment vector $M_{t'}$ that acts along the positive direction for the t'-axis direction, are evaluated as

$$q_{2h} = \frac{M_{t'} + \left(\frac{a_{p1} + b_{bf}\tan\theta}{2}\right)V_{h'}}{a_{p1}b_2\left(\ell_{emb1} - a_{p1}\right)} \tag{8.206}$$

$$q_{1h} = \frac{q_{2h}a_{p1}b_2 + V_{h'}}{a_{p1}b_1} \tag{8.207}$$

The effective-bearing widths, b_1 and b_2, for the bearing stresses q_{1h} and q_{2h}, respectively, are given by

$$b_1 = b_{bf} + b_{tf} - t_w \tag{8.208}$$

$$b_2 = b_1 \tag{8.209}$$

where, t_w is the web thickness for the PC girder. The bearing stress q_{2h} that is shown in Fig 8.73d to be acting downward on the top flange of the PC girder models the effect of a tensile force in the vertical legs of U-shaped ties that the ISU researchers recommend to be installed along the embedment length ℓ_{emb1} of each PC girder. This reinforcement should be positioned to straddle over a PC girder. The horizontal portion of each U-shaped bar should be located near the top surface of the bridge deck, and each vertical leg of each U-shaped bar should extend along one side of the girder web and extend into the abutment-pile cap. The embedment length for these U-shaped bars in the pile cap should be sufficient to develop the yield strength of each leg of this reinforcement. Since the girder forces and moments are reversible, the required area for this U-shaped reinforcement is required over each half of the embedment length ℓ_{emb1}. If this U-shaped

reinforcement is not present, the hooked #p-bars that are shown in Fig. 8.73a along the back face of the abutment backwall, would need to develop the bearing stress q_{2h} at the top flange of the PC girder. However, since these vertical bars are not located adjacent to the bearing stress q_{2h}, the effectiveness of these vertical bars in resisting the required force is questionable.

Since the inside face of the top and bottom flanges of a PC girder are inclined at the angles ζ_{tf} and ζ_{bf}, respectively, as shown in Fig. 8.73c, the concrete-bearing stresses q_{1h} and q_{2h}, respectively, for these inside surfaces of the flanges are the vertical components of the normal, concrete-bearing stress q_1 and q_2, respectively. These normal bearing stresses are expressed as

$$q_1 = \frac{q_{1h}}{\cos \xi_{tf}} \tag{8.210}$$

$$q_2 = \frac{q_{2h}}{\cos \xi_{bf}} \tag{8.211}$$

The concrete-bearing stress $q_{3\ell}$, which corresponds to an axial-force vector $P_{\ell'}$ that acts along the negative direction for the ℓ-axis direction, as shown in Fig 8.73d, is given by

$$q_{3\ell} = \frac{P_{\ell'}}{A_{girder}} \tag{8.212}$$

For the connection shown in Fig. 8.73, the total of the factored-level, concrete-bearing stresses in both the horizontal and vertical directions must be less than the design, concrete-bearing stress, $\Phi_c q_n$, for the concrete in both the PC girder and abutment backwall, where the resistance factor, Φ_c, is set equal to 0.65 for concrete

bearing, as specified by the ACI Code (2003). Since the 28-day, concrete-compressive strength, f_c', for a PC girder is higher than that for an abutment backwall, the bearing stresses on the concrete in the backwall that surrounds the PC girder will govern the bearing-strength-limit state. With respect to nominal, concrete-bearing stresses, the ISU researchers believe that this connection is not the same as the connection between an abutment pile and an abutment-pile cap. The differences in these connections involve the type of material for the connected members and confinement-reinforcement conditions for the surrounding concrete. The pile-to-pile-cap connection involves a large steel insert in a concrete mass that is confined by spiral-bar reinforcement, while the girder-to-backwall connection involves a large concrete insert in a concrete mass that is not confined by steel-bar reinforcement. In addition, the ratio of volume of the surrounding concrete to that of the inserted member is significantly smaller for the connection involving the PC girder than that for the connection involving the steel pile. Therefore, the ISU researchers recommend that the high, nominal, concrete-bearing stress that was established by Burdette, et al. (1983) for a specific type of a large steel insert in a concrete slab should not be used for the connections between the PC girders and the abutment backwall. Instead, nominal, concrete-bearing stresses, q_n, that are equal to $0.85f_c$' and $1.7f_c$', which are specified by the ACI Code (2002), for unconfined concrete and confined concrete, respectively, should be used near a concrete surface and within the interior regions of a concrete volume, respectively.

The shear strength of the concrete in the abutment backwall that is beyond the end of a PC girder needs to be investigated for a potential, punching-shear-type failure that may be caused by the concrete-bearing stress q_{u3}, which is associated with the

girder axial load, $P_{\ell'}$. To generate a punching-shear failure in this portion of the abutment, a three or four-sided, wedge shape must develop through concrete. This type of a shear failure is a function of the effective depth to the tension reinforcement in the shear-failure zone. When an abutment has a skewed-alignment, as shown in Fig. 8.73a, the effective depth varies across the width of the PC girder from the distances d_{eff1} to d_{eff2} that are measured along embedment lengths ℓ_{emb1} and ℓ_{emb2}, respectively. Since the concrete along all of the surfaces of a wedge-shape failure needs to fracture in shear for a punching-shear failure to occur, the ISU researchers suggest that the average of these two effective depths should be used as the effective depth, d_{eff}, to evaluate the punching-shear strength. The width at the mid-depth of this wedge shaped is assumed to be equal to the average of the top-flange width, b_{tf}, and bottom-flange width, b_{bf}, plus the effective depth d_{eff}. Since the construction joint between the abutment backwall and the abutment pile cap is keyed and is crossed by large-sized reinforcing bars (#p-bars), the location for the mid-depth of this wedge shape is assumed at a distance of $d_{eff}/2$ below the bottom flange of the PC girder. For a three-sided, wedge-shaped failure, the vertical shear planes extend to the top surface of the RC bridge deck. For a four-sided, wedge-shaped failure, the mid-depth of the fourth shear plane is assumed at a distance of $d_{eff}/2$ above the top flange of the PC girder. The punching-shear strength for this connection is the least shear strength for the three-sided or four-sided, wedge-shaped failures. As discussed in Section 8.8.5.2, the nominal, punching-shear strength, V_c, of the concrete is the lowest strength that is established from Eqs. 8.187, 8.188, and 8.189.

8.9. Pile design

The selection of a design specification to apply for the design of the piles for the abutment backwall was made after comparing specific steel-design provisions of the AASHTO Standard Specifications for Highway Bridges (1996), AASHTO Load and Resistance Factor Design (LRFD) Bridge Design Specifications (1998), AISC Allowable Stress Design (ASD) Specifications for Structural Steel Buildings (1989), and the AISC LRFD Specifications for Structural Steel Buildings (1999). The abutment piles are members that are subjected to combined forces, which can involve axial compression and bi-axial bending moments. Strength conditions for members with combined forces are expressed in the form of interaction relationships. The interaction equations for the load-factor method and the service-load method in the AASHTO Standard Specifications are essentially factored versions and identical versions, respectively, of the interaction equations in the AISC ASD Specifications. The AISC LRFD Specifications presented a new set of interaction equations for combined forces in members and the AASHTO LRFD Specifications has essentially adopted those same interaction expressions. Because an LRFD approach to design is more rational than that for a service-load approach or an ASD approach, the ISU researchers selected the AASHTO LRFD Specifications for investigating the more accurate interaction relationships (Eqs. 8-199 and 8-200) between axial load and biaxial bending of the abutment piles. To evaluate the interaction limit state involving axial load and bending moments, the ISU researchers used the load factors from the AASHTO Standard Specification that were presented in Section 8.1. For these interaction relationships, the AASHTO LRFD Specifications sets the axial-compression resistance factor, ϕ_c, and the bending-moment resistance factor, ϕ_f,

equal to 0.90 and 1.00, respectively. Even though the AASHTO Standard Specifications does not explicitly provide resistance factors for axial compression and bending moment, this specification uses an implied resistance factor ϕ_f, which is the same as that in the AASHTO LRFD Specifications, and an implied resistance factor ϕ_c, which is equal to 0.85. For a slightly more conservative evaluation of the design resistance of a pile for an integral abutment, the ISU researchers used the implied resistance factors from the AASHTO Standard Specifications.

Article 10.7.1.3 in the AASHTO LRFD Specifications (1998) requires a pile to have adequate bearing and structural resistances and tolerable settlements and lateral displacements. Other design criteria include pile-group, scour, and negative-skin friction effects. The material presented in this section will emphasize the resistance of pile as a structural member. Article 6.5 in the AASHTO LRFD Specifications requires that steel structures satisfy strength-limit states, service-limit states, fatigue and fracture-limit states, and extreme-event-limit states. For an integral-abutment pile, only strength-limit states and a limit state for pile ductility will be considered in the following sections.

8.9.1. Strength-limit-state for combined axial compression and bending

An abutment pile in an integral-abutment bridge is a structural member that is subjected to combined, axial compression and bending. Article 6.9.2.2 in the AASHTO LRFD Specification (1998) provides two interaction equations, which are re-written here as Eqs. 8.213 and 8.214. The governing, strength-limit state is established by the axial-load ratio, P_u/P_r.

For $\frac{P_u}{P_r} < 0.2$,

$$\frac{P_u}{2.0P_r} + \left(\frac{M_{ux}}{M_{rx}} + \frac{M_{uy}}{M_{ry}}\right) \leq 1.0 \tag{8.213}$$

For $\frac{P_u}{P_r} \geq 0.2$,

$$\frac{P_u}{P_r} + \frac{8}{9}\left(\frac{M_{ux}}{M_{rx}} + \frac{M_{uy}}{M_{ry}}\right) \leq 1.0 \tag{8.214}$$

where, P_u is the factored-level, axial-compressive load; M_{ux} is the factored-level, bending moment, including second-order bending effects with respect to bending about the x-axis; M_{uy} is the factored-level, bending moment, including second-order bending effects with respect to bending about the y-axis; P_r is the factored-level, axial-compressive resistance when only axial load is present ($P_r = \phi_c P_n$, where ϕ_c is the resistance factor for axial compression and P_n is the nominal compressive resistance); M_{rx} is the factored-level, flexural resistance for bending about the x-axis when only x-axis bending is present ($M_{rx} = \phi_f M_{nx}$, where ϕ_f is the resistance factor for flexure and M_{nx} is the nominal, x-axis, bending resistance); and M_{ry} is the factored-level, flexural resistance for bending about the y-axis when only y-axis bending is present ($M_{ry} = \phi_f M_{ny}$, where M_{ny} is the nominal, y-axis, bending resistance) for an abutment pile. The factored-level, flexural resistance, M_r, includes flange and web-local buckling effects, as well as lateral-torsional buckling for strong-axis bending (AASHTO LRFD Specifications, Article 6.10.4).

The moments M_{ux} and M_{uy} may be determined either by a second-order, elastic analysis that accounts for moment magnification, which is caused by the factored-level,

axial load and the induced, lateral displacement, or by the approximate procedure that is provided in Article 4.5.3.2.2b of the AASHTO LRFD Specifications (1998).

Previous research on integral-abutment, pile design that was conducted by Greimann, et al. (1987a) at Iowa State University recommends that the moment, M_u should be only the PΔ-moment due to gravity loads that are amplified by the factored-level, axial load as given by

$$M_u = M_{u-gravity} + \frac{P_{pile}\Delta}{2} \tag{8.215}$$

where, $M_{u\text{-}gravity}$ is the first-order, factored-level, gravity-load, bending moment at the top of a fixed-head, abutment pile that acts about the t-axis of the bridge; P_{pile} is the first-order, factored-level, axial force in the pile at the pile head; and Δ is the lateral displacement of the top of the pile. The bending moment $M_{u\text{-}gravity}$ and the axial force P_{pile} include the bending moments and axial forces that are induced by the dead, live, and impact loads that act on the bridge superstructure. The bending moment in a pile that is induced by the thermal movement of a bridge, is assumed not to have a significant effect on the pile capacity. However, the pile must be sufficiently ductile to accommodate the lateral displacement at the top of the pile. Greimann, et al. (1987a) provides additional discussion regarding the justification for neglecting the bending moments in an integral-abutment pile due to thermal movements of a bridge superstructure. The design requirements for pile ductility are discussed in Section 8.9.2.

8.9.2. Limit state for pile ductility

The ductility of an integral-abutment pile is sufficient when a ductility-limit state is satisfied. This limit state can be expressed either in terms of a rotation capacity and a rotation demand at the plastic-hinge location in a pile or in terms of a displacement capacity and a displacement demand at the top of the pile. The rotation capacity or displacement capacity includes both elastic and inelastic components. Factors that affect the rotation or displacement capacity relate to the loading on the pile, geometry of the pile cross section, and moment versus curvature relationship for the pile cross section. Factors that affect the rotation or displacement demand relate to the horizontal displacements of the abutment and the vertical rotation of the abutment in a plane that is parallel to the bridge length. These factors, which affect the ductility-limit state for an integral-abutment pile are discussed in the following sections.

8.9.2.1. Inelastic-rotation capacity for a compact, simply-supported beam

Lukey and Adams (1969) investigated the moment-rotation characteristics of rolled, I-shaped beams subjected to moment gradients along their laterally unsupported lengths. These researchers experimentally tested I-shaped beams that had different flange width, b_f, to flange thickness, t_f, ratios and beam depth, d, to web thickness, t_w, ratios. The beams were laterally braced at their ends and at the mid-span, as shown in Fig. 8.75. The beams were simply-supported at the ends of a single span of length, L. A single, concentrated, transverse load was applied to the web-stiffener plates at the mid-span of the beam. Displaced-geometric conditions for the beam when elastic behavior; initial, theoretical-plastic, moment strength, M_p, behavior; and inelastic behavior are shown in Figs. 8.76a, 8.76b, and 8.76c, respectively. The relative angles $\theta_{e\text{-simple}}$, $\theta_{p\text{-simple}}$,

and $\theta_{i\text{-simple}}$ at the mid-span of the simply-supported beam are the angles between the tangent lines to the elastic curve for the displaced shape of the beam that are drawn through the supports when elastic behavior; theoretical and initial M_p behavior; and inelastic behavior, respectively, occurs for the beam. Symmetry requires that the beam rotations at each support equal one-half of those relative, mid-span angles. The moment diagram for the beam, when the mid-span moment equals M_p, is shown in Fig. 8.76d. Figure 8.77 shows a non-dimensionalized, moment-curvature relationship for a beam whose element, width-to-thickness ratios are small enough to prevent local buckling of those elements, until the displaced shape of the beam corresponds to the geometrical conditions shown in Fig. 8.76c. During the early-load stage shown in Fig. 8.76a, elastic behavior occurs and the mid-span moment, M, is less than the moment at first yield, which is labeled in Fig. 8.77. As the load P increases, a plastic hinge begins to form at the mid-span of the beam, as shown in Figs. 8.76b and 8.76c. Due to strain hardening of the outer fibers of the flanges, the moment M can exceed M_p, as shown in Fig. 8.77. Inelastic rotation occurs at the plastic-hinge location as the deflection of the beam increases. The dashed lines that are shown in Fig. 8.77 represent the behavior that is assumed in simple-plastic-bending theory. When the mid-span moment equals the moment M_p (Point A in Fig. 8.77), the relative mid-span angle is the angle $\theta_{p\text{-simple}}$, which is shown in Fig. 8.76b. Applying the moment-area method for the simple beam, the angle $\theta_{p\text{-simple}}$ is expressed as

$$\theta_{p\text{-simple}} = \frac{M_p L}{2EI} \tag{8.216}$$

For the inelastic behavior shown in Fig. 8.76c, the relative, mid-span angle, $\theta_{i\text{-simple}}$, is equal to the sum of the relative, mid-span angle $\theta_{p\text{-simple}}$ that is associated with the plastic- hinge formation, which is assumed for simple-plastic theory, and the inelastic-rotation angle, $\theta_{ip\text{-simple}}$, between the tangent lines to the curve of the displaced shape of the beam on each side of the plastic-hinge location. This angular relationship is expressed by

$$\theta_{i-\text{simple}} = \theta_{p-\text{simple}} + \theta_{ip-\text{simple}} \tag{8.217}$$

Figure 8.77 shows an actual and an idealized, non-dimensional, moment-rotation (M-θ) behavior that occur for bending at a cross section for a steel beam. The abscissa scale is the relative, mid-span rotation, θ, and represents the relative, mid-span angles shown in Fig. 8.76, and the ordinate scale is the ratio of the moment resistance, M, to the plastic-moment strength, M_p, for the cross section. The angles θ_y, θ_p, and θ_u are the relative, mid-span angles at first yielding of the extreme fibers in the cross section; at the initial development of the M_p-strength for the idealized behavior (Point A in Fig. 5.77); and the relative angle when the strain-hardening, moment resistance decreases to the M_p-strength due to buckling. The buckling can be flange-local buckling, web-local buckling, or lateral-torsional buckling. When buckling causes the moment M to be reduced to the M_p-strength, the relative, mid-span angle $\theta_{i\text{-simple}}$, shown in Fig. 8.76c, is equal to the angle θ_u, shown in Fig. 8.77, which is the maximum, relative, mid-span angle, $\theta_{imax\text{-simple}}$, and the angle $\theta_{p\text{-simple}}$ is equal to the inelastic-rotation capacity, θ_{ipc}, at the plastic-hinge location. For this condition, the inelastic-rotation capacity of the idealized, simple-beam, plastic hinge is given by

$$\theta_{ipc\text{-}simple} = \theta_{imax\text{-}simple} - \theta_{p\text{-}simple} \tag{8.218}$$

8.9.2.2. Moment reversal effects on inelastic-rotation capacity

A condition for full-load reversal of a simply-supported beam is illustrated in Fig. 8.78. A simply-supported beam resists a variable-magnitude, concentrated load (either P_{down} or P_{up}) at the mid-span as shown in Fig. 8.78a. The loads P_{down} and P_{up} act downward and upwards, respectively. The geometrical conditions for a load in one of the directions are similar to those shown in Fig. 8.75. For this discussion, the magnitude of the loads P_{down} and P_{up} are equal. The cross section of the beam is shown in Fig. 8.78b. Figure 8.78c shows the moment-curvature (M-ϕ) relationship for the cross section of the beam that is free of residual stresses. The presence of residual stresses will reduce the moment M for which the moment-curvature behavior remains linear and elastic. The slope of the linear portions of the M-ϕ curves is the flexural rigidity EI for the beam, where E is the modulus of elasticity and I is the moment of inertia for the beam cross section with respect to the axis of bending. The curvatures ϕ_p and ϕ_y are the curvatures when the moment strength of the cross section for the beam is equal to the theoretical, plastic-moment strength, M_p, and theoretical, yield-moment strength, M_y, respectively, according to simple-plastic-beam theory that is represented by the straight solid and dotted-line extensions shown in Fig. 8.78c.

The Path OAC represents the moment-curvature relationship for the load P_{down}. At Point C, the load P_{down} equals its maximum value, P_{max}, when the top flange of the beam is in compression. If the load P_{up} is applied instead of P_{down}, the moment-curvature

relationship is represented by dashed Path OA'I. The curvature range from Points B to C and from Points B' to I represent the inelastic-curvature capacity, $\phi_{ic\text{-}simple}$, which equals $R\phi_p$, for unidirectional loading on a simply-supported beam where, R is the inelastic-curvature, capacity factor.

If at Point C, the load P_{down} is gradually reduced to zero and the load P_{up} is gradually applied, the moment-curvature relationship is linear between Points C and F for a range of moment equal to $2M_y$. At Point F, yielding of the beam cross section begins with the top flange of the beam in tension. At Point I, the load P_{up} equals the load P_{max}. To complete the hysteresic cycle, the load P_{up} is gradually reduced and the load P_{down} is gradually applied until the load P_{down} is again equal to the load P_{max}. The corresponding portion of the moment-curvature relationship is represented by the solid line from Points I to C.

Figures 8.79 and 8.80 show the vertical distribution of the strains and stresses, respectively, in the beam cross-section that are associated with moment-curvature (M-ϕ) Points A to L shown in Fig. 8.78c. Linear strains exist throughout the beam cross section that is subjected to alternating plasticity for all points of the moment-rotation behavior shown in Fig. 8.78c. The corresponding stresses are linear only within the regions of the beam cross section where elastic behavior occurs during the load and unloading of the beam. When the strain at a point in the beam cross section exceeds the yield strain, restrained yielding occurs for those beam fibers. The yielding is restrained by the other fibers of the beam cross section that are experiencing elastic behavior and by the displacement controlled loading that produces the loads P_{down} and P_{up}. The shape factor, ξ, shown in Figs. 8.79 and 8.80 for a beam cross section is given by

$$\xi = \frac{M_p}{M_y} = \frac{\phi_p}{\phi_y} \tag{8.219}$$

where, ϕ_p and ϕ_y are the beam curvatures associated with the moment strengths M_p and M_y, respectively, that are shown in Figs. 8.77 and 8.78c. With reference to Fig. 8.78c, the inelastic-curvature capacity, $\phi_{ic\text{-}rev\text{-}simple}$, for a full-reversal of loads on a simply-supported beam is given by

$$\phi_{ic\text{-}rev\text{-}simple} = 2\phi_{ic\text{-}simple} \tag{8.220}$$

Therefore, the inelastic-rotation capacity of the simply-supported, I-shaped beam with compact elements that is subjected to a full-reversal of a mid-span, concentrated load (+P to -P) is equal to two times the inelastic-rotation capacity of that same beam when it is subjected to a uni-directional, mid-span, concentrated load P.

8.9.2.3. Flange local-buckling effects on inelastic-rotation capacity

The compression flange of an I-shaped section is classified as compact when the width-to-thickness (b/t) ratio for the portion of the flange between the flange tip and the mid-width of the flange does not exceed a limiting b/t-ratio. Both Articles 6.10.4.1.3 and B5.1 in the AASHTO LRFD Specifications (1998) and the AISC LRFD Specifications in the AISC Manual of Steel Construction (2001), respectively, present the same limiting b/t ratio. According to Table B5.1 in the AISC LRFD Specification, compact, I-shape sections with $\frac{b_f}{2t_f} \leq 0.38\sqrt{\frac{E}{F_y}}$, where $b_f/2t_f$ is the width-to-thickness ratio for the flange of an I-shaped cross section, E is the modulus of elasticity for steel and F_y is the yield

stress for the steel, have an inelastic-rotation capacity, $\theta_{ipc\text{-}simple}$, of at least three times the rotation $\theta_{p\text{-}simple}$ for uni-directional, x-axis (strong-axis) bending.

When a beam is subjected to cyclic load, in which a repeated sequence of full-reverse loading occurs, the inelastic-rotation capacity of the beam will be reduced because of the Bauschinger Effect (Bruneau, et al., 1998). For a given transverse displacement, a beam that would not experience flange-local buckling, web-local buckling, or lateral-torsional buckling under monotonic loading could buckle during cyclic loading (Bruneau, et al., 1998). For a beam subjected to repeated-cyclic load, the ISU researchers recommend the use of the AISC (2001) seismic-design, compact-section criteria. Therefore, the $\frac{b_f}{2t_f}$ limit of $0.38\sqrt{\frac{E}{F_y}}$ should be replaced with the $\frac{b_f}{2t_f}$ limit of $0.31\sqrt{\frac{E}{F_y}}$.

When an I-shaped, non-compact, column is subjected to only axial compression, flange-local buckling will not occur if $\frac{b_f}{2t_f} \le 0.56\sqrt{\frac{E}{F_y}}$. Strong-axis bending or axial compression subjects the flange of an I-shape to essentially uniform compression; therefore, if $\frac{b_f}{2t_f} \ge 0.56\sqrt{\frac{E}{F_y}}$, the cross section has no inelastic-rotation capacity. The inelastic-rotation capacity of I-shaped cross sections with $0.31\sqrt{\frac{E}{F_y}} \le \frac{b_f}{2t_f} \le 0.56\sqrt{\frac{E}{F_y}}$ can be assumed to vary linearly between three and zero, respectively. Justification for using a linear variation for the moment-rotation relationship of a partially-compact cross section

is provided by the AISC-ASD Specification (1989). In Chapter F of that specification, a linear equation (ASD Eq. F1-3) is used to represent the allowable-bending stress for a partially-compact cross section that has the width-to-thickness ratio for the flange element of an I-shaped beam between that ratio for a compact element and a non-compact element. Salmon and Johnson (1996) graphically illustrate this concept in Fig. 7.5.1 of that textbook.

The AISC LRFD seismic-design $\frac{b_f}{2t_f}$ limit of $0.31\sqrt{\frac{E}{F_y}}$ is equal to 8.80 and 7.47 for steels with a yield stress equal to 36 ksi and 50 ksi, respectively; and the AISC LRFD column-design $\frac{b_f}{2t_f}$ limit of $0.56\sqrt{\frac{E}{F_y}}$ is equal to 15.9 and 13.5 for steels with a yield stress equal to 36 ksi and 50 ksi, respectively. Since the seismic-design b/t-limits for both grades of steel are exceeded for all of the rolled HP-shapes, the flanges for an HP-shaped pile are not classified as compact. Two HP shapes have flange b/t-ratios that exceed the column-design b/t-limit for 50-grade steel. These shapes are the HP12X53 and the HP14X73, which have a flange b/t-ratio equal to 13.8 and 14.4, respectively. According to Table 2-1 in the AISC Manual of Steel Construction (2001) the preferred material specification for an HP shape is A36 steel. However, the actual yield strength of the steel will normally be higher than 36 ksi. The ISU researchers recommend that the HP12X53 and HP14X73 shapes not be used for piles in integral-abutment bridges when the actual yield strength of the steel for these shapes exceeds about 48 ksi and 44 ksi, respectively.

For uni-directional loading, the inelastic-rotation capacity for a simple-span beam is expressed as

$$\theta_{ipc-simple} = \varphi_{rc}\left(3\theta_{p-simple}\right) C_i \tag{8.221}$$

in which, the compression-flange, local-buckling factor, C_i, is given by

$$C_i = \left[\frac{0.56\sqrt{\frac{E}{F_y}} - \frac{b_f}{2t_f}}{0.25\sqrt{\frac{E}{F_y}}}\right] \tag{8.222}$$

where, $0 \le C_i \le 1$ and ϕ_{rc}, is the resistance factor for compression that is applied to the inelastic-rotation capacity for the pile (ϕ_{rc} = 0.85).

8.9.2.4. Inelastic-rotation capacity of a fixed-head pile

Figure 8.81 shows displaced shapes of a fixed-end beam at various stages of transverse displacement or side-sway. Figure 8.81b shows the rotations and displaced shape of the beam when the end moments are equal to the plastic moment, M_p, at Point A in Fig. 8.77. The rotation at the mid-span of the fixed-end beam is denoted as the angle $\frac{1}{2}\theta_{p-fixed}$, which is equal to the end rotation $\frac{1}{2}\theta_{p-simple}$ for the simply-supported beam shown in Fig. 8.76b. Applying the moment-area method to Fig. 8.81b and using the portion of the moment diagram shown in Fig. 8.81e, the rotation $\theta_{p\text{-fixed}}$ is equal to the rotation $\theta_{p\text{-simple}}$ for the simple beam that is given by Eq. 8.216.

As the transverse displacement increases, plastic hinges form at the fixed supports of the beam, as shown in Fig. 8.81c. For clarity, the plastic hinges are shown to

be in the beam rather than directly at a support. For this displacement condition, the rotation at the mid-span of the beam is given by

$$\frac{1}{2}\theta_{i-fixed} = \frac{1}{2}\theta_{p-fixed} + \theta_{ip-fixed} \tag{8.223}$$

where, $\theta_{ip\text{-}fixed}$ is the inelastic rotation of the plastic hinge at the fixed supports (Fig. 8.81c). Figure 8.81d show a re-assembly of the displaced shape for the beam shown in Fig. 8.81c. The right half of the span shown in Fig. 8.81c is drawn as the left half of the span shown in Fig. 8.81d. The left half of the span shown in Fig. 8.81c was inverted and drawn as the right half of the span shown in Fig. 8.81d. The displaced shape shown in Fig. 8.81d is identical to the displaced shape for the simply-supported beam shown in Fig. 8.76c. The end rotation, $\frac{1}{2}\theta_{i-simple}$ of the simple-span beam corresponds with the mid-span rotation, $\frac{1}{2}\theta_{i\text{-}fixed}$, of the fixed-end beam. A comparison of the displaced shapes shown in Figs. 8.81d and 8.81c, reveals that the inelastic rotation at a plastic hinge in the fixed-end beam is equal to one-half of the inelastic rotation at the plastic hinge for the simple-span beam. This relationship is expressed by

$$\theta_{ip\text{-}fixed} = \frac{1}{2}\theta_{ip-simple} \tag{8.224}$$

A fixed-head, abutment pile in an integral-abutment bridge that has an effective-cantilever length, L_e, as determined by Eq. 8.23, and is subjected to transverse displacements of the pile head is mathematically equivalent to the fixed-end beam that has a length L and is laterally displaced at one end as shown in Fig. 8.81. The moment-

rotation relationships for the fixed-head pile are similar to that shown in Fig. 8.77 for the simple-span beam. The inelastic-rotation capacity of the plastic hinge at the fixed head for the pile (right end of the beam shown in Fig. 8.81c) and at the assumed fixed end at the bottom of the equivalent cantilever for the pile (left end of the beam, shown in Fig. 8.81c) is equal to the inelastic-rotation capacity for the left half of the plastic hinge in the simple beam shown in Fig. 8.76c. Then, from Eq. 8.221 for uni-directional lateral loading, the inelastic-rotation capacity for an abutment pile is given by

$$\theta_{ic} = \left[\frac{\theta_{ipc-simple}}{2} = \phi_{rc}\left(\frac{3}{2}\theta_{p-simple}\right)C_i \right] \tag{8.225}$$

8.9.2.5. Inelastic-rotation capacity at different temperature phases

As discussed in Section 8.5, there are two displacement sequences to consider for the design of an integral abutment bridge: initial expansion and initial contraction. When a bridge becomes integral, the average, bridge temperature, $T_{construction}$, will be between the minimum and maximum, average, bridge temperature ($T_{max\ ave}$ and $T_{min\ ave}$, respectively). If the absolute value for the temperature change $T_{max\ ave} - T_{construction}$ and the absolute value for the temperature change $T_{min\ ave} - T_{constructoin}$ are not equal for either the initial-expansion, displacement sequence or the initial-contraction, displacement sequence, the inelastic-rotation capacity of the abutment piles will be smaller than that associated with an equal temperature change for both the expansion and contraction of a bridge. When moment reversals occur on a pile cross section that has a non-linear, moment versus rotation relationship, which is similar to that shown in Fig. 8.82, the inelastic-rotation capacity, θ_c, of the cross section is dependent on the load path. If a

uni-directional moment acts on a pile cross section, the inelastic-rotation capacity is governed by $\theta_c \leq 3\theta_p C_i$, where θ_p is the plastic rotation associated with the plastic-moment capacity, M_p, of the pile cross section and C_i is the compression-flange, local-buckling factor for the pile cross section. If a full-reversal of moment acts on a pile cross section, the inelastic-rotation capacity is governed by $\theta_c \leq 6\theta_p C_i$. When a full-moment-reversal does not act on a pile cross section, the inelastic-rotation capacity is governed by $3\theta_p C_i \leq \theta_c \leq 6\theta_p C_i$. To account for the variable inelastic-rotation capacity of the pile cross section that is associated with the temperature phases, a temperature-phase factor, D_i, that must be applied to the inelastic-rotation capacity.

For the initial thermal expansion or initial thermal contraction of a bridge superstructure (Displacement Cases 1 or 2, respectively),

$$D_i = 1 \tag{8.226}$$

For subsequent temperature cycles involving re-expansion of a bridge superstructure (Displacement Case 3),

$$D_i = \left(\frac{\Delta T_1}{\Delta T_2} + 1 \right) \tag{8.227}$$

where, ΔT_1 equals the minimum, absolute value of ($T_{max\ ave} - T_{construction}$) and ($T_{min\ ave} - T_{construction}$) and ΔT_2 equals the maximum absolute value of ($T_{max\ ave} - T_{construction}$) and ($T_{min\ ave} - T_{construction}$), as described in Section 8.6.1, Displacement Case 1 (initial expansion but without concrete creep and concrete shrinkage) and Displacement Case 2 (long-term contraction but without concrete creep and shrinkage).

Figures 8.82a and 8.82b show an idealized, moment-rotation relationship for a cross section at the top of an integral-abutment pile for a bridge that is first subjected to an initial expansion that is followed by a contraction and then a re-expansion and to an initial contraction that is followed by an expansion and then a re-contraction, respectively. If an integral-abutment bridge is not symmetric, unequal displacements will occur at each abutment, and the effects of temperature-induced, abutment displacements need to be evaluated at each abutment. Extending the discussion in Section 8.9.2.4 and applying Eq. 8.225, the inelastic-rotation capacity, θ_{ic}, for an abutment pile is expressed as

$$\theta_{ic} = \phi_{rc}\left(\frac{3}{2}\theta_{p-simple}\right)C_i D_i \tag{8.228}$$

8.9.2.6. Biaxial-bending effects on inelastic-rotation capacity

The inelastic-rotation capacity for bending about the y-axis (weak-axis) of an I-shaped cross section is also limited by flange-local buckling. The compressive strain in the flange controls flange-local buckling. For x-axis (strong-axis) bending of an I-shaped cross section, the strain in the flange has a negligible gradient. For y-axis (weak-axis) bending of this same shape, a large, strain gradient occurs in the flange that will produce a higher, inelastic-rotation capacity than that for x-axis bending. However, due to the lack of published work describing the inelastic-rotation capacity, for y-axis bending of an I-shaped cross section, the inelastic-rotation capacity for the y-axis bending is conservatively assumed to be the same as the inelastic-rotation capacity of x-axis

bending. The inelastic-rotation capacities, θ_{icx} and θ_{icy}, are given by Eqs. 8.229 and 8.230, respectively, which are re-written forms of Eq. 8.228 for x-axis and y-axis bending.

$$\theta_{icx} = \phi_{rc}\left(\frac{3}{2}\theta_{px-simple}\right)C_iD_i \tag{8.229}$$

$$\theta_{icy} = \phi_{rc}\left(\frac{3}{2}\theta_{py-simple}\right)C_iD_i \tag{8.230}$$

8.9.2.7. Inelastic-rotation demand for a fixed-end beam

The inelastic-rotation demand for the fixed-end beam shown in Fig. 8.81 that is subjected to a uni-directional displacement shown in Fig. 8.81c can be evaluated by applying the basic, slope-deflection equation, which is written as

$$M_p = \frac{2EI}{L}\left(-2\theta_i - \theta_i + \frac{3\Delta}{L}\right) \tag{8.231}$$

where, M_p is the internal moment at the right end of the beam; EI is the flexural-rigidity of the beam with respect to the axis of bending; L is the span length; and $2\theta_l$, θ_l, and Δ are two times the inelastic rotation at the right end of the beam, the inelastic rotation at the left end of the beam, and the lateral displacement at the right support relative to the left support, respectively. When the displacement Δ induces member-end moments that are less than the moment M_p, member-end rotations do not occur because the supports are fixed against rotation. Inelastic, member-end rotations occur simultaneously and at equivalent magnitudes when the displacement Δ is greater than the displacement $\Delta_{p\text{-fixed}}$ shown in Fig. 8.81b. When strain-hardening effects are neglected for the extreme fibers of the cross section for the beam, the member-end moments remain constant and equal

to the plastic-moment strength, M_p, throughout the inelastic rotation θ_i. Solving Eq. 8.231 for the inelastic rotation, θ_I, and incorporating the expression for the rotation $\theta_{p\text{-simple}}$ that is given by Eq. 8.216,

$$\theta_i = \frac{\Delta}{L} - \left(\frac{\theta_{p-simple}}{3} \right) \tag{8.232}$$

8.9.2.8. Inelastic-rotation demand for uniaxial bending of a fixed-head pile

The inelastic-rotation demand for a fixed-head, integral-abutment pile, with an effective-cantilever length, L_e, that is subjected to a partial reversal of the lateral displacement that induces uniaxial bending of the pile is mathematically similar to the fixed-end beam shown in Fig. 8.81c. With displacement reversals, inelastic, member-end rotations will occur at each end of the equivalent-cantilever pile during the expansion and contraction of the bridge superstructure, when the lateral displacement on each side of the constructed position for the pile induces the displaced shape shown in Fig. 8.81c. At the top of the abutment pile, the inelastic-rotation demand, $\theta_{i\text{-partrev}}$, is the sum of the inelastic rotations on each side of the constructed position for the pile. The total, lateral displacement at the top of the pile can be expressed as a proportion of the largest, lateral displacement, Δ, on one side of the constructed position for the pile. The amount of displacement in each direction is directly proportional with the change in the average, bridge temperature. The D_i-factor that was introduced for defining the inelastic-rotation capacity for the pile cross section at the location of the plastic hinge will be applied to define the total, lateral displacement, $D_i\Delta$, and the total, member-end moments, D_iM_p.

Again, the slope-deflection equation, which is written as Eq. 8.233 is used to calculate the inelastic-rotation demand for a fixed-head, integral-abutment pile.

$$D_i M_p = \frac{2EI}{L}\left(-2\theta_{id-partrev} - \theta_{id-partrev} + \frac{3D_i\Delta}{L_e}\right) \tag{8.233}$$

Solving Eq. 8.233 for $\theta_{id\text{-}partrev}$ and incorporating the expression for the rotation $\theta_{p\text{-}simple}$ that is given by Eq. 8.216, with the length L_e for the equivalent length for the abutment pile substituted for the length L for the simple-span beam,

$$\theta_{id-partrev} = \left[\frac{\Delta}{L_e} - \frac{1}{3}(\theta_{p-simple})\right]D_i \tag{8.234}$$

As shown in Fig. 8.83, additional, inelastic-rotation demand at the top of the fixed-head pile is required to accommodate the abutment rotation, θ_w, which is in a vertical plane that is parallel to the longitudinal direction of the bridge, due to the presence of the factored-level, live and impact loads when the bridge is at its maximum, expanded position that corresponds to the pile conditions shown in Fig. 8.81a, or due to the removal of these loads when the bridge is at its maximum, contracted position that corresponds to the pile conditions shown in Fig. 8.81c. Figure 8.81b shows the relative, rotated position of the abutment for the contraction of the bridge superstructure when the live load is still on the bridge deck. The rotation θ_w is at the elastic rotation of the bridge superstructure at the abutment location. The magnitude of this rotation is a function of the flexural stiffness of the composite PC girders and the rotational restraint provided by the abutment piles. Once a plastic hinge has formed at the top of the piles, the piles will

not provide any additional rotational restraint to the end of the bridge superstructure, as the inelastic rotation at the top of the pile is increased by the rotation θ_w. If these gravity, live loads were applied before the abutments displaced laterally, the bridge superstructure and abutment piles form part of a frame system, as shown in Fig. 8.36. However, since the total, flexural stiffness for all of the composite girders is substantially greater than the total, flexural stiffness for all of the piles in one abutment, the rotational restraint provided by the elastically behaving abutment piles is not significant, and the ends of the girders can be assumed to be pinned. For the non-displaced-pile position, the rotation θ_w at the end of a girder will induce a rotation at the top of a pile equal to the rotation θ_w because for this pile position a rigid joint exists between the bridge superstructure and the abutment piles. An induced rotation θ_w at the top of an elastic, equivalent-cantilever pile will produce a moment, M_w, at the top of the pile given by

$$M_w = \left(\frac{4EI}{L_e}\right)\theta_w \tag{8.235}$$

where, EI is the flexural rigidity for the abutment pile and L_e is the equivalent-cantilever for the pile that is based on the moment equivalency ($L_e = L_{em}$). Solving Eq. 8.235 for the rotation θ_w,

$$\theta_w = \left(\frac{L_e}{4EI}\right)M_w \tag{8.236}$$

Another rotational demand at the top of the fixed-head, integral-abutment pile is caused by a vertical-temperature gradient through the depth of a bridge superstructure. For a positive, vertical-temperature gradient the end span of a bridge will experience a

downward curvature over a distance from the abutment to an inflection point near the pier and an upward displacement in the span. A negative, vertical-temperature gradient in the end span for a bridge will induce an upward curvature and a downward displacement in the span. When an abutment is displaced to the maximum-bridge-expansion position, the abutment rotation, θ_{tg}, which is in a vertical plane that is parallel to the longitudinal direction of the bridge, that is caused by a negative, vertical-temperature gradient is in the opposite direction to the inelastic rotation at the plastic-hinge location at the top of the pile that is induced by the bridge expansion. Similarly, when an abutment is displaced to the maximum-bridge-contraction position, the abutment rotation, θ_{tg}, that is produced by a positive, vertical-temperature gradient is in the opposite direction to the inelastic rotation that is caused by the bridge contraction. Figure 8.83 can be used to illustrate the effect of these two, vertical-temperature gradient and bridge-expansion conditions when the rotation θ_w is replaced by the rotation θ_{tg}.

To determine the significance of the rotation θ_{tg} in comparison to that for the rotation θ_w on the inelastic-rotation demand for the plastic hinge at the top of an abutment pile, two structural analyses of the Guthrie County Bridge were performed using the simplified-frame model shown in Fig. 8.36. The first analysis involved the application of a uniform-gravity load to approximate a live load on the bridge deck for the evaluation of the rotation θ_w. The second analysis involved application of the AASHTO recommended negative, vertical-temperature gradient for the bridge superstructure for the evaluation of the rotation θ_{tg}. Those analyses revealed that the abutment rotation that would be induced by the negative, vertical-temperature gradient were more than an order-of-magnitude less than the abutment rotation induced by the uniform-gravity load.

Therefore, the rotation θ_{tg} will not significantly affect the inelastic-rotation demand at the top of a fixed-head, integral-abutment pile. Then, the total, inelastic-rotation demand, θ_{id}, at the top of the pile is given by

$$\theta_{id} = \theta_{id\text{-}partrev} + \theta_w \tag{8.237}$$

Substituting the rotation θ_w from Eq. 8.236 and the inelastic rotation $\theta_{id\text{-}partrev}$ from Eq. 8.234 into Eq. 8.237, the inelastic-rotation demand for the plastic hinge at the pile head is given by

$$\theta_{id} = \left(\frac{\Delta}{L_e} - \frac{\theta_{p-simple}}{3}\right)D_i + \frac{M_w L_e}{4EI} \tag{8.238}$$

8.9.2.9. Inelastic-rotation demand for biaxial bending of a fixed-head pile

When an integral-abutment pile is subjected to biaxial bending, the abutment displacements dℓ, which are along the longitudinal direction of the bridge, and the displacements dt, which are in the transverse direction to the bridge length, must be resolved as x-axis and y-axis displacements, Δ_x and Δ_y, respectively, for the pile. The displacements Δ_x and Δ_y are functions of the bridge-skew angle and the particular pile orientation shown in Fig. 8.14. The inelastic-rotation demands, θ_{idx} and θ_{idy}, are obtained from Eqs. 8.239 and 8.240, respectively, which are re-written forms of Eq. 8.238 for x-axis and y-axis bending.

$$\theta_{idx} = \left(\frac{\Delta_y}{L_{ex}} - \frac{\theta_{px-simple}}{3}\right)D_i + \frac{M_{wx} L_{ex}}{4EI_x} \tag{8.239}$$

$$\theta_{idy} = \left(\frac{\Delta x}{L_{ey}} - \frac{\theta_{py-simple}}{3}\right)D_i + \frac{M_{wy} L_{ey}}{4EI_y} \tag{8.240}$$

8.9.2.10. Displacement-ductility limit state for uniaxial bending of fixed-head piles

The rotational-ductility limit state for uniaxial bending of a fixed-head, integral-abutment pile, which requires that the inelastic-rotation demand that is expressed by Eq. 8.238 must be less than or equal to the inelastic-rotation capacity that is expressed by Eq. 8.228, is expressed as

$$\left\{\left[\left(\frac{\Delta}{L_e}-\frac{1}{3}(\theta_{p-simple})\right)\right]D_i+\frac{M_w L_e}{4EI}\right\}\leq\left[\phi_{rc}\left(\frac{3}{2}\theta_{p-simple}\right)C_i D_i\right] \tag{8.241}$$

Substituting the expression for $\theta_{p\text{-simple}}$ from Eq. 8.216, with the length L changed to L_e, into Eq. 8.241 and simplifying, the displacement-ductility, limit state for uniaxial bending of a fixed-head, integral-abutment pile is given by

$$\Delta\leq\Delta_p\left[\phi_{rc}\left(\frac{9}{2}\right)C_i+1-\left(\frac{3M_w}{2M_p D_i}\right)\right] \tag{8.242}$$

with,

$$\Delta_p=\frac{M_p L_e^2}{6EI} \tag{8.243}$$

where, Δ is the calculated, horizontal displacement of the pile head at factored-load levels that is induced by a temperature change of the bridge superstructure; Δ_p is the horizontal displacement at the pile head that is associated with the theoretical, initial M_p behavior shown in Fig. 8.81b; ϕ_{rc} is the resistance factor that is associated with compressive strains on the flange element of the HP-shaped, pile cross section (ϕ_{rc} =

0.85); C_i is the compression-flange, local-buckling factor, which is evaluated by Eq. 8.222; D_i is the temperature-phase factor, which is calculated from Eqs. 8.226 or 8.227 depending on the particular temperature case for bridge expansion or contraction, as discussed in Section 8.9.2.5); M_w is the moment induced at the top of the pile by the factored-level live loads, including impact effects; M_p is the plastic-moment strength and EI is the flexural rigidity of the pile with respect to the axis of bending; and L_e is the equivalent-cantilever length that is associated with horizontal stiffness of the backfill behind the abutment ($L_e = L_{eh}$), which is evaluated from Eq. 8.23.

The term $\left(\frac{3M_w}{2M_pD_i}\right)$ in Eq. 8.242 will be less than unity. If this term is set equal to one, a conservative expression for the factored-load-level, displacement-ductility, limit state for uniaxial bending of a fixed-head, integral-abutment pile is written as

$$\Delta \leq \phi_{rc}\left(\frac{9}{2}\right)C_i\Delta_p \tag{8.244}$$

Equation 8.244 specifies that the displacement demand, Δ, must be equal to or less than the displacement capacity, Δ_c. Therefore, the displacement capacity for uniaxial bending of a fixed-head, integral-abutment pile is given by

$$\Delta_c = \phi_{rc}\left(\frac{9}{2}\right)C_i\Delta_p \tag{8.245}$$

Equation 8.245 is graphically illustrated in Fig. 8.84. The hatched-vertical lines on each side of the figure represent the pile, uniaxial-bending, displacement capacity. As long as the pile-head displacement, $d\ell$, along the longitudinal direction of the bridge, which is

also in the direction of one of the principal axes for the HP-shaped pile, remains between the displacement limits shown in the figure, the pile has adequate ductility. The hysteresis loops shown in the figure represent the design-moment strength versus displacement relationship for longitudinal, expansion and contraction of a bridge superstructure.

8.9.2.11. Displacement-ductility limit state for biaxial bending of fixed-head piles

The rotational-ductility limit state for biaxial bending of a fixed-head, integral-abutment pile that was presented by Greimann et al. (1987b) is re-written here as Eq. 8.246.

$$\left(\frac{\theta_{idx}}{\theta_{icx}}\right)+\left(\frac{\theta_{idy}}{\theta_{icy}}\right)\leq 1 \tag{8.246}$$

For this linear, interaction relationship, the rotations θ_{icx} and θ_{icy} are the inelastic-rotation capacities for x-axis and y-axis bending, respectively for the HP-shaped pile, which are expressed by Eqs. 8.229 and 8.230, respectively. The rotations θ_{idx} and θ_{idy} are the inelastic-rotation demands for x-axis and y-axis bending, respectively, for the HP-shaped pile, which are expressed by Eqs. 8.239 and 8.240, respectively.

The displacement-ductility limit state for biaxial bending of a fixed-head, integral-abutment pile that was presented by Greimann et al. (1987b) is re-written here as Eq. 8.247.

$$\left(\frac{\Delta_x}{\Delta_{cx}}\right)+\left(\frac{\Delta_y}{\Delta_{cy}}\right)\leq 1 \tag{8.247}$$

with,

$$\Delta_x = (d\ell) \cos \theta_r - (dt) \sin \theta_r \tag{8.248}$$

$$\Delta_y = (d\ell) \sin \theta_r + (dt) \cos \theta_r \tag{8.249}$$

where, the displacements Δ_x and Δ_y are total components of the displacements $d\ell$ and dt in the x-axis and y-axis directions, respectively, for a pile. The pile-skew angle, θ_r, is the angle between the t-axis for the bridge and the y-axis for an abutment pile. The displacements Δ_{cx} and Δ_{cy} are the displacement capacities in the x-axis and y-axis directions, respectively, at the top of the pile for y-axis bending and x-axis bending, respectively, for an abutment pile. These displacement capacities are given by Eqs. 8.250 and 8.251 which are re-written forms of Eq. 8.237 for x-axis and y-axis bending, respectively.

$$\Delta_{cx} = \phi_{rc} \frac{9}{2} C_i \Delta_{px} \tag{8.250}$$

$$\Delta_{cy} = \phi_{rc} \frac{9}{2} C_i \Delta_{py} \tag{8.251}$$

where, Δ_{px} and Δ_{py} are the lateral displacements at the top of an abutment pile in the x-axis and y-axis directions, respectively, for the pile that are associated with the theoretical, initial M_{py} and M_{px}, respectively, behavior. In summary, the pile ductility (Eq. 8.247) should be checked for Displacement Case 1 (without concrete creep and shrinkage) and Displacement Case 2 (without concrete creep and shrinkage), where the displacement $d\ell$ is given in Section 8.6 and the upper bound for the displacement dt is dt_{max} that is described in Section 8.7.6. Additionally, Eq. 8.247 should be checked for re-expansion of the bridge superstructure (Displacement Case 3) with double the ductility

capacities (See Section 8.9.2.5) or, alternatively, with one-half of the displacement $\Delta\ell_{re\text{-}expand}$ from Section 8.6.1.

8.9.3. Capacity to transfer load from a pile to the soil strata

Article 10.7.3.2 of the AASHTO-LRFD Specifications (1998) states that the bearing resistance of piles may be estimated using analytical or in-situ, test methods. The bearing resistance of a pile in soil is derived from the tip resistance and/or skin-friction resistance along the length of the pile.

The seasonal-cyclic, lateral displacement of an integral-abutment pile will not affect its tip resistance. However, these lateral displacements will create a gap between the pile and the surrounding soil near the top of the pile that will reduce the pile length that provides the frictional resistance of the pile. Figure 8.85 shows the length of the pile where the lateral displacement of a pile is greater than a critical-lateral displacement, y_{max}, for which the skin-frictional resistance of the pile is affected by the magnitude of the lateral displacement. The length, ℓ', of a pile that is available to resist the vertical load by skin friction is given by

$$\ell' = \ell - \ell_n \tag{8.252}$$

where, ℓ is the total pile length and ℓ_n is the length of the pile that is ineffective for vertical, skin-frictional resistance. The laterally unrestrained length, ℓ_u, for a pile is the length of the pile that is above the undisturbed-soil strata. This length includes the depth of a pre-bored hole for the pile. Figure 8.86, which was presented by Greimann et al. (1987a), is used to evaluate the length ℓ_n for a prescribed displacement y_{max}. Fleming, et al. (1985) suggested that the displacement y_{max} is about 2 percent of the pile diameter.

The critical pile length, ℓ_c, which was discussed in Section 8.5, is evaluated from Eq. 8.24.

8.10. Maximum bridge length

The maximum length of an integral-abutment bridge is often limited by the ductility of the abutment piles. These piles must have adequate moment-rotation capacity to accommodate the horizontal displacements of the abutments. Brief explanations are presented for the analysis procedures that are used to establish the maximum, bridge length for a particular orientation of the abutment piles in a non-skewed or a skewed, integral-abutment bridge when Eq. 8.235 controls the pile design.

8.10.1. Non-skewed bridge

For a symmetric, non-skewed, integral-abutment bridge that has the webs of the abutment piles oriented perpendicular to the longitudinal axis of the bridge, Eq. 8.243 reduces to

$$d\ell \leq \Delta_{cx} \tag{8.253}$$

since, $\theta_r = 0$ and $dt = 0$. Substituting the expression for the displacement capacity, Δ_{cx}, for y-axis bending of the abutment pile from Eq. 8.250 into Eq. 8.253,

$$d\ell \leq \phi_{rc}\left(\frac{9}{2}\right) C_i\, \Delta_{px} \tag{8.254}$$

From Eq. 8.32, 8.36, and 8.39, the displacement $d\ell$ is rewritten as

$$d\ell = \Gamma\, \varepsilon_\ell\, \ell \tag{8.255}$$

with,

$$\varepsilon_\ell = \alpha_e \, \Delta T \tag{8.256}$$

where, ε_ℓ is the average, longitudinal strain in the bridge superstructure; α_e is the effective α-coefficient for the bridge superstructure; ℓ is the distance from the "point-of-fixity" for the bridge to the abutment where the displacement $d\ell$ is evaluated; and Γ and ΔT are the uncertainty factor and change in the average, bridge temperature. Recall that the concrete-creep and concrete-shrinkage strains are neglected for the design and ductility requirements for the integral-abutment piles, as discussed in Section 8.4.4. When the same soil conditions exist behind each abutment and if the bridge is symmetric, the length ℓ equals one-half of the total, bridge length, L. Rewriting Eq. 8.255 for a change in the length variables and equating the strain ε_ℓ to the free expansion or contraction of the bridge superstructure,

$$d\ell = \frac{1}{2}\Gamma\alpha_e(\Delta T)\, L \tag{8.257}$$

Substituting Eq. 8.257 into Eq. 8.254 and solving for the bridge length, L,

$$L \le \frac{\phi_{rc}\left(9C_i\Delta_{px}\right)}{\Gamma\,\alpha_e(\Delta T)} \tag{8.258}$$

The maximum length for a non-skewed, symmetric bridge, will be the shortest length that is calculated by applying Eq. 8.258 for the three, critical-pile displacements that correspond with the maximum expansion (Displacement Case 1), maximum contraction (Displacement Case 2), and maximum re-expansion (Displacement Case 3) of the bridge

superstructure, which were described in Section 8.6.1. Stated another way, the maximum bridge length will be the length that is associated with the largest factored temperature (Γ times ΔT) for the three displacement cases. Chapter 9 presents numerical solutions for the maximum length of an integral-abutment bridge without skew. The effect of a change in the steel-yield strength for the abutment piles on the maximum bridge length is presented in two examples.

8.10.2. Skewed bridge

The maximum length for a skewed, integral-abutment bridge cannot be expressed in a closed-form, mathematical equation because the transverse displacement, dt, for an abutment is calculated by the iterative algorithm in the program Transmove. The longitudinal displacement $d\ell$, for an abutment, which is assumed to be the free expansion or contraction for a temperature increase or decrease, respectively, of the skewed-bridge superstructure, is also expressed by Eq. 8.31.

The pile-head, displacement demands, which are expressed by Eqs. 8.248 and 8.249, and the pile-head, displacement capacities, which are given by Eqs. 8.250 and 8.251, for biaxial displacements at the fixed-head of an abutment pile are substituted into the displacement-ductility, interaction expression (Eq. 8.247) to obtain the expanded form of the displacement-ductility, interaction expression for the pile that is subjected to either a uni-direction displacement or to a reversal of displacements. This biaxial-displacement relationship for a skewed, integral-abutment bridge is given by

$$\left[\frac{(d\ell)\cos\theta_r - (dt)\sin\theta_r}{\phi_{rc}\left(\frac{9}{2}\right)C_i\Delta_{px}}\right] + \left[\frac{(d\ell)\sin\theta_r + (dt)\cos\theta_r}{\phi_{rc}\left(\frac{9}{2}\right)C_i\Delta_{py}}\right] \le 1 \qquad (8.259)$$

Solving Eq. 8.259 for the displacement $d\ell$,

$$d\ell \le \left[\frac{\phi_{rc}\left(\frac{9}{2}\right)C_i\Delta_{px}\Delta_{py} + dt\left(\Delta_{py}\sin\theta_r - \Delta_{px}\cos\theta_r\right)}{\left(\Delta_{py}\cos\theta_r + \Delta_{px}\sin\theta_r\right)}\right] \qquad (8.260)$$

Again, setting the displacement $d\ell$ equal to the free expansion or contraction of the bridge superstructure, as expressed by Eq. 8.255, and assuming that the same soil conditions exist behind each abutment and that the bridge is symmetric, the bridge length, L, is given by

$$L \le \left[\frac{2}{\Gamma\alpha_e(\Delta T)}\right]\left[\frac{\phi_{rc}\left(\frac{9}{2}\right)C_i\Delta_{px}\Delta_{py} + dt\left(\Delta_{py}\sin\theta_r - \Delta_{px}\cos\theta_r\right)}{\left(\Delta_{py}\cos\theta_r + \Delta_{px}\sin\theta_r\right)}\right] \qquad (8.261)$$

The maximum bridge length for a skewed, symmetric, integral-abutment bridge will be the shortest length that is calculated by applying Eq. 8.261 for the three, critical-pile displacements that correspond with the maximum expansion (Displacement Case 1), maximum contraction (Displacement Case 2), and maximum re-expansion (Displacement Case 3) of the bridge superstructure, which were described in Section 8.6.1. Stated another way, the maximum bridge length will be the length that is

associated with the largest factored temperature (Γ times ΔT) for the three displacement cases. However, an iterative solution of Eq. 8.261 is required, since the displacement dt is a function of the maximum bridge length. An iterative procedure that can be used involves the following steps:

Step 1: Select the appropriate displacement factor Γ; coefficient of thermal expansion and contraction α_e; and the change in the average, bridge temperature ΔT.

Step 2: Estimate the maximum bridge length, L_{max}.

Step 3: Establish the transverse displacement, dt, of the abutment.

Step 4: Calculate the length L_{max} using Eq. 8.261.

Step 5: Compare the lengths L_{max} from Steps 2 and 4.

Step 6: Repeat Steps 2 through 5 until acceptable convergence is obtained for the length L_{max}.

A close approximation for the maximum bridge length can be determined if the displacement dt is set equal to the maximum transverse displacement, dt_{max}, of the abutment (see Section 8.6.2.6). The displacement dt_{max} can be predicted by the Transmove program (see Appendix B). Chapter 9 presents numerical solutions for the maximum length of an integral-abutment bridge with a 40-deg. skew. The effect of a change in the steel-yield strength for the abutment piles on the maximum bridge length is presented in two examples.

8.11. Pile Orientation

Vann, et al., (1973) noted that the lowest strength of an I-shaped beam that is predicted by the individual consideration of the mathematical models for flange-local

buckling, web-local buckling, and lateral-torsional buckling is larger than the strength for the same beam when interaction occurs between either flange-local buckling and web-local buckling or flange-local buckling and lateral-torsional buckling. If the HP-shaped, abutment piles for an integral-abutment bridge are oriented with their webs perpendicular to the longitudinal axis of the bridge, the piles will be subjected to only y-axis (weak-axis), flexural bending for non-skewed bridges and non-skewed bridges with small skew angles and to primarily y-axis, flexural bending for skewed bridges with moderate and large skew angles, when a bridge superstructure expands and contracts with changes in the average, bridge temperature. Web-local buckling and lateral-torsional buckling will not occur with y-axis, flexural bending of an I-shaped cross section. Therefore, with this orientation for an HP-shaped, abutment pile, interaction will not occur for the flexural-bending, failure modes; and only flange-local buckling may affect the flexural-bending strength and the associated moment-rotation capacity, as discussed in Section 8.9.2.3 for the abutment piles.

For y-axis (weak-axis) bending of an abutment pile, a linearly-varying, strain gradient is induced in the flange, and for x-axis (strong-axis) bending of that same pile an essentially constant strain is induced in the flange. The potential for flange-local buckling is greater when the flange element is subjected to constant, compressive strain than when this element is subjected to a linearly varying, compressive strain. Although the ISU researchers have used the same generic term for the inelastic-rotation capacity for both the y-axis and x-axis bending of the pile, the rotation θ_{py} is larger than the rotation θ_{px}.

When the webs of HP-shaped, abutment piles are oriented perpendicular to the longitudinal direction of an integral-abutment bridge, the piles will provide the least resistance to the longitudinal expansion and contraction of a bridge superstructure. Even if the abutment piles are oriented for only x-axis, (strong-axis) flexural bending when temperature changes occur in the bridge superstructure, the reduction in the longitudinal displacements of the bridge would be negligible compared to those displacements for y-axis, flexural bending of the abutment piles. In addition, the transverse-movement study, which is presented in Section 8.6.2, revealed that the smallest, transverse displacements of the abutment are induced for a skewed, integral-abutment bridge when the abutment piles are subjected to primarily y-axis, flexural bending as the bridge expands and contracts. The ISU researchers recommend that the HP-shaped, abutment piles should be oriented with their webs perpendicular and their flanges parallel to the longitudinal direction of the bridge for both non-skewed and skewed, integral-abutment bridges. Therefore, the ISU researchers recommend the discontinuation of the current, Iowa DOT practice that permits a bridge contractor to orientate the webs of the abutment-backwall piles in a direction that is parallel to the front face of the abutment for bridge-skew angles of up to 30 deg.

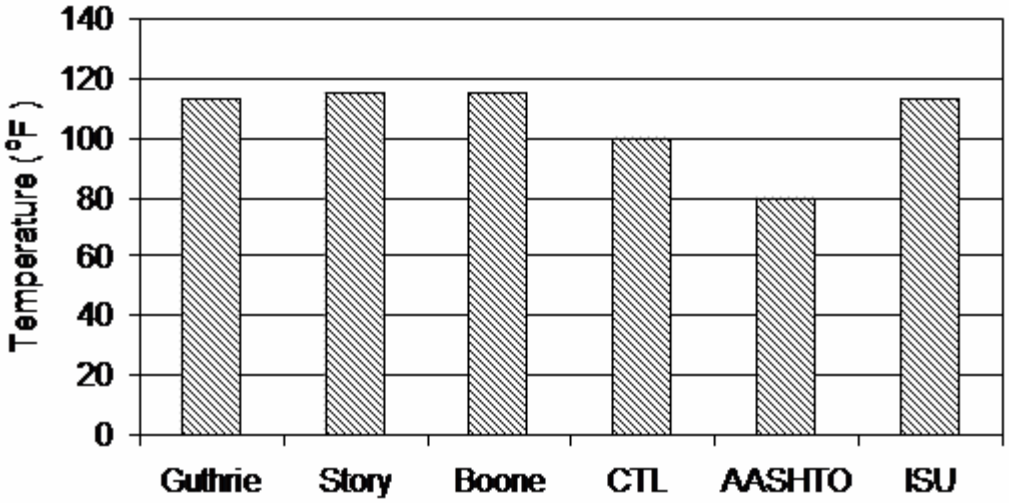

Figure 8.1. Recommended and experimental, temperature ranges

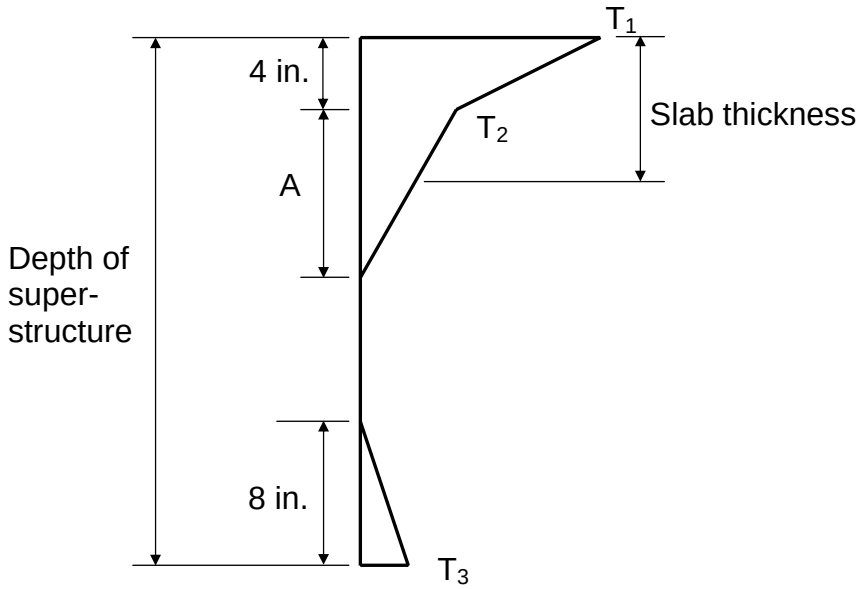

Figure 8.2. Temperature gradient through the depth of a bridge superstructure (adapted from AASHTO-LRFD, 1998)

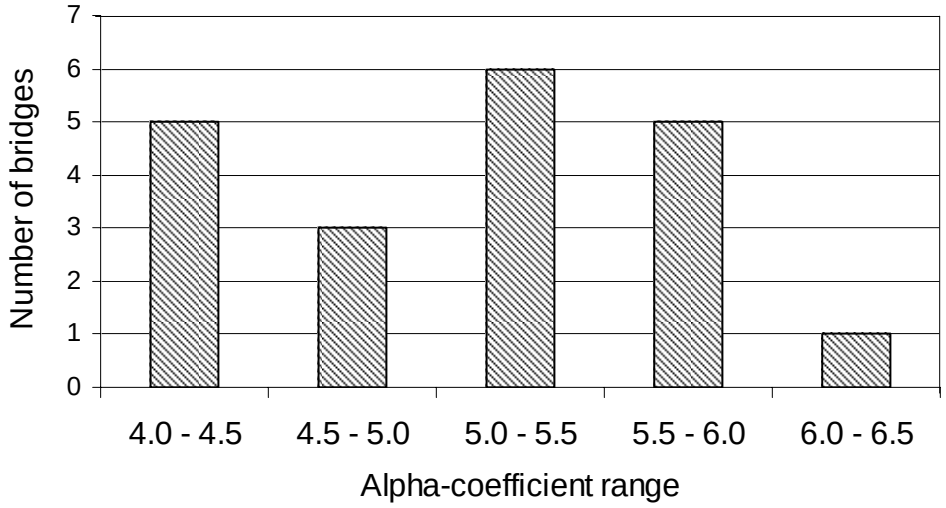

Figure 8.3. Alpha-coefficients for 100%-dry concrete from selected bridge decks in the State of Iowa

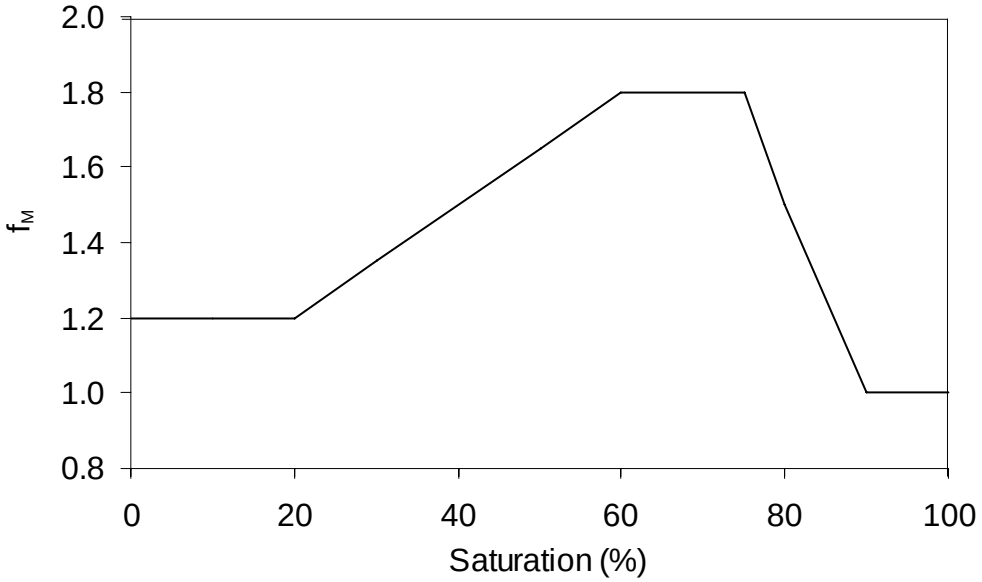

Figure 8.4. Moisture-correction factor

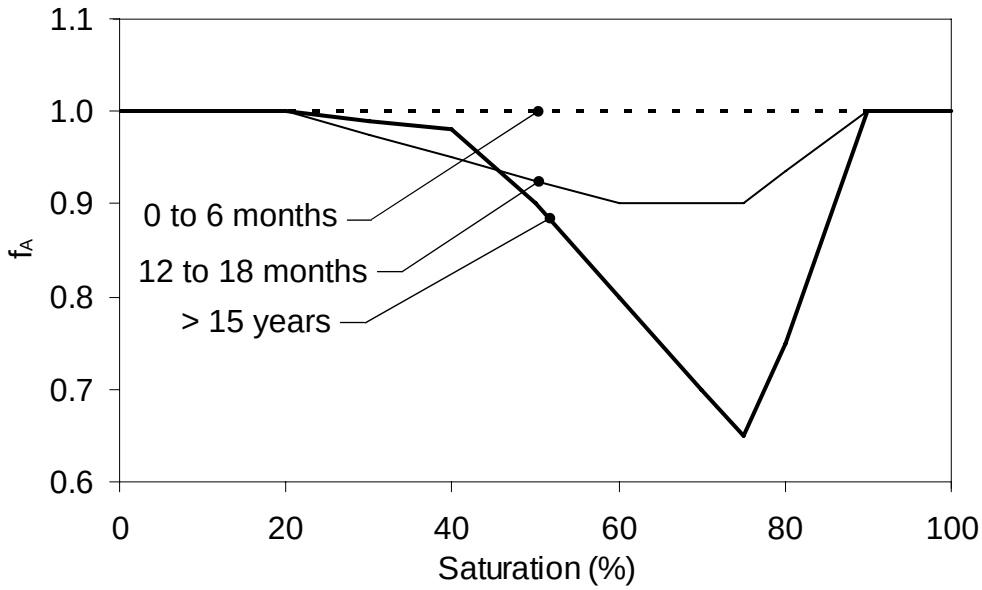

Figure 8.5. Concrete-age-correction factor

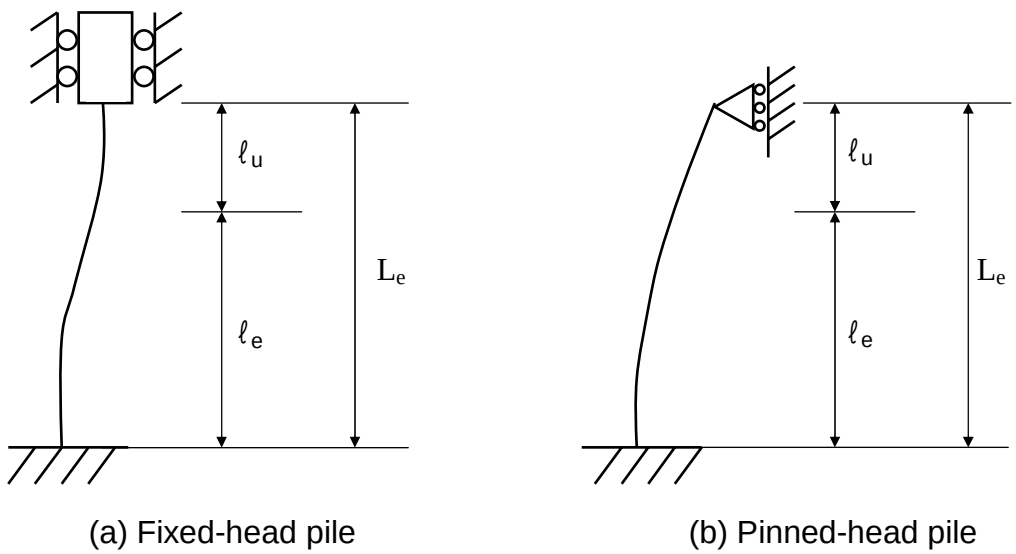

Figure 8.6. Equivalent cantilevers for an abutment pile

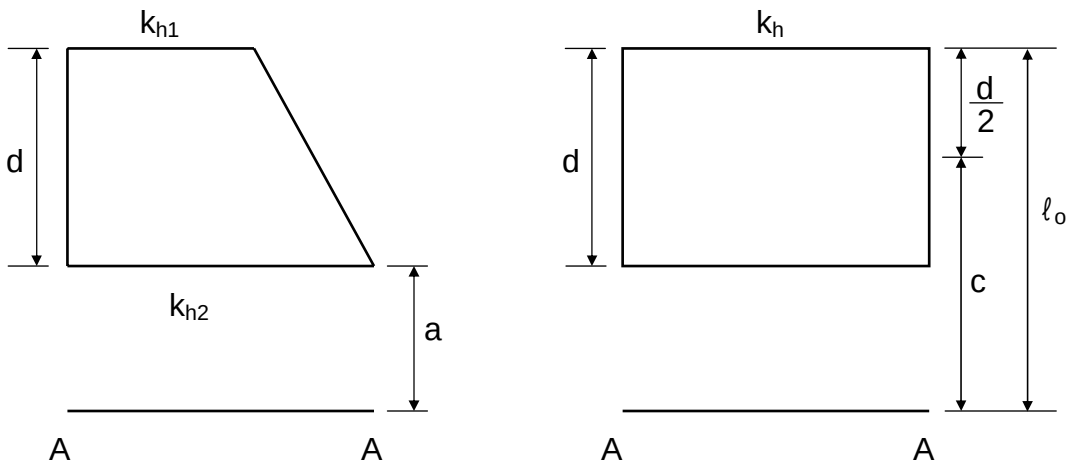

$$I_k = k_{h1}\left[\frac{d^3}{36} + \frac{d}{2}\left(a + \frac{2d}{3}\right)^2\right] + k_{h2}\left[\frac{d^3}{36} + \frac{d}{2}\left(a + \frac{d}{3}\right)^2\right]$$

$$I_k = k_h\left[\frac{d^3}{12} + dc^2\right]$$

(a) Linearly varying soil stiffness

(b) Uniform soil stiffness

Figure 8.7. Second moment of the distributed, horizontal stiffness of the soil within a soil layer about a reference line A-A

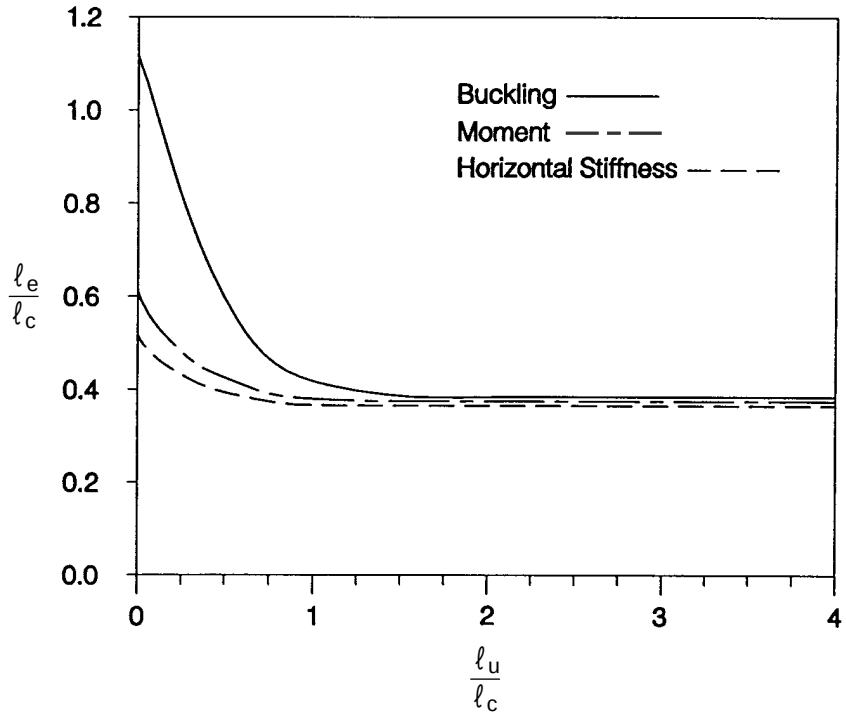

(a) Fixed-head pile

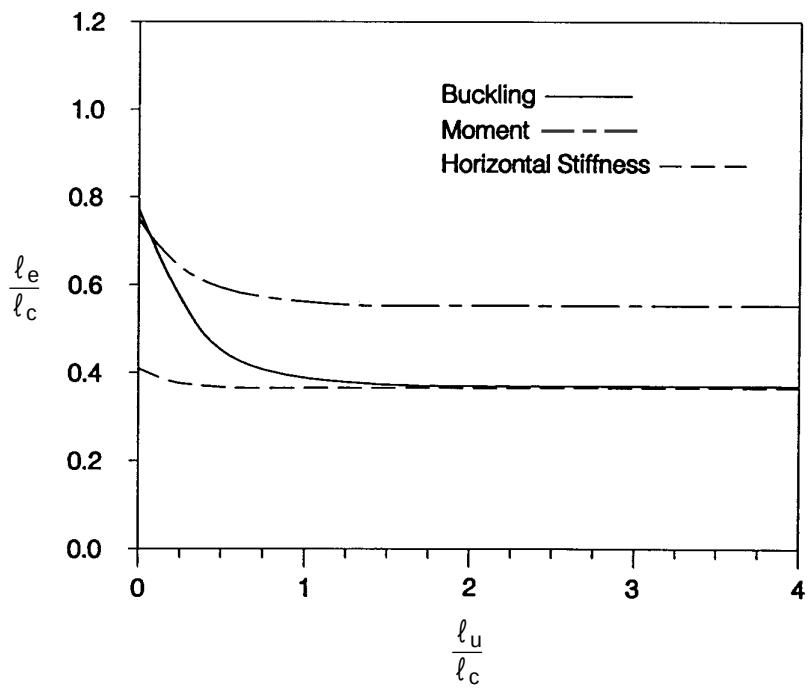

(b) Pinned-head pile

Figure 8.8. Equivalent-cantilever lengths for piles in a uniform soil

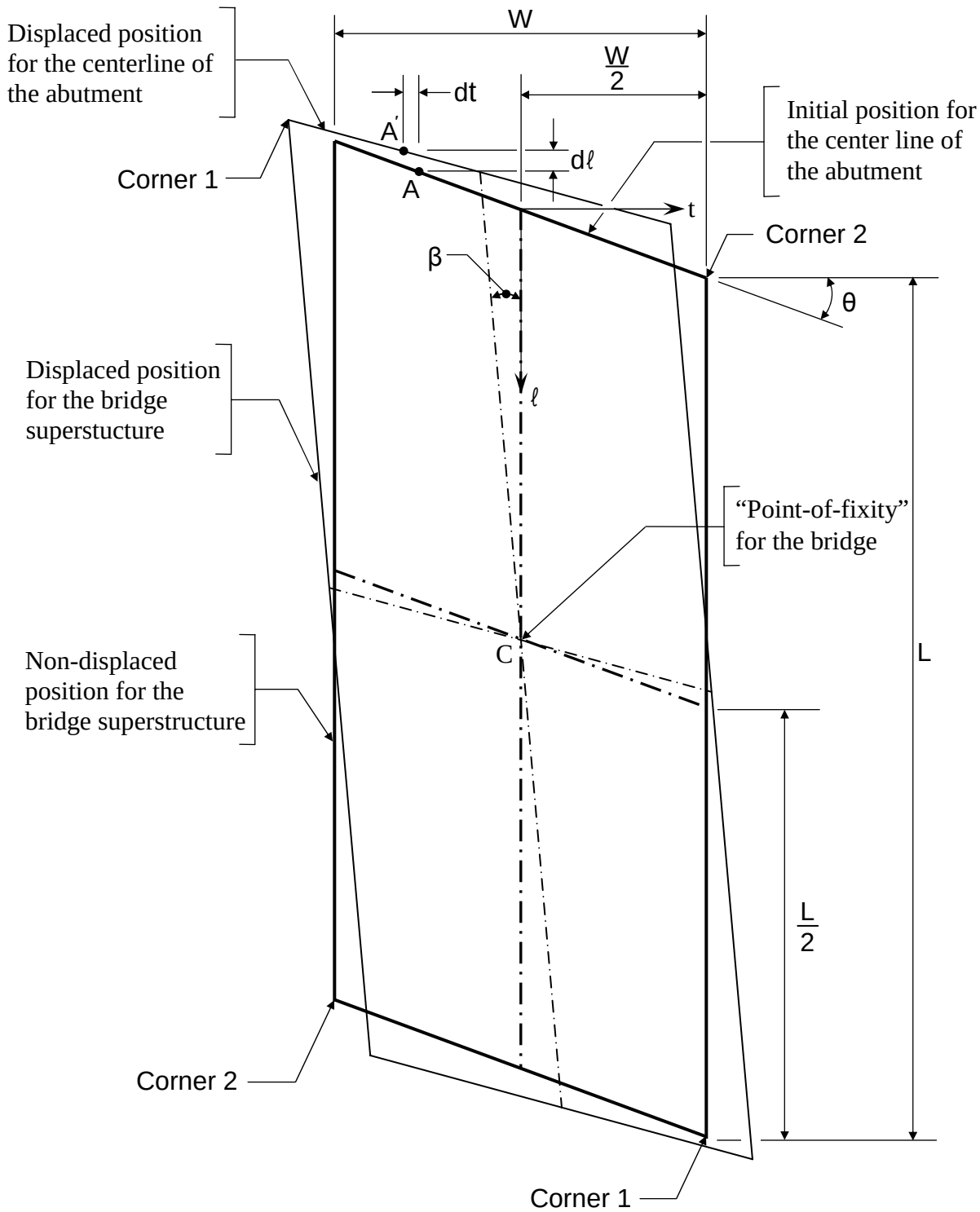

Figure 8.9. Longitudinal displacement and horizontal rotation of a symmetric, single-span, integral-abutment, bridge superstructure

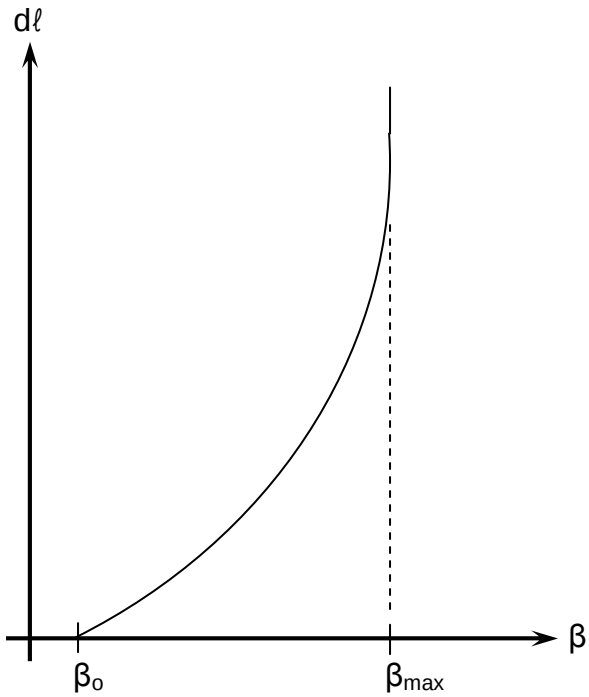

Figure 8.10. Relationship between the horizontal rotation of an integral-abutment bridge and the longitudinal displacement of an integral abutment

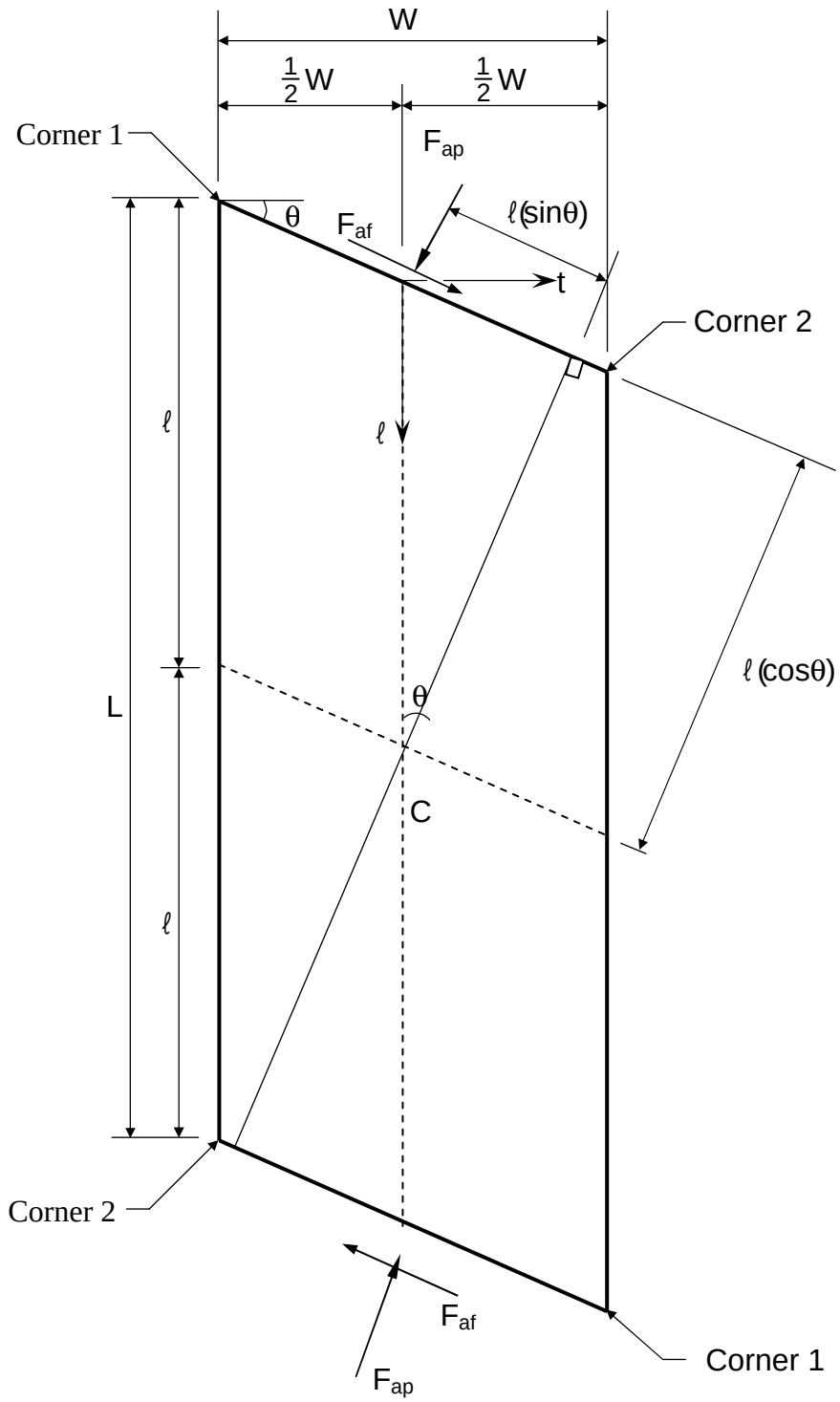

Figure 8.11. Simplified model for transverse displacements of an abutment

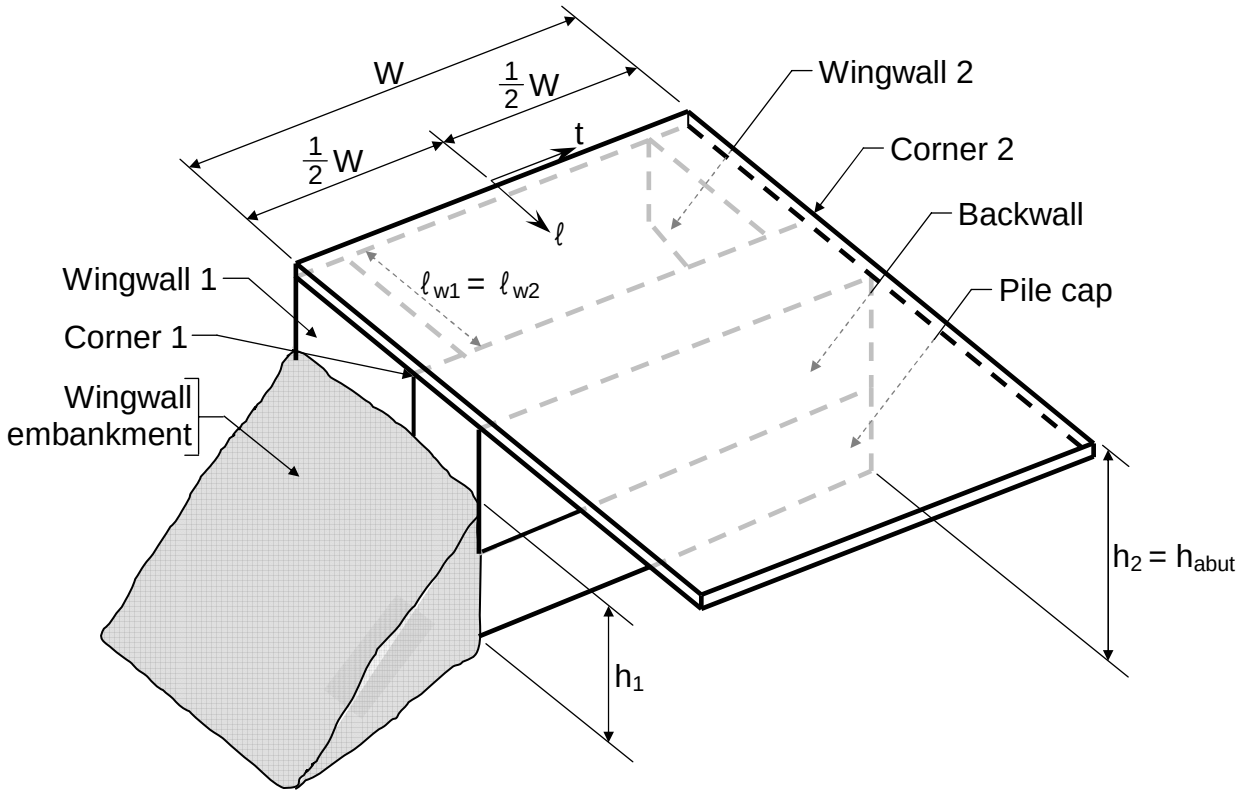

Note: Soil berm and soil embankment along Wingwall 2 are not shown for figure clarity

Figure 8.12. Parameters that affect the transverse displacements of an abutment

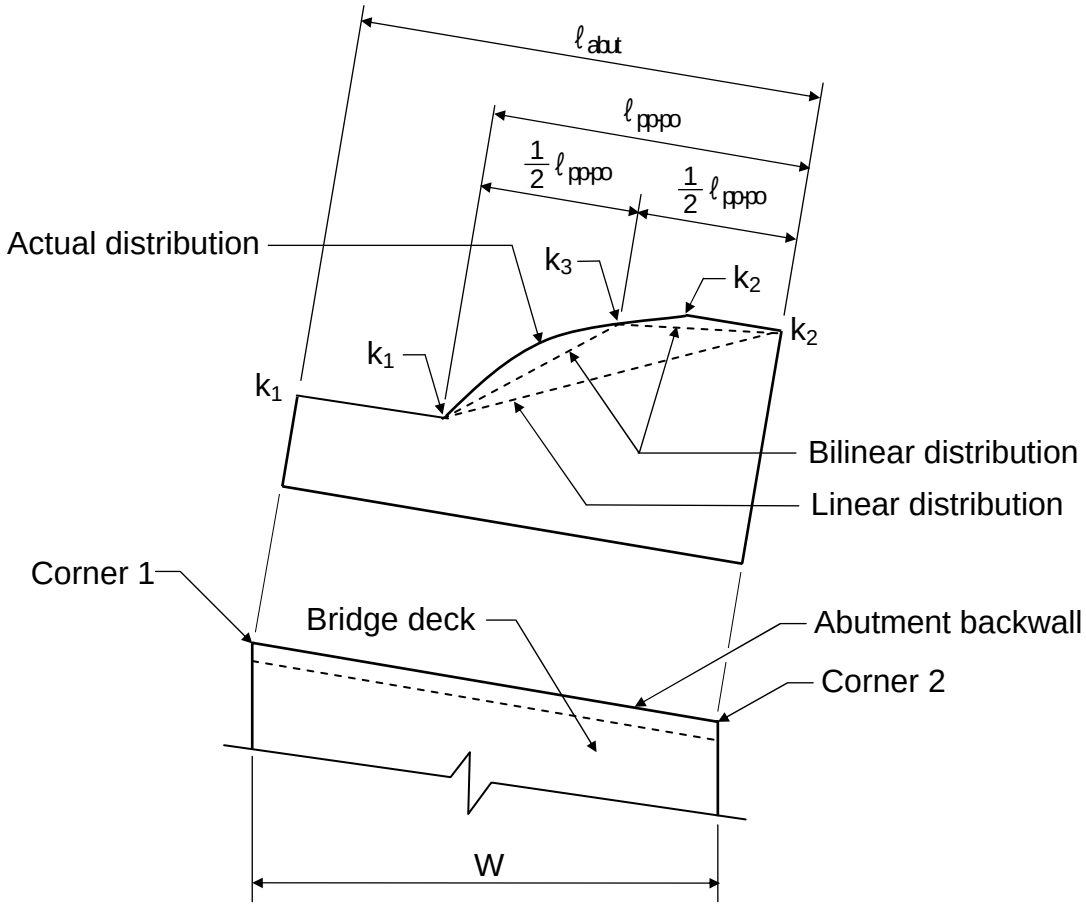

Figure 8.13. Soil-pressure coefficients for the abutment backfill

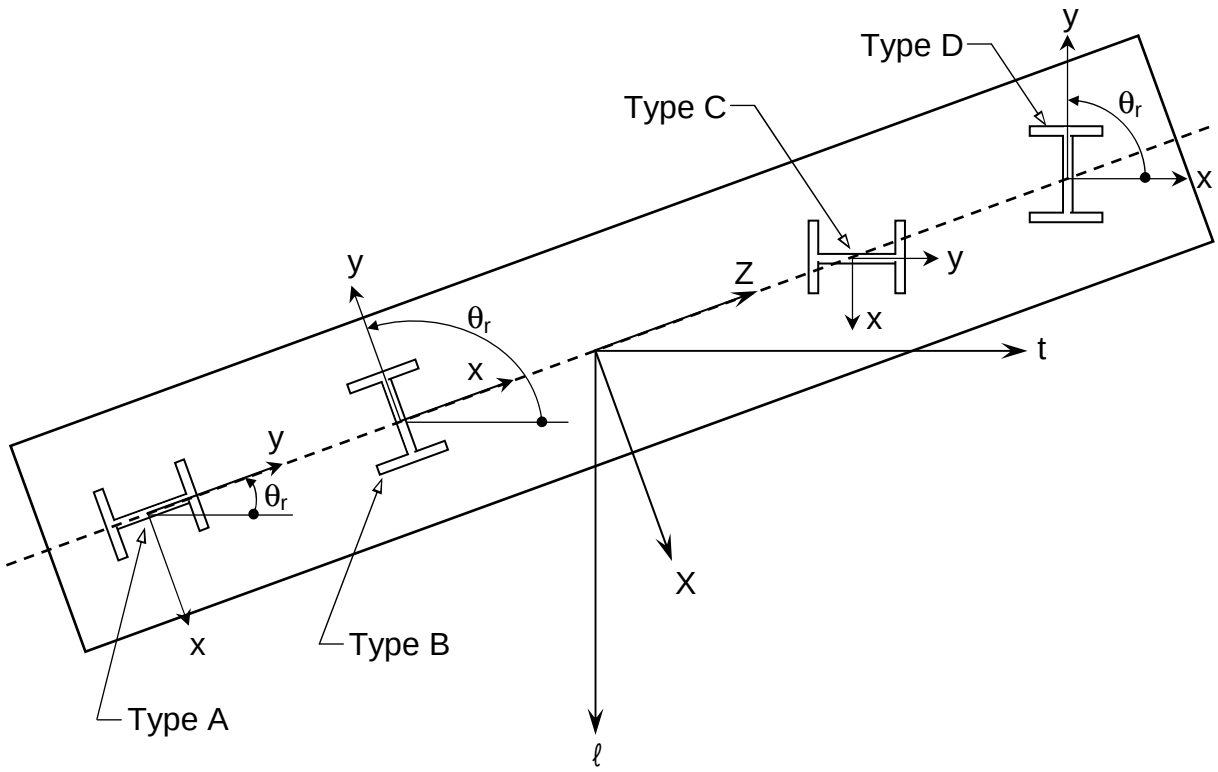

Figure 8.14. Pile orientations for integral abutments

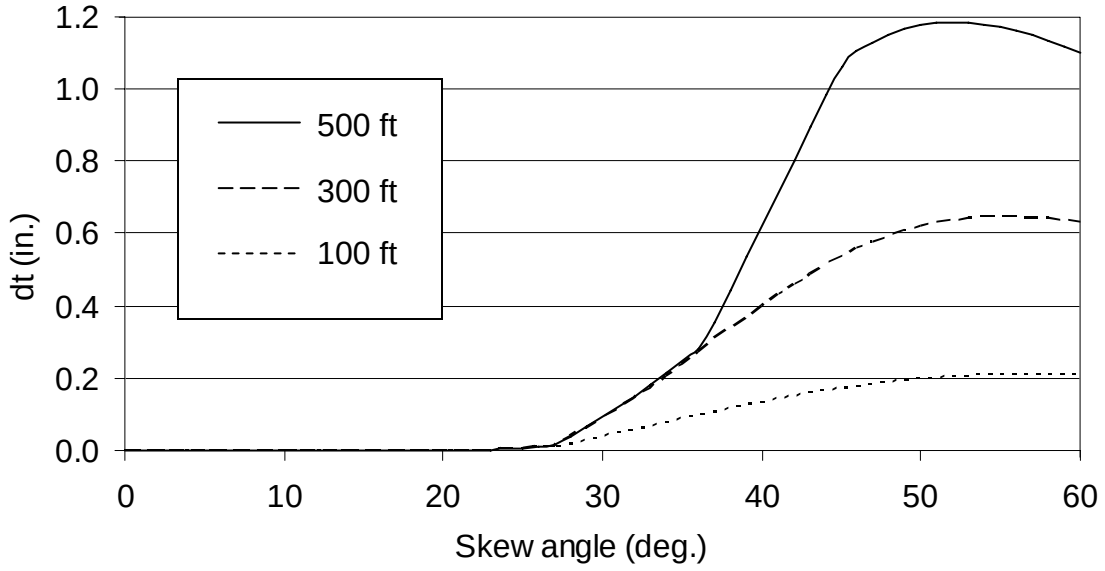

Figure 8.15. Influence of the bridge length on the abutment displacement dt

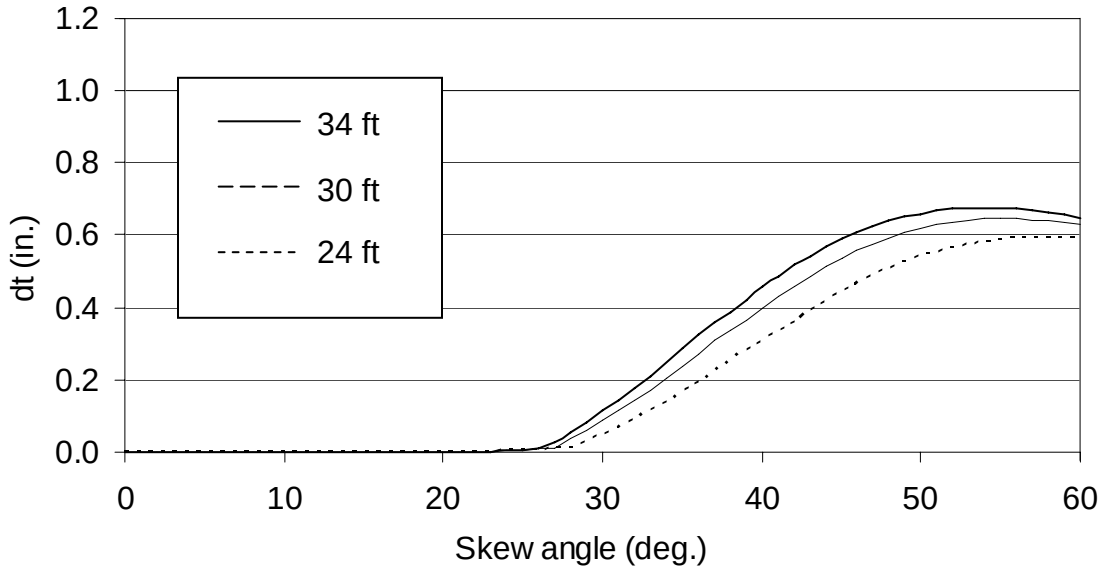

Figure 8.16. Influence of the bridge width on the abutment displacement dt

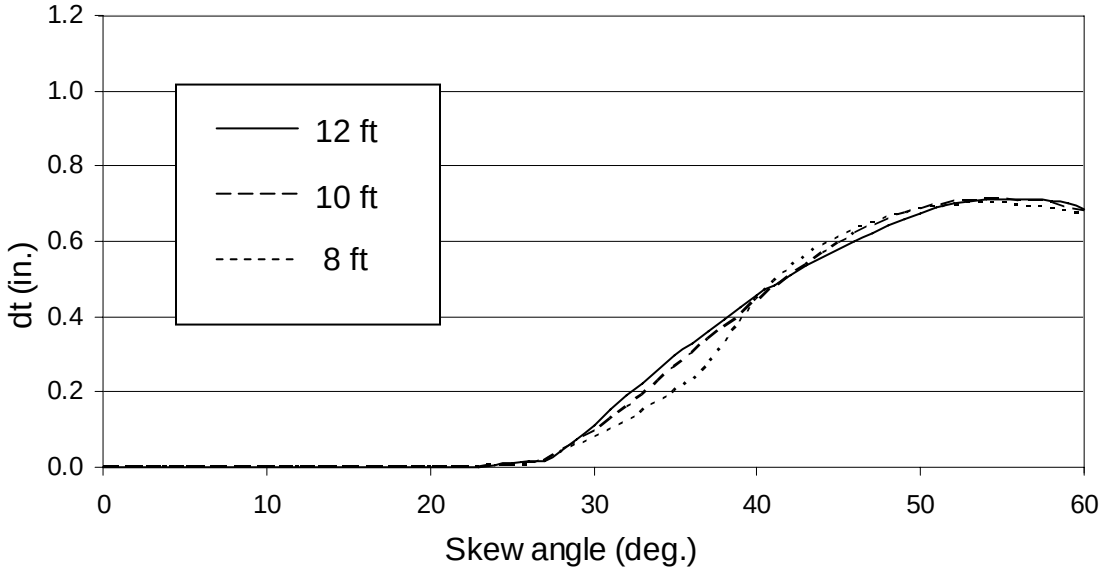

Figure 8.17. Influence of the abutment height on the abutment displacement dt

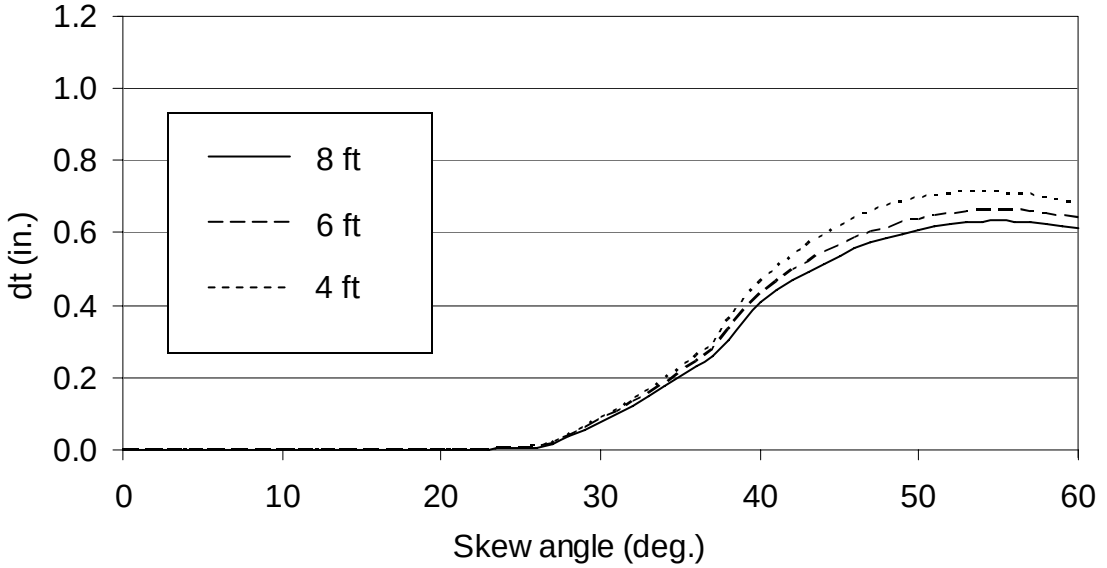

Figure 8.18. Influence of the wingwall-embankment height on the abutment displacement dt

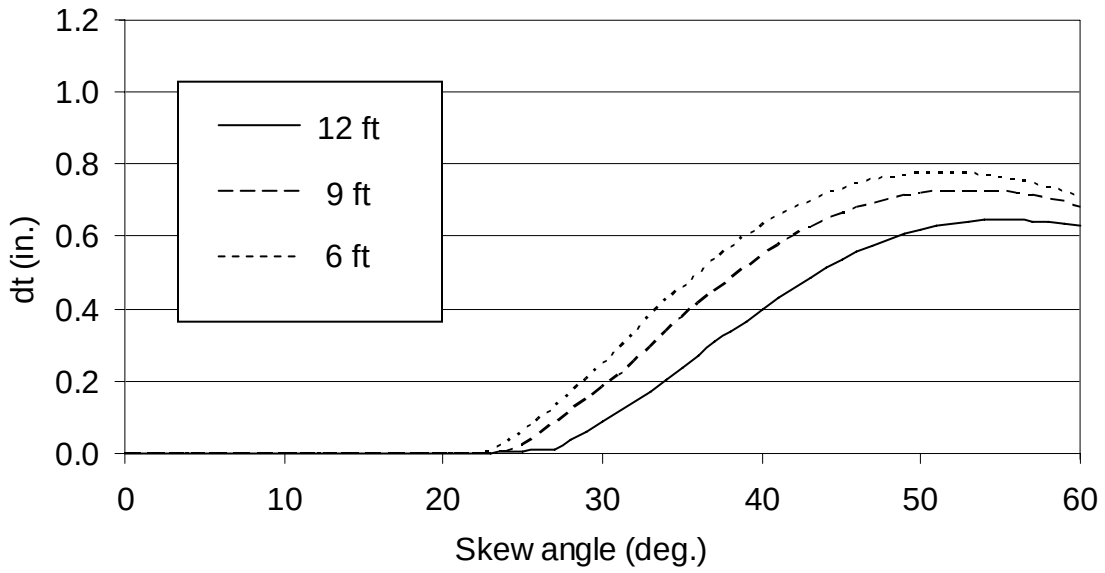

Figure 8.19. Influence of the wingwall length on the abutment displacement dt

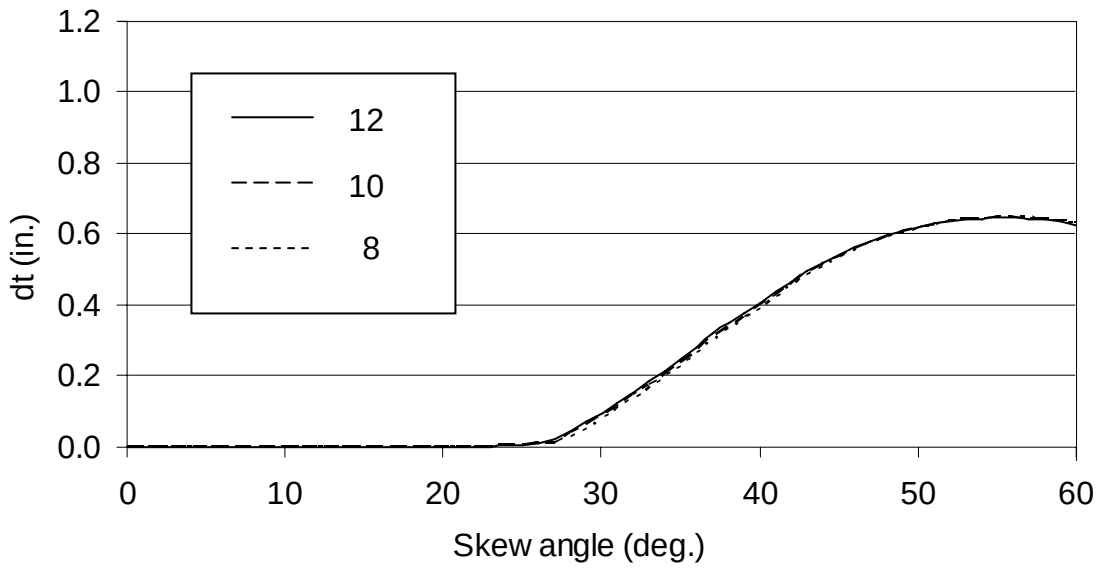

Figure 8.20. Influence of the number of backwall piles on the abutment displacement dt

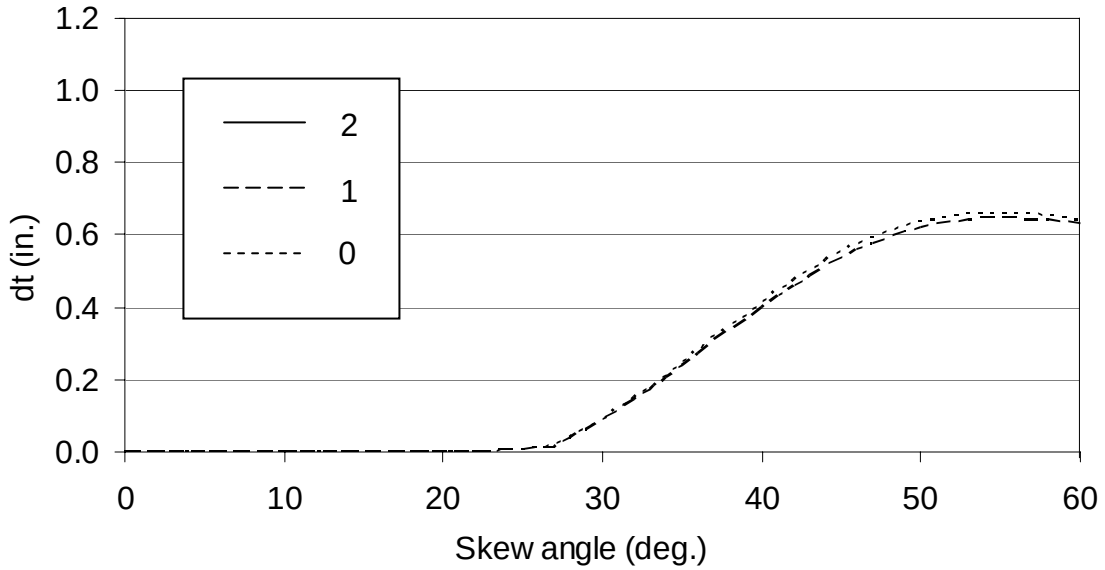

Figure 8.21. Influence of the number of sidewall piles on the abutment displacement dt

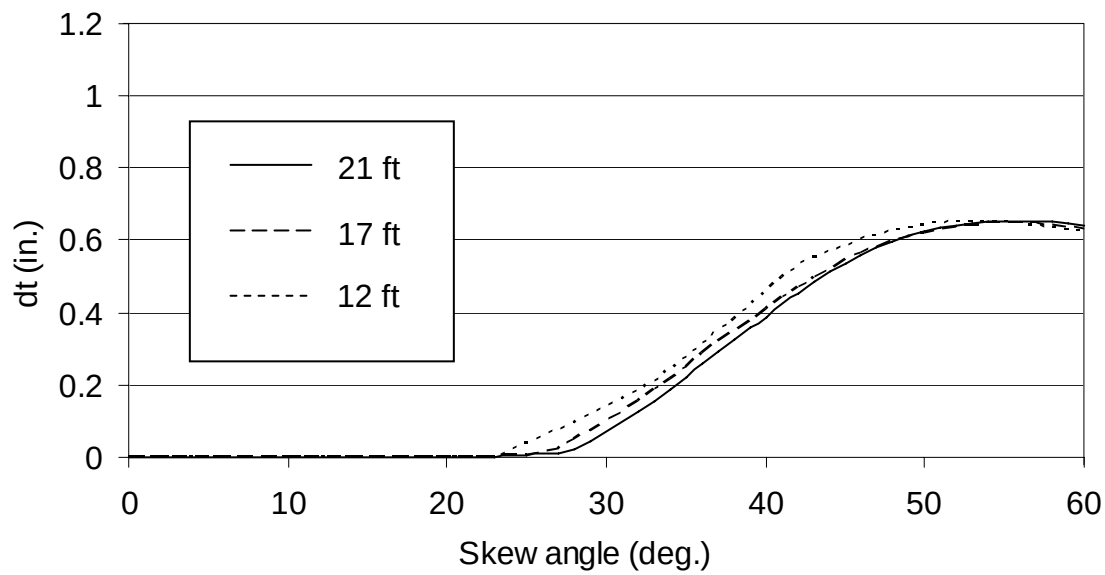

Figure 8.22. Influence of the backwall and sidewall pile, equivalent-cantilever length on the abutment displacement dt

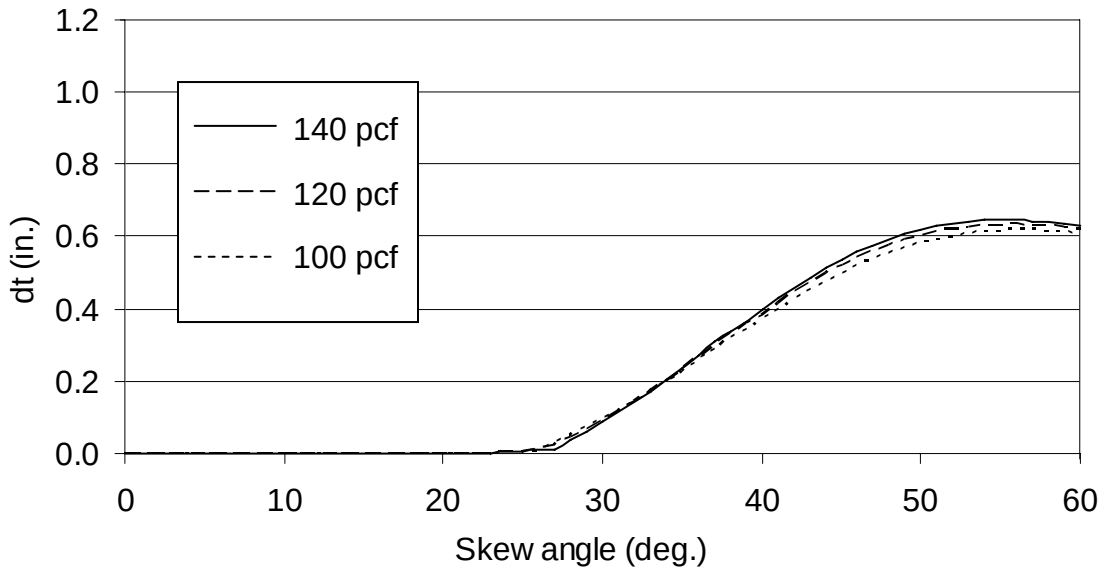

Figure 8.23. Influence of the soil unit-weight on the abutment displacement dt

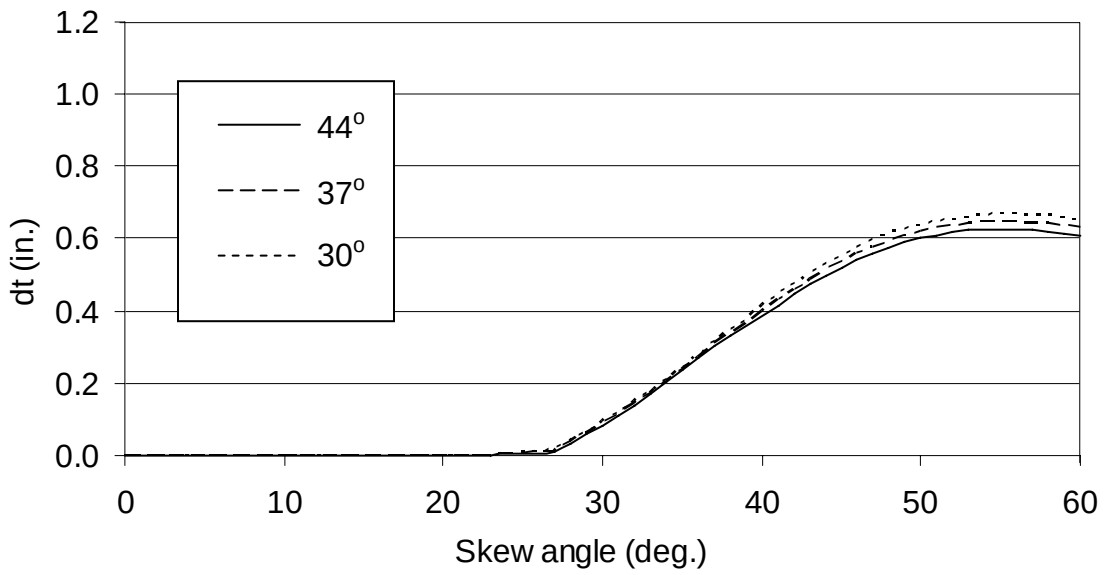

Figure 8.24. Influence of the soil-internal-friction angle on the abutment displacement dt

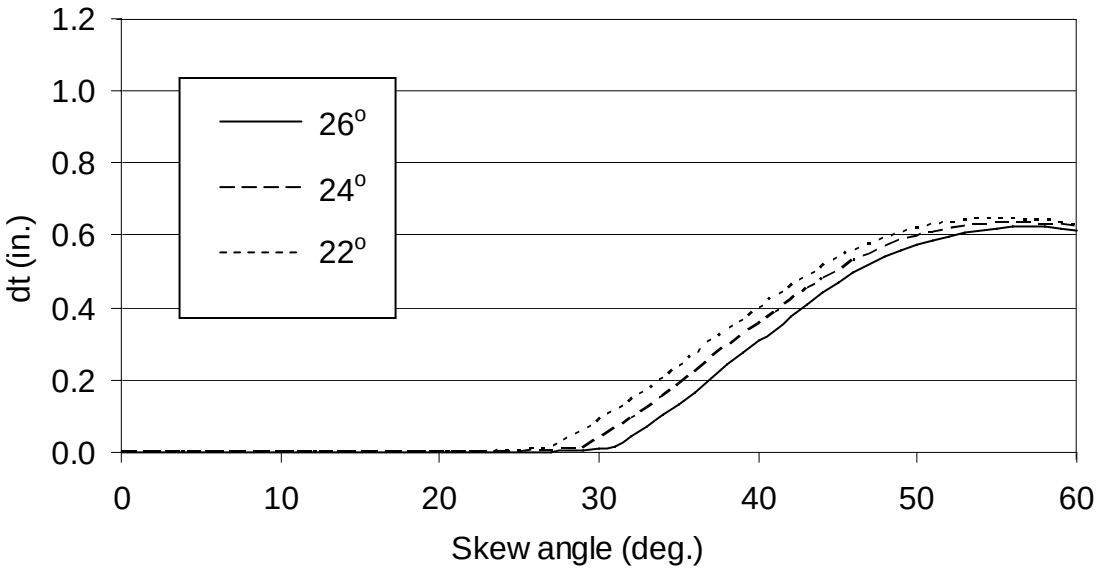

Figure 8.25. Influence of the soil-to-abutment, surface-frictional angle on the abutment displacement dt

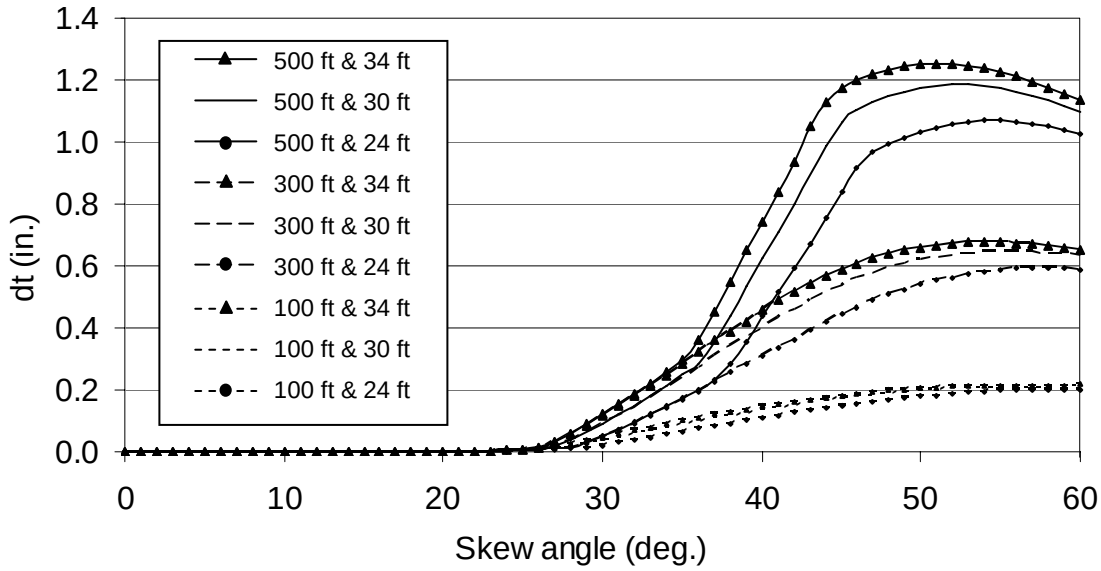

Figure 8.26. Influence of both the bridge length and bridge width on the abutment displacement dt

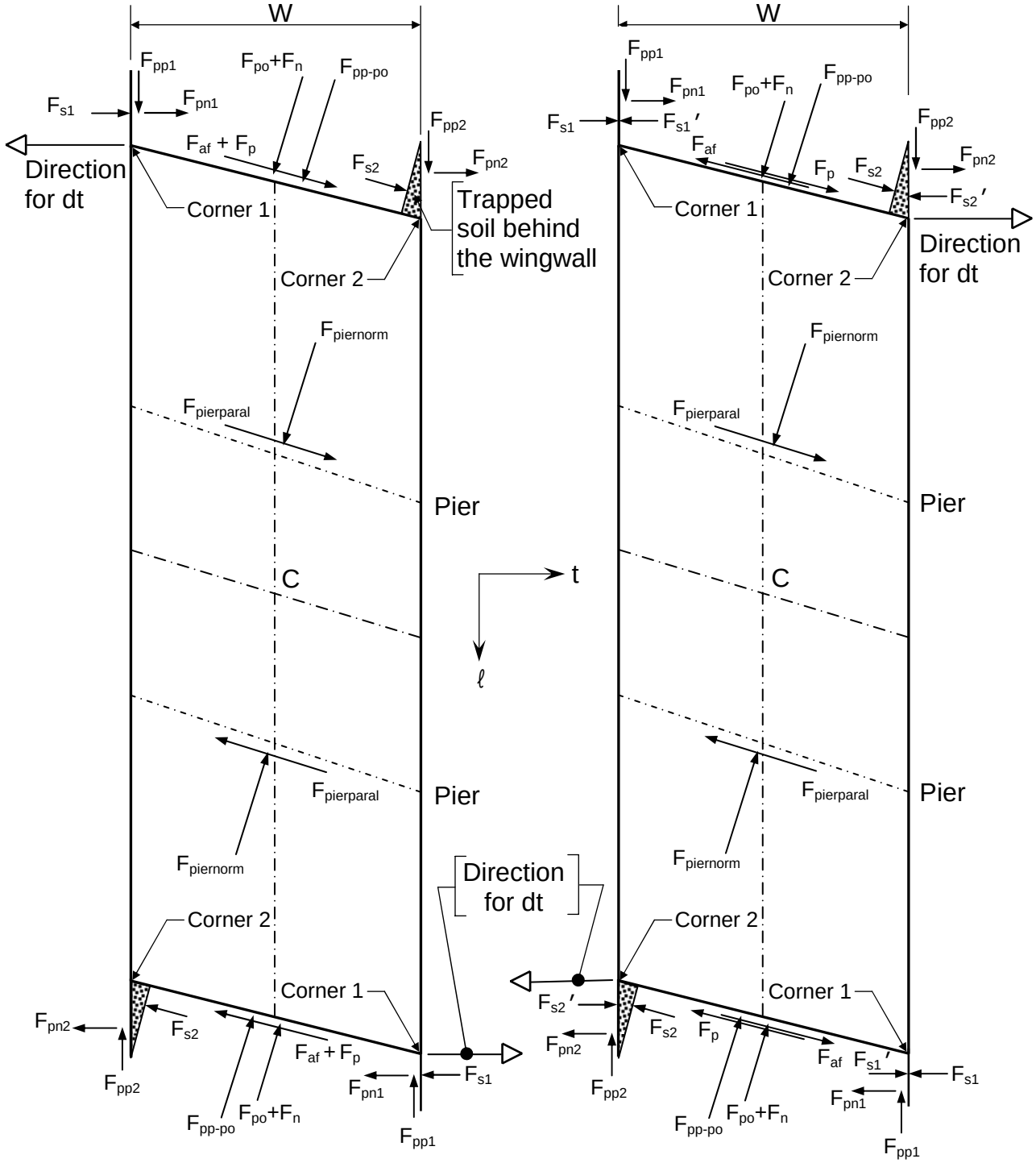

(a) Forces during an expansion phase

(b) Forces during a subsequence contraction phase

Figure 8.27. Forces governing the transverse displacement of the bridge during an expansion and a subsequence contraction

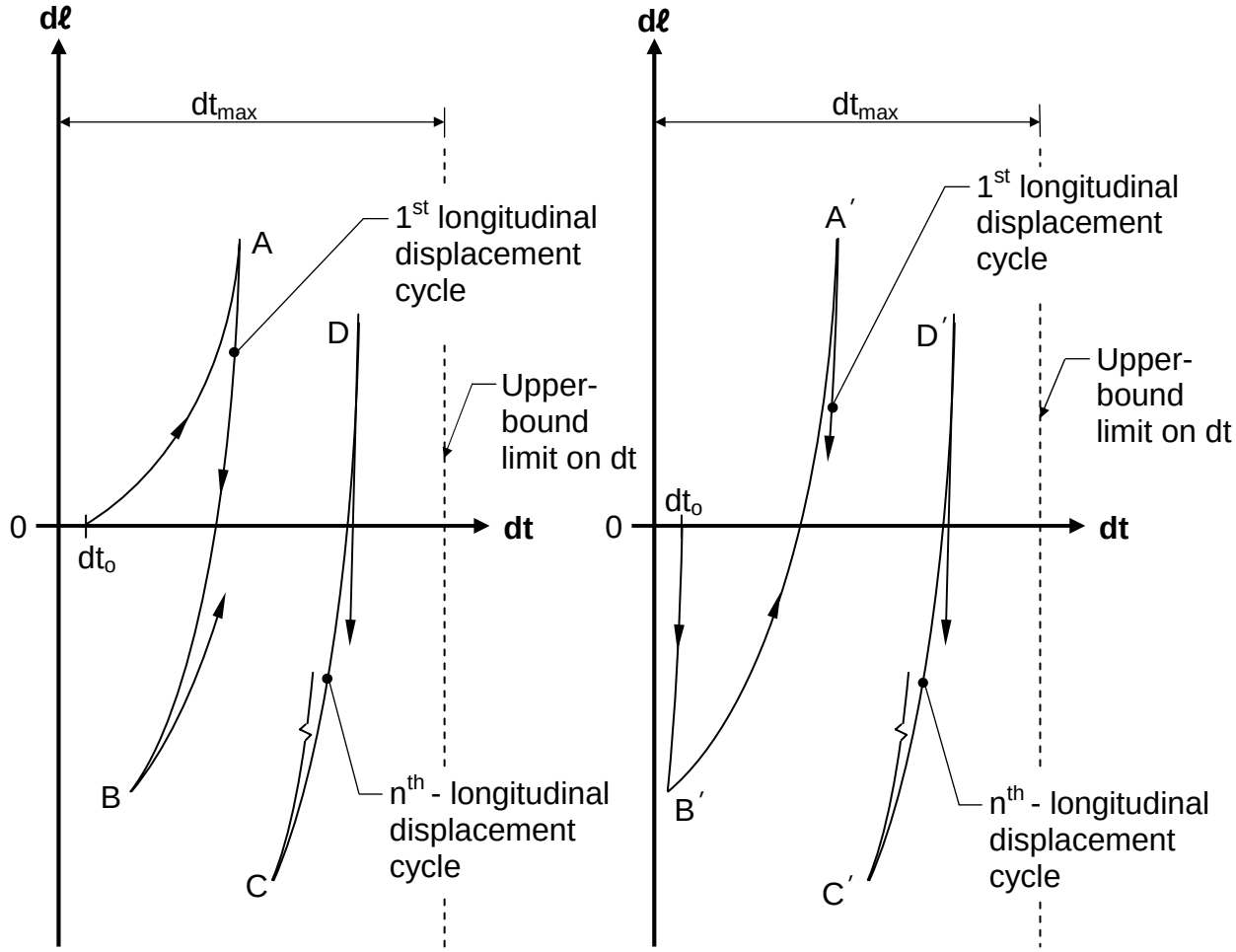

(a) Initial longitudinal expansion (b) Initial longitudinal contraction

Figure 8.28. Relationship between the transverse and longitudinal displacements of an integral abutment

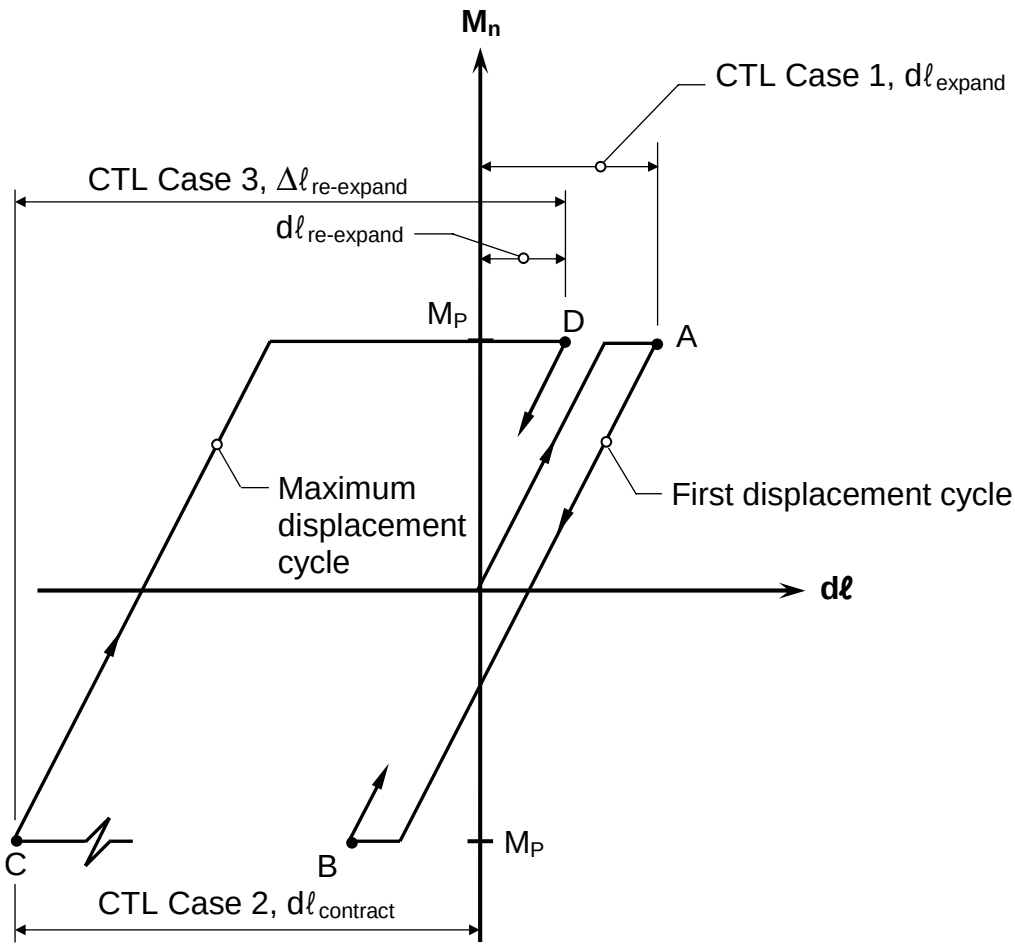

(a) Displacement cycles after initial expansion

Figure 8.29. Pile moment resistance versus displacement relationship (Adapted from Oesterle, et al., 1999)

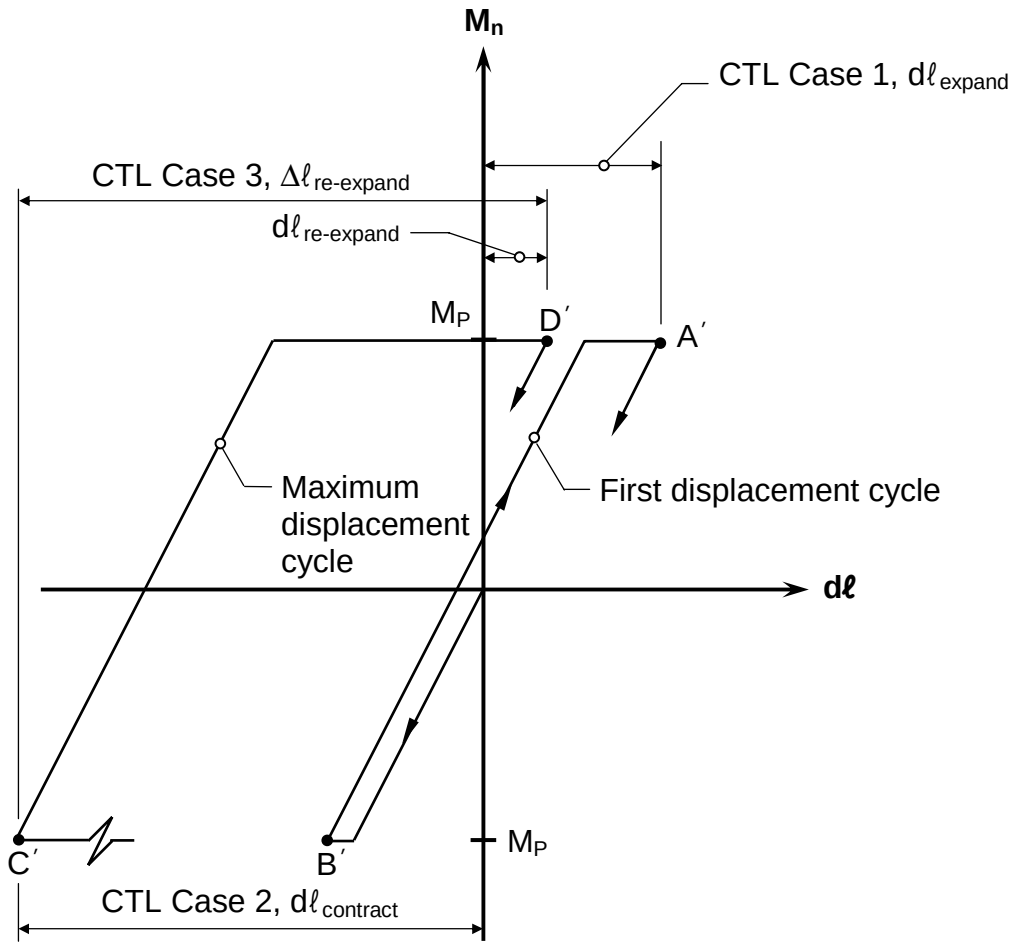

(b) Displacement cycles after initial contraction

Figure 8.29 (continued)

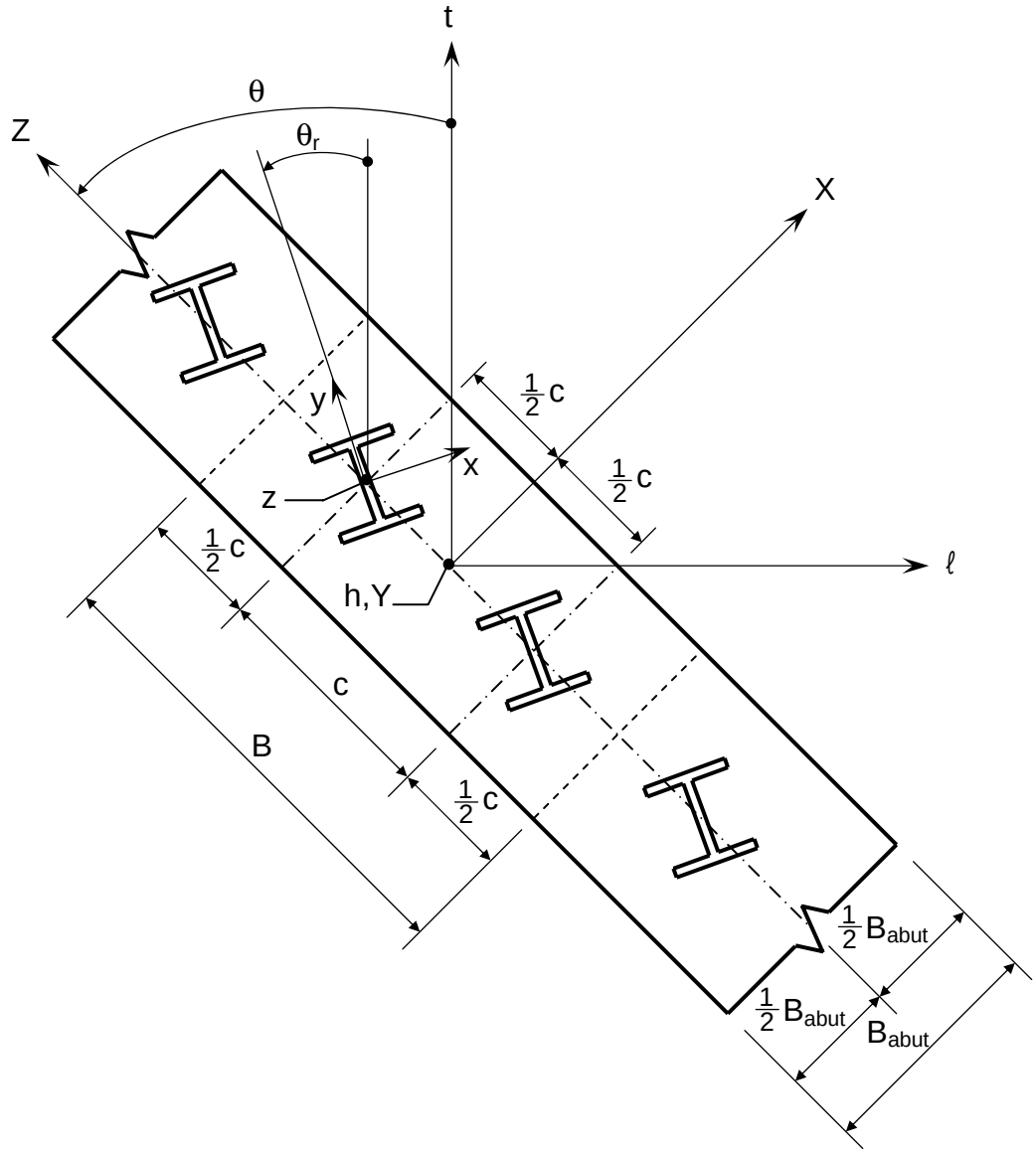

Figure 8.30. Coordinate axes for an integral-abutment bridge, integral abutment, and abutment-backwall piles

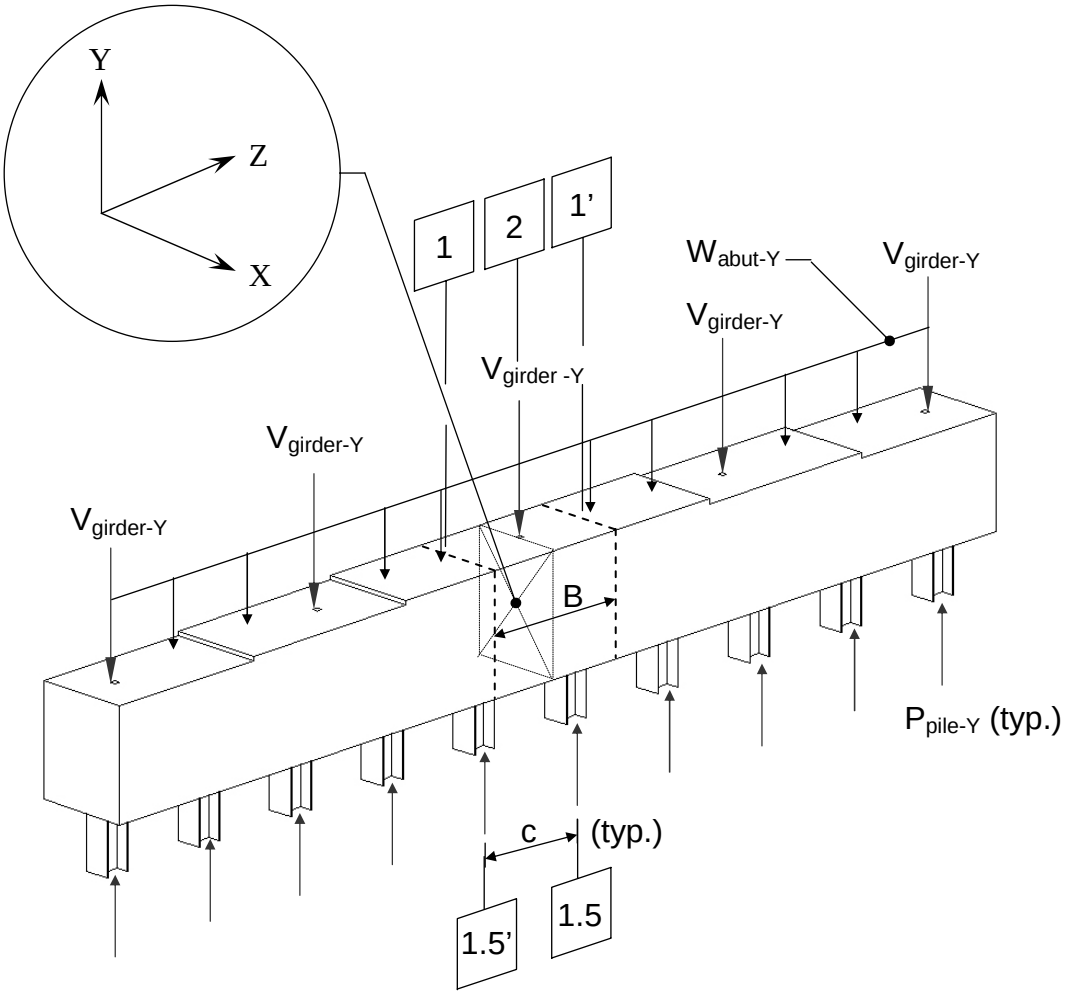

Figure 8.31. Gravity loads on a backwall-pile cap

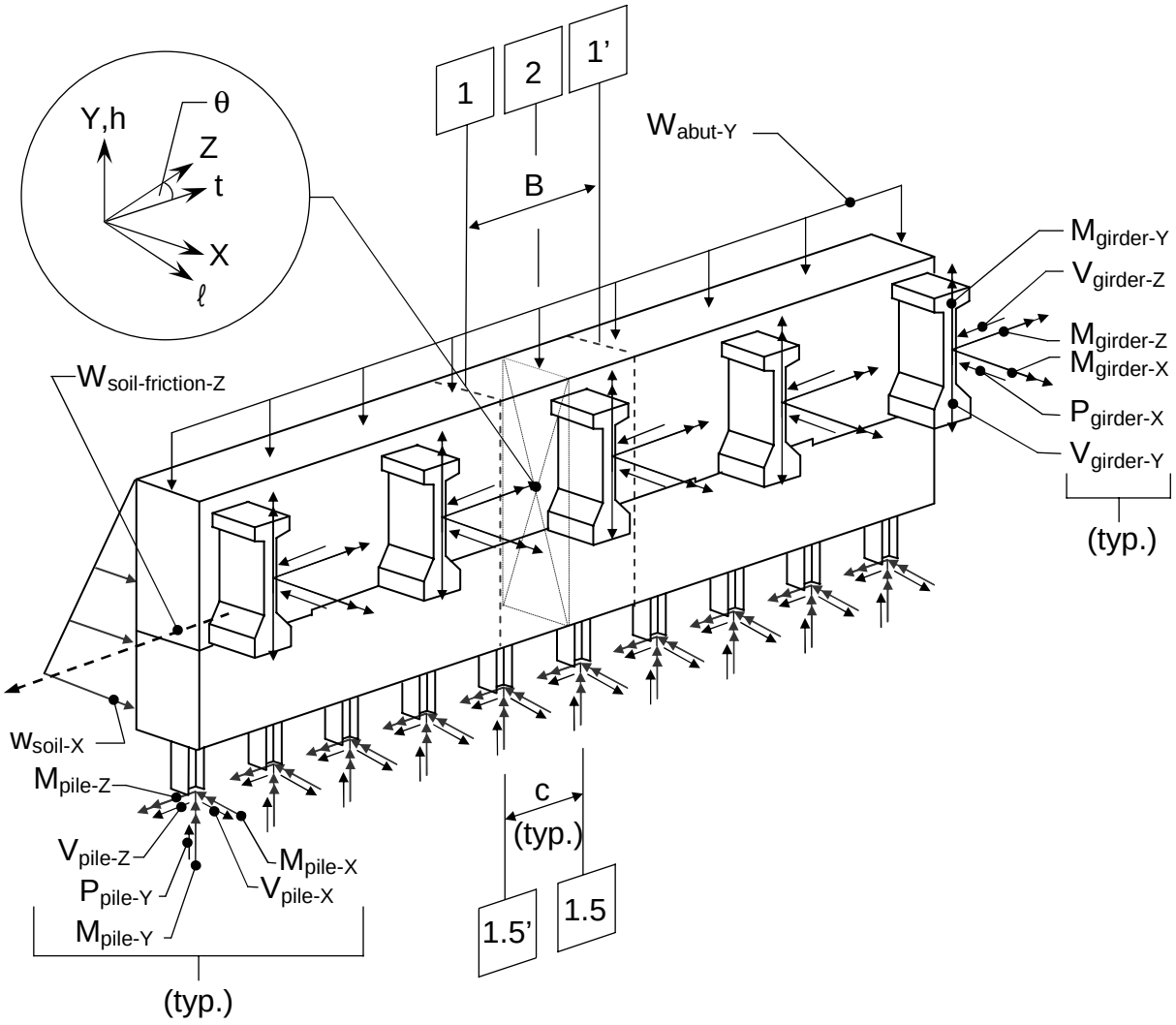

Figure 8.32. Gravity and thermally-induced loads on an integral abutment without common sidewalls and wingwalls

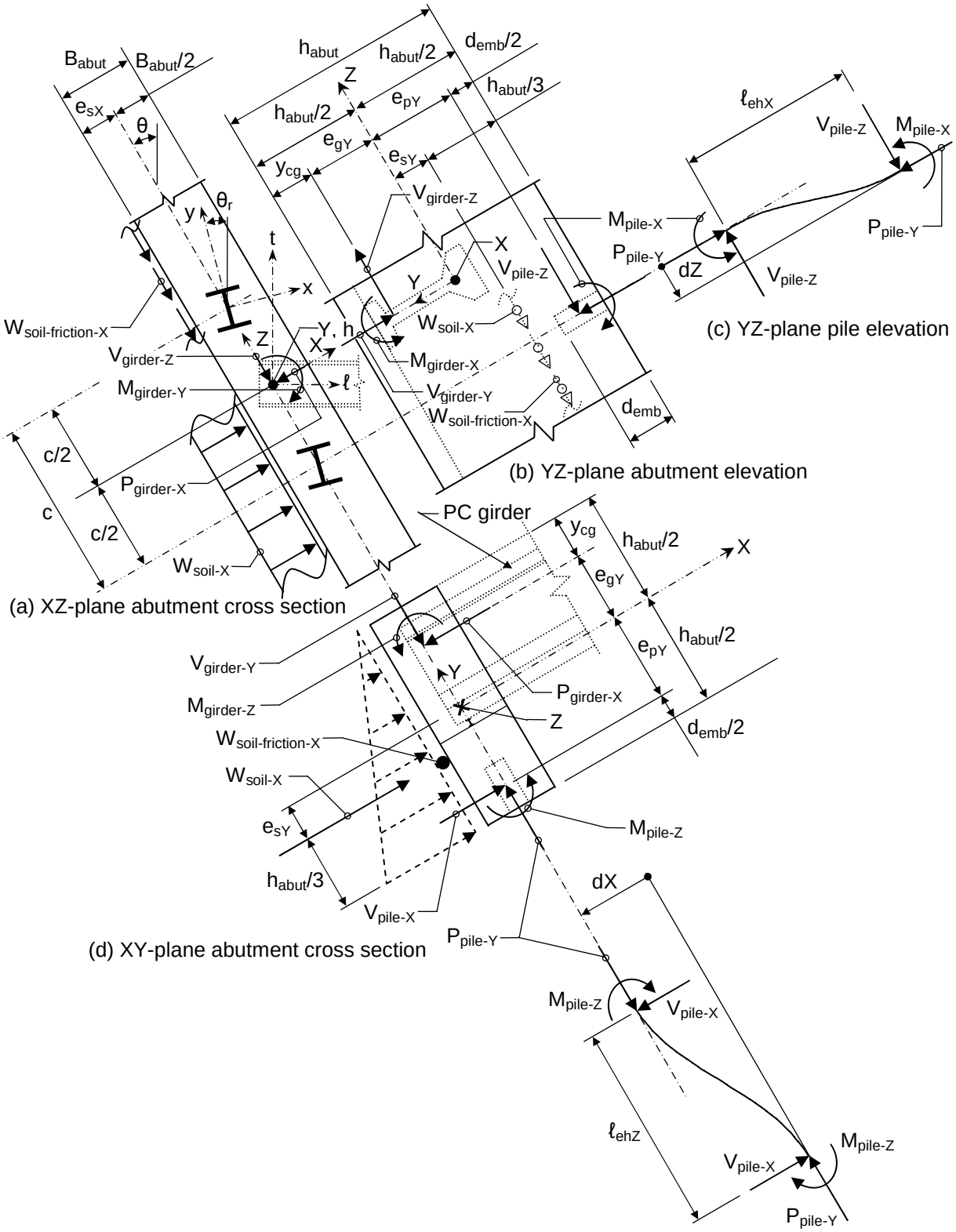

Figure 8.33. Abutment force geometry for bridge superstructure expansion

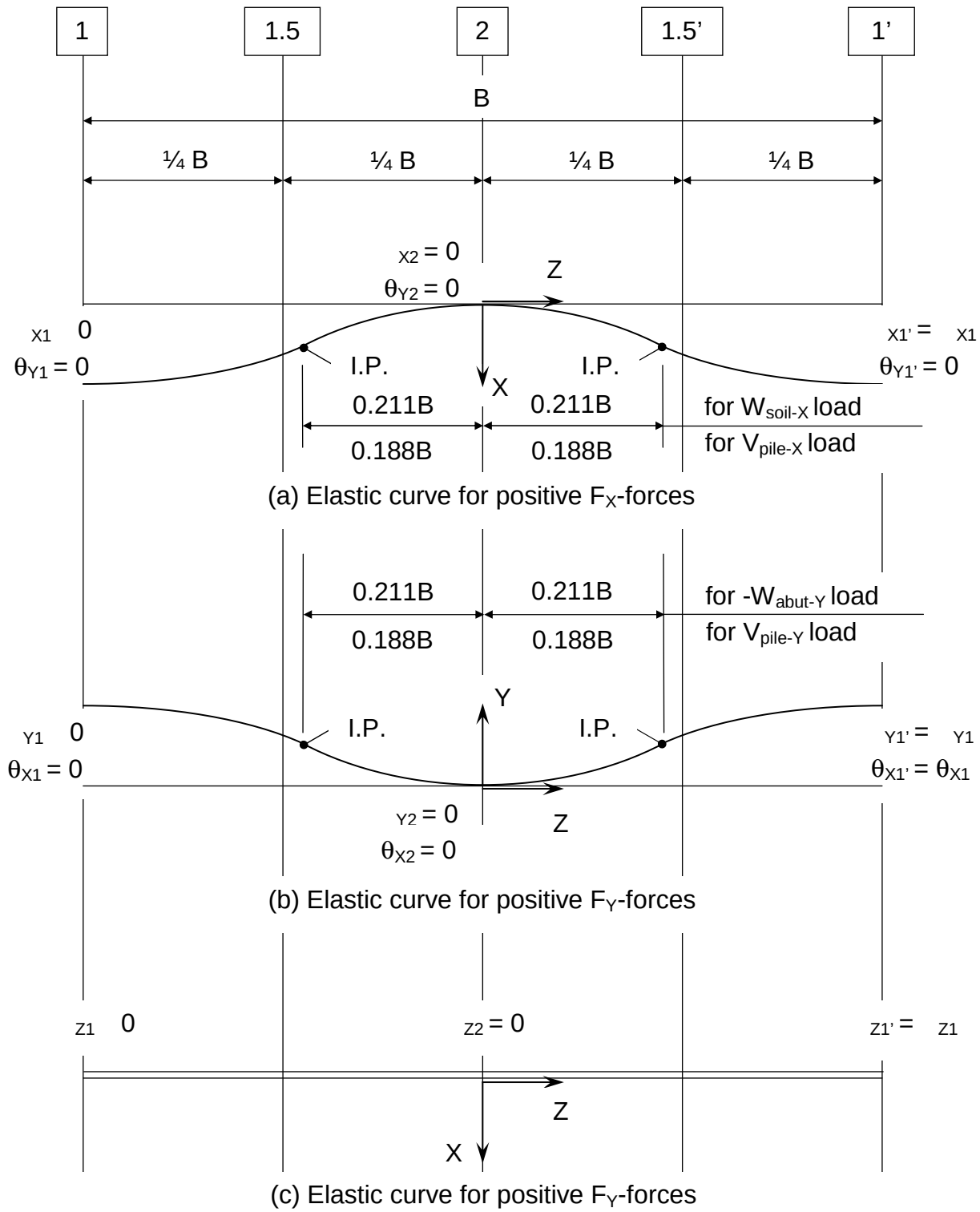

Figure 8.34. Displaced shapes for the central portion of an abutment

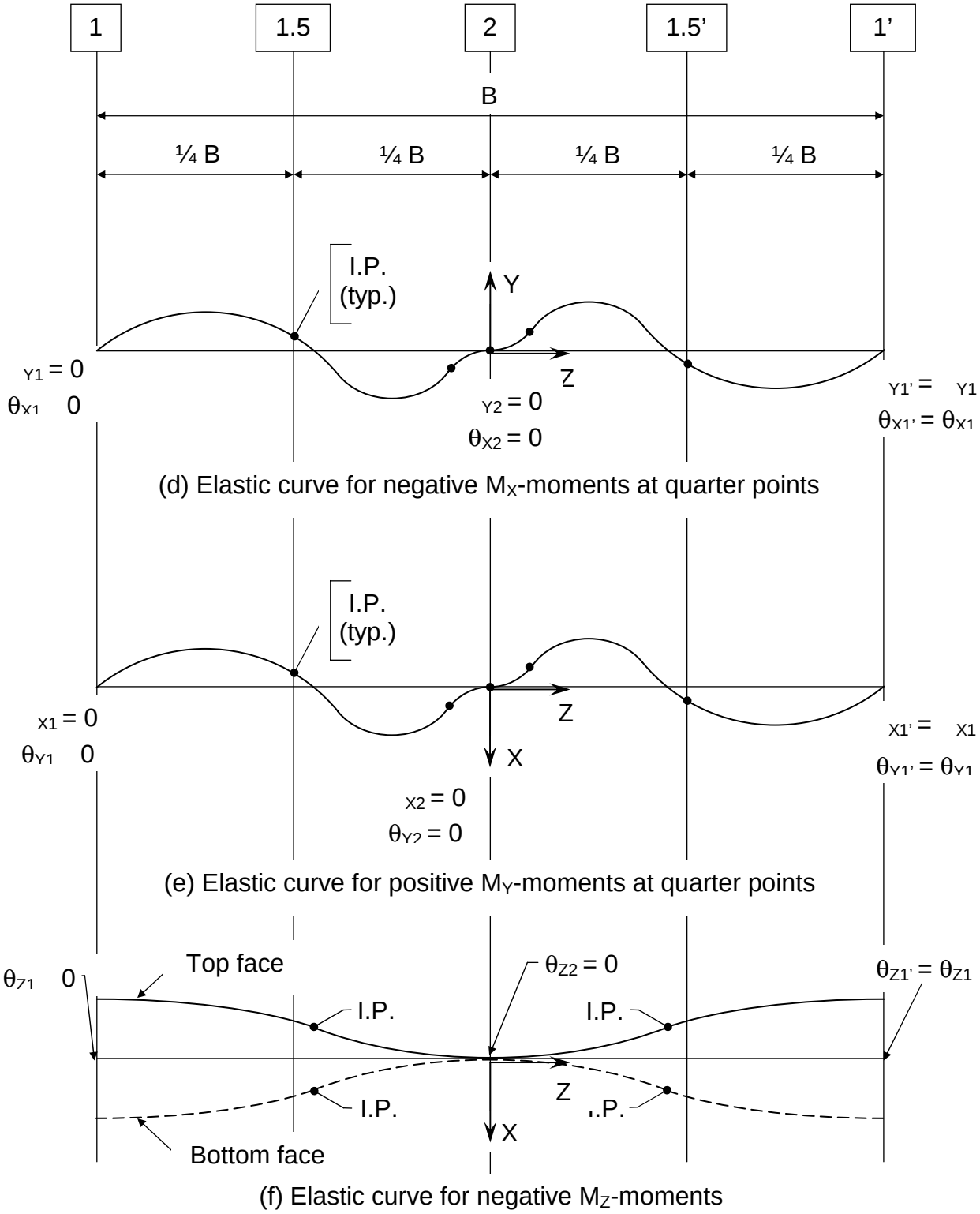

Figure 8.34. (cont'd.)

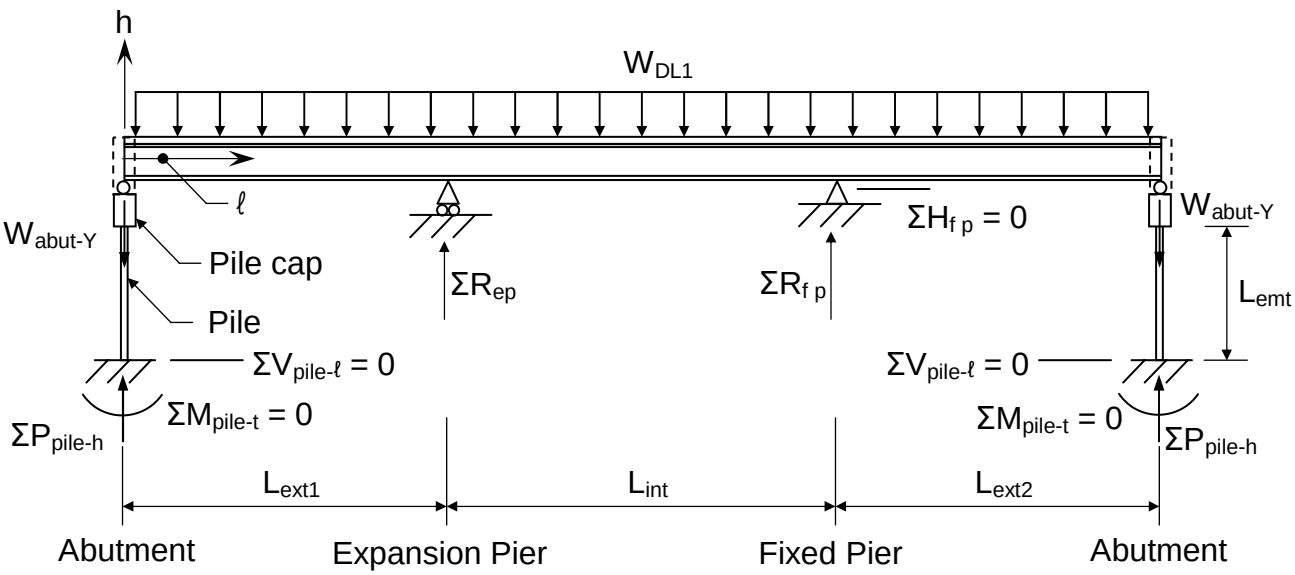

Figure 8.35. Simplified-frame model in the ℓh-plane for an integral-abutment bridge with gravity loads before the abutments become composite members

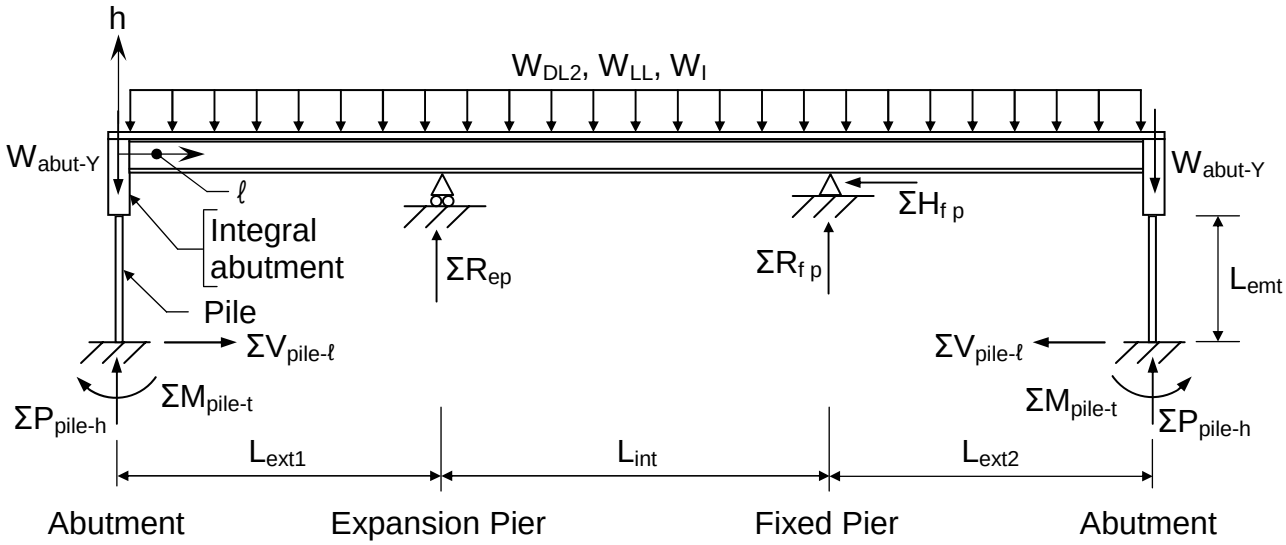

Figure 8.36. Simplified-frame model in the ℓh-plane for an integral-abutment bridge with gravity loads after the abutments become composite members

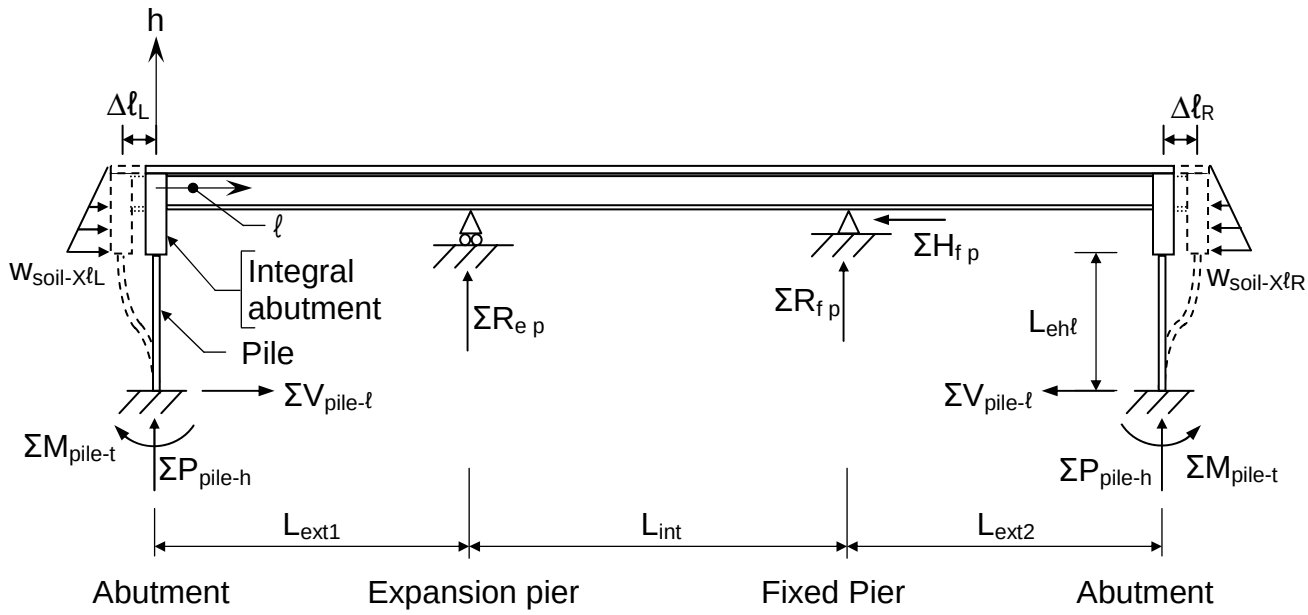

Figure 8.37. Simplified-frame model in the ℓh-plane for an integral-abutment bridge with a thermally induced expansion and without a vertical-temperature gradient

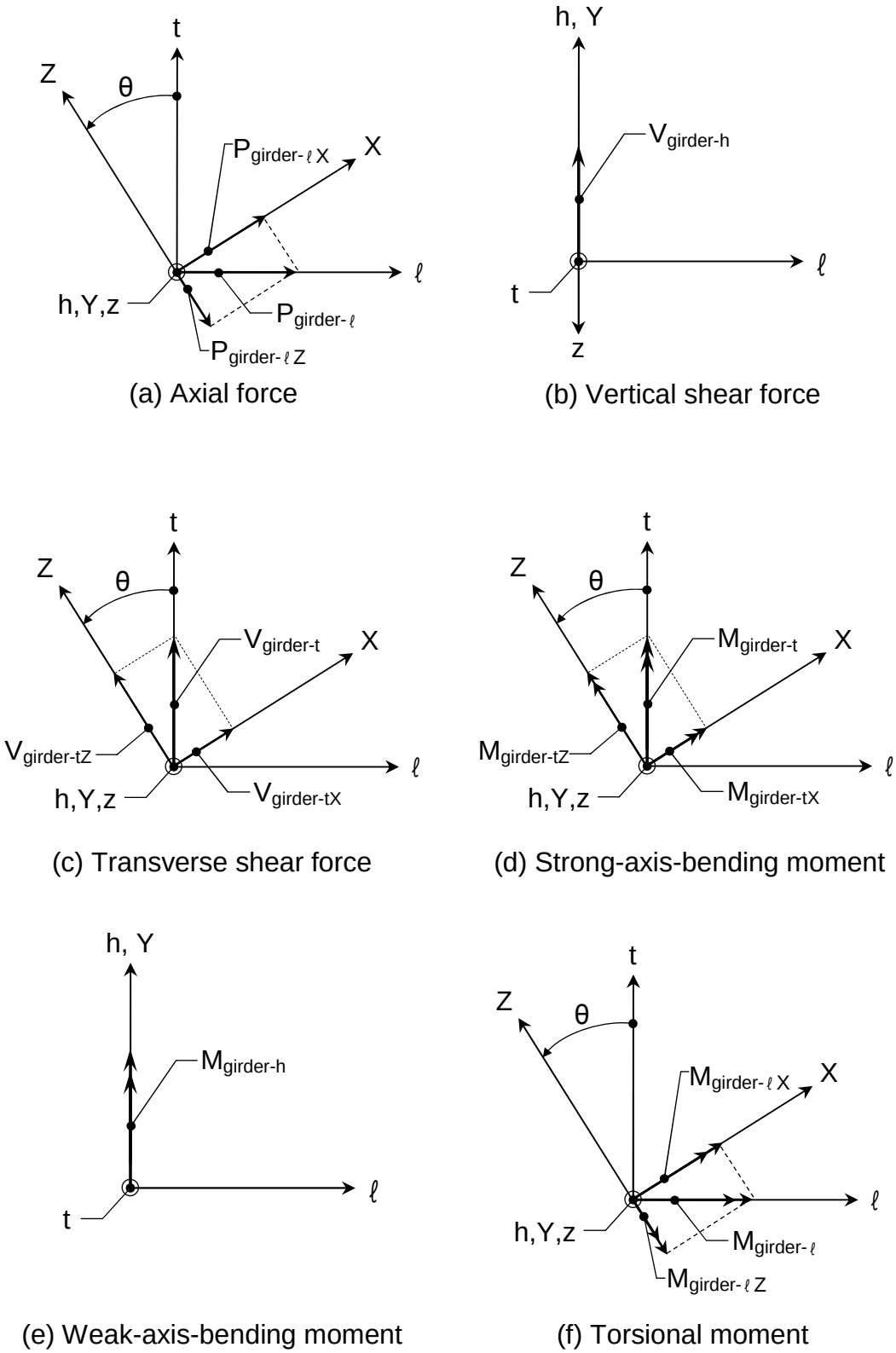

Figure 8.38. Components for the member-end forces for a PC girder that act on an abutment for Analysis Method 1

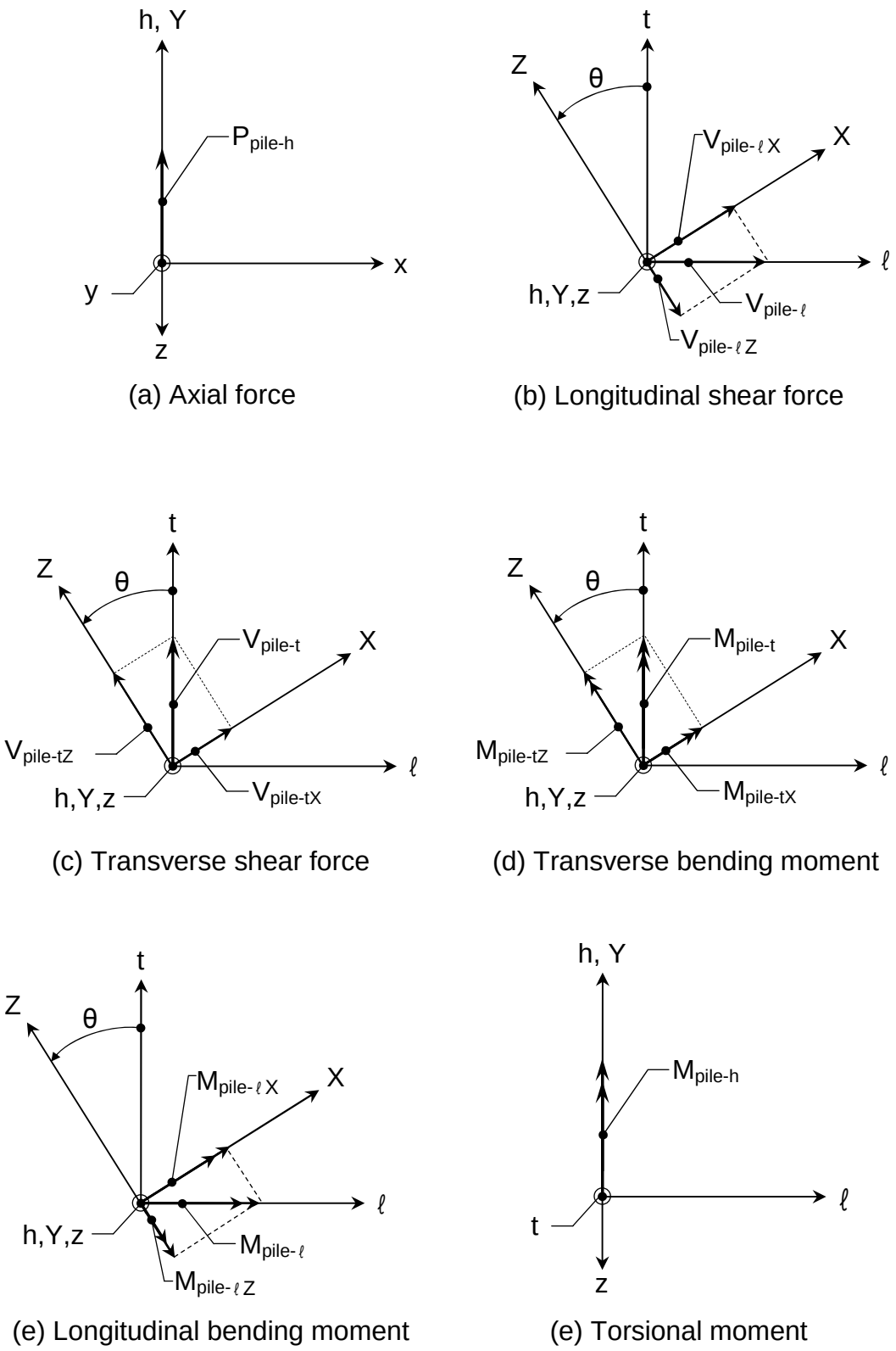

Figure 8.39. Components for the member-end forces for an HP-shaped pile that act on an abutment for Analysis Method 1

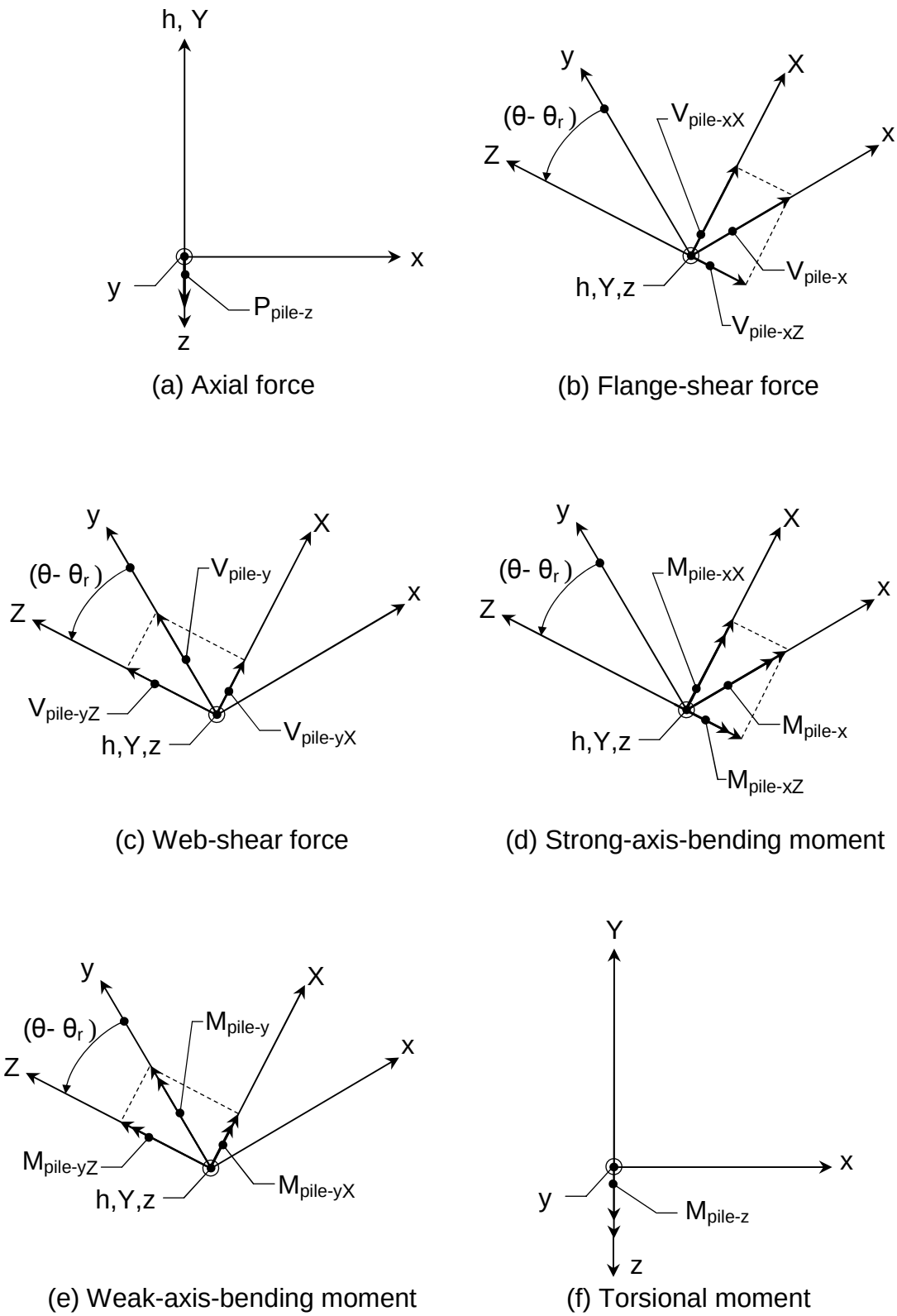

Figure 8.40. Components for the member-end forces for an HP-shaped pile that act on an abutment for Analysis Method 2

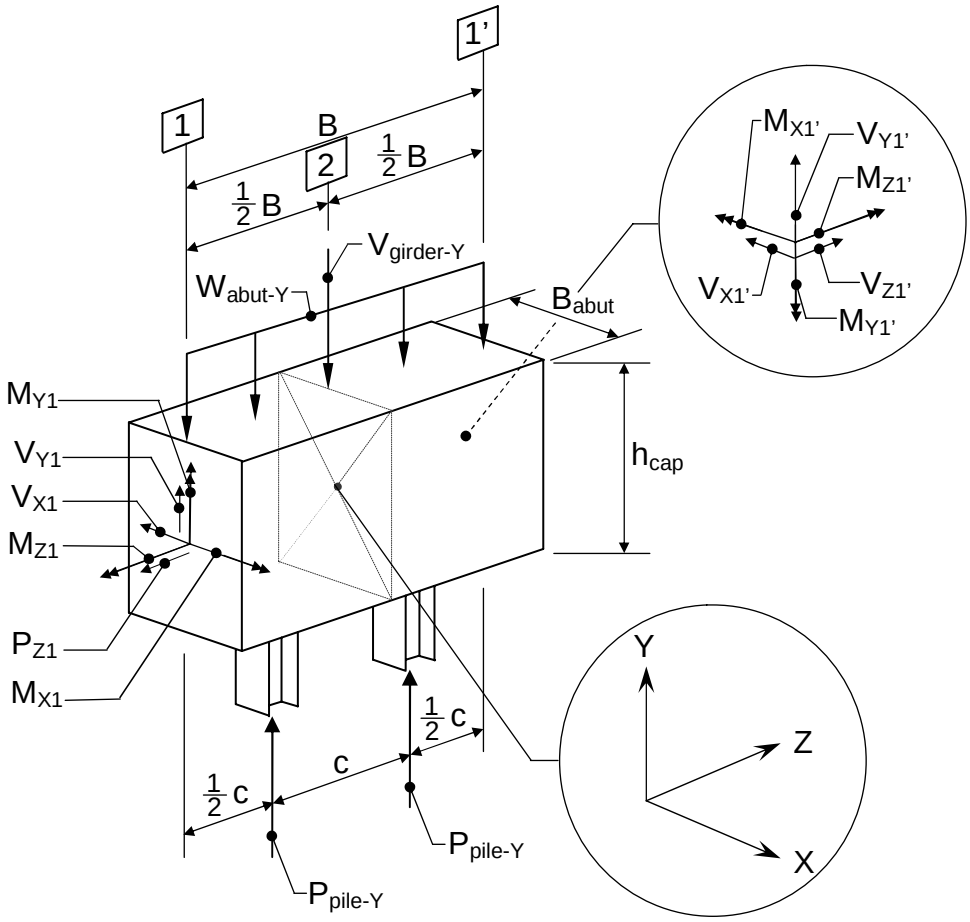

Figure 8.41. Gravity loads on the central portion of an abutment-pile cap

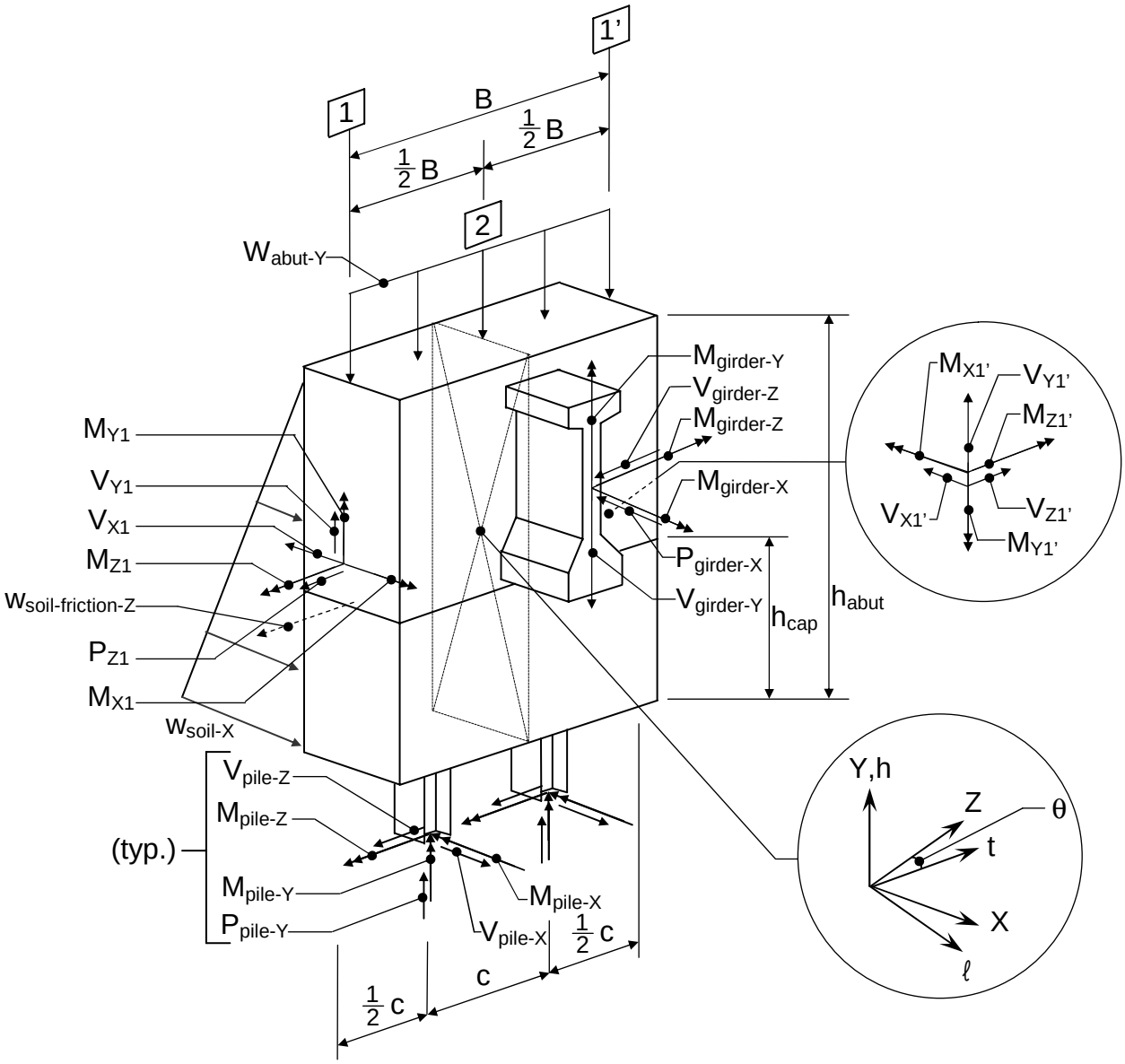

Figure 8.42. Gravity and thermally-induced loads on the central portion of an integral abutment

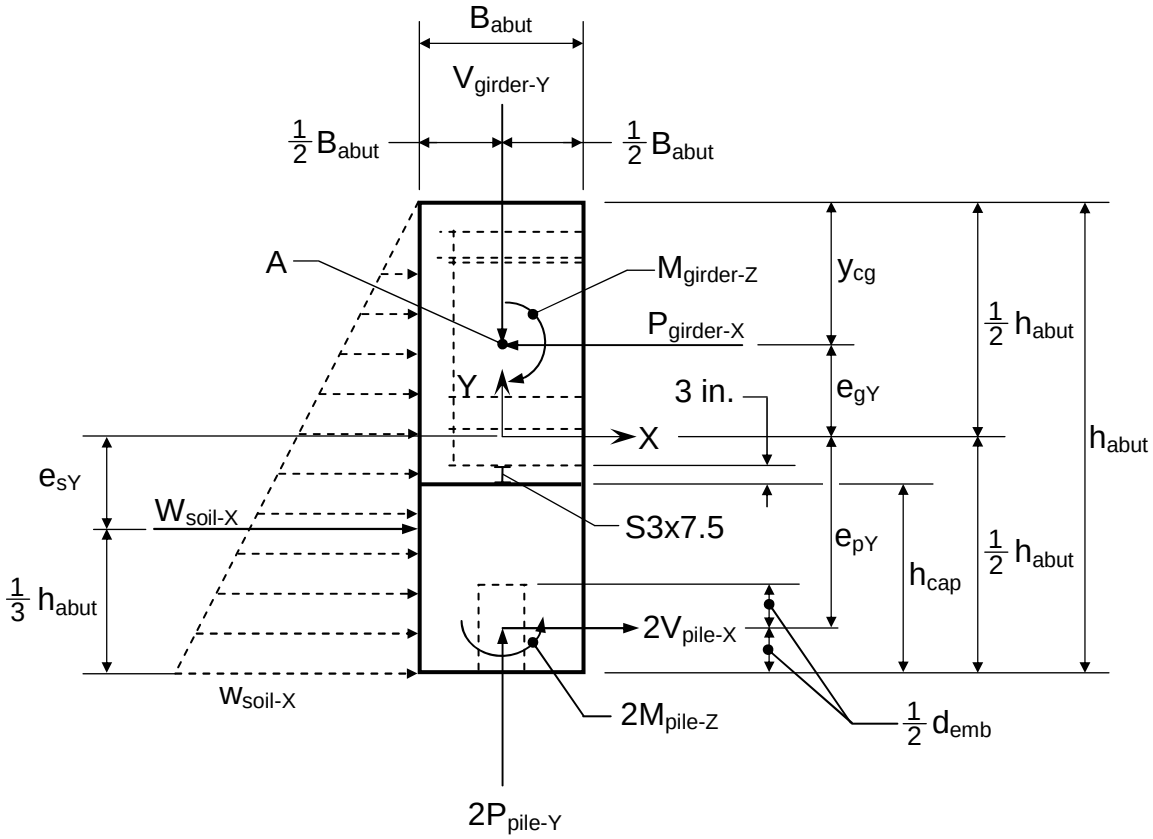

Figure 8.43. Free-body diagram in the vertical XY-plane for the central portion of an integral abutment

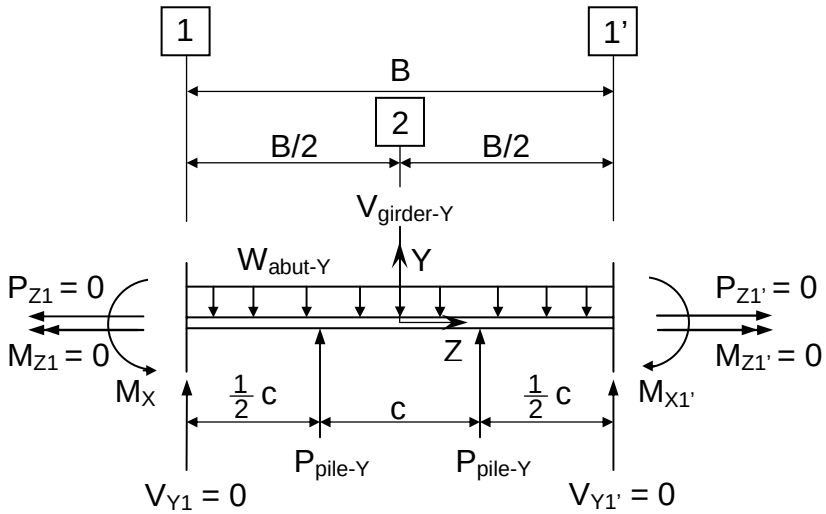

Figure 8.44. Free-body diagram in the vertical YZ-plane for the central portion of an abutment-pile cap

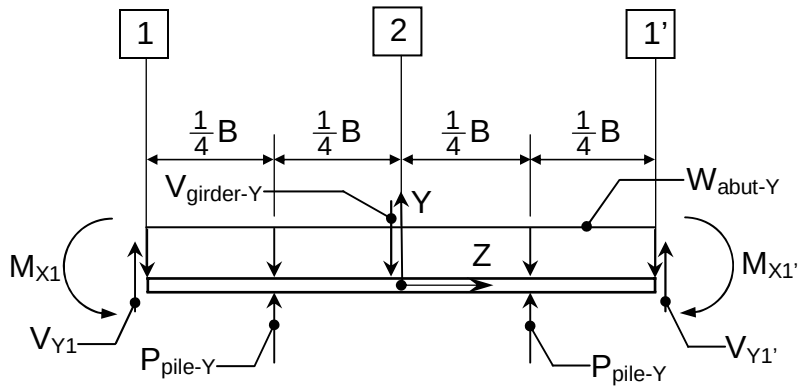

(a) Symmetric – flexural forces in the YZ-plane

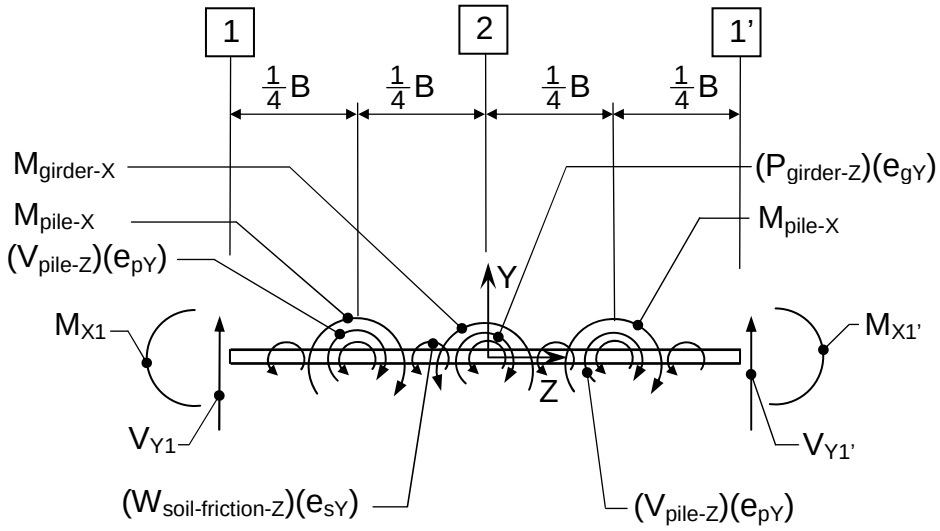

(b) Asymmetric-flexural forces in the YZ-plane

Figure 8.45. Free-body diagrams for the central portion of an integral-abutment

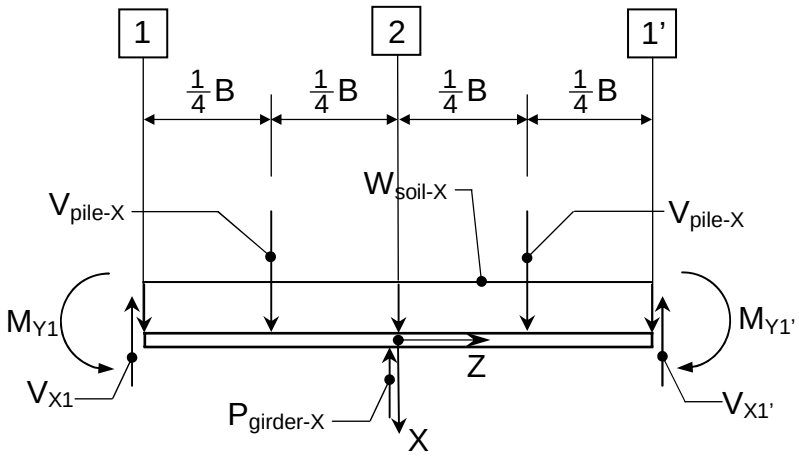

(c) Symmetric-flexural forces in the XZ-plane

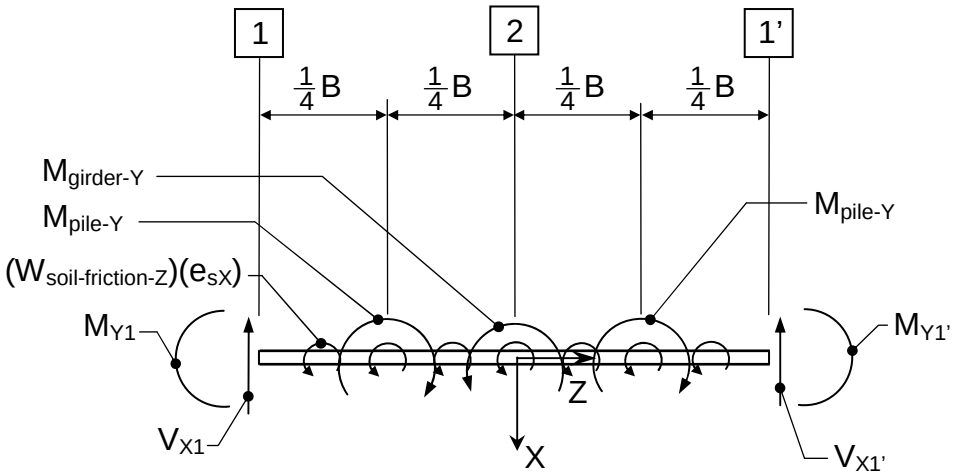

(d) Assymetric-frictional forces in the YZ-plane

Figure 8.45. (cont'd)

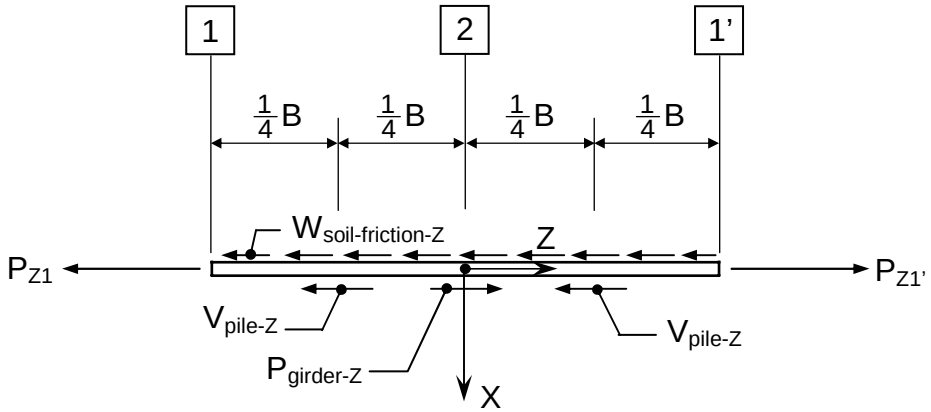

(e) Axial loads along the Z-axis

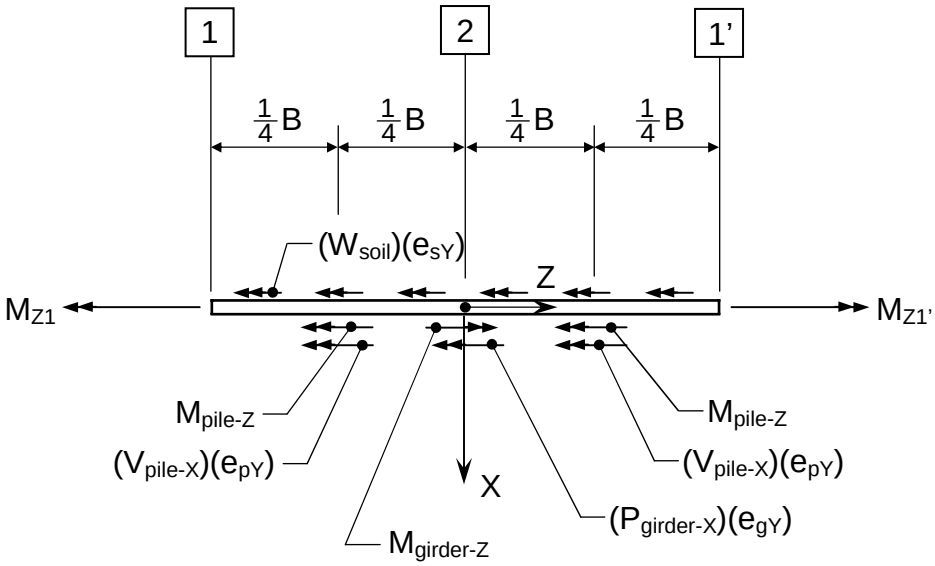

(f) Torsional moments along the Z-axis

Figure 8.45. (cont'd)

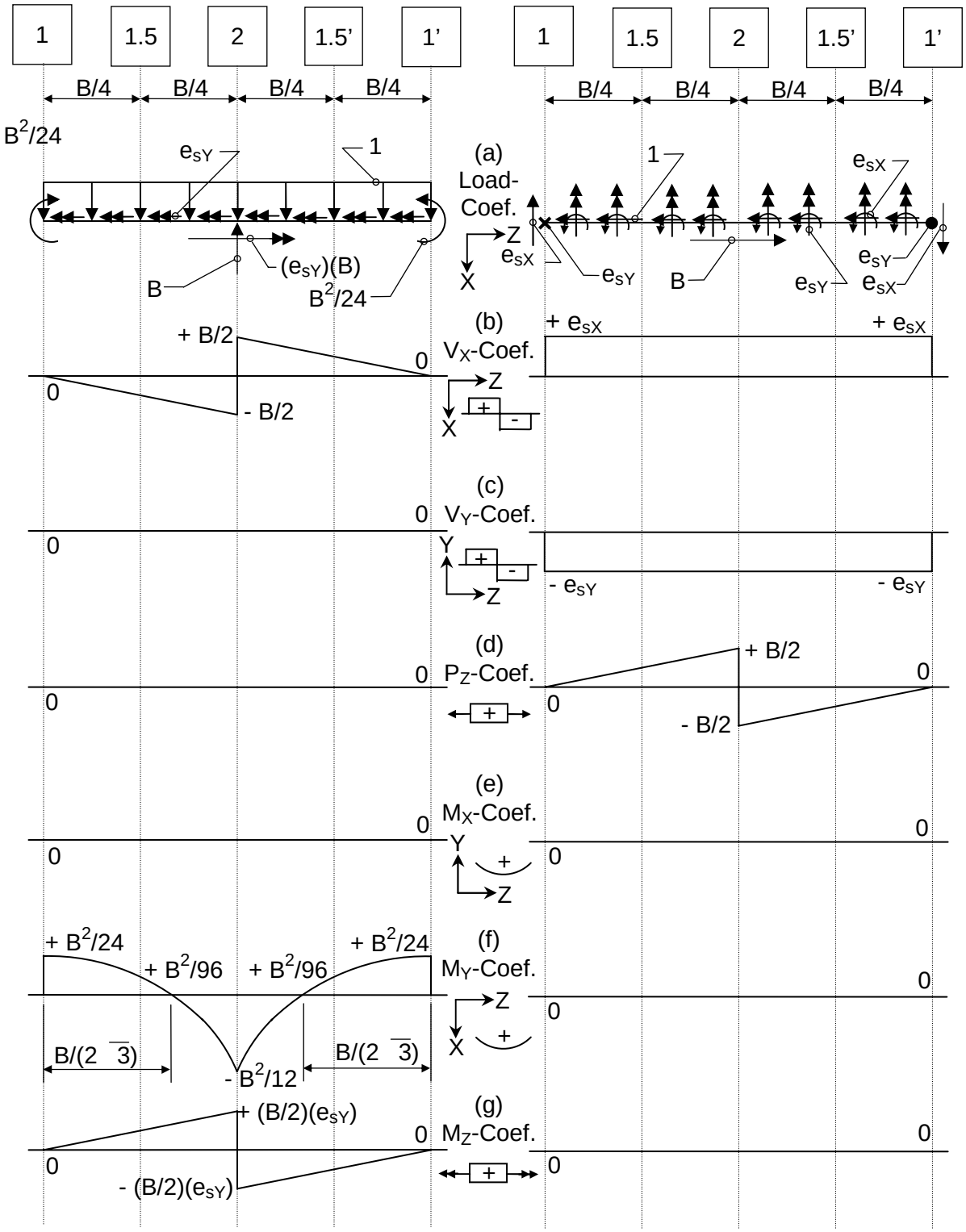

Figure 8.46. Force coefficients for $W_{soil\text{-}X}$

Figure 8.47. Force coefficients for $W_{soil\text{-}friction\text{-}Z}$

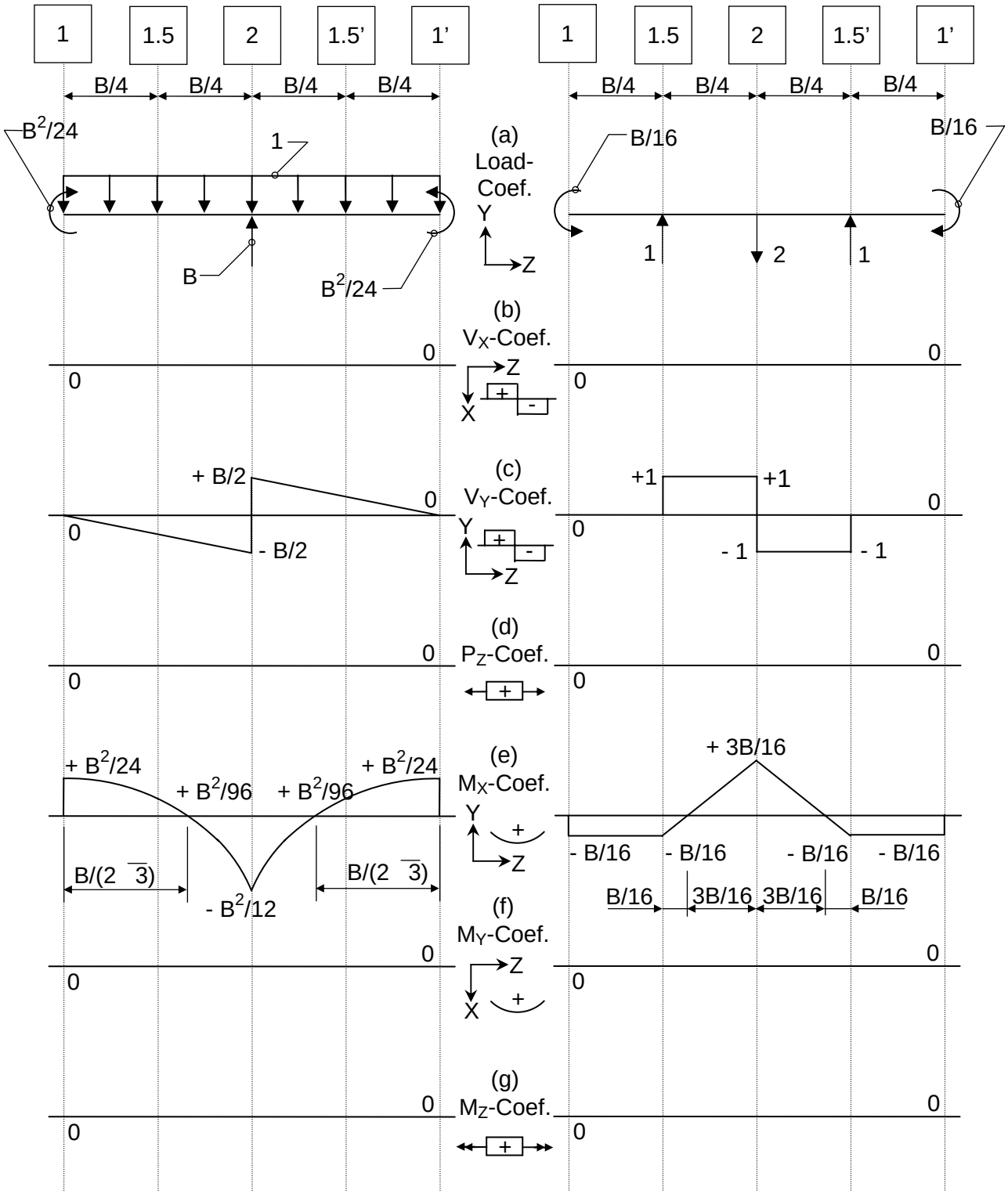

Figure 8.48. Force coefficients for $W_{abut\text{-}Y}$

Figure 8.49. Force coefficients for $P_{pile\text{-}Y}$

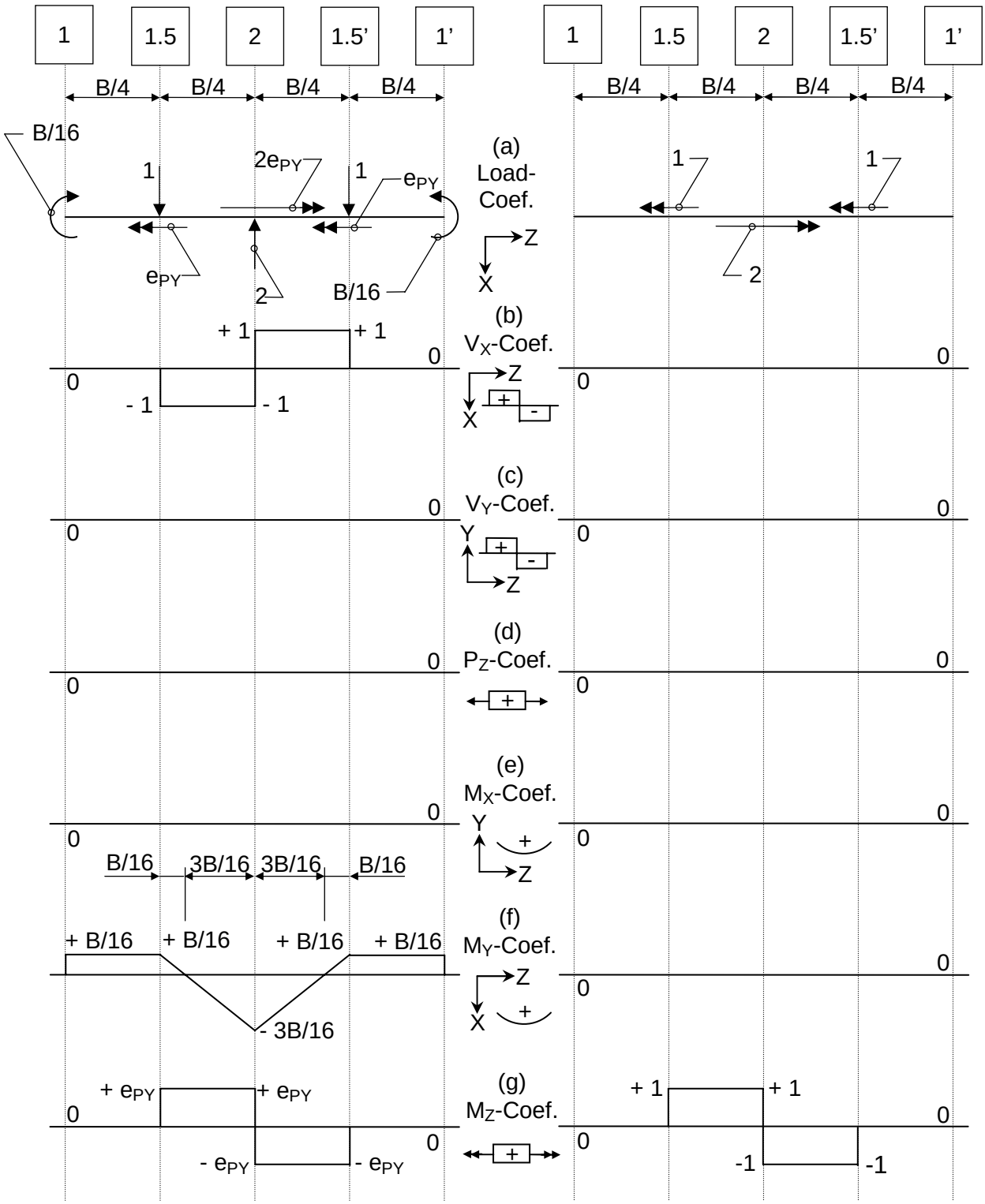

Figure 8.50. Force coefficients for $V_{pile\text{-}X}$

Figure 8.51. Force coefficients for $M_{pile\text{-}Z}$

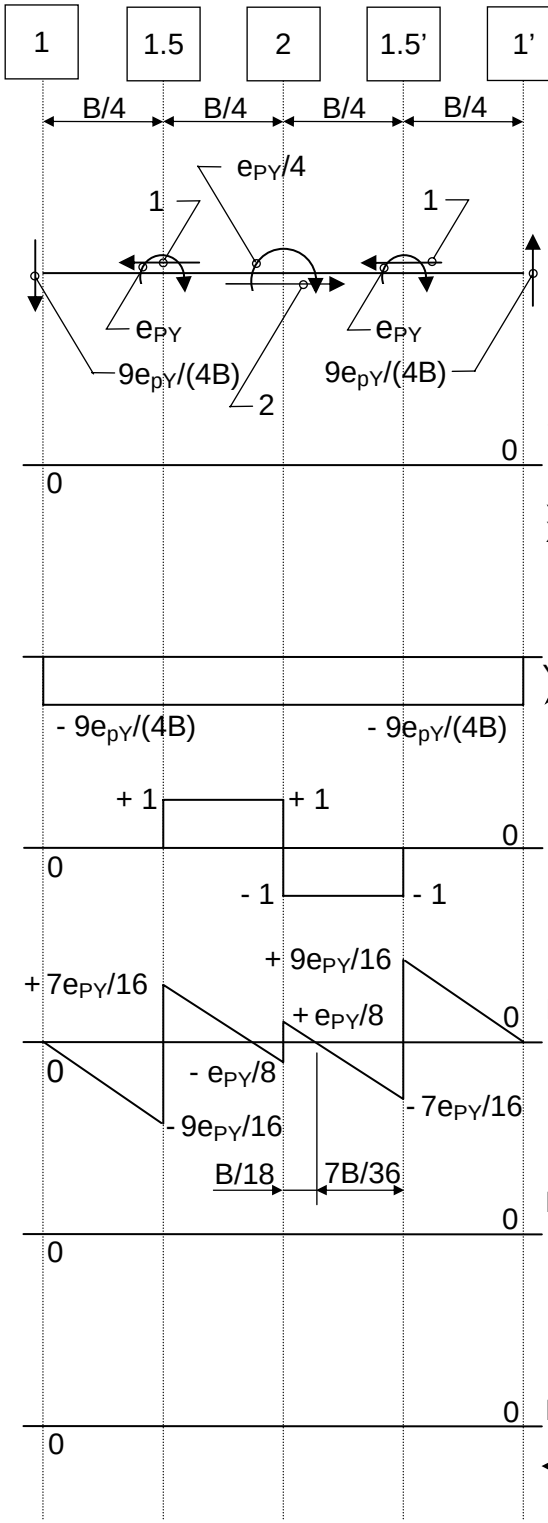

Figure 8.52. Force coefficients for $V_{pile\text{-}Z}$

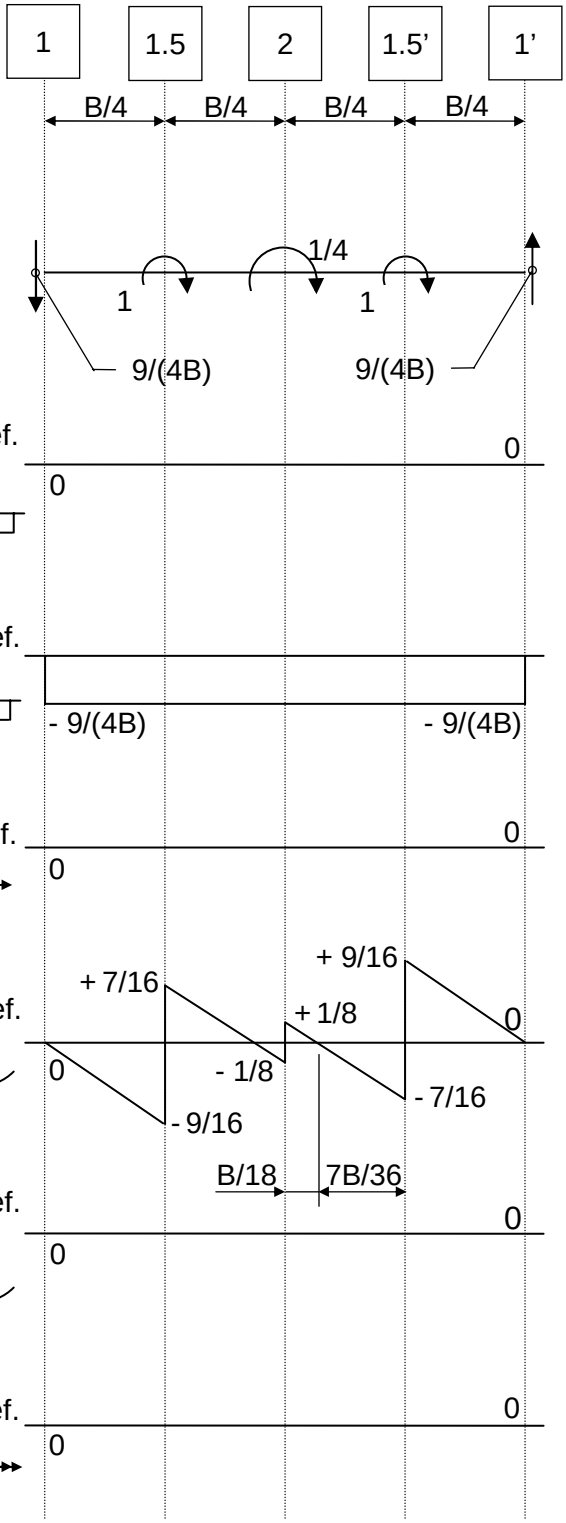

Figure 8.53. Force coefficients for $M_{pile\text{-}X}$

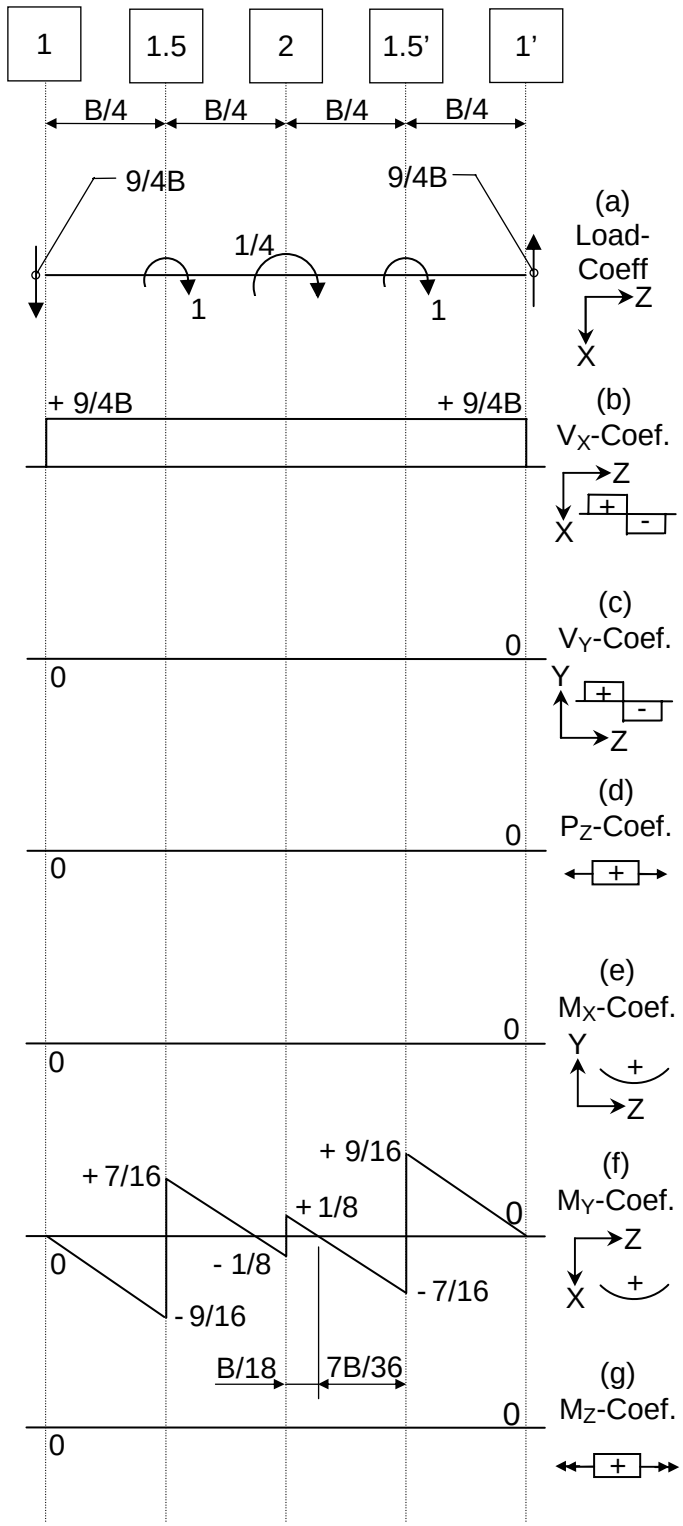

Figure 8.54. Force coefficients for $M_{pile\text{-}Y}$

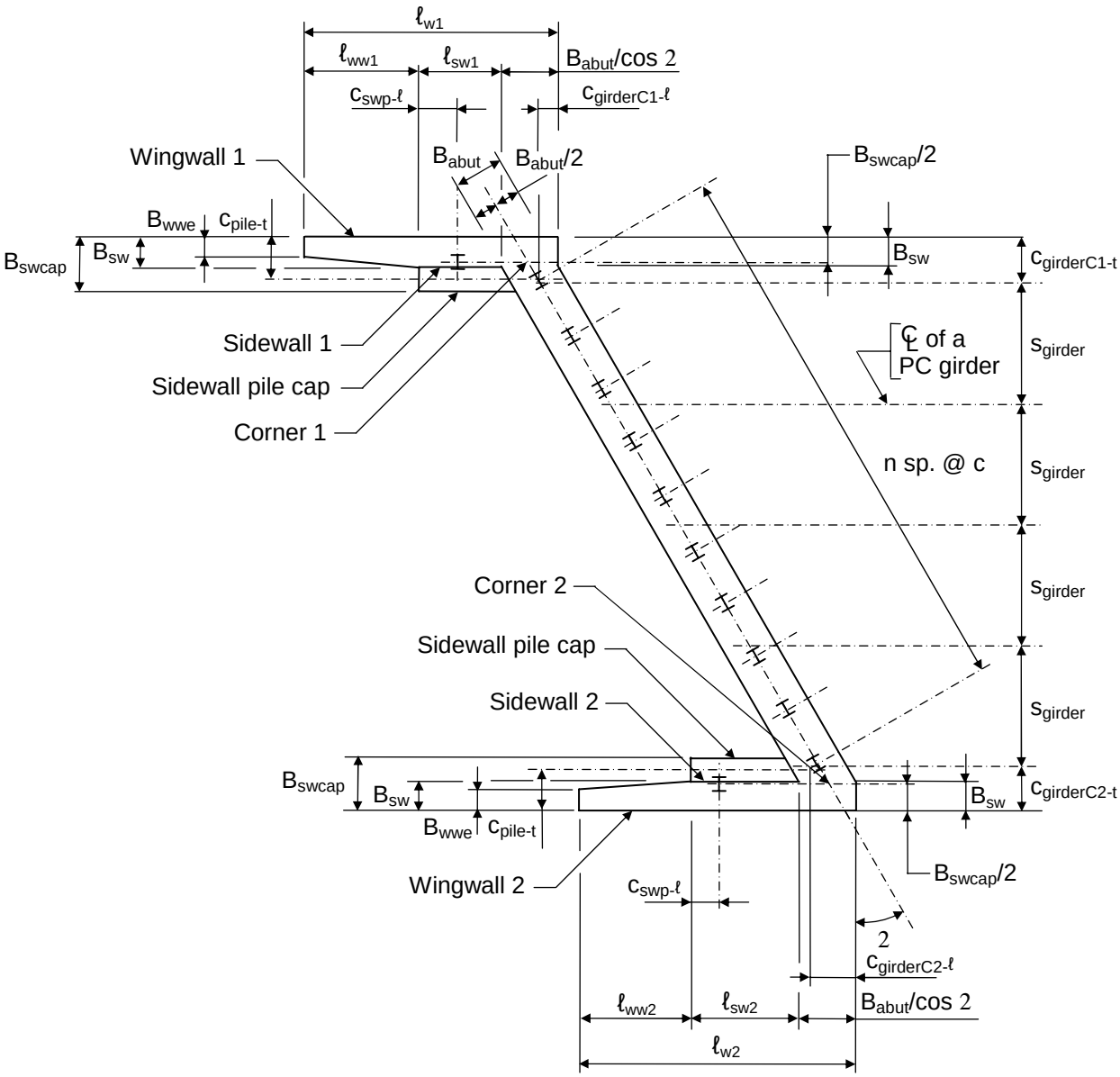

Figure 8.55. Plan view of an integral abutment

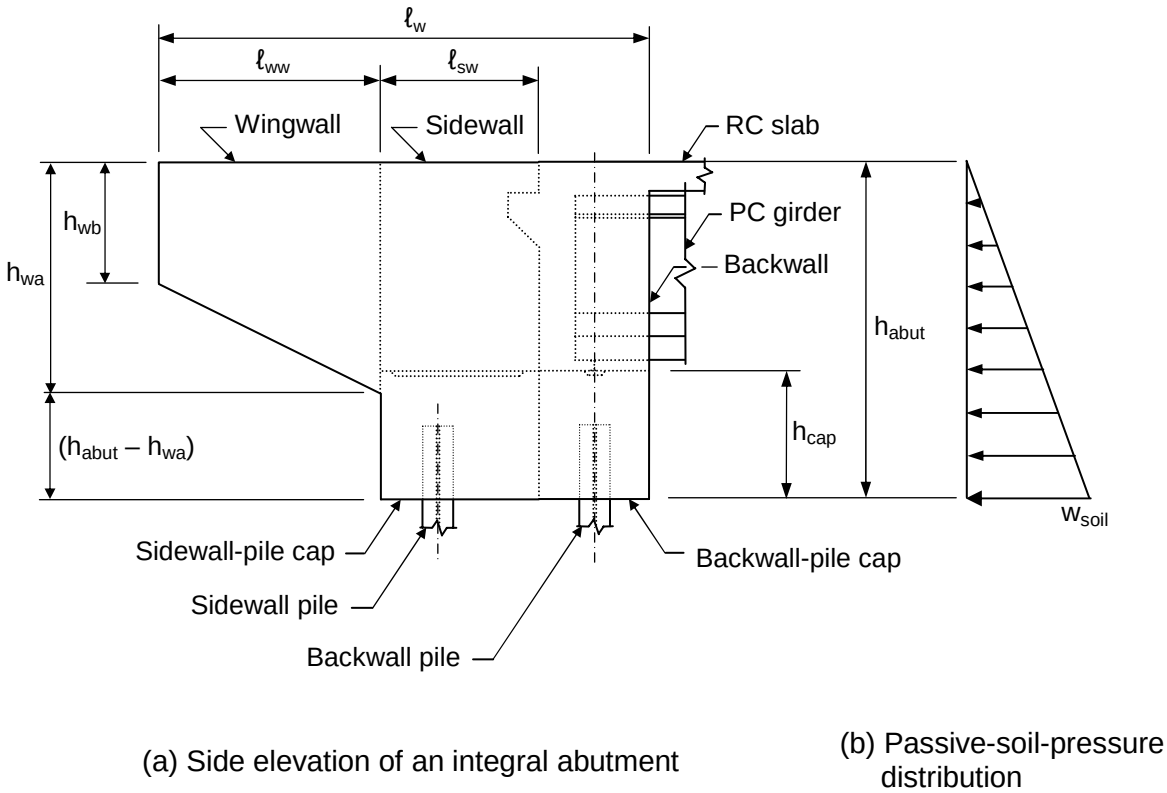

Figure 8.56. Side-elevation view of an integral abutment

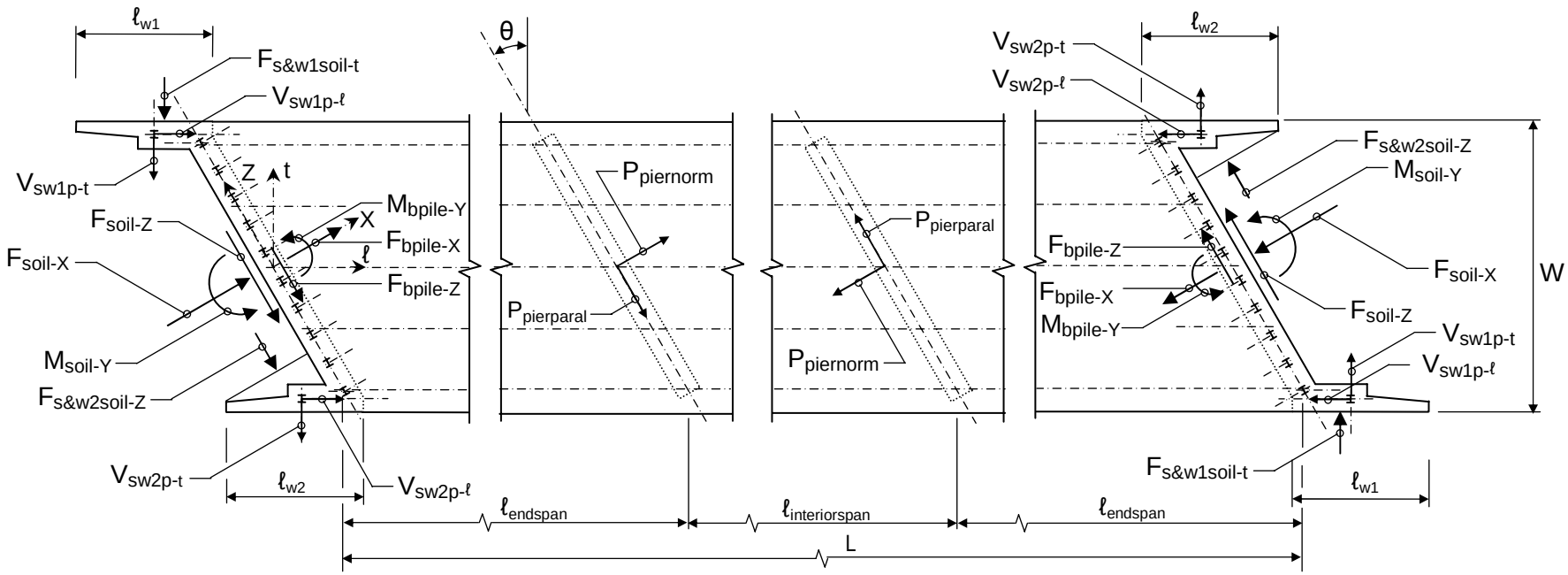

Figure 8.57. Forces induced by thermal expansion of an integral-abutment bridge

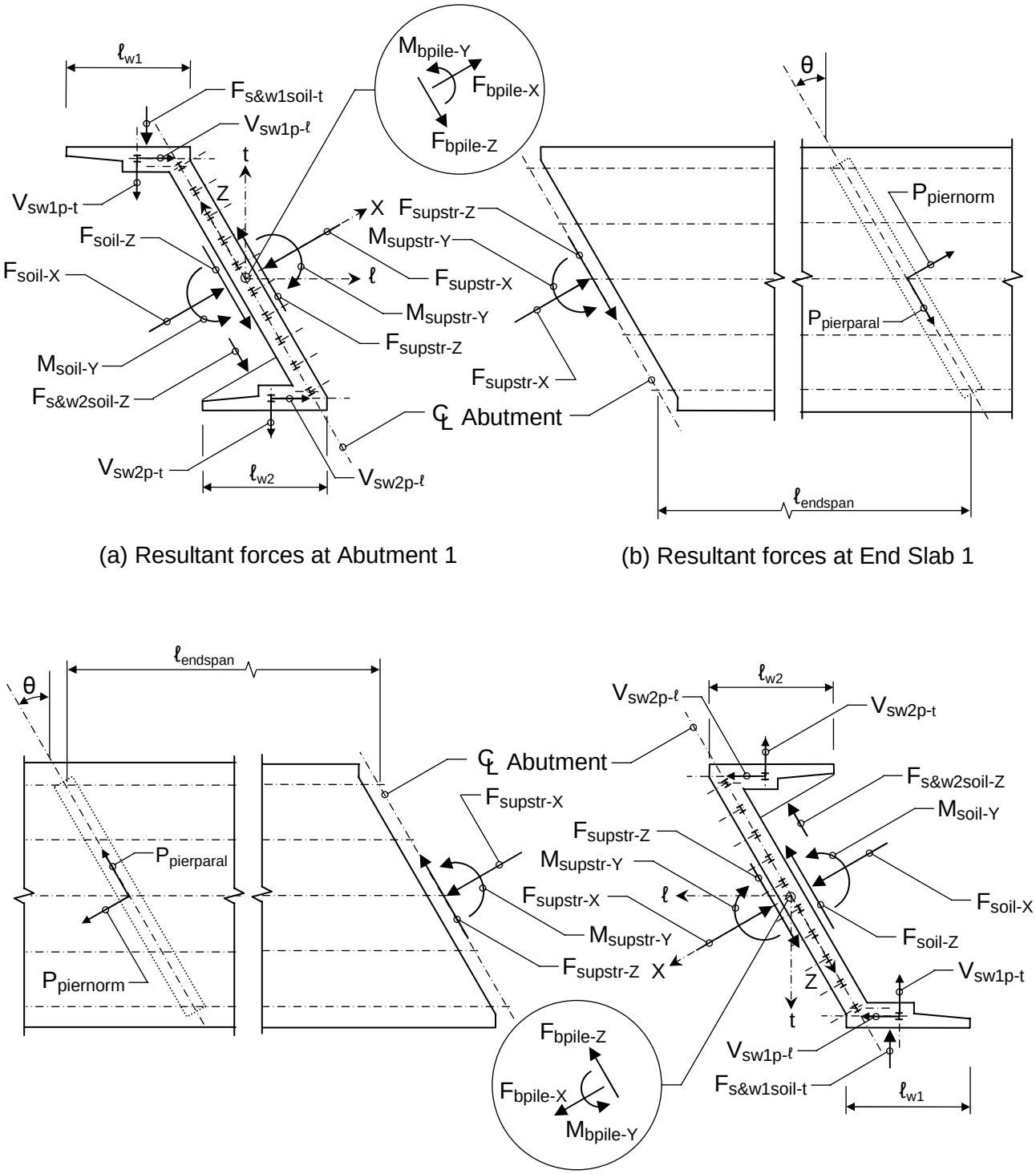

Figure 8.58. Abutment and superstructure forces that are induced by a thermal expansion of an integral-abutment bridge

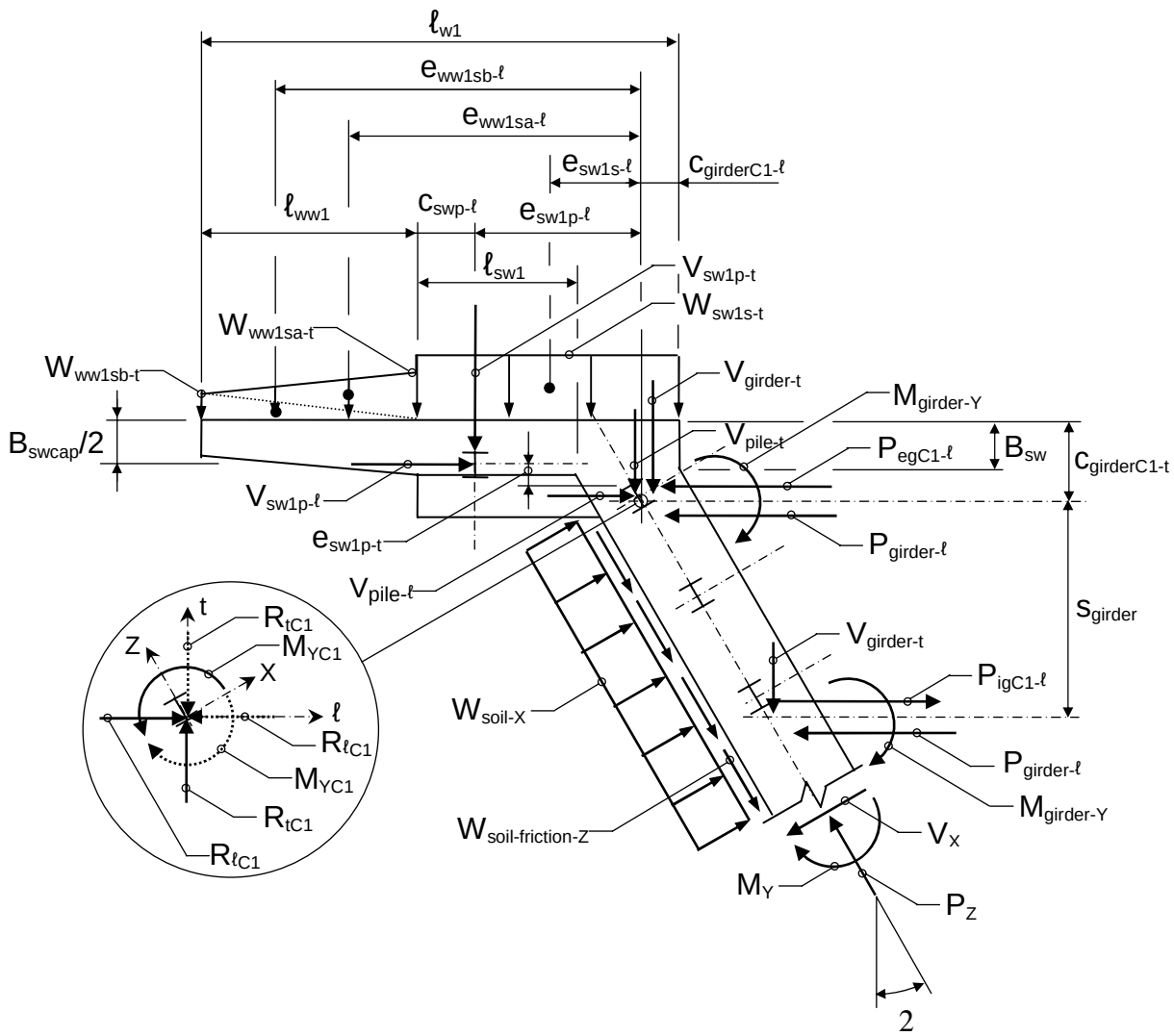

(a) Corner 1 of an abutment

Figure 8.59. Free-body diagrams for the corners of an integral abutment

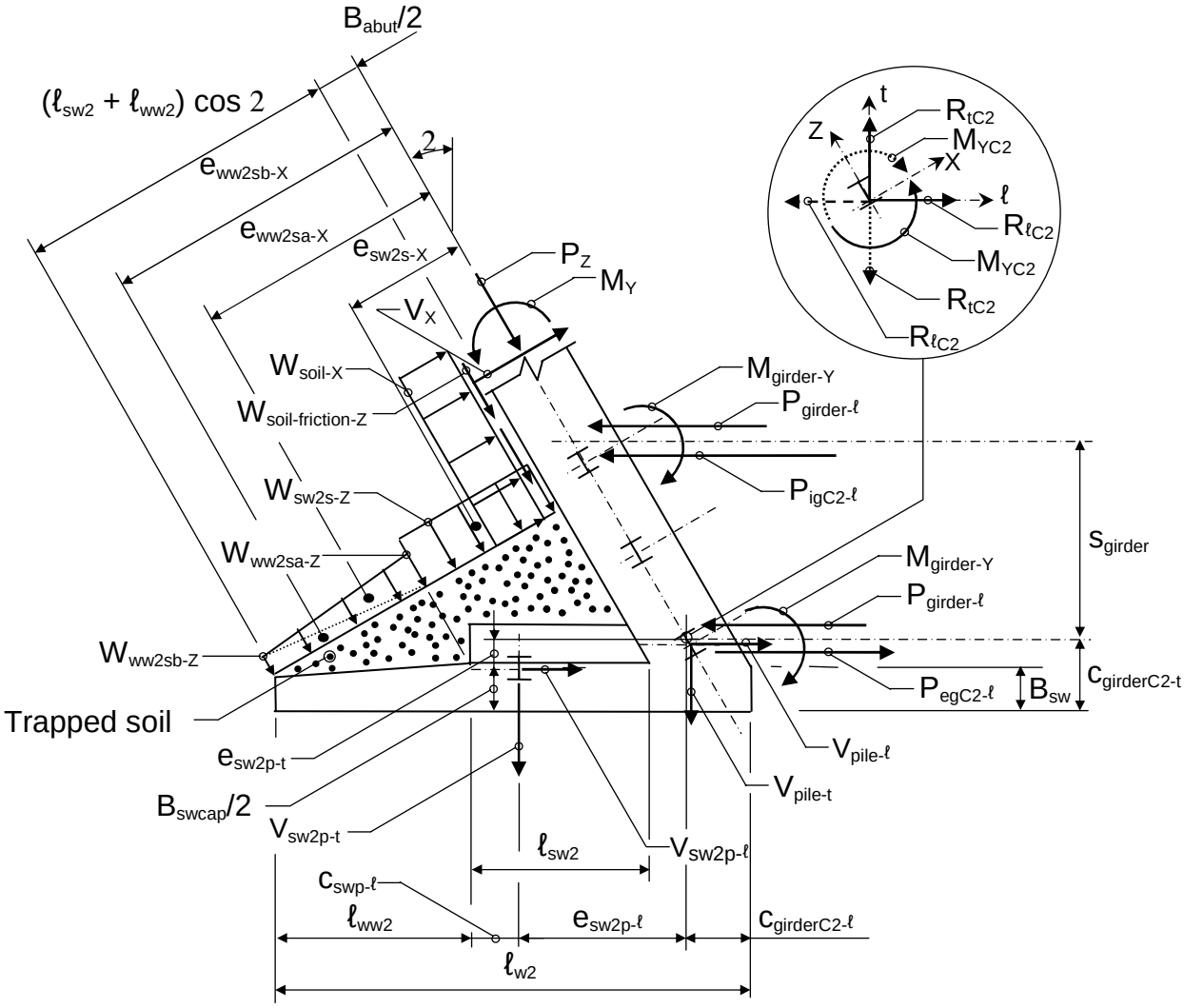

(b) Corner 2 of an abutment

Figure 8.59. (cont'd.)

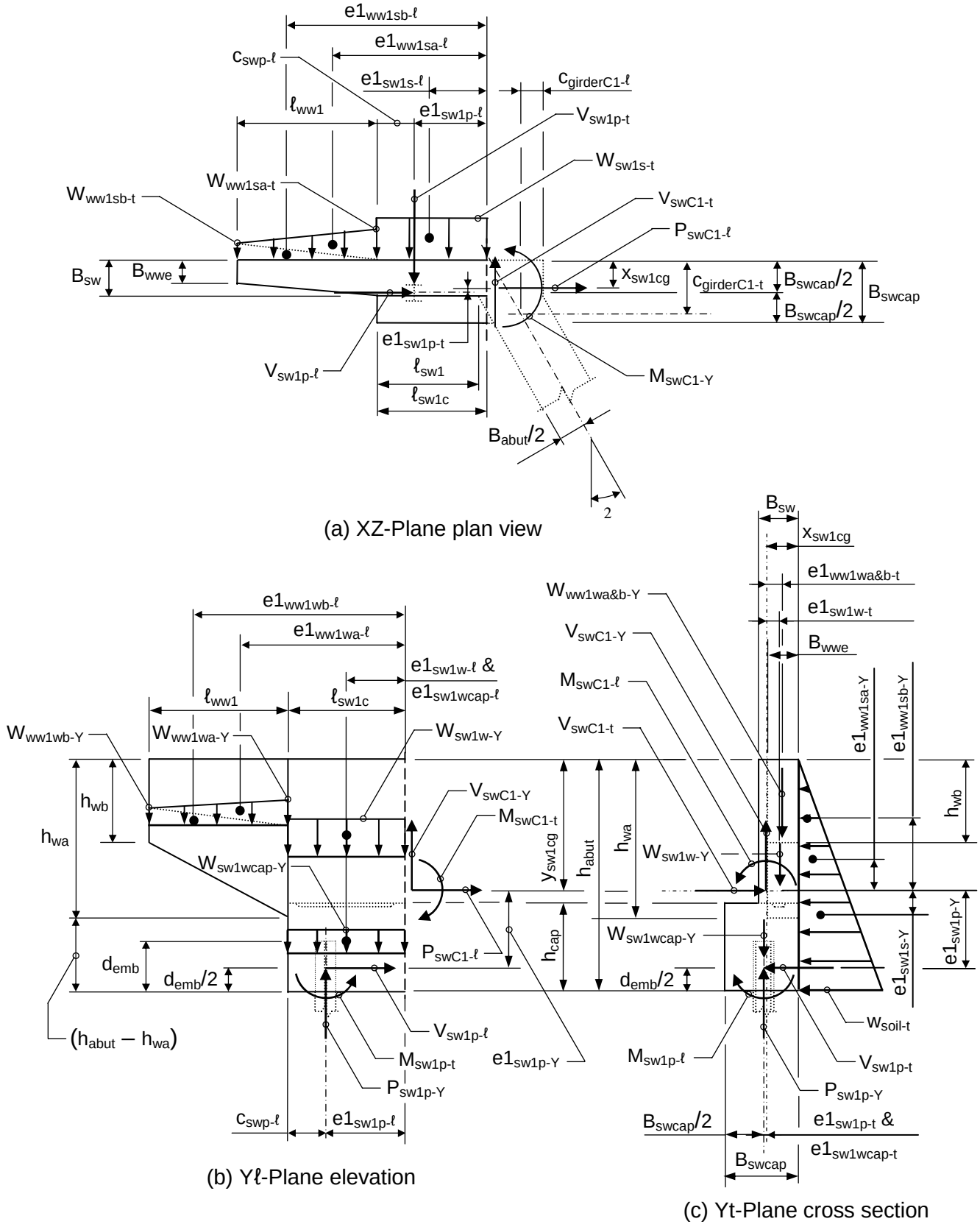

Figure 8.60. Wingwall and sidewall at Corner 1 of an integral-abutment

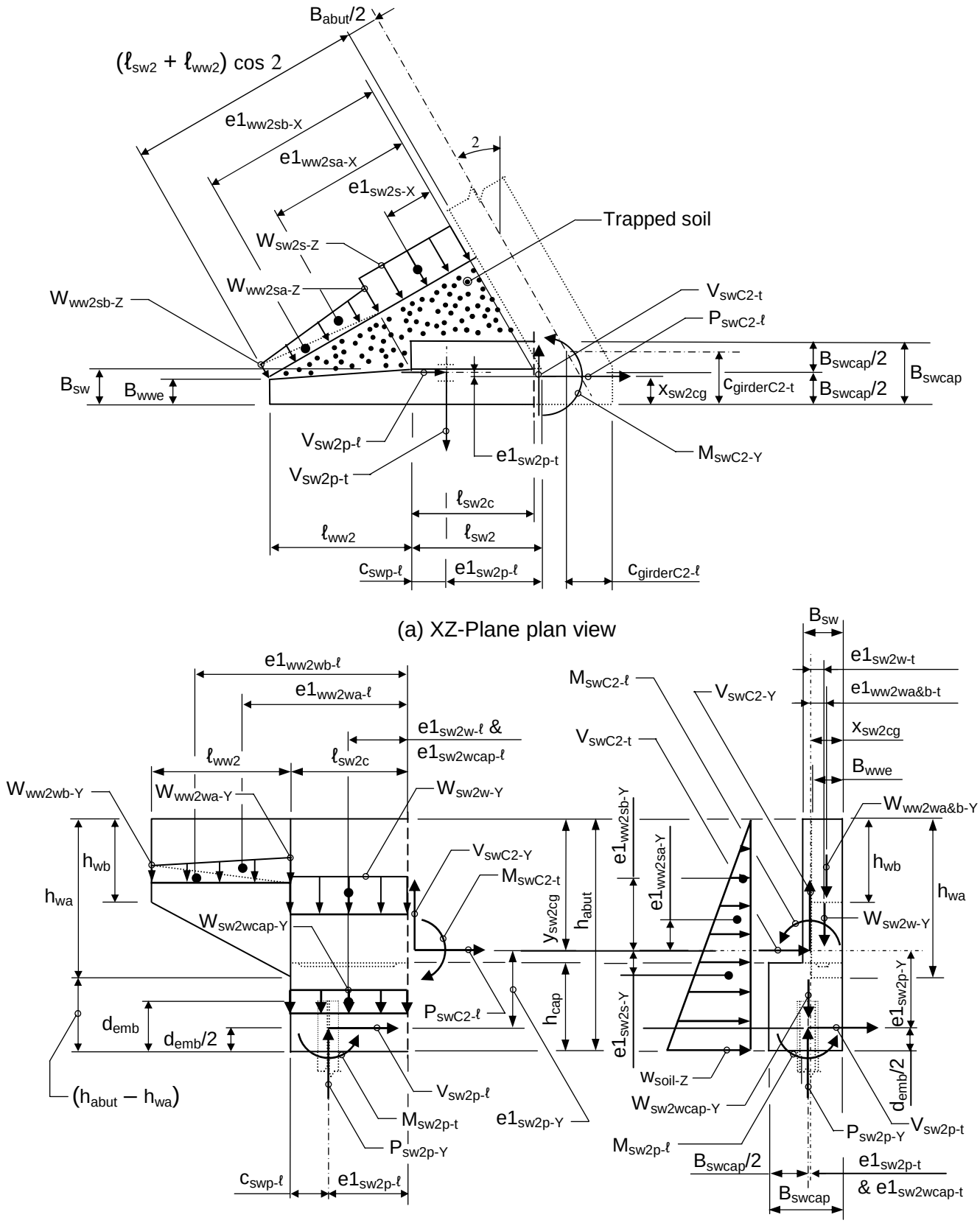

Figure 8.61. Wingwall and sidewall at Corner 2 of an integral-abutment

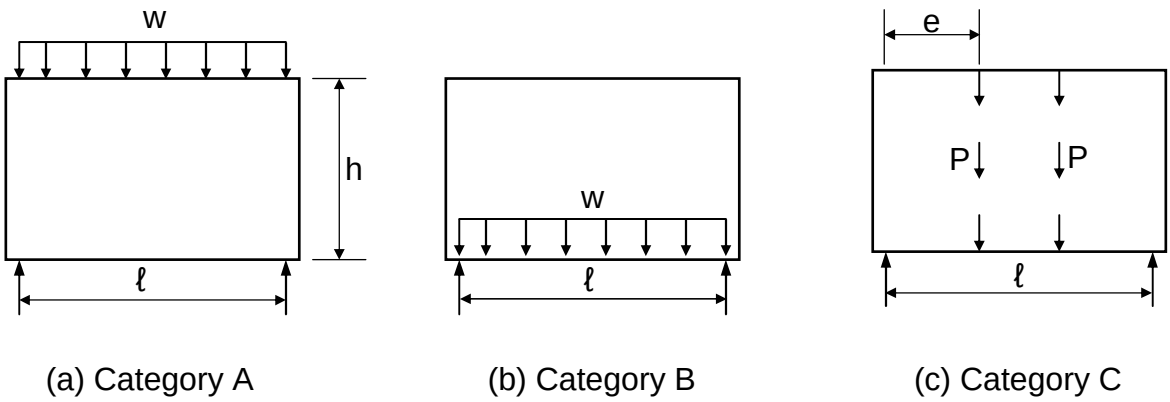

Figure 8.62. Loads on deep-flexural members

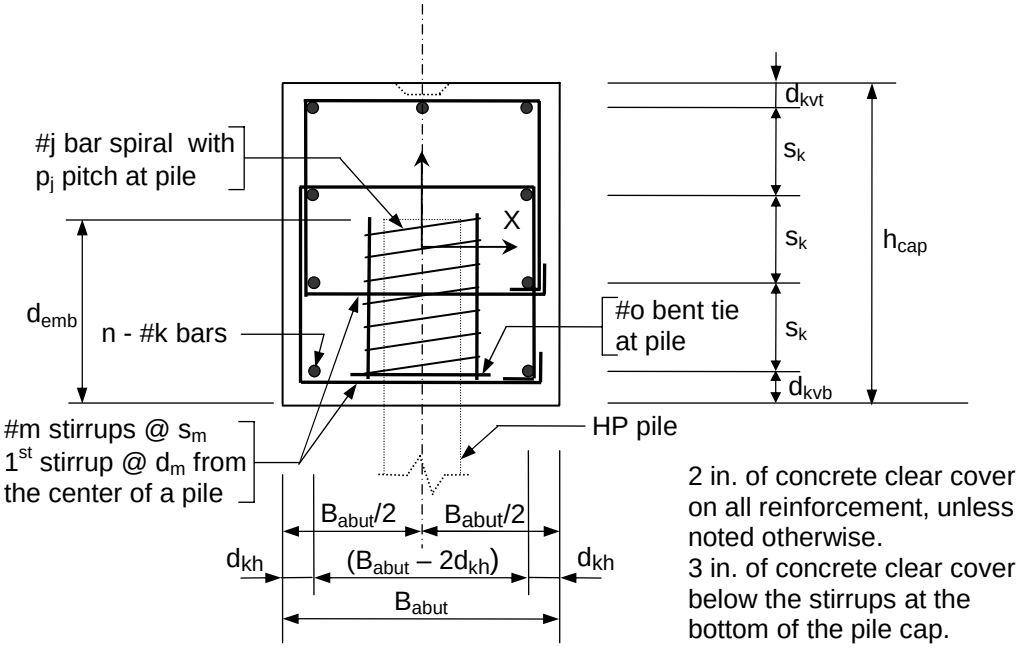

Figure 8.63. Reinforcement for a backwall-pile cap

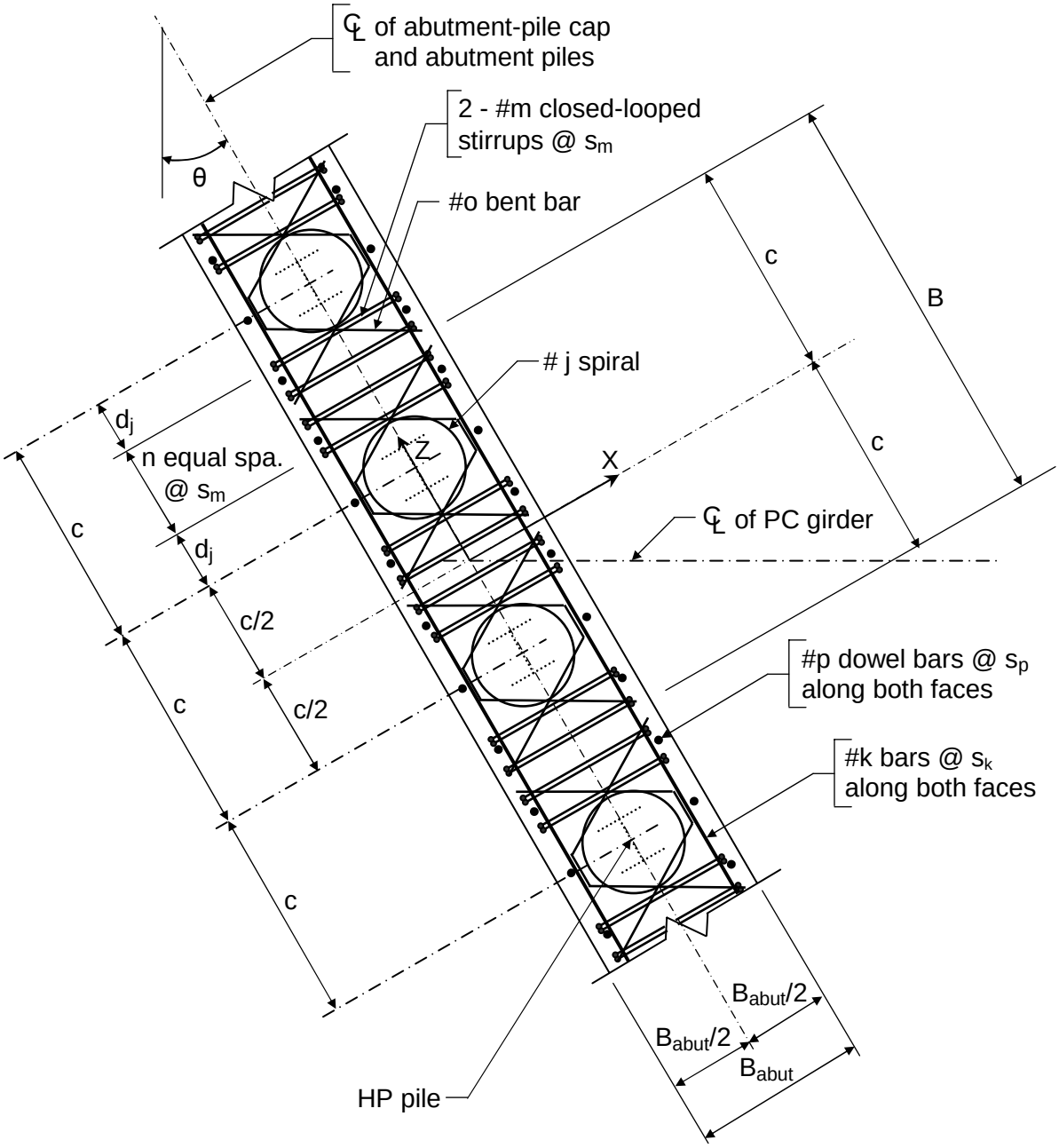

Figure 8.64. Partial XZ-plane cross section of a backwall-pile cap

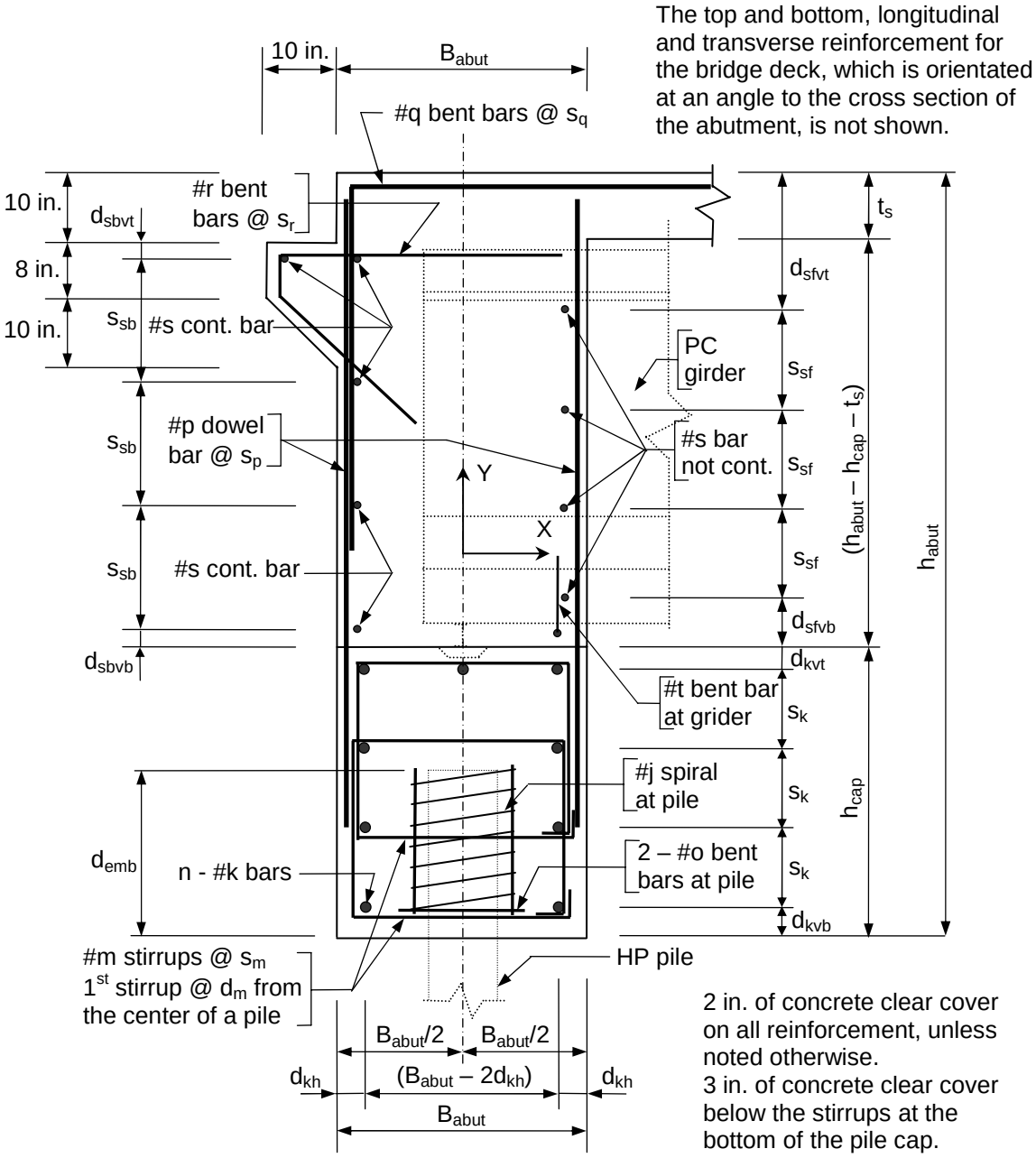

Figure 8.65. Reinforcement for an abutment backwall

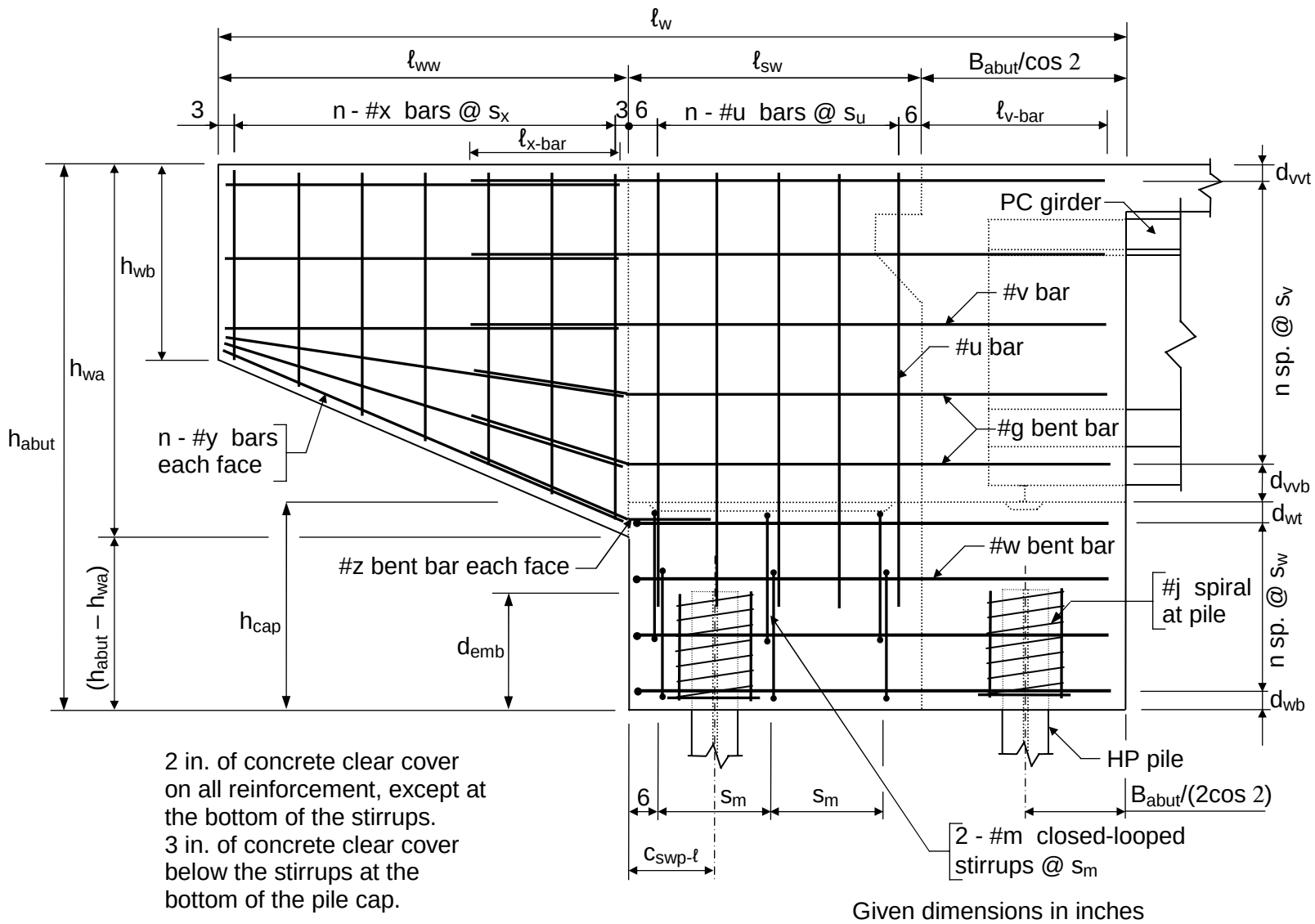

Figure 8.66. Reinforcement for a wingwall, sidewall, and sidewall-pile-cap

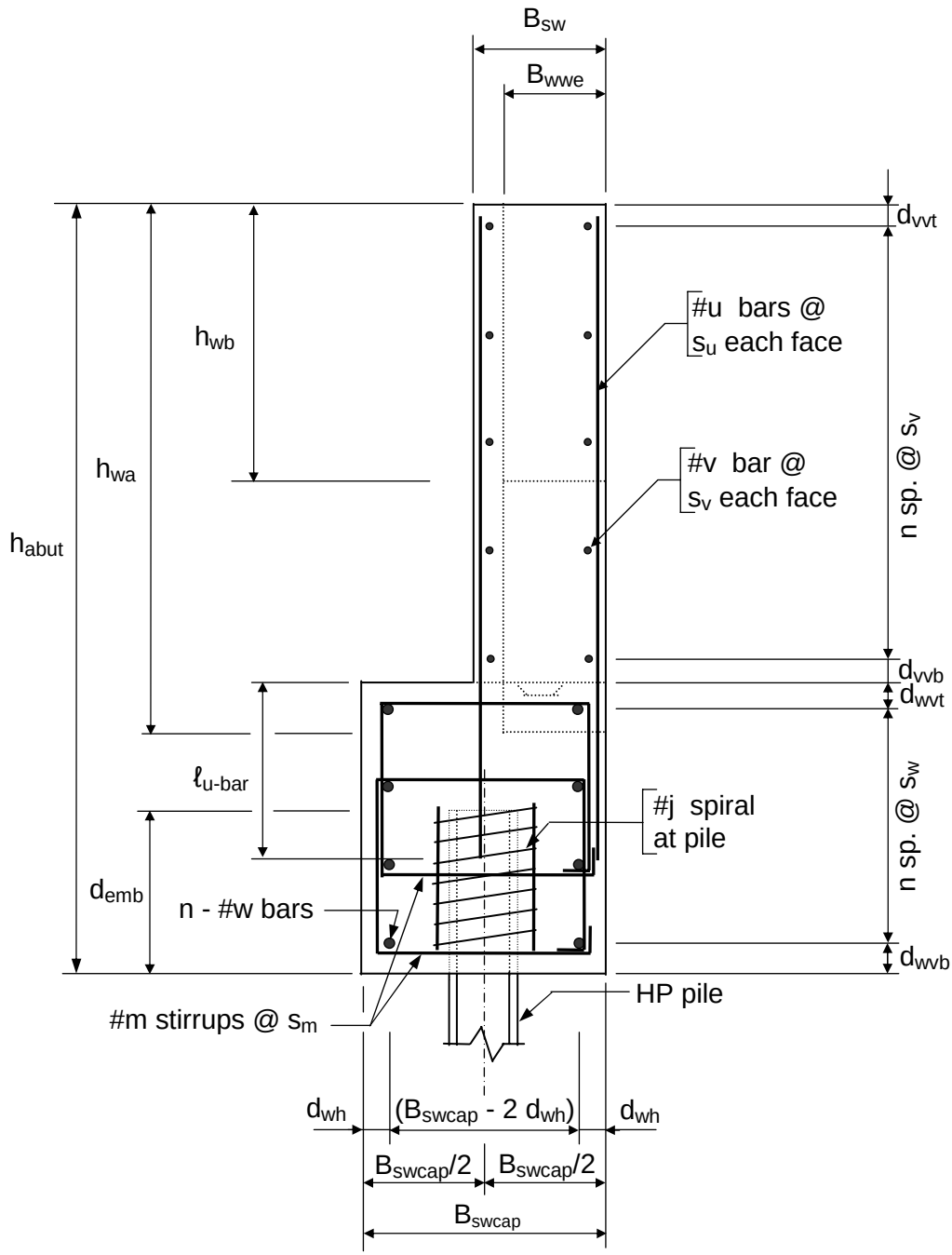

2 in. of concrete clear cover on all reinforcement, except at the bottom of the stirrups.
3 in. of concrete clear cover below the stirrups at the bottom of the pile cap.

Figure 8.67. Reinforcement for a sidewall and a sidewall-pile cap

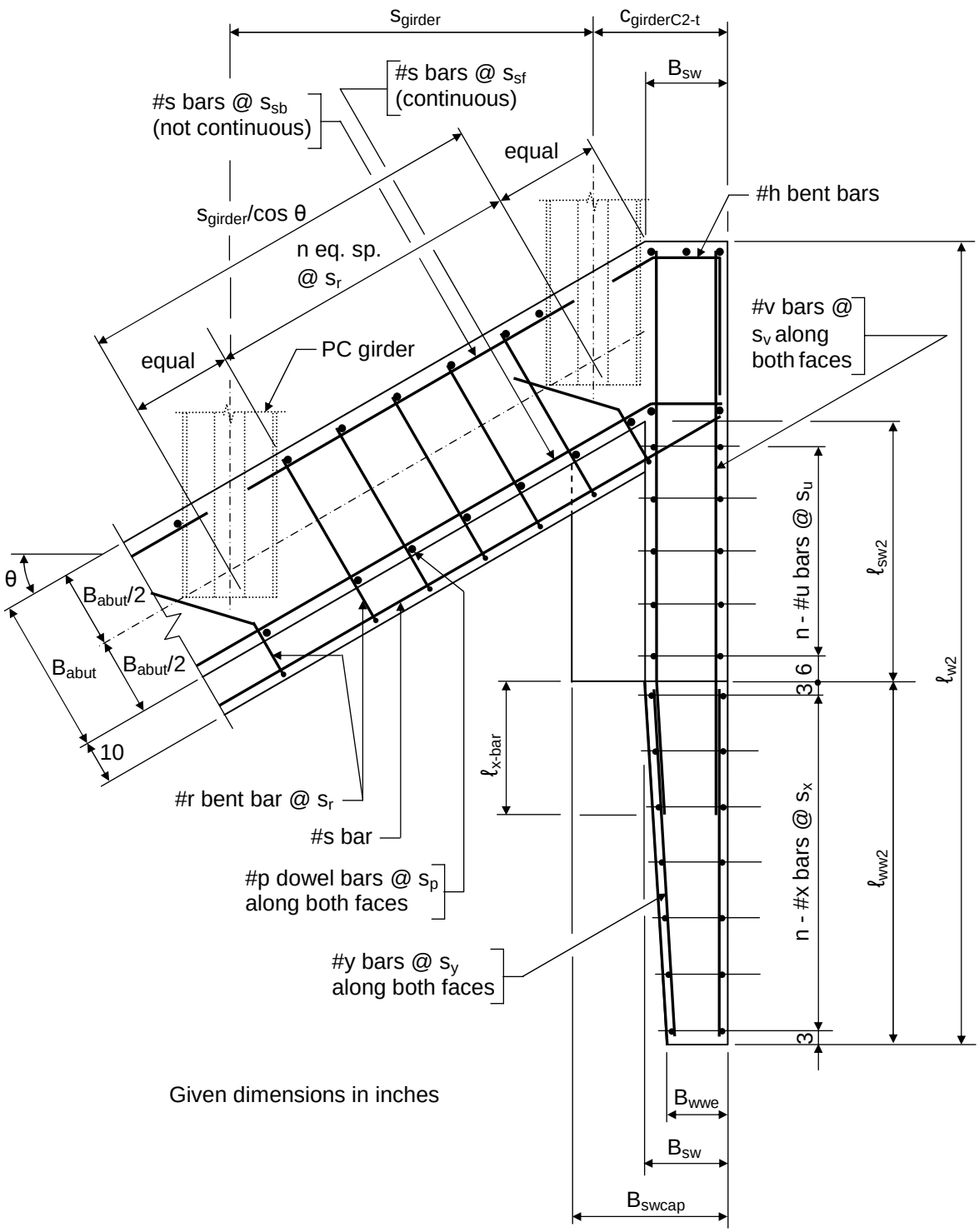

Figure 8.68. Abutment reinforcement in an XY-plane above the pile cap near Corner 2

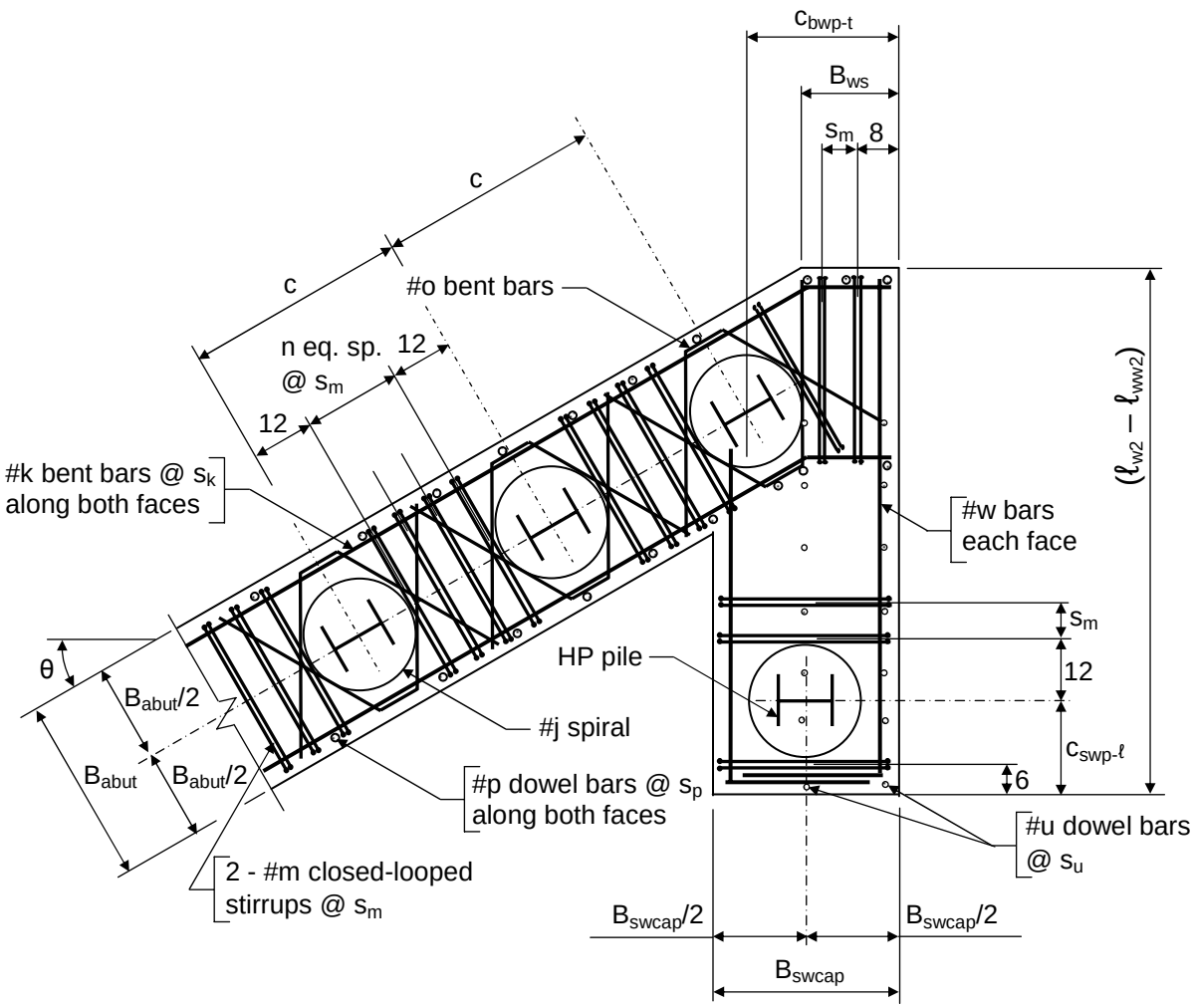

Given dimensions in inches

Figure 8.69. Abutment reinforcement in an XY-plane within the pile cap near Corner 2

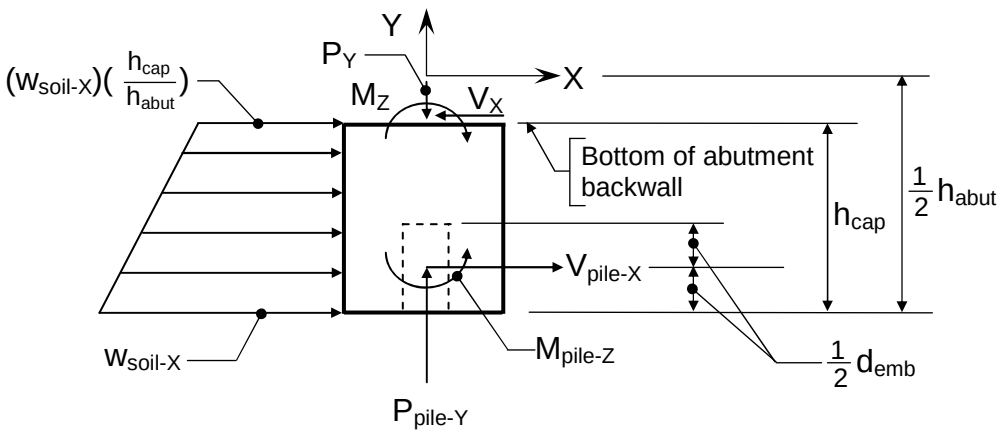

Figure 8.70. Free-body diagram of an abutment-pile cap with thermally-induced forces

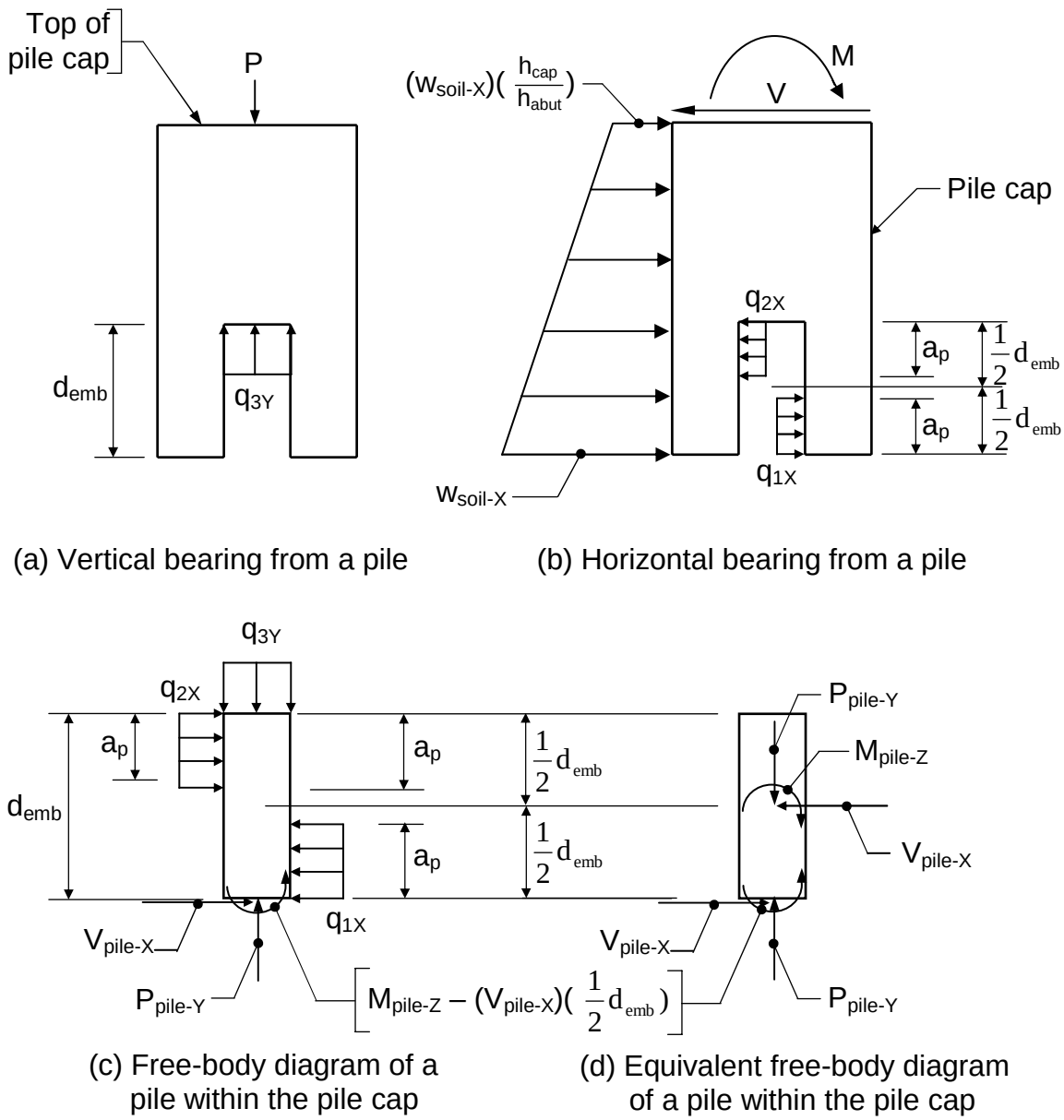

(a) Vertical bearing from a pile

(b) Horizontal bearing from a pile

(c) Free-body diagram of a pile within the pile cap

(d) Equivalent free-body diagram of a pile within the pile cap

Figure 8.71. Pile-to-pile-cap connection

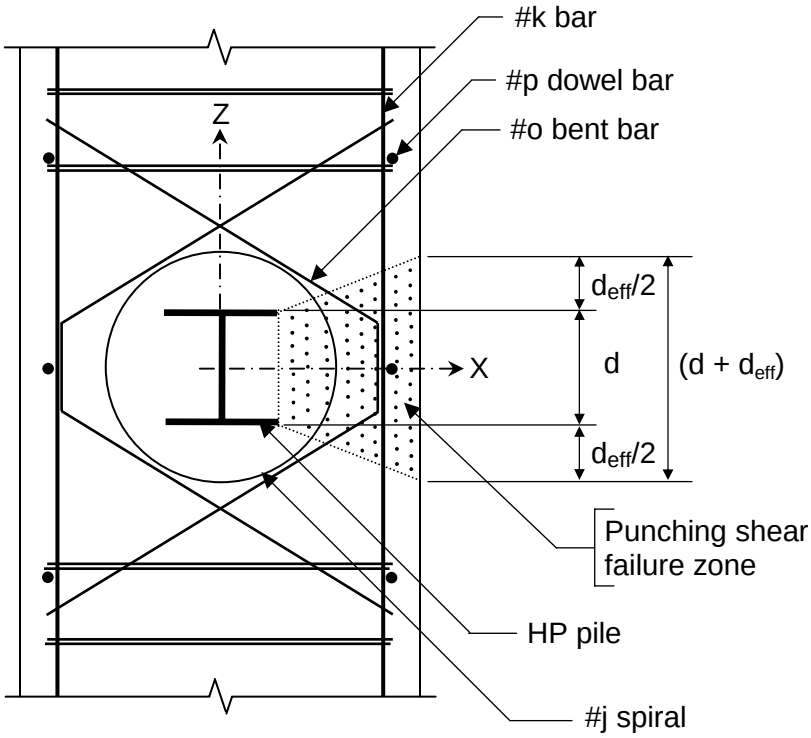

(c) Plan view cross section of pile cap at the location of an abutment pile

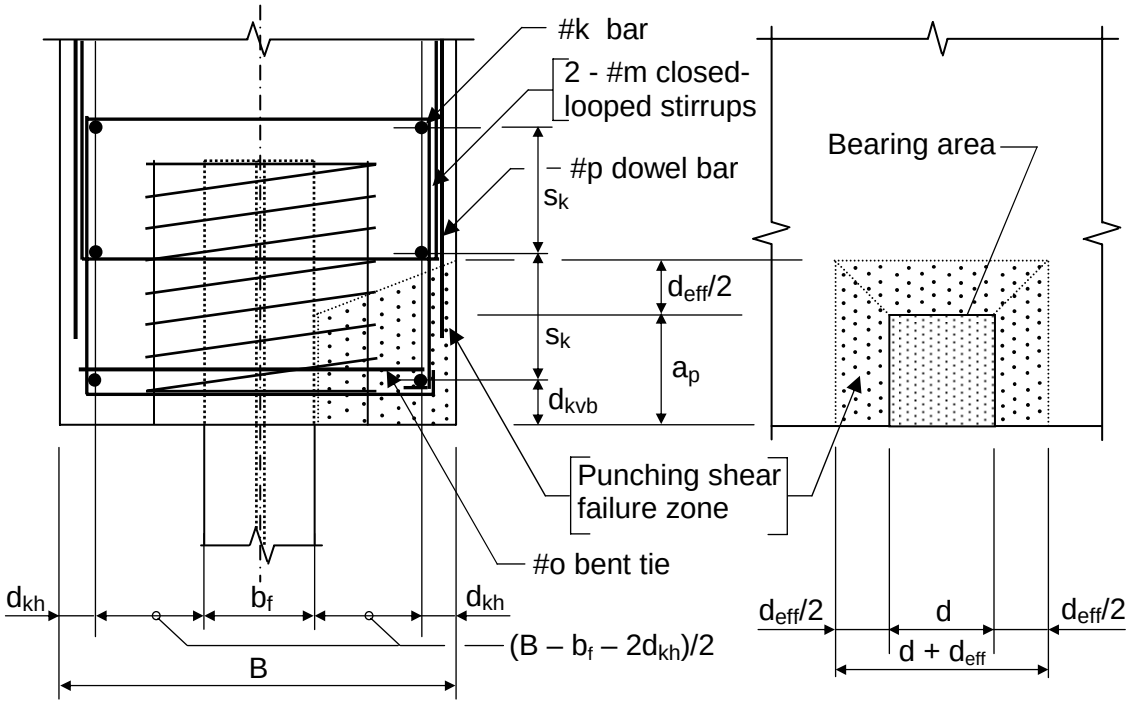

(a) Vertical cross section of pile cap at the location of an abutment pile

(b) Concrete bearing area of an abutment pile at the bottom of the pile cap

Figure 8.72. Concrete punching-shear failure at an abutment pile

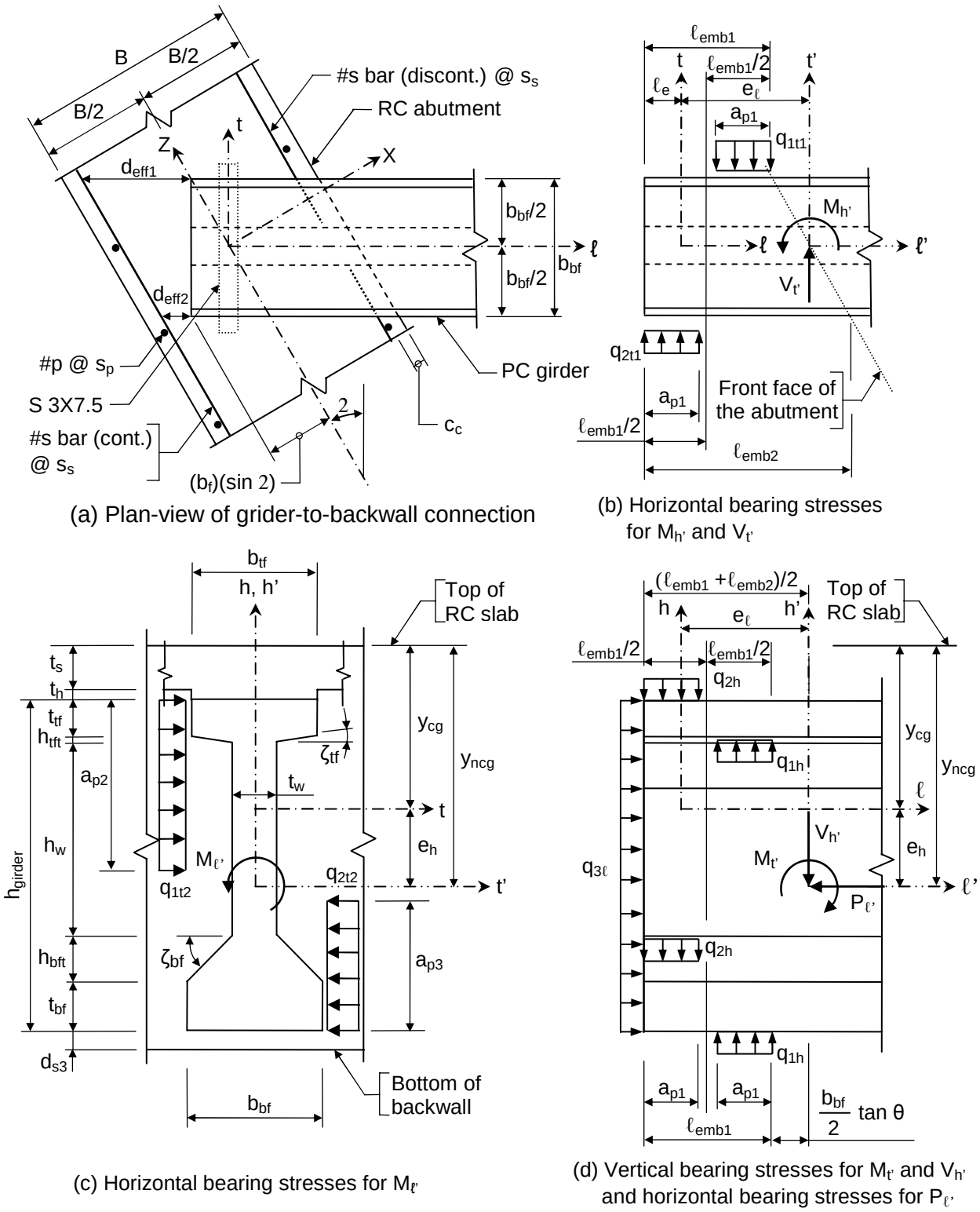

Figure 8.73. Concrete bearing stresses at the end of a PC girder

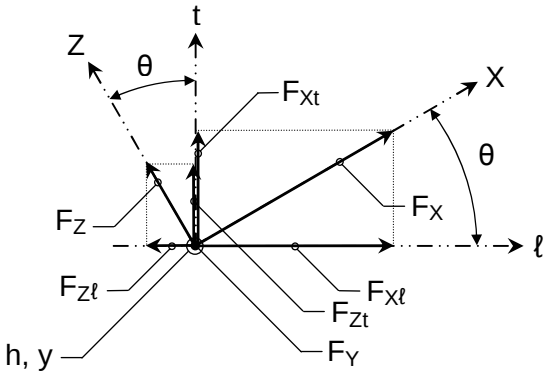

(a) Force and force components

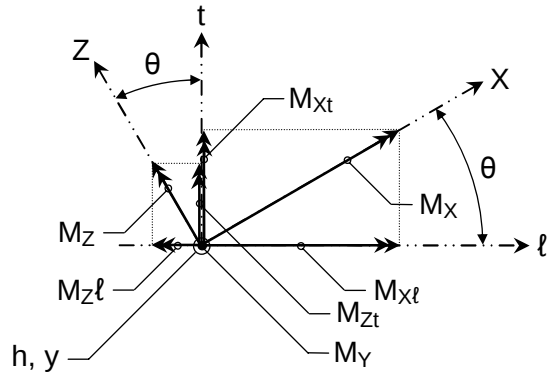

(b) Moment and moment components

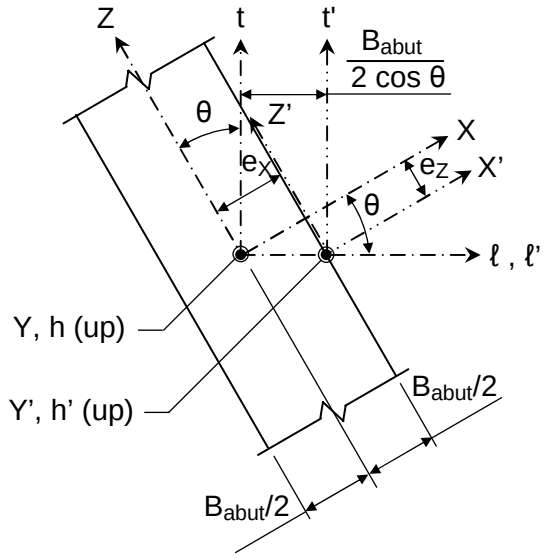

(c) Abutment and superstructure coordinate axes

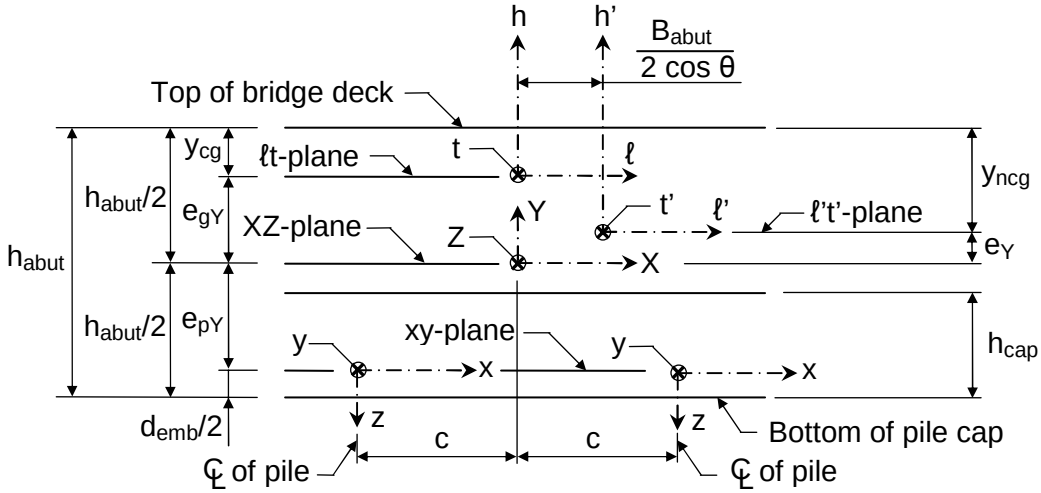

(d) Horizontal planes at an integral abutment

Figure 8.74. PC girder member-end forces that act on an integral abutment

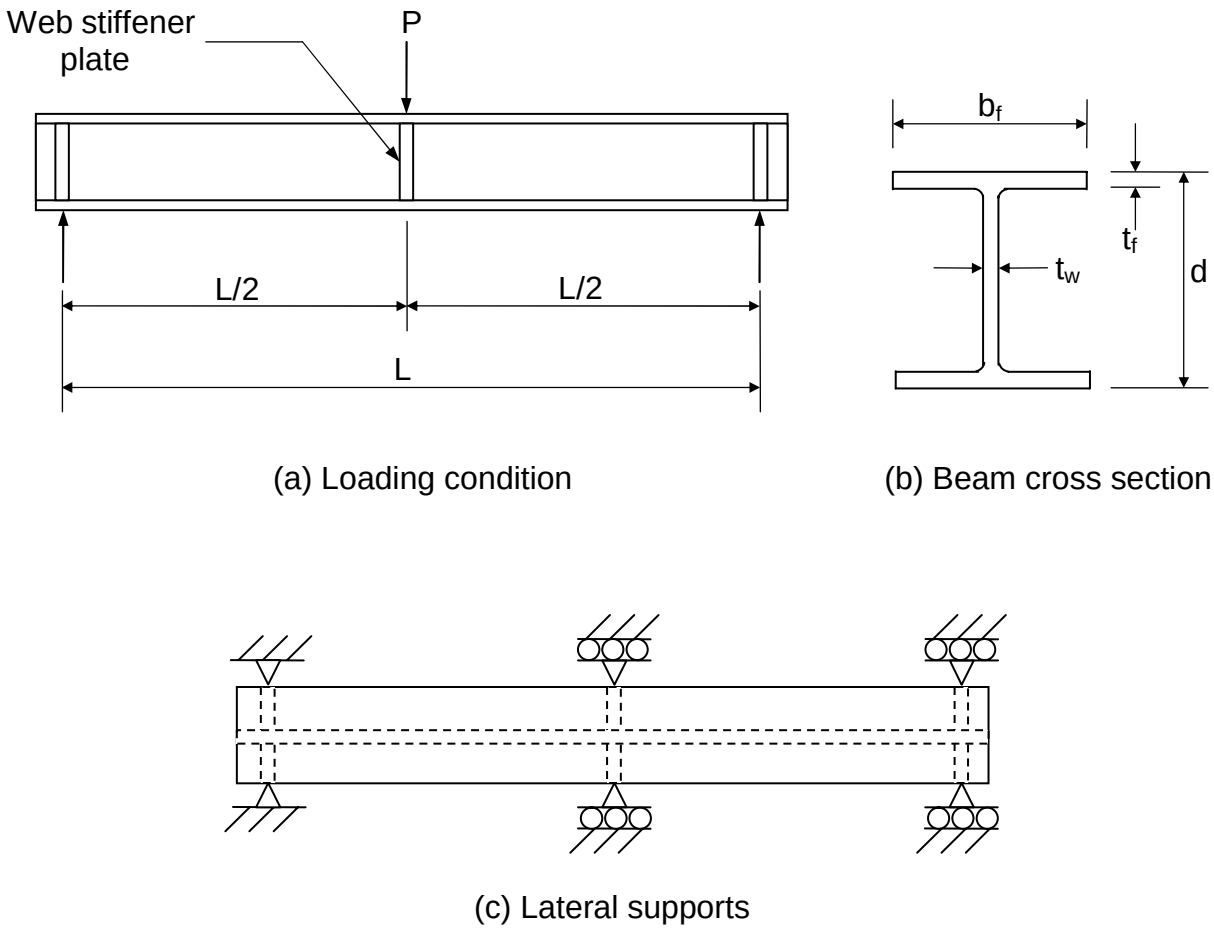

(a) Loading condition

(b) Beam cross section

(c) Lateral supports

Figure 8.75. Geometric conditions for a simply-supported beam with a concentrated load at the midspan

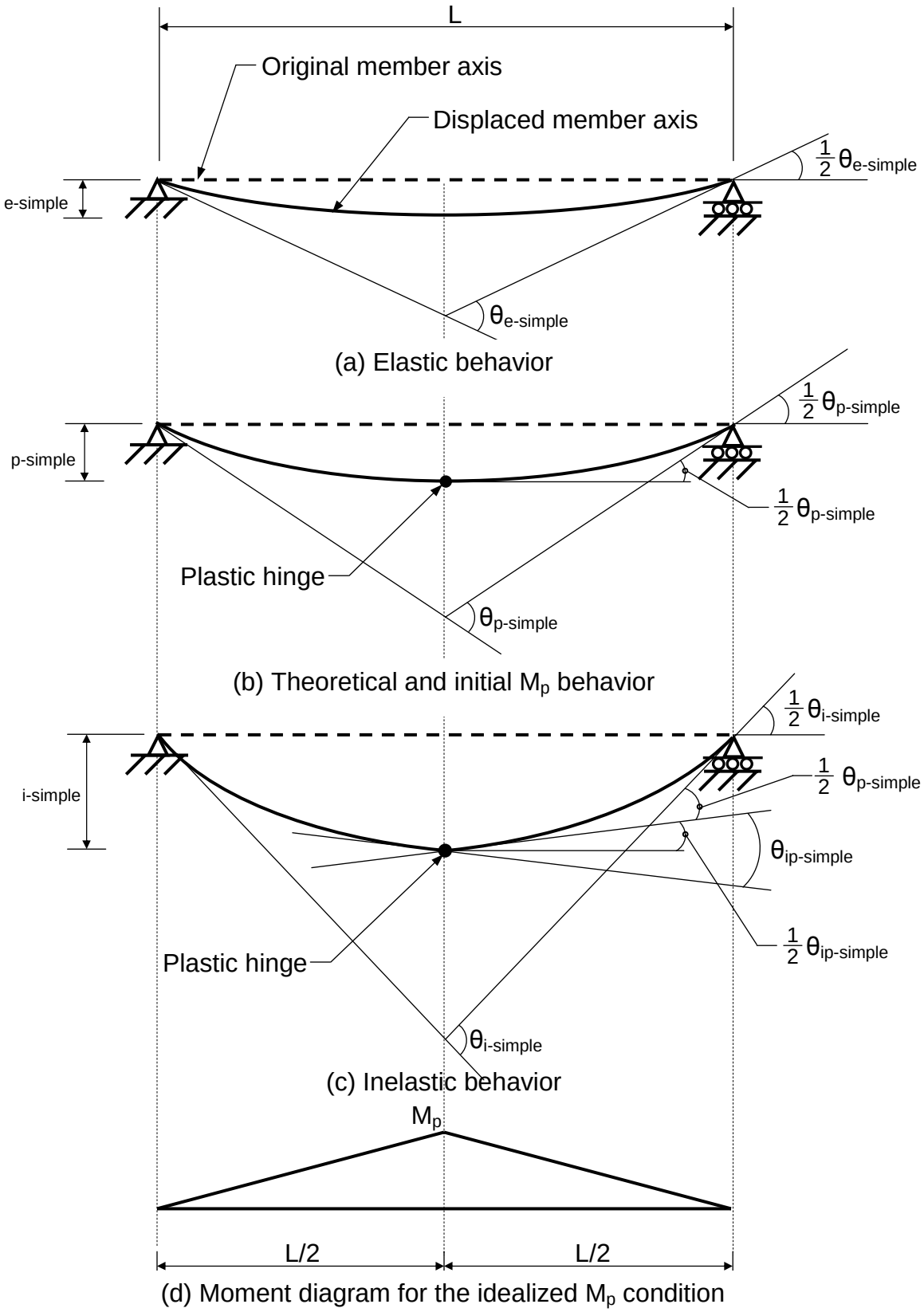

Figure 8.76. Displacements for a simply-supported beam loaded at the mid-span

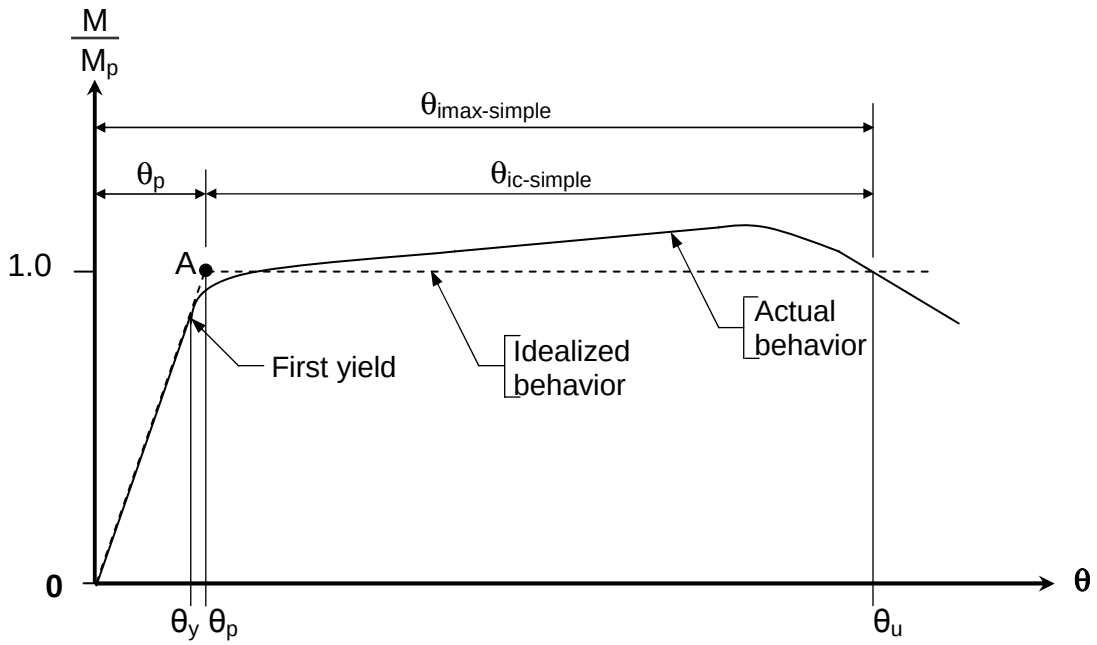

Figure 8.77. Moment-rotation relationship

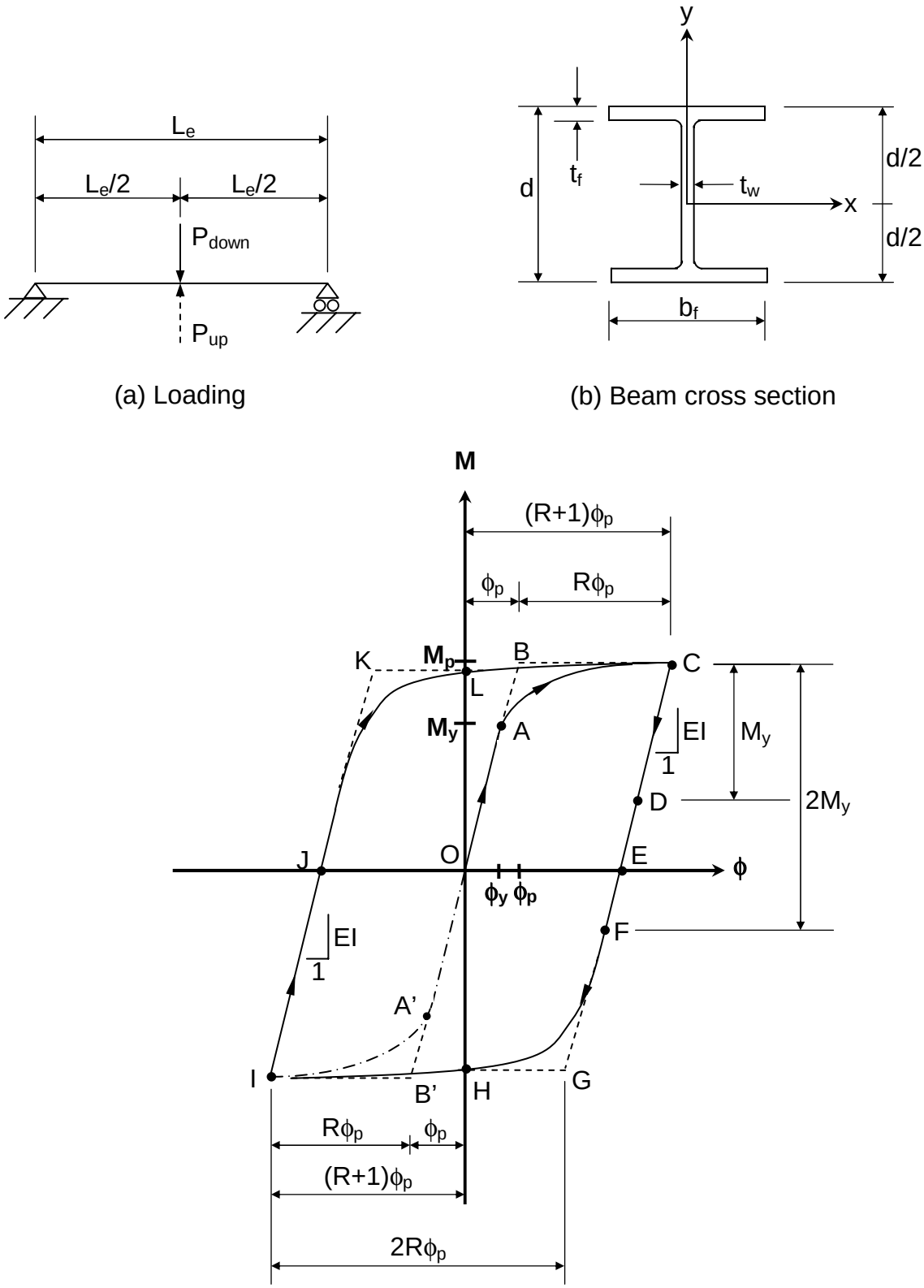

(a) Loading

(b) Beam cross section

(c) Moment-curvature relationship

Figure 8.78. Alternating plasticity

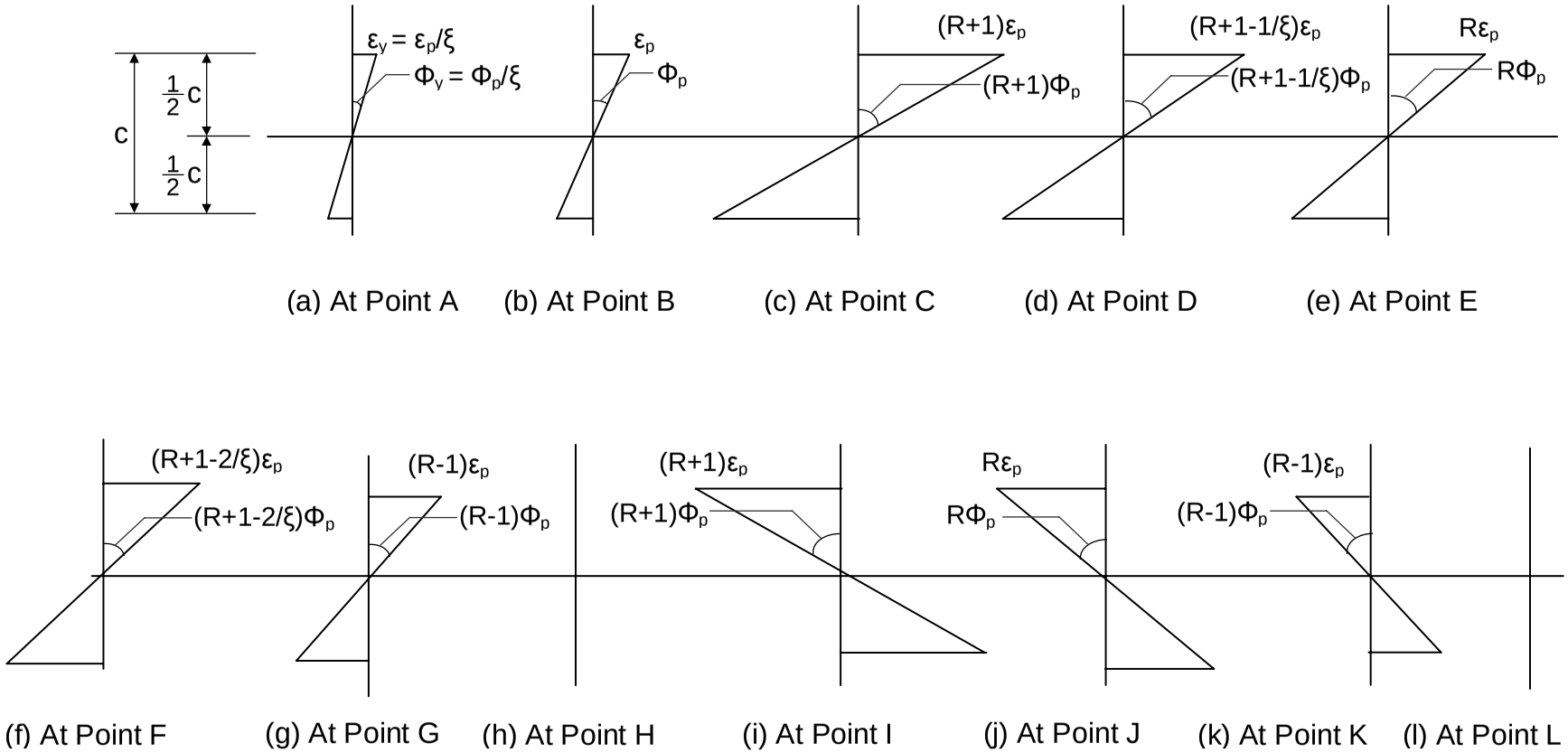

Figure 8.79. Strain distributions that correspond to M-ϕ points shown in Fig. 8.78

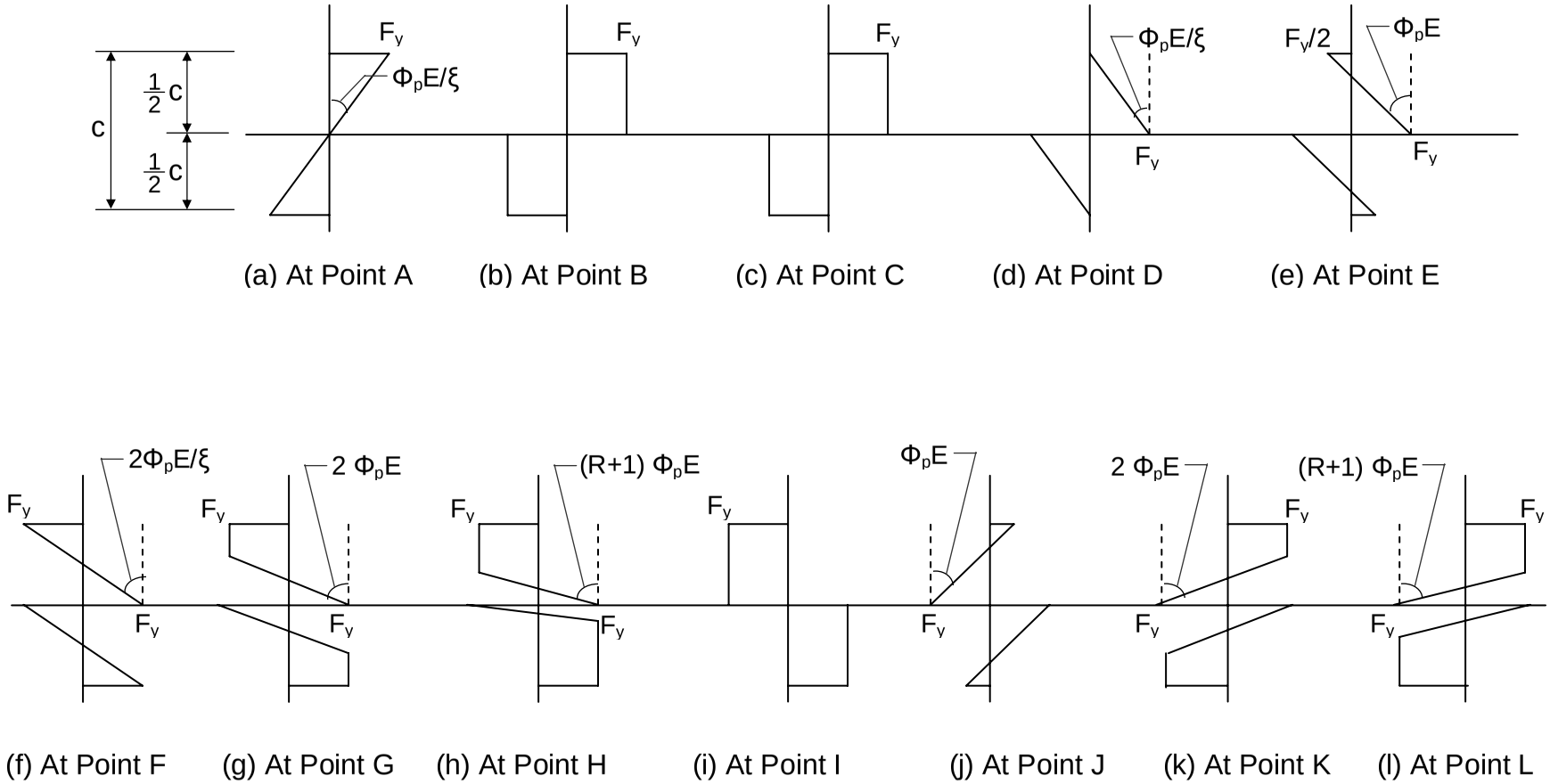

Figure 8.80. Stress distributions that correspond to M-ϕ points shown in Fig. 8.78

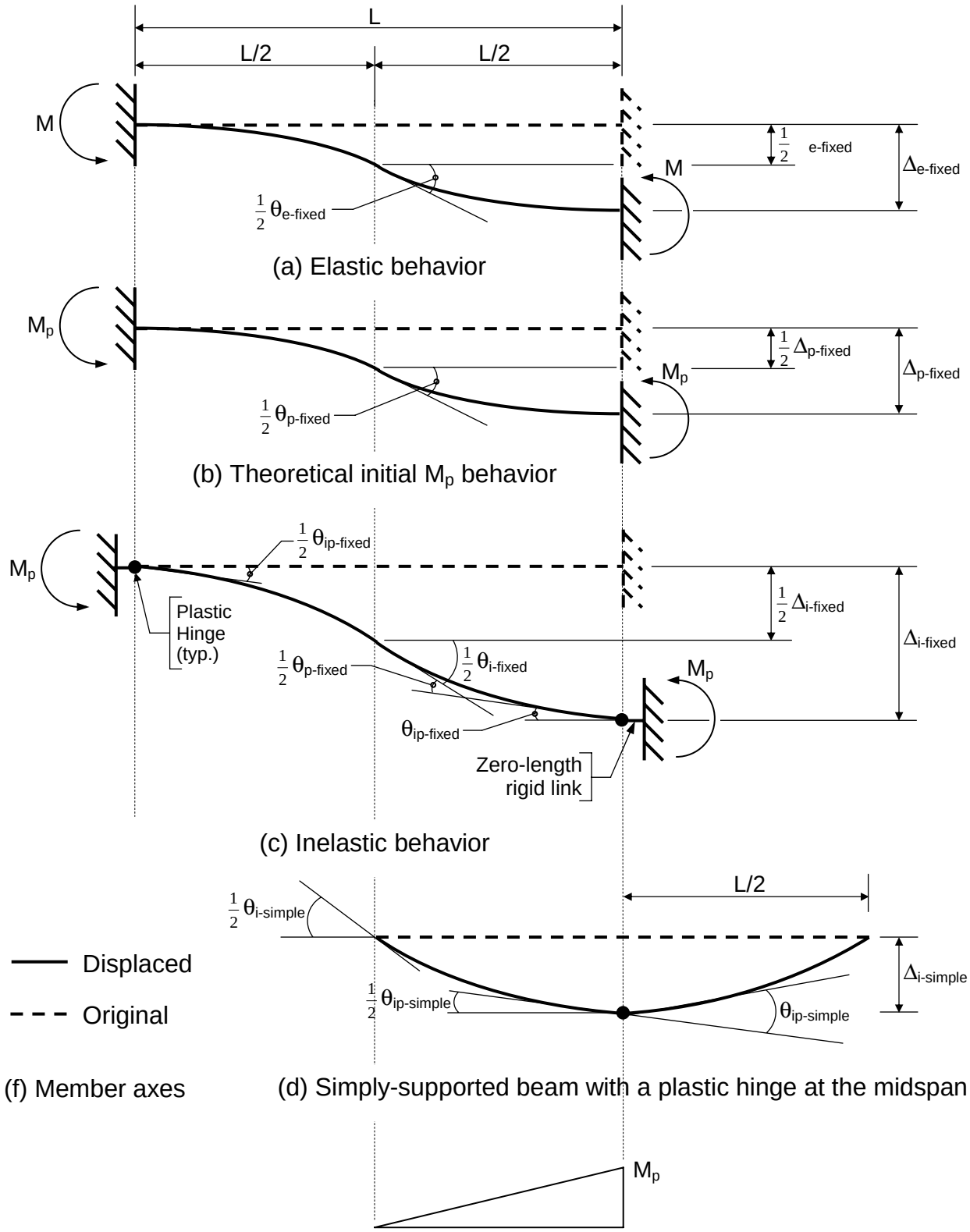

Figure 8.81. Fixed-end beam with sidesway

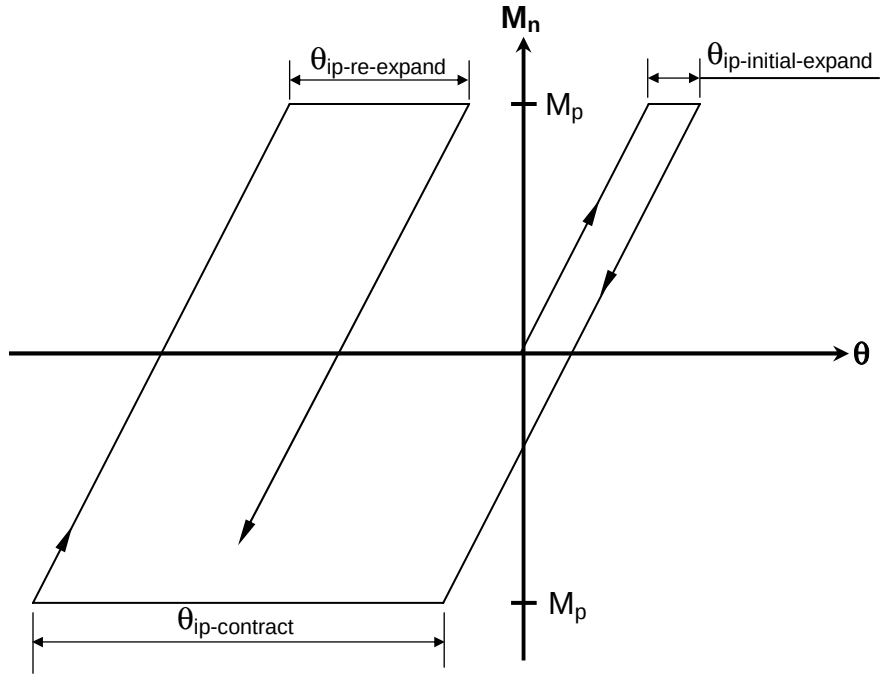

(a) Initial expansion, contraction, and re-expansion

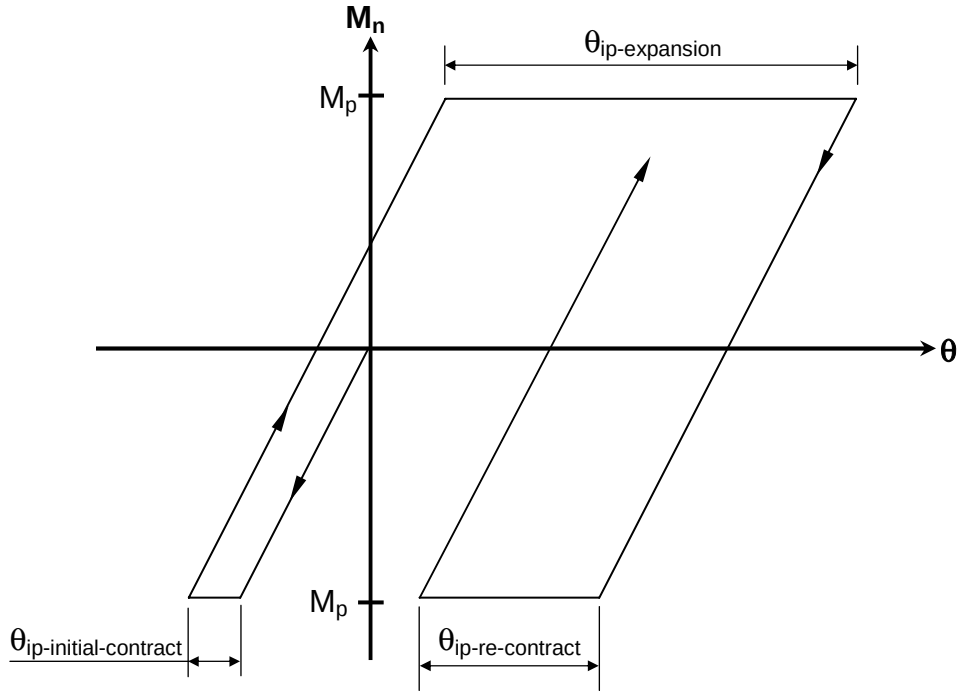

(b) Initial contraction, expansion, and re-contraction

Figure 8.82. Moment-rotation relationship for an abutment pile associated with temperature changes for a bridge superstructure

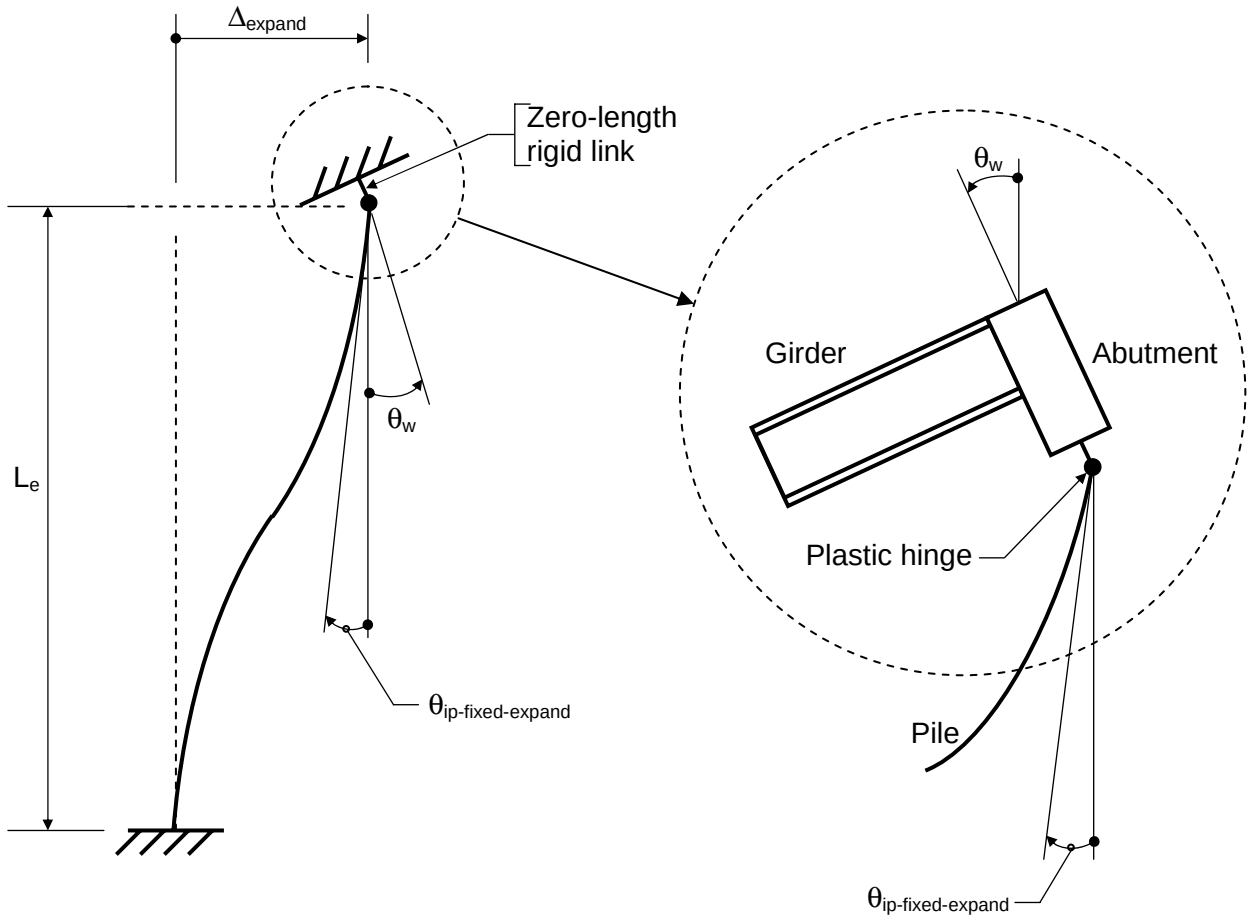

(a) Bridge expansion with the application of the live load

Figure 8.83. Inelastic-hinge rotation due to live load

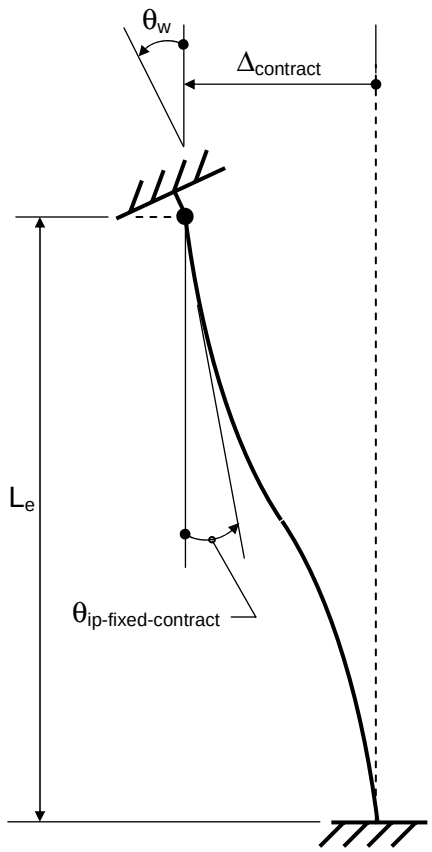

(b) Bridge contraction with the application of the live load

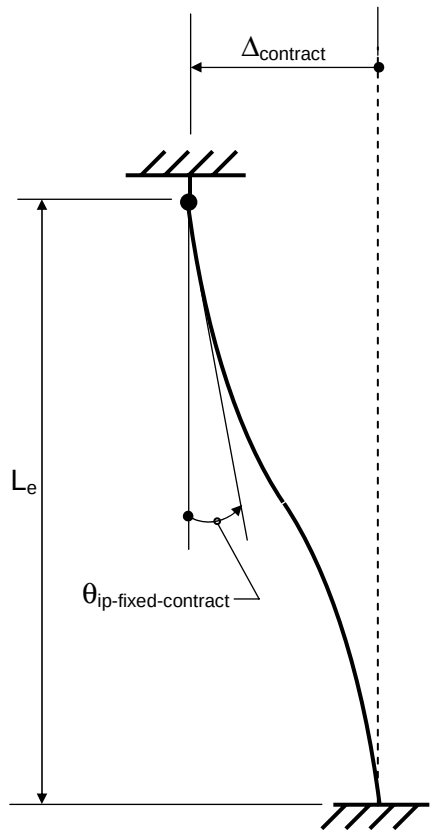

(c) Bridge contraction with the removal of the live load

Figure 8.83. (Continued)

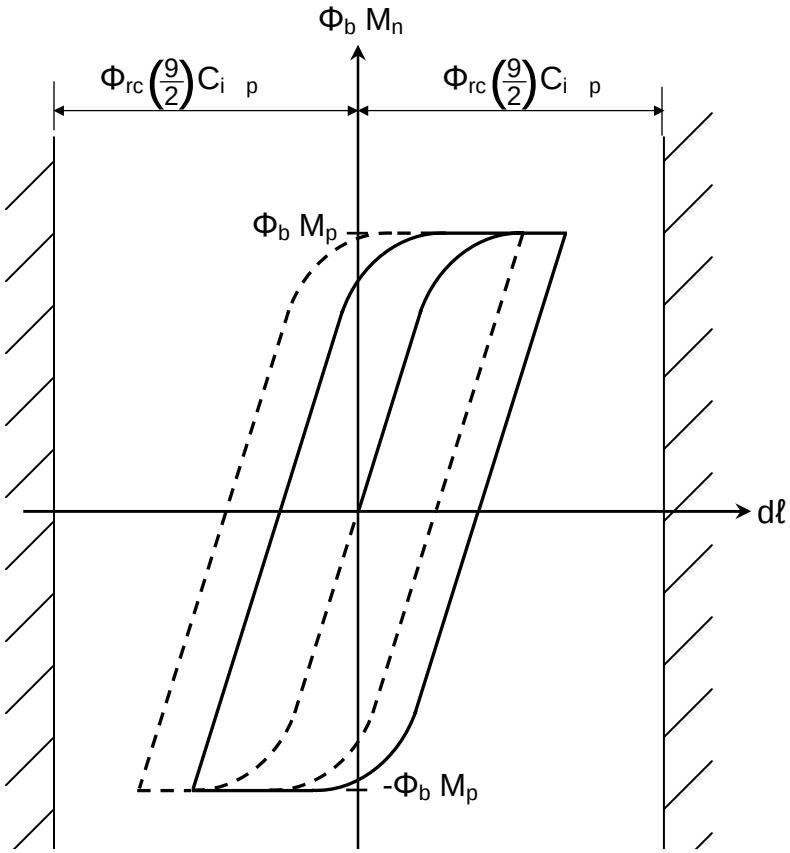

Figure 8.84. Uniaxial-displacement, ductility-limit state for a pile

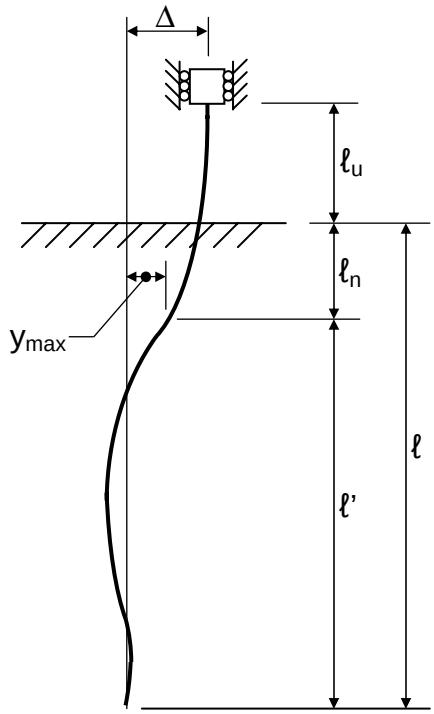

Figure 8.85. Soil-pile system for determining the skin-frictional resistance of a pile

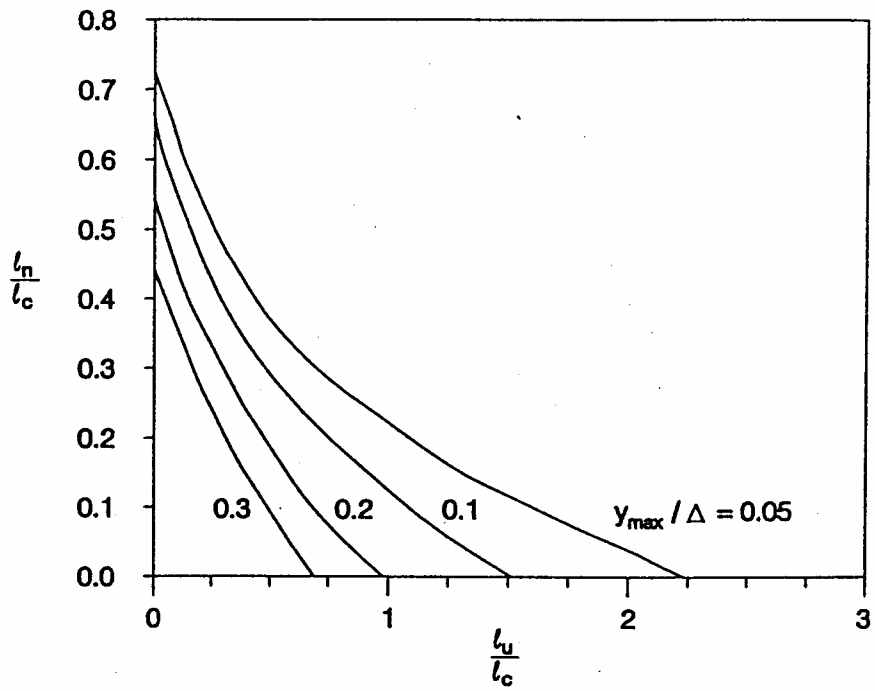

(a) Displacement for a fixed-head pile embedded in a uniform soil

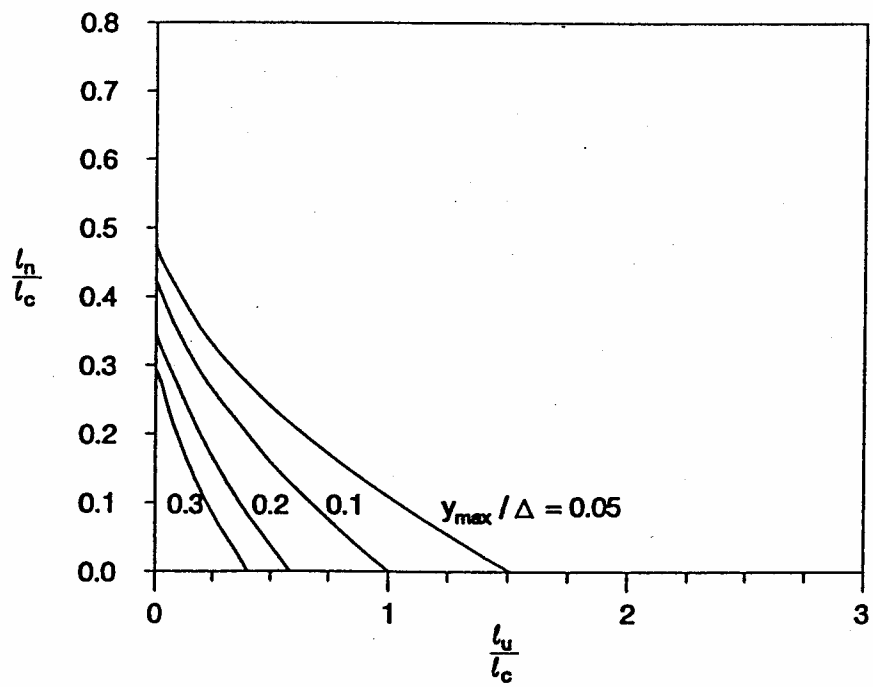

(b) Displacement for a pinned-head pile embedded in a uniform soil

Figure 8.86. Horizontal displacement effects of a pile on the pile length for vertical, skin-frictional resistance

Table 8.1. Load combinations (AASHTO Specifications, 1996)

Col. No.		1	2	3	3A	4	5	6	7	8	9	10	11	12	13
Group (N)		γ	β-Factors												
			D	$(L+I)_n$	$(L+I)_p$	CF	E	B	SF	W	WL	LF	R+S+T	EQ	ICE
Load Factor Design	I	1.3	1	1.67	0	1	1.3	1	1	0	0	0	0	0	0
	IA	1.3	1	2.2	0	0	0	0	0	0	0	0	0	0	0
	IB	1.3	1	0	1	1	1.3	1	1	0	0	0	0	0	0
	II	1.3	1	0	0	0	1.3	1	1	1	0	0	0	0	0
	III	1.3	1	1	0	1	1.3	1	1	0.3	1	1	0	0	0
	IV	1.3	1	1	0	1	1.3	1	1	0	0	0	1	0	0
	V	1.25	1	0	0	0	1.3	1	1	1	0	0	1	0	0
	VI	1.25	1	1	0	1	1.3	1	1	0.3	1	1	1	0	0
	VII	1.3	1	0	0	0	1.3	1	1	0	0	0	0	1	0
	VIII	1.3	1	1	0	1	1.3	1	1	0	0	0	0	0	1
	IX	1.2	1	0	0	0	1.3	1	1	1	0	0	0	0	1
	X	1.3	1	1.67	0	0	1.3	0	0	0	0	0	0	0	0

Table 8.2. Average bridge temperature based on air temperatures

Bridge	Coldest Day			Hottest Day		
	$T_{min\ air}$ (°F)	$T_{min\ ave}$ (°F)		$T_{max\ air}$ (°F)	$T_{max\ ave}$ (°F)	
		Eq. 4.13	Eq. 8.5		Eq. 4.13	Eq. 8.6
Guthrie County	-25	-12	-16	93	101	100
Story County	-16	-11	-7	96	104	103

Table 8.3. Experimentally-measured and recommended, average, bridge, temperatures

PC Girder Bridges		Average Bridge Temperatures (°F)		
		Minimum	Maximum	Range
Experimentally Measured	Guthrie County Bridge	-12	101	113
	Story County Bridge	-11	104	115
	Boone River Bridge (Girton, et al. 1989)	-15	100	115
Recommend (Des Moines, Iowa area)	CTL (Oesterle, et al. 1999)	0	100	100
	AASHTO – LFRD Specification (1998) (cold climate, has at least 14 days/yr below 32°F)	0	80	80
	ISU recommendation	-6	109	115

Table 8.4. Average design temperatures for concrete-girder bridges in Iowa (Roeder, 2003)

Cities in the State of Iowa	Minimum average bridge temperature (°F)	Maximum average bridge temperature (°F)
Burlington	-4	109
Cedar Rapids	-8	109
Des Moines	-6	109
Dubuque	-9	108
Mason City	-13	109
Ottumwa	-4	109
Sioux City	-9	111
Waterloo	-9	109

Table 8.5. Volume proportion for typical concrete mixes (Ng,1999)

Concrete Mix	Cement Paste	Fine Aggregate	Coarse Aggregate
Iowa DOT C4	0.337	0.331	0.332
Iowa DOT D57	0.372	0.314	0.314
Iowa DOT D57-6	0.372	0.377	0.251
Raider Precast Concrete	0.343	0.329	0.328
Iowa Precast Concrete	n.a.	n.a.	n.a.

Table 8.6. Specified alpha coefficients for various types of aggregates

Aggregate Type	Alpha Coefficient (10^6 in./in./°F)		
	ACI (1998)	AASHTO (1989)	PCA (1988)
Basalt	3.6	5.0	4.8
Chert	6.6	n.a.	n.a.
Dolerite	3.8	5.3	n.a.
Granite	3.8	5.3	5.3
Gravel	n.a.	6.9	6.0
Limestone	3.1	4.0	3.8
Marble	4.6	2.4 to 4.1	n.a.
Quartz	6.2	6.4	6.6
Quartzite	5.7	7.1	n.a.
Sandstone	5.2	6.5	6.5
Siliceous	4.6	n.a.	n.a.

Table 8.7. Experimental and predicted alpha coefficients for concrete-core specimens at 100%-dry condition (Ng, 1999)

Concrete	Alpha Coefficients (10^6 in./in./°F)			
	Average Experimental	Predicted Value Using Eq. 8.8		
		ACI (1998)	AASHTO (1989)	PCA (1988)
Guthrie County Bridge Deck	5.9	n.a.[a]	5.9	5.7
Story County Bridge Deck	4.8	4.8	5.1	5.1
Raider Precast Girder	4.2	4.8	5.1	5.1
Iowa Precast Girder	4.3	4.7 - 5.0[b]	5.1 – 5.2[b]	5.1 – 5.3[b]

[a]ACI does not provide an alpha-coefficient for gravel coarse aggregate.
[b]Predicted value based on concrete-mix design, C4, D57, and D57-6 (see Table 8.5).

Table 8.8. Predicted alpha coefficients

Concrete	Alpha Coefficients (10^6 in./in./°F)	
	Ng[a] (1999)	Eq. 8.9
Guthrie County Bridge Deck	6.4	6.6
Story County Bridge Deck	5.3	5.9
Guthrie and Story County Bridge Girders[a]	4.7	5.8
Effective concrete alpha-coefficient (Guthrie)	5.4	6.1
Effective concrete alpha-coefficient (Story)	5.0	5.8

[a]Raider Precast Concrete mix proportions were used, since the mix proportions were not available for these girders.

Table 8.9. Experimental and theoretical, longitudinal displacements

Parameters		Experimental Re-Expansion	Theoretical Re-Expansion	
			With Experimental ΔT and α_e	With Theoretical ΔT and α_c by Eq. 8.9
Guthrie County Bridge	Temperature range (°F)	113	113	115
	α_e-coefficient by Eq. 8.10 (10^6in./in./°F)	5.4	5.4	6.1
	North abutment displacement (in.)	1.20	1.17	1.35
	South abutment displacement (in.)	0.61	1.17	1.35
	Change in bridge length (in.)	1.81	2.34	2.70
Story County Bridge	Temperature range (°F)	115	114	115
	α_e-coefficient by Eq. 8.10 (10^6 in./in./°F)	5.0	5.0	5.8
	East abutment displacement (in.)	0.44	0.68	0.81
	West abutment displacement (in.)	0.54	0.68	0.81
	Change in bridge length (in.)	0.98	1.36	1.62

Table 8.10. Parameters for transverse displacements

Parameters		Base Value	Lower Bound	Upper Bound
Bridge Geometry	W (ft)	30	24	34
	L (ft)	300	100	500
	$h_{abut} = h_2$ (in.)	120	96	144
	h_1 (in.)	72	48	96
	$\ell_{w1} = \ell_{w2}$ (in.)	100	72	144
Pile Properties	N_{pa}	10	8	12
	$N_{p1} = N_{p2}$	0	0	1
	L_e (ft)	17	12	21
	Orientation	Type-C	Type-C	Type-C
Soil Properties	γ (pcf)	140	100	140
	ϕ (deg.)	37	30	44
	δ (deg.)	24	22	26

Table 8.11. Summary of parameter studies

Parameters	η	$0° \leq \theta \leq \eta$		$\eta \leq \theta \leq 60°$	
		Relationship	Influence	Relationship	Influence
Bridge length	60°	positive	significant	positive	significant
Bridge width	60°	positive	significant	positive	significant
Abutment backwall height	40°	positive	moderate	insignificant	negligible
Abutment wingwall height	40°	negative	minor	negative	moderate
Common sidewall and wingwall length	60°	negative	significant	negative	significant
Number of abutment backwall piles	60°	insignificant	negligible	insignificant	negligible
Number of abutment wingwall piles	60°	insignificant	negligible	insignificant	negligible
Pile effective length	50°	negative	significant	insignificant	negligible
Soil unit weight	35°	insignificant	negligible	positive	minor
Soil internal-frictional angle	40°	insignificant	negligible	negative	minor
Soil-abutment surface frictional angle	50°	negative	significant	negative	minor

Table 8.12. Relative geometric conditions at three cross sections of an abutment

Loading			Displacements									Rotations								
Type	Component direction	Geo-metry	X1	Y1	Z1	X1.5	Y1.5	Z1.5	X2	Y2	Z2	θ_{X1}	θ_{Y1}	θ_{Z1}	$\theta_{X1.5}$	$\theta_{Y1.5}$	$\theta_{Z1.5}$	θ_{X2}	θ_{Y2}	θ_{Z2}
$W_{soil\text{-}X}$	$+ F_X$	Sym.	0			0			0				0			0			0	
$W_{soil\text{-}X}$	$- M_Z$	Sym.												0			0			0
$W_{soil\text{-}friction\text{-}Z}$	$- F_Z$	Asym.			0			0			0									
$W_{soil\text{-}friction\text{-}Z}$	$- M_X$	n.a.		0			0			0		0			0			0		
$W_{soil\text{-}friction\text{-}Z}$	$+ M_Y$	n.a.	0			0			0				0			0			0	
$W_{abut\text{-}Y}$	$- F_Y$	Sym.		0			0			0		0			0			0		
$P_{pile\text{-}Y}$	$+ F_Y$	Sym.		0			0			0		0			0			0		
$V_{pile\text{-}X}$	$+ F_X$	Sym.	0			0			0				0			0			0	
$V_{pile\text{-}X}$	$- M_Z$	Sym.												0			0			0
$M_{pile\text{-}Z}$	$- M_Z$	Sym.												0			0			0
$V_{pile\text{-}Z}$	$- F_Z$	Asym.			0			0			0									
$V_{pile\text{-}Z}$	$- M_X$	Asym.		0			0			0		0			0			0		
$M_{pile\text{-}X}$	$- M_X$	Asym.		0			0			0		0			0			0		
$M_{pile\text{-}Y}$	$- M_Y$	Asym.	0			0			0				0			0			0	

Table 8.13. Zero-magnitude internal forces for XY-planes of symmetry and asymmetry

Load Type	Zero-Magnitude Internal Forces for Geometrically-Symmetric Conditions	Zero-Magnitude Internal Forces for Geometrically-Asymmetric Conditions
$W_{soil\text{-}X}$	V_{X1}, M_{Z1}, $V_{X1'}$, and $M_{Z1'}$ V_{Yi}, P_{Zi}, and M_{Xi}	n.a.
$W_{soil\text{-}friction\text{-}Z}$	n.a.	P_{Z1}, $P_{Z1'}$, M_{Xi}, and M_{Yi} M_{Zi}
$W_{abut\text{-}Y}$	V_{Y1} and $V_{Y1'}$ V_{Xi}, P_{Zi}, M_{Yi}, and M_{Zi}	n.a.
$P_{pile\text{-}Y}$	V_{Y1} and $V_{Y1'}$ V_{Xi}, P_{Zi}, M_{Yi}, and M_{Zi}	n.a.
$V_{pile\text{-}X}$	V_{X1}, $V_{X1'}$; M_{Z1}, and $M_{Z1'}$ V_{Yi}, P_{Zi}, and M_{Xi}	n.a.
$M_{pile\text{-}Z}$	M_{Z1} and $M_{Z1'}$ V_{Xi}, V_{Yi}, P_{Zi}, M_{Xi}, and M_{Yi}	n.a.
$V_{pile\text{-}Z}$	n.a.	P_{Z1}, $P_{Z1'}$, M_{X1}, and $M_{X1'}$ V_{Xi}, M_{Yi}, and M_{Zi}
$M_{pile\text{-}X}$	n.a.	M_{X1} and $M_{X1'}$ V_{Xi}, P_{Zi}, M_{Yi}, and M_{Zi}
$M_{pile\text{-}Y}$	n.a.	M_{Y1} and $M_{Y1'}$ V_{Xi}, P_{Zi}, M_{Xi}, and M_{Zi}

Table 8.14. Internal-force coefficients at three cross sections for an abutment

Loading	X-Axis-Shear Forces			Y-Axis-Shear Forces			Axial Forces		
Type	V_{X1}	$V_{X1.5}$	V_{X2}	V_{Y1}	$V_{Y1.5}$	V_{Y2}	P_{Z1}	$P_{Z1.5}$	P_{Z2}
$W_{soil\text{-}X}$	0	-B/4	-B/2, + B/2	0	0	0	0	0	0
$W_{soil\text{-}friction\text{-}Z}$	+ e_{sX}	+ e_{sX}	+ e_{sX}	- e_{sY}	- e_{sY}	- e_{sY}	0	+ B/4	+ B/2, - B/2
$W_{abut\text{-}Y}$	0	0	0	0	- B/4	- B/2, + B/2	0	0	0
$P_{pile\text{-}Y}$	0	0	0	0	0, + 1	+ 1, – 1	0	0	0
$V_{pile\text{-}X}$	0	0, - 1	- 1, + 1	0	0	0	0	0	0
$M_{pile\text{-}Z}$	0	0	0	0	0	0	0	0	0
$V_{pile\text{-}Z}$	0	0	0	- $9e_{pY}/(4B)$	- $9e_{pY}/(4B)$	- $9e_{pY}/(4B)$	0	0, + 1	+ 1, - 1
$M_{pile\text{-}X}$	0	0	0	- 9/(4B)	- 9/(4B)	- 9/(4B)	0	0	0
$M_{pile\text{-}Y}$	+ 9/(4B)	+ 9/(4B)	+ 9/(4B)	0	0	0	0	0	0
Loading	X-Axis-Bending Moments			Y-Axis-Bending Moments			Torsional Moments		
Type	M_{X1}	$M_{X1.5}$	M_{X2}	M_{Y1}	$M_{Y1.5}$	M_{Y2}	M_{Z1}	$M_{Z1.5}$	M_{Z2}
$W_{soil\text{-}X}$	0	0	0	+ $B^2/24$	+ $B^2/96$	- $B^2/12$	0	+ $Be_{sY}/4$	+ $Be_{sY}/2$, - $Be_{sY}/2$
$W_{soil\text{-}friction\text{-}Z}$	0	0	0	0	0	0	0	0	0
$W_{abut\text{-}Y}$	+ $B^2/24$	+ $B^2/96$	- $B^2/12$	0	0	0	0	0	0
$P_{pile\text{-}Y}$	- B/16	- B/16	+ 3B/16	0	0	0	0	0	0
$V_{pile\text{-}X}$	0	0	0	+ B/16	+ B/16	- 3B/16	0	0, + e_{pY}	+ e_{pY}, - e_{pY}
$M_{pile\text{-}Z}$	0	0	0	0	0	0	0	0, + 1	+1, - 1
$V_{pile\text{-}Z}$	0	-$9e_{pY}/16$, + $7e_{pY}/16$	-$e_{pY}/8$, + $e_{pY}/8$	0	0	0	0	0	0
$M_{pile\text{-}X}$	0	- 9/16, + 7/16	- 1/8, + 1/8	0	0	0	0	0	0
$M_{pile\text{-}Y}$	0	0	0	0	- 9/16, + 7/16	- 1/8, + 1/8	0	0	0

Table 8.15. Effective girder-reaction coefficients at the center of gravity of an abutment

Load type	F_X[a]	F_Y[b]	F_Z[c]	M_X[d]	M_Y[e]	M_Z[f]
$W_{soil\text{-}X}$	- B	0	0	0	0	+ (B)(e_{sy})
$W_{soil\text{-}friction\text{-}X}$	0	0	+ B	0	0	0
$W_{abutl\text{-}Y}$	0	+ B	0	0	0	0
$P_{pile\text{-}Y}$	0	- 2	0	0	0	0
$V_{pilel\text{-}X}$	+ 2	0	0	0	0	+ 2e_{py}
$M_{pile\text{-}Z}$	0	0	0	0	0	+ 2
$V_{pile\text{-}Z}$	0	0	+ 2	- e_{py}/4	0	0
$M_{pile\text{-}X}$	0	0	0	- 1/4	0	0
$M_{pile\text{-}Y}$	0	0	0	0	- 1/4	0

[a] Force vector is directed along the positive X-axis direction of the abutment.
[b] Force vector is directed along the positive Y-axis direction of the abutment.
[c] Force vector is directed along the positive Z-axis direction of the abutment.
[d] Moment vector is directed along the positive X-axis direction of the abutment.
[e] Moment vector is directed along the positive Y-axis direction of the abutment.
[f] Moment vector is directed along the positive Z-axis direction of the abutment.

9. DESIGN EXAMPLES

This chapter presents examples for part of the integral abutment and pile design process that was described in Chapter 8. The geometrical conditions and material properties for the Guthrie County Bridge were chosen for the parameters in the design examples that involve the application of the load combination associated with thermal loading from AASHTO Standard Specification (1996). A complete design for integral abutments and their piles should check all of the appropriate load cases.

The Guthrie County Bridge, which is located just south of the Town of Panora, Iowa on Route P28 where the highway crosses the Middle Raccoon River, is a three-span-continuous, approximately 318-ft long by 33-ft wide, PC-girder, integral-abutment bridge with a right-side-ahead, 30-deg., skew angle. A plan view of the bridge; a plan view of the south abutment; a vertical cross section through the south abutment; and the east elevation of the south abutment for this bridge, are shown in Figs. 9.1, 9.2, 9.3, and 9.4, respectively. A U-shaped, integral abutment was constructed at each end of the bridge, with a single row of ten, HP10X42, steel piles, which are located under the reinforced-concrete (RC) backwall and an HP10X42 pile, which is located under each sidewall. The piles under the RC backwall are oriented with their webs parallel to the abutment face while, the sidewall piles are oriented with the webs perpendicular to the longitudinal axis of the bridge. The piles were driven to a depth of at least 45 ft and into the shale bedrock at the south abutment and to a depth of at least 40 ft and into the shale bedrock at the north abutment. Figure 9.5 shows the soil profile down to a depth of about 40 ft at the south abutment. Pre-bored holes that were filled with bentonite slurry

were specified for the abutment piles. Additional descriptive information about the Guthrie County Bridge was presented in Chapter 3.

9.1. Average bridge temperature

A discussion regarding average bridge temperatures was presented in Section 8.2.1. In this section of Chapter 9 an example are presented to illustrate the calculation of the average bridge temperature for the Guthrie County Bridge.

Example 9.1 _____

Determine the minimum and maximum, average, bridge temperatures and the corresponding average, bridge-temperature range for the Guthrie County Bridge.

Solution:

Choose the appropriate, maximum and minimum, average, bridge temperatures from Table 8.4. The temperatures that are listed in this table are based on Roeder's (2003) research. The Guthrie County Bridge is located about one mile south of Panora, Iowa and about 45 miles west of Des Moines, Iowa. Since the bridge is relatively close to Des Moines, Iowa, use the minimum and maximum, average, bridge temperatures for that city. Then, from Table 8.4, $T_{min\ ave}$ = -6 °F and $T_{max\ avg}$ = 109 °F and, the average temperature range for the bridge is evaluated by Eq. 8.7 as

$$\Delta T_{average} = 109\ °F - (-6\ °F) = 115\ °F \tag{9.1}$$

9.2. Alpha coefficient for concrete

There are two approaches that can be applied to compute a coefficient of thermal expansion and contraction (α-coefficient) for concrete, depending on whether or not an

experimental, 100%-dry-concrete, α-coefficient is known. If an experimental, 100%-dry-concrete, α-coefficient is known, the concrete α-coefficient for design can be computed by multiplying the experimental α-coefficient by the α-coefficient ratio given in Table A.5. If an experimental, 100%-dry-concrete, α-coefficient is not known, the concrete α-coefficient for design can be computed using the revised, Emanuel and Hulsey's (1977) expression (Eq. 8.9) that accounts for a 45%-moisture-saturation condition and an outside, temperature-exposure condition.

Further discussion regarding the coefficient of thermal expansion and contraction for concrete was presented in Section 8.3. In this section of Chapter 9, examples are presented to illustrate the calculation of the coefficient to thermal expansion and contraction for the bridge deck, bridge girders, and bridge superstructure of the Guthrie County Bridge.

9.2.1. Bridge deck

Example 9.2 _____

Calculate the α-coefficient for the concrete deck of the Guthrie County Bridge, if an experimental, 100%-dry-concrete, α-coefficient is known.

Solution:

From Table 8.7, the average, experimental, 100%-dry-concrete α-coefficient for the bridge deck of the Guthrie County Bridge is 5.9×10^{-6} in./in./°F. From Table A.5, the α-coefficient ratio for the Iowa DOT, C4 mix is equal to 1.10. Then, the α-coefficient for the concrete in the bridge deck is calculated using Eq. A.2 as

$$\alpha_c = 1.1\ \alpha_{dry} = (1.10)(5.9 \times 10^{-6}\ \text{in./in./°F}) = 6.5 \times 10^{-6}\ \text{in./in./°F}. \qquad (9.2)$$

Example 9.3

Calculate the α-coefficient for the concrete deck of the Guthrie County Bridge, if an experimental, 100%-dry-concrete, α-coefficient is not known.

Solution:

The concrete for the bridge deck of the Guthrie County Bridge is an Iowa DOT, C4-mix design with sandstone, fine aggregate and a gravel, coarse aggregate. From Table 8.5, the Iowa DOT, C4-mix-design, proportions by volume for the cement paste, fine aggregate, and coarse aggregate are β_p = 0.337, β_{FA} = 0.331, and β_{CA} = 0.332, respectively. The α-coefficient, α_s, for a saturated and hardened, neat-cement paste is equal to 6.0 x 10^{-6} in./in./°F. From Table 8.6, the maximum of the α-coefficients that are specified by either ACI (1998), AASHTO (1989), or PCA (1988) for sandstone fine aggregate and gravel coarse aggregate in the C4-mix are α_{FA} = 6.5 x 10^{-6} in./in./°F and α_{CA} = 6.9 x 10^{-6} in./in./°F, respectively. The α-coefficient of the concrete in the bridge deck is calculated from Eq. 8.9 as:

$$\alpha_c = 0.86\left(1.58\beta_P\alpha_S + \beta_{FA}\alpha_{FA} + \beta_{CA}\alpha_{CA}\right)$$

$$= 0.86\ [(1.58)(0.337)(6.0 \times 10^{-6}) + (0.331)(6.5 \times 10^{-6}) + (0.332)(6.9 \times 10^{-6})]$$

$$= 6.6 \times 10^{-6}\ \text{in./in./°F} \qquad (9.3)$$

The α-coefficients for the concrete in the deck of the Guthrie County Bridge that were computed by both methods (Example 2 and Example 3) are essentially the same.

9.2.2. Bridge girders

Example 9.4

Establish an approximate value for the α-coefficient of the PC girders in the Guthrie County Bridge. Since the specific the concrete-mix proportions by volume for the PC girders in the Guthrie County Bridge are not available, use the concrete-mix proportion for the girders from Raider Precast Concrete that were core drilled to obtain concrete specimens. These girders, which had sandstone fine aggregate and limestone coarse aggregate, are assumed to be representative of those materials in the concrete for the PC girders in the Guthrie County Bridge.

Solution:

From Table 8.5, the Raider Precast Concrete, mix-design proportions by volume are β_P = 0.343, β_{FA} = 0.329, and β_{CA} = 0.328. After selecting the α-coefficients for the sandstone and limestone aggregates from Table 8.6, the maximum α-coefficient of the concrete in the PC girders is computed using Eq. 8.9 as:

$$\alpha_c = 0.86(1.58\beta_P\alpha_S + \beta_{FA}\alpha_{FA} + \beta_{CA}\alpha_{CA})$$

$$= 0.86\ [(1.58)(0.343)(6.0 \times 10^{-6}) + (0.329)(6.5 \times 10^{-6}) + (0.328)(4.0 \times 10^{-6})]$$

$$= 5.8 \times 10^{-6}\ \text{in./in./°F.} \qquad (9.4)$$

9.2.3. Bridge superstructure

The PC-girder haunch and slab-thickness detail on Sheet 14 of 28 of the design drawings (Iowa DOT File No. 54398) for the Guthrie County Bridge specify a minimum thickness of 7.5 in. for the bridge deck within the center, one-third length of each span and a bridge-deck width of 33 ft – 2 in. Because of a positive camber for the PC

girders, the predicted slab thickness at the abutments and piers was 9.5 and 9.75 in., respectively. An effective α-coefficient for a bridge superstructure, which is expressed by Eq. 8.10, accounts for the differences in the axial rigidities and α-coefficients of the concrete elements that are in the superstructure.

Example 9.5

Determine the effective α-coefficient for the superstructure of the Guthrie County Bridge. Use the α-coefficients for the bridge deck and girders that were calculated in Examples 3 and 4. The concrete-compressive strengths of the girders and deck are 6000 and 3500 psi, respectively.

Solution:

Five, Iowa DOT, LXD105 girders support the deck for the Guthrie County Bridge. Each girder has a cross-sectional area that is equal to 638.75 in.^{2} The axial rigidities (E_gA_g) and (E_dA_d) for all five girders and the deck, respectively, are:

$$E_gA_g = 57\sqrt{f_c'}A_g = 57\sqrt{6000}\left[(5)(638.75)\right] = 1.41\text{x}10^7 \text{ kips} \tag{9.5}$$

$$E_dA_d = 57\sqrt{f_c'}A_d = 57\sqrt{3000}\left[(398)(7.5)\right] = 1.01\text{x}10^7 \text{ kips} \tag{9.6}$$

Substituting the α-coefficients that were calculated by Eq. 8.9 for Examples 3 and 4 and the EA-values for the five, PC girders from Eq. 9.5 and RC deck from Eq. 9.6 into Eq. 8.10, the effective α-coefficient for the Guthrie County Bridge is evaluated as

$$\alpha_e = \frac{(\alpha_g E_g A_g) + (\alpha_d E_d A_d)}{(E_g A_g + E_d A_d)} = \left[\frac{(5.8\text{x}10^{-6})(1.41\text{x}10^7) + (6.6\text{x}10^{-6})(1.01\text{x}10^7)}{(1.41\text{x}10^7) + (1.01\text{x}10^7)}\right]$$

$$= 6.1 \text{ x } 10^{-6} \text{ in./in./°F.} \tag{9.7}$$

9.3. Equivalent-cantilever length

As discussed in Section 8.5, equivalent-cantilever lengths are used to model three distinct behaviors of an integral-abutment pile in soil. These lengths are functions of the horizontal stiffness of the soil around the pile, the length of the pile that is below the depth of a pre-bored hole, the depth of the pre-bored hole, and the flexural rigidity of the pile with respect to the plane of curvature. The example presented in this section of Chapter 9 illustrates the evaluation of the effective-cantilever length for the horizontal-stiffness equivalency. A similar approach can be used to establish the effective-cantilever lengths of an abutment pile for the elastic-buckling and bending-moment equivalencies.

Example 9.6

Calculate the effective-cantilever length for the horizontal-stiffness equivalency that is associated with y-axis (weak-axis) bending of the HP10X42, abutment piles for the Guthrie County Bridge. The piles have an 8-ft deep, pre-bored hole. Figure 9.5 shows the horizontal stiffness of the soil at the south abutment. This stiffness profile was developed from Tables 5.5 and 5.6, as described in Section 5.2. An expanded view of the upper 20 feet of the soil-stiffness profile is shown in Fig. 9.6. Assume that the horizontal stiffness of the soil at the north abutment is the same as that at the south abutment.

Solution:

The calculation of the effective, horizontal stiffness, k_e, of the layered soil follows the procedure that was discussed in Section 8.5.

Step 1: Assume an initial value of the horizontal stiffness, k_e, for the layered soil that is equal to 300 ksf.

Step 2: Calculate an active length, ℓ_o, from the bottom of the pre-bored hole for a pile in bending by applying Eq. 8.26 as:

$$\ell_o = 2\sqrt[4]{\frac{EI_y}{k_e}} = 2\sqrt[4]{\frac{(29{,}000)(71.7)}{(300)(12)^2}} = 5.27 \text{ ft} \qquad (9.8)$$

Step 3: Calculate the second moment, I_k, of each layer of soil that is above the depth $z = \ell_o$ about the line, A-A, at the depth of ℓ_o shown in Figs. 8.7 and 9.5. The dimensional parameters for Fig. 9.5 are:

d_1 = 3.77 ft (the depth of the first soil layer),

d_2 = 0.50 ft (the depth of the second soil layer),

$d_3 = (\ell_o - 3.77 - 0.50) = (5.27 - 3.77 - 0.50) = 1.00$ ft

(the depth of the third soil layer within the length ℓ_o),

$a_1 = (\ell_o - d_1) = (5.27 - 3.77) = 1.50$ ft,

$a_2 = (\ell_o - d_1 - d_2) = (5.27 - 3.77 - 0.50) = 1.00$ ft, and

$$c_3 = \left[\frac{(\ell_o - d_1 - d_2)}{2}\right] = 0.50 \text{ ft.}$$

With these dimensional parameters, calculate the second-moment of the soil, horizontal stiffness for the three, soil layers using Figs. 8.7 and 9.5 and Eq. 8.27.

$$I_k = \int_o^{\ell_o} k_h(z)(\ell_o - z)^2 dz \qquad [8.27]$$

For the first soil layer,

$$I_{k1} = 309\left[\frac{3.77^3}{36} + \frac{3.77}{2}\left(1.50 + \frac{2(3.77)}{3}\right)^2\right] + 376\left[\frac{3.77^3}{36} + \frac{3.77}{2}\left(1.50 + \frac{3.77}{3}\right)^2\right]$$

$$= 15{,}787 \text{ k-ft} \tag{9.9}$$

For the second soil layer,

$$I_{k2} = 376\left[\frac{0.50^3}{36} + \frac{0.50}{2}\left(1.00 + \frac{2(0.50)}{3}\right)^2\right] + 329.5\left[\frac{0.50^3}{36} + \frac{0.50}{2}\left(1.00 + \frac{0.50}{3}\right)^2\right]$$

$$= 282 \text{ k-ft} \tag{9.10}$$

For the third soil layer,

$$I_{k3} = \left\{329.5\left[\frac{1.0^3}{12} + 1.0\left(0.5^2\right)\right]\right\} = 109 \text{ k-ft} \tag{9.11}$$

The total for the second moment of the soil, horizontal stiffness, I_k, is calculated as

$$I_k = (I_{k1} + I_{k2} + I_{k3}) = 16{,}179 \text{ k-ft.} \tag{9.12}$$

Step 4: Use Eq. 8.28 to determine a new estimate for the horizontal stiffness, k_e, of the layered soil as

$$k_e = \left(\frac{3I_k}{\ell_o^{\,3}}\right) = \left[\frac{3(16{,}179)}{(5.27)^3}\right] = 332 \text{ ksf} \tag{9.13}$$

Step 5: Return to Step 2 and repeat Steps 2, 3, and 4 until the stiffness converges to k_e = 331 ksf.

From Eqs. 8.25 and 8.24 with the y-axis, flexural rigidity, EI_y, equal to 14,440 k-ft^2, the relative-stiffness factor, R, for a pile in soil and the critical pile length, ℓ_c, respectively, are given by

$$R = \sqrt[4]{\frac{EI_y}{k_e}} = \sqrt[4]{\frac{14{,}400}{331}} = 2.57 \text{ ft} \tag{9.14}$$

$$\ell_c = (4R) = 4(2.57) = 10.28 \text{ ft} \tag{9.15}$$

For an 8-ft deep, pre-bored hole that is filled with bentonite slurry, the length ℓ_u is equal to 8 ft. Then, the ratio of the lengths ℓ_u and ℓ_c is equal to

$$\frac{\ell_u}{\ell_c} = \left(\frac{8}{10.28}\right) = 0.778 \tag{9.16}$$

The connection between a pile and the abutment for the Guthrie County Bridge is modeled as a rigid joint. Since the flexural stiffness of a composite bridge girder is significantly greater than that for a pile, the top of the pile is essentially fixed against rotation. To calculate the equivalent-cantilever length L_{ehy} for a pile that is based on horizontal stiffness of the layered soil, apply Fig. 8.8a to obtain

$$\frac{\ell_{ehy}}{\ell_c} = 0.38 \tag{9.17}$$

Substituting the critical length ℓ_c from Eq. 9.15 into Eq. 9.17 and solving Eq. 9.17 for the length ℓ_{ehy},

$$\ell_{ehy} = 0.38(10.28) = 3.90 \text{ ft} \tag{9.18}$$

Then, the equivalent-cantilever length L_{ehy} is calculated from Eq. 8.23 as

$$L_{ehy} = (\ell_{ehy} + \ell_u) = (3.90 + 8.00) = 11.90 \text{ ft} \tag{9.19}$$

For the Guthrie County Bridge, all of the equivalent-cantilever lengths L_{eh}, L_{em}, and L_{eb} that were discussed in Section 8.5 are listed in Table 9.1 for the x-axis and y-axis of the HP10X42 piles.

9.4. Abutment longitudinal displacements

A discussion regarding the longitudinal displacements for integral abutments was presented in Section 8.6.1. In this section of Chapter 9, an example is presented to illustrate the calculation of the longitudinal displacements of the abutments for the Guthrie County Bridge. Three temperature conditions are considered to evaluate the longitudinal displacements of the abutments that are associated with the initial expansion, initial contraction, and re-expansion of the bridge superstructure.

Example 9.7 _____

Compute the abutment displacements along the longitudinal direction of the 318-ft long, integral-abutment, Guthrie County Bridge for the initial expansion, initial contraction, and re-expansion of the superstructure, using the procedures discussed in Section 8.6. Assume that a 60 °F temperature occurred when the bridge became an integral structure during the construction of the bridge.

Solution:

Step 1: Assume the mean, construction temperature, $T_{construction}$ = 60 °F.

Step 2: As established in Section 9.1, $T_{min\ ave}$ = -6 °F and $T_{max\ ave}$ = 109 °F.

Step 3: The 318-ft long, three-span, Guthrie County Bridge has an expansion pier (south pier) and a fixed pier (north pier). If thermally-induced, longitudinal

displacements do not occur at the fixed pier, the fixed pier is the "point-of-fixity" for the superstructure. Experimental evidence for the Guthrie County Bridge indicated that the fixed pier did not noticeably affect the thermal, longitudinal movements of the integral abutments. The relative, longitudinal movement at the pier-to-girder joint and the pier flexibility did not significantly restrain the thermal expansion of the Guthrie County Bridge. The soil conditions behind the integral abutments have a more significant effect on the relative movement along the longitudinal direction of a bridge. For the Guthrie County Bridge, the abutment that is closest to the fixed pier had the largest thermal movement. Therefore, with regards to the longitudinal displacements of an integral abutment for the Guthrie County Bridge, this bridge can be assumed to behave as a symmetric bridge. Then, the length, ℓ, from the "point-of-fixity" to an integral abutment is equal to one-half of the total bridge length. Using Eq. 8.29, the length ℓ is computed as

$$\ell = \frac{1}{2}\,(318\ \text{ft})\left(\frac{12\ \text{in.}}{1\ \text{ft}}\right) = 1{,}908\ \text{in.} \tag{9.20}$$

Step 4: Compute the abutment displacement in the longitudinal direction of the bridge due to the initial, maximum expansion of the bridge using Eqs. 8.30, 8.31, and 8.32

$$\Delta T_{expand} = (T_{max\ ave} - T_{construction}) = (109 - 60) = 49\ °F \tag{9.21}$$

$$(\varepsilon_{th})_{expand} = \alpha_e(\Delta T_{expand}) = (6.1 \times 10^{-6})(49) = 299 \times 10^{-6}\ \text{in./in.} \tag{9.22}$$

$$d\ell_{expand} = \Gamma(\varepsilon_{th})_{expand}\,\ell = (1.60)(299 \times 10^{-6})(1908) = 0.91\ \text{in.} \tag{9.23}$$

Step 5: Use Eqs. 8.33 and 8.34 to compute the abutment displacement in the longitudinal direction of the bridge due to the maximum contraction of the bridge.

$$\Delta T_{contract} = (T_{min\ ave} - T_{construction}) = (-6\ -60) = -\ 66\ ^{\circ}F \tag{9.24}$$

$$(\varepsilon_{th})_{contract} = \alpha_e(\Delta T_{contract}) = (6.1 \times 10^{-6})(-\ 66) = -\ 403 \times 10^{-6}\ \text{in./in.} \tag{9.25}$$

The thermal contraction for the bridge is obtained from Eq. 8.36 as

$$d\ell_{contract} = \Gamma(\varepsilon_{th})_{contract}\,\ell = (1.35)(-\ 403 \times 10^{-6})(1908) = -\ 1.04\ \text{in.} \tag{9.26}$$

Following the discussion in Section 8.6, the combination of concrete creep and shrinkage will be approximated by a compressive strain of 500 micro-strain, so that the total, maximum, long-term contraction for the bridge is obtained from Eq. 8.36 as

$$d\ell_{contract} = (1.35)(-\ 403\ -\ 500)(10^{-6})(1908) = -\ 2.33\ \text{in.} \tag{9.27}$$

Step 6: Compute the abutment displacement in the longitudinal direction of the bridge due to the re-expansion of the bridge using Eqs. 8.37, 8.38, and 8.39.

$$\Delta T_{re\text{-}expand} = (T_{max\ ave} - T_{min\ ave}) = 109 - (-\ 6) = 115\ ^{\circ}F \tag{9.28}$$

$$(\varepsilon_{th})_{re\text{-}expand} = \alpha_e(\Delta T_{re\text{-}expand}) = (6.1 \times 10^{-6})(115) = 702 \times 10^{-6}\ \text{in./in.} \tag{9.29}$$

$$\Delta\ell_{re\text{-}expand} = \Gamma(\varepsilon_{th})_{re\text{-}expand}\,\ell = (1.20)(702 \times 10^{-6})(1908) = 1.61\ \text{in.} \tag{9.30}$$

Note that the change in the longitudinal displacement $\Delta\ell_{re\text{-}expand}$ is a displacement range, and this displacement is not an absolute displacement from the original, undisplaced position of the abutment (see Section 8.8.1 and Fig. 8.29).

9.5. Abutment transverse displacements

A discussion regarding the transverse displacements for integral abutments was presented in Section 8.6.2. In this section of Chapter 9, an example is presented to illustrate the calculation of the transverse displacements of the abutments for the Guthrie County Bridge.

Example 9.8 _____

Calculate the maximum transverse movement of the integral abutments for the Guthrie County Bridge.

Solution:

The Transmove software (see Appendix B) was used to compute the maximum, transverse displacement of an integral abutment. Input data for the software program include bridge length, L (318 ft); bridge width, W (34 ft); abutment height, h_{abut} (9.33 ft); height of soil on a wingwall, h_1 (about 8.5 ft); bridge-skew angle, θ (30 degrees); and pile-skew angle, θ_r, (30 degrees, see Figs. 8.14 and 8.32). The wingwalls for the Guthrie County Bridge are trapezoidal in shape. A rectangular wingwall with a height of 9.33 ft and a length, ℓ_{w1}, of 8.6 ft has approximately the same area. There are ten, HP10X42 piles under the abutment backwall, and there is one, HP10X42 pile under each sidewall. The cross-sectional properties of the pile are listed in the Transmove

interface that is shown in Fig. 9.7, and the pile-effective lengths are given in Table 9.1. For this bridge site, the soil density, γ; friction angle ϕ; and abutment/soil friction angle, γ are 140 pcf, 37 deg., and 22 deg., respectively. The effective, coefficient of thermal expansion and contraction, α_e, for the bridge superstructure was calculated in Eq. 9.7. As noted in Fig. 9.7, the upper-bound, transverse displacement, dt_{max}, for an abutment of the Guthrie County Bridge was computed as 0.030 in.

9.6. Abutment design

As discussed in Section 8.8 the elevation of the soil beneath an abutment affects the design requirements for the abutment. The pile cap for the abutment backwall should be designed to resist all dead loads, including the self weight of the pile cap and uncured concrete weight in the abutment backwall, girder-dead-load reactions, and slab and curb dead loads. The composite, backwall and backwall-pile cap should be designed for all dead loads and live loads, including impact, and for soil pressures that are induced by the thermal expansion and contraction of the bridge superstructure.

9.6.1. Backwall-pile-cap design

For the Guthrie County Bridge, the height, h_{abut}, and width, B_{abut}, of the abutment are 9.33 ft and 3.00 ft, respectively. Along the back of an abutment, a trapezoidal-shaped corbel, which varies in depth from 8 in. to 18 in. and has a 10-in. width, supports the approach slab to the bridge. The abutment piles are spaced at about 3.62 ft on center. The length B of a central portion of the abutment is 7.25 ft. This length is equal to two times the spacing of the abutment piles, as illustrated in Figs. 8.31 and 8.32. For this bridge, the Iowa DOT, LDX, PC girders are spaced at 7.00 ft on center or at about

8.03 ft along the length of the skewed, pile cap. The girders support a nominal, 8-in.-thick RC slab and have an end-span length of about 106 ft. The anticipated camber in the PC girders produced an average girder-haunch height and an average slab thickness of about 1.08 in. and 8.04 in., respectively. The girder reactions were computed using these dimensions. As suggested in Section 8.8, if the girder reactions occurred at alternate mid-spans between the abutment piles, the analysis of the abutment for internal forces would be simplified, due to symmetry and asymmetry conditions. Therefore, a 7.25-ft girder spacing rather than the actual 8.03-ft girder spacing along the length of the pile cap was used in the evaluation of the pile-cap design for an abutment backwall of the Guthrie County Bridge.

Example 9.9

For the Guthrie County Bridge, calculate the factored-level, dead loads that need to be resisted by a pile cap for an abutment backwall.

Solution:

The service-level, uniform, dead load of the pile cap and abutment backwall is calculated as

$$W_{abut-Y} = 0.150\left[(9.33)(3.0) + \left(\frac{8+18}{(2)(12)}\right)\left(\frac{10}{12}\right)\right] = 4.33\ \text{k/ft} \qquad (9.31)$$

For the design of the pile cap, only dead loads are present, therefore, the AASHTO Load Group IV should be applied where the load factor on the dead load is equal to 1.3. Then, the factored-level, uniform dead load, $W_{uabut-Y}$, of the pile cap and abutment backwall is equal to 5.63 k/ft. Assuming that the PC girders are simply supported at the pile cap and at the first pier during the construction of the bridge, the service-level,

girder, dead-load reaction, $V_{girder\text{-}Y}$, on the pile cap that includes the self-weight of the girder, deck, and girder haunch was calculated to be equal to 71.2 kips. Again applying the 1.3 load factor, the factored-level dead-load girder reaction, $V_{ugirder\text{-}Y}$, is equal to 92.5 kips. Using the free-body diagram in Fig. 8.41 and knowing that the vertical shear forces V_{uy1} and $V_{uy1'}$ on the planes of symmetry at Cross Sections 1 and 1', respectively, are equal to zero, the factored-level, axial load, $P_{upile\text{-}Y}$, in a abutment-backwall pile is equal to 66.7 kips.

Example 9.10

For the Guthrie County Bridge, calculate the factored-level, internal forces that occur at Cross Sections 1, 1.5 and 2 of a pile cap for an abutment backwall.

Solution:

Analysis Method 2 that was discussed in Section 8.8.2.2 and the internal-force coefficients that are given in Table 8.14 were applied to calculate the factored-level, internal forces for the backwall-pile cap. The non-zero, factored-level loads need to be resisted by the pile cap for an abutment backwall of the Guthrie County Bridge are the loads $W_{uabt\text{-}Y}$ and $P_{upile\text{-}Y}$, which were computed in Example 9.9 to be equal to 5.63 kips/ft and 66.7 kips, respectively. The resulting, internal forces at the Cross Sections 1, 1.5, and 2 for the backwall-pile cap are listed in Table 9.2.

Example 9.11

For the Guthrie County Bridge, compute the shear-force, bending-moment, and torsional-moment design strengths at the critical cross sections of a pile cap for an abutment backwall.

Solution:

Figure 9.8 shows a cross-sectional view of a backwall-pile cap and the steel-reinforcing bars that were used in the pile cap for the Guthrie County Bridge. The dimensions and bar sizes and locations that are shown in these figures were obtained from the Iowa DOT design drawings for this bridge. Each abutment pile is embedded 24 in. into the bottom of the pile cap. A #2 bar spiral with two, 7/8 C 0.69, spiral spacers was placed around each of the abutment piles within the pile cap. A total of 9 - #8 bars were used as longitudinal reinforcement for a pile cap. Four of these bars were equally spaced in each vertical face of the pile cap, and the remaining #8 bar was placed at the mid-width and in the top face of the pile cap just below the formed keyway. Two, sets of #5-bar, closed-looped stirrups with a 90°-corner bend were used around the longitudinal reinforcement. These stirrup pairs, which were vertically offset from each other, were spaced at 6.5-in. on center with the first pair of stirrups located at a distance of 12 in. from the center of an abutment pile. At the bottom of the pile cap, 2 - #6 bars, which were bent into a flared-channel shape, were used around each pile to reinforce the concrete in the bottom of the pile cap for resistance to the forces that a pile would induce at the bottom of the pile cap during expansion and contraction of the bridge superstructure.

The ACI Building Code (2002) was applied to establish the design strengths, ϕR_n, of a pile cap for the Y-axis-shear force, $\phi_v V_{nY}$; positive, X-axis-bending moment, $\phi_b M_{nX}^{+}$; negative, X-axis-bending moment, $\phi_b M_{nX}^{-}$; and torsional moment, $\phi_b T_n$. The pile cap is classified as a deep-flexural member for vertical loads, since the depth of the pile cap is large in comparison with the close spacing of the abutment piles. Therefore, the

horizontal spacing of the #5, closed-looped stirrups and the vertical spacing of the #8, longitudinal bars should satisfy the reinforcement-spacing requirements that are given in Article 11.8 of the ACI Code (2002). Even if the effective depth for the tension reinforcement in the pile cap is taken as the 37.8-in., which is the distance between the top of the pile cap and the center of the bottom layer of longitudinal reinforcement, the vertical spacing of the #8 bars should not exceed about 7.5 in. on center. Since an 11.5-in. vertical spacing was used for these bars, potential concrete cracking could occur between these longitudinal bars.

An upper bound can be established for the Y-axis, design-shear strength. If the vertical spacing of the #8 bars did not exceed the ACI requirement, the y-axis, design-shear strength, $\phi_v V_{nY}$, would be equal to about 197 kips, when a shear-resistance factor, Φ_v, that is equal to 0.75 was applied as specified in Article 9.3.2.3 of the ACI Code. This shear strength was evaluated using the 28-day, concrete-compressive strength, f_c', of 3,500 psi and a yield strength of the shear reinforcement, F_{ys}, of 60,000 psi that were listed on the design drawings for the Guthrie County Bridge. Since the vertical spacing of these bars exceeds the ACI requirement, the ISU researchers believe that the $\phi_v V_{nY}$-design-shear strength should be limited to the shear strength of a plain-concrete beam. When the ACI Eq. (22-9) in Article 22.5.4 and a shear-resistance factor, ϕ_v, which is equal to 0.55 from Article 9.3.5 of the ACI Code are applied for a plain-concrete cross section, a lower bound for the design-shear strength is equal to 62.5 kips. Table 9.3 lists a lower bound, ISU suggested, and upper bound, design-shear strengths for the abutment-pile cap when shear forces act in the Y-axis direction of the pile cap.

The X-axis-bending, design-moment strength for a reinforced-concrete cross section of the pile cap was computed by applying compatibility of the bending strains throughout the depth of the cross section. As specified by the ACI Code (2002), the maximum compressive strain, ε_c, at the extreme-compression fiber of the cross section was set equal to 0.003 in./in. and a linear distribution for the longitudinal strains were assumed to occur throughout the depth of the cross section. The location of the neutral axis for X-axis bending was established for static equilibrium of the internal longitudinal forces in the concrete and in the #8 bars. The concrete strength f_c' and the yield-strength, F_y, for the longitudinal reinforcement were set equal to 3,500 psi and 60,000 psi, respectively. The positive and negative, X-axis-bending, design-moment strengths, $\phi_b M_{nX}^+$ and $\phi_b M_{nX}^-$, respectively, were computed to be equal to 532 k-ft and 682 k-ft, respectively. However, to prevent the occurrence of a non-ductile, flexural failure that would occur for non-reinforced (plain-concrete) beam, the ACI Code (2002) requires that at least a minimum amount of tension reinforcement needs to be provided in the cross section, unless the moment strength, which is provided by the actual amount of tension steel in the beam, is greater than four-thirds of the required, factored-level bending moment, $\Phi_b M_n$. If the effective depth to the tension reinforcement is assumed to be equal to the distance from the extreme-compressive fiber of the cross section to the depth of the centroid for the two layers of #8 bars that are closest to the tension face of the cross section, the minimum amount of tension reinforcement that should be used in a cross section of the pile cap for positive and negative, X-axis-bending moment is equal to 3.84 in.^{2} and 4.10 in.^{2}, respectively. The pile cap contains 4 - #8 bars for the bottom two rows of steel, which have a total area equal to 3.16 in.^{2}, and 5 - #8 bars for

the top two rows of bars, which have a total area equal to 3.95 in.^{2}. Since these areas are less than the ACI minimum areas for tension steel, the X-axis-bending, design-moment strength for a plain-concrete cross section was computed using the ACI Eq. (22-2) in Article 22.5.1 with a resistance factor for bending, Φ_b, equal to 0.55, as specified in Article 9.5.3 of the ACI Code. The resulting lower-bound, moment strength was equal to 133 k-ft.

Since the moment strength associated with a plain-concrete cross section is very conservative, the ISU researchers recommend that the computed, X-axis-bending, design-moment strengths be set equal to three-fourths of the calculated values for the reinforced-concrete pile cap. The three-quarters factor will effectively account for the four-thirds, moment-strength exception given in the ACI Code. Then, the design-moment strengths $\phi_b M_{nX}^+$ and $\phi_b M_{nX}^-$ become 399 k-ft and 568 k-ft, respectively. The lower bound, ISU suggested, and upper bound for these design-moment strengths are listed in Table 9.3.

Even though the pile cap by itself is not subjected to torsional moments before an abutment becomes integral with the bridge superstructure, the design, torsional-moment strength was evaluated for the pile cap to establish a possible, lower-bound, torsional strength for an integral abutment. As long as the moment strength across the joint between the backwall-pile cap and the backwall is adequate, the torsional strength of an integral abutment should not be less that that strength for just the abutment-pile cap. Article 11.6.1 of the ACI Code (2002) specifies that if the factored-level, torsional moment, T_u, does not exceed one-quarter of the concrete-cracking, torsional-moment strength, T_{cr}, torsion can be neglected for the design of the concrete member. Then, a

lower-bound for the design-torsional-moment strength, $\phi_v T_{nZ}$, of an XY-plane cross section of a backwall-pile cap was computed to be equal to 50.4 k-ft.

As noted in Commentary Article R11.6.1 of the ACI Code, once the concrete cracks due to torsional strains, concrete does not resist any torsion. The closed-looped stirrups and the longitudinal bars that are distributed around the perimeter of the cross section are assumed to resist all the total, factored-level, torsional moment. An upper-bound for the design-torsional-moment strength, $\phi_v T_{nZ}$, for the backwall-pile cap was computed by applying ACI Eq. (11-21) in Article 11.6.3.6 and using the torsion-resistance factor, ϕ_v, equal to 0.75, as specified in Article 9.3.2.3 of the ACI Code. Since only one leg of a closed-looped tie that extends for the full height of a cross section is considered effective for resisting torsion, only a single leg for the pair of the closed-looped stirrups, which are spaced at 6.5 in. on center, is actually effective in resisting a torsional moment for a cross section of the pile cap. The torsional-moment strength for the pile cap was computed to be equal to 324 k-ft. This computed torsional strength accounts for satisfying the ACI Code requirements for the minimum amount of closed-looped ties to resist the combined effect of flexural shear and torsional shear (ACI Article 11.6.5.2), the minimum amount of longitudinal reinforcement for resisting torsion (ACI Article 11.6.5.3), for the maximum spacing of the closed-looped ties (ACI Article 11.6.6.1), and for the minimum diameter of the longitudinal bars (ACI Article 11.6.6.1). The computed torsional strength does not account for not meeting the ACI Code requirements for the maximum spacing of the longitudinal bars around the perimeter of the cross section for the pile cap (ACI Article 11.6.6.2) and for the

anchorage of the closed-looped ties (ACI Article 11.6.4.2, which states that a 135-deg. standard hook around a longitudinal bar is needed to properly anchor a tie bar).

The closed-looped ties that were used in the Guthrie County Bridge have a 90-deg. hook that is wrapped around a longitudinal bar. The spacing of the #8 longitudinal bars along the vertical faces of a pile cap satisfies the ACI Code spacing requirement, but the spacing of these bars along the top and bottom faces of the pile cap does not satisfy the ACI Code spacing requirement. Table 9.3 lists the lower bound, ISU suggested, and upper bound, torsional-moment-design strengths.

Example 9.12

For the Guthrie County Bridge, evaluate the bending-moment interaction relationship and the shear-force interaction relationship for the critical cross sections of the pile cap for an abutment backwall.

Solution:

The factored-level load effects, R_u, for the V_{uY}-shear force along its local Y-axis and for the M_{uX}-bending moment of the pile-cap cross section about its local X-axis are listed in Table 9.2; and the lower bound, ISU suggested, and upper-bound, design strengths, ϕR_n, for the Y-axis-shear force, $\phi_v V_{nY}$; positive, X-axis bending moment, $\phi_b M_{nX}^{+}$; negative, X-axis bending moment, $\phi_b M_{nX}^{-}$; and torsional moment, $\phi_v T_{nZ}$ are listed in Table 9.3. For a backwall-pile cap, the interaction relationships for biaxial bending (Eq. 8.177) and biaxial shear and torsional moment (Eq. 8.178) simplify to uni-axial bending and uni-axial shear, respectively. The ISU suggested values for the design strengths that are listed in Table 9.3 were used to evaluate the strength requirements at several critical sections along the length of the backwall-pile cap. The

direction of the curvature for the factored-level, bending moments and the corresponding bending-moment, design strength was established by the sign for the combined-loading, factored-level, bending moment that is shown in Table 9.2.

At Section 1:

$$\left(\frac{M_{uX}^{+}}{\varphi_b M_{nX}^{+}} + \frac{M_{uY}}{\varphi_b M_{nY}}\right) = \left(\frac{17.9}{339} + 0\right) = 0.053 < 1.0 \tag{9.32}$$

$$\left(\frac{V_{uX}}{\varphi_v V_{nX}} + \frac{V_{uY}}{\varphi_v V_{nY}} + \frac{T_{uZ}}{\varphi_v T_{nZ}}\right) = (0 + 0 + 0) = 0.0 < 1.0 \tag{9.33}$$

At Section 1.5:

$$\left(\frac{M_{uX}^{+}}{\varphi_b M_{nX}^{+}} + \frac{M_{uY}}{\varphi_b M_{nY}}\right) = \left(\frac{27.1}{339} + 0\right) = 0.080 < 1.0 \tag{9.34}$$

$$\left(\frac{V_{uX}}{\varphi_v V_{nX}} + \frac{V_{uY}}{\varphi_v V_{nY}} + \frac{T_{uZ}}{\varphi_v T_{nZ}}\right) = \left(0 + \frac{56.5}{62.5} + 0\right) = 0.904 < 1.0 \tag{9.35}$$

At Section 2:

$$\left(\frac{M_{uX}^{-}}{\varphi_b M_{nX}^{-}} + \frac{M_{uY}}{\varphi_b M_{nY}}\right) = \left(\frac{66.0}{568} + 0\right) = 0.116 < 1.0 \tag{9.36}$$

$$\left(\frac{V_{uX}}{\varphi_v V_{nX}} + \frac{V_{uY}}{\varphi_v V_{nY}} + \frac{T_{uZ}}{\varphi_v T_{nZ}}\right) = \left(0 + \frac{46.3}{62.5} + 0\right) = 0.741 < 1.0 \tag{9.37}$$

The backwall-pile cap satisfies the uniaxial-bending-moment requirements and the uniaxial-shear force requirements at Cross Sections 1, 1.5, and 2, as shown by Eqs. 9.32 thru 9.37.

9.6.2. Composite backwall and backwall-pile-cap design

For a general description of the integral abutments and PC girders for the Guthrie County Bridge, see Section 9.6.1.

Example 9.13

For the Guthrie County Bridge, calculate the factored-level loads that need to be resisted by a composite, abutment backwall and backwall-pile cap.

Solution:

For an integral-abutment design, the bridge expansion and re-expansion phases with passive-soil pressures will govern over the bridge-contraction phase. When the maximum, abutment displacement in the longitudinal direction of a bridge occurs, the passive-soil pressure coefficient, k_p, for the soil behind the abutment is approximated by applying Fig. 5.12. For a sand backfill behind the abutment, the maximum, passive-soil-pressure coefficient is equal to 4.0, and the soil weighs140 pcf. Following the rationale of Analysis Method 2 and applying Eq. 8.65, the service-level, passive-soil pressure at the base of the 9.33-ft-high abutment is computed as

$$w_{soil\text{-}X} = k_{pmax}\, \gamma\, h_{abut} = 4.0(140)(9.33)/1000 = 5.22 \text{ k/ft}^2 \qquad (9.38)$$

When the load factors γ and β_E are each set equal to 1.3 for the AASHTO Load Group IV, load combination that is represented by Eq. 8.4, the factored-level, passive-soil pressure, $w_{usoil\text{-}X}$, is equal to 8.83 k/ft^2. Applying Eq. 8.79 the resultant force for the factored-level, distributed, soil pressure along the back of the abutment is given by

$$W_{usoil\text{-}X} = (w_{usoil\text{-}X})(h_{abut})\ /2 = (8.83)(9.33)/2 = 41.2 \text{ k/ft} \qquad (9.39)$$

With a soil-to-abutment, surface-friction angle, γ, of 22 degrees, the frictional force behind the abutment, according to Eq. 8.78, is expressed as

$$W_{usoil\text{-}friction\text{-}Z} = (W_{usoil\text{-}X})(\tan \gamma) = (41.2) \tan (22^{o}) = 16.6 \text{ k/ft} \quad (9.40)$$

When a dead-load factor, γ, which is equal to 1.3 for the AASHTO Load Group IV, is applied to the service-level dead load of the composite, backwall and backwall-pile cap from Eq. 9.31, the factored-level, dead weight of the combined pile cap and backwall for an abutment, $W_{uabut\text{-}Y}$, at the Guthrie County Bridge is equal to 5.63 k/ft.

From the "abutments notes" on Sheets 6 and 7 of 28 of the design drawings for the Guthrie County Bridge, the vertical-load capacity for an abutment pile is specified to be at least 37 tons or 74.0 kips. Then, the minimum, factored-level, axial force in a pile for Analysis Method 2 is given by

$$P_{upile\text{-}Y} = 1.3(74.0) = 96.2 \text{ kips} \quad (9.41)$$

Following the discussion in Section 8.8.2.2, the maximum, factored-level, shear force and bending-moment that a pile can apply to the abutment are limited by the plastic-moment capacity of the piles. For an A36-steel (F_y = 36 ksi), HP10x42 pile, the plastic-moment capacities for x-axis and y-axis bending are computed as

$$M_{px} = Z_x F_y = (48.3)(36)/12 = 144.9 \text{ k-ft} \quad (9.42)$$

$$M_{py} = Z_y F_y = (21.8)(36)/12 = 65.4 \text{ k-ft} \quad (9.43)$$

For thermal expansion, the longitudinal and transverse displacements at the pile head were calculated as 0.91 in. and 0.030 in., respectively, as presented in Sections 9.4 and 9.5, respectively. Equations 8.248 and 8.249 were used to transform the pile

displacements from the ℓ-axis and t-axis directions to the x-axis and y-axis directions for the abutment-pile orientation at the Guthrie County Bridge.

$$\Delta_x = [(d\ell)\cos\theta_r - (dt)\sin\theta_r] = [(0.91)\cos(30^o) - (0.030)\sin(30^o)] = 0.773 \text{ in.} \qquad (9.44)$$

$$\Delta_y = [(d\ell)\sin\theta_r + (dt)\cos\theta_r] = [(0.91)\sin(30^o) + (0.030)\cos(30^o)] = 0.481 \text{ in.} \qquad (9.45)$$

The displacements, Δ_{px} and Δ_{py}, associated with the uni-axial, plastic moments M_{px} and M_{py} are calculated in Eqs. 9.106 and 9.107 as 1.30 in. and 1.25 in., respectively. A substitution of uni-axial plastic moment capacities and these four displacements into Eq. 8.59 and 8.60 and applying a load factor, γ, of 1.3, the reduced, plastic-moment capacities for x-axis and y-axis bending, respectively, are computed as

$$M_{upile\text{-}x} = \gamma M_{px}\left[\frac{(\Delta_y/\Delta_{py})}{(\Delta_x/\Delta_{px}) + (\Delta_y/\Delta_{py})}\right] = 1.3(144.9)\left[\frac{\left(\frac{0.479}{1.25}\right)}{\left(\frac{0.774}{1.30}\right) + \left(\frac{0.479}{1.25}\right)}\right] = 73.8\,\text{k} - \text{ft} \qquad (9.46)$$

$$M_{upile\text{-}y} = \gamma M_{py}\left[\frac{(\Delta_x/\Delta_{px})}{(\Delta_x/\Delta_{px}) + (\Delta_y/\Delta_{py})}\right] = 1.3(65.4)\left[\frac{\left(\frac{0.774}{1.30}\right)}{\left(\frac{0.774}{1.30}\right) + \left(\frac{0.479}{1.25}\right)}\right] = 51.7\ \text{k} - \text{ft} \qquad (9.47)$$

The maximum, factored-level, shear forces in an abutment pile that are associated with the plastic-moment capacities for x-axis and y-axis bending of an abutment pile are calculated using Eqs. 8.61 and 8.62, respectively, which are rewritten here at factored-load levels as

$$V_{upile-x} = \frac{2M_{upile-y}}{L_{ehy}} = \frac{2(51.7)}{11.9} = 8.69 \text{ kips} \tag{9.48}$$

$$V_{upile-y} = \frac{2M_{upile-x}}{L_{ehx}} = \frac{2(73.8)}{13.2} = 11.2 \text{ kips} \tag{9.49}$$

If the torsional moments, M_{pile-z}, in a pile are neglected, the pile forces with respect to the X, Y, and Z-axes of an integral abutment are obtained from the pile forces with respect to the x, y, and z-axes of a pile by applying the transformation Eqs. 8.63 and 8.64. For the Guthrie County Bridge, the bridge-skew angle, 2, and the pile-skew angle, 2_r, are both equal to 30°. The factored-level, axial force, biaxial shear forces, biaxial bending moments, and torsional moment for an abutment pile with respect to the X, Y, and Z-axes of an integral abutment are evaluated as

$$\begin{Bmatrix} V_{upile-X} \\ P_{upile-Y} \\ V_{upile-Z} \end{Bmatrix} = \begin{bmatrix} \cos(\theta-\theta_r) & 0 & \sin(\theta-\theta_r) \\ 0 & -1 & 0 \\ -\sin(\theta-\theta_r) & 0 & \cos(\theta-\theta_r) \end{bmatrix} \begin{Bmatrix} V_{upile-x} \\ P_{upile-z} \\ V_{upile-y} \end{Bmatrix} = \begin{bmatrix} 1 & 0 & 0 \\ 0 & -1 & 0 \\ 0 & 0 & 1 \end{bmatrix} \begin{Bmatrix} 8.69 \\ 96.2 \\ 11.2 \end{Bmatrix} = \begin{Bmatrix} 8.69\,k \\ 96.2\,k \\ 11.2\,k \end{Bmatrix} \tag{9.50}$$

$$\begin{Bmatrix} M_{upile-X} \\ M_{upile-Y} \\ M_{upile-Z} \end{Bmatrix} = \begin{bmatrix} \cos(\theta-\theta_r) & 0 & \sin(\theta-\theta_r) \\ 0 & -1 & 0 \\ -\sin(\theta-\theta_r) & 0 & \cos(\theta-\theta_r) \end{bmatrix} \begin{Bmatrix} M_{upile-x} \\ M_{upile-z} \\ M_{upile-y} \end{Bmatrix} = \begin{bmatrix} 1 & 0 & 0 \\ 0 & -1 & 0 \\ 0 & 0 & 1 \end{bmatrix} \begin{Bmatrix} 73.8 \\ 0.00 \\ 51.7 \end{Bmatrix} = \begin{Bmatrix} 73.8\,k-ft \\ 0.00\,k-ft \\ 51.7\,k-ft \end{Bmatrix} \tag{9.51}$$

Example 9.14

For the Guthrie County Bridge, calculate the factored-level, internal forces that act on Cross Sections 1, 1.5, and 2 of a composite, abutment backwall and backwall-pile cap.

Solution:

Analysis Method 2 that was discussed in Section 8.8.2.2 and the internal-force coefficients that are given in Table 8.14 were applied to calculate the factored-level, internal forces for a composite, abutment backwall and backwall-pile cap. Additional parameters required for the calculations are the vertical and horizontal eccentricities for the horizontal forces from the soil and the vertical eccentricity for the horizontal forces from the pile, which were calculated using Eqs. 8.67, 8.68, and 8.70, respectively, as e_{sY} = 1.56 ft, e_{sX} = 1.50 ft, and e_{pY} = 3.67 ft, respectively (see Fig. 8.43). The resulting, internal forces at the Cross Sections 1, 1.5, and 2 for the integral abutment are listed in Table 9.4.

Example 9.15 _____

Establish the shear-force, bending-moment, and torsional-moment design strengths of cross sections of a composite abutment backwall and backwall-pile cap for the Guthrie County Bridge.

Solution:

Figure 9.9 shows a cross-sectional view of a composite, abutment backwall and backwall-pile cap and the steel-reinforcing bars that were used in an abutment for the Guthrie County Bridge. The dimensions and bar sizes and locations that are shown in this figure was obtained from the Iowa DOT design drawings for this bridge. For a description of the reinforcement in the pile-cap portion of the integral abutment see Section 9.6.1. The horizontal #5 bars along the inside face of the abutment backwall terminate at the face of the PC girders that are extended into the abutment and bear on a short length of a structural steel S3X7.5, while the horizontal #5 bars along the outside

face of the abutment backwall extend past the ends of the PC girders. The vertical #8 bars along the inside and outside faces of the abutment tie together the abutment backwall to the pile cap. These bars extend about 26 in. into the pile cap. Along the inside face of the abutment, these vertical bars are extended into the thickness of the RC slab, which is cast monolithically with the abutment backwall. Along the outside face of the abutment, these #8 vertical bars are lapped with #8 bars that are bent in a vertical plane and extend horizontally into the RC slab. Because the Guthrie County Bridge has a 30-deg.-skew angle, the longitudinal and transverse reinforcement in the bridge deck will not contribute to the bending-moment and torsional-moment resistances of the integral abutment, since this steel reinforcement is orientated at an angle to the X-axis and Z-axis of the integral abutment.

The ACI Building Code (2002) was applied to establish the design strengths, ϕR_n, of an integral abutment for the Y-axis-shear force, $\phi_v V_{nY}$; X-axis-shear force, $\phi_v V_{nX}$; positive, X-axis bending moment, $\phi_b M_{nX}^+$; negative X-axis bending moment, $\phi_b M_{nX}^-$; positive, Y-axis bending moment, $\phi_b M_{nY}^+$; negative Y-axis bending moment, $\phi_b M_{nY}^-$; and torsional moment, $\phi_b T_{nZ}$. The integral abutment is classified as a deep-flexural member for both vertical and horizontal loads, since the depth of the abutment is large in comparison to the close spacing of the abutment piles and the width of the abutment is large in comparison to the close spacing of the PC girders, respectively. Therefore, the horizontal spacing of the vertical reinforcement and the vertical spacing of the longitudinal bars needs to satisfy the reinforcement spacing requirements that are given in Article 11.8 of the ACI Code (2002). An upper bound for the Y-axis, design-shear strength, $\phi_v V_{nY}$, was established by considering only the #8 bars along the outside face

of the abutment. The shear reinforcement needs to cross any potential diagonal concrete crack to provide resistance to shear and have adequate bar development at each end. The top of the vertical #8 bars that are spaced at 14.5 in. on center are lapped with the #8 bent bars that are at the same spacing and are hooked into the RC slab, and the bottom of these bars lapped with the closed-looped #5 ties that are spaced at 6.5 in on center. The computed $\phi_v V_{nY}$-shear-design strength was equal to 538 kips. Since the minimum area of shear reinforcement and the horizontal spacing of the vertical #8 bars and the minimum area of the longitudinal reinforcement and vertical spacing of the horizontal #5 bars does not satisfy the area and spacing requirements of Article 11.8 of the ACI Code, a lower bound for the Y-axis, design-shear strength, $\phi_v V_{nY}$, was established by considering only the shear strength of a plain-concrete cross section. Using ACI Eq. (22-9) to calculate the nominal-shear strength and applying the shear-resistance factor, Φ_v, equal to 0.55 from Article 9.3.5 of the ACI Code, the computed $\phi_v V_{nY}$-shear-design strength was equal to 169 kips. These two, shear-design strengths along with the ISU suggested shear-design strength are listed in Table 9.5.

An upper bound for the $\Phi_v V_{nX}$-design-shear strength was established by considering the area of shear reinforcement to consist of the horizontal portion of the #8 bent bars that are spaced at 14.5 in. on center at the top of the abutment and the four, horizontal legs of the #5 closed-looped ties that are spaced at 6.5 in. on center at the bottom of the abutment. The computed $\phi_v V_{nX}$-shear-design strength was equal to 679 kips. Since the minimum area of shear reinforcement that consists of the #8 bent bars and the four legs of the #5 closed-looped ties and the spacing of the longitudinal #8 bars and the minimum area and spacing of the longitudinal and the reinforcement along

the top and bottom faces of the abutment does not satisfy the area and spacing requirements of Article 11.8 of the ACI Code, a lower bound for the X-axis, design-shear strength, $\phi_v V_{nX}$, was established by considering only the shear strength of a plain-concrete cross section. Using ACI Eq. (22-9) to calculate the nominal-shear strength and applying the shear-resistance factor, Φ_v, equal to 0.55 from Article 9.3.5 of the ACI Code, the computed $\phi_v V_{nX}$-shear-design strength was equal to 169 kips. These two, shear-design strengths along with the ISU suggested shear-design strength are listed in Table 9.5.

Strain compatibility was applied to establish the positive and negative, design-moment strengths for X-axis and Y-axis bending of the cross section of an integral abutment for the Guthrie County Bridge. Positive, X-axis-bending moments and positive, Y-axis-bending moments cause compressive strains along the top and back face, respectively, of the abutment. The approach that was used was the same as that which was discussed in Section 9.6.1. Since the minimum area of tension reinforcement that is specified by Eq. (10-3) in Article 10.5.1 of the ACI Code (2002) was not provided in the cross sections of the composite, backwall and backwall-pile cap for the four, design-moment strengths ($\Phi_b M_{nX}^+$, $\Phi_b M_{nX}^-$, $\Phi_b M_{nY}^+$, and $\Phi_b M_{nY}^-$), an upper bound for a particular design-moment strength was set equal to three-fourths of the computed, design-moment strength based on strain compatibility. The resulting $\Phi_b M_{nX}^+$, $\Phi_b M_{nX}^-$, $\Phi_b M_{nY}^+$, and $\Phi_b M_{nY}^-$ moment strengths were equal to 2,338 k-ft; 953 k-ft; 552 k-ft; and 580 k-ft, respectively. Lower bounds for these moment strengths were established by considering the abutment to be a plain-concrete member. Using the ACI Eq. (22-2) to evaluate the nominal-moment strengths and applying the bending-

moment-resistance factor that is equal to 0.55 as specified in Article 9.3.5 of the ACI Code, the design-moment strengths $\Phi_b M_{nX}^+$ and $\Phi_b M_{nX}^-$ were equal to 953 k-ft and the design-moment strengths $\Phi_b M_{nY}^+$ and and $\Phi_b M_{nY}^-$ were equal to 317 k-ft. The lower bound, ISU suggested, and upper bound design-moment strengths for an integral abutment for the Guthrie County Bridge are listed in Table 9.5.

The torsional-moment design strength, $\Phi_v T_{nZ}$, of an integral abutment for the Guthrie County Bridge is limited because closed-ties were not used throughout the depth of the abutment and because only a small amount of longitudinal reinforcement was used in the abutment backwall. Closed-looped ties and significant longitudinal reinforcement were only used in the backwall-pile cap. If the reinforcement in the entire composite, backwall and backwall-pile cap were omitted, the abutment would behave as a plain-concrete member. Then, the concrete would experience cracking due to torsion when the applied torsional moment exceeded the torsional-cracking moment that is evaluated by Eq. 9.46. This equation is provided in the Commentary to Article 11.6.1 of the ACI Code (2002).

$$T_{cr} = 4\sqrt{f_c'}\left[\frac{\left(A_{cp}\right)^2}{p_{cp}}\right] = 4\left[\left(\frac{\sqrt{3000}}{(1000)(12)}\right)\right]\left[\frac{(3897)^2}{288.5}\right] = 1{,}038\ \text{k-ft} \qquad (9.52)$$

where, f_c' is the 28-day concrete-compressive strength, A_{cp} is the area that is enclosed by the perimeter of the concrete cross section, and p_{cp} is the perimeter of the concrete cross section. A 2-in. thickness of concrete at the bottom of the abutment-pile cap that is cast in contact with the earth needs to be neglected for the evaluation of the torsional strength of the cross section.

Article 11.6.1 of the ACI Code states that if the factored-level torsion-moment, T_u, is less than one-quarter of the torsional-cracking, design-moment strength, $\Phi_v T_{cr}$, torsional moments can be neglected for the design of the cross section. The torsional-resistance factor, Φ_v, is equal to 0.75, as specified in Article 9.3.2.2 of the ACI Code. Then, a lower bound for the torsional-moment, design strength, $\Phi_v T_{nZ}$, is equal to 195 k-ft. Even though Chapter 22 of the ACI Code that applies for structural, plain concrete does not address torsional-moment design strength, an upper bound for the $\Phi_v T_{nZ}$-strength was obtained by applying a Φ_v-factor equal to 0.55 to the torsional-cracking moment. The resulting $\Phi_v T_{nZ}$-strength was equal to 571 k-ft. (Even though Article 9.3.5 of the ACI Code does not specify a Φ_v-factor for torsion of plain concrete, this article lists the same value of the resistance factor for flexure, compression, shear, and bearing on structural, plain concrete. Therefore, using a Φ_v-factor equal to 0.55 for torsion seems to be appropriate.)

The design, torsional-moment strength, $\Phi_v T_{nZ}$, for the composite, abutment backwall and pile cap should not be less than that strength for only the abutment-pile cap, as long as the connection along the horizontal plane between the pile cap and the abutment backwall has sufficient bending-moment strength to transfer the torsional moment from the vertical cross sections of the backwall to the vertical cross sections of the pile cap. In Section 9.6.1, the torsional-moment design strength of the pile cap was determined to be equal to 324 k-ft. The lower bound, ISU suggested, and upper bound for the design-moment strengths $\Phi_v T_{nZ}$ are listed in Table 9.5.

The factored-level load effects, R_u, for the V_{uY}-shear force and V_{uX}-shear force along its local Y-axis and X-axis, respectively; M_{uX}-bending moment and M_{uY}-bending

moment of the abutment cross section about its local X-axis and Y-axis, respectively; and for the T_{uZ}-torsional moment, about its local Z-axis are listed in Table 9.4; and the design strengths, ϕR_n, for the Y-axis-shear force, $\phi_v V_{nY}$; X-axis-shear force, $\phi_v V_{nX}$; positive, X-axis bending moment, $\phi_b M_{nX}^{+}$; negative X-axis bending moment, $\phi_b M_{nX}^{-}$; positive, Y-axis bending moment, $\phi_b M_{nY}^{+}$; negative Y-axis bending moment, $\phi_b M_{nY}^{-}$; and torsional moment, $\phi_v T_{nZ}$ are listed in Table 9.5. The interaction relationships for biaxial bending (Eq. 8.177) and biaxial shear and torsional shear (Eq. 8.178) need to be evaluated at several critical sections along the length of the integral abutment. The direction of the curvature for the factored-level, bending moments and the corresponding bending-moment, design strength was established by the sign for the combined-loading, factored-level, bending moment that is shown in Table 9.4.

At Section 1:

$$\left(\frac{M_{uX}^{-}}{\varphi_b M_{nX}^{-}} + \frac{M_{uY}^{+}}{\varphi_b M_{nY}^{+}}\right) = \left(\frac{31.3}{953} + \frac{94.1}{552}\right) = 0.203 < 1.0 \tag{9.53}$$

$$\left(\frac{V_{uX}}{\varphi_v V_{nX}} + \frac{V_{uY}}{\varphi_v V_{nY}} + \frac{T_{uZ}}{\varphi_v T_{nZ}}\right) = \left(\frac{25.0}{169} + \frac{61.6}{169} + \frac{0}{571}\right) = 0.512 < 1.0 \tag{9.54}$$

At Section 1.5:

$$\left(\frac{M_{uX}^{-}}{\varphi_b M_{nX}^{-}} + \frac{M_{uY}^{+}}{\varphi_b M_{nY}^{+}}\right) = \left(\frac{105.1}{953} + \frac{26.5}{552}\right) = 0.158 < 1.0 \tag{9.55}$$

$$\left(\frac{V_{uX}}{\varphi_v V_{nX}} + \frac{V_{uY}}{\varphi_v V_{nY}} + \frac{T_{uZ}}{\varphi_v T_{nZ}}\right) = \left(\frac{58.4}{169} + \frac{71.8}{169} + \frac{200.1}{571}\right) = 1.12 > 1.0 \tag{9.56}$$

At Section 2:

$$\left(\frac{M_{uX}^{+}}{\varphi_b M_{nX}^{+}}+\frac{M_{uY}^{-}}{\varphi_b M_{nY}^{-}}\right)=\left(\frac{120.4}{2338}+\frac{192.2}{580}\right)=0.383<1.0 \tag{9.57}$$

$$\left(\frac{V_{uX}}{\varphi_v V_{nX}}+\frac{V_{uY}}{\varphi_v V_{nY}}+\frac{T_{uZ}}{\varphi_v T_{nZ}}\right)=\left(\frac{183.0}{169}+\frac{137.4}{169}+\frac{316.0}{571}\right)=2.45>1.0 \tag{9.58}$$

The composite, abutment backwall and backwall-pile cap satisfies the interaction relationship Eqs. 9.53, 9.55, and 9.57 for biaxial-moment strength at Cross Sections 1, 1.5, and 2, respectively, and satisfies the interaction relationship Eq. 9.54 for biaxial-shear strength and torsional-moment strength at Cross Section 1. However, the composite, backwall and backwall-pile cap violates the interaction relationship Eqs. 9.56 and 9.58 for biaxial-shear strength and torsional-moment strength at Cross Section 1.5 by about 12 percent and at Cross Section 2 by about 145 percent. The ISU researchers recommend that the amount of reinforcement and the spacing of the shear and torsion reinforcement in the composite, backwall and backwall-pile cap be modified to significantly increase the design strengths for shear and torsion.

9.6.3. Connections

Discussion regarding the design of connections for integral abutments was presented in Section 8.8.5. In this section of Chapter 9, strength-limit states were investigated for three, integral-abutment connections for the Guthrie County Bridge. These connections are the connections between the abutment backwall and the backwall-pile cap, between a backwall pile and the backwall-pile cap, and between an interior PC girder and an abutment backwall. Examples that evaluate the strength for these connections are presented in Sections 9.6.3.1, 9.6.3.2, and 9.6.3.3, respectively.

9.6.3.1. Backwall-to-pile-cap connection

The construction joint between the backwall-pile cap and the abutment backwall needs to transfer an axial force, P_{uY}, shear forces V_{ux} and V_{uZ}, and bending moments, M_{uX} and M_{uZ}. These forces are induced with respect to the X, Y, and Z-axes of an abutment by the soil pressures that act on the vertical faces of the pile cap and by the end forces from the abutment piles.

Example 9.16 _____

Calculate the required factored-level forces that need to be resisted along the connection between a pile cap and an abutment backwall for an integral abutment of the Guthrie County Bridge.

Solution:

Figure 9.10 shows an XY-plane cross section of a backwall-pile cap for the Guthrie County Bridge. The factored-level forces that act on the pile cap from the soil and from each of the HP10X42 piles that are below the abutment backwall are shown in the figure. The factored-level, passive-soil pressure, $w_{usoil\text{-}X}$, was computed by multiplying the service-level, passive-soil pressure, $w_{soil\text{-}X}$, which was evaluated in Eq. 9.34, by the product of the γ-load factor and the β_E-load factor. Both of these load factors are equal to 1.3 for the AASHTO Load Group IV, as shown in Eq. 8.4. The factored-level axial force, shear force, and bending moment for an abutment pile were computed by Eqs. 9.50 and 9.51. The factored-level, axial force, P_{uY}, shear force, V_{uX}, and bending moment, M_{uZ}, at the interface between the bottom of the abutment backwall and the top of the pile cap are also shown in Fig. 9.10.

Figure 9.11 shows an XZ-plane cross section through a portion of the length of a backwall-pile cap for the Guthrie County Bridge. The vertical #8 bars at 14.5 in. on center that are in the front and back faces of the pile cap extend across the construction joint between the pile cap and the backwall of the abutment. An 87-in.-long section, of an abutment, which is the center-to-center spacing of the abutment piles, was selected as a tributary width for checking the strength of the connection between a pile cap and an abutment backwall. Each vertical cross section at the ends of this section of an abutment is either a plane of symmetry or asymmetry, depending on the particular load that is applied to the abutment. Therefore, the soil pressures on the back face of the pile cap and the forces from the two piles that are within this 87-in. length are resisted only along the connection between the pile cap and the abutment backwall. The forces P_{uY}, V_{uX}, and, M_{uZ} are not uniformly distributed along this length of the abutment. As discussed in Section 8.8.4.1, Oesterle, et al. (1999) recommended that 75 percent of the total area of vertical reinforcement across this construction joint be located within 25 percent of the center-to-center spacing for the PC girders on each side of a girder and that 25 percent of this reinforcement be located within the center 50 percent of the abutment length between the girders.

The total factored-level forces along the construction joint between a pile cap and an abutment backwall that act over the 87-in. length of an abutment were computed as

$$P_{uY} = 2P_{upile\text{-}Y} = 2(96.2) = 192.4 \text{ kips} \tag{9.59}$$

$$V_{uX} = 2\,V_{upile-X} + \frac{1}{2}\left(w_{usoil-X}\right)B\left(h_{cap}\right)\left[1+\left(\frac{h_{cap}}{h_{abut}}\right)\right]$$

$$= 2(8.64) + \frac{1}{2}(8.83)(7.25)\left(\frac{42}{12}\right)\left[1 + \left(\frac{42}{112}\right)\right] = 171.3 \text{ kips} \qquad (9.60)$$

$$M_{uZ} = 2M_{upile-Z} + 2V_{upile-X}\left(h_{cap} - \frac{1}{2}d_{emb}\right) + \frac{1}{6}\left(w_{usoil-X}\right)B\,h_{cap}^2\left[2 + \left(\frac{h_{cap}}{h_{abut}}\right)\right]$$

$$= 2(51.33) + 2(8.64)\left(\frac{42-12}{12}\right) + \frac{1}{6}(8.83)(7.25)\left(\frac{42}{12}\right)^2\left[2 + \left(\frac{42}{112}\right)\right] = 456.3\text{k} - \text{ft} \qquad (9.61)$$

The magnitudes of these forces in terms of forces per foot along the portion of the abutment adjacent to a PC girder were computed by multiplying these forces by the reinforcement-distribution, r_d, factor that is expressed by Eq. 9.62 to incorporate the reinforcement distribution that was recommended by Oesterle, et al.

$$r_d = (0.75)\left[\frac{12}{\left(\frac{87}{4}\right) + \left(\frac{87}{4}\right)}\right] \qquad (9.62)$$

The resulting P_{uY}, V_{uX}, and, M_{uZ}-forces at the interface between a pile cap and an abutment backwall were 39.8 k/ft, 35.4 k/ft, and 94.4 k-ft/ft, respectively. If the total of the forces along this joint were uniformly distributed along the 87-in. length for this section of an abutment, these forces would have been 26.5 k/ft, 23.6 k/ft, and 62.9 k-ft/ft, respectively. The resulting, non-uniformly-distributed forces are equal to 1.5 times the magnitude of the uniformly-distributed forces.

Example 9.17 _____

Determine the flexural-bending, design strength, $\Phi_b M_{nZ}$, and the shear-friction, design strength, $\Phi_v V_{nX}$, along the construction joint between a backwall-pile cap and an

abutment backwall for the Guthrie County Bridge and compare those strengths with the required, factored-level bending moment, M_{uZ}, and shear-friction force, V_{uX}.

Solution:

Strain-compatibility conditions were applied to the doubly-reinforced, horizontal cross section shown in Fig. 9.11 to establish the design strength, $\Phi_b M_{nZ}$. A 2-in. concrete clear cover was assumed for the vertical #8 bars that are spaced at 14.5 in. on center. The amount of tension reinforcement that was used in the tension face of the horizontal cross section does not satisfy the minimum reinforcement requirements that are specified in Articles 10.5 and 7.12 of the ACI Code (2002). To satisfy the ACI requirement of providing four-thirds the area of tension steel that is required to resist the factored-level moment when less than the minimum amount of tension steel is present in a cross section, three-fourths of the design-moment strength that was computed by applying strain compatibility was used for the $\Phi_b M_{nZ}$-strength. The resulting moment strength was equal to 73.1 k-ft/ft, which is less than the required factored-level bending moment of 94.4 k-ft/ft. Insufficient moment strength exists at the interface between a backwall-pile cap and the abutment backwall. The 14.5-in spacing for the vertical #8 bars does not satisfy the recommendations by Oesterle, et al. (2002). These researchers recommended that the spacing of these vertical bars should not exceed 11 in. as computed from Eqs. 8.179 and 8.180.

Article 11.7.4 of the ACI Code (2002) was applied to evaluate the shear-friction design strength for the construction joint between the abutment backwall and the backwall-pile cap. The coefficient-of-friction between the top of the pile cap and the bottom of the abutment backwall is a function of the surface condition between these

two parts of the abutment. For concrete that is cast against a hardened concrete surface that is not intentionally roughened, the ACI Code specifies a coefficient of friction μ equal to 0.6λ, where the factor λ is set equal to 1.0 for normal-weight concrete. When a resistance factor Φ equal to 0.75 is used, the shear-friction design strength for this connection is computed as

$$\varphi\, V_n = \varphi\, A_{vf}\; f_y\, \mu = 0.75\left[2(0.79)\left(\frac{12}{14.5}\right)\right](60)\left[(0.6)(1.0)\right] = 35.3\,\text{k/ft} \qquad (9.63)$$

where, A_{vf} is the area of the shear-friction reinforcement. This design strength does not account for the strength of the concrete keyway that is present along the length of the abutment. Since the required, factored-level shear-friction force was equal to 35.4 k/ft, the shear capacity is sufficient across the interface between the backwall-pile cap and the abutment backwall.

9.6.3.2. Pile-to-pile-cap connection

The pile cap must have adequate strength to support the vertical-bearing force, P_{ebv}, which is expressed by Eq. 8.181, and horizontal-bearing force, P_{ebH}, which is expressed by Eq. 8.182, without crushing the concrete. Also, when the force P_{ebH} is directed towards the front or back face of the pile cap, the pile cap must have adequate strength to prevent a “punching-type” failure of the pile head through that vertical face of the pile cap. See Section 8.8.5.2 for additional discussion regarding the pile-to-pile-cap connection.

Example 9.18 _____

Evaluate the vertical, bearing strength of the concrete at the top of a pile in a backwall-pile cap for the Guthrie County Bridge and compare this strength with the factored-level, axial load, $P_{upile\text{-}Y}$, in the pile.

Solution:

Figure 9.12 shows details for the pile-to-pile-cap connection for an HP10X42 pile at the Guthrie County Bridge. The factored-level, axial load in the pile was computed to be equal to 96.2 kips. Some of the load in a pile will be transferred to the pile cap by skin friction between the pile and the surrounding concrete along the embedment length of the pile into the pile cap and by end bearing of the pile on the concrete at the end of the pile. If only end bearing at the top of a pile is considered to transfer the vertical load in a pile to the pile cap, the induced, factored-level, bearing stress, q_{u3Y}, is equal to 7.76 ksi. For a pile that is embedded into concrete, Wassermann and Walker (1996) recommended a nominal, concrete-bearing stress that is equal to $3.78f_c'$. The ISU researchers recommend using this nominal, concrete-bearing stress for an abutment pile that is subjected to an axial-compressive force, biaxial-shear forces, and biaxial-bending moments, rather than the more liberal, nominal, concrete-bearing stress of $8f_c'$ that was recommended by AISI (1980) for HP-shaped piles that are subjected to only an axial-compressive load. Then, the design, concrete-bearing stress for a pile in concrete would be expressed as $3.78\Phi_c f_c'$. When a resistance factor, Φ_c, for bearing on concrete, which is given in Article 9.3.2.4 of the ACI Code (2002), is equal to 0.65 and the 28-day, concrete-compressive strength, f_c', is equal to 3,500 psi, the design, concrete-bearing stress was computed to be equal to 8.60 ksi. This design-bearing

resistance is greater than the calculated, factored-level, concrete-bearing stress q_{u3Y}. Therefore, an end-bearing plate was not required at the top of a backwall pile to increase the end-bearing area and reduce the factored-level, concrete-bearing stresses.

Example 9.19 _____

Evaluate the horizontal, bearing strength of the concrete in a pile cap at the top of an abutment pile for the Guthrie County Bridge and compare that strength with the factored-level, concrete-bearing stress.

Solution:

Two free-body diagrams in the XY-plane for the portion of an abutment pile that is embedded within the backwall-pile cap are shown in Figs. 9.12c and 9.12d. The horizontal-bearing stresses q_{u1X} and q_{u2X}, which are induced by the pile forces $V_{upile\text{-}X}$ and $M_{upile\text{-}Z}$, are assumed to be rectangular stress blocks that have a height equal to that of a Whitney Stress Block for reinforced-concrete design by the ACI Code (2002). The neutral axis for zero-bending strain is located at the mid-height of the pile embedment length into the pile cap. The dimension a_p for the compressive-bearing stresses is given by

$$a_p = \left[\beta_1\left(\frac{d_{emb}}{2}\right)\right] = \left[0.85\left(\frac{24.0}{2}\right)\right] = 10.20\,\text{in.} \tag{9.64}$$

Each abutment pile was surrounded by spiral reinforcement along the pile-embedment length. The #2-bar spiral is 21-in. in diameter and has 7 turns on a 3-in. pitch. If the effect of the spiral reinforcement on increasing the effective-bearing width of a pile on the concrete outside of the spiral is neglected, the width, b, for the concrete-bearing-stress volume is the cross-sectional, depth-dimension, d, for an HP10X42. The

factored-level, concrete-bearing stresses q_{u2x} and q_{u1x} in the XY-plane of the pile cap for an abutment backwall were computed using Eqs. 8.184 and 8.183, respectively, as

$$q_{u2X} = \left[\frac{M_{upile-Z} + \left(\frac{a_p}{2}\right)\left(V_{upile-X}\right)}{a_p\ b\left(d_{emb} - a_p\right)} \right] = \left[\frac{51.33(12) + \left(\frac{10.20}{2}\right)(8.64)}{10.20(9.7)\left(24.00 - 10.20\right)} \right] = 0.483\,\text{ksi} \tag{9.65}$$

$$q_{u1X} = \left[q_{u2X} + \frac{V_{upile-X}}{a_p\ b} \right] = \left[0.483 + \frac{8.64}{10.20(9.7)} \right] = 0.571\,\text{ksi} \tag{9.66}$$

By a similar analysis, the factored-level, concrete-bearing stresses, q_{u1Z} and q_{u2Z}, which are induced by the pile forces $V_{upile-Z}$ and $M_{upile-X}$, were computed to be equal to 0.777 ksi and 0.670 ksi, respectively. The design, concrete-bearing stress, $\Phi_c q_n$, was evaluated in Example 9.18 to be equal to 8.60 ksi. Since the computed, X-axis and Z-axis, factored-level, concrete-bearing stresses at the two locations along the length of the pile embedment are less than the design, concrete-bearing stresses for those locations, the 24-in.-long, pile-embedment length into the pile cap is sufficient to transfer the pile forces into the pile cap.

Example 9.20 _____

For the Guthrie County Bridge, evaluate the punching-shear-strength, limit state that is associated with the factored-level, concrete-bearing stresses along the embedment length of a pile in a backwall-pile cap.

Solution:

A “punching-shear” failure through a vertical face of the pile cap may occur with large, horizontal, concrete-bearing stresses, which are directed normal to the face of the

pile cap, as shown in Fig. 9.12b. These bearing stresses are induced by the pile forces $V_{upile\text{-}X}$ and $M_{upile\text{-}Z}$ that are shown in Fig. 9.12c. The concrete-bearing stress q_{u1X}, which is expressed by Eq. 9.66, is larger than the concrete-bearing stress q_{u2X}, which is expressed by Eq. 9.65. At the location of the stress q_{u1X}, the perimeter for a concrete "punching shear" failure is smaller than that associated with the stress q_{u2X} because of the free edge at the bottom of the pile cap.

Figure 9.13 shows a cross-sectional-plan view, a vertical cross section, and an elevation of the concrete-bearing area adjacent to an abutment-backwall pile at the bottom of a backwall-pile cap for the Guthrie County Bridge. A portion of the spiral reinforcement and two legs of a #6-bent bar pass through the sides of the potential punching-shear failure surfaces. Article 11.12 of the ACI Code (2002) was applied to determine the design strength for concrete-punching shear. The concrete strength is a function of the dimensions for the loaded-concrete area and the perimeter, b_o, of the concrete-failure surface. For the concrete-bearing stress q_{u1X}, the loaded-concrete area has the dimensions of the Whitney-Stress Block depth, a_p, by the depth, d, of the HP10X42 cross section. For the abutment piles of the Guthrie County Bridge, the ratio, β_c, of the longer-to-shorter dimensions of the loaded-concrete area is equal to 1.053; the bearing-condition edge factor, α_s, is equal to 30 for a concrete-punching-shear failure shape that occurs at the bottom of the pile cap, where one edge of that failure surface is truncated by a concrete face; and b_o is equal to 49.76 in. The nominal concrete strength, V_c, is the smallest of the nominal strengths that are evaluated by Eqs. 8.187, 8.188, and 8.189. These three nominal strengths are given by

$$V_c = \left[\left(2+\frac{4}{\beta_c}\right)\sqrt{f'_c}\ b_o d_{eff}\right] = \left[\frac{\left(2+\frac{4}{1.053}\right)\sqrt{3500}\,(49.76)(9.83)}{1000}\right] = 168\ \text{kips} \qquad (9.67)$$

$$V_c = \left[\left(\frac{\alpha_s d_{eff}}{b_o}+2\right)\sqrt{f'_c}\ b_o d_{eff}\right] = \left[\frac{\left(\frac{(30)(9.83)}{49.76}+2\right)\sqrt{3500}\,(49.76)(9.83)}{1000}\right] = 229\ \text{kips} \qquad (9.68)$$

$$V_c = \left[4\sqrt{f'_c}\ b_o d_{eff}\right] = \left[\frac{4\sqrt{3500}\,(49.76)(9.83)}{1000}\right] = 116\ \text{kips} \qquad (9.69)$$

Equation 9.69 establishes the nominal, concrete-punching-shear strength of 116 kips. If the strength effects of the two legs of the #6-bent ties and the #2-bar, spiral loops that cross the concrete-punching-shear failure surfaces are neglected, the design, concrete-punching-shear strength, $\Phi_v V_n$, is equal to 86.8 kips. The factored-level, shear force that acts on the failure surface is equal to the applied load for the bearing of the pile on the concrete at the bottom of the pile cap. This force is expressed as

$$V_u = \left(q_{u1X} a_p d\right) = \left[(0.571)(10.20)(9.7)\right] = 56.5\ \text{kips} \qquad (9.70)$$

The design, concrete-punching-shear strength is greater than the required, factored-level, concrete-punching-shear strength. Therefore, the strength-limit state for a concrete-punching-shear failure is not violated for the backwall-pile cap.

9.6.3.3. Girder-to-backwall connection

As discussed in Section 8.8.5.3, the internal forces that occur at the connection between a PC girder and an abutment backwall were assumed to induce vertical and horizontal, concrete-bearing stresses that act around the perimeter and at the end of a girder that is embedded into the abutment backwall. For factored-level loads that act on the bridge superstructure and substructure, the computed, factored-level, concrete-bearing stresses must not exceed the design, concrete-bearing stresses. Also, the factored-level, horizontal, concrete-bearing stresses that act on the vertical plane at the end of a girder are limited by the punching-shear strength of the concrete in the abutment backwall that is behind the girder.

Example 9.21 _____

Compute the factored-level, concrete-bearing stresses that act at the end of an interior, PC girder that is embedded into an abutment backwall for the Guthrie County Bridge. Compare these stresses to the design, concrete-bearing strength of the abutment backwall.

Solution:

Figure 9.14 shows the concrete-bearing stresses that act around the perimeter and at the end of an interior, PC girder for the Guthrie County Bridge. These bearing stresses were induced by the girder, member-end forces that were resolved at a point that corresponds with the center of gravity for the “LDX” PC girder at the front face of the abutment backwall. The presence of concrete for the RC slab and haunch was neglected to simplify the evaluation of these bearing stresses. Therefore, only the concrete-bearing stresses that act on the girder were considered to resist the member-

end forces. For an interior girder, the factored-level, girder forces and moments at the front face of the abutment backwall were evaluated using the combined, factored-level, girder reactions that are listed in Table 9.6 and the transformation matrices that were part of Eqs. 8.195 and 8.196. These forces and moments were calculated as

$$\begin{Bmatrix} P_{u\ell'} \\ V_{uh'} \\ V_{ut'} \end{Bmatrix} = \begin{bmatrix} \cos\theta & 0 & -\sin\theta \\ 0 & 1 & 0 \\ \sin\theta & 0 & \cos\theta \end{bmatrix} \begin{Bmatrix} F_{uX} \\ F_{uY} \\ F_{uZ} \end{Bmatrix} = \begin{bmatrix} 0.866 & 0 & -0.500 \\ 0 & 1 & 0 \\ 0.500 & 0 & 0.866 \end{bmatrix} \begin{Bmatrix} -282 \\ -152 \\ +143 \end{Bmatrix} = \begin{Bmatrix} +316\text{ kips} \\ -152\text{ kips} \\ -17.2\text{ kips} \end{Bmatrix} \quad (9.71)$$

$$\begin{Bmatrix} M_{u\ell'} \\ M_{uh'} \\ M_{ut'} \end{Bmatrix} = \begin{bmatrix} \cos\theta & 0 & -\sin\theta \\ 0 & 1 & 0 \\ \sin\theta & 0 & \cos\theta \end{bmatrix} \left\{ \begin{Bmatrix} M_{uX} \\ M_{uY} \\ M_{uZ} \end{Bmatrix} + \begin{bmatrix} 0 & +e_Z & +e_Y \\ -e_Z & 0 & -e_X \\ -e_Y & +e_X & 0 \end{bmatrix} \begin{Bmatrix} F_{uX} \\ F_{uY} \\ F_{uZ} \end{Bmatrix} \right\}$$

$$= \begin{bmatrix} 0.866 & 0 & -0.500 \\ 0 & 1 & 0 \\ 0.500 & 0 & 0.866 \end{bmatrix} \left\{ \begin{Bmatrix} -28.7 \\ 0 \\ +633 \end{Bmatrix} + \begin{bmatrix} 0 & +0.866 & +1.12 \\ -0.866 & 0 & -1.50 \\ -1.12 & +1.50 & 0 \end{bmatrix} \begin{Bmatrix} -282 \\ -152 \\ +143 \end{Bmatrix} \right\}$$

$$= \begin{Bmatrix} -360\text{ ft-kips} \\ +472\text{ ft-kips} \\ +624\text{ ft-kips} \end{Bmatrix} \quad (9.72)$$

The width a_{p1} of the Whitney Stress Block and the factored-level, concrete-bearing stresses q_{u2t1} and q_{u1t1}, which are shown in Fig. 9.14b, were computed as

$$a_{p1} = \beta_1 \left(\frac{\ell_{emb1}}{2} \right) = 0.85 \left(\frac{20.43}{2} \right) = 8.68\text{ in.} \quad (9.73)$$

$$q_{u2t1} = \left[\frac{M_{uh'} + \left(\frac{a_{p1} + b_{bf} \tan\theta}{2} \right) V_{ut'}}{a_{p1} h_{girder} \left(\ell_{emb1} - a_{p1} \right)} \right]$$

$$= \left[\frac{472(12) + \left(\frac{8.68 + 22\tan 30^{o}}{2} \right)(-17.2)}{8.68(54)(20.48 - 8.68)} \right] = 0.99 \text{ ksi} \tag{9.74}$$

$$q_{u1t1} = \left[q_{u1t2} + \left(\frac{V_{ut'}}{a_{p1} h_{girder}} \right) \right] = \left[0.995 + \left(\frac{-17.2}{8.68(54)} \right) \right] = 0.96 \text{ ksi} \tag{9.75}$$

The widths a_{p2} and a_{p3} of the Whitney Stress Blocks and the factored-level, concrete-bearing stresses q_{u2t2} and q_{u1t2}, which are shown in Fig. 9.14c, were calculated as

$$a_{p2} = \left[\beta_1 \left(y_{ncg} - t_s - t_h \right) \right] = \left[0.85(40.88 - 9.5 - 1.75) \right] = 25.19 \text{ in.} \tag{9.76}$$

$$a_{p3} = \left[\beta_1 \left(h_{girder} - y_{ncg} + t_s + t_h \right) \right] = \left[0.85(54 - 40.88 + 9.5 + 1.75) \right] = 20.72 \text{ in.} \tag{9.77}$$

$$q_{u2t2} = \left[\frac{M_{ut'}}{a_{p3} \ell_{emb1} \left(h_{girder} - \frac{a_{p2}}{2} - \frac{a_{p3}}{2} \right)} \right]$$

$$= \left[\frac{-360(12)}{20.72(20.43)\left(54 - \frac{25.19}{2} - \frac{20.72}{2} \right)} \right] = -0.33 \text{ ksi} \tag{9.78}$$

$$q_{u1t2} = \left[\left(\frac{a_{p3}}{a_{p2}} \right) q_{u2t2} \right] = \left[\left(\frac{20.72}{25.19} \right)(-0.329) \right] = -0.27 \text{ ksi} \tag{9.79}$$

Since the concrete-bearing stresses q_{u1t1} and q_{u2t1}, which are shown in Fig. 9.14b, and the concrete-bearing stresses q_{u1t2} and q_{u2t2}, which are shown in Fig. 9.14c, act in the horizontal direction against the vertical faces of the PC girders, these stresses

need to be combined to establish the total, factored-level, concrete-bearing stresses q_{u1t} and q_{u2t} that acts on the sides of a girder. The total of these horizontal, concrete-bearing stresses were evaluated as

$$q_{u1t} = \left(q_{u1t1} - q_{u1t2}\right) = \left[0.96 - (-0.27)\right] = 1.23 \text{ ksi} \tag{9.80}$$

$$q_{u2t} = \left(q_{u2t1} - q_{u2t2}\right) = \left[0.99 - (-0.33)\right] = 1.32 \text{ ksi} \tag{9.81}$$

As discussed in Section 8.8.5.3, the ISU researchers recommend using the ACI Code (2002), design, concrete-bearing stress, $\Phi_c q_n$, which is a function of the amount of concrete confinement around the location of the bearing area, rather than the higher bearing stress that was suggested by Burdette, et al. (1983) for a particular, large steel insert in a concrete slab. For concrete bearing near the front face of an abutment backwall and for concrete bearing near embedded end of a PC girder, the ACI Code, non-confined, concrete-bearing-design stress, $\Phi_c q_{n1}$ and the confined, concrete-bearing stress, $\Phi_c q_{n2}$, respectively, are expressed as

$$\varphi_c q_{n1} = \left[\left(\varphi_c\right)(0.85)\left(f_c^{'}\right)\right] = \left[(0.65)(0.85)(3.5)\right] = 1.93 \text{ ksi} \tag{9.82}$$

$$\varphi_c q_{n2} = \left[\left(\varphi_c\right)(1.9)\left(f_c^{'}\right)\right] = \left[(0.65)(1.9)(3.5)\right] = 3.87 \text{ ksi} \tag{9.83}$$

Since the calculated, factored-level, concrete-bearing stresses q_{u1t} and q_{u2t} are less than the design, concrete-bearing stresses $\Phi_c q_{n1}$ and $\Phi_c q_{n2}$, respectively, the concrete-bearing-strength, limit state was satisfied regarding these bearing stresses.

The factored-level, concrete-bearing stresses q_{u2h} and q_{u1h}, which are shown in Fig. 9.14d, were computed as

$$q_{u2h} = \left[\frac{M_{ut'} + \left(\frac{a_{p1} + b_{bf} \tan\theta}{2} \right) V_{uh'}}{a_{p1} b_2 \left(\ell_{emb1} - a_{p1} \right)} \right] = \left[\frac{(+624)(12) + \left(\frac{8.68 + 22 \tan 30^o}{2} \right)(+152)}{8.68(35)(20.43 - 8.68)} \right] = 2.55 \text{ ksi}$$

(9.84)

$$q_{u1h} = \left[\frac{q_{u2h} a_{p1} b_2 + V_{uh'}}{a_{p1} b_1} \right] = \left[\frac{2.551(8.68)(35) + 152}{8.68(35)} \right] = 3.05 \text{ ksi} \qquad (9.85)$$

The concrete-bearing stresses q_{u1} and q_{u2} that act normal to the sloped inside face of the top and bottom flanges, respectively, of the PC girder were evaluated as

$$q_{u1} = \left(\frac{q_{u1h}}{\cos \xi_{tf}} \right) = \left(\frac{3.05}{\cos 8.75^o} \right) = 3.09 \text{ ksi} \qquad (9.86)$$

$$q_{u2} = \left(\frac{q_{u2h}}{\cos \xi_{bf}} \right) = \left(\frac{2.55}{\cos\ 45^o} \right) = 3.61 \text{ksi} \qquad (9.87)$$

The calculated, factored-level, concrete-bearing stresses q_{u1h} and q_{u1} exceeded the unconfined, design, concrete-bearing stress, $\Phi_c q_{n1}$, by about 60 percent; while, the calculated, factored-level, concrete-bearing stresses q_{u2h} and q_{u2} are about 34 percent and 7 percent, respectively, less than the confined, design, concrete-bearing stress, $\Phi_c q_{n2}$. The apparent violation of the bearing-strength, limit state along the embedment length ℓ_{emb1} may be based on modeling simplifications for the bearing conditions of an interior, PC girder on the skewed, integral abutment. Recall that the smaller of the embedment lengths ℓ_{emb1} and ℓ_{emb2} was selected to analyze these vertical bearing

stresses. If a longer embedment length was used for the PC girders, the magnitude of these concrete-bearing stresses would be reduced. A more precise analysis of the connection between a PC girder and the abutment backwall should be performed, to determine if a longer embedment length should have been provided to satisfy the strength-limit state for concrete bearing.

The horizontal, concrete-bearing stress, $q_{u3\ell}$, at the end of an interior PC girder was calculated as

$$q_{u3\ell} = \left(\frac{P_{u\ell'}}{A_{girder}}\right) = \left(\frac{316}{639}\right) = 0.49 \text{ ksi} \tag{9.88}$$

Since this stress is significantly smaller than the confined, design, concrete-bearing stress, the concrete-bearing-strength, limit state for the abutment backwall is satisfied for the concrete beyond the end of an interior, PC girder.

This example evaluated concrete-bearing stresses for an interior, PC girder of the Guthrie County Bridge. A similar analysis should be performed to establish the concrete-bearing stresses for an exterior, PC girder. For an exterior girder, the member-end forces that are associated with the effective width for a portion of the integral abutment and bridge superstructure are smaller than those for an interior girder. However, additional member-end forces that are associated with the soil pressures and gravity loads for a sidewall with its pile foundation and wingwall will exist for an exterior girder.

Example 9.22 _____

Investigate the punching-shear strength of the abutment backwall at the end of an interior, PC girder for the Guthrie County Bridge.

Solution:

Figures 9.14a and 9.14c show a plan view and a girder-cross-sectional view, respectively, of the connection between a PC girder and an integral-abutment backwall for the Guthrie County Bridge. As discussed in Section 8.8.5.3, to generate a punching-shear failure in the concrete beyond the end of the girder, a three-sided of a four-sided, wedge-shaped failure must develop through concrete in this portion of the abutment. The ACI Code (2002) represents the shear strength of the concrete along the inclined surfaces of the wedge-shaped failure to be a function of the effective depth to the tension reinforcement for flexural behavior of the member within the punching-shear failure region. Since the abutments for this bridge have a 30°-skewed alignment, the effective depth to the horizontal, #5-bar along the back face of an abutment varies between 3.91 in. and 16.61 in. For a concrete-punching-shear failure to occur in an abutment backwall, the concrete along all of the planes of the wedge-shaped failure needs to fracture in shear. Therefore, an average, effective depth of 10.26 in. can be used to evaluate the punching-shear strength for the concrete beyond the end of an interior girder for the Guthrie County Bridge. The shear strength of a three-sided, wedge-shaped, punching-shear failure for this bridge is lower than that for a four-sided, wedge-shaped, punching-shear failure. For a three-sided, wedge shape, the bearing-condition-edge factor, α_s, is equal to 30, and the perimeter, b_o, and the ratio, β_c, of the long-to-short dimensions of the loaded area are given by

$$b_o = \left[\left(\frac{b_{bf} + b_{tf}}{2}\right) + d_{eff}\right] + 2\left(h_{girder} + t_s + t_h + \frac{d_{eff}}{2}\right)$$

$$= \left\{ \left[\left(\frac{22+20}{2} \right) + 10.26 \right] + 2\left(54 + 9.50 + 1.75 + \frac{10.26}{2} \right) \right\} = 172\,\text{in.} \qquad (9.89)$$

$$\beta_c = \left[\frac{h_{girder}}{\left(\frac{b_{bf} + b_{tf}}{2} \right)} \right] = \left[\frac{54}{\left(\frac{22+20}{2} \right)} \right] = 2.57 \qquad (9.90)$$

The nominal-shear strength, V_c, of the concrete is the smaller of the three shear strengths that are established by evaluating Eqs. 8.187, 8.188, and 8.189. These strengths are calculated as

$$V_c = \left[\left(2 + \frac{4}{\beta_c} \right) \sqrt{f_c^{'}}\ b_o d_{eff} \right] = \left[\left(2 + \frac{4}{2.57} \right) \left(\frac{\sqrt{3500}}{1000} \right) (172)(10.26) \right] = 371\,\text{kips} \qquad (9.91)$$

$$V_c = \left[\left(\frac{\alpha_s d_{eff}}{b_o} + 2 \right) \sqrt{f_c^{'}}\ b_o d_{eff} \right] = \left\{ \left[\frac{(30)(10.26)}{172} + 2 \right] \frac{\sqrt{3500}}{1000} (172)(10.26) \right\} = 396\,\text{kips} \qquad (9.92)$$

$$V_c = \left(4\sqrt{f_c^{'}}\ b_o d_{eff} \right) = \left[4\left(\frac{\sqrt{3500}}{1000} \right) (172)(10.26) \right] = 418\,\text{kips} \qquad (9.93)$$

Equation 9.91 establishes the nominal, concrete-punching-shear strength of 371 kips. When a resistance factor, Φ_v, of 0.75 is applied to the governing, nominal, concrete-shear strength, the corresponding design, shear strength, $\Phi_v V_n$, is equal to 278 kips. At the location of an interior PC girder, the required, factored-level, shear strength, V_u, is equal to the 316-kip, factored-level, axial force, $P_{u\ell'}$ in the girder. A 14-percent overstress exists for a punching-shear failure mechanism of the concrete beyond the end of an interior, PC girder in the Guthrie County Bridge.

9.7 Pile Design

A discussion regarding the design of a pile for an abutment backwall of an integral-abutment bridge was presented in Section 8.9. In this section of Chapter 9, examples are presented to illustrate the calculation of the strength-limit state for interaction behavior involving axial compression and biaxial bending and the ductility-limit state of the abutment-backwall piles for the Guthrie County Bridge.

9.7.1. Strength limit state

Example 9.23 _____

Evaluate the axial-compression and biaxial-bending, interaction, strength-limit state for an abutment-backwall pile of the Guthrie County Bridge. For the purpose of this example, a simplified structural analysis, which was similar to Analysis Method 1 that was discussed in Section 8.9.2, was performed to calculate the axial force, shear force, and bending moment in the ℓh-plane of the bridge superstructure, when only dead, live, and live-impact loads (gravity loads) were applied to the bridge. This analysis predicted an 81-kip, axial force, $P_{upile\text{-}Y}$; a 2.3-kip, shear force, $V_{upile\text{-}\ell}$; and a 169 in.-kip bending moment, $M_{ut\text{-}gravity}$, that acted in the ℓh-plane of the bridge superstructure and at the top of an abutment pile. The shear force, $V_{upile\text{-}\ell}$, and the bending moment, $M_{u\ell\text{-}gravity}$, that act in the ht-plane of the bridge superstructure and at the top of an abutment-backwall pile were assumed to be equal to zero.

Solution:

Following the discussion related to Eq. 8.215, factored-level, second-order, bending moments, M_{ut2nd}, ($P_{upile\text{-}Y}\Delta_\ell$-moments) that act about an axis that is parallel to

the t-axis of the bridge superstructure are induced in an abutment-backwall pile for both thermal expansion and contraction of the bridge superstructure. Since the longitudinal displacements of an integral abutment, which are induced by thermal contraction are larger than those displacements that are induced by thermal expansion, the $P_{upile\text{-}Y}\Delta_\ell$-moments that are associated with thermal contraction will govern for the pile design. For the strength evaluation of an abutment-backwall pile, concrete creep and shrinkage of the bridge superstructure will be conservatively included in the evaluation of the displacement Δ_ℓ by Eq. 8.36. With the displacement Δ_ℓ set equal to the displacement $d\ell_{contract}$ that was computed using Eq. 9.27, the factored-level, second-order, bending moment, M_{ut2nd}, at the top of an abutment-backwall pile, which is induced by the displacement of the pile head in a direction that is parallel to the ℓ-axis of the bridge superstructure, is expressed as

$$M_{ut2nd} = \left(\frac{P_{upile\text{-}Y}\, d\ell_{contract}}{2}\right) = \left[\frac{(81)(2.33)}{2}\right] = 94 \text{ in.-kips} \tag{9.94}$$

The total bending moment, in an abutment-backwall pile is equal to the sum of the first-order, bending moment (gravity-moment) and the second-order, bending moment (PΔ-moment). For an abutment-backwall pile of the Guthrie County Bridge, the total, factored-level, bending moment, M_{ut} that acts about an axis that is parallel to the t-axis for the bridge superstructure is given by

$$M_{ut} = \left(M_{ut-gravity} + M_{ut2nd}\right) = (169 + 94) = 263 \text{ in.-kips} \tag{9.95}$$

The transverse displacements, dt, of the abutment will also induce second-order, bending moments, $M_{u\ell 2nd}$, ($P_{upile\text{-}Y}\Delta_t$-moments) that act about an axis that is parallel to the ℓ-axis of the bridge superstructure are induced in an abutment-backwall pile for both thermal expansion and contraction of the bridge superstructure. However, since the displacement dt at the top of an abutment-backwall pile is normally significantly smaller than the displacement dℓ, moment $M_{u\ell 2nd}$ will be smaller than the moment M_{ut2nd}. If the displacement dt is set equal to the maximum transverse displacement, dt_{max}, of the abutment, a conservative solution will be obtained for this PΔ-moment. From Section 9.5 the displacement, dt_{max}, for this bridge is limited to 0.030 in. The second-order, bending moment, $M_{u\ell 2nd}$, at the top of an abutment-backwall pile, which is induced by the displacement of the pile head in a direction that is parallel to the t-axis of the bridge superstructure, is expressed as

$$M_{u\ell 2nd} = \left(\frac{P_{upile\text{-}Y}\,dt_{max}}{2}\right) = \left[\frac{(81)(0.028)}{2}\right] = 1 \text{ in.-kips} \tag{9.96}$$

For abutment-backwall pile of the Guthrie County Bridge, the total, factored-level, bending moment, $M_{u\ell}$ that acts about an axis that is parallel to the ℓ-axis for the bridge superstructure, is given by

$$M_{u\ell} = \left(M_{u\ell-gravity} + M_{u\ell 2nd}\right) = (0+1) = 1 \text{ in.-kips} \tag{9.97}$$

The bending moments M_{ut} and $M_{u\ell}$ need to be resolved into bending-moment components M_{ux} and M_{uy} about the x-axis and y-axis, respectively, of a pile. For the Guthrie County Bridge, these moment components are given by

$$M_{ux} = \left(M_{ut}\sin\theta_r + M_{u\ell}\cos\theta_r\right) = \left[(263)\left(\sin 30^o\right) + (1)\left(\cos 30^o\right)\right] = 132 \text{ in.-kips} \qquad (9.98)$$

$$M_{uy} = \left(M_{ut}\cos\theta_r - M_{u\ell}\sin\theta_r\right) = \left[(263)\left(\cos 30^o\right) - (1)\left(\sin 30^o\right)\right] = 227 \text{ in.-kips} \qquad (9.99)$$

where, positive-moment vectors for the moments $M_{u\ell}$ and M_{ut} are directed along the positive ℓ-axis and positive t-axis directions, respectively.

For a fixed-head pile, the design, effective-length factors, K_x and K_y for flexural buckling about the x-axis and y-axis, respectively, are both equal to 0.65. For the HP10X42 piles at the Guthrie County Bridge, Table 9.1 lists the equivalent-length, L_{ebx}, for flexural buckling about the x-axis at 15.5 ft; the equivalent-length, L_{eby}, for flexural buckling about the y-axis at 12.6 ft; and the equivalent-length, L_{emx}, for x-axis bending at 13.5 ft. The AASHTO Standard Specification for Highway Bridges (1998) has implied, resistance factors and for axial compression, ϕ_c, and bending, ϕ_f, which are equal to 0.85 and 1.00, respectively. Applying these design parameters, the design strengths of an HP10X42, which is a non-compact section, are evaluated as

$$P_r = 348 \text{ kips} \qquad (9.100)$$

$$M_{rx} = 1739 \text{ in.-kip} \qquad (9.101)$$

$$M_{ry} = 784 \text{ in.-kips} \qquad (9.102)$$

A substitution of the required, factored-level strengths and the design strengths into Eq. 8.214 gives

$$\frac{P_u}{P_r} + \frac{8}{9}\left(\frac{M_{ux}}{M_{rx}} + \frac{M_{uy}}{M_{ry}}\right) = \left[\frac{81}{348} + \frac{8}{9}\left(\frac{132}{1739} + \frac{287}{784}\right)\right] = 0.626 < 1.0 \qquad (9.103)$$

Equation 9.103 shows that an HP10X42 pile for an abutment backwall of the Guthrie County Bridge satisfies the strength-interaction-limit state.

9.7.2. Pile ductility

The displacements that are induced by temperature changes and concrete creep and shrinkage for an integral abutment in the ℓh-plane of the bridge superstructure and along the longitudinal direction of the Guthrie County Bridge were evaluated in Section 9.4. As discussed in Section 8.4.4, concrete creep and shrinkage contributions to the bridge longitudinal movements can be neglected when evaluating the ductility performance of an integral-abutment pile. Pile ductility needs to be evaluated for the displacement conditions at the pile head of maximum expansion (Displacement Case 1), maximum contraction (Displacement Case 2), and maximum re-expansion (Displacement Case 3) of the bridge superstructure. For Displacement Cases 1 and 2, the total change in the average bridge temperature, ΔT, is used to evaluate pile ductility. However, for pile ductility that is associated with Displacement Case 3, the change in the average bridge temperature is set equal to one-half of the total temperature change to account for the long-term, steady-state position of the abutment piles along the longitudinal axis of the bridge. This pile position is associated with no flexural-bending strains in the piles and is effected by soil consolidation and soil creep behind the abutment and along the length of the abutment piles, as discussed in Section 8.7.1.

The ductility of the abutment backwall piles for the Guthrie County Bridge that is evaluated in Examples 9.24 and 9.25 illustrates a proposed, pile-ductility, limit state that was presented by the ISU researchers in Section 8.9.2. This limit state represents a

proposed modification by the ISU researchers to the present, pile-ductility limit state that was developed by Greimann, et al. (1987a and 1987b) and was incorporated by the Office of Bridges and Structures in the Iowa Department of Transportation (Iowa DOT) into their design standards for integral-abutment bridges. To date (June of 2005), the proposed, pile-ductility limit state has not been adopted by the Iowa DOT and should not be applied by bridge designers for the State of Iowa.

Example 9.24 _____

Evaluate the ductility requirement for an abutment-backwall pile for the Guthrie County Bridge.

Solution:

For the Guthrie County Bridge, the thermally-induced, longitudinal displacements at the top of a pile for an abutment backwall were calculated in Section 9.4 as 0.91 in., -1.04 in., and 1.61 in. for maximum expansion, maximum contraction, and maximum re-expansion, respectively, of the bridge superstructure, when the displacements are neglected for concrete creep and shrinkage. These three displacements include the temperature-induced, displacement-factors (Γ-factors) of 1.60, 1.35, and 1.25, for Displacement Cases 1, 2, and 3, respectively, which were recommended by Oesterle, et al. (1999). The longitudinal displacement that governs the pile-ductility, limit state is the largest of 0.91 in., 1.04 in., and one-half of 1.61 in. These predicted displacements indicate that the thermal expansion and re-expansion of the bridge superstructure will not govern the ductility-limit state for the abutment piles. Therefore, pile ductility will be checked for only thermal contraction of the bridge superstructure. From Section 9.5 the

maximum, transverse displacement, dt_{max}, for an integral abutment in this bridge is limited to 0.030 in. For the thermal contraction of the superstructure of the Guthrie County Bridge, the horizontal displacements in the x-axis and y-axis directions at the top of an abutment pile are evaluated by Eqs. 8.248 and 8.249, respectively.

$$\Delta_x = \left[(d\ell)\cos\theta_r - (dt)\sin\theta_r\right] = \left[(-1.04)\cos\left(30^o\right) - (+0.030)\ \sin\left(30^o\right)\right] = -0.92\,\text{in.} \quad (9.104)$$

$$\Delta_y = \left[(d\ell)\sin\theta_r + (dt)\cos\theta_r\right] = \left[(-1.04)\sin\left(30^o\right) + (+0.030)\ \cos\left(30^o\right)\right] = -0.49\,\text{in.} \quad (9.105)$$

where, the pile-skew angle, θ_r, is equal to 30 deg. This angle is measured between the t-axis for the bridge superstructure and the y-axis for an abutment pile, as shown in Figs. 8.14 and 8.30.

For an HP10X42 abutment-backwall pile at the Guthrie County Bridge, the local-buckling factor, C_i, which is expressed by Eq. 8.222, and the horizontal displacements, which are expressed by rewritten forms of Eq. 8.243 for x-axis and y-axis bending moments at the pile head that are associated with the plastic-moment resistances M_{py} and M_{px}, are respectively given by

$$C_i = \left[\frac{0.56\sqrt{\dfrac{E}{F_y}} - \dfrac{b_f}{2t_f}}{0.25\sqrt{\dfrac{E}{F_y}}}\right] = \left[\frac{0.56\sqrt{\dfrac{29000}{36}} - 12.0}{0.25\sqrt{\dfrac{29000}{36}}}\right] = 0.528 \quad (9.106)$$

$$\Delta_{px} = \frac{M_{py}L_{emy}{}^2}{6EI_y} = \frac{(65.4)(12)[(12.0)12]^2}{6(29000)71.7} = 1.30\ \text{in.} \quad (9.107)$$

$$\Delta_{py} = \frac{M_{px}L_{emx}{}^2}{6EI_x} = \frac{(144.9)(12)[(13.5)12]^2}{6(29000)210} = 1.25\ \text{in.} \quad (9.108)$$

where, the equivalent lengths L_{emx} and L_{emy} for x-axis and y-axis bending moment, respectively, were obtained from Table 9.1. The displacement capacities for an HP10X42 abutment-backwall pile along its x-axis direction and y-axis direction at the Guthrie County Bridge are expressed by Eqs. 8.250 and 8.251, respectively. The displacement capacities Δ_{cx} and Δ_{cy} are respectively evaluated as

$$\Delta_{cx} = \left[(\phi_{rc}) \frac{9}{2} C_i \Delta_{px} \right] = \left[(0.85) \left(\frac{9}{2} \right) (0.528)(1.30) \right] = 2.62 \text{ in.} \tag{9.109}$$

$$\Delta_{cy} = \left[(\phi_{rc}) \frac{9}{2} C_i \Delta_{py} \right] = \left[(0.85) \left(\frac{9}{2} \right) (0.528)(1.25) \right] = 2.52 \text{ in.} \tag{9.110}$$

A substitution of the pile-head displacements that includes a Γ-factor, as discussed in Section 8.6.1, and the pile-displacement capacities into Eq. 8.247 gives

$$\left(\frac{\Delta_x}{\Delta_{cx}} + \frac{\Delta_y}{\Delta_{cy}} \right) = \left(\frac{0.92}{2.62} + \frac{0.49}{2.52} \right) = 0.546 \leq 1.0 \tag{9.111}$$

Equation 9.111 shows that the A36-steel, HP10X42, piles for an abutment backwall satisfy the ductility-limit state.

The availability of A36-steel, HP-shaped steel piles with a yield strength equal to 36 ksi is limited, since trends in metallurgy are producing steels with higher yield strengths than the specified, minimum-yield strengths. If the yield strength of the abutment-backwall piles is actually closer to 50 ksi, the ductility-limit state will be different from that for steel with 36-ksi yield strength.

Example 9.25

Re-evaluate the ductility requirement for an abutment-backwall pile for the Guthrie County Bridge if the yield strength of the HP10X42, steel pile is equal to 50 ksi.

Solution:

The displacements Δ_x and Δ_y that were calculated from Eqs. 9.104 and 9.105, respectively, remain the same at -0.92 in., -0.49 in., respectively. The local-buckling factor, C_i, which is expressed by Eq. 8.222 is significantly affected by a change in the steel-yield strength, as shown by Eq. 9.112.

$$C_i = \left[\frac{0.56\sqrt{\frac{E}{F_y}} - \frac{b_f}{2t_f}}{0.25\sqrt{\frac{E}{F_y}}}\right] = \left[\frac{0.56\sqrt{\frac{29000}{50}} - 12.0}{0.25\sqrt{\frac{29000}{50}}}\right] = 0.237 \qquad (9.112)$$

For a 36-ksi-yield strength the C_i-factor was equal to 0.528. The displacements Δ_{px}, and Δ_{px} will increase when the yield strength is changed from 36 ksi to 50 ksi, as shown by Eqs. 9.113 and 9.114, respectively.

$$\Delta_{px} = \left(\frac{M_{py}L_{emy}{}^2}{6EI_y}\right) = \left\{\frac{(90.8)(12)[(12.0)(12)]^2}{6(29000)(71.7)}\right\} = 1.81\text{in.} \qquad (9.113)$$

$$\Delta_{px} = \left(\frac{M_{px}L_{emx}{}^2}{6EI_x}\right) = \left\{\frac{(201.2)(12)[(13.5)(12)]^2}{6(29000)(210)}\right\} = 1.74 \text{ in.} \qquad (9.114)$$

The displacement capacities Δ_{cx} and Δ_{cy} for an HP10X42, 50-grade steel, abutment-backwall pile along its x-axis direction and y-axis direction, respectively, at the Guthrie County Bridge are calculated as

$$\Delta_{cx} = \left[\phi_{rc}\left(\frac{9}{2}\right)C_i\Delta_{px}\right] = \left[(0.85)\left(\frac{9}{2}\right)(0.237)(1.81)\right] = 1.64 \text{ in.} \tag{9.115}$$

$$\Delta_{cy} = \left[\phi_{rc}\left(\frac{9}{2}\right)C_i\Delta_{py}\right] = \left[(0.85)\left(\frac{9}{2}\right)(0.237)(1.74)\right] = 1.58 \text{ in.} \tag{9.116}$$

A substitution of the pile-head displacements that includes a Γ-factor, as discussed in Section 8.6.1, and the pile-displacement capacities into Eq. 8.247 gives

$$\left(\frac{\Delta_x}{\Delta_{cx}} + \frac{\Delta_y}{\Delta_{cy}}\right) = \left(\frac{0.92}{1.64} + \frac{0.49}{1.58}\right) = 0.871 \leq 1.0 \tag{9.117}$$

Equation 9.117 shows that if the yield strength of the HP10X42 piles is equal to 50 ksi rather than 36 ksi, the abutment backwall piles would still satisfy the ductility-limit state.

9.8. Maximum bridge length

Many design-limit states, geometric conditions, and material properties affect the maximum permissible length of an integral-abutment bridge. Therefore, a specific maximum length can not be specified for all non-skewed or all skewed, PC-girder, integral-abutment bridges. Regarding the affect of the design-limit states on the length of a bridge, only the ductility requirements for the abutment-backwall piles will be considered in this section of the report. The biaxial-displacement relationship for a fixed-head, abutment-backwall pile in a skewed, integral-abutment bridge that was

presented in Section 8.10.2 will be applied to estimate the maximum bridge length. To simplify the iterative solution procedure for computing the maximum bridge length, the transverse displacement, dt, of the abutment will be set equal to the maximum transverse displacement, dt_{max}. The displacement dt_{max} is determined by the procedure presented in Appendix B and implemented in the Transmove software. With this approximation, the maximum bridge length is expressed as

$$L \le \left[\frac{2}{\Gamma\,\alpha_e(\Delta T)}\right]\left[\frac{\phi_{rc}\left(\frac{9}{2}\right)C_i\Delta_{px}\Delta_{py} + dt_{max}\left(\Delta_{py}\sin\theta_r - \Delta_{px}\cos\theta_r\right)}{\left(\Delta_{py}\cos\theta_r + \Delta_{px}\sin\theta_r\right)}\right] \qquad [8.261]$$

The maximum bridge length will be the minimum length that is established from Eqs. 8.261, when the longitudinal and transverse displacements of the abutment-backwall piles and the Γ-displacement factor are set equal to those parameters that are associated with the maximum expansion, maximum contraction, or maximum re-expansion of the bridge superstructure. When the effective, coefficient of expansion and contraction, α_e-coefficient, is based on experimentally-measured α-coefficients for the PC girders and the RC bridge deck, Oesterle, et al.'s (1999), Γ-factors are set equal to 1.60, 1.35, and 1.25 for Displacement Cases 1, 2, and 3, respectively. When the α_e-coefficient, is based on Emanuel and Husley's (1977) expression (Eq. 8.8) for the PC girders and the RC bridge deck, Oesterle, et al.'s (1999), Γ-factors are set equal to 2.05, 1.45, and 1.25 for Displacement Cases 1, 2, and 3, respectively. These three thermal conditions for the bridge superstructure were discussed in Section 8.6.1, and the

associated longitudinal displacements for an integral abutment were denoted as Displacement Cases 1, 2, and 3, respectively, in Section 8.7.1.

The maximum bridge lengths that are evaluated in Examples 9.26 and 9.31 illustrate the application of an approach that is based on the proposed, pile-ductility limit state, which was presented by the ISU researchers in Section 8.9.2. The application of this proposed approach will produce a predicted, maximum bridge length that may be larger or smaller than that length, which is predicted by a previous method that was presented by Greimann, et al. (1987a and 1987b). To date (June of 2005), the proposed approach to establish the maximum bridge length has not been adopted by the Office of Bridges and Structures in Iowa DOT and should not be applied by bridge designers for the State of Iowa. Currently, an Iowa DOT, design standard exists for the determination of the maximum length for non-skewed and skewed, integral-abutment bridges.

Example 9.26 _____

Determine the maximum length of an integral-abutment bridge that, except for the pile-skew angle, θ_r, and the bridge-skew angle, θ, has the same geometric and material parameters as those for the Guthrie County Bridge. Assume that the α_e-coefficient, which is equal to 6.1×10^{-6} for the bridge superstructure, was based on experimentally-measured α-coefficients for the PC girders and the RC bridge deck. Establish the effect of either y-axis (weak-axis) bending or x-axis (strong-axis) bending of the abutment-backwall piles on the maximum bridge length, when the bridge-skew angle varies between 0 deg. and 45 deg.

Solution:

Many parameters affect the variables in Eq. 8.261. The geometric and material parameters that are listed in Table 9.7 will be used in this example. The abutment piles are HP10X42, A36-steel piles that are driven through 8-ft deep, pre-bored holes. When the pile-skew angle, 2_r, for the ten, abutment-backwall piles is equal to 0 deg. or 90 deg., these piles are orientated with their webs parallel to the t-axis (transverse axis) or ℓ-axis (longitudinal axis), respectively, of the bridge superstructure. These pile orientations were respectively shown in Fig. 8.14 as a Type-C or a Type-D, pile orientation during a thermal expansion or contraction of the bridge superstructure. The pile-skew angle for each sidewall pile was 0 deg. For the pile-ductility-limit state, the effective lengths of a pile that need to be calculated are those lengths that are associated with the curvatures for the elastic curve of a pile with respect to both the x-axis and y-axis of a pile cross section for both the horizontal-stiffness and bending-moment equivalencies. The effective lengths L_{ebx} and L_{eby} for flexural-buckling equivalency of a pile were not needed, since these lengths are associated with the axial compressive strength of a pile and with moment magnification for the limit state involving axial compression and biaxial-bending moments. The approach that was used to establish the effective lengths of a pile was presented in Section 8.5. Example 9.6 illustrates the calculation of the effective length L_{ehy}. For each principal axis of a pile cross section, Tables 9.1 and 9.7 list the effective lengths for the horizontal-stiffness and bending-moment equivalencies, and Table 9.1 also lists the effective lengths for the flexural-buckling equivalencies for the abutment piles in the Guthrie County Bridge.

The change in the average bridge temperature is a parameter that has the most significant affect on the maximum length for an integral-abutment bridge. Table 9.7 lists the three critical temperature changes that need to be considered in the evaluation of the maximum bridge length. These temperature changes were multiplied by the associated Γ-factor, as recommended by Oesterle, et al. (1999), to account for uncertainties that are related to the displacement of an abutment pile head in a direction that is parallel to the longitudinal direction of the bridge superstructure. As shown in Table 9.7, a Γ-factor that was equal to 1.60, 1.35, and 1.25 was used for Displacement Cases 1, 2, and 3, respectively, that had a change in the average temperature for the bridge superstructure that was equal to 49 ^{o}F, 66 ^{o}F, and one-half of 115 ^{o}F, respectively. For re-expansion of the bridge superstructure (Displacement Case 3), one-half of the change in the temperature was applied to account for the effect of soil consolidation and soil creep on the long-term location for the horizontal position of an abutment pile along the length of the bridge that corresponds with the steady-state condition of flexural-bending strains in the pile, which was discussed in Section 8.7.1. Displacement Case 2, which corresponds with the maximum contraction of the bridge superstructure, controlled the maximum length of a bridge that has most of the geometric and material properties (including the soil properties behind the abutments) that are the same as those for the Guthrie County Bridge.

Figure 9.15 shows two graphs for the maximum bridge length, L_{max}, versus the bridge-skew angle, 2, for integral-abutment bridges that have two different orientations for the backwall piles. These graphs were developed for the geometric and material properties that are listed in Table 9.7. This figure shows that longer, integral-abutment

bridges can be constructed when the backwall piles are orientated for weak-axis bending than when these piles are orientated for strong-axis bending. Also, this figure shows that when the bridge-skew angle is about 40 deg., the greatest difference occurs in the maximum bridge lengths for the two pile orientations. Maximum bridge lengths of about 800 ft or 770 ft occur for bridge-skew angles less that about 25 deg. and when the backwall piles are orientated for weak-axis bending or strong-axis bending, respectively. For bridge-skew angles between 0 deg. and about 25 deg. transverse displacements do not occur for the integral abutments for either pile orientation.

The graphical results that were shown in Fig. 9.15 for this example depend on very specific design parameters. Bridge designers should not assume that the design parameters that were used to generate these graphs are representative of those design parameters that are associated with any proposed, integral-abutment bridge. As illustrated by Examples 9.29, 9.30, and 9.31, if some of the design parameters are changed from those listed in Table 9.7, the predicted, maximum bridge length can vary considerably from the lengths shown in Fig. 9.7. Also, Example 9.26 has only addressed a proposed, pile-ductility limit state. Other limit states, which may limit the maximum bridge length, need to be addressed for a final design of an integral-abutment bridge.

Example 9.27 _____

Calculate the maximum bridge length for a non-skewed, integral-abutment bridge that, except for the bridge-skew angle and the pile-skew angle for the abutment-backwall piles, has the geometric and material properties that are listed in Table 9.7.

The abutment piles are orientated for y-axis (weak-axis) bending for bridge expansion and contraction, and the α_e-coefficient is based on experimental measurements.

Solution:

From Table 9.7, the critical, factored-temperature change corresponds with the maximum contraction (Displacement Case 2) of the bridge superstructure. The maximum bridge length is computed using Eq. 8.258.

$$L \le \left[\frac{\phi_{rc}\left(9C_i\Delta_{px}\right)}{\Gamma\,\alpha_e(\Delta T)}\right] = \left[\frac{(0.85)(9)(0.528)(1.30)}{(1.35)(0.0000061)(66)(12)}\right] = 805 \text{ ft} \qquad (9.118)$$

where, the design parameters C_i and Δ_{px} were computed using Eqs. 9.106 and 9.107, respectively.

Example 9.28 _____

Calculate the maximum bridge length for a 40-deg.-skewed, integral-abutment bridge that, except for the bridge-skew angle and the pile-skew angle for the abutment-backwall piles, has the geometric and material properties that are listed in Table 9.7. The abutment piles are orientated for y-axis (weak-axis) bending for bridge expansion and contraction, and the α_e-coefficient is based on experimental measurements.

Solution:

From Table 9.7, the critical, factored-temperature change corresponds with the maximum contraction (Displacement Case 2) of the bridge superstructure. The maximum bridge length is computed using an iterative solution for Eq. 8.261, with the pile-head displacement dt set equal to dt_{max} for an abutment-backwall pile.

Step 1: Select the displacement factor Γ equal to 1.35; coefficient of thermal expansion and contraction α_e equal to 6.1×10^{-6} in./in.; and the change in the average, bridge temperature ΔT equal to 66 °F.

Step 2: Estimate the maximum bridge length, L_{max} at 500 ft.

Step 3: Establish the transverse displacement, dt_{max}, of the abutment using the Transmove software (dt_{max} = 0.698 in.).

Step 4: Calculate the length L_{max} using Eq. 9.119.

$$L \le \left[\frac{2}{\Gamma\,\alpha_e(\Delta T)}\right]\left[\frac{\phi_{rc}\left(\frac{9}{2}\right)C_i\Delta_{px}\Delta_{py} + dt_{max}\left(\Delta_{py}\sin\theta_r - \Delta_{px}\cos\theta_r\right)}{\left(\Delta_{py}\cos\theta_r + \Delta_{px}\sin\theta_r\right)}\right] \qquad (9.119)$$

where, the design parameter Δ_{py} is calculated using Eq. 9.108 and the remaining terms are expressed in Eqs. 9.120 through 9.123.

$$\frac{2}{\Gamma\,\alpha_e(\Delta T)} = \left[\frac{2}{(1.35)(0.0000061)(66)}\right] = 3{,}680 \text{ in./in.} \qquad (9.120)$$

$$\phi_{rc}\left(\frac{9}{2}\right)C_i\Delta_{px}\Delta_{py} = \left[(0.85)\left(\frac{9}{2}\right)(0.528)(1.30)(1.25)\right] = 3.282 \text{ in.}^2 \qquad (9.121)$$

$$dt_{max}\left(\Delta_{py}\sin\theta_r - \Delta_{px}\cos\theta_r\right) = 0.698\left[(1.25)\left(\sin 0^o\right) - (1.30)\left(\cos 0^o\right)\right]$$

$$= -0.907 \text{ in}^2. \qquad (9.122)$$

$$\left(\Delta_{py}\cos\theta_r + \Delta_{px}\sin\theta_r\right) = \left[(1.25)\left(\cos 0^o\right) + (1.30)\left(\sin 0^o\right)\right] = 1.25 \text{ in.} \qquad (9.123)$$

Substituting these terms into Eq. 9.116 gives

$$L \le 3680\left[\frac{3.282+(-0.907)}{1.25(12)}\right] = 583 \text{ ft} \tag{9.124}$$

Step 5: Compare the lengths L_{max} from Steps 2 and 4. The assumed maximum bridge length of 500 ft is less than the calculated, maximum bridge length of 583 ft.

Step 6: Repeat Steps 2 through 5 until acceptable convergence is obtained for the length L_{max}.

Step 2: Estimate the maximum bridge length, L_{max}, at 580 ft.

Step 3: Establish the transverse displacement, dt_{max}, of the abutment using the Transmove software (dt_{max} = 0.703 in.).

Step 4: Calculate the length L_{max} using Eq. 9.119, where

$$dt_{max}\left(\Delta_{py}\sin\theta_r - \Delta_{px}\cos\theta_r\right) = 0.703\left[(1.25)\left(\sin 0^\circ\right) - (1.30)\left(\cos 0^\circ\right)\right]$$

$$= -0.914 \text{ in.}^2 \tag{9.125}$$

Substituting the terms evaluated by Eqs. 9.120, 9.121, 9.123, and 9.125 into Eq. 9.116 gives

$$L \le 3680\left[\frac{3.282+(-0.914)}{1.25(12)}\right] = 581 \text{ ft} \tag{9.126}$$

Step 5: Compare the lengths L_{max} from Steps 2 and 4. The assumed maximum bridge length of 580 ft is sufficiently close to the calculated, maximum bridge length of 581 ft.

Therefore, to satisfy the ductility-limit state for the abutment piles, the maximum length for a 40-deg.-skewed, integral-abutment bridge that has the abutment-backwall piles orientated at a 0-deg.-skew angle and that has the other geometric and material properties that match those for the Guthrie County Bridge is equal to 581 ft. As shown in Fig. 9.15, this length corresponds with the maximum bridge length that is obtained from the intersection point between the graph for weak-axis bending of the abutment-backwall piles and the abscissa value for a 40-deg.-bridge-skew angle.

Example 9.29

Re-solve Example 9.27 if 50-grade steel is used for the abutment piles.

Solution:

The maximum bridge length is computed using Eq. 8.258.

$$L \le \left[\frac{\phi_{rc}\left(9C_i\Delta_{px}\right)}{\Gamma\,\alpha_e(\Delta T)} \right] = \left[\frac{(0.85)(9)(0.237)(1.81)}{(1.35)(0.0000061)(66)(12)} \right] = 503 \text{ ft} \tag{9.127}$$

where, the design parameters C_i and Δ_{px} are evaluated using Eqs. 9.112 and 9.113, respectively. The change in the yield strength of the steel piles from 36 ksi to 50 ksi has significantly altered the inelastic-rotation capacity of the HP10X42 steel piles. The resulting decrease in pile ductility has reduced the maximum bridge length from 803 ft to 503 ft.

Example 9.30

Re-solve Example 9.28 if 50-grade steel is used for the abutment piles.

Solution:

The iterative solution for the maximum bridge length is started at Step 2 for re-solving Example 9.28. After some initial iterative steps, the last iteration cycle is as follows:

Step 2: Estimate the maximum bridge length, L_{max}, at 300 ft.

Step 3: Establish the transverse displacement, dt_{max}, of the abutment using the Transmove software (dt_{max} = 0.670 in.).

Step 4: Calculate the length L_{max} using Eq. 9.119, where the design parameter Δ_{py} is calculated using Eq. 9.108 and the remaining terms are expressed in Eqs. 9.128 through 9.130.

$$\phi_{rc}\left(\frac{9}{2}\right)C_i\Delta_{px}\Delta_{py} = \left[(0.85)\left(\frac{9}{2}\right)(0.237)(1.81)(1.74)\right] = 2.855 \text{ in.}^2 \qquad (9.128)$$

$$dt_{max}\left(\Delta_{py}\sin\theta_r - \Delta_{px}\cos\theta_r\right) = 0.670\left[(1.74)\left(\sin 0^\circ\right) - (1.81)\left(\cos 0^\circ\right)\right]$$

$$= -1.166 \text{ in.}^2 \qquad (9.129)$$

$$\left(\Delta_{py}\cos\theta_r + \Delta_{px}\sin\theta_r\right) = \left[(1.74)\left(\cos 0^o\right) + (1.81)\left(\sin 0^o\right)\right] = 1.74 \text{ in.} \qquad (9.130)$$

Substituting the terms evaluated by Eqs. 9.120, 9.128, 9.129, and 9.130 into Eq. 9.116 gives

$$L \le 3680\left[\frac{2.855 + (-1.166)}{1.74(12)}\right] = 298 \text{ ft} \qquad (9.131)$$

Step 5: Compare the lengths L_{max} from Steps 2 and 4. The assumed maximum bridge length of 300 ft is sufficiently close to the calculated, maximum bridge length of 298 ft.

The change in the yield strength of the steel piles from 36 ksi to 50 ksi has significantly altered the inelastic-rotation capacity of the HP10X42 steel piles. The resulting decrease in pile ductility has reduced the maximum bridge length from 581 ft to 298 ft.

Example 9.31 _____

Re-solve Example 9.27 if 50-grade steel is used for the abutment piles, and the α_e-coefficient is based on Emanuel and Husley's (1977) expression for determining the α-coefficient for the PC girders and the RC bridge deck.

Solution:

Since the effective, coefficient of expansion and contraction for the bridge superstructure was based on the use of Emanuel and Husley's expression, Oesterle, et al.'s (1999), Γ-factors become 2.05, 1.45, and 1.25 for Displacement Cases 1, 2, and 3, respectively. The corresponding Γ(ΔT)-values become 100 ^{o}F, 96 ^{o}F, and 72 ^{o}F, respectively, rather than the Γ(ΔT)-values that are listed in Table 9.7. The change in the Γ-factors causes Displacement Case 1, rather than Displacement Case 2, to limit the maximum bridge length, which is computed using Eq. 8.258.

$$L \le \left[\frac{\phi_{rc}\left(9C_i\Delta_{px}\right)}{\Gamma\,\alpha_e(\Delta T)}\right] = \left[\frac{(0.85)(9)(0.237)(1.81)}{(2.05)(0.0000061)(49)(12)}\right] = 446 \text{ ft} \qquad (9.127)$$

where, the design parameters C_i and Δ_{px} are evaluated using Eqs. 9.112 and 9.113, respectively. The change in the yield strength of the steel piles from 36 ksi to 50 ksi and

the change from experimentally-measured α-coefficients to analytically-calculated α-coefficients for the PC girders and the RC bridge deck has significantly altered the inelastic-rotation capacity of the HP10X42 steel piles. The resulting decrease in pile ductility has reduced the maximum bridge length from 803 ft to 446 ft.

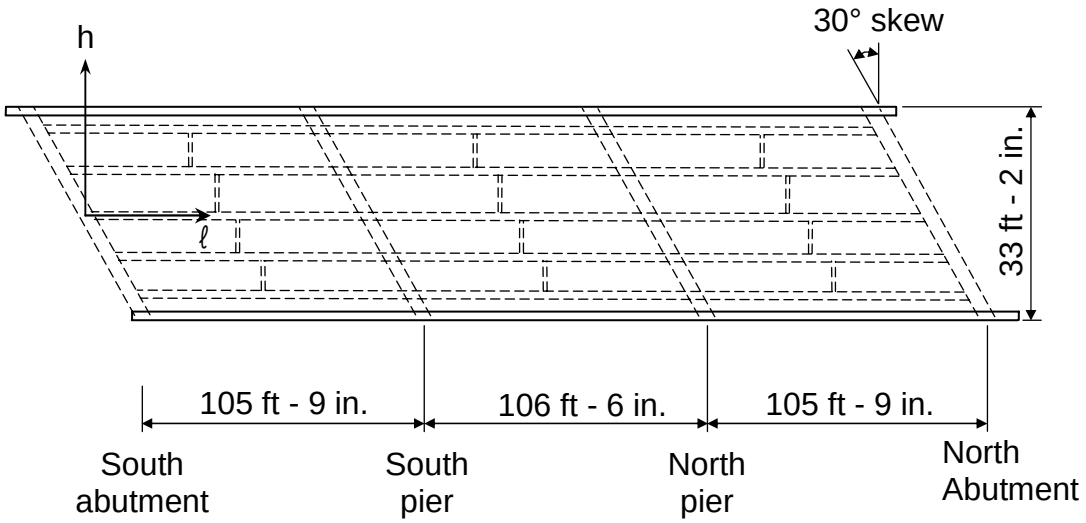

Figure 9.1. Plan view of the Guthrie County Bridge (not to scale)

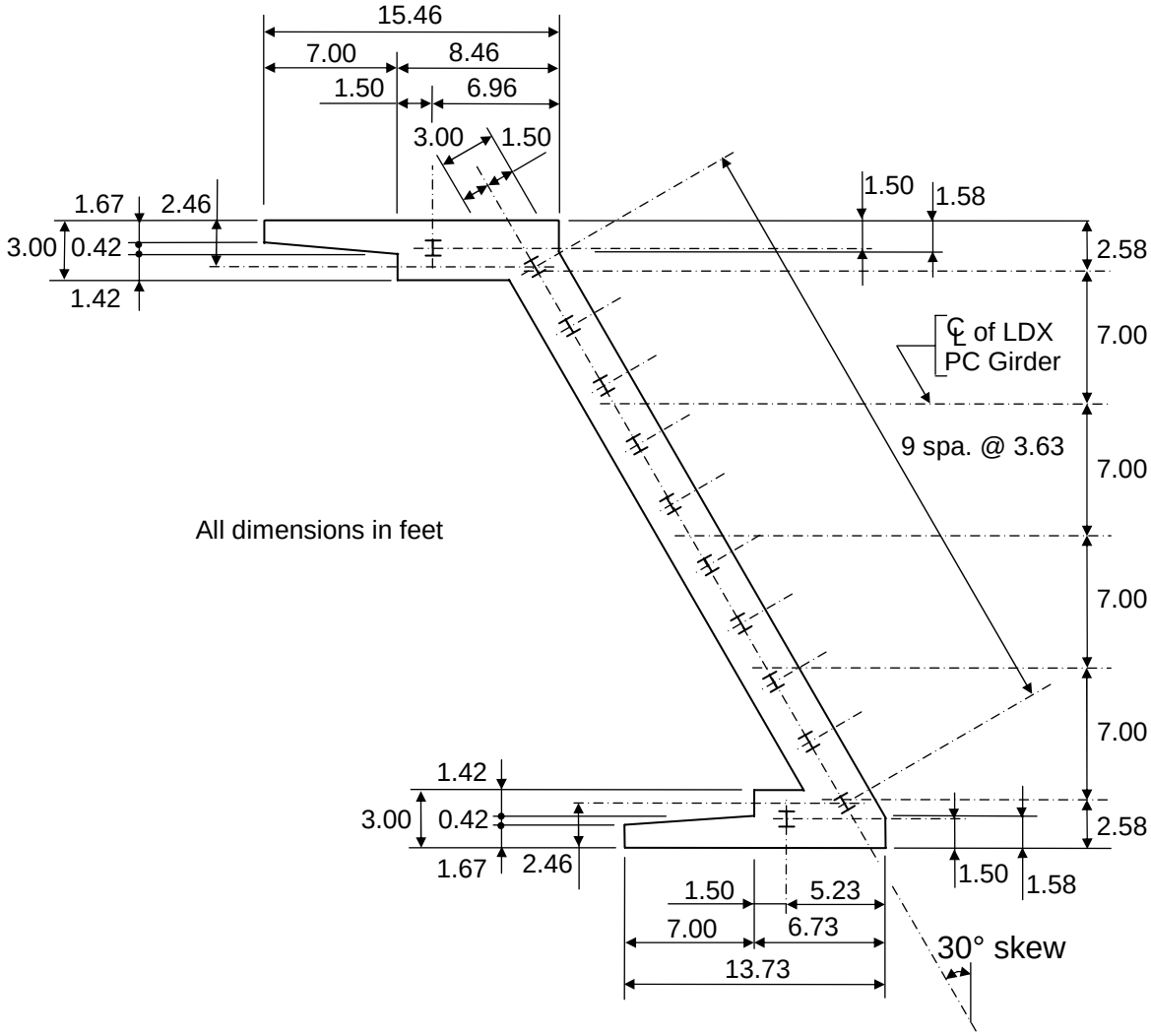

Figure 9.2. Plan view of the south abutment for the Guthrie County Bridge

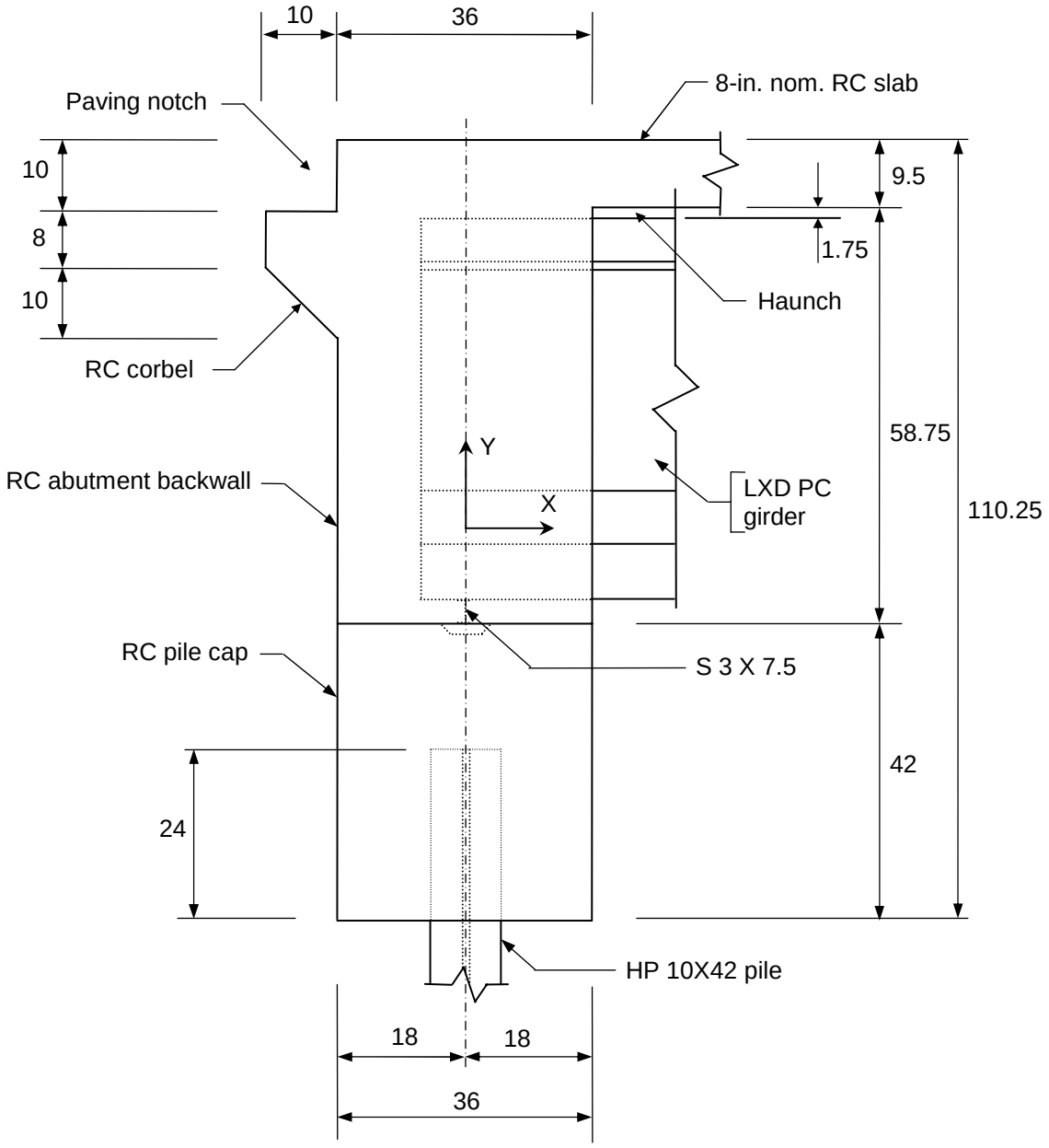

All dimensions are in inches

Figure 9.3. Vertical cross section of the south abutment for the Guthrie County Bridge (adapted from the Iowa DOT bridge drawings – File No. 54398)

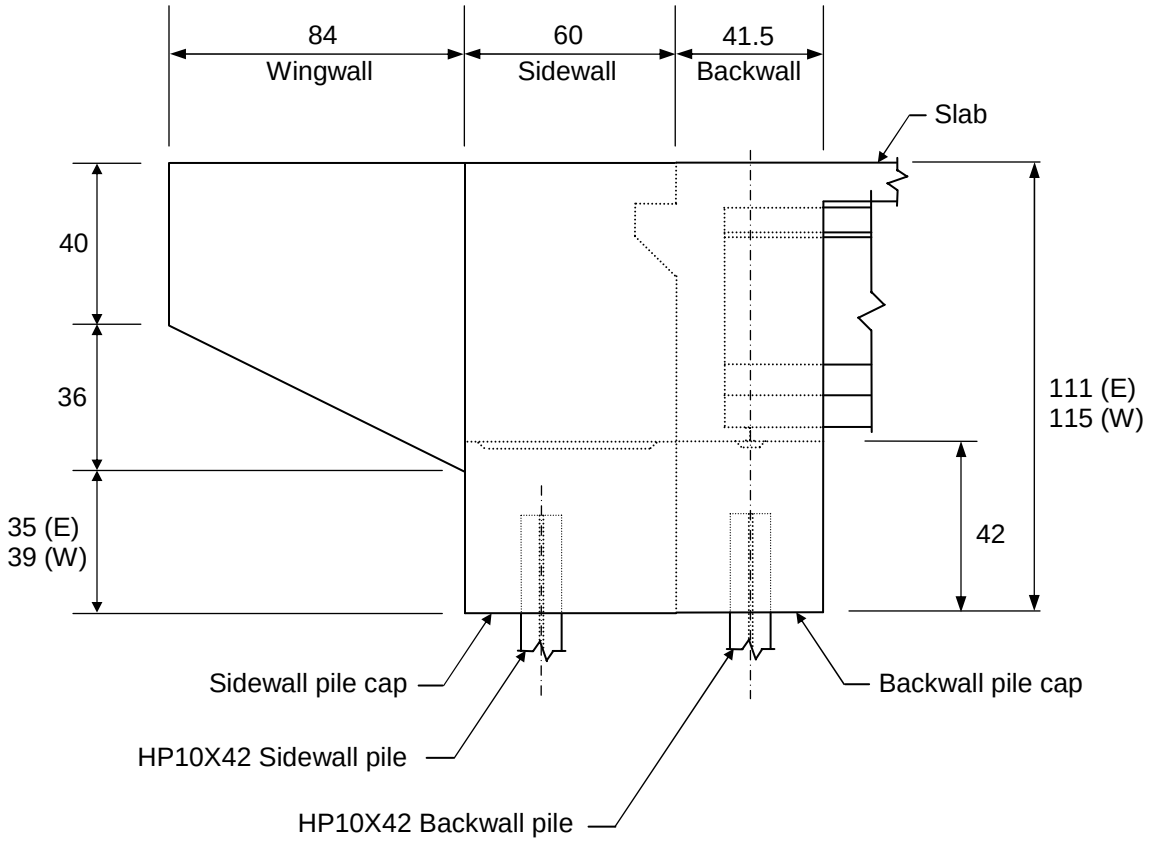

All dimensions are in inches

Figure 9.4. East elevation of the south abutment for the Guthrie County Bridge (adapted from the Iowa DOT bridge drawings – File No. 54398)

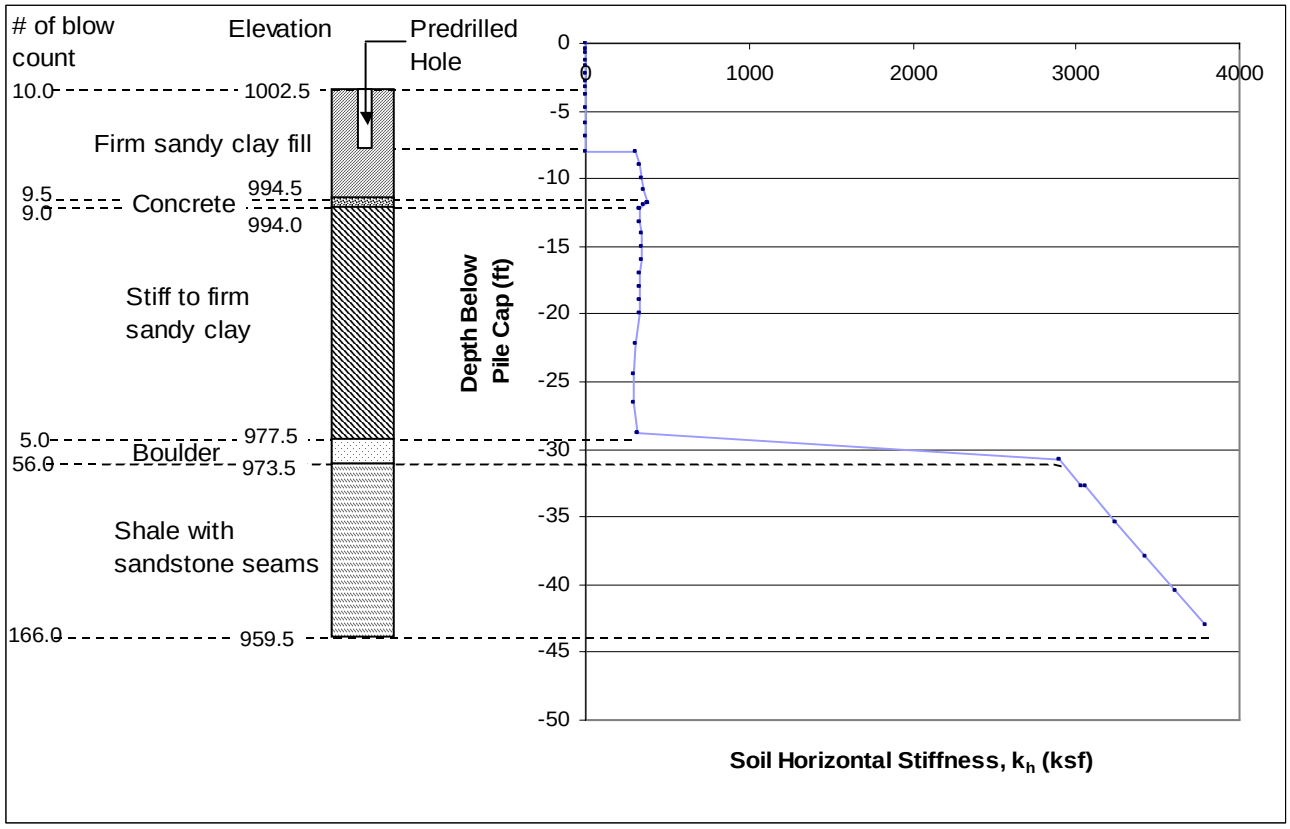

Figure 9.5. Soil profile and horizontal stiffness at the south abutment of the Guthrie County Bridge

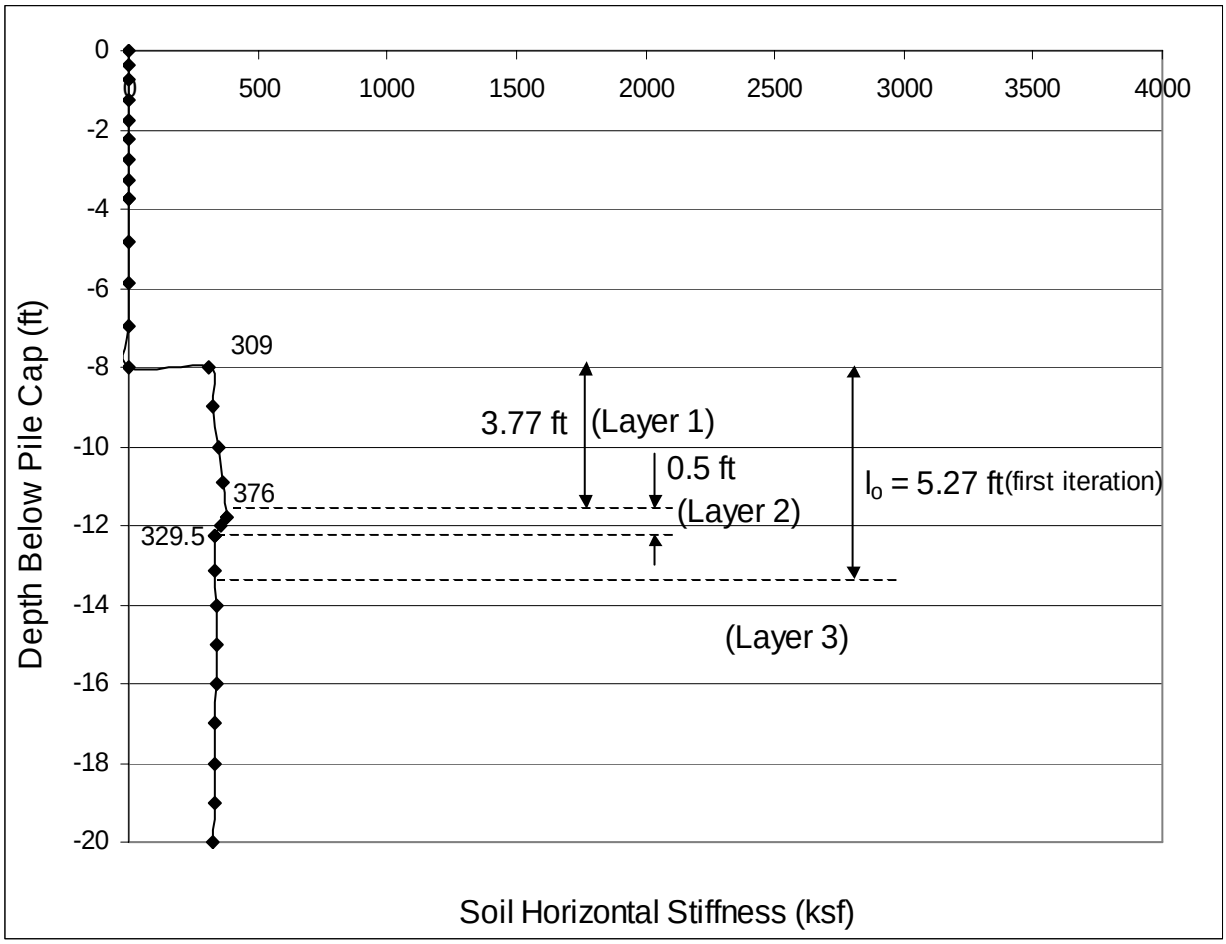

Figure 9.6. Horizontal stiffness of the upper 20 ft of soil at the south abutment of the Guthrie County Bridge

Click here for Instruction

Sample Input | Analyze | dt_{max} 0.0297 inches | Clear

Bridge Geometry		Pile Properties		Soil Properties		Miscelleneous	
L (ft)	318	N_{pa}	10	γ (pcf)	140	α_e (10^{+6} in./in./ ^{0}F)	6.1
W (ft)	34	$N_{p1} = N_{p2}$	1	φ (deg.)	37		
$h_{abut} = h_2$ (ft)	9.33	E (ksi)	29,000	δ (deg.)	22		
h_1 (ft)	8.5	F_y (ksi)	36				
$P_{w1}=P_{w2}$ (ft)	8.6	I_x (in.^{4})	210				
θ (deg.)	30	Z_x (in.^{3})	48.3				
θ_r (deg.)	30	I_y (in.^{4})	71.7				
		Z_y (in.^{3})	21.8				
		L_{ehx} (ft)	13.2				
		L_{ehy} (ft)	11.9				

Figure 9.7. Transmove software parameters for the Guthrie County Bridge

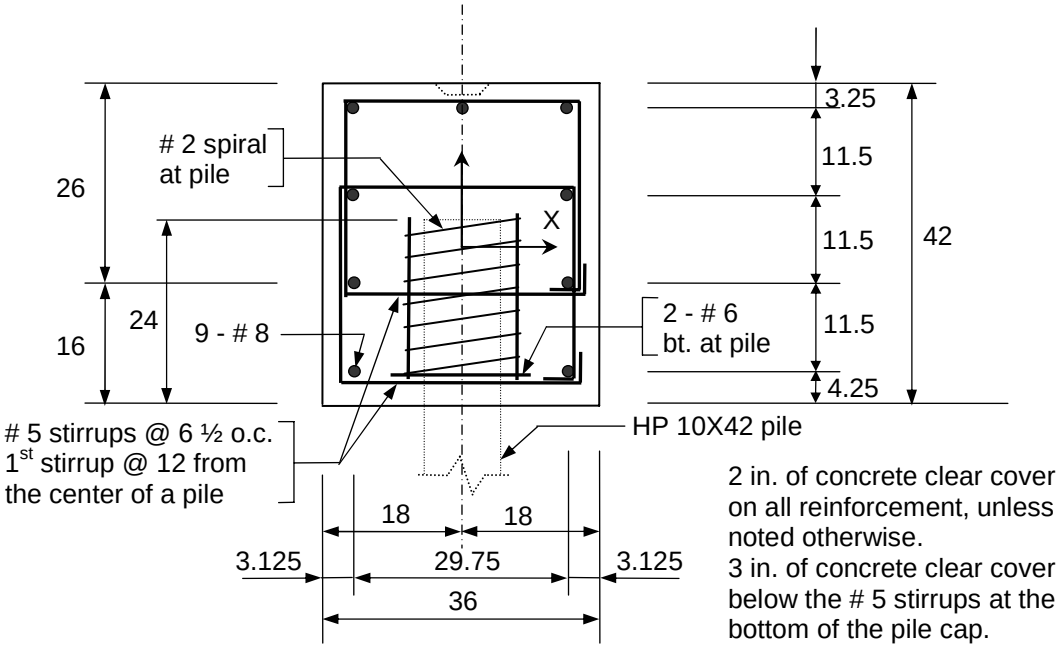

All dimensions are in inches

Figure 9.8. Backwall-pile-cap reinforcement for the Guthrie County Bridge (adapted from the Iowa DOT bridge drawings – File No. 54398)

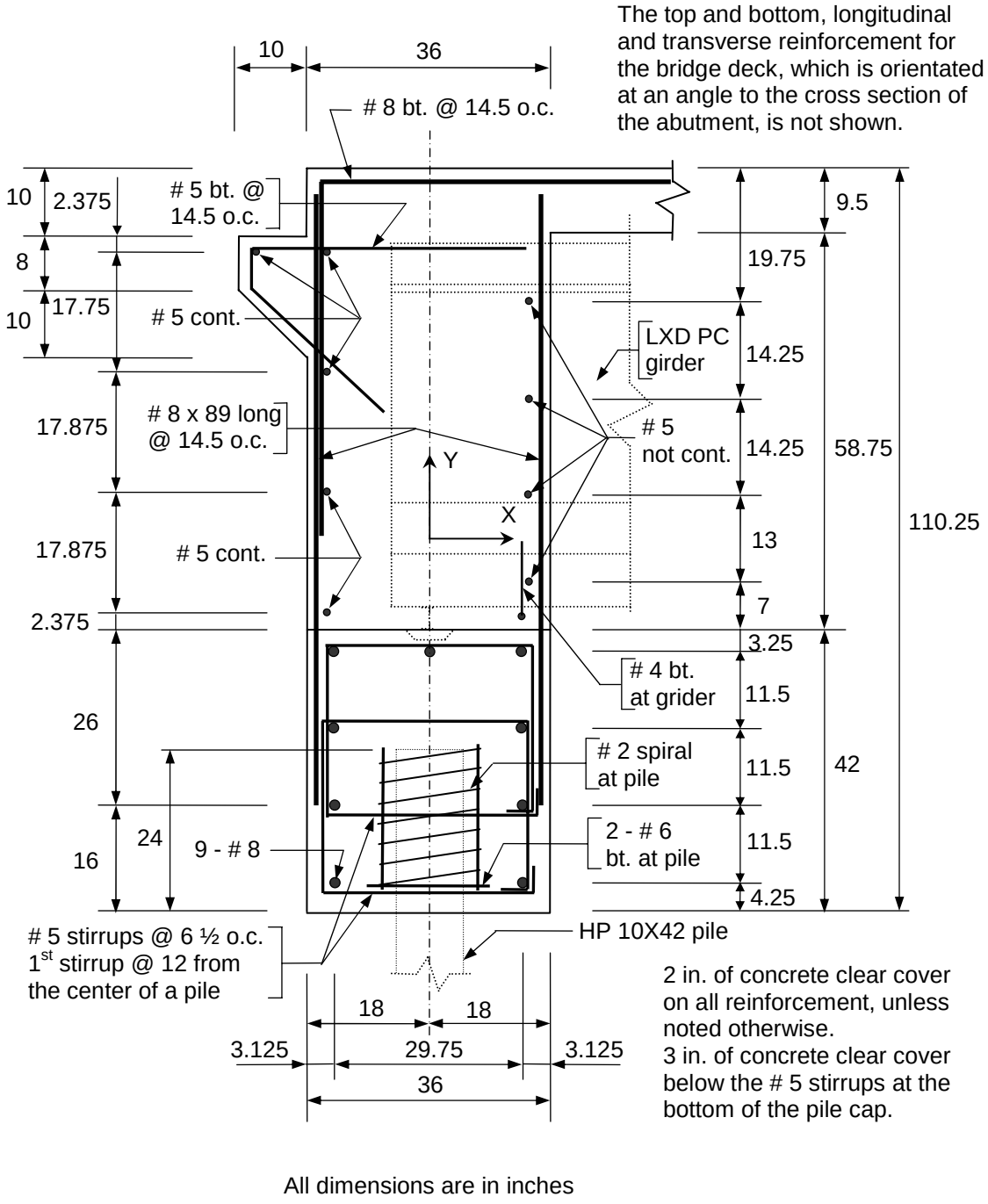

Figure 9.9. Composite backwall and backwall-pile-cap reinforcement for the Guthrie County Bridge (adapted from the Iowa DOT bridge drawings – File No. 54398)

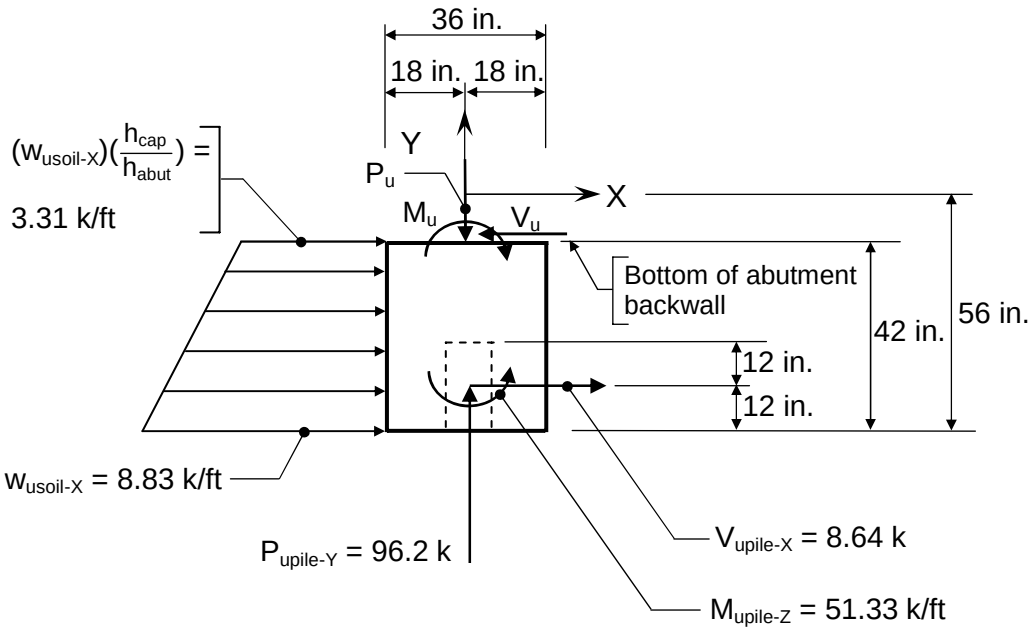

Figure 9.10. Free-body diagram of a backwall-pile cap with factored-level, thermally-induced forces for the Guthrie County Bridge

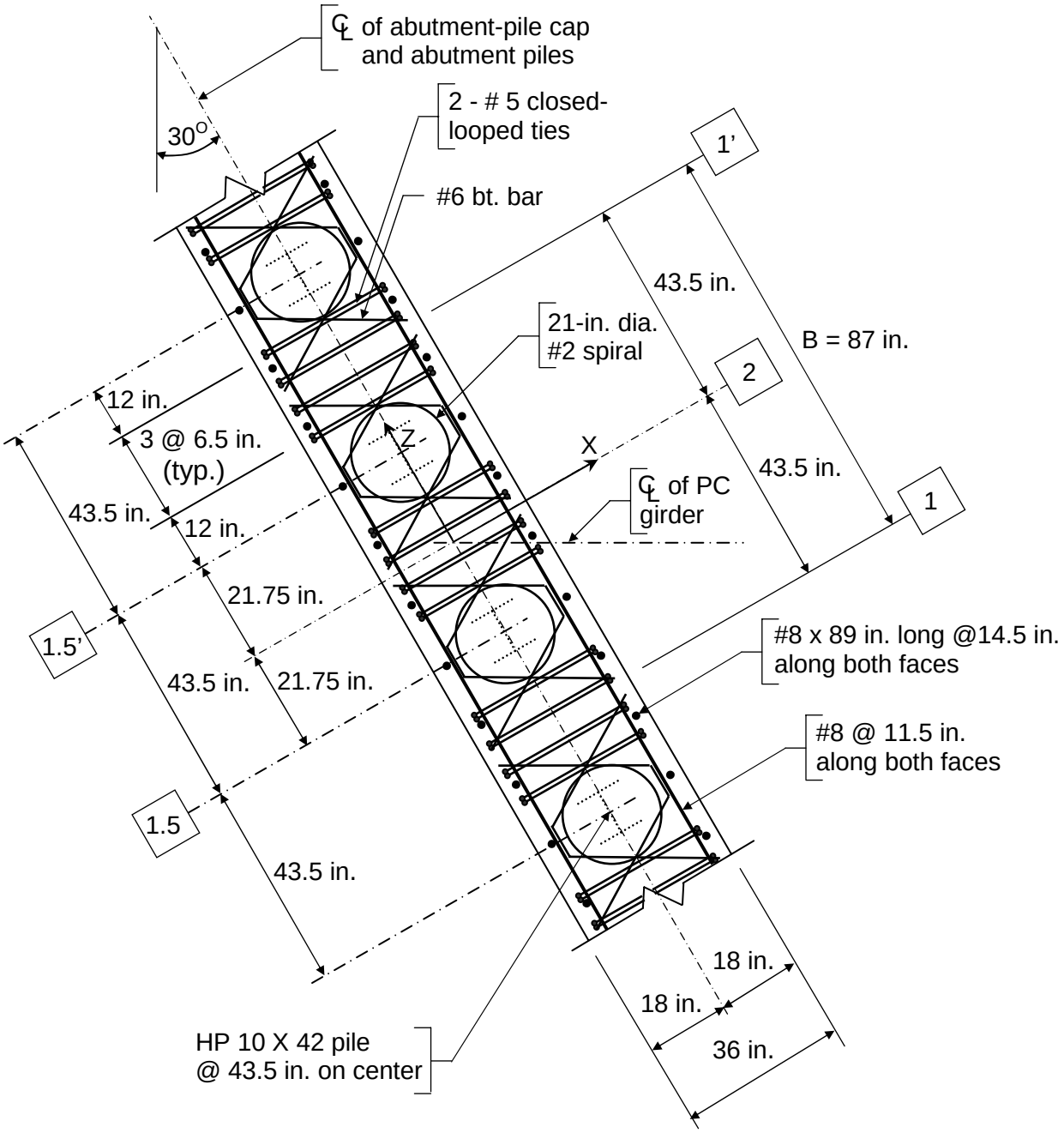

Figure 9.11. Partial XZ-plane cross section of a backwall-pile cap for the Guthrie County Bridge

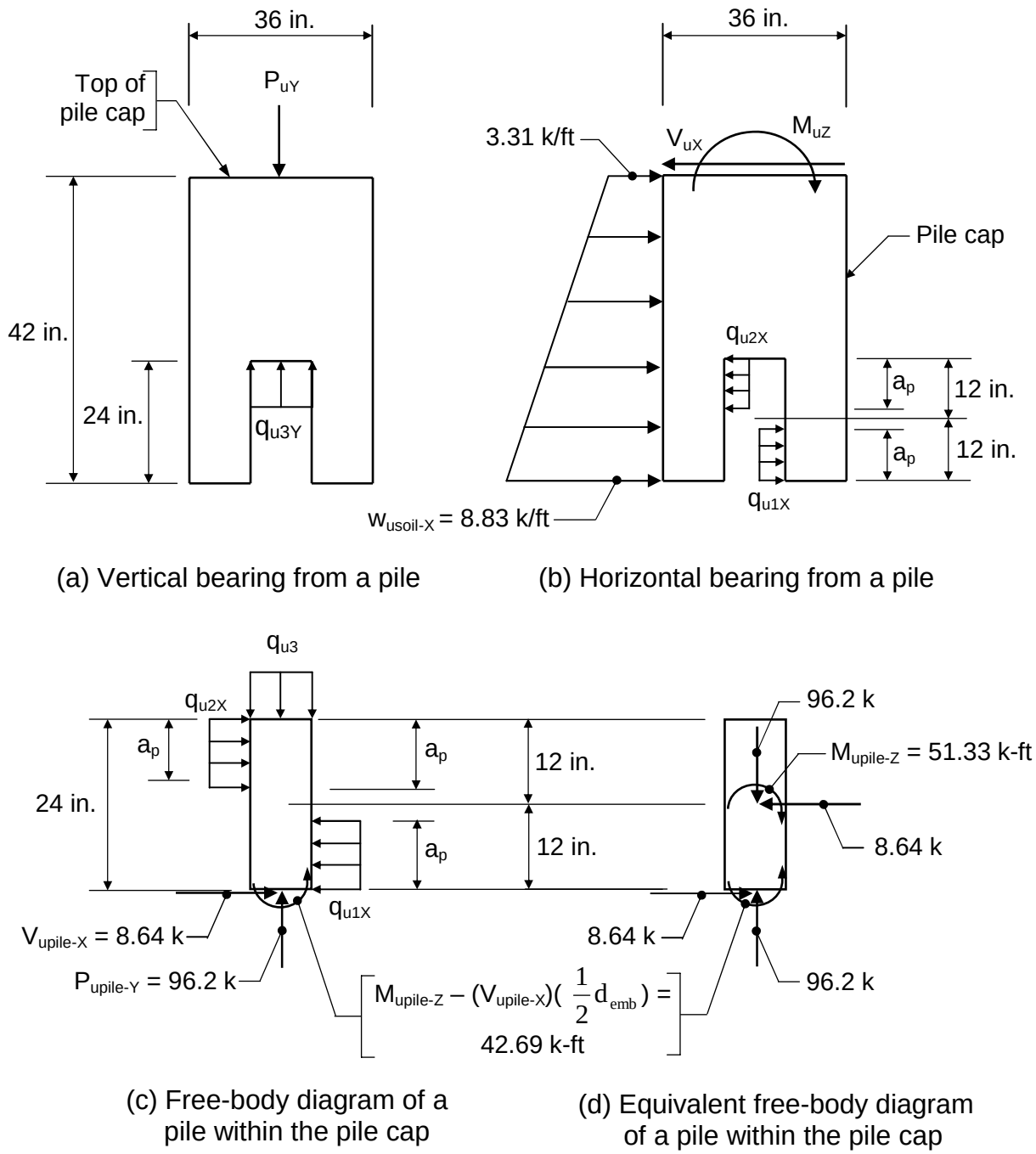

Figure 9.12. Pile-to-pile-cap connection in the XY-plane for the Guthrie County Bridge

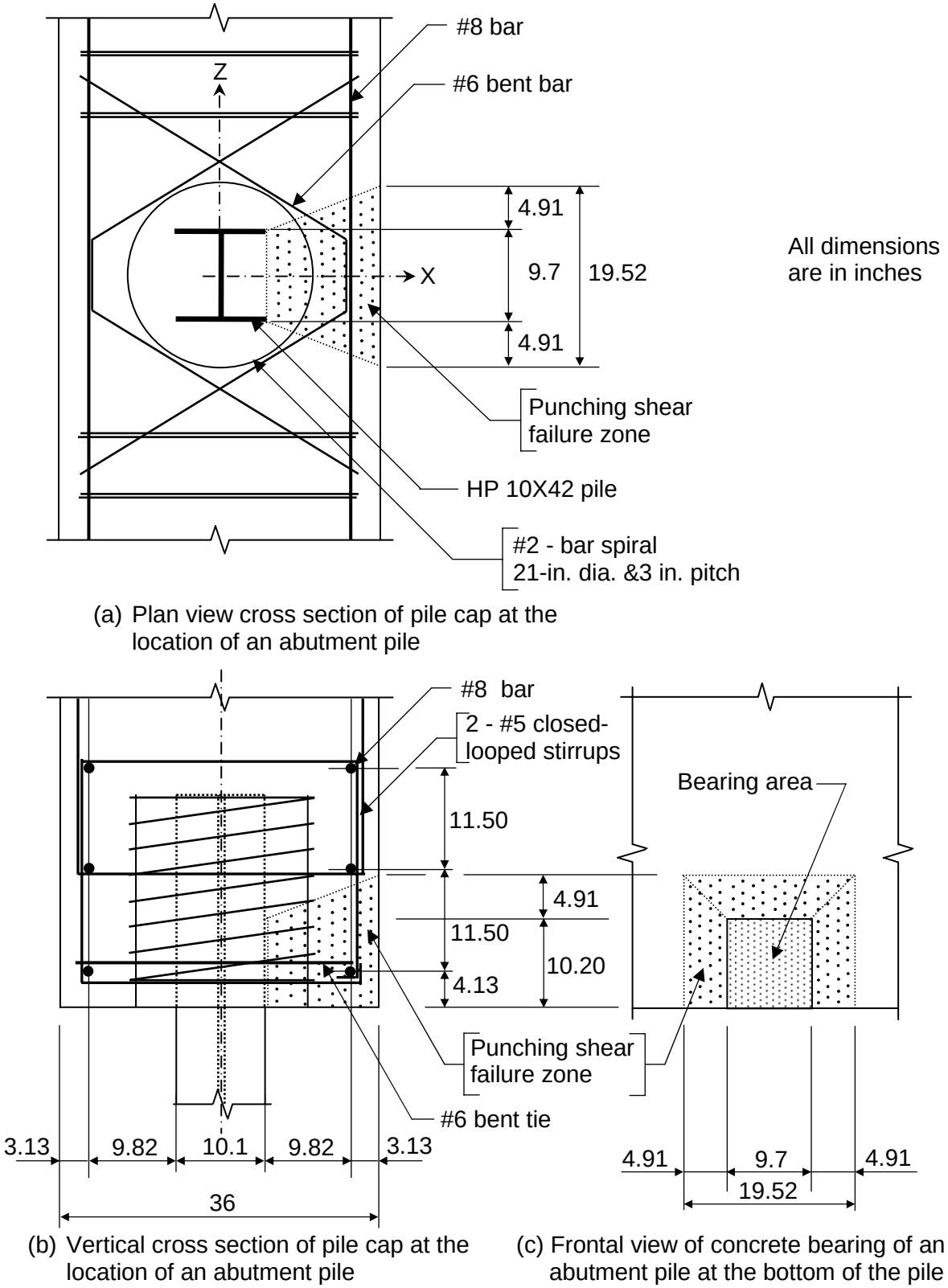

Figure 9.13. Concrete punching-shear failure at an abutment pile

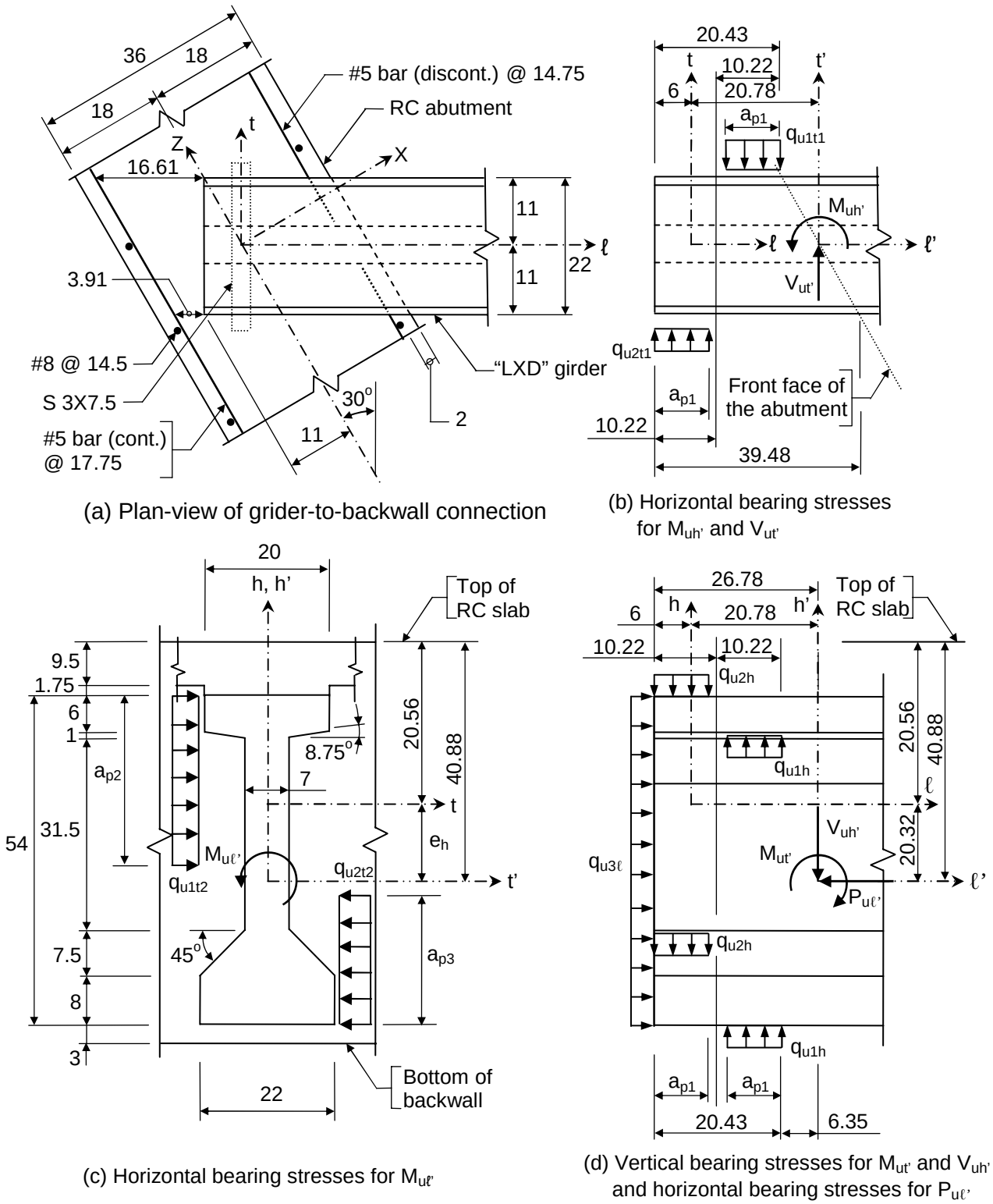

(a) Plan-view of grider-to-backwall connection

(b) Horizontal bearing stresses for $M_{uh'}$ and $V_{ut'}$

(c) Horizontal bearing stresses for $M_{u\ell'}$

(d) Vertical bearing stresses for $M_{ut'}$ and $V_{uh'}$ and horizontal bearing stresses for $P_{u\ell'}$

Note: All dimensions are in inches.

Figure 9.14. Concrete bearing stresses at the end of a PC girder for the Guthrie County Bridge

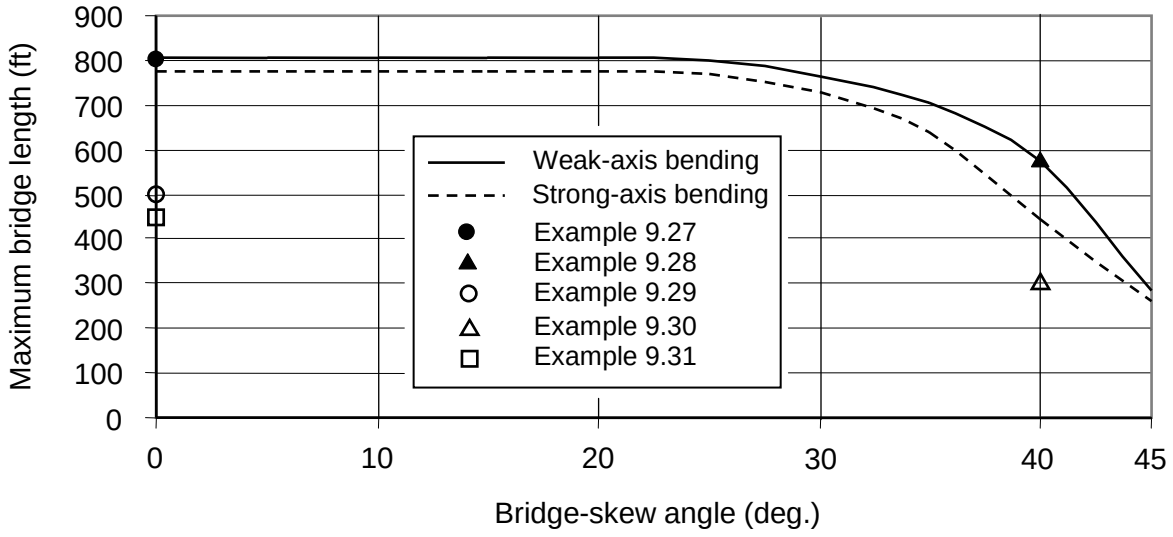

Figure 9.15. Maximum bridge length for skewed, integral-abutment bridges (see Table 9.7 for the geometric and material parameters)

Table 9.1. Equivalent cantilever lengths for the abutment piles at the Guthrie County Bridge

Equivalent Length	x-axis (ft)	y-axis (ft)
Horizontal stiffness	13.2	11.9
Bending moment	13.5	12.0
Buckling load	15.5	12.6

Table 9.2. Factored-level internal forces using AASHTO Load Group IV with a D-Load Factor of 1.3 for a pile cap of an abutment backwall at the Guthrie County Bridge

Loading		X-Axis-Shear Forces		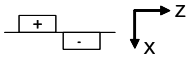	Y-Axis-Shear Forces		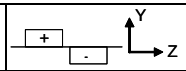	Axial Forces		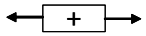
Type	Value	V_{uX1}	$V_{uX1.5}$	V_{uX2}	V_{uY1}	$V_{uY1.5}$	V_{uY2}	P_{uZ1}	$P_{uZ1.5}$	P_{uZ2}
$W_{usoil\text{-}X}$	0	0	0	0	0	0	0	0	0	0
$W_{usoil\text{-}friction\text{-}Z}$	0	0	0	0	0	0	0	0	0	0
$W_{uabut\text{-}Y}$	5.63	0	0	0	0	-10.2	-20.4, +20.4	0	0	0
$P_{upile\text{-}Y}$	66.7	0	0	0	0	0, +66.7	+66.7, -66.7	0	0	0
$V_{upile\text{-}X}$	0	0	0	0	0	0	0	0	0	0
$M_{upile\text{-}Z}$	0	0	0	0	0	0	0	0	0	0
$V_{upile\text{-}Z}$	0	0	0	0	0	0	0	0	0	0
$M_{upile\text{-}X}$	0	0	0	0	0	0	0	0	0	0
$M_{upile\text{-}Y}$	neglect	neglect	neglect	neglect	0	0	0	0	0	0
Combined		0	0	0	0	-10.2, +56.5	+46.3, -46.3	0	0	0
Loading		X-Axis-Bending Moments		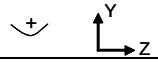	Y-Axis-Bending Moments		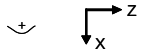	Torsional Moments		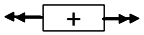
Type	Value	M_{uX1}	$M_{uX1.5}$	M_{uX2}	M_{uY1}	$M_{uY1.5}$	M_{uY2}	M_{uZ1}	$M_{uZ1.5}$	M_{uZ2}
$W_{usoil\text{-}X}$	0	0	0	0	0	0	-180.4	0	0	0
$W_{usoil\text{-}friction\text{-}Z}$	0	0	0	0	0	0	0	0	0	0
$W_{uabut\text{-}Y}$	5.63	+12.3	+3.1	-24.7	0	0	0	0	0	0
$P_{upile\text{-}Y}$	66.7	-30.2	-30.2	+90.7	0	0	0	0	0	0
$V_{upile\text{-}X}$	0	0	0	0	0	0	0	0	0	0
$M_{upile\text{-}Z}$	0	0	0	0	0	0	0	0	0	0
$V_{upile\text{-}Z}$	0	0	0	0	0	0	0	0	0	0
$M_{upile\text{-}X}$	0	0	0	0	0	0	0	0	0	0
$M_{upile\text{-}Y}$	neglect	0	0	0	0	0	0	0	0	0
Combined		-17.9	-27.1	+66.0	0	0	0	0	0	0

Units: Loads - Uniform load in k/ft, forces in kips, and moments in k-ft
Internal forces - Shear forces in kips, axial force in kips, and moments in k-ft

Table 9.3. Design strengths for a pile cap of an abutment backwall at the Guthrie County Bridge

ϕR_n	Design Strength Limits			Comments
	Lower Bound	ISU Suggestion	Upper Bound	
$\phi_v V_{nY}$	62.5[a] k	62.5[a] k	197[b] k	Horizontal and vertical spacing of the stirrups violates the deep-beam provisions in Art. 11.8 of ACI (2002).
$\phi_b M_{nX}^{+}$	133[a] k-ft	399[c] k-ft	399[c] k-ft	Longitudinal tension steel violates the minimum reinforcement provisions in Art. 10.5 of ACI (2002).
$\phi_b M_{nX}^{-}$	133[a] k-ft	568[c] k-ft	568[c] k-ft	Longitudinal tension steel violates the minimum reinforcement provisions in Art. 10.5 of ACI (2002).
$\phi_v T_{nZ}$	50.4[d] k-ft	324[g] k-ft	324[e] k-ft	Spacing and distribution of the longitudinal steel violates the maximum spacing provision in Art. 11.6.6 of ACI (2002).

[a] Based only on the strength of plain concrete.
[b] Computed using only the area of both legs of a single #5, closed-looped bar @ 6.5 in. o.c.
[c] Three-fourths of the reinforced-concrete, bending-moment strength.
[d] One-quarter of the plain-concrete, cracking, torsional-moment strength.
[e] Computed using the area of one leg of a single #5, closed-looped bar @ 6.5 in. o.c.
[g] The pile cap is not subjected to torsional moments until after the entire abutment becomes intergral with the bridge superstructure and soil pressures act on the backwall of the abutment. This torsional-moment strength is a lower bound for the torsional-moment strength for the integral abutment if the construction joint between the pile cap and the abutment backwall has adequate bending-moment strength with respect to an axis that is parallel to the X-axis for the abutment (see Table 9.5).

Table 9.4. Factored-level internal forces using AASHTO Load Group IV with a D, L and I, E, and T-Load Factors of 1.3, 1.3, 1.69, and 1.3, respectively, for a composite backwall and backwall-pile cap at the Guthrie County Bridge

Loading		X-Axis-Shear Forces		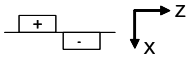	Y-Axis-Shear Forces		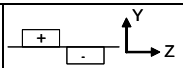	Axial Forces		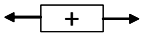
Type	Value	V_{uX1}	$V_{uX1.5}$	V_{uX2}	V_{uY1}	$V_{uY1.5}$	V_{uY2}	P_{uZ1}	$P_{uZ1.5}$	P_{uZ2}
$W_{usoil\text{-}X}$	41.2	0	-74.7	-149.3, +149.3	0	0	0	0	0	0
$W_{usoil\text{-}friction\text{-}Z}$	16.6	+25.0	+25.0	+25.0	-26.0	-26.0	-26.0	0	+30.2	+60.3, -60.3
$W_{uabut\text{-}Y}$	5.63	0	0	0	0	-10.2	-20.4, +20.4	0	0	0
$P_{upile\text{-}Y}$	96.2	0	0	0	0	0, +96.2	+96.2, -96.2	0	0	0
$V_{upile\text{-}X}$	8.69	0	0, -8.7	-8.7, +8.7	0	0	0	0	0	0
$M_{upile\text{-}Z}$	51.7	0	0	0	0	0	0	0	0	0
$V_{upile\text{-}Z}$	11.2	0	0	0	-12.7	-12.7	-12.7	0	0, +11.2	+11.2, -11.2
$M_{upile\text{-}X}$	73.8	0	0	0	-22.9	-22.9	-22.9	0	0	0
$M_{upile\text{-}Y}$	neglect	neglect	neglect	neglect	0	0	0	0	0	0
Combined		+25.0	-49.7, -58.4	-133.0, +183.0	-61.6	-71.8, +24.4	+14.2, -137.4	0	+30.2, +41.4	+71.5, -71.5
Loading		X-Axis-Bending Moments		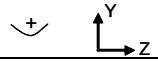	Y-Axis-Bending Moments		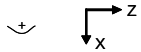	Torsional Moments		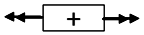
Type	Value	M_{uX1}	$M_{uX1.5}$	M_{uX2}	M_{uY1}	$M_{uY1.5}$	M_{uY2}	M_{uZ1}	$M_{uZ1.5}$	M_{uZ2}
$W_{usoil\text{-}X}$	41.2	0	0	0	+90.2	+22.6	-180.4	0	+116.5	+232.9, -232.9
$W_{usoil\text{-}friction\text{-}Z}$	16.6	0	0	0	0	0	0	0	0	0
$W_{uabut\text{-}Y}$	5.63	+12.3	+3.1	-24.7	0	0	0	0	0	0
$P_{upile\text{-}Y}$	96.2	-43.6	-43.6	+130.8	0	0	0	0	0	0
$V_{upile\text{-}X}$	8.69	0	0	0	+3.9	+3.9	-11.8	0	0, +31.9	+31.9, -31.9
$M_{upile\text{-}Z}$	51.7	0	0	0	0	0	0	0	0, +51.7	+51.7, -51.7
$V_{upile\text{-}Z}$	11.2	0	-23.1, +18.0	-5.1, +5.1	0	0	0	0	0	0
$M_{upile\text{-}X}$	73.8	0	-41.5, +32.3	-9.2, +9.2	0	0	0	0	0	0
$M_{upile\text{-}Y}$	neglect	0	0	0	0	neglect	neglect	0	0	0
Combined		-31.3	-105.1, +9.8	+91.8, +120.4	+94.1	+26.5	-192.2	0	+116.5,+200.1	+316.5,-316.5

Units: Loads - Uniform load in k/ft, forces in kips, and moments in k-ft
Internal forces - Shear forces in kips, axial force in kips, and moments in k-ft

Table 9.5. Design strengths for a composite backwall and backwall-cap at the Guthrie County Bridge

ϕR_n	Design Strength Limits			Comments
	Lower Bound	ISU Suggestion	Upper Bound	
$\phi_v V_{nY}$	169[a] k	169[a] k	538[b] k	Horizontal and vertical spacing of the stirrups violates the deep-beam provisions and the amount of vertical and horizontal steel violates the minimum reinforcement provisions in Art. 11.8 of ACI (2002).
$\phi_v V_{nX}$	169[a]k	169[a]k	679[c] k	Horizontal and vertical spacing of the stirrups violates the deep-beam provisions and the amount of vertical and horizontal steel violates the minimum reinforcement provisions in Art. 11.8 of ACI (2002).
$\phi_b M_{nX}^{+}$	953[a] k-ft	2,338[d] k-ft	2,338[d] k-ft	Longitudinal tension steel violates the minimum reinforcement provisions in Art. 10.5 of ACI (2002).
$\phi_b M_{nX}^{-}$	892[d] k-ft	953[a] k-ft	953[a] k-ft	Longitudinal tension steel violates the minimum reinforcement provisions in Art. 10.5 of ACI (2002).
$\phi_b M_{nY}^{+}$	317[a] k-ft	552[d] k-ft	552[d] k-ft	Longitudinal tension steel violates the minimum reinforcement provisions in Art. 10.5 of ACI (2002).
$\phi_b M_{nY}^{-}$	317[a] k-ft	580[d] k-ft	580[d] k-ft	Longitudinal tension steel violates the minimum reinforcement provisions in Art. 10.5 of ACI (2002).
$\phi_v T_{nZ}$	324[e] k-ft	571[f] k-ft	571[f] k-ft	Closed-looped ties were not provided in the abutment backwall, which violates Art. 11.6.4 of ACI (2002). Spacing and distribution of the longitudinal steel violates the maximum spacing provision in Art. 11.6.6 of ACI (2002).

[a] Based only on the strength of plain-concrete.
[b] Computed using the area of the #8 bar @ 14.5 in. o.c. along the back of the abutment.
[c] Computed using the area of 4 - #5 bar @ 6.5 in. o.c. & 1 - #8 bar @ 14.5 in. o.c.
[d] Three-fourths of the reinforced-concrete, bending-moment strength.
[e] Torsional-moment strength of only the pile cap (see Table 9.3). The construction joint between the pile cap and the abutment backwall must have adequate bending-moment strength with respect to an axis that is parallel to the X-axis for the abutment.
[f] 55 percent of the plain-concrete, cracking, torsional-moment strength.

Table 9.6. Effective girder reactions at the center of gravity of a composite backwall and backwall-pile cap at the Guthrie County Bridge

Load		Forces			Moments		
Type	Value	F_X[a]	F_Y[b]	F_Z[c]	M_X[d]	M_Y[e]	M_Z[f]
$W_{usoil\text{-}X}$	41.2	- 299	0	0	0	0	+ 466
$W_{usoil\text{-}friction\text{-}Z}$	16.6	0	0	+ 120.4	0	0	0
$W_{uabut\text{-}Y}$	5.63	0	+ 40.8	0	0	0	0
$P_{upile\text{-}Y}$	96.2	0	- 192.4	0	0	0	0
$V_{upile\text{-}X}$	8.69	+ 17.4	0	0	0	0	+ 63.8
$M_{upile\text{-}Z}$	51.7	0	0	0	0	0	+ 103.4
$V_{upile\text{-}Z}$	11.2	0	0	+ 22.4	- 10.3	0	0
$M_{upile\text{-}X}$	73.8	0	0	0	- 18.4	0	0
$M_{upile\text{-}Y}$	neglect	0	0	0	0	neglect	0
Combined		- 282	- 152	+ 143	- 28.7	0	+ 633

[a] Force vector is directed along the positive X-axis direction of the abutment.
[b] Force vector is directed along the positive Y-axis direction of the abutment.
[c] Force vector is directed along the positive Z-axis direction of the abutment.
[d] Moment vector is directed along the positive X-axis direction of the abutment.
[e] Moment vector is directed along the positive Y-axis direction of the abutment.
[f] Moment vector is directed along the positive Z-axis direction of the abutment.

Table 9.7. Geometric and material parameters for the maximum bridge length (based on many of the parameters for the Guthrie County Bridge)

Parameters		Values
Bridge length, L		varied
Bridge width, W		34 ft
Abutment backwall height, h_2		9.33 ft
Soil embankment height, h_1		8.5 ft
Wingwall length, $\ell_{1w} = \ell_{2w}$		8.6 ft
Bridge-skew angle, θ		0 deg. thru 45 deg.
Backwall-pile-skew angle, θ_r, for weak-axis or strong-axis bending		0 deg. or 90 deg.
Wingwall/sidewall-pile-skew angle for weak-axis bending		0 deg.
Number of abutment backwall piles, N_{pa}		10
Number of abutment sidewall piles, $N_{p1} = N_{p2}$		1
Modulus of elasticity, E		29,000 ksi
Pile yield stress, F_y		36 ksi
Pile shape		HP10X42
Pile effective length for x-axis, horizontal-stiffness equivalency, L_{ehx}		13.2 ft
Pile effective length for y-axis, horizontal-stiffness equivalency, L_{ehy}		11.9 ft
Pile effective length for x-axis, bending-moment equivalency, L_{emx}		13.5 ft
Pile effective length for y-axis, bending-moment equivalency, L_{emy}		12.0 ft
Soil unit weight, γ		140 lb/ft^3
Soil internal-frictional angle, Φ		37 deg.
Soil-abutment surface frictional angle, δ		22 deg.
Effective coefficient of thermal expansion and contraction, α_e		6.1 x 10^{-6} in./in./°F
(Γ)(T)	Displacement Case 1, with Γ = 1.60 [a] and T = 49 °F	78 °F
	Displacement Case 2, with Γ = 1.35 [b] and T = 66 °F	89 °F [d]
	Displacement Case 3, with Γ = 1.25 [c] and T = (115/2) = 57.5°F	72 °F
	[a] Γ = 1.60 for an experimentally measured α-coefficient and Γ = 2.05 for an α-coefficient by Emanuel and Husley's (1977) expression that is given by Eq. 8.8. [b] Γ = 1.35 for an experimentally measured α-coefficient and Γ = 1.45 for an α-coefficient by Emanuel and Husley's (1977) expression that is given by Eq. 8.8. [c] Γ = 1.25 for both an experimentally measured α-coefficient and an α-coefficient by Emanuel and Husley's (1977) expression that is given by Eq. 8.8. [d] Displacement Case 2 controls for Case 1 with Γ = 1.60 and Case 2 with Γ = 1.35.	

10. CLOSING REMARKS

10.1. Summary

The objectives of the research program were to evaluate the state-of-the-art for prestressed concrete (PC), integral-abutment, bridge design, to validate the assumptions that are incorporated in the current-design procedures for these types of bridges when they are subjected to thermal-loading conditions, and, as appropriate, to revise and improve the current-design procedures for this type of a bridge, as that design relates to the thermally-induced displacements and forces in the abutments and abutment piles. The research program involved the following seven aspects:

(1) A review of the published literature for integral-abutment bridges

(2) Long-term, experimental monitoring of two, multiple-span, PC-girder, integral-abutment bridges in the State of Iowa

(3) Finite-element modeling and analyses of the superstructures and substructures, which included the soil conditions behind the abutments and around the abutment piles, for the monitored bridges

(4) Comparative studies of the analytically-predicted and experimentally-measured, horizontal displacements of the integral abutments and strains in the abutment piles and PC girders that were induced by temperature changes in the bridge superstructures

(5) Investigations of the strength-limit states for the design of the abutment backwall, pile cap, and piles and for the connections between a pile and a pile cap, an abutment pile cap and an abutment backwall, and a PC girder and an abutment backwall

(6) Analytical studies of rotation capacity and rotation demand for an HP-shaped pile, which is subjected to uni-axial or biaxial bending, that is caused by uni-directional or reversal of displacements of the top of the pile

(7) Design examples to illustrate some of the formulated recommendations for the design of an integral abutment and its pile foundation

The literature review for integral-abutment bridges covered the current-design practice in the United States and Canada, field studies, analytical studies, and design models of integral-abutment bridges. The published field studies included discussion and investigations of the longitudinal displacements of integral abutments, soil pressures behind an abutment, strains in bridge girders, rotations of an abutment, and vertical-temperature gradients through the depth of the bridge girders. The published analytical studies of field-monitoring programs addressed bridge deck and girder, vertical-temperature gradients; two-dimensional, temperature distributions; ambient-air temperatures; and solar radiation. Many published articles presented analytical models that were used to study the interaction between an abutment and the soil backfill, axial forces and bending moments in the superstructure due to the thermal expansion of the bridge, interaction between the girders and the deck, interaction between soil and piles, effect of the piers on the bridge longitudinal displacements, and pile strains induced by temperature changes in the bridge superstructure. The topics in the literature include integral-abutment-design recommendations for the design-temperature ranges; vertical-temperature gradients in the superstructure; upper bounds and lower bounds for the coefficient of thermal expansion and contraction of concrete; backfill material behind the abutments; maximum, bridge length; and maximum, bridge-skew angle. Other topics in

the literature include discussions on longitudinal and transverse displacements of abutments, problems related to the approach slabs, integral verses semi-integral abutments, pile behavior, and moment-rotation relationships for cross sections of steel beams.

The primary objective of the field study of Guthrie County Bridge and Story County Bridge was to measure the horizontal and transverse displacements of integral abutments, relative displacements between the PC girders and the pier caps, longitudinal strains in the abutment piles and PC-girder flanges that are caused by thermal loading, and vertical-temperature and horizontal-temperature distributions in the bridge superstructures. The instrumentation devices that were installed at each bridge included displacement transducers, tilt-meters, strain gages, and thermocouples. Each PC-girder bridge was selected for the geometric conditions of long, span lengths; moderate, skew angles; and abutment geometry. One of the bridges has straight-line, integral abutments with a single, vertical row of piles. The other bridge has U-shaped, integral abutments with a single, vertical row of piles under the backwall and one vertical pile under each sidewall.

Finite-element studies for the Guthrie County Bridge and Story County Bridge were performed using the ANSYS (Swanson, 1992) computer software. The analytical models included the bridge deck; PC girders; piers; abutments; steel piles; steel, intermediate diaphragms; and soil. Linear-material properties were used for the reinforced-concrete members, prestressed-concrete members, and structural-steel members. Linear springs were used to represent the soil behind the abutments and along the lengths and at the tip of the abutment piles. The coefficient of thermal

expansion and contraction for the concrete members were based on laboratory tests that were conducted on concrete-core specimens, which were taken from the bridge decks and similar, PC-girder webs.

The ISU recommended, design procedures for an integral-abutment bridge include the design-temperature range for a bridge; vertical-temperature gradient for a bridge superstructure; longitudinal and transverse displacements for an integral abutment; concrete creep and shrinkage effects on the longitudinal expansion and contraction of a bridge superstructure; coefficients of thermal expansion and contraction of the bridge members; equivalent-cantilever lengths that are based on horizontal stiffness, maximum bending moment, and flexural buckling equivalencies for the abutment piles; strength-limit states for an integral-abutment backwall, pile cap, and piles and for the abutment connections to the PC girders and the piles; and a ductility-limit state for an abutment pile, which is based on the longitudinal and transverse displacements of an integral abutment. A computer program (Transmove) is presented to estimate the transverse displacements for an abutment of a skewed, integral-abutment bridge, and a user interface for the program is provided to assist bridge engineers in using the program. To illustrate many of the strength-limit states and the ISU design recommendations for integral abutments, annotated examples are provided for the Guthrie County Bridge. Examples for this bridge are given to address the effect that the steel grade for the abutment piles has on the pile-ductility, limit state. Also, examples are presented for the evaluation of the maximum length for non-skewed and skewed, integral-abutment bridges. For those examples, many of the geometric and material properties were taken to be the same as those for the Guthrie County Bridge.

10.2. Conclusions

The bridge-monitoring programs for the Guthrie County Bridge and Story County Bridge revealed that the maximum, average, bridge temperature occurred on a hot summer day during the early evening hours and the minimum, average, bridge temperature occurred on a cold winter day just before sunrise at both bridges. The maximum, bridge temperature lagged behind and exceeded the measured, air temperature. Vertical-temperature gradients through the depth of the bridge superstructures were much larger during the summer due to solar radiation than those gradients during the winter. Negative, vertical-temperature gradients occurred more frequently during the winter than during the summer.

The measured, longitudinal displacements of the abutments correlated well with the recorded changes in the average, bridge temperatures. The longitudinal displacements, which were measured at each abutment of the Guthrie County Bridge, were not equal. Even though the distance from the fixed pier to the north abutment was about twice as long as the distance from the fixed pier to the south abutment for this bridge, the experimentally-measured, longitudinal displacements at the south abutment were about twice as large as those displacements at the north abutment. The ISU researchers attributed this apparent inconsistency in the abutment displacements to the differences in the horizontal stiffness for the soil behind each abutment for this bridge, the ability for limited relative movements to occur between the bridge superstructure and the pier cap for the fixed pier, and the flexibility of the fixed and expansion piers. The experimentally-measured, longitudinal displacements of the abutments for the Story County Bridge were essentially equal to each other. Both of the monitored bridges

experienced transverse displacements of the abutments and relative, longitudinal displacements between the center, PC girder and the RC diaphragms at both piers.

The maximum, biaxial-bending strains at a flange tip of the HP-shaped, monitored piles at the Guthrie County Bridge, which were extrapolated from the experimentally-measured strains on the outside face of the flanges, exceed the specified, minimum-yield strain of the steel. For the Story County Bridge, the maximum, experimentally-based, extrapolated, biaxial-bending strains in the monitored piles were equal to approximately 73 percent of the steel-yield strain. However, when this strain is superimposed with the sum of the axial-compressive strain due to the dead load of the bridge and the residual-compressive strain in the flange tips, the longitudinal strains for a portion of one flange of the pile exceeded the steel-yield strain. The experimentally-measured, longitudinal strains in the monitored, PC girders at the selected locations for both bridges were well within acceptable limits.

The finite-element models over estimated the experimentally-measured, vertical rotations and longitudinal displacements of the abutments for both bridges. The cause was not determined for the discrepancy between the predicted and measured deformations. A series of finite-element models were developed that had the movements of the monitored abutment set equal to the measured movements. For these finite-element models, the pile strains and the differences between the longitudinal strains in the top and bottom flanges of selected PC girders correlate reasonably well with the experimental results. The predicted, transverse displacements for the abutments were not completely confirmed because of lack of reliable, experimental data.

For the application of the load combination associated with thermal loading from AASHTO Standard Specification (1996), the evaluation of the strength-limit states for the integral abutments and the strength and ductility-limit states for the abutment-backwall piles for the Guthrie County Bridge produced the following results:

(1) The backwall-pile cap satisfies the uni-axial-bending-moment requirements and the uni-axial-shear force requirements at Cross Sections 1, 1.5, and 2 that are located at the mid-span of the pile cap between two, abutment-backwall piles; at an abutment-backwall pile; and at an interior, PC girder, respectively, as shown in Figs. 8.31, 8.41, and 8.44. The span of the pile cap where Cross Section 1 is located does not directly support an interior girder.

(2) The composite, abutment backwall and backwall-pile cap satisfies the interaction relationship for biaxial-moment strength at Cross Sections 1, 1.5, and 2 and satisfies the interaction relationship for biaxial-shear strength and torsional-moment strength at Cross Section 1. However, the composite, backwall and backwall-pile cap violates the interaction relationship for biaxial-shear strength and torsional-moment strength at Cross Section 1.5 by about 12 percent and at Cross Section 2 by about 145 percent. These cross sections, which are shown in Figs. 8.32, 8.42, and 8.45, were at the same locations as those same cross sections for the abutment-pile cap. The overstress conditions were caused by the small, shear resistance for shear forces that are directed along the height and width of the cross section for the abutment and by the small, torsional resistance for the abutment.

(3) At the construction joint between a backwall-pile cap and the abutment backwall, the shear-force resistance is sufficient across the interface between these parts of the abutment.

(4) The design-bearing resistance at the top of an abutment pile is greater than the required, factored-level concrete-bearing stress. Therefore, an end-bearing plate was not required at the top of a backwall pile.

(5) For an abutment pile, the computed, horizontal, factored-level, concrete-bearing stresses that are directed along the length and width of the abutment-pile cap and occur along the length of the pile embedment length are less than the design, concrete-bearing stresses for those locations. Therefore, the 24-in.-long, pile-embedment length into the pile cap is sufficient to transfer the pile forces into the pile cap.

(6) The design, concrete-punching-shear strength for an abutment-pile cap at the location of a pile is sufficient to resist the factored-level, horizontal, concrete-bearing stresses that are induced by the pile end forces.

(7) For the connection between an interior, PC girder and an abutment backwall, the calculated, factored-level, concrete-bearing stresses that act on the abutment backwall along the sides of the girder are less than the design, concrete-bearing stresses; therefore, the concrete-bearing-strength, limit state was satisfied regarding these bearing stresses.

(8) For the connection between an interior, PC girder and an abutment backwall, the calculated, factored-level, concrete-bearing stresses that act on the abutment backwall adjacent to the front face of the abutment and in a direction that is normal

to the bottom flange and normal to the sloped surface of the top flange of a PC girder exceeded the unconfined, design, concrete-bearing stress by about 60 percent. The unconfined, concrete-bearing stress was considered to be applicable, since the bearing stresses occur adjacent to the front face of the abutment. The apparent violation of the bearing-strength, limit state along the girder-embedment length may be based on modeling simplifications for the bearing conditions of an interior, PC girder on the skewed, integral abutment. A more precise analysis of the connection between a PC girder and the abutment backwall should be performed, to determine if a longer embedment length should have been provided to satisfy the strength-limit state for concrete bearing.

(9) For the connection between an interior, PC girder and an abutment backwall, the calculated, factored-level, concrete-bearing stresses that act on the abutment backwall along the last half of the girder-embedment length near the end of a PC girder and in a direction that is normal to the top flange and normal to the sloped surface of the bottom flange of a PC girder are less than and slightly less than, respectively, the confined, design, concrete-bearing stress. Therefore, the concrete-bearing limit state is satisfied for these bearing stresses.

(10) For the connection between an interior, PC girder and an abutment backwall, the calculated, factored-level, concrete-bearing stresses that act on the abutment backwall at the end of a PC girder are significantly smaller than the confined, design, concrete-bearing stress. Therefore, the concrete-bearing-strength, limit state for the abutment backwall is satisfied for the concrete beyond the end of an interior, PC girder.

(11) A 14-percent overstress exists for a punching-shear failure mechanism of the concrete beyond the end of an interior PC girder.

(12) An HP10X42 pile for an abutment backwall satisfies the strength-interaction-limit state.

(13) An HP10X42 pile for an abutment backwall satisfies the ductility-limit state.

10.3. Design recommendations

Based on the research findings that are related to this work and previous research by ISU and other researchers, the ISU researchers have formulated new and confirmed previous recommendations for the design of integral-abutment bridges. The ISU design recommendations, which were presented in Chapter 8 and were demonstrated in Chapter 9, for the expansion and contraction of a bridge superstructure, abutment-pile cap, composite backwall and pile cap, abutment-backwall piles, abutment-backwall-to-pile-cap connection, pile-to-pile-cap connection, and girder-to-backwall connection are as listed in Sections 10.3.1, 10.3.2, 10.3.3, 10.3.4, 10.3.5, 10.3.6, and 10.3.7, respectively.

10.3.1. Expansion and contraction of a bridge superstructure

(1) Minimum and maximum, average, bridge temperatures should be obtained from the bridge-temperature maps that were developed by Roeder (2003) and that are presented as “Procedure B” in Article 3.12.2.1 of the AASHTO LRFD Bridge Design Specifications (AASHTO, 2004).

(2) Positive and negative, vertical-temperature gradients through the depth of a bridge superstructure should be established using the AASHTO LRFD Specifications (1998).

(3) Coefficients of thermal expansion and contraction (α-coefficients) should be evaluated from the revised, Emanuel and Hulsey's (1977) equation when experimental data are not available or from Appendix A when experimental data are available for the concrete, bridge members.

(4) An effective, coefficient of thermal expansion and contraction (α_e-coefficient) for a bridge superstructure should be evaluated from an axial-rigidity, weighted-average expression.

(5) The ISU researchers believe that since the rates of soil consolidation and soil creep are faster than the rates of concrete creep and concrete shrinkage, concrete creep and shrinkage can be neglected when evaluating the ductility demand of the abutment piles, which is associated with the maximum expansion, maximum contraction, and re-expansion of the bridge superstructure. However concrete creep and shrinkage strains do affect the movements of the bridge superstructure. Therefore, these concrete strains need to be considered for the design of the approach slabs. If for some reasons, the concrete creep and shrinkage strains can not be evaluated by accurate methods, a strain of 500 micro-strains should be used to approximate the total of these concrete-material strains.

(6) Construction temperature when the bridge becomes integral should be near the middle of the temperature range for the bridge to provide the greatest, inelastic-rotation capacity for the HP-shaped, abutment piles.

(7) Abutment-pile-head displacements along the longitudinal direction of a bridge need to be amplified by a Γ-factor, as recommended by Oesterle, et al. (1999), to account for uncertainties in these displacements. When experimentally-measured α-coefficients are used to calculate the effective, coefficient of expansion and contraction, α_e-coefficient, of a bridge superstructure, a Γ-factor that is equal to 1.60, 1.35, and 1.25 should be used for maximum expansion (Displacement Case 1), maximum contraction (Displacement Case 2), and re-expansion (Displacement Case 3), respectively, of a bridge superstructure. When Emanuel and Husley's (1977) expression is used to calculate the α_e-coefficient, the Γ-factor should be set equal to 2.05, 1.45, and 1.25, respectively, for these displacement cases.

(8) The actual temperature range for Displacement Case 3, should also be used to determine the maximum, passive-soil pressure that acts on the abutment for the abutment design.

(9) Maximum lengths for non-skewed and skewed, integral-abutment bridges are functions of many parameters and should be determined for a specific bridge, rather than for a generic bridge.

10.3.2. Abutment-pile cap

(10) The spacing and amount of flexural and shear reinforcement should satisfy the maximum spacing and minimum reinforcement amounts that are specified by the ACI Code (2002).

(11) An abutment-pile cap should be designed to resist all dead loads, since the soil beneath the pile cap may settle prior to curing of the concrete in the abutment backwall.

10.3.3. Composite backwall and pile cap

(12) A composite, abutment-pile cap and backwall should be designed to resist all dead and live loads, since the soil beneath the pile cap will settle. Also, the abutment must be designed for passive-soil pressures that act against the back of the abutment and along the sidewalls and wingwalls when the bridge-skew angle is large enough to cause a horizontal rotation of the bridge superstructure.

(13) When the axial force has an insignificant effect on the design of the composite backwall and pile cap, the member needs to be designed for the interaction of biaxial-bending moments and for the interaction of biaxial-shear forces and torsion.

(14) If the magnitude of the required bending moment that induces tensile strains in the front face of an abutment at the location of a PC girder or if the magnitude of the required torsional moment in an abutment requires continuity of the longitudinal steel along the front face of an abutment, PVC sleeves should be placed through the webs of the PC girders to permit the horizontal reinforcing bars to pass through the girder webs and be lapped with the longitudinal bars in this face of the abutment backwall. The horizontal alignment of these PVC sleeves would need to correspond with the skew angle for the bridge.

(15) When required for the bending-moment strength and torsional-moment strength of an abutment in a skewed, integral-abutment bridge, additional longitudinal reinforcement must be used along the length of the abutment and be located within the thickness of the bridge deck.

(16) When passive-soil pressure acts on a sidewall and wingwall, the portion of the abutment backwall between the exterior girder and the first-interior girder will be

subjected to significant, horizontal-bending moment. The longitudinal reinforcement in the vertical faces of the backwall that is required to resist this moment should be extended to the first-interior girder. To accommodate this reinforcement placement in the front face of the backwall, the horizontal reinforcement must pass through the web of the exterior, PC girder. Again, PVC sleeves would need to be placed through the webs of the exterior girders prior to casting the concrete for these girders.

(17) When passive-soil pressure acts on the outside face of an abutment sidewall and wingwall, the acute angle between the sidewall and the abutment backwall will tend to close and cause a vertical concrete crack to develop in the front face of the backwall adjacent to the exterior, PC girder. A similar situation exists at the obtuse-angle corner of the abutment. To reinforce the abutment at these locations, corner bars should be extended through PVC sleeves that pass through the web of the exterior girder. These corner bars should be lapped with the horizontal bars in the front face of the abutment backwall and with the horizontal bars that are in the outside face of the abutment sidewall. At this same joint, when passive-soil pressures act on the inside face of the sidewall and wingwall, the acute-angle corner of the abutment will tend to open and induce tension in the horizontal bars that are in the back face of the abutment backwall. Minimal embedment length is available for a straight-end extension of these horizontal bars into the abutment sidewall. Again, a similar situation exists at the obtuse-angle corner of the abutment. If the thickness of the sidewall is not large enough to fully develop these horizontal bars, a standard ACI hook should be used at this end of those bars to provide sufficient anchorage.

(18) The spacing and amount of flexural and shear reinforcement should satisfy the maximum spacing and minimum reinforcement amounts that are specified by the ACI Code (2002). The amount of reinforcement and the spacing of the shear and torsion reinforcement that is presently specified for the standard details for a composite, backwall and backwall-pile cap should be modified to significantly increase the design strengths for shear and torsion.

10.3.4. Abutment-backwall piles

(19) The webs of HP-shaped, abutment piles should be oriented with their webs perpendicular and their flanges parallel to the longitudinal direction of the bridge for both non-skewed and skewed, integral-abutment bridges. Therefore, the current, Iowa DOT practice that permits a bridge contractor to orientate the web of an HP-shaped, abutment-backwall pile in a direction that is parallel to the front face of the abutment for bridge-skew angles of up to 30 deg. should be discontinued.

(20) Pre-bored holes should be used for the abutment piles to increase the flexibility of the piles for movements of the pile head.

(21) A material with a low stiffness, such as bentonite, should be placed in the pre-bored holes after the piles are driven and cutoff at their proper elevations.

(22) Since an integral-abutment pile is subjected to repeated-cyclic load, the AISC (2001) seismic-design, compact-section criteria should be applied to establish the limiting width-to-thickness ratios for the flange and web elements in a pile cross section. The seismic-design b/t-limits for the flanges of either an A36 steel or a 50-grade steel, HP-shaped pile are exceeded for all of the rolled HP-shapes. Therefore, these pile shapes are not compact shapes. Since the HP12X53 and

HP14X73 shapes have flange b/t-ratios that exceed the column-design b/t-limit for 50-grade steel, these shapes should not be used for piles in integral-abutment bridges when the actual yield strength of the steel for these shapes exceeds about 48 ksi and 44 ksi, respectively.

(23) For the AASHTO (1996) load combination that includes temperature, the integral-abutment piles must be designed for the strength-limit state of combined axial load and bending moments, which includes only the pile moments that are determined from a braced-frame analysis of the bridge for gravity loads and the gravity-induced, $P\Delta$-moments that are caused by the pile axial load, P, and the thermally-induced, lateral displacement, Δ, at the top of the pile. The bending moment that is caused by the lateral movement and flexural stiffness of a pile may be neglected (Greimann, et al., 1987a). The bending moment in a pile that is induced by the thermal movement of a bridge, is assumed not to have a significant effect on the pile capacity. However, the pile must be sufficiently ductile to accommodate the lateral displacement at the top of the pile.

(24) Transverse displacement for an integral abutment and the tops of the abutment-backwall piles can be approximately evaluated by the Transmove program that is presented in Appendix B.

(25) Integral-abutment piles must satisfy displacement-ductility, limit states that involve the expansion and contraction of the bridge superstructure. The element-width-to-thickness ratios for an HP-shaped pile should be correlated with the seismic-design, compact-section limits for those ratios that are specified in the AISC LRFD Specifications (2001) to establish the compression-flange, local-buckling factor, C_i.

(26) For the required ductility of the abutment piles that is associated with Displacement Case 3, a temperature range that is equal to one-half of the actual temperature range should be used to account for the effects of soil consolidation and soil creep.

(27) Since the rotation about the "point-of-fixity" of the superstructure for an integral-abutment bridge is small and since the torsional resistance of an HP-shape pile is small in comparison to its bending-moment resistances, the torsional-moment in the abutment piles can be neglected for establishing the forces that act on an integral abutment.

10.3.5. Abutment-backwall-to-pile-cap connection

(28) For the connection between an abutment backwall and the pile cap, a uniform distribution of vertical reinforcement should be used across this construction joint for the front and back faces of an abutment. The amount of reinforcement must be at least equal to the maximum amount of reinforcement that was recommended by Oesterle, et al. (1999). The spacing for this reinforcement must satisfy Eqs. 8.179 and 8.180. Also, the reinforcement across this joint must satisfy the shear-friction requirements, bar-development-length requirements, and dowel-bar requirements in Articles 11.7, 12.1, and 15.8, respectively, of the ACI Building Code (2002).

(29) The vertical reinforcement across the joint between the abutment backwall and the pile cap must develop the required moment strength and shear strength to resist the passive-soil pressure and pile-end forces that act on the pile cap.

10.3.6. Pile-to-pile-cap connection

(29) Since the pile bending moments needs to be effectively resisted near the mid-depth of the pile-embedment length into the bottom of the pile cap, adequate anchorage below the mid-depth of the pile-embedment length must be provided for the vertical, dowel-bar between the abutment backwall and the pile cap. The dowel bars may need to be extended to the bottom of the pile cap and an ACI 90-deg. Standard hook may need to be used at the end of these bars to develop the required tensile strength for this reinforcement.

(30 For the connection between an abutment pile and an abutment-pile cap that has spiral reinforcement around the pile, the ISU researchers believe that the portion of a steel pile that is embedded into the pile cap is representative of a large steel insert in a mass of concrete. Therefore, a design, concrete-bearing stress of $2.46f_c'$ (0.65 times $3.78f_c'$) can be used along the sides of the pile-embedment length. For bearing at the top of an embedded, HP-shaped pile, the same design, concrete-bearing stress should be used, rather than a more liberal design concrete-bearing stress of 5.20fc' (0.65 times $8f_c'$) that is based on the pile-cap research for AISI (1980). This higher bearing stress at the top of a pile could be used if the abutment piles were subjected only to axial-compressive loads. Since the abutment piles are subjected to axial compression, biaxial-bending moments, and biaxial-shear forces, the design, concrete-bearing stress should probably be somewhere between $2.46f_c'$ and $5.20f_c'$. For most applications, the computed, factored-level, concrete-bearing stress at the top of an abutment pile will be less than the lower-bound, design, concrete-bearing stress. Therefore, a pile-cap plate, which is similar to a base plate

for a column, would not be needed across the pile head to reduce the concrete-bearing stresses.

(31) Spiral-reinforcement and/or bent-bar reinforcement may be needed to resist the horizontal bearing stresses along the embedment depth of the piles in the abutment-pile cap.

10.3.7. Girder-to-backwall connection

(32) The connection between a PC girder and an abutment backwall should be analyzed and designed for the vertical and horizontal, concrete-bearing stresses, that are induced by the member-end forces for the girder. These bearing stresses can be calculated by applying of the same static-equilibrium, analysis technique that was used to determine the concrete-bearing stresses for an abutment pile that is embedded into a pile cap. However, the high, nominal, concrete-bearing stress that was established by Burdette, et al. (1983) for a specific type of a large steel insert in a concrete slab should not be used for the connections between the PC girders and the abutment backwall. This connection is not the same as the connection between an abutment pile and an abutment-pile cap. The differences in these connections involve the type of material for the connected members and confinement-reinforcement conditions for the surrounding concrete. For the girder-to-backwall connection, the nominal, concrete-bearing stresses that are equal to $0.85f_c'$ and $1.7f_c'$, which are specified by the ACI Code (2002), for unconfined concrete and confined concrete, respectively, should be used near a concrete surface and within the interior regions of a concrete volume, respectively.

(33) The vertical, concrete-bearing stresses that act upwards on abutment backwall along the top flange of a PC girder must be resisted by U-shaped ties that should be installed along the embedment length of each girder. This reinforcement should be positioned to straddle over a girder. The horizontal portion of each U-shaped bar should be located near the top surface of the bridge deck, and each vertical leg of each U-shaped bar should extend along one side of the girder web and should be anchored into the abutment-pile cap. The embedment length for these U-shaped bars in the pile cap should be sufficient to develop the yield strength of each leg of this reinforcement. Since the girder forces and moments are reversible, the required area for this U-shaped reinforcement should be distributed over each half of the girder-embedment length.

10.4. Recommendation for further study

Laboratory studies should be conducted for determining the moment-rotation relationships for y-axis (weak-axis) bending of HP-shaped, pile, cross sections. The rotation capacity of abutment piles subjected to axial load and high-amplitude, cyclic load deserves further experimental investigation. After these moment-rotation relationships are established, a more accurate (and possibly more liberal) displacement-ductility, limit state can be developed for HP-shaped, abutment piles.

Since only two, PC-girder bridges were monitored during this research and one other PC-girder bridge was monitored during a previous ISU research study, the experimentally-measured displacements, rotations, member strains, and temperatures that are presented in this report may not be entirely representative of those bridge responses and temperatures for other PC-girder, integral-abutment bridges in the State

of Iowa. Further experimental studies that involve bridge-monitoring programs would contribute to a better understanding of the behavior of integral-abutment bridges with longer lengths, larger-skew angles, horizontally-curved alignments, and abutments supported by PC piles. When long-term, monitoring programs are conducted for integral-abutment bridges, additional precautions need to be taken to minimize the loss of data due to moisture infiltration into the electrical connections for the instrumentation devices. Soil-pressure transducers should be used to measure soil pressures that act on the abutment.

More confirmation and revisions are needed for the analytical model (the program Transmove) that was used to predict the transverse displacements of an integral abutment. Future studies should focus on the correlation between the field-measured and theoretically-predicted, transverse displacements of an integral abutment and on the soil-frictional angle with the abutment for numerous types of dry and saturated soil. The present version of the program was written for predicting the transverse displacement of an integral abutment when only counter-clockwise rotations of the bridge superstructure occur about the “point-of-fixity” for a bridge that has the bridge-skew-angle direction matching the bridge geometry which is shown in Figs. B.1 and B.2. Revisions to the program Transmove should be made to account for a net clockwise rotation of the bridge superstructure for that same bridge geometry. Another modification to the program Transmove should include the presence of “fixed” piers that would restrain the rotation of the bridge superstructure. This program modification would need to account for any potential, relative, longitudinal displacements that may occur between a pier diaphragm and the PC girders.

Additional finite-element studies of integral-abutment bridges should further address the soil interaction with the abutment and the abutment piles. More information about the in-situ backfill behind the abutment and the soil surrounding the piles should be obtained for these finite-element studies. The use of non-linear, soil springs should be considered to model the lateral stiffness of the soil for the finite-element models.

11. REFERENCES

American Association of State Highway and Transportation Officials (AASHTO). (2004). LRFD Bridge Design Specifications, 3rd ed., Washington, D.C.

American Association of State Highway and Transportation Officials (AASHTO). (1998). LRFD Bridge Design Specifications, 2nd ed., Washington, D.C.

American Association of State Highway and Transportation Officials (AASHTO). (1996). Standard Specifications for Highway Bridges, 16th ed., Washington, D.C.

American Association of State Highway and Transportation Officials (AASHTO). (1994). LRFD Bridge Design Specifications, 1st ed., Washington, D.C.

American Association of State Highway and Transportation Officials (AASHTO). (1989). Guide Specifications – Thermal Effects in Concrete Bridge Superstructures, Washington, D.C.

Abendroth, Robert E. and Greimann, Lowell F. (1989a). "Rational Design Approach for Integral Abutment Bridge Piles", Transportation Research Record 1223, TRB, National Research Council, Washington, D.C., 12-23.

Abendroth, Robert E. and Greimann, Lowell F. (1989b). "Abutment Pile Design for Jointless Bridges", Journal of Structural Engineering, American Society of Civil Engineers, 115 (11), 2914-2929.

American Concrete Institute Committee 209 (ACI Committee 209). (1998). "Prediction of Creep, Shrinkage, and Temperature Effects in Concrete Structures," ACI 209R-98, Detroit, Michigan.

American Concrete Institute (ACI). (1999). Building Code Requirements for Structural Concrete (ACI 318-99) and Commentary (ACI 318R-99), Farmington Hills, Michigan.

American Concrete Institute (ACI). (2002). Building Code Requirements for Structural Concrete (ACI 318-02) and Commentary (ACI 318R-02), Farmington Hills, Michigan.

Adams, P. F., Lay, M. G., and Galambos, T. V. (1965). "Experiments on High-Strength Steel Beams," Bulletin No. 110, Welding Research Council, 1-16.

American Institute of Steel Construction (AISC). (1989). Manual of Steel Construction-Allowable Stress Design, 9th ed., Chicago, Illinois.

American Institute of Steel Constructoin (AISC). (1994). Manual of Steel Construction – Load and Resistance Factor Design, 2nd ed., Chicago, Illinois.

American Institute of Steel Construction (AISC). (2001). Manual of Steel Construction-Load and Resistance Factor Design, 3rd ed., Chicago, Illinois.

American Iorn and Steel Institute (AISI). (1982). "The Steel Pile Pile Cap Connection", Washington, DC, 1-40.

Alampalli, Sreenivas and Yannotti, Arthur P. (1998). "In-Service Performance of Integral Bridges and Jointless Decks", Transportation Research Record 1624, TRB, National Research Council, Washington, D.C., 1-7.

Amde, A. M. (formerly Wolde-Tinsae, A. M.), Chini, S. A., and Mafi, M. (1997). "Model Study of H-Piles Subjected to Combined Loading," Geotechnical and Geological Engineering, Chapman & Hall, 15 (4), 343-355.

Arsoy, Sami and Ducan, J. M. (2002). "Lateral Load Behavior of Piles Supporting Integral Bridges", Transportation Research Board Annual Meeting CD-ROM.

Arsoy, Sami, Ducan, J. M. and Barker, R. M. (2002). "Performance of Piles Supporting Integral Bridges", Transportation Research Record 1808, TRB, National Research Council, Washington, D.C., 162-167.

American Society of Heating, Refrigeration, and Air Conditioning Engineers. (ASHRAE). (1993). Fundamentals Handbook, New York, New York.

American Society for Testing Materials (ASTM). (1993). "Standard Test Method for Linear Thermal Expansion of Solid Materials by Thermomechanical Analysis", E831-93, Philadelphia, Pennsylvania, 552-556.

Barkan, D. D. (1992). "Dynamics of Bases and Foundations," McGraw-Hill, New York.

Barker, R. M., Duncan, J. M., Rojiani, K. B., Ooi, P. S. K., Tan, C. K., and Kim, S. G. editors (1991). Manuals for the Design of Bridge Foundations, National Cooperative Highway Research Program Report 343, Transportation Research Board.

Bruneau, Michel, Uang, Chia-Ming, and Whittaker, Andrew. (1998). Ductile Design of Steel Structures, McGraw Hill, New York, New York.

Burdette, E. G., Jones, W. D., and Fricke, K. E. (1983). "Concrete Bearing Capacity Around Large Inserts," Journal of Structural Engineering, American Society of Civil Engineers, 109 (6), 1375-1386.

Burke, M. P. (1987). "Bridge Approach Pavements, Integral Bridges, and Cycle-Control Joints", Transportation Research Record 1113, TRB, National Research Council, Washington, D.C., 54-65.

Burke, M. P., Jr. (1993). “Integral Bridges: Attributes and Limitations,” Transportation Research Board 1393, TRB, National Research Council, Washington, D.C., 1-8.

Burke, Martin P. Jr. (1999). “Cracking of Concrete Decks and Other Problems with Integral-Type Bridges”, Transportation Research Record 1688, TRB, National Research Council, Washington, D.C., 131-138.

Canadian Geotechnical Society. (1992). Canadian Foundation Engineering Manual, 3rd Ed., Toronto, Canada.

Chen, Y. (1997a). “Assessment of Pile Effective Lengths and their Effects on Design-I Assessment”, Computers and Structures, Pergamon, Elsevier Sciences Ltd., New York, New York, 62 (2), 265-286.

Chen, Y. (1997b). “Assessment of Pile Effective Lengths and their Effects on Design-II. Practical Applications”, Computers and Structures, Pergamon, Elsevier Sciences Ltd., New York, New York, 62 (2), 287-312.

Chen, Yohchia. (1997c). “Explicit Calculation of Effective Lengths for Friction Piles”, Journal of Engineering Technology, American Society for Engineering Education, Washington, D.C., 14-17.

Clayton, C. R. I., Milititsky, J., and Woods, R. I. (1993). Earth Pressure and Earth-Retaining Structures, Blackie Academic and Professional, Glascow.

Clough, G. W. and Duncan, J. M. (1991). “Earth Pressures” Foundation Engineering Handbook, 2nd ed., edited by H. Y. Fung, Van Nostrand Reinhold, New York.

Collins, M. P. and Mitchell, D. (1997). Prestressed Concrete Structures, Response Publications, Canada.

Daali, M. L. and Korol, R. M. (1994). “Local Buckling Rules for Rotation Capacity,” Engineering Journal, American Institute of Steel Construction, 31 (2), 41-47.

Dally, J. and Riley, B. (1991). Experimental Stress Analysis, 3rd Edition, McGraw-Hill, Inc., New York.

Darley, P. and Alderman, G. H. (1995). “Measurement of Thermal Cyclic Movements on Two Portal Frame Bridges on the M1,” Transportation Research Laboratory Report 165, Transport Research Laboratory, England.

Darley, P., Carder, D. R., and Alderman, G. H. (1996). “Seasonal Thermal Effects on the Shallow Abutment of an Integral Bridge in Glasgow”, Transportation Laboratory Report 178, Transport Research Laboratory, England.

Davisson, M. T. (1970). “Lateral Load Capacity of Piles,” Transportation Research Record 333, TRB, National Research Council, Washington, D.C., 104-112.

Desai, C. S. and Wu, T. H. (1976). “A General Function for Stress-Strain Curves,” Proceedings of the 2nd International Conference on Numerical Methods in Geomechanics, American Society of Civil Engineers, Vol. 1, 306-318.

Department of the Navy. (1971). Design Manual - Soil Mechanics, Foundations and Earth Structures, Naval Facilities Engineering Command, Alexandria, Virginia.

Duncan, J. M. and Chang, C. -Y. (1970). “Nonlinear Analysis of Stress and Strain in Soils,” Journal of the Soil Mechanics and Foundation Engineering Division, Proceedings of the American Society of Civil Engineers, 96 (SM5), 1629-1653.

Elbadry, Mamdouh M. and Amin, Ghali. (1983). “Temperature Variations in Concrete Bridges”, Journal of Structural Engineering, American Society of Civil Engineering, 109 (10), 2355-2374.

Emanuel, J. H. and Hulsey, J. L. (1977). “Prediction of the Thermal Coefficient of Expansion of Concrete,” Journal of the American Concrete Institute, 74 (4), 149-155.

Fleming, W. G., Weltman, A. J., Randolph, M. F., and Elson, W. K. (1985). Piling Engineering, Halsted Press, New York.

Filz, G. M., Boyer, R. D., and Davidson, R. R. (1997). “Bentonite-Water Slurry Rheology and Cutoff Wall Trench Stability,” Geotechnical Special Publication, American Society of Civil Engineers, No. 71.

Finn, W. D., Lee, K. W., and Martin, G. R. (1977). “An Effective Stress Model for Liquefaction,” Journal of the Geotechnical Engineering Division, American Society of Civil Engineers, 103 (GT6), 517-533.

Girton, D. D., Hawkinson, T. R., and Greimann, L. F. (1989). “Validation of Design Recommendations for Integral Abutment Piles,” Final Report, Iowa DOT Project HR-292, Highway Division, Iowa Department of Transportation, Ames, Iowa.

Girton, D. D., Hawkinson, T. R., and Greimann, L. F. (1991). “Validation of Design Recommendations for Integral Abutment Piles,” Journal of Structural Engineering, American Society of Civil Engineers, 117 (7), 2117-2134.

Greimann, L. F., Abendroth, R. E., Johnson, D. E., and Ebner, P. B. (1987a). “Pile Design and Tests for Integral Abutment Bridges,” Final Report, Iowa DOT Project HR-273, Highway Division, Iowa Department of Transportation, Ames, Iowa.

Greimann, L. F., Abendroth, R. E., Johnson, D. E., and Ebner, P. B. (1987b). Addendum to: “Pile Design and Tests for Integral Abutment Bridges,” Final Report, Iowa DOT Project HR-273, Highway Division, Iowa Department of Transportation, Ames, Iowa.

Greimann, L. F., Yang, P. S., Edmunds, S. K., and Wolde-Tinsae, A. M. (1984). “Design of Piles for Integral Abutment Bridges”, Final Report, Iowa DOT Project No. HR-252, Iowa Department of Transportation, ISU-ERI-Ames 84286.

Georgia Institute of Technology (1991). GTSTRUDL User’s Manual, GTICES Systems Laboratory, Atlanta, Georgia, Vol. 1, Revision M.

Ha, N. B. and O'Neill, M. W. (1981). "Field Study of Pile Group Action (Appendix A)." Final Report, Federal Highway Administration, Washington, D.C.

Hoppe, E. J. and Gomez, J. P. (1996). “Field Study of an Integral Backwall Bridge”, Final Report, Project 97-R7, Virginia Transportation Research Council.

Huang, Jimin, French, Catherine, and Shield, Carol (2004). “Behavior of Concrete Integral Abutment Bridges.” Final Report. Minnesota Department of Transportation, Research Services Section, St. Paul, Minnesota.

Hulsey, J. L. and Powell, D. T. (1993). “Rational Weather Model for Highway Structures”, Transportation Research Record 1393, TRB, National Research Council, Washington, D.C., 54-64.

Husain, I. and Bagnaroil, D. (1996). “Integral Abutment Bridge” Report SO-96-01, Structures Office, Ontario Ministry of Transportation, Ontario, Canada.

Husain, Iqbal and Bagnariol, Dino. (1998). “Design and Performance of Jointless Bridges in Ontario”, Transportation Research Record, 1696, TRB, National Research Council, Washington, D.C., 109-121.

Ingram, Earl E., Burdette, Edwin G., Goodpasture, David W., and Deatherage, Harold J. (2003). “Evaluation of Applicability of Typical Column Design Equations to Steel H-Piles Supporting Integral Abutments”, Engineering Journal, American Institute of Steel Construction, 40 (1), 50-58.

Jorgenson, James L. (1983). “Behavior of Abutment Piles in Integral Abutment in Response to Bridge Movements”, Transportation Research Record 903, TRB, National Research Council, Washington, D.C., 72-79.

Kamel, M. R., Benak, J. V., Tadros, M. K., and Jamshidi, M. (1996). “Prestressed Concrete Piles in Jointless Bridges,” PCI Journal, 41 (2), 56-67.

Kato, Ben. (1989). “Rotation Capacity of H-Section Members as Determined by Local Buckling”, J. Construct. Steel Research, 0143-974X, Elsevier Science Publishers Ltd, Great Britain, United Kingom, 95-109.

Kemp, A. R. (1985). “Interaction of Plastic Local and Lateral Buckling”, Journal of Structural Engineering, American Society of Civil Engineers, 111 (10), 2181-2196.

Kemp, A. R. (1986). “Factors Affecting the Rotation Capacity of Plastically Designed Members”, The Structural Engineer, London, England, 64B (2), 28-35.

Kemp, A. R. (1991). “Available Rotation Capacity in Steel and Composite Beams”, The Structural Engineer, London, England, 69 (5), 88-97.

Kemp, A. R. (1996). “Inelastic Local and Lateral Buckling in Design Codes”, Journal of Structural Engineering, American Society of Civil Engineers, 122 (4), 374-382.

Kirkpatrick, C. (1997). “Instrumentation for Field Testing of Integral Abutment Bridges,” M.S. Creative Component Report, Iowa State University, Ames, Iowa.

Koch, J.C. and Schaefer, V.R. (1992). “Void Development Under Bridge Approaches”, Final Report, South Dakota Department of Transportation, Pierre, South Dakota.

Kuhlmann, U. (1989). “Definition of Flange Slenderness Limits on the Basis of Rotation Capacity Values”, J. Constr. Steel Res., Vol. 14, 21-40.

Kunin, J. and Alampalli, S. (1999). “Integral Abutment Bridges: Current Practice in the United States and Canada,” Special Report 132, New York State Department of Transportation.

Kunin, Jonathan and Alampalli, Sreenivas. (2000). “Integral Abutment Bridges: Current Practice in United States and Canada”, Journal of Performance of Constructed Facilities, American Society of Civil Engineers, 14 (3), 104-111.

Lawver, A., French, C., and Shield, C. K. (2000). “Field Performance of an Integral Abutment Bridge,” Paper presented at the Transportation Research Board 79th Annual Meeting, Washington, D.C..

Lee, D. J. (1994). Bridge Bearings and Expansion Joints, 2nd ed., E & FN Spon, United Kingdom.

Lehane, B. M., Keogh, D. L., and O’Brien, E. J. (1999). “Simplified Elastic Model for Restraining Effects of Backfill Soil on Integral Bridges,” Computers and Structures, Pergamon, Elsevier Services Ltd., New York, New York, 73 (1-5), 303-313.

Loveall, Clellan L. (1985). “Jointless Bridge Decks”, Civil Engineering, American Society of Civil Engineers, November, 64-67.

Lukey, A. F. and Adams, P. R. (1969). “Rotation Capacity of Wide Flanged Beams Under Moment Gradient”, Journal of the Structural Division, American Society of Civil Engineers, 95 (ST6), 1173-1188.

MacGregor, James G., Kennedy, D.J. Laurie, Bartlett, F. Michael, Chernenko, Diana, Maes, Marc A., and Dunaszegi, Laszlo. (1997). “Design Criteria and Load and Resistance Factors for the Confederation Bridge”, Canadian Journal of Civil Engineering, National Research Council Canada, University of Toronto Press, Inc., 24 (6), 882-897.

Martin, P. P.(1975). “Nonlinear Methods for Dynamic Analysis of Ground Response,” Ph.D. Thesis, University of California at Berkley.
Matlock, H., and Reese, L. C. (1960). "Generalized Solutions for Laterally Loaded Piles," Journals of the Soil Mechanics and Foundation Division, American Society of Civil Engineers, 86 (SM5), 63-91.

Measurements Group, Inc. (1983). “Temperature–Induced Apparent Strain and Gage Factor Variation in Strain Gages,“ Technical Note TN-504, Raleigh, North Carolina.

Mitchell, James K. (1993). Fundamentals of Soil Behavior, 2nd ed., John Wiley and Sons, Inc., New York, 187-189.

Moorty, Shashi, and Roeder, Charles W. (1992). “Temperature-Dependent Bridge Movements”, Journal of Structural Engineering, American Society of Engineers, 118 (4), 1090-1105.

Ng, Wei Chei. (1999). “Thermal Expansion and Contraction of Concrete”, M.S. Creative Component Report, Iowa State University, Ames, Iowa.

Nilson, Arthur H. and Winter, George. (1991). Design of Concrete Structures, 11th ed., McGraw-Hill, Inc., New York.

Oesterle, R. G., Tabatabai, H., Lawson, T. J., Refai, T. M., Volz, J. S., and Scanlon, A. (1999). “Jointless and Integral Abutment Bridges” Draft Summary Report, Construction Technology Laboratories, Skokie, Illinois.

O’Neill, M. W. and Murchison, J. M. (1983). “An Evaluation of p-y Relationships in Sands,” University of Houston, Report GT-DF02-83, American Petroleum Institute.

Portland Cement Association (PCA). (1988). “Design and Control of Concrete Mixtures,” 13th ed., Kosmatha, Steven H. and Panarese, William C., Skokie, Illinois.

Precast/Prestressed Concrete Institute (PCI). (2001). The State of the Art of Precast/Prestressed Integral Bridges, Chicago, Illinois.

Pentas, Herodotos, A., Avent R. Richard, Gopu, V. K. A., and Rebello, K. J. (1994a). "Field Study of Longitudinal Movements in Composite Bridges," Transportation Research Record 1476, TRB, National Research Council, Washington, D.C., 117-128.

Pentas, H. A., Avent, R. R., Gopu, V. K. A., and Rebellow, K. J. (1994b). "Field Study of Bridge Temperatures in Composite Bridges", Transportation Research Record 1460, TRB, National Research Council, Washington, D.C., 42-52.

Potgieter, I. C. and Gamble, W. L. (1989). "Non-Linear Temperature Distributions in Bridges at Different Locations in the United States", PCI Journal, 34 (4), 80-103.

Poulos, H. G., and Davis, E. H. (1980). Pile Foundation Analysis and Design, John Wiley and Sons, Inc., New York.

Pyke, R. (1979). "Nonlinear Soil Models for Irregular Cyclic Loadings," Journal of the Geotechnical Engineering Division, American Society of Civil Engineers, 105 (GT6), 715-726.

Reid, R. A., Soupir, S. P., and Schaefer, V. R. (1998). "Mitigation and Void Development Under Bridge Approach Slabs Using Rubber Tire Chips", Geotechnical Special Publication-Recycled Materials, Oct. 18-21, 37-50.

Roctest, Inc. (1997). "Tiltmeter Temperature Coefficients: Sources, Definitions and Use to Improve Accuracy", Document B-95-1005, Rev. C.

Roeder, Charles W. (2003). "Proposed Design Method for Thermal Bridge Movements," Journal of Bridge Engineering, American Society of Civil Engineers, 8 (1), 12-19.

Russell, H. G. and Gerken, L. J. (1994). "Jointless Bridges – The Knowns and the Unknowns," Concrete International, American Concrete Institute, 16 (4), 44-48.

Salmon, Charles G. and Johnson, John E. (1996). Steel Structures – Design and Behavior, 4th ed., Harper Collins, New York, New York.

Sandford, Thomas C. and Elgaaly, Muhamed. (1994). "Skew Effects on Backfill Pressures at Frame Bridge Abutment," Transportation Research Record 1415, TRB, National Research Council, Washington, D.C., 1-11.

Sayers, Brad H. (2000). "Experimental and Analytical Study of Integral Abutment Bridges," M.S. Thesis, Iowa State University, Ames, Iowa.

Siros, K. A. (1995). "Three Dimensional Analysis of Integral Bridges", Ph.D. Dissertation, West Virginia University, Morgantown, West Virginia.

Springman, S. M., Norrish, A. R. M., and Ng, C. W. W. (1996). "Cyclic Loading of Sand Behind Integral Bridge Abutments," Transportation Research Laboratory, TRL Report 146, United Kingdom.

Streeter. V. L., Wylie, E. B., and Richard, F. E. Jr. (1974). “Soil Motions Computations by Characteristic Methods,” Journal of the Geotechnical Engineering Division, American Society of Civil Engineers, 100 (GT3), 247-263.

Swanson Analysis Systems, Inc. (1992). ANSYS User’s Manual, Revision 5.0, Houston, Texas.

Takanashi, Koichi and Udagawa, Kuniaki. (1989). “Behaviors of Steel and Composite Beams at Various Displacement Rates”, Journal of Structural Engineering, 115 (8), 2067-2081.

Thippeswamy, Hemanth K. and GangaRao, V. S. (1995). “Analysis of In-Service Jointless Bridges”, Transportation Research Record 1476, TRB, National Research Council, Washington, D.C., 162-170.

Thomas, M. E. (1999). “Field Study of Integral Abutment Bridges,” M.S. Thesis, Iowa State University, Ames, Iowa.

Ting, J. M. and Faraji, S. (1998). “Streamlined Analysis and Design of Integral Abutment Bridges,” Technical Report, Department of Civil and Environmental Engineering, University of Massachusetts, Lowell, Massachusetts.

Toshihiro, Miki. (1997). “Elasto-Plastic Behavior of Steel Cantilever Columns with Variable Cross-Section Subjected to Horizontally Cyclic Load,” Structural Eng./Earthquake Eng., JSCE, 14 (1), 51s-61s.

United States Steel Corporation. (1965). Highway Structures Design Handbook. Vol. 1. Pittsburgh, Pennsylvania.

Vann, W. P., Thompson, L. E., Whalley, L. E., and Ozier, L. D. (1973). “Cyclic Behavior of Rolled Steel Members”, Proceedings of the 5th World Conference on Earthquake Engineering, Vol. 1, International Association of Earthquake Engineering, Rome, Italy, 1187-1193.

Wang, Chu-Kia and Salmon, Charles G. (1998). Reinforced Concrete Design, 6th ed., Addision Wesley Educational Publishers, Inc., New York.

Wasserman, Edward P. (1987). “Jointless Bridge Decks”, Engineering Journal, American Institute of Steel Construction, Chicago, Illinois, 24 (3), 93-100.

Wasserman, E. P. and Walker, J. H. (1996). “Integral Abutments for Steel Bridges,” Highway Structures Design Handbook, VII, Chapter 5, American Iron and Steel Institute, Washington, D.C.

Wasserman, Edward P. (2001). “Design of Integral Abutments for Jointless Bridges”, Structure, National Council of Structural Engineers, Council of American Structural Engineers, and Structural Engineering Institute, May, 24-33.

Weaver, W. Jr. and Gere, J. M. (1990). Matrix Analysis of Framed Structures, 3rd Edition, Van Nostrand Reinhold, New York, New York.

Winklehorn, H. F. and Fang, H. Y., editors. (1975). Foundation Engineering Handbook, Van Nostrand Reinhold Co., New York, New York.

Wolde-Tinsae, A. M., Greimann, L. F., and Yang, P. S. (1982). “Nonlinear Pile Behavior in Integral Abutment Bridges,” Final Report, Iowa DOT Project HR-227, Highway Division, Iowa Department of Transportation, Ames, Iowa.

Wolde-Tinsae, Amde M. and Klinger, James E. (1987). “Integral Abutment Bridge Design and Construction”, Final Report, FHWA/MD-87/04, Maryland Department of Transportation, National Technical Information Service, Springfield, Virginia.

Wolde-Tinsae, Amde M., Klinger, James E., and White, Elmer J. (1988). “Performance of Jointless Bridges”, Journal of Performance of Constructed Facilities, American Society of Civil Engineers, 2 (2), 111-124.

Yang, P. S., Wolde-Tinsae, A. M., and Greimann, L. F. (1985). “Effects of Predrilling and Layered Soils on Piles”, Journal of Geotechnical Engineering, American Society of Civil Engineers, 111 (1), 18-31.

Zederbaum, J. (1969). “Factors Influencing the Longitudinal Movement of Concrete Bridge System with Special Reference to Deck Contraction,” Concrete Bridge Design, ACI publication SP-23. American Concrete Institute, Detroit, Michigan, 75-95.

APPENDIX A. ALPHA-COEFFICIENT STUDY

Ng (1999) investigated the coefficient of thermal expansion and contraction (α-coefficient) of the concrete in reinforced-concrete bridge decks and precast concrete (PC) girders. Figure A.1 shows the geographical locations in the State of Iowa where concrete-core specimens were taken from bridges decks and from the web elements of PC girders that were at the production facilities for two, precast-concrete producers. These specimens were tested in the laboratory to determine the α-coefficient for the concrete in the core samples. The county in the State of Iowa, specimen label, specimen length, concrete age, Iowa-DOT mix number, and course aggregate for the concrete-core specimens that were taken from the bridge decks and PC girders are listed in Table A.1 and Table A.2, respectively.

All of the specimens were tested accordance with the ASTM (1993), α-coefficient, test standard. Alpha-coefficients for the concrete in the core specimens were determined for 40 °F to 190 ^{o}F and 40 °F to 140 ^{o}F temperature ranges. All of the specimens were tested at a 100%-dry condition. Only the concrete-core specimens from the Guthrie County Bridge and Story County Bridge and from the two PC producers were also tested at a 100%-saturated condition. The experimentally-determined α-coefficients for the concrete-core specimens from the bridge decks and PC girders, are listed in Tables A.3 and A.4, respectively. For a particular core specimen, the α-coefficient for the concrete at the 100%-saturated condition were lower than the α-coefficient for the concrete at the 100%-dry condition. The ranges in the experimental α-coefficients for the 100%-dry condition of the concrete-core specimens that were taken from bridge decks are shown in Fig. A.2.

Tables A.3 and A.4 also list α-coefficients for the concrete in the core specimens, which were predicted by applying Eq. 8.8 and using the α-coefficients for the aggregates in the concrete as specified suggested by ACI (1998), AASHTO (1989), and PCA (1988) (see Table 8.6). The differences between the experimentally-determined and analytically-predicted, α-coefficients for the concrete were less than about 15 percent.

Ng (1999) also examined the effects of concrete-mix designs and moisture contents on the α-coefficient for concrete. The α-coefficients for different moisture contents of the concrete for the Iowa DOT Class C4, D57, and D57-6 (see Table 8.5) concrete mixes were calculated using Eq. 8.8. Figures A-3 and A-4 show the relationship between a non-dimensionalized α-coefficient (α-coefficient ratio) and the moisture content for the three, Iowa DOT, concrete-mix designs that contain limestone course aggregate and gravel course aggregate, respectively. The α-coefficient ratio is given by

$$\alpha\text{-coefficient ratio} = \frac{\text{Predicted } \alpha\text{-coefficient for known moisture content}}{\text{Predicted } \alpha\text{-coefficient for the 100\%-dry condition}} \qquad \text{(A.1)}$$

where, Eq. 8.8 was applied to evaluate the predicted α-coefficients. These figures show that the moisture content of the concrete has a large effect, while the concrete-mix proportions have a very small effect, on the magnitude of the α-coefficient for concrete. For both types of coarse aggregate, the α-coefficient ratio is greater than unity for moisture contents (saturation percentages) between about 20 to 73 percent. The maximum magnitude for this ratio was approximately equal to 1.10, which occurred at about 40%-moisture content. Table A.5 lists the maximum, α-coefficient ratio for the

three, Iowa-DOT, concrete-mix designs and for the concrete in the selected PC girders at Raider Precast Concrete.

If experimental results are available for the α-coefficient of the concrete at the 100%-dry condition, the maximum magnitude for the α-coefficient of the concrete that will occur for any moisture content can be approximated by

$$\alpha_c = 1.1\,\alpha_{dry} \tag{A.2}$$

where, α_{dry} is the α-coefficient of the concrete at the 100%-dry condition. If experimental results are not available for the α-coefficient of the concrete at the 100%-dry condition, a revised Emanuel and Hulseys' (1977) equation (Eq. 8.9) should be used to predict the α-coefficient of the concrete.

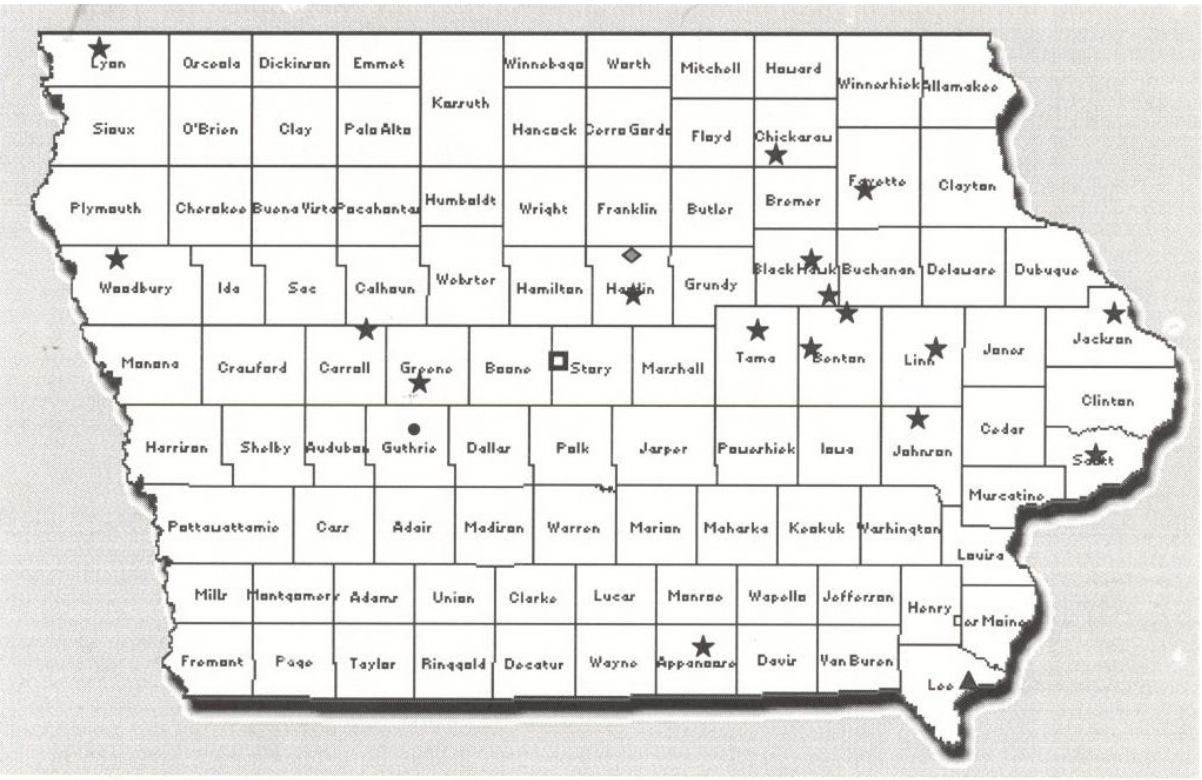

- ● Guthrie County Bridge
- ◻ Story County Bridge
- ★ Other Bridge Decks
- ▲ Raider Concrete
- ◇ Iowa Falls Concrete

Figure A.1. Geographical locations in the State of Iowa for concrete-core specimens.

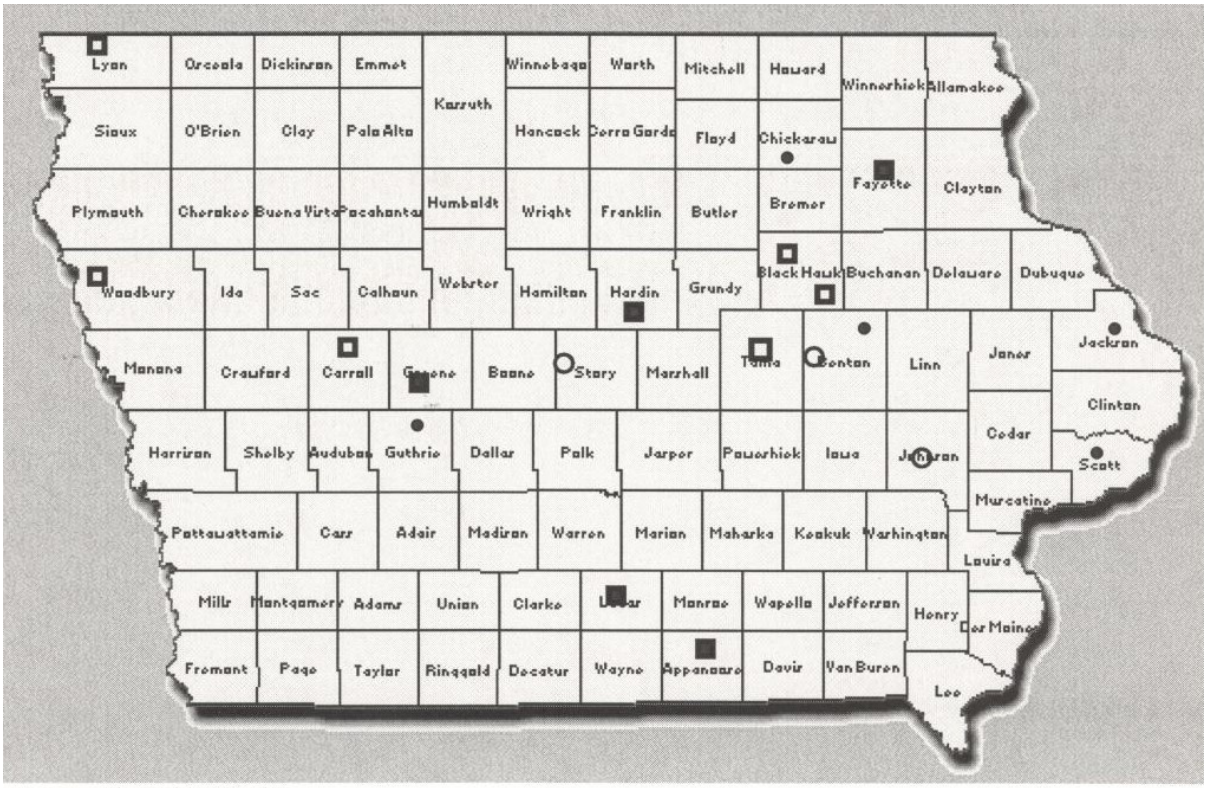

α-Range for Bridge Decks
(10^{-6} in./in./°F)
100% dry

- ■ 4.0 – 4.5
- ○ 4.5 – 5.0
- □ 5.0 – 5.5
- ● 5.5 – 6.0

Figure A.2. Ranges for the α-coefficients for bridge decks in the State of Iowa

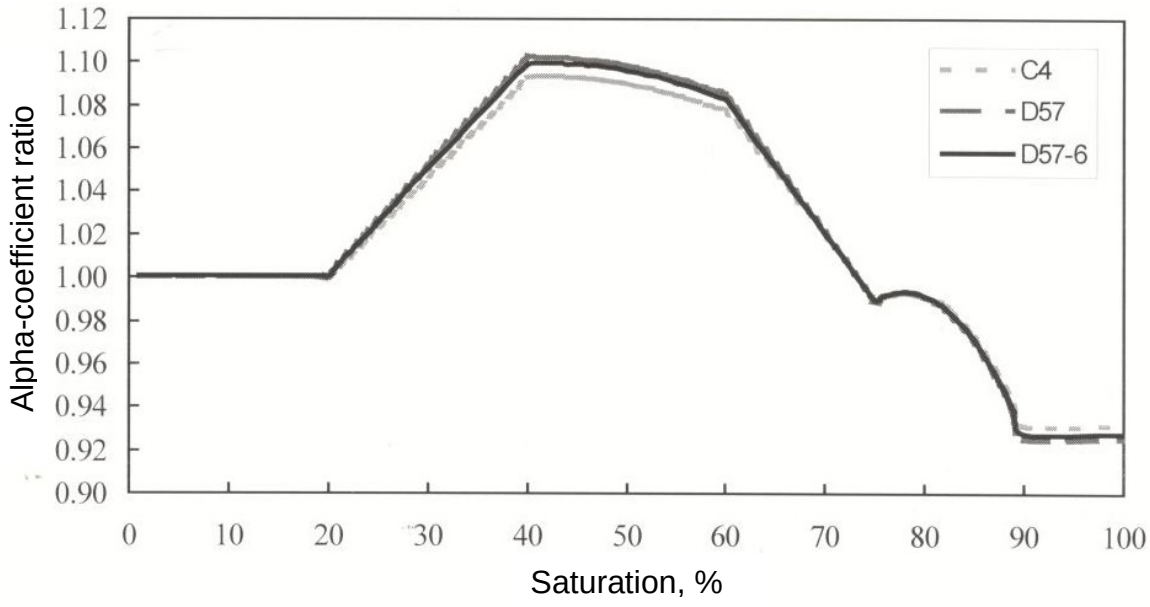

Figure A.3. Alpha-coefficient ratio for concrete with limestone coarse aggregate

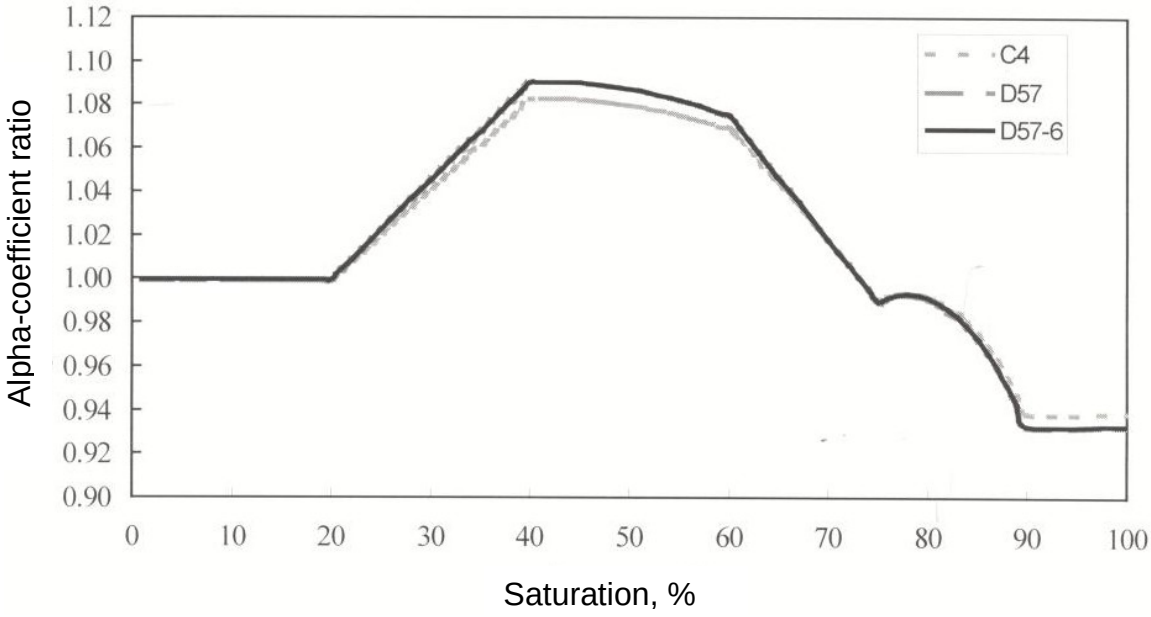

Figure A.4. Alpha-coefficient ratio for concrete with gravel coarse aggregate

Table A.1. Concrete-core specimens from bridge decks

County	Specimen Label	Specimen Length (in.)	Concrete Age (yrs.)	Iowa DOT Mix Number	Coarse Aggregate
Appanoose	0476.4 2	6.1	21	D57-6	limestone
Appanoose	0476.4 D	5.1	21	D57-6	limestone
Benton	0643.5 I	4.7	17	D57-6	limestone
Benton	0643.5 III	5.1	17	D57-6	limestone
Benton	0688.7 N	5.5	20	D57-6	limestone
Benton	0688.7 M	4.7	20	D57-6	limestone
Benton	0688.7 F	5.1	20	D57-6	limestone
Black Hawk	0761.5 I	4.6	15	D57-6	limestone
Black Hawk	0761.5 III	5.6	15	D57-6	limestone
Black Hawk	0761.5 IV	4.9	15	D57-6	limestone
Black Hawk	0757.1 I	5.1	15	D57-6	limestone
Black Hawk	0757.1 II	5.3	15	D57-6	limestone
Carroll	1411.6 N	4.7	15	C4	limestone
Carroll	1411.6 F	5.9	15	C4	limestone
Chickasaw	1910.0 1	5.6	15	C4	limestone
Chickasaw	1910.0 2	5.5	15	C4	limestone
Chickasaw	1910.0 3	4.8	15	C4	limestone
Fayette	3364.6 C	4.9	7	C4	limestone
Green	3712.3 N	5.2	6	C4	limestone
Green	3712.3 M	5	6	C4	limestone
Guthrie	C1	--	8	C4	gravel
Guthrie	C2	4.5 (3.6+0.9)[a]	8	C4	gravel
Guthrie	C3	5.4 (3.8+1.6)[a]	8	C4	gravel
Guthrie	C4	5.6 (4.4+1.2)[a]	8	C4	gravel
Guthrie	C5	--	8	C4	gravel
Guthrie	C6	5.6 (4.1+1.5)[a]	8	C4	gravel
Hardin	4227.3	6.1	14	C4	limestone
Jackson	4926.7 III	4.9	13	D57-6	gravel
Johnson	5293.7 2	4.8	15	D57-6	limestone
Linn	5713.7 N	5.2	12	D57-6	limestone
Linn	5713.7 M	5.5	12	D57-6	limestone
Linn	5713.7 F	5.7	12	D57-6	limestone
Lucas	5931.7 N	5	7	C4	limestone
Lucas	5931.7 F	5.3	7	C4	limestone
Lyon	6011.6	4.8	23	D57	gravel
Scott	8224.1 I	5.1	18	D57-6	limestone
Scott	8224.1 II	4.8	18	D57-6	limestone
Scott	8224.1 III	5	18	D57-6	limestone
Story	NE	5.3	17	D57	limestone
Story	NC	5.1	17	D57	limestone
Story	NW	5.5	17	D57	limestone
Story	SE	5.4	17	D57	limestone
Story	SC	5.4	17	D57	limestone
Story	SW	5.4	17	D57	limestone
Tama	8600.5 N	4.9	10	D57-6	limestone
Tama	8600.5 M	5.2	10	D57-6	limestone
Tama	8600.5 F	5.3	10	D57-6	limestone
Woodbury	9708.3 I	4.9	21	D57	gravel

[a]Original layer (gravel) thickness + overlay (limestone) thickness

Table A.2. Concrete-core specimens from PC girders

Precaster	Specimen Label	Specimen Length (in.)	Concrete Age (yrs.)	Iowa DOT Mix Number	Coarse Aggregate
Raider	bm 1-1	6.2	unknown	unknown	limestone
Raider	bm 1-2	6.2	unknown	unknown	limestone
Raider	bm 1-3	6.3	unknown	unknown	limestone
Raider	bm 2-4	6.1	unknown	unknown	limestone
Raider	bm 2-5	6.3	unknown	unknown	limestone
Raider	bm 2-6	6.4	unknown	unknown	limestone
Iowa Falls	1	6.3	unknown	unknown	limestone
Iowa Falls	2	6.1	unknown	unknown	limestone
Iowa Falls	3	6.3	unknown	unknown	limestone
Iowa Falls	4	6.5	unknown	unknown	limestone
Iowa Falls	5	6.3	unknown	unknown	limestone
Iowa Falls	6	6.4	unknown	unknown	limestone

Table A.3. Alpha coefficients for concrete-core specimens taken from bridge decks

County	Specimen Label	Experimental $\alpha \times 10^{+6}$ (in./in./°F)			Predicted $\alpha \times 10^{+6}$ (in./in./°F) by Eq. 8.8		
		100% dry		100% saturated	100% dry (100% saturated)		
		40 °F to 190 °F	40 °F to 140 ° F	40 °F to 140 °F	ACI (1998)	AASHTO (1989)	PCA (1988)
Appanoose	0476.4 2	4.21	3.9	n.a.	5	5.2	5.3
Appanoose	0476.4 D	4.15	6.97	n.a.	5	5.2	5.3
Benton	0643.5 I	5.67	5.5	n.a.	5	5.2	5.3
Benton	0643.5 III	5.7	5.57	n.a.	5	5.2	5.3
Benton	0688.7 N	4.94	4.78	n.a.	5	5.2	n.a.
Benton	0688.7 M	5.15	5.13	n.a.	5	5.2	n.a.
Benton	0688.7 F	4.96	4.82	n.a.	5	5.2	n.a.
Black Hawk	0761.5 I	5.83	5.77	n.a.	5	5.2	n.a.
Black Hawk	0761.5 III	5.07	5.06	n.a.	5	5.2	n.a.
Black Hawk	0761.5 IV	5.62	5.54	n.a.	5	5.2	n.a.
Black Hawk	0757.1 I	5.64	5.38	n.a.	5	5.2	n.a.
Black Hawk	0757.1 II	5.58	5.42	n.a.	5	5.2	n.a.
Carroll	1411.6 N	5.38	5.26	n.a.	4.7	5.1	n.a.
Carroll	1411.6 F	5.11	5.12	n.a.	4.7	5.1	n.a.
Chickasaw	1910.0 1	5.86	5.74	n.a.	4.7	5.1	n.a.
Chickasaw	1910.0 2	6.18	5.98	n.a.	4.7	5.1	n.a.
Chickasaw	1910.0 3	6.21	5.89	n.a.	4.7	5.1	n.a.
Fayette	3364.6 C	4.42	4.22	n.a.	4.7	5.1	n.a.
Green	3712.3 N	3.86	4.05	n.a.	4.7	5.1	n.a.
Green	3712.3 M	4.17	4.19	n.a.	n.a.	n.a.	n.a.
Guthrie	C2	6.14	6.32	5.92	n.a.	5.9 (5.5)	5.7 (5.3)
Guthrie	C3	6.03	6.06	5.57	n.a.	5.9 (5.5)	5.7 (5.3)
Guthrie	C4	5.86	5.89	5.51	n.a.	5.9 (5.5)	5.7 (5.3)
Guthrie	C6	5.74	5.68	5.4	n.a.	5.9 (5.5)	5.7 (5.3)
Hardin	4227.3	4.52	4.35	n.a.	4.7	5.1	5.1
Jackson	4926.7 III	5.72	5.56	n.a.	n.a.	5.9	5.1
Johnson	5293.7 2	5.08	4.88	n.a.	5	5.2	5.3
Linn	5713.7 N	4.96	4.7	n.a.	5	5.2	5.3
Linn	5713.7 M	5.26	5.1	n.a.	5	5.2	5.3
Linn	5713.7 F	4.93	4.87	n.a.	5	5.2	5.3
Lucas	5931.7 N	4.4	4.45	n.a.	4.7	5.1	5.1
Lucas	5931.7 F	4.27	4.2	n.a.	4.7	5.1	5.1
Lyon	6011.6	5.28	5.1	n.a.	n.a.	5.9	5.7
Scott	8224.1 I	5.9	5.97	n.a.	5	5.2	5.3
Scott	8224.1 II	6.03	6.05	n.a.	5	5.2	5.3
Scott	8224.1 III	5.86	5.85	n.a.	5	5.2	5.3
Story	NE	4.95	4.93	4.58	4.8 (4.4)	5.1 (4.7)	5.1 (4.7)
Story	NC	4.89	4.87	4.32	4.8 (4.4)	5.1 (4.7)	5.1 (4.7)
Story	NW	4.83	4.69	4.42	4.8 (4.4)	5.1 (4.7)	5.1 (4.7)
Story	SE	4.98	4.85	4.63	4.8 (4.4)	5.1 (4.7)	5.1 (4.7)
Story	SC	4.96	4.89	4.64	4.8 (4.4)	5.1 (4.7)	5.1 (4.7)
Story	SW	4.88	4.63	4.2	4.8 (4.4)	5.1 (4.7)	5.1 (4.7)
Tama	8600.5 N	5.31	5.22	n.a.	5	5.2	5.3
Tama	8600.5 M	5.25	5.15	n.a.	5	5.2	5.3
Tama	8600.5 F	5.24	5.06	n.a.	5	5.2	5.3
Woodbury	9708.3 I	5.46	5.39	n.a.	n.a.	5.9	5.7

Table A.4. Alpha coefficients for concrete-core specimens taken from PC girders

Producer	Specimen Label	Experimental α x 10^{+6} (in./in./°F)			Experimental α x 10^{+6} (in./in./°F) by Eq. 8.8		
		100% dry		100% saturated	100% dry (100% saturated)		
		40 °F to 190 °F	40 °F to 140 °F	40 °F to 140 °F	ACI (1998)	AASHTO (1989)	PCA (1988)
Raider	bm 1-1	4.36	4.06	3.87	4.8	5.1	5.1
Raider	bm 1-2	4.35	4.07	3.83	4.8	5.1	5.1
Raider	bm 1-3	4.41	4.31	3.97	4.8	5.1	5.1
Raider	bm 2-4	4.3	4.13	3.92	4.8	5.1	5.1
Raider	bm 2-5	4.4	4.12	3.78	4.8	5.1	5.1
Raider	bm 2-6	4.41	4.25	3.97	4.8	5.1	5.1
Iowa Falls	1	4.6	4.33	4.09	4.7–5.0[a] (4.4-4.6)[a]	4.7–5.0[a] (4.4-4.6)[a]	5.1–5.3[a] (4.7-4.9)[a]
Iowa Falls	2	4.61	4.42	4.08	4.7–5.0[a] (4.4-4.6)[a]	4.7–5.0[a] (4.4-4.6)[a]	5.1–5.3[a] (4.7-4.9)[a]
Iowa Falls	3	4.65	4.4	4.2	4.7–5.0[a] (4.4-4.6)[a]	4.7–5.0[a] (4.4-4.6)[a]	5.1–5.3[a] (4.7-4.9)[a]
Iowa Falls	4	4.54	4.27	4.02	4.7–5.0[a] (4.4-4.6)[a]	4.7–5.0[a] (4.4-4.6)[a]	5.1–5.3[a] (4.7-4.9)[a]
Iowa Falls	5	4.76	4.62	4.25	4.7–5.0[a] (4.4-4.6)[a]	4.7–5.0[a] (4.4-4.6)[a]	5.1–5.3[a] (4.7-4.9)[a]
Iowa Falls	6	4.74	4.61	4.18	4.7–5.0[a] (4.4-4.6)[a]	4.7–5.0[a] (4.4-4.6)[a]	5.1–5.3[a] (4.7-4.9)[a]

[a]Predicted value based on concrete-mix design C4, D57, D57-6 (see Table 8.6)

Table A.5. Maximum, alpha-coefficient ratio

Concrete Mix	Alpha-Coefficient Ratio	
	Limestone	Gravel
Iowa DOT C4	1.10	1.09
Iowa DOT D57	1.09	1.08
Iowa DOT D57-6	1.10	1.09

APPENDIX B. TRANSMOVE SOFTWARE

B.1. Force equilibrium for an integral abutment

Figure B.1 shows a plan view for one half of a skewed, symmetric, integral-abutment bridge. Forces that are induced by thermal elongation and a counter-clockwise, rigid-body rotation, β, of the bridge superstructure are shown acting on the abutment. The definitions for the parameters that are shown in the figure are:

F_{af} = horizontal force that acts along the length of an abutment and is induced by the coefficient of friction of the soil against the abutment backwall and the forces F_{po} and $F_{pp\text{-}po}$;

F_n = sum of the components of the horizontal forces that are induced by the displacement at the top of each of the abutment-backwall piles (N_{pa} piles) and that acts normal to the abutment length;

F_p = sum of the components of the horizontal forces that are induced by the displacement at the top of each of the abutment-backwall piles (N_{pa} piles) and that acts parallel to the abutment length;

F_{pn1} = sum of the components of the horizontal forces that are induced by the displacement at the top of each of the Sidewall 1 piles (N_{p1} piles) and that acts normal to the length, ℓ_{w1}, of the common sidewall and wingwall;

F_{pp1} = sum of the components of the horizontal forces that are induced by the displacement at the top of each of the Sidewall 1 piles (N_{p1} piles) and that acts parallel to the length, ℓ_{w1}, of the common sidewall and wingwall;

F_{pn2} = sum of the components of the horizontal forces that are induced by the displacement at the top of each of the Sidewall 2 piles (N_{p2} piles) and that acts normal to the length, ℓ_{w2}, of the common sidewall and wingwall;

F_{pp2} = sum of the components of the horizontal forces that are induced by the displacement at the top of each of the Sidewall 2 piles (N_{p2} piles) and that acts parallel to the length, ℓ_{w2}, of the common sidewall and wingwall;

F_{po} = horizontal force that is induced by the at-rest-soil-pressure p_o and that acts normal to the backwall of the abutment and over the height, h_{abut}, and length, ℓ_{abut}, of the abutment;

$F_{pp\text{-}po}$ = horizontal force that is induced by the difference between the passive-soil pressures p_{p2} and p_{p3} and the at-rest-soil pressure p_o and that acts normal to the back of the abutment and over the height, h_{abut}, and length, $\ell_{pp\text{-}po}$, of the abutment that is subjected to the passive-soil pressure;

F_{s1} = horizontal force that is induced by the passive-soil pressure p_{pw1} and that acts normal to Sidewall and Wingwall 1 and over the height, h_1, and length, ℓ_{w1}, of the abutment;

F_{s2} = horizontal force that is induced by the passive-soil pressure p_{pw2} and that acts normal to Sidewall and Wingwall 2 and over the height, h_2, and length, ℓ_{w2}, of the abutment;

L = bridge length;

W = bridge width;

P = distance from the "point-of-fixity" for the bridge to the abutment (for the program Transmove, P = L/2);

P_{1w} = total length of Sidewall and Wingwall 1 for the abutment;

P_{2w} = total length of Sidewall and Wingwall 2 for the abutment;

P_{abut} = abutment length (P_{abut} = W/cos θ);

$P_{pp\text{-}po}$ = length of the abutment that is subjected to passive-soil pressure (when the entire length of the abutment is subjected to passive-soil pressure, the length $P_{pp\text{-}po}$ = the length P_{abut} and p_{p1} = the passive-soil pressure that acts normal to the backwall of the abutment at Corner 1);

p_o = at-rest-soil pressure that acts normal to the backwall of the abutment;

p_{p2} = passive-soil pressure that acts normal to the backwall of the abutment at Corner 2;

p_{p3} = passive-soil pressure that acts normal to the backwall of the abutment at the mid-point of the length $P_{pp\text{-}po}$;

p_{pw1} = passive-soil pressure that acts normal to Sidewall and Wingwall 1 of the abutment;

p_{pw2} = passive-soil pressure that acts normal to Sidewall and Wingwall 2 of the abutment;

θ = skew angle for a bridge (angle between the t-axis for the bridge and the Z-axis for an abutment).

The active-soil pressure p_o that acts behind the abutment backwall; the passive-soil pressures p_{p2}, p_{p3}, and possibly pp1, if the entire abutment backwall is subjected to passive-soil pressure, that act behind the abutment backwall; the passive-soil pressure p_{pw1} and that acts on and Wingwall 1; and the passive-soil pressure p_{pw2} that acts on and Wingwall 2 were evaluated using the Husain and Bagnaroil (1996) design curves shown in Fig. 5.10b. For each particular Δ/h ratio, where Δ is the horizontal displacement that is normal to and at the top of a wall segment and h is the height of the soil against that wall segment, a soil-pressure coefficient, k, per unit area of that wall segment is obtained from Fig. 5.10b for the soil behind the wall. The soil pressure that is induced by the movement of a wall is given by

$$p = k \gamma h \tag{B.1}$$

where, γ is the unit weight of the soil.

The soil forces F_{po} and $F_{pp\text{-}po}$ that act on the abutment backwall, the soil force F_{s1} that acts on Sidewall and Wingwall 1, and the soil force F_{s2} that acts on Sidewall and Wingwall 2 of the abutment are equal to the volume of the soil-pressure distributions that act normal to the walls of the abutment and involve the soil pressures p_o; p_{p2}-p_o, p_{p3}-p_o, and possible p_{p1}-p_o; p_{p1w}; and p_{p2w}, respectively. The soil force F_{af} that acts on the abutment is a function of the soil-pressure distributions that act normal to the backwall of the abutment and soil-to-abutment, surface-friction angle, δ, between the concrete wall and the soil. This soil force acts parallel to the length of the abutment backwall.

An integral-abutment bridge has specific locations for the piles that support the backwall and sidewalls of an abutment. To simplify the input for the program Transmove, an outer pile for an abutment backwall was placed at each end (Corner 1 and Corner 2) of the abutment length and the rest of the piles for an abutment backwall were evenly spaced along the length of the abutment backwall. This simplification in the location of the abutment-backwall piles will not significantly affect the transverse displacement of an integral abutment, since many piles are used to support an abutment backwall. Another simplification for the input into the program Transmove involves the location of the pile(s) for each sidewall. The pile(s) for Sidewall 1 were positioned at the mid-length of Sidewall and Wingwall 1, and the pile(s) for Sidewall 2 were positioned at the mid-length of Sidewall and Wingwall 2. If only wingwalls are used for an abutment (the abutment does not have any sidewalls), there are no sidewall piles ($N_{p1} = N_{p2} = 0$). The pile forces F_n and F_p that act on the abutment backwall, the pile forces F_{pn1} and F_{pp1} that act on Sidewall 1, and the pile forces F_{pn2} and F_{pp2} that act on Sidewall 2 are equal to the sum of the horizontal-components of the individual, pile forces that are in the direction of these F-forces.

B.2. Displacement and force expressions

For the program Transmove, a sign convention for horizontal displacements and rotation of a bridge superstructure was established with respect to the bridge geometry that is shown in Figs. B.1 and B.2. When an increase in the average temperature of the bridge superstructure causes an expansion of the bridge superstructure, positive longitudinal displacements are directed towards the soil backfill behind an abutment, positive rotations of a bridge superstructure about the “point-of-fixity” for the bridge were

taken as counter-clockwise rotations, and positive transverse displacements are directed towards the acute corner (Corner 2) of the bridge deck, as shown by the labeled displacements in Fig. B.2.

The displacements dt_1 and $d\ell_1$, which are measured along the transverse and longitudinal directions, respectively, of the bridge and occur at Corner 1 of the abutment, are a functions of the displacements dR_{1t}, $dR_{1\ell}$, and $d\ell$, as shown in Fig. B.3a. The displacements dR_{1t} and $dR_{1\ell}$ are the displacement components, which are directed along the transverse and longitudinal directions, respectively, of the bridge, for the relative displacement, dR_1, that occurs at Corner 1 of an abutment for a horizontal rotation, β, of the bridge superstructure about the "point-of fixity" for the bridge. The displacement $d\ell$ is the change in the length of the bridge superstructure between the "point-of-fixity" for the bridge and the abutment. The displacements dt_1 and $d\ell_1$ are expressed as

$$dt_1 = dR_1 \cos\alpha_1 \tag{B.2}$$

$$d\ell_1 = d\ell - dR_1 \sin\alpha_1 \tag{B.3}$$

where, α_1 is the rotation angle between a line that is drawn parallel to the transverse axis (t-axis) for the bridge and a line drawn along the displacement dR_1. The displacement dR_1 is given by

$$dR_1 = \beta\left[\left(\frac{W}{2}\right)^2 + \left(\ell + \frac{W}{2}\tan\theta\right)^2 + d\ell\right]^{\frac{1}{2}} \tag{B.4}$$

where, W is the width of the abutment; ℓ is the distance from the "point-of-fixity" for the bridge to the abutment; and θ is the skew angle for the bridge. The displacement $d\ell$ is evaluated as

$$d\ell = \alpha_e \quad T\ell \tag{B.5}$$

where, T is the change in the average temperature of the bridge superstructure and α_e is the effective coefficient of thermal expansion and contraction of the bridge superstructure, which is established from Eq. 8.10. The displacement $d\ell$ is assumed to be the free (unrestrained), longitudinal expansion of the bridge superstructure. The angle α_1 is expressed as

$$\alpha_1 = \tan^{-1}\left(\frac{\frac{W}{2}}{\ell + \frac{W}{2}\tan\theta + d\ell}\right) \tag{B.6}$$

The displacements dn_1, and dp_1, which are measured normal and parallel, respectively, to the length of the abutment and occur at Corner 1 of the abutment, are functions of the displacements dR_{1n}, dR_{1p}, $d\ell_n$, and $d\ell_p$. The displacements dR_{1n} and $d\ell_n$ and dR_{1p} and $d\ell_p$ are displacement components that are directed normal and parallel, respectively, to the abutment length of the relative displacement dR_1 and the length $d\ell$, as shown Fig. B3a. The displacements dn_1, and dp_1 are given by

$$dn_1 = ABS\left(+dR_1 \sin(\theta + \alpha_1) - d\ell\cos\theta\right) \tag{B.7}$$

$$dp_1 = dR_1 \cos(\theta + \alpha_1) + d\ell\sin\theta \tag{B.8}$$

The absolute-value function is needed in Eq. B.7 to prevent a negative value for the distance dn_1, which would occur if the elongated and rotated position for Corner 1 is above the line that is an extension of the abutment length for the initial position of the abutment.

The displacements dt_2 and $d\ell_2$, which are measured along transverse and longitudinal directions, respectively, of the bridge and occur at Corner 2 of the abutment,

are functions of the displacements dR_{t2} and $dR_{\ell 2}$. The displacements dR_{t2} and $dR_{\ell 2}$ are the displacement components that are directed along the transverse and longitudinal directions, respectively, of the bridge for the relative displacement, dR_2, at Corner 2 of an abutment for the rotation, β, and the displacement dℓ of the bridge superstructure, as shown in Fig. B.3b. The displacements dt_2 and $d\ell_2$ are expressed as

$$dt_2 = dR_2 \cos\alpha_2 \tag{B.9}$$

$$d\ell_2 = d\ell + dR_2 \sin\alpha_2 \tag{B.10}$$

where, α_2 is the rotation angle between a line that is drawn parallel to the transverse axis (t-axis) for the bridge and a line drawn along the displacement dR_2. The displacement dR_2 is given by

$$dR_2 = \beta\left[\left(\frac{W}{2}\right)^2 + \left(\ell - \frac{W}{2}\tan\theta + d\ell\right)^2\right]^{\frac{1}{2}} \tag{B.11}$$

and the angle α_2 is evaluated by

$$\alpha_2 = \tan^{-1}\left(\frac{\frac{W}{2}}{\ell - \frac{W}{2}\tan\theta + d\ell}\right) \tag{B.12}$$

The displacements dn_2, and dp_2, which are measured normal and parallel, respectively, to the length of the abutment and occur at Corner 2 of the abutment, are functions of the displacements dR_{n2}, dR_{p2}, $d\ell_n$, and $d\ell_p$. The displacements dR_{n2} and $d\ell_n$ and dR_{p2} and $d\ell_p$ are displacement components that are directed normal and parallel, respectively, to the abutment length of the relative displacement dR_2 and the length dℓ, as shown Fig. B3b. The displacements dn_1, and dp_1 are given by

$$dn_2 = -dR_2 \sin(\theta - \alpha_2) + d\ell \cos\theta \tag{B.13}$$

$$dp_2 = dR_2 \cos(\theta - \alpha_2) + d\ell \sin\theta \tag{B.14}$$

The displacements dn_3 and dt_3, which are measured normal and transverse respectively, to the length of the abutment and occur at the mid-length of the abutment are evaluated as

$$dn_3 = \frac{1}{2}(dn_1 + dn_2) \tag{B.15}$$

$$dt_3 = \beta(\ell + d\ell) \tag{B.16}$$

The maximum transverse displacement, dt_{max}, of an integral abutment occurs when the angle β is equal to the maximum angle β_{max}. Then, the displacement dt_3 equals the displacement dt_{max}.

The at-rest-soil-pressure force, F_{po}, and net-passive-soil-pressure force, $F_{pp\text{-}po}$, which is based on the difference between the passive-soil pressure and the at-rest-soil pressure, that act on the backwall for an integral abutment, which are shown in Fig. B.1 for a counter-clockwise rotation of the bridge superstructure, are expressed as

$$F_{po} = \frac{1}{2}\gamma k_o h_{abut}{}^2 \frac{W}{\cos\theta} \tag{B.17}$$

$$F_{pp-po} = \frac{1}{2}\gamma\left[\frac{1}{4}(k_{n1} + 2k_{n3} + k_{n2}) - k_o\right] h_{abut}{}^2 \ell_{pp-po} \tag{B.18}$$

where, γ is the unit weight of the soil; k_o is the Rankine, at-rest-soil-pressure coefficient; h_{abut} is the height of the soil embankment against the abutment backwall; kn_1, kn_2, and kn_3 are the passive-soil-pressure coefficients for the soil pressures that act normal to the abutment backwall at Corner 1, at Corner 2, and at the mid-point of the length $l_{pp\text{-}po}$, respectively; and $\ell_{pp\text{-}po}$, which is the length of the abutment that is subjected to passive-soil pressure, is calculated by

$$\ell_{pp-po} = \frac{x - dt_2}{\cos(\theta - \beta)} \tag{B.19}$$

where the distance, x, which is the transverse distance between Corner 2 and the location along the length of the abutment where the soil pressure is equal to the at-rest-soil pressure (see Fig. B.3b), is given by

$$x = \frac{d\ell_2 - dt_2 \tan(\theta - \beta)}{\tan\theta - \tan(\theta - \beta)} \tag{B.20}$$

For a counter-clockwise rotation of the bridge superstructure, the soil-friction force, F_{af}, that acts on the backwall for an integral abutment as shown in Fig. B.1, is a function of the total normal force against the abutment backwall and the coefficient of friction between the concrete backwall and the soil. This force is expressed as

$$F_{af} = (F_{po} + F_{pp-po})\tan\delta \tag{B.21}$$

where, δ is the soil-to-abutment, surface-friction angle.

The passive-soil-pressure forces F_{s1} and F_{s2} that act on Sidewall and Wingwall 1 and Sidewall and Wingwall 2, respectively, of an integral abutment, as shown in Fig. B.1 for a counter-clockwise rotation of the bridge superstructure, are given by

$$F_{s1} = \frac{1}{4}\gamma k_{pw1} h_1^2 \ell_{1w} \tag{B.22}$$

$$F_{s2} = \frac{1}{2}\gamma k_{pw2} h_2^2 \ell_{2w} \cos\theta \tag{B.23}$$

where, k_{pw1} and k_{pw2} are the passive-soil pressure coefficients for the soil that acts against Sidewall and Wingwall 1 and Sidewall and Wingwall 2, respectively; h_1 and h_2 are the soil-embankment heights at Corner 1 and Corner 2, respectively; and ℓ_{1w} and ℓ_{2w} are the lengths of Sidewall and Wingwall 1 and Sidewall and Wingwall 2, respectively. In the horizontal plane, the distribution of the passive-soil pressure against

the outside face of Sidewall and Wingwall 1 is assumed to be triangular in shape with zero soil pressure acting at Corner 1. At this corner, the height of the soil embankment matches the elevation for the berm in front of the abutment. In the horizontal plane, the distribution of the passive-soil pressure against inside face of Sidewall and Wingwall 2 is assumed to be rectangular in shape. At Corner 2 for the abutment, the height of the soil embankment is the same as that for the soil behind the abutment.

Since pile-skew angle, θ_r, defines the orientation of the backwall piles, the displacements $d\ell_i$ and dt_i at the ith backwall pile, which are in the longitudinal direction and transverse direction, respectively, of the bridge, need to be resolved into components along the x-axis and y-axis of that pile. The displacements $d\ell_i$ and dt_i were established by using the longitudinal and transverse displacements $d\ell_1$ and dt_1, respectively, at Corner 1, the longitudinal and transverse displacements $d\ell_2$ and dt_2, respectively, at Corner 2, and the distance that the ith backwall pile is from Corner 2 of the abutment. For each backwall pile, the displacements dx_i and dy_i along the x-axis and y-axis, respectively, for the cross section of the pile at the top of the ith backwall pile are given by

$$dx_i = d\ell_i \sin\theta_r + dt_i \cos\theta_r \tag{B.24}$$

$$dy_i = d\ell_i \cos\theta_r - dt_i \sin\theta_r \tag{B.25}$$

The horizontal forces F_{xi} and F_{yi} that are at the top of the ith backwall pile and in the x-axis and y-axis directions, respectively, of the pile cross section are established from

$$F_{xi} = k_x\, dx_i \le V_{py} \tag{B.26}$$

$$F_{yi} = k_y\, dy_i \le V_{px} \tag{B.27}$$

where, k_x and k_y are the flexural stiffness of an HP-shaped sidewall pile with respect to bending about the strong-axis (x-axis) and weak-axis (y-axis), respectively, of the pile cross section; and V_{py} and V_{px} are the lateral loads (y-axis-shear force and x-axis-shear force, respectively, in the pile that correspond to the plastic-moment resistances of the pile for x-axis bending and y-axis bending, respectively) at the top of a pile. These shear forces act along the y-axis and x-axis directions, respectively, of the pile cross section. The elastic, x-axis, flexural stiffness, k_x, and the elastic, y-axis, flexural stiffness, k_y, of a pile that is fixed against rotation at each end of an equivalent-cantilever length and that is subjected to a lateral displacement along the y-axis and x-axis, respectively, of the pile cross section is defined by

$$k_x = \frac{12\,E\,I_x}{L_{ehx}^{\;2}} \tag{B.28}$$

$$k_y = \frac{12\,E\,I_y}{L_{ehy}^{\;2}} \tag{B.29}$$

where, E is the modulus of elasticity (Young's modulus) for steel; I_x and I_y are the moment of inertias of an HP-shaped pile with respect to the x-axis and y-axis, respectively, of the pile cross section; and L_{ehx} and L_{ehy} are the equivalent-cantilever lengths that are based on the horizontal-stiffness equivalency for x-axis bending and y-axis bending, respectively, of the pile cross section. The y-axis-shear force and x-axis-shear force in a pile that has fixed-ends and experiences a relative, laterally displacement along the y-axis and x-axis, respectively, at one end of an equivalent-cantilever length versus the other end of that length are respectively expressed as

$$V_{py} = 2F_y\,Z_x\,L_{ehx} \tag{B.30}$$

$$V_{px} = 2F_y\ Z_y\ L_{ehy} \tag{B.31}$$

where, F_y is the yield stress for steel and Z_x and Z_y are the plastic-section modulus with respect to the x-axis and y-axis, respectively, of the pile cross section. After the horizontal forces F_{xi} and F_{yi} were calculated, components of these forces were resolved into directions that were normal and parallel to the length of the abutment. The horizontal forces F_{ni} and F_{pi}, that act normal and parallel, respectively, to the length of the abutment and occur at the top of the ith pile are given by

$$F_{ni} = F_{xi}\sin(\theta - \theta_r) + F_{yi}\cos(\theta - \theta_r) \tag{B.32}$$

$$F_{pi} = F_{xi}\cos(\theta - \theta_r) + F_{yi}\sin(\theta - \theta_r) \tag{B.33}$$

The total horizontal forces F_n and F_p that act normal and parallel, respectively, to the abutment are expressed as

$$F_n = \sum_{i=1}^{N_{pa}} F_{ni} \tag{B.34}$$

$$F_p = \sum_{i=1}^{N_{pa}} F_{pi} \tag{B.35}$$

where, N_{pa} is the number of piles in the abutment backwall.

For the program Transmove, the piles in the sidewalls of an integral abutment were oriented with the web of the HP-shaped pile in the transverse direction of the bridge. With this pile alignment, pile-head movements along the longitudinal direction of a bridge superstructure will produce only weak axis (y-axis) bending of the pile cross section, while pile-head movements along the transverse direction of the bridge will produce only strong axis (x-axis) bending of the pile cross section. The horizontal

forces F_{pn1} and F_{pn2} for the pile(s) in Sidewall 1 and the pile(s) in Sidewall 2, respectively, that act in the transverse direction for the bridge, and the horizontal forces F_{pp1} and F_{pp2} for the pile(s) in Sidewall 1 and the pile(s) in Sidewall 2, respectively, that act in the longitudinal direction for the bridge are given by

$$F_{pn1} = N_{p1} k_x \, dt_{s1} \leq N_{p1} V_{py} \tag{B.36}$$

$$F_{pn2} = N_{p2} k_x \, dt_{s2} \leq N_{p2} V_{py} \tag{B.37}$$

$$F_{pp1} = N_{p1} k_y \, d\ell_{s1} \leq N_{p1} V_{px} \tag{B.38}$$

$$F_{pp2} = N_{p2} k_y \, d\ell_{s2} \leq N_{p2} V_{px} \tag{B.39}$$

where, N_{p1} and N_{p2} are the number of piles in Sidewall 1 and Sidewall 2, respectively. The displacements dt_{s1} and dt_{s2} are the horizontal displacements of the abutment in the transverse direction of the bridge at the mid-length of Sidewall and Wingwall 1 and Sidewall and Wingwall 2, respectively; and dP_{s1} and dP_{s2} are the horizontal displacements of the abutment in the longitudinal direction of the bridge at the mid-length of Sidewall and Wingwall 1 and Sidewall and Wingwall 2, respectively.

Table B.1 lists the point of application for the soil forces and pile forces that act on an integral abutment and the eccentricity for each of these forces with respect to the "point-of-fixity for a bridge. When a thermal expansion occurs for the bridge superstructure, the fourth column and the fifth column in this table indicate the direction of these forces and the direction of the resulting moment of these forces with respect to the "point-of-fixity" for the bridge, respectively, which are associated with the bridge-geometrical conditions that are shown in Figs. B.1 and B.2. The expression for the eccentricity of the force F_n for the backwall piles was written for the ith backwall pile, where d_{c2i} is the distance from the ith backwall pile to Corner 2.

B.3. Program installation

The following steps are used to install the program Transmove:

Step 1: Copy the file “Transmove.xls” from the CD to the computer hard drive.

Step 2: Open Microsoft Excel version 2000 or later.

Step 3: Select the “Tools” icon in Microsoft Excel.

Step 4: Select the “Macro” icon from the “Tools” window.

Step 5: Select the “Security” icon from the “Macro“ window.

Step 6: Set the security level to “Medium” from the Security window.

Step 7: Close Microsoft Excel.

Step 8: Re-open Microsoft Excel.

Step 9: Select the “Open” icon in Microsoft Excel.

Step 10: Select the file “Transmove.xls” from the sub-directory where the program “Transmove” was saved.

Step 11: Select the “Enable Macros” icon from the Microsoft Excel window to activate the program “Transmove”.

B.4. Program interface

The computer program Transmove was written in the Visual C++ program language, which is compatible with Microsoft Excel. Figure B.4 shows the user-interface for the software. The input parameters that are need for to execute the program include the bridge geometry, pile properties, soil properties, and a miscellaneous property. The parameters for the bridge geometry are the total bridge length, L; bridge width, W; soil-embankment heights, h_{abut} and h_1, against the abutment backwall and Sidewall and Wingwall 1, respectively; Sidewall and Wingwall 1 and

Sidewall and Wingwall 2 lengths, ℓ_{1w} and ℓ_{2w} ($\ell_{1w} = \ell_{2w}$), respectively; bridge-skew angle, θ; and pile-skew angle, θ_r. For counter-clockwise rotations β of the bridge superstructure about the "point-of-fixity" for the bridge, the soil-embankment height h_2 along Sidewall and Wingwall 2 are the same as that for the abutment backwall. The pile properties are the number of piles for the abutment backwall, N_{pa} , number of piles for Sidewall 1 and Sidewall 2, N_{p1} and N_{p2} ($N_{p1} = N_{p2}$), respectively; modulus of elasticity, E, and yield stress, F_y, for the piles; x-axis and y-axis moment of inertias, I_x and I_y, respectively; x-axis and y-axis plastic-section modulus, Z_x and Z_y, respectively; and equivalent-cantilever lengths L_{ehx} and L_{ehy} for x-axis bending and y-axis bending, respectively, that are based on the horizontal-stiffness equivalency. The soil properties are the unit weight, γ; angle-of-internal friction, ϕ; and soil-to-abutment, surface-friction angle, δ. The miscellaneous parameter is the effective α-coefficient, α_e, of the bridge superstructure. An example that shows the values for the input parameters for the Guthrie County Bridge is included within the Transmove program. This example can be accessed by selecting the icon labeled "Sample Input" from the "User Interface".

B.5. Program algorithm

The algorithm of the Transmove program is summarized by the flowchart shown in Fig. B.5. The input data from the "User Interface" is used by the program to compute the soil and pile forces and the corresponding moment for those forces about the "point-of-fixity" for the bridge superstructure. The algorithm for the program increases the temperature of the bridge superstructure by 1° F and re-computes the soil and pile forces and the corresponding moments for these forces about the "point-of fixity" for the bridge. As the temperature of the bridge superstructure is increased, the bridge will

elongate along its displaced longitudinal axis. If the sum of the moments for the soil and pile forces about the “point-of-fixity” is greater than zero (counter-clockwise moments for these forces were considered to be positive moments), the bridge will rotate in a counter-clockwise direction until moment equilibrium is established for the rotated bridge for the bridge geometry that is shown in Figs. B.1 and B.2. Once moment equilibrium is satisfied, the program algorithm increases the temperature for the bridge superstructure by another 1 ^{o}F, and a new rotated position for the bridge is established to re-satisfy moment equilibrium. The original version of the program Transmove required the user to input the construction temperature and the temperature range for the bridge. The algorithm for the program would terminate the expansion and any rotation of the bridge when the temperature of the bridge superstructure was equal to the maximum temperature for the bridge. When the maximum temperature was obtained, the transverse displacement, dt, of the integral abutment may have been less than the potential, maximum transverse displacement, dt_{max}. The ISU researchers decided to revise the algorithm for the program to prevent the displacement dt from being less that the displacement dt_{max}. Therefore, the latest version of the program Transmove does not require a user to input a construction temperature or a temperature range. Now, the program algorithm has a preset temperature range of 300 ^{o}F. With this extremely large, temperature range, the possibility was eliminated that the displacement dt would be less than the displacement dt_{max}. Even though moment equilibrium for the soil and pile forces about the “point-of-fixity” for the bridge will not be satisfied with a 300 ^{o}F change in the bridge temperature, the predicted displacement dt_{max} for the abutment will be correct.

B.6. Program limitations

The program Transmove can only be used to predict the transverse displacement of an integral abutment that is caused by a longitudinal expansion of the bridge superstructure and a corresponding counter-clockwise rotation β of the bridge superstructure about the "point-of-fixity for the bridge. These conditions will produce the soil-pressure distributions and soil-force and pile-force directions that are shown in Fig. B.1 and the displacements at Corner 1 and Corner 2 of the abutment that are shown in Fig. B.3. After the maximum transverse displacement, dt_{max}, for the abutment has occurred, the bridge will begin to rotate in the clockwise direction as the temperature of the bridge superstructure is increased further due to a potentially large, abutment-pile force, F_p. This pile force has a larger eccentricity with respect to the "point-of-fixity for the bridge than that for the corresponding large, abutment-pile force F_n. (Figure B.3 shows the force directions and Table B.1 lists the force eccentricities.) If a net, clockwise-rotation angle β for the bridge superstructure occurs, Fig. B.1 does not show the correct soil-pressure distributions and soil-force and pile-force directions and Fig. B.3 does not show the correct abutment displacement directions.

The algorithm for the program Transmove, which is based on the research by Oesterle, et al. (1999), was written with specific geometry for an integral-abutment bridge. Regardless of the direction of the bridge-skew angle, θ, for the actual bridge, the direction for the bridge-skew angle needs to match the direction that is shown in Figs. B.1, B.2, and B.3. Therefore, the angle θ needs to satisfy the relationship $0\ ^{o}F \leq \theta < +90\ ^{o}F$. Also, the pile-skew angle, θ_r, of the abutment backwall piles needs to satisfy the relationship $0\ ^{o}F \leq \theta_r < +90\ ^{o}F$, regardless of the direction of the skew angle for

those piles in the actual bridge. The orientation for the sidewall piles that is used by the program has the web of the HP-shaped pile parallel to the transverse direction of the bridge. Therefore, the pile-skew angle for the sidewall piles is preset in the program Transmove to 0 deg. The orientation of the sidewall piles can not be changed by the user of the program. The abutment wingwalls or combined sidewall and wingwalls are assumed to be parallel to the longitudinal direction of the bridge. Therefore, a bridge with flared wingwalls can not be analyzed by the program Transmove. The piles that support the abutment backwall are assumed to be evenly distributed along the length of the backwall with one pile located at each end to the backwall. The pile(s) for the abutment sidewalls are assumed to be located at the mid-length of the common sidewall and wingwalls. Other pile locations can not be used with the program Transmove. Since the length ℓ is not part of the input data, the program Transmove sets the length ℓ equal to one-half of the bridge length, L.

To predict the maximum transverse displacement, $dt_{max,}$ for an integral abutment, the program Transmove was written to initially assume that the average temperature of a bridge superstructure is equal to that temperature which occurs on the coldest day. Therefore, the bridge is assumed to be at its maximum contracted position and only bridge expansion will occur for a change in the average temperature for the bridge. In the program algorithm, the temperature is gradually increased by 1 ^{o}F temperature increments until the total temperature change, T, is equal to 300 ^{o}F. Figure B.6 shows two displacement paths for a point on an integral abutment, when incremental increases occur in the temperature of a bridge superstructure. The solid line in the figure represents the displacement path for a point on an integral abutment over many cycles

of bridge expansion and contraction, and the dashed line in the figure represents the displacement path for that same point which is predicted by the program Transmove. Even though the two displacement paths are different, the resulting displacements dt_{max} that are associated with either displacement path will be the same.

The temperature-induced change in the length $d\ell$, which is predicted by Eq. B.5, is based on the minimally conservative assumption that free expansion of a bridge superstructure is essentially the same as the restrained expansion of an actual bridge. Restraint to bridge expansion is provided by the soil backfill behind the abutments, and the abutment backwall and sidewall piles. The horizontal stiffness of the soil that is against the abutment backwall and wingwalls or common wingwall and sidewalls is modeled by an elastic-plastic, displacement-resistance relationship. The elastic stiffness for the soil is based on the slope of a secant line that was drawn on the graph for the passive-soil-pressure coefficient, k, verses the horizontal-displacement parameter, /h, for medium-dense sand that is shown in Fig. 5.10b. This non-dimensionalized slope for the horizontal stiffness of the soil is equal to 450. The full-passive-soil-pressure coefficient, k_p, was set equal to 4.0 to correspond with full-passive-soil pressure for medium-dense sand, as shown in that same figure. Other horizontal stiffness and full-passive-soil-pressure coefficients can not be used with the program Transmove, unless the program code is change in the portion of the program that can be accessed by selecting the page icon “Program” located at the bottom of the Excel window.

B.7. Program execution

The following steps are used to execute the program Transmove:

Step 1: Select on the “Click here for instruction” button to read information about the program Transmove

Step 2: Enter the bridge length, L; bridge width, W; soil embankment height behind the abutment backwall, h_{abut}; soil embankment height along Sidewall and Wingwall 1, h_1; length of Sidewall and Wingwall 1, P_{1w}; bridge-skew angle, 2; pile-skew angle 2$_r$; number of backwall piles, N_{pa}, number of piles, N_{p1}, for each sidewall; modulus of elasticity, E, and yield stress, F_y, for the piles; strong axis (x-axis) moment of inertia, I_x, and plastic-section modulus, Z_x, and weak axis (y-axis) moment of inertia, I_y, and plastic-section modulus, Z_y, of the pile cross section; equivalent-cantilever lengths, L_{ehx} and L_{ehy}, of a pile for x-axis bending and y-axis bending, respectively, that are based on the horizontal-stiffness equivalency; unit-weight of the soil, γ; angle-of-internal friction, ϕ, of the soil; soil-to-abutment, surface-friction angle, δ; effective coefficient of thermal expansion and contraction, α_e, of the bridge superstructure in the empty cells of the “User Interface”. Use the proper units that are shown next to the variable.

Step 3: Select on the “Analyze” icon. After the program has completed the analysis of the bridge, the maximum transverse displacement for the integral abutment will appear in the box to the right of the label “dt_{max}”.

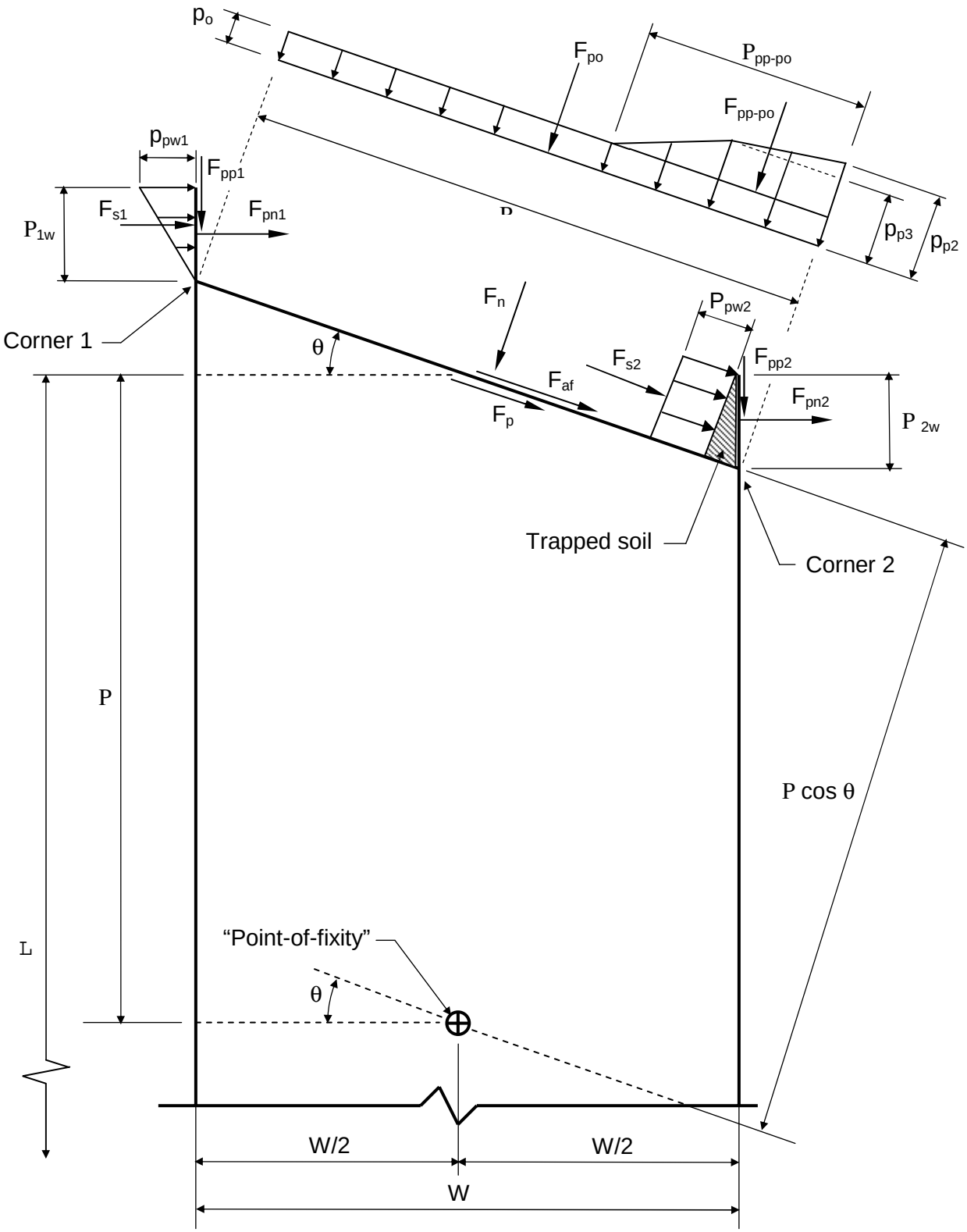

Figure B.1. Forces on an integral abutment for a skewed bridge due to thermal elongation and rigid-body rotation of the bridge superstructure (adapted from Oesterle et al., 1999)

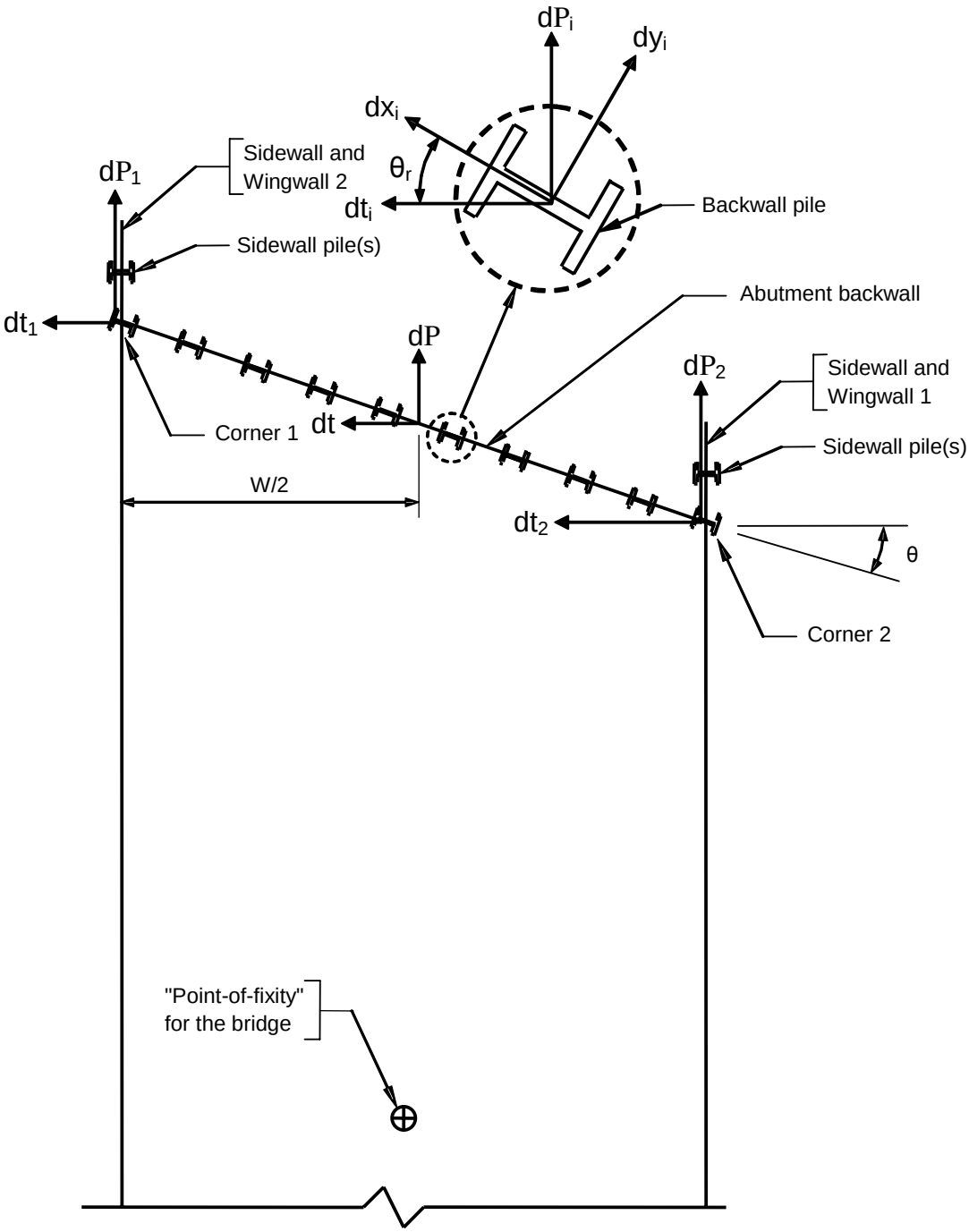

Figure B.2. Positive displacements for an abutment in the program Transmove

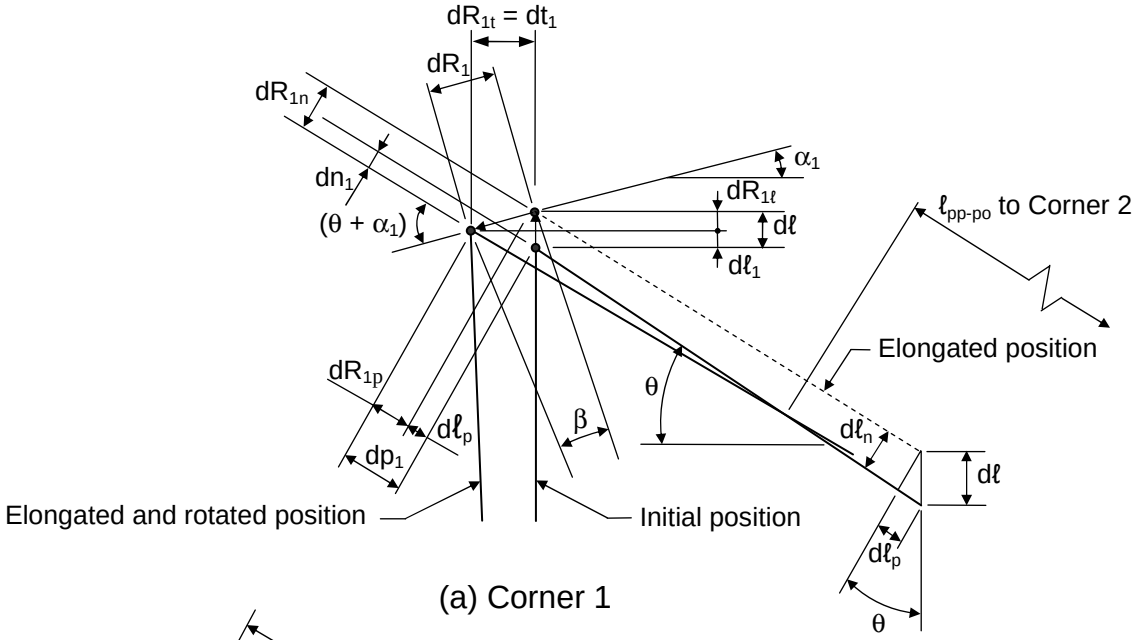

(a) Corner 1

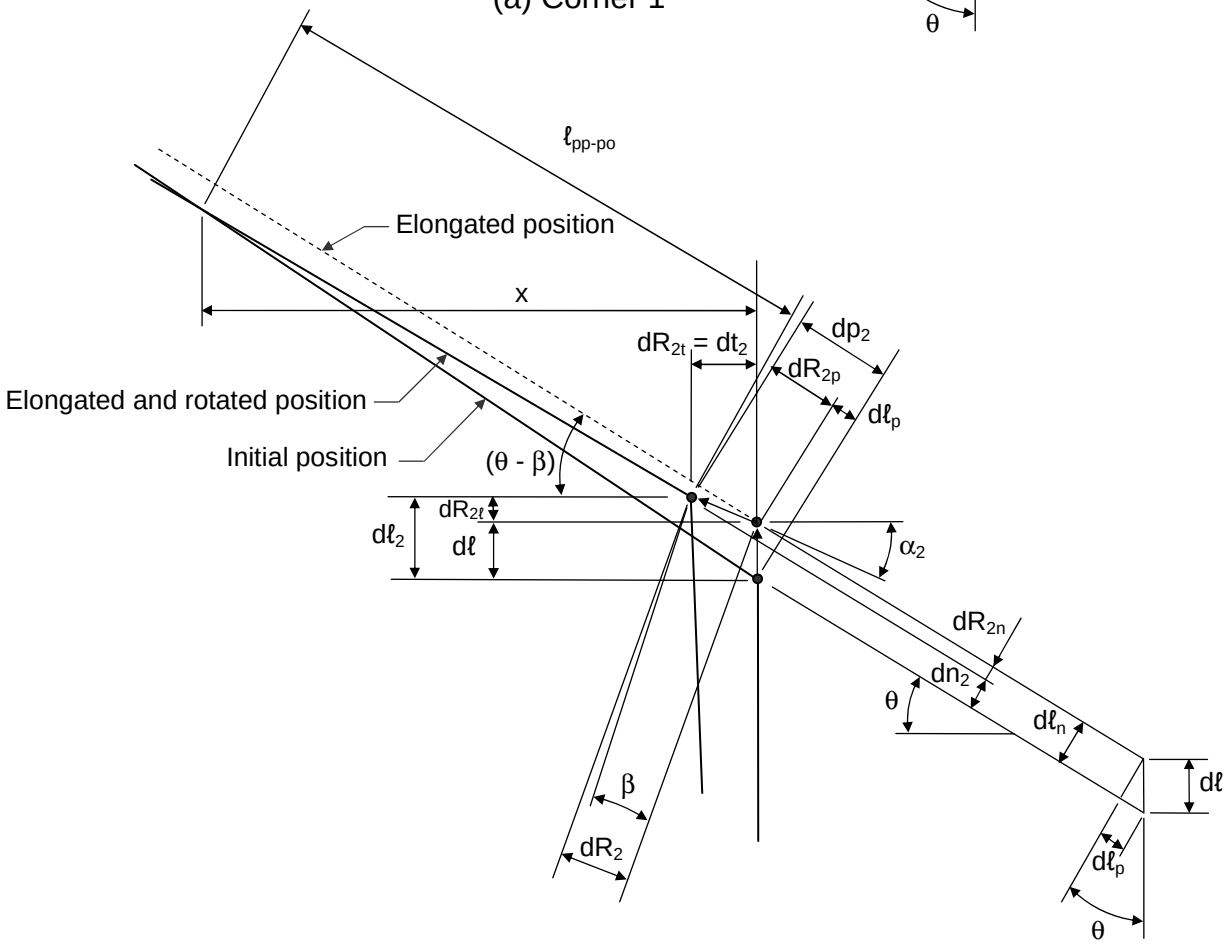

(a) Corner 2

Figure B.3. Displacements at the abutment corners (Adapted from Oesterle, et al. (1999)

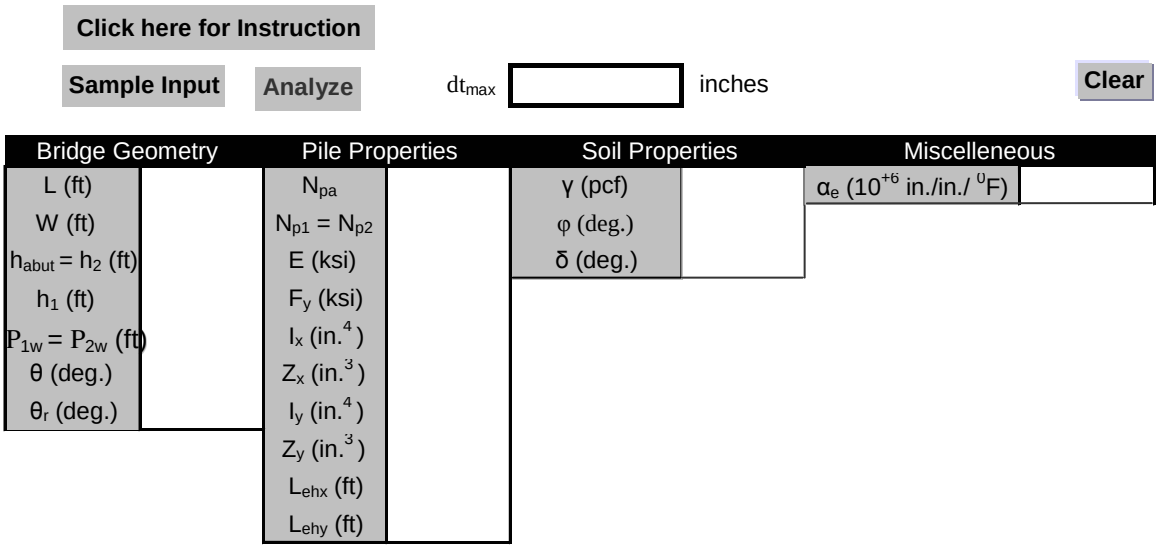

Figure B.4. User-interface for the Transmove software

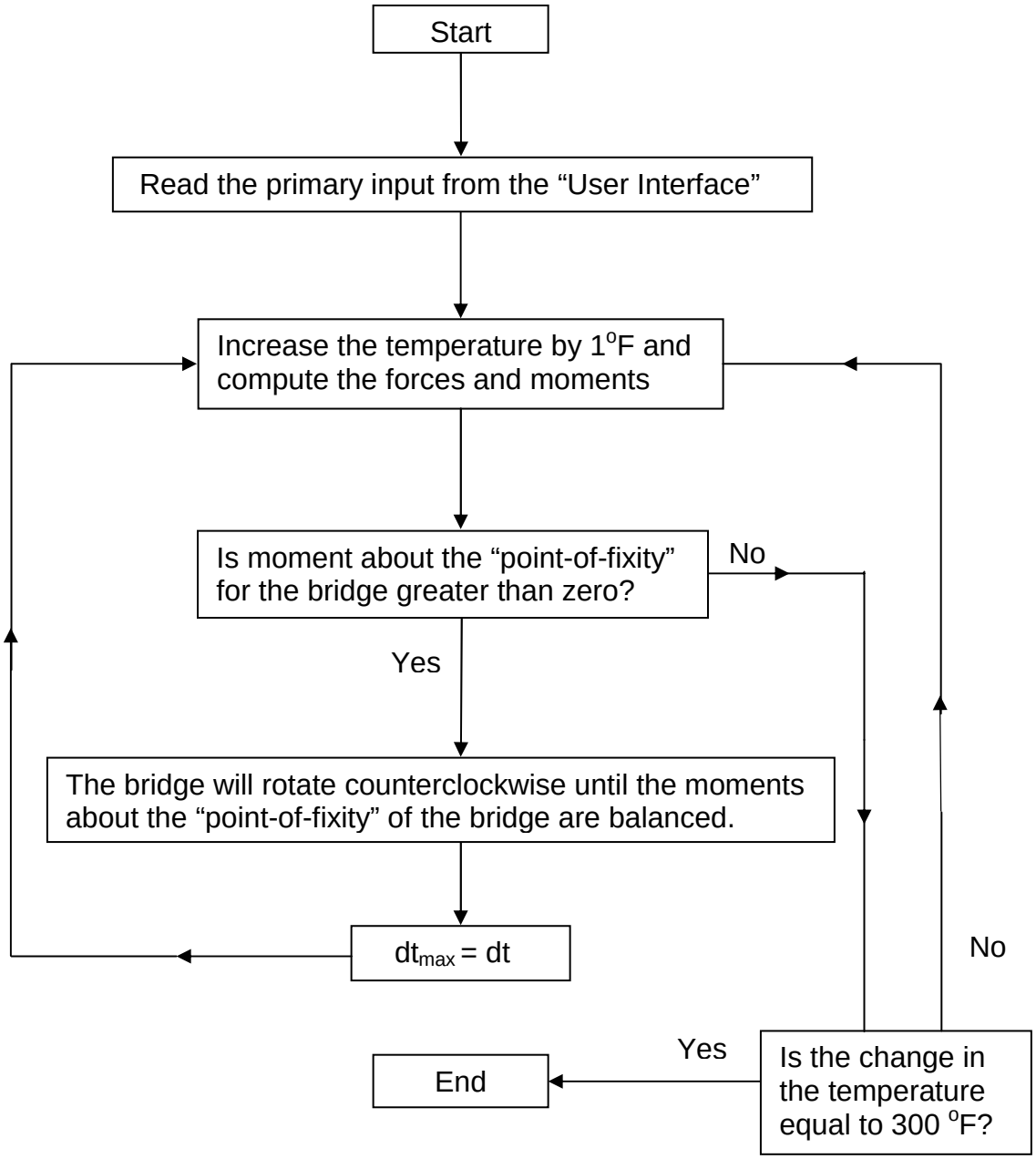

Figure B.5. Flowchart for the algorithm of the program Transmove

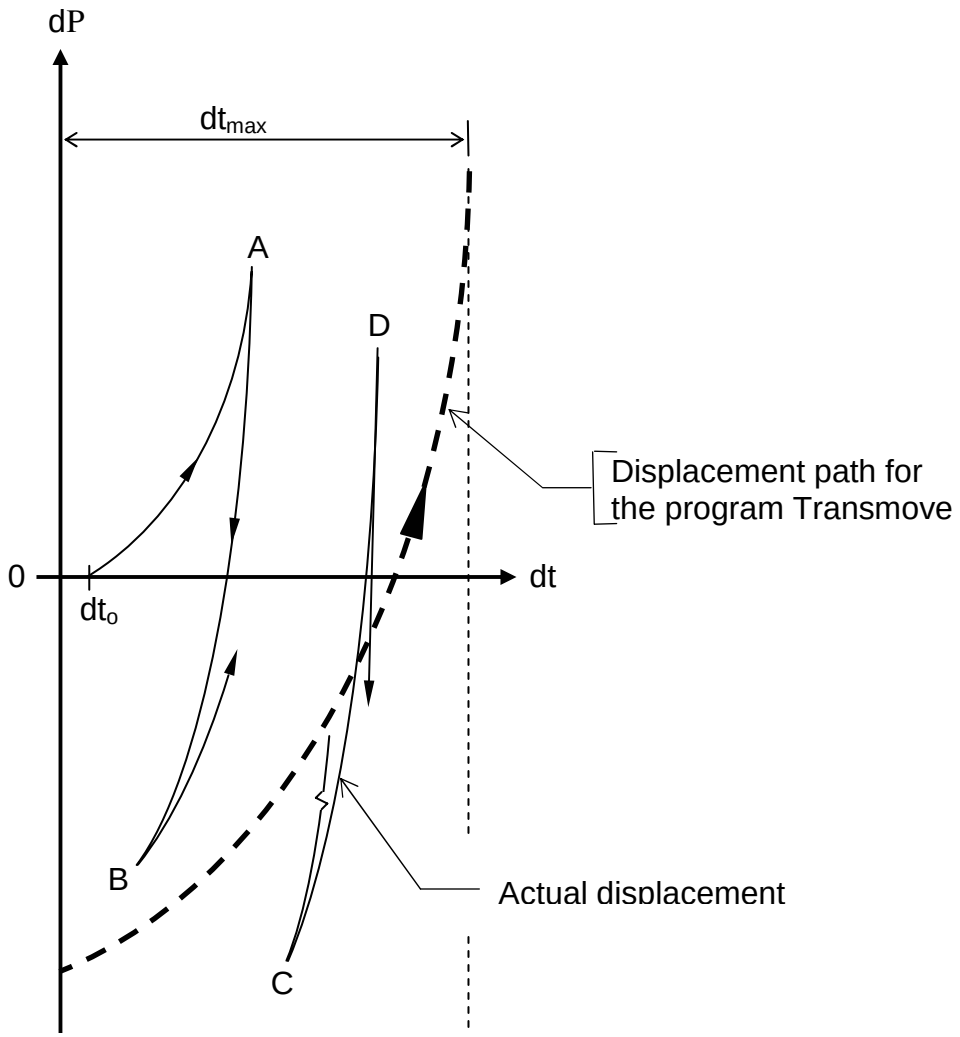

Figure B.6. Displacement paths in the horizontal plane

Table B.1. Soil and pile forces on an integral abutment

Force	Point-of-application	Eccentricity from the "point-of-fixity"	Positive direction for force	Moment direction
F_{af}	Centroid of the resultant soil-pressure that acts on the backwall	$(\ell + d\ell)\cos\theta$		clockwise
F_{pn1}	Mid-length of Sidewall and Wingwall 1	$\ell + d\ell + \frac{W}{2}\tan\theta + \frac{\ell_{1w}}{2}$	→	clockwise
F_{pp1}	Mid-length of Sidewall and Wingwall 1	$\frac{W}{2}$	↓	counter-clockwise
F_{pn2}	Mid-length of Sidewall and Wingwall 2	$\ell + d\ell - \frac{W}{2}\tan\theta + \frac{\ell_{2w}}{2}$	→	clockwise
F_{pp2}	Mid-length of Sidewall and Wingwall 2	$\frac{W}{2}$	↓	clockwise
F_n	Centroid for the horizontal resistance for the N_{pa} piles	for each pile: $d_{c2i} - \frac{W}{4} + (\ell + d\ell)\sin\theta$		counter-clockwise
F_p	Centroid for the horizontal resistance for the N_{pa} piles	$(\ell + d\ell)\cos\theta$		clockwise
F_{po}	Mid-length of the abutment backwall	$\ell \sin\theta$		counter-clockwise
$F_{pp\text{-}po}$	Centroid for the net-passive-soil-pressure distribution along the length $P_{pp\text{-}po}$	$\ell\sin\theta - \frac{W}{4} + \left(\frac{\ell_{pp-po}}{24}\right)\left(\frac{5k_{n1} - 12k_o + 6k_{n3} + k_{n2}}{\left(\frac{k_{n1} + 2k_{n3} + k_{n2}}{4}\right) - k_o}\right)$		counter-clockwise
F_{s1}	Centroid of the triangular, passive-soil-pressure distribution on Sidewall and Wingwall 1	$\ell + d\ell + \frac{W}{2}\tan\theta + \frac{2\ell_{1w}}{3}$	→	clockwise
F_{s2}	Centroid of the rectangular, passive-soil-pressure distribution on Sidewall and Wingwall 2	$\ell + d\ell - \frac{W}{2}\tan\theta + \frac{2\ell_{2w}}{3}$		clockwise